frontiers | Research Topics

Bioactive agents for functionalization of biomaterials for precise tissue engineering

Edited by
Gang Wu, Rui Guo, Jenneke Klein-Nulend and Kaili Lin

Published in
Frontiers in Bioengineering and Biotechnology

FRONTIERS EBOOK COPYRIGHT STATEMENT

The copyright in the text of individual articles in this ebook is the property of their respective authors or their respective institutions or funders. The copyright in graphics and images within each article may be subject to copyright of other parties. In both cases this is subject to a license granted to Frontiers.

The compilation of articles constituting this ebook is the property of Frontiers.

Each article within this ebook, and the ebook itself, are published under the most recent version of the Creative Commons CC-BY licence. The version current at the date of publication of this ebook is CC-BY 4.0. If the CC-BY licence is updated, the licence granted by Frontiers is automatically updated to the new version.

When exercising any right under the CC-BY licence, Frontiers must be attributed as the original publisher of the article or ebook, as applicable.

Authors have the responsibility of ensuring that any graphics or other materials which are the property of others may be included in the CC-BY licence, but this should be checked before relying on the CC-BY licence to reproduce those materials. Any copyright notices relating to those materials must be complied with.

Copyright and source acknowledgement notices may not be removed and must be displayed in any copy, derivative work or partial copy which includes the elements in question.

All copyright, and all rights therein, are protected by national and international copyright laws. The above represents a summary only. For further information please read Frontiers' Conditions for Website Use and Copyright Statement, and the applicable CC-BY licence.

ISSN 1664-8714
ISBN 978-2-83251-289-0
DOI 10.3389/978-2-83251-289-0

About Frontiers

Frontiers is more than just an open access publisher of scholarly articles: it is a pioneering approach to the world of academia, radically improving the way scholarly research is managed. The grand vision of Frontiers is a world where all people have an equal opportunity to seek, share and generate knowledge. Frontiers provides immediate and permanent online open access to all its publications, but this alone is not enough to realize our grand goals.

Frontiers journal series

The Frontiers journal series is a multi-tier and interdisciplinary set of open-access, online journals, promising a paradigm shift from the current review, selection and dissemination processes in academic publishing. All Frontiers journals are driven by researchers for researchers; therefore, they constitute a service to the scholarly community. At the same time, the *Frontiers journal series* operates on a revolutionary invention, the tiered publishing system, initially addressing specific communities of scholars, and gradually climbing up to broader public understanding, thus serving the interests of the lay society, too.

Dedication to quality

Each Frontiers article is a landmark of the highest quality, thanks to genuinely collaborative interactions between authors and review editors, who include some of the world's best academicians. Research must be certified by peers before entering a stream of knowledge that may eventually reach the public - and shape society; therefore, Frontiers only applies the most rigorous and unbiased reviews. Frontiers revolutionizes research publishing by freely delivering the most outstanding research, evaluated with no bias from both the academic and social point of view. By applying the most advanced information technologies, Frontiers is catapulting scholarly publishing into a new generation.

What are Frontiers Research Topics?

Frontiers Research Topics are very popular trademarks of the *Frontiers journals series*: they are collections of at least ten articles, all centered on a particular subject. With their unique mix of varied contributions from Original Research to Review Articles, Frontiers Research Topics unify the most influential researchers, the latest key findings and historical advances in a hot research area.

Find out more on how to host your own Frontiers Research Topic or contribute to one as an author by contacting the Frontiers editorial office: frontiersin.org/about/contact

Bioactive agents for functionalization of biomaterials for precise tissue engineering

Topic editors

Gang Wu — Academic Centre for Dentistry Amsterdam, VU Amsterdam, Netherlands

Rui Guo — Jinan University, China

Jenneke Klein-Nulend — University of Amsterdam and Vrije Universiteit Amsterdam, Amsterdam Movement Sciences, Netherlands

Kaili Lin — Shanghai Jiao Tong University, China

Citation

Wu, G., Guo, R., Klein-Nulend, J., Lin, K., eds. (2023). *Bioactive agents for functionalization of biomaterials for precise tissue engineering*. Lausanne: Frontiers Media SA. doi: 10.3389/978-2-83251-289-0

Table of contents

06 Editorial: Bioactive agents for functionalization of biomaterials for precise tissue engineering
Gang Wu

08 A Multifunctional AIE Nanoprobe as a Drug Delivery Bioimaging and Cancer Treatment System
Keqi Hu, Daquan Zhou, Linlin Rao, Peng Wang, Chunxiang Xiang and Feng Chen

22 Modifying a 3D-Printed Ti6Al4V Implant with Polydopamine Coating to Improve BMSCs Growth, Osteogenic Differentiation, and *In Situ* Osseointegration *In Vivo*
Hui Wang, Changyong Yuan, Kaili Lin, Rui Zhu and Shilei Zhang

31 Enhanced Spontaneous Antibacterial Activity of δ-MnO_2 by Alkali Metals Doping
Yali Yan, Ning Jiang, Xin Liu, Jie Pan, Mai Li, Chunrui Wang, Pedro H. C. Camargo and Jiale Wang

42 Macrophage-Derived Exosomes Promote Bone Mesenchymal Stem Cells Towards Osteoblastic Fate Through microRNA-21a-5p
Kun Liu, Xin Luo, Zhao-Yong Lv, Yu-Jue Zhang, Zhen Meng, Jun Li, Chun-Xiu Meng, Hui-Fen Qiang, Cai-Yao Hou, Lei Hou, Feng-Zhen Liu and Bin Zhang

54 Advancement of Gallium and Gallium-Based Compounds as Antimicrobial Agents
Fupeng Li, Fengxiang Liu, Kai Huang and Shengbing Yang

69 Photothermal 2D Nanosheets Combined With Astragaloside IV for Antibacterial Properties and Promoting Angiogenesis to Treat Infected Wounds
Lichang Liu, Wenfeng Wang, Weihong Hong, Yuyan Jin, Lichun Wang, Sujun Liu, Ailin Wang and Xusheng Liu

82 Traditional Chinese Medicine Compound-Loaded Materials in Bone Regeneration
Guiwen Shi, Chaohua Yang, Qing Wang, Song Wang, Gaoju Wang, Rongguang Ao and Dejian Li

102 Platelet-Activating Biominerals Enhanced Injectable Hydrogels With Superior Bioactivity for Bone Regeneration
Xin Chen, Jiajun Yan, Yingying Jiang, Yunshan Fan, Zhengran Ying, Shuo Tan, Zhi Zhou, Junjian Liu, Feng Chen and Shisheng He

113 Adaptive Gelatin Microspheres Enhanced Stem Cell Delivery and Integration With Diabetic Wounds to Activate Skin Tissue Regeneration
Ming Shi, Yunfen Gao, Lim Lee, Ting Song, Jianhua Zhou, Ling Yan and Yan Li

128 β-Cyclodextrin and Oligoarginine Peptide-Based Dendrimer-Entrapped Gold Nanoparticles for Improving Drug Delivery to the Inner Ear
Jia Luo, XueXin Lin, LiLing Li, JingQian Tan and Peng Li

144 Advances in Regenerative Sports Medicine Research
Liren Wang, Jia Jiang, Hai Lin, Tonghe Zhu, Jiangyu Cai, Wei Su, Jiebo Chen, Junjie Xu, Yamin Li, Jing Wang, Kai Zhang and Jinzhong Zhao

165 Approaches to Biofunctionalize Polyetheretherketone for Antibacterial: A Review
Yihan Wang, Shutao Zhang, Bin'en Nie, Xinhua Qu and Bing Yue

180 The Osteoinductivity of Calcium Phosphate-Based Biomaterials: A Tight Interaction With Bone Healing
Yuchen Zhang, Tianyu Shu, Silin Wang, Zhongbo Liu, Yilong Cheng, Ang Li and Dandan Pei

189 Treatment of Acute Wounds With Recombinant Human-Like Collagen and Recombinant Human-Like Fibronectin in C57BL/6 Mice Individually or in Combination
Yunqing Dong, Weidong Zhu, Xiaoxuan Lei, Xin Luo, Qi Xiang, Xuanru Zhu, Qiao Pan, Panshi Jin and Biao Cheng

203 Biomimetic Design and Fabrication of Sericin-Hydroxyapatite Based Membranes With Osteogenic Activity for Periodontal Tissue Regeneration
Piaoye Ming, Pengcheng Rao, Tianli Wu, Jianghua Yang, Shi Lu, Binbin Yang, Jingang Xiao and Gang Tao

219 Quercetin-Coating Promotes Osteogenic Differentiation, Osseointegration and Anti-Inflammatory Properties of Nano-Topographic Modificated 3D-Printed Ti6Al4V Implant
Nian Liu, Hui Wang, Zeyu Fu, Chuxi Zhang, Wenyu Hui, Jinyang Wu, Yong Zhang and Shilei Zhang

230 Stem Cells-Loaded 3D-Printed Scaffolds for the Reconstruction of Alveolar Cleft
Dongyuan Luo, Boying Chen and Yu Chen

239 A Modified Hyaluronic Acid–Based Dissolving Microneedle Loaded With Daphnetin Improved the Treatment of Psoriasis
Shiya Peng, Liuhanghang Cheng, Qian Wu, Yuanchao Li, Lei Ran, Wei Wang, Ke Huang, Rong Zhu, Sihong Xue, Chunli Zhou, Weidong Zhu, Biao Cheng, Xiaobing Fu and Rupeng Wang

253 Customized Barrier Membrane (Titanium Alloy, Poly Ether-Ether Ketone and Unsintered Hydroxyapatite/Poly-l-Lactide) for Guided Bone Regeneration
Yilin Shi, Jin Liu, Mi Du, Shengben Zhang, Yue Liu, Hu Yang, Ruiwen Shi, Yuanyuan Guo, Feng Song, Yajun Zhao and Jing Lan

270 Mesoporous Polydopamine Loaded Pirfenidone Target to Fibroblast Activation Protein for Pulmonary Fibrosis Therapy
Qi Fang, Shaoyu Liu, Jiangyu Cui, Ruiyue Zhao, Qian Han, Peng Hou, Youcai Li, Jie Lv, Xiaoyao Zhang, Qun Luo and Xinlu Wang

282 Real-Time MRI Monitoring of GelMA-Based Hydrogel-Loaded Kartogenin for *In Situ* Cartilage Regeneration
Hanyuan Zhang, Weijun Fang, Tingting Zhao, Huabing Zhang, Liang Gao, Jingya Li, Rujing Wang and Weiping Xu

294 Researching progress on bio-reactive electrogenic materials with electrophysiological activity for enhanced bone regeneration
Shaojie Dong, Yuwei Zhang, Yukun Mei, Yifei Zhang, Yaqi Hao, Beilei Liang, Weijiang Dong, Rui Zou and Lin Niu

309 Sulfated carboxymethyl cellulose and carboxymethyl κ-carrageenan immobilization on 3D-printed poly-ε-caprolactone scaffolds differentially promote pre-osteoblast proliferation and osteogenic activity
Sonia Abbasi-Ravasjani, Hadi Seddiqi, Ali Moghaddaszadeh, Mohammad-Ehsan Ghiasvand, Jianfeng Jin, Erfan Oliaei, Rommel Gaud Bacabac and Jenneke Klein-Nulend

330 Kappa-carrageenan-Functionalization of octacalcium phosphate-coated titanium Discs enhances pre-osteoblast behavior and osteogenic differentiation
Wei Cao, Jianfeng Jin, Gang Wu, Nathalie Bravenboer, Marco N. Helder, Engelbert A. J. M. Schulten, Rommel G. Bacabac, Janak L. Pathak and Jenneke Klein-Nulend

frontiers | Frontiers in Bioengineering and Biotechnology

TYPE Editorial
PUBLISHED 31 January 2023
DOI 10.3389/fbioe.2023.1141827

Check for updates

OPEN ACCESS

EDITED AND REVIEWED BY
Hasan Uludag,
University of Alberta, Canada

*CORRESPONDENCE
Gang Wu,
g.wu@acta.nl

SPECIALTY SECTION
This article was submitted to Biomaterials, a section of the journal Frontiers in Bioengineering and Biotechnology

RECEIVED 10 January 2023
ACCEPTED 18 January 2023
PUBLISHED 31 January 2023

CITATION
Wu G (2023), Editorial: Bioactive agents for functionalization of biomaterials for precise tissue engineering.
Front. Bioeng. Biotechnol. 11:1141827.
doi: 10.3389/fbioe.2023.1141827

COPYRIGHT
© 2023 Wu. This is an open-access article distributed under the terms of the Creative Commons Attribution License (CC BY). The use, distribution or reproduction in other forums is permitted, provided the original author(s) and the copyright owner(s) are credited and that the original publication in this journal is cited, in accordance with accepted academic practice. No use, distribution or reproduction is permitted which does not comply with these terms.

Editorial: Bioactive agents for functionalization of biomaterials for precise tissue engineering

Gang Wu*

Department of Oral Cell Biology, Academic Centre for Dentistry Amsterdam (ACTA), University of Amsterdam (UvA) and Vrije Universiteit Amsterdam (VU), Amsterdam, Netherlands

KEYWORDS

bioactive agents, precise tissue engineering, bone regeneration, skin disease, antibacterial, biofunctionalisation

Editorial on the Research Topic
Bioactive agents for functionalization of biomaterials for precise tissue engineering

Tissue engineering is a multidisciplinary technology to improve or replace biological tissues. Biomaterial scaffolds are an indispensable element in tissue engineering. A large variety of biomaterial scaffolds are widely adopted to facilitate the precise engineering of various tissues. The biomaterial scaffolds can be naturally derived or synthesized organic, inorganic, metallic, and hybrid materials. To facilitate precise tissue engineering, biomaterials can be further bio-functionalized by various bioactive agents. Bioactive agents can be naturally derived or synthetic cytokines, growth factors, extracellular vesicles, small-molecules, and peptides with one or multiple functions, such as osteoinduction, osteoconduction, anti-inflammation, anti-cancer, and anti-osteoclast. The methods to integrate bioactive agents into implants may include internal incorporation, electrostatic deposition, surface modification and entrapment.

To provide a scientific forum for the researchers in this field, we started this Research Topic—Bioactive agents for functionalization of biomaterials for precise tissue engineering in August 2021. Until now, 1 mini review, 6 reviews and 17 original research articles have been published with 191 authors involved. We hereby sincerely thank the excellent contributions of all these researchers to this successful Research Topic.

Similar as in our previous Research Topic (Advanced Biomaterials and Systems Releasing Bioactive Agents for Precise Tissue Regeneration), bone regeneration is still the hottest topic with 13 articles (1 mini review, 3 review and 9 original researches) published. One mini-review and one review summarized the key advances of two major bone-repairing components in clinic: calcium phosphate and barrier membrane. To facilitate pro-osteogenic functionalization of different biomaterials, various types of bioactive agents have been introduced and investigated in this Research Topic. The most investigated type in this Research Topic is plant-derived bioactive agents, such as k-carrageenan, sulfated carboxymethyl cellulose and quercetin, as well as animal-derived dopamine and sericin. Chen et al. reported platelet-activating biominerals enhanced injectable hydrogels with superior bioactivity for bone regeneration. Furthermore, one review summarized the application of traditional chinese medicine compound in functionalizing biomaterials for bone regeneration. Two research articles applied stem cells and M1 macrophage-derived exosomes as bioactive elements to promote osteogenic differentiation. Apart from these bioactive agents, bone regeneration may also be achieved by applying bio-reactive electrogenesis materials with electrophysical activity.

In additional to bone tissue, cartilage regeneration was also achieved using Kartogenin-loaded GelMA hydrogel. Wang et al. reviewed the advances in regenerative sports medicine research.

Apart from bone and cartilage regeneration, three research articles discussed novel biofunctionalized biomaterials to treat skin diseases. Dong et al. reported the application of recombinant human-like collagen and fibronectin in treating acute skin wounds. Shi et al. applied adaptive gelatin microspheres as a stem cell delivery system to activate skin tissue regeneration in diabetic wounds. Peng et al. applied a daphnetin-loaded, modified hyaluronic acid-based dissolving microneedle to improve the treatment of psoriasis.

In addition to reports in the development of novel regenerative materials, a series of studies have focused on antibacterial functionalization of biomaterials. One review summarized the developments of the approaches to functionalize polyetheretherketone with antibacterial properties. Another review focused on the advancement of gallium and gallium-based compounds as antimicrobial agents. Liu et al. applied a novel astragaloside IV-loaded photothermal 2D nanosheet to treat infected wounds with its antibacterial and angiogenic properties. And Yan et al. presented a study on enhancing spontaneous antibacterial activity of δ-MnO2 by alkali Metals doping.

Apart from the above-mentioned Research Topic, original research articles have been presented to develop novel functionalized biomaterials for the treatment of pulmonary fibrosis, inner ear, and cancer. For example, Fang et al., developed a antifibrosis drug pirfenidone-functionalized mesoporous polydopamine for the treatment of pulmonary fibrosis. Interestingly, the authors also introduced an inhibitor of fibroblast activation protein, a 97 kDa type II transmembrane protein only overexpressed on the membrane of aberrantly activated fibroblast, onto the surface of polydopamine to facilitate the targeting to the lesion. Similarly, Hu et al. combined PLA polymer, malignant tumor-targeting T7 peptide, aggregation-induced emission-based fluorophore (tetrastyrene) and anti-tumor drug (Temozolomide) to develop a novel nanoprobe to target, bioimage and treat glioma. Luo et al. adopted β-cyclodextrin and oligoarginine peptide (Arg8)-modified dendrimer-entrapped gold nanoparticle as a drug delivery system to inner ear. All these studies showed a multi-functionalization pattern.

In summary, this Research Topic covers many recent advances in bioactive agents-functionalized biomaterials to treat various diseases, which contribute significantly to the progress of precise tissue regeneration.

Author contributions

All authors listed have made a substantial, direct, and intellectual contribution to the work and approved it for publication.

Conflict of interest

The authors declare that the research was conducted in the absence of any commercial or financial relationships that could be construed as a potential conflict of interest.

Publisher's note

All claims expressed in this article are solely those of the authors and do not necessarily represent those of their affiliated organizations, or those of the publisher, the editors and the reviewers. Any product that may be evaluated in this article, or claim that may be made by its manufacturer, is not guaranteed or endorsed by the publisher.

frontiers in Bioengineering and Biotechnology

ORIGINAL RESEARCH
published: 08 November 2021
doi: 10.3389/fbioe.2021.766470

A Multifunctional AIE Nanoprobe as a Drug Delivery Bioimaging and Cancer Treatment System

Keqi Hu[1†], Daquan Zhou[1†], Linlin Rao[1], Peng Wang[1], Chunxiang Xiang[2] and Feng Chen[1*]*

[1]*Department of Neurosurgery, Xiangyang Central Hospital, Affiliated Hospital of Hubei University of Arts and Science, Xiangyang, China,* [2]*Department of Pathology, Xiangyang Central Hospital, Affiliated Hospital of Hubei University of Arts and Science, Xiangyang, China*

Of all malignant brain tumors, glioma is the deadliest and most common, with a poor prognosis. Drug therapy is considered as a promising way to stop the progression of disease and even cure tumors. However, the presence of blood brain barrier (BBB) and blood tumor barrier (BTB) limits the delivery of these therapeutic genes. In this work, an intelligent cell imaging and cancer therapy drug delivery system targeting the blood-brain barrier and the highly expressed transferrin receptors (TfR) in gliomas has been successfully constructed, and an amphiphilic polymer (PLA-PEG-T7/TPE) with aggregation-induced emission (AIE) properties has been designed and successfully synthesized. PLA-PEG-T7/TPE self-assembled polymer micelles showed significant AIE effect in aqueous solution with good biocompatibility. Therefore, it can be used for potential biological imaging applications. In addition, drug-carrying micelles showed typical behavior of regulating drug release. Inhibition of cell proliferation *in vitro* showed that the drug-loaded micelles had dose-dependent cytotoxicity to LN229 cells. In the *in vivo* anti-tumor experiment, PLA-PEG-T7/TPE/TMZ had the best therapeutic effect. These results indicated that T7 functionalized PLA-PEG was a promising platform for nasopharyngeal cancer drug combination therapy.

Keywords: drug delivery, aggregation-induced emission, imaging, PLA-PEG, T7 peptide, cancer treatment

OPEN ACCESS

Edited by:
Kaili Lin,
Shanghai Jiao Tong University, China

Reviewed by:
Zhong Cao,
Sun Yat-sen University, China
Aristeidis Papagiannopoulos,
National Hellenic Research Foundation, Greece

****Correspondence:***
Chunxiang Xiang
chunxianghuanle@163.com
Feng Chen
chenfenghuanle@163.com

[†]These authors have contributed equally to this work

Specialty section:
This article was submitted to Biomaterials, a section of the journal Frontiers in Bioengineering and Biotechnology

Received: *29 August 2021*
Accepted: *13 October 2021*
Published: *08 November 2021*

Citation:
Hu K, Zhou D, Rao L, Wang P, Xiang C and Chen F (2021) A Multifunctional AIE Nanoprobe as a Drug Delivery Bioimaging and Cancer Treatment System. Front. Bioeng. Biotechnol. 9:766470. doi: 10.3389/fbioe.2021.766470

INTRODUCTION

Glioblastoma (GBM) is the most common primary brain tumor of the central nervous system with a high mortality rate, with a 5-year relative survival rate of 4.5% after diagnosis in the United States (Stupp et al., 2017; Ladomersky et al., 2019). Chemotherapy is one of the most commonly used methods to treat glioma (Teresa et al., 2018; Hanna et al., 2020). Unfortunately, many chemotherapeutic drugs often cause serious side effects because they do not distinguish between cancer cells and healthy cells. To overcome this problem, nanoscale drug delivery systems have been developed to enhance the anticancer activity of these chemotherapeutic drugs and reduce side effects (Nuk et al., 2020; Griffith et al., 2021; Malekjani and Jafari, 2021).

At present, most drug delivery systems can only deliver drugs to cancer cells, and the distribution and release of drug delivery systems in cancer cells cannot be monitored. In order to further develop and optimize drug delivery systems, a multifunctional nanomedicine platform for imaging diagnosis and therapy is needed (Zhao et al., 2017; Wang et al., 2020). The usual approach is to integrate fluorescent dyes into the drug delivery system. However, most conventional fluorescent dyes are toxic, and due to their aggregation-induced quenching (ACQ) effect, the fluorescence quenching in

the aggregation state greatly limits their applications in biomedical applications (Gang et al., 2009; Su et al., 2020). Therefore, it is necessary to develop new fluorescent molecules to avoid ACQ effect. Recently, Tang and others have developed a new class of fluorophores with aggregation-induced emission (AIE) properties. Unlike ACQ-influenced conventional fluorophores, AIE-based fluorophores, such as tetrastyrene (TPE), exhibit high emission efficiency in the polymerized state (Long et al., 2014; Gao and Tang, 2017; Lin et al., 2017). Using these unique AIE characteristics, many fluorescent probes with AIE characteristics have been extensively studied by Liu et al. (Gao et al., 2017; Mao et al., 2020; Shi et al., 2020; Liu et al., 2021). These probes have strong fluorescence properties and excellent cell imaging capabilities. Therefore, the development of fluorescence delivery systems based on AIE dyes is considered to be a promising strategy for simultaneous imaging and therapy.

Another obstacle is the concentration of chemotherapies in gliomas, which means that drug delivery systems must cross different biological barriers, particularly the blood brain barrier (BBB) and blood tumor barrier (BTB) of gliomas (Fortin, 2012). It has been reported that brain capillary endothelial cells and many malignant tumor cells have overexpression of transferrin receptor (TfR), which is significantly higher than that of other normal cells (Yoon et al., 2017; Arumov et al., 2020; Wan et al., 2020). Since high concentrations of endogenous transferrin may be a competitive inhibition of the transferrin modified gene delivery system (Lee et al., 2010), the peptide T7 targeting the TfR (His-Ala-Ile-Tyr-Pro-Arg-His) was found to have a similar affinity with transferrin (Han et al., 2010; Kuang et al., 2013; Tang et al., 2019). Moreover, T7 peptide is a small molecule of peptide. It has the advantages of easy chemical synthesis, good stability, and little steric hindrance, and it has good clinical application potential. Therefore, we selected T7 peptides to design gene delivery systems that cross the blood-brain barrier and target brain tumors.

In recent years, polymer micelles have been widely used in the field of medicine as a new delivery carrier due to their unique advantages (Liu et al., 2020; Wu et al., 2021). PLA was the most common biodegradable polymer because it was easy to be degraded and produces non-toxic degradation products which can be eliminated by metabolism (Wang et al., 2018; Shang et al., 2019).

In this study, a covalent bond of polyethylene glycol (PEG) was formed on the surface of PLA to modify T7, and PLA-PEG-T7 was obtained for loading temozolomide and tetrastyrene, as well as for cell imaging and drug delivery. The material can be self-assembled into micelles, in which the tetrastyrene core serves as the optical recognition code for cell imaging, and the biocompatible PEG serves as the micelle shell, with long blood circulation time. The tumor targeting effect of PLAA-PEG-T7 as a drug carrier was evaluated *in vitro* and *in vivo*. The intracellular transport of PLA-PEG-T7/TPE/TMZ NPs was systematically evaluated.

EXPERIMENTAL SECTION

Materials

All chemical reagents were purchased from commercial suppliers and can be used without further purification. PLA-PEG-NH_2 was purchased from Xi'an Ruixi Biotechnology Co., Ltd. Temozolomide and tetraphenylvinyl were purchased from Shanghai Aladdin Biochemical Technology Co., Ltd. (Shanghai, China). In addition, 1-ethyl-3 -(3-dimethylaminopropyl) carbodiimide hydrochloride and N-hydroxysuccinimide (EDC and NHS) were purchased from Macklin Biochemical Technology Co., Ltd. (Shanghai, China). Cell culture reagents included DMEM medium, fetal bovine serum, trypsin, penicillin-streptomycin, and phosphate buffer saline, available from Gibco BRL (Carlsbad, California, United States). Cell Counting Kit-8 (CCK-8) was purchased from Beyotime Institute of Biotechnology (Shanghai, China). Annexin V-PE Apoptosis Kit was purchased from Beckton, Dickinson and Inc. (United States). T7 peptide was synthesized by Sangon Bioengineering Co., Ltd. (Shanghai, China). LN229 (glioma cell line) was provided by Southern Medical University (Guangzhou, China).

Synthesis of PLA-PEG-T7

The coupling of PLA-PEG-NH_2 and T7 was achieved by amide reaction. Specifically, 8 mg of EDC and 10 mg of NHS were added to 3 ml of T7 solution and stirred for 4 h. Then, 20 mg of PLA-PEG-NH_2 was added dropwise to the above solution, and reacted at room temperature overnight. Finally, the co-polymer was precipitated with cold methanol for 12 h and washed out by same solvent and then lyophilized again to obtain pure PLA-PEG-T7.

Synthesis of PLA-PEG-T7/TMZ/TPE

PLA-PEG-T7/TMZ/TPE nanoparticles were prepared by double emulsion solvent evaporation method. First, 4 mg of TMZ was dissolved in HCl solution (200 μl, 0.1 M) to form aqueous phase. Then 10 mg of PLA-PEG-T7 and 3 mg of TPE were dissolved in 2 ml of dichloromethane (DCM) to form oil phase. The aqueous phase was added to the oil phase and the resulting mixture was emulsified with an ultrasonic processor for 120 s to form the initial emulsion. The emulsion was then dropped into 1% PVA (10 ml) solution and emulsified again. The homogeneous emulsion was stirred overnight at room temperature to devolatilize the DCM. The PLA-PEG-T7/TMZ/TPE nanoparticles were centrifuged at 13,000 × g for 20 min at 4°C and placed in water for subsequent use.

The loading amount of TMZ was characterized by measuring the UV-Vis absorption peak at 327 nm. The linear regression equation ($y = 0.0486x + 0.0493$, $R^2 = 0.998$) of TMZ was obtained through the standard curve.

Characterization

Chemical structure of PLA-PEG-NH_2 and PLA-PEG-T7 was characterized by ^1H NMR spectroscopy (300 MHz, Varian, United States) using Deuterated chloroform ($CDCl_3$) as the solvent. The shape, size, and morphology of the synthesized nanomaterials were studied with transmission electron microscopy (JEOL TEM-1210) at 120 kV and Zetasizer Nano ZS (Malvern) apparatus. Fourier transform infrared spectrum of all samples were collected in a PerkinElmer Spectrum 100 FT-IR spectrometer (PerkinElmer Inc., United States) under the

transmittance mode with KBr plates. Excitation and emission spectra of samples were recorded using a FLS920P Edinburgh Analytical Instrument. Confocal optical micrographs were analyzed by performing confocal laser scanning microscope (CLSM, Leica SP8, Nikon, Japan).

In Vitro Drug Release

Dialysis bag method was used to study the release of TMZ *in vitro*. Firstly, 1 ml of 6 mg/ml of PLA-PEG-T7/TMZ was placed in a dialysis bag (molecular weight cut off = 2000 Da). Then, the dialysis bag was placed in a 15 ml centrifuge tube with 3 ml PBS (pH = 6.5) as the release medium. The centrifuge tube was placed at 37°C and shaken at 100 rpm to simulate the release of TMZ *in vitro*. Then, 1 ml of the release solution was removed at regular intervals and 1 ml of fresh PBS was added to the centrifuge tube. The absorption value of the liquid at 329 nm, the concentration at the corresponding time point, and the cumulative release rate were calculated.

Cytotoxicity of PLA-PEG-T7

The cytotoxicity of PLA-PEG-T7 was measured on L929 cells using the CCK-8 assay. Briefly, the L929 cells (5×10^3 cells per well) were seeded in 96-well plates (Corning, United States) for 12 h. The cells were then incubated with fresh cell medium containing PLA-PEG-T7 with concentrations ranging from 0 to 320 μg/ml and incubated for 24 h. After treatment, cells were washed with PBS and added with fresh cell medium containing 10% CCK-8 to all wells. Finally, the absorbance at 450 nm was tested by a microplate reader (Thermo Scientific, United States). L929 cells incubated with RPMI 1640 medium were used as control groups.

T7 Targeting Ability Assay

Cellular uptake of PLA-PEG-T7/TPE complex with and without T7 functionalization was analyzed to confirm the targeting ability of T7. In detail, LN229 cells were seeded in 24-well plate with a density of 5×10^4 cells/well and incubated in a 37°C humidified incubator (5% CO_2) for 12 h. Then, PLA-PEG/TPE or PLA-PEG-T7/TPE complex was added to treat the cells and incubated for different time. After each interval (0.5, 1, 2, 4, and 6 h), cells in each group were washed by PBS, trypsinized, centrifuged, and resuspended in 200 μl PBS. Finally, samples were measured using flow cytometry and the corresponding fluorescent intensity was quantified by Flow Jo 7.6.1 software.

In Vitro BBB-Transport Efficiency

In order to test the *trans*-BBB efficiency of PLA-PEG-T7/TPE, an *in vitro* BBB model was established in a transwell cell culture system. The bEnd.3 cells (5×10^4 per insert) were seeded in the upper transwell and cultured for 7 days with a trans endothelial resistance (TEER) exceeded 200 ω·cm (Stupp et al., 2017). Finally, the following channels were detected by confocal microscope under the same optical conditions at different time points. For transport analysis, transfer the cross-well insert to a new 24-well plate containing 5×10^5 LN229 cells. PLA-PEG/TPE and PLA-PEG-T7/TPE nanoparticles were added to the transwell insert and left for 24 h. Then stain with phalloidin staining solution for 1 h. Observation of the co-stained fluorescence signal of TPE and phalloidin with confocal laser scanning microscope.

Endocytosis Pathway Analysis

For this study, LN229 cell culture was performed as described above. Referring to the method of selecting the dose of each inhibitor, the cells were precultured in DMEM containing 10 μg/ml chlorpromazine, 200 μM genistein, 200 nM wortmannin, or 5 μg/ml cytochalasin B. After 3 h of pretreatment, the culture medium was taken out, the PLA-PEG-T7/TPE complex containing inhibitor was added, and the culture was continued for 2 h. Cells treated with PBS or incubated at 4°C were set as controls. Next, the cells are trypsinized and centrifuged for flow cytometry detection. FlowJo software was used to analyze the average fluorescence of each group compared with untreated cells.

Inhibition Cell Proliferation *in Vitro*

Temozolomide (TMZ) was a commonly used anti-tumor drug, which has a strong toxic effect on cancer cells. In order to measure the effect of co-administration of PLA-PEG/TMZ/TPE on LN229 cells survival rate, CCK-8 assay was performed. Briefly, LN229 cells were planted into 96-well plate at a density of 1×10^4/cell. Next, 12 h after seeding, the cells were exposed to PLA-PEG/TMZ/TPE with drug concentrations for 24 h. Then, 100 μl of CCK-8 solution (10%) was added to each well and incubated at 37°C in 5% CO_2 atmosphere for 1 h. Next, absorbance of each sample was measured at 450 nm using a microplate reader.

Apoptosis Assay

LN229 cells were inoculated in 24-well plates with a density of 5×10^4 cells/well and cultured overnight in an incubator. The original medium was then replaced by complete medium containing PBS, TMZ, PLA-PEG-T7, and PLA-PEG-T7/TMZ/TPE and incubated for 24 h. After the experiment, the cells were washed with PBS and digested with trypsin, then the supernatant was removed by centrifugation, and the cells were resuspended in 200 μl binding buffer and stained for 15 min by adding 5 μL Annexin V-PE and 5 μl 7-AAD. The apoptosis of the cells in different treatment groups was analyzed by flow cytometry.

Cell Cycle Assay

In short, LN229 cells were cultured as described in the cell uptake test. Then, the cells were treated with various preparations (PBS, PLA-PEG-T7, TMZ, PLA-PEG-T7/TMZ). After 24 h, the cells were fixed with 70% ethanol. Before analysis, the fixed cells were stained with ribonuclease A and propidium iodide. Next, we analyzed the cells by flow cytometry and analyzed the cell cycle by cell cycle analysis software.

Scratch Healing Assay

LN229 cells were seeded in a 24-well plate at a density of 5×10^4 cells/well and cultured overnight. After culturing overnight, a line was created on the bottom using a 10 μL pipette tip. PLA-PEG-T7, PLA-PEG/TMZ, PLA-PEG-T7/TMZ suspended in serum-free DMEM were used to culture LN229 cells. Serum-free DMEM was used as control group. The scratch was photographed for

different time intervals (0, 12, and 24 h) using an inverted fluorescence microscope.

Biocompatibility Evaluation

Morphology of Red Blood Cells

Firstly, fresh whole blood was centrifuged at 1,000×g for 5 min, and the lower layer of red blood cells (RBC) were collected. Three concentrations of PLA-PEG-T7 (0.1, 0.2, and 0.5 mg/ml) were reconfigured by PBS, and PBS served as negative control group. Each sample was mixed with an appropriate amount of red blood cells and incubated for 1 h. The red blood cells were collected by centrifugation, washed with PBS, and then fixed by 4% paraformaldehyde for 1 h.

As for the SEM sample preparation, fixed erythrocytes were placed on glass slides and dehydrated with 70, 85, 95, and 100% ethanol in turn. The dehydration time was 10 min each time. After the treated samples were naturally air-dried, then sprayed with gold, and the morphologies of red blood cells were observed by scanning electron microscopy (SEM).

Hemolysis Assay *in Vitro*

PBS aqueous solution of PLA-PEG-T7 with different concentrations of 0.1, 0.2, and 0.5 mg/ml was prepared. Deionized water and PBS were used as positive and negative controls, respectively. Next, 4 ml of samples with different concentrations were put into a centrifuge tube, and 200 μl of 16% red blood cell suspension was added for co-incubation. The supernatants were collected by centrifugation at the preset time points (1, 3, 5, 8, 18, and 24 h) at 1,000×g for 5 min. The absorbance of each sample at 540 nm was measured by microplate analyzer, and the hemolysis rate was calculated by the following formula:

$$\text{Hemolysis rate } (\%) = (\text{A-C})/(\text{B-C}) \times 100\%$$

where A, B, and C represented the absorbance of the experimental group, the positive control group, and the negative control group respectively (three groups were parallel for each sample).

APTT and PT

In total, 270 μl of platelet lean plasma was mixed with 30 μl of PLA-PEG-T7 solutions of different concentrations (0.01, 0.1, 0.2, and 0.5 mg/ml in PBS) at room temperature, and the corresponding detection reagents were added. The activated partial thromboplastin time (APTT) and prothrombin time (PT) of each mixture were determined by automatic coagulation analysis instrument.

In Vivo Fluorescence Imaging

The animal experiment was carried out with the help of Jinan University and all animal experimental protocols have been approved by the Animal Protection and Use Committee of Jinan University. For evaluating the targeting ability of PLA-PEG-T7, tumor-bearing nude mice with a tumor size of about 100 mm^3 were selected and injected 100 μl of PLA-PEG-Cy5 complex and PLA-PEG-T7-Cy5 complex via tail vein. At different time intervals, the nude mice were subjected to fluorescence imaging using the small animal live imager (FX Pro Bruker). At 8 h after injection, the nude mice were sacrificed to take out hearts, livers, spleen, lungs, kidneys, and tumors, and then the main organs and tumor were imaged (excitation wavelength: 630 nm, emission wavelength: 700 nm) *ex vivo*.

Tumor Inhibition Assay

For the tumor suppression test, tumor-bearing mice were randomly divided into five treatment groups: PBS control group, PLA-PEG-T7, TMZ, PLA-PEG/TPE/TMZ, and PLA-PEG-T7/TPE/TMZ. Each group included three mice that were injected every 2 days. Tumor volume was measured with an electronic caliper and calculated as 1/2 × shortest diameter (Stupp et al., 2017) × longest diameter. At the same time, the body weight of the mice was recorded. After 10 treatments, the tumors were collected and weighed.

Histological Analysis

The collected tumors were immersed in tissue fixator for routine paraffin embedding and cut into tissue sections with a thickness of 4 μm. Then, the sections were stained with hematoxylin and eosin (H&E). For immunohistochemical analysis, the level of tumor apoptosis was evaluated by the terminal deoxynucleotidyl transferase deoxyuridine triphosphate nick end labeling (TUNEL) assay. In addition, the expression of Ki67 and CD31 in tumor sections were also detected.

In Vivo Biocompatibility Evaluation

Histological analysis: After the mice were euthanized, the heart, liver, spleen, lung, kidney, and other major organs were collected, immersed in paraformaldehyde fixative, embedded in conventional paraffin, and sliced into 4 μm thick tissue sections. Then the sections were stained with hematoxylin and eosin and imaged with a fluorescence microscope.

Blood chemistry assay: After 21 days of treatment, the mouse blood was collected and centrifuged at 3,000 rpm for 5 min to obtain the serum in the supernatant. Then, the kidneys (UREA, UA, and CREA), liver functions (AST, ALT, and ALB), blood glucose (GLU), Low Density Lipoprotein Cholesterol (LDL), and myocardial enzymes (LDH) were evaluated through blood parameters.

RESULTS AND DISCUSSION

Synthesis and Characterization of Products

Transferrin receptor (TfR) is highly expressed in brain capillaries. Targeting TfR has long represented an attractive way to penetrate the BBB (Ullman et al., 2020). Both PLA and PEG are FDA-approved biodegradable polymer materials that can be used in the human body and have good biocompatibility. In this study, PLA-PEG micelle was designed and grafted T7 peptide to target transferrin receptors at brain capillaries to penetrate BBB.

T7 was grafted on PLA-PEG micellar through amide reaction. **Figure 1A** showed the ^{1}H NMR spectra of PLA-PEG and PLA-PEG-T7. The chemical shift that occurred at 7.3 ppm

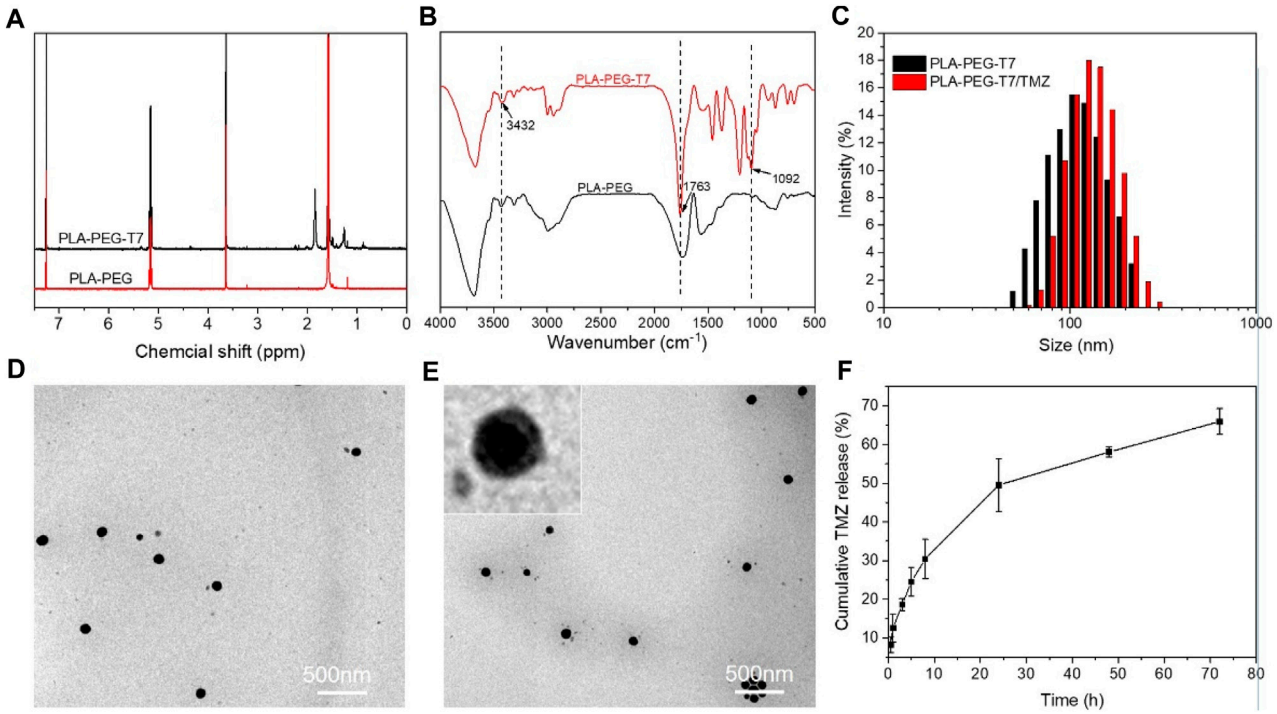

FIGURE 1 | Characterizations of PLA-PEG-T7. **(A)** ^{1}H NMR spectra of PLA-PEG and PLA-PEG-T7. **(B)** FTIR spectra of PLA-PEG and PLA-PEG-T7. **(C)** Size distribution of PLA-PEG-T7 and PLA-PEG-T7/MZ. **(D)**TEM image of PLA-PEG-T7. **(E)** TEM image of PLA-PEG-T7/TMZ. **(F)** Cumulative TMZ release (%) from PLA-PEG-T7/TMZ in PBS buffer (pH = 6.5) values at different time intervals.

corresponded to the solvent peak of $CDCl_3$. Chemical shift at 5.1–5.2 ppm corresponds to the H atom on the last methyl of the lactic acid unit, 3.6–3.7 ppm corresponds to the H atom on the CH_2 of the block copolymer polyethyleneglycol unit, 1.5–1.6 ppm corresponds to the H atom on the block methyl of polylactic acid unit, and 1.9–1.7 ppm and 1.3–1.2 ppm newly appeared peaks are a series of proton peaks on T7[32]. FTIR measurement showed that PLA-PEG-T7 was successfully synthesized (**Figure 1B**). The absorption peak at 1,092 cm^{-1} was attributed to C-O-C stretch of PEG segments. The strong absorption peak at 1756 cm^{-1} belonged to -C=O stretch, indicating the formation of PLA segments. The broad absorption peak at 3,243 cm^{-1} was -OH stretching, which was practically eliminated from the spectrum of PLA-PEG block copolymers. The results showed that T7 was successfully grafted onto the block polymer.

DLS and TEM image showed that PLA-PEG-T7 micellar had average diameter of about 100 nm and the distribution was uniform (**Figures 1C,D**). After loading with TMZ, the micelles still remain regular spherical shape. DLS showed that the particle size of PLA-PEG-T7/TMZ increased slightly and TEM image showed a diameter distribution of about 100–200 nm (**Figures 1C–E**). PLA-PEG-T7 and PLA-PEG-T7/TPE/TMZ were suspended in PBS to observe the stability. And the change in average particle size was measured by DLS within 24 h. As shown in **Supplementary Figure S1**, the diameter of the PLA-PEG-T7/TPE/TMZ micelles changed little from 106 to 135 nm, behaved higher stability than PLA-PEG-T7 alone.

Drug Release

Due to the layered structure of PLA-PEG-T7, hydrophobic drugs TMZ could be encapsulated in the cavity structure of PLA-PEG-T7 during the formation process, and the loading amount of TMZ in the PLA-PEG-T7/TMZ composite was 69 mg/g. In order to investigate the release behavior of PLA-PEG-T7/TMZ, acidic environment (pH = 6.5) was prepared to stimulate the tumor tissue. TMZ was slowly released in the first few hours, but increased after 8 h. By 72 h, the cumulative drug release reached 65%, indicating that PLA-PEG-T7 could release the drug slowly and solve the problem of sudden drug release (**Figure 1F**). Previous reports using PLA-PEG micelle to carry Paclitaxel (PTX), the release curve is similar to this study. Nearly 85% PTX released to PBS (pH = 5.0), while 70% PTX released to PBS (pH = 7.4) (Cai et al., 2020). The higher release amounts owing to the more acidic environment.

In Vitro BBB-Transport Efficiency

The unique BBB of the brain makes it difficult for traditional chemotherapy to achieve better therapeutic effects. It is urgent for drugs to effectively penetrate the BBB to target tumor cells and exert therapeutic effects. As a tumor-targeting peptide, T7 peptide can bind to TfR with significantly greater affinity (Tang et al., 2019; Yu et al., 2019). The *in vitro* BBB-crossing efficiency of PLA-PEG-T7/TPE in the transwell system was shown in **Figure 2C**. CLSM showed that compared with the PLA-PEG/TPE group, the PLA-PEG-T7/TPE group had more TPE

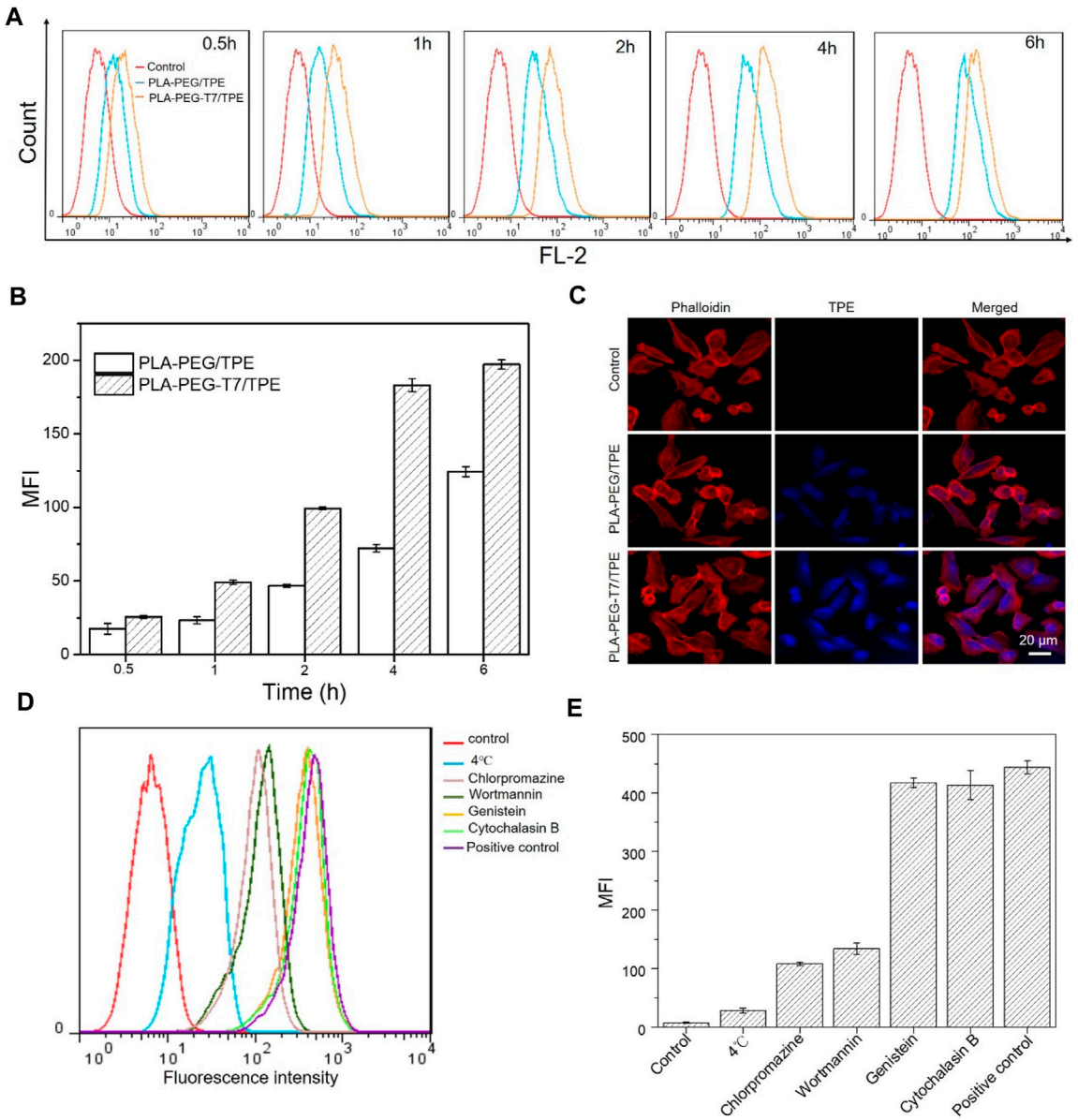

FIGURE 2 | (A) Flow cytometry analysis of fluorescence peak figure in LN229 cells incubated with PLA-PEG/TPE and PLA-PEG-T7/TPE for different time. **(B)** Mean fluorescence intensity (MFI) in LN229 cells incubated with PLA-PEG/TPE and PLA-PEG-T7/TPE for different time. **(C)** Confocal laser scanning microscopy (CLSM) shows the uptake of TPE into LN229 cells between PLA-PEG/TPE and PLA-PEG-T7/TPE a groups in a two-compartment BBB model. **(D)** Flow cytometry analysis of the effect of various inhibitors on the endocytosis of PLA-PEG-T7/TPE into LN229 cells. **(E)** The effect of various inhibitors on the endocytosis of PLA-PEG-T7/TPE in LN229 cells.

accumulation in the cytoplasm, which indicated that PLA-PEG-T7/TPE nanoparticles crossed the BBB more easily.

T7 Targeting Ability Assay

Efficient uptake of by *in vivo* cells was the key to achieving the biological performance of material design (Patalag et al., 2021). To verify the targeting of T7 on LN229 cells, cell uptakes of PLA-PEG/TPE and PLA-PEG-T7/TPE were also compared by flow cytometry as shown in **Figure 2A**. As expected, the fluorescence intensity of PLA-PEG-T7/TPE with T7 function was strongest at the same time point, indicating a significant increase in the absorption of PLA-PEG-T7/TPE by LN229 cells (**Figure 2B**). This suggests that T7-targeted peptides can significantly enhance the endocytosis efficiency of the PLA-PEG-T7/TPE nano micelle.

Endocytosis Pathway Analysis

For nanocarriers, endocytosis is a prerequisite for entering cells, and endocytosis is usually achieved by phagocytosis, macrocytosis, clathrin-dependent endocytosis, and clathrin-independent endocytosis. In order to explore the pathway of

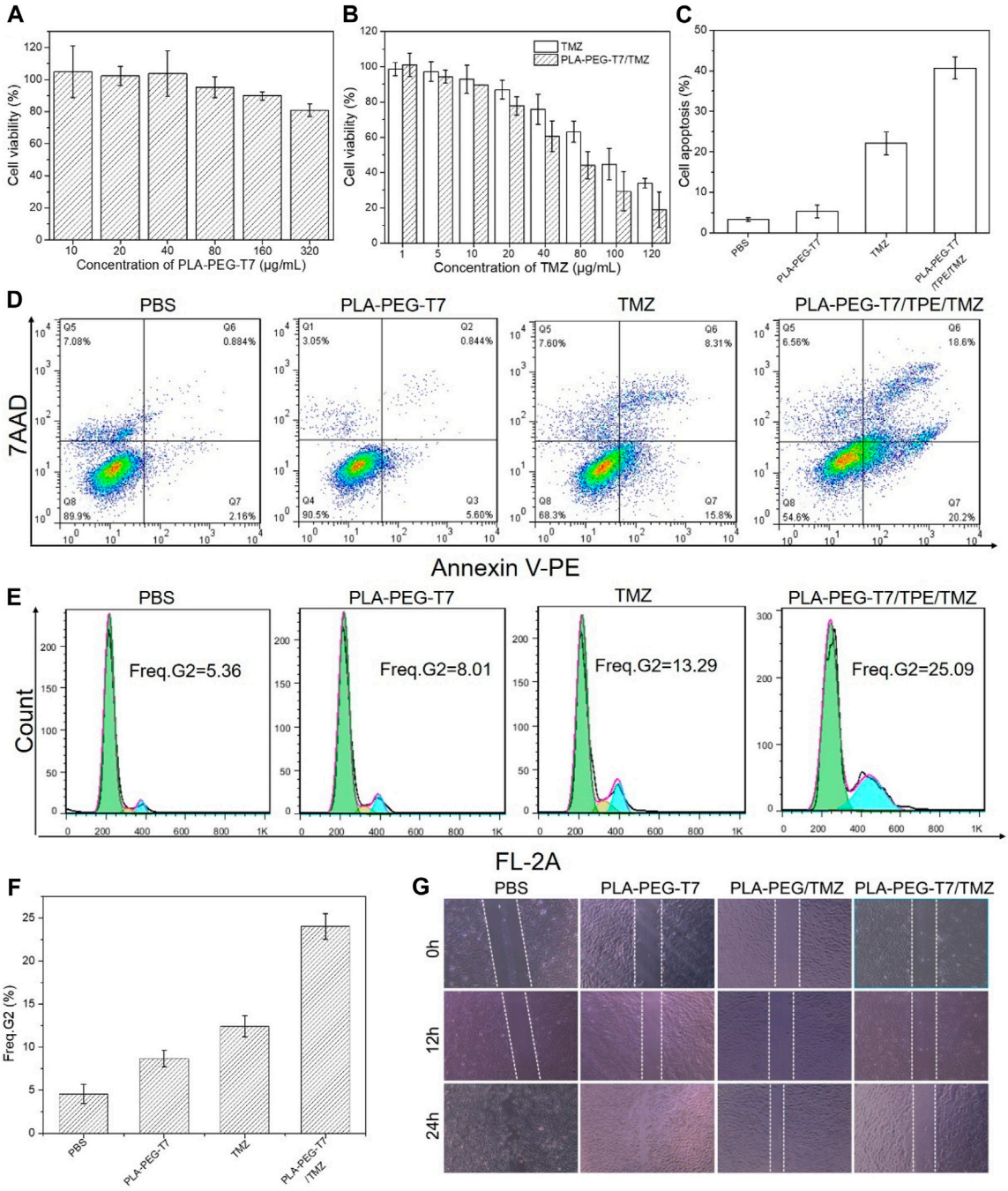

FIGURE 3 | (A) *In vitro* cytotoxicity of PLA-PEG-T7 with different concentrations on LN229 cells over an evaluation period of 24 h. **(B)** Cell viability of LN229 cells pretreated by TMZ and PLA-PEG-T7/TMZ with different concentrations. **(C)** Result histogram of apoptotic LN229 cells. **(D)** Apoptosis analysis by flow cytometry after LN229 cells incubated with various formulations using Annexin-V PE and 7-ADD dual-staining method. **(E)** Flow cytometry analysis of cell cycle in LN229 cells. **(F)** Freq. G2 of cell cycle in LN229 cells. **(G)** Scratch diagram of LN229 cells after treatment in different experimental groups.

the PLA-PEG-T7/TPE complex into LN229 cells, several specific drug inhibitors were used, such as chlorpromazine (an inhibitor of clathrin-dependent endocytosis), genistein Flavonoids (inhibitors of vesicle-mediated endocytosis), wortmannin (specific inhibitors of macrocytosis), and cytochalasin B (specific inhibitors of phagocytosis) to block specific endocytosis pathways. The results of the endocytosis pathway were shown in **Figures 2D,E**. Similar to other reports, low temperature (4°C) significantly inhibits cellular uptake compared with the normal 37°C, indicating that the endocytosis process is energy-dependent. In addition, chlorpromazine also significantly inhibits the uptake of PLA-PEG-T7/TPE by LN229

cells, and the fluorescence intensity was reduced by 70% compared with the control group, indicating that clathrin-dependent endocytosis is the main endocytic pathway for PLA-PEG-T7/TPE complex entering LN229 cells.

Cytotoxicity of PLA-PEG-T7

For *in vivo* applications, an important requirement for nanocarriers was to have low cytotoxicity. In order to investigate the cytotoxicity of PLA-PEG-T7 *in vitro*, CCK-8 method was used in this study to detect the survival rate of L929 cells under different concentrations of PLA-PEG-T7. When the concentration was 80 μg/ml, the survival rate of cells was 95%, indicating the toxicity of copolymer to cells was very small. With the further increase of polymer concentration, cell viability gradually decreased. Even at high concentrations (320 μg/ml), the survival rate of cells was more than 80%, which means that the PLA-PEG-T7 nano micelle had good biocompatibility (**Figure 3A**).

Inhibition of Cell Proliferation

The CCK-8 method further confirmed the feasibility of PLA-PEG-T7/TMZ to inhibit the proliferation of LN229 cells *in vitro*. After 24 h incubation, the *in vitro* cytotoxicity of TMZ and PLA-PEG-T7/TMZ was determined. As shown in **Figure 3B**, different experimental groups had inhibitory effects on cells and were concentration-dependent. The results showed that TMZ and PLA-PEG-T7/TMZ had anti-tumor activity against LN229 cell lines at appropriate concentrations. Compared with TMZ alone, PLA-PEG-T7/TMZ showed better tumor inhibition effect.

In Vitro Apoptosis Assessments

We also used flow cytometry to study the apoptotic effect of PLA-PEG-T7/TMZ on LN229 cells. LN229 cells treated with different preparations were stained with Annexin V-PE and 7-ADD. Flow cytometry quantitatively analyzes the apoptotic cell population after drug treatment. As shown in **Figures 3C,D**, after 24 h of incubation with blank PLA-PEG-T7, the apoptosis of these cells was negligible compared with the PBS control, indicating that it was non-toxic to LN229 cells at the measured concentration. TMZ and PLA-PEG-T7/TMZ could significantly induce LN229 cell apoptosis. The apoptotic rates of TMZ and PLA-PEG-T7/TMZ cells were 20.13% and 42.46%, respectively. Compared with TMZ, the apoptosis rate of LN229 cells treated with PLA-PEG-T7/TMZ was significantly increased. These results indicate that the nanocarrier loading strategy can effectively deliver drugs to cells and induce tumor cell apoptosis, which has potential application prospects in the comprehensive treatment of tumors.

Cell Cycle

The DNA content was analyzed by flow cytometry to determine the effect of PLA-PEG-T7/TMZ on cell cycle progression. As reflected in the G2 cell population shown in **Figures 3E,F**, no significant difference was observed in the cells treated between the blank PLA-PEG-T7 and the PBS control. However, the cells treated with TMZ showed a significantly larger cell population in the G2, 13.9% or 25.09%, respectively, which was much higher than the 5.36% of the PBS control, indicating that TMZ can inhibit intracellular DNA replication and induce cell apoptosis.

Scratch Healing Assay

Through the wound healing test, the inhibitory effect of PLA-PEG-T7/TMZ on the migration of LN229 cells was studied. As shown in **Figure 3G**, after 24 h of incubation, complete wound closure of blank PLA-PEG-T7 was observed. However, the cells treated with TMZ still retained a large area of uncovered wound. For the drug delivery system, the largest uncovered wound area was observed, indicating that PLA-PEG-T7/TMZ can effectively inhibit the migration of LN229 cells and help improve the anti-tumor efficacy.

In Vivo Fluorescence Imaging

The targeting ability of PLA-PEG-T7 was evaluated by fluorescence imaging experiments. The experimental results are shown in **Figure 4A**. Compared with PLA-PEG-Cy5 without targeting, PLA-PEG-T7-Cy5 modified with T7 was injected intravenously for 1 h, when the tumor site has obvious fluorescent signal. The fluorescent signal at the tumor site was significantly enhanced 3 h after the injection. The experimental results showed that the modification of T7 enhanced the material's tumor targeting. At 8 h after injection, the nude mice were sacrificed, and tumors and normal tissues were collected for *ex vivo* imaging (**Figure 4B**). The tumors treated with PLA-PEG-T7-Cy5 showed obvious fluorescent signals, indicating that the nanomaterials were delivered to the tumor.

In Vivo Assays

Encouraged by the good combination therapy of LN229 cells outside the recipient, the anti-tumor effect of PLA-PEG-T7/TPE/TMZ was studied through the treatment of nude mice carrying LN229 tumors. **Figures 5A,B** show representative tumor images and tumor growth curves treated with various preparations. It was found that the blank PLA-PEG-T7 had no effect on the growth of the LN229 tumor, and there was no significant difference in the growth curve of the PBS control. The group treated with TMZ showed significant anti-tumor effects. In particular, tumors treated with PLA-PEG-T7/TPE/TMZ showed a smaller volume than tumors treated with free TMZ, indicating that PLA-PEG-T7/TPE/TMZ drugs can enter LN229 cells more due to the targeting effect, and showed better anti-tumor effect *in vivo*, which is consistent with the *in vitro* apoptosis test. That means PLA-PEG-T7 delivery of drugs may be a promising strategy for the treatment of cancer. During the *in vivo* experiment, the changes in the weight of the mice were recorded, and it was considered to be a key factor reflecting the safety and side effects of the single formula food used. As shown in **Figure 5C**, the weight of each group of mice increased, so the PLA-PEG-T7/TPE/TMZ preparation was safe for mice during *in vivo* tumor treatment.

Histologic and Immunohistochemical Analysis

The hematoxylin-eosin (H&E) staining method was also used to analyze the tumor necrosis after the material treatment. H&E

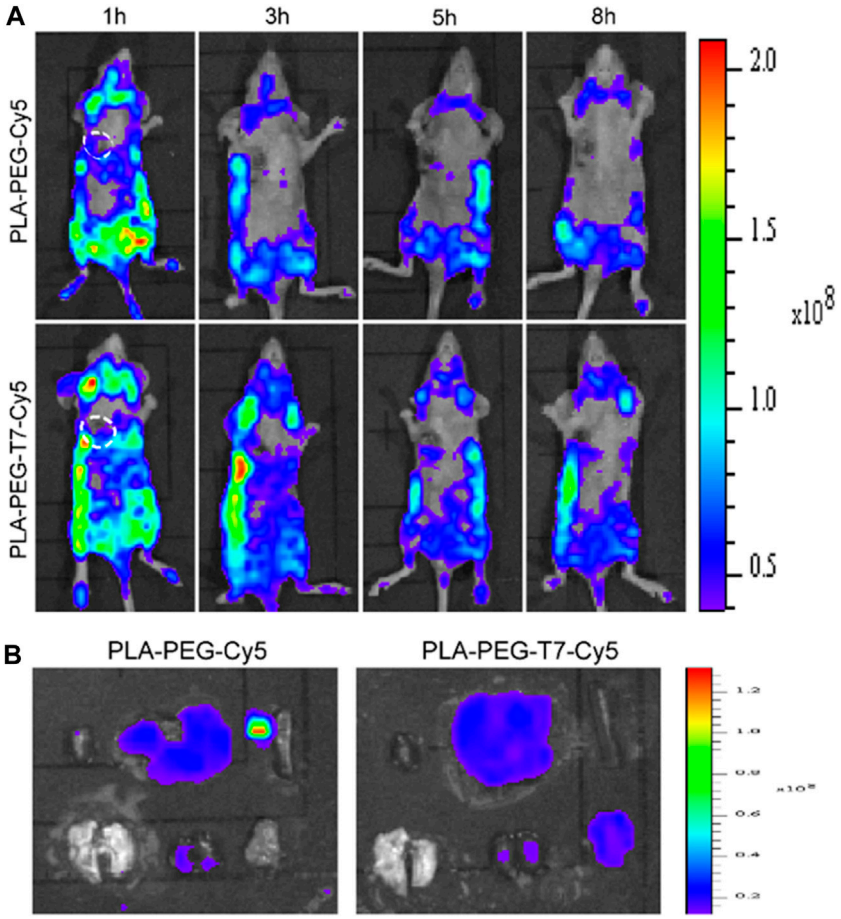

FIGURE 4 | (A) *In vivo* fluorescence images of LN229 tumor-bearing nude mice at different time points. **(B)** *Ex vivo* fluorescence imaging of various organs and tumors of LN229 tumor-bearing mice after injection.

images showed that PLA-PEG-T7/TPE/TMZ treatment induced the largest necrotic tumor area, in which the largest number of nuclei were deformed (**Figure 5E**). A terminal deoxynucleotidyl transferase-mediated dUTP nick end labeling (TUNEL) assay was performed to further evaluate the *in vivo* apoptotic effects of different treatment methods. Similarly, PLA-PEG-T7/TPE/TMZ induced the highest percentage of apoptosis-positive tumor cells, confirming its strongest anti-cancer activity *in vivo*. CD31 and Ki67 immunohistochemical staining were also performed on each group of tumor sections to monitor the changes in blood vessel density and tumor tissue proliferation activity, respectively. The CD31 stained images showed that the tumor tissue vascular density was greatly reduced after PLA-PEG-T7/TPE/TMZ treatment, indicating that APLA-PEG-T7/TPE/TMZ can effectively inhibit the angiogenesis of tumor tissues. The Ki67 stained image indicated that PLA-PEG-T7/TPE/TMZ treatment also significantly inhibited the proliferation activity of tumor cells.

In addition, major organs were excised from BALB/C nude mice for further histological analysis to evaluate the safety of the preparation. A representative photograph of the H&E stained sample was shown in **Figure 6A**. Compared with the PBS control, most of the preparations treated organs have no visible damage, indicating that most of the preparations have good biological safety. This result once again confirmed the safety and necessity of the PLA-PEG-T7 vector.

The blood chemistry parameters used to assess kidney, liver, blood lipids, blood sugar, and myocardial enzyme functions in each group were also tested (**Figure 6B**). Compared with PBS control mice, no significant changes in blood parameters were observed in the mice treated with PLA-PEG/TMZ/TPE and PLA-PEG-T7/TMZ/TPE. Therefore, we concluded that the PLA-PEG-T7/TMZ/TPE complex is a safe material and is expected to be used in the diagnosis and treatment of cancer *in vivo*.

Biocompatibility

Through hemolysis test and red blood cell morphological changes, the blood compatibility of PLA-PEG-T7 was studied. As shown in **Figure 7B**, 0.5 mg/ml PPLA-PEG-T7 did not produce any hemolysis (the hemolysis rate was less than 5%). In addition, the effect of PLA-PEG-T7 on red blood cells was further

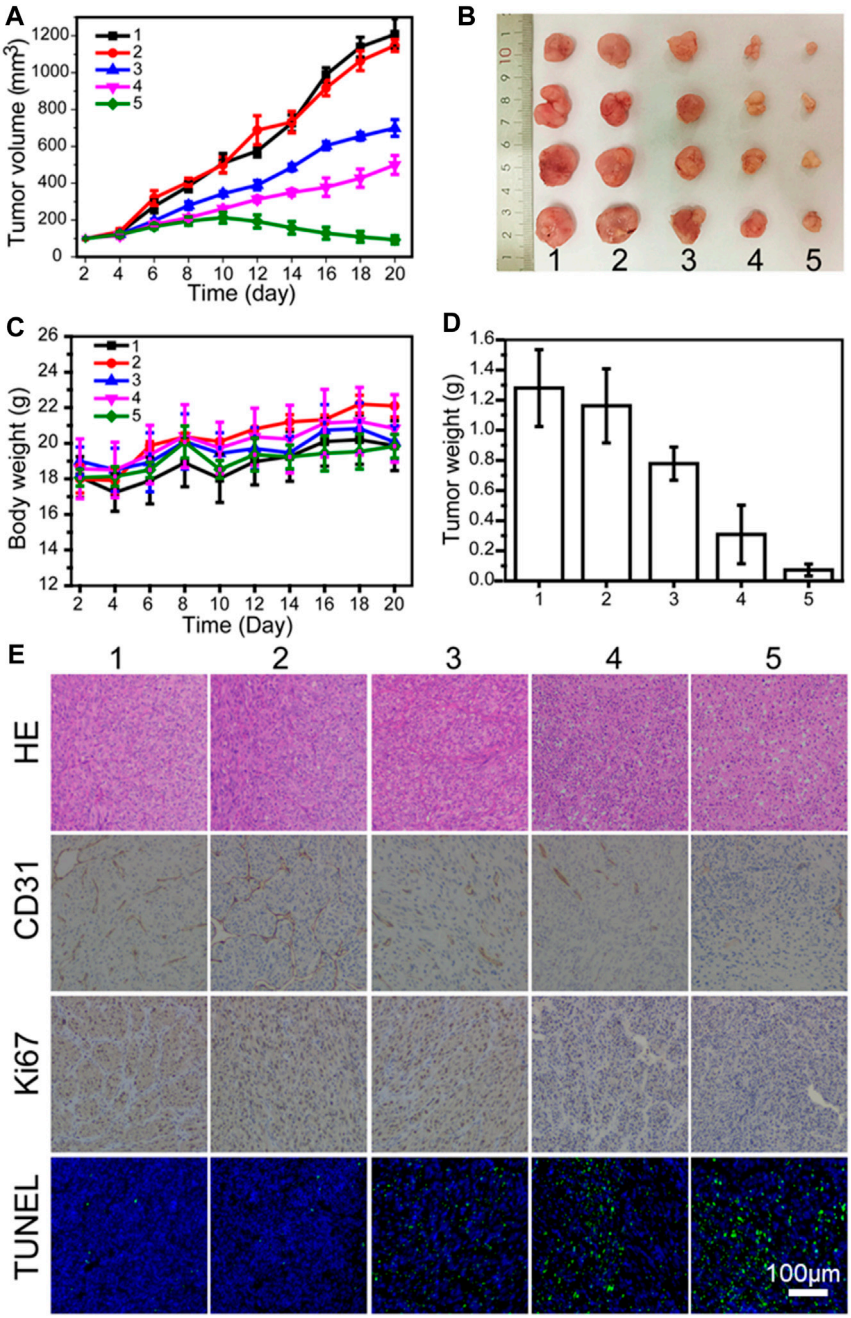

FIGURE 5 | (A) *In vivo* tumor growth curves of LN229 tumor-bearing mice treated with different formulations. **(B)** Representative image of LN229 tumors at the 21st day. **(C)** Body weight changes of mice treated with different formulations during the treatment. **(D)** The tumor weights excised from different groups after 21 days treatment. **(E)** Immunohistochemical analyses of H&E, TUNEL, CD31, and Ki67 for LN229 tumor tissues after the last treatment with different formulations *in vivo* (200 ×) (1: PBS; 2: PLA-PEG-T7; 3: TMZ; 4: PLA-PEG/TMZ/TPE; 5: PLA-PEG-T7/TMZ/TPE).

evaluated. As shown in **Figure 7A**, the excellent blood biocompatibility of PLA-PEG-T7 is further confirmed. The results showed that in the concentration range of 0.1–0.5 mg/ml, the morphology of red blood cells did not change after treatment with PLA-PEG-T7. The reason why PLA-PEG-T7 has excellent blood biocompatibility is the presence of PEG fragments.

In addition, APTT/PT analysis was performed to further evaluate the blood safety of PLA-PEG-T7. As shown in **Figure 7C**, compared with the PBS group, different concentrations of PLA-PEG-T7 had no obvious effect on APTT and PT. It proved that PLA-PEG-T7 had good blood compatibility within a specific concentration range.

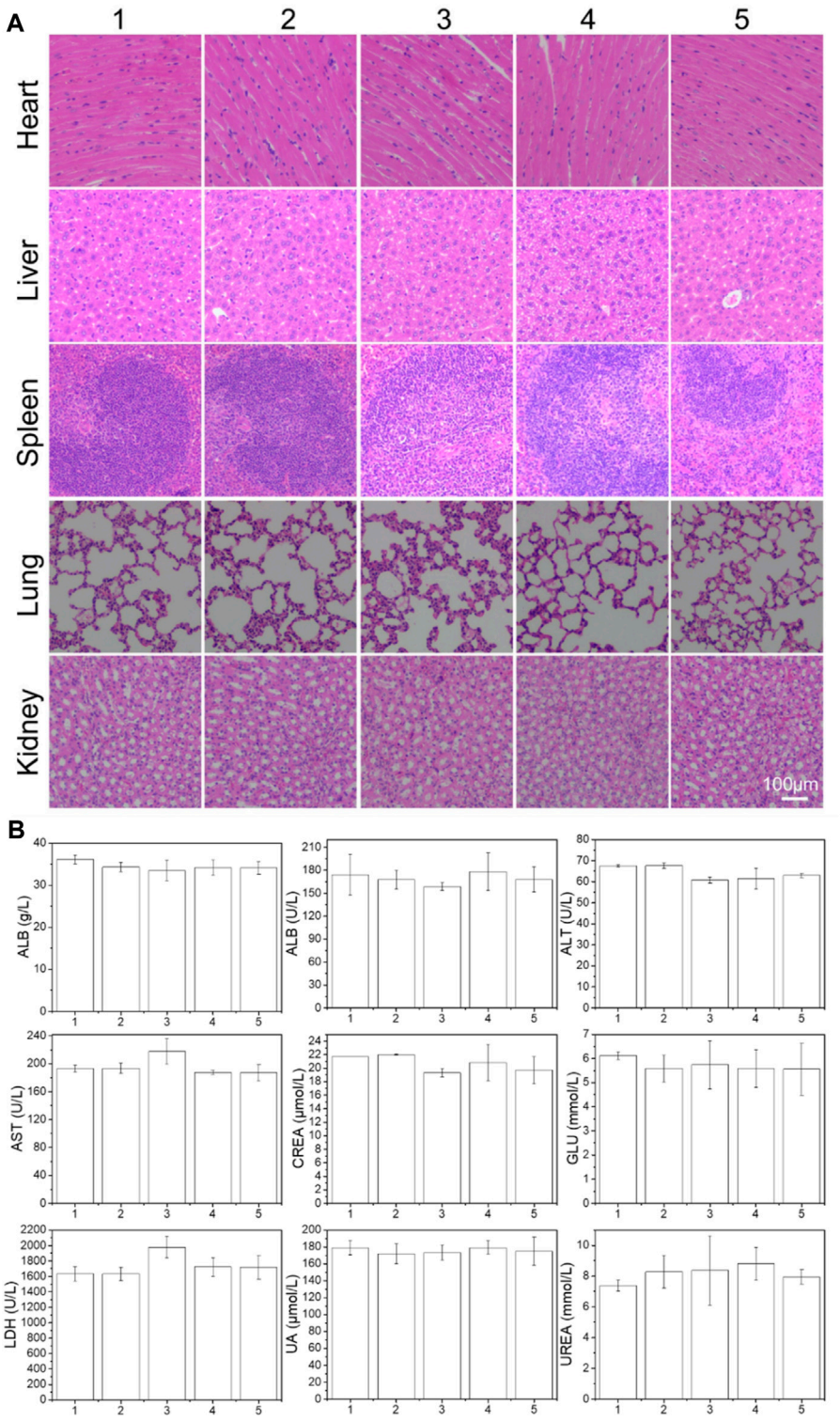

FIGURE 6 | (A) Histologic assessments of major organs in mice (200×) treated with different formulations. **(B)** Serum levels of albumin (ALB), alkaline phosphatase (ALP), alanine aminotransferase (ALT), aspartate aminotransferase (AST), lactate dehydrogenase (LDH), glucose (GLU), creatinine (CREA), uric acid (UA), and urea (UREA) of mice after 21 days treatment of different formulations. (1: PBS; 2: PLA-PEG-T7; 3: TMZ; 4: PLA-PEG/TMZ/TPE; 5: PLA-PEG-T7/TMZ/TPE).

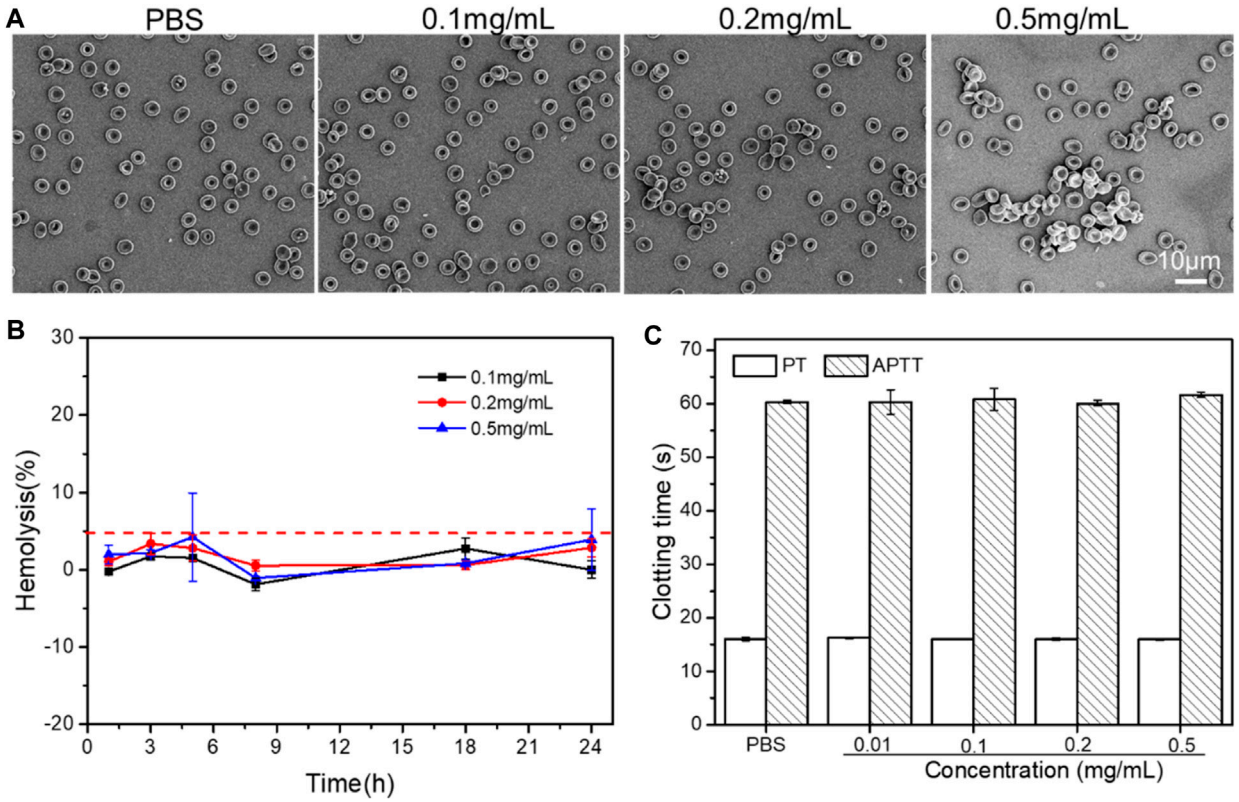

FIGURE 7 | (A) Effect of PLA-PEG-T7 with different concentrations on the aggregation and morphology of RBCs. **(B)** Effect of PLA-PEG-T7with different concentrations on the hemolysis. **(C)** Effect of PLA-PEG-T7with different concentrations on the APTT/PT.

CONCLUSION

Polylactic acid-polyethylene glycol bioabsorbable micelles have many advantages as a drug delivery system, such as biocompatibility and sustained release of drugs. This research developed a new micellar carrier for co-delivery of TMZ and TPE. Drug-free micelles do not affect the viability of cells. For the anti-tumor effect of PLA-PEG-T7/TPE/TMZ, it was found that PLA-PEG-T7/TPE/TMZ was much better than the free TMZ formulation used. PLA-PEG-T7/TPE/TMZ has a good inhibitory effect on the proliferation of LN229 cells *in vitro*, and a good inhibitory effect on LN229 tumors *in vivo*. In addition, PLA-PEG-T7 shows non-toxicity and excellent blood compatibility, indicating that it is a promising drug delivery vehicle in the comprehensive treatment of tumors.

DATA AVAILABILITY STATEMENT

The raw data supporting the conclusions of this article will be made available by the authors, without undue reservation.

ETHICS STATEMENT

The animal study was reviewed and approved by the Animal Protection and Use Committee of Jinan University.

AUTHOR CONTRIBUTIONS

Conceptualization, FC and CX; methodology, KH; software, KH; validation, DZ and LR; formal analysis, PW; investigation, PW.; resources, FC; data curation, KH; writing—original draft preparation, DZ; writing—review and editing, FC and CX; visualization, KH; supervision, FC; project administration, FC; funding acquisition, FC. All authors have read and agreed to the published version of the manuscript.

FUNDING

This study was supported by Xiangyang science and technology plan project in the medical and health field (2020ZD19).

SUPPLEMENTARY MATERIAL

The Supplementary Material for this article can be found online at: https://www.frontiersin.org/articles/10.3389/fbioe.2021.766470/full#supplementary-material

REFERENCES

Arumov, A., Liyanage, P. Y., Trabolsi, A., Roberts, E. R., Li, L., Ferreira, B. C. L. B., et al. (2020). Optimized Doxorubicin Chemotherapy for Diffuse Large B-Cell Lymphoma Exploits Nanocarrier Delivery to Transferrin Receptors. *Cancer Res.* 81 (3), 763–775. doi:10.1158/0008-5472.can-20-2674

Cai, Y., Xu, Z., Shuai, Q., Zhu, F., Xu, J., Gao, X., et al. (2020). Tumor-targeting Peptide Functionalized PEG-PLA Micelles for Efficient Drug Delivery. *Biomater. Sci.* 8 (8), 2274–2282. doi:10.1039/c9bm02036e

Fortin, D. (2012). The Blood-Brain Barrier: Its Influence in the Treatment of Brain Tumors Metastases. *Ccdt* 12 (3), 247–259. doi:10.2174/156800912799277511

Gang, Q., Zhong, Z., Min, L., Yu, D., and Ma, D. (2009). Simple and Efficient Near-Infrared Organic Chromophores for Light-Emitting Diodes with Single Electroluminescent Emission above 1000 Nm. *Adv. Mater.* 21 (1), 111–116.

Gao, M., and Tang, B. Z. (2017). Aggregation-induced Emission Probes for Cancer Theranostics. *Drug Discov. Today* 22 (9), 1288–1294. doi:10.1016/j.drudis.2017.07.004

Gao, X., Feng, G., Manghnani, P. N., Hu, F., Jiang, N., Liu, J., et al. (2017). A Two-Channel Responsive Fluorescent Probe with AIE Characteristics and its Application for Selective Imaging of Superoxide Anions in Living Cells. *Chem. Commun.* 53 (10), 1653–1656. doi:10.1039/c6cc09307h

Griffith, J. I., Sarkaria, J. N., and Elmquist, W. F. (2021). Efflux Limits Tumor Drug Delivery Despite Disrupted BBB. *Trends Pharmacol. Sci.* 42 (6), 426–428. doi:10.1016/j.tips.2021.03.001

Han, L., Huang, R., Liu, S., Huang, S., and Jiang, C. (2010). Peptide-Conjugated PAMAM for Targeted Doxorubicin Delivery to Transferrin Receptor Overexpressed Tumors. *Mol. Pharm.* 7 (6), 2156–2165. doi:10.1021/mp100185f

Hanna, C., Lawrie, T. A., Rogozińska, E., Kernohan, A., Jefferies, S., Bulbeck, H., et al. (2020). Treatment of Newly Diagnosed Glioblastoma in the Elderly: a Network Meta-Analysis. *Cochrane Database Syst. Rev.* 3 (3), CD013261. doi:10.1002/14651858.CD013261.pub2

Kuang, Y., An, S., Guo, Y., Huang, S., Shao, K., Liu, Y., et al. (2013). T7 Peptide-Functionalized Nanoparticles Utilizing RNA Interference for Glioma Dual Targeting. *Int. J. Pharmaceutics* 454 (1), 11–20. doi:10.1016/j.ijpharm.2013.07.019

Ladomersky, E., Scholtens, D. M., Kocherginsky, M., Hibler, E. A., Bartom, E. T., Otto-Meyer, S., et al. (2019). The Coincidence between Increasing Age, Immunosuppression, and the Incidence of Patients with Glioblastoma. *Front. Pharmacol.* 10, 200. doi:10.3389/fphar.2019.00200

Lee, J. H., Engler, J. A., Collawn, J. F., and Moore, B. A. (2010). Receptor Mediated Uptake of Peptides that Bind the Human Transferrin Receptor. *Eur. J. Biochem.* 268 (7), 2004–2012. doi:10.1046/j.1432-1327.2001.02073.x

Lin, G., Manghnani, P. N., Mao, D., Teh, C., Li, Y., Zhao, Z., et al. (2017). Robust Red Organic Nanoparticles for *In Vivo* Fluorescence Imaging of Cancer Cell Progression in Xenografted Zebrafish. *Adv. Funct. Mater.* 27 (31), 1701418. doi:10.1002/adfm.201701418

Liu, J., Hu, F., Wu, M., Tian, L., Gong, F., Zhong, X., et al. (2021). Bioorthogonal Coordination Polymer Nanoparticles with Aggregation-Induced Emission for Deep Tumor-Penetrating Radio- and Radiodynamic Therapy. *Adv. Mater.* 33 (9), e2007888. doi:10.1002/adma.202007888

Liu, S., Wang, J., Tang, F., Wang, N., Li, L., Yao, C., et al. (2020). Aqueous Systems with Tunable Fluorescence Including White-Light Emission for Anti-counterfeiting Fluorescent Inks and Hydrogels. *ACS Appl. Mater. Inter.* 12 (49), 55269–55277. doi:10.1021/acsami.0c16815

Long, C., Jiang, Y., Han, N., Hu, R., and Tang, B. Z. (2014). Rational Design of Aggregation-Induced Emission Luminogen with Weak Electron Donor-Acceptor Interaction to Achieve Highly Efficient Undoped Bilayer OLEDs. *Acs Appl. Mater. Inter.* 6 (19), 17215–17225.

Malekjani, N., and Jafari, S. M. (2021). Modeling the Release of Food Bioactive Ingredients from Carriers/nanocarriers by the Empirical, Semiempirical, and Mechanistic Models. *Compr. Rev. Food Sci. Food Saf.* 20 (1), 3–47. doi:10.1111/1541-4337.12660

Mao, D., Hu, F., Yi, Z., Kenry, K., Xu, S., Yan, S., et al. (2020). AIEgen-Coupled Upconversion Nanoparticles Eradicate Solid Tumors through Dual-Mode ROS Activation. *Sci. Adv.* 6 (26), eabb2712. doi:10.1126/sciadv.abb2712

Nuk, A., Jiang, N., Xj, A., Tm, A., Hc, A., and Liang, H. A. (2020). Escape from Abluminal LRP1-Mediated Clearance for Boosted Nanoparticle Brain Delivery and Brain Metastasis Treatment. *Acta Pharmaceutica Sinica B* 11 (5), 1341–1354.

Patalag, L. J., Ahadi, S., Lashchuk, O., Jones, P. G., Ebbinghaus, S., and Werz, D. B. (2021). GlycoBODIPYs: Sugars Serving as a Natural Stock for Water-Soluble Fluorescent Probes of Complex Chiral Morphologyoluble Fluorescent Probes of Complex Chiral Morphology. *Angew. Chem. Int. Ed. Engl.* 60 (16), 8766–8771. doi:10.1002/anie.202016764

Shang, M., Wang, K., Guo, L., Duan, S., Lu, Z., and Li, J. (2019). Development of Novel ST68/PLA-PEG Stabilized Ultrasound Nanobubbles for Potential Tumor Imaging and Theranostic. *Ultrasonics* 99, 105947. doi:10.1016/j.ultras.2019.105947

Shi, X., Sung, S. H. P., Lee, M. M. S., Kwok, R. T. K., Sung, H. H. Y., Liu, H., et al. (2020). A Lipophilic AIEgen for Lipid Droplet Imaging and Evaluation of the Efficacy of HIF-1 Targeting Drugs. *J. Mater. Chem. B* 8 (7), 1516–1523. doi:10.1039/c9tb02848j

Stupp, R., Taillibert, S., Kanner, A., Read, W., Steinberg, D. M., Lhermitte, B., et al. (2017). Effect of Tumor-Treating Fields Plus Maintenance Temozolomide vs Maintenance Temozolomide Alone on Survival in Patients with Glioblastoma. *Jama* 318 (23), 2306. doi:10.1001/jama.2017.18718

Su, Y., Lv, C., Zhang, Y., Liu, S., Xie, Z., and Zheng, M. (2020). Fluorescent Nanoparticles with Ultralow Chromophore Loading for Long-Term Tumor-Targeted Imaging. *Acta Biomater.* 111, 398–405. doi:10.1016/j.actbio.2020.05.013

Tang, J., Wang, Q., Yu, Q., Qiu, Y., Mei, L., Wan, D., et al. (2019). A Stabilized Retro-Inverso Peptide Ligand of Transferrin Receptor for Enhanced Liposome-Based Hepatocellular Carcinoma-Targeted Drug Delivery. *Acta Biomater.* 83, 379–389. doi:10.1016/j.actbio.2018.11.002

Teresa, P., James, P., Taylor, B., Giorgio, C., Sharareh, G., Jessica, M. R., et al. (2018). Developmental Phosphoproteomics Identifies the Kinase CK2 as a Driver of Hedgehog Signaling and a Therapeutic Target in Medulloblastoma. *Signal* 11 (547), eaau5147.

Ullman, J. C., Arguello, A., Getz, J. A., Bhalla, A., Mahon, C. S., Wang, J., et al. (2020). Brain Delivery and Activity of a Lysosomal Enzyme Using a Blood-Brain Barrier Transport Vehicle in Mice. *Sci. Transl. Med.* 12 (545), eaay1163. doi:10.1126/scitranslmed.aay1163

Wan, J., Li, Y., Jin, K., Guo, J., Xu, J., and Wang, C. (2020). Robust Strategy for Antibody-Polymer-Drug Conjugation: Significance of Conjugating Orientation and Linker Charge on Targeting Ability. *ACS Appl. Mater. Inter.* 12 (21), 23717–23725. doi:10.1021/acsami.0c04471

Wang, S., Luo, Y., Zhou, J., Wang, M., and Wang, Y. (2018). PLA-PEG-FA NPs for Drug Delivery System: Evaluation of Carrier Micro-structure, Degradation and Size-Cell Proliferation Relationship. *Mater. Sci. Eng. C* 91, 297–302. doi:10.1016/j.msec.2018.05.049

Wang, Y., Zu, M., Ma, X., Jia, D., Lu, Y., Zhang, T., et al. (2020). Glutathione-Responsive Multifunctional "Trojan Horse" Nanogel as a Nanotheranostic for Combined Chemotherapy and Photodynamic Anticancer Therapy. *ACS Appl. Mater. Inter.* 12 (45), 50896–50908. doi:10.1021/acsami.0c15781

Wu, Z., Zhang, P., Wang, P., Wang, Z., and Luo, X. (2021). Using Copper Sulfide Nanoparticles as Cross-Linkers of Tumor Microenvironment Responsive Polymer Micelles for Cancer Synergistic Photo-Chemotherapy. *Nanoscale* 13 (6), 3723–3736. doi:10.1039/d0nr06866g

Yoon, D. J., Chen, K. Y., Lopes, A. M., Pan, A. A., Shiloach, J., Mason, A. B., et al. (2017). Mathematical Modeling of Mutant Transferrin-Crm107 Molecular Conjugates for Cancer Therapy. *J. Theor. Biol.* 416, 88–98. doi:10.1016/j.jtbi.2017.01.008

Yu, M., Su, D., Yang, Y., Qin, L., Hu, C., Liu, R., et al. (2019). D-T7 Peptide-Modified PEGylated Bilirubin Nanoparticles Loaded with Cediranib and Paclitaxel for Antiangiogenesis and Chemotherapy of Glioma. *ACS Appl. Mater. Inter.* 11 (1), 176–186. doi:10.1021/acsami.8b16219

Zhao, D., Hu, Q., Qi, L., Wang, J., Wu, H., Zhu, G., et al. (2017). Magnetic Resonance (MR) Imaging for Tumor Staging and Definition of Tumor Volumes on Radiation Treatment Planning in Nonsmall Cell Lung Cancer. *Medicine* 96 (8), e5943. doi:10.1097/md.0000000000005943

Conflict of Interest: The authors declare that the research was conducted in the absence of any commercial or financial relationships that could be construed as a potential conflict of interest.

Publisher's Note: All claims expressed in this article are solely those of the authors and do not necessarily represent those of their affiliated organizations, or those of the publisher, the editors and the reviewers. Any product that may be evaluated in this article, or claim that may be made by its manufacturer, is not guaranteed or endorsed by the publisher.

Copyright © 2021 Hu, Zhou, Rao, Wang, Xiang and Chen. This is an open-access article distributed under the terms of the Creative Commons Attribution License (CC BY). The use, distribution or reproduction in other forums is permitted, provided the original author(s) and the copyright owner(s) are credited and that the original publication in this journal is cited, in accordance with accepted academic practice. No use, distribution or reproduction is permitted which does not comply with these terms.

frontiers in Bioengineering and Biotechnology

ORIGINAL RESEARCH
published: 30 November 2021
doi: 10.3389/fbioe.2021.761911

Modifying a 3D-Printed Ti6Al4V Implant with Polydopamine Coating to Improve BMSCs Growth, Osteogenic Differentiation, and *In Situ* Osseointegration *In Vivo*

Hui Wang[1†], Changyong Yuan[2†], Kaili Lin[1], Rui Zhu[3]* and Shilei Zhang[1]**

[1]Department of Oral and Cranio-Maxillofacial Surgery, Shanghai Ninth People's Hospital, College of Stomatology, Shanghai Jiao Tong University School of Medicine, National Clinical Research Center for Oral Diseases, Shanghai Key Laboratory of Stomatology and Shanghai Research Institute of Stomatology, Shanghai, China, [2]School of Stomatology, Xuzhou Medical University, Xuzhou, China, [3]Key Laboratory of Spine and Spinal Cord Injury Repair and Regeneration of Ministry of Education, Orthopaedic Department of Tongji Hospital, School of Medicine, Tongji University, Shanghai, China

OPEN ACCESS

Edited by:
Lia Rimondini,
University of Eastern Piedmont, Italy

Reviewed by:
Claudia Dellavia,
University of Milan, Italy
Xiao Gong,
Wuhan University of Technology, China

***Correspondence:**
Kaili Lin
linkaili@sjtu.edu.cn
lklecnu@aliyun.com
Rui Zhu
zhurui08@hotmail.com
Shilei Zhang
leinnymd@hotmail.com

[†]These authors have contributed equally to this work

Specialty section:
This article was submitted to Biomaterials, a section of the journal Frontiers in Bioengineering and Biotechnology

Received: 20 August 2021
Accepted: 10 November 2021
Published: 30 November 2021

Citation:
Wang H, Yuan C, Lin K, Zhu R and Zhang S (2021) Modifying a 3D-Printed Ti6Al4V Implant with Polydopamine Coating to Improve BMSCs Growth, Osteogenic Differentiation, and In Situ Osseointegration In Vivo. Front. Bioeng. Biotechnol. 9:761911. doi: 10.3389/fbioe.2021.761911

Nowadays, 3D printing technology has been applied in dentistry to fabricate customized implants. However, the biological performance is unsatisfactory. Polydopamine (PDA) has been used to immobilize bioactive agents on implant surfaces to endow them with multiple properties, such as anti-infection and pro-osteogenesis, benefiting rapid osseointegration. Herein, we fabricated a PDA coating on a 3D-printed implant surface (3D-PDA) *via* the *in situ* polymerization method. Then the 3D-PDA implants' pro-osteogenesis capacity and the osseointegration performance were evaluated in comparison with the 3D group. The *in vitro* results revealed that the PDA coating modification increased the hydrophilicity of the implants, promoting the improvement of the adhesion, propagation, and osteogenic differentiation of bone marrow-derived mesenchymal stem cells (BMSCs) *in vitro*. Additionally, the 3D-PDA implant improved osteointegration performance *in vivo*. The present study suggested that PDA coating might be a feasible strategy to optimize 3D-printed implant surfaces, making a preliminary research basis for the subsequent work to immobilize bioactive factors on the 3D-printed implant surface.

Keywords: 3D printing, titanium alloy implants, surface modification, polydopamine, osteogenesis

1 INTRODUCTION

Simplification of the manufacturing process and clinical procedures, and decreases in treatment time are the trends of implant dentistry. When an immediate implant technique is implemented, the implant needs to be inserted into the tooth socket immediately after tooth extraction, which can effectively preserve the height and width of the alveolar and minimize the margin bone adsorption during the healing stage of extraction socket (Koh et al., 2010). Hence, the demand for fabricating customized dental implants to precisely suit the extraction socket and obtain ideal primary stability is dramatically increasing. Fortunately, in recent years, the 3D printing technique has been applied in the orthopedic field and dentistry for its ability to fabricate customized products rapidly and effectively (van Noort 2012; Zhang et al., 2020). Based on a computer-aided design (CAD) file, 3D printing can fabricate personalized implants (Figliuzzi et al., 2012; Oladapo et al., 2021). More

importantly, 3D printing could produce porous implants to make the elasticity modulus similar to natural bone, avoiding the stress shielding effect and minimizing associated bone adsorption (Sidambe 2014; Shah et al., 2016; Vijayavenkataraman et al., 2020).

Our former study found that a 3D-printed Ti6Al4V implant could obviously improve osseointegration in a rat condyle implant model compared to the implant prepared by traditional machining technology after implantation for 3 weeks. However, there was no significant difference between them in the longer term. Moreover, compared to a sand-blasting with large grit and acid-etching titanium implant (SLA), which is prevalently used in clinic, the osseointegration performance of a 3D-printed Ti6Al4V implant was inferior and not ideal (Zhang et al., 2019; Zhang et al., 2020). Therefore, it is urgent to find effective ways to overcome the unsatisfactory osseointegration performance of 3D-printed implants.

Lots of research has confirmed that the surface characteristics play essential roles in dominating implant fate (Hotchkiss et al., 2016; Zhang et al., 2021). Hence, it may be a promising strategy to make surface modifications on 3D-printed implants. So far, physical modifications, including topography, roughness, wettability, and chemical component modification have been successfully applied to the implant surface (Xia et al., 2018; Zhang et al., 2019; Liu et al., 2020; Xue et al., 2020). For example, sand-blasting, acid-etching (Zhang et al., 2020), micro-arc oxidation (Shimabukuro et al., 2019), alkali-heat treatment (Wang et al., 2018) have been proved to promote osteogenic cell lineage differentiation and implant osseointegration.

In effect, the above studies have mainly focused on providing the osteogenic property to implants for the sake of enhancing the osseointegration performance. Actually, many other factors participate in the implant osseointegration process (DAr et al., 2018; Guder et al., 2020). When the implant is placed into the human body, it can be regarded as a foreign substance, activating biological response cascades (Chen et al., 2016). Briefly, the immune cells can recognize it, and then they secrete a variety of inflammatory cytokines and chemokines, and recruit fibroblasts, endothelial cells, bone marrow mesenchymal cells (BMSCs), and other repair cells to migrate toward the implant surface to participate in the osseointegration repair process (Landen et al., 2016). Therefore, it is desired to endow an implant with multiple properties, including regulating immune cells function, promoting angiogenesis and an antimicrobial property (Chen et al., 2017; Bai et al., 2018; Zhang et al., 2021).

With the emergence and development of biochemical surface modification, bioactive agents, such as protein, peptide, growth factor, and drugs have been tentatively applied to implant surfaces. Nowadays, many techniques can immobilize the above bioactive agents, mainly classified into three kinds, protein adsorption, covalent immobilization by physical methods, or by chemical methods (Stewart et al., 2019). By assembling multiple bioactive factors on the surface, the implant would become multifunctional. Among these methods, one of the bioinspired methods, polydopamine (PDA), has attracted the attention of researchers because of its simplicity, convenience, and efficiency (Jin et al., 2020; Zeng et al., 2020; Tang et al., 2021; Wang et al., 2021; Zhuang et al., 2021).

PDA is the self-polymerized product of dopamine in an alkaline aqueous solution in the dark. Previous research confirmed that polydopamine can powerfully adhere to a large variety of material surfaces and apparently enhance hydrophilicity and biocompatibility, which is a universal method to functionalize material surfaces (Ku et al., 2010; Zeng et al., 2020; Owji et al., 2021; Tang et al., 2021). More importantly, PDA has been successfully applied to immobilize bioactive agents on implant surfaces because of numerous chemical functional groups, especially imine, amine, and catechol groups. Due to those functional groups, on the one hand, PDA can be strongly covalent with the implant surface; on the other hand, it can chelate metal ions and immobilize various bioactive factors (Lee et al., 2009). For example, Chien et al. (Chien and Tsai 2013) improved the osteogenesis of BMSCs by using polydopamine to immobilize Arg-Gly-Asp peptides, hydroxyapatite (HA), and bone morphogenic protein-2 (BMP-2) on the titanium implant surface. Poh et al. (Poh et al., 2010) utilized polydopamine to functionalize an implant surface with vascular endothelial growth factor (VEGF), which could improve human dermal microvascular endothelial cells' (HDMECs) adhesion and multiplication, and human mesenchymal stem cells' (hMSCs) differentiation. Using a layer by layer assemble process, Li et al. (Li et al., 2016) fabricated a hybrid coating consisting of HA, Ag nanoparticles, and chitosan on a polydopamine-modified titanium implant surface, which enhanced antimicrobial and osteogenic activity.

Overall, as mentioned before, our previous study has successfully designed and fabricated a customized 3D-printed implant. In the current research, we primarily focused on studying the biocompatibility and *in vivo* application of 3D-printed implants modified by appropriate surface modification techniques. As a bio-inspired polymer, PDA has been used as a crosslinking agent to immobilize bioactive factors on implant surfaces and modify implants biocompatibility. However, to the best of our knowledge, the research about immobilizing bioactive agents on 3D-printed Ti6Al4V implants by PDA is limited. Hence, to improve the 3D-printed Ti6Al4V implant surface, it is meaningful to explore the potential application of PDA coating *in vivo*. Therefore, in the current applied study, we tried to assemble the 3D-printed implant with a PDA coating and preliminarily studied its surface characteristics, biocompatibility, biosecurity, and osseointegration capability *in vivo*. Based on the present study results, in future work, we further intend to immobilize multiple bioactive factors on the 3D-printed implants' surface and study its application.

2 MATERIALS AND METHODS

2.1 Fabrication of Samples

The 3D-printed Ti6Al4V implants (Ø 2 mm × 4 mm) and plates (side length: 10 mm, height: 2 mm) were fabricated by an EOS laser printing system (EOS GmbH Munchen, Germany) as previously demonstrated (Wang et al., 2018). In short, the

20–50 μm Ti6Al4V alloy powers were exploited as raw materials, and then the samples were additively manufactured layer by layer (Wang et al., 2021). All the specimens were ultrasonically washed in acetone, ethanol, and distilled water, respectively, for 15 min. For the sake of fabricating the PDA coating on the specimens, the 3D-printed Ti6Al4V implants and disks were soaked in prepared dopamine solution (2 mg/ml in 10 mM Tris buffer at pH 8.5) at room temperature in the dark according to former research (Xi et al., 2009). After undergoing the polymerization reaction of dopamine monomers for 24 h, a layer of PDA was formed and deposited on the sample surfaces. Then the specimens were ultrasonically rinsed in distilled water to remove free dopamine monomers. Afterward, the samples were dried at room temperature and labeled as the 3D-PDA group. The 3D-printed Ti6Al4V implants and disks without PDA coating were named the 3D group and used as control.

2.2 Specimen Surface Characterization

The surface topography of the 3D-PDA and 3D groups were characterized *via* scanning electron microscopy (SEM, SU8220, Hitachi, Japan). To verify whether the PDA coating was prepared on the 3D-PDA surface, a Raman spectroscopy image was obtained using a Raman spectroscope (RW2000, Renishaw, England) at a 524 nm source wavelength. Moreover, the PDA coating thickness was detected by spectroscopic ellipsometer at the polarized angle of 70° (UVISEL, HORIBA, France). Besides, the discrepancy of hydrophilicity between the two kinds of specimens was evaluated by a surface-contact angle machine (Optical Contact Angle and interface tension meter, SL200 KS, SOLON TECH, China). The surface chemical composition of the PDA coating on the 3D-PDA group was detected by X-ray photoelectron spectroscopy (XPS, Escalab250Xi, Thermo Scientific, United States).

2.3 *In Vitro* Studies

2.3.1 Separation and Cultivation of Bone Marrow-Derived Mesenchymal Stem Cells (BMSCs)

Sprague Dawley (SD) rats approximately 2 weeks old were purchased from the Shanghai SLAC Laboratory Animal Co. Ltd (Shanghai, China) and used in the current study. All the animal experiments and procedures were performed according to the approval and guidance of the Institutional Animal Care and Use Committee of Tongji University (Shanghai, China). The process of isolating BMSCs coincided with former research (Wang et al., 2018). Then the harvested primary cells were cultured in alpha-modified Eagle's medium (α-MEM, Hyclone, United States) with 1% penicillin/streptomycin solution and 10% fetal bovine serum (Hyclone, United States). Cells were cultured at 37°C in a humidified atmosphere containing 5% CO_2. Until 80–90% convergence was reached, the cells were sub-cultured and the two to four passages of BMSCs were used in the subsequent research.

2.3.2 Cell Morphology and Adhesion Observation

To evaluate the form of BMSCs on the two group surfaces, 1×10^4 cells were cultivated on each specimen. After culturing for 24 h, the cells were rinsed three times with phosphate buffer saline (PBS) and immobilized with 4% paraformaldehyde (PFA) overnight at 4°C. Then the samples were dehydrated with hierarchical ethanol series sequentially, freezing dried, and sprayed with gold before scanning *via* SEM.

TABLE 1 | Primer sequences utilized for RT-PCR.

Gene	Primer sequences (F = forward; R = reverse)
BSP	F: 5′-AGAAAGAGCAGCACGGTTGAGT-3′
	R: 5′-GACCCTCGTAGCCTTCATAGCC-3′
OCN	F: 5′-GCCCTGACTGCATTCTGCCTCT-3′
	R: 5′-TCACCACCTTACTGCCCTCCTG-3′
COL-1	F: 5′-GCCTCCCAGAACATCACCTA-3′
	R: 5′-GCAGGGACTTCTTGAGGTTG-3′
OPN	F: 5′-CCAAGCGTGGAAACACACAGCC-3′
	R: 5′-GGCTTTGGAACTCGCCTGACTG-3′
β-actin	F: 5′-GTAAAGACCTCTATGCCAACA-3′
	R: 5′-GGACTCATCGTACTCCTGCT-3′

2.3.3 Cell Multiplication Activity Assay

For the cell proliferation assay, 2×10^4 cells were cultured on the 3D-PDA and 3D groups. At days 1, 4 and 7, samples were rinsed with PBS three times and cultured in medium added with 10% CCK-8 (CCK-8, Beyotime, China) working solution for 3 h at 37°C in the dark. Afterward, the solution absorbance was detected at a 405 nm wavelength by utilizing a microplate reader (Biotek, United States).

2.3.4 The Alkaline Phosphatase (ALP) Activity Trial

BMSCs were cultivated (2×10^4/well) on the two kinds of sample surfaces to measure the ALP activity performance at days 4 and 7. For quantitative analysis of ALP activity, samples were flushed with PBS and soaked in 1% TritonX-100 (Beyotime, China). After centrifuging at 4°C (12,000 rpm × 10 min), supernatants were obtained. The ALP kit (JianCheng Bioengineering Institute, Nanjing, China) and the BCA protein trial kit (Beyotime, China) were used to test the ALP activity and total protein concentration, respectively. Ultimately, the results were computed and normalized to the total protein level.

2.3.5 Isolation RNA and Quantitative Real-Time PCR (PT-PCR) Assay

BMSCs were cultivated on the different groups for 4 and 7 days to detect the osteogenesis-related gene expression level. Subsequently, the cells from each group were dissolved in Trizol reagent (Invitrogen, United States) and the total RNA was refined. Afterward, 1 μg of RNA was transcribed in reverse into cDNA by using a Prime-Script™ RT reagent kit (Takara Bio, Japan). Primers utilized in this research were synthesized by Sangon Biotech (Shanghai) Co., Ltd and are listed in **Table 1**, including osteocalcin (OCN), osteopontin (OPN), bone sialoprotein (BSP), and collagen type 1 (COL-1). The β-actin gene was used as a reference for normalization. All RT-RCR procedures were performed on the Light Cycler 96 Real-Time PCR System (Roche, Switzerland) by utilizing the SYBR Green PCR reaction mix (Roche, Basel, Switzerland) under the

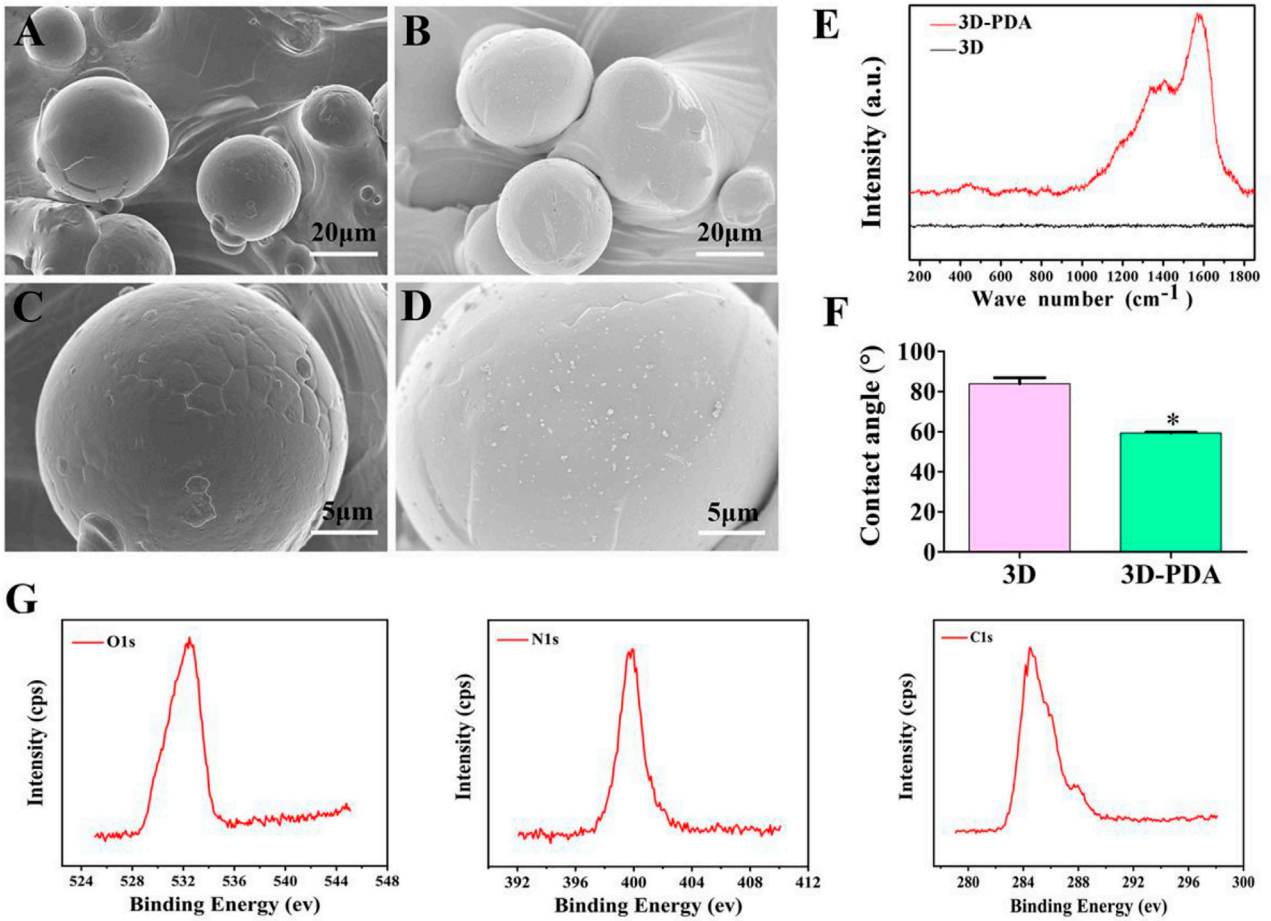

FIGURE 1 | SEM images of 3D **(A,C)** and 3D-PDA **(B,D)** at low **(A,B)** and high magnifications **(C,D)**. Raman spectra analysis **(E)**, water contact angle **(F)** of 3D and Q15 3D-PDA group surfaces, and X-ray photoelectron spectroscopy spectra of the 3D-PDA surface **(G)**. *$p < 0.05$.

instructions of the manufacturers. All the experiments were conducted in triplicate.

2.4 *In Vivo* Studies

2.4.1 Animal Surgical Operation

In order to evaluate the osseointegration performance of the two kinds of implants, 10 SD rats weighing approximately 280 g were used in the trial. All the animal assays were authorized and performed according to the instructions of the Institutional Animal Care and Use Committee of Tongji University (Shanghai, China). The rat femoral condyle model was used in the current study and the surgical procedures were demonstrated previously (Wang et al., 2018). In short, the bilateral femoral condyles of the recipient rats were shaved and disinfected after anesthesia. Then the lateral surface of the femoral condyle was exposed, and a hole perpendicular to the long axis of the femoral condyle was prepared. Afterward, either the 3D and 3D-PDA implants were randomly inserted into the left or right femoral condyle holes. In the end, the muscle and skin were sutured in layers. After 4 weeks, the implants in the rat femoral condyles were harvested, and subsequently immobilized in 4% PFA before histological analysis.

2.4.2 Histological and Histomorphometric Analyzation

Hard-tissue slicing was utilized for histological and histomorphometric observation and analysis. Briefly, the harvested samples were fixed in 4% PFA for 24 h. Then they were washed in distilled deionized water and then dehydrated in grade ethanol series from 70 to 100%. Subsequently, the samples were embedded in a light-curing one-component resin (Technovit 7200VLC, kulzers, Friedrichsdorf, Germany). After 15 h, the polymerized samples were cut longitudinally into 200-μm-thick sections with a diamond circular saw system (Exakt 300 CL, Exakt Apparatebau, Germany), and then ground and polished to around 30 μm thickness using a grinding system (Exakt 400 CS, Exakt Apparatbau, Germany).

After being stained by Van Gieson's picrofuchsine, the sections were observed and photographed by a microscope (Olympus, Japan). And Image-Pro Plus 6.0 software was used to perform histomorphometric analysis and compute the bone-implant contact (BIC) percentage in the cancellous bone. BIC was

calculated as the percentage of the length of direct contact to the total length of the implant surface.

2.5 Statistical Analysis

Using SPSS 22.0 statistical software, all the data were demonstrated as means ± standard deviation (SD). Independent *t*-test or paired *t*-test were conducted to compare the statistic difference between the 3D and 3D-PDA groups. The distinction was considered statistically significant at $p < 0.05$.

3 RESULTS AND DISCUSSION

3.1 Characterization Analysis of Prepared Samples

Figures 1A–D show the topography of the 3D and 3D-PDA sample surfaces. Both of them exhibited similar micro-scale surface morphology at low magnification. Briefly, spherical Ti6Al4V particles with sizes from 20 to 50 μm were distributed disorderly and fused on the relatively flat substrate. More importantly, granular PDA aggregates with nanometer size were evenly deposited and dispersed on the 3D-PDA samples, which was demonstrated clearly at high magnification (**Figure 1D**). The Raman spectra (**Figure 1E**) images showed that the 3D-PDA group showed the typical peaks of polydopamine at approximately 1,350 and 1,580 cm^{-1} in contrast to the 3D group. The results proved that PDA coating was fabricated on the 3D sample surface successfully. As measured by spectroscopic ellipsometer, the PDA coating thickness was approximately 30 nm.

Surface free energy (SFE) dominates the interplay between the surface, aqueous biological environment, and proteins. What is more, SFE can be reflected by water contact angle (WCA) measurements. In general, based on a WCA >90° or <90°, a surface could be classified as hydrophobic (low SFE) or hydrophilic (high SFE). And at WCA >150° or <5°, the surface could be further defined as super-hydrophilic and super-hydrophobic (Wei et al., 2020; Han and Gong 2021; Zhang et al., 2021). As presented in **Figure 1F**, the water contact angle of 3D-PDA was obviously lower than that of the 3D group, which suggested that the surface of the 3D-PDA group had better hydrophilicity and higher SFE. Previous research finds that PDA contains many amino and hydroxyl aqueous functional groups, which can provide a hydrophobic surface with a hydrophilic group to improve the hydrophilicity of the biological materials (Ku et al., 2010; Li et al., 2019). The hydrophilic surface is beneficial to the adhesion of extracellular matrix proteins and more RGD (R-arginine, G-glycine, D-aspartic acid) sequence sitesexposure, which has an essential role in osteoblast adhesion, propagation, and differentiation. As the XPS results showed (**Figure 1G**), the element peaks of O1s, N1s, and C1s were detected on the surface of the 3D-PDA group, which showed that the PDA coating was deposited successfully.

3.2 The Influence of a PDA-Coated Surface on the Adhesion of BMSCs

The SEM results show the effect of the PDA-coated surface on the adhesion of BMSCs after seeding for 24 h (**Figure 2**). Both BMSCs on the two kinds of samples could grow and extend toward the three-dimensional direction. Moreover, BMSCs also could adhere from one particle to another or the substrate. Compared to the 3D group, BMSCs on the 3D-PDA sample surface spread well and had plentiful filopodia and lamellipodia, which suggested that the 3D-printed titanium surface with a PDA coating could facilitate cell adhesion. It is well known that the implant surface properties, for example, topography, wettability, and charge, could impact the conformation and orientation of the cell adhesive proteins. Then the complex cell adhesion process, including cell attachment, cell spread, cytoskeleton organization, and so on could be changed, further triggering the subsequent cell response cascades (Lebaron and Athanasiou 2000). Therefore, favorable cell adhesion is beneficial to cell survival, proliferation, differentiation, and osseointegration *in vivo*.

3.3 The Impact of the PDA-Coated Surface on the Propagation and Osteogenic Differentiation of BMSCs

The proliferation of BMSCs cultured on 3D and 3D-PDA samples were detected by the CCK-8 test (**Figure 3A**). There was no significant distinction between the two groups at day 1. However, the 3D-PDA samples showed higher proliferative activity than the 3D group with the increase of culturing time to 4 and 7 days. Higher cell propagation leads to increased cell colonization on the implant surface and enhances cell-cell communications. The cell-cell communications play a dramatic role in responding to external stimulus, regulating cell function development and osteoblast differentiation, resulting in larger lumps of bone tissue around the implant (Civitelli 2008; Zhao et al., 2010).

After being cultivated for 4 and 7 days, the ALP activity of BMSCs cultured on the two kinds of specimens was evaluated (**Figure 3B**). At days 4 and 7, BMSCs incubated on the 3D-PDA surface presented prominent ALP activity. It has been illuminated that ALP activity is an early indicator of BMSCs differentiation into osteoblasts and osteogenesis (Birmingham et al., 2012). Hence, the 3D-printed titanium implant surface with a PDA coating could promote BMSCs osteogenic differentiation. The osteogenic gene expression levels of BMSCs were detected by using RT-PCR, and the results are shown in **Figure 3C**. Despite the fact that the COL-1 expression level of BMSCs cultivated on 3D and 3D-PDA samples presented no significant difference at day 4, all of the OCN, OPN, and BSP expression levels of BMSCs on the 3D-PDA group were dramatically higher than that on the 3D group at each timepoint. At the process of BMSCs differentiated into mature osteoblasts, the osteogenic gene expression and local factor production were intricately regulated. At the early stage of BMSCs osteogenic differentiation, the OPN and BSP facilitated osteoprogenitor cell adhesion to the mineralized extracellular matrix and the hydroxyapatite deposition, which takes an important role in the initiation of bone formation and mineralization. COL-1 is the primary component of collagen extra cell matrix, which indicates the deposition and maturation of the bone matrix (Valenti et al., 2008). At the late stage of

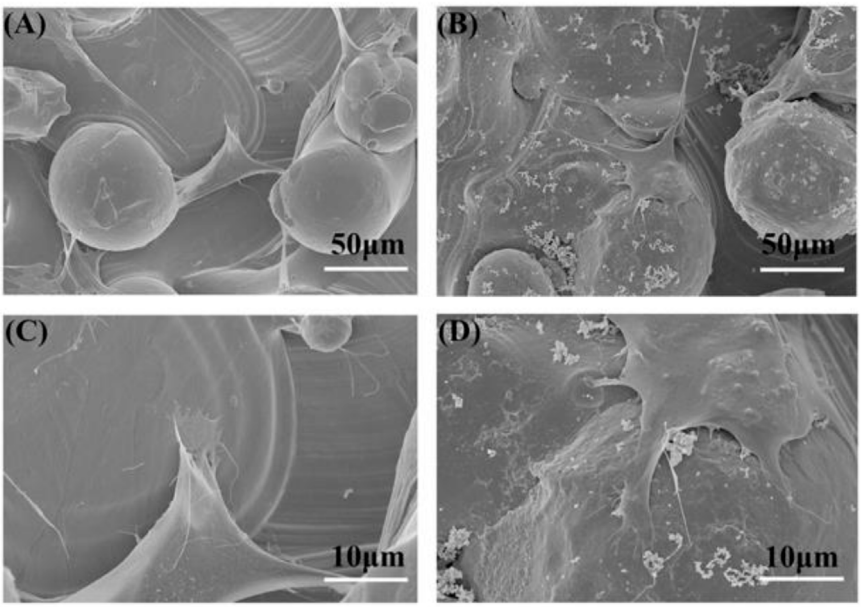

FIGURE 2 | SEM images of adherent cells on the 3D **(A,C)** and 3D-PDA **(B,D)** samples after 24 h of culture at low **(A,B)** and high **(C,D)** magnifications.

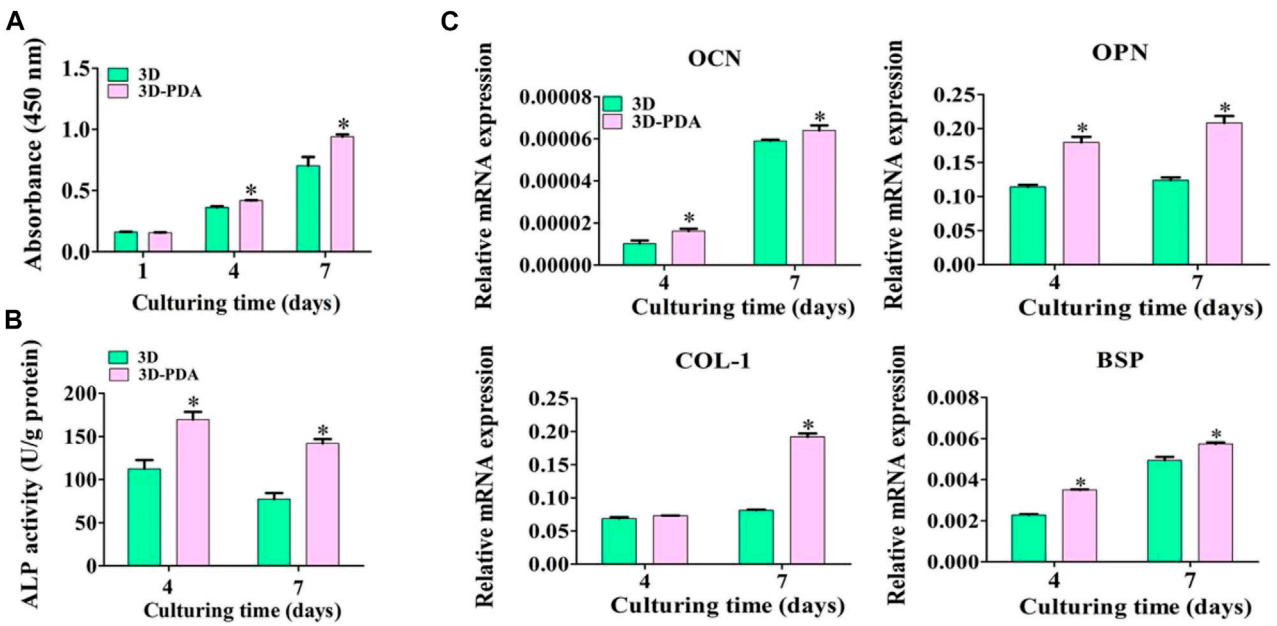

FIGURE 3 | Propagation of BMSCs on the 3D and 3D-PDA samples by CCK-8 test after seeding for 1, 4, and 7 days **(A)**. ALP activity **(B)** and RT-PCR analysis of the osteogenic gene expression levels **(C)** after culturing BMSCs for 4 and 7 days on the 3D and 3D-PDA group surfaces. *$p < 0.05$.

BMSCs osteogenic differentiation, OCN showed that premature osteoblasts developed into mature osteoblasts and bone matrix mineralization increased (Lin et al., 2013). As the above results suggested, the 3D-printed Ti6Al4V implants with a PDA coating might stimulate the osteogenic differentiation of BMSCs.

3.4 *In Vivo* Study

The *in vivo* osseointegration performance of 3D and 3D-PDA implants was studied by implanting them into rat femoral condyles for 4 weeks. As shown in **Figure 4**, compared to the 3D group, a large number of new bone tissues formed and deposited directly on the interface between the 3D-PDA

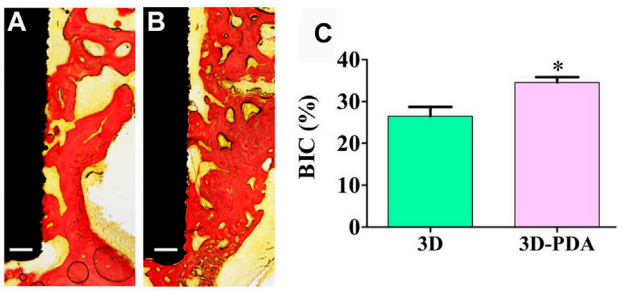

FIGURE 4 | Histological images of hard-tissue slicing of 3D **(A)** and 3D-PDA **(B)** implants after implantation at week 4, scale bar = 200 μm, histomorphometry quantitive analysis of BIC percentages on implant surfaces **(C)**; $^{*}p < 0.05$.

implant and host bone (**Figures 4A,B**). And the histomorphometry quantification analysis of BIC percentages on the different implant surfaces further demonstrated that 3D-PDA had a significantly higher BIC percentage than that of the 3D group (**Figure 4C**). The above results implied that the 3D-printed Ti6Al4V with a PDA coating owned better osseointegration ability *in vivo*.

Taking the *in vitro* and *in vivo* results into consideration together, the 3D-printed Ti6Al4V implants with a PDA coating exhibited favorable biocompatibility and osteogenic differentiation *in vitro* and osseointegration *in vivo*. The fate of implant osseointegration depends on the cell response to the implant surface. And the surface characteristics of implant materials exert a vital influence on the cell-material interactions. In the present research, the 3D-printed Ti6Al4V implant obtained superior hydrophilicity after being modified with the PDA coating. Previous research indicates that hydrophilicity plays an important role in altering cell adhesion, propagation, and osteogenic differentiation of BMSCs (Leal-Egaña et al., 2013), which was confirmed in the present study. Hence, the advantage in improving cell response to implant material surface leads to more bone matrix deposition, mineralization, and more new bone formed rapidly to stabilize the implant.

4. CONCLUSION

It is essential to improve surface characteristics, promoting the biocompatibility and osseointegration performance of personalized 3D-printed dental implants. In the present research, the 3D-printed Ti6Al4V implant surface was successfully modified with a PDA coating, which apparently increased the hydrophilicity. Furthermore, the BMSCs adhesion, propagation, and osteogenic differentiation *in vitro* and the osteointegration *in vivo* on the PDA coating-modified implant surface were dramatically enhanced. The results suggest that PDA coating might be a feasible and favorable strategy to optimize 3D-printed implant surfaces. Moreover, the study suggests a preliminary research basis for following work to immobilize bioactive factors on 3D-printed implant surfaces.

DATA AVAILABILITY STATEMENT

The raw data supporting the conclusions of this article will be made available by the authors, without undue reservation.

ETHICS STATEMENT

The animal study was reviewed and approved by the Institutional Animal Care and Use Committee of Tongji University (Shanghai, China).

AUTHOR CONTRIBUTIONS

HW performed the experiment and wrote the original draft. CY helped to prepare the manuscript and gave some conceptualization on this manuscript. KL, RZ and SZ led the conceptualization and project administration, and supervised the writing and editing of the manuscript. All authors contributed to the article and approved the submitted version.

ACKNOWLEDGMENTS

The authors acknowledge the support provided by the National Natural Science Foundation of China (82072396, 81871490), the Science and Technology Commission of Shanghai Municipality (21490711700), the Interdisciplinary Program of Shanghai Jiao Tong University (YG2021ZD12), the Program of Shanghai Academic/Technology Research Leader (19XD1434500), the Open Project of State Key Laboratory of Oral Diseases (SKLOD2021OF01), and Two-Hundred Talent (20191819).

REFERENCES

Bai, L., Du, Z., Du, J., Yao, W., Zhang, J., Weng, Z., et al. (2018). A Multifaceted Coating on Titanium Dictates Osteoimmunomodulation and Osteo/angio-Genesis towards Ameliorative Osseointegration. *Biomaterials* 162, 154–169. doi:10.1016/j.biomaterials.2018.02.010

Birmingham, E., Niebur, G. L., Niebur, G., McHugh, P., Shaw, G., Barry, F., et al. (2012). Osteogenic Differentiation of Mesenchymal Stem Cells Is Regulated by Osteocyte and Osteoblast Cells in a Simplified Bone Niche. *eCM* 23, 13–27. doi:10.22203/ecm.v023a02

Chen, Z., Bachhuka, A., Han, S., Wei, F., Lu, S., Visalakshan, R. M., et al. (2017). Tuning Chemistry and Topography of Nanoengineered Surfaces to Manipulate Immune Response for Bone Regeneration Applications. *ACS Nano* 11, 4494–4506. doi:10.1021/acsnano.6b07808

Chen, Z., Klein, T., Murray, R. Z., Crawford, R., Chang, J., Wu, C., et al. (2016). Osteoimmunomodulation for the Development of Advanced Bone Biomaterials. *Mater. Today* 19, 304–321. doi:10.1016/j.mattod.2015.11.004

Chien, C.-Y., and Tsai, W.-B. (2013). Poly(dopamine)-assisted Immobilization of Arg-Gly-Asp Peptides, Hydroxyapatite, and Bone Morphogenic Protein-2 on Titanium to Improve the Osteogenesis of Bone Marrow Stem Cells. *ACS Appl. Mater. Inter.* 5, 6975–6983. doi:10.1021/am401071f

Civitelli, R. (2008). Cell-cell Communication in the Osteoblast/osteocyte Lineage. *Arch. Biochem. Biophys.* 473, 188–192. doi:10.1016/j.abb.2008.04.005

DAr, H. Y., Azam, Z., Anupam, R., Mondal, R. K., and Srivastava, R. K. (2018). Osteoimmunology: The Nexus between Bone and Immune System. *Front. Biosci. (Landmark Ed.* 23, 464–492. doi:10.2741/4600

Figliuzzi, M., Mangano, F., and Mangano, C. (2012). A Novel Root Analogue Dental Implant Using CT Scan and CAD/CAM: Selective Laser Melting Technology. *Int. J. Oral Maxill. Surg.* 41, 858–862. doi:10.1016/j.ijom.2012.01.014

Guder, C., Gravius, S., Burger, C., Wirtz, D. C., and Schildberg, F. A. (2020). Osteoimmunology: A Current Update of the Interplay between Bone and the Immune System. *Front. Immunol.* 11, 58. doi:10.3389/fimmu.2020.00058

Han, X., and Gong, X. (2021). *In Situ*, One-Pot Method to Prepare Robust Superamphiphobic Cotton Fabrics for High Buoyancy and Good Antifouling. *ACS Appl. Mater. Inter.* 13, 31298–31309. doi:10.1021/acsami.1c08844

Hotchkiss, K. M., Reddy, G. B., Hyzy, S. L., Schwartz, Z., Boyan, B. D., and Olivares-Navarrete, R. (2016). Titanium Surface Characteristics, Including Topography and Wettability, Alter Macrophage Activation. *Acta Biomater.* 31, 425–434. doi:10.1016/j.actbio.2015.12.003

Jin, A., Wang, Y., Lin, K., and Jiang, L. (2020). Nanoparticles Modified by Polydopamine: Working as "Drug" Carriers. *Bioactive Mater.* 5, 522–541. doi:10.1016/j.bioactmat.2020.04.003

Koh, R. U., Rudek, I., and Wang, H.-L. (2010). Immediate Implant Placement: Positives and Negatives. *Implant Dent.* 19, 98–108. doi:10.1097/id.0b013e3181d47eaf

Ku, S. H., Ryu, J., Hong, S. K., Lee, H., and Park, C. B. (2010). General Functionalization Route for Cell Adhesion on Non-wetting Surfaces. *Biomaterials* 31, 2535–2541. doi:10.1016/j.biomaterials.2009.12.020

Landén, N. X., Li, D., and Ståhle, M. (2016). Transition from Inflammation to Proliferation: a Critical Step during Wound Healing. *Cell. Mol. Life Sci.* 73, 3861–3885. doi:10.1007/s00018-016-2268-0

Leal-Egaña, A., Díaz-Cuenca, A., and Boccaccini, A. R. (2013). Tuning of Cell-Biomaterial Anchorage for Tissue Regeneration. *Adv. Mater.* 25, 4049–4057.

Lebaron, R. G., and Athanasiou, K. A. (2000). Extracellular Matrix Cell Adhesion Peptides: Functional Applications in Orthopedic Materials. *Tissue Eng.* 6, 85–103. doi:10.1089/107632700320720

Lee, H., Rho, J., and Messersmith, P. B. (2009). Facile Conjugation of Biomolecules onto Surfaces via Mussel Adhesive Protein Inspired Coatings. *Adv. Mater.* 21, 431–434. doi:10.1002/adma.200801222

Li, D., Li, Y., Shrestha, A., Wang, S., Wu, Q., Li, L., et al. (2019). Effects of Programmed Local Delivery from a Micro/Nano-Hierarchical Surface on Titanium Implant on Infection Clearance and Osteogenic Induction in an Infected Bone Defect. *Adv. Healthc. Mater.* 8, 1900002. doi:10.1002/adhm.201900002

Li, M., Liu, X., Xu, Z., Yeung, K. W. K., and Wu, S. (2016). Dopamine Modified Organic-Inorganic Hybrid Coating for Antimicrobial and Osteogenesis. *ACS Appl. Mater. Inter.* 8, 33972–33981. doi:10.1021/acsami.6b09457

Lin, K., Xia, L., Gan, J., Zhang, Z., Chen, H., Jiang, X., et al. (2013). Tailoring the Nanostructured Surfaces of Hydroxyapatite Bioceramics to Promote Protein Adsorption, Osteoblast Growth, and Osteogenic Differentiation. *ACS Appl. Mater. Inter.* 5, 8008–8017. doi:10.1021/am402089w

Liu, L., Wang, X., Zhou, Y., Cai, M., Lin, K., Fang, B., et al. (2020). The Synergistic Promotion of Osseointegration by Nanostructure Design and Silicon Substitution of Hydroxyapatite Coatings in a Diabetic Model. *J. Mater. Chem. B* 8, 2754–2767. doi:10.1039/c9tb02882j

Oladapo, B. I., Zahedi, S. A., Ismail, S. O., Omigbodun, F. T., Bowoto, O. K., Olawumi, M. A., et al. (2021). 3D Printing of PEEK-cHAp Scaffold for Medical Bone Implant. *Bio-des. Manuf.* 4, 44–59. doi:10.1007/s42242-020-00098-0

Owji, N., Mandakhbayar, N., Gregory, D. A., Marcello, E., Kim, H.-w., Roy, I., et al. (2021). Mussel Inspired Chemistry and Bacteria Derived Polymers for Oral Mucosal Adhesion and Drug Delivery. *Front. Bioeng. Biotechnol.* 9, 663764. doi:10.3389/fbioe.2021.663764

Poh, C. K., Shi, Z., Lim, T. Y., Neoh, K. G., and Wang, W. (2010). The Effect of VEGF Functionalization of Titanium on Endothelial Cells *In Vitro*. *Biomaterials* 31, 1578–1585. doi:10.1016/j.biomaterials.2009.11.042

Shah, F. A., Snis, A., Matic, A., Thomsen, P., and Palmquist, A. (2016). 3D Printed Ti6Al4V Implant Surface Promotes Bone Maturation and Retains a Higher Density of Less Aged Osteocytes at the Bone-Implant Interface. *Acta Biomater.* 30, 357–367. doi:10.1016/j.actbio.2015.11.013

Shimabukuro, M., Tsutsumi, Y., Yamada, R., Ashida, M., Chen, P., Doi, H., et al. (2019). Investigation of Realizing Both Antibacterial Property and Osteogenic Cell Compatibility on Titanium Surface by Simple Electrochemical Treatment. *ACS Biomater. Sci. Eng.* 5, 5623–5630. doi:10.1021/acsbiomaterials.8b01058

Sidambe, A. (2014). Biocompatibility of Advanced Manufactured Titanium Implants-A Review. *Materials* 7, 8168–8188. doi:10.3390/ma7128168

Stewart, C., Akhavan, B., Wise, S. G., and Bilek, M. M. M. (2019). A Review of Biomimetic Surface Functionalization for Bone-Integrating Orthopedic Implants: Mechanisms, Current Approaches, and Future Directions. *Prog. Mater. Sci.* 106, 100588. doi:10.1016/j.pmatsci.2019.100588

Tang, Y., Tan, Y., Lin, K., and Zhu, M. (2021). Research Progress on Polydopamine Nanoparticles for Tissue Engineering. *Front. Chem.* 9, 727123. doi:10.3389/fchem.2021.727123

Valenti, M. T., Carbonare, L. D., Donatelli, L., Bertoldo, F., Zanatta, M., and Lo Cascio, V. (2008). Gene Expression Analysis in Osteoblastic Differentiation from Peripheral Blood Mesenchymal Stem Cells. *Bone* 43, 1084–1092. doi:10.1016/j.bone.2008.07.252

van Noort, R. (2012). The Future of Dental Devices Is Digital. *Dental Mater.* 28, 3–12. doi:10.1016/j.dental.2011.10.014

Vijayavenkataraman, S., Gopinath, A., and Lu, W. F. (2020). A New Design of 3D-Printed Orthopedic Bone Plates with Auxetic Structures to Mitigate Stress Shielding and Improve Intra-operative Bending. *Bio-des. Manuf.* 3, 98–108. doi:10.1007/s42242-020-00066-8

Wang, H., Liu, J., Wang, C., Shen, S. G., Wang, X., and Lin, K. (2021). The Synergistic Effect of 3D-Printed Microscale Roughness Surface and Nanoscale Feature on Enhancing Osteogenic Differentiation and Rapid Osseointegration. *J. Mater. Sci. Techn.* 63, 18–26. doi:10.1016/j.jmst.2019.12.030

Wang, H., Zhang, X., Wang, H., Zhang, J., Li, J., Ruan, C., et al. (2018). Enhancing the Osteogenic Differentiation and Rapid Osseointegration of 3D Printed Ti6Al4V Implants via Nano-Topographic Modification. *J. Biomed. Nanotechnol.* 14, 707–715. doi:10.1166/jbn.2018.2551

Wang, X., Zhao, H., Liu, Z., Wang, Y., Lin, D., Chen, L., et al. (2021). Polydopamine Nanoparticles as Dual-Task Platform for Osteoarthritis Therapy: A Scavenger for Reactive Oxygen Species and Regulator for Cellular Powerhouses. *Chem. Eng. J.* 417, 129284. doi:10.1016/j.cej.2021.129284

Wei, D. W., Wei, H., Gauthier, A. C., Song, J., Jin, Y., and Xiao, H. (2020). Superhydrophobic Modification of Cellulose and Cotton Textiles: Methodologies and Applications. *J. Bioresources Bioproducts* 5, 1–15. doi:10.1016/j.jobab.2020.03.001

Xi, Z.-Y., Xu, Y.-Y., Zhu, L.-P., Wang, Y., and Zhu, B.-K. (2009). A Facile Method of Surface Modification for Hydrophobic Polymer Membranes Based on the Adhesive Behavior of Poly(DOPA) and Poly(dopamine). *J. Membr. Sci.* 327, 244–253. doi:10.1016/j.memsci.2008.11.037

Xia, L., Xie, Y., Fang, B., Wang, X., and Lin, K. (2018). *In Situ* modulation of Crystallinity and Nano-Structures to Enhance the Stability and Osseointegration of Hydroxyapatite Coatings on Ti-6Al-4V Implants. *Chem. Eng. J.* 347, 711–720. doi:10.1016/j.cej.2018.04.045

Xue, T., Attarilar, S., Liu, S., Liu, J., Song, X., Li, L., et al. (2020). Surface Modification Techniques of Titanium and its Alloys to Functionally Optimize Their Biomedical Properties: Thematic Review. *Front. Bioeng. Biotechnol.* 8, 603072. doi:10.3389/fbioe.2020.603072

Zeng, J., Wang, Y., Sun, Z., Chang, H., Cao, M., Zhao, J., et al. (2020). A Novel Biocompatible PDA/IR820/DAP Coating for Antibiotic/photodynamic/photothermal Triple Therapy to Inhibit and Eliminate Staphylococcus aureus Biofilm. *Chem. Eng. J.* 394, 125017. doi:10.1016/j.cej.2020.125017

Zhang, C., Zhang, T., Geng, T., Wang, X., Lin, K., and Wang, P. (2021). Dental Implants Loaded with Bioactive Agents Promote Osseointegration in Osteoporosis: A Review. *Front. Bioeng. Biotechnol.* 9, 591796. doi:10.3389/fbioe.2021.591796

Zhang, J., Liu, J., Wang, C., Chen, F., Wang, X., and Lin, K. (2020). A Comparative Study of the Osteogenic Performance between the Hierarchical Micro/

submicro-Textured 3D-Printed Ti6Al4V Surface and the SLA Surface. *Bioactive Mater.* 5, 9–16. doi:10.1016/j.bioactmat.2019.12.008

Zhang, J., Zhang, L., and Gong, X. (2021). Large-Scale Spraying Fabrication of Robust Fluorine-free Superhydrophobic Coatings Based on Dual-Sized Silica Particles for Effective Antipollution and Strong Buoyancy. *Langmuir* 37, 6042–6051. doi:10.1021/acs.langmuir.1c00706

Zhang, J., Zhou, W., Wang, H., Lin, K., and Chen, F. (2019). 3D-printed Surface Promoting Osteogenic Differentiation and Angiogenetic Factor Expression of BMSCs on Ti6Al4V Implants and Early Osseointegration *In Vivo*. *J. Mater. Sci. Techn.* 35, 336–343. doi:10.1016/j.jmst.2018.09.063

Zhang, P., Yang, K., Zhou, Z., Zhu, X., Li, W., Cao, C., et al. (2020). Customized Borosilicate Bioglass Scaffolds with Excellent Biodegradation and Osteogenesis for Mandible Reconstruction. *Front. Bioeng. Biotechnol.* 8, 610284. doi:10.3389/fbioe.2020.610284

Zhang, T., Jiang, M., Yin, X., Yao, P., and Sun, H. (2021). Mechanism of Exosomes Involved in Osteoimmunity Promoting Osseointegration Around Titanium Implants with Small-Scale Topography. *Front. Bioeng. Biotechnol.* 9, 682384. doi:10.3389/fbioe.2021.682384

Zhang, X., Li, H., Liu, J., Wang, H., Sun, W., Lin, K., et al. (2019). Amorphous Carbon Modification on Implant Surface: a General Strategy to Enhance Osteogenic Differentiation for Diverse Biomaterials via FAK/ERK1/2 Signaling Pathways. *J. Mater. Chem. B* 7, 2518–2533. doi:10.1039/c8tb02850h

Zhao, L., Mei, S., Chu, P. K., Zhang, Y., and Wu, Z. (2010). The Influence of Hierarchical Hybrid Micro/nano-Textured Titanium Surface with Titania Nanotubes on Osteoblast Functions. *Biomaterials* 31, 5072–5082. doi:10.1016/j.biomaterials.2010.03.014

Zhuang, Y., Zhang, C., Cheng, M., Huang, J., Liu, Q., Yuan, G., et al. (2021). Challenges and Strategies for *In Situ* Endothelialization and Long-Term Lumen Patency of Vascular Grafts. *Bioactive Mater.* 6, 1791–1809. doi:10.1016/j.bioactmat.2020.11.028

Conflict of Interest: The authors declare that the research was conducted in the absence of any commercial or financial relationships that could be construed as a potential conflict of interest.

Publisher's Note: All claims expressed in this article are solely those of the authors and do not necessarily represent those of their affiliated organizations, or those of the publisher, the editors and the reviewers. Any product that may be evaluated in this article, or claim that may be made by its manufacturer, is not guaranteed or endorsed by the publisher.

Copyright © 2021 Wang, Yuan, Lin, Zhu and Zhang. This is an open-access article distributed under the terms of the Creative Commons Attribution License (CC BY). The use, distribution or reproduction in other forums is permitted, provided the original author(s) and the copyright owner(s) are credited and that the original publication in this journal is cited, in accordance with accepted academic practice. No use, distribution or reproduction is permitted which does not comply with these terms.

frontiers in Bioengineering and Biotechnology

ORIGINAL RESEARCH
published: 04 January 2022
doi: 10.3389/fbioe.2021.788574

Enhanced Spontaneous Antibacterial Activity of δ-MnO_2 by Alkali Metals Doping

Yali Yan[1†], Ning Jiang[2†], Xin Liu[3], Jie Pan[4,5]*, Mai Li[1], Chunrui Wang[1], Pedro H. C. Camargo[6] and Jiale Wang[1,7]**

[1]College of Science, Donghua University, Shanghai, China, [2]Department of Oral and Craniomaxillofacial Science, Shanghai Key Laboratory of Stomatology, College of Stomatology, Ninth People's Hospital, Shanghai Jiao Tong University School of Medicine, Shanghai, China, [3]Department of Dental Materials, Shanghai Key Laboratory of Stomatology, Shanghai Biomaterials Research and Testing Center, National Center for Stomatology, National Clinical Research Center for Oral Diseases, Shanghai Ninth People's Hospital, Shanghai Jiao Tong University School of Medicine, College of Stomatology, Shanghai Jiao Tong University, Shanghai, China, [4]Department of Orthodontics, Shanghai Stomatological Hospital, Fudan University, Shanghai, China, [5]Shanghai Key Laboratory of Craniomaxillofacial Development and Diseases, Fudan University, Shanghai, China, [6]Department of Chemistry, University of Helsinki, Helsinki, Finland, [7]Shanghai Institute of Intelligent Electronics and Systems, Donghua University, Shanghai, China

OPEN ACCESS

Edited by:
Rui Guo,
Jinan University, China

Reviewed by:
Ehsan Nazarzadeh Zare,
Damghan University, Iran
Yan Li,
Sun Yat-sen University, China

***Correspondence:**
Xin Liu
liuxin0556@163.com
Jie Pan
jiepan@fudan.edu.cn
Jiale Wang
jiale.wang@dhu.edu.cn

†These authors have contributed equally to this work

Specialty section:
This article was submitted to Biomaterials, a section of the journal Frontiers in Bioengineering and Biotechnology

Received: *02 October 2021*
Accepted: *15 November 2021*
Published: *04 January 2022*

Citation:
Yan Y, Jiang N, Liu X, Pan J, Li M, Wang C, Camargo PHC and Wang J (2022) Enhanced Spontaneous Antibacterial Activity of δ-MnO_2 by Alkali Metals Doping. Front. Bioeng. Biotechnol. 9:788574. doi: 10.3389/fbioe.2021.788574

Recently, the widespread use of antibiotics is becoming a serious worldwide public health challenge, which causes antimicrobial resistance and the occurrence of superbugs. In this context, MnO_2 has been proposed as an alternative approach to achieve target antibacterial properties on *Streptococcus* mutans (S. mutans). This requires a further understanding on how to control and optimize antibacterial properties in these systems. We address this challenge by synthesizing δ-MnO_2 nanoflowers doped by magnesium (Mg), sodium (Na), and potassium (K) ions, thus displaying different bandgaps, to evaluate the effect of doping on the bacterial viability of S. mutans. All these samples demonstrated antibacterial activity from the spontaneous generation of reactive oxygen species (ROS) without external illumination, where doped MnO_2 can provide free electrons to induce the production of ROS, resulting in the antibacterial activity. Furthermore, it was observed that δ-MnO_2 with narrower bandgap displayed a superior ability to inhibit bacteria. The enhancement is mainly attributed to the higher doping levels, which provided more free electrons to generate ROS for antibacterial effects. Moreover, we found that δ-MnO_2 was attractive for *in vivo* applications, because it could nearly be degraded into Mn ions completely following the gradual addition of vitamin C. We believe that our results may provide meaningful insights for the design of inorganic antibacterial nanomaterials.

Keywords: MnO_2, doping, antibacterial property, reactive oxygen species, alkali metal ions

INTRODUCTION

Manganese oxides (MnO_2) have been extensively studied due to the structural multiformity. The various structures, corresponding to different chemical and physical properties, have been widely applied in catalysis, batteries, sensors, molecular sieves, energy storage, etc. (Dawadi et al., 2020; Ye et al., 2020; Marciniuk et al., 2021; Ouyang et al., 2021; Wang et al., 2021). Particularly, δ-MnO_2 has attracted considerable attention due to its unique layered structure, where its bandgap can be tuned

by filling ions between the layers (Luo et al., 2000; Wang et al., 2017). Herein, δ-MnO_2 samples with different bandgaps, doped by alkali metals such as magnesium (Mg), sodium (Na), or potassium (K), has been used as antibacterial materials.

Recently, the abuse of antibiotics is becoming a serious worldwide public health challenge, which causes antimicrobial resistance and the occurrence of superbugs (Podder et al., 2018; Teng et al., 2020). It not only prolongs treatment but also declines life expectancy due to higher morbidity/mortality risk (Podder et al., 2018; Liu et al., 2020; Estes et al., 2021). These serious public health challenges require the development of new bactericidal methods (Herman and Herman, 2014; Gatadi et al., 2021). With the development of nanotechnology, new antibacterial agents have arisen (Herman and Herman, 2014; Liu et al., 2020). These nanoscale agents may provide more effective and/or more convenient routes (Dizaj et al., 2014; Herman and Herman, 2014). Particularly, nanomaterials based on inorganic metal oxide semiconductors, i.e., CuO, ZnO, MgO, etc., have been considered as alternative antibacterial materials (Zhang et al., 2010; Bafekr and Jalal, 2018; Hong et al., 2018; Chandra et al., 2019; Ogunyemi et al., 2020; Zhang et al., 2010; Baruah et al., 2021; Haider et al., 2021; Han et al., 2021; Qian et al., 2021), whose activities can easily be tuned by altering their morphology and/or component (Prasanna and Vijayaraghavan, 2015).

Generally, reactive oxygen species (ROS) can injure biomolecules by its strong oxidation potential (Sharifi et al., 2012; Prasanna and Vijayaraghavan, 2015; Podder et al., 2018; Yao et al., 2020). The oxidant activity of metal oxide semiconductor nanomaterials usually originates from light-induced oxidative properties to generate ROS, including hydroxyl radicals (·OH), superoxide anions radicals ($\cdot O_2^-$), and singlet oxygen ($^1O_2$) (Podder et al., 2018). The generation of ROS under light exposure comes from the photo-generated electron-hole pairs excited on the appropriate band levels through the absorption of light, which interact with water and then produce ROS (Hirakawa and Nosaka, 2002; Prasanna and Vijayaraghavan, 2015). In addition to photoexcitation, the ROS can also be produced by electrons trapped by the defects at the surface of materials in the absence of light (Prasanna and Vijayaraghavan, 2015; Hao et al., 2017). However, we found that doped agents, which can provide free electrons to induce the production of ROS, also result in the antibacterial activity without external light exposure. MnO_2 has five different phases (α, β, γ, λ, and δ) and the different properties of each phase make it be extensively studied in the fields of catalysis (Suib, 2008; Truong et al., 2012; Zhou et al., 2017). Moreover, MnO_2 can effectively enhance the produce of ·OH in the aqueous solution *via* the excitation and formation of electron-hole pairs (Das et al., 2017; Xiao et al., 2018; Chhabra et al., 2019). Particularly, δ-MnO_2, with a unique layered crystalline structure, has aroused much investigation. By changing the quantity of filling ions between MnO_2 layers, its doping level can easily be tuned (Golden et al., 1986; Luo et al., 2008; Geng et al., 2016).

We report herein the synthesis of δ-MnO_2 nanoflowers doped by Mg, Na, and K ions to evaluate the effect of doping on the bacterial viability of *Streptococcus* mutans (S. mutans), a recognized cariogenic bacterium (Song et al., 2020; Afrasiabi et al., 2021). Here, the antibacterial properties of δ-MnO_2 were probed in the dark (without external illumination). It was observed that all δ-MnO_2 nanoflowers demonstrated an excellent antibacterial activity without external light exposure. Our data showed that in doped MnO_2 nanoflowers the free electrons due to doping could induce the production of ROS, resulting in the antibacterial activity. Moreover, δ-MnO_2 nanoflowers with narrower bandgap displayed a superior antibacterial ability, in which higher doping levels, providing more free electrons to induce the production of ROS, led to better antibacterial properties (following the order: $K^+ > Na^+ > Mg^{2+}$). Furthermore, following the gradual addition of vitamin C, the δ-MnO_2 could nearly be degraded into Mn ions completely, making this materials potential for *in vivo* applications (Liu et al., 2021).

EXPERIMENTAL SECTION

Materials and Instrumentation

Potassium permanganate ($KMnO_4$, >99.5%, Sinopharm), sodium permanganate monohydrate ($NaMnO_4 \cdot H_2O$, ≥97%, Sigma-Aldrich), magnesium permanganate hydrate ($Mg(MnO_4)_2 \cdot xH_2O$, Sigma-Aldrich), manganese sulfate monohydrate ($MnSO_4 \cdot H_2O$, >99.0%, Sigma-Aldrich), superoxide dismutase (SOD, 15KU, Gunn reagent), vitamin C (VC, 99%, Adamas), and all the chemicals were used without any further purification. De-ionized (DI) water (18.2 MΩ) was used throughout the experiments.

SEM images were obtained by field-emission scanning electron microscopy (FESEM, Hitachi S-4800) which worked at 5 kV. To prepare the samples of SEM, the aqueous suspension including the nanoflowers was dripped on a Si wafer, followed by drying under the air condition. HRTEM images were obtained with a high-resolution transmission electron microscopy (HRTEM, TECHAI G2S-TWIN) operated at 200 kV. To prepare the samples of HRTEM, the alcoholic suspension including the nanoflowers was dripped on a copper grid, followed by drying under the air condition. UV-VIS spectra were obtained from the powder of MnO_2 with a Shimadzu UV-3600 spectrophotometer. X-ray diffraction (XRD) was characterized by a Rigaku D/Max-2550. X-ray photoelectron spectroscopy (XPS) was carried out using a Thermo Science ESCALAB 250Xi with monochromatic Al Kα (1486.7 eV). The binding energy (BE) was scaled, which regarded the C 1s line at 284.6 eV as the standard for calibration. All data were processed by using the CasaXPS software. The electron spin resonance (ESR) spectra were conducted on a Bruker A300 Electron Paramagnetic Resonance (EPR) Spectrometer.

Synthesis of MnO_2 Nanoflowers

MnO_2 nanoflowers were synthesized through hydrothermal methods as reported previously (Hu et al., 2019; Zhu et al., 2019). For K-doped MnO_2 nanoflowers, 1.0 g $KMnO_4$ and 0.4 g $MnSO_4$ were added into the Teflon-lined stainless steel autoclave, together with 30 ml DI water. After stirring for 30 min, the Teflon-lined stainless-steel autoclave was heated and stirred at

140°C for 1 h and then cooled down to room temperature. The obtained MnO_2 nanoflowers were washed three times with ethanol and three times with DI water by successive cycles of centrifugation and removal of supernatant. Finally, the materials were dried at 60°C for 12 h in a vacuum oven for further use. The Na-doped and Mg-doped samples were prepared with the same procedure, except that the 1.0 g $KMnO_4$ was replaced by 1.012 g $NaMnO_4{\cdot}H_2O$ or 0.84 g $Mg(MnO_4)_2{\cdot}xH_2O$, respectively.

Bacteria Culture of *Streptococcus* Mutans

Streptococcus mutans (S. mutans) (UA159) were obtained from Shanghai Key Laboratory of Stomatology, Ninth People's Hospital, Shanghai Jiao Tong University School of Medicine (Shanghai, China). S. mutans was cultured in brain heart infusion broth (BHI broth, Difco laboratories, United States) at 37°C in anaerobic system (N_2 80%, H_2 10%, CO_2 10%). Bacteria were harvested at the exponential growth phase for the use of subsequent experiments.

Bacterial Viability Test by MTT Assay

The bacterial viability was assessed by 3-[4,5-dimethylthiazol-2-yl]-2,5-diphenyl tetrazolium bromide (MTT) assay. Briefly, S. mutans suspensions at a density of 1×10^6 colony forming units (CFUs)/ml were treated with the different concentrations of Mg-, Na-, and K-doped MnO_2 nanoflowers (100, 200, 400, and 800 μg/ml) in BHI at 37°C under standard anaerobic conditions (N_2 80%, H_2 10%, CO_2 10%) for 24 h. After 24 h of anaerobic culture, 5 mg/ml MTT solution was added to each well and incubated in dark for 2 h. The supernatant was discarded, and the substrate was reacted in solution by dimethyl sulfoxide (DMSO). The absorbance was tested at 490 nm wavelength using a microplate reader (Bio-Rad, United States). All samples were performed in triplicate. The negative control was the S. mutans group without MnO_2 nanoflowers treatment. By comparing the OD values (490 nm) of the negative control with that of Mg-, Na-, and K-doped MnO_2 nanoflowers, the inhibition percentage of bacterial viability was calculated by using the equation: [(OD (negative control)-OD (sample))/OD (negative control)]×100%.

Biofilm Formation Test by Crystal Violet Assay

Firstly, 1 × 1 cm sterile glass slides were placed in a 24-well plate, and 50 μl ~10^6 CFU/ml S. mutans was added to each well. Then, 150 μl suspensions with different concentrations of Mg-, Na-, and K-doped MnO_2 nanoflowers (100, 200, 400, and 800 μg/ml) were added into the mixture, respectively. In addition, 200 μl ~10^6 CFU/ml S. mutans was added to the control wells and anaerobically cultured for 24 h at 37°C. After 24 h of anaerobic culture, the crystal violet was fixed with methanol, stained with 0.1% (w/v) crystal violet, moistened with sterile double steam water, and washed overnight. After drying, the crystal violet was dissolved with 90% ethanol and the absorbance was tested at 550 nm wavelength using a microplate reader (Bio-Rad, United States). All samples were performed in triplicate. The negative control was the biofilm without MnO_2 nanoflowers. By comparing the OD values (550 nm) of the negative control with that of Mg-, Na-, and K-doped MnO_2 nanoflowers, the inhibition percentage of biofilm formation was calculated by using the equation: [(OD (negative control)-OD (sample))/OD (growth control)]×100%

In vitro Cytotoxicity Assays

The mouse fibroblast cell line (L929) was obtained from the cell bank of the Chinese Academy of Sciences (Shanghai, China) and cultured in minimum essential medium (Gibco, Life Technologies, Carlsbad, CA) supplemented with 10% fetal bovine serum and 100 U/ml penicillin–streptomycin (Gibco, CA), at 37°C and 5% CO_2 humidified atmosphere. Cells without any exposure to nanoparticles served as the negative control. Cytotoxicity was assessed by using the MTT assay. Briefly, to evaluate the mitochondrial function and cell viability of L929 cells treated with different concentrations of Mg-, Na-, and K-doped MnO_2 nanoflowers (100, 200, 400, and 800 μg/ml), cells were seeded at a density of 10^4 cells/well on 96-well plates and then treated with particles at different concentrations for 24 h. After 24 h treatment, MTT solution (20 μl, 5 mg/ml) (Amersco, Solon, OH, United States) was added into each well and incubated for an additional 4 h in 37°C incubator. Subsequently, 150 μl DMSO was added to dissolve the formazan crystals. The absorbance at 570 and 630 nm was measured by a microplate reader (Multiskan GO, Thermo Scientific, MA, United States).

ESR Determination

ESR spectroscopy was employed to detect ROS using 5,5-dimethyl-1-pyrroline-N-oxide (DMPO) as a spin trap (Bosnjakovic and Schlick, 2006; Szterk et al., 2011). DMPO traps ·OH to form DMPO–·OH spin adduct which gives a quadrant signal. It also traps $\cdot O_2^-$ to form DMPO–·O_2^- spin adduct which also gives a quadrant signal. To suspension of MnO_2, DMPO was added and the ESR spectra were recorded. All the experiments were performed in dark.

The Calculation of Atomic Ratios

Take K-doped MnO_2 nanoflowers as example, the atomic radio between Mn and K was obtained with the quantitative analysis of high-resolution XPS spectra. We regarded I^{Mn} and I^K as the Mn and K intensities from one Mn and K atom, respectively. The total intensities of Mn $2p_{3/2}$ and K $2p_{3/2}$ can be expressed by following expression (Hu et al., 2019; Zhu et al., 2019):

$$I_{(TOT)}(\mathrm{Mn\ 2p}) = \frac{I^{Mn}k^{Mn}}{1-k^2} \quad (1)$$

$$I_{(TOT)}(\mathrm{K\ 2p}) = \frac{I^{K}k^{K}}{1-k^2} \quad (2)$$

where the layer-by-layer attenuation factor is given by $k = \exp(-c/\lambda \sin\theta)$. The c is the depth of atoms, λ is the photoelectron inelastic mean free path, and θ is the takeoff angle relative to the sample surface. Owing to the isotropic property of nanoflowers, k

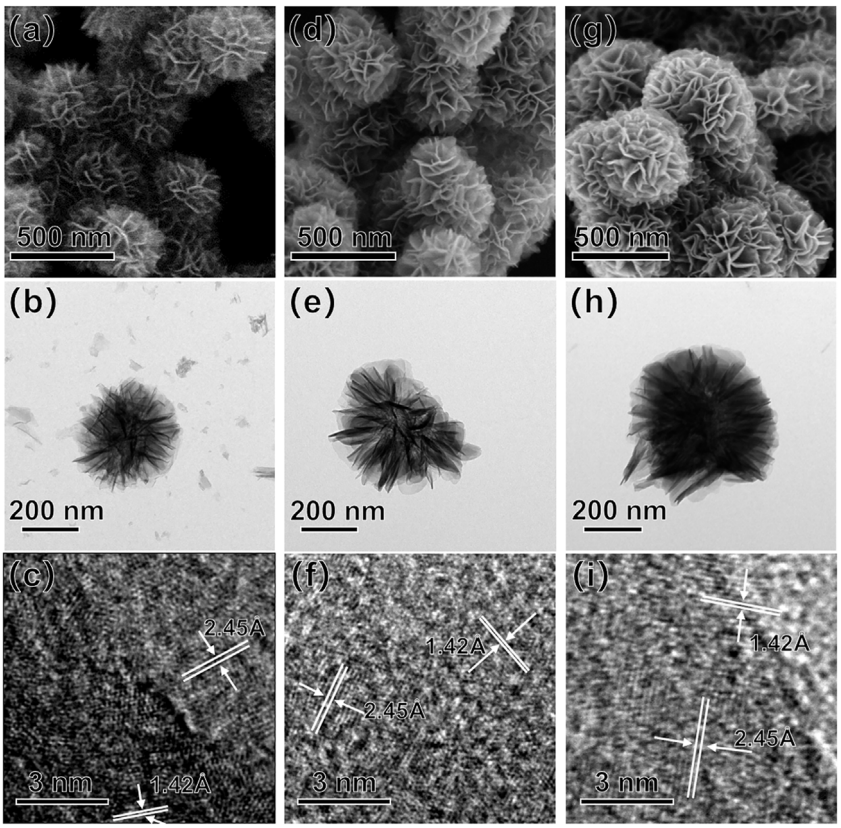

FIGURE 1 | SEM **(A,D,G)**, TEM **(B,E,H)**, and HRTEM **(C,F,I)** images of Mg-, Na-, and K-doped δ-MnO_2 nanoflowers.

should be integrated to obtain the average. Thus, the layer-by-layer attenuation factor is given by the following expression:

$$k = \frac{\int_0^{\pi} \exp\left(-\frac{c}{\lambda \sin\theta}\right) d\theta}{\int_0^{\pi} d\theta} \quad (3)$$

The parameter c can be obtained by XRD. The photoelectron inelastic mean free path (λ_{Mn} = 1.73 nm, λ_K = 2.25 nm) was calculated by using the National Institute of Standards and Technology (NIST) database.

RESULTS AND DISCUSSION

We started by using $Mg(MnO_4)_2$ as precursor to synthesize Mg-doped δ-MnO_2 materials. **Figure 1A** shows the SEM image of Mg-doped MnO_2, which presented a flower-like morphology and the size was ~380 nm in diameter. **Supplementary Figure S1A** shows the XRD patterns of Mg-doped δ-MnO_2 nanoflowers. All the peaks correspond to the crystal planes of δ-MnO_2 (Hu et al., 2019; Li et al., 2019), and no other crystalline phases were detected. **Figures 1B,C** present the TEM and HRTEM images of Mg-doped MnO_2 nanoflowers. The lattice spacings of 1.42 and 2.45 Å coincide with the (110) and (101) interlayer distance in δ-MnO_2. This is also supported by the SAED patters shown in **Supplementary Figure S2A**.

The band gap for the Mg-doped MnO_2 nanoflowers was calculated as 1.13 eV from the UV-VIS spectrum shown in **Supplementary Figure S3A**. The narrower bandgap observed here relative to the previously reported (Sakai et al., 2005; John et al., 2016) might be attributed to the doping of Mg^{2+} ions between layers of MnO_2 (Luo et al., 2000; Wang et al., 2017; Hu et al., 2019; Zhu et al., 2019), which will be discussed later.

Figure 2A shows the XPS survey spectrum of Mg-doped MnO_2. It was detected that, with a ~15 min UV exposure, surface C contamination has a ~8 times minor intensity relative to that of Mn $2p_{3/2}$. The binding energy (BE) values of different elements were presented in **Supplementary Table S1**. The Mn $2p_{3/2}$ core-level spectrum in **Figure 2D** presented two components. The main peak labeled I with low BE at 642.3 eV is due to bulk-coordinated Mn, and the other peak with high BE at 645.1 eV (peak II) corresponds to MnO_2 interacted with absorbed oxygen from air (Selvakumar et al., 2015; Li et al., 2017; Hu et al., 2019; Tang et al., 2020). However, no signal corresponding to reduced Mn^{3+}, which is known to occur as a result of the formation of oxygen vacancies, was observed (Selvakumar et al., 2015). **Figure 2E** shows the O 1s core-level spectrum, which presented three components. The main peak (BE 529.9 eV)

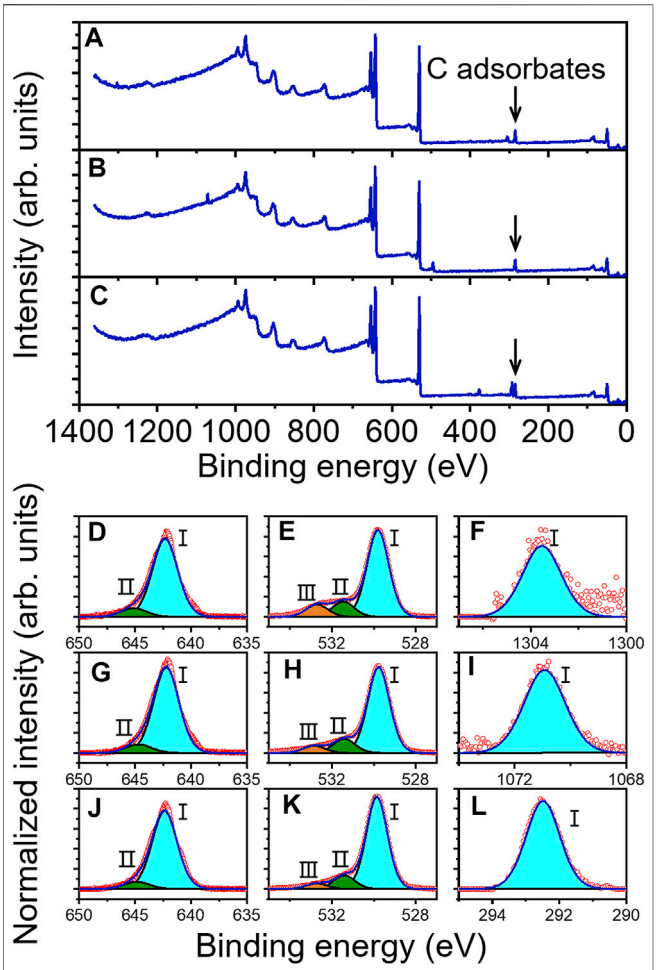

FIGURE 2 | Survey XPS scan of **(A)** Mg-doped, **(B)** Na-doped, and **(C)** K-doped δ-MnO_2 nanoflowers. Core-level spectra for Mg-doped **(D–F)**, Na-doped **(G–I)**, and K-doped δ-MnO_2 nanoflowers **(J–L)**: **(D,G,J)** Mn $2p_{3/2}$, **(E,H,K)** O 1s, **(F)** Mg 1s, **(I)** Na 1s, and **(L)** K $2p_{3/2}$.

labeled I is due to bulk-coordinated oxygen. Peak II (BE 531.5 eV) and peak III (BE 532.9 eV) are attributed to the surface component and the carbonate or hydroxyl groups chemically bound on the surface, respectively (Tang et al., 2020; Arunpandiyan et al., 2021). **Figure 2F** presents the Mg 1s spectrum which only has one component. The BE of Mg 1s is 1303.5 eV, which is higher than that of Mg_2Si (~1302.3 eV) and $Mg(OH)_2$ (~1303 eV) (Esaka et al., 2016; Jiang et al., 2017). The results indicate that Mg^{2+} is chemically bound to MnO_2 (Nefedov, 1977). In the Mg 1s spectrum only one component was observed, suggesting that all Mg^{2+} ions were filled between the MnO_2 layers (Hu et al., 2019).

Since the biocompatibility of materials is a prerequisite for their intended use in the human body, *in vitro* cytotoxicity studies of Mg-doped MnO_2 nanoflowers were carried out prior to antibacterial testing. Specifically, L929 mouse fibroblastic cells were exposed for 24 h to different concentrations (0, 100, 200, 400, and 800 μg/ml) of MnO_2 nanoflowers and then the cell viability was determined using the MTT assay, a well-established colorimetric method to evaluate the cytotoxicity of biomedical device according to ISO 10993-5:2009. After 24 h of incubation, the cell viability of L929 cells was more than 90% with the concentration of Mg-doped MnO_2 nanoflowers at 100–400 μg/ml, whereas it was reduced to 66 ± 5.7% when the dose was increased up to 800 μg/ml (**Supplementary Figure S4**), suggesting that the MnO_2 nanoflowers exhibited no or low cytotoxicity even at high concentration. When the concentration was higher than 400 μg/ml, an apparent decrease in cell viability was found, indicating high dose of MnO_2 nanoparticles could induce cell death, which was consistent with our previous studies showing high concentrations of silica nanoparticles could induce cell necrosis in endothelial cells (Liu and Sun, 2010). It might be attributed to the higher cellular uptake of nanoparticles, which could directly damage cell plasma membranes and thus cause cell necrosis (Liu and Sun, 2010).

Then, the antibacterial activity of Mg-doped MnO_2 sample was evaluated by detection of the bacterial viability and biofilm formation of S. mutans (Bijle et al., 2020; Daood et al., 2020; Song et al., 2020). Firstly, MTT assay was applied to evaluate the effect of Mg-doped MnO_2 sample on the bacterial viability of S. mutans. As shown in **Figure 3A**, Mg-doped MnO_2 can effectively inhibit bacterial viability. When the Mg-doped MnO_2 nanoflowers at 100, 200, 400, and 800 μg/ml concentration were added, the percentage of inhibition was 11.86 ± 2.18, 13.73 ± 1.45, 16.0 ± 1.83, and 20.79 ± 0.94%, respectively, reflecting that as the concentration of Mg-doped MnO_2 nanoflowers increases, the inhibition of bacterial viability shows an upward trend.

Generally, the MTT assay for assessment of antibacterial activity revealed the function of bacterial dehydrogenase system involved in metabolism (He et al., 2015). Furthermore, bacterial biofilm formation is known to increase resistance against the antibiotic and plays a critical role in the pathogenesis of infections (Banerjee et al., 2020). Then, we also examined the effect of Mg-doped MnO_2 nanoflowers on S. mutans biofilm formation by crystal violet staining (Asgharpour et al., 2019; Chan et al., 2020; Jiang et al., 2020; Song et al., 2020), and the results showed the same trend as the MTT assay (**Figure 3B**). In the presence of Mg-doped MnO_2, the inhibition percentage of biofilm formation was 4.1 ± 1.45% at 100 μg/ml, 21.02 ± 0.49% at 200 μg/ml, 39.86 ± 1.59% at 400 μg/ml, and 51.99 ± 1.18% at 800 μg/ml concentration, respectively, showing a dose-dependent enhanced antibacterial activity and reduced biofilm formation against S. mutans induced by Mg-doped MnO_2 nanoflowers. Interestingly, these antibacterial tests were all performed in the dark.

From the above results, it was intriguing to find that the Mg-doped δ-MnO_2 nanoflowers exhibited spontaneous antibacterial properties in the dark. Since it is established that ROS is responsible for antibacterial activity in the dark (Prasanna and Vijayaraghavan, 2015), their formation was investigated by electron spin resonance (ESR) using DMPO as a quencher without external illumination. **Figures 4A,B** show the characteristic DMPO-·O_2^- and DMPO-·OH signals in the case of Mg-doped MnO_2 nanoflowers at 800 μg/ml concentration (Peng et al., 2021; Zong et al., 2021). The results show that

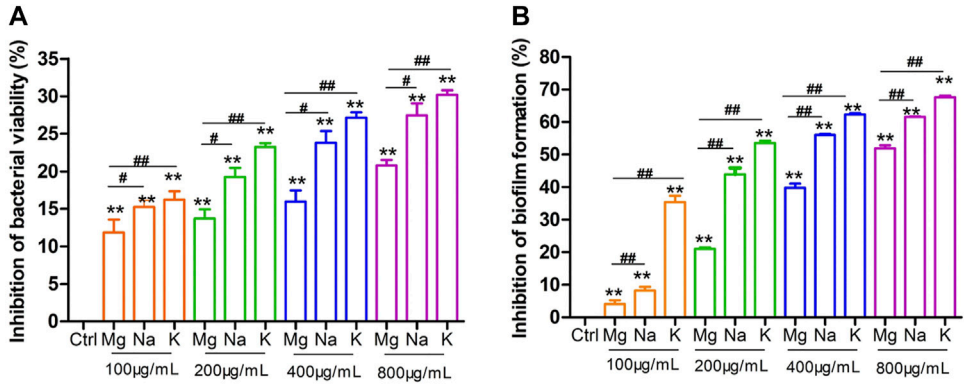

FIGURE 3 | The inhibition effect of Mg-, Na-, and K-doped δ-MnO_2 nanoflowers on S. mutans bacterial viability and biofilm formation at 24 h. **(A)** Bacterial viability by MTT assay. **(B)** Biofilm formation by crystal violet assay. Bacteria without nanoparticle treatment served as the negative control. Data represents mean ± standard deviation (SD), $n = 3$. $^{**}p < 0.01$ vs. the negative control group; $^{\#\#}p < 0.01$ significant difference as compared groups.

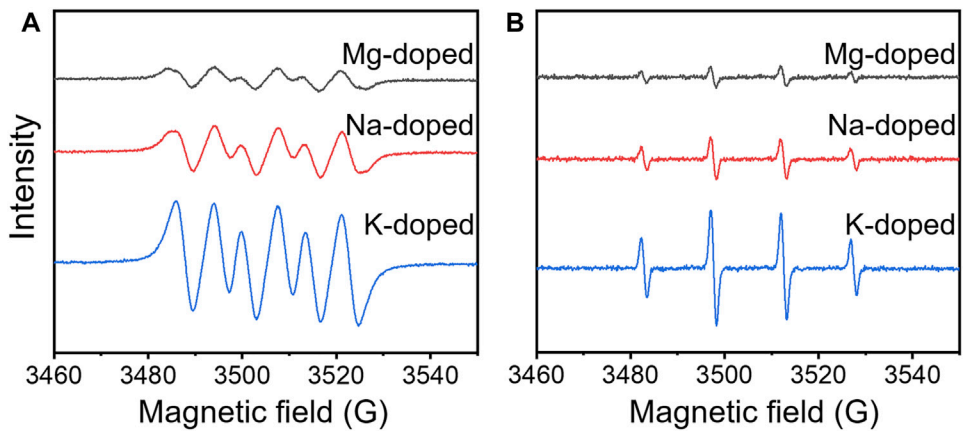

FIGURE 4 | ESR spin trapping spectra of **(A)** DMPO-·O_2^- and **(B)** DMPO-·OH on Mg-, Na-, and K-doped δ-MnO_2 nanoflowers in the dark.

both superoxide radicals (O_2^-) and hydroxyl radical (OH) were generated under dark conditions.

It has been reported that ZnO and MgO nanoparticles produced ROS in the dark due to the transfer of electrons trapped by the oxygen vacancies at the surface of materials (Prasanna and Vijayaraghavan, 2015; Hao et al., 2017). However, in our case, the presence of oxygen vacancies on the δ-MnO_2 surface was not detected from the XPS results (Selvakumar et al., 2015). For the Mg 1s core-level spectrum in **Figure 2F**, it can be observed that Mg is chemically bound to MnO_2, and thus, the valence electrons of Mg were transferred to MnO_2, becoming free electrons. It implies that the production of ROS in the dark might be produced by the free electrons in δ-MnO_2 coming from doping.

In order to further confirm this hypothesis, $NaMnO_4$ and $KMnO_4$ were employed to synthesize the Na- and K-doped δ-MnO_2 as similarly described for Mg-doped δ-MnO_2. In this case, it has been established that these δ-MnO_2 samples can enable higher doping levels relative to Mg-doped δ-MnO_2, which can lead to an increase number of free electrons (Hu et al., 2019). **Figures 1D,G** present their SEM images. These MnO_2 samples showed similar flower-like morphology as that of Mg-doped ones, and the sizes were ~460 nm in diameter (Na-doped MnO_2) and ~500 nm in diameter (K-doped MnO_2), respectively. From the XRD patterns in **Supplementary Figures S1B,C**, it was observed that they all presented very similar crystalline structures to Mg-doped sample. **Figures 1E,H** present their TEM images. The HRTEM images depicted in **Figures 1F,I**, as well as SAED patterns in **Supplementary Figure S2B,C**, display the same lattice spacings (1.42 and 2.45 Å) of MnO_2 as that of Mg-doped δ-MnO_2. The bandgaps were calculated from UV-VIS spectra (**Supplementary Figures S3B,C**, respectively), which were 1.06 (Na-doped MnO_2) and 0.75 eV (K-doped MnO_2), respectively.

Figures 2B,C display the XPS survey spectra of Na- and K-doped MnO_2. In **Figure 2I,L**, it presented only one component in both Na 1s and K $2p_{3/2}$ spectra. The BE of Na 1s (1070.9 eV) is higher than that of NaOH (~1069.6 eV), while

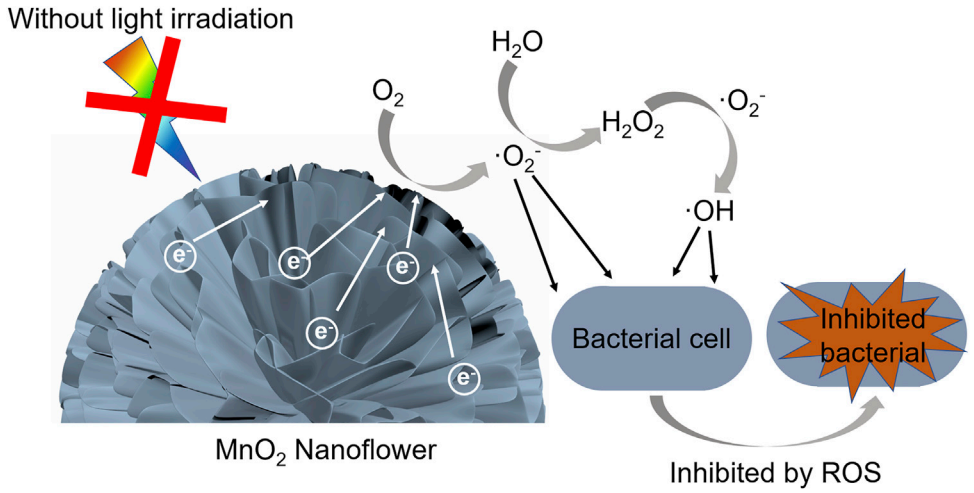

FIGURE 5 | Schematic diagram for the mechanism of antibacterial activity on doped δ-MnO_2.

the BE of K $2p_{3/2}$ (292.5 eV) is higher than that of KF (~292.2 eV) (Oh et al., 2013). Thus, it indicates that Na^+ or K^+ ions were also filled between the layers of MnO_2 (Hu et al., 2019). In **Figures 2G,J**, Mn $2p_{3/2}$ core-level spectra presented 2 components, which was consistent with the Mg-doped MnO_2 sample. The BE of peak II are 644.9 (Na-doped MnO_2) and 644.7 eV (K-doped MnO_2), respectively, which are 0.2 and 0.4 eV lower than the corresponding peaks of Mg-doped MnO_2. Meanwhile, the BE of peak II and III of O 1s peak for Na-doped and K-doped samples also shift to lower BE values relative to those of Mg-doped sample. These variations demonstrate that between MnO_2 and doped ions, it occurred a charge transfer (Luo et al., 2000; Gupta et al., 2018). The reason can be explained by the different doping levels as follows.

The atomic ratios calculated from the XPS data for Mg/Mn (Mg-doped MnO_2), Na/Mn (Na-doped MnO_2), and K/Mn (K-doped MnO_2) were 1:626, 1:52, and 1:7, respectively. Details on these calculations are described in the experimental section (Hu et al., 2019; Zhu et al., 2019). This difference might be that the bigger size of ions results in larger interaction between ions and MnO_2 layers, because the ions presented the size of K^+>Na^+>Mg^{2+} (Hu et al., 2019). Therefore, the difference in the amounts of doping ions in MnO_2 results in the variance in the bandgap values, and meanwhile contribute to the lower BE of Mn and O peaks in Na- and K-doped samples relative to those of Mg-doped ones.

Then, MnO_2 doped by Na^+ and K^+ ions were employed to evaluate the effect of free electrons quantity on the bacterial viability and biofilm formation of S. mutans in the dark. *In vitro* cytotoxicity studies were also tested. The experimental procedure was the same as that of Mg-doped MnO_2 samples, and the results were described in **Supplementary Figure S4**. Consistent with the cytotoxicity results of Mg-doped MnO_2, neither Na- nor K-doped MnO_2 had a significant effect on cell viability at concentration below 400 μg/ml, while a slight reduction in cell viability was observed at 800 μg/ml. Thus, the MTT assay showed no significant cytotoxicity for MnO_2 against L929 cells when the concentration was no more than 400 μg/ml. It was noted that K-doped MnO_2 had the least cytotoxicity, while Mg-doped MnO_2 displayed higher cytotoxicity than Na-doped MnO_2 sample. According to ISO 10993-5:2009, the biocompatibility of K-doped MnO_2 was very much within the acceptable limits even at a concentration as high as 800 μg/ml.

Subsequently, we used both the MTT assay and crystal violet staining assay to evaluate the effect of MnO_2 nanoflowers with different doping on the bacterial viability and biofilm formation of S. mutans. As shown in **Figure 3A**, the inhibition of S. mutans bacterial viability exposed to Na-doped MnO_2 nanoflowers at 100, 200, 400, and 800 μg/ml concentration was 15.25 ± 1.11, 19.26 ± 1.39, 23.81 ± 1.83, and 27.46 ± 1.82%, respectively. Meanwhile the inhibition with K-doped MnO_2 at concentrations of 100, 200, 400, and 800 μg/ml was 16.22 ± 1.38, 23.26 ± 0.65, 27.13 ± 0.98, and 30.20 ± 0.77%, respectively, reflecting that as the concentrations of MnO_2 nanoflowers increases, the antibacterial activity shows an upward trend.

From **Figure 3B**, in the presence of Na-doped MnO_2, the inhibition of biofilm formation was 8.25 ± 1.48% at 100 μg/ml, 44.0 ± 2.40% at 200 μg/ml, 56.0 ± 0.46% at 400 μg/ml, and 61.57 ± 0.24% at 800 μg/ml, respectively. In the presence of K-doped MnO_2, the inhibition of biofilm formation was 35.44 ± 2.28% at 100 μg/ml, 53.56 ± 1.00% at 200 μg/ml, 62.38 ± 0.46% at 400 μg/ml, and 67.61 ± 0.61% at 800 μg/ml, respectively. Obviously, both MTT assay and crystal violet staining have shown that K-doped MnO_2 has the superior antibacterial and antibiofilm formation ability, which is better than that of Na-doped sample. Meanwhile, the Mg-doped MnO_2 had the lowest antibacterial activity. Therefore, these results confirm the hypothesis that higher doping levels could provide more free electrons, which enhanced the antibacterial properties in doped δ-MnO_2.

Figures 4A,B also show the characteristic DMPO-·O_2^- and DMPO-·OH signals in the case of Na- and K-doped MnO_2 (Peng et al., 2021; Zong et al., 2021). The results show that both O_2^- and

OH produced in the dark were following the order of $K^+>Na^+>Mg^{2+}$, which further confirm that the production of ROS in the dark might be produced by the free electrons in δ-MnO_2 coming from doping.

In aqueous solutions, the free electrons in δ-MnO_2 coming from doping can transfer to the water around it and form $\cdot O_2^-$, while ·OH is known as a derivative of O_2^- (Morrison et al., 1988; Xu et al., 2020; Yao et al., 2020). To clarify the role of O_2^- in the mechanism of ROS production, ESR was then carried out with the addition of superoxide dismutase (SOD), a well-known superoxide scavenger (Carre et al., 2013; Piccaro et al., 2014; Jiang et al., 2016). The results in **Supplementary Figure S5** demonstrate that in the dark both DMPO-$\cdot O_2^-$ and DMPO-·OH signal disappeared in the presence of SOD, revealing that ROS mediated through superoxide plays a major role in antibacterial activity without external illumination (Prasanna and Vijayaraghavan, 2015; Ijaz et al., 2020). Thus, the antibacterial mechanism of doped δ-MnO_2 could be proposed as in **Figure 5**. When the alkali metal atoms are chemically bound to MnO_2 by doping, the valence electrons of alkali metals will transfer to MnO_2. Then, the doped MnO_2 can provide free electrons to induce the production of O_2^- in aqueous solutions, which could penetrate into the bacteria cell membrane and then damage cellular components such as DNA and proteins (Xia et al., 2008; Kasemets et al., 2009; Dadi et al., 2019), resulting in the antibacterial activity without external illumination. Furthermore, by comparing the δ-MnO_2 with different doping level, the ROS generation following the doping levels of $K^+>Na^+>Mg^{2+}$ can be observed. With higher doping levels, more free electrons can be transferred to MnO_2, which induce the production of more ROS, and thus present superior antibacterial activity. Compared to the antibacterial activities of MnO_2 with other iron oxide nanoparticles such as ZnO, CuO, Fe_3O_4, and Al_2O_3 (**Supplementary Table S2**), it was observed that MnO_2 displayed a superior antibacterial ability.

Supplementary Figure S6 presented the controllable degradation behavior of δ-MnO_2. Following the gradual addition of vitamin C into the suspension with δ-MnO_2 samples, it started to fade color, which indicated that MnO_2 could be degraded in the presence of vitamin C. When the quantity of vitamin C was 14 times over MnO_2 samples, it observed a nearly complete degradation of MnO_2 into water soluble Mn ions, which can be rapidly excreted from the body, making this materials potential for *in vivo* applications, presenting not only an outstanding antibacterial efficacy but also an excellent biosafety (Liu et al., 2021).

CONCLUSION

δ-MnO_2 nanoflowers doped by Mg, Na, and K ions were successful synthesized and their bandgap tunable antibacterial properties and controllable degradability mediated by vitamin C were systematically investigated. Interestingly, it was observed that all the samples showed antibacterial activity in the dark, and the antibacterial activity increased with doping levels, which was favored in the $K^+>Na^+>Mg^{2+}$ order. Our data suggest that doped MnO_2 can provide free electrons to induce the production of ROS and result in the antibacterial activity in the dark. Moreover, it is shown that higher doping levels can provide more free electrons, which enhance the antibacterial activity of the δ-MnO_2 materials. Following the gradual addition of vitamin C, MnO_2 nanoflowers could nearly be degraded into water soluble Mn ions completely, indicating that these materials also display biosafety. We believe that our results shed light on the design and fabrication of antibacterial nanomaterials with tailored properties.

DATA AVAILABILITY STATEMENT

The original contributions presented in the study are included in the article/**Supplementary Material**. Further inquiries can be directed to the corresponding authors.

AUTHOR CONTRIBUTIONS

YY (investigation, writing—original draft); NJ (methodology, investigation, analysis); XL (conceptualization, project administration); JP (conceptualization, funding acquisition); ML (investigation, analysis); CW (investigation, analysis); PC (methodology, analysis); JW (conceptualization, project administration, funding acquisition).

FUNDING

This work was supported by Shanghai Natural Science Foundation (20ZR1401700), the National Natural Science Foundation of China (21703031, 81971751, 22005046, and 61376017), Shanghai Science and Technology Innovation Fund (19ZR1445500, 20Y11904100), innovative research team of high-level local universities in Shanghai (SSMU-ZDCX20180900), and the Research Discipline fund No. KQYJXK2020 from Ninth People's Hospital, Shanghai Jiao Tong University School of Medicine, and College of Stomatology, Shanghai Jiao Tong University.

SUPPLEMENTARY MATERIAL

The Supplementary Material for this article can be found online at: https://www.frontiersin.org/articles/10.3389/fbioe.2021.788574/full#supplementary-material

REFERENCES

Afrasiabi, S., Bahador, A., and Partoazar, A. (2021). Combinatorial Therapy of Chitosan Hydrogel-Based Zinc Oxide Nanocomposite Attenuates the Virulence of Streptococcus Mutans. *BMC Microbiol.* 21, 62. doi:10.1186/s12866-021-02128-y

Arunpandiyan, S., Vinoth, S., Pandikumar, A., Raja, A., and Arivarasan, A. (2021). Decoration of CeO2 Nanoparticles on Hierarchically Porous MnO2 Nanorods and Enhancement of Supercapacitor Performance by Redox Additive Electrolyte. *J. Alloys Compd.* 861, 158456. doi:10.1016/j.jallcom.2020.158456

Asgharpour, F., Moghadamnia, A. A., Zabihi, E., Kazemi, S., Ebrahimzadeh Namvar, A., Gholinia, H., et al. (2019). Iranian Propolis Efficiently Inhibits Growth of Oral Streptococci and Cancer Cell Lines. *BMC Complement. Altern. Med.* 19, 266. doi:10.1186/s12906-019-2677-3

Banerjee, S., Vishakha, K., Das, S., Dutta, M., Mukherjee, D., Mondal, J., et al. (2020). Antibacterial, Anti-biofilm Activity and Mechanism of Action of Pancreatin Doped Zinc Oxide Nanoparticles against Methicillin Resistant *Staphylococcus aureus*. *Colloids Surf. B Biointerfaces* 190, 110921. doi:10.1016/j.colsurfb.2020.110921

Baruah, R., Yadav, A., and Das, A. M. (2021). Livistona Jekinsiana Fabricated ZnO Nanoparticles and Their Detrimental Effect towards Anthropogenic Organic Pollutants and Human Pathogenic Bacteria. *Spectrochimica Acta A: Mol. Biomol. Spectrosc.* 251, 119459. doi:10.1016/j.saa.2021.119459

Bijle, M. N., Neelakantan, P., Ekambaram, M., Lo, E. C. M., and Yiu, C. K. Y. (2020). Effect of a Novel Synbiotic on Streptococcus Mutans. *Sci. Rep.* 10, 7951. doi:10.1038/s41598-020-64956-8

Bosnjakovic, A., and Schlick, S. (2006). Spin Trapping by 5,5-Dimethylpyrroline-N-Oxide in Fenton media in the Presence of Nafion Perfluorinated Membranes: Limitations and Potential. *J. Phys. Chem. B* 110, 10720–10728. doi:10.1021/jp061042y

Carré, G., Benhamida, D., Peluso, J., Muller, C. D., Lett, M.-C., Gies, J.-P., et al. (2013). On the Use of Capillary Cytometry for Assessing the Bactericidal Effect of TiO2. Identification and Involvement of Reactive Oxygen Species. *Photochem. Photobiol. Sci.* 12, 610–620. doi:10.1039/c2pp25189b

Chan, A., Ellepola, K., Truong, T., Balan, P., Koo, H., and Seneviratne, C. J. (2020). Inhibitory Effects of Xylitol and Sorbitol on Streptococcus Mutans and Candida Albicans Biofilms Are Repressed by the Presence of Sucrose. *Arch. Oral Biol.* 119, 104886. doi:10.1016/j.archoralbio.2020.104886

Chandra, H., Patel, D., Kumari, P., Jangwan, J. S., and Yadav, S. (2019). Phyto-mediated Synthesis of Zinc Oxide Nanoparticles of Berberis Aristata: Characterization, Antioxidant Activity and Antibacterial Activity with Special Reference to Urinary Tract Pathogens. *Mater. Sci. Eng. C* 102, 212–220. doi:10.1016/j.msec.2019.04.035

Chhabra, T., Kumar, A., Bahuguna, A., and Krishnan, V. (2019). Reduced Graphene Oxide Supported MnO2 Nanorods as Recyclable and Efficient Adsorptive Photocatalysts for Pollutants Removal. *Vacuum* 160, 333–346. doi:10.1016/j.vacuum.2018.11.053

Dadi, R., Azouani, R., Traore, M., Mielcarek, C., and Kanaev, A. (2019). Antibacterial Activity of ZnO and CuO Nanoparticles against Gram Positive and Gram Negative Strains. *Mater. Sci. Eng. C* 104, 109968. doi:10.1016/j.msec.2019.109968

Daood, U., Burrow, M. F., and Yiu, C. K. Y. (2020). Effect of a Novel Quaternary Ammonium Silane Cavity Disinfectant on Cariogenic Biofilm Formation. *Clin. Oral Invest.* 24, 649–661. doi:10.1007/s00784-019-02928-7

Das, S., Samanta, A., and Jana, S. (2017). Light-Assisted Synthesis of Hierarchical Flower-like MnO2 Nanocomposites with Solar Light Induced Enhanced Photocatalytic Activity. *ACS Sustain. Chem. Eng.* 5, 9086–9094. doi:10.1021/acssuschemeng.7b02003

Dawadi, S., Gupta, A., Khatri, M., Budhathoki, B., Lamichhane, G., and Parajuli, N. (2020). Manganese Dioxide Nanoparticles: Synthesis, Application and Challenges. *Bull. Mater. Sci.* 43, 277. doi:10.1007/s12034-020-02247-8

Dizaj, S. M., Lotfipour, F., Barzegar-Jalali, M., Zarrintan, M. H., and Adibkia, K. (2014). Antimicrobial Activity of the Metals and Metal Oxide Nanoparticles. *Mater. Sci. Eng. C* 44, 278–284. doi:10.1016/j.msec.2014.08.031

Esaka, F., Nojima, T., Udono, H., Magara, M., and Yamamoto, H. (2016). Non-destructive Depth Analysis of the Surface Oxide Layer on Mg2 Si with XPS and XAS. *Surf. Interf. Anal.* 48, 432–435. doi:10.1002/sia.5939

Estes, L. M., Singha, P., Singh, S., Sakthivel, T. S., Garren, M., Devine, R., et al. (2021). Characterization of a Nitric Oxide (NO) Donor Molecule and Cerium Oxide Nanoparticle (CNP) Interactions and Their Synergistic Antimicrobial Potential for Biomedical Applications. *J. Colloid Interf. Sci.* 586, 163–177. doi:10.1016/j.jcis.2020.10.081

Gatadi, S., Madhavi, Y. V., and Nanduri, S. (2021). Nanoparticle Drug Conjugates Treating Microbial and Viral Infections: A Review. *J. Mol. Struct.* 1228, 129750. doi:10.1016/j.molstruc.2020.129750

Geng, Z., Wang, Y., Liu, J., Li, G., Li, L., Huang, K., et al. (2016). δ-MnO2-Mn3O4 Nanocomposite for Photochemical Water Oxidation: Active Structure Stabilized in the Interface. *ACS Appl. Mater. Inter.* 8, 27825–27831. doi:10.1021/acsami.6b09984

Golden, D. C., Dixon, J. B., and Chen, C. C. (1986). Ion Exchange, thermal Transformations, and Oxidizing Properties of Birnessite. *Clays and Clay Minerals* 34, 511–520. doi:10.1346/ccmn.1986.0340503

Gupta, V. K., Fakhri, A., Azad, M., and Agarwal, S. (2018). Synthesis and Characterization of Ag Doped ZnS Quantum Dots for Enhanced Photocatalysis of Strychnine as a Poison: Charge Transfer Behavior Study by Electrochemical Impedance and Time-Resolved Photoluminescence Spectroscopy. *J. Colloid Interf. Sci.* 510, 95–102. doi:10.1016/j.jcis.2017.09.043

Haider, M. K., Ullah, A., Sarwar, M. N., Saito, Y., Sun, L., Park, S., et al. (2021). Lignin-mediated *In-Situ* Synthesis of CuO Nanoparticles on Cellulose Nanofibers: A Potential Wound Dressing Material. *Int. J. Biol. Macromolecules* 173, 315–326. doi:10.1016/j.ijbiomac.2021.01.050

Han, X., Zhang, G., Chai, M., and Zhang, X. (2021). Light-assisted Therapy for Biofilm Infected Micro-arc Oxidation TiO2 Coating on Bone Implants. *Biomed. Mater.* 16, 025018. doi:10.1088/1748-605x/abdb72

Hao, Y.-J., Liu, B., Tian, L.-G., Li, F.-T., Ren, J., Liu, S.-J., et al. (2017). Synthesis of {111} Facet-Exposed MgO with Surface Oxygen Vacancies for Reactive Oxygen Species Generation in the Dark. *ACS Appl. Mater. Inter.* 9, 12687–12693. doi:10.1021/acsami.6b16856

He, J., Zhu, X., Qi, Z., Wang, C., Mao, X., Zhu, C., et al. (2015). Killing Dental Pathogens Using Antibacterial Graphene Oxide. *ACS Appl. Mater. Inter.* 7, 5605–5611. doi:10.1021/acsami.5b01069

Herman, A., and Herman, A. P. (2014). Nanoparticles as Antimicrobial Agents: Their Toxicity and Mechanisms of Action. *J. Nanosci. Nanotech.* 14, 946–957. doi:10.1166/jnn.2014.9054

Hirakawa, T., and Nosaka, Y. (2002). Properties of O2- and OH Formed in TiO2 Aqueous Suspensions by Photocatalytic Reaction and the Influence of H2O2 and Some Ions. *Langmuir* 18, 3247–3254. doi:10.1021/la015685a

Hong, W.-E., Hsu, I.-L., Huang, S.-Y., Lee, C.-W., Ko, H., Tsai, P.-J., et al. (2018). Assembled Growth of 3D Fe3O4@Au Nanoparticles for Efficient Photothermal Ablation and SERS Detection of Microorganisms. *J. Mater. Chem. B* 6, 5689–5697. doi:10.1039/c8tb00599k

Hu, S., Liu, X., Wang, C., Camargo, P. H. C., and Wang, J. (2019). Tuning Thermal Catalytic Enhancement in Doped MnO2-Au Nano-Heterojunctions. *ACS Appl. Mater. Inter.* 11, 17444–17451. doi:10.1021/acsami.9b03879

Ijaz, M., Zafar, M., Islam, A., Afsheen, S., and Iqbal, T. (2020). A Review on Antibacterial Properties of Biologically Synthesized Zinc Oxide Nanostructures. *J. Inorg. Organomet. Polym.* 30, 2815–2826. doi:10.1007/s10904-020-01603-9

Javedani Bafekr, J., and Jalal, R. (2018). *In Vitro* antibacterial Activity of Ceftazidime, unlike Ciprofloxacin, Improves in the Presence of ZnO Nanofluids under Acidic Conditions. *IET nanobiotechnol.* 12, 640–646. doi:10.1049/iet-nbt.2017.0119

Jiang, J., Zhang, C., Zeng, G.-M., Gong, J.-L., Chang, Y.-N., Song, B., et al. (2016). The Disinfection Performance and Mechanisms of Ag/lysozyme Nanoparticles Supported with Montmorillonite clay. *J. Hazard. Mater.* 317, 416–429. doi:10.1016/j.jhazmat.2016.05.089

Jiang, M., Yan, L., Li, K. a., Ji, Z. h., and Tian, S. g. (2020). Evaluation of Total Phenol and Flavonoid Content and Antimicrobial and Antibiofilm Activities of Trollius Chinensis Bunge Extracts on Streptococcus Mutans. *Microsc. Res. Tech.* 83, 1471–1479. doi:10.1002/jemt.23540

Jiang, Y.-Z., Wang, Y.-L., Wang, C.-Y., Bai, L.-M., Li, X., and Li, Y.-B. (2017). Magnesium Hydroxide Whisker Modified via *In Situ* Copolymerization of N-Butyl Acrylate and Maleic Anhydride. *Rare Met.* 36, 997–1002. doi:10.1007/s12598-016-0826-0

John, R. E., Chandran, A., Thomas, M., Jose, J., and George, K. C. (2016). Surface-defect Induced Modifications in the Optical Properties of α-MnO2 Nanorods. *Appl. Surf. Sci.* 367, 43–51. doi:10.1016/j.apsusc.2016.01.153

Kasemets, K., Ivask, A., Dubourguier, H.-C., and Kahru, A. (2009). Toxicity of Nanoparticles of ZnO, CuO and TiO2 to Yeast *Saccharomyces cerevisiae*. *Toxicol. Vitro* 23, 1116–1122. doi:10.1016/j.tiv.2009.05.015

Lakshmi Prasanna, V., and Vijayaraghavan, R. (2015). Insight into the Mechanism of Antibacterial Activity of ZnO: Surface Defects Mediated Reactive Oxygen Species Even in the Dark. *Langmuir* 31, 9155–9162. doi:10.1021/acs.langmuir.5b02266

Li, K., Li, H., Xiao, T., Long, J., Zhang, G., Li, Y., et al. (2019). Synthesis of Manganese Dioxide with Different Morphologies for Thallium Removal from Wastewater. *J. Environ. Manage.* 251, 109563. doi:10.1016/j.jenvman.2019.109563

Li, Y., Xu, Z., Wang, D., Zhao, J., and Zhang, H. (2017). Snowflake-like Core-Shell α-MnO2@δ-MnO2 for High Performance Asymmetric Supercapacitor. *Electrochimica Acta* 251, 344–354. doi:10.1016/j.electacta.2017.08.146

Liu, W., Ge, H., Ding, X., Lu, X., Zhang, Y., and Gu, Z. (2020). Cubic Nano-Silver-Decorated Manganese Dioxide Micromotors: Enhanced Propulsion and Antibacterial Performance. *Nanoscale* 12, 19655–19664. doi:10.1039/d0nr06281b

Liu, X., Sui, B., Camargo, P. H. C., Wang, J., and Sun, J. (2021). Tuning Band gap of MnO2 Nanoflowers by Alkali Metal Doping for Enhanced Ferroptosis/phototherapy Synergism in Cancer. *Appl. Mater. Today* 23, 101027. doi:10.1016/j.apmt.2021.101027

Liu, X., and Sun, J. (2010). Endothelial Cells Dysfunction Induced by Silica Nanoparticles through Oxidative Stress via JNK/P53 and NF-Kb Pathways. *Biomaterials* 31, 8198–8209. doi:10.1016/j.biomaterials.2010.07.069

Luo, J., Zhang, Q., Garcia-Martinez, J., and Suib, S. L. (2008). Adsorptive and Acidic Properties, Reversible Lattice Oxygen Evolution, and Catalytic Mechanism of Cryptomelane-type Manganese Oxides as Oxidation Catalysts. *J. Am. Chem. Soc.* 130, 3198–3207. doi:10.1021/ja077706e

Luo, J., Zhang, Q., and Suib, S. L. (2000). Mechanistic and Kinetic Studies of Crystallization of Birnessite. *Inorg. Chem.* 39, 741–747. doi:10.1021/ic990456l

Marciniuk, G., Ferreira, R. T., Pedroso, A. V., Ribas, A. S., Ribeiro, R. A. P., de Lázaro, S. R., et al. (2021). Enhancing Hydrothermal Formation of α-MnO2 Nanoneedles over Nanographite Structures Obtained by Electrochemical Exfoliation. *Bull. Mater. Sci.* 44, 62. doi:10.1007/s12034-020-02336-8

Morrison, C. J., Isenberg, R. A., and Stevens, D. A. (1988). Enhanced Oxidative Mechanisms in Immunologically Activated versus Elicited Polymorphonuclear Neutrophils: Correlations with Fungicidal Activity. *J. Med. Microbiol.* 25, 115–121. doi:10.1099/00222615-25-2-115

Nefedov, V. I. (1977). X-Ray Photoelectron Spectra of Halogens in Coordination Compounds. *J. Electron Spectrosc. Relat. Phenomena* 12, 459–476. doi:10.1016/0368-2048(77)85097-4

Ogunyemi, S. O., Zhang, M., Abdallah, Y., Ahmed, T., Qiu, W., Ali, M. A., et al. (2020). The Bio-Synthesis of Three Metal Oxide Nanoparticles (ZnO, MnO2, and MgO) and Their Antibacterial Activity against the Bacterial Leaf Blight Pathogen. *Front. Microbiol.* 11, 588326. doi:10.3389/fmicb.2020.588326

Oh, J. H., Kang, Y. S., and Kang, S. W. (2013). Poly(vinylpyrrolidone)/KF Electrolyte Membranes for Facilitated CO2 Transport. *Chem. Commun.* 49, 10181–10183. doi:10.1039/c3cc46253f

Ouyang, Q., Wang, L., Ahmad, W., Rong, Y., Li, H., Hu, Y., et al. (2021). A Highly Sensitive Detection of Carbendazim Pesticide in Food Based on the Upconversion-MnO2 Luminescent Resonance Energy Transfer Biosensor. *Food Chem.* 349, 129157. doi:10.1016/j.foodchem.2021.129157

Peng, Y.-P., Liu, C.-C., Chen, K.-F., Huang, C.-P., and Chen, C.-H. (2021). Green Synthesis of Nano-Silver-Titanium Nanotube Array (Ag/TNA) Composite for Concurrent Ibuprofen Degradation and Hydrogen Generation. *Chemosphere* 264, 128407. doi:10.1016/j.chemosphere.2020.128407

Piccaro, G., Pietraforte, D., Giannoni, F., Mustazzolu, A., and Fattorini, L. (2014). Rifampin Induces Hydroxyl Radical Formation in *Mycobacterium tuberculosis*. *Antimicrob. Agents Chemother.* 58, 7527–7533. doi:10.1128/aac.03169-14

Podder, S., Chanda, D., Mukhopadhyay, A. K., De, A., Das, B., Samanta, A., et al. (2018). Effect of Morphology and Concentration on Crossover between Antioxidant and Pro-oxidant Activity of MgO Nanostructures. *Inorg. Chem.* 57, 12727–12739. doi:10.1021/acs.inorgchem.8b01938

Qian, F., Zheng, Y., Pan, N., Li, L., Li, R., and Ren, X. (2021). Synthesis of Polysiloxane and its Co-application with Nano-SiO2 for Antibacterial and Hydrophobic Cotton Fabrics. *Cellulose* 28, 3169–3181. doi:10.1007/s10570-021-03704-1

Sakai, N., Ebina, Y., Takada, K., and Sasaki, T. (2005). Photocurrent Generation from Semiconducting Manganese Oxide Nanosheets in Response to Visible Light. *J. Phys. Chem. B* 109, 9651–9655. doi:10.1021/jp0500485

Selvakumar, K., Senthil Kumar, S. M., Thangamuthu, R., Ganesan, K., Murugan, P., Rajput, P., et al. (2015). Physiochemical Investigation of Shape-Designed MnO2 Nanostructures and Their Influence on Oxygen Reduction Reaction Activity in Alkaline Solution. *J. Phys. Chem. C* 119, 6604–6618. doi:10.1021/jp5127915

Sharifi, S., Behzadi, S., Laurent, S., Laird Forrest, M., Stroeve, P., and Mahmoudi, M. (2012). Toxicity of Nanomaterials. *Chem. Soc. Rev.* 41, 2323–2343. doi:10.1039/c1cs15188f

Sikora, P., Augustyniak, A., Cendrowski, K., Nawrotek, P., and Mijowska, E. (2018). Antimicrobial Activity of Al2O3, CuO, Fe3O4, and ZnO Nanoparticles in Scope of Their Further Application in Cement-Based Building Materials. *Nanomaterials* 8, 212. doi:10.3390/nano8040212

Song, Y.-M., Zhou, H.-Y., Wu, Y., Wang, J., Liu, Q., and Mei, Y.-F. (2020). *In Vitro* Evaluation of the Antibacterial Properties of Tea Tree Oil on Planktonic and Biofilm-Forming Streptococcus Mutans. *AAPS Pharmscitech* 21, 227. doi:10.1208/s12249-020-01753-6

Suib, S. L. (2008). Porous Manganese Oxide Octahedral Molecular Sieves and Octahedral Layered Materials. *Acc. Chem. Res.* 41, 479–487. doi:10.1021/ar7001667

Szterk, A., Stefaniuk, I., Waszkiewicz-Robak, B., and Roszko, M. (2011). Oxidative Stability of Lipids by Means of EPR Spectroscopy and Chemiluminescence. *J. Am. Oil Chem. Soc.* 88, 611–618. doi:10.1007/s11746-010-1715-6

Tang, X., Wang, C., Gao, F., Ma, Y., Yi, H., Zhao, S., et al. (2020). Effect of Hierarchical Element Doping on the Low-Temperature Activity of Manganese-Based Catalysts for NH3-SCR. *J. Environ. Chem. Eng.* 8, 104399. doi:10.1016/j.jece.2020.104399

Teng, X., Liu, X., Cui, Z., Zheng, Y., Chen, D.-f., Li, Z., et al. (2020). Rapid and Highly Effective Bacteria-Killing by polydopamine/IR780@MnO2-Ti Using Near-Infrared Light. *Prog. Nat. Sci. Mater. Int.* 30, 677–685. doi:10.1016/j.pnsc.2020.06.003

Truong, T. T., Liu, Y., Ren, Y., Trahey, L., and Sun, Y. (2012). Morphological and Crystalline Evolution of Nanostructured MnO2 and its Application in Lithium-Air Batteries. *ACS Nano* 6, 8067–8077. doi:10.1021/nn302654p

Wang, M., Shen, M., Zhang, L., Tian, J., Jin, X., Zhou, Y., et al. (2017). 2D-2D MnO2/g-C3n4 Heterojunction Photocatalyst: *In-Situ* Synthesis and Enhanced CO2 Reduction Activity. *Carbon* 120, 23–31. doi:10.1016/j.carbon.2017.05.024

Wang, Z., Yan, X., Wang, F., Xiong, T., Balogun, M.-S., Zhou, H., et al. (2021). Reduced Graphene Oxide Thin Layer Induced Lattice Distortion in High Crystalline MnO2 Nanowires for High-Performance Sodium- and Potassium-Ion Batteries and Capacitors. *Carbon* 174, 556–566. doi:10.1016/j.carbon.2020.12.071

Xia, T., Kovochich, M., Liong, M., Mädler, L., Gilbert, B., Shi, H., et al. (2008). Comparison of the Mechanism of Toxicity of Zinc Oxide and Cerium Oxide Nanoparticles Based on Dissolution and Oxidative Stress Properties. *ACS Nano* 2, 2121–2134. doi:10.1021/nn800511k

Xiao, L., Sun, W., Zhou, X., Cai, Z., and Hu, F. (2018). Facile Synthesis of Mesoporous MnO2 Nanosheet and Microflower with Efficient Photocatalytic Activities for Organic Dyes. *Vacuum* 156, 291–297. doi:10.1016/j.vacuum.2018.07.045

Xu, H., Ma, R., Zhu, Y., Du, M., Zhang, H., and Jiao, Z. (2020). A Systematic Study of the Antimicrobial Mechanisms of Cold Atmospheric-Pressure Plasma for Water Disinfection. *Sci. Total Environ.* 703, 134965. doi:10.1016/j.scitotenv.2019.134965

Yao, H., Huang, Y., Li, X., Li, X., Xie, H., Luo, T., et al. (2020). Underlying Mechanisms of Reactive Oxygen Species and Oxidative Stress Photoinduced by Graphene and its Surface-Functionalized Derivatives. *Environ. Sci. Nano* 7, 782–792. doi:10.1039/c9en01295h

Ye, X., Jiang, X., Chen, L., Jiang, W., Wang, H., Cen, W., et al. (2020). Effect of Manganese Dioxide crystal Structure on Adsorption of SO2 by DFT and Experimental Study. *Appl. Surf. Sci.* 521, 146477. doi:10.1016/j.apsusc.2020.146477

Zhang, L., Pornpattananangkul, D., Hu, C.-M., and Huang, C.-M. (2010). Development of Nanoparticles for Antimicrobial Drug Delivery. *Cmc* 17, 585–594. doi:10.2174/092986710790416290

Zhou, G., Liu, H., Ma, Z., Li, H., and Pei, Y. (2017). Spatially Confined Li-Oxygen Interaction in the Tunnel of α-MnO2 Catalyst for Li-Air Battery: A First-

Principles Study. *J. Phys. Chem. C* 121, 16193–16200. doi:10.1021/acs.jpcc.7b01855

Zhu, K., Wang, C., Camargo, P. H. C., and Wang, J. (2019). Investigating the Effect of MnO2 Band gap in Hybrid MnO2-Au Materials over the SPR-Mediated Activities under Visible Light. *J. Mater. Chem. A.* 7, 925–931. doi:10.1039/c8ta09785b

Zong, W., Guo, Z., Wu, M., Yi, X., Zhou, H., Jing, S., et al. (2021). Synergistic Multiple Active Species Driven Fast Estrone Oxidation by δ-MnO2 in the Existence of Methanol. *Sci. Total Environ.* 761, 143201. doi:10.1016/j.scitotenv.2020.143201

Conflict of Interest: The authors declare that the research was conducted in the absence of any commercial or financial relationships that could be construed as a potential conflict of interest.

Publisher's Note: All claims expressed in this article are solely those of the authors and do not necessarily represent those of their affiliated organizations, or those of the publisher, the editors, and the reviewers. Any product that may be evaluated in this article, or claim that may be made by its manufacturer, is not guaranteed or endorsed by the publisher.

Copyright © 2022 Yan, Jiang, Liu, Pan, Li, Wang, Camargo and Wang. This is an open-access article distributed under the terms of the Creative Commons Attribution License (CC BY). The use, distribution or reproduction in other forums is permitted, provided the original author(s) and the copyright owner(s) are credited and that the original publication in this journal is cited, in accordance with accepted academic practice. No use, distribution or reproduction is permitted which does not comply with these terms.

frontiers in Bioengineering and Biotechnology

ORIGINAL RESEARCH
published: 05 January 2022
doi: 10.3389/fbioe.2021.801432

Macrophage-Derived Exosomes Promote Bone Mesenchymal Stem Cells Towards Osteoblastic Fate Through microRNA-21a-5p

Kun Liu[1,2], Xin Luo[2], Zhao-Yong Lv[2], Yu-Jue Zhang[2], Zhen Meng[2], Jun Li[2], Chun-Xiu Meng[2], Hui-Fen Qiang[3], Cai-Yao Hou[2], Lei Hou[2], Feng-Zhen Liu[2,3] and Bin Zhang[1,2]**

[1]Department of Oral and Maxillofacial Surgery, School and Hospital of Stomatology, Shandong University and Shandong Provincial Key Laboratory of Oral Tissue Regeneration and Shandong Engineering Laboratory for Dental Materials and Oral Tissue Regeneration, Jinan, China, [2]Liaocheng People's Hospital, Medical College of Liaocheng University, Liaocheng, China, [3]Department of Materials Science and Engineering, Liaocheng University, Liaocheng, China

OPEN ACCESS

Edited by:
Kaili Lin,
Shanghai Jiao Tong University, China

Reviewed by:
Youtao Xie,
Shanghai Institute of Ceramics (CAS), China
Xuening Chen,
Sichuan University, China

***Correspondence:**
Feng-Zhen Liu
ldcllfz@163.com
Bin Zhang
zhangbinlc@sdu.edu.cn

Specialty section:
This article was submitted to Biomaterials, a section of the journal Frontiers in Bioengineering and Biotechnology

Received: 25 October 2021
Accepted: 08 December 2021
Published: 05 January 2022

Citation:
Liu K, Luo X, Lv Z-Y, Zhang Y-J, Meng Z, Li J, Meng C-X, Qiang H-F, Hou C-Y, Hou L, Liu F-Z and Zhang B (2022) Macrophage-Derived Exosomes Promote Bone Mesenchymal Stem Cells Towards Osteoblastic Fate Through microRNA-21a-5p. Front. Bioeng. Biotechnol. 9:801432. doi: 10.3389/fbioe.2021.801432

The effective healing of a bone defect is dependent on the careful coordination of inflammatory and bone-forming cells. In the current work, pro-inflammatory M1 and anti-inflammatory M2 macrophages were co-cultured with primary murine bone mesenchymal stem cells (BMSCs), *in vitro*, to establish the cross-talk among polarized macrophages and BMSCs, and as well as their effects on osteogenesis. Meanwhile, macrophages influence the osteogenesis of BMSCs through paracrine forms such as exosomes. We focused on whether exosomes of macrophages promote osteogenic differentiation. The results indicated that M1 and M2 polarized macrophage exosomes all can promote osteogenesis of BMSCs. Especially, M1 macrophage-derived exosomes promote osteogenesis of BMSCs through microRNA-21a-5p at the early stage of inflammation. This research helps to develop an understanding of the intricate interactions among BMSCs and macrophages, which can help to improve the process of bone healing as well as additional regenerative processes by local sustained release of exosomes.

Keywords: macrophage, exosomes, microRNA-21a-5p, BMSCs, osteogenic differentiation

INTRODUCTION

Rehabilitation of extensive bone defects is a formidable challenge in modern medical science. However, owing to their outstanding capacity for bringing about osteogenic differentiation, bone marrow mesenchymal stem cells (BMSCs) have become the osteogenous seed cells of bone tissue engineering and cytotherapy in recent years (Li Z. et al., 2020; Sui et al., 2019). The regeneration activities of BMSCs may be attributed to the diverse mechanisms of molecular cross-talk between BMSCs and adjacent cells (Thurairajah et al., 2017). Recent studies have determined that the macrophage-BMSCs crosstalk is substantially useful for the healing of bone defects (Pajarinen et al., 2019; Vallés et al., 2020).

Macrophages are an important part of innate immunity. Depending on the environment macrophages display different phenotypes. The two major phenotype classifications include M1 (pro-inflammatory, classically activated macrophages) and M2 (anti-inflammatory or alternative activated macrophages). This functional plasticity of macrophages has been conceptualized as

macrophage polarization. Furthermore, the polarization state of macrophages is fluid and can rapidly sense changes in the microenvironment and switch between M1 and M2 (Muñoz et al., 2020; Li J. et al., 2020). In an *in vitro* setting, exposure to Th1 cytokines, like TNF-α and IFN-γ or lipopolysaccharide (LPS), and polarizes macrophages into the M1 phenotype. Th2 cytokines, for instance, IL-4, and IL-13 polarize the M2 phenotype. The overall balance of M1/M2 macrophages controls the ultimate fate of organs in inflammation or injury. M1 macrophages increase the release of pro-inflammatory cytokines when an organ is infected or inflamed. In the later stages of inflammation, M2 macrophages secrete anti-inflammatory cytokines to suppress the inflammation and promote tissue repair (Selders et al., 2017; Krzyszczyk et al., 2018; Oishi and Manabe, 2018; Shapouri-Moghaddam et al., 2018; Meng et al., 2021). The imbalance of the inflammatory milieu, therefore, leads to abnormal bone repair during bone healing (Vallés et al., 2020). A recent study found that co-cultured macrophages and mesenchymal stem cells can be induced to undergo osteogenic differentiation, with M2 macrophages being the most successful at promoting the generation of new bone tissue (Loi et al., 2016; Zhang et al., 2017; Nathan et al., 2019). Furthermore, quite a few studies have shown that an initial proinflammatory phase modulated by M1 macrophages promotes osteogenesis in BMSCs (Tu et al., 2015; Lu et al., 2017; Romero-López et al., 2020; Xia et al., 2020). However, the mechanism of M1 macrophages promoting osteogenic differentiation at the early stage of inflammation is still rather ambiguous.

Exosomes, as key components of the macrophage-derived cell-conditioned medium, may play an important role. Exosomes are membrane microvesicles with a diameter of 30–200 nm that are derived from endosomes. Exosomes, which carry microRNAs (miRNAs), can be released into their environment (media) and then taken up by distal cells, in which they regulate biological processes (Li et al., 2017; Li and Jiang, 2019). Xiong et al. discovered that there was a substantial overexpression of microRNA-5106 in exosomes derived from M2 macrophages, but not in those derived from M1 macrophages, and that BMSCs osteogenic differentiation would be promoted by the exosomal miRNA by direct targeting of the Salt-inducible kinase 2 and 3 (SIK2 and SIK3) genes (Xiong et al., 2020). However, Xie et al. found that M1 macrophage exosomes support cell osteogenic differentiation (Xia et al., 2020).

This study aimed to see how macrophage-derived exosomal miRNAs affected BMSCs differentiation during the early stages of the pro-inflammatory response. We demonstrated that the miR-21a-5p is highly enriched in exosomes secreted by M1 macrophages and that it can be transferred to BMSCs to induce osteoblastic differentiation *in vitro*. Lian et al. show that miR-21-5p may be a potential pro-osteogenesis regulator (Lian et al., 2018). In addition, Huang et al. found that miR-21-5p targets SKP2 to reduce osteoclastogenesis in a mouse model of osteoporosis (Huang et al., 2021). MiR-21a-5p is highly homologous with miR-21-5p (Budak et al., 2016). To suggest new strategies for promoting bone regeneration, we investigated the molecular mechanism of M1 macrophages promoting the bone formation of BMSCs at an early stage. These findings will enhance our understanding of macrophage-BMSCs crosstalk at the cellular-molecular level and contribute to the development of treatments of bone defects.

MATERIALS AND METHODS

Macrophage Polarization and Preparation of CMs

Murine RAW264.7 (ATCC, United States) was incubated in a complete medium (DMEM; Gibco, Grand Island, United States) supplemented with streptomycin/penicillin (1%, Hyclone, United States) and fetal bovine serum (10%, FBS; Gibco, Grand Island, United States). In each well of a six-well plate, 1×10^6 cells were plated for each group. Macrophages were incubated with 100 ng/ml Lipopolysaccharide (LPS, Solarbio, China) and 20 ng/ml INF-γ (Beyotime, China) to induce M1 polarization, while 20 ng/ml IL-4 (Peprotech, United States) induced M2 polarization (Zhang et al., 2017; Xia et al., 2020). As a control, M0 macrophages were incubated in a complete culture medium. The cells were washed three times in PBS followed by incubation with a complete medium after 24 h. The medium supernatants derived from macrophage were centrifuged after collection for 20 min at 1950 g after another 24 h of culturing. The conditioned medium (CM) comprising M0, M1, and M2 cell cultures were given the respective names CM0, CM1, and CM2. As a control, the entire medium (Norm) was used. Quantitative real-time polymerase chain reaction (qRT-PCR), flow cytometry, and fluorescence staining and imaging were used to identify the phenotypes of polarized cells (as activated by IL-4 or LPS plus INF-γ) and unpolarized cells (complete culture medium).

Isolation and Identification of BMSCs

Sipeifu Biotechnology Co., Ltd provided C57BL/6J mice (4 weeks old, male) (Beijing, China). The Animal Use and Care Committee of the Liaocheng People's Hospital inspected and approved the entire animal work. Removal of C57BL/6J mice's femurs and tibias was carried out aseptically. The bone marrow tissues were flushed and incubated in α-MEM medium supplemented with streptomycin (1%), penicillin (1%), and FBS (10%). The cells cultures were maintained for 7–10 days, with the medium being changed every 3 days. BMSCs were identified by flow cytometry and used in subsequent experiments.

Isolation and Identification of Macrophage-Derived Exosomes

Isolation of Macrophage-Derived Exosomes

RAW264.7 cells were incubated in a polarization medium for 24 h before being washed twice with PBS to eliminate any residual cytokines. After that, the cells were cultured in α-MEM (Gibco, Grand Island, United States) supplemented with 10% exosome-depleted FBS and 1% penicillin/streptomycin. FBS was centrifuged at 100,000 g for 18 h to extract bovine exosomes using a Beckman Optima XE L-80 XP ultracentrifuge (45 Ti

rotor) (Beckman Coulter. Inc., United States). The CM formed by the M0, M1, and M2 macrophages was collected separately after 24 h. To extract cells and debris, individual CM specimen was centrifuged at 2,000 g for 30 min at 4°C. The complete exosome isolation (from cell culture medium) reagent was used to separate exosomes from CM samples (Invitrogen, Carlsbad, CA, United States) (Romero-López et al., 2020). Xia et al. used a similar method to extract the exosomes secreted by macrophages (Xia et al., 2020). The CM was moved to a new tube, and each CM supernatant received 0.5 volume of total exosome isolation reagent. Vortex was used to thoroughly combine the mixtures, followed by their incubation at 4°C overnight. After incubation, centrifuge the samples for 1 h at 4°C at 10,000 × g. Finally, 1 ml CM exosomes (designated M0-Exos, M1-Exos, and M2-Exos) were suspended in 100 μl PBS.

Identification of Macrophage-Derived Exosomes

The M2-Exos, M1-Exos, and M0-Exos were directed to Novogene Co., Ltd. in Beijing, China, for identification, which included transmission electron microscope (TEM) observation, nanoparticle tracking analysis (NTA), and identification of precise markers by flow cytometry for nanoparticle analysis (NanoFCM).

For one minute, exosomes were dropped on copper. The floating liquid was soaked by the filter paper after 10 μl of uranyl acetate was applied dropwise to the copper mesh for 1 min for precipitation. The grids were dried at room temperature for a few minutes. A Hitachi HT-7700 transmission electron microscope was used to examine the samples (Tokyo, Japan).

Nanoparticle tracking analysis (NTA) was employed for the assessment of particle size and exosome concentration. N30E was used to weigh exosomes (NanoFCM, Xiamen, China). Specific markers CD81 and CD63 were extracted from M1-Exos and M2-Exos to detect the expression of exosome protein.

Internalization of the Exosomes by BMSCs

The exosomes were labeled by employing PKH67 fluorescent cell linker kits (Sigma-Aldrich, St. Louis, MI, United States) following the protocol from the manufacturer. In a nutshell, 20 μl of exosomes were diluted in 1 ml of diluent C and 6 μl of PKH67 dye. The labeled exosomes were washed in PBS for 70 min at 100,000 g. Finally, BMSCs were incubated with PKH67-labeled exosomes for 6 h at 37°C. The uptake of exosomes by BMSCs was observed making use of a confocal laser microscope (FV1000; Olympus, Tokyo, and Japan).

Effects of Macrophage-Derived Exosomes on BMSCs Osteogenic Differentiation

BMSCs were seeded in 24-well plates, at a density of 2×10^5 cells per well. α-MEM full medium (with 10% FBS and 1% penicillin and streptomycin) was supplemented with 10 nM dexamethasone, 50 μg/ml vitamin C and 10 mM glycerophosphate to make osteogenic medium. To the osteogenic media employed for culturing BMSC, M0-Exos, M1-Exos, or M2-Exos were added at a concentration of 1 μg/ml (Qian et al., 2020). Nothing was added to the osteogenic medium as a blank control (CON). The cells were harvested after 7 days to be stained for alkaline phosphatase (ALP) and qRT-PCR analysis. The cells were harvested after 14 days for alizarin red S staining and activity analysis.

Microarray Analysis

The Illumina se50 platform was used to sequence RNA from M1-Exos and M2-Exos (NEB, United States). The Agilent Bioanalyzer 2,100 system's RNA Nano 6000 Assay Kit (Agilent Technologies, CA, United States) was utilized to test RNA integrity. Multiplex Small RNA Library Prep Set for Illumina (NEB, United States) was employed for building sequencing libraries, and index codes were added to each sample's sequences. DNA High Sensitivity Chips were used to evaluate library efficiency on the Agilent Bioanalyzer 2,100 device. Small RNAs were reverse transcribed, amplified, and sequenced on the Illumina HiSeq 2,500 platform, which provided 50-bp single-end reads. The samples were analyzed by DESeq based on negative binomial distribution and evaluated by fold change and Qvalue. The differential microRNAs were screened with Qvalue < 0.05 and log2 (foldchange) > 1. The overall distribution of differentially represented miRNAs is inferred using a volcanic map.

RAW264.7 Transfection

Lentiviral Infection Induces Knockdown and Overexpression of miR-21a-5p

The Gene Corporation provided the lentivirus Lv-mmu-miR-21a-5p-knockdown, overexpression and the negative regulation lentivirus (Genechem Co., Ltd, Shanghai, China). Following incubation for 24 h at 37°C, the RAW264.7 cells were plated into 6-well plates at a density of 2×10^5 cells/well and grown to 20–40% confluence. The RAW264.7 cells were then infected with the lentivirus at a multiplicity of infection (MOI) equivalent to 20. The cells in the shNC,Lv-NC group were transfected with NC lentivirus, while the cells in the shmiR-21a-5p group received Lv-mmu-miR-21a-5p knockdown, Lv-miR-21a-5p group received Lv-mmu-miR-21a-5p-overexpression.For 12–16 h, and the cells were cultured in an improved infection solution. A regular medium containing serum was then utilized to replace the cell culture medium. After 24 h, the cells were washed twice in PBS, and the 48-h puromycin (3 μg/ml) was used for screening.

The rate of green fluorescent protein-positive cells was then calculated using a fluorescence microscope for assessing transfection efficiency. To confirm the knockdown of miR-21a-5p, reverse transcription quantitative polymerase chain reaction (qRT-PCR) was employed for detecting the target genes STAT3, PTEN, and SMAD7. To confirm the overexpression of miR-21a-5p, reverse transcription quantitative polymerase chain reaction (qRT-PCR) was employed for detecting miR-21a-5p.

Effects of M1-Exos Derived miR-21a-5p on BMSCs Osteogenic Differentiation

In four groups of cells, 1×10^6 RAW264.7 cells were seeded per well in 6-well plates. The cells were induced into M1 respectively. The exosomes were generated and named shNC, shmiR-21a-5p, Lv-NC, and Lv-miR-21a-5p. QRT-PCR was used to confirm the expression of miR-21a-5p in exosomes (Horwood, 2016).

The exosomes were added to the osteogenic medium used to culture BMSCs at a concentration of 1 μg/ml 7 days later, the cells were harvested in order to be stained for alkaline phosphatase

TABLE 1 | Primer sequences used in this study.

Gene	Primer	Sequences (5′-3′)
CD206	Forward	AGACGAAATCCCTGCTACTG
	Reverse	CACCCATTCGAAGGCATTC
CD86	Forward	CTGCTCATCATTGTATGTCAC
	Reverse	ACTGCCTTCACTCTGCATTTG
Runx2	Forward	AAATGCCTCCGCTGTTATGAA
	Reverse	GCTCCGGCCCACAAATCT
OCN	Forward	CCGGGAGCAGTGTGAGCTTA
	Reverse	AGGCGGTCTTCAAGCCATACT
BMP-2	Forward	TGACTGGATCGTGGCACCTC
	Reverse	CAGAGTCTGCACTATGGCATGGTTA
ALP	Forward	AGGGTGGGTAGTCATTTGCATAG
	Reverse	GAGGCATACGCCATCACATG
OPN	Forward	ATCTCACCATTCGGATGAGTCT
	Reverse	TGTAGGGACGATTGGAGTGAAA
STAT3	Forward	ATTAA GGGCA GTGAG GACAT
	Reverse	GCCTT GCCTT CCTAA ATACC
PTEN	Forward	AATTC CCAGT CAGAG GCGCT ATGT
	Reverse	GATTG CAAGT TCCGC CACTG A
SMAD7	Forward	GCTAT TCCAG AAGAT GCTGT TC
	Reverse	GTTGC TGAGC TGTTC TGATT TG
miR-21a-5p	Forward	CGCTAG CTTATCAGAC TGA
	Reverse	CTCAACTGGTGTCGTGGA
miR-146a-5p	Forward	CGCTGAGA ACTGAATTCC A
	Reverse	CTCAACTGGTGTCGTGGA
miR-3473b	Forward	CGAGGGCT GGAGAGATG
	Reverse	CTCAACTGGTGTCGTGGA
U6	Forward	CTCGCTTCGGCAGCACA
	Reverse	AACGCTTCACGAATTTGCGT
GAPDH	Forward	TGACCACAGTCCATGCCATC
	Reverse	GACGGACACATTGGGGGTAG

(ALP) and qRT-PCR analysis. The cells were again harvested after 14 days to be stained with alizarin red S and activity analysis.

Flow Cytometric Analysis

Flow cytometry was used to examine the cell surface markers of BMSCs and RAW 264.7 cells. RAW264.7 macrophage cells were inoculated into a six-well plate with 1×10^6 cells inoculated per well. The cells incubated with 20 ng/ml IFN-γ and 100 ng/ml LPS were named as group M1, and group M2 was incubated with 20 ng/ml IL-4, group M0 was cultured with complete medium.

After 24 h, RAW 264.7 cells were digested by trypsin and the supernatant was removed after centrifugation. The three groups (M0, M1, M2) were then suspended with 1 ml PBS and added to 5 μl APC anti-mouse CD206 and FITC anti-mouse CD86 (Biolegend, San Diego, CA, United States). APC anti-mouse CD206 was employed for intracellular flow cytometry. The cells were resuspended with 0.5 ml permeabilization wash buffer (1 x) and centrifuged at 350 g for 5 min, discarding the supernatant later. Resuspension of the cells was done with 1 ml PBS and 5 μl APC anti-mouse CD206 was added.

The antibodies utilized for identifying BMSCs are mentioned as follows: PE/Cy5 anti-mouse CD44 Antibody, APC anti-mouse CD106 Antibody, FITC anti-mouse CD45 Antibody (BioLegend, San Diego, CA, United States). These antibodies were then suspended together with 1 ml PBS.

Cell antigen staining was analyzed using a FACSC alibur analyzer and Cell Quest software (BD Biosciences).

Quantitative Real-Time Polymerase Chain Reaction

For cellular mRNA, the RNA pure complete RNA quick isolation kit (BioTeke, Beijing, China) was used, whereas Trizol (Invitrogen, United States) was employed for miRNA, thereby completing the extraction of total RNA. First-strand cDNA was synthesized using PrimeScript™ RT Master Mix Kit (TaKaRa Bio Inc., Shiga, Japan) and the first-strand cDNA of miRNA Synthesis (stem ring method) (Sangon Biotech Co., Ltd. Shanghai, China). Later, using an Applied Biosystems 7500HT Real-Time PCR machine and SYBR PremixExTaqTMII, qRT-PCR analysis was carried out (Tli RNaseH Plus; TaKaRa, Tokyo, Japan). Primer sequences used in this study are summarized in **Table 1**. Gene expression was normalized to GAPDH (for cellular mRNA) and U6 (for miRNA) using the ΔΔCt method.

Fluorescence Staining and Imaging

Macrophage polarization (M0, M1, and M2) was identified by fluorescence staining and imaging. The three groups of cells were fixed for 30 min at room temperature in 4% paraformaldehyde (MP Biomedicals, Santa Ana, CA, United States). 0.1% Triton X-100 (Sigma-Aldrich, St. Louis, MO, United States) in PBS containing 0.1% Tween-20 was used to permeabilize the cells, after washing them with PBS thrice (5 min each). The cells were blocked with 3% BSA (Sigma-Aldrich) for 30 min at room temperature. After that, samples were allowed to incubate overnight at 4°C with primary antibodies, which included rabbit anti-iNOS IgG (Abcam, United States) and mouse anti-Arginase (Abcam, United States), Anti-CD86 Antibody (Abcam, United States), and Anti-Mannose Receptor Antibody (Abcam, United States) (Abcam, United States). Secondary antibodies included Cy3-labeled Goat Anti-Rat IgG (Beyotime, Shanghai, China), Cy3-labeled Goat Anti-Mouse IgG (Beyotime, Shanghai, China), and Alexa Fluor 488-labeled Goat Anti-Mouse IgG (Beyotime, Shanghai, China), and cells were counterstained with 6-diamidino-2-phenylindole (DAPI) (Beyotime, Shanghai, China) solution at 1 μg/ml. Images were obtained using a fluorescence microscope was used to capture the images (BX51; Olympus, Tokyo, and Japan).

Statistical Analyses

All data are presented as the mean and standard deviation (±SD) from at least three independent experiments. Statistically signifcant differences were determined by one-way ANOVA and independent unpaired parametric 2-tailed Student's *t* test. All statistical analysis was performed on GraphPad Prism 7 (GraphPad Software). *p* values of less than 0.05 were considered significant and denoted with an asterisk.

RESULTS

Characterization of Polarized Macrophages

Flow cytometry, qRT-PCR, and immunofluorescent staining were used to assess the expression of phenotype markers associated with M1 and M2 macrophages. RAW264.7 induced

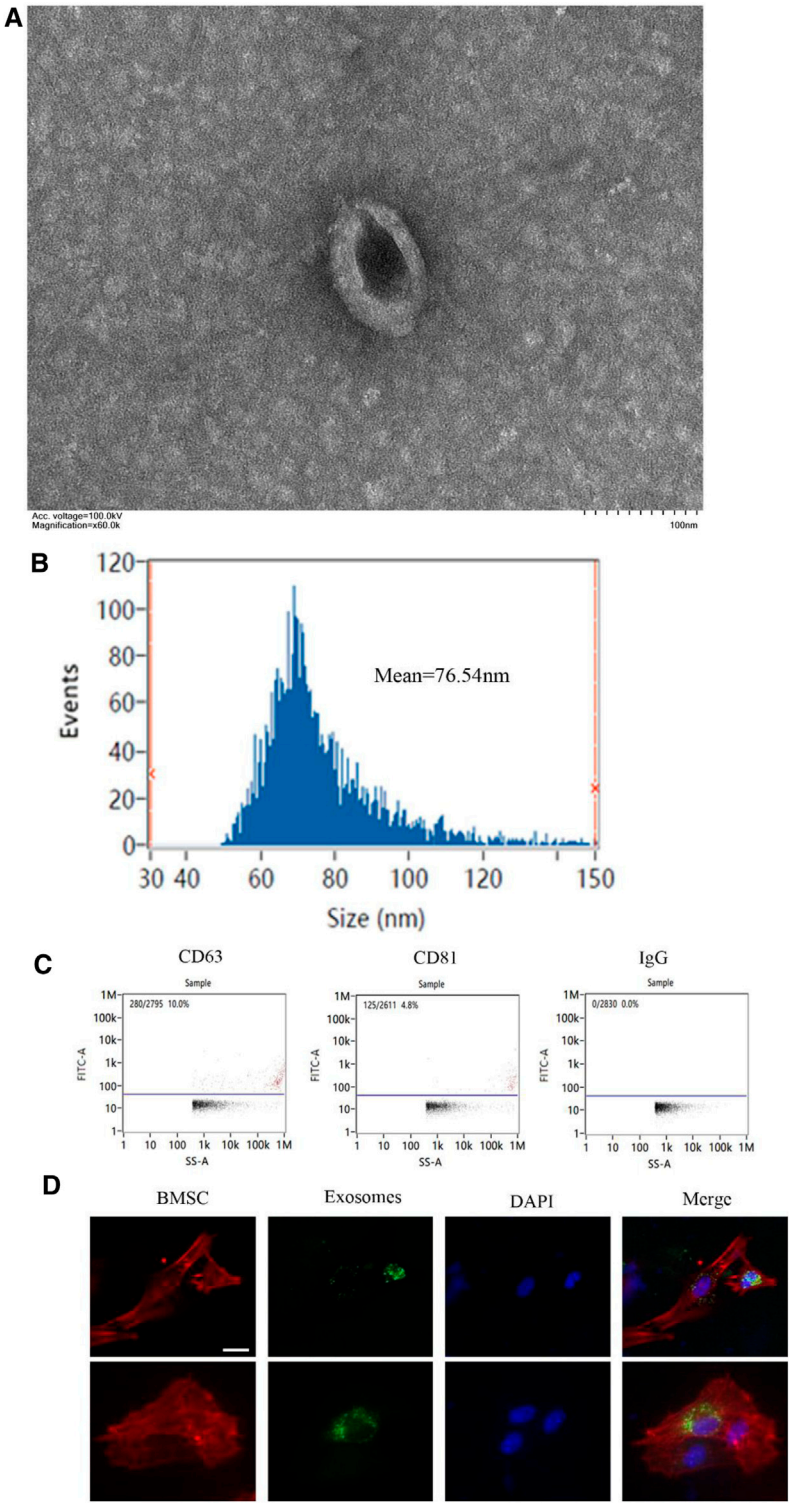

FIGURE 1 | Identification of exosomes generated by macrophages. **(A)** The morphology of exosomes under transmission electron microscope (scale bar: 100 nm); **(B)** The size distribution curve of the exosomes was determined by nanoparticle tracking analysis; **(C)** The expression of exosome marker proteins CD81 and CD63 was analyzed by flow cytometry; **(D)** Representative immunofluorescence images showing the internalization of PKH67-labeled BMDM-derived exosomes (green) by BMSCs stained with phalloidine (red) at 6 h. Cell nuclei were stained with DAPI (blue), white arrows indicate exosomes (green). Scale bars, 10 μm. *p <0.05 and **p < 0.01.

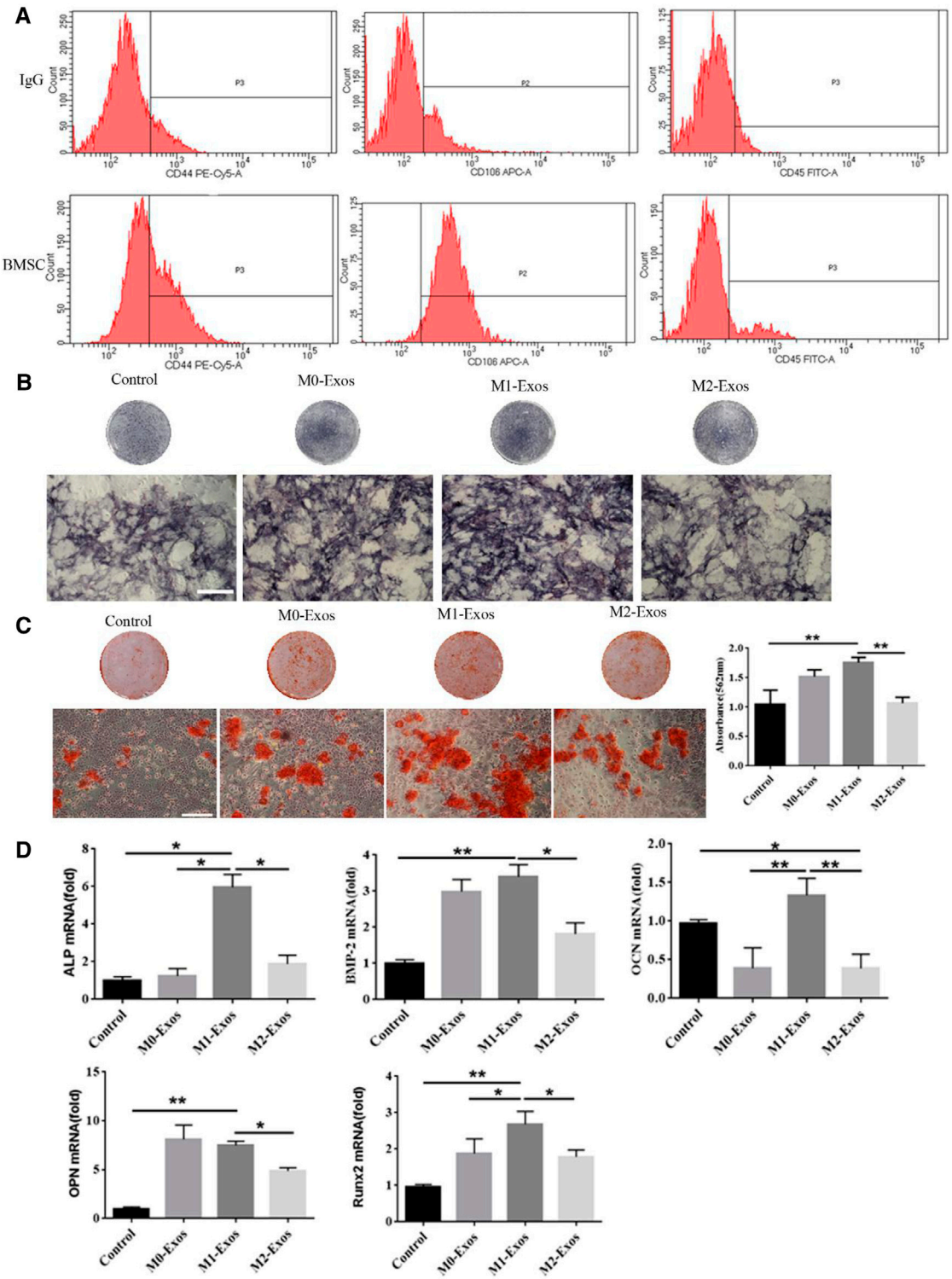

FIGURE 2 | M1-Exos promote osteogenic differentiation of BMSCs. **(A)** Identification of BMSCs markers by flow cytometry. **(B)** ALP stainingand in BMSCs (Scale bars, 100 μm). **(C)** Alizarin red S staining and quantification in BMSCs (Scale bars, 100 μm); **(D)** The expression of osteogenic gene was detected by qRT-PCR. Data are presented as mean ± SD. $^{*}p < 0.05$, $^{**}p < 0.01$ represent significant differences between the indicated columns.

by IFN-γ plus LPS was named as group M1, and RAW264.7 induced by IL-4 was named as group M2. Cells were incubated in a normal complete medium as an unpolarized phenotype (M0). CD86 and CD206 being M1 and M2 surface markers, respectively. Flow cytometric analysis revealed a stronger CD86 expression in M1 whereas CD206 was highly expressed in M2 (Additional file: **Supplementary Figure S1A**). Analysis of mRNA expression of CD86 and CD206 in macrophages was carried out using qRT-PCR. Our results demonstrated a significant rise in the CD86 mRNA expression in M1 macrophages. In addition, CD206 was found to be significantly up-regulated in M2 macrophages (Additional file: **Supplementary Figure S1B**). An immunofluorescence assay was used to confirm the polarization of macrophages. iNOS and CD86 (M1-specific markers) staining was observed to be much stronger in M1 macrophages whereas the staining of Arg-1 and CD206 (M2-specific markers) was manifested much strongly in M2 macrophages (Additional file: **Supplementary Figure S1C**). We successfully induced M1 and M2 phenotypes in macrophages.

Identification of Exosomes Generated by Macrophages

The exosomes were extracted from M1 and M2 macrophages' CM. Transmission electron microscopy was employed to examine the morphology of exosomes. As shown in **Figure 1A**, exosomes were elliptical vesicles with bilayer membranes (**Figure 1A**). These exosomes have a diameter of 30–150 nm, according to nanoparticle tracking analysis (**Figure 1B**). Exosomal markers CD81 and CD63 were clearly expressed by flow cytometry for nanoparticle analysis (**Figure 1C**). Fluorescence microscope imaging revealed the presence of PKH67 spots in recipient fibroblasts after incubation, indicating that macrophage's exosomes were delivered to BMSCs (**Figure 1D**).

M1-Exos Promote Osteogenic Differentiation of BMSCs

Next, we extracted mouse BMSCs and the expression of markers was identified by flow cytometry studied. The results indicated that BMSCs were successfully extracted treated (**Figure 2A**). The impact of exosomes secreted by macrophages on osteogenic differentiation of BMSCs was investigated. For the incubation of BMSCs, M0-Exos, M1-Exos, and or M2-Exos were added to the osteogenic medium. The control group received the same amount of osteogenic medium. In BMSCs treated with Exos-based osteogenic medium for 7–14 days, we measured ALP activity, osteogenesis-related gene expression, and alizarin red S staining. The results indicated that M1 and M2 polarized macrophage exosomes all can promote osteogenesis of BMSCs. In M1-Exos, there were more ALP-positive cells (**Figure 2B**). M1-Exos BMSCs formed more calcium deposits than other types, according to Alizarin Red S staining. According to quantitative analysis, BMSCs in M1-Exos provided the most mineralized nodules (**Figure 2C**). Expression of the osteogenic genes ALP, BMP-2, OPN, OCN, and Runx2 were then measured by qRTPCR. Compared with other groups, the mRNA levels of these genes were significantly increased in M1-Exos group (**Figure 2D**). This finding further indicated that M1 may promote the early stages of osteogenesis mainly through exosomes.

Differential miRNAs of M1-Exos and M2-Exos were Detected by Small RNA-seq Technology

To explore the mechanism of M1-Exos promoting osteogenesis of BMSCs, we made use of miRNA microarray for comparing the differentially-expressed miRNAs in M1-Exos and M2-Exos. The difference of miRNA expression between M1-Exos and M2-Exos was detected by independent hierarchical clustering and demonstrated using a heat map (**Figure 3A**). As demonstrated in **Figure 3B**, a volcano plot illustrates the expression variance in the number of differentially-expressed miRNAs at different p-values and fold changes. Based on a threshold set at (>2.0 fold change and $p < 0.05$) for the microarray data, a total of 8 differentially expressed mRNAs were identified in M1-Exos in comparison with the M2-Exos macrophage samples, of which two miRNAs (miR-3473b, miR-146a-5p) were up-regulated whereas six of them (miR-342-5p, mmu-miR-451a, miR-365-2-5p, miR-182-5p, miR-122-5p, and miR-122b-3p) were down-regulated. Although microarray analysis showed that miR-21a-5p had no significant difference M1-Exos and M2-Exos, it was the most abundant microRNA in M1-Exos (**Figure 3C**). Therefore, we verified the expression of miR-3473b and miR-146a-5p as well as miR-21a-5p via qRT-PCR. The results revealed that miR-21a-5p was significantly up-regulated in M1-Exos compared with M2-Exos (**Figure 3C**). To evaluate concordance in gene expression intensities between RNA-seq and qRT-PCR, we calculated expression correlation between qRT-qPCR C_T-values and log transformed RNA-seq expression values (Everaert et al., 2017). High expression correlations were observed between RNA-seq and qRT-PCR expression intensities (Pearson correlation, $R^2 = 0.845$) (**Figure 3D**).

MiR-21a-5p Induces Osteogenic Differentiation of BMSCs *In Vitro*

We intended to investigate whether miR-21a-5p was a crucial genetic factor that influenced BMSCs osteogenic differentiation since it was the most abundant microRNA and its levels were found to increase dramatically in M1-Exos (Zhang et al., 2017). Lentivirus transfection was utilized for knocking down miR-21a-5p in M1 macrophage and the knockdown rate was 80%, thereby suggesting that individual genes have been successfully knocked down (**Figure 4A**). qRT-PCR verified the expression of miR-21a-5p′s target genes SMAD7, PTEN, and STAT3. The outcome revealed that the gene expression of SMAD7, PTEN, and STAT3 increased after the knockdown of mir-21a-5p (**Figure 4B**). M1 transfected with shmiR-21a-5p, as well as M1 with shNC were cultured in a 10 cm culture dish. The exosomes were extracted from the supernatant of each group and added to the osteogenic induction medium to incubate BMSCs. The results demonstrated

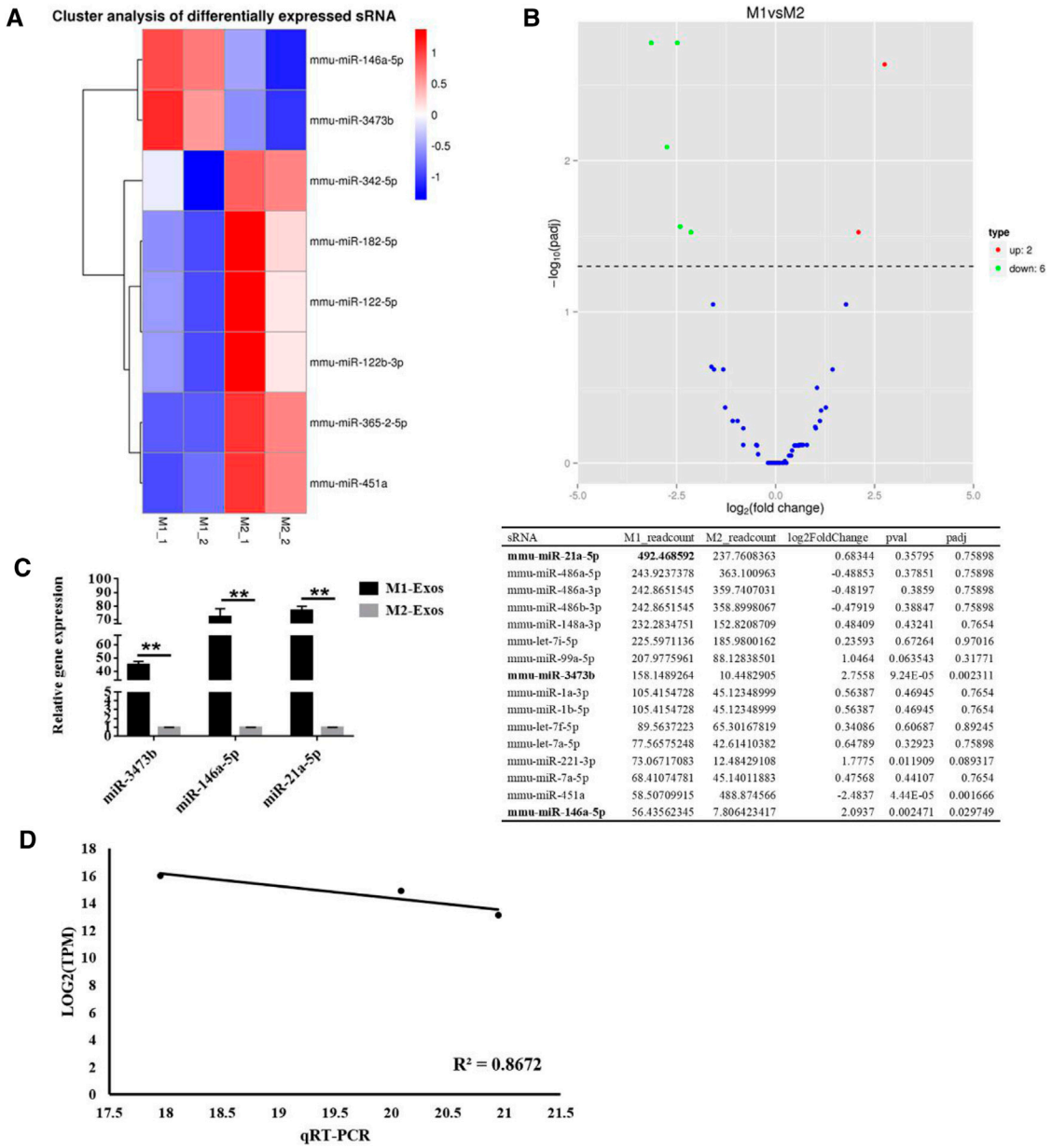

sRNA	M1_readcount	M2_readcount	log2FoldChange	pval	padj
mmu-miR-21a-5p	**492.468592**	237.7608363	0.68344	0.35795	0.75898
mmu-miR-486a-5p	243.9237378	363.100963	-0.48853	0.37851	0.75898
mmu-miR-486a-3p	242.8651545	359.7407031	-0.48197	0.3859	0.75898
mmu-miR-486b-3p	242.8651545	358.8998067	-0.47919	0.38847	0.75898
mmu-miR-148a-3p	232.2834751	152.8208709	0.48409	0.43241	0.7654
mmu-let-7i-5p	225.5971136	185.9800162	0.23593	0.67264	0.97016
mmu-miR-99a-5p	207.9775961	88.12838501	1.0464	0.063543	0.31771
mmu-miR-3473b	158.1489264	10.4482905	2.7558	9.24E-05	0.002311
mmu-miR-1a-3p	105.4154728	45.12348999	0.56387	0.46945	0.7654
mmu-miR-1b-5p	105.4154728	45.12348999	0.56387	0.46945	0.7654
mmu-let-7f-5p	89.5637223	65.30167819	0.34086	0.60687	0.89245
mmu-let-7a-5p	77.56575248	42.61410382	0.64789	0.32923	0.75898
mmu-miR-221-3p	73.06717083	12.48429108	1.7775	0.011909	0.089317
mmu-miR-7a-5p	68.41074781	45.14011883	0.47568	0.44107	0.7654
mmu-miR-451a	58.50709915	488.874566	-2.4837	4.44E-05	0.001666
mmu-miR-146a-5p	56.43562345	7.806423417	2.0937	0.002471	0.029749

FIGURE 3 | Identifcation of diferentially expressed miRNAs between M1-Exos and M2-Exos. **(A)** Heat map identifed the diferently expressed miRNAs of M1-Exos and M2-Exos. Red and blue were used to indicate the up-regulated and down-regulated genes respectively. $n = 2$ for each group. M1, Exosomes were extracted from medium of M1 macrophage medium; M2, Exosomes were extracted from medium of M1 macrophage medium; **(B)** Volcano plot comparing the levels of gene expression between M1-Exos and M2-Exos. Red and green dots represent upregulated and downregulated miRNAs (>2.0 fold change and $p < 0.05$). **(C)** The expression of miR-3473b, miR-146a-5p and miR-21a-5p was detected by qRT-PCR. Data are presented as mean ± SD. $^{**}p < 0.01$ represent significant differences between the indicated columns. **(D)** Gene expression correlation between qRT-PCR and RNA-seq data. Te Pearson correlation coefficients and linear regression line are indicated.

that there were fewer ALP positive cells in the shmiR-21a-5p group (**Figure 4C**). Alizarin red S staining revealed that the shmiR-21a-5p group had the least calcium deposition of all, and the quantitative analysis showed that the mineralized nodules were also the least (**Figure 4D**). The expression of osteogenic genes OCN, BMP-2, ALP, OPN, and Runx2 was detected by qRT-PCR. In comparison to shNC, the mRNA levels of these genes in the shmiR-21a-5p group were substantially lower (**Figure 4E**). Next, we used the same method to overexpress miR-21a-5p to detect osteogenic differentiation of BMSCs (**Figure 5A**). The outcome revealed that the gene expression of miR-21a-5p increased (**Figure 5B**). Moreover, there were more ALP positive cells in the Lv-miR-21a-5p group (**Figure 5C**). Alizarin red S staining showed the most

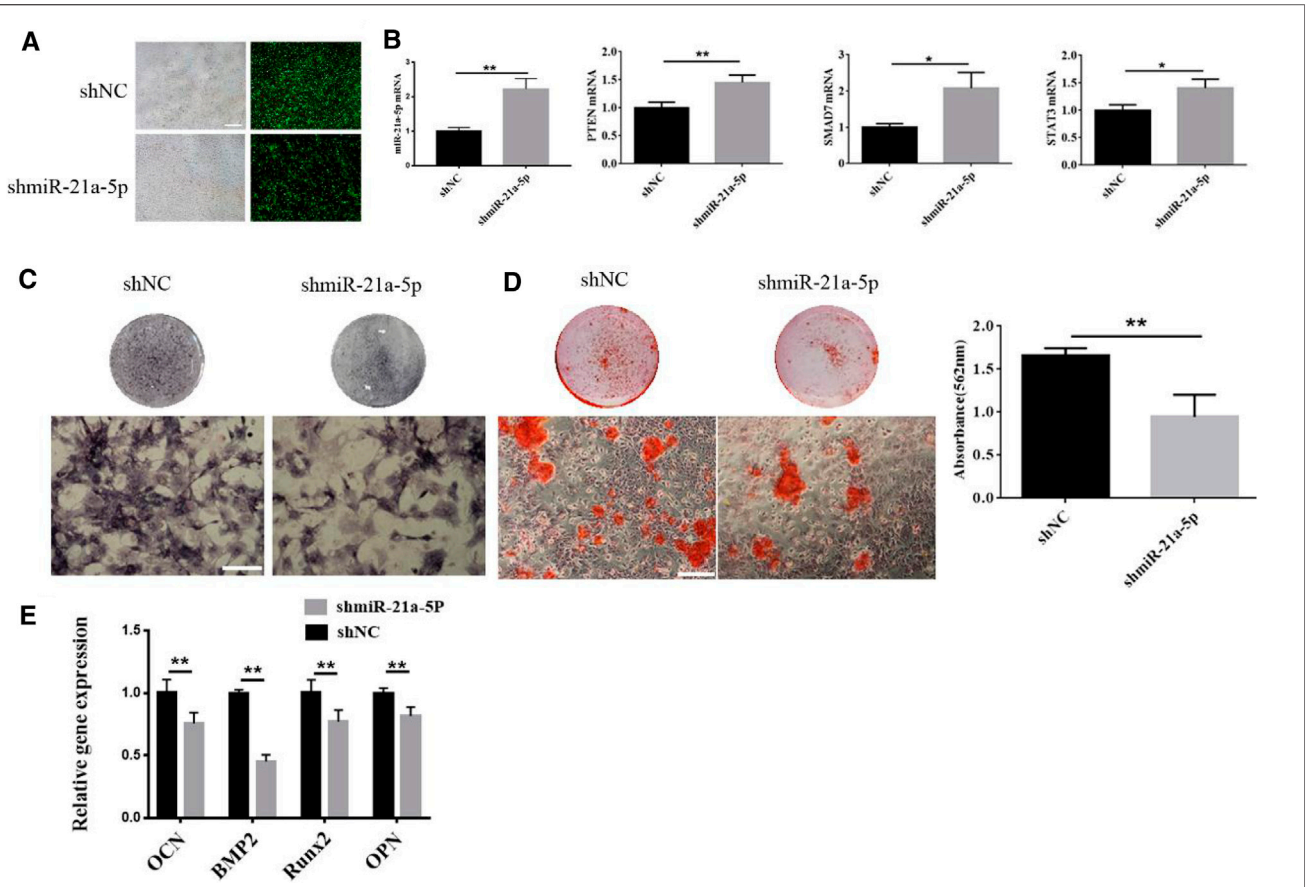

FIGURE 4 | Effect of knocking down miR-21a-5p in M1 macrophages on osteogenic differentiation of BMSCs. **(A)** sh-miR-21a-5p were knocked down using a lentiviral transfection technique. **(B)** qPT-PCR was used to verify the expression of miR-21a-5p, SMAD7, PTEN, and STAT3. $^{**}p < 0.01$. **(C)** ALP staining in BMSCs (Scale bars, 100 μm). **(D)** Alizarin red S staining and quantification in BMSCs (Scale bars, 100 μm). **(E)** The expression of osteogenic gene was detected by qRT-PCR (7 days).Data are presented as mean ± SD. $^{*}p < 0.05$, $^{**}p < 0.01$ represent significant differences between the indicated columns.

calcium deposition in the Lv-miR-21a-5p group, and quantitative analysis showed the most mineralized nodules (**Figure 5D**). The expression of osteogenic genes ALP, OPN, BMP2, Runx2, and COL-1 was detected by qRT-PCR (7 days). The mRNA levels of these genes were significantly higher in the Lv-miR-21a-5p group compared to Lv-NC (**Figure 5E**).

DISCUSSION

Bone defect repair has always been a difficult problem in clinical treatment, due to the destruction of the inflammatory microenvironment. Macrophages have an indispensable role in the control of bone regeneration in normal bones, contributing to inflammation and debridement of the injury site (Pajarinen et al., 2019). Macrophages can polarize from a nonpolarized state to M1 and M2, making them important targets for therapeutic. Studies have shown that macrophage polarization can promote osteoblast differentiation (Horwood, 2016). MSCs co-cultured with M2 macrophages results in substantially increased MSCs mineralization due to soluble factors, according to studies. M0 and M1 macrophages, in particular, only stimulated MSCs osteogenic differentiation in the early stage of co-culture (Zhang et al., 2017). The significance of an original, transient inflammatory process mediated by M1 macrophage-BMSCs cross-talk in enhancing osteoblast differentiation was highlighted by our findings. Lu et al. found that exposing BMSCs to a high density of pro-inflammatory M1 macrophages stimulated them to achieve their maximum pro-osteogenic capacity and immune-modulatory effect by reciprocally modulating an ideal transfer of macrophages from M1 to M2 phenotype for optimal bone healing (Lu et al., 2017). Zhang et al. co-cultured MSCs with M0, M1, and M2 macrophages and measured ALP activity at 7, 14, and 28 days, respectively. The results revealed that M1 macrophages and M2 macrophages had the advantage of promoting osteogenic differentiation at 7 and 28 days, respectively, (Zhang et al., 2017).

Macrophage-derived exosomes have become a research hotspot in recent years. Exosomes, which are secreted by almost all cells and widely present in various body fluids, are nano-sized vesicles of 30–150 nm in diameter. Exosomes from various kinds of cells contain 194 lipids, 4,400 proteins, 764 miRNAs, and 1,639 mRNAs approximately, suggesting their complexity as well as the diversity of function (Pegtel and

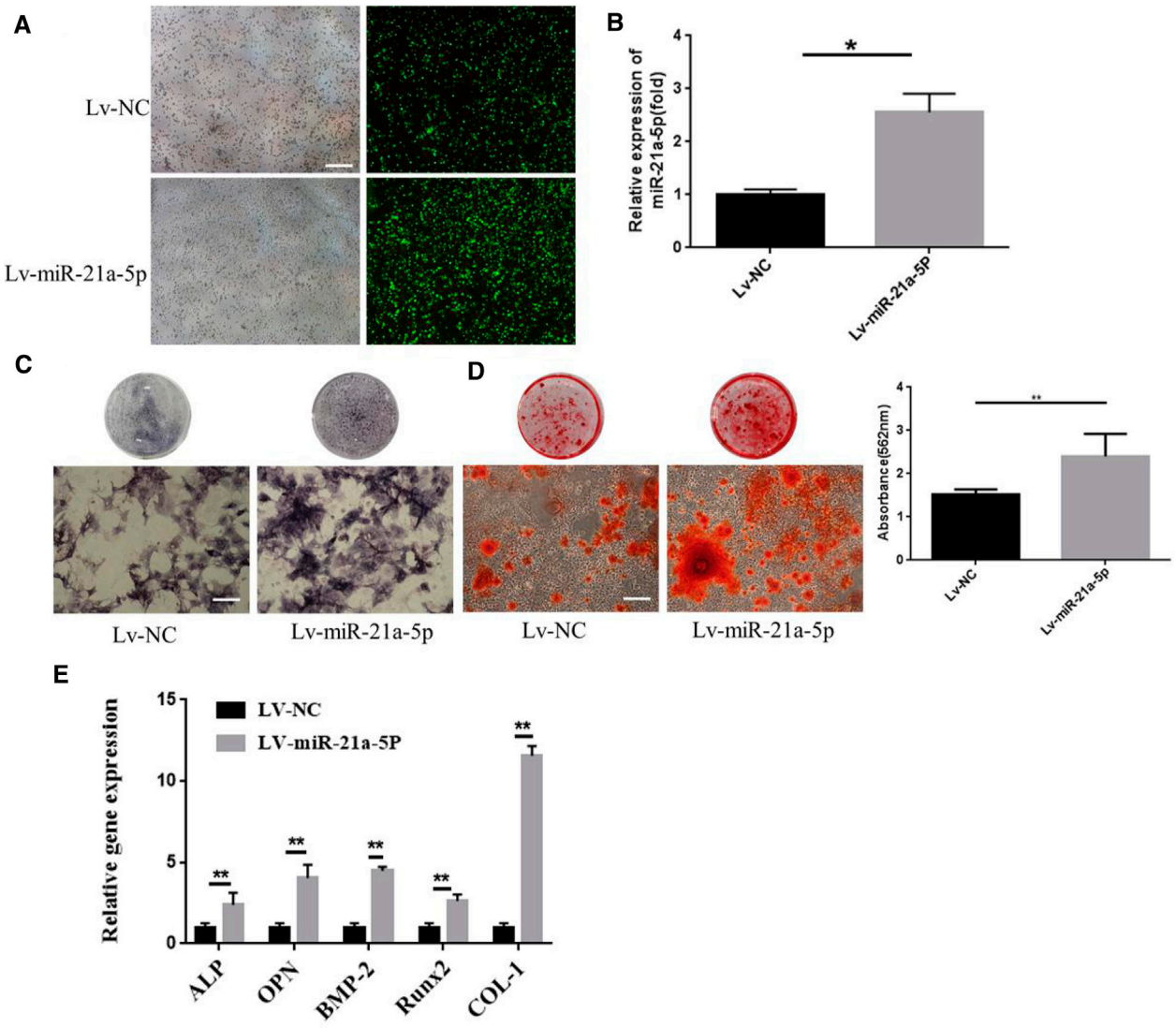

FIGURE 5 | Effect of miR-21a-5p overexpression in M1 macrophages on osteogenic differentiation of BMSCs. **(A)** MiR-21a-5p was overexpressed using lentivirus transfection technique. **(B)** QPT-PCR was used to verify the expression of miR-21a-5p. **(C)** ALP staining in BMSCs (Scale bars, 100 μm). **(D)** Alizarin red S staining and quantification in BMSCs (Scale bars, 100 μm). **(E)** The expression of osteogenic gene was detected by qRT-PCR. Data are presented as mean ± SD. $^{*}p < 0.05$, $^{**}p < 0.01$ represent significant differences between the indicated columns.

Gould, 2019; Zhang et al., 2019). The influence of M1 and M2 exosomes upon BMSCs osteogenic differentiation were investigated. The exosomes secreted by M0, M1, M2 were added to the osteogenic induction medium of BMSCs for 7 and 14 days and macrophage exosomes were all found to facilitate osteogenic differentiation of BMSCs. And M1 exosomes are more effective. This is consistent with the research results of Xia et al. (2020). Upon bone injury, monocytes are recruited to the wound site and differentiate into activated macrophages. In the early stages of injury mainly polarized to M1 macrophages (Vallés et al., 2020). We speculate that the M1 phenotype is essential for early osteogenic differentiation. In exosomes, 80% of the content is miRNA. Exosomes, which are secreted by macrophages, enhance the inflammatory response of receptor cells by controlling the levels of microRNAs (miRNAs) and play an important role in cell-to-cell contact (Li et al., 2019). We used microarray analysis to discover that miR-21a-5p is the main miRNA enriched in M1 exosomes, which may play a role in bone formation/regeneration promotion or inhibition. We knocked down and overexpressed miR-21a-5p in M1 macrophages to verify whether miR-21a-5p affects the osteogenic differentiation of BMSCs. The results showed that when BMSCs were incubated with exosomes secreted by M1 macrophages with a miR-21a-5p knockdown, the number of ALP positive cells and mineralized nodules were decreased, and the expression of osteogenic related genes was decreased. Meanwile, M1 macrophage exosomes overexpressing miR-21a-5p promoted the osteogenic differentiation of BMSCs.

The present data indicates that M1 macrophagy-derived exosomes miR-21a-5p induces BMSCs towards osteoblastic fate in the early stage of osteogenesis. The findings suggested that the M1 macrophage-BMSCs crosstalk could aid osteogenesis by stimulating osteoblast differentiation through paracrine signaling.

Many studies have demonstrated the effects of MSCs priming with pro-inflammatory cytokines or growth factors (Noronha et al., 2019). This is consistent with our point of view. In addition, exosomes were added at a low concentration of 1 μg/ml. One study indicated that low-inflammatory macrophages could activate autophagy in BMSCs to improve osteogenesis (Yang et al., 2021).These observations highlight the importance of an initial, transient inflammatory phase during bone healing.

Modern research showed that exosome is an effective and potent additive to produce advanced immunomodulatory and bone regeneration materials. There are results showed the exosomes loaded sulfonated polyetheretherketone (SPEEK) promoted macrophage polarization via the NF-κB pathway to enhance BMSCs osteogenic differentiation (Fan et al., 2021). So, the application of bone biomaterials combined with exosomes in bone tissue engineering may be promising.

The findings that co-culturing of BMSCs with exosomes secreted by M1 macrophages enhances osteogenesis of the BMSCs suggest the feasibility of targeting BMSCs-macrophage crosstalk for bone repair. Besides, the mechanism of M1 macrophage-derived exosomes miR-21a-5p inducing osteogenic differentiation of BMSCs needs further study and should be modeled by animal experiments, so as to open up a new therapeutic scheme for macrophages to repair bone defects.

CONCLUSION

The effect of macrophage exosomes on BMSCs osteogenic differentiation was investigated in this research. The results indicated that M1 and M2 polarized macrophage exosomes all can promote osteogenesis of BMSCs. Especially, M1 macrophage exosomes have a stronger ability at the early stage of inflammation.The enhanced osteogenesis mediated by M1 macrophage exosomes is related to the miR-21a-5p. Understanding the regulatory effect of M1 macrophage exosome miRNA on BMSCs will aid in designing effective strategies to guide the fate of BMSCs and improve the regeneration results and have immense potential for optimizing fracture therapies.

DATA AVAILABILITY STATEMENT

The original contributions presented in the study are included in the article/**Supplementary Material**, further inquiries can be directed to the corresponding authors.

AUTHOR CONTRIBUTIONS

XL, Z-YL, Y-JZ, JL, C-XM, H-FQ, C-YH, LH assisted KL performed all experimental work of this article. KL wrote and XL edited the manuscript. F-ZL reviewed this manuscript, contributed, and approved the final manuscript. ZM, F-ZL, and BZ contributed to the conception, design, and leadership of the program.

FUNDING

This work was in part supported by the Science Foundation of Shandong Province of China (Grant Nos: ZR2021MH026 and ZR2019PH090) and Medicine and Health Science Technology Development plan of Shandong Province of China (Grant No: 202108020440), and Liaocheng People's Hospital Youth Fund Project (Grant No: LYQN201914).

SUPPLEMENTARY MATERIAL

The Supplementary Material for this article can be found online at: https://www.frontiersin.org/articles/10.3389/fbioe.2021.801432/full#supplementary-material

REFERENCES

Budak, H., Bulut, R., Kantar, M., and Alptekin, B. (2016). MicroRNA Nomenclature and the Need for a Revised Naming Prescription. *Brief. Funct. Genomics* 15, 65–71. doi:10.1093/bfgp/elv026

Everaert, C., Luypaert, M., Maag, J. L. V., Cheng, Q. X., Dinger, M. E., Hellemans, J., et al. (2017). Benchmarking of RNA-Sequencing Analysis Workflows Using Whole-Transcriptome RT-qPCR Expression Data. *Sci. Rep.* 7, 1559. doi:10.1038/s41598-017-01617-3

Fan, L., Guan, P., Xiao, C., Wen, H., Wang, Q., Liu, C., et al. (2021). Exosome-functionalized Polyetheretherketone-Based Implant with Immunomodulatory Property for Enhancing Osseointegration. *Bioact Mater.* 6, 2754–2766. doi:10.1016/j.bioactmat.2021.02.005

Horwood, N. J. (2016). Macrophage Polarization and Bone Formation: A Review. *Clinic Rev. Allerg Immunol.* 51, 79–86. doi:10.1007/s12016-015-8519-2

Huang, Y., Yang, Y., Wang, J., Yao, S., Yao, T., Xu, Y., et al. (2021). miR-21-5p Targets SKP2 to Reduce Osteoclastogenesis in a Mouse Model of Osteoporosis. *J. Biol. Chem.* 296, 100617. doi:10.1016/j.jbc.2021.100617

Krzyszczyk, P., Schloss, R., Palmer, A., and Berthiaume, F. (2018). The Role of Macrophages in Acute and Chronic Wound Healing and Interventions to Promote Pro-wound Healing Phenotypes. *Front. Physiol.* 9, 419. doi:10.3389/fphys.2018.00419

Li, J., Zhang, Y.-J., Lv, Z.-Y., Liu, K., Meng, C.-X., Zou, B., et al. (2020). The Observed Difference of Macrophage Phenotype on Different Surface Roughness of Mineralized Collagen. *Regen. Biomater.* 7, 203–211. doi:10.1093/rb/rbz053

Li, L., and Jiang, D. (2019). Hypoxia-responsive miRNA-21-5p Inhibits Runx2 Suppression by Targeting SMAD7 in MC3T3-E1 Cells. *J. Cel Biochem* 120, 16867–16875. doi:10.1002/jcb.28944

Li, M., Wang, T., Tian, H., Wei, G., Zhao, L., and Shi, Y. (2019). Macrophage-derived Exosomes Accelerate Wound Healing through Their Anti-

inflammation Effects in a Diabetic Rat Model. *Artif. Cell Nanomed Biotechnol* 47, 3793–3803. doi:10.1080/21691401.2019.1669617

Li, X., Guo, L., Liu, Y., Su, Y., Xie, Y., Du, J., et al. (2017). MicroRNA-21 Promotes Osteogenesis of Bone Marrow Mesenchymal Stem Cells via the Smad7-Smad1/5/8-Runx2 Pathway. *Biochem. Biophysical Res. Commun.* 493, 928–933. doi:10.1016/j.bbrc.2017.09.119

Li, Z., Gu, Y., Lin, Z., Ma, H., and Zhang, S. (2020). Cordycepin Promotes Osteogenesis of Bone Marrow-Derived Mesenchymal Stem Cells and Accelerates Fracture Healing via Hypoxia in a Rat Model of Closed Femur Fracture. *Biomed. Pharmacother.* 125, 109991. doi:10.1016/j.biopha.2020.109991

Lian, F., Zhao, C., Qu, J., Lian, Y., Cui, Y., Shan, L., et al. (2018). Icariin Attenuates Titanium Particle-Induced Inhibition of Osteogenic Differentiation and Matrix Mineralization via miR-21-5p. *Cell Biol Int* 42, 931–939. doi:10.1002/cbin.10957

Loi, F., Córdova, L. A., Zhang, R., Pajarinen, J., Lin, T.-h., Goodman, S. B., et al. (2016). The Effects of Immunomodulation by Macrophage Subsets on Osteogenesis *In Vitro*. *Stem Cel Res Ther* 7, 15. doi:10.1186/s13287-016-0276-5

Lu, L. Y., Loi, F., Nathan, K., Lin, T.-h., Pajarinen, J., Gibon, E., et al. (2017). Pro-inflammatory M1 Macrophages Promote Osteogenesis by Mesenchymal Stem Cells via the COX-2-Prostaglandin E2 Pathway. *J. Orthop. Res.* 35, 2378–2385. doi:10.1002/jor.23553

Meng, C., Liu, K., Lv, Z., Zhang, Y., Li, J., Luo, X., et al. (2021). Inflammation and Immunity Gene Expression Profiling of Macrophages on Mineralized Collagen. *J. Biomed. Mater. Res.* 109, 1328–1336. doi:10.1002/jbm.a.37124

Muñoz, J., Akhavan, N. S., Mullins, A. P., and Arjmandi, B. H. (2020). Macrophage Polarization and Osteoporosis: A Review. *Nutrients* 12, 2999. doi:10.3390/nu12102999

Nathan, K., Lu, L. Y., Lin, T., Pajarinen, J., Jämsen, E., Huang, J.-F., et al. (2019). Precise Immunomodulation of the M1 to M2 Macrophage Transition Enhances Mesenchymal Stem Cell Osteogenesis and Differs by Sex. *Bone Jt. Res.* 8, 481–488. doi:10.1302/2046-3758.810.BJR-2018-0231.R2

Noronha, N. C., Mizukami, A., Caliári-Oliveira, C., Cominal, J. G., Rocha, J., Covas, D. T., et al. (2019). Priming Approaches to Improve the Efficacy of Mesenchymal Stromal Cell-Based Therapies. *Stem Cel Res Ther* 10, 131. doi:10.1186/s13287-019-1224-y

Oishi, Y., and Manabe, I. (2018). Macrophages in Inflammation, Repair and Regeneration. *Int. Immunol.* 30, 511–528. doi:10.1093/intimm/dxy054

Pajarinen, J., Lin, T., Gibon, E., Kohno, Y., Maruyama, M., Nathan, K., et al. (2019). Mesenchymal Stem Cell-Macrophage Crosstalk and Bone Healing. *Biomaterials* 196, 80–89. doi:10.1016/j.biomaterials.2017.12.025

Pegtel, D. M., and Gould, S. J. (2019). Exosomes. *Annu. Rev. Biochem.* 88, 487–514. doi:10.1146/annurev-biochem-013118-111902

Qian, M., Wang, S., Guo, X., Wang, J., Zhang, Z., Qiu, W., et al. (2020). Hypoxic Glioma-Derived Exosomes Deliver microRNA-1246 to Induce M2 Macrophage Polarization by Targeting TERF2IP via the STAT3 and NF-Kb Pathways. *Oncogene* 39, 428–442. doi:10.1038/s41388-019-0996-y

Romero-López, M., Li, Z., Rhee, C., Maruyama, M., Pajarinen, J., O'Donnell, B., et al. (2020). Macrophage Effects on Mesenchymal Stem Cell Osteogenesis in a Three-Dimensional *In Vitro* Bone Model. *Tissue Eng. A* 26, 1099–1111. doi:10.1089/ten.TEA.2020.0041

Selders, G. S., Fetz, A. E., Radic, M. Z., and Bowlin, G. L. (2017). An Overview of the Role of Neutrophils in Innate Immunity, Inflammation and Host-Biomaterial Integration. *Regen. Biomater.* 4, 55–68. doi:10.1093/rb/rbw041

Shapouri-Moghaddam, A., Mohammadian, S., Vazini, H., Taghadosi, M., Esmaeili, S. A., Mardani, F., et al. (2018). Macrophage Plasticity, Polarization, and Function in Health and Disease. *J. Cel Physiol* 233, 6425–6440. doi:10.1002/jcp.26429

Sui, B.-D., Hu, C.-H., Liu, A.-Q., Zheng, C.-X., Xuan, K., and Jin, Y. (2019). Stem Cell-Based Bone Regeneration in Diseased Microenvironments: Challenges and Solutions. *Biomaterials* 196, 18–30. doi:10.1016/j.biomaterials.2017.10.046

Thurairajah, K., Broadhead, M., and Balogh, Z. (2017). Trauma and Stem Cells: Biology and Potential Therapeutic Implications. *Int. J. Mol. Sci.* 18, 577. doi:10.3390/ijms18030577

Tu, B., Liu, S., Liu, G., Yan, W., Wang, Y., Li, Z., et al. (2015). Macrophages Derived from THP-1 Promote the Osteogenic Differentiation of Mesenchymal Stem Cells through the IL-23/IL-23R/β-catenin Pathway. *Exp. Cel Res.* 339, 81–89. doi:10.1016/j.yexcr.2015.10.015

Vallés, G., Bensiamar, F., Maestro-Paramio, L., García-Rey, E., Vilaboa, N., and Saldaña, L. (2020). Influence of Inflammatory Conditions provided by Macrophages on Osteogenic Ability of Mesenchymal Stem Cells. *Stem Cel Res Ther* 11, 57. doi:10.1186/s13287-020-1578-1

Xia, Y., He, X.-T., Xu, X.-Y., Tian, B.-M., An, Y., and Chen, F.-M. (2020). Exosomes Derived from M0, M1 and M2 Macrophages Exert Distinct Influences on the Proliferation and Differentiation of Mesenchymal Stem Cells. *PeerJ* 8, e8970. doi:10.7717/peerj.8970

Xiong, Y., Chen, L., Yan, C., Zhou, W., Yu, T., Sun, Y., et al. (2020). M2 Macrophagy-Derived Exosomal miRNA-5106 Induces Bone Mesenchymal Stem Cells towards Osteoblastic Fate by Targeting Salt-Inducible Kinase 2 and 3. *J. Nanobiotechnol* 18, 66. doi:10.1186/s12951-020-00622-5

Yang, L., Xiao, L., Gao, W., Huang, X., Wei, F., Zhang, Q., et al. (2021). Macrophages at Low-Inflammatory Status Improved Osteogenesis via Autophagy Regulation. *Tissue Eng. Part. A.* 10, 1089. doi:10.1089/ten.TEA.2021.0015

Zhang, Y., Böse, T., Unger, R. E., Jansen, J. A., Kirkpatrick, C. J., and van den Beucken, J. J. J. P. (2017). Macrophage Type Modulates Osteogenic Differentiation of Adipose Tissue MSCs. *Cell Tissue Res* 369, 273–286. doi:10.1007/s00441-017-2598-8

Zhang, Y., Liu, Y., Liu, H., and Tang, W. H. (2019). Exosomes: Biogenesis, Biologic Function and Clinical Potential. *Cell Biosci* 9, 19. doi:10.1186/s13578-019-0282-2

Conflict of Interest: The authors declare that the research was conducted in the absence of any commercial or financial relationships that could be construed as a potential conflict of interest.

Publisher's Note: All claims expressed in this article are solely those of the authors and do not necessarily represent those of their affiliated organizations, or those of the publisher, the editors and the reviewers. Any product that may be evaluated in this article, or claim that may be made by its manufacturer, is not guaranteed or endorsed by the publisher.

Copyright © 2022 Liu, Luo, Lv, Zhang, Meng, Li, Meng, Qiang, Hou, Hou, Liu and Zhang. This is an open-access article distributed under the terms of the Creative Commons Attribution License (CC BY). The use, distribution or reproduction in other forums is permitted, provided the original author(s) and the copyright owner(s) are credited and that the original publication in this journal is cited, in accordance with accepted academic practice. No use, distribution or reproduction is permitted which does not comply with these terms.

frontiers in Bioengineering and Biotechnology

REVIEW
published: 04 February 2022
doi: 10.3389/fbioe.2022.827960

Advancement of Gallium and Gallium-Based Compounds as Antimicrobial Agents

Fupeng Li, Fengxiang Liu, Kai Huang* and Shengbing Yang**

Shanghai Key Laboratory of Orthopaedic Implants, Department of Orthopaedic Surgery, Shanghai Ninth People's Hospital, Shanghai Jiao Tong University School of Medicine, Shanghai, China

With the abuse and misuse of antibiotics, antimicrobial resistance has become a challenging issue in the medical system. Iatrogenic and non-iatrogenic infections caused by multidrug-resistant (MDR) pathogens pose serious threats to global human life and health because the efficacy of traditional antibiotics has been greatly reduced and the resulting socio-economic burden has increased. It is important to find and develop non-antibiotic-dependent antibacterial strategies because the development of new antibiotics can hardly keep pace with the emergence of resistant bacteria. Gallium (III) is a multi-target antibacterial agent that has an excellent antibacterial activity, especially against MDR pathogens; thus, a gallium (III)-based treatment is expected to become a new antibacterial strategy. However, some limitations of gallium ions as antimicrobials still exist, including low bioavailability and explosive release. In recent years, with the development of nanomaterials and clathrates, the progress of manufacturing technology, and the emergence of synergistic antibacterial strategies, the antibacterial activities of gallium have greatly improved, and the scope of application in medical systems has expanded. This review summarizes the advancement of current optimization for these key factors. This review will enrich the knowledge about the efficiency and mechanism of various gallium-based antibacterial agents and provide strategies for the improvement of the antibacterial activity of gallium-based compounds.

Keywords: gallium (Ga(III)), antibacterial, iron matabolism, optimization, bioavailability

OPEN ACCESS

Edited by:
Jenneke Klein-Nulend, Academic Centre for Dentistry Amsterdam, Netherlands

Reviewed by:
Muhammad Aqeel Bhutto, University of Sindh, Pakistan
Javier Alberto Garza Cervantes, Autonomous University of Nuevo León, Mexico

****Correspondence:***
Fengxiang Liu
liu_fengxiang@126.com
Kai Huang
kaihuang@shsmu.edu.cn
Shengbing Yang
shengbingyang@shsmu.edu.cn

Specialty section:
This article was submitted to Biomaterials, a section of the journal Frontiers in Bioengineering and Biotechnology

Received: *02 December 2021*
Accepted: *13 January 2022*
Published: *04 February 2022*

Citation:
Li F, Liu F, Huang K and Yang S (2022) Advancement of Gallium and Gallium-Based Compounds as Antimicrobial Agents. Front. Bioeng. Biotechnol. 10:827960. doi: 10.3389/fbioe.2022.827960

1 INTRODUCTION

The emergence of drug-resistant bacteria has greatly reduced the therapeutic effect of traditional antibiotics, posing a great challenge to the global medical systems and requiring the research and development of novel non-antibiotic-dependent antibacterial strategies (Roope et al., 2019) to combat drug resistance. Gallium is a semi-metallic element whose citrate buffered nitrate form was approved by the United States Food and Drug Administration (FDA) for clinical use in the treatment of malignant tumor-related hypercalcemia and autoimmune diseases in 2003 (Leyland-Jones, 2003). Noteworthy, its antibacterial effect has gradually attracted attention in recent years.

In 1931, Levaditi et al. (1931) found that intravenous injection of gallium tartrate could eliminate both syphilis in rabbits and *Trypanosoma evansi* in mice. Moreover, Yukihiro et al. (Britigan et al., 2000; Kaneko et al., 2007; Lessa et al., 2012) found that gallium has a strong killing effect on *Pseudomonas aeruginosa*, a multi-drug resistant opportunistic pathogen that is also the main pathogenic bacterium responsible for respiratory failure in patients with pulmonary cystic

TABLE 1 | Summary of the use of gallium and gallium-compounds as antimicrobial agents.

Optimization strategies	Gallium and gallium-based compounds	Antimicrobial effects	References
coordination compound	gallium citrate, gallium maltolate, gallium tartrate, tris(8-quinolinolato) gallium (III) (KP46), and gallium (III) complexes of a-N-heterocyclic thiosemicarbazones	improved solubility and not poor bactericidal effects on drug-resistant Gram-negative and Gram-positive bacteria, including *P. aeruginosa*, *Acinetobacter baumannii*, *M. tuberculosis*, and methicillin-resistant *Staphylococcus aureus*	Bonchi et al. (2014), Piatek et al. (2020), Lessa et al. (2012)
	Ga_2L_3 $(bpy)_2$, (L = 2,2′-bis(3-hydroxy-1,4naphthoquinone); bpy = 2,2′-bipyridine)	exert bactericidal effects on drug-resistant *P. aeruginosa* and *S. aureus* in an iron-containing environment	Wang et al. (2021b)
	$GaMe_2(L)$ and Ga $(Me)_2L$	improved antibacterial activity than quinolinolate alone	Duffin et al. (2020)
nanomaterial-based vehicles	Lipo-Ga-GEN	improved antibacterial activity than the corresponding drugs without liposomes	Halwani et al. (2008)
	gallium-NAC	more gallium ions were deposited in *P. aeruginosa* cells in the gallium-NAC treatment group than in the traditional gallium citrate treatment group	Young et al. (2019)
	gallium-containing siderophores and heme analogues: desferoxamine-gallium, Ga-protoporphyrin IX, Ga-deuteroporphyrin, Ga-mesoporphyrin, Ga-hematoporphyrin, Ga-octaethylporphyrin, and Ga-porphine	not all siderophores combined with an antibacterial agent show increased antibacterial activity. Ga-protoporphyrin IX showed the best antibacterial effect	Kelson et al. (2013)
	ciprofloxacin-siderophore	decreased uptake of gallium and antibacterial potency compared to ciprofloxacin alone both in iron replete and deplete conditions	Sanderson et al. (2020)
	bioresponsive antibacterial nanomaterials based on gallium (III) and iron (III) cross-linked polysaccharide materials		
improved bioavailability of gallium	Lin et al. (2021), Best et al. (2020)		
alloys and scaffold composites	Ga-doped titanium alloys	long-lasting release of Ga (III) and strong antibacterial effects on multidrug-resistant *S. aureus* for at least 3 days	Cochis et al. (2019)
	Ga-doped magnesium alloys	effective in the treatment of osteomyelitis	Gao et al. (2019)
	eutectic gallium–indium alloys	time-increasing bactericidal effects against Gram-positive bacteria	Li et al. (2021b)
	bioglasses doped with gallium	sustained release of gallium ions and time-increasing bactericidal effects	Kurtuldu et al. (2021), Mehrabi et al. (2020), Wang et al. (2021a), Siqueira et al. (2019), Song et al. (2019), Lapa et al. (2019), Ciraldo et al. (2021), Keenan et al. (2017), Rahimnejad Yazdi et al. (2018)
	gallium-doped zinc borate bioactive glass	sustained and controlled release of gallium for at least 28 days	Rahimnejad Yazdi et al. (2018)
	phosphate glass, hydroxyapatite, PCL and hydrogel, collagen, poly (4-hydroxybutyrate), silk fibroin, Ca titanate	sustained release of gallium ions and play an excellent bactericidal effect against common pathogens, such as *E. coli*, *S. aureus*, and *P. aeruginosa*, both *in vivo* and *in vitro*	Lapa et al. (2020), Pajor et al. (2020), Rastin et al. (2021), Xu et al. (2019), Muller et al. (2021), Mehrabi et al. (2020), Rodriguez-Contreras et al. (2020)
layered double hydroxide	gallium (Ga)–strontium (Sr) layered double hydroxides	sustained release of Ga ions and time-increasing bactericidal effects	Li et al. (2021a)
	gallium (Ga)–zinc (Zn) layered double hydroxides	sustained release of Ga ions and time-increasing bactericidal effects	Donnadio et al. (2021)
Synergistic strategies	ciprofloxacin, colistin, meropenem, and tobramycin	restored the bactericidal effect of traditional antibiotics and reversed the drug resistance of resistant bacteria	Rezzoagli et al. (2020)
	tetracycline	improved antibacterial activity of gallium nitrate both *in vitro* and *in vivo*	Kang et al. (2021)
	poly (ethylene glycol)-desferrioxamine/gallium (PEG-DG) conjugates	Increase bacterial susceptibility to vancomycin	Qiao et al. (2021a)
	a xenosiderophore-conjugated cationic random copolymer	0.31 of FICI for *P. aeruginosa*	Qiao et al. (2021b)

(Continued on following page)

TABLE 1 | (*Continued*) Summary of the use of gallium and gallium-compounds as antimicrobial agents.

Optimization strategies	Gallium and gallium-based compounds	Antimicrobial effects	References
	a gallium-chitosan complex	improved antibacterial activity than that of single chitosan	Akhtar et al. (2020)
	ciprofloxacin-functionalized desferrichrome	improved antibacterial activity than that of ciprofloxacin alone	Pandey et al. (2019)
	metal ions	silver ions, zinc ions, Cd, Se, and Ga had good synergistic effects	Aziz (2019), Pormohammad and Turner (2020); Vaidya et al. (2019), Yoon et al. (2006)
	gallium-substituted hemoglobin combined with Ag nanoparticles	improved antibacterial activity	Morales-de-Echegaray et al. (2020)
	gallium-porphyrin, gallium-substituted hemoglobin, phthalocyanine, indocyanine green (ICG), hollow titanium dioxide nanotubes and gallium ions	improved antibacterial activity	Morales-de-Echegaray et al. (2020); Shisaka et al. (2019), Xie et al. (2021), Rahimnejad Yazdi et al. (2018)
	nitrates and gallium ions	induce antibacterial activity against *P. aeruginosa* under both aerobic and anaerobic conditions	Zemke et al. (2020)
	graphene foam and gallium ions	improved antibacterial activity	Slate et al. (2021)

fibrosis. The ideal bactericidal effect of gallium ions can be achieved even at micromolar concentration levels. In addition, gallium at such low concentrations can remove the biofilm formed by *P. aeruginosa*, which is difficult to eliminate by traditional antibiotics. Furthermore, Choi et al. (2017, 2019) demonstrated that gallium also has bactericidal effects against common drug-resistant bacteria, such as *Mycobacterium tuberculosis*, *Klebsiella pneumoniae*, and other Gram-negative bacteria.

Currently, it is believed that the mechanism underlying the gallium antibacterial effect is related to gallium uptake by bacteria as an iron mimic. Considering that gallium is a redox inert metal that cannot be reduced under physiological conditions, gallium-substituted enzymes cannot exert the functions of the corresponding iron-dependent enzymes, which are indispensable for bacterial proliferation; thus, iron metabolism is disturbed, leading to bacterial death (Kelson et al., 2013). Iron is an indispensable nutrient for bacterial proliferation, especially for bacteria that establish infections *in vivo*. Therefore, it is difficult for bacteria to evolve resistance to gallium by reducing uptake, because it would reduce iron uptake as well. Consequently, it is believed that gallium-based compounds may become the next generation of antibiotics because of their scavenging effect on resistant bacteria.

Although gallium has definite antibacterial effects, it is almost completely hydrolyzed into insoluble hydroxide under physiological conditions. Therefore, it is difficult to release adequate quantities of gallium (III) to play an antibacterial role due to its extremely low bioavailability (Bonchi et al., 2014). In contrast, the prevention and treatment of iatrogenic infections caused by implants or internal incisions requires the maintenance of antimicrobial agent concentrations above the minimum inhibitory concentration (MIC) at the infection foci, and the explosive release of an element in a short period of time would hardly meet the clinical needs (Zhang et al., 2015; Shao et al., 2016; Ning et al., 2018).

Besides, in contrast with the treatment of respiratory infections, implant-related anti-infective materials have to be implanted *in vivo* in the form of scaffolds, requiring good biomechanical properties and releasing antibacterial agents in a sustained manner. Finally, a combination of drugs with different antibacterial mechanisms could produce stronger synergistic antibacterial effects than a single antibacterial component; this has become a research hotspot. Various combinations of gallium ions and clinically applied antibiotics or other non-antibiotic antimicrobial agents are expected to potentiate the antibacterial effect of gallium (III) and enable the traditional antibiotics to be applied in the treatment of drug-resistant bacteria through synergistic effects (Garcia-Contreras et al., 2013). This review summarizes the above-mentioned methods for improving the antibacterial effect of gallium, explores the putative antibacterial mechanism of gallium, and provides ideas for the development of novel gallium-based antibacterial strategies and for promoting the clinical transformation of gallium-based drugs (**Table 1**).

TABLE 2 | Similarities between gallium and iron ions.

	Gallium (III)	Iron (III)
Octahedral ion radius	0.620 Å	0.645 Å
Tetrahedral ion radius	0.47 Å	0.49 Å
Ionization potential	64 eV	54.8 eV
Ionization affinity	30.71 eV	30.65 eV

2 BIOCHEMICAL PROPERTIES OF GALLIUM AND IRON IONS

Gallium is an element of group IIIA of the periodic table, with an atomic number of 31 and a molecular weight of 69.72 g/mol. The chemical behavior of gallium is close to that of Fe(III) in terms of its electrical charge, ion diameter, coordination number, electron affinity, tendency to form ionic bonds, ionization potential, and

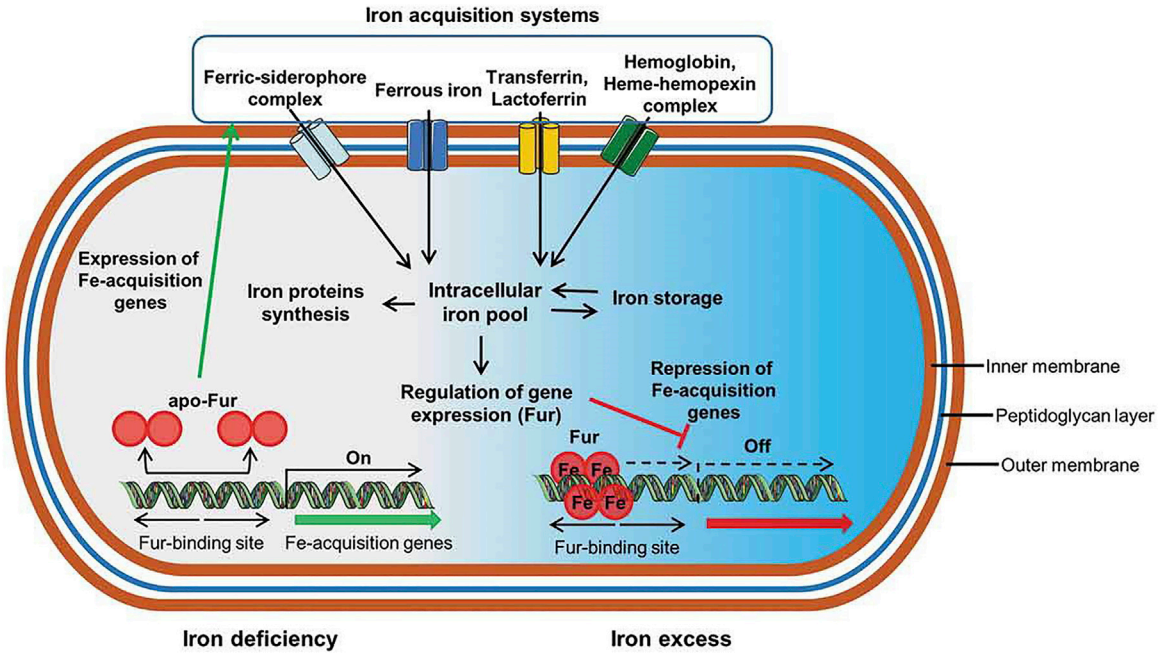

FIGURE 1 | Schematic representation of critical iron acquisition mechanisms and pathways in bacteria. Both Gram-negative and Gram-positive bacteria have evolved multiple sophisticated systems to acquire iron from the environment, including trivalent iron containing siderophores, hemes, heme proteins, heme analogues, and transferrin/lactoferrin. Due to the similarity between gallium and iron, the above pathways are also suitable for gallium transport, providing the possibility of targeted therapy for gallium (Seyoum et al., 2021).

electron configuration. The exact parameters are summarized in **Table 2**. Another similarity between these elements is the extensive hydrolysis that occurs in neutral aqueous solutions, with the consequent formation of various hydroxide species, such as $Ga(OH)_4$ and $Ga(OH)_3$, for that Ga(III) ions, having low polarization and a small size, are hard acids with high affinity for hydroxide ions (Nielsen et al., 2021). Although gallium hydroxide precipitates under physiological conditions, it is soluble under acidic or alkaline conditions. When the pH of the solution changes from low to high, gallium hydroxide changes from a dissolved state to a precipitated state in the form of $Ga(OH)_3$ and then back to a dissolved state as $Ga(OH)_4$. However, it is worth noting that gallium is a redox inert element that cannot be reduced to Ga(II) under physiological conditions (Centola et al., 2020).

The proteins responsible for iron transport *in vivo*, such as transferrin and lactoferrin, can also bind stably with gallium. However, gallium-transporter complexes are more sensitive to acidic pH than iron-transporter complexes, and strong dissociation of gallium ions can occur at pH 6.1 (Bonchi et al., 2014).

3 ANTIBACTERIAL MECHANISM OF GALLIUM IONS

3.1 Iron Uptake

Iron is an essential nutrient for the survival and proliferation of both bacteria and cells; it is a universal cofactor of oxidoreductases that participates in a variety of critical metabolic pathways *in vivo*, such as DNA synthesis, electron transfer, and anti-oxidative stress (Andrews et al., 2003). As a result, bacteria that colonize a host and establish an infection require more iron than free living bacteria to maintain their fundamental nutrient needs for growth. Due to the low bioavailability of iron in the body, bacteria have evolved a complicated iron uptake mechanism, whereby continuous evolution and mutation, to compete with cells and other microorganisms in the body for iron to survive and reproduce. At present, most studies believe that bacteria mainly obtain iron from the outside world in three ways (**Figure 1**): 1) siderophore-based systems, 2) heme/hemeprotein-based systems, and 3) transferrin and lactoferrin-based systems (Kelson et al., 2013).

Siderophores (Wilson et al., 2016) are small molecules secreted by microorganisms; siderophores can specifically recognize and bind to ferric ions from the host or other exogenous sources. In addition, bacteria simultaneously secrete heme carriers to capture hemes and heme analogues in the host. Heme is an important prosthetic group of human heme proteins, such as hemoglobin and myoglobin, which are responsible for oxygen transport. Kelson et al. (2013) systematically summarized the siderophores and heme carriers secreted by common pathogens. For example, pyoverdine and pyochelin, two types of siderophores secreted by *P. aeruginosa*, are critical for iron acquisition by this bacterium.

Bacteria can acquire iron depending on siderophores or heme carriers, but bacteria can also directly interact with iron sources, such as iron or hemes, and transport them into the cell through membrane receptors. Gram-positive bacteria specifically recognize the surrounding iron or iron-containing siderophores and hemes through receptors on the cytoplasmic membrane and then transport them to the cytoplasm where trivalent iron is dissociated from the complex and reduced to divalent iron for further use. In Gram-negative bacteria, the iron source is first recognized by an outer membrane receptor and then transported into the periplasm where it may enter the cell through the plasma membrane.

3.2 Iron Contender

Owing to the extremely similar biochemical characteristics of gallium and iron, it is difficult for biological systems to distinguish between gallium (III) and iron (III) and their corresponding compounds, such as iron protoporphyrin and gallium protoporphyrin; this is also the basis for the specific uptake of gallium by bacteria according to the above-mentioned pathways. Therefore, gallium can be used as an antagonist of iron to competitively bind to iron-dependent proteins, thus affecting the function and activity of related enzymes. In summary, gallium could be firmly bound to the siderophores that should be combined with iron, reducing the amount of iron obtained, and gallium complexes enter the bacterial cells as Trojan horses, but cannot undergo redox, interrupting the normal enzyme metabolism.

3.3 Disturbance of Iron Metabolism

Considering that gallium (III) cannot be reduced to divalent gallium under physiological conditions, when an enzyme that regularly has iron as a cofactor replaces it for gallium, its activity is affected, and its related biochemical processes are interrupted. It is believed that the inhibition of bacterial activity caused by iron metabolism disorders is mainly due to the inactivation of deoxynucleotide reductase. However, other important factors include the electron transfer, Krebs cycle, and protein synthesis. Ribonucleotide reductase (Kircheva & Dudev, 2021) is an indispensable iron-containing enzyme that participates in DNA replication and is essential for bacterial proliferation.

Recent studies have shown that oxidative stress caused by iron metabolism disorders plays a pivotal role in the antibacterial effect of gallium. Interestingly, it has been shown that the overexpression of NADPH-producing enzymes can counteract the oxidative stress evoked by gallium (Beriault et al., 2007). Zeng et al. (2021) also found that *Escherichia coli* strains with mutations in the *evgS* gene, encoding ROS detoxification enzymes, developed tolerance to gallium nitrate. Besides, the antibacterial effect of gallium ions on aerobic bacteria is better than that on anaerobic bacteria, which also indicates that reactive oxygen may be involved in the antibacterial mechanism of gallium (Zemke et al., 2020). The molecular mechanism of the antibacterial action of gallium ions remains to be further explored.

In addition to inhibiting bacterial proliferation by disturbing the activity of iron-containing enzymes such as deoxyribonucleotide reductase, gallium ions can reduce the production of virulence factors. Among virulence factors, biofilm formation is a crucial mechanism for multidrug resistance (Zhang et al., 2021). Bacteria secrete extracellular polymers to protect them from external antibiotics and the host immune system. In addition, the phenotypes of bacteria inhabiting biofilms are altered compared to that of planktonic bacteria. The proliferation rate tends to be lower, and the sensitivity to antibiotics is significantly reduced. Kang and Kirienko (2018) demonstrated that iron is indispensable for the formation of biofilms. Inactivation of pyoverdine, a key siderophore for *P. aeruginosa*, prevents biofilm formation; however, supplementation with ferric citrate can restore this ability. Therefore, gallium, as an iron antagonist, can affect the virulence of bacteria by reducing the iron content. A proteomic analysis suggested that gallium ions could reduce the expression abundance of quorum-sensing and swarming motility related proteins in *P. aeruginosa*; these proteins play a fundamental role in bacterial virulence and dissemination (Piatek et al., 2020).

4 OPTIMIZATION OF GALLIUM-BASED COMPOUNDS

4.1 Development of Gallium-Based Clathrates

Gallium ions are highly hydrolyzable under physiological conditions, and trivalent gallium ions are almost completely hydrolyzed into insoluble hydroxides in the body, leading to extremely low bioavailability. Consequently, there are few gallium ions entering bacterial cells *in vivo* to play an antibacterial role. At present, the problem of precipitation caused by the hydrolysis of gallium is mainly solved by chelating various organic ligands with gallium to form complexes with increased water solubility. The precipitation of hydroxides may be prevented by surrounding the gallium cation with an appropriate ligand sphere, rendering it stable to hydrolysis. Furthermore, the pharmacokinetics of gallium-based drugs is closely related to their coordination chemistry, and different ligands have a profound impact on the water solubility of gallium-based drugs. Currently, mature gallium salts and gallium-based coordination compounds, such as gallium nitrate, gallium chloride, gallium citrate, gallium maltolate, gallium tartrate, tris(8-quinolinolato) gallium (III) (KP46), and gallium (III) complexes of a-N-heterocyclic thiosemicarbazones, with improved solubility and not poor bactericidal effects on drug-resistant Gram-negative and Gram-positive bacteria, including *P. aeruginosa*, *Acinetobacter baumannii*, *M. tuberculosis,* and methicillin-resistant *Staphylococcus aureus*, are being tested.

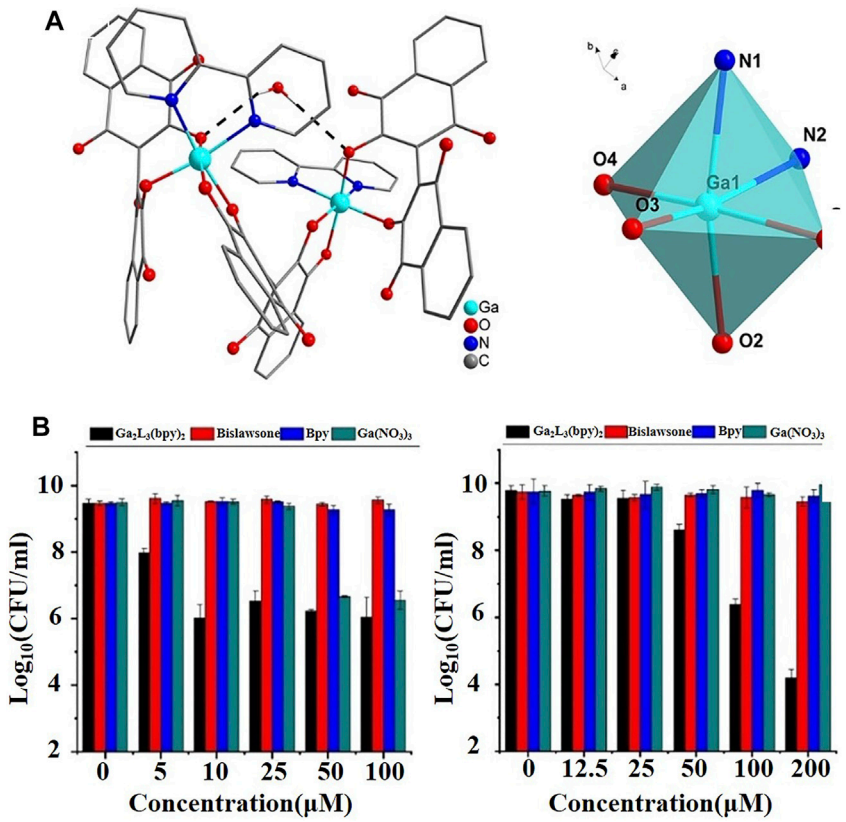

FIGURE 2 | (A) Molecular structure of $[Ga_2L_3(bpy)_2]$·H2O as determined by single-crystal X-ray structure analysis (left), and schematic representation of the coordination environment of the Ga(III) ion (right) (Wang et al., 2021b). **(B)** Antibacterial effect of $[Ga_2L_3(bpy)_2]$ on drug-sensitive *P. aeruginosa* ATCC 15692 (left) and drug-sensitive *S. aureus* ATCC 6538 (right) compared with those of gallium nitrate, bpy, and bislawsone (Wang et al., 2021b).

Bonchi et al. (2014) systematically summarized the pharmacological properties and antibacterial activities of the gallium salts and gallium-based complexes mentioned above. Among them, gallium maltoate, as a second-generation gallium-based coordinated complex, may be used in an oral or topical way with obviously improved bioavailability of gallium ions compared to that of gallium nitrate. Piatek et al. (2020), using quantitative proteomics, further revealed that gallium maltoate exerted antibacterial effects by inhibiting the quorum-sensing system in *P. aeruginosa*. Similar to gallium maltoate, KP46 was also designed to improve the oral bioavailability of gallium ions. Thiosemicarbazones, antibacterial and antitumor drugs, can also be applied as ligands to form complexes with gallium ions (Enyedy et al., 2012). Lessa et al. (2012) demonstrated that gallium-based compounds coordinated with 2-formylpyridine-, 2-acetylpyridine-, and 2-benzoylpyridine-derived thiosemicarbazones not only potentiated the antibacterial activity of gallium ions due to their increased bioavailability, but also improved the antibacterial activity and spectrum of thiosemicarbazones. New gallium complexes have also been developed with the continuous discovery of ligands. Wang et al. (2021b) synthesized a lipophilic ligand, $Ga_2L_3(bpy)_2$, (L = 2,2′-bis(3-hydroxy-1,4naphthoquinone); bpy = 2,2′-bipyridine) (**Figure 2A**), which had excellent bactericidal effects on drug-resistant *P. aeruginosa* and *S. aureus* in an iron-containing environment, with MIC of 10 and 100 μM, respectively (**Figure 2B**). The antibacterial effect was superior to that of gallium alone. More interestingly, the lipophilic gallium ligand delayed the emergence of bacterial resistance. Duffin et al. (2020) synthesized a series of eight alkyl gallium complexes of general formulae $[GaMe_2(L)]$ and $[Ga(Me)_2L]$ to increase the release of gallium and promote a reaction with transferrin and lactoferrin. The antibacterial activity of alkyl gallium (III) quinolinolate was three times that of quinolinolate alone. It is worth noting that the category and quantity of alkyl gallium (III) quinolinolate had a certain influence on the lipid solubility of the complex, providing a reference for the development of new antibacterial gallium-based complexes. In addition, gallium-based complexes with tranexamic acid and pyrophosphate as ligands have achieved

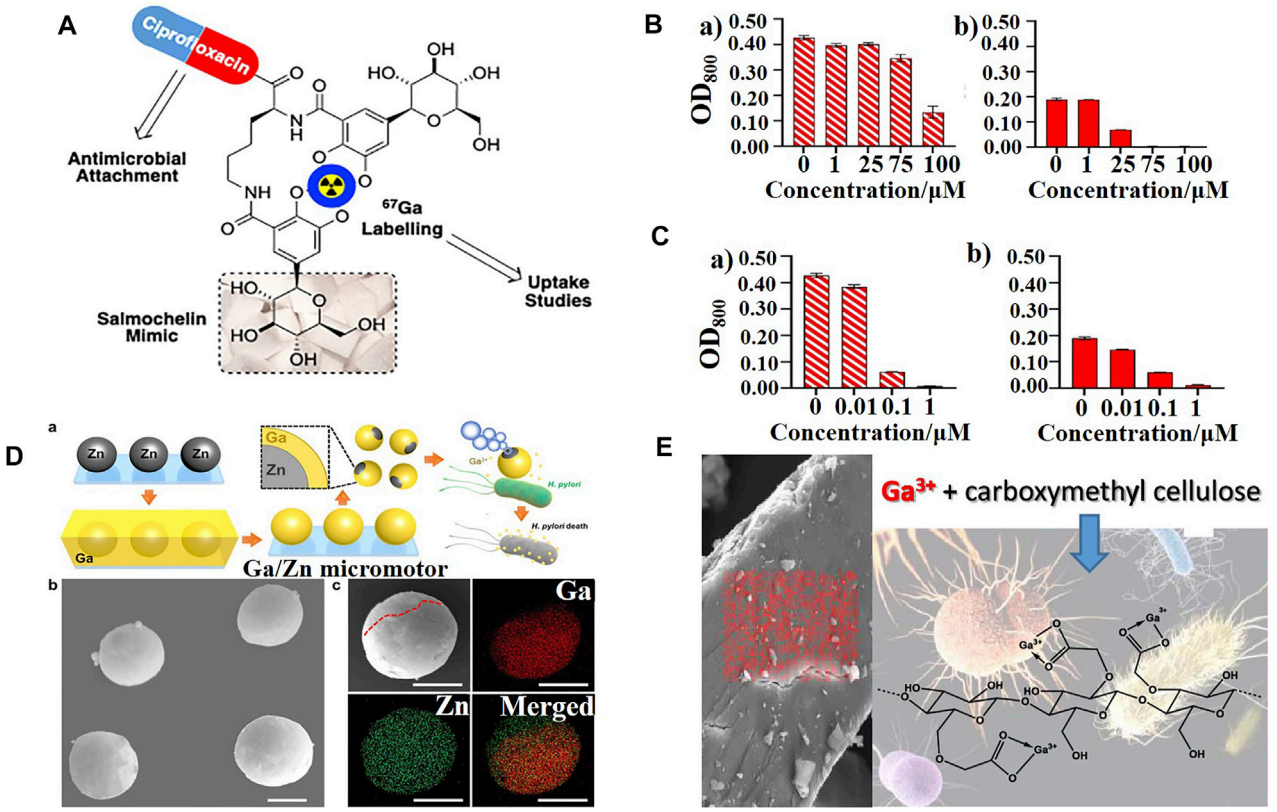

FIGURE 3 | (A) Schematic representation of a ciprofloxacin–siderophore Trojan horse antimicrobial (Sanderson et al., 2020). **(B,C)** Growth status of *E. coli* K12 (BW25113) in the presence of **(B)** ciprofloxacin–siderophores and **(C)** ciprofloxacin after 48 h with **(a)** sufficient iron levels or **(b)** scarce iron (Sanderson et al., 2020). **(D)** Schematic representation of the synthesis and antibacterial mechanism of Janus Ga/Zn micromotors and their characterization (Lin et al., 2021). **(E)** Scheme of gallium molecules encapsulated by carboxymethyl cellulose (CMC) (Best et al., 2020).

great success as antitumor agents, given the similarity of bacterial and tumor metabolisms (El-Habeeb and Refat, 2019). Their application in the field of antibacterial therapy is worthy of further study (Greenfield et al., 2019).

4.2 Advancement in the Development of Nanomaterial-Based Vehicles for Loading Gallium Ions

The emergence of diverse nanomaterials provides an excellent platform for loading gallium ions. On the one hand, the ideal nanomaterial surface-capping agent could improve the biocompatibility of gallium ions and increase the therapeutic window range; on the other hand, it could effectively reduce the hydrolysis of gallium (III), thus, releasing more gallium ions at the infection site. Halwani et al. (2008) used liposomes as carriers to encapsulate and transport gallium ions and improve their bioavailability by taking advantage of the lipophilic characteristics of liposomes. The complexes demonstrated excellent antimicrobial activity against *P. aeruginosa* and the corresponding biofilms compared to $Ga(NO_3)_3$ alone. Lipo-Ga-GEN, liposomes carrying both gallium ions and gentamicin (0.6 μM for Ga and 8 mg/L for GEN, respectively), inhibited bacterial growth completely, while other formulations failed to achieve the same effect at the same drug concentrations. In addition, Lipo-Ga-GEN, Lipo-Ga (liposomes carrying gallium ions only), and Lipo-GEN (liposomes carrying gentamicin only) exhibited better antibacterial activities than the corresponding drugs without liposomes (Halwani et al., 2008), providing another way to improve the bioavailability of gallium. Similar to liposomes, N-acetyl-cysteine (NAC), a thiol-substituted derivative of the amino acid L-cysteine, has been used as a surface-capping agent for gallium because of its excellent biocompatibility and water solubility (Young et al., 2019). The amount of gallium ions released by the NAC-coated gallium particles was much higher than that of the gallium particles without NAC coating. Noteworthy, more gallium ions were deposited in *P. aeruginosa* cells in the gallium-NAC treatment group than in the traditional gallium citrate treatment group, indicating that NAC promoted the absorption of gallium ions.

In addition, the construction of gallium-containing siderophores and heme analogues, taking advantage of the iron uptake pathway, provides another strategy for the

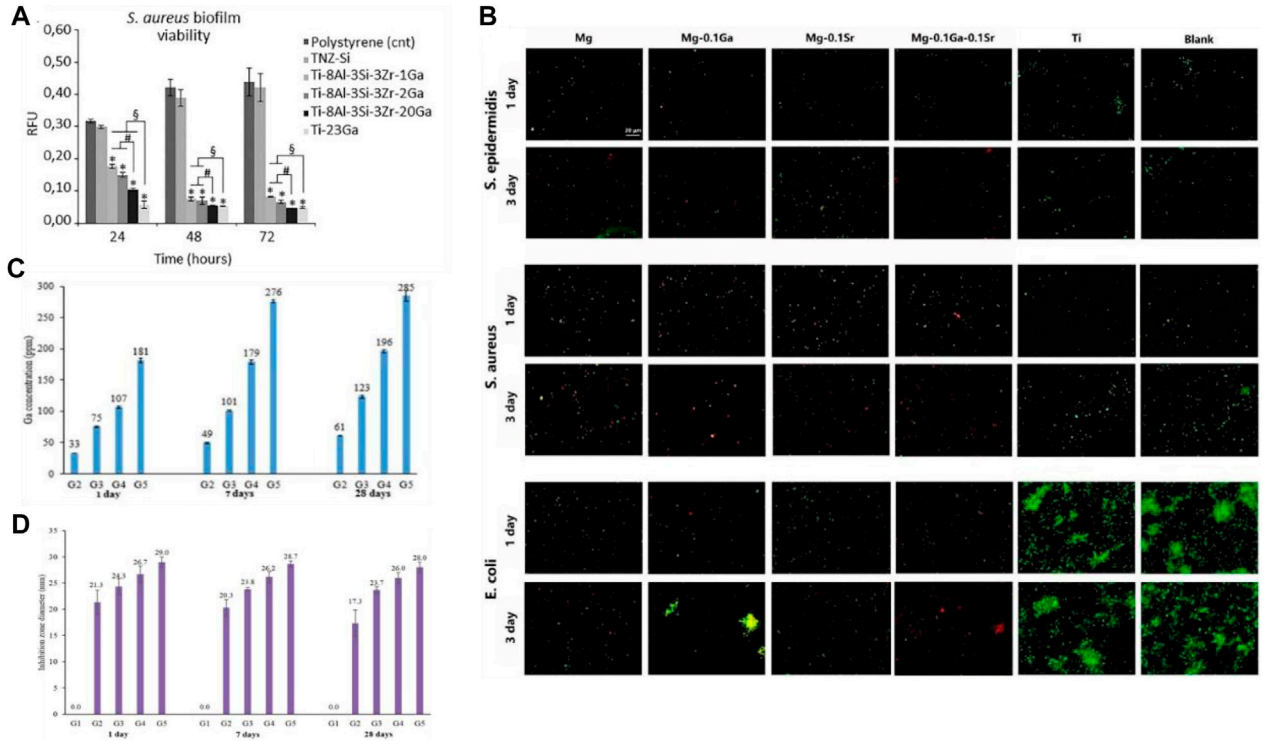

FIGURE 4 | (A) Antibacterial effect of metallurgical gallium additions to titanium alloys against *S. aureus* biofilm formation (Cochis et al., 2019). **(B)** Fluorescent images of biofilms formed by *Staphylococcus epidermidis*, *S. aureus*, and *E. coli* on pure Mg, Mg-0.1 Ga, Mg-0.1 Sr, Mg-0.1 Ga-0.1 Sr, and c.p. Ti surfaces at days 1 and 3; biofilms were detected through live-dead staining (Gao et al., 2019). **(C)** Accumulated concentration of gallium ions released from different borate glasses with increased gallium content (0, 2.5, 5, 10, and 15 Wt % Ga) after being immersed in deionized water for 1, 7, and 28 days at 37°C (Rahimnejad Yazdi et al., 2018). **(D)** Evaluation of long-time antibacterial activity of the borate glasses against *P. aeruginosa* after 1, 7, and 28 days of incubation; inhibition was determined by measuring inhibition zone diameters (Rahimnejad Yazdi et al., 2018).

preparation of gallium-loaded nanomaterials. The targeted accumulation of gallium in bacterial cells depends mainly on the formation of couplings with endogenous siderophores or hemes. Through the Trojan horse strategy, gallium is transported into bacterial cells with the help of the bacteria's own iron acquisition receptors. The antibacterial activities of common gallium-siderophores and gallium-heme conjugates have been summarized by Kelson et al. (2013), including those of desferoxamine-gallium, Ga-protoporphyrin IX, Ga-deuteroporphyrin, Ga-mesoporphyrin, Ga-hematoporphyrin, Ga-octaethylporphyrin, and Ga-porphine. Among them, Ga-protoporphyrin IX, as a heme analogue, showed the best antibacterial effect and had a good bactericidal effect on both Gram-positive and Gram-negative bacteria for perturbing the metabolism of heme. It is worth noting that not all siderophores combined with an antibacterial agent show increased antibacterial activity (Frangipani et al., 2014).

Sanderson et al. (2020) synthesized a novel ciprofloxacin-siderophore antimicrobial (**Figure 3A**) by incorporating key design features of salmochelin, a stealth siderophore expressed by many Enterobacteriaceae; however, it decreased the uptake of gallium and antibacterial potency compared to ciprofloxacin alone both in iron replete and deplete conditions (**Figures 3B,C**). Frangipani et al. (2014) compared the antibacterial activity of several commonly used siderophore-gallium complexes with gallium nitrate alone, and the results were similar to those described above. Only the complex formed with the endogenous siderophore, the pyochelin-gallium complex, significantly potentiated the antibacterial activity of gallium ions, whereas those with ferrichrome, desferrioxamine, and pyoverdine, alleviated the antibacterial effect of gallium nitrate. These results suggest that the type of siderophore and the size and polar surface area of the corresponding conjugate remain significant challenges in the design of Trojan horse antimicrobials, which may prevent gallium from being recognized by receptors of the outer membrane.

In addition to gallium-ligand and gallium-iron/heme carriers, Lin et al. (2021) provided a new strategy: the active uptake of gallium by bubble-propelled Janus gallium/zinc micromotors that, at an acidic microenvironment, can increase the gallium content in bacteria (**Figure 3D**). Based on the same principle, Best et al. (2020) prepared a family of bioresponsive antibacterial

nanomaterials based on gallium (III) and iron (III) cross-linked polysaccharide materials (**Figure 3E**), to which *P. aeruginosa* was specifically responsive, to improve the bioavailability of gallium ions.

4.3 Construction of Gallium-Doped Alloys and Scaffold Composites

Although gallium has a definite antibacterial effect, existing gallium-based drugs, including gallium nitrate, tend to quickly release gallium (III) *in vivo*, reaching the maximum concentration in an extremely short time and failing to exert an antibacterial effect. Opportunities for iatrogenic infections exist anytime, and it is particularly critical that the concentration of an antibacterial agent at infective sites is maintained above the MIC. The controlled and sustained release of antibacterial agents is of great significance for the prevention and treatment of clinically common implant-related infections and skin incision-related infections. In addition, gallium salts and gallium-based complexes are mostly administered intravenously or orally, while local treatments tend to be safer, which is of great clinical significance for local infection control.

Innovations in biomaterials, such as hydrogels and bioglasses, as well as improvements in manufacturing processes, such as coating technology, 3D printing technology, and metallurgy technology, make it possible for gallium-loaded scaffolds and alloys to be applied in the body as tissue engineering materials. In view of the low melting point (15.5°C) of gallium and its similarity with aluminum, it is possible to microalloy gallium with other biocompatible metals. Cochis et al. (2019) investigated Ga-doped titanium alloys using metallurgical methods, and the results demonstrated that these alloys ensured long-lasting release of Ga (III) and strong antibacterial effects on multidrug-resistant *S. aureus* for at least 3 days, showing a high potential for the treatment of implant-related infections in orthopedics. After metallurgical addition of gallium, the antibacterial activity of titanium alloys was significantly improved compared with that of polystyrene, and the antibacterial activity could still be observed after 3 days. Although the antibacterial activity over longer periods of time was not studied, the effect would be expected to be good after observing the trend. In addition, with the increase in gallium content, the antibacterial activity of the alloy gradually improved; however, the mechanical properties of the titanium alloy might also be affected, making it necessary to further explore the optimal gallium loading amount (**Figure 4A**).

Similarly, through gallium-strontium microalloying, magnesium alloys (Gao et al., 2019) have also been shown to be effective in the treatment of osteomyelitis. Compared with titanium, magnesium is degradable under physiological conditions with certain advantages in the treatment of bone infections; moreover, magnesium allows for the sustained release of gallium (III). According to the observations from fluorescent imaging studies (**Figure 4B**), magnesium alloys combined with gallium almost eliminated *S. aureus* and *E. coli* after 3 days. The red fluorescence intensity of the Ga-containing magnesium alloy increased gradually and reached a maximum on the third day, indicating the slow-release effect of gallium ions. Besides, 3D printed gallium-based liquid metals such as eutectic gallium–indium alloys have also shown time-increasing bactericidal effects against Gram-positive bacteria (Li K. et al., 2021).

With the development of manufacturing technology and the constant updating of biological materials, an increasing number of materials are used as scaffolds to store antibacterial agents to achieve a slow release. Mesoporous bioactive glasses (Kurtuldu et al., 2021) have been widely applied *in vivo* in non-weight-bearing parts of the body such as the oral cavity, in orthopedics, and in skin tissues where they act as repair materials and drug-loading scaffolds (Mehrabi et al., 2020). Recently, bioglasses doped with gallium have been gradually used as antibacterial materials against bone defect infections (Wang et al., 2021a), caries infections (Siqueira et al., 2019; Song et al., 2019), and skin incision infections (Lapa et al., 2019). The *in vitro* ion release curves from these gallium-loaded complexes show that gallium can be continuously released for nearly 550 h and that the concentration of gallium ions can reach 20 ppm on day 21 (Ciraldo et al., 2021), which may be attributed to the network structure and composition of the bioglass, especially to its calcium content (Keenan et al., 2017; Rahimnejad Yazdi et al., 2018).

Rahimnejad Yazdi et al. (2018) synthesized a gallium-doped zinc borate bioactive glass exhibiting a sustained and controlled release of gallium for at least 28 days. Interestingly, different gallium contents resulted in different gallium ion release curves (**Figure 4C**) and different antibacterial effects (**Figure 4D**). The cumulative concentrations of gallium (III) in all gallium-loaded bioglasses under a simulated body fluid environment increased gradually, and the highest gallium content reached 285 ppm on day 28. The controlled release of gallium ions was consistent with the sustained bacteriostatic activity against *P. aeruginosa* over 28 days. Other biomaterials, including phosphate glass (Lapa et al., 2020), hydroxyapatite (Pajor et al., 2020), PCL and hydrogel (Rastin et al., 2021), collagen (Xu et al., 2019), poly (4-hydroxybutyrate) (Muller et al., 2021), silk fibroin (Mehrabi et al., 2020), and Ca titanate (Rodriguez-Contreras et al., 2020), have also been proven to compound with gallium for a sustained release of gallium ions and to play an excellent bactericidal effect against common pathogens, such as *E. coli*, *S. aureus*, and *P. aeruginosa*, both *in vivo* and *in vitro*.

The successful synthesis of gallium-sustained release materials is of great clinical significance. On the one hand, hydrogel, bioceramics, and other materials with good biocompatibility can be directly used as tissue engineering scaffolds for the repair of infectious defects. On the other hand, chemical processes, such as electrophoretic deposition, thermochemical treatment (Rodriguez-Contreras et al., 2020), solid-state method (Pajor et al., 2020), radio-frequency magnetron sputtering (Stan et al., 2020), and gel/sol can form antibacterial coatings (Pajor et al., 2020; Rodriguez-Contreras et al., 2020; Stan et al., 2020; Almohandes et al., 2021; Centurion et al., 2021) containing

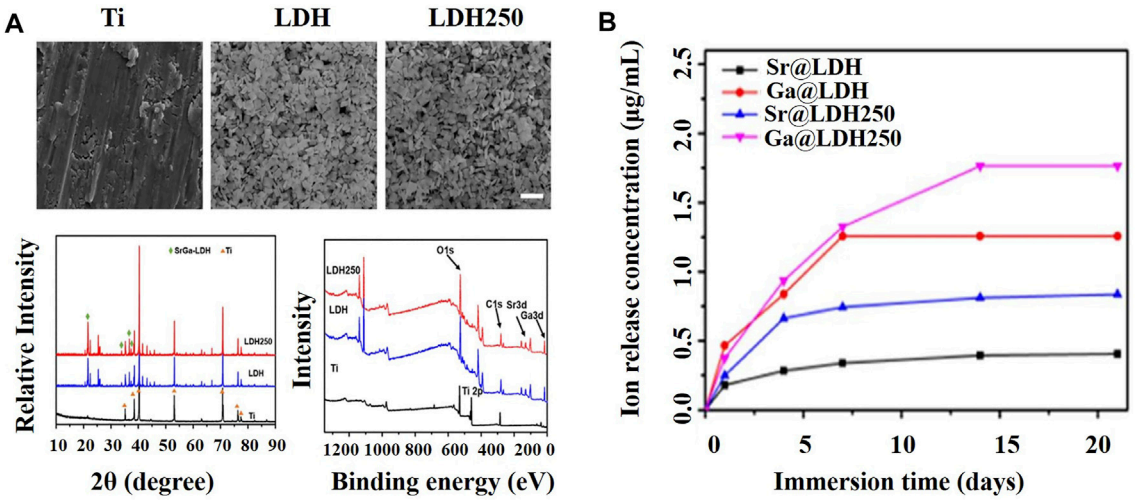

FIGURE 5 | (A) Characterization of Ti, LDH, and LDH250 substrates (Li K. et al., 2021). **(B)** The cumulative release of gallium and strontium ions from the layered double hydroxide (LDH) and layered double hydroxide calcined at 250°C (LDH 250) was observed within 20 days of soaking in PBS solution (Li K. et al., 2021).

gallium on the surface of implants to prevent and treat iatrogenic infections. The controlled release of gallium by the above materials mainly benefits from their biodegradability, porous network structure, and adjustable porosity.

4.4 Design of Gallium-Containing Layered Double Hydroxide

LDHs are layered solids described by the general formula $[M(II)_{1-x}M(III)_x\ (OH)_2](A^{n-})_{x/n}{\cdot}nH2O$, where M(II) is a divalent cation, M(III) is a trivalent cation, and A^{n-} represents the anions that balance the positive charges of the lamellae. LDHs have attracted considerable attention as drug release platforms and bone tissue engineering materials based on their excellent biocompatibility (Taviot-Guého et al., 2018). The region between layers can store a large amount of bioactive ions where drugs are released in a sustained manner. In addition, LDHs can also be combined with other materials such as hydroxyapatite without affecting their own structure (Donnadio et al., 2021), which is beneficial for realizing the multi-functionalization of gallium-containing materials. Li K. et al. (2021) and Donnadio et al. (2021) constructed and characterized gallium (Ga)–strontium (Sr) layered double hydroxides (**Figure 5A**) and gallium (Ga)–zinc (Zn) layered double hydroxides, respectively, both of which exhibited sustained release of Ga ions. On day 21, the concentrations of Ga (III) released from LDH 250 and LDH reached almost 1.75 and 1.25 μg/ml, respectively (**Figure 5B**).

4.5 Synergistic Antimicrobial Effects Between Gallium and Other Antibacterial Agents

Recently, the combination of multiple antibacterial agents to achieve enhanced antibacterial effects has become a research hotspot (Pormohammad & Turner, 2020). With the excessive use of antibiotics and metal ions, bacteria gradually acquire drug resistance through horizontal gene transmission or gene mutation (Sutterlin et al., 2017). Some researchers have isolated bacterial strains that are resistant to gallium ions (Garcia-Contreras et al., 2013). The combination of two or more drugs with different antimicrobial mechanisms may reduce or delay the emergence of antimicrobial resistance by attacking different bacterial targets (Cottarel & Wierzbowski, 2007; Fischbach, 2011). In addition, the combined use of multiple antibacterial agents can reduce the therapeutic dose and concentration of a single antibacterial agent, thus reducing toxicity and side reactions, increasing the treatment window, and improving biological safety (Harrison et al., 2008).

The diversity of existing antibacterial agents has promoted a diversity of combinations with gallium ions. Among them, the combination of traditional antibiotics and gallium-based antimicrobials has attracted considerable attention. Rezzoagli et al. (2020) evaluated the synergistic antibacterial effect of gallium ions in combination with four clinically common antibiotics (ciprofloxacin, colistin, meropenem, and tobramycin) using a 9 × 9 drug concentration matrix. The results showed that gallium ions not only restored the bactericidal effect of traditional antibiotics, but also reversed the drug resistance of resistant bacteria. A research conducted by Kang et al. (2021) demonstrated that tetracycline could inhibit the biosynthesis of the endogenous siderophore pyoverdine at concentrations lower than the MIC, thus enhancing the antibacterial activity of gallium nitrate both *in vitro* and *in vivo*. In other words, gallium ions could reduce the concentration of conventional antibiotics for treatment, allowing antibiotics to play a role in the treatment of resistant bacteria. In addition to gallium nitrate, the Ga(III)-based compounds mentioned above, including Ga-siderophores and Ga-porphyrin, were used as adjuvants of antibiotics for

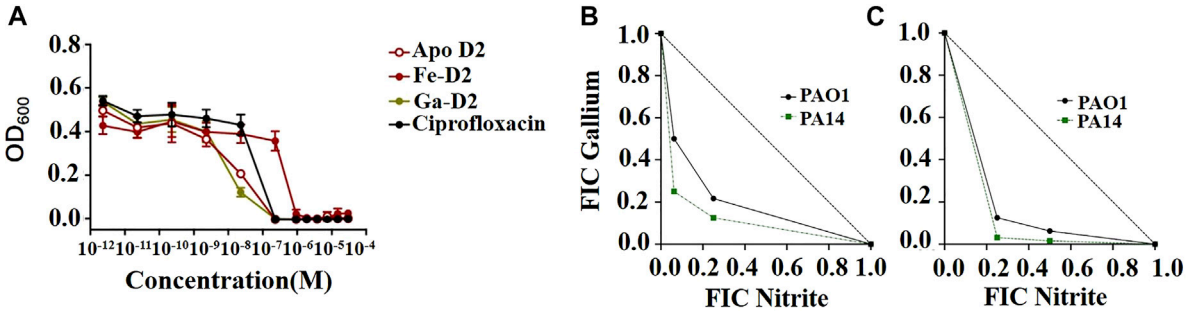

FIGURE 6 | (A) MIC assays using a gallium-based complexes of ciprofloxacin-functionalized desferrichrome (D2) against *E. coli* K12 indicated that the Ga-D2 complex has a greater antibacterial potential when compared to that of ciprofloxacin alone (Pandey et al., 2019). **(B,C)** Synergistic antibacterial activity between nitrite and Ga^{3+}. The isobolograms show the results of checkerboard assays for *P. aeruginosa* PAO1 and PA14 showing the fractional inhibitory concentration (FICs) of the two compounds in combination under **(B)** aerobic and **(C)** anaerobic conditions (Zemke et al., 2020).

antibacterial purposes. Both gallium-porphyrin and gallium-heme targeted the bacterial iron metabolism pathway because they were specifically and directly recognized and absorbed by bacterial membrane receptors. Therefore, gallium complexes bound to antibiotics entered bacterial cells, increasing antibiotic sensitivity, and playing a synergistic role. For example, protoporphyrin IX, which serves as a heme analogue, has been demonstrated to have enhanced antibacterial activity against several bacterial species by targeting cytochromes and interfering with cellular respiration (Hijazi et al., 2017).

Pandey et al. (2019) demonstrated that ciprofloxacin-functionalized desferrichrome exhibited a MIC of 0.23 μM for *E. coli*, in accordance with its parent fluoroquinolone antibiotic, and showed potent against *P. aeruginosa*, *S. aureus*, and *K. pneumoniae* with MICs of 3.8, 0.94, and 12.5 μM, respectively. The dose-response curve showed that the antibacterial effect of ciprofloxacin-functionalized gallium- desferrichrome conjugates was superior to that of ciprofloxacin alone (**Figure 6A**). In addition to using antibiotics directly, Qiao et al. (2021a) introduced PEG to further increase bacterial susceptibility to vancomycin, demonstrating excellent antibacterial activity.

Considering the excellent synergistic antibacterial effects of traditional antibiotics and gallium ions, combined antibacterial treatments with gallium and non-antibiotic antibacterial agents has also been explored. Akhtar et al. (2020) prepared a gallium-chitosan complex and performed *in vitro* experiments that showed that the antibacterial rate of the complex against *E. coli* was above 90% compared with that of single chitosan. Qiao et al. (2021b) developed a triple combination strategy, as follows: 1) cationic guanidine moieties and short alkyl quaternary ammonium salts were chosen to destroy the bacterial membrane, 2) deferoxamine (DFO)-gallium conjugated to the above copolymer (namely the pGQ-DG complex) was used to disrupt iron metabolism, and 3) vancomycin (VAN) was finally added. The study demonstrated that the fractional inhibitory concentration index (FICI) of sub-MIC concentrations of pGQ-DG combined with VAN was 0.31 in *P. aeruginosa*, confirming their synergy—when FICI values are lower than 0.5, there is a synergistic effect between the drugs tested (Yoon et al., 2006). However, no obvious synergistic effects were observed in *E. coli* between VAN and pGQ-DG. This indicates that the synergistic antibacterial effect between drugs is not absolute and that the synergistic effect will be either enhanced or weakened depending on the bacterial species. It is critical to find optimal synergistic antibacterial formulations for specific pathogens. *In vivo* experiments demonstrated that the three-drug combination had a strong synergistic effect and could achieve the same effect as colistin in the elimination of *P. aeruginosa*, simultaneously accelerating the healing of infected wounds.

Several studies investigated the antimicrobial synergies between different metal ions, and fractional inhibitory concentration and fractional bactericidal concentration assays were used to evaluate synergistic intensity (Yoon et al., 2006; Aziz, 2019; Vaidya et al., 2019; Pormohammad & Turner, 2020). The results showed that silver ions, zinc ions, Cd, Se, and Ga had good synergistic effects. According to Morales-de-Echegaray et al. (2020), the antibacterial activity of gallium-substituted hemoglobin combined with Ag nanoparticles showed multiple amplifications. In addition, antibacterial photodynamic treatment has also been used in combination with gallium to treat bacterial infections. In several studies, gallium-porphyrin, gallium-substituted hemoglobin, phthalocyanine, indocyanine green (ICG), and hollow titanium dioxide nanotubes were used as photosensitizers to couple with gallium (Morales-de-Echegaray et al., 2020; Shisaka et al., 2019; Xie et al., 2021; Yang et al., 2020). Under near-infrared light irradiation, photosensitizers catalyze the production of reactive oxygen substances such as singlet oxygen which has membrane permeability and can cause irreversible oxidative damage to cell membranes, DNA, and lipids (Imlay, 2013). This synergistic mechanism may occur because gallium affects the activity of bacterial antioxidant enzymes by interfering with their iron metabolism, increasing the sensitivity of bacteria to oxidative stress; thus, the reactive oxygen species produced by the action of photosensitizers may promote the killing of bacteria.

Similarly, Zemke et al. (2020) combined nitrates and gallium, where nitrates served as nitric oxide donors—a type of reactive oxygen species—, to induce antibacterial activity against *P. aeruginosa* under both aerobic and anaerobic conditions

(**Figures 6B**,C). Slate et al. (2021) used the sharp nanomorphology of non-metallic graphene and its derivatives to destroy bacterial cell membranes, they simultaneously used gallium that slowly released from graphene foam to interfere with bacterial iron metabolism, which also had a positive synergistic effect.

5 CONCLUSION AND PROSPECTIVE VIEWS

With the recent development of coordination chemistry, an increasing number of organic ligands have been developed to chelate gallium. Therefore, gallium-based compounds have enhanced solubility and improved bioavailability. The coating of biomaterials responsive to an infected microenvironment can greatly increase the gallium ion concentration at the infected site. In addition, further elucidation of the mechanism of gallium acquisition will provide the basis for targeted antibacterial therapy; simultaneously, the constant research on mesoporous materials, bioceramics, hydrogels, bacterial microenvironment-responsive materials, and coating technologies could provide new options for the modification and loading of gallium-based antibacterial agents to realize the sustained and controllable release of gallium (III) and greatly improve the antibacterial effect of this element.

Furthermore, the combined use of various antibacterial agents results in exciting synergistic antibacterial effects. At present, there is a variety of antibacterial drugs, including antibiotics, chitosan, antibacterial peptides, and metal ions, as well as complex antibacterial treatments, such as photothermal treatment, chemical dynamic treatment, photodynamic treatment, and physical destruction. All these antibacterial drugs and methods could be used in combination with gallium, and their combined antibacterial effects remain to be explored. The continuous optimization of the key factors affecting the antibacterial efficiency of gallium will provide the possibility for gallium to be used in the clinic.

However, gallium, as an antibacterial agent, also faces some challenges. Gallium has no indications for patients with specific pathological conditions. Due to its immunosuppressive effect, long-term use of gallium could lead to decreased immune capacity of the body, which is unfortunate for patients with immune deficiencies. In contrast, the antibacterial activity of gallium might be beneficial for patients with hemochromatosis and thalassemia, which cause pathological iron overload. Considering the susceptibility and severity of an infection in these patients, it would be of great clinical significance to successfully use gallium-based antibacterial agents to treat such infections.

Although gallium ions, as multi-target antimicrobial agents, have been demonstrated to have definite and excellent bactericidal effects against pathogens that are resistant to traditional antibiotics, the potency of gallium-based antimicrobials is relatively lower than that of some existing antibacterial drugs. Gallium maltoate has an MIC of more than 250 μg/ml against *P. aeruginosa*, much higher than some clinical antibiotics, such as murepavadin (MIC = 2 μg/ml) and colistin (MIC = 1 μg/ml) (Ekkelenkamp et al., 2020; Piatek et al., 2020). Combination therapies with gallium-based antibacterial agents are expected to further reduce the concentration of gallium ions, so as to be better applied in the treatment of drug-resistant bacteria in the clinic. In addition, understanding the exact antibacterial mechanism of gallium ions remains a long way off. Although gallium has been demonstrated to play an antibacterial role by interrupting iron metabolism, there have been no reports on the proteins or enzymes on which gallium ions act. The identification of gallium ion targets is of great significance for improving gallium antibacterial effects and tackling drug resistance. More research is proposed to focus on the molecular mechanism of the antibacterial activity of gallium in the future. Finally, in recent years, the successful synthesis of various metal–organic frameworks, covalent-organic frameworks, hydrogen-bonded organic frameworks, and other emerging nanomaterials with ultra-high specific surface areas, satisfactory biocompatibility, biodegradability, and high density with uniformly distributed catalytic active sites has greatly promoted the development of antibacterial agents and enriched antimicrobial strategies. However, their combined use with gallium ions is rarely reported, and we believe that this direction possesses promising research prospects.

AUTHOR CONTRIBUTIONS

FL: writing the manuscript. KH, FL, and SY: revising and editing the manuscript. All authors contributed to the article and approved the submitted version.

FUNDING

This work was funded by the National Natural Science Foundation of China (81802178, 92068205 and 81871790), the Shanghai Science and Technology Development Fund (20QC1400800 and 21QA1405400).

REFERENCES

Akhtar, M. A., Hadzhieva, Z., Dlouhý, I., and Boccaccini, A. R. (2020). Electrophoretic Deposition and Characterization of Functional Coatings Based on an Antibacterial Gallium (III)-chitosan Complex. *Coatings* 10 (5), 483. doi:10.3390/coatings10050483

Almohandes, A., Abrahamsson, I., Dahlén, G., and Berglundh, T. (2021). Effect of Biofilm Formation on Implant Abutments with an Anti-bacterial Coating: A Pre-clinical *In Vivo* Study. *Clin. Oral Impl Res.* 32 (6), 756–766. doi:10.1111/clr.13745

Andrews, S. C., Robinson, A. K., and Rodríguez-Quiñones, F. (2003). Bacterial Iron Homeostasis. *Fems Microbiol. Rev.* 27, 215–237. doi:10.1016/s0168-6445(03)00055-x

Aziz, W. J. (2019). Synthesis of CdSe and CdSe:Ga Nanostructures for Antibacterial Application. *Bull. Mater. Sci.* 42 (4), 148. doi:10.1007/s12034-019-1830-4

Bériault, R., Hamel, R., Chenier, D., Mailloux, R. J., Joly, H., and Appanna, V. D. (2007). The Overexpression of NADPH-Producing Enzymes Counters the Oxidative Stress Evoked by Gallium, an Iron Mimetic. *Biometals* 20 (2), 165–176. doi:10.1007/s10534-006-9024-0

Best, M. G., Cunha-Reis, C., Ganin, A. Y., Sousa, A., Johnston, J., Oliveira, A. L., et al. (2020). Antimicrobial Properties of Gallium(III)- and Iron(III)-loaded Polysaccharides Affecting the Growth of *Escherichia coli, Staphylococcus aureus*, and *Pseudomonas aeruginosa, In Vitro*. *ACS Appl. Bio Mater.* 3 (11), 7589–7597. doi:10.1021/acsabm.0c00811

Bonchi, C., Imperi, F., Minandri, F., Visca, P., and Frangipani, E. (2014). Repurposing of Gallium-Based Drugs for Antibacterial Therapy. *Biofactors* 40 (3), 303–312. doi:10.1002/biof.1159

Britigan, B. E., Rasmussen, G. T., Olakanmi, O., and Cox, C. D. (2000). Iron Acquisition from *Pseudomonas aeruginosa* Siderophores by Human Phagocytes: an Additional Mechanism of Host Defense through Iron Sequestration? *Infect. Immun.* 68 (3), 1271–1275. doi:10.1128/IAI.68.3.1271-1275.2000

Centola, G., Xue, F., and Wilks, A. (2020). Metallotherapeutics Development in the Age of Iron-Clad Bacteria. *Metallomics* 12 (12), 1863–1877. doi:10.1039/d0mt00206b

Centurion, F., Namivandi-Zangeneh, R., Flores, N., Tajik, M., Merhebi, S., Abbasi, R., et al. (2021). Liquid Metal-Triggered Assembly of Phenolic Nanocoatings with Antioxidant and Antibacterial Properties. *ACS Appl. Nano Mater.* 4 (3), 2987–2998. doi:10.1021/acsanm.1c00125

Choi, S.-r., Britigan, B. E., Moran, D. M., and Narayanasamy, P. (2017). Gallium Nanoparticles Facilitate Phagosome Maturation and Inhibit Growth of Virulent *Mycobacterium tuberculosis* in Macrophages. *PLoS One* 12 (5), e0177987. doi:10.1371/journal.pone.0177987

Choi, S.-r., Britigan, B. E., and Narayanasamy, P. (2019). Dual Inhibition of *Klebsiella pneumoniae* and *Pseudomonas aeruginosa* Iron Metabolism Using Gallium Porphyrin and Gallium Nitrate. *ACS Infect. Dis.* 5 (9), 1559–1569. doi:10.1021/acsinfecdis.9b00100

Ciraldo, F. E., Arango-Ospina, M., Goldmann, W. H., Beltrán, A. M., Detsch, R., Gruenewald, A., et al. (2021). Fabrication and Characterization of Ag- and Ga-doped Mesoporous Glass-coated Scaffolds Based on Natural marine Sponges with Improved Mechanical Properties. *J. Biomed. Mater. Res.* 109 (8), 1309–1327. doi:10.1002/jbm.a.37123

Cochis, A., Azzimonti, B., Chiesa, R., Rimondini, L., and Gasik, M. (2019). Metallurgical Gallium Additions to Titanium Alloys Demonstrate a strong Time-Increasing Antibacterial Activity without Any Cellular Toxicity. *ACS Biomater. Sci. Eng.* 5 (6), 2815–2820. doi:10.1021/acsbiomaterials.9b00147

Cottarel, G., and Wierzbowski, J. (2007). Combination Drugs, an Emerging Option for Antibacterial Therapy. *Trends Biotechnol.* 25 (12), 547–555. doi:10.1016/j.tibtech.2007.09.004

Donnadio, A., Bini, M., Centracchio, C., Mattarelli, M., Caponi, S., Ambrogi, V., et al. (2021). Bioinspired Reactive Interfaces Based on Layered Double Hydroxides-Zn Rich Hydroxyapatite with Antibacterial Activity. *ACS Biomater. Sci. Eng.* 7 (4), 1361–1373. doi:10.1021/acsbiomaterials.0c01643

Duffin, R. N., Blair, V. L., Kedzierski, L., and Andrews, P. C. (2020). Alkyl Gallium(III) Quinolinolates: a New Class of Highly Selective Anti-leishmanial Agents. *Eur. J. Med. Chem.* 186, 111895. doi:10.1016/j.ejmech.2019.111895

Ekkelenkamp, M. B., Cantón, R., Díez-Aguilar, M., Tunney, M. M., Gilpin, D. F., Bernardini, F., et al. (2020). Susceptibility of *Pseudomonas aeruginosa* Recovered from Cystic Fibrosis Patients to Murepavadin and 13 Comparator Antibiotics. *Antimicrob. Agents Chemother.* 64 (2), e01541–19. doi:10.1128/AAC.01541-19

El-Habeeb, A. A., and Refat, M. S. (2019). Synthesis, Structure Interpretation, Antimicrobial and Anticancer Studies of Tranexamic Acid Complexes towards Ga(III), W(VI), Y(III) and Si(IV) Metal Ions. *J. Mol. Struct.* 1175, 65–72. doi:10.1016/j.molstruc.2018.07.099

Enyedy, É. A., Petrasheuskaya, T. V., Kiss, M. A., Wernitznig, D., Wenisch, D., Keppler, B. K., et al. (2021). Complex Formation of an Estrone-Salicylaldehyde Semicarbazone Hybrid with Copper(II) and Gallium(III): Solution Equilibria and Biological Activity. *J. Inorg. Biochem.* 220, 111468. doi:10.1016/j.jinorgbio.2021.111468

Fischbach, M. A. (2011). Combination Therapies for Combating Antimicrobial Resistance. *Curr. Opin. Microbiol.* 14 (5), 519–523. doi:10.1016/j.mib.2011.08.003

Frangipani, E., Bonchi, C., Minandri, F., Imperi, F., and Visca, P. (2014). Pyochelin Potentiates the Inhibitory Activity of Gallium on *Pseudomonas aeruginosa*. *Antimicrob. Agents Chemother.* 58 (9), 5572–5575. doi:10.1128/AAC.03154-14

Gao, Z., Song, M., Liu, R.-L., Shen, Y., Ward, L., Cole, I., et al. (2019). Improving *In Vitro* and *In Vivo* Antibacterial Functionality of Mg Alloys through Micro-alloying with Sr and Ga. *Mater. Sci. Eng. C* 104, 109926. doi:10.1016/j.msec.2019.109926

García-Contreras, R., Lira-Silva, E., Jasso-Chávez, R., Hernández-González, I. L., Maeda, T., Hashimoto, T., et al. (2013). Isolation and Characterization of Gallium Resistant *Pseudomonas aeruginosa* Mutants. *Int. J. Med. Microbiol.* 303 (8), 574–582. doi:10.1016/j.ijmm.2013.07.009

Greenfield, T. J., Julve, M., and Doyle, R. P. (2019). Exploring the Biological, Catalytic, and Magnetic Properties of Transition Metal Coordination Complexes Incorporating Pyrophosphate. *Coord. Chem. Rev.* 384, 37–64. doi:10.1016/j.ccr.2018.12.011

Halwani, M., Yebio, B., Suntres, Z. E., Alipour, M., Azghani, A. O., and Omri, A. (2008). Co-encapsulation of Gallium with Gentamicin in Liposomes Enhances Antimicrobial Activity of Gentamicin against *Pseudomonas aeruginosa*. *J. Antimicrob. Chemother.* 62 (6), 1291–1297. doi:10.1093/jac/dkn422

Harrison, J. J., Turner, R. J., Joo, D. A., Stan, M. A., Chan, C. S., Allan, N. D., et al. (2008). Copper and Quaternary Ammonium Cations Exert Synergistic Bactericidal and Antibiofilm Activity against *Pseudomonas aeruginosa*. *Antimicrob. Agents Chemother.* 52 (8), 2870–2881. doi:10.1128/AAC.00203-08

Hijazi, S., Visca, P., and Frangipani, E. (2017). Gallium-protoporphyrin IX Inhibits *Pseudomonas aeruginosa* Growth by Targeting Cytochromes. *Front. Cell. Infect. Microbiol.* 7, 12. doi:10.3389/fcimb.2017.00012

Imlay, J. A. (2013). The Molecular Mechanisms and Physiological Consequences of Oxidative Stress: Lessons from a Model Bacterium. *Nat. Rev. Microbiol.* 11 (7), 443–454. doi:10.1038/nrmicro3032

Kaneko, Y., Thoendel, M., Olakanmi, O., Britigan, B. E., and Singh, P. K. (2007). The Transition Metal Gallium Disrupts *Pseudomonas aeruginosa* Iron Metabolism and Has Antimicrobial and Antibiofilm Activity. *J. Clin. Invest.* 117 (4), 877–888. doi:10.1172/JCI30783

Kang, D., and Kirienko, N. V. (2018). Interdependence between Iron Acquisition and Biofilm Formation in *Pseudomonas aeruginosa*. *J. Microbiol.* 56 (7), 449–457. doi:10.1007/s12275-018-8114-3

Kang, D., Revtovich, A. V., Deyanov, A. E., and Kirienko, N. V. (2021). Pyoverdine Inhibitors and Gallium Nitrate Synergistically Affect *Pseudomonas aeruginosa*. *mSphere* 6, e0040121. doi:10.1128/mSphere.00401-21

Keenan, T. J., Placek, L. M., Hall, M. M., and Wren, A. W. (2017). Antibacterial and Antifungal Potential of Ga-bioactive Glass and Ga-bioactive Glass/polymeric Hydrogel Composites. *J. Biomed. Mater. Res.* 105 (5), 1102–1113. doi:10.1002/jbm.b.33655

Kelson, A. B., Carnevali, M., and Truong-Le, V. (2013). Gallium-based Anti-infectives: Targeting Microbial Iron-Uptake Mechanisms. *Curr. Opin. Pharmacol.* 13 (5), 707–716. doi:10.1016/j.coph.2013.07.001

Kircheva, N., and Dudev, T. (2021). Competition between Abiogenic and Biogenic Metal Cations in Biological Systems: Mechanisms of Gallium's Anticancer and Antibacterial Effect. *J. Inorg. Biochem.* 214, 111309. doi:10.1016/j.jinorgbio.2020.111309

Kurtuldu, F., Mutlu, N., Michálek, M., Zheng, K., Masar, M., Liverani, L., et al. (2021). Cerium and Gallium Containing Mesoporous Bioactive Glass Nanoparticles for Bone Regeneration: Bioactivity, Biocompatibility and Antibacterial Activity. *Mater. Sci. Eng. C* 124, 112050. doi:10.1016/j.msec.2021.112050

Łapa, A., Cresswell, M., Campbell, I., Jackson, P., Goldmann, W. H., Detsch, R., et al. (2020). Gallium- and Cerium-Doped Phosphate Glasses with Antibacterial Properties for Medical Applications. *Adv. Eng. Mater.* 22 (9), 1901577. doi:10.1002/adem.201901577

Łapa, A., Cresswell, M., Campbell, I., Jackson, P., Goldmann, W. H., Detsch, R., et al. (2019). Ga and Ce Ion-Doped Phosphate Glass Fibres with Antibacterial Properties and Their Composite for Wound Healing Applications. *J. Mater. Chem. B* 7 (44), 6981–6993. doi:10.1039/c9tb00820a

Lessa, J. A., Parrilha, G. L., and Beraldo, H. (2012). Gallium Complexes as New Promising Metallodrug Candidates. *Inorg. Chim. Acta* 393, 53–63. doi:10.1016/j.ica.2012.06.003

Levaditi, C., Bardet, J., Tchakirian, A., and Vaisman, A. (1931). Therapeutic Properties of Gallium in Syphilis and Trypanosomiasis. *C. R. Acad. Bulg. Sci.* 192 (18), 1142–1143.

Leyland-Jones, B. (2003). Treatment of Cancer-Related Hypercalcemia: the Role of Gallium Nitrate. *Semin. Oncol.* 30, 13–19. doi:10.1016/s0093-7754(03)00171-4

Li, K., Tian, H., Guo, A., Jin, L., Chen, W., and Tao, B. (2021a). Gallium (Ga)-strontium (Sr) Layered Double Hydroxide Composite Coating on Titanium Substrates for Enhanced Osteogenic and Antibacterial Abilities. *J. Biomed. Mater. Res* 110 (2), 273–286. doi:10.1002/jbm.a.37284

Li, L., Chang, H., Yong, N., Li, M., Hou, Y., and Rao, W. (2021b). Superior Antibacterial Activity of Gallium Based Liquid Metals Due to Ga3+ Induced Intracellular ROS Generation. *J. Mater. Chem. B* 9 (1), 85–93. doi:10.1039/d0tb00174k

Lin, Z., Gao, C., Wang, D., and He, Q. (2021). Bubble-Propelled Janus Gallium/Zinc Micromotors for the Active Treatment of Bacterial Infections. *Angew. Chem. Int. Ed.* 60 (16), 8750–8754. doi:10.1002/anie.202016260

Mehrabi, T., Mesgar, A. S., and Mohammadi, Z. (2020). Bioactive Glasses: A Promising Therapeutic Ion Release Strategy for Enhancing Wound Healing. *ACS Biomater. Sci. Eng.* 6 (10), 5399–5430. doi:10.1021/acsbiomaterials.0c00528

Morales-de-Echegaray, A. V., Lin, L., Sivasubramaniam, B., Yermembetova, A., Wang, Q., Abutaleb, N. S., et al. (2020). Antimicrobial Photodynamic Activity of Gallium-Substituted Haemoglobin on Silver Nanoparticles. *Nanoscale* 12 (42), 21734–21742. doi:10.1039/c9nr09064a

Müller, A., Fessele, C., Zuber, F., Rottmar, M., Maniura-Weber, K., Ren, Q., et al. (2021). Gallium Complex-Functionalized P4HB Fibers: a Trojan Horse to Fight Bacterial Infection. *ACS Appl. Bio Mater.* 4 (1), 682–691. doi:10.1021/acsabm.0c01221

Nielsen, I. G., Sommer, S., Dippel, A.-C., Skibsted, J., and Iversen, B. B. (2021). Pair Distribution Function and 71Ga NMR Study of Aqueous Ga3+ Complexes. *Chem. Sci.* 12 (43), 14420–14431. doi:10.1039/d1sc05190c

Ning, L. G., Kang, E.-T., Wang, Y. B., Hu, X. F., and Xu, L. Q. (2018). Recent Developments in Controlled Release of Antibiotics. *Cpd* 24 (8), 911–925. doi:10.2174/1381612824666180315094947

Pajor, K., Pajchel, Ł., Zgadzaj, A., Piotrowska, U., and Kolmas, J. (2020). Modifications of Hydroxyapatite by Gallium and Silver Ions-Physicochemical Characterization, Cytotoxicity and Antibacterial Evaluation. *Ijms* 21 (14), 5006. doi:10.3390/ijms21145006

Pandey, A., Savino, C., Ahn, S. H., Yang, Z., Van Lanen, S. G., and Boros, E. (2019). Theranostic Gallium Siderophore Ciprofloxacin Conjugate with Broad Spectrum Antibiotic Potency. *J. Med. Chem.* 62 (21), 9947–9960. doi:10.1021/acs.jmedchem.9b01388

Piatek, M., Griffith, D. M., and Kavanagh, K. (2020). Quantitative Proteomic Reveals Gallium Maltolate Induces an Iron-Limited Stress Response and Reduced Quorum-sensing in *Pseudomonas aeruginosa*. *J. Biol. Inorg. Chem.* 25 (8), 1153–1165. doi:10.1007/s00775-020-01831-x

Pormohammad, A., and Turner, R. J. (2020). Silver Antibacterial Synergism Activities with Eight Other Metal(loid)-Based Antimicrobials against *Escherichia coli, Pseudomonas aeruginosa*, and *Staphylococcus aureus*. *Antibiotics* 9 (12), 853. doi:10.3390/antibiotics9120853

Qiao, J., Liu, Z., Cui, S., Nagy, T., and Xiong, M. P. (2021). Synthesis and Evaluation of an Amphiphilic Deferoxamine:gallium-Conjugated Cationic Random Copolymer against a Murine Wound Healing Infection Model of *Pseudomonas aeruginosa*. *Acta Biomater.* 126, 384–393. doi:10.1016/j.actbio.2021.03.005

Qiao, J., Purro, M., Liu, Z., and Xiong, M. P. (2021). Effects of Polyethyelene Glycol-Desferrioxamine:gallium Conjugates on *Pseudomonas aeruginosa* Outer Membrane Permeability and Vancomycin Potentiation. *Mol. Pharmaceutics* 18 (2), 735–742. doi:10.1021/acs.molpharmaceut.0c00820

Rahimnejad Yazdi, A., Torkan, L., Stone, W., and Towler, M. R. (2018). The Impact of Gallium Content on Degradation, Bioactivity, and Antibacterial Potency of Zinc Borate Bioactive Glass. *J. Biomed. Mater. Res.* 106 (1), 367–376. doi:10.1002/jbm.b.33856

Rastin, H., Ramezanpour, M., Hassan, K., Mazinani, A., Tung, T. T., Vreugde, S., et al. (2021). 3D Bioprinting of a Cell-Laden Antibacterial Polysaccharide Hydrogel Composite. *Carbohydr. Polym.* 264, 117989. doi:10.1016/j.carbpol.2021.117989

Rezzoagli, C., Archetti, M., Mignot, I., Baumgartner, M., and Kümmerli, R. (2020). Combining Antibiotics with Antivirulence Compounds Can Have Synergistic Effects and Reverse Selection for Antibiotic Resistance in *Pseudomonas aeruginosa*. *PLoS. Biol.* 18 (8), e3000805. doi:10.1371/journal.pbio.3000805

Rodríguez-Contreras, A., Torres, D., Guillem-Marti, J., Sereno, P., Ginebra, M. P., Calero, J. A., et al. (2020). Development of Novel Dual-Action Coatings with Osteoinductive and Antibacterial Properties for 3D-Printed Titanium Implants. *Surf. Coat. Technology* 403, 126381. doi:10.1016/j.surfcoat.2020.126381

Roope, L. S. J., Smith, R. D., Pouwels, K. B., Buchanan, J., Abel, L., Eibich, P., et al. (2019). The challenge of Antimicrobial Resistance: what Economics Can Contribute. *Science* 364 (6435), 41. doi:10.1126/science.aau4679

Sanderson, T. J., Black, C. M., Southwell, J. W., Wilde, E. J., Pandey, A., Herman, R., et al. (2020). A Salmochelin S4-Inspired Ciprofloxacin Trojan Horse Conjugate. *ACS Infect. Dis.* 6 (9), 2532–2541. doi:10.1021/acsinfecdis.0c00568

Seyoum, Y., Baye, K., and Humblot, C. (2021). Iron Homeostasis in Host and Gut Bacteria - a Complex Interrelationship. *Gut Microbes* 13 (1), e1874855. doi:10.1080/19490976.2021.1874855

Shao, W., Liu, H., Wang, S., Wu, J., Huang, M., Min, H., et al. (2016). Controlled Release and Antibacterial Activity of Tetracycline Hydrochloride-Loaded Bacterial Cellulose Composite Membranes. *Carbohydr. Polym.* 145, 114–120. doi:10.1016/j.carbpol.2016.02.065

Shisaka, Y., Iwai, Y., Yamada, S., Uehara, H., Tosha, T., Sugimoto, H., et al. (2019). Hijacking the Heme Acquisition System of Pseudomonas aeruginosa for the Delivery of Phthalocyanine as an Antimicrobial. *ACS Chem. Biol.* 14, 1637–1642. doi:10.1021/acschembio.9b00373

Siqueira, R. L., Alves, P. F. S., da Silva Moraes, T., Casemiro, L. A., da Silva, S. N., Peitl, O., et al. (2019). Cation-doped Bioactive Ceramics: *In Vitro* Bioactivity and Effect against Bacteria of the Oral Cavity. *Ceramics Int.* 45 (7), 9231–9244. doi:10.1016/j.ceramint.2019.02.001

Slate, A. J., Karaky, N., Crowther, G. S., Butler, J. A., Banks, C. E., McBain, A. J., et al. (2021). Graphene Matrices as Carriers for Metal Ions against Antibiotic Susceptible and Resistant Bacterial Pathogens. *Coatings* 11 (3), 352. doi:10.3390/coatings11030352

Song, H.-K., Yoo, K.-H., Yoon, S.-Y., Na, H. S., Chung, J., Son, W.-S., et al. (2019). *In Vitro* effect of Gallium-Doped Bioactive Glass on Enamel Anti-demineralization and Bond Strength of Orthodontic Resins. *Appl. Sci.* 9 (22), 4918. doi:10.3390/app9224918

Stan, G. E., Tite, T., Popa, A.-C., Chirica, I. M., Negrila, C. C., Besleaga, C., et al. (2020). The Beneficial Mechanical and Biological Outcomes of Thin Copper-Gallium Doped Silica-Rich Bio-Active Glass Implant-type Coatings. *Coatings* 10 (11), 1119. doi:10.3390/coatings10111119

Sütterlin, S., Dahlö, M., Tellgren-Roth, C., Schaal, W., and Melhus, A. (2017). High Frequency of Silver Resistance Genes in Invasive Isolates of *Enterobacter* and *Klebsiella* Species. *J. Hosp. Infect.* 96 (3), 256–261. doi:10.1016/j.jhin.2017.04.017

Taviot-Guého, C., Prévot, V., Forano, C., Renaudin, G., Mousty, C., and Leroux, F. (2018). Tailoring Hybrid Layered Double Hydroxides for the Development of Innovative Applications. *Adv. Funct. Mater.* 28 (27), 1703868. doi:10.1002/adfm.201703868

Vaidya, M., McBain, A. J., Banks, C. E., and Whitehead, K. A. (2019). Single and Combined Antimicrobial Efficacies for Nine Metal Ion Solutions against *Klebsiella pneumoniae, Acinetobacter Baumannii* and *Enterococcus Faecium*. *Int. Biodeterioration Biodegradation* 141, 39–43. doi:10.1016/j.ibiod.2018.06.017

Wang, M., Yang, Y., Chi, G., Yuan, K., Zhou, F., Dong, L., et al. (2021). A 3D Printed Ga Containing Scaffold with Both Anti-infection and Bone Homeostasis-Regulating Properties for the Treatment of Infected Bone Defects. *J. Mater. Chem. B* 9 (23), 4735–4745. doi:10.1039/d1tb00387a

Wang, Z., Li, J., Benin, B. M., Yu, B., Bunge, S. D., Abeydeera, N., et al. (2021). Lipophilic Ga Complex with Broad-Spectrum Antimicrobial Activity and the Ability to Overcome Gallium Resistance in Both P*seudomonas aeruginosa* and *Staphylococcus aureus*. *J. Med. Chem.* 64 (13), 9381–9388. doi:10.1021/acs.jmedchem.1c00656

Wilson, B. R., Bogdan, A. R., Miyazawa, M., Hashimoto, K., and Tsuji, Y. (2016). Siderophores in Iron Metabolism: from Mechanism to Therapy Potential. *Trends Mol. Med.* 22 (12), 1077–1090. doi:10.1016/j.molmed.2016.10.005

Xie, T., Qi, Y., Li, Y., Zhang, F., Li, W., Zhong, D., et al. (2021). Ultrasmall Ga-ICG Nanoparticles Based Gallium ion/photodynamic Synergistic Therapy to Eradicate Biofilms and Against Drug-Resistant Bacterial Liver Abscess. *Bioact. Mater.* 6 (11), 3812–3823. doi:10.1016/j.bioactmat.2021.03.032

Xu, Z., Chen, X., Tan, R., She, Z., Chen, Z., and Xia, Z. (2019). Preparation and Characterization of a Gallium-Loaded Antimicrobial Artificial Dermal Scaffold. *Mater. Sci. Eng. C* 105, 110063. doi:10.1016/j.msec.2019.110063

Yang, J., Wang, C., Liu, X., Yin, Y., Ma, Y., Gao, Y., et al. (2020). Gallium-Carbenicillin Framework Coated Defect-Rich Hollow TiO2 as a Photocatalyzed Oxidative Stress Amplifier against Complex Infections. *Adv. Funct. Mater.* 30 (43), 2004861. doi:10.1002/adfm.202004861

Yoon, S. S., Coakley, R., Lau, G. W., Lymar, S. V., Gaston, B., Karabulut, A. C., et al. (2006). Anaerobic Killing of Mucoid *Pseudomonas aeruginosa* by Acidified Nitrite Derivatives under Cystic Fibrosis Airway Conditions. *J. Clin. Invest.* 116 (2), 436–446. doi:10.1172/jci24684

Young, M., Ozcan, A., Lee, B., Maxwell, T., Andl, T., Rajasekaran, P., et al. (2019). N-acetyl Cysteine Coated Gallium Particles Demonstrate High Potency against *Pseudomonas aeruginosa* PAO1. *Pathogens* 8 (3), 120. doi:10.3390/pathogens8030120

Zemke, A. C., Madison, C. J., Kasturiarachi, N., Pearce, L. L., and Peterson, J. (2020). Antimicrobial Synergism toward *Pseudomonas aeruginosa* by Gallium(III) and Inorganic Nitrite. *Front. Microbiol.* 11, 2113. doi:10.3389/fmicb.2020.02113

Zeng, J., Wu, L., Liu, Z., Lv, Y., Feng, J., Wang, W., et al. (2021). Gain-of-Function Mutations in Acid Stress Response (evgS) Protect *Escherichia coli* from Killing by Gallium Nitrate, an Antimicrobial Candidate. *Antimicrob. Agents Chemother.* 65 (3), e01595–20. doi:10.1128/AAC.01595-20

Zhang, Y., Pan, X., Wang, L., and Chen, L. (2021). Iron Metabolism in *Pseudomonas aeruginosa* Biofilm and the Involved Iron-Targeted Anti-biofilm Strategies. *J. Drug Target.* 29 (3), 249–258. doi:10.1080/1061186x.2020.1824235

Zhang, Z., Tang, J., Wang, H., Xia, Q., Xu, S., and Han, C. C. (2015). Controlled Antibiotics Release System through Simple Blended Electrospun Fibers for Sustained Antibacterial Effects. *ACS Appl. Mater. Inter.* 7 (48), 26400–26404. doi:10.1021/acsami.5b09820

Conflict of Interest: The authors declare that the research was conducted in the absence of any commercial or financial relationships that could be construed as a potential conflict of interest.

Publisher's Note: All claims expressed in this article are solely those of the authors and do not necessarily represent those of their affiliated organizations, or those of the publisher, the editors and the reviewers. Any product that may be evaluated in this article, or claim that may be made by its manufacturer, is not guaranteed or endorsed by the publisher.

Copyright © 2022 Li, Liu, Huang and Yang. This is an open-access article distributed under the terms of the Creative Commons Attribution License (CC BY). The use, distribution or reproduction in other forums is permitted, provided the original author(s) and the copyright owner(s) are credited and that the original publication in this journal is cited, in accordance with accepted academic practice. No use, distribution or reproduction is permitted which does not comply with these terms.

frontiers in Bioengineering and Biotechnology

ORIGINAL RESEARCH
published: 09 February 2022
doi: 10.3389/fbioe.2021.826011

Photothermal 2D Nanosheets Combined With Astragaloside IV for Antibacterial Properties and Promoting Angiogenesis to Treat Infected Wounds

*Lichang Liu[1], Wenfeng Wang[1], Weihong Hong[1], Yuyan Jin[1], Lichun Wang[1], Sujun Liu[1], Ailin Wang[2] and Xusheng Liu[3]**

[1]Department of Nephrology, Zhuhai Hospital of Guangdong Provincial Hospital of Chinese Medicine, Zhuhai, China, [2]Second Clinical Medical College, Guangzhou University of Chinese Medicine, Guangzhou, China, [3]Department of Nephrology, Guangdong Provincial Hospital of Chinese Medicine, Guangzhou, China

OPEN ACCESS

Edited by:
Gang Wu,
Academic Centre for Dentistry Amsterdam, Netherlands

Reviewed by:
Huaping Tan,
Nanjing University of Science and Technology, China
Bing Tang,
First Affiliated Hospital of Sun Yat-sen University, China

***Correspondence:**
Xusheng Liu
liuxu801@126.com

Specialty section:
This article was submitted to Biomaterials, a section of the journal Frontiers in Bioengineering and Biotechnology

Received: 30 November 2021
Accepted: 27 December 2021
Published: 09 February 2022

Citation:
Liu L, Wang W, Hong W, Jin Y, Wang L, Liu S, Wang A and Liu X (2022) Photothermal 2D Nanosheets Combined With Astragaloside IV for Antibacterial Properties and Promoting Angiogenesis to Treat Infected Wounds. Front. Bioeng. Biotechnol. 9:826011. doi: 10.3389/fbioe.2021.826011

Bacterial infection, inflammatory disorder, and poor angiogenesis of tissue in chronic wounds are the main reasons why wounds are difficult to heal. In this study, a novel MSN-PEG@AS/BP nano-spray was designed to solve these issues. Astragaloside IV (AS) was loaded in mesoporous silica nanoparticles (MSN) to enhance angiogenesis and regulate inflammation, and the two-dimensional (2D) nanosheet black phosphorus (BP) was used to kill bacteria through a photothermal effect. Under thermal decomposition, the covalent bond of polyethylene glycol (PEG) was broken, releasing AS to promote the proliferation of fibroblasts, the formation of blood vessels, and the resolution of inflammation. AS can promote the polarization of the anti-inflammatory (M2) macrophage phenotype to enhance the deposition of extracellular matrix and the formation of blood vessels. Besides, BP showed a significant photothermal effect and nearly 99.58% of *Escherichia coli* and 99.13% of *Staphylococcus aureus* were killed in an antibacterial study. This nano-spray would be a novel therapeutic agent for infected wound treatment.

Keywords: infected wound healing, anti-inflammatory, photothermal therapy, Astragaloside IV (AS), black phosphorus (BP) nanosheets

1 INTRODUCTION

The skin is the largest organ of the human body. When the skin is severely damaged, it will seriously threaten human health (Moreira and Marques, 2022). In fact, chronic wounds are currently facing a huge challenge in the global healthcare system. Despite a series of treatments for wounds in clinic, there are still some hard-to-heal wounds (Clark and Price, 2004). The annual cost for treating chronic wounds in the United States exceeds 25 billion U.S. dollars. Some chronic wounds that are difficult to heal, such as diabetic foot ulcers and venous ulcers of the lower extremities, may lead to infection, sepsis, amputation, and even death (Sen et al., 2009). Therefore, wound dressings that can effectively treat chronic wounds are urgently needed.

Chronic wounds are often accompanied with persistent infection, excessive inflammation, and damaged tissue (Cavanagh et al., 2005). Bacterial infection is a major factor hindering the healing of chronic wounds. The biofilm formed by bacterial infection not only destroys the host's immune

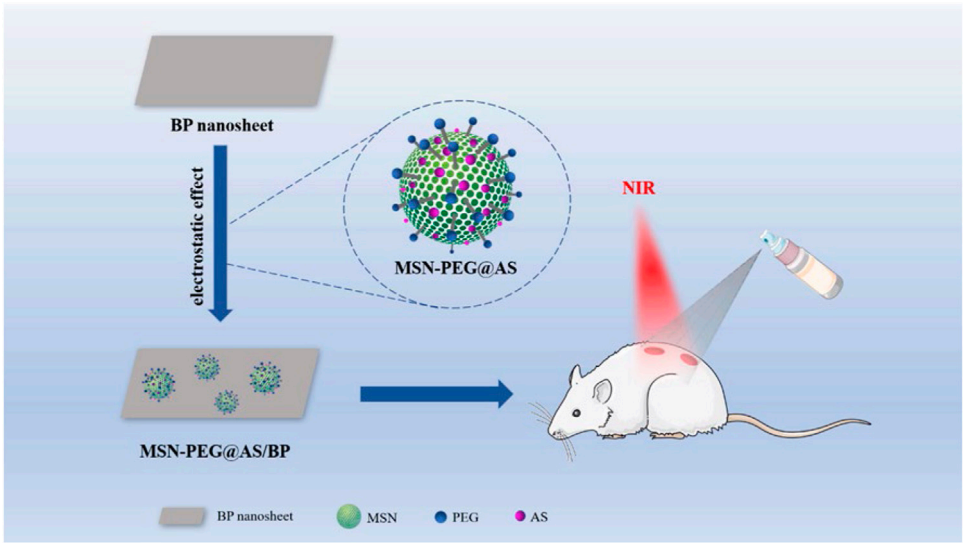

SCHEME 1 | Schematic illustration of the construction of the MSN-PEG@AS/BP multifunctional nano-spray for bacteria-infected wound, enhancing angiogenesis and regulating inflammation.

system, but also forms a barrier that hinders the tight junction of epithelial cells, resulting in chronic wounds that cannot be closed (Metcalf and Bowler, 2013). Traditional treatment method is to use a lot of antibiotics on the infected wounds. However, bacterial resistance may occur during treatment. In order to avoid the long-term use of antibiotics that leads to bacterial resistance, photothermal therapy (PTT) was chosen as new way to treat the infected wounds. Due to its non-invasiveness, high-efficiency bactericidal properties, and low toxicity, PTT has attracted widespread attention in recent years (Chen et al., 2020). The emergence of black phosphorus (BP) nanosheets provides a new method to solve the problem of bacterial resistance. BP has an excellent photothermal conversion effect that can destroy bacterial biofilms under NIR irradiation (Miao et al., 2019). In addition, the large surface area and planar structure of BP provide convenience for loading wound healing drugs (Wang et al., 2015). Moreover, BP has excellent biocompatibility and biodegradability, and its degradation products in aqueous media are non-toxic phosphate and phosphonate (Huang et al., 2018).

Excessive inflammation is another major problem in wound healing, which leads to growth factor and ECM degradation, and hinders the formation of new granulation tissue and blood vessels (Eming et al., 2014). Macrophages play an essential role in the resolution of inflammation. The conversion of the M1 phenotype of macrophages to the M2 phenotype is conducive to changing the wound microenvironment from a pro-inflammatory state to an anti-inflammatory state (Larouche et al., 2018). Previous studies have shown that a certain concentration of silicon ions can promote the polarization of macrophages to the M2 phenotype (Zhu et al., 2020). Nano-silica is widely used as drug carriers, and the silicon ions produced during the degradation process can control inflammation. Meanwhile, nano-silica can also be used as a carrier to release other drugs. Mesoporous silica nanoparticles (MSN) are newly derived by a template etching method (Nguyen et al., 2020). Compared to nano-silica, MSN effectively solves the problem of drug loading efficiency and sustained release kinetics due to its high surface area and ordered mesoporous channels (Zhang et al., 2017).

Astragaloside IV (AS), the main component of Astragalus, has been demonstrated to be the most effective biologically active compound to promote skin cell proliferation (Lee et al., 2018). As reported in the literature, AS regulates nitric oxide (NO) and growth factors through the JAK2/STAT3 pathway to induce angiogenesis in umbilical vein endothelial cells (Wang et al., 2013). In addition, AS could downregulate the pro-inflammatory cytokines and upregulate anti-inflammatory cytokines, such as transforming growth factor-β (TGF-β), in the inflammation site, and trigger the transition of the macrophage phenotype to the anti-inflammatory state (M2) (Chen et al., 2012). Anti-inflammatory macrophages contribute to the production of extracellular matrix (ECM) and wound contraction. Meanwhile, M2 macrophages guide the tunnel of endothelial migration and release angiogenic factors, thereby promoting angiogenesis. Chen et al. have confirmed that AS can promote wound re-epithelialization, angiogenesis, and ECM remodeling (Chen et al., 2012).

In this research, we loaded AS in the mesopores of aminated MSN (MSN-NH_2), and complex with BP through electrostatic adsorption to produce MSN-PEG@AS/BP nano-spray. The photothermal effect of this nano-spray irradiated by NIR laser can generate local high temperature to destroy the structure and metabolism of bacteria, thereby killing them. Considering that the photothermal effect of BP caused physical

changes (phase transition, swelling, and solubility) in MSN, which limited the release rate of AS, we designed a thermally responsive PEG shell grafted on the MSN surface loaded with AS and BP. When PEG is thermally decomposed, the covalent bond is broken to trigger the release of the drug (Saint-Cricq et al., 2015). The nano-spray reported here is a new way to treat bacteria-infected wound (**Scheme 1**).

2 EXPERIMENTAL SECTION

2.1 Materials

Cetyl trimethyl ammonium chloride (CTAC), ethyl orthosilicate (TEOS), 3-aminopropyltriethoxysilane (APTES), p-toluenesulfonyl chloride, p-hydroxybenzaldehyde, Astragaloside IV (AS), anhydrous magnesium sulfate ($MgSO_4$), dichloromethane (CH_2Cl_2), ethanol, methylbenzene, and methanol were purchased from Macklin (Shanghai, China). Triethanolamine (TEA) and polyethylene glycol (PEG) were purchased from Aladdin Industrial Corporation (Shanghai, China). Hydrochloric acid (HCl) and sodium chloride (NaCl) were purchased from Sinopharm Chemical Reagent Co., Ltd. (Shanghai, China). BP crystal was purchased from Nanjing XFNANO Materials Tech. Co. Ltd. (Nanjing, China). All other reagents used in the experiment were of analytical grade and no further purification was required.

2.2 Synthesis of MSN-NH_2

MSN was synthesized by a template etching method (Wu et al., 2018). Briefly, CTAC (2 g) and TEA (0.1 g) were dissolved in 20 ml of deionized water at 95°C for 1 h under stirring. Then, 1.5 ml of TEOS was added in the above solution. After stirring for 1 h, the mixture was centrifuged at 15,000 *g* for 15 min and washed three times with ethanol to obtain the MSN.

For amination modification, the product was dispersed in 50 ml of ethanol. Two hundred microliters of APTES was added to the solution and refluxed for 4 h at 60°C under stirring. The mixture was then centrifuged and washed with deionized water to obtain the aminated mesoporous silica (MSN-NH_2). The final product MSN-NH_2 was dispersed in ethanol and stored at 4°C.

2.3 Synthesis of Dibenzaldehyde-Terminated Polyethylene Glycol (OHC-PEG-CHO)

OHC-PEG-CHO was prepared by a two-step process (Yang et al., 2017). Polyethylene glycol (16 g, 4 mmol) was added to azeotropically dry until most of the toluene was distilled, and then anhydrous CH_2Cl_2 (50 ml) and triethanolamine (2.22 ml, 16 mmol) were added to it. After cooling to 0°C, p-toluenesulfonyl chloride solution (1.24 ml, 60 mM, dissolved in CH_2Cl_2) was added dropwise to the above mixture during 30 min and stirred for 24 h at room temperature, and then 100 ml of deionized water was added and the mixture was extracted five times with 25 ml of CH_2Cl_2. The organic layer was washed by 1 M HCl and saturated NaCl solution and dried with excess anhydrous $MgSO_4$. After CH_2Cl_2 was removed with a rotary evaporator, the concentrated solution was precipitated with 200 ml of cold ether. The precipitate was dried in a vacuum oven at 40°C to obtain polyethylene glycol-p-toluenesulfonate.

Then, 24 g of polyethylene glycol-p-toluenesulfonate was dissolved in 60 ml of DMF solution. After this, p-hydroxybenzaldehyde (1.98 g, 16.24 mmol) and K_2CO_3 (2.24 g, 16.24 mmol) were added to the mixture and stirred for 3 days at 80°C. After cooling to room temperature, 50 ml of deionized water was added to the mixture and then extracted with CH_2Cl_2 and precipitated with cold ether. After drying in a vacuum drying oven at 40°C, the OHC-PEG-CHO was obtained.

2.4 Synthesis of MSN-PEG

Twenty milligrams of MSN-NH_2 synthesized in **Section 2.2** was dispersed in water, and OHC-PEG-CHO (20 mg) was added and stirred for 2 h. The final product MSN-PEG was obtained by centrifuging at 12,000 rpm for 10 min, and the precipitate was redispersed in deionized water and stored at 4°C.

2.5 Preparation of BP

BP was prepared by peeling off BP nanocrystals according to the literature (Aksoy et al., 2020; Zhang et al., 2021). Twenty-five milligrams of BP powder was added to 50 ml of deionized water from which dissolved oxygen had been removed to reduce the oxidation of BP. Then, the mixture was pulverized ultrasonically for 12 h (900 W, SCIENTZ, Ningbo, China). After the color of the BP solution turned dark brown, it was centrifuged at 1,500 rpm for 12 min to remove unstripped BP, and the supernatant was collected and further centrifuged. The supernatant was further centrifuged at 7,800 rpm for 20 min to obtain the BP nanosheets.

2.6 Preparation of MSN-PEG@AS/BP Nanoparticles

Five milligrams of AS and 20 mg of MSN-NH_2 were dissolved in 10 ml of methanol accompanied with magnetic stirring for 24 h. Then, the mixture was centrifuged at 12,000 rpm for 30 min and washed three times with deionized water. The supernatant was collected to calculate the drug loading amount. The resulting precipitate MSN-NH_2@AS was redispersed in water, and 1 mg of BP was added with stirring. After stirring for 30 min, 20 mg of OHC-PEG-CHO was added and stirred for another 2 h. The final product MSN-PEG@AS/BP was obtained by centrifugation and redispersed in deionized water for storage at 4°C.

2.7 Characterization of MSN-PEG@AS/BP

The chemical structures of PEG and OHC-PEG-CHO were confirmed by Fourier transform infrared (FT-IR) spectroscopy (Thermo Electron Scientific Instruments Corp., Fitchburg, WI, United States) and high-resolution proton nuclear magnetic resonance (^{1}H NMR, Burke, Germany). Morphology of nanoparticles and nanosheets was observed by a Zeiss EM902 transmission electron microscope (TEM; Carl Zeiss, Germany). Dispersion of nanomaterials was dropped on the copper mesh and dried under room temperature before observation. The size distribution of nanomaterials was analyzed using dynamic laser scatterometer (DLS, Malvern, Zeta Sizer Nano ZS).

Concentration of nanomaterials used for DLS testing was 1 mg/ml.

2.8 Photothermal Performance Evaluation

The photothermal performance of BP was explored from laser power density and concentration of BP. BP (50 μg/ml, 1 ml) was dispersed in water and irradiated with 808 nm near-infrared (NIR) laser with different laser powers (0.5, 1, 1.5, and 2 W/cm^2) for 5 min at room temperature and temperature was recorded every 10 s. The photothermal effects of BP at various concentrations (20, 30, 40, and 50 μg/ml) were measured following a similar procedure with a laser power density of 1.5 W/cm^2. To study the photothermal stability of BP, 1 ml of BP solution (40 μg/ml) was repeatedly irradiated with 808 nm NIR laser (2 W/cm^2, 5 min) five times.

2.9 Material Stability Evaluation

MSN-PEG@AS was dispersed in the PBS buffer (pH = 7.4), and the particle size distribution was measured daily using DLS for 5 days.

2.10 Drug Loading and Release Assay

The concentration of AS was measured by a high-performance liquid chromatograph (HPLC) at 205 nm (mobile phase: methanol; 0.8 ml/min) (Szabo et al., 1994). The standard curve of AS is shown in **Supplementary Figure S1**. The supernatant collected in **Section 2.6** was filtered with a 0.22-μm filter and re-dissolved in methanol. The concentration of AS in the supernatant was determined by the standard curve. Drug loading amount and encapsulation efficiency of MSN were calculated by **Eqs 1**, **2** (Pham et al., 2021).

$$\text{Drug loading amount}\,(\%) = W_1/W_0 \times 100\% \quad (1)$$

$$\text{Encapsulation efficiency}\,(\%) = W_1/W_2 \times 100\% \quad (2)$$

where W_0 is the total mass of MSN, W_1 is the mass of AS loaded in MSN, and W_2 is the feed amount of AS for drug loading.

MSN-PEG@AS (0.5 mg) was placed in a dialysis bag, and shaken in 2 ml of PBS (pH = 7.4) at 37°C. Release solution (0.2 ml) was taken out, respectively, and the same amount of PBS buffer was added at the same time at different time points (1, 2, 4, 6, 8, 12, 24, 36, 48, and 96 h). The AS concentration was detected by HPLC, and the cumulative release percentage of AS was calculated as reported (Zhang et al., 2017; Chen et al., 2021).

2.11 *In Vitro* Antibacterial Activity Evaluation

The antibacterial properties of the nanomaterials were evaluated with Gram-positive *Staphylococcus aureus* (*S. aureus*) and Gram-negative *Escherichia coli* (*E. coli*). Two hundred microliters of nanomaterials suspension (100 μg/ml) was co-incubated with 100 μl of bacteria suspension (1 × 10^6 CFU/ml), and the MSN-PEG/BP + NIR group was exposed to NIR (2 W/cm^2) laser for 5 min. After that, 1.7 ml of LB medium was added and incubated at 37°C for 4 h. The diluted bacterial suspension (100 μl) was inoculated on LB agar plates and cultured at 37°C for 24 h. Number of colonies was counted and the antibacterial ratio was calculated by **Eq. 3**.

$$\text{Antibacterial ratio}\,(\%) = \left(N_{control} - N_{sample}\right)/N_{control} \times 100\% \quad (3)$$

where $N_{control}$ is the average number of colonies in the control sample and N_{sample} is the average bacterial colony in the nanomaterials-treated sample.

2.12 Cytotoxicity and Live/Dead Staining of L929

L929 in the logarithmic growth phase were used for cytotoxicity assay. Firstly, L929 cells were seeded on a 96-well plate at a density of 1 × 10^4/well and incubated in a 5% carbon dioxide incubator at 37°C for 24 h. Then, the culture medium was refreshed with culture medium containing 100 μg/ml of nanomaterials and co-incubated for another 24 h. Cell viability was detected using CCK-8 assay per the manufacturer's instruction, and the optical density at 450 nm was read by a microplate reader. L929 cells co-cultured with nanomaterials in 48 well-plates were further stained by a Live/Dead staining kit (Thermal Fisher, United States). Dead cells were stained with red fluorescence, while live cells were stained with green fluorescence.

2.13 *In Vitro* Tube Formation of MSN-PEG@AS/BP

Matrigel (Corning, United States) diluted with serum-free medium at a ratio of 1:1 was added in 48 well-plates and then placed at 37°C to form a gel. HUVECs at a cell density of 10,000 per well were added to the well plate. After the cells adhere to the Matrigel, each group of culture media containing nanomaterials was added separately and incubated at 37°C. Images of HUVEC were taken by an inverted fluorescence microscope at selected time points.

2.14 *In Vivo* Infected Full-Thickness Skin Defect Model

Animals were treated in accordance with protocols evaluated and approved by the Ethics Committee of Zhuhai Hospital of Guangdong Provincial Hospital of Chinese Medicine. SD rats (200 g) were randomly divided into five groups, namely, Control (treated with PBS), MSN-PEG@AS, MSN-PEG/BP + NIR, MSN-PEG@AS/BP, or MSN-PEG@AS/BP + NIR. The rats were weighed before the operation and anesthetized with 3% sodium pentobarbital (45–60 mg/kg) intraperitoneally. Hair on the back of rats was shaved and disinfected with iodophor. Full thickness skin on the back was completely removed with tissue scissors to create a 12-mm round defect. The wound was then infected with a mixture of 40 μl of *E. coli* (1 × 10^8 CFU/ml) and *S. aureus* (1 × 10^8 CFU/ml) suspension for 1 day before treatment. One hundred microliters of nano-spray (100 μg/ml) was used on the defect every 2 days. The MSN-PEG@AS/BP + NIR group was exposed to NIR laser (2 W/cm^2) for 5 min after each treatment. Wound area was photographed by a digital camera, and the wound area was evaluated using IPP 6.0 software.

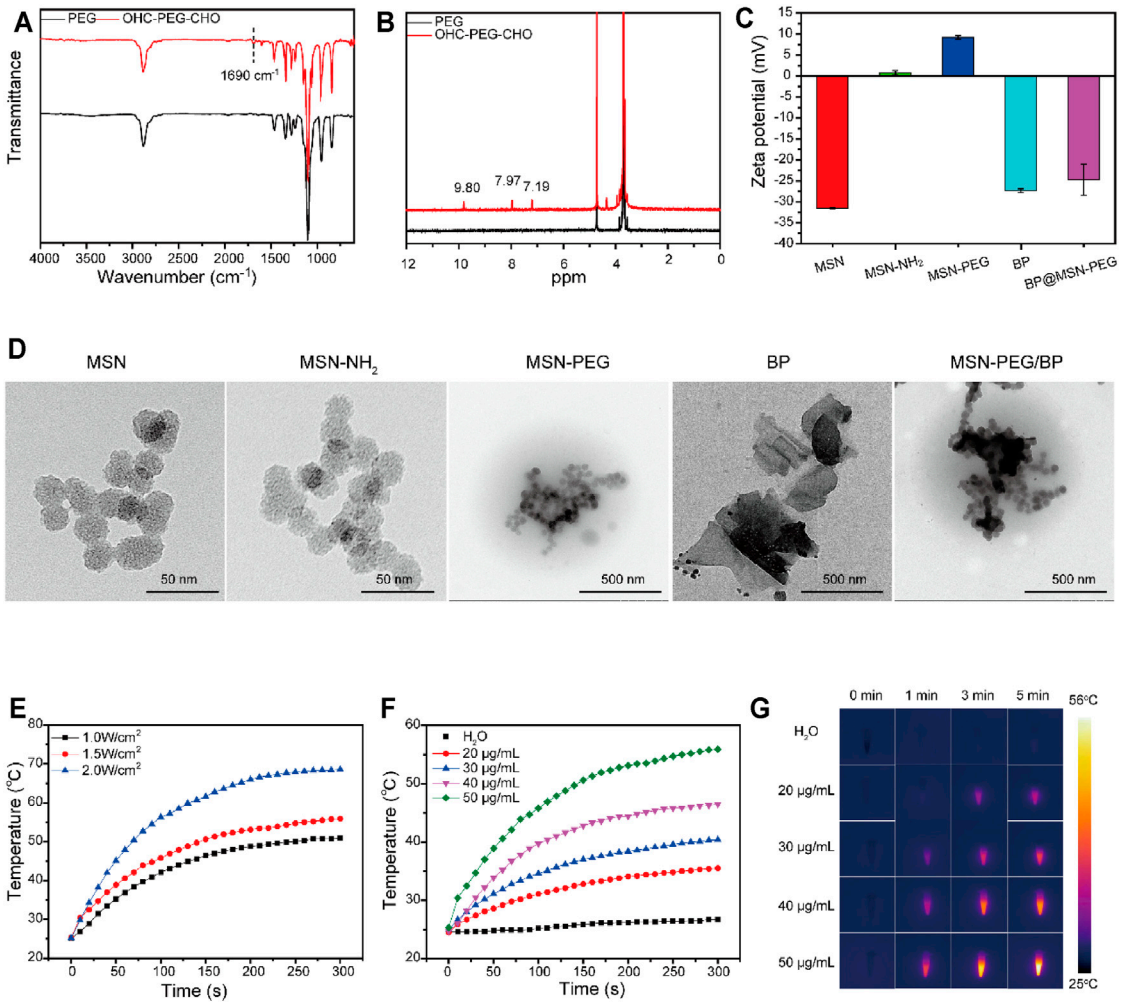

FIGURE 1 | Characterizations of AS@MSN-PEG/BP. **(A)** FTIR spectra of PEG and OHC-PEG-CHO. **(B)** ^{1}H NMR spectra of PEG and OHC-PEG-CHO. **(C)** Zeta potential of MSN, MSN-NH2, MSN-PEG, BP, and MSN-PEG/BP. **(D)** TEM image of MSN, MSN-NH2, MSN-PEG, BP, and MSN-PEG/BP. **(E)** Photothermal temperature increase of BP solution (50 μg/ml) under different NIR light irradiation (0.5, 1, 1.5, and 2 W/cm^2). **(F)** Photothermal temperature increase of DI water and BP solution with different concentrations (20, 30, 40 and 50 μg/ml). **(G)** Photothermal imaging of DI water and BP solution with different concentrations (20, 30, 40, and 50 μg/ml) under NIR light irradiation (1.5 W/cm^2, 0–5 min).

2.15 *In Vivo* Antibacterial Performance Analysis

Bacterial number in wounds was evaluated on day 3. Tissue was harvested and homogenate in normal saline, and then 100 μl of diluted homogenate was spread on the Gram-negative bacteria selection medium and mannitol salt agar medium plates, separately. The culture plate was incubated at 37°C for 24 h for colony counting.

2.16 Histological and Immunofluorescence Analysis

Skin harvested at 3, 7, 10, and 14 days was fixed in 4% paraformaldehyde for more than 24 h and embedded in paraffin. Tissues were sliced into 4-μm-thick sections and stained according to the manufacturer's instruction. H&E and Masson staining were used to observe the tissue repair at days 3, 7, 10 and 14. Immunofluorescence staining of TNF-α, TGF-β-1, and IL-10 was used to assess the inflammation level of tissue at days 3 and 7. Immunofluorescence staining of CD31 and α-SMA were used to assess the angiogenesis of tissue at day 7.

2.17 Statistical Analysis

Each sample was tested three times in parallel, and the results were expressed in terms of average and standard deviation. The significance was analyzed using GraphPad Prism 7.0. One-way analysis of variance (ANOVA) was performed to evaluate the

significance of the experimental data. The statistical significance was $^{*}p < 0.05$, $^{**}p < 0.01$, and $^{***}p < 0.001$.

3 RESULTS AND DISCUSSION

3.1 Synthesis and Characterization of MSN-PEG@AS/BP

To prepare the thermally responsive PEG shell for MSN, OHC-PEG-CHO was firstly synthesized as PEG was modified with benzaldehyde groups (Deng et al., 2010). The FT-IR spectra of OHC-PEG-CHO showed the absorption peak at 1,690 cm^{-1} corresponding to the C=O stretching vibration absorption peak (**Figure 1A**). The ^{1}H NMR spectra of PEG and OHC-PEG-CHO showed that the absorption peak at the chemical shift ppm = 9.80 corresponded to the hydrogen on the aldehyde group. Both FT-IR and ^{1}H NMR results confirmed the successful modification (**Figure 1B**).

Aminated MSN was then derived to form MSN-PEG nanoparticles through Schiff base reaction. The zeta-potentials of MSN, MSN-NH_2, and MSN-PEG (**Figure 1C**) were −31.5 ± 0.2, 0.794 ± 0.47, and 9.25 ± 0.48 mV, respectively. Obviously, when MSN was modified by amination, the surface charge changed to positive (Aquib et al., 2021). The change of surface charge of MSN was attributed to the appearance of amino groups in MSN (Yang et al., 2017). Compared with MSN-NH_2, the surface charge of MSN-PEG had a slight increase, perhaps due to the large number of unreacted amino groups on the surface of MSN nanoparticles (von Baeckmann et al., 2021). As shown in **Supplementary Figure S2**, DLS analysis showed that the particle size of MSN, MSN-NH_2, and MSN-PEG in PBS solution was approximately 200–260 nm. In addition, the TEM images of MSN and MSN-NH_2 showed that both MSN and MSN-NH_2 were approximately spherical porous nanoparticles (**Figure 1D**), with a particle size of about 20–30 nm. In the TEM image of MSN-PEG, the nanospheres showed an inconspicuous porous structure, and the color deepened, indicating that the PEG shell was successfully modified on the surface of the MSN. The coating of PEG to MSN was due to the Schiff base reaction between MSN-NH_2 and OHC-PEG-CHO.

The BP nanosheets were peeled ultrasonically from the BP crystals (Ouyang et al., 2018). **Figure 1D** shows that the BP nanosheets presented a layer structure with a size of 200–600 nm. BP has a negative zeta potential of −27.3 ± 0.451 mV (**Figure 1C**) (Kong et al., 2020), which can be used for coating with MSN-PEG due to its electrostatic effect. TEM image of MSN-PEG/BP showed that MSN-PEG nanoparticles were successfully deposed on the surface of BP nanosheets (**Figure 1D**).

Stability of MSN-PEG@AS was also detected. **Supplementary Figure S3** showed a particle size distribution of MSN-PEG@AS in PBS buffer within 5 days. The size distribution was increased from 400 nm to about 800 nm in the first 4 days and finally stabilized, owing to the electrostatic effect between MSN-PEG@AS and BP. Finally, the complex showed a stable diameter, indicating that the MSN-PEG@AS/BP have formed a stable complex.

3.2 *In Vitro* Photothermal Performance of BP Nanosheets

Photothermal capability of BP is one of the most interesting characteristics for researchers in the field of biomedical engineering, that BP can be used as a new antibacterial agent. The photothermal performance of BP (50 μg/ml) under 808-nm NIR laser irradiation with different power densities is displayed in **Figure 1E**. With the laser power densities increased (1.0–2.0 W/cm^2), the temperature of BP increased rapidly and the maximum temperature also increased from 50.9°C to 68.6°C.

Temperature changes of BP solution with different concentrations (20–50 μg/ml) at fixed power density (1.5 W/cm^2) were also recorded (**Figures 1F,G**). When the 808-nm NIR laser irradiated for 5 min, the temperature of the BP solution with a concentration of 50 μg/ml reached 55.9°C and increased by 30.6°C. In comparison, the temperature of 40, 30, and 20 μg/ml BP solutions increased by 21.8, 15.4, and 11.0°C, respectively. The temperature of water only increased by 2.1°C in 5 min and showed no obvious change. It could be observed that under the same irradiation time, temperature improved with the increased concentration of the BP solution, which displayed obvious concentration dependence (Shao et al., 2016). Additionally, the temperature of the BP solution increased rapidly in a short time under the irradiation of the NIR laser and gradually slows down until it stabilizes with the increase of irradiation time.

Photothermal stability was also analyzed as shown in **Supplementary Figure S4**. After three cycles of repeated NIR laser irradiation, the temperature increase of BP was about 25.9°C, and the temperature could still rise sharply in a short period of time without significant difference compared to the first cycle, indicating its excellent photothermal stability as reported (Liu et al., 2020).

3.3 *In Vitro* Drug Loading and Release Behavior

To verify the drug loading and release ability of the MSN-PEG@AS, the AS loading and release was investigated. Drug loading and encapsulation efficiency of AS was 8.12 and 70.7%, respectively, according to HPLC determination. **Supplementary Figure S5** shows the *in vitro* release curve of MSN-PEG@AS. AS showed a quick release in the first 8 h, and nearly 40% released. Most of the AS molecules entrapped in the MSN were quickly released into the aqueous medium. The initial sharp burst was due to the rapid leaching of AS from the hole. The release gradually slowed down in the later period, because the concentration of AS in the aqueous medium gradually increased, and the release balance was gradually reached (Xue and Shi, 2004). The release balance showed that 91.32 ± 2.75% of AS was released at 96 h. That means, AS can take effect within 4 days, confirming the sustained-release effect of MSN and providing support for reducing the frequency of administration.

3.4 *In Vitro* Antibacterial Activity Evaluation

The antibacterial activity against *E. coli* and *S. aureus* was evaluated. As shown in **Figure 2A**, the MSN-PEG group

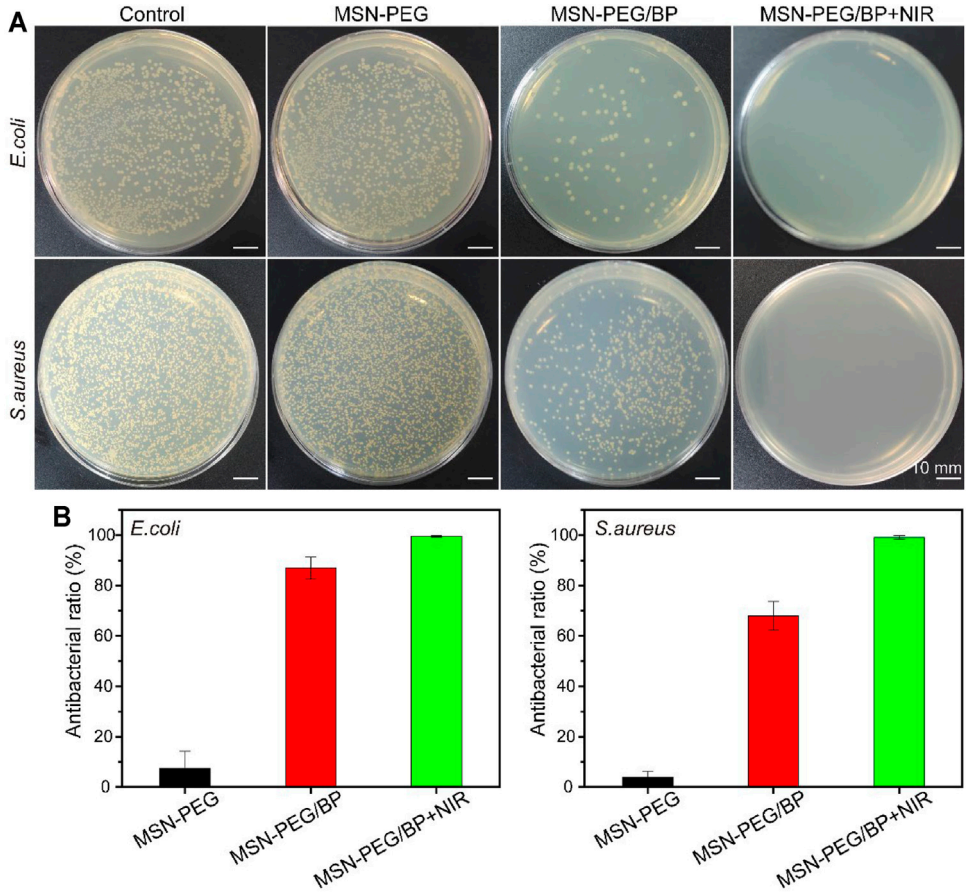

FIGURE 2 | (A) Agar Petri dish images of *E. coli* and *S. aureus* bacterial colonies after the treatments and **(B)** their corresponding survival rates *in vitro*: (1) Control, (2) MSN-PEG, (3) MSN-PEG/BP, and (4) MSN-PEG/BP + NIR.

caused the death of only a very small number of *E. coli* and *S. aureus*, which was equivalent to that of the control group. In contrast, the number of *E. coli* and *S. aureus* treated by MSN-PEG/BP without NIR group was significantly reduced, indicating that BP itself can cause certain bacterial toxicity in the absence of NIR. Xiong et al. have clearly demonstrated that the sharp edges of BP nanosheets can cause bacterial membrane damage (Xiong et al., 2018). The bacteria treated with MSN-PEG/BP were almost completely killed under NIR irradiation, which is attributed to the toxicity of BP to bacteria and the high temperature under NIR laser irradiation. **Figure 2B** quantitatively showed the outstanding antibacterial effect of MSN-PEG/BP, with antibacterial rates of 99.58% (*E. coli*) and 99.13% (*S. aureus*), respectively. Therefore, MSN-PEG/BP has a great potential for antibacterial applications.

3.5 Evaluation of Biocompatible and Angiogenic Potential

Cell cytotoxicity against L929 cells was conducted to evaluate the biocompatibility of the materials. **Figure 3A** shows that the live/dead staining of L929 co-incubated with nanomaterials. Green fluorescence represents the live cells, while red fluorescence indicates the dead cells. The cells showed a good spread morphology, and the number gradually increased with the extension of the culture time. All cells co-cultured with nanomaterials did not show red fluorescence, which means nanomaterials based on MSN-PEG and BP has no obvious cytotoxicity to L929.

The cell viability of L929 cells treated with different nanomaterials was quantitively analyzed using the CCK-8 kit and is displayed in **Figure 3B**. All groups showed cell viability higher than 97.5% after culturing for 24 h, indicating no cytotoxicity according to ISO 10993-5:2009. Nanomaterials containing AS all promoted the proliferation of L929, suggesting that AS can promote the proliferation of fibroblasts as described in the literature (Chen et al., 2012).

Furthermore, the pro-angiogenic properties of the prepared materials were evaluated using Matrigel by the tube formation assay. Compared with the control group, the effect of tubule formation in the MSN-PEG group was negligible (**Figure 3C**). On the contrary, the MSN-PEG@AS group and MSN-PEG/BP group have more tubule formation and branch points than the MSN-

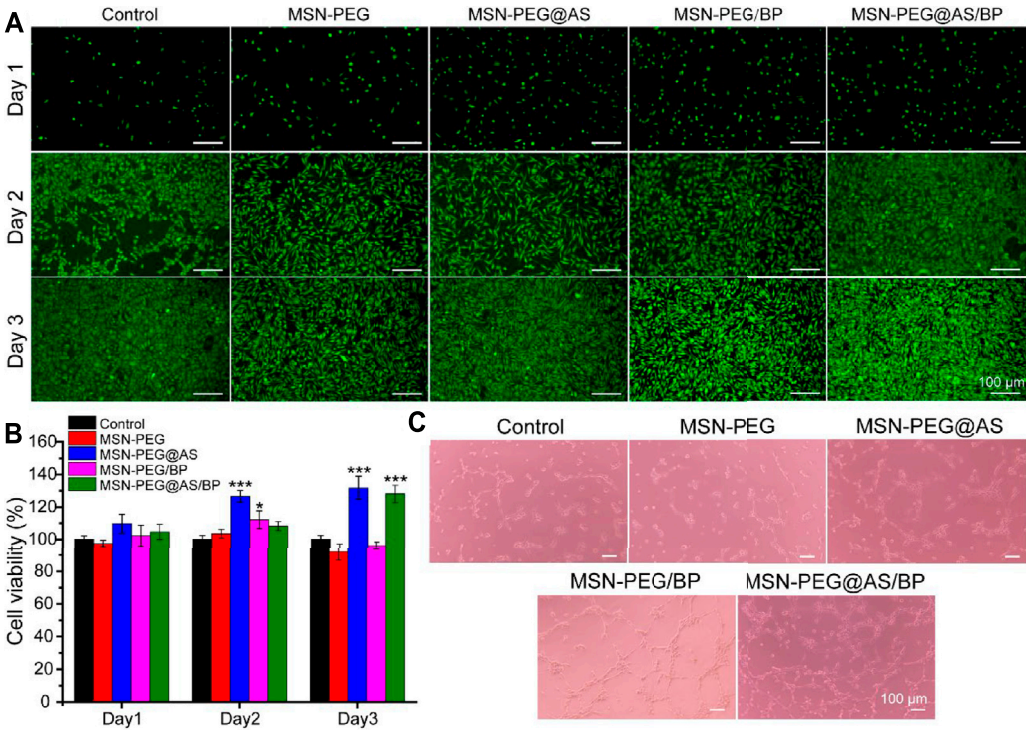

FIGURE 3 | (A) Live/dead staining and **(B)** cytotoxicity assay of L929 cells at different time points. **(C)** The angiogenic potential of HUVEC treated with different nanomaterials (100 μg/ml).

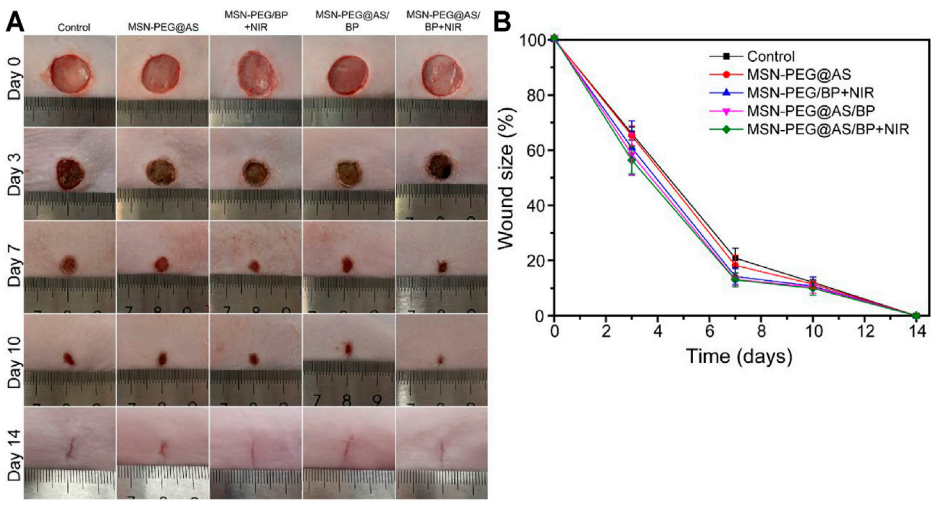

FIGURE 4 | (A) Digital image of wound healing at day 0, 3, 7, 10, and 14 with different treatments. **(B)** Quantification of wound closure rate (Control, MSN-PEG@AS, MSN-PEG@BP + NIR, MSN-PEG@AS/BP, and MSN-PEG@AS/BP + NIR).

PEG group, which is probably due to AS and BP affecting the formation of blood vessels (Wang et al., 2013; Qian et al., 2019). In addition, the MSN-PEG@AS/BP group had maximal tubule formation and branch points, indicating the best angiogenesis effect compared to other groups.

3.6 *In Vivo* Wound Healing and Antibacterial Ability

The *in vivo* application of the MSN-PEG@AS further confirmed the successful treatment of chronic wounds. Healthy SD rats were

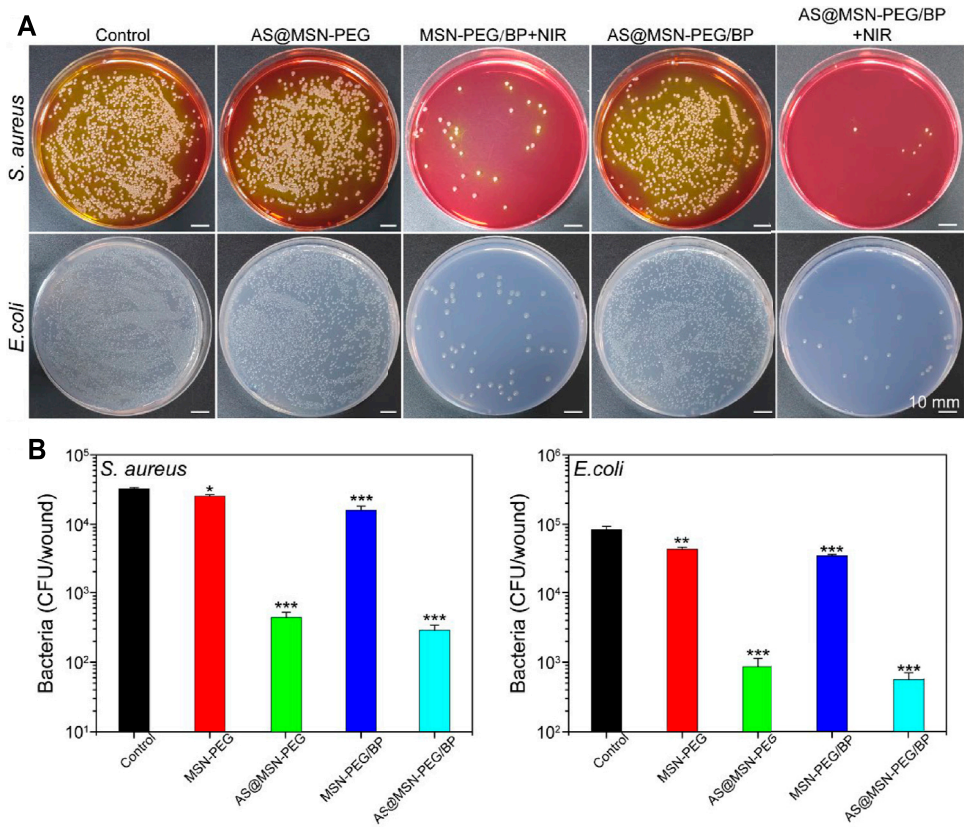

FIGURE 5 | (A) Digital images of *E. coli* and *S. aureus* bacterial colony-forming units, obtained from the wound tissue (day 3) under various experimental conditions (Control, MSN-PEG@AS, MSN-PEG@BP + NIR, MSN-PEG@AS/BP, and MSN-PEG@AS/BP + NIR). **(B)** Quantitative results of standard plate counting assay after 24 h (n = 3).

randomly divided into five groups: Control, MSN-PEG@AS, MSN-PEG/BP + NIR, MSN-PEG@AS/BP, and MSN-PEG@AS/BP + NIR. The images of the wounds were taken by a digital camera for gross observation (**Figure 4A**). The relative wound area showed the nanomaterials with AS leading to a smaller wound area, which was conspicuously smaller than the control group, indicating that the AS could promote wound healing as reported in the literature (Lee et al., 2018). Moreover, the wound healing in the rats treated with MSN-PEG@AS/BP with or without NIR irradiation occurred faster than in the rats treated without BP at day 3.

More specifically, **Figure 4B** further confirmed this finding as the wound size of the MSN-PEG@AS/BP with NIR irradiation group was smaller than that of the group without NIR irradiation. At days 7 and 10, MSN-PEG@AS/BP with NIR irradiation-treated wound showed the smallest area, 56.3% and 12.5%, respectively, which revealed that the MSN-PEG@AS/BP with NIR irradiation could be used for the bacteria-infected wound *in vivo* with the assistance of photothermal effects.

3.7 *In Vivo* Antibacterial Performance Analysis

The *in vivo* antibacterial performance of the materials was evaluated by the full-thickness skin defect model mentioned above. We collected the infected skin tissue in the wounds and tested the bacterial viability by a colony counting assay to quantitatively evaluate the growth of bacteria in the wound on day 3. The growth of bacteria in the wounds was observed in **Figure 5A**. The colony numbers of *E. coli* and *S. aureus* in the MSN-PEG/BP + NIR group and MSN-PEG@AS/BP + NIR group were much lower than those of other groups. Moreover, nearly 30,000–15,000 CFU/wound of *E. coli* and 3000-8000 CFU/wound of *S. aureus* were still alive in the wound site in the control group, MSN-PEG@AS group, and MSN-PEG@AS/BP without NIR irradiation group (**Figure 5B**). In contrast, the number of *E. coli* and *S. aureus* colonies in the group with NIR irradiation was much lower than that in the group without NIR irradiation, about 500-800 CFU/wound and 200-400 CFU/wound, respectively. The colony count statistics of wounds in different groups demonstrated that the good antibacterial effect *in vivo* was attribute to the high temperature caused by BP with NIR irradiation.

3.8 Wound Histological Analysis

The wound healing quality was further evaluated by H&E and Masson staining. After 3 days of treatment, the granulation tissue was observed in the wounds. Additionally, compared with the control group, the thickness of the granulation tissue in the nano-spray-treated groups was significantly higher at days 3, 7, and 10 (**Figure 6**). In the early stage of wound healing, the secreted pro-

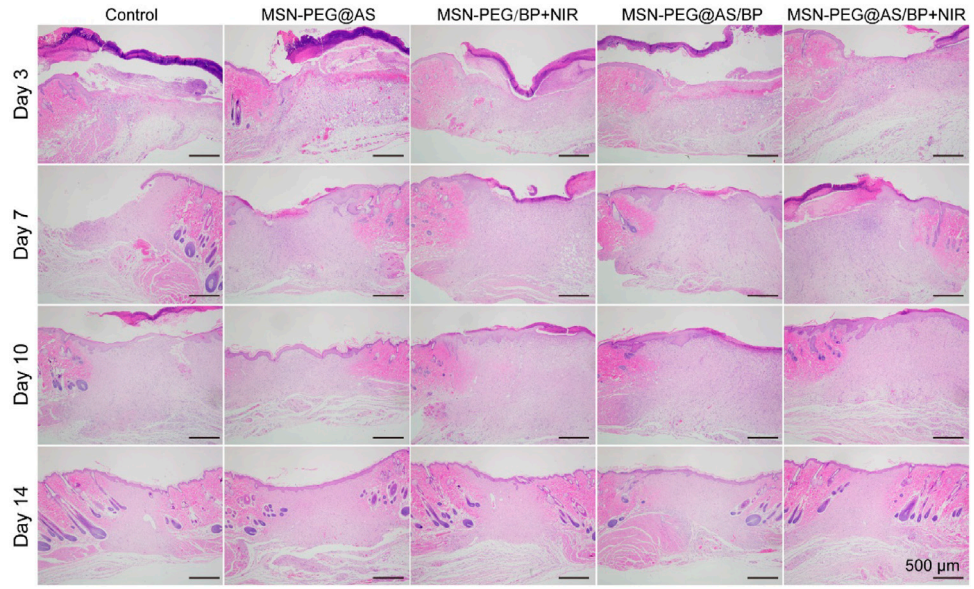

FIGURE 6 | H&E staining of wound sections at days 0, 3, 7, 10, and 14 with different treatments (Control, MSN-PEG@AS, MSN-PEG@BP + NIR, MSN-PEG@AS/BP, and MSN-PEG@AS/BP + NIR).

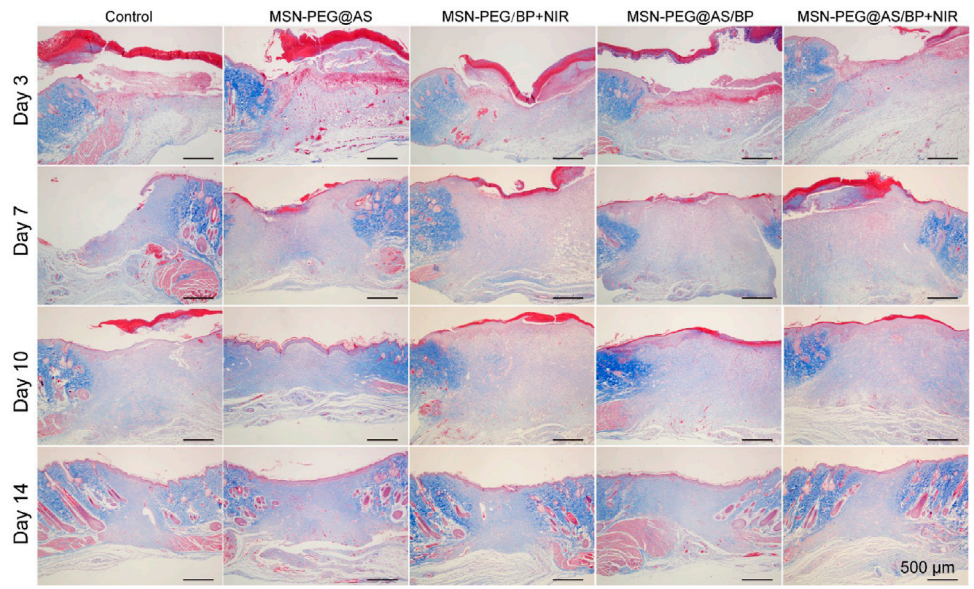

FIGURE 7 | Masson staining of wound sections at days 0, 3, 7, 10, and 14 with different treatments (Control, MSN-PEG@AS, MSN-PEG@BP + NIR, MSN-PEG@AS/BP, and MSN-PEG@AS/BP + NIR).

inflammatory cytokines and growth factors promote the proliferation of fibroblasts, the differentiation of immune cells, and the deposition of ECM to form the new granulation tissue. At day 7, the intact neoepidermis layer was formed in the wound sites of the MSN-PEG/BP + NIR group, the MSN-PEG@AS/BP with NIR group, and the MSN-PEG@AS/BP without NIR irradiation group compared with other groups. In contrast, the little granulation tissue and the thin neoepidermis layer were barely observed in the wounds treated with PBS and MSN-PEG@AS. In fact, the epithelium of the MSN-PEG@AS/BP + NIR group was smoother and more regulated than that of the MSN-PEG@AS/BP group, and follicles began to develop around the wound.

Besides, Masson staining was applied to different groups to reflect the deposition of collagen. Similarly, there was a larger collagen deposition area at wound with dense collagen fibers in the MSN-PEG@AS/BP + NIR group (**Figure 7**). As one of the

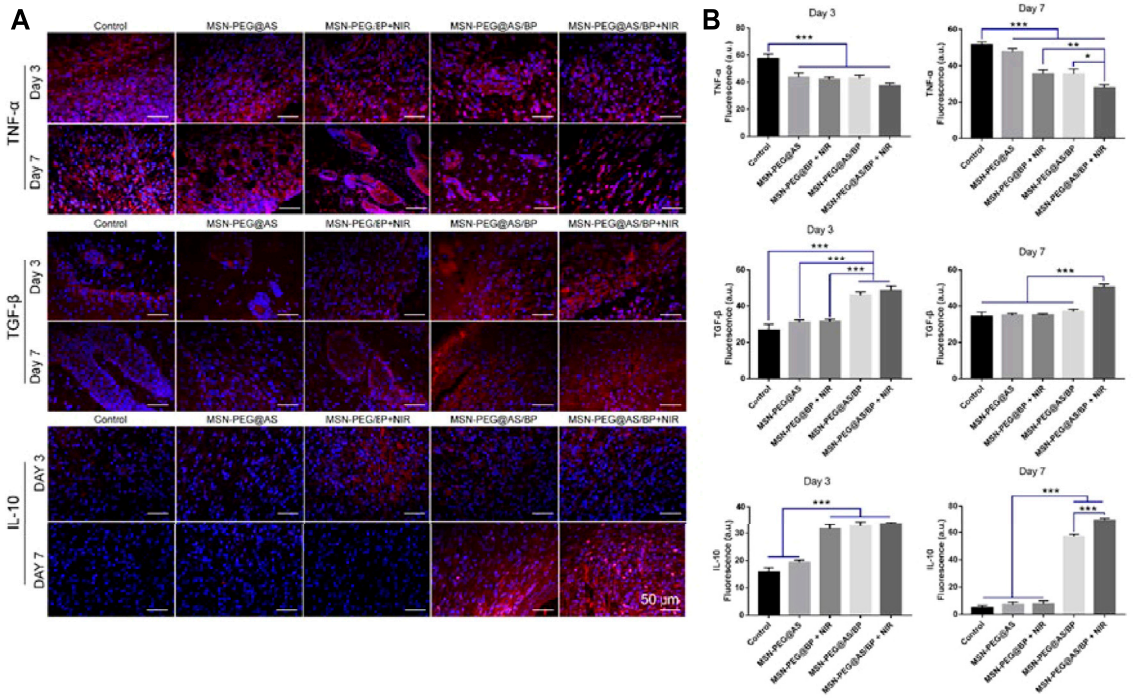

FIGURE 8 | (A) Immunofluorescence staining of TNF-α, TGF-β, and IL-10 in the wounds at Day 3 and Day 7. **(B)** Quantitative analysis of Immunofluorescence staining of TNF-α, TGF-β, and IL-10 in the wounds at Day 3 and Day 7.

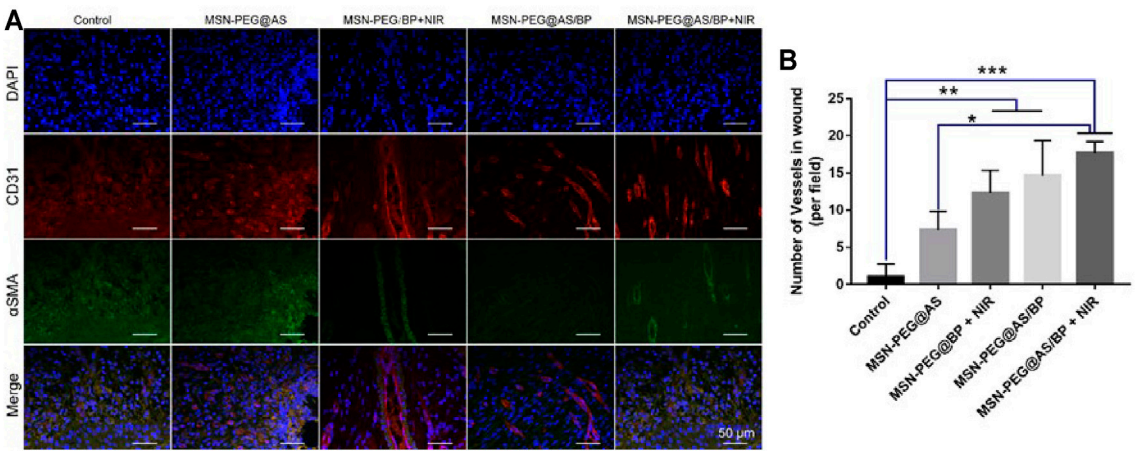

FIGURE 9 | (A) Immunofluorescence staining of DAPI, CD31, and α-SMA in the wounds at Day 7. **(B)** Quantitative analysis of number of blood vessels.

main components of the dermis, the deposition of collagen plays an important role in wound healing. The increased collagen content in the wound demonstrated a faster wound regeneration rate promoted by the MSN-PEG@AS/BP with NIR.

3.9 *In Vivo* Anti-Inflammatory and Angiogenesis

In order to further explore the changes in the wound microenvironment after treatment, we analyzed the skin samples by immunofluorescence staining. Tumor necrosis factor-alpha (TNF-α) secreted by proinflammatory macrophages has negative effects on the wound microenvironment (Ashcroft et al., 2012). **Figure 8A** shows that the positive expression of TNF-α in each group of wounds on the seventh day was lower than that on the third day. The expression of TNF-α in wounds treated with MSN-PEG@AS/BP with NIR was significantly lower than that of other groups. The low expression of TNF-α could lead to less ECM proteolysis, which is consistent with the H&E staining results mentioned above. **Figure 8B** is the fluorescence quantitative

analysis corresponding to **Figure 8A**, and the above analysis results can be observed from it more intuitively.

Moreover, we also detected the positive expression of TGF-β and IL-10 in the samples. The literature has reported that TGF-β triggers fibroblasts and myofibroblasts to produce new ECM, which plays a central role in fibrinogenesis (Schiller et al., 2004). Besides, IL-10 is an anti-inflammatory cytokine that could induce polarization of macrophages (Ferrante and Joseph Leibovich, 2012). Compared to day 3, the expression of TGF-β and IL-10 at the wound site was significantly upregulated on day 7, and the expression in the MSN-PEG@AS/BP with NIR group was the most. Briefly, MSN-PEG@AS/BP can regulate the secretion of anti-inflammatory cytokines and inhibit the expression of TNF-α to change the wound microenvironment from a pro-inflammatory into a pro-resolution state and promote matrix regeneration and vascular remodeling.

In addition, we detected the expression of CD31 and α-SMA in the samples on day 7 to assess the formation of blood vessels. Angiogenesis is essential for the healing of chronic wounds. Compared with other groups, the expression of CD31 and α-SMA was almost invisible in the wound treated by the control group and MSN-PEG@AS group (**Figure 9A**). However, the co-localizations of CD31 and α-SMA positive staining treated by the MSN-PEG@AS/BP with NIR group were significantly more than the other groups, which is consistent with the less expression of TNF-α mentioned above. A prior study reported that the reduction of TNF-α promotes the expression of α-MSA in human dermal fibroblasts (Goldberg et al., 2007). **Figure 9B** shows the statistics of blood vessel density at the corresponding wound site. The results also demonstrated that the addition of MSN-PEG@AS/BP with NIR had a noteworthy effect on promoting angiogenesis during the wound healing process.

4 CONCLUSION

In summary, we reported novel photothermal 2D nanosheets combined with AS (MSN-PEG@AS/BP) that have antibacterial properties and that promote angiogenesis to treat infected wounds. The MSN-loaded AS exhibits excellent angiogenesis and anti-inflammatory properties, which showed excellent cytocompatibility and played a powerful regulation effect for inflammatory response and enhanced the formation of blood vessels *in vivo*. In addition, the 2D nanosheet BP showed outstanding photothermal property, favorable photothermal stability, and excellent antibacterial effect with antibacterial rates of 99.58% (*E. coli*) and 99.13% (*S. aureus*). Therefore, as an antibacterial and biocompatibility nano-spray, MSN-PEG@AS/BP may be an outstanding candidate for infected wound treatment.

DATA AVAILABILITY STATEMENT

The original contributions presented in the study are included in the article/**Supplementary Material**, further inquiries can be directed to the corresponding author.

ETHICS STATEMENT

The animal study was reviewed and approved by Zhuhai Hospital of Guangdong Provincial Hospital of Chinese Medicine.

AUTHOR CONTRIBUTIONS

LL: Conceptualization, Methodology, Investigation, Data Curation, Visualization, Writing—Original Draft. WW: Methodology, Validation, Formal analysis, Visualization. WH: Data Curation. YJ: Resources, Visualization. LW: Investigation, Resources. SL: Validation; Formal analysis. AW: Visualization. XL: Writing—Review and Editing, Supervision, Project administration, Funding acquisition.

FUNDING

This study was supported by the introduction of the high-level health team project in Zhuhai.

SUPPLEMENTARY MATERIAL

The Supplementary Material for this article can be found online at: https://www.frontiersin.org/articles/10.3389/fbioe.2021.826011/full#supplementary-material

REFERENCES

Aksoy, İ., Küçükkeçeci, H., Sevgi, F., Metin, Ö., and Hatay Patir, I. (2020). Photothermal Antibacterial and Antibiofilm Activity of Black Phosphorus/Gold Nanocomposites against Pathogenic Bacteria. *ACS Appl. Mater. Inter.* 12 (24), 26822–26831. doi:10.1021/acsami.0c02524

Aquib, M., Zhang, H., Raza, F., Banerjee, P., Bavi, R., Kesse, S., et al. (2021). Delivery of Repurposed Disulfiram by Aminated Mesoporous Silica Nanoparticles for Anticancer Therapy. *J. Mol. Liquids*, 117065. doi:10.1016/j.molliq.2021.117065

Ashcroft, G. S., Jeong, M.-J., Ashworth, J. J., Hardman, M., Jin, W., Moutsopoulos, N., et al. (2012). Tumor Necrosis Factor-Alpha (TNF-α) Is a Therapeutic Target for Impaired Cutaneous Wound Healing. *Wound Repair Regen.* 20 (1), 38–49. doi:10.1111/j.1524-475x.2011.00748.x

Cavanagh, P. R., Lipsky, B. A., Bradbury, A. W., and Botek, G. (2005). Treatment for Diabetic Foot Ulcers. *The Lancet* 366 (9498), 1725–1735. doi:10.1016/s0140-6736(05)67699-4

Chen, J., Han, X., Deng, J., Zhang, J., Li, L., Ni, J., et al. (2021). An Injectable Hydrogel Based on Phenylboronic Acid Hyperbranched Macromer Encapsulating Gold Nanorods and Astragaloside IV Nanodrug for Myocardial Infarction. *Chem. Eng. J.* 413, 127423. doi:10.1016/j.cej.2020.127423

Chen, X., Peng, L.-H., Li, N., Li, Q.-M., Li, P., Fung, K.-P., et al. (2012). The Healing and Anti-scar Effects of Astragaloside IV on the Wound Repair *In Vitro* and *In Vivo*. *J. Ethnopharmacology* 139 (3), 721–727. doi:10.1016/j.jep.2011.11.035

Chen, Y., Gao, Y., Chen, Y., Liu, L., Mo, A., and Peng, Q. (2020). Nanomaterials-based Photothermal Therapy and its Potentials in Antibacterial Treatment. *J. Controlled Release* 328, 251–262. doi:10.1016/j.jconrel.2020.08.055

Clark, M., and Price, P. E. (2004). Is Wound Healing a True Science or a Clinical Art? *The Lancet* 364 (9443), 1388–1389. doi:10.1016/s0140-6736(04)17240-1

Deng, G., Tang, C., Li, F., Jiang, H., and Chen, Y. (2010). Covalent Cross-Linked Polymer Gels with Reversible Sol–Gel Transition and Self-Healing Properties. *Macromolecules* 43 (3), 1191–1194. doi:10.1021/ma9022197

Eming, S. A., Martin, P., and Tomic-Canic, M. (2014). Wound Repair and Regeneration: Mechanisms, Signaling, and Translation. *Sci. Transl Med.* 6 (265), 265sr6. doi:10.1126/scitranslmed.3009337

Ferrante, C. J., and Joseph Leibovich, S. (2012). Regulation of Macrophage Polarization and Wound Healing. *Adv. Wound Care* 1 (1), 10–16. doi:10.1089/wound.2011.0307

Goldberg, M. T., Han, Y.-P., Yan, C., Shaw, M. C., and Garner, W. L. (2007). TNF-α Suppresses α-Smooth Muscle Actin Expression in Human Dermal Fibroblasts: An Implication for Abnormal Wound Healing. *J. Invest. Dermatol.* 127 (11), 2645–2655. doi:10.1038/sj.jid.5700890

Huang, X.-W., Wei, J.-J., Zhang, M.-Y., Zhang, X.-L., Yin, X.-F., Lu, C.-H., et al. (2018). Water-Based Black Phosphorus Hybrid Nanosheets as a Moldable Platform for Wound Healing Applications. *ACS Appl. Mater. Inter.* 10 (41), 35495–35502. doi:10.1021/acsami.8b12523

Kong, N., Ji, X., Wang, J., Sun, X., Chen, G., Fan, T., et al. (2020). ROS-mediated Selective Killing Effect of Black Phosphorus: Mechanistic Understanding and its Guidance for Safe Biomedical Applications. *Nano Lett.* 20 (5), 3943–3955. doi:10.1021/acs.nanolett.0c01098

Larouche, J., Sheoran, S., Maruyama, K., and Martino, M. M. (2018). Immune Regulation of Skin Wound Healing: Mechanisms and Novel Therapeutic Targets. *Adv. Wound Care* 7 (7), 209–231. doi:10.1089/wound.2017.0761

Lee, S.-Y., Chang, W.-L., Li, Z.-X., Kirkby, N. S., Tsai, W.-C., Huang, S.-F., et al. (2018). Astragaloside VI and Cycloastragenol-6- O -Beta-D-Glucoside Promote Wound Healing *In Vitro* and *In Vivo*. *Phytomedicine* 38, 183–191. doi:10.1016/j.phymed.2017.12.003

Liu, H., Zhu, X., Guo, H., Huang, H., Huang, S., Huang, S., et al. (2020). Nitric Oxide Released Injectable Hydrogel Combined with Synergistic Photothermal Therapy for Antibacterial and Accelerated Wound Healing. *Appl. Mater. Today* 20, 100781. doi:10.1016/j.apmt.2020.100781

Metcalf, D. G., and Bowler, P. G. (2013). Biofilm Delays Wound Healing: A Review of the Evidence. *Burns Trauma* 1 (1), 5–12. doi:10.4103/2321-3868.113329

Miao, Y., Shi, X., Li, Q., Hao, L., Liu, L., Liu, X., et al. (2019). Engineering Natural Matrices with Black Phosphorus Nanosheets to Generate Multi-Functional Therapeutic Nanocomposite Hydrogels. *Biomater. Sci.* 7 (10), 4046–4059. doi:10.1039/c9bm01072f

Moreira, H. R., and Marques, A. P. (2022). Vascularization in Skin Wound Healing: where Do We Stand and where Do We Go? *Curr. Opin. Biotechnol.* 73, 253–262. doi:10.1016/j.copbio.2021.08.019

Nguyen, T. L., Cha, B. G., Choi, Y., Im, J., and Kim, J. (2020). Injectable Dual-Scale Mesoporous Silica Cancer Vaccine Enabling Efficient Delivery of Antigen/adjuvant-Loaded Nanoparticles to Dendritic Cells Recruited in Local Macroporous Scaffold. *Biomaterials* 239, 119859. doi:10.1016/j.biomaterials.2020.119859

Ouyang, J., Liu, R.-Y., Chen, W., Liu, Z., Xu, Q., Zeng, K., et al. (2018). A Black Phosphorus Based Synergistic Antibacterial Platform against Drug Resistant Bacteria. *J. Mater. Chem. B* 6 (39), 6302–6310. doi:10.1039/c8tb01669k

Pham, L. M., Kim, E.-C., Ou, W., Phung, C. D., Nguyen, T. T., Pham, T. T., et al. (2021). Targeting and Clearance of Senescent Foamy Macrophages and Senescent Endothelial Cells by Antibody-Functionalized Mesoporous Silica Nanoparticles for Alleviating Aorta Atherosclerosis. *Biomaterials* 269, 120677. doi:10.1016/j.biomaterials.2021.120677

Qian, Y., Yuan, W.-E., Cheng, Y., Yang, Y., Qu, X., and Fan, C. (2019). Concentrically Integrative Bioassembly of a Three-Dimensional Black Phosphorus Nanoscaffold for Restoring Neurogenesis, Angiogenesis, and Immune Homeostasis. *Nano Lett.* 19 (12), 8990–9001. doi:10.1021/acs.nanolett.9b03980

Saint-Cricq, P., Deshayes, S., Zink, J. I., and Kasko, A. M. (2015). Magnetic Field Activated Drug Delivery Using Thermodegradable Azo-Functionalised PEG-Coated Core-Shell Mesoporous Silica Nanoparticles. *Nanoscale* 7 (31), 13168–13172. doi:10.1039/c5nr03777h

Schiller, M., Javelaud, D., and Mauviel, A. (2004). TGF-β-induced SMAD Signaling and Gene Regulation: Consequences for Extracellular Matrix Remodeling and Wound Healing. *J. Dermatol. Sci.* 35 (2), 83–92. doi:10.1016/j.jdermsci.2003.12.006

Sen, C. K., Gordillo, G. M., Roy, S., Kirsner, R., Lambert, L., Hunt, T. K., et al. (2009). Human Skin Wounds: A Major and Snowballing Threat to Public Health and the Economy. *Wound Repair Regen.* 17 (6), 763–771. doi:10.1111/j.1524-475x.2009.00543.x

Shao, J., Xie, H., Huang, H., Li, Z., Sun, Z., Xu, Y., et al. (2016). Biodegradable Black Phosphorus-Based Nanospheres for *In Vivo* Photothermal Cancer Therapy. *Nat. Commun.* 7, 12967. doi:10.1038/ncomms12967

Szabo, G. K., Browne, H. K., Ajami, A., and Josephs, E. G. (1994). Alternatives to Least Squares Linear Regression Analysis for Computation of Standard Curves for Quantitation by High Performance Liquid Chromatography: Applications to Clinical Pharmacology. *J. Clin. Pharmacol.* 34 (3), 242–249. doi:10.1002/j.1552-4604.1994.tb03993.x

von Baeckmann, C., Kählig, H., Lindén, M., and Kleitz, F. (2021). On the Importance of the Linking Chemistry for the PEGylation of Mesoporous Silica Nanoparticles. *J. Colloid Interf. Sci.* 589, 453–461. doi:10.1016/j.jcis.2020.12.004

Wang, S.-G., Xu, Y., Chen, J.-D., Yang, C.-H., and Chen, X.-H. (2013). Astragaloside IV Stimulates Angiogenesis and Increases Nitric Oxide Accumulation via JAK2/STAT3 and ERK1/2 Pathway. *Molecules* 18 (10), 12809–12819. doi:10.3390/molecules181012809

Wang, X., Jones, A. M., Seyler, K. L., Tran, V., Jia, Y., Zhao, H., et al. (2015). Highly Anisotropic and Robust Excitons in Monolayer Black Phosphorus. *Nat. Nanotech* 10 (6), 517–521. doi:10.1038/nnano.2015.71

Wu, H., Li, F., Wang, S., Lu, J., Li, J., Du, Y., et al. (2018). Ceria Nanocrystals Decorated Mesoporous Silica Nanoparticle Based ROS-Scavenging Tissue Adhesive for Highly Efficient Regenerative Wound Healing. *Biomaterials* 151, 66–77. doi:10.1016/j.biomaterials.2017.10.018

Xiong, Z., Zhang, X., Zhang, S., Lei, L., Ma, W., Li, D., et al. (2018). Bacterial Toxicity of Exfoliated Black Phosphorus Nanosheets. *Ecotoxicology Environ. Saf.* 161, 507–514. doi:10.1016/j.ecoenv.2018.06.008

Xue, J. M., and Shi, M. (2004). PLGA/mesoporous Silica Hybrid Structure for Controlled Drug Release. *J. Controlled Release* 98 (2), 209–217. doi:10.1016/j.jconrel.2004.04.023

Yang, X., Liu, G., Peng, L., Guo, J., Tao, L., Yuan, J., et al. (2017). Highly Efficient Self-Healable and Dual Responsive Cellulose-Based Hydrogels for Controlled Release and 3D Cell Culture. *Adv. Funct. Mater.* 27 (40), 1703174. doi:10.1002/adfm.201703174

Zhang, Q., Shen, C., Zhao, N., and Xu, F.-J. (2017). Redox-Responsive and Drug-Embedded Silica Nanoparticles with Unique Self-Destruction Features for Efficient Gene/Drug Codelivery. *Adv. Funct. Mater.* 27 (10), 1606229. doi:10.1002/adfm.201606229

Zhang, Y., Jiang, Q., Lang, P., Yuan, N., and Tang, J. (2021). Fabrication and Applications of 2D Black Phosphorus in Catalyst, Sensing and Electrochemical Energy Storage. *J. Alloys Compounds* 850, 156580. doi:10.1016/j.jallcom.2020.156580

Zhu, Y., Ma, Z., Kong, L., He, Y., Chan, H. F., and Li, H. (2020). Modulation of Macrophages by Bioactive Glass/sodium Alginate Hydrogel Is Crucial in Skin Regeneration Enhancement. *Biomaterials* 256, 120216. doi:10.1016/j.biomaterials.2020.120216

Conflict of Interest: The authors declare that the research was conducted in the absence of any commercial or financial relationships that could be construed as a potential conflict of interest.

Publisher's Note: All claims expressed in this article are solely those of the authors and do not necessarily represent those of their affiliated organizations, or those of the publisher, the editors and the reviewers. Any product that may be evaluated in this article, or claim that may be made by its manufacturer, is not guaranteed or endorsed by the publisher.

Copyright © 2022 Liu, Wang, Hong, Jin, Wang, Liu, Wang and Liu. This is an open-access article distributed under the terms of the Creative Commons Attribution License (CC BY). The use, distribution or reproduction in other forums is permitted, provided the original author(s) and the copyright owner(s) are credited and that the original publication in this journal is cited, in accordance with accepted academic practice. No use, distribution or reproduction is permitted which does not comply with these terms.

frontiers in Bioengineering and Biotechnology

REVIEW
published: 18 February 2022
doi: 10.3389/fbioe.2022.851561

Traditional Chinese Medicine Compound-Loaded Materials in Bone Regeneration

Guiwen Shi[1†], *Chaohua Yang*[1,2†], *Qing Wang*[1]*, *Song Wang*[1], *Gaoju Wang*[1], *Rongguang Ao*[3]* *and Dejian Li*[3]*

[1]Department of Orthopaedics, Affiliated Hospital of Southwest Medical University, Luzhou, China, [2]Department of Orthopaedics, The First Affiliated Hospital of Chongqing Medical University, Chongqing, China, [3]Department of Orthopaedics, Shanghai Pudong Hospital, Fudan University Pudong Medical Center, Shanghai, China

Bone is a dynamic organ that has the ability to repair minor injuries via regeneration. However, large bone defects with limited regeneration are debilitating conditions in patients and cause a substantial clinical burden. Bone tissue engineering (BTE) is an alternative method that mainly involves three factors: scaffolds, biologically active factors, and cells with osteogenic potential. However, active factors such as bone morphogenetic protein-2 (BMP-2) are costly and show an unstable release. Previous studies have shown that compounds of traditional Chinese medicines (TCMs) can effectively promote regeneration of bone defects when administered locally and systemically. However, due to the low bioavailability of these compounds, many recent studies have combined TCM compounds with materials to enhance drug bioavailability and bone regeneration. Hence, the article comprehensively reviewed the local application of TCM compounds to the materials in the bone regeneration *in vitro* and *in vivo*. The compounds included icariin, naringin, quercetin, curcumin, berberine, resveratrol, ginsenosides, and salvianolic acids. These findings will contribute to the potential use of TCM compound-loaded materials in BTE.

Keywords: traditional Chinese medicine, osteogenesis, bone defect, bone regeneration, bone tissue engineering, drug delivery

OPEN ACCESS

Edited by:
Kaili Lin,
Shanghai Jiao Tong University, China

Reviewed by:
Xiaojun Zhou,
Donghua University, China
Changchun Zhou,
Sichuan University, China

***Correspondence:**
Qing Wang
wqspine2004@163.com
Rongguang Ao
yst-2008@126.com
Dejian Li
ldj880820@163.com

[†]*These authors have contributed equally to this work and share first authorship*

Specialty section:
This article was submitted to Biomaterials, a section of the journal Frontiers in Bioengineering and Biotechnology

Received: *10 January 2022*
Accepted: *26 January 2022*
Published: *18 February 2022*

Citation:
Shi G, Yang C, Wang Q, Wang S, Wang G, Ao R and Li D (2022) Traditional Chinese Medicine Compound-Loaded Materials in Bone Regeneration. Front. Bioeng. Biotechnol. 10:851561. doi: 10.3389/fbioe.2022.851561

INTRODUCTION

Critical-sized bone defects caused by severe trauma, infections, tumors, and genetic disorders that cannot be spontaneously repaired within a patient's lifetime are a major clinical challenge and require external intervention to guide and accelerate the healing process (Roddy et al., 2018). Furthermore, bone regeneration can be impacted by the absence of osteoblasts or poor microvessel formation at the site of bone defects due to various comorbidities, such as diabetes, genetic factors, smoking and alcohol abuse, and inappropriate treatment (Tang et al., 2016; Holmes, 2017). For the regeneration of bone defects in clinical practice, even though bone transplantation, such as autograft and allograft, is the most commonly used and effective method, it is limited by the insufficient supply of tissue in the donor site, and patients must undergo additional surgery with increasing the risk of infection and hematoma and the cost of the procedure, and increases the risk of immune responses and rejection (Keating et al., 2005; Cancedda et al., 2007; Delloye et al., 2007).

To overcome the issues with bone transplantation and provide a new method for the regeneration of bone defects, researchers have developed bioactive bone-substitute materials

TABLE 1 | Overview of representative studies providing release profiles kinetics obtained from the use of TCM compound delivery systems.

Compound	Carrier	Drug content	Initial burst release (time)	Total accumulative release (time)	Reference
Icariin	CPC tablet	1 mg	2% (1 day)	6% (15 days)	Zhao et al. (2010)
	injectable CPC	2 mg	35% (7 days)	85% (30 days)	Huang et al., (2013)
	PLGA/TCP scaffold	0.16, 0.32, and 0.64%	N	90% (14 weeks)	Lai et al. (2018b)
	SF/PLCL nanofbrous membrane	10^{-5} mol/L	47.54 ± 0.06% (5 days)	82.09 ± 1.86% (30 days)	Yin et al. (2017)
	HA/alginate scaffold	10^{-5} mol/L	N	69.07 ± 8.16% (40 days)	Xie et al. (2019)
	PLGA microspheres	4×10^{-3} M	N	57.5 ± 5.0 μg/ml (28 days)	Yuan et al. (2020)
	HA/CS coated Ti	1.5×10^{-5} mol/L, 3×10^{-5} mol/L, 6×10^{-5} mol/L	N	100% (14 days)	Song et al. (2018b)
Naringin	PCL/PEG-b-PCL nanoscaffold	3.33 mg/ml	20% (1 day)	93% (90 days)	Ji et al. (2014)
	CS microspheres/PLLA scaffold	59.39 ± 3.43%	N	90% (30 days)	Guo et al. (2017)
	PLGA/PLLA/PDLLA blend fibers	0.7wt%	Y	82% (21 days)	Guo et al. (2018)
		7.0wt%	Y	11% (21 days)	
	SF/HA scaffold	0.1%	70% (20 h)	90% (80 days)	Zhao et al. (2021)
Quercetin	CDHA scaffold	200 μM	N	50% (60 days)	Tripathi et al. (2015)
	PD-PLLA scaffold	8.33 μg	3 μg, 12 h	6.26 μg (24 days)	Chen et al. (2019)
		10.84 μg	3 μg, 12 h	9.03 μg (24 days)	
		13.07 μg	3 μg, 12 h	11.15 μg (24 days)	
	PLGA microspheres	7.67 ± 0.10%	N	50% (30 days)	Lee et al. (2018)
	nHA microspheres	200 μM	6.39 ± 0.20% (1 h)	74.68 ± 1.33% (28 days)	Zhou et al. (2017)
Curcumin	PCL nanofibers	1wt%	N	70% (12 days)	Jain et al. (2016)
	Liposomes/TCP scaffold	68%	N	17% (60 days)	Sarkar and Bose, (2019)
	CS nanoparticles-SF/HAMA hydrogel	10%	N	77.1% (32 days)	Yu et al. (2021a)
	HA coated Ti6Al4V	25 μg	17% (24 h)	93% (22 days)	Sarkar and Bose, (2020)
Berberine	PCL/COL scafolds	50 μg/ml	8.63 ± 0.50% (1 day)	61.4% (27 days)	Ma et al. (2021b)
	PCL/PVP-MC/CS Bilayer Membrane	10 μM	30% (1 day)	65% (28 days)	Zhang et al. (2021b)
Resveratrol	PCL nanofibers	0.1:9.9 (w/w)	Y	28.6 ± 1.4 μM (35 days)	Riccitiello et al. (2017)
	PLA nanofibers	0.1:9.9 (w/w)	Y	12.3 ± 1.8 μM (35 days)	Riccitiello et al. (2017)
	PCL scaffold	5.5% (w/w)	N	64% (12 days)	Kamath et al. (2014)
	PEGDA/TCS Hydrogel	1,066 μM/g	N	71.5% (32 days)	Fan et al. (2021)
	SLNs/GelMA scaffold	0.08 wt%	14% (12 h)	75% (28 days)	Wei et al. (2021)
Salvianolic acids	CS/HA scaffold	10^{-7} mol	N	35% (56 days)	Ji et al. (2019)
Ginsenosides	Gelatin microspheres/Sr-α-CaS Scaffold	2.51%	N	85% (120 h)	Luo et al. (2020)

CPC, calcium phosphate cement; PLGA, poly (lactic-coglycolic acid); TCP, b-calcium phosphate; SF, Silk fbroin; HA, hydroxyapatite; PCL, poly (ε-caprolactone); PEG, poly (ethylene glycol); CS, Chitosan; PLLA, Poly (l-lactic acid); PDLLA, poly (D, L-lactic acid); CDHA, calcium-deficient hydroxyapatite; PD, polydopamine; HAMA, hyaluronic acid esterified by methacrylate; COL, collagen; PVP, polyvinylpyrrolidone; MC, mineralized collagen; TCS, Thiolated chitosan; SLN, solid lipid nanoparticles; GelMA, Gelatin methacrylate; Sr-α-CaS, strontium-calcium sulfate hemihydrate.

with integration of scaffolds, biologically active molecules, stem cells, or demineralized bone matrix in bone tissue engineering (BTE) in recent years (Agarwal and García, 2015). To further increase the ability of bone regeneration, researchers have added different cell types, drugs, and active agents to the scaffold for osteointegration, osteoinduction, and osteoconduction of the bone grafts, and these factors are delivered to the bone defect sites together (Martin and Bettencourt, 2018). Osteoinductive molecules, including growth factors such as bone morphogenetic protein-2 (BMP-2), still have issues including the method of combining with scaffolds, a short half-life, an unstable release, a high cost, and rapid degradation, which are major shortcomings and limit the clinical use of these molecules (James et al., 2016). Therefore, development of cost-effective alternative molecules with good safety and higher efficacies than growth factors is urgently needed.

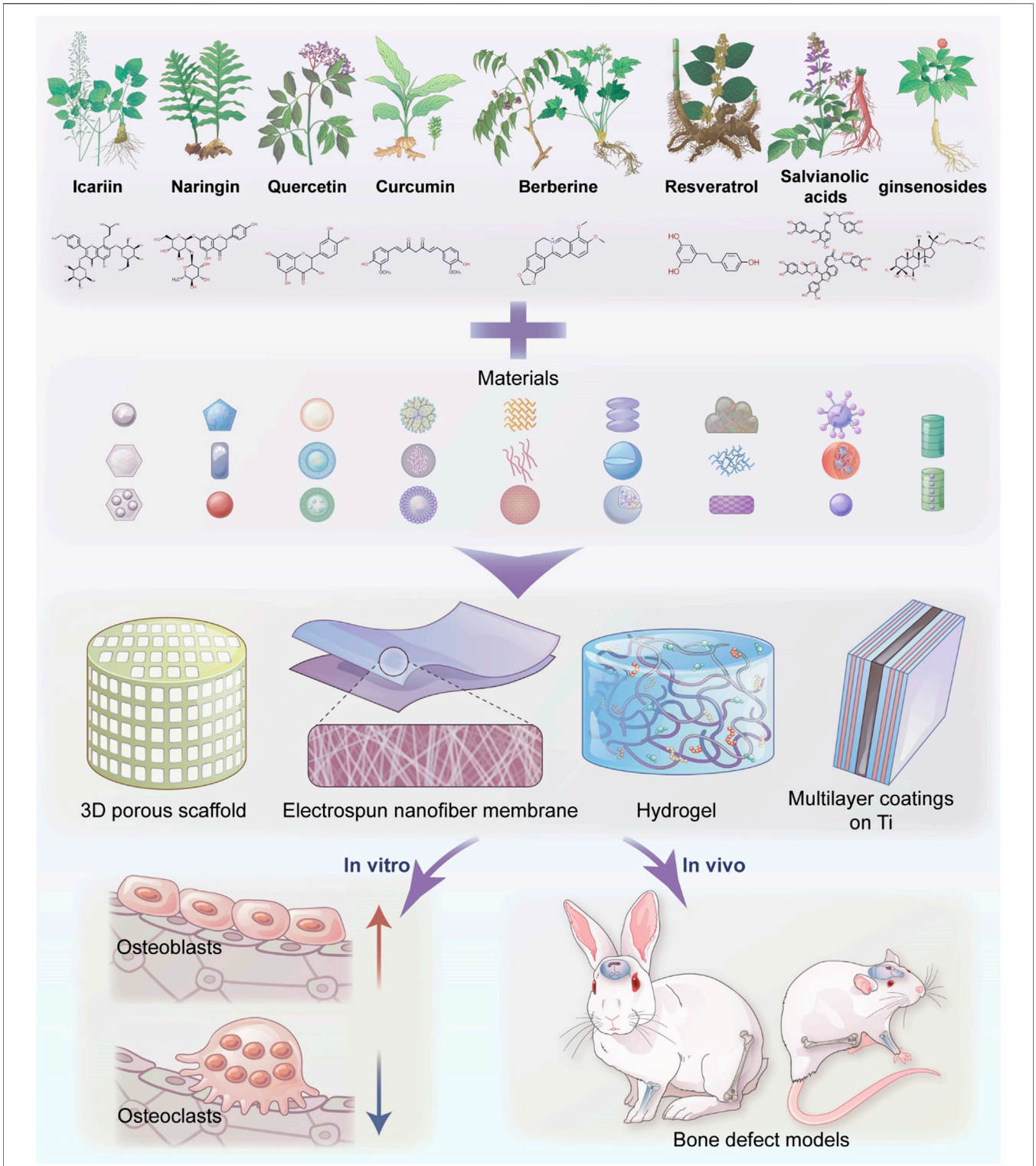

FIGURE 1 | Schematic presentation of the application of traditional Chinese medicine-loaded materials in BTE.

Traditional Chinese medicines (TCMs) with different pharmacological activities have been used for centuries among the Chinese population as safe, economic, and effective drugs (Zeng and Gu, 2021). TCMs are often used in combination to form a formula, and have shown therapeutic effects on bone regeneration in clinical and animal studies (Che et al., 2016).

Recent studies also have pointed out that the application of combination TCM prescriptions to bone substitutes has achieved satisfactory results in bone tissue regeneration (Yao et al., 2006; Wang et al., 2015b). Compounds isolated from TCMs play an increasingly important role in existing drugs with the development of modern separation techniques and have been reported to enhance bone formation and inhibit bone resorption through their effects on cell signaling pathways, influencing osteoblast and osteoclast differentiation (Zhong et al., 2019; Zhang et al., 2020). TCM compounds represent naturally abundant, cost-efficient agents with potential uses in bone regeneration. However, in the conventional systemic route, drug delivery occurs via the circulatory system, which may result in many disadvantages, such as systemic toxicity, side effects, renal and liver complications, drug interactions, poor distribution to the targeted tissue, and decreased patient compliance (Soundarya et al., 2017). Local drug delivery systems of biomaterials overcome these restrictions with limited side effects, high concentrations in the targeted tissue, and little systemic uptake (Li et al., 2017a). Additionally, a sustained and controlled local release system improves the drug release profiles by releasing the desired amount of drug at a controlled rate and time with protection from surrounding factors, such as protection from degradation, and increased drug safety and efficacy (Tang et al., 2021).

Therefore, this article reviewed the various strategies of loading materials with compounds of TCMs that achieve drug delivery and have positive effects on bone regeneration *in vitro* and *in vivo* locally (summarized in **Table 1** and **Figure 1**). The purpose is to summarize the latest research progress of relevant studies and to emphasize that applying TCM compounds to materials can optimize drug delivery and release and improve the ability of materials in BTE.

FLAVONOIDS

Icariin

Icariin is a flavonoid constituent isolated from the traditional Chinese herb *Epimedium pubescens* as its main active compound. Icariin has been proven to not only enhance osteoblast proliferation, differentiation, and mineralization and the expression of bone-related genes and proteins but also inhibit the transformation of osteoblasts into adipocytes and the formation and differentiation of osteoclasts, thereby promoting bone formation and inhibiting bone resorption (Hsieh et al., 2011; Zhang et al., 2012; Song et al., 2013a; Wei et al., 2016; Xue et al., 2016; Zhang et al., 2016; Ye et al., 2017; Wang F. et al., 2020). In addition, icariin could combine with estrogen receptors and affect bone regeneration via estrogen receptor pathways due to the similarity of its structure to that of estrogen and could increase angiogenesis by stimulating endothelial cell migration, proliferation, and tubulogenesis (Chung et al., 2008; Nian et al., 2009; Song et al., 2013b). Locally administered icariin to the fracture was shown to accelerate bone healing by reducing oxidative stress (Gürbüz et al., 2019). However, icariin has a low bioavailability and a short half-life (1–2 h); complete exposure of icariin molecules to fluid environments *in vivo* led to a substantial loss of bioactivity, and the molecules were easily eliminated from the body (Yang W. et al., 2012). Osseointegration requires a long period of time (3–6 months), and thus, long-term and stable drug release to the surrounding tissue is needed for local administration of icariin with appropriate carriers.

Icariin combined with calcium phosphate-based bioactive materials has been shown to contribute to bone formation *in vitro* and *in vivo* with minimal changes in the surface microstructure, bioactivity and biocompatibility, and sustained drug release. Icariin-loaded calcium phosphate cement (CPC) significantly promoted new bone and blood vessel formation when implanted in the mouse calvarial defect model compared with CPC at 4 and 6 weeks (Zhao et al., 2010). The 2000 μM icariin-loaded CPC also enhanced osteogenesis and angiogenesis of ovariectomized (OVX) rats with calvarial defects, as shown by fluorochrome-labeling histomorphometric analysis, van Gieson's picro fuchsin, and Microfil perfusion analysis at 8 weeks (Wu et al., 2017). Porous β-TCP disks were soaked in icariin solution and shown to promote proliferation and osteoblastic differentiation of rat Ros17/28 cells and induce new bone formation after back intramuscular implantation in rats for 3 months, whereas no obvious osteogenic evidence was detected in the control group (Zhang et al., 2011). In addition, *Staphylococcus* aureus-contaminated radius defects were completely repaired with the significantly improved formation of lamellar bone and recanalization of the marrow cavity at 12 weeks when icariin and vancomycin were introduced to CPC (Huang et al., 2013). However, the degradation of CPC was very low *in vivo*, and the osteoinduction of CPC was limited.

Icariin delivery porous PHBV scaffolds could strongly enhance the proliferation of human osteoblast-like MG-63 cells (2.3-fold) and preosteoblast MC3T3-E1 cells (1.7-fold) compared with that of cell culture plates and promote the cell proliferation of MG-63 cells by stimulating the transcription of key BMP genes and extracellular matrix (ECM) genes and inhibiting the transcription of TGF-β1 and Col-I, as shown by RT-PCR assays (Xia et al., 2013). Small intestinal submucosa (SIS) can be produced as multiple layers to provide local, slow release of icariin for more than 30 days. The icariin-loaded SIS affected osteoblast differentiation of MC3T3-E1 cells by upregulating the expression of osteogenic differentiation markers (Alp, Bsp, and Ocn) and resulted in a higher new bone formation ratio in mouse calvarial defect models than the raw SIS scaffolds at 4 and 8 weeks (Li M. et al., 2017). A study demonstrated that icariin significantly improved the healing capacity of 45S5 Bioglass seeded with ASCs. The icariin-doped 45S5 Bioglass seeded with ASCs significantly induced new bone formation as well as neovascularization in the rat calvarial bone defect model with complete repair and complete degradation of the scaffold at 12 weeks, as shown by micro-CT imaging and histological and immunohistological staining (Jing et al., 2018). When icariin was used in combination with gelatin/bioactive glass (45S5 composition)-based scaffolds, the crosslinked gelatin network was shown to be a suitable candidate for sustained release, and loading with icariin enhanced the formation of hydroxyapatite (HA) in all

samples after immersion in simulated body fluid (SBF) for 14 days, as characterized by Fourier-transform infrared spectroscopy (FTIR) and scanning electron microscopy (SEM) (Reiter et al., 2019). Icariin was also successfully incorporated into the nanofibrous membrane by electrospinning and contributed to the attachment, proliferation, and osteogenic differentiation of MC3T3-E1 cells or rat BMMSCs (Yin et al., 2017; Gong et al., 2018). The icariin-incorporated SF/PLCL nanofibrous membrane can realize the controlled and sustained release of drugs and resulted in faster and more effective osteogenesis in calvarial defects of rats at 4, 8, and 12 weeks, as shown by quantitative analysis of μ-CT images and histological analysis (Gong et al., 2018).

Icariin was absorbed by hydroxyapatite (HA) and encapsulated by chitosan (CS) by freeze–drying technology, the icariin release kinetics were governed by the degradation of the CS and HA components and icariin release lasted for more than 90 days. The icariin-loaded CS/HA scaffold not only resulted in higher adhesion and proliferation of hBMSCs and mouse BMSCs with higher expression of ALP activity and mineralized nodules than either the blank control or CS/HA scaffold but also had osteoinductive functions at an early stage according to X-ray results, indicating better bone repair abilities with a high BMD and complete degradation of the scaffolds in a rabbit radius defect model at 12 weeks, as shown by histological observations (Wu et al., 2009; Fan et al., 2012). Alginate scaffolds with HA exhibited a sustained release of icariin for longer than 40 days *in vitro* and enhanced stimulatory effects on the relative expression levels of osteogenic and Wnt signaling pathway genes of rabbit BMSCs, as shown by RT-PCR and Western blotting. Icariin-loaded HAA was shown to repair critical-sized radius defects in rabbits through the mediation of the coupling processes of osteogenic induction and the inhibition of osteoclast activity with better radiographic Lane-Sandhu scoring and histological scoring compared with those of the HAA, icariin, and control groups at 4 and 12 weeks (Xie et al., 2019). For long-term efficacy in promoting osteogenesis, icariin was incorporated into the PLGA/β-TCP scaffold by low-temperature 3D printing technology, and release from the scaffold could last at least 14 weeks because it was encapsulated in PLGA to protect the contents from the sensitive environment *in vitro* and enzymatic degradation *in vivo*. Analysis of the bioactive composite scaffold revealed that icariin could facilitate MC3T3-E1 cell ingrowth into the scaffold and regulate osteoblastic differentiation with increased mRNA expression levels of OC and BSP by quantitative real-time PCR. In addition, when the icariin-loaded PLGA/β-TCP scaffold was implanted into the bone tunnel of the distal femora of SAON rabbits, increased temporal new bone and fast MAR within the bone defect region were identified at 8 weeks, and the newly formed bone replaced the degraded scaffold and possessed a higher mechanical strength than that in the PLGA/β-TCP group (Lai Y. et al., 2018).

To decrease the release rate of icariin and overcome the frequently observed burst release problem, researchers used icariin-loaded CS/nHA microspheres, which exhibit sustained release behavior that can be ascribed not only to electrostatic interactions between reactive negative hydroxyl (-OH) groups of icariin and positive amine groups (-NH2) of CS but also to the homogeneous dispersion of HA nanoparticles inside the CS organic matrix. The composite microspheres provided a suitable microenvironment for osteoblast attachment and proliferation, as shown by inverted fluorescence microscopy, MTT assays, cytotoxicity assays, Hoechst 33,258 staining, and PI fluorescence staining (Chen J. et al., 2015). Icariin was preloaded onto $MgO/MgCO_3$ particles and then encapsulated into PLGA microspheres to improve the hydrophobicity and achieve sustained release over a prolonged period. A moderate dose of icariin-loaded microspheres strongly increased the proliferation and differentiation of rat BMSCs and increased the BV/TV (41.3 ± 4.7%) and BMD (488.7 ± 55.8 mg/cm^3) values with high expression of OCN based on micro-CT images and immunohistochemical staining at 16 weeks after implantation into rat calvarial defects (Yuan et al., 2020). An icariin-loaded core-shell (COL/CS microspheres-COL/PCL/HA) scaffold with sustained release of icariin was shown to have excellent osteoinductivity and osteoconductivity and promoted new bone formation with increased BMD, Conn.Dn, and expression of ALP, COL1, OPN, and OC according to micro-CT, histological, and histochemical assessments of *in vivo* tibial bone defects in rabbit models at 12 weeks (Zhao et al., 2020).

Icariin was loaded onto TiO2 nanotubes and then sealed with chitosan/gelatin multilayer coatings by the LbL self-assembly technique, and the composite structure improved osseointegration by promoting osteoblastic proliferation of rat osteoblasts by upregulating the expression of bone-related genes and proteins while downregulating RANKL mRNA expression compared with those of the pure Ti, NT, NT/LbL, and NT/icariin groups after *in vitro* culture for 7 days (Feng et al., 2016). A study noted that PLGA coating by the overlay method and the mixing method could enhance the loading and sustained release properties of the icariin/TiO_2 nanotube composite coating and promote the long-term stable release of the drug in 10–12 days to the surrounding tissue (Wang et al., 2019). The icariin-immobilized HA/CS multilayer on the PTL-primed Ti rods via the LbL system displayed a sustained and controlled release profile that lasted more than 14 days and promoted the adhesion, proliferation, and differentiation of mouse preosteoblastic cells in the early stage. The icariin load increased osteogenesis of rat femoral defects with elevated new bone formation and accelerated the speed of local bone mineralization around the implant locally according to histological assessments at 2 weeks postimplantation (Song Y. et al., 2018).

Naringin

Naringin, a flavanone glycoside, is considered the main effective component in the epiphytic fern *Drynaria fortunei* and is also commonly found in tomatoes, grapefruits, and other members of the *Citrus genus*. Administration of naringin increased the *in vitro* expression of BMP and the activation of the Wnt/β-catenin and extracellular signal-related kinase (Erk) pathways, thereby promoting osteoblastic proliferation and differentiation from stem cell precursors for bone formation (Wu et al., 2008; Wang D. et al., 2015; Lin et al., 2016; Liu et al., 2017; Wang

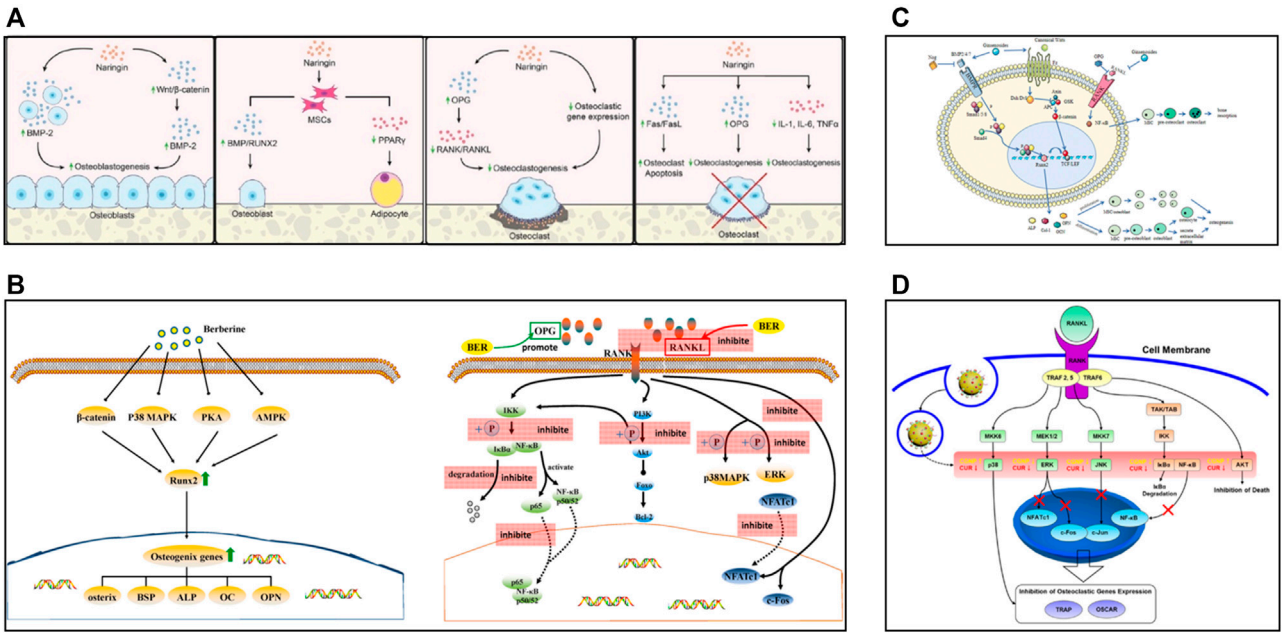

FIGURE 2 | (A) *In vitro* effects of naringin, reproduced with permission (Yu et al., 2020). **(B)** Schematic diagram of some osteogenic pathways and genes influenced by berberine, and schematic diagram of berberine inhibiting osteoclasts by affecting the binding of RANK and RANKL, reproduced with permission (Zhang et al., 2021a). **(C)** Schematic diagram of the bone remodeling mechanism and the role of ginsenosides, reproduced with permission (Yang N. et al., 2020). **(D)** Biological mechanism leading to inhibition of osteoclast differentiation of BMMs by CURCGNPs through RANKL-induced signaling pathways, reproduced with permission (Heo et al., 2014).

et al., 2017; Yu et al., 2020) (**Figure 2**). Naringin also inhibited osteoclastogenesis by both modifying RANK/RANKL interactions and inducing apoptosis in osteoclasts *in vitro* (Ang et al., 2011; Yu et al., 2013; Li F. et al., 2014; Yu et al., 2020) (**Figure 2**). In addition, naringin has estrogen-like effects and is known to bind to the estrogen receptor (Pang et al., 2010; Wong et al., 2013). Although naringin has the potential to accelerate bone regeneration, its biological activities are dose-dependent. Naringin is relatively nontoxic in the range of 1–200 μg/ml in various cell lines but is cytotoxic at high concentrations, as revealed by an increase in apoptosis (Tsui et al., 2008). Moreover, naringin exhibits low bioavailability following oral administration owing to its poor water solubility and dissolution rates. Naringin has low bioavailability and undergoes extensive metabolism *in vivo*. Therefore, it is necessary to explore biomaterial-based platforms for immobilizing or protecting naringin from degradation and for achieving sustained spatiotemporally controlled release to optimize its function.

Naringin with a collagen matrix carrier exhibited better early bone remodeling and bone formation after grafting into full-thickness parietal bone defects of rabbits than that of autogenous endochondral bone graft alone and that of collagen matrix alone, as shown by histological analysis at 2 weeks (Wong and Rabie, 2006). Naringin was immobilized on ozonated CS with a reduced initial burst release and slow and sustained release in 2 weeks because of stronger intermolecular forces between naringin and chitosan. Immobilized naringin could enhance the osteoconductivity of CS with high expression of osteogenic proteins, activation of receptor Smad1, and suppression of inhibitory Smad6 (Li C. H. et al., 2014). Naringin was incorporated in the PCL/PEG-b-PCL nanofibers by the electrospinning technique, resulting in a low concentration release, a slow-release effect prolonged to 90 days, and a total release of more than 93%. Naringin-loaded PCL/PEG-b-PCL nanoscaffolds were superior in supporting MC3T3-E1 preosteoblastic cell line attachment, proliferation, differentiation, and mineralization. Moreover, naringin-loaded PCL/PEG-b-PCL nanoscaffolds could effectively suppress osteoclasts, as shown by TRAP staining in a critical-size defect model of mouse calvarial bone after 14 days of implantation (Ji et al., 2014). In addition, naringin-loaded mPEG-MS-PLA micelles with high drug encapsulation efficiency (87.8 ± 4%) achieved sustained drug release under both physiological and endolysosomal conditions. The naringin-loaded nanocarriers were readily internalized by hASCs and effectively promoted the osteogenic differentiation of hASCs with more pronounced ALP and OPN expression and increased matrix mineralization (Lavrador et al., 2018). Naringin was embedded into PLGA/PLLA/PDLLA fibers via electrospinning and showed very close to sustained and steady drug liberation for 21 days, and the naringin-loaded fibers increased the viability and enhanced the proliferation of MC3T3-E1 cells compared with the mats without naringin (Guo et al., 2018).

A naringin-loaded porous biodegradable gelatin/β-TCP composite enhanced bone regeneration with good osteoconductive activity. The composite accelerated the ingrowth of new bone into a defect site, as shown by radiographic analysis, and complete osseointegration of the biodegradable implant with newly formed bone replacing a significant amount of the composites, as shown by histological H&E staining, after implantation in a rabbit calvarial defect model at 8 weeks (Chen et al., 2013). The hydroxyl groups in naringin were immobilized by the carboxylic end groups of SF and HA through chemical bonding with slow and sustained release of naringin from SF/HA scaffolds. The naringin-loaded scaffold promoted the osteogenic differentiation of hUCMSCs by activating the PI3K/Akt, VEGF, and HIF-1 signaling pathways demonstrated by gene microarray assays and enhanced bone formation at the site of reconstruction in rabbit distal femur defects, as shown by μCT and histological analyses at 4 weeks after scaffold implantation. Moreover, naringin promoted HUVEC growth and activated vascularization of SF/HA scaffolds (Zhao et al., 2021).

Naringin-loaded microspheres embedded in the PLLA matrix via thermal-induced phase separation partially rescued the observed MC3T3-E1 cell cytotoxic effect of the anti-inflammatory drug parthenolide and enhanced periodontal bone regeneration for a long period of time after implantation into rat fenestration defects (Guo et al., 2017). Naringin-loaded PCL/PEG-b-PCL microspheres were incorporated into SAIB depots to effectively reduce burst release with double diffusion barriers. In addition, this injected construct increased new bone formation by 53.1% after 8 weeks in an *in vivo* calvarial bone defect rat model with enhanced expression levels of Runx-2 and OCN (Yang et al., 2019).

Loading naringin was proven to enhance the bioactivity of Ti-based biomaterials. Naringin-loaded TiO_2 nanotubes with CS coating enhanced osteoblast spreading, proliferation, ALP activity, and late-stage osteoblast mineralization with slow release of naringin (Lai M. et al., 2018). Naringin was loaded by mixing and soaking in GelMA incorporated on a TiO_2 nanorod coating to achieve degradation-type release and diffusion-type release. The release of naringin notably upregulated the expression of the osteogenic genes ALP, RUNX-2, and COL-1 and promoted the attachment, osteogenesis, and mineralization of MSCs. The degradation-type release of naringin-M was shown to enhance the osteogenic differentiation of MSCs more effectively because naringin not only physically absorbed on GelMA but also covalently bonded with GelMA during the curing process (Shao et al., 2019). Naringin-loaded mineralized collagen coatings with MOFs led to a strengthened controlled release behavior that effectively reduced the burst release quantity by nearly 50%. The coating improved rat MSC adhesion and the expression of Col I, OC and RUNX2, as shown by RT-PCR analysis, at 14 days of culture and led to the highest MSC mineralization after 21 days of culture, as shown by Alizarin Red S (ARS) staining (Yu et al., 2017). Naringin-decorated ZnO nanoparticles were applied to functionalize Ti implants and exhibited great potential for osteoblast proliferation and differentiation (Yang Y. et al., 2020). Naringin can be loaded in multilayers to create a sustained release of naringin from micro-Ti surfaces using a layer-by-layer technique, enhance the differentiation of osteoblasts, consistent with qRT-PCR analysis of osteoblast genes, including Runx2, ALP, Col I, OCN, OPN, and OPG, and inhibit osteoclast formation, as shown by qRT-PCR analysis of the expression of osteoclastic differentiation-related genes, including CTSK, NFAT, TRAP, and VATP (Shen et al., 2021).

Quercetin

Quercetin is a flavonoid that is a component of Chinese medicines such as *Sambucus williamsii* and is ubiquitously found in vegetables and fruits. Quercetin promoted proliferation, differentiation, and mineralization in the osteoblastic lineage with a concomitant increase in the expression of osteogenic genes, and the concentration of quercetin needed for proliferation and differentiation may be cell type dependent (Prouillet et al., 2004; Kim et al., 2007; Srivastava et al., 2013; Zhou and Lin, 2014). Quercetin also has inhibitory effects on formation, proliferation, and maturation and decreases osteoclastic bone resorption *in vitro* by binding to estrogen receptors (Wattel et al., 2004; Woo et al., 2004). In addition, quercetin inhibited osteoblast apoptosis and oxidative stress and promoted antioxidant expression, adipocyte apoptosis, and osteoclast apoptosis (Hsu and Yen, 2006; Guo et al., 2012; Messer et al., 2015; Messer et al., 2016; Zhang et al., 2017). Despite the fact that many articles have reported the osteogenic activity of quercetin, most previous studies have assessed quercetin by directly adding it to cell culture media *in vitro* or through oral administration (Yuan et al., 2018). Quercetin has the drawbacks of low solubility in aqueous media, weak lipid solubility, and poor permeability, oral bioavailability, and biodegradation (Patel et al., 2012; Anandam and Selvamuthukumar, 2014). Therefore, a local sustained-release system of quercetin in bone defect areas must be developed. A recent study noted that quercetin-loaded composite materials could achieve sustained release of quercetin during a test period of 120 days without any initial burst (Raja et al., 2021).

The quercetin-loaded CDHA scaffold fabricated by a fabrication process involving original room temperature 3D printing showed steady release with the biodegradation of CaP and constant release for 60 days *in vitro* without any initial burst. By the addition of quercetin, the scaffold resulted in superior osteoblast proliferation of MC3T3-E1 cells and suppressed RAW 264.7 cell proliferation, as shown by calorimetric MTS assays and fluorescence microscopy images. In addition, quercetin-loaded scaffolds significantly increased preosteoblast cell differentiation and mineralization with the upregulation of COL I, RUNX-2, ALP, BSP, and OC expression, as shown by real-time PCR analysis, whereas osteoclast cell differentiation was dramatically suppressed with decreased TRAP activity (Tripathi et al., 2015). Quercetin-functionalized HA was synthesized by phase transition from monetite and enhanced human osteoblast-like MG63 proliferation and inhibited osteoclast precursor 2T-110 viability according to WST1

results at 7 and 14 days. The presence of quercetin in the composite materials enhanced OB differentiation with increased ALP and COL I expression and inhibited the differentiation of osteoclasts with high OPG/RANKL ratios and low CATK levels, as shown by immunoenzymatic assays (Forte et al., 2016). In addition, quercetin provided antioxidant properties to HA and counteracted the negative effect of oxidative stress on osteoblast viability and differentiation in an H_2O_2-induced oxidative stress environment while maintaining their inhibitory effect on osteoclasts (Forte et al., 2017).

Quercetin-loaded collagen matrix promoted the formation of new bone across parietal bone defects of rabbits after grating for 14 days, as shown by histological qualitative assessment (Wong and Rabie, 2008). The quercetin-immobilized 3D-printed PLLA scaffold achieved effective and sustainable release with the aid of a PDA layer via covalent and noncovalent interactions. Quercetin-loaded scaffolds enhanced the proliferation, differentiation, and mineralization of MC3T3-E1 cells, consistent with the qRT-PCR analysis of osteoblast genes and Western blot analysis of protein expression, including that of OCN, COL-I, ALP, and Runx-2. The concentration of quercetin and the biological activity of the scaffolds showed a dose-dependent relationship (Chen et al., 2019).

Quercetin-inlaid SF/HA scaffolds (0.03 wt%) promoted rabbit BMSC proliferation and osteogenic differentiation with prominent upregulation of Col I, OCN, and Runx2 RNA expression shown by real-time PCR analysis after seeding scaffolds for 28 days. The quercetin-loaded scaffolds also enhanced new bone formation with increased values of BMD, BV, BV/TV, BS, Tb.N, and Tb.Th by micro-CT 6 weeks after implantation into the calvarial defects of rats (Song J. E. et al., 2018). A subsequent study indicated that 25 μM quercetin-containing DC/HAp sponges also promoted new bone formation with increased BMD and BV 8 weeks after implantation (Song et al., 2020). Quercetin-containing MSCS/PCL composite scaffolds promoted WJMSC proliferation and stimulated WJMSC mineralized nodule formation and calcium deposition. Moreover, precipitation of apatite on the surface of the scaffold was observed after immersion for 28 days in a SBF solution (Khha et al., 2021). The complexes formed by the interaction between quercetin and vanadium or copper were shown to have osteogenic effects, as they stimulated matrix mineralization, calcium deposition, and expression of ALP, COL1, Runx-2, and osteoblast-specific microRNA (pre-miR-15b) in murine osteoblastic MC3T3-E1 cells and human osteoblast-like MG63 cells (Ferrer et al., 2006; Vimalraj et al., 2018). Quercetin-zinc metal complex-incorporated PCL/gelatin nanofiber scaffolds generated by electrospinning enhanced cellular activity, adhesion, and proliferation and stimulated osteogenic differentiation with higher expression of Runx2 and type 1 collagen shown by RT-PCR analysis and bone mineralization with improved relative OC and ONC expression, as shown by enzyme-linked immunosorbent assay (ELISA) kits (Preeth et al., 2021).

Quercetin-loaded nHA bioceramic microspheres resulted in favorable drug loading and sustained release capacity for up to 28 days. The presence of quercetin strongly enhanced new bone formation with increased BMD and Tb.Th values in the femur defects of OVX rats at 8 weeks, as shown by micro-CT results. In addition, the percentages of polychrome sequential fluorescence labeling of new mineralized tissue in the quercetin-loaded nHA group were significantly higher than those in the nHA group, and more newly formed bone tissue penetrated into the top of the defect of the quercetin-loaded nHA group, whereas only limited new bone formation was shown on the bottom of the defect of the nHA group by V-G picro fuchsin (Zhou et al., 2017). Quercetin-loaded biodegradable PLGA microspheres had prolonged release profiles without burst drug release and resulted in enhanced osteogenic differentiation and mineralization of stem cell spheroids according to ALP assays, ARS staining, and RT-PCR (Lee et al., 2018).

Kaempferol

Kaempferol is found widely in *Kaempferia galangal L.*, *Ginkgo biloba L.*, *Thesium chinense T.*, *Aloe vera*, *Rosmarinus officinalis*, *Hippophae Rhamnoides L.,* and *hawthorn*, and showed osteogenic property with various molecular mechanisms (Lee et al., 2014; Sharma and Nam, 2019; Liu et al., 2021). Different delivery carriers including nanostructured lipid or layer-by-layer nano-matrix efficiently improve the oral bioavailability of kaempferol (Kumar et al., 2012; Gupta et al., 2013; Du et al., 2019). A recent study showed that 58S BG coated with Zein achieve could sustained release of kaempferol in 9 days. The concentration with 20 μM sample was not toxic for BMSC cells according to the MTT results (Ranjbar et al., 2021). In addition, kaempferol-loaded TiO_2 showed sustained release within 168 h, and promoted the rat BMSCs proliferation and osteogenic differentiation with increasing mRNA expressions of Runx2, OCN, ON, OPN, and ALP *in vitro* culture, and promoted new bone formation surrounding the TiO_2 implants at 2 and 4 weeks after implantation *iv vivo* (Tsuchiya et al., 2018).

Puerarin

Puerarin, the major compound derived from the root of the *Pueraria lobata* (*Gegen*), has a positive effect on bone health based on the results of *in vitro* experiments and animal studies (Park et al., 2017; Zeng et al., 2018; Kulczyński et al., 2021). However, there were limited studies in local application in combination with materials. Puerarin was first mixed with collagen matrix grafted into rabbits' skull defects, and produced 554% more new bone than the absorbable collagen sponge alone at 2 weeks according to histological analysis (Wong and Rabie, 2007). In addition, puerarin-loaded Ti surface promotes osteogenic differentiation and mineralization of MC3T3-E1 cells with increasing ALP activity, Type I collagen synthesis, and osteocalcin release (Yang F. et al., 2012).

ALKALOID

Curcumin

Curcumin, a principal alkaloid compound extracted from *Curcuma longa Linn*, as well as from several other members of the ginger family Zingiberaceae, accounts for 77% of turmeric

extracts. Curcumin could enhance the proliferation of osteoblasts, induce the expression of related genes, affect osteoclast activity, and inhibit bone resorption by suppressing osteoclastogenesis by inhibiting NF-κB and its ligand RANKL (Ozaki et al., 2000; Hie et al., 2009; Gu et al., 2012; Son et al., 2018; Abdullah et al., 2020; Liang et al., 2020). In addition, oral curcumin administration enhanced the closure of critical-sized defects and bone repair around titanium implants in streptozotocin-induced diabetic rats (Cirano et al., 2018). In addition to its ability to regenerate bone, curcumin also exhibits anticancer and antioxidant properties (Naeini et al., 2019; Li et al., 2020; Ma B. et al., 2021). However, the bioavailability of curcumin is limited due to low aqueous solubility, extremely rapid systemic elimination, and inadequate tissue absorption and degradation (Anand et al., 2007). The high concentration of curcumin caused by inappropriate release behavior is not conducive to cell adhesion and proliferation (Scharstuhl et al., 2009; Jain et al., 2016; Kim et al., 2017). Therefore, the bioavailability and sustained-release kinetics of curcumin have been improved through biomaterial-based administration methods used for the inhibition of osteoclasts and osteosarcoma (Dhule et al., 2012; Heo et al., 2014; Chen X. et al., 2015; Kheiri Manjili et al., 2017; Verma et al., 2019) (**Figure 2**). Curcumin-loaded PBAE particle-embedded calcium sulfate hemihydrate composites showed sustained-release kinetics in 4 weeks controlled by the degradation of PBAE during dissolution of CS over time (Orellana et al., 2013). A study noted that curcumin-loaded Ti using poly (dopamine) as an anchor did not adversely affect osteoblast attachment, proliferation, apoptosis, differentiation, or calcium deposition in cell culture (He et al., 2015).

The curcumin-encapsulated CS-BG composite improved the morphological parameters with increased bone/tissue volume, osteoblast/bone surface, and osteoblast number and decreased osteoclast/bone surface and mechanical properties with bone hardness of newly formed bone in defects of the femoral condyle irradiated with 1.5 Gy of 60 Co for 7 days after 30 days of implantation (Jebahi et al., 2015). Curcumin-loaded PCL nanofibers (1 wt%) enhanced MC3T3-E1 osteogenic differentiation and mineralization with increased gene and protein expression of Alpl, Runx2, Bglap, Spp1, and Bmp2 at day 21 after seeding *in vitro*, as shown using a combination of qPCR and Western blots (Jain et al., 2016). Curcumin-loaded collagen nanofiber membranes enhanced DPSC proliferation and differentiation with increased ALP activity and expression of osteoblastic genes and associated proteins, including Runx-2 and OCN. In addition, the jaw defect of dogs was completely filled with new bone after just 28 days of implantation, as confirmed by histological testing, while the commercial membrane area remained empty (Ghavimi et al., 2020).

Curcumin-loaded PCL-PEG and PLGA-PEG coatings enabled continuous release of curcumin from the HA matrix for 22 days and enhanced hFOB proliferation with apatite formation at cell culture day 11 by FESEM and MTT cell viability assays. Curcumin-loaded PCL-PEG enhanced the osteogenic properties of the β-TCP scaffold with increased osteoid formation and mineralization of the newly formed bone by modified Masson Goldner trichrome staining and H&E staining and ECM formation by collagen staining after 6 weeks in an *in vivo* study (Bose et al., 2018). Curcumin-loaded microspheres were incorporated into the CHA scaffold to achieve drug release from the composite scaffolds for up to 30 days. The curcumin-loaded scaffold alleviated the negative impacts of diabetic serum on the proliferation, migration, and osteogenic differentiation of rat BMSCs with increased expression of Nrf2 and HO-1 and decreased production of H_2O_2, thiobarbituric acid reacting substances (TBARS), and intracellular reactive oxygen species (ROS). Moreover, the presence of curcumin in the composite materials enhanced new bone formation within the calvarial defect, as shown by micro-CT and H&E staining, compared to that of the diabetes group at 8 weeks postoperatively and activated vascular recruitment with higher protein expression of PECAM-1 and VEGF, as shown by Western blots (Li and Zhang, 2018). In addition, curcumin/alendronate-coloaded NPs decorated with hyaluronic acid increased the MC3T3-E1 cell growth rate determined using crystal violet staining, promoted cell differentiation with higher collagen deposition as shown by VG staining from days 7 to 21, and enhanced ECM mineralization with high calcium and phosphate deposition, as shown by ARS and von Kossa staining and EDX microanalysis from days 7 to 21. Moreover, the nanoformulation could stimulate bone formation by upregulating the levels of BMP-2, Runx 2, and OCN, as shown by using sandwich ELISAs (Dong et al., 2018).

A study demonstrated that various amounts of curcumin/BMP-2-loaded poly-L-lysine/hyaluronic acid hydrogels resulted in increased MG-63 cell proliferation after 3 days of culture, and by controlling the amounts of curcumin and BMP-2, the hydrogels showed better osteogenesis with higher *in vitro* ALP activity and calcium deposition and better *in vivo* new bone regeneration, as shown by micro-CT analyses. Notably, the incorporation of greater than 15 μM curcumin had negative effects on the proliferation of human osteosarcoma MG-63 cells (Kim et al., 2017). Successful treatment of osteosarcoma requires postsurgical bone defect repair as well as the complete eradication of bone tumor cells in the surrounding tissues (Ma et al., 2018). Curcumin-loaded liposomes exhibited more controlled and sustained release for 60 days by the thin-film hydration method. Porous 3DP TCP scaffolds with curcumin-encapsulated liposomes promoted hFOB cell proliferation, as determined by MTT assays; attachment and growth, as determined by FESEM at days 3, 7, and 11; and early osteoblast differentiation at day 11, as determined by ALP assays. Moreover, the presence of liposomal curcumin resulted in a 96% decrease in *in vitro* MG-63 cell proliferation and viability and almost no or very poor cell attachment after 11 days of incubation (Sarkar and Bose, 2019). Curcumin-loaded HA-coated Ti6Al4V implants showed controlled and sustained drug delivery from HA-coated Ti implants at pH 7.4 and pH 5.0 for 22 days in the presence of vitamin K2. The curcumin/vitamin K-loaded implant enhanced *in vitro* hFOB cell attachment and proliferation for 11 days and inhibited MG-63 cell attachment and proliferation with 95 and 92% lower

osteosarcoma cell viability at days 7 and 11, respectively, according to the MTT results and FESEM images. In addition, curcumin/vitamin K enhanced bone formation around the implant and improved contact between the tissue and implant, as shown by modified Masson Goldner staining, after 120 h of femoral epicondyle defect surgery in a rat distal femur model (Sarkar and Bose, 2020). Curcumin-loaded CS nanoparticle-encapsulated SF/HAMA hydrogels exhibited pH-responsive release and had a lower drug release rate and were maintained at 32 days. The *in vitro* proliferative response of the hydrogels with an equivalent curcumin concentration of 150 μg/ml decreased the MG-63 cell survival rate and improved the viability of MC3T3-E1 cells, consistent with the results of live and dead cells stained with fluorescent dye (Yu Q. et al., 2021). The curcumin microsphere/IR820 coloaded hybrid methylcellulose hydrogel induced more tumor cell apoptosis due to localized hyperthermia-accelerated curcumin release and promoted osteogenic differentiation, as shown by ALP and ARS staining and a microplate reader at days 7 and 14. The curcumin-loaded hydrogel with chemo-co-thermal efficacy and thermal-accelerated curcumin release efficiently eliminated osteosarcoma and promoted tibial bone defect regeneration according to micro-CT analysis, H&E staining, and Masson staining (Tan et al., 2021).

Berberine

Berberine is a quaternary ammonium isoquinoline alkaloid and is mainly extracted from traditional Chinese herbs, such as *Coptidis chinensis Franch*. (family Ranunculaceae), *Phellodendron chinense Schneid*. (family Rutaceae), and *Mahonia bealei* (*Fort*.) *Carr*. (family Berberidaceae). Berberine can promote the proliferation and differentiation of osteoblasts and inhibit the production of osteoclasts to promote bone regeneration (Tao et al., 2016; Dinesh and Rasool, 2018; Han and Kim, 2019; Yang B. et al., 2020; Zhang et al., 2021a) (**Figure 2**). However, berberine was found to have low pharmacological activity because of its low bioavailability resulting from poor solubility, a short half-life, and a substantial first-pass effect in the intestines, and developing a new berberine delivery strategy has been used to address these problems (Liu et al., 2016). Studies have shown that combining different materials can control the release behavior but only emphasizes the anti-infective effects (Zou et al., 2009; Cai et al., 2018). Berberine-coated mannosylated liposomes abrogated the increased osteoclast formation in BMM cells, inhibited the bone resorptive activity of osteoclasts, and upregulated miR-23a levels to inhibit GSK-3β phosphorylation (Sujitha and Rasool, 2019).

Berberine-loaded porous n-HA/PA66 composite scaffolds coated with chitosan achieved continuous berberine release and were maintained for 150 h in PBS solution. The *in vitro* cytotoxicity test showed that the berberine-loaded scaffold had good cell adhesive and proliferative capacities by phase contrast micrographs, SEM photographs, and MTT tests (Huang et al., 2011). Berberine-loaded porous CPC with sustained release of berberine for as long as 9–10 days promoted cell proliferation and differentiation with significantly increased ALP activity and mineral deposition, which was consistent with the expression levels of ALP, OCN, and BMP2 and RUNX2 in BMSCs originating from rats with osteoporosis cultured for 14 days *in vitro*. In addition, with berberine, the local BMD and BV/TV values were substantially higher than those of the porous CPC group or control group, as shown by micro-CT analysis, and the new bone formation area was substantially greater than those of the porous CPC group and the control group, as shown by van Gieson staining, 8 weeks after implantation *in vivo* in critical-size calvarial defects in an OVX rat model (Wang et al., 2021). Berberine-loaded PCL/COL electrospun scaffolds could release drug stably for up to 27 days with a low burst release and promote osteogenic differentiation of DPSCs with upregulated expression levels of osteogenic genes (ALP, BMP2, OCN, and COL-1) in coculture on the scaffolds after 7 and 14 days, as shown by RT-PCR. The presence of quercetin could elevate the bone defect repair ability of the scaffold. An *in vivo* study showed that the defect in the berberine-loaded scaffold group was almost repaired by newly formed minerals with a higher bone mineral density and increased BV/TV, as shown by micro-CT analysis, and an increase in the newly formed bone diameter and newly formed bone area in the defect edge, as shown by H&E and Masson staining, at 8 weeks after implantation in the critical bone defect of rats (Ma L. et al., 2021). A 10 mmol/L berberine-loaded PCL/PVP-MC/CS bilayer membrane could promote MC3T3-E1 cell proliferation and attachment *in vitro*, as shown by MTT assays and confocal laser confocal microscopy, and stimulate bone tissue repair with thicker lamellar bone and higher bone density, as shown by CT, H&E, and Goldner's trichrome staining, when implanted into a femoral bone defect in adult rats for 4 and 8 weeks (Zhang et al., 2021a).

STILBENES, PHENOLIC ACIDS, AND TERPENOIDS

Resveratrol

Resveratrol is a nonflavonoid polyphenol phytoalexin with a stilbene structure found in the traditional Chinese medicine *Reynoutria japonica Houtt*. Resveratrol promotes bone formation by promoting osteoblast proliferation and osteogenic differentiation and antagonizing osteoclast differentiation through different signaling pathways (Mizutani et al., 1998; Dai et al., 2007; He et al., 2010; Tseng et al., 2011; Dosier et al., 2012; Erdman et al., 2012; Shakibaei et al., 2012; Zhao et al., 2018). Resveratrol also stimulated BMP-2 production by osteoblasts through Src kinase-dependent ER activation, increased the serum concentration of BMP-2, and prevented femoral bone loss in OVX rats (Mizutani et al., 2000; Su et al., 2007). In addition, resveratrol has antioxidant and anti-inflammatory biological activities (Chung et al., 2011; Zhou et al., 2019). Several studies have shown that resveratrol can positively affect the repair of rat skull defects through oral administration (Casarin et al., 2014; Pino et al., 2017; Franck et al., 2018). In recent clinical trials, orally administered resveratrol failed to show any significant effect on a panel of biomarkers of bone turnover and calcium metabolism (Asis et al., 2019). The clinical use of resveratrol has been limited mainly by

its low aqueous solubility and rapid metabolism and poor chemical stability, resulting in low bioavailability (Baur and Sinclair, 2006). Combining resveratrol with various materials for a local controlled delivery system may provide a new route through which to deliver this agent to a local target and strengthen its potency (Peng et al., 2010; Teskac and Kristl, 2010).

Resveratrol-loaded porous PCL scaffolds generated by vapor phase grafting and coupling could increase the ALP activity of rat BMSCs, as shown by pNPP analysis and a TRACP and ALP double staining kit, and increased matrix production and mineralization of the cell–scaffold cocultures, as shown by toluidine blue, von Kossa and Alizarin Red staining *in vitro*. The resveratrol-loaded scaffold also enhanced the bone regeneration of *in vivo* rat calvarial defects, as shown by X-ray and histological analysis, which demonstrated higher X-ray density and greater areas of bone-like structures that were positively stained for BSP after implantation for 8 weeks (Li et al., 2011). The resveratrol-loaded collagen scaffolds released over twice as much resveratrol as the blank collagen scaffold. The incorporation of resveratrol enhanced the scaffold mineralization of hASC osteogenic differentiation in the scaffolds, as shown by flow cytometry analysis and Alizarin Red and von Kossa staining, and promoted the bone regeneration calvarial defects of the rat models at 3 months, as shown by micro-CT (Wang et al., 2018).

Resveratrol-loaded electrospun PCL and PLA nanofibers with sustained release for 35 days could promote STRO-1+ cell osteogenic differentiation with higher mRNA levels of the early-stage osteoblast differentiation markers RUNX2 and OSX and the late-stage markers OCN, ONN, OPN, and BSP, which were evaluated by quantitative RT-PCR, but only the PLA nanofibers with lower resveratrol release could inhibit RANKL-induced osteoclast differentiation via the downregulation of CTSK expression and a reduction in TRAP activity (Riccitiello et al., 2017). Resveratrol-loaded PLA/OMMT composite nanofibrous scaffolds showed slower and more controlled release because resveratrol can be trapped within the OMMT plates and interact chemically with CTAB. The presence of resveratrol promoted antioxidant activity with 83.75% radical scavenging and enhanced hASC osteogenic differentiation with the increased expression levels of ALP, OCN, and OPN after culturing for 14 and 21 days (Karimi-Soflou et al., 2021).

Resveratrol-loaded albumin nanoparticle-entrapped PCL scaffolds showed sustained release without a burst effect. The scaffold with the addition of resveratrol increased hMBSC activity, as determined by MTT assays; ALP activity, as determined by BCIP-NBT assays on days 8 and 12; and increased calcium deposition, as determined by von Kossa staining on day 16 after the addition of quercetin (Kamath et al., 2014). Resveratrol-loaded 3D PLGA-sintered microsphere scaffolds promoted osteogenic differentiation with greater ALP expression and higher amounts of calcium in hMSCs cultured *in vitro* at 7, 14, and 21 days. Moreover, resveratrol-loaded scaffolds downregulated the expression of inflammatory markers while stimulating the expression of angiogenic genes (Rutledge et al., 2016). Resveratrol-encapsulated n-HA/CS composite microspheres suppressed TNF-α, IL-1β, and iNOS mRNA expression in RAW 264.7 cells cultured on composite microspheres for 3 and 7 days and had no significant effect on the viability of these cells. Resveratrol-loaded microspheres promoted the proliferation of BMSCs, enhanced the osteodifferentiation of BMSCs by upregulating the levels of osteogenic Runx2, ALP, Col-1, and OCN, as determined by RT-qPCR analysis at 14 days, and resulted in higher levels of calcium deposition than those of BMSCs, as determined by ARS staining. In addition, the microspheres enhanced entochondrostosis and the bone remodeling capacity in a dose-dependent manner according to micro-CT analysis and Masson's trichrome and H&E staining when implanted into *in vivo* bone defects of osteoporotic rat femoral condyles at 6 weeks (Li et al., 2021). Resveratrol/angiopoietin-2-loaded PEGDA/TCS hydrogels induced new blood vessel reconstruction earlier through the autophagy pathway and resulted in new bone tissue almost completely formed and a network structure in the *in vivo* defect area at 8 weeks in a relatively hypoxic environment, as demonstrated by histology, immunofluorescence, immunohistochemistry, and Masson staining (Fan et al., 2021). Resveratrol-loaded SLNs/GelMA hydrogels exhibited long-term slow release of the drug from the scaffolds, and the drug concentration was maintained at the necessary level for 28 days. The hydrogel promoted both early-stage and late-stage osteogenic differentiation of BMSCs *in vitro* with increased expression of osteogenic genes, including Alp, Ocn, Runx2, and Opn, as shown by RT-qPCR. The presence of resveratrol promoted new bone to completely cover *in vivo* rat cranial defects with a 50% BV/TV ratio shown by micro-CT and 80% thickness of normal bone tissue shown by H&E staining and Masson's trichrome staining at 8 weeks post-operation (Wei et al., 2021).

Salvianolic Acids

Salvianolic acids are water-soluble components extracted from *Salvia miltiorrhiza*, and more than 50 hydrophilic compounds, including salvianolic acids A and B, which are the most abundant, have been isolated. Salvianolic acids A and B promoted osteogenesis of osteoblasts and bone marrow stromal cells and enhanced angiogenesis *in vitro* and *in vivo* to accelerate early-stage fracture healing (Lay et al., 2003; Cui et al., 2009; Cui et al., 2012; He and Shen, 2014; Tang et al., 2014; Xu et al., 2014).

Salvianolic acid B-loaded CS microspheres immobilized on alginate-coated HA scaffolds exhibited an initial burst release followed by sustained release over 30 days and obviously promoted rat calvarial osteoblast attachment, uniform distribution, and proliferation after cell culture for 3 and 7 days, as shown by SEM observation and Alamar Blue assays (Li et al., 2016). The salvianolic acid B-loaded CS/HA scaffold showed that the release of salvianolic acid B lasted for more than 56 days. The addition of salvianolic acid B promoted the proliferation of MC3T3-E1 cells at 3 and 5 days, as evaluated by the CCK-8 method, and increased ALP expressed by MC3T3-E1 cells after 7 and 14 days of culture. The addition of salvianolic acid B also enhanced bone regeneration of rabbit radius bone defects with higher BV/TV values, as shown by CT examinations, and a higher percentage of bone formation shown by HE staining

at 6 and 12 weeks. In addition, the addition of salvianolic acid B enhanced the angiogenic bioactivities of the scaffold with increased VEGF activity *in vitro* and increased expression of CD34 *in vivo* (Ji et al., 2019). Salvianolic acid B-loaded PLGA/β-TCP composite scaffolds steadily released salvianolic acid B from the PLGA/β-TCP scaffold in 30 days, but the release kinetics were gradually reduced after 10 days. The addition of salvianolic acid B promoted GFP transgenic rat MSC proliferation, as measured by Alamar Blue assays. The addition of salvianolic acid B promoted osteogenic differentiation of GFP transgenic rat MSCs, with calcium deposition and ALP activity determined by ARS and ALP staining. Salvianolic acid B enhanced the mRNA levels of the osteogenic markers Runx2, OCN, and Cal1a1, as determined by qPCR. After 8 weeks of implantation, salvianolic acid B increased new bone formation, the bone volume ratio, and neovascularization in a dose-dependent manner, as shown by micro-CT analysis and histological analysis, and increased the expression of OCN and CD31, as shown by immunohistochemistry assays (Lin et al., 2019). Salvianolic acid B-loaded SF/GO scaffolds generated through physical adsorption and covalent bonding could load large doses and exhibited continuous release *in vitro* for at least 4 weeks. The scaffold promoted the proliferation, osteogenic differentiation, and mineralization of rBMSCs *in vitro*, and enhanced the expression of the osteogenic genes ALP, COL1, RUNX2, and OCN and upregulated the expression of the angiogenesis marker genes VEGF and HIF-1α, as determined by qRT-PCR. When the scaffold was implanted to the defect after 8 weeks, a large amount of new bone was formed at the defect site with good interfacial integration and increased number of neovessels according to the results of Micro-CT, van Gieson, H&E, and Masson staining (Wang W. et al., 2020). The salvianolic acid B-loaded MBG scaffold consistently released drug for nearly 30 days. The addition of salvianolic acid B to the MBG scaffold further promoted rBMSC proliferation, as determined by CCK-8 assays on days 1, 3, and 7, osteogenic differentiation with high ALP expression and calcified nodules, as determined by alkaline phosphatase staining and Alizarin Red staining on days 7 and 14, which was consistent with the upregulation of osteogenic differentiation-related genes. The addition of salvianolic acid B enhanced the bone regenerative ability of MBG scaffolds by micro-CT, sequential polychrome label analysis, and van Gieson's and immunohistochemistry staining 8 weeks after implantation in rat cranial bone defects (Wu et al., 2021).

Salvianolic acid A-loaded liposomes provided substantial local distribution of high concentrations of the drug and improved retention (lasting beyond 20 days for one injection) of the drug at the fracture site, improving the healing of prednisone-induced delayed fracture union in mice. The liposome was able to reverse the decline of bone in TCA, effectively reducing the cartilaginous callus area and chondrocyte area in the total callus area shown by safranin O and H&E staining on the 18th day. Immunohistochemistry analyses suggested that osteogenesis (Osterix) and angiogenesis (PECAM-1)-related protein expression was increased by liposome treatment in the callus. The liposomes increased the callus BV/TV, BS/TV, connectivity density, and BMC, as shown by micro-CT analysis. Liposome treatment could shorten fracture healing by at least 22 days (from >64 to 42 days) with improved structural strength and apparent material strength (Liu et al., 2018). Salvianolic acid A-loaded liposome-incorporated collagen sponges promoted bone formation at the fracture site of a rabbit model of radius nonunion. Micro-CT showed significantly increased union callus formation with elevated BV and TV values in the 4th week postsurgery. Histological images showed increased bone areas in the callus, and immunofluorescence images showed increased expression of collagen II, P-HDAC3, VEGFA, osteocalcin, and RUNX2 in the callus (Zhou et al., 2020).

Notably, all the above-mentioned studies have demonstrated that salvianolic acid-loaded materials can promote angiogenesis both *in vitro* and *in vivo*.

Ginsenosides

Ginsenosides are the main triterpene glycoside compounds present in the plants of the *genus Panax* (*ginseng*), which belongs to the Araliaceae family. Based on diverse structural characteristics, ginsenosides can be divided into the following three types: protopanaxadiol (PPD), protopanaxatriol (PPT), and oleanane. Ginsenosides, such as Rb1, Rg1, Re, Rb2, and Rh1, have positive effects on bone regeneration, promoting osteoblast-related cell proliferation and osteogenesis and inhibiting the activity of osteoclasts (Cheng et al., 2012; Siddiqi et al., 2014; Gu et al., 2016; Kim et al., 2016; Cong et al., 2017; Yang N. et al., 2020) (**Figure 2**).

The ginsenoside Rb1-loaded 3D MSCS/PCL composite scaffold led to larger and more tightly arranged HA aggregates and improved attachment to the scaffolds after 3 days of immersion in SBF. The scaffold promoted adhesion and proliferation of hDPSCs, as shown by PrestoBlue assays and F-actin fluorescent staining; osteogenic differentiation and expression of osteogenesis-related markers such as ALP, OPN, and OC, as shown by ELISAs; and bone mineralization, as shown by Alizarin Red S staining. Moreover, according to the results of immunohistochemistry, the GR-containing MSCS scaffolds had substantially increased collagen formation, mineralization of bone defect areas, and greater proportions of calcified hard tissue than those of the others 4 and 8 weeks after implantation in the critical-size bone defect in a rabbit model, as shown by H&E, Masson's trichrome, and von Kossa staining. The scaffold enhanced the proliferation of hDPSCs, increased expression of osteogenic-related proteins, and effectively inhibited inflammation. The scaffold strongly increased collagen formation, mineralization of the bone defect area, and the proportions of calcified hard tissue compared with the others and was progressively degraded by the newly formed bone tissue during regeneration after 4 and 8 weeks of implantation (Chen et al., 2021).

Ginsenoside compound K is one of the major metabolites detected in blood after the oral administration of the ginsenosides Rb1 and Rb2. The ginsenoside compound K-loaded porous FSC: CH:BCP scaffold promotes the attachment of osteoblast-like MG-63 cell lines and subsequent spreading and proliferation of cells, as shown by MTT assays and cell adhesion and inverted

fluorescence staining images (Muthukumar et al., 2016). Further research from the same team showed that the ginsenoside compound K-loaded CH:BCP microspheres could promote rat BMSC proliferation shown by CLSM and DNA quantification and osteogenic properties with increased osteogenic marker expression of OPN, OCN, and Col I shown by RT-PCR analysis (Thangavelu et al., 2020).

Ginsenoside Rg1-loaded PPF microspheres resulted in a slow *in vitro* release from microsphere/scaffold composites, maintaining local *in vivo* concentrations at angiogenic levels for an adequate duration and thus enhancing bone regeneration (Salarian et al., 2016). The ginsenoside Rg1-loaded GM/Sr-α-CaS scaffold achieved sustained release without drug burst. A scaffold with a low concentration of ginsenoside Rg1 accelerated MC3T3-E1 *in vitro* osteogenic differentiation with higher ALP activity at 14 and 21 days and vascularization with higher expression of VEGF, as shown by RT-qPCR at 1, 7, 14, and 21 days. Moreover, the ginsenoside Rg1-loaded scaffold promoted bone regeneration of rat calvarial defects in 12 weeks with a new bone volume of approximately 83.3%, and BMD increased to 1,133 mg/cm^3, as shown by micro-CT, with many new bones and collagen fibers shown by HE staining, safranin O-fast green staining, and Masson staining. In addition, the new bone had higher OCN expression (Luo et al., 2020).

Ursolic Acid

Ursolic acid is a pentacyclic triterpenoid compound extracted from Ligustrum lucidum and Eriobotrya japonica, stimulated osteoblast differentiation, and inhibited osteoclast differentiation (Cao et al., 2018; Tan et al., 2019; Zheng et al., 2020). Ursolic acid also inhibited osteolysis, inflammation, and osteoclastogenesis caused by titanium wear particles (Peng et al., 2018). Ursolic acid-loaded collagen sponges were implanted onto the calvarial bones of mice, the thickness of newly formed woven bone in ursolic acid-treated mice was increased about 7-fold relative to vehicle-treated mice after 3 weeks with a high proportion of positive immunostaining of BMP-2 (Lee et al., 2008). Ursolic acid-loaded mesoporous bioglass/chitosan porous scaffolds with continuous release for 72 h promoted *in vitro* MC3T3-E1 cell proliferation and osteogenic effects with increasing ALP activity and expression level of COL1, RUNX2 genes. The scaffold remarkably promoted new bone formation in rat critical-size calvarial bone defect with high BV/TV (40.15 ± 3.29%), BMD, and MAR (5.89 ± 0.18 μm/d) according to Micro-CT and histological results at 12 weeks (Ge et al., 2019). Ursolic acid-loaded mesoporous hydroxylapatite/chitosan scaffolds enhanced the controlled release of drugs in 72 h with hydrogen bonding between the mesoporous structure and polar group in the scaffold. The scaffold showed better *in vitro* osteogenesis and bone mineralization ability with the expression of genes and proteins related to new bone formation and differentiation. The scaffold promoted the bone regeneration in ability rat skull defect model at 12 weeks with increase in volume, density, BMD, and MAR of new bone formation with higher osteogenic-related proteins (Yu X. et al., 2021).

CONCLUSION AND PROSPECTS

Integrating materials with TCM compounds delivery has been proven to be effective substitutes for bone defect regeneration without adverse side effects, primarily in preclinical cell-based or experimental animal studies. Combining different compounds with different materials through different economical and effective preparation methods not only improves the release behavior of compounds, but also improves the biocompatibility, mechanical properties, osteoconductivity, and osteoinductivity of biomaterials. Although the effective concentration of the compounds is different for different cells, with the help of these materials, the drug can maintain the appropriate concentration with continuous and controlled release, promote the proliferation and osteogenic differentiation of various cells with osteogenic potential, and inhibit the activity of osteoclasts by regulating different signal pathways. This synergy further enhances its comprehensive biological activity in the process of bone regeneration, effectively promoting the development in BTE. However, the optimum concentration of compounds is different *in vivo* and *in vitro*, and the rate at which drugs clear in the human body follows different kinetics compared with that in controlled *in vitro* experiments. Although current studies have described attempts to improve the release behavior of compounds, almost no research mentions the pharmaceutical behavior of compounds *in vivo*. Therefore, the major issue to be addressed is the scale-up of the compound release profile in an *in vivo* model. Material types and loading strategies deserve further attention and optimization to promote the efficiencies and efficacies of compound delivery systems. In addition, these compounds have antioxidative, antibacterial, anti-inflammatory, and antitumor cell proliferative abilities and promote angiogenesis. The study of bone defect models under corresponding environments should be carried out for applications in clinical treatment. In addition, the current research is limited to the reconstruction of bone defect models in mice, rats, or rabbits, and most of them are calvarial defect models that cannot fully simulate the process of human bone regeneration and cannot soon be translated into clinical practice. Therefore, the development of more ideal preclinical studies on bone defects in large animals models (horses, sheep, dogs, and pigs) is necessary for the future, followed by transfer to human clinical trials.

AUTHOR CONTRIBUTIONS

QW, RA, and DL designed the study. GS and CY wrote the paper with help from all the authors. SW and GW were involved in document retrieval. All the authors read and approved the final form of the manuscript.

FUNDING

This work was supported by the Young Medical Talents Training Program of Pudong Health Committee of Shanghai (Grant No. PWRq 2021-08), the Youth Science and Technology Project of Health Commission of Shanghai Pudong New Area (Project no. PW2020B-5), the Talents Training Program of Pudong Hospital affiliated to Fudan University (Project no. PX202001), the Scientific Research Foundation provided by Pudong Hospital affiliated to Fudan University (Project no. YJRCJJ201906), China Postdoctoral Science Foundation (2021M692119).

SUPPLEMENTARY MATERIAL

The Supplementary Material for this article can be found online at: https://www.frontiersin.org/articles/10.3389/fbioe.2022.851561/full#supplementary-material

REFERENCES

Abdullah, A. O., He, J., Yang, X., Liu, F., and Liu, Y. (2020). The Impact of Curcumin on Bone Osteogenic Promotion of MC3T3 Cells under High Glucose Conditions and Enhanced Bone Formation in Diabetic Mice. *Coatings* 10 (3), 258. doi:10.3390/coatings10030258

Agarwal, R., and García, A. J. (2015). Biomaterial Strategies for Engineering Implants for Enhanced Osseointegration and Bone Repair. *Adv. Drug Deliv. Rev.* 94, 53–62. doi:10.1016/j.addr.2015.03.013

Anand, P., Kunnumakkara, A. B., Newman, R. A., and Aggarwal, B. B. (2007). Bioavailability of Curcumin: Problems and Promises. *Mol. Pharm.* 4 (6), 807–818. doi:10.1021/mp700113r

Anandam, S., and Selvamuthukumar, S. (2014). Fabrication of Cyclodextrin Nanosponges for Quercetin Delivery: Physicochemical Characterization, Photostability, and Antioxidant Effects. *J. Mater. Sci.* 49 (23), 8140–8153.

Ang, E. S., Yang, X., Chen, H., Liu, Q., Zheng, M. H., and Xu, J. (2011). Naringin Abrogates Osteoclastogenesis and Bone Resorption via the Inhibition of RANKL-Induced NF-Kb and ERK Activation. *FEBS Lett.* 585 (17), 2755–2762. doi:10.1016/j.febslet.2011.07.046

Asis, M., Hemmati, N., Moradi, S., Nagulapalli Venkata, K. C., Mohammadi, E., Farzaei, M. H., et al. (2019). Effects of Resveratrol Supplementation on Bone Biomarkers: a Systematic Review and Meta-Analysis. *Ann. N. Y Acad. Sci.* 1457 (1), 92–103. doi:10.1111/nyas.14226

Baur, J. A., and Sinclair, D. A. (2006). Therapeutic Potential of Resveratrol: the *In Vivo* Evidence. *Nat. Rev. Drug Discov.* 5 (6), 493–506. doi:10.1038/nrd2060

Bose, S., Sarkar, N., and Banerjee, D. (2018). Effects of PCL, PEG and PLGA Polymers on Curcumin Release from Calcium Phosphate Matrix for *In Vitro* and *In Vivo* Bone Regeneration. *Mater. Today Chem.* 8, 110–120. doi:10.1016/j.mtchem.2018.03.005

Cai, B., Zou, Q., Zuo, Y., Mei, Q., Ma, J., Lin, L., et al. (2018). Injectable Gel Constructs with Regenerative and Anti-infective Dual Effects Based on Assembled Chitosan Microspheres. *ACS Appl. Mater. Inter.* 10 (30), 25099–25112. doi:10.1021/acsami.8b06648

Cancedda, R., Giannoni, P., and Mastrogiacomo, M. (2007). A Tissue Engineering Approach to Bone Repair in Large Animal Models and in Clinical Practice. *Biomaterials* 28 (29), 4240–4250. doi:10.1016/j.biomaterials.2007.06.023

Cao, S., Tian, X. L., Yu, W. X., Zhou, L. P., Dong, X. L., Favus, M. J., et al. (2018). Oleanolic Acid and Ursolic Acid Improve Bone Properties and Calcium Balance and Modulate Vitamin D Metabolism in Aged Female Rats. *Front. Pharmacol.* 9, 1435. doi:10.3389/fphar.2018.01435

Casarin, R. C., Casati, M. Z., Pimentel, S. P., Cirano, F. R., Algayer, M., Pires, P. R., et al. (2014). Resveratrol Improves Bone Repair by Modulation of Bone Morphogenetic Proteins and Osteopontin Gene Expression in Rats. *Int. J. Oral Maxillofac. Surg.* 43 (7), 900–906. doi:10.1016/j.ijom.2014.01.009

Che, C. T., Wong, M. S., and Lam, C. W. (2016). Natural Products from Chinese Medicines with Potential Benefits to Bone Health. *Molecules* 21 (3), 239. doi:10.3390/molecules21030239

Chen, C. Y., Shie, M. Y., Lee, A. K., Chou, Y. T., Chiang, C., and Lin, C. P. (2021). 3D-Printed Ginsenoside Rb1-Loaded Mesoporous Calcium Silicate/Calcium Sulfate Scaffolds for Inflammation Inhibition and Bone Regeneration. *Biomedicines* 9 (8). doi:10.3390/biomedicines9080907

Chen, J., Pan, P., Zhang, Y., Zhong, S., and Zhang, Q. (2015a). Preparation of Chitosan/nano Hydroxyapatite Organic-Inorganic Hybrid Microspheres for Bone Repair. *Colloids Surf. B Biointerfaces* 134, 401–407. doi:10.1016/j.colsurfb.2015.06.072

Chen, K. Y., Lin, K. C., Chen, Y. S., and Yao, C. H. (2013). A Novel Porous Gelatin Composite Containing Naringin for Bone Repair. *Evid. Based Complement. Alternat Med.* 2013, 283941. doi:10.1155/2013/283941

Chen, S., Zhu, L., Wen, W., Lu, L., Zhou, C., and Luo, B. (2019). Fabrication and Evaluation of 3D Printed Poly(l -lactide) Scaffold Functionalized with Quercetin-Polydopamine for Bone Tissue Engineering. *ACS Biomater. Sci. Eng.* 5 (5), 2506–2518. doi:10.1021/acsbiomaterials.9b00254

Chen, X., Zou, L. Q., Niu, J., Liu, W., Peng, S. F., and Liu, C. M. (2015b). The Stability, Sustained Release and Cellular Antioxidant Activity of Curcumin Nanoliposomes. *Molecules* 20 (8), 14293–14311. doi:10.3390/molecules200814293

Cheng, B., Li, J., Du, J., Lv, X., Weng, L., and Ling, C. (2012). Ginsenoside Rb1 Inhibits Osteoclastogenesis by Modulating NF-Kb and MAPKs Pathways. *Food Chem. Toxicol.* 50 (5), 1610–1615. doi:10.1016/j.fct.2012.02.019

Chung, B. H., Kim, J. D., Kim, C. K., Kim, J. H., Won, M. H., Lee, H. S., et al. (2008). Icariin Stimulates Angiogenesis by Activating the MEK/ERK- and PI3K/Akt/eNOS-dependent Signal Pathways in Human Endothelial Cells. *Biochem. Biophys. Res. Commun.* 376 (2), 404–408. doi:10.1016/j.bbrc.2008.09.001

Chung, E. Y., Kim, B. H., Hong, J. T., Lee, C. K., Ahn, B., Nam, S. Y., et al. (2011). Resveratrol Down-Regulates Interferon-γ-Inducible Inflammatory Genes in Macrophages: Molecular Mechanism via Decreased STAT-1 Activation. *J. Nutr. Biochem.* 22 (10), 902–909. doi:10.1016/j.jnutbio.2010.07.012

Cirano, F. R., Pimentel, S. P., Casati, M. Z., Corrêa, M. G., Pino, D. S., Messora, M. R., et al. (2018). Effect of Curcumin on Bone Tissue in the Diabetic Rat: Repair of Peri-Implant and Critical-Sized Defects. *Int. J. Oral Maxillofac. Surg.* 47 (11), 1495–1503. doi:10.1016/j.ijom.2018.04.018

Cong, F., Liu, J., Wang, C., Yuan, Z., Bi, L., Liang, J., et al. (2017). Ginsenoside Rb2 Inhibits Osteoclast Differentiation through Nuclear Factor-kappaB and Signal Transducer and Activator of Transcription Protein 3 Signaling Pathway. *Biomed. Pharmacother.* 92, 927–934. doi:10.1016/j.biopha.2017.05.115

Cui, L., Li, T., Liu, Y., Zhou, L., Li, P., Xu, B., et al. (2012). Salvianolic Acid B Prevents Bone Loss in Prednisone-Treated Rats through Stimulation of Osteogenesis and Bone Marrow Angiogenesis. *PLoS One* 7 (4), e34647. doi:10.1371/journal.pone.0034647

Cui, L., Liu, Y. Y., Wu, T., Ai, C. M., and Chen, H. Q. (2009). Osteogenic Effects of D+beta-3,4-dihydroxyphenyl Lactic Acid (Salvianic Acid A, SAA) on Osteoblasts and Bone Marrow Stromal Cells of Intact and Prednisone-Treated Rats. *Acta Pharmacol. Sin* 30 (3), 321–332. doi:10.1038/aps.2009.9

Dai, Z., Li, Y., Quarles, L. D., Song, T., Pan, W., Zhou, H., et al. (2007). Resveratrol Enhances Proliferation and Osteoblastic Differentiation in Human Mesenchymal Stem Cells via ER-dependent ERK1/2 Activation. *Phytomedicine* 14 (12), 806–814. doi:10.1016/j.phymed.2007.04.003

Delloye, C., Cornu, O., Druez, V., and Barbier, O. (2007). Bone Allografts: What They Can Offer and what They Cannot. *J. Bone Jt. Surg Br* 89 (5), 574–579. doi:10.1302/0301-620x.89b5.19039

Dhule, S. S., Penfornis, P., Frazier, T., Walker, R., Feldman, J., Tan, G., et al. (2012). Curcumin-loaded γ-cyclodextrin Liposomal Nanoparticles as Delivery Vehicles for Osteosarcoma. *Nanomedicine* 8 (4), 440–451. doi:10.1016/j.nano.2011.07.011

Dinesh, P., and Rasool, M. (2018). Berberine Inhibits IL-21/IL-21R Mediated Inflammatory Proliferation of Fibroblast-like Synoviocytes through the Attenuation of PI3K/Akt Signaling Pathway and Ameliorates IL-21

Mediated Osteoclastogenesis. *Cytokine* 106, 54–66. doi:10.1016/j.cyto.2018.03.005

Dong, J., Tao, L., Abourehab, M. A. S., and Hussain, Z. (2018). Design and Development of Novel Hyaluronate-Modified Nanoparticles for Combo-Delivery of Curcumin and Alendronate: Fabrication, Characterization, and Cellular and Molecular Evidences of Enhanced Bone Regeneration. *Int. J. Biol. Macromol* 116, 1268–1281. doi:10.1016/j.ijbiomac.2018.05.116

Dosier, C. R., Erdman, C. P., Park, J. H., Schwartz, Z., Boyan, B. D., and Guldberg, R. E. (2012). Resveratrol Effect on Osteogenic Differentiation of Rat and Human Adipose Derived Stem Cells in a 3-D Culture Environment. *J. Mech. Behav. Biomed. Mater.* 11, 112–122. doi:10.1016/j.jmbbm.2011.08.014

Du, Q., Chen, J., Yan, G., Lyu, F., Huang, J., Ren, J., et al. (2019). Comparison of Different Aliphatic Acid Grafted N-Trimethyl Chitosan Surface-Modified Nanostructured Lipid Carriers for Improved Oral Kaempferol Delivery. *Int. J. Pharm.* 568, 118506. doi:10.1016/j.ijpharm.2019.118506

Erdman, C. P., Dosier, C. R., Olivares-Navarrete, R., Baile, C., Guldberg, R. E., Schwartz, Z., et al. (2012). Effects of Resveratrol on Enrichment of Adipose-Derived Stem Cells and Their Differentiation to Osteoblasts in Two-And Three-Dimensional Cultures. *J. Tissue Eng. Regen. Med.* 6 (Suppl. 3), s34–46. doi:10.1002/term.513

Fan, D., Liu, H., Zhang, Z., Su, M., Yuan, Z., Lin, Y., et al. (2021). Resveratrol and Angiogenin-2 Combined with PEGDA/TCS Hydrogel for the Targeted Therapy of Hypoxic Bone Defects via Activation of the Autophagy Pathway. *Front. Pharmacol.* 12, 618724. doi:10.3389/fphar.2021.618724

Fan, J., Bi, L., Wu, T., Cao, L., Wang, D., Nan, K., et al. (2012). A Combined Chitosan/nano-Size Hydroxyapatite System for the Controlled Release of Icariin. *J. Mater. Sci. Mater. Med.* 23 (2), 399–407. doi:10.1007/s10856-011-4491-4

Feng, X., Wei, L., Shao, L., Chen, L., Zhang, Y., and Liu, C. (2016). Self-assembly Chitosan/gelatin Composite Coating on Icariin-Modified TiO2 Nanotubes for the Regulation of Osteoblast Bioactivity. *Mater. Des.*

Ferrer, E. G., Salinas, M. V., Correa, M. J., Naso, L., Barrio, D. A., Etcheverry, S. B., et al. (2006). Synthesis, Characterization, Antitumoral and Osteogenic Activities of Quercetin Vanadyl(IV) Complexes. *J. Biol. Inorg. Chem.* 11 (6), 791–801. doi:10.1007/s00775-006-0122-9

Forte, L., Torricelli, P., Boanini, E., Gazzano, M., Rubini, K., Fini, M., et al. (2016). Antioxidant and Bone Repair Properties of Quercetin-Functionalized Hydroxyapatite: An *In Vitro* Osteoblast-Osteoclast-Endothelial Cell Co-culture Study. *Acta Biomater.* 32, 298–308. doi:10.1016/j.actbio.2015.12.013

Forte, L., Torricelli, P., Boanini, E., Rubini, K., Fini, M., and Bigi, A. (2017). Quercetin and Alendronate Multi-Functionalized Materials as Tools to Hinder Oxidative Stress Damage. *J. Biomed. Mater. Res. A.* 105 (12), 3293–3303. doi:10.1002/jbm.a.36192

Franck, F. C., Benatti, B. B., Andia, D. C., Cirano, F. R., Casarin, R. C., Corrêa, M. G., et al. (2018). Impact of Resveratrol on Bone Repair in Rats Exposed to Cigarette Smoke Inhalation: Histomorphometric and Bone-Related Gene Expression Analysis. *Int. J. Oral Maxillofac. Surg.* 47 (4), 541–548. doi:10.1016/j.ijom.2017.08.004

Ge, Y. W., Lu, J. W., Sun, Z. Y., Liu, Z. Q., Zhou, J., Ke, Q. F., et al. (2019). Ursolic Acid Loaded-Mesoporous Bioglass/chitosan Porous Scaffolds as Drug Delivery System for Bone Regeneration. *Nanomedicine* 18, 336–346. doi:10.1016/j.nano.2018.10.010

Ghavimi, M. A., Bani Shahabadi, A., Jarolmasjed, S., Memar, M. Y., Maleki Dizaj, S., and Sharifi, S. (2020). Nanofibrous Asymmetric Collagen/curcumin Membrane Containing Aspirin-Loaded PLGA Nanoparticles for Guided Bone Regeneration. *Sci. Rep.* 10 (1), 18200. doi:10.1038/s41598-020-75454-2

Gong, M., Chi, C., Ye, J., Liao, M., Xie, W., Wu, C., et al. (2018). Icariin-loaded Electrospun PCL/gelatin Nanofiber Membrane as Potential Artificial Periosteum. *Colloids Surf. B Biointerfaces* 170, 201–209. doi:10.1016/j.colsurfb.2018.06.012

Gu, Q., Cai, Y., Huang, C., Shi, Q., and Yang, H. (2012). Curcumin Increases Rat Mesenchymal Stem Cell Osteoblast Differentiation but Inhibits Adipocyte Differentiation. *Pharmacogn Mag.* 8 (31), 202–208. doi:10.4103/0973-1296.99285

Gu, Y., Zhou, J., Wang, Q., Fan, W., and Yin, G. (2016). Ginsenoside Rg1 Promotes Osteogenic Differentiation of rBMSCs and Healing of Rat Tibial Fractures through Regulation of GR-dependent BMP-2/SMAD Signaling. *Sci. Rep.* 6, 25282. doi:10.1038/srep25282

Guo, C., Hou, G. Q., Li, X. D., Xia, X., Liu, D. X., Huang, D. Y., et al. (2012). Quercetin Triggers Apoptosis of Lipopolysaccharide (LPS)-induced Osteoclasts and Inhibits Bone Resorption in RAW264.7 Cells. *Cell Physiol Biochem* 30 (1), 123–136. doi:10.1159/000339052

Guo, Z., Bo, D., He, P., Li, H., Wu, G., Li, Z., et al. (2017). Sequential Controlled-Released Dual-Drug Loaded Scaffold for Guided Bone Regeneration in a Rat Fenestration Defect Model. *J. Mater. Chem. B* 5 (37), 7701–7710. doi:10.1039/c7tb00909g

Guo, Z., Wu, S., Li, H., Li, Q., Wu, G., and Zhou, C. (2018). *In Vitro* evaluation of Electrospun PLGA/PLLA/PDLLA Blend Fibers Loaded with Naringin for Guided Bone Regeneration. *Dent Mater. J.* 37 (2), 317–324. doi:10.4012/dmj.2016-220

Gupta, G. K., Kumar, A., Khedgikar, V., Kushwaha, P., Gautam, J., Nagar, G. K., et al. (2013). Osteogenic Efficacy Enhancement of Kaempferol through an Engineered Layer-By-Layer Matrix: a Study in Ovariectomized Rats. *Nanomedicine (Lond)* 8 (5), 757–771. doi:10.2217/nnm.12.171

Gürbüz, K., Yerer, M. B., Gürbüz, P., and Halıcı, M. (2019). Icariin Promotes Early and Late Stages of Fracture Healing in Rats. *Eklem Hastalik Cerrahisi* 30 (3), 282–288. doi:10.5606/ehc.2019.66796

Han, S. Y., and Kim, Y. K. (2019). Berberine Suppresses RANKL-Induced Osteoclast Differentiation by Inhibiting C-Fos and NFATc1 Expression. *Am. J. Chin. Med.* 47 (2), 439–455. doi:10.1142/s0192415x19500228

He, R., Hu, X., Tan, H. C., Feng, J., Steffi, C., Wang, K., et al. (2015). Surface Modification of Titanium with Curcumin: a Promising Strategy to Combat Fibrous Encapsulation. *J. Mater. Chem. B* 3 (10), 2137–2146. doi:10.1039/c4tb01616e

He, X., Andersson, G., Lindgren, U., and Li, Y. (2010). Resveratrol Prevents RANKL-Induced Osteoclast Differentiation of Murine Osteoclast Progenitor RAW 264.7 Cells through Inhibition of ROS Production. *Biochem. Biophys. Res. Commun.* 401 (3), 356–362. doi:10.1016/j.bbrc.2010.09.053

He, X., and Shen, Q. (2014). Salvianolic Acid B Promotes Bone Formation by Increasing Activity of Alkaline Phosphatase in a Rat Tibia Fracture Model: a Pilot Study. *BMC Complement. Altern. Med.* 14, 493. doi:10.1186/1472-6882-14-493

Heo, D. N., Ko, W. K., Moon, H. J., Kim, H. J., Lee, S. J., Lee, J. B., et al. (2014). Inhibition of Osteoclast Differentiation by Gold Nanoparticles Functionalized with Cyclodextrin Curcumin Complexes. *ACS Nano* 8 (12), 12049–12062. doi:10.1021/nn504329u

Hie, M., Yamazaki, M., and Tsukamoto, I. (2009). Curcumin Suppresses Increased Bone Resorption by Inhibiting Osteoclastogenesis in Rats with Streptozotocin-Induced Diabetes. *Eur. J. Pharmacol.* 621 (1-3), 1–9. doi:10.1016/j.ejphar.2009.08.025

Holmes, D. (2017). Non-union Bone Fracture: a Quicker Fix. *Nature* 550 (7677), S193. doi:10.1038/550S193a

Hsieh, T. P., Sheu, S. Y., Sun, J. S., and Chen, M. H. (2011). Icariin Inhibits Osteoclast Differentiation and Bone Resorption by Suppression of MAPKs/NF-Kb Regulated HIF-1α and PGE(2) Synthesis. *Phytomedicine* 18 (2-3), 176–185. doi:10.1016/j.phymed.2010.04.003

Hsu, C. L., and Yen, G. C. (2006). Induction of Cell Apoptosis in 3T3-L1 Pre-adipocytes by Flavonoids Is Associated with Their Antioxidant Activity. *Mol. Nutr. Food Res.* 50 (11), 1072–1079. doi:10.1002/mnfr.200600040

Huang, D., Zuo, Y., Zou, Q., Zhang, L., Li, J., Cheng, L., et al. (2011). Antibacterial Chitosan Coating on Nano-Hydroxyapatite/polyamide66 Porous Bone Scaffold for Drug Delivery. *J. Biomater. Sci. Polym. Ed.* 22 (7), 931–944. doi:10.1163/092050610x496576

Huang, J., Pang, l., Chen, Z., and Tan, X. (2013). Dual-delivery of Vancomycin and Icariin from an Injectable Calcium Phosphate Cement-Release System for Controlling Infection and Improving Bone Healing. *Mol. Med. Rep.* 8 (4), 1221–1227.

Jain, S., Krishna Meka, S. R., and Chatterjee, K. (2016). Curcumin Eluting Nanofibers Augment Osteogenesis toward Phytochemical Based Bone Tissue Engineering. *Biomed. Mater.* 11 (5), 055007. doi:10.1088/1748-6041/11/5/055007

James, A. W., Lachaud, G., Jia, S., Asatrian, G., and Soo, C. (2016). A Review of the Clinical Side Effects of Bone Morphogenetic Protein-2. *Tissue Eng. B Rev.* 22 (4), 284.

Jebahi, S., Saoudi, M., Farhat, L., Oudadesse, H., Rebai, T., Kabir, A., et al. (2015). Effect of Novel Curcumin-Encapsulated Chitosan-Bioglass Drug on Bone and

Skin Repair after Gamma Radiation: Experimental Study on a Wistar Rat Model. *Cell Biochem Funct* 33 (3), 150–159. doi:10.1002/cbf.3098

Ji, C., Bi, L., Li, J., and Fan, J. (2019). Salvianolic Acid B-Loaded Chitosan/hydroxyapatite Scaffolds Promotes the Repair of Segmental Bone Defect by Angiogenesis and Osteogenesis. *Int. J. Nanomedicine* 14, 8271–8284. doi:10.2147/ijn.S219105

Ji, Y., Wang, L., Watts, D. C., Qiu, H., You, T., Deng, F., et al. (2014). Controlled-release Naringin Nanoscaffold for Osteoporotic Bone Healing. *Dent Mater.* 30 (11), 1263–1273. doi:10.1016/j.dental.2014.08.381

Jing, X., Yin, W., Tian, H., Chen, M., Yao, X., Zhu, W., et al. (2018). Icariin Doped Bioactive Glasses Seeded with Rat Adipose-Derived Stem Cells to Promote Bone Repair via Enhanced Osteogenic and Angiogenic Activities. *Life Sci.* 202, 52–60. doi:10.1016/j.lfs.2018.02.026

Kamath, M. S., Ahmed, S. S., Dhanasekaran, M., and Santosh, S. W. (2014). Polycaprolactone Scaffold Engineered for Sustained Release of Resveratrol: Therapeutic Enhancement in Bone Tissue Engineering. *Int. J. Nanomedicine* 9, 183–195. doi:10.2147/ijn.S49460

Karimi-Soflou, R., Mohseni-Vadeghani, E., and Karkhaneh, A. (2021). Controlled Release of Resveratrol from a Composite Nanofibrous Scaffold: Effect of Resveratrol on Antioxidant Activity and Osteogenic Differentiation. *J. Biomed. Mater. Res. A.* doi:10.1002/jbm.a.37262

Keating, J. F., Simpson, A. H., and Robinson, C. M. (2005). The Management of Fractures with Bone Loss. *J. Bone Jt. Surg Br* 87 (2), 142–150. doi:10.1302/0301-620x.87b2.15874

Kheiri Manjili, H., Ghasemi, P., Malvandi, H., Mousavi, M. S., Attari, E., and Danafar, H. (2017). Pharmacokinetics and *In Vivo* Delivery of Curcumin by Copolymeric mPEG-PCL Micelles. *Eur. J. Pharm. Biopharm.* 116, 17–30. doi:10.1016/j.ejpb.2016.10.003

Khha, B., Cyc, A., Cyc, C., Ywccd, E., and Cplab, F. (2021). The Synergistic Effects of Quercetin-Containing 3D-Printed Mesoporous Calcium Silicate/calcium Sulfate/poly-ε-Caprolactone Scaffolds for the Promotion of Osteogenesis in Mesenchymal Stem Cells - ScienceDirect. *J. Formos. Med. Assoc.*

Kim, D. S., Takai, H., Arai, M., Araki, S., Mezawa, M., Kawai, Y., et al. (2007). Effects of Quercetin and Quercetin 3-glucuronide on the Expression of Bone Sialoprotein Gene. *J. Cel Biochem* 101 (3), 790–800. doi:10.1002/jcb.21233

Kim, E. C., Yoon, S. J., Noh, K., and Lee, D. W. (2017). Dual Effect of Curcumin/BMP-2 Loaded in HA/PLL Hydrogels on Osteogenesis *In Vitro* and *In Vivo*. *J. Nanosci Nanotechnol* 17 (1), 143–152. doi:10.1166/jnn.2017.12380

Kim, H. M., Kim, D. H., Han, H. J., Park, C. M., Ganipisetti, S. R., Valan Arasu, M., et al. (2016). Ginsenoside Re Promotes Osteoblast Differentiation in Mouse Osteoblast Precursor MC3T3-E1 Cells and a Zebrafish Model. *Molecules* 22 (1). doi:10.3390/molecules22010042

Kulczyński, B., Gramza-Michałowska, A., Suliburska, J., and Sidor, A. (2021). Puerarin-an Isoflavone with Beneficial Effects on Bone Health. *Front. Biosci. (Landmark Ed.* 26 (12), 1653–1667. doi:10.52586/5058

Kumar, A., Gupta, G. K., Khedgikar, V., Gautam, J., Kushwaha, P., Changkija, B., et al. (2012). *In Vivo* efficacy Studies of Layer-By-Layer Nano-Matrix Bearing Kaempferol for the Conditions of Osteoporosis: a Study in Ovariectomized Rat Model. *Eur. J. Pharm. Biopharm.* 82 (3), 508–517. doi:10.1016/j.ejpb.2012.08.001

Lai, M., Jin, Z., Yan, M., Zhu, J., Yan, X., and Xu, K. (2018a). The Controlled Naringin Release from TiO(2) Nanotubes to Regulate Osteoblast Differentiation. *J. Biomater. Appl.* 33 (5), 673–680. doi:10.1177/0885328218809239

Lai, Y., Cao, H., Wang, X., Chen, S., Zhang, M., Wang, N., et al. (2018b). Porous Composite Scaffold Incorporating Osteogenic Phytomolecule Icariin for Promoting Skeletal Regeneration in Challenging Osteonecrotic Bone in Rabbits. *Biomaterials* 153, 1–13. doi:10.1016/j.biomaterials.2017.10.025

Lavrador, P., Gaspar, V. M., and Mano, J. F. (2018). Bioinstructive Naringin-Loaded Micelles for Guiding Stem Cell Osteodifferentiation. *Adv. Healthc. Mater.* 7 (19), e1800890. doi:10.1002/adhm.201800890

Lay, I. S., Chiu, J. H., Shiao, M. S., Lui, W. Y., and Wu, C. W. (2003). Crude Extract of Salvia Miltiorrhiza and Salvianolic Acid B Enhance *In Vitro* Angiogenesis in Murine SVR Endothelial Cell Line. *Planta Med.* 69 (1), 26–32. doi:10.1055/s-2003-37034

Lee, H., Nguyen, T. T., Kim, M., Jeong, J. H., and Park, J. B. (2018). The Effects of Biodegradable Poly(lactic-co-glycolic Acid)-based Microspheres Loaded with Quercetin on Stemness, Viability and Osteogenic Differentiation Potential of Stem Cell Spheroids. *J. Periodontal Res.* 53.

Lee, S. U., Park, S. J., Kwak, H. B., Oh, J., Min, Y. K., and Kim, S. H. (2008). Anabolic Activity of Ursolic Acid in Bone: Stimulating Osteoblast Differentiation *In Vitro* and Inducing New Bone Formation *In Vivo*. *Pharmacol. Res.* 58 (5-6), 290–296. doi:10.1016/j.phrs.2008.08.008

Lee, W. S., Lee, E. G., Sung, M. S., and Yoo, W. H. (2014). Kaempferol Inhibits IL-1β-stimulated, RANKL-Mediated Osteoclastogenesis via Downregulation of MAPKs, C-Fos, and NFATc1. *Inflammation* 37 (4), 1221–1230. doi:10.1007/s10753-014-9849-6

Li, C. H., Wang, J. W., Ho, M. H., Shih, J. L., Hsiao, S. W., and Thien, D. V. (2014a). Immobilization of Naringin onto Chitosan Substrates by Using Ozone Activation. *Colloids Surf. B Biointerfaces* 115, 1–7. doi:10.1016/j.colsurfb.2013.11.006

Li, D., Nie, W., Chen, L., Miao, Y., Zhang, X., Chen, F., et al. (2017a). Fabrication of Curcumin-Loaded Mesoporous Silica Incorporated Polyvinyl Pyrrolidone Nanofibers for Rapid Hemostasis and Antibacterial Treatment. *Rsc Adv.* 7 (13), 7973–7982.

Li, F., Sun, X., Ma, J., Ma, X., Zhao, B., Zhang, Y., et al. (2014b). Naringin Prevents Ovariectomy-Induced Osteoporosis and Promotes Osteoclasts Apoptosis through the Mitochondria-Mediated Apoptosis Pathway. *Biochem. Biophys. Res. Commun.* 452 (3), 629–635. doi:10.1016/j.bbrc.2014.08.117

Li, J., Wang, Q., Zhi, W., Wang, J., Feng, B., Qu, S., et al. (2016). Immobilization of Salvianolic Acid B-Loaded Chitosan Microspheres Distributed Three-Dimensionally and Homogeneously on the Porous Surface of Hydroxyapatite Scaffolds. *Biomed. Mater.* 11 (5), 055014. doi:10.1088/1748-6041/11/5/055014

Li, L., Yu, M., Li, Y., Li, Q., Yang, H., Zheng, M., et al. (2021). Synergistic Anti-inflammatory and Osteogenic N-HA/resveratrol/chitosan Composite Microspheres for Osteoporotic Bone Regeneration. *Bioact Mater.* 6 (5), 1255–1266. doi:10.1016/j.bioactmat.2020.10.018

Li, M., Gu, Q., Chen, M., Zhang, C., Chen, S., and Zhao, J. (2017b). Controlled Delivery of Icariin on Small Intestine Submucosa for Bone Tissue Engineering. *Mater. Sci. Eng. C Mater. Biol. Appl.* 71, 260–267. doi:10.1016/j.msec.2016.10.016

Li, X., Chen, Y., Mao, Y., Dai, P., Sun, X., Zhang, X., et al. (2020). Curcumin Protects Osteoblasts from Oxidative Stress-Induced Dysfunction via GSK3β-Nrf2 Signaling Pathway. *Front. Bioeng. Biotechnol.* 8, 625. doi:10.3389/fbioe.2020.00625

Li, Y., Dånmark, S., Edlund, U., Finne-Wistrand, A., He, X., Norgård, M., et al. (2011). Resveratrol-conjugated Poly-ε-Caprolactone Facilitates *In Vitro* Mineralization and *In Vivo* Bone Regeneration. *Acta Biomater.* 7 (2), 751–758. doi:10.1016/j.actbio.2010.09.008

Li, Y., and Zhang, Z. Z. (2018). Sustained Curcumin Release from PLGA Microspheres Improves Bone Formation under Diabetic Conditions by Inhibiting the Reactive Oxygen Species Production. *Drug Des. Devel Ther.* 12, 1453–1466. doi:10.2147/dddt.S154334

Liang, Z., Xue, Y., Wang, T., Xie, Q., Lin, J., and Wang, Y. (2020). Curcumin Inhibits the Migration of Osteoclast Precursors and Osteoclastogenesis by Repressing CCL3 Production. *BMC Complement. Med. Ther.* 20 (1), 234. doi:10.1186/s12906-020-03014-2

Lin, F. X., Du, S. X., Liu, D. Z., Hu, Q. X., Yu, G. Y., Wu, C. C., et al. (2016). Naringin Promotes Osteogenic Differentiation of Bone Marrow Stromal Cells by Up-Regulating Foxc2 Expression via the IHH Signaling Pathway. *Am. J. Transl Res.* 8 (11), 5098–5107.

Lin, S., Cui, L., Chen, G., Huang, J., Yang, Y., Zou, K., et al. (2019). PLGA/β-TCP Composite Scaffold Incorporating Salvianolic Acid B Promotes Bone Fusion by Angiogenesis and Osteogenesis in a Rat Spinal Fusion Model. *Biomaterials* 196, 109–121. doi:10.1016/j.biomaterials.2018.04.004

Liu, C. S., Zheng, Y. R., Zhang, Y. F., and Long, X. Y. (2016). Research Progress on Berberine with a Special Focus on its Oral Bioavailability. *Fitoterapia* 109, 274–282. doi:10.1016/j.fitote.2016.02.001

Liu, H., Yi, X., Tu, S., Cheng, C., and Luo, J. (2021). Kaempferol Promotes BMSC Osteogenic Differentiation and Improves Osteoporosis by Downregulating miR-10a-3p and Upregulating CXCL12. *Mol. Cel Endocrinol* 520, 111074. doi:10.1016/j.mce.2020.111074

Liu, M., Li, Y., and Yang, S. T. (2017). Effects of Naringin on the Proliferation and Osteogenic Differentiation of Human Amniotic Fluid-Derived Stem Cells. *J. Tissue Eng. Regen. Med.* 11 (1), 276–284. doi:10.1002/term.1911

Liu, Y., Jia, Z., Akhter, M. P., Gao, X., Wang, X., Wang, X., et al. (2018). Bone-targeting Liposome Formulation of Salvianic Acid A Accelerates the Healing of Delayed Fracture Union in Mice. *Nanomedicine* 14 (7), 2271–2282. doi:10.1016/j.nano.2018.07.011

Luo, P., Yu, L., Lin, Q., Wang, C., Yang, D., and Tang, S. (2020). Strontium Modified Calcium Sulfate Hemihydrate Scaffold Incorporating Ginsenoside Rg1/Gelatin Microspheres for Bone Regeneration. *Front. Bioeng. Biotechnol.* 8, 888. doi:10.3389/fbioe.2020.00888

Ma, B., Guan, G., Lv, Q., and Yang, L. (2021a). Curcumin Ameliorates Palmitic Acid-Induced Saos-2 Cell Apoptosis via Inhibiting Oxidative Stress and Autophagy. *Evid. Based Complement. Alternat Med.* 2021, 5563660. doi:10.1155/2021/5563660

Ma, H., Li, T., Huan, Z., Zhang, M., Yang, Z., Wang, J., et al. (2018). 3D Printing of High-Strength Bioscaffolds for the Synergistic Treatment of Bone Cancer. *Npg Asia Mater.*

Ma, L., Yu, Y., Liu, H., Sun, W., Lin, Z., Liu, C., et al. (2021b). Berberine-releasing Electrospun Scaffold Induces Osteogenic Differentiation of DPSCs and Accelerates Bone Repair. *Sci. Rep.* 11 (1), 1027. doi:10.1038/s41598-020-79734-9

Martin, V., and Bettencourt, A. (2018). Bone Regeneration: Biomaterials as Local Delivery Systems with Improved Osteoinductive Properties. *Mater. Sci. Eng. C Mater. Biol. Appl.* 82, 363–371. doi:10.1016/j.msec.2017.04.038

Messer, J. G., Hopkins, R. G., and Kipp, D. E. (2015). Quercetin Metabolites Up-Regulate the Antioxidant Response in Osteoblasts Isolated from Fetal Rat Calvaria. *J. Cel Biochem* 116 (9), 1857–1866. doi:10.1002/jcb.25141

Messer, J. G., La, S., Hopkins, R. G., and Kipp, D. E. (2016). Quercetin Partially Preserves Development of Osteoblast Phenotype in Fetal Rat Calvaria Cells in an Oxidative Stress Environment. *J. Cel Physiol* 231 (12), 2779–2788. doi:10.1002/jcp.25392

Mizutani, K., Ikeda, K., Kawai, Y., and Yamori, Y. (2000). Resveratrol Attenuates Ovariectomy-Induced Hypertension and Bone Loss in Stroke-Prone Spontaneously Hypertensive Rats. *J. Nutr. Sci. Vitaminol (Tokyo)* 46 (2), 78–83. doi:10.3177/jnsv.46.78

Mizutani, K., Ikeda, K., Kawai, Y., and Yamori, Y. (1998). Resveratrol Stimulates the Proliferation and Differentiation of Osteoblastic MC3T3-E1 Cells. *Biochem. Biophys. Res. Commun.* 253 (3), 859–863. doi:10.1006/bbrc.1998.9870

Muthukumar, T., Aravinthan, A., Sharmila, J., Kim, N. S., and Kim, J. H. (2016). Collagen/chitosan Porous Bone Tissue Engineering Composite Scaffold Incorporated with Ginseng Compound K. *Carbohydr. Polym.* 152, 566–574. doi:10.1016/j.carbpol.2016.07.003

Naeini, M. B., Momtazi, A. A., Jaafari, M. R., Johnston, T. P., Barreto, G., Banach, M., et al. (2019). Antitumor Effects of Curcumin: A Lipid Perspective. *J. Cel Physiol.* doi:10.1002/jcp.28262

Nian, H., Ma, M. H., Nian, S. S., and Xu, L. L. (2009). Antiosteoporotic Activity of Icariin in Ovariectomized Rats. *Phytomedicine* 16 (4), 320–326.

Orellana, B. R., Thomas, M. V., Dziubla, T. D., Shah, N. M., Hilt, J. Z., and Puleo, D. A. (2013). Bioerodible Calcium Sulfate/poly(β-Amino Ester) Hydrogel Composites. *J. Mech. Behav. Biomed. Mater.* 26, 43–53. doi:10.1016/j.jmbbm.2013.05.021

Ozaki, K., Kawata, Y., Amano, S., and Hanazawa, S. (2000). Stimulatory Effect of Curcumin on Osteoclast Apoptosis. *Biochem. Pharmacol.* 59 (12), 1577–1581. doi:10.1016/s0006-2952(00)00277-x

Pang, W. Y., Wang, X. L., Mok, S. K., Lai, W. P., Chow, H. K., Leung, P. C., et al. (2010). Naringin Improves Bone Properties in Ovariectomized Mice and Exerts Oestrogen-like Activities in Rat Osteoblast-like (UMR-106) Cells. *Br. J. Pharmacol.* 159 (8), 1693–1703. doi:10.1111/j.1476-5381.2010.00664.x

Park, K. H., Gu, D. R., Jin, S. H., Yoon, C. S., Ko, W., Kim, Y. C., et al. (2017). Pueraria Lobate Inhibits RANKL-Mediated Osteoclastogenesis via Downregulation of CREB/PGC1β/c-Fos/NFATc1 Signaling. *Am. J. Chin. Med.* 45 (8), 1725–1744. doi:10.1142/s0192415x17500938

Patel, A. R., Heussen, P. C., Hazekamp, J., Drost, E., and Velikov, K. P. (2012). Quercetin Loaded Biopolymeric Colloidal Particles Prepared by Simultaneous Precipitation of Quercetin with Hydrophobic Protein in Aqueous Medium. *Food Chem.* 133 (2), 423–429. doi:10.1016/j.foodchem.2012.01.054

Peng, H., Xiong, H., Li, J., Xie, M., Liu, Y., Bai, C., et al. (2010). Vanillin Cross-Linked Chitosan Microspheres for Controlled Release of Resveratrol. *Food Chem.* 121 (1), 23–28.

Peng, M., Qiang, L., Xu, Y., Li, C., Li, T., and Wang, J. (2018). Modification of Cysteine 179 in IKKβ by Ursolic Acid Inhibits Titanium-Wear-Particle-Induced Inflammation, Osteoclastogenesis, and Hydroxylapatite Resorption. *Mol. Pharm.* 15 (11), 5244–5251. doi:10.1021/acs.molpharmaceut.8b00747

Pino, D. S., Casarin, R. C., Pimentel, S. P., Cirano, F. R., Corrêa, M. G., and Ribeiro, F. V. (2017). Effect of Resveratrol on Critical-Sized Calvarial Defects of Diabetic Rats: Histometric and Gene Expression Analysis. *J. Oral Maxillofac. Surg.* 75 (12), 2561. e2510. doi:10.1016/j.joms.2017.07.167

Preeth, D. R., Saravanan, S., Shairam, M., Selvakumar, N., and Rajalakshmi, S. (2021). Bioactive Zinc(II) Complex Incorporated PCL/gelatin Electrospun Nanofiber Enhanced Bone Tissue Regeneration. *Eur. J. Pharm. Sci.* 160 (90), 105768.

Prouillet, C., Mazière, J. C., Mazière, C., Wattel, A., Brazier, M., and Kamel, S. (2004). Stimulatory Effect of Naturally Occurring Flavonols Quercetin and Kaempferol on Alkaline Phosphatase Activity in MG-63 Human Osteoblasts through ERK and Estrogen Receptor Pathway. *Biochem. Pharmacol.* 67 (7), 1307–1313. doi:10.1016/j.bcp.2003.11.009

Raja, N., Park, H., Choi, Y. J., and Yun, H. S. (2021). Multifunctional Calcium-Deficient Hydroxyl Apatite-Alginate Core-Shell-Structured Bone Substitutes as Cell and Drug Delivery Vehicles for Bone Tissue Regeneration. *ACS Biomater. Sci. Eng.* 7 (3), 1123–1133. doi:10.1021/acsbiomaterials.0c01341

Ranjbar, F. E., Foroutan, F., Hajian, M., Ai, J., Farsinejad, A., Ebrahimi-Barough, S., et al. (2021). Preparation and Characterization of 58S Bioactive Glass Based Scaffold with Kaempferol-Containing Zein Coating for Bone Tissue Engineering. *J. Biomed. Mater. Res. B Appl. Biomater.* 109 (9), 1259–1270. doi:10.1002/jbm.b.34786

Reiter, T., Panick, T., Schuhladen, K., Roether, J. A., Hum, J., and Boccaccini, A. R. (2019). Bioactive Glass Based Scaffolds Coated with Gelatin for the Sustained Release of Icariin. *Bioact Mater.* 4 (1), 1–7. doi:10.1016/j.bioactmat.2018.10.001

Riccitiello, F., De Luise, A., Conte, R. D., Aniello, S., Vittoria, V., Di Salle, A., et al. (2017). Effect of Resveratrol Release Kinetic from Electrospun Nanofibers on Osteoblast and Osteoclast Differentiation. *Eur. Polym. J.* 99, 289–297.

Roddy, E., DeBaun, M. R., Daoud-Gray, A., Yang, Y. P., and Gardner, M. J. (2018). Treatment of Critical-Sized Bone Defects: Clinical and Tissue Engineering Perspectives. *Eur. J. Orthop. Surg. Traumatol.* 28 (3), 351–362. doi:10.1007/s00590-017-2063-0

Rutledge, K. E., Cheng, Q., and Jabbarzadeh, E. (2016). Modulation of Inflammatory Response and Induction of Bone Formation Based on Combinatorial Effects of Resveratrol. *J. Nanomed Nanotechnol* 7 (1). doi:10.4172/2157-7439.1000350

Salarian, M., Samimi, R., Xu, W. Z., Wang, Z., Sham, T. K., Lui, E. M. K., et al. (2016). Microfluidic Synthesis and Angiogenic Activity of Ginsenoside Rg(1)-Loaded PPF Microspheres. *ACS Biomater. Sci. Eng.* 2 (11), 1872–1882. doi:10.1021/acsbiomaterials.6b00222

Sarkar, N., and Bose, S. (2020). Controlled Delivery of Curcumin and Vitamin K2 from Hydroxyapatite-Coated Titanium Implant for Enhanced *In Vitro* Chemoprevention, Osteogenesis, and *In Vivo* Osseointegration. *ACS Appl. Mater. Inter.* 12 (12), 13644–13656. doi:10.1021/acsami.9b22474

Sarkar, N., and Bose, S. (2019). Liposome-Encapsulated Curcumin-Loaded 3D Printed Scaffold for Bone Tissue Engineering. *ACS Appl. Mater. Inter.* 11 (19), 17184–17192. doi:10.1021/acsami.9b01218

Scharstuhl, A., Mutsaers, H. A., Pennings, S. W., Szarek, W. A., Russel, F. G., and Wagener, F. A. (2009). Curcumin-induced Fibroblast Apoptosis and *In Vitro* Wound Contraction Are Regulated by Antioxidants and Heme Oxygenase: Implications for Scar Formation. *J. Cel Mol Med* 13 (4), 712–725. doi:10.1111/j.1582-4934.2008.00339.x

Shakibaei, M., Shayan, P., Busch, F., Aldinger, C., Buhrmann, C., Lueders, C., et al. (2012). Resveratrol Mediated Modulation of Sirt-1/Runx2 Promotes Osteogenic Differentiation of Mesenchymal Stem Cells: Potential Role of Runx2 Deacetylation. *PLoS One* 7 (4), e35712. doi:10.1371/journal.pone.0035712

Shao, Y., You, D., Lou, Y., Li, J., Ying, B., Cheng, K., et al. (2019). Controlled Release of Naringin in GelMA-Incorporated Rutile Nanorod Films to Regulate Osteogenic Differentiation of Mesenchymal Stem Cells. *ACS Omega* 4 (21), 19350–19357. doi:10.1021/acsomega.9b02751

Sharma, A. R., and Nam, J. S. (2019). Kaempferol Stimulates WNT/β-catenin Signaling Pathway to Induce Differentiation of Osteoblasts. *J. Nutr. Biochem.* 74, 108228. doi:10.1016/j.jnutbio.2019.108228

Shen, K., Zhang, X., Tang, Q., Fang, X., Zhang, C., Zhu, Z., et al. (2021). Microstructured Titanium Functionalized by Naringin Inserted Multilayers for Promoting Osteogenesis and Inhibiting Osteoclastogenesis. *J. Biomater. Sci. Polym. Ed.*, 1–17. doi:10.1080/09205063.2021.1949098

Siddiqi, M. H., Siddiqi, M. Z., Ahn, S., Kim, Y. J., and Yang, D. C. (2014). Ginsenoside Rh1 Induces Mouse Osteoblast Growth and Differentiation through the Bone Morphogenetic Protein 2/runt-Related Gene 2 Signalling Pathway. *J. Pharm. Pharmacol.* 66 (12), 1763–1773. doi:10.1111/jphp.12306

Son, H. E., Kim, E. J., and Jang, W. G. (2018). Curcumin Induces Osteoblast Differentiation through Mild-Endoplasmic Reticulum Stress-Mediated Such as BMP2 on Osteoblast Cells. *Life Sci.* 193, 34–39. doi:10.1016/j.lfs.2017.12.008

Song, J. E., Tian, J., Kook, Y. J., Thangavelu, M., and Khang, G. (2020). A BMSCs-laden Quercetin/duck's Feet Collagen/hydroxyapatite Sponge for Enhanced Bone Regeneration. *J. Biomed. Mater. Res. A* 108 (3).

Song, J. E., Tripathy, N., Lee, D. H., Park, J. H., and Khang, G. (2018a). Quercetin Inlaid Silk Fibroin/Hydroxyapatite Scaffold Promotes Enhanced Osteogenesis. *ACS Appl. Mater. Inter.* 10 (39), 32955–32964. doi:10.1021/acsami.8b08119

Song, L., Zhao, J., Zhang, X., Li, H., and Zhou, Y. (2013a). Icariin Induces Osteoblast Proliferation, Differentiation and Mineralization through Estrogen Receptor-Mediated ERK and JNK Signal Activation. *Eur. J. Pharmacol.* 714 (1-3), 15–22.

Song, L., Zhao, J., Zhang, X., Li, H., and Zhou, Y. (2013b). Icariin Induces Osteoblast Proliferation, Differentiation and Mineralization through Estrogen Receptor-Mediated ERK and JNK Signal Activation. *Eur. J. Pharmacol.* 714 (1-3), 15–22. doi:10.1016/j.ejphar.2013.05.039

Song, Y., Ma, A., Ning, J., Zhong, X., Zhang, Q., Zhang, X., et al. (2018b). Loading Icariin on Titanium Surfaces by Phase-Transited Lysozyme Priming and Layer-By-Layer Self-Assembly of Hyaluronic Acid/chitosan to Improve Surface Osteogenesis Ability. *Int. J. Nanomedicine* 13, 6751–6767. doi:10.2147/ijn.S174953

Soundarya, S. P., Sanjay, V., Menon, A. H., Dhivya, S., and Selvamurugan, N. (2017). Effects of Flavonoids Incorporated Biological Macromolecules Based Scaffolds in Bone Tissue Engineering. *Int. J. Biol. Macromolecules*, S0141813017321876.

Srivastava, S., Bankar, R., and Roy, P. (2013). Assessment of the Role of Flavonoids for Inducing Osteoblast Differentiation in Isolated Mouse Bone Marrow Derived Mesenchymal Stem Cells. *Phytomedicine* 20 (8-9), 683–690. doi:10.1016/j.phymed.2013.03.001

Su, J. L., Yang, C. Y., Zhao, M., Kuo, M. L., and Yen, M. L. (2007). Forkhead Proteins Are Critical for Bone Morphogenetic Protein-2 Regulation and Anti-tumor Activity of Resveratrol. *J. Biol. Chem.* 282 (27), 19385–19398. doi:10.1074/jbc.M702452200

Sujitha, S., and Rasool, M. (2019). Berberine Coated Mannosylated Liposomes Curtail RANKL Stimulated Osteoclastogenesis through the Modulation of GSK3β Pathway via Upregulating miR-23a. *Int. Immunopharmacol* 74, 105703. doi:10.1016/j.intimp.2019.105703

Tan, B., Wu, Y., Wu, Y., Shi, K., Han, R., Li, Y., et al. (2021). Curcumin-Microsphere/IR820 Hybrid Bifunctional Hydrogels for *In Situ* Osteosarcoma Chemo-Co-Thermal Therapy and Bone Reconstruction. *ACS Appl. Mater. Inter.* 13 (27), 31542–31553. doi:10.1021/acsami.1c08775

Tan, H., Zhao, C., Zhu, Q., Katakura, Y., Tanaka, H., Ohnuki, K., et al. (2019). Ursolic Acid Isolated from the Leaves of Loquat (Eriobotrya Japonica) Inhibited Osteoclast Differentiation through Targeting Exportin 5. *J. Agric. Food Chem.* 67 (12), 3333–3340. doi:10.1021/acs.jafc.8b06954

Tang, D., Tare, R. S., Yang, L. Y., Williams, D. F., Ou, K. L., and Oreffo, R. O. (2016). Biofabrication of Bone Tissue: Approaches, Challenges and Translation for Bone Regeneration. *Biomaterials* 83, 363–382. doi:10.1016/j.biomaterials.2016.01.024

Tang, H., Hosein, A., and Mattioli-Belmonte, M. (2021). Traditional Chinese Medicine and Orthopedic Biomaterials: Host of Opportunities from Herbal Extracts. *Mater. Sci. Eng. C Mater. Biol. Appl.* 120, 111760. doi:10.1016/j.msec.2020.111760

Tang, Y., Jacobi, A., Vater, C., Zou, X., and Stiehler, M. (2014). Salvianolic Acid B Protects Human Endothelial Progenitor Cells against Oxidative Stress-Mediated Dysfunction by Modulating Akt/mTOR/4EBP1, P38 MAPK/ATF2, and ERK1/2 Signaling Pathways. *Biochem. Pharmacol.* 90 (1), 34–49. doi:10.1016/j.bcp.2014.04.008

Tao, K., Xiao, D., Weng, J., Xiong, A., Kang, B., and Zeng, H. (2016). Berberine Promotes Bone Marrow-Derived Mesenchymal Stem Cells Osteogenic Differentiation via Canonical Wnt/β-Catenin Signaling Pathway. *Toxicol. Lett.* 240 (1), 68–80. doi:10.1016/j.toxlet.2015.10.007

Teskac, K., and Kristl, J. (2010). The Evidence for Solid Lipid Nanoparticles Mediated Cell Uptake of Resveratrol. *Int. J. Pharm.* 390 (1), 61–69. doi:10.1016/j.ijpharm.2009.10.011

Thangavelu, M., Adithan, A., John Peter, J. S., Hossain, M. A., Kim, N. S., Hwang, K. C., et al. (2020). Ginseng Compound K Incorporated Porous Chitosan/biphasic Calcium Phosphate Composite Microsphere for Bone Regeneration. *Int. J. Biol. Macromol* 146, 1024–1029. doi:10.1016/j.ijbiomac.2019.09.228

Tripathi, G., Raja, N., and Yun, H. S. (2015). Effect of Direct Loading of Phytoestrogens into the Calcium Phosphate Scaffold on Osteoporotic Bone Tissue Regeneration. *J. Mater. Chem. B* 3 (44), 8694–8703. doi:10.1039/c5tb01574j

Tseng, P. C., Hou, S. M., Chen, R. J., Peng, H. W., Hsieh, C. F., Kuo, M. L., et al. (2011). Resveratrol Promotes Osteogenesis of Human Mesenchymal Stem Cells by Upregulating RUNX2 Gene Expression via the SIRT1/FOXO3A axis. *J. Bone Miner Res.* 26 (10), 2552–2563. doi:10.1002/jbmr.460

Tsuchiya, S., Sugimoto, K., Kamio, H., Okabe, K., Kuroda, K., Okido, M., et al. (2018). Kaempferol-immobilized Titanium Dioxide Promotes Formation of New Bone: Effects of Loading Methods on Bone Marrow Stromal Cell Differentiation *In Vivo* and *In Vitro*. *Int. J. Nanomedicine* 13, 1665–1676. doi:10.2147/ijn.S150786

Tsui, V. W., Wong, R. W., and Rabie, A. B. (2008). The Inhibitory Effects of Naringin on the Growth of Periodontal Pathogens *In Vitro*. *Phytother Res.* 22 (3), 401–406. doi:10.1002/ptr.2338

Verma, A. H., Kumar, T. S. S., Madhumathi, K., Rubaiya, Y., Ramalingan, M., and Doble, M. (2019). Curcumin Releasing Eggshell Derived Carbonated Apatite Nanocarriers for Combined Anti-cancer, Anti-inflammatory and Bone Regenerative Therapy. *J. Nanosci Nanotechnol* 19 (11), 6872–6880. doi:10.1166/jnn.2019.16640

Vimalraj, S., Rajalakshmi, S., Raj Preeth, D., Vinoth Kumar, S., Deepak, T., Gopinath, V., et al. (2018). Mixed-ligand Copper(II) Complex of Quercetin Regulate Osteogenesis and Angiogenesis. *Mater. Sci. Eng. C Mater. Biol. Appl.* 83, 187–194. doi:10.1016/j.msec.2017.09.005

Wang, C. C., Wang, C. H., Chen, H. C., Cherng, J. H., Chang, S. J., Wang, Y. W., et al. (2018). Combination of Resveratrol-Containing Collagen with Adipose Stem Cells for Craniofacial Tissue-Engineering Applications. *Int. Wound J.* 15 (4), 660–672. doi:10.1111/iwj.12910

Wang, D., Ma, W., Wang, F., Dong, J., Wang, D., Sun, B., et al. (2015a). Stimulation of Wnt/β-Catenin Signaling to Improve Bone Development by Naringin via Interacting with AMPK and Akt. *Cel Physiol Biochem* 36 (4), 1563–1576. doi:10.1159/000430319

Wang, D., Zhang, P., Mei, X., and Chen, Z. (2021). Repair Calvarial Defect of Osteoporotic Rats by Berberine Functionalized Porous Calcium Phosphate Scaffold. *Regen. Biomater.* 8 (3), rbab022. doi:10.1093/rb/rbab022

Wang, F. F., Li, Y., and Liu, H. C. (2019). A Study on PLGA Sustained Release Icariin/titanium Dioxide Nanotube Composite Coating. *Eur. Rev. Med. Pharmacol. Sci.* 23 (3), 911–917. doi:10.26355/eurrev_201902_16974

Wang, F., Yang, Z., He, W., Song, Q., Wang, K., and Zhou, Y. (2020a). Effects of Icariin on the Proliferation and Osteogenic Differentiation of Human Amniotic Mesenchymal Stem Cells. *J. Orthop. Surg. Res.* 15 (1), 578. doi:10.1186/s13018-020-02076-9

Wang, H., Li, C., Li, J., Zhu, Y., Jia, Y., Zhang, Y., et al. (2017). Naringin Enhances Osteogenic Differentiation through the Activation of ERK Signaling in Human Bone Marrow Mesenchymal Stem Cells. *Iran J. Basic Med. Sci.* 20 (4), 408–414. doi:10.22038/ijbms.2017.8582

Wang, W., Liu, Y., Yang, C., Jia, W., and Li, X. (2020b). Delivery of Salvianolic Acid B for Efficient Osteogenesis and Angiogenesis from Silk Fibroin Combined with Graphene Oxide. *ACS Biomater. Sci. Eng.* 6 (6), 3539–3549. doi:10.1021/acsbiomaterials.0c00558

Wang, W. L., Sheu, S. Y., Chen, Y. S., Kao, S. T., Fu, Y. T., Kuo, T. F., et al. (2015b). Enhanced Bone Tissue Regeneration by Porous Gelatin Composites Loaded

with the Chinese Herbal Decoction Danggui Buxue Tang. *PLoS One* 10 (6), e0131999. doi:10.1371/journal.pone.0131999

Wattel, A., Kamel, S., Prouillet, C., Petit, J. P., Lorget, F., Offord, E., et al. (2004). Flavonoid Quercetin Decreases Osteoclastic Differentiation Induced by RANKL via a Mechanism Involving NF Kappa B and AP-1. *J. Cel Biochem* 92 (2), 285–295. doi:10.1002/jcb.20071

Wei, B., Wang, W., Liu, X., Xu, C., Wang, Y., Wang, Z., et al. (2021). Gelatin Methacrylate Hydrogel Scaffold Carrying Resveratrol-Loaded Solid Lipid Nanoparticles for Enhancement of Osteogenic Differentiation of BMSCs and Effective Bone Regeneration. *Regen. Biomater.* 8 (5), rbab044. doi:10.1093/rb/rbab044

Wei, Q., Zhang, J., Hong, G., Chen, Z., Deng, W., He, W., et al. (2016). Icariin Promotes Osteogenic Differentiation of Rat Bone Marrow Stromal Cells by Activating the ERα-Wnt/β-Catenin Signaling Pathway. *Biomed. Pharmacother.* 84, 931–939. doi:10.1016/j.biopha.2016.09.107

Wong, K. C., Pang, W. Y., Wang, X. L., Mok, S. K., Lai, W. P., Chow, H. K., et al. (2013). Drynaria Fortunei-Derived Total Flavonoid Fraction and Isolated Compounds Exert Oestrogen-like Protective Effects in Bone. *Br. J. Nutr.* 110 (3), 475–485. doi:10.1017/s0007114512005405

Wong, R., and Rabie, B. (2007). Effect of Puerarin on Bone Formation. *Osteoarthritis Cartilage* 15 (8), 894–899. doi:10.1016/j.joca.2007.02.009

Wong, R. W., and Rabie, A. B. (2006). Effect of Naringin Collagen Graft on Bone Formation. *Biomaterials* 27 (9), 1824–1831. doi:10.1016/j.biomaterials.2005.11.009

Wong, R. W., and Rabie, A. B. (2008). Effect of Quercetin on Preosteoblasts and Bone Defects. *Open Orthop. J.* 2, 27–32. doi:10.2174/1874325000802010027

Woo, J. T., Nakagawa, H., Notoya, M., Yonezawa, T., Udagawa, N., Lee, I. S., et al. (2004). Quercetin Suppresses Bone Resorption by Inhibiting the Differentiation and Activation of Osteoclasts. *Biol. Pharm. Bull.* 27 (4), 504–509. doi:10.1248/bpb.27.504

Wu, J. B., Fong, Y. C., Tsai, H. Y., Chen, Y. F., Tsuzuki, M., and Tang, C. H. (2008). Naringin-induced Bone Morphogenetic Protein-2 Expression via PI3K, Akt, C-Fos/c-Jun and AP-1 Pathway in Osteoblasts. *Eur. J. Pharmacol.* 588 (2-3), 333–341. doi:10.1016/j.ejphar.2008.04.030

Wu, L., Wei, Z., He, S., Bi, Y., Cao, Y., and Wang, W. (2021). Mesoporous Bioactive Glass Scaffold Delivers Salvianolic Acid B to Promote Bone Regeneration in a Rat Cranial Defect Model. *Curr. Drug Deliv.* 18 (3), 323–333. doi:10.2174/1567201817666200916091253

Wu, T., Nan, K. H., Chen, J. D., Jin, D., Jiang, S., Zhao, P. R., et al. (2009). A New Bone Repair Scaffold Combined with Chitosan/hydroxyapatite and Sustained Releasing Icariin. *Chin. Sci. Bull.*

Wu, Y., Cao, L., Xia, L., Wu, Q., Wang, J., Wang, X., et al. (2017). Evaluation of Osteogenesis and Angiogenesis of Icariin in Local Controlled Release and Systemic Delivery for Calvarial Defect in Ovariectomized Rats. *Sci. Rep.* 7 (1), 5077. doi:10.1038/s41598-017-05392-z

Xia, L., Li, Y., Zheng, Z., Yao, D., Liu, H., and Liu, H. (2013). Icariin Delivery Porous PHBV Scaffolds for Promoting Osteoblast Expansion *In Vitro*. *Mater. Sci. Eng. C Mater. Biol. Appl.* 33 (6), 3545–3552.

Xie, Y., Sun, W., Yan, F., Liu, H., and Cai, L. (2019). Icariin-loaded Porous Scaffolds for Bone Regeneration through the Regulation of the Coupling Process of Osteogenesis and Osteoclastic Activity. *Int. J. Nanomedicine* 14, 6019–6033.

Xu, D., Xu, L., Zhou, C., Lee, W. Y., Wu, T., Cui, L., et al. (2014). Salvianolic Acid B Promotes Osteogenesis of Human Mesenchymal Stem Cells through Activating ERK Signaling Pathway. *Int. J. Biochem. Cel Biol* 51, 1–9. doi:10.1016/j.biocel.2014.03.005

Xue, L., Jiang, Y., Han, T., Zhang, N., Qin, L., Xin, H., et al. (2016). Comparative Proteomic and Metabolomic Analysis Reveal the Antiosteoporotic Molecular Mechanism of Icariin from Epimedium Brevicornu Maxim. *J. Ethnopharmacol* 192, 370–381. doi:10.1016/j.jep.2016.07.037

Yang, B., Sun, H., Xu, X., Zhong, H., Wu, Y., and Wang, J. (2020a). YAP1 Inhibits the Induction of TNF-α-Stimulated Bone-Resorbing Mediators by Suppressing the NF-Kb Signaling Pathway in MC3T3-E1 Cells. *J. Cel Physiol* 235 (5), 4698–4708. doi:10.1002/jcp.29348

Yang, F., Zhang, R., He, F., Wang, X. X., Zhao, S., and Yang, G. (2012a). Osteoblast Response to Puerarin-Loaded Porous Titanium Surfaces: an *In Vitro* Study. *J. Biomed. Mater. Res. A.* 100 (6), 1419–1426. doi:10.1002/jbm.a.34080

Yang, N., Liu, D., Zhang, X., Li, J., Wang, M., Xu, T., et al. (2020b). Effects of Ginsenosides on Bone Remodelling for Novel Drug Applications: a Review. *Chin. Med.* 15, 42. doi:10.1186/s13020-020-00323-z

Yang, W., Yu, X. C., Chen, X. Y., Zhang, L., Lu, C. T., and Zhao, Y. Z. (2012b). Pharmacokinetics and Tissue Distribution Profile of Icariin Propylene Glycol-Liposome Intraperitoneal Injection in Mice. *J. Pharm. Pharmacol.* 64 (2), 190–198. doi:10.1111/j.2042-7158.2011.01388.x

Yang, X., Almassri, H. N. S., Zhang, Q., Ma, Y., Zhang, D., Chen, M., et al. (2019). Electrosprayed Naringin-Loaded Microsphere/SAIB Hybrid Depots Enhance Bone Formation in a Mouse Calvarial Defect Model. *Drug Deliv.* 26 (1), 137–146. doi:10.1080/10717544.2019.1568620

Yang, Y., Tao, B., Gong, Y., Chen, R., Yang, W., Lin, C., et al. (2020c). Functionalization of Ti Substrate With pH-Responsive Naringin no Nanoparticles for the Reconstruction of Large Bony After Osteosarcoma Resection. *J. Biomed. Mater. Res. A.* 108 (11), 2190–2205. doi:10.1002/jbm.a.36977

Yao, C. H., Liu, B. S., Liu, C. G., and Chen, Y. S. (2006). Osteogenic Potential Using a Malleable, Biodegradable Composite Added Traditional Chinese Medicine: *In Vitro* and *In Vivo* Evaluations. *Am. J. Chin. Med.* 34 (5), 873–886. doi:10.1142/s0192415x06004351

Ye, Y., Jing, X., Li, N., Wu, Y., Li, B., and Xu, T. (2017). Icariin Promotes Proliferation and Osteogenic Differentiation of Rat Adipose-Derived Stem Cells by Activating the RhoA-TAZ Signaling Pathway. *Biomed. Pharmacother.* 88, 384–394. doi:10.1016/j.biopha.2017.01.075

Yin, L., Wang, K., Lv, X., Sun, R., Yang, S., Yang, Y., et al. (2017). The Fabrication of an ICA-SF/PLCL Nanofibrous Membrane by Coaxial Electrospinning and its Effect on Bone Regeneration *In Vitro* and *In Vivo*. *Sci. Rep.* 7 (1), 8616. doi:10.1038/s41598-017-07759-8

Yu, K. E., Alder, K. D., Morris, M. T., Munger, A. M., Lee, I., Cahill, S. V., et al. (2020). Re-appraising the Potential of Naringin for Natural, Novel Orthopedic Biotherapies. *Ther. Adv. Musculoskelet. Dis.* 12, 1759720x20966135. doi:10.1177/1759720x20966135

Yu, M., You, D., Zhuang, J., Lin, S., Dong, L., Weng, S., et al. (2017). Controlled Release of Naringin in Metal-Organic Framework-Loaded Mineralized Collagen Coating to Simultaneously Enhance Osseointegration and Antibacterial Activity. *ACS Appl. Mater. Inter.* 9 (23), 19698–19705. doi:10.1021/acsami.7b05296

Yu, Q., Meng, Z., Liu, Y., Li, Z., Sun, X., and Zhao, Z. (2021a). Photocuring Hyaluronic Acid/Silk Fibroin Hydrogel Containing Curcumin Loaded CHITOSAN Nanoparticles for the Treatment of MG-63 Cells and ME3T3-E1 Cells. *Polymers (Basel)* 13 (14). doi:10.3390/polym13142302

Yu, X., Wang, Y., Liu, X., Ge, Y., and Zhang, S. (2021b). Ursolic Acid Loaded-Mesoporous Hydroxylapatite/Chitosan Therapeutic Scaffolds Regulate Bone Regeneration Ability by Promoting the M2-type Polarization of Macrophages. *Int. J. Nanomedicine* 16, 5301–5315. doi:10.2147/ijn.S323033

Yu, X., Zhao, X., Wu, T., Zhou, Z., Gao, Y., Wang, X., et al. (2013). Inhibiting Wear Particles-Induced Osteolysis with Naringin. *Int. Orthop.* 37 (1), 137–143. doi:10.1007/s00264-012-1668-5

Yuan, Z., Min, J., Zhao, Y., Cheng, Q., Wang, K., Lin, S., et al. (2018). Quercetin Rescued TNF-Alpha-Induced Impairments in Bone Marrow-Derived Mesenchymal Stem Cell Osteogenesis and Improved Osteoporosis in Rats. *Am. J. Transl Res.* 10 (12), 4313–4321.

Yuan, Z., Wan, Z., Wei, P., Lu, X., Mao, J., Cai, Q., et al. (2020). Dual-Controlled Release of Icariin/Mg2+ from Biodegradable Microspheres and Their Synergistic Upregulation Effect on Bone Regeneration. *Adv. Healthc. Mater.* 9.

Zeng, K. W., and Gu, M. Y. (2021). Annual Advances of Integrative Pharmacology in 2020. *Traditional Med. Res.* 6 (4), 1–12. doi:10.12032/TMR20210616237

Zeng, X., Feng, Q., Zhao, F., Sun, C., Zhou, T., Yang, J., et al. (2018). Puerarin Inhibits TRPM3/miR-204 to Promote MC3T3-E1 Cells Proliferation, Differentiation and Mineralization. *Phytother Res.* 32 (6), 996–1003. doi:10.1002/ptr.6034

Zhang, D., Fong, C., Jia, Z., Cui, L., Yao, X., and Yang, M. (2016). Icariin Stimulates Differentiation and Suppresses Adipocytic Transdifferentiation of Primary Osteoblasts through Estrogen Receptor-Mediated Pathway. *Calcif Tissue Int.* 99 (2), 187–198. doi:10.1007/s00223-016-0138-2

Zhang, D., Zhang, J., Fong, C., Yao, X., and Yang, M. (2012). Herba Epimedii Flavonoids Suppress Osteoclastic Differentiation and Bone Resorption by

Inducing G2/M Arrest and Apoptosis. *Biochimie* 94 (12), 2514–2522. doi:10.1016/j.biochi.2012.06.033

Zhang, F., Huang, X., Qi, Y., Qian, Z., Ni, S., Zhong, Z., et al. (2020). Juglanin Inhibits Osteoclastogenesis in Ovariectomized Mice via the Suppression of NF-Kb Signaling Pathways. *Front. Pharmacol.* 11, 596230. doi:10.3389/fphar.2020.596230

Zhang, L., Tian, Z., Li, W., Wang, X., Man, Z., and Sun, S. (2017). Inhibitory Effect of Quercetin on Titanium Particle-Induced Endoplasmic Reticulum Stress (ERS)-related Apoptosis and in Vivoosteolysis. *Biosci. Rep.* 37 (4). doi:10.1042/bsr20170961

Zhang, X., Guo, Y., Li, D. X., Wang, R., Fan, H. S., Xiao, Y. M., et al. (2011). The Effect of Loading Icariin on Biocompatibility and Bioactivity of Porous β-TCP Ceramic. *J. Mater. Sci. Mater. Med.* 22 (2), 371–379. doi:10.1007/s10856-010-4198-y

Zhang, Y., Ma, J., and Zhang, W. (2021a). Berberine for Bone Regeneration: Therapeutic Potential and Molecular Mechanisms. *J. Ethnopharmacol* 277, 114249. doi:10.1016/j.jep.2021.114249

Zhang, Y., Wang, T., Li, J., Cui, X., Jiang, M., Zhang, M., et al. (2021b). Bilayer Membrane Composed of Mineralized Collagen and Chitosan Cast Film Coated with Berberine-Loaded PCL/PVP Electrospun Nanofiber Promotes Bone Regeneration. *Front. Bioeng. Biotechnol.* 9, 684335. doi:10.3389/fbioe.2021.684335

Zhao, H., Tang, J., Zhou, D., Weng, Y., Qin, W., Liu, C., et al. (2020). Electrospun Icariin-Loaded Core-Shell Collagen, Polycaprolactone, Hydroxyapatite Composite Scaffolds for the Repair of Rabbit Tibia Bone Defects. *Int. J. Nanomedicine* 15, 3039–3056. doi:10.2147/ijn.S238800

Zhao, J., Ohba, S., Komiyama, Y., Shinkai, M., Chung, U. I., and Nagamune, T. (2010). Icariin: a Potential Osteoinductive Compound for Bone Tissue Engineering. *Tissue Eng. Part. A.* 16 (1), 233–243. doi:10.1089/ten.TEA.2009.0165

Zhao, X. E., Yang, Z., Zhang, H., Yao, G., Liu, J., Wei, Q., et al. (2018). Resveratrol Promotes Osteogenic Differentiation of Canine Bone Marrow Mesenchymal Stem Cells through Wnt/Beta-Catenin Signaling Pathway. *Cell Reprogram* 20 (6), 371–381. doi:10.1089/cell.2018.0032

Zhao, Z. H., Ma, X. L., Zhao, B., Tian, P., Ma, J. X., Kang, J. Y., et al. (2021). Naringin-inlaid Silk Fibroin/hydroxyapatite Scaffold Enhances Human Umbilical Cord-Derived Mesenchymal Stem Cell-Based Bone Regeneration. *Cell Prolif* 54 (7), e13043. doi:10.1111/cpr.13043

Zheng, H., Feng, H., Zhang, W., Han, Y., and Zhao, W. (2020). Targeting Autophagy by Natural Product Ursolic Acid for Prevention and Treatment of Osteoporosis. *Toxicol. Appl. Pharmacol.* 409, 115271. doi:10.1016/j.taap.2020.115271

Zhong, Z., Qian, Z., Zhang, X., Chen, F., Ni, S., Kang, Z., et al. (2019). Tetrandrine Prevents Bone Loss in Ovariectomized Mice by Inhibiting RANKL-Induced Osteoclastogenesis. *Front. Pharmacol.* 10, 1530. doi:10.3389/fphar.2019.01530

Zhou, C., and Lin, Y. (2014). Osteogenic Differentiation of Adipose-Derived Stem Cells Promoted by Quercetin. *Cel Prolif* 47 (2), 124–132. doi:10.1111/cpr.12097

Zhou, L., Wu, H., Gao, X., Zheng, X., Chen, H., Li, H., et al. (2020). Bone-Targeting Liposome-Encapsulated Salvianic Acid A Improves Nonunion Healing through the Regulation of HDAC3-Mediated Endochondral Ossification. *Drug Des. Devel Ther.* 14, 3519–3533. doi:10.2147/dddt.S263787

Zhou, T., Yan, Y., Zhao, C., Xu, Y., Wang, Q., and Xu, N. (2019). Resveratrol Improves Osteogenic Differentiation of Senescent Bone Mesenchymal Stem Cells through Inhibiting Endogenous Reactive Oxygen Species Production via AMPK Activation. *Redox Rep.* 24 (1), 62–69. doi:10.1080/13510002.2019.1658376

Zhou, Y., Wu, Y., Ma, W., Jiang, X., Takemra, A., Uemura, M., et al. (2017). The Effect of Quercetin Delivery System on Osteogenesis and Angiogenesis under Osteoporotic Conditions. *J. Mater. Chem. B* 5 (3), 612–625. doi:10.1039/c6tb02312f

Zou, Q., Li, Y., Zhang, L., Zuo, Y., Li, J., and Li, J. (2009). Antibiotic Delivery System Using Nano-Hydroxyapatite/chitosan Bone Cement Consisting of Berberine. *J. Biomed. Mater. Res. A.* 89 (4), 1108–1117. doi:10.1002/jbm.a.32199

Conflict of Interest: The authors declare that the research was conducted in the absence of any commercial or financial relationships that could be construed as a potential conflict of interest.

Publisher's Note: All claims expressed in this article are solely those of the authors and do not necessarily represent those of their affiliated organizations, or those of the publisher, the editors, and the reviewers. Any product that may be evaluated in this article, or claim that may be made by its manufacturer, is not guaranteed or endorsed by the publisher.

Copyright © 2022 Shi, Yang, Wang, Wang, Wang, Ao and Li. This is an open-access article distributed under the terms of the Creative Commons Attribution License (CC BY). The use, distribution or reproduction in other forums is permitted, provided the original author(s) and the copyright owner(s) are credited and that the original publication in this journal is cited, in accordance with accepted academic practice. No use, distribution or reproduction is permitted which does not comply with these terms.

frontiers in Bioengineering and Biotechnology

ORIGINAL RESEARCH
published: 07 March 2022
doi: 10.3389/fbioe.2022.826855

Platelet-Activating Biominerals Enhanced Injectable Hydrogels With Superior Bioactivity for Bone Regeneration

Xin Chen[1†], Jiajun Yan[1†], Yingying Jiang[1†], Yunshan Fan[1], Zhengran Ying[1], Shuo Tan[1], Zhi Zhou[1], Junjian Liu[1], Feng Chen[1,2]* and Shisheng He[1]**

[1]Department of Orthopedic, Spinal Pain Research Institute, Shanghai Tenth People's Hospital, Tongji University School of Medicine, Shanghai, China, [2]National Engineering Research Center for Nanotechnology, Shanghai, China

OPEN ACCESS

Edited by:
Gang Wu,
VU Amsterdam, Netherlands

Reviewed by:
Xingge Yu,
Shanghai Ninth People's Hospital, China
Yan Su,
Genome Institute of Singapore, Singapore

***Correspondence:**
Junjian Liu
jjliu@tongji.edu.cn
Feng Chen
fchen@tongji.edu.cn
Shisheng He
tjhss7418@tongji.edu.cn

†These authors have contributed equally to this work and share first authorship

Specialty section:
This article was submitted to Biomaterials, a section of the journal Frontiers in Bioengineering and Biotechnology

Received: 01 December 2021
Accepted: 14 February 2022
Published: 07 March 2022

Citation:
Chen X, Yan J, Jiang Y, Fan Y, Ying Z, Tan S, Zhou Z, Liu J, Chen F and He S (2022) Platelet-Activating Biominerals Enhanced Injectable Hydrogels With Superior Bioactivity for Bone Regeneration. Front. Bioeng. Biotechnol. 10:826855. doi: 10.3389/fbioe.2022.826855

Refractory bone fracture, which is difficult to be treated, is a common clinical disease. Taking inspiration from the natural process of bone regeneration, we provide a biomimetic strategy to develop a new injectable biomaterial for repairing bone defects, which is mainly composed of platelets, fibrins, and biominerals. Biomineral nanoparticles (EACPNs) with an amorphous phase are prepared by an enzyme-catalyzed route and display a platelet-activating property. The composite hydrogel (EPH) of EACPNs, fibrins, and platelets is injectable, and has similar chemical properties to natural materials in bone regeneration. The dried EPH samples display a highly porous structure, which would be favorable for cell attachment and growth. The results from *in vitro* studies indicate that EPH has high biocompatibility and superior bioactivity in promoting the osteogenic differentiation of rat bone marrow stem cells (rBMSCs). Furthermore, the results from *in vivo* studies clearly indicate that EPH can induce the formation of new collagen and vessels in the defect area, thus leading to faster regeneration of bone defects at 2 weeks. Our study provides a strategy for designing new biomimetic materials, which may be favorable in the treatment of refractory bone fracture.

Keywords: calcium phosphate, biominerals, hydrogels, platelets, bone regeneration

INTRODUCTION

Refractory bone fracture disease is a constant problem among orthopedic patients in hospitals that leads to a serious impact on the health and quality of life. Biomaterials with high biocompatibility and bioactivity that promote bone regeneration will be promising in the treatment of refractory bone fractures and can be implanted into defect areas by a simple injection (Xu et al., 2020). However, it is still a critical problem to prepare such high-performance bone repair materials in orthopedic research fields. Fortunately, the natural bone regeneration process has provided great inspiration for developing such high-performance biomaterials.

The natural healing process of bone defects is a multistep process involving blood and various cells (e.g., immunological cells, osteoclasts, fibroblasts, and osteoblasts). In the early stage of bone regeneration, a hematoma is formed at the bone defect site by the coagulation of blood, and then the fibroblasts penetrate into the defect area to build a fibrous callus (De Pascale et al., 2015). The formation of hematoma plays an essential role. The activated platelets in the hematoma release a variety of growth factors and cytokines to promote tissue regeneration,

including vascular endothelial growth factor (VEGF), fibroblast growth factor (FGF), platelet-derived growth factor (PDGF), and transforming growth factor β (TGF-β) (Ruggeri, 2002; Giusti et al., 2020). Moreover, the fibrinogen in plasma can transform into a tightly packed gel with a network microstructure, which can combine with the aforementioned growth factors to enhance tissue regeneration (Boswell et al., 2012; Mussano et al., 2016). The fibrinogen/platelet gels promote cell proliferation and induce the deposition of a new extracellular matrix (ECM), which is beneficial for the repair of damaged bone tissues (Aravamudhan et al., 2013; Shiu et al., 2014). Then, over many weeks, osteoblasts gradually transform the callus into a bone tissue through a biomineralization process.

Biomineralization is a complex process that produces heterogeneous minerals, leading to the hardening or stiffening of mineralized tissues in vertebrates (Wegst et al., 2015). The biomineralization process in mineralized tissues is usually regulated by osteoblasts, various molecules, and inorganic ions. Osteoblasts not only produce the collagenous extracellular matrix (ECM) but also secrete calcium phosphate (ACP) nanogranules, which are generated in mitochondria and further induce the subsequent mineralization of collagen to form the hierarchical structure of a bone (Martin and Matthews, 1970; Sutfin et al., 1971; Sayegh et al., 1974; Landis et al., 1993; Mahamid et al., 2010; Boonrungsiman et al., 2012; Niu et al., 2017; Lotsari et al., 2018; Reznikov et al., 2018). Due to the similar chemical properties to inorganic constituents of bone, synthetic calcium phosphate has been prepared and widely used in bone regeneration. Calcium phosphate-based biomaterials can promote bone repair (Kim et al., 2017; González Díaz et al., 2018) by supporting mineral crystal growth on the ECM and then promoting bone mineralization (Zhai et al., 2010; Wang et al., 2012; Wang et al., 2019).

Through the understanding of the bone formation process, we think that the combined use of calcium phosphate-based biominerals with natural constituents in bone regeneration may provide a new strategy to design functional biomaterials. Our previous work reported an enzymatic strategy to synthesize biominerals of amorphous calcium phosphate nanoparticles (EACPNs), which can promote the proliferation and osteogenic differentiation of hBMSCs (Jiang et al., 2018). The EACPNs may affect the activation of platelets and further lead to an acceleration of bone regeneration. However, there is no report on the effect of EACPNs on platelets and their combined use in bone regeneration, which will be significant for the design and construction of new biomaterials.

Herein, we developed a strategy to prepare injectable composite hydrogels for bone defect repair by combining the use of EACBN biominerals and platelets. EACPNs have been prepared with an enzyme-catalyzed route and display a platelet-activating property. *In vitro* studies have indicated that the composite hydrogel has high cell biocompatibility and superior bioactivity in inducing osteogenic differentiation of stem cells. Moreover, the *in vivo* experiment clearly shows the high performance of this composite hydrogel in promoting bone regeneration.

EXPERIMENTAL

Materials

The adenosine 5′-triphosphate disodium salt hydrate (Na_2ATP) and alkaline phosphatase (ALP) powders were purchased from Sigma–Aldrich (United States). Fibrin sealant kits were obtained from Shanghai RAAS Blood Products Co., Ltd. (China). Other chemicals used in material preparation were obtained from Aladdin Industrial Corporation (Shanghai, China) if there was no special declaration. All the chemicals were used as received without further purification.

Enzyme-Catalyzed Synthesis of Biominerals

EACPNs were prepared *via* an enzymatic reaction strategy reported in our previous work (Jiang et al., 2018). Briefly, $CaCl_2$ (66.0 mg) was dissolved into deionized water (30.0 ml), and then aqueous solution (30.0 ml) containing Na_2ATP (110.0 mg) was added drop-wise into the above Ca^{2+} solution under magnetic stirring. Then, 6.0 μl of alkaline phosphatase solution (6.0 U ml^{-1}) was added to the above mixed reactive solution. The whole reaction was conducted for 3 h in a constant temperature bath (37°C), and the pH value was maintained at 8.0–8.5 by adding NaOH solution (0.2 M) throughout the reaction process. Finally, the products were collected by centrifugation and separately washed with DI water and ethanol three times. Then, the samples were freeze-dried for storage or further use.

Interaction Between Platelets and EACBN Biominerals

Platelets were derived from commercial platelet solutions, which were supplied by the Shanghai Blood Center (Shanghai, China). Typically, 4 ml of platelet solution was separated by centrifugation at 8,000 rpm min^{-1} for 3 min at room temperature, and then 3 ml of the supernatant was subsequently removed. The remaining plasma and platelets that were concentrated 4 times were mixed and collected for further use. Then, EACPNs (10 mg/ml) were mixed with the above platelet solution, and after a certain period of reaction at 37°C, their fluidity was observed to determine the time for the material to activate platelets and promote coagulation. Platelets in the resting state were used as a control. In addition, we observed the morphology of platelets interacting with EACPNs by scanning electron microscopy (SEM).

Preparation of EACPN-Platelet Injectable Hydrogels

In the preparation of the hydrogel, we used two reactive solutions that were put into two different syringes. A reaction can occur when these two solutions are mixed at the same time, and then the solutions turn into hydrogels. Typically, 400.0 μg of EACPNs was dispersed into 20.0 μl of fibrinogen solution (40 mg/ml), and then 10 μl of 4 times concentrated platelet solution was added into the

above solution under magnetic stirring to obtain Solution A. Fibrinogen was dissolved according to the manufacturer's instructions. Thereafter, 20 μl of thrombin solution with a concentration of 500 IU/ml was prepared as solution B. Finally, when Solution A and Solution B were mixed, an EACBN–platelet composite hydrogel (EPH) was obtained. The control sample of platelet hydrogel (PH) was prepared in the same way without adding EACPNs. Moreover, the other control sample of fibrinogen hydrogel (FH) was prepared by directly mixing 20 μl of fibrinogen solution with 20 μl of thrombin solution without adding EACPNs or platelets. The as-prepared EPH, PH, and FH were further freeze-dried *via* lyophilization for further characterization.

Swelling Ratio of Materials

To study the influence of EACPNs on the swelling ratio of samples, the different samples were injected into round molds, and then cylindrical samples (5 mm in diameter and 5 mm in height) were obtained. All the samples were freeze-dried and immersed in PBS solution (37°C 120 rpm) after being washed with PBS solution and weighed separately. The dry weight of each sample was Wd. After immersing in the PBS solution for different times, each sample was weighed again to obtain its wet weight (Ww).

The formulation to acquire the swelling ratio is as follows:

$$\text{Swelling ratio} = (\text{Ww} - \text{Wd})/\text{Wd} \cdot 100\%.$$

Material Characterization

Mechanical strength is important for the regeneration of defective bones. To acquire the mechanical properties of the samples, different cylindrical samples (5 mm in diameter and 5 mm in height) were prepared and compressed at a constant speed of 5 mm min^{-1}. The accurate diameter and height of each sample were recorded before testing. At least three samples were measured to obtain the mechanical properties of the samples.

Cell Activity

Rat bone marrow mesenchymal stem cells (rBMSCs) were derived from the femurs of Sprague–Dawley (SD) rats and were provided by the Shanghai SLAC Experimental Animal Center (Shanghai, China). The cells were cultured in Dulbecco's minimum essential medium (DMEM, Sigma Life Science) supplemented with 10% fetal bovine serum (FBS) and 1% penicillin–streptomycin (PS) at 37°C under a 5% CO_2 humidified atmosphere. All the following tests were conducted using rBMSCs from the third to the fifth passages. The freeze-dried gels were irradiated in ultraviolet light for 60 min, immersed in 1,000 μl of raw DMEM at room temperature for 24 h, and then centrifuged at 8,000 rpm to extract the supernatant. The supernatant extracted from freeze-dried EPH was diluted with DMEM for different ratios. Then, rBMSCs were co-cultured with the extracted supernatant supplemented with 10% FBS and 1% PS in a 96-well plate with a cell concentration of 3,000 cells per well for 48 h to evaluate the cell viability of the samples with a CCK-8 assay (Beyotime Biotechnology, Shanghai, China).

In addition, to evaluate whether the ACPN–platelet composite hydrogel has the ability to induce chemotaxis of cells, human umbilical vein endothelial cells (HUVECs, Cell Bank of the Chinese Academy of Sciences, Shanghai, China) were seeded into a 6-well plate at a concentration of 2×10^4 cells per well and co-cultured with the extracted supernatant of FH, PH, and EPH (at 24 h). Then, the cells were preserved and stained with crystal violet staining solution (Beyotime, China) and observed under an inverted fluorescence microscope (Leica, Germany).

Alkaline Phosphatase (ALP) Staining

To assess the ALP activity of the supernatant-treated rBMSCs at Days 7 and 14, the co-cultured cells were washed with PBS, fixed in 4% paraformaldehyde for 20 min and stained with an Alkaline Phosphatase Kit (Beyotime Biotechnology, Shanghai, China). Optical images were taken using a Leica inverted microscope.

Real-Time Quantitative PCR

The rBMSCs co-cultured with the supernatant in a 6-well plate were washed with PBS and collected at 14 days. Then, the total RNA in rBMSCs was isolated by TRIzol reagent (Thermo Fisher Scientific, American). The TaKaRa reagents PrimeScript RT Master Mix and SYBR Premix Ex Taq were used for RNA reverse transcription and RT–qPCR, respectively. The expression of osteocalcin (OCN), osteopontin (OPN), and Runx2 was measured. The data were normalized to the expression of glyceraldehyde 3-phosphate dehydrogenase and analyzed by the control Ct ($2^{-\Delta\Delta Ct}$) method.

In Vivo Experiment

The animal experiment was performed according to the plan approved by the Ethics Committee of Shanghai Tenth People's Hospital. Twenty 6-week-old male Sprague–Dawley (SD) rats were provided by the Shanghai SLAC Experimental Animal Center and were randomly divided into 4 groups. All rats were given food and water in the absence of specific pathogens (12 h light/dark cycle, 23°C). The operation was performed aseptically on the right femur. After inhaling isoflurane anesthesia, the rat's surgical area was scraped and disinfected with iodophor. The skin was cut by a scalpel and peeled off from the muscle space to the bone surface. Then, a unilateral bone penetrating the defect with a diameter of 2.4 mm was made at the middle and lower parts of the femur using a tungsten steel ball drill. Later, the prepared gels were implanted, and the muscular layer and skin were sutured. The bone defects that were unfilled were set as the blank group, and bone defects that were filled by injection with FH, PH, and EPH hydrogels were prepared under aseptic conditions.

Two weeks later, all the rats were euthanized, and the femurs with defects were fixed with 4% paraformaldehyde for 48 h at 4°C. The femurs were scanned by micro-CT (SkyScan1276,

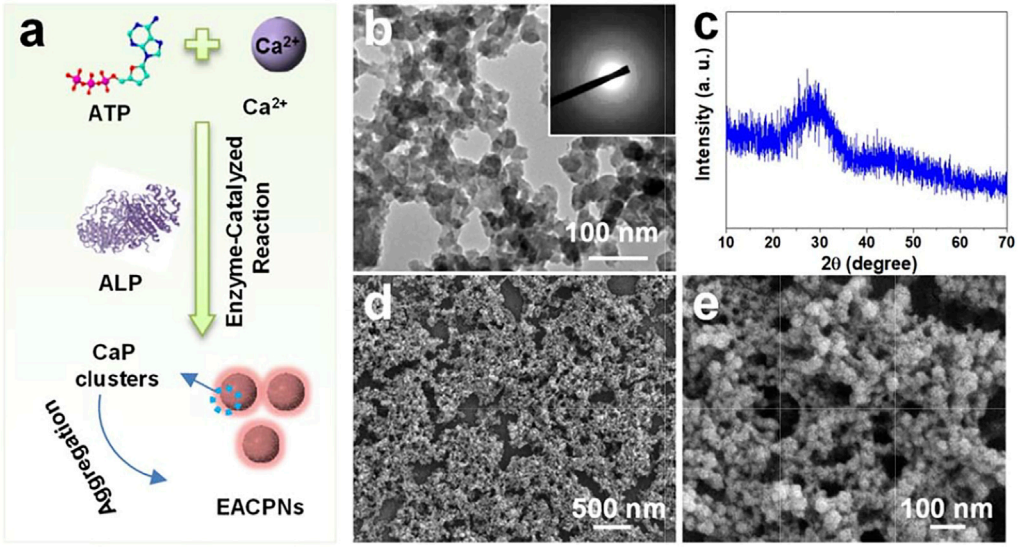

FIGURE 1 | Schematic illustration of preparation and characterization of EACPNs. **(A)** The enzyme-catalyzed reaction route for the preparation of EACPNs; characterization results of TEM **(B)**, XRD **(C)**, and SEM **(D,E)** of EACPNs.

Bruker Corporation, United States) and reconstructed *via* SkyScan NRecon software. Indices such as bone volume/tissue volume (BV/TV), trabecular thickness (Tb.Th), number (Tb.N), and separation (Tb.Sp) were analyzed using SkyScan CT-Analyzer software to evaluate the effect of bone defect repair. For the hematoxylin–eosin and Masson staining, the fixed femur samples were decalcified with EDTA solution for 1 month. The decalcified specimens were embedded in paraffin, and the sections were stained with H&E and Masson. All chemicals were purchased from Wuhan Service Bio Technology Co., Ltd., China. Representative images were taken by a Leica vertical microscope.

Statistical Analysis

The data were analyzed *via* SPSS 24.0 software. One-way ANOVA and *t*-tests were used to compare between groups. All data are expressed as the average ±SD. Each experiment contained at least three repeats. Only when $^{*}p < 0.05$, $^{**}p < 0.01$, and $^{***}p < 0.001$, the difference was regarded as statistically significant.

RESULTS AND DISCUSSION

Preparation and Characterization of EACPNs

Figure 1A displays the route of the enzyme-catalyzed reaction for the preparation of EACPNs. **Figure 1B** shows transmission electron microscopy (TEM) micrographs of EACPNs, in which the samples display an amorphous structure of nanoparticles with a diameter of 20–50 nm. The selected-area electron diffraction (SAED) pattern (insert) also shows a typical pattern of an amorphous structure. These results agree well with the XRD pattern of the EACPNs in **Figure 1C**. Furthermore, the SEM micrographs (**Figures 1D,E**) of EACPNs display a spherical morphology, which is consistent with the TEM results.

In the reaction process, the ALP enzyme acts as a cleaver to hydrolyze phosphate ions, which react with calcium ions to form EACPNs from ATP molecules. After the enzyme-catalyzed reaction, some ATP molecules can transform to ADP and AMP. The molecules of ATP/ADP/AMP can interact with the calcium ions of mineral clusters and inhibit the crystallization of these clusters. Then, these mineral clusters form amorphous aggregates of EACPNs.

The Interaction Between EACPNs and Platelets

In an *in vitro* study of the interaction between EACPNs and platelets, we found that EACPNs and platelets have a significant interaction that can promote platelet activation and coagulation (**Figure 2**). When EACPNs are incubated with platelets for approximately 2 min, we can observe that the originally flowing platelet solution loses its fluidity and can be stably fixed on the bottom of the inverted centrifuge tube (**Figure 2D**). SEM micrographs of platelets in the resting state and EACBN-treated platelets are shown in **Figure 2**. The platelets in the resting state showed a smooth discoid shape (**Figures 2B,C**). In contrast, after treatment with EACPNs, there was a significant change in the morphologies of platelets, which displayed a typical activated state with many channels of the open canalicular system (OCS) (**Figures 2D,E**).

We think that the activation of platelets is related to the large amount of ADP molecules in EACPNs. In our previous study, we revealed the content of ADP molecules in EACPNs

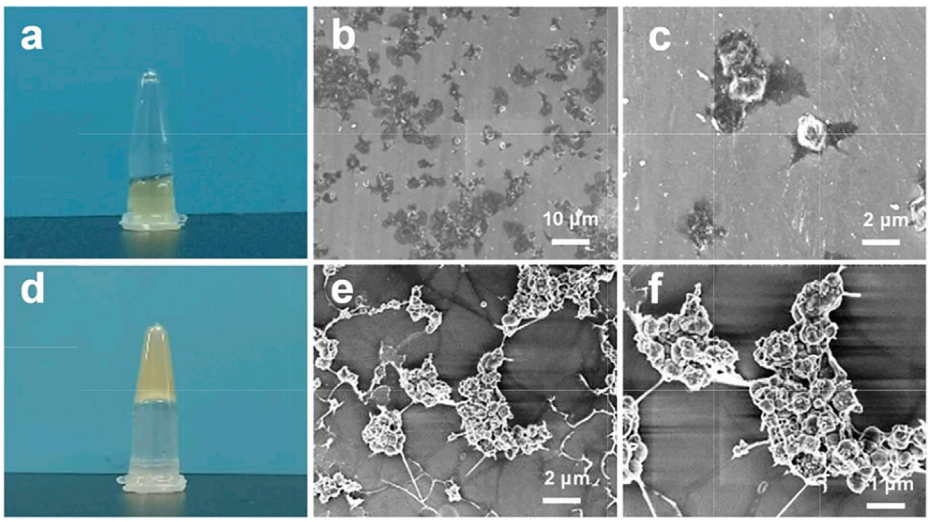

FIGURE 2 | Digital photographs and SEM micrographs of platelets in resting states **(A–C)** and EACPN-treated platelets **(D–F)**.

by a high-performance liquid chromatography (HPLC) method, which indicated that there is approximately 0.15 g of ADP molecules in each gram of EACPNs (Jiang et al., 2018). It has been reported that ADP, as a soluble agonist released by activated cells, can trigger platelet activation through GPCRs, thereby promoting coagulation formation (Yun et al., 2016).

As fragments of blood cells, platelets (in an activated state) play essential roles in defense against excessive blood loss and wound repair. For example, in the bone regeneration process, platelets play a critical role in the hematoma formation process and in blood coagulation, which provide the supporting sites and environment for the growth of different cells. Activated platelets also release a variety of growth factors and cytokines to promote the proliferation or differentiation of bone repair-related cells. Platelets have been widely used in promoting tissue regeneration, including stomatology (Attia et al., 2020), maxillofacial surgery (Chou et al., 2020), trauma, and orthopedics (Hohmann et al., 2021). Therefore, we believe that the combination of EACPNs and platelets is a potential choice in developing bioactive materials for bone defect repair.

Characterization of EACPN–Platelet Hydrogels

After mixing solutions of EACPNs, platelets, and fibrinogen/thrombin, a hydrogel of EPH was obtained. The natural coagulation of blood contains much fibrinogen from blood. The platelet solution is concentrated and short of fibrinogen. Therefore, we have added fibrinogen to the preparation process of EPH. The hydrogels of PH (without EACPNs) and FH (without platelets) were used as control samples. The as-prepared FH, PH, and EPH were freeze-dried *via* lyophilization for further characterization.

Figure 3 displays the SEM micrographs and element distribution of EPH and control samples. As shown in **Figures 3A–I**, typical 3D structures with interconnected micropores were observed in all samples of dried FH, PH, and EPH hydrogels. There is no significant difference in the morphologies with low magnification among these three samples, which have large pores with diameters of 100–500 μm. However, in the SEM images with high magnification, we find that there are significant differences among the three samples. On the wall of the porous structure, the FH sample has a smooth surface structure. In contrast, the PH and EPH samples have rough surfaces with a large number of activated platelets.

The EACPNs are small and can be encased in the wall of the porous structure, which cannot be clearly observed in the SEM micrographs. Therefore, the results of element mappings are given to illustrate the distribution of EACPNs. **Figures 3I,K** display the element distributions of C, Ca, and P in the selected areas of the control samples of PH and EPH, which show that the contents of calcium and phosphorus in EPH are significantly higher than those in PH. The distribution of calcium and phosphorus is consistent with the distribution of carbon, which indicates the successful incorporation of EACPNs in the EPH sample. Compared with the control sample of PH, the amount of calcium and phosphate increased from 0.51 to 0.56 % to 2.71 and 2.80 %, respectively. Moreover, the results of reconstructed micro-CT images of dried hydrogels of PH and EPH are given in **Supplementary Figure S1**, which display the difference in the mineral density of the two samples. The images also perfectly display the internal interconnected structure inside the EPH sample. The obvious difference in mineral density between the PH and EPH samples can be well explained by the addition of EACPNs to the EPH sample.

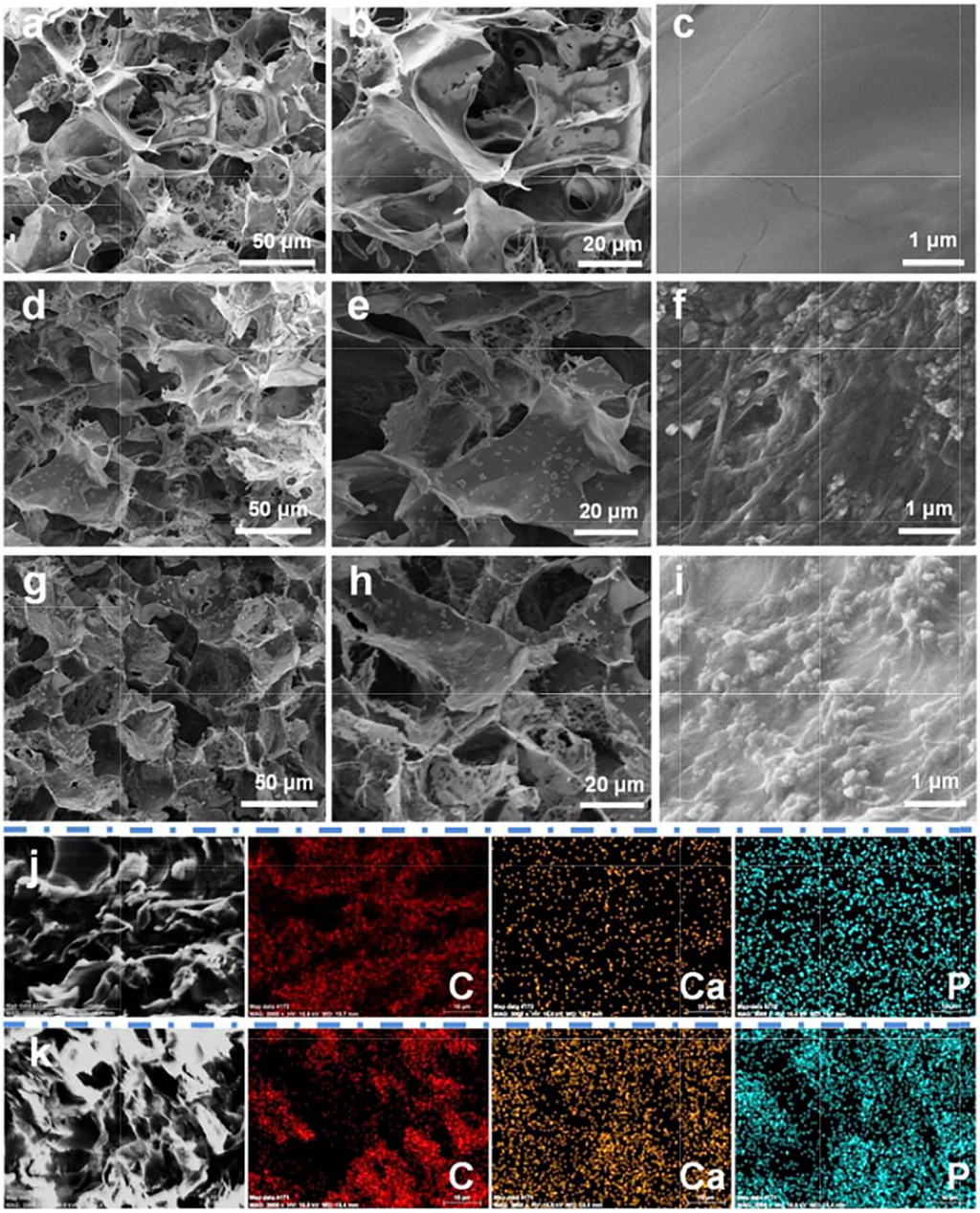

FIGURE 3 | SEM micrograph and element distribution mappings of EACPN–platelet hydrogels and control samples. **(A–I)** SEM micrographs of freeze-dried hydrogels of FH **(A–C)**, PH **(D–F)**, and EPH **(G–I)**; **(J,K)** C, Ca, and P distribution mappings of selected areas of control sample of PH **(J)** and EPH **(K)**.

Furthermore, the results of the swelling ratio and mechanical properties of the three materials are also given in **Supplementary Figures S2A,B**. The image of the swelling ratio shows that dried EPH could absorb the surrounding liquid in a short time and reach equilibrium in a shorter time than the samples of dried samples of FH and PH. Moreover, from the results of mechanical tests, a stronger mechanical bearing capacity was obtained in the EPH group than in the other two groups. The results may be explained by the addition of EACPNs into the EPH samples, which may affect the mechanical properties by a reinforcement effect. These results indicate that the addition of EACPNs can affect the physical properties of materials.

The FTIR spectra of EACPNs, FH, PH, and EPH are shown in **Supplementary Figure S3**. The broad absorption bands in the spectra of all samples at 3,200–3,600 cm^{-1} originate from the water molecules adsorbed by the samples. In the spectra of EACPNs and EPH, the absorption peaks at approximately

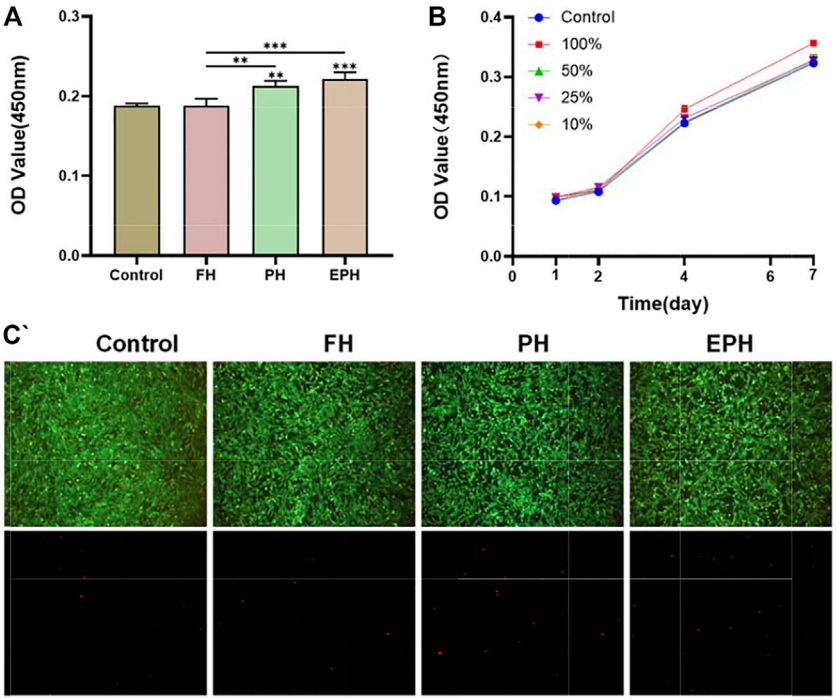

FIGURE 4 | (A) Cell viability of rBMSCs co-cultured with the corresponding extracted supernatant from FH, PH, and EPH for 48 h. **(B)** The proliferation curve of rBMSCs treated with a series of diluted supernatant of EPH. **(C)** Fluorescence images of dead/live cell staining after incubation with extracted supernatant of FH, PH, and EPH. Fluorescence microscopy images of four groups stained with calcein–AM/PI.

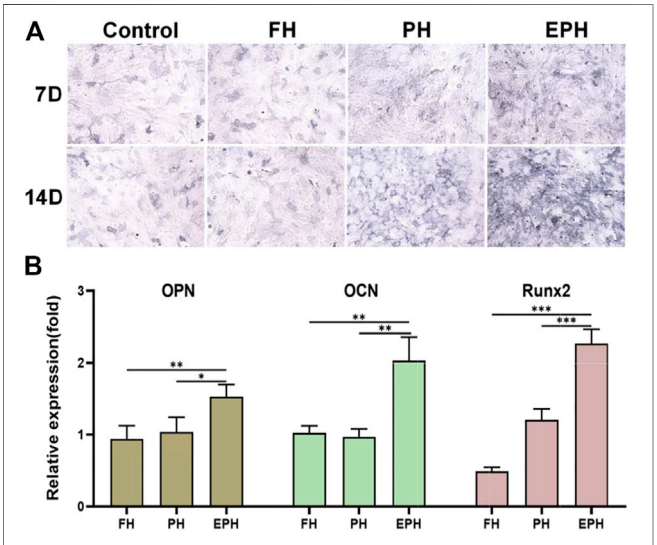

FIGURE 5 | (A) ALP staining of rBMSCs incubated with the supernatant of hydrogels of FH, PH, and EPH for 7 and 14 days, respectively. **(B)** The expression of osteopontin (OPN), osteocalcin (OCN), Osterix, and Runx2 genes of rBMSCs incubated with the supernatant of FH, PH, and EPH for 14 days, respectively.

1,109 cm^{-1} and 563 cm^{-1} are higher than those of FH and PH, which can be assigned to the asymmetric stretching vibration of PO_4^{3-}. The absorption peaks at approximately 1,649 cm^{-1} originate from adenosine or other organic molecules from platelets, which correspond to the stretching mode of C=N. These FTIR spectra indicate the components of the samples, which are consistent with the above element mapping results.

In Vitro Biocompatibility and Bioactivity of EPH

To further evaluate the *in vitro* biocompatibility of FH, PH, and EPH, rBMSCs were co-cultured with the extracted supernatant of hydrogel samples. As shown in **Figure 4A**, the OD values from the CCK-8 assay of the PH and EPH groups were higher than those of the control, and FH showed a similar value as the control. The results reveal the high biocompatibility of EPH, PH, and FH. Afterward, a series of dilutions of EPH supernatant were used to further explore the effect of EPH on the proliferation of rBMSCs. The results in **Figure 4B** show that all the groups cultured with supernatants show good proliferation curves. The proliferation rate of rBMSCs treated with 100% supernatant was slightly faster than that of rBMSCs in the other groups. Furthermore, there was no significant difference in the live/dead cell staining of the four groups, which also indicated the good biocompatibility of these hydrogels (**Figure 4C**).

Thereafter, the effects of FH, PH, and EPH on the osteogenic differentiation of rBMSCs were studied. The

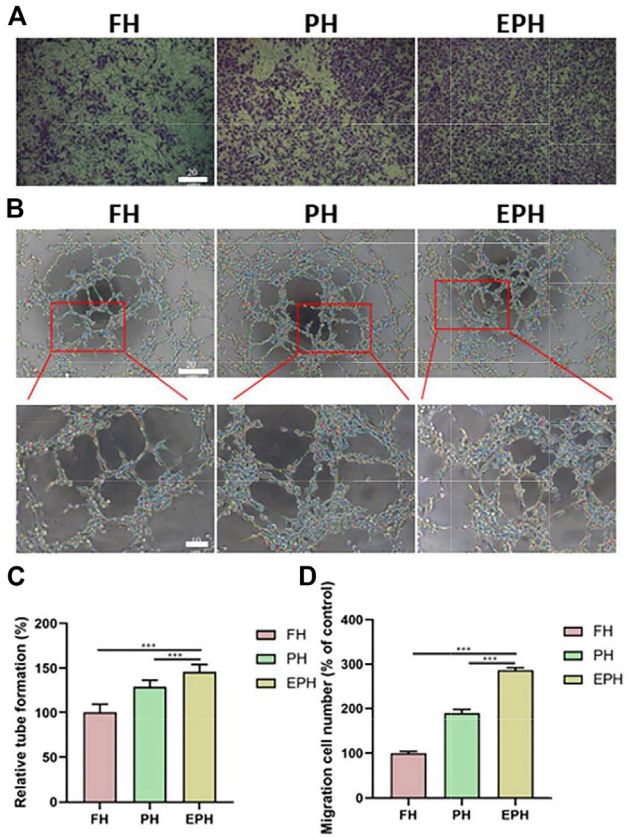

FIGURE 6 | (A) Transwell migration assay of HUVECs incubated with the extracted supernatant of FH, PH, and EPH hydrogels for 24 h, respectively; **(B)** The tube formation of HUVECs incubated with the extracted supernatant of FH, PH, and EPH for 24 h, respectively. **(C)** Quantitative data of the formed tube in **(B)**; **(D)** Quantitative data of the migration cell number obtained from transwell assay.

results of alkaline phosphatase (ALP) staining are given in **Figure 5A**. The images show that the ALP activity of rBMSCs incubated with the supernatant of EPH was higher than that of the control and the other groups. Then, the total RNA of OPN, OCN, and Runx2 expressed in rBMSCs was also studied (**Figure 5B**). The results clearly indicated that the examined genes were obviously upregulated after treatment with the supernatant of EPH, which was obviously higher than that of FH and PH.

In addition, we evaluated the effects of FH, PH, and EPH on the migration and tube formation properties of HUVECs. In **Figures 6A,D**, the images and analyzed data obtained from the transwell assay clearly show that the supernatant from PH and EPH can promote the migration of HUVECs compared with that from FH. Furthermore, we investigated the angiogenic capacity of HUVECs using *in vitro* tube formation experiments. As shown in **Figures 6B,C**, the images and analyzed data show that PH and EPH had significantly better effects on the tube formation ability of HUVECs than FH materials. This result can be easily understood because it is well known that platelets and the abundant growth factors in platelets may contribute to the migration, growth, and angiogenesis of vascular endothelial cells.

In Vivo Studies of EPH in a Rat Defect Model

The *in vivo* performance of EPH materials has been investigated using a rat defect model in the femoral bone with a diameter of 2.4 mm, which is a small defect that mimics bone fractures. **Figure 7A** displays a schematic illustration of the preparation and application of EPH in repairing an *in vivo* bone defect model. **Figure 7B** shows the results of reconstructed micro-CT images of the bone defects in the femoral bones of the rats after treatment with EPH and controls for 2 weeks. The images clearly display that there is more regenerative bone formed in the EPH group from both the front and sectional views. The regenerative bone in defect areas is highlighted and shown in the third row of **Figure 7B**. Obviously, EPH provides a significant promotion of the formation of new cortical and cancellous bone. Micro-CT quantitative analysis further confirmed that EPH has a superior capacity in promoting bone regeneration. However, a large difference was not observed among the four groups in trabecular thickness (Tb.Th) (**Figure 7C**), and it can be seen that the bone volume/tissue volume (BV/TV) in the EPH group increased from 20 to 43% compared with those of the other groups (**Figure 7D**). Moreover, the trabecular number (Tb.N) also significantly improved in the EPH group (**Figure 7E**), while the decreased trabecular septum (Tb.Sp) further indicated the improvement in bone mass after treatment with EPH (**Figure 7F**).

Then, histological evaluation was performed by hematoxylin–eosin (H&E) staining and the Masson trichrome staining (**Figure 8**). As we can see from the front of the femur specimens, there is a small amount of new bone collagen and new vessels in the defect area of the blank control and FH groups. Moreover, the amount of bone collagen and the distribution were relatively improved in the PH group, and there were more new vessels. However, a large amount of continuous new bone collagen was found in the EPH group, showing better woven bone formation than the other three groups, and the bone defects were almost completely filled.

The excellent *in vivo* behavior of EPH as a bone repair material can be explained as follows: First, platelets and fibrinogen in EPH are natural, endogenous, degradable materials that can provide mechanical support for cell growth and attachment. Second, platelets release a large number of growth factors, which effectively induce chemotaxis of various cells and promote cell proliferation (El-Sharkawy et al., 2007). In addition, platelets and fibrinogen have the ability to increase vascular permeability and promote angiogenesis (Kubota et al., 2004). Finally, EACPNs combined in the scaffold can further induce the osteogenic differentiation of rBMSCs *via* a favorable interaction. Our previous study proved that EACPNs can enter cells by an endocytosis effect and can then cause autophagy and activate the AMPK pathway in BMSCs, which promotes the osteogenic differentiation of these cells (Jiang et al., 2018). The good performance of EPH in promoting bone defect repair is caused by the abovementioned factors, and it has good potential for future clinical application.

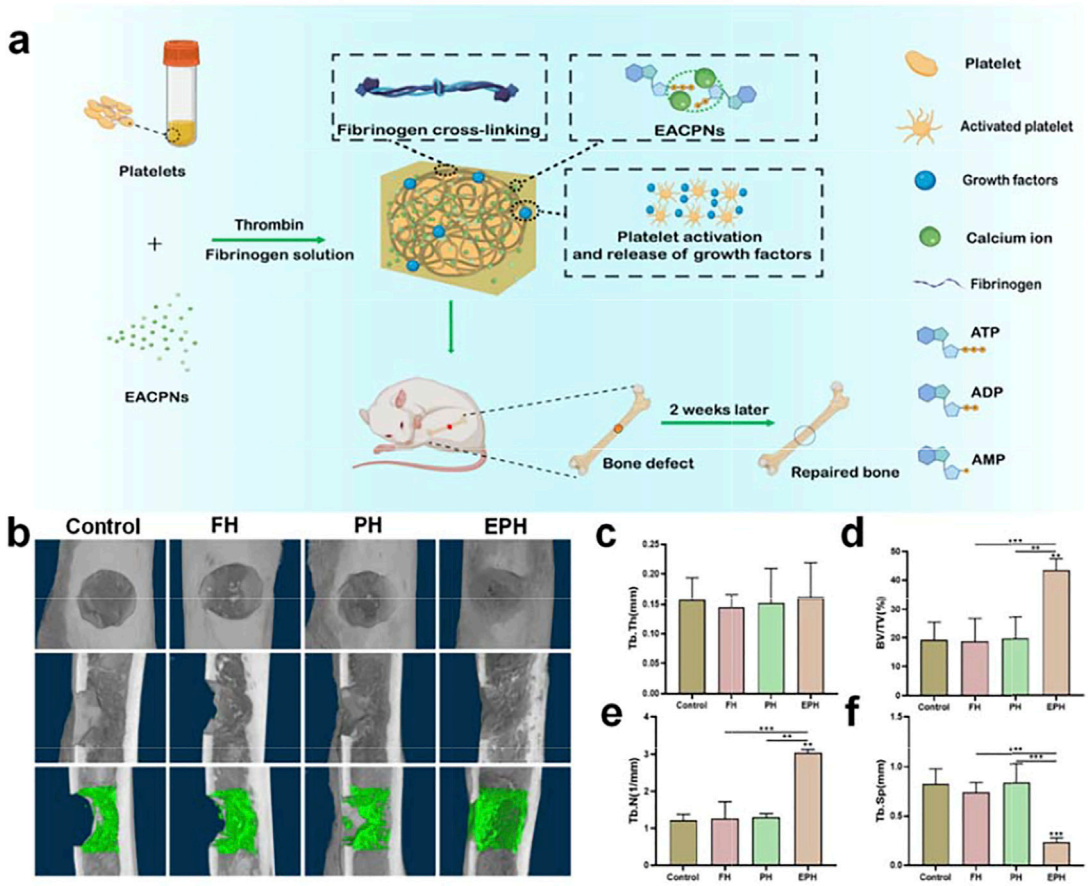

FIGURE 7 | (A) Schematic illustration of the preparation and application of EPH and controls in the repair of an *in vivo* femoral defect model with a diameter of 2.4 mm; **(B)** reconstructed micro-CT images of the defects treated with EPH and controls for 2 weeks post-op (First row: front view; second row: sectional view; third row: regenerative areas highlighted from the sectional view); **(C–F)** the analysis results of the trabecular thickness (Tb.Th) **(C)**, bone volume density (BV/TV); and **(D)** trabecular number (Tb.N) **(E)** and trabecular separation (Tb.Sp) **(F)** of the defective areas after treated with the samples for 2 weeks.

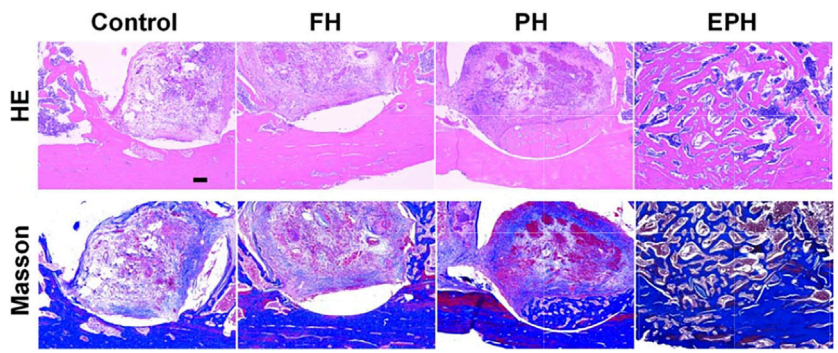

FIGURE 8 | Optical images of histological samples with hematoxylin and eosin (H&E) staining and Masson's trichrome staining. The scale bar in images is 200 μm.

CONCLUSION

In this study, a biomimetic hybrid hydrogel of EPH inspired by the formation of natural bone was designed and successfully prepared by using EACPNs, fibrin, and platelets. EACPNs, which have an amorphous structure and display a platelet-activating property, have been prepared by an enzyme-catalyzed route. After mixing with fibrin and platelets, the composite hydrogel

of EPH with an injectable property is prepared, with excellent biocompatibility and bioactivity. EPH promoted the osteogenic differentiation of rBMSCs, which displayed the upregulated expression of OPN, OCN, Runx2, and Col I. Moreover, EPH displayed remarkable *in vivo* performance in promoting the regeneration of bone defects with a small size of 2.4 mm in 2 weeks by inducing the formation of new collagen and vessels in the defect area. Thus, this study provides a new strategy for constructing bioactive and injectable materials *via* a biomimetic strategy for effective bone regeneration.

DATA AVAILABILITY STATEMENT

The original contributions presented in the study are included in the article/**Supplementary Material**, further inquiries can be directed to the corresponding authors.

ETHICS STATEMENT

The animal study was reviewed and approved by the Ethics Committee of Shanghai Tenth People's Hospital.

AUTHOR CONTRIBUTIONS

XC, JY, and YJ performed the experiments and analyzed the data. YF, ZY, ST, and ZZ summarized the methods and analyzed the data. XC, YJ, and FC wrote the manuscript. JL, FC, and SH designed and supervised the project.

FUNDING

This study was supported by grants from the National Natural Science Foundation of China (31771081), the Science and Technology Commission of Shanghai Municipality (19JC1414300, 19441901900, 19ZR1439700, and 22S31903300), and S&T Innovation 2025 Major Special Programme of Ningbo (2018B10040).

SUPPLEMENTARY MATERIAL

The Supplementary Material for this article can be found online at: https://www.frontiersin.org/articles/10.3389/fbioe.2022.826855/full#supplementary-material

REFERENCES

Aravamudhan, A., Ramos, D. M., Nip, J., Harmon, M. D., James, R., Deng, M., et al. (2013). Cellulose and Collagen Derived Micro-nano Structured Scaffolds for Bone Tissue Engineering. *J. Biomed. Nanotechnology* 9 (4), 719–731. doi:10.1166/jbn.2013.1574

Attia, S., Narberhaus, C., Schaaf, H., Streckbein, P., Pons-Kühnemann, J., Schmitt, C., et al. (2020). Long-Term Influence of Platelet-Rich Plasma (PRP) on Dental Implants after Maxillary Augmentation: Retrospective Clinical and Radiological Outcomes of a Randomized Controlled Clinical Trial. *J. Clin. Med.* 9, 355. doi:10.3390/jcm9020355

Boonrungsiman, S., Gentleman, E., Carzaniga, R., Evans, N. D., McComb, D. W., Porter, A. E., et al. (2012). The Role of Intracellular Calcium Phosphate in Osteoblast-Mediated Bone Apatite Formation. *Proc. Natl. Acad. Sci.* 109 (35), 14170–14175. doi:10.1073/pnas.1208916109

Boswell, S. G., Cole, B. J., Sundman, E. A., Karas, V., and Fortier, L. A. (2012). Platelet-rich Plasma: a Milieu of Bioactive Factors. *Arthrosc. J. Arthroscopic Relat. Surg.* 28 (3), 429–439. doi:10.1016/j.arthro.2011.10.018

Chou, T. M., Chang, H. P., and Wang, J. C. (2020). Autologous Platelet Concentrates in Maxillofacial Regenerative Therapy. *Kaohsiung J. Med. Sci.* 36 (5), 305–310. doi:10.1002/kjm2.12192

De Pascale, M. R., Sommese, L., Casamassimi, A., and Napoli, C. (2015). Platelet Derivatives in Regenerative Medicine: an Update. *Transfus. Med. Rev.* 29 (1), 52–61. doi:10.1016/j.tmrv.2014.11.001

El-Sharkawy, H., Kantarci, A., Deady, J., Hasturk, H., Liu, H., Alshahat, M., et al. (2007). Platelet-rich Plasma: Growth Factors and Pro- and Anti-inflammatory Properties. *J. Periodontol.* 78 (4), 661–669. doi:10.1902/jop.2007.060302

Giusti, I., D'Ascenzo, S., Macchiarelli, G., and Dolo, V. (2020). *In Vitro* evidence Supporting Applications of Platelet Derivatives in Regenerative Medicine. *Blood Transfus.* 18 (2), 117–129. doi:10.2450/2019.0164-19

González Díaz, E. C., Shih, Y. V., Nakasaki, M., Liu, M., and Varghese, S. (2018). Mineralized Biomaterials Mediated Repair of Bone Defects through Endogenous Cells. *Tissue Eng. Part. A.* 24 (13-14), 1148–1156. doi:10.1089/ten.TEA.2017.0297

Hohmann, E., Tetsworth, K., and Glatt, V. (2021). Platelet-Rich Plasma versus Corticosteroids for the Treatment of Plantar Fasciitis: A Systematic Review and Meta-Analysis. *Am. J. Sports Med.* 49 (5), 1381–1393. doi:10.1177/0363546520937293

Jiang, Y. Y., Zhou, Z. F., Zhu, Y. J., Chen, F. F., Lu, B. Q., Cao, W. T., et al. (2018). Enzymatic Reaction Generates Biomimic Nanominerals with Superior Bioactivity. *Small* 14 (51), e1804321. doi:10.1002/smll.201804321

Kim, H. D., Jang, H. L., Ahn, H.-Y., Lee, H. K., Park, J., Lee, E.-s., et al. (2017). Biomimetic Whitlockite Inorganic Nanoparticles-Mediated *In Situ* Remodeling and Rapid Bone Regeneration. *Biomaterials* 112, 31. doi:10.1016/j.biomaterials.2016.10.009

Kubota, S., Kawata, K., Yanagita, T., Doi, H., Kitoh, T., and Takigawa, M. (2004). Abundant Retention and Release of Connective Tissue Growth Factor (CTGF/CCN2) by Platelets. *J. Biochem.* 136 (3), 279–282. doi:10.1093/jb/mvh126

Landis, W. J., Song, M. J., Leith, A., McEwen, L., and McEwen, B. F. (1993). Mineral and Organic Matrix Interaction in Normally Calcifying Tendon Visualized in Three Dimensions by High-Voltage Electron Microscopic Tomography and Graphic Image Reconstruction. *J. Struct. Biol.* 110 (1), 39–54. doi:10.1006/jsbi.1993.1003

Lotsari, A., Rajasekharan, A. K., Halvarsson, M., and Andersson, M. (2018). Transformation of Amorphous Calcium Phosphate to Bone-like Apatite. *Nat. Commun.* 9 (1), 4170. doi:10.1038/s41467-018-06570-x

Mahamid, J., Aichmayer, B., Shimoni, E., Ziblat, R., Li, C., Siegel, S., et al. (2010). Mapping Amorphous Calcium Phosphate Transformation into Crystalline mineral from the Cell to the Bone in Zebrafish Fin Rays. *Proc. Natl. Acad. Sci.* 107 (14), 6316–6321. doi:10.1073/pnas.0914218107

Martin, J. H., and Matthews, J. L. (1970). 34 Mitochondrial Granules in Chondrocytes, Osteoblasts and Osteocytes. *Clin. Orthopaedics Relat. Res.* 68, 273–278. doi:10.1097/00003086-197001000-00035

Mussano, F., Genova, T., Munaron, L., Petrillo, S., Erovigni, F., and Carossa, S. (2016). Cytokine, Chemokine, and Growth Factor Profile of Platelet-Rich Plasma. *Platelets* 27 (5), 467–471. doi:10.3109/09537104.2016.1143922

Niu, L.-n., Jee, S. E., Jiao, K., Tonggu, L., Li, M., Wang, L., et al. (2017). Collagen Intrafibrillar Mineralization as a Result of the Balance between Osmotic Equilibrium and Electroneutrality. *Nat. Mater* 16 (3), 370–378. doi:10.1038/nmat4789

Reznikov, N., Bilton, M., Lari, L., Stevens, M. M., and Kroger, R. (2018). Fractal-like Hierarchical Organization of Bone Begins at the Nanoscale. *Science* 360, eaao2189. doi:10.1126/science.aao2189

Ruggeri, Z. M. (2002). Platelets in Atherothrombosis. *Nat. Med.* 8 (11), 1227–1234. doi:10.1038/nm1102-1227

Sayegh, F. S., Solomon, G. C., and Davis, R. W. (1974). Ultrastructure of Intracellular Mineralization in the Deer??s Antler. *Clin. Orthopaedics Relat. Res.* 99, 267–284. doi:10.1097/00003086-197403000-00030

Shiu, H. T., Goss, B., Lutton, C., Crawford, R., and Xiao, Y. (2014). Formation of Blood Clot on Biomaterial Implants Influences Bone Healing. *Tissue Eng. B: Rev.* 20 (6), 697–712. doi:10.1089/ten.teb.2013.0709

Sutfin, L. V., Holtrop, M. E., and Ogilvie, R. E. (1971). Microanalysis of Individual Mitochondrial Granules with Diameters Less Than 1000 Angstroms. *Science* 174 (4012), 947–949. doi:10.1126/science.174.4012.947

Wang, X., Deng, Y., Li, S., Wang, G., Qin, E., Xu, X., et al. (2012). Biomineralization-based Virus Shell-Engineering: towards Neutralization Escape and Tropism Expansion. *Adv. Healthc. Mater.* 1 (4), 443–449. doi:10.1002/adhm.201200034

Wang, Y., Hu, X., Zhang, L., Zhu, C., Wang, J., Li, Y., et al. (2019). Bioinspired Extracellular Vesicles Embedded with Black Phosphorus for Molecular Recognition-Guided Biomineralization. *Nat. Commun.* 10 (1), 2829. doi:10.1038/s41467-019-10761-5

Wegst, U. G. K., Bai, H., Saiz, E., Tomsia, A. P., and Ritchie, R. O. (2015). Bioinspired Structural Materials. *Nat. Mater* 14 (1), 23–36. doi:10.1038/nmat4089

Xu, Q., Liang, J., Xue, H., Liu, Y. E., Cao, L., Li, X., et al. (2020). Novel Injectable and Self-Setting Composite Materials for Bone Defect Repair. *Sci. China Mater.* 63 (5), 876–887. doi:10.1007/s40843-019-1233-7

Yun, S. H., Sim, E. H., Goh, R. Y., Park, J. I., and Han, J. Y. (2016). Platelet Activation: The Mechanisms and Potential Biomarkers. *Biomed. Res. Int.* 2016, 9060143. doi:10.1155/2016/9060143

Zhai, H., Jiang, W., Tao, J., Lin, S., Chu, X., Xu, X., et al. (2010). Self-Assembled Organic-Inorganic Hybrid Elastic Crystal via Biomimetic Mineralization. *Adv. Mater.* 22 (33), 3729–3734. doi:10.1002/adma.201000941

Conflict of Interest: The authors declare that the research was conducted in the absence of any commercial or financial relationships that could be construed as a potential conflict of interest.

The reviewer XY declared a shared parent affiliation, with no collaboration, with one of the authors FC to the handling editor at the time of the review.

Publisher's Note: All claims expressed in this article are solely those of the authors and do not necessarily represent those of their affiliated organizations, or those of the publisher, the editors, and the reviewers. Any product that may be evaluated in this article, or claim that may be made by its manufacturer, is not guaranteed or endorsed by the publisher.

Copyright © 2022 Chen, Yan, Jiang, Fan, Ying, Tan, Zhou, Liu, Chen and He. This is an open-access article distributed under the terms of the Creative Commons Attribution License (CC BY). The use, distribution or reproduction in other forums is permitted, provided the original author(s) and the copyright owner(s) are credited and that the original publication in this journal is cited, in accordance with accepted academic practice. No use, distribution or reproduction is permitted which does not comply with these terms.

frontiers | Frontiers in Bioengineering and Biotechnology

ORIGINAL RESEARCH
published: 01 April 2022
doi: 10.3389/fbioe.2022.813805

Adaptive Gelatin Microspheres Enhanced Stem Cell Delivery and Integration With Diabetic Wounds to Activate Skin Tissue Regeneration

Ming Shi[1,2,3], *Yunfen Gao*[1,2], *Lim Lee*[4], *Ting Song*[1,2], *Jianhua Zhou*[1,2], *Ling Yan*[4] *and Yan Li*[1,2]*

[1]*Guangdong Provincial Key Laboratory of Sensor Technology and Biomedical Instrument, School of Biomedical Engineering, Shenzhen Campus of Sun Yat-sen University, Shenzhen, China,* [2]*Guangdong Provincial Engineering and Technology Center of Advanced and Portable Medical Devices, Sun Yat-sen University, Guangzhou, China,* [3]*Department of Scientific Research Center, The Seventh Affiliated Hospital, Sun Yat-Sen University, Shenzhen, China,* [4]*Department of Plastic and Cosmetic Surgery, The Third Affiliated Hospital, Sun Yat-sen University, Guangzhou, China*

The delayed and complicated diabetic wound healing raises clinical and social concerns. The application of stem cells along with hydrogels is an attractive therapeutic approach. However, low cell retention and integration hindered the performance. Herein, gelatin microspheres were fabricated for local delivery of adipose-derived stem cells (from rats, rADSCs), and the effect of rADSCs with microspheres on diabetic wound healing was examined. Uniform, well-dispersed microspheres were fabricated using the microfluidic technique. Due to geometry differences, the proteinase degradation rate for microspheres was four times that of the bulk hydrogel. The obtained gelatin microspheres supported cell's adhesion and proliferation and provided a suitable microenvironment for rADSC survival. For *in vivo* animal tests, rADSCs were labeled with CM-Dil for tracking purposes. Microspheres were well embedded in the regenerated tissue and demonstrated good biocompatibility and an adaptive biodegradation rate. Histological examination revealed rADSC-loaded gelatin microspheres that significantly accelerated wound healing *via* promoting M2 macrophage polarization, collagen deposition, angiogenesis associated with peripheral nerve recovery, and hair follicle formation. Notably, the relative fluorescence intensity around the hair follicle was 17-fold higher than that of the blank group, indicating rADSC participated in the healing process *via* exosomes. Taken together, the rADSC-laden gelatin microspheres provided a promising strategy for local stem cell delivery to improve diabetic wound healing.

Keywords: adipose-derived stem cells, gelatin microspheres, diabetic wound healing, tissue regeneration, exosome

OPEN ACCESS

Edited by:
Kaili Lin,
Shanghai Jiao Tong University, China

Reviewed by:
Zhuang Yu,
Shanghai Jiao Tong University, China
Feng Chen,
Zhejiang University of Technology, China

***Correspondence:**
Yan Li
liyan99@mail.sysu.edu.cn

Specialty section:
This article was submitted to Biomaterials, a section of the journal Frontiers in Bioengineering and Biotechnology

Received: *12 November 2021*
Accepted: *16 February 2022*
Published: *01 April 2022*

Citation:
Shi M, Gao Y, Lee L, Song T, Zhou J, Yan L and Li Y (2022) Adaptive Gelatin Microspheres Enhanced Stem Cell Delivery and Integration With Diabetic Wounds to Activate Skin Tissue Regeneration. Front. Bioeng. Biotechnol. 10:813805. doi: 10.3389/fbioe.2022.813805

INTRODUCTION

Diabetes has become a global epidemic (Wimmer et al., 2019). The high and growing incidence presented considerable challenges to health care systems (Matoori et al., 2021). A major associated complication was poor or delayed wound healing, which may lead to diabetic foot ulcers (Armstrong et al., 2017). The pathogenesis of diabetic wounds was complicated and multifaceted, including neuropathy and microvascular abnormalities (Falanga, 2005). Optimum cutaneous wound healing required a well-orchestrated integration of complex biological and

molecular events, including cell migration and proliferation, angiogenesis, extracellular matrix (ECM) deposition, and remodeling. However, this orderly sequence of cellular and molecular events was disrupted in diabetic wounds.

Current clinical treatments for diabetic wounds involved offloading, debridement, eradicating infected tissue, and maintaining moisture microenvironment (Kavitha et al., 2014). These strategies are mainly aimed at a fast wound closure rather than addressing the underlying pathophysiology and usually result in wound recurrence, leading to treatment failure and maybe amputation (Cavanagh et al., 2005; Falanga, 2005). Numerous approaches such as applying growth factors, anti-inflammatory drugs, matrix metalloproteinase (MMP) inhibitors, scaffolds, and injection of stem cells on diabetic wounds have been evaluated. However, limited performance was reported (Patel et al., 2019). Due to the multifactorial origins of wound etiology, there were no simple methods that aimed at the persistence of wounds in diabetic patients.

Stem cell-based therapy was an attractive approach for the treatment of chronic nonhealing wounds (Dehkordi et al., 2019). There was a growing interest in the potential of adipose-derived stem cells (ADSCs) for diabetic wound healing applications. ADSCs have been shown to promote revascularization and reepithelialization through secretion of proangiogenic factors, such as epidermal growth factor and vascular endothelial growth factor (Kuo et al., 2016), and also have the potential to activate local stem cell niches, reduce oxidative stress, and modulate immune responses (Takemitsu et al., 2012). Combined with the fact that they were easy to isolate, relatively abundant in fatty tissue, and harvested in large numbers with minimal donor site morbidity (Kokai et al., 2014), ADSCs demonstrated a great potential to be used for diabetic wounds. A local injection that directly delivered ADSCs at injury sites causes minimal invasion and thus has gained popularity for clinical applications (Li et al., 2012). However, harsh diabetic wound microenvironment factors such as hypoxia, ischemia, and the persistence inflammation result in upregulation of MMPs (Nguyen et al., 2018), leading to low cell retention and engraftment efficiency, which significantly compromised the clinical performance of stem cell therapies.

To address this hurdle, one potential strategy was to suspend cells in a hydrogel matrix that provided a suitable microenvironment. Because of its superior biocompatibility and controllable physical and functional properties, hydrogel has gained extensive attention for medical wound dressing (Yang et al., 2021). Natural ECM protein such as collagen or its denatured form gelatin retained cell adhesion motifs, and MMP-mediated degradability became popular (Santoro et al., 2014). Dong et al. improved the survival ratio of ADSCs in diabetic wounds using a gelatin-based hydrogel delivery system (Dong et al., 2017). Another research that encapsulated ADSCs in gelatin bulk hydrogel displayed a promoting effect on neovascularization and wound closure (Dong et al., 2018). However, when applied on the wound bed, the limited interface between the bulk hydrogel and the wound resulted in poor tissue infiltration and thus a low survival of stem cells. Therefore, the establishment of alternative hydrogel in other geometries as stem cell delivery vehicles was highly demanded.

Recent advances in tissue engineering have demonstrated the versatility and efficacy of hydrogel microparticles as drug and cell delivery depots (Newsom et al., 2019). Compared with the bulk hydrogel, such geometry endowed microspheres with a large surface area that facilitated nutrient and waste diffusion and thereby maintained the viability of encapsulated cells (Chen et al., 2006). Microparticles also provided mechanical support to the regenerated tissue. Such function was inherently affected by the degradation (Qian et al., 2018). Hence, adaptive material was needed, of which the degradation rate should match well with the tissue regeneration. In addition, our previous research demonstrated that, after being applied on the wound surface, hydrogel microparticles functioned as scaffolds and were gradually embedded in the regenerated skin tissue (Shi et al., 2019a). This finding suggested that hydrogel microspheres could be a suitable carrier for local delivery of ADSCs to improve diabetic wound healing. Although various bulk hydrogels have been studied, microspheres such as gelatin hydrogel microspheres entrapping ADSCs have rarely been applied on wounds. Furthermore, the mechanism of gelatin microspheres along with the encapsulation of ADSCs on diabetic wound healing was still not clear.

Hence, the performance of stem cell therapy together with gelatin hydrogel microspheres on diabetic wound healing was investigated. Gelatin was selected because it had MMP-mediated degradability (Santoro et al., 2014), whereas diabetic wounds were rich in MMPs (Nguyen et al., 2018). Gelatin microspheres were fabricated to encapsulate ADSCs from SD rats (rADSCs) using the microfluidic technique. The properties and the feasibility of gelatin microspheres as a stem cell delivery platform were systematically characterized, including cross-linking degree, proteinase degradation, adhesion and proliferation behaviors of fibroblast cells, and viability and morphology of encapsulated rADSCs. Finally, *in vivo* performances were evaluated in the full-thickness skin diabetic wound model; CM-Dil-labeled rADSCs were encapsulated in microspheres to investigate whether the transplanted rADSCs were involved in the healing process.

MATERIALS AND METHODS

Materials

Gelatin (type A) was obtained from Sigma-Aldrich (St. Louis, MO, USA). Genipin was purchased from Wako (Japan). Dulbecco's modified eagle medium—basic (DMEM), penicillin/streptomycin antibiotics, fetal bovine serum (FBS), collagenase type I, and trypsin–ethylenediaminetetraacetic acid were supplied by Gibco (Carlsbad, CA, USA). Endothelial cell medium was purchased from ScienCell Research Laboratories (Carlsbad). Peanut oil was from Arawana (Guangzhou, China). Ninhydrin, $SnCl{\cdot}2H_2O$, ethylene glycol monomethyl ether, and streptozotocin (STZ) were from Macklin (Shanghai, China). Actin cytoskeleton, focal adhesion staining kit (FAK-100), and pentobarbital sodium were from Merck (Billerica, MA, USA). Cell Counting Kit-8 (CCK-8) was purchased from Dojindo (Shanghai, China). Cell Tracker TM CM-DiI (C7000) was from Molecular Probes (Eugene, USA). β3-tubulin (D71G9)

rabbit mAb and Neurofilament-L (DA2) mouse mAb were purchased from Cell Signaling Technology (Danvers, MA, USA). All other chemicals and reagents were of analytical grade. All reagents were used as received.

Preparation of Uniform Gelatin Microspheres

Monodisperse gelatin microspheres were fabricated using a microfluidic device consisting of two syringe needles and a polytetrafluoroethylene tube (inner/outer diameters were 0.3 and 0.6 mm, respectively). Briefly, a 26 G needle was first connected with the polytetrafluoroethylene tube, and then, a 31 G needle was inserted into the tube at an appropriate position, keeping the needle concentric within the tube. All connections were sealed with acrylic adhesive glue. The internal phase was gelatin/phosphate-buffered saline (PBS) solution (10% w/v, 37°C), and the flow rate was set as 5 μl/min. Peanut oil was the continuous phase, at a flow rate of 100 μl/min. Gelatin microspheres were collected in 10°C peanut oil for 10 min, and then, these batch microspheres were further incubated in 4°C ice bath for another 10 min for complete gelation. Genipin/PBS solution (0.5% w/v, 1 ml) was added into the microsphere/peanut oil suspension (containing 50-mg microspheres) at room temperature (~23°C) for cross-linking. After centrifugation to remove the supernatant, microspheres were rinsed three times with DMEM (containing 5% FBS). The collected microspheres were stored in PBS for subsequent characterizations.

To obtain sterile microspheres, gelatin/PBS solution, peanut oil, genipin solution, and PBS were sterilized by filtration, and all fabrication procedures were performed in a laminar flow hood.

Characterizations of Gelatin Microspheres

The cross-linking degree of gelatin microspheres was quantified using a ninhydrin assay, which was defined as the percentage of amino groups reacted with the cross-linking agent (Liang et al., 2003). One milliliter of ninhydrin solution was added into each sample containing 50-mg gelatin microspheres, which were cross-linked with genipin for 0, 1, 2, or 4 h (n = 3). After incubated at 100°C for 20 min, isopropanol (50% w/v, 5 ml) was added, and 1-ml supernatant was taken out to measure the absorbance at 570 nm. For the following tests, microspheres cross-linked for 1 h were used.

In vitro proteinase degradation of microspheres was monitored following similar procedures reported elsewhere (Turner et al., 2017). In brief, microspheres (100 mg/ml) were suspended in collagenase type I solution (0.75 mg/ml) at 37°C. Because the reaction between genipin and amino acids formed blue molecules, which showed the maximum absorbance at 590 nm and also released into the solution due to proteinase degradation of gelatin, absorbance at 590 nm of the supernatant was measured every 90 s.

The morphology of hydrogel microspheres was observed under a light microscope, and the average particle size was calculated using ImageJ. After freeze-drying, surface morphology was observed using a scanning electron microscope (Quanta 400F, FEI, Netherlands).

Adhesion and proliferation behaviors of fibroblast cells (NIH-3T3) on sterile gelatin microspheres were investigated. Microspheres were placed in a non-treated 48-well plate (50 mg/well), whereas a treated 48-well plate was used as the control group (TCP). NIH-3T3 cells were seeded at a density of 5×10^4 cells/well. On days 1 and 3, cell viability was measured using a CCK-8 assay (n = 3). Cytoskeleton staining was carried out on day 2, following the manufacturer's instructions. Images were taken using a confocal laser scanning microscope (CLSM, FV3000, Olympus, Japan).

Preparation and Characterizations of Adipose-Derived Stem Cells From Rats-Loaded Gelatin Microspheres

rADSCs were isolated from rats following our previous procedures (Shi et al., 2019b). Cells at passages 3–4 were mixed with gelatin/PBS solution. In the suspension, gelatin concentration was 10%, and cell density was 5×10^6 cells/ml. A total of 100 μl of cell suspension was loaded in a syringe as internal phase, and other parameters were followed as described in *Preparation of Uniform Gelatin Microspheres*. After rinsing, rADSC-loaded gelatin microspheres (rADSC/MS), which contained 5×10^5 cells per sample, were cultured in DMEM/FBS medium. On days 1 and 7, live/dead assay and cytoskeleton staining were performed and observed under CLSM.

For *in vitro* coculture and *in vivo* tests, rADSCs were labeled with CM-Dil before being entrapped in gelatin microspheres. In brief, 1 mg/ml CM-Dil stock solution was diluted with PBS at 1: 500. rADSCs were rinsed with PBS. After adding CM-Dil solution, cells were incubated for 30 min at room temperature and then kept in a refrigerator at 4°C for 15 min to enhance CM-Dil labeling the plasma membrane. After the staining process, the cells were rinsed with PBS.

CM-Dil-labeled rADSC/MS were cocultured with human umbilical vein endothelial cells (HUVECs, a gift from Quan Daping group in School of Materials Science and Engineering, Sun Yat-sen University) to investigate whether exosomes from rADSCs were uptaken by HUVECs. HUVECs were seeded on Petri dishes for CLSM at a density of 5,000 cells/cm^2 and cultured in an endothelial cell medium. CM-Dil-labeled rADSC/MS were placed in the transwell. After cocultured in the endothelial cell medium for 5 days, HUVECs were fixed, stained with 4′,6-diamidino-2-phenylindole, and observed under CLSM. HUVECs being solo-cultured were also observed.

Application of Gelatin Microspheres on Full-Thickness Skin Wound of Type I Diabetes Mellitus Rats

The *in vivo* test was approved by the Institutional Animal Care and Use Committee of Sun Yat-sen University. Type I diabetes mellitus (TIDM) was induced in Sprague-Dawley rats (SD rats, 250–300 g, 8 weeks old) according to routine procedures (Kuo et al., 2009). Briefly, after fasting for 1 day, tail vein blood was taken to measure the fasting blood glucose. STZ solution (1% w/v) was injected intraperitoneal at 50 mg/kg. The model was considered

successfully induced when the initial blood glucose value was <8.9 mmol/L and the random blood glucose after injection of STZ solution was ≥16.7 mmol/L for three consecutive days.

TIDM rats were randomly divided into three groups (n = 5). After anesthetized with 3% sodium pentobarbital solution, three circular full-thickness excisions with a diameter of 8 mm were created on the back of each rat. MS (100 mg) and rADSC/MS (100 mg containing 5×10^5 cells) were applied on wound beds; wound without any treatment was set as the control group. Wounds were then covered with a transparent dressing and further fastened with a self-adhesive bandage for protection. On days 3, 7, and 14, wounds were photographed using a digital camera, and ImageJ was used to measure the wound area. The wound contraction was calculated using **Eq. 1**:

$$Wound\ contraction\ (\%) = (A_0 - A_t)/A_0 \times 100\% \quad (1)$$

where A_0 is the wound area on day 0, and A_t is the wound area at the indicated time point.

On days 3, 7, and 14, rats were killed by injection of excessive 3% sodium pentobarbital solution. Optical coherence tomography (OCT) analysis was first used to observe the distribution of gelatin microspheres in the wound bed. The scanning wavelength was 1,310 nm.

Histological and Immunohistochemistry Staining Analysis

The full-thickness skin around the wound (1.5 × 1.5 cm) was removed, fixed in paraformaldehyde solution, paraffin-embedded, and sectioned for hematoxylin/eosin staining, and Masson's Trichrome staining and CD31 immunohistochemical staining were performed as previous (Shi et al., 2019a). Sectioned tissue without any staining was observed under CLSM to investigate whether CM-Dil-labeled cells were present.

Immunofluorescence Analysis

For neuronal marker staining, sections were first repaired using ethylenediaminetetraacetic acid antigen retrieval solution (pH 9.0) for 5 min at 100°C and blocked with 3% BSA solution for 30 min. After rinsing, sections were probed overnight at 4°C with the following primary antibodies: β3-tubulin (1:200, Cell Signaling Technology) or Neurofilament-L (1:100, Cell Signaling Technology). Sections were then washed and incubated with Alexa Fluor 488 conjugated goat anti-rabbit or rabbit anti-mouse secondary antibodies (1:500, Invitrogen) for 1 h at 37°C, correspondingly.

To investigate the inflammatory response, immunofluorescence analysis of CD68 (1:1,000, Invitrogen) and CD206 (1:200, Proteintech) was performed similarly as earlier. Sections were then incubated with Alexa Fluor 647 conjugated goat anti-rabbit or Alexa Fluor 568 conjugated rabbit anti-mouse secondary antibodies (1:500, Invitrogen) for 1 h at 37°C, respectively.

To evaluate exosomes, CD63 primary antibody (1:200, Affinity) was selected and incubated with sections at 4°C overnight, then treated with Alexa Fluor 647 conjugated goat anti-rabbit secondary antibody.

Nuclei were counterstained with 4′,6-diamidino-2-phenylindole for 10 min. Sections were observed using a CLSM.

Statistical Analysis

All data were shown as mean ± standard deviation, and the difference between groups was analyzed with Student's paired T-test. $p < 0.05$ indicated that difference was statistically significant.

RESULTS

Characterizations of Gelatin Microspheres

Gelatin microspheres were prepared using a microfluidic method. Precooled peanut oil (~10°C) was used as the collecting phase to rapidly gelatinize microdroplets. As shown in **Figures 1A,B**, uniform microspheres with a narrow size distribution were obtained, for which the average diameter was 267 ± 12 μm. Then, genipin/PBS solution was added to cross-link microspheres. This introduced a nucleophilic agent to initiate the cross-linking reaction of genipin with itself, thereby forming an oligomeric cross-linking agent that produces a high degree of intermolecular binding (Liang et al., 2004). The reaction was carried out at 23°C to ensure that the precooled microspheres were not dissolved and cross-linked at an appropriate rate and formed a stable structure; when compared with 10 or 4°C, cross-linking temperature of 23°C had minimum influences on cell viability. As shown in **Figures 1C,D**, after reaction for 1 h, gelatin microspheres were still well-dispersed and stable at 37°C. The average diameter was 361 ± 7 μm, slightly bigger than that in the oil phase. Based on the ninhydrin assay (**Figure 1E**), it was found that the cross-linking degree positively correlated with the cross-linking time. Because cells showed a more spread morphology within soft hydrogel matrix (Sung et al., 2018), 1 h was selected. After lyophilization, scanning electron microscope image (**Figure 1F**) showed that the particle was no longer spherical, whereas the size was slightly increased. This may be due to the freeze-drying process. The lyophilized microspheres had a mesh-liked surface, indicating that microspheres were porous.

Gelatin microspheres were developed to be applied on diabetic wounds rich in MMPs, such as MMP2 and MMP9 (Gooyit et al., 2014). As MMPs and collagenase shared common target sites to cleave amide linkages within the repeating peptide motif QPQGLAK in gelatin (Fonseca et al., 2014), collagenase (type I) was used to compare the degradation rates of gelatin hydrogel in different shapes. The prepared microspheres were stable in PBS longer than 7 days. When collagenase was introduced, the degradation was much faster. As shown in **Figure 1G**, within 10 min, microspheres were completely degraded. The rate was higher than that reported in the literature, where microspheres were degraded within 14 min (Turner et al., 2017). The difference was probably because of the slightly lower cross-linking degree for the microspheres here. As for the bulk hydrogels, which were fabricated following the same parameters for microspheres, fourfold longer time (*i.e.*, 44 min) was needed (**Figure 1H**). Microspheres had a much higher

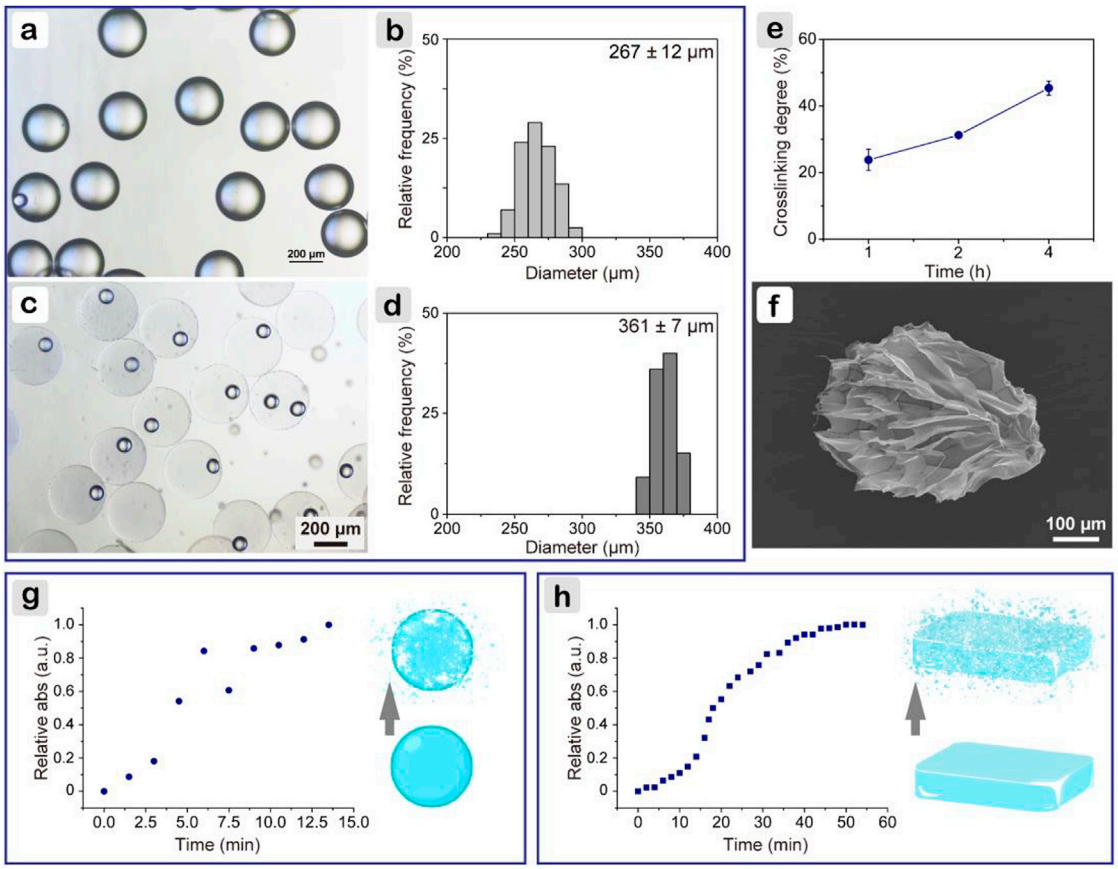

FIGURE 1 | Characterizations of gelatin microspheres. **(A)** Light microscope image of microspheres in precooled peanut oil, and **(B)** corresponding particle size distribution; **(C)** after cross-linking for 1 h, and **(D)** corresponding particle size distribution; **(E)** cross-linking degree of gelatin microspheres; **(F)** scanning electron microscope image of gelatin microsphere after lyophilization; change of relative absorbance at 590 nm for microspheres **(G)** and bulk hydrogel **(H)** with proteinase degradation time.

specific surface area than bulk hydrogels, which facilitated enzyme infiltration and further contributed to a faster degradation rate.

In Vitro Cell Tests for Gelatin Microspheres as Adipose-Derived Stem Cells From Rats Delivery Platform

The proliferation rate of fibroblasts (NIH-3T3) was measured using the CCK-8 assay (**Figure 2A**), where the MS group showed close values with the TCP group on days 1 and 3. Cell adhesion behaviors were further investigated. After growing for 2 days, all cells spread well on the microsphere surface (**Figure 2B**). The well-organized actin filament structure and presence of vinculin were observed. On gelatin microspheres that were fabricated using the double emulsion method and also cross-linked with genipin, osteoblasts on large microspheres (200–300 μm) had a larger spread out morphology and a faster proliferation rate than on small microspheres (75–160 μm) during 7 days of culture (Lau et al., 2010). Thus, also considering the particle size effect on cell proliferation, it was reasonable that gelatin microspheres here supported cell adhesion and proliferation.

To determine the suitability of gelatin microspheres as delivery vehicles for stem cells, live/dead assay and cytoskeleton staining for the encapsulated rADSCs were conducted. After culturing for 7 days and live/dead staining, microspheres were scanned with CLSM for 100 layers, and a three-dimensional (3D) image was then reconstructed. As shown in **Figure 2C**, all rADSCs were green, whereas nearly no red cells were detected, demonstrating that most cells were still viable. On the first day, the cells were spherical; actin without filament structure was detected, whereas vinculin structures were present. After 7 days of culture, rADSCs spread out, and a large number of filopodia structures formed (**Figure 2D**), which may be the result of the gradual interactions between cells and gelatin matrix (Baeckkyoung et al., 2018). The changes of cell spreading morphologies with culture time were similar to the reported results that within soft gelatin matrix, development of filopodia and actin filament in stem cells was easier than that within the rigid matrix (Zhao et al., 2016; Sung et al., 2018).

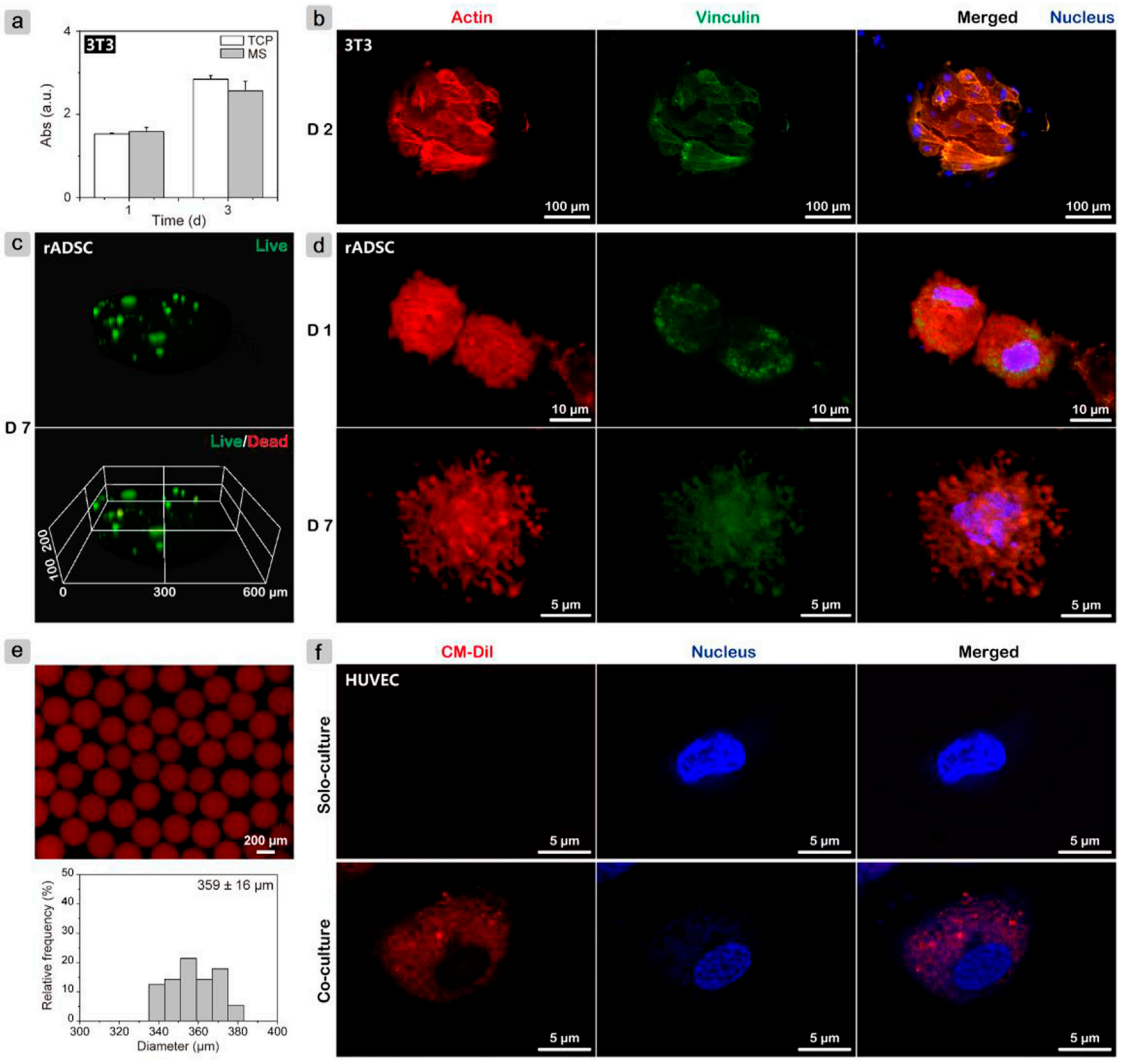

FIGURE 2 | *In vitro* cell test results. **(A)** Monitoring proliferation of NIH-3T3 cells on gelatin microspheres using CCK-8 assay; **(B)** CLSM images of NIH-3T3 cells after growing on microspheres for 2 days and cytoskeleton staining to evaluate adhesion behavior. **(C)** Live/dead assay and **(D)** cytoskeleton staining of rADSCs inside gelatin microspheres after culturing for 7 days to investigate cell viability and spreading morphology, respectively. **(E)** Fluorescence image of CM-Dil-labeled rADSC/MS and corresponding particle size distribution. **(F)** CLSM images of HUVECs after cocultured with CM-Dil-labeled rADSC/MS and solo-cultured for 5 days.

The fabricated gelatin microspheres did not only facilitate the adhesion and proliferation of fibroblast cells but also maintained the cell viability of the encapsulated rADSCs. For MSCs, the therapeutic potential to accelerate cutaneous wound healing was found to be related to exosomes (Shabbir et al., 2015). Red fluorescent lipophilic dye (Dil)-labeled exosomes from Dil-labeled synovium MSCs were found to be in the perinuclear region of human dermal microvascular endothelial cells (Tao et al., 2017). To investigate whether exosomes from rADSCs in gelatin microspheres were internalized by other types of cells, rADSC/MS with CM-Dil-labeled rADSCs were fabricated. As shown in **Figure 2E**, the gelatin matrix demonstrated autofluorescence property at ~600 nm because of cross-linking (Solorio et al., 2010). When compared with blank microspheres, the one entrapping cell showed a broader size distribution. Coculture was carried out in HUVEC medium (ECM medium), in which rADSCs also proliferated well (**Supplementary Figure S1**). After 5 days, red fluorescent exosomes were observed inside HUVECs (**Figure 2F**). This phenomenon confirmed that exosomes were slowly released from rADSCs and eventually internalized by HUVECs seeded on TCP. The release and uptaking of exosomes may improve diabetic wound healing.

Adipose-Derived Stem Cells From Rats Improving Diabetic Wound Healing

Full-thickness wounds of TIDM rats were established to evaluate the performance of rADSC/MS on wound healing. The digital images of wounds within 14 days are shown in

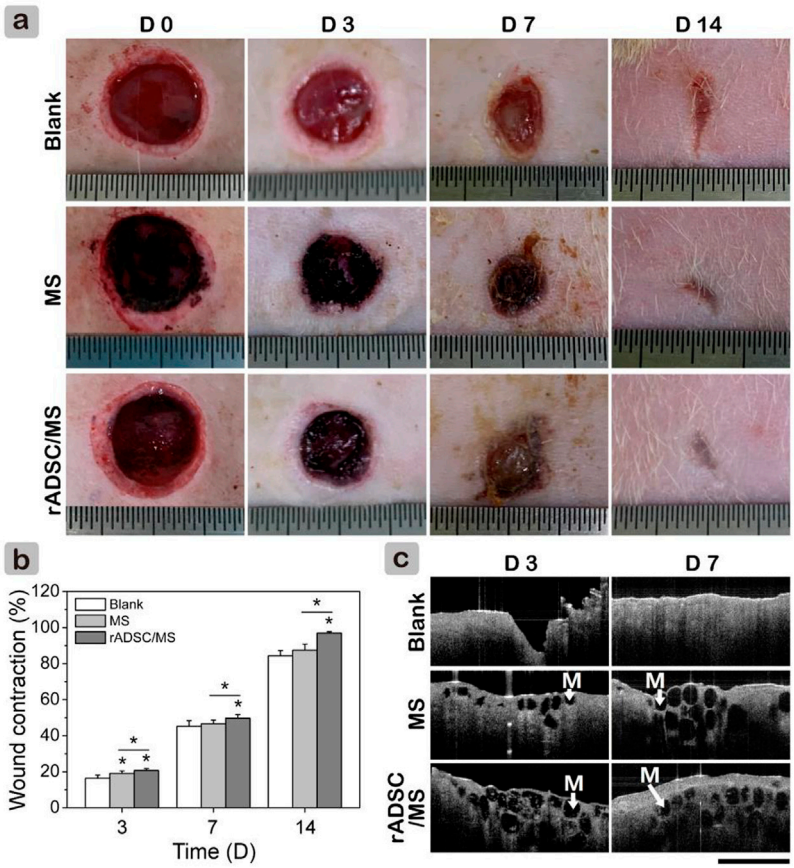

FIGURE 3 | Effects of gelatin microspheres on wound healing in diabetic rats. **(A)** Wound healing process within 14 days was recorded in photographs. Length between adjacent lines on ruler is 0.5 mm. **(B)** Wound contraction was calculated based on these images (data = mean ± SD, $n = 5$, $^*p < 0.05$). **(C)** OCT scanning images for section view of regenerate granulation tissue. Black circles (also "M") in wound area represent gelatin microspheres. Scale bar is 2 mm.

Figure 3A. Microspheres attached wound beds tightly. When compared with the blank group, both the MS and rADSC/MS groups appeared to have less bleeding; during the following healing process, these groups showed a more rapid wound contraction. On day 14, the rADSC/MS group nearly completely healed with regenerated smooth skin, whereas the blank group only healed ~80%. At each time point, the contraction value for the rADSC/MS group was significantly higher than that for the MS and blank groups (**Figure 3B**). To detect microsphere integration, OCT was used to scan the wounds *in situ*. As shown in **Figure 3C**, the regenerated tissue was around and over microspheres in both the MS and rADSC/MS groups, showing that microspheres were gradually integrated into the regenerated skin tissue from days 3–7.

Macroscopic results demonstrated that rADSC/MS accelerated diabetic wound contraction. To gain further insights, histological analysis was performed. As shown in **Figure 4A**, on day 3, granulation tissue was observed in all groups, and a few microspheres were detected for both the MS and rADSC/MS groups. The bonding between granulation tissue and microspheres was not strong enough; therefore, the distribution of microspheres on wound sections was probably affected by the embedding and following processes. On day 7, granulation tissues grew around microspheres in both the MS and rADSC/MS groups. A migrating reepithelialization layer from the wound edge to the center gradually formed over the microspheres. This trend was evident for the rADSC/MS group, demonstrating that the wound was in a rapid healing rate. Neutrophils clustered at the microsphere edge, showing a certain inflammatory response. On day 14, both epidermis and dermis layers were reestablished for all groups, whereas the structure of the dermis layer was different. For rADSC/MS, the regenerated dermis was close to the normal tissue; plenty of growing hair follicles and sebaceous glands were present, and no layers of remaining microspheres were detected. As for the MS group, hair follicles and sebaceous glands gradually formed from wound edges over undegraded microspheres. For the blank group, there was no hair follicle or sebaceous gland observed, indicating that the wound healing was much slower. Additionally, in subdermal layers of the MS and rADSC/MS groups, there were much more large blood vessels than the blank group.

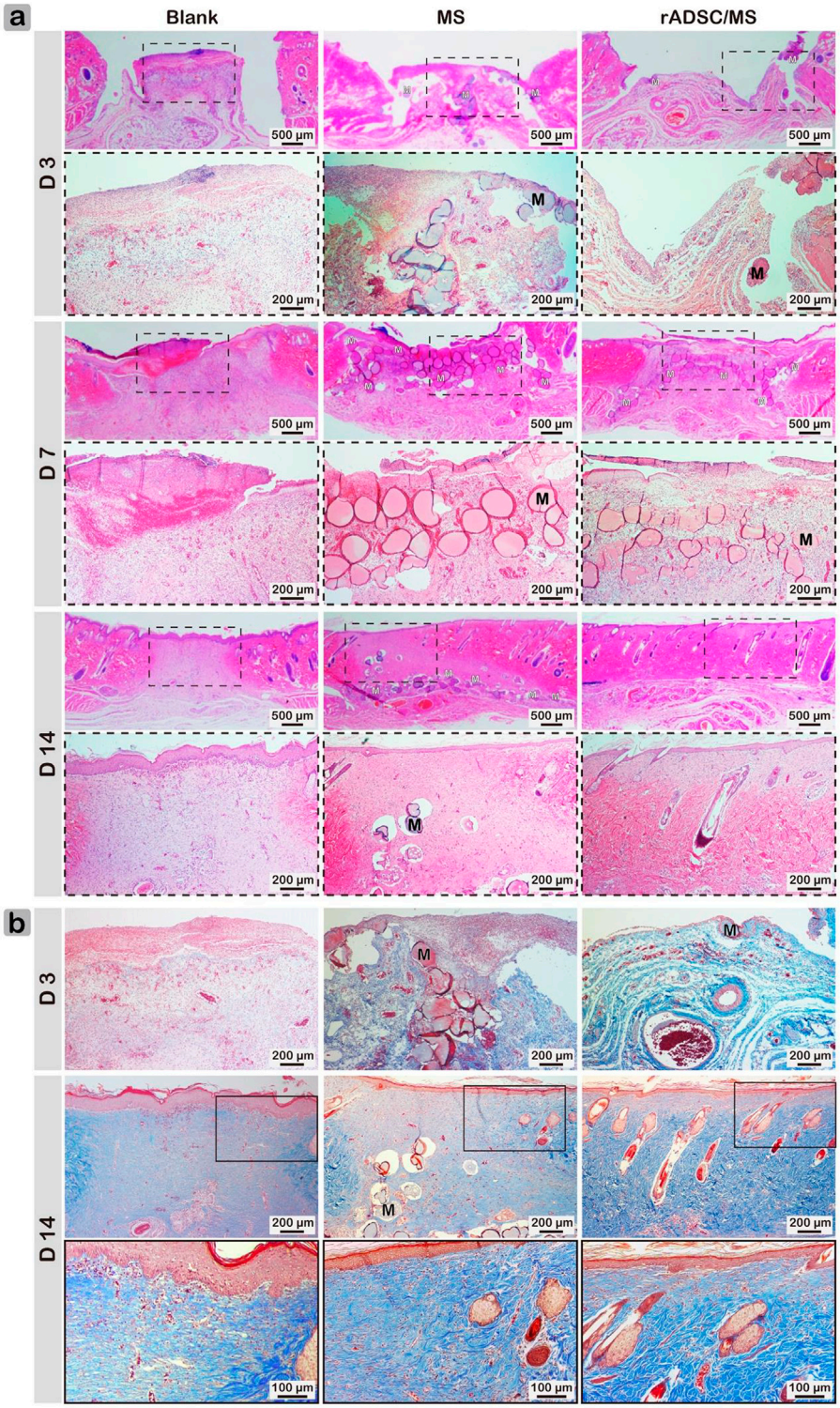

FIGURE 4 | Representative **(A)** hematoxylin/eosin- and **(B)** Masson's Trichrome-stained wound sections for blank, MS, and rADSC/MS groups on days 3, 7, and 14. "M" represents gelatin microspheres. Microspheres functioned as scaffolds to fasten wound healing and enhance collagen deposition; with encapsulation of rADSCs, enhancing effect was more significant. On day 14, arrangement of collagen fibers for rADSC/MS group was similar to unwounded skin.

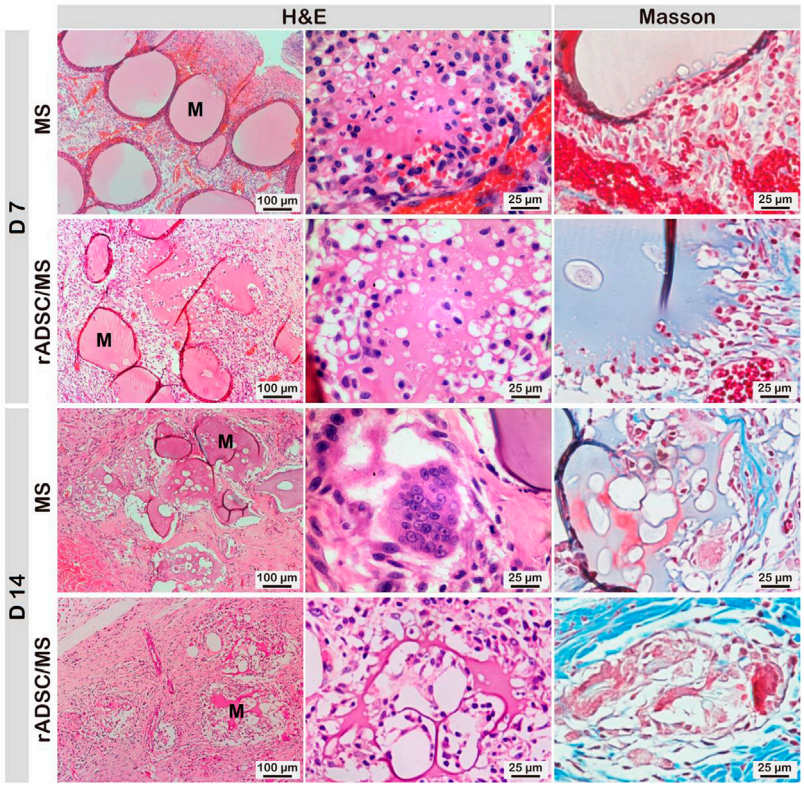

FIGURE 5 | Biocompatibility and biodegradability of gelatin microspheres during wound healing. Degradation rate of microspheres in rADSC/MS group appeared to be faster than that in MS group. "M" represents gelatin microspheres.

Collagen is susceptible to glycosylation, which reduces its sensitivity to enzymes and further affects metabolism, repair, and renewal (Abiko and Selimovic, 2010). Factors such as increased level of MMP9 in diabetic skin impair collagen accumulation leading to impaired wound healing (Li et al., 2013). Therefore, Masson's Trichrome staining was performed to determine the formation and distribution of collagen fibers (**Figure 4B**). The blank group always showed the least collagen production. Compared with the MS group, collagen deposition in the rADSC/MS group was more significant. On day 14, dense collagen formed, and collagen fibers arranged in a neat manner similar to normal tissues, whereas neither the MS group nor the blank group had mature collagen fibers.

Mechanism of Adipose-Derived Stem Cells From Rats on Improving Diabetic Wound Healing

During wound healing, gelatin microspheres were embedded in the regenerated skin tissue for both the MS and rADSC/MS groups. Gelatin is hydrolyzed from collagen, with good biocompatibility and biodegradability (Sivadas et al., 2008). As shown in **Figure 5**, the degradation of gelatin microspheres in the rADSC/MS group was faster. On day 7, nearly intact microspheres with neutrophils gathering on the surface were present in the MS group; for the rADSC/MS group, a lighter inflammation response was detected, and most microspheres became porous. Such a porous structure may facilitate the signaling between rADSCs and the host tissue. On day 14, in the MS group, microspheres became porous, whereas microspheres of the rADSC/MS group were basically degraded. Besides neutrophils, macrophages also took part. Regarding the faster degradation rate for the rADSC/MS group, entrapping rADSCs may result in slightly higher water content in microspheres, as gelatin hydrogel with a higher water content degraded faster when subcutaneously implanted into mice back (Tabata, 1998). The tissue regeneration rate adaptively matched with the microsphere degradation rate, especially for the rADSC/MS group, where the collagen fibers around microsphere debris arranged neatly.

Macrophages were key factors in the inflammatory–proliferation phase transition, which mainly contained two subtypes: classically activated M1 with pro-inflammatory properties and alternatively activated M2 exhibiting anti-inflammatory and pro-wound healing functions (Wynn et al., 2013). On day 7, co-staining results of CD68 and CD206 demonstrated a much higher percentage of M2 macrophages in the regenerated tissues of the rADSC/MS group than the other two groups (**Figures 6A,C**). This phenomenon indicated that the wound was in the process of healing. As for the blank group, more $CD68^{+}$ cells were still present, showing an

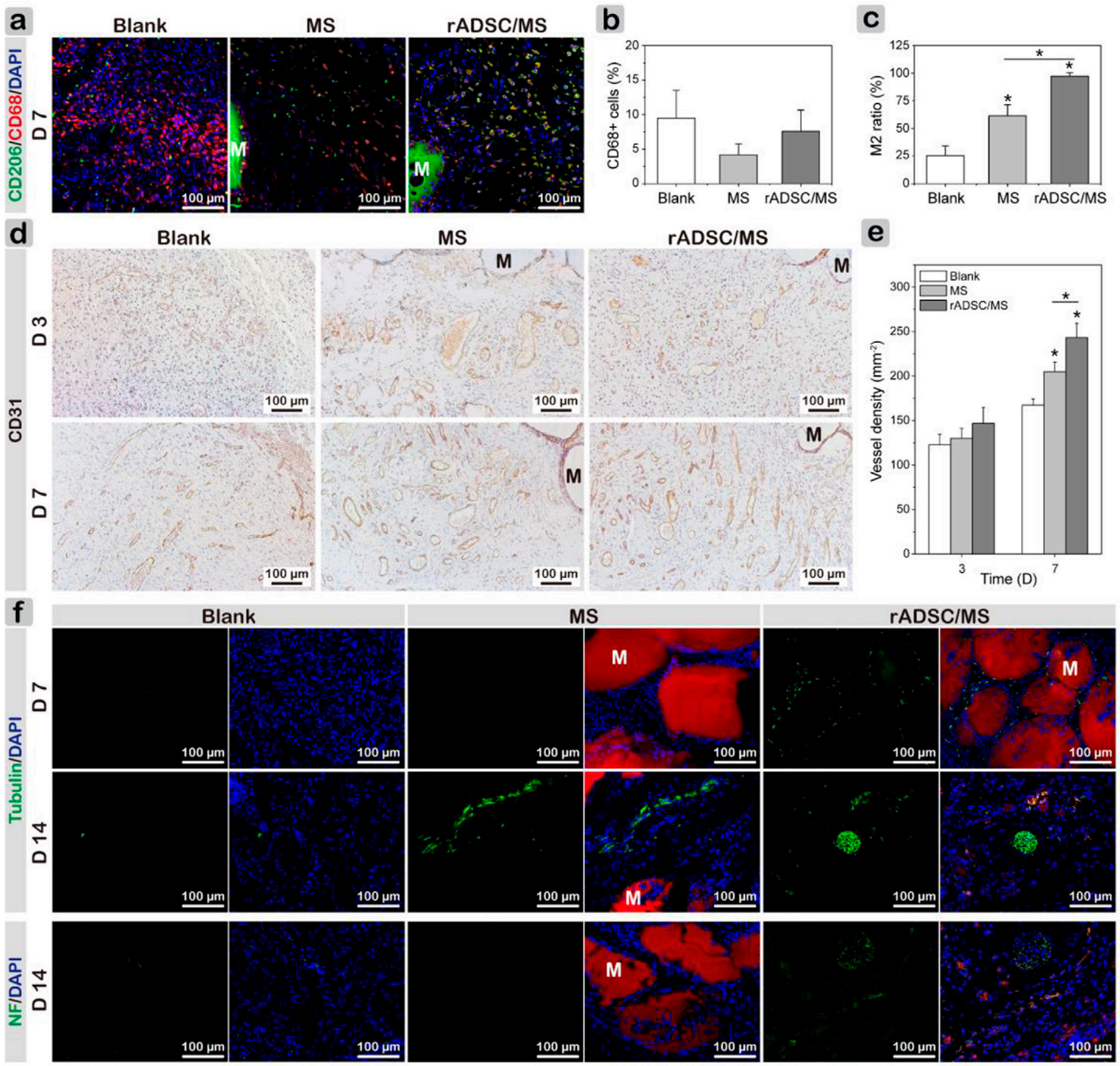

FIGURE 6 | Investigating mechanism of MS and rADSC/MS on promoting diabetic wound healing by evaluating macrophage polarization, angiogenesis, and neurogenesis during wound healing. **(A)** Representative CLSM images for all groups on day 7 showing increased presence of M2 macrophages around microspheres, as evidenced by co-staining of CD68 and CD206. CD68 antibody was conjugated with Alexa Fluor 647 (650/668 nm), and CD206 antibody was conjugated with Alexa Fluor 568 (578/603 nm). **(B)** Percentage of $CD68^+$ cells; **(C)** M2 macrophage ratio of CD206 + $CD68^+$ cells to $CD68^+$ cells. **(D)** Representative CD31 immunohistochemical staining images of wound sections on days 3 and 7 and **(E)** corresponding quantitative results of vessel density. **(F)** Immunofluorescence images of sections revealing distribution of newly regenerated neurons (tubulin) and axon (Neurofilament-L) in all groups on days 7 and 14, respectively. Tubulin and Neurofilament-L antibodies were conjugated with Alexa Fluor 488 (495/518 nm). "M" represents gelatin microspheres. Fluorescence intensity was calculated using ImageJ. Data = mean ± SD, $n = 3$, $^*p < 0.05$ when compared with blank or MS group.

excessive inflammatory response (**Figure 6B**). This may illustrate the delayed wound healing. The encapsulation of rADSCs in the rADSC/MS group may regulate the polarization of macrophages to the M2 subtype and thus promote wound healing.

Local ischemia results from microvascular complications, and hyperglycemia inhibits angiogenesis in diabetes, which considerably delays wound healing (Botusan et al., 2008). Thus, the reestablishment of the vascular network is crucial.

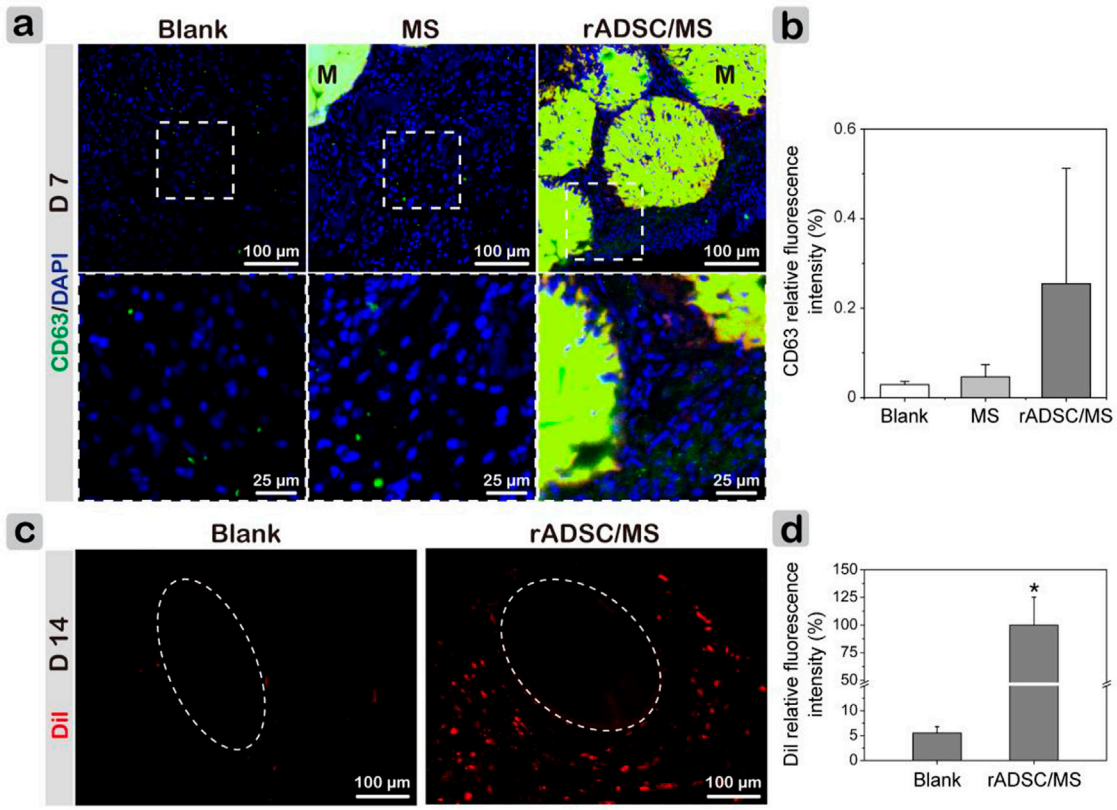

FIGURE 7 | Investigating paracrine performance of encapsulated rADSCs during wound healing. **(A)** CD63 staining results showing presence of exosomes in regenerated tissues on day 7. Local magnified images were also shown. CD68 antibody was conjugated with Alexa Fluor 647 (650/668 nm). "M" represents gelatin microspheres. **(B)** CD63 fluorescence intensity of three groups on day 7. **(C)** CLSM images of wound sections without any staining on day 14. Dotted circles represent hair bulbs in subdermal layer, and rADSCs in gelatin microspheres were labeled with CM-DiI (DiI). **(D)** Corresponding DiI relative fluorescence intensity for blank and rADSC/MS groups. Intensity was calculated using ImageJ. Data = mean ± SD, $n = 3$, $^*p < 0.05$ when compared with blank group.

Immunohistochemical staining of CD31 for tissue sections and quantitative analysis of vessel densities based on CD31-positive capillaries were performed. **Figure 6D** shows that on both days 3 and 7, a large number of blood vessels regenerated. With healing time, the density of CD31-positive capillaries increased, where on day 7, the value of the MS group was significantly higher than that for the blank group, and the rADSC/MS group had the highest value (**Figure 6E**). On day 14, vessel density decreased in all groups (**Supplementary Figure S2**) because vascularization mainly occurred in the early stage of wound healing. These comparisons indicated that gelatin microspheres showed a certain promoting effect on angiogenesis; when rADSCs were entrapped, the promoting effect was stronger (rADSC/MS).

Diabetic peripheral neuropathy is the most common chronic complication (Galuppo et al., 2014). Besides looking at tissue regeneration, it was also important to observe the distribution of peripheral nerves. Thus, immunofluorescent staining of β III-tubulin and Neurofilament-L was conducted (**Figure 6F**). For the blank group, very few expressions for these two proteins were observed. In the rADSC/MS group, positive expressions of β III-tubulin around gelatin microspheres were observed on day 7. Such protein expression correlates with the early phase of neural differentiation, implying that neurogenesis began. On day 14, a relatively mature bundle of nerve fibers around degraded microspheres in the subdermal layer appeared; some β III-tubulin-positive cells co-fluoresced with red color (**Supplementary Figure S3**), demonstrating that these cells may be related with rADSCs (CM-DiI labeled). The presence of axon marker (Neurofilament-L) also demonstrated the promoting effects of rADSC/MS on neurogenesis, inducing axon's growth into the wound bed.

It was of great interest to investigate whether rADSCs are involved during wound healing. As *in vitro* coculture tests showed that rADSCs released exosomes that were internalized by other cells, immune fluorescence staining of exosome marker CD63 was performed on tissue sections

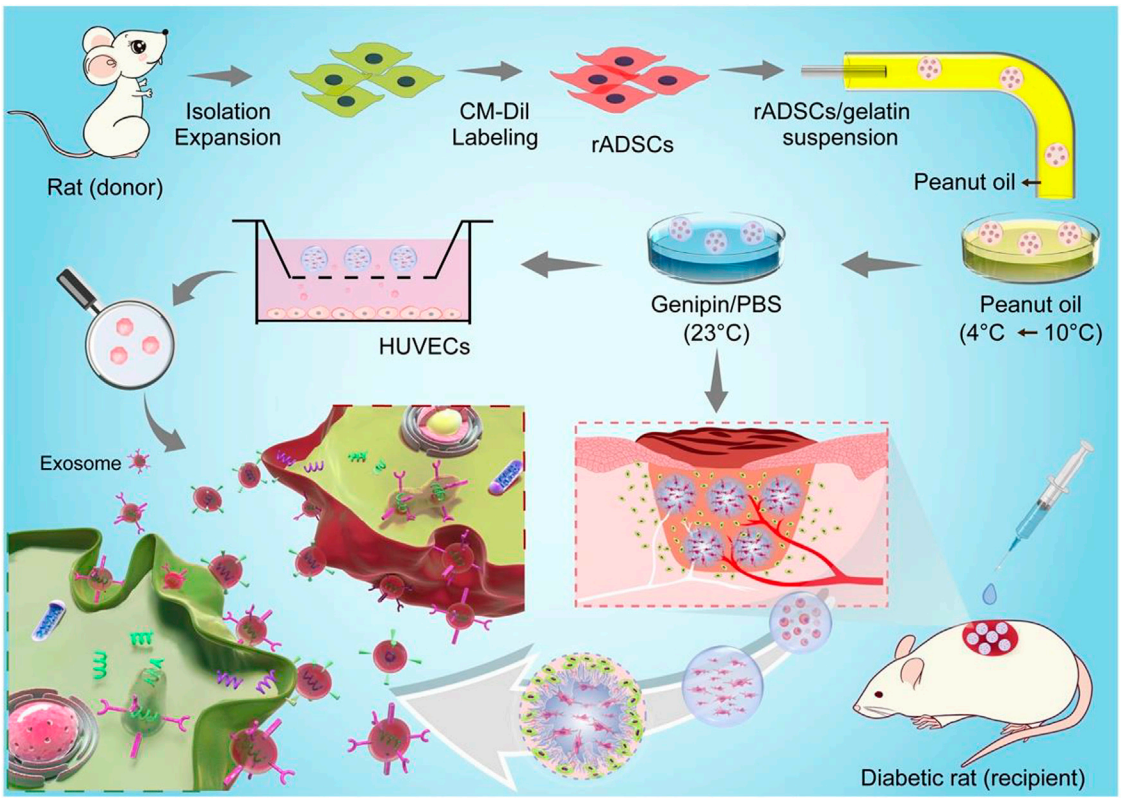

FIGURE 8 | Schemes for preparation of CM-DiI-labeled rADSCs-laden gelatin microspheres and application for diabetic wound healing. rADSCs were isolated and labeled with CM-DiI after expansion and then encapsulated in gelatin microspheres using a microfluidic method. After cross-linking, microspheres were applied in a full-thickness diabetic wound to enhance wound healing, including reepithelialization, angiogenesis (red tube), and nerve regeneration (white tube). Gelatin matrix degraded along with tissue regeneration in wound bed, and entrapped rADSCs influenced surrounding cells *via* paracrine effect. Schematic diagram for paracrine effect was shown on left corner; exosomes were released from CM-DiI-labeled rADSC (red) and uptaken by recipient cell.

(Nakazaki et al., 2021). On day 3, exosomes were observed in granulation tissues, and the fluorescence intensity of CD63 was slightly higher in the rADSCs/MS group (**Supplementary Figure S4**). On day 7, exosomes arose between microspheres in rADSCs/MS, and the fluorescent intensity was much higher than in other groups (**Figures 7A,B**). Here, rADSCs were labeled with CM-Dil. On day 14, as shown in **Figure 7C** (full-thickness results are shown in **Supplementary Figure S5**), plenty of red fluorescent cells around hair follicles were observed in the rADSC/MS group, whereas few fluorescent cells were detected in the same area for the blank group. The corresponding fluorescence intensities of the rADSC/MS group were 17-fold higher than that of the blank group (**Figure 7D**). Furthermore, plenty of fluorescent cells around the undegraded microsphere were also observed in the rADSC/MS group. As for the MS group, remaining autofluorescent gelatin microspheres were present, and no fluorescent cells were around (**Supplementary Figure S5**). Also, combined with the *in vitro* coculture results that red fluorescent exosomes were observed inside HUVECs, it can be inferred that these entrapped rADSCs remained viable during wound healing, and the paracrine effects may be through exosomes.

DISCUSSIONS

In this study, genipin–cross-linked gelatin microspheres were fabricated to deliver stem cells for diabetic wound healing (**Figure 8**), where the strategy did not only fasten wound closure but also enhanced functional recovery, including revascularization and regeneration of peripheral nerves and hair follicles.

Among various hydrogel materials, gelatin has attracted wide interest as a scaffold material because it retains intrinsic integrin-binding ligands for cell adhesion and can be easily cross-linked with genipin, a plant-derived cross-linker (Bigi et al., 2002). The genipin concentration and cross-linking time were two major factors influencing the viability of encapsulated cells and the elastic stiffness of cross-linked hydrogel. A total of 0.5% w/v genipin in a medium for 60 min maintained ~87% viability of MSCs, and the value decreased to ~80% at 1% w/v genipin for only 30 min (Baeckkyoung et al., 2018). Here, using a low concentration of 0.5% w/v cross-linking for 1 h did not only minimize the cytotoxicity of genipin but also resulted in a soft gelatin matrix. Additionally, encapsulation in gelatin microspheres may further protect rADSCs from genipin, as MSCs within 3D gelatin microgels exhibited significantly elevated viability as ~90% compared with 2D monolayer

culture with the viability of ~55% over 7 days in the pro-inflammatory environment (Baeckkyoung et al., 2018). Here, the high cell viability of rADSCs inside gelatin microspheres ensured the applicability to treat diabetic wounds.

A major challenge in MSC-based therapy for diabetic wound treatment has been associated with poor cell survival and integration (Wu et al., 2010). When injection of ADSC suspension in PEG-gelatin hydrogel into diabetic wounds, a remarkable decrease of ~40% cell viability as early as 2-h post-transplanting was detected (Dong et al., 2018). The main reasons included mechanical damage during injection, lack of cell-matrix adhesions, and the harmful inflammatory conditions at the injured site (Rustad et al., 2012). Here, encapsulating rADSCs inside gelatin microspheres provided a suitable microenvironment in the early stage of transplantation. After initial integration (**Figure 3C**), microspheres along with rADSCs well participated in the tissue regeneration (**Figure 4**). It was reported that GFP-labeled ADSCs migrated and accumulated in the subdermal layer of the wound margin on day 10 after injection and expressed vascular endothelial growth factor in the peri-wound area to activate neoangiogenesis. However, no fluorescent cells were observed around accessory organelles in the cutaneous layer (Kuo et al., 2016). It seemed that the local existence of ADSCs was crucial. Here, when rADSCs/MS were applied on diabetic wounds, gelatin microspheres were well integrated into the regenerated tissue to avail full local utilization of the entrapped rADSCs.

To restore tissue function, scaffold degradation was required to balance with tissue regrowth (Griffin et al., 2021). Here, gelatin microspheres may attract MMPs within diabetic wounds, resulting in the local enrichment of MMPs and microsphere degradation. The speculation was supported by the significant difference that gelatin microspheres were stable longer than 7 days in PBS, whereas *in vivo* microspheres became porous on day 7. As for the rADSC/MS group, microspheres were nearly completely degraded on day 14. This was much faster than the reported result, where the degradation time of gelatin hydrogel containing ADSCs was ~28 days (Dong et al., 2018). Compared with bulk hydrogel, the degradation of microspheres was faster. This was confirmed by the *in vitro* results that 10 min for microspheres compared with 44 min for bulk hydrogels were needed to degrade completely in collagenase solution. An appropriate degradation rate of scaffolds may guide fibroblasts infiltration, promote granulation tissue formation, and also prevent excessive contraction and fibrosis (Nyame et al., 2015), thus resulting in smooth skin for the rADSC/MS group.

Gelatin microspheres were well integrated into wounds and gradually degraded during tissue regrowth. ADSCs have been shown to secrete massive growth factors to improve fibroblast proliferation (Kim et al., 2011). Such paracrine effects were affected by the distance between MSCs and surrounded cells. The value was reported to be less than 200 μm to preferentially promote tube formation of HUVECs because of a significant increase in Ang-1 secretion (Piard et al., 2019). Here, the small size (~360 μm) of gelatin microspheres provided an appropriate distance. The paracrine effect of encapsulated rADSCs through exosomes was proved by both *in vitro* coculture (**Figure 2F**) and *in vivo* wound healing results (**Figures 7C,D**). Exosomes from MSCs were internalized by other cells and activated several signaling pathways, including Akt, ERK, and STAT3, enhancing proliferation and migration of fibroblasts and also angiogenesis (Shabbir et al., 2015). Furthermore, the 3D culture of ADSCs was found to improve the paracrine effect (Tomaszewski et al., 2019). Hence, for the rADSC/MS group, wound healing was significantly improved (**Figure 4**).

Recent studies found that *in vitro* co-encapsulation of ADSCs with early-stage follicles in an alginate-based 3D culture system supported follicular development through secretion of cytokines that promoted follicular survival, antrum formation, and meiotic competence (Green et al., 2019). Here, regeneration of hair follicles in the rADSC/MS group was much faster, whereas significantly more fluorescent cells around hair follicles than other groups were detected; these findings indicated that rADSCs might participate in the formation of follicles during wound healing. New hair follicles were reported to reprogram myofibroblasts that were abundant in dermal scar tissue to differentiate into adipocytes by activating the BMP-ZFP423 pathway during mouse wound healing. The depletion of myofibroblasts has been viewed as a main anti-scarring strategy (Plikus et al., 2017). Here, adipocytes were detected at the area close to the new hair follicles for both the MS and rADSC/MS groups on day 14 (**Supplementary Figure S6**), which might originate from myofibroblasts. Thus, it was reasonable that the deposition of well-organized collagen fibers was the fastest in the rADSC/MS group, as the regeneration of hair follicles was the earliest (**Figure 4**).

With a high specific surface area and appropriate *in vivo* degradation rate, gelatin microspheres facilitated tissue infiltration, enabling granulation tissue to grow tightly around these microspheres. Therefore, the presence of rADSCs in the gelatin matrix further contributed to the fastest wound closure, angiogenesis, collagen deposition, and peripheral nerve recovery. Hence, the rADSC/MS group showed better performance on improving diabetic wound healing than only gelatin microspheres.

CONCLUSION

Gelatin microspheres were developed for local delivery of rADSCs to promote diabetic wound healing. Uniform, well-dispersed gelatin microspheres with desired biocompatibility and degradation properties were obtained, which provided a suitable microenvironment for rADSCs survival, avoiding direct exposure to the complex microenvironment of diabetic wounds. Because of MMP-mediated degradation, gelatin microspheres may improve the local microenvironment of diabetic wounds, leading to faster and better wound healing when compared with the blank group. The encapsulation of rADSCs in the rADSC/MS group

promoted M2 polarization and peripheral nerve recovery and further facilitated angiogenesis and collagen and follicle formation, ultimately accelerating wound healing. The degradation rate of the rADSC/MS group matched well with tissue regeneration. Nevertheless, these data still could not provide direct evidence regarding whether rADSCs differentiated into adult somatic cells. Further investigations were needed. Taken together, gelatin microspheres showed great potential as a stem cell delivery vehicle and also as scaffold materials to improve diabetic wound healing.

DATA AVAILABILITY STATEMENT

The original contributions presented in the study are included in the article/**Supplementary Material**; further inquiries can be directed to the corresponding author.

ETHICS STATEMENT

The animal study was reviewed and approved by the Institutional Animal Care and Use Committee of Sun Yat-sen University.

AUTHOR CONTRIBUTIONS

MS and YL conceived the study and were in charge of overall direction and planning. MS, YG, and LL performed the measurements, MS and TS were involved in planning and supervising the work, and MS, JZ, and LY processed the experimental data and performed the analysis. MS drafted the manuscript and designed the figures with help from YG. All authors discussed the results and commented on the manuscript.

FUNDING

This work was supported in part by the Shenzhen Basic Research Project (no. JCYJ20190807155805818) and the project for Science and Technology New Star of Zhujiang in Guangzhou City (no. 201906010082).

SUPPLEMENTARY MATERIAL

The Supplementary Material for this article can be found online at: https://www.frontiersin.org/articles/10.3389/fbioe.2022.813805/full#supplementary-material

REFERENCES

Abiko, Y., and Selimovic, D. (2010). The Mechanism of Protracted Wound Healing on Oral Mucosa in Diabetes. Review. *Bosn J. Basic Med. Sci.* 10, 186–191. doi:10.17305/bjbms.2010.2683

Armstrong, D. G., Boulton, A. J. M., and Bus, S. A. (2017). Diabetic Foot Ulcers and Their Recurrence. *N. Engl. J. Med.* 376, 2367–2375. doi:10.1056/nejmra1615439

Baeckkyoung, S., Jess, K., Bing, Y., and Min-Ho, K. (2018). Colloidal Gelatin Microgels with Tunable Elasticity Support the Viability and Differentiation of Mesenchymal Stem Cells under Pro-inflammatory Conditions. *J. Biomed. Mater. Res. A* 106, 2753–2761. doi:10.1002/jbm.a.36505

Bigi, A., Cojazzi, G., Panzavolta, S., Roveri, N., and Rubini, K. (2002). Stabilization of Gelatin Films by Crosslinking with Genipin. *Biomaterials* 23, 4827–4832. doi:10.1016/s0142-9612(02)00235-1

Botusan, I. R., Sunkari, V. G., Savu, O., Catrina, A. I., Grunler, J., Lindberg, S., et al. (2008). Stabilization of HIF-1 Is Critical to Improve Wound Healing in Diabetic Mice. *Proc. Natl. Acad. Sci.* 105, 19426–19431. doi:10.1073/pnas.0805230105

Cavanagh, P. R., Lipsky, B. A., Bradbury, A. W., and Botek, G. (2005). Treatment for Diabetic Foot Ulcers. *The Lancet* 366, 1725–1735. doi:10.1016/s0140-6736(05)67699-4

Chen, R., Curran, S., Curran, J., and Hunt, J. (2006). The Use of Poly(l-Lactide) and RGD Modified Microspheres as Cell Carriers in a Flow Intermittency Bioreactor for Tissue Engineering Cartilage. *Biomaterials* 27, 4453–4460. doi:10.1016/j.biomaterials.2006.04.011

Dong, Y., Rodrigues, M., Kwon, S. H., Li, X., Sigen, A., Brett, EA, et al. (2018). Acceleration of Diabetic Wound Regeneration Using an In Situ-Formed Stem-Cell-Based Skin Substitute. *Adv. Healthc. Mater.* 7, 1800432. doi:10.1002/adhm.201800432

Dong, Y., Rodrigues, X., Kwon, S. H., Kosaric, N., Khong, S., Gao, Y., et al. (2017). Injectable and Tunable Gelatin Hydrogels Enhance Stem Cell Retention and Improve Cutaneous Wound Healing. *Adv. Funct. Mater.* 27, 1606619. doi:10.1002/adfm.201606619

Falanga, V. (2005). Wound Healing and its Impairment in the Diabetic Foot. *The Lancet* 366, 1736–1743. doi:10.1016/s0140-6736(05)67700-8

Fonseca, K. B., Granja, P. L., and Barrias, C. C. (2014). Engineering Proteolytically-Degradable Artificial Extracellular Matrices. *Prog. Polym. Sci.* 39, 2010–2029. doi:10.1016/j.progpolymsci.2014.07.003

Galuppo, M., Giacoppo, S., Bramanti, P., and Mazzon, E. (2014). Use of Natural Compounds in the Management of Diabetic Peripheral Neuropathy. *Molecules* 19, 2877–2895. doi:10.3390/molecules19032877

Gooyit, M., Peng, Z., Wolter, W. R., Pi, H., Ding, D., Hesek, D., et al. (2014). A Chemical Biological Strategy to Facilitate Diabetic Wound Healing. *ACS Chem. Biol.* 9, 105–110. doi:10.1021/cb4005468

Green, L. J., Zhou, H., Padmanabhan, V., and Shikanov, A. (2019). Adipose-derived Stem Cells Promote Survival, Growth, and Maturation of Early-Stage Murine Follicles. *Stem Cel Res Ther* 10, 102. doi:10.1186/s13287-019-1199-8

Griffin, D. R., Archang, M. M., Kuan, C.-H., Weaver, W. M., Weinstein, J. S., Feng, A. C., et al. (2021). Activating an Adaptive Immune Response from a Hydrogel Scaffold Imparts Regenerative Wound Healing. *Nat. Mater.* 20, 560–569. doi:10.1038/s41563-020-00844-w

Kavitha, K. V., Tiwari, S., Purandare, V. B., Khedkar, S., Bhosale, S. S., and Unnikrishnan, A. G. (2014). Choice of Wound Care in Diabetic Foot Ulcer: A Practical Approach. *Wjd* 5, 546–556. doi:10.4239/wjd.v5.i4.546

Kim, E. K., Li, G., Lee, T. J., and Hong, J. P. (2011). The Effect of Human Adipose-Derived Stem Cells on Healing of Ischemic Wounds in a Diabetic Nude Mouse Model. *Plast. Reconstr. Surg.* 128, 387–394. doi:10.1097/prs.0b013e31821e6de2

Kokai, L. E., Marra, K., and Rubin, J. P. (2014). Adipose Stem Cells: Biology and Clinical Applications for Tissue Repair and Regeneration. *Translational Res.* 163, 399–408. doi:10.1016/j.trsl.2013.11.009

Kuo, Y.-R., Wang, C.-T., Cheng, J.-T., Kao, G.-S., Chiang, Y.-C., and Wang, C.-J. (2016). Adipose-derived Stem Cells Accelerate Diabetic Wound Healing through the Induction of Autocrine and Paracrine Effects. *Cel Transpl.* 25, 71–81. doi:10.3727/096368915x687921

Kuo, Y.-R., Wang, C.-T., Wang, F.-S., Chiang, Y.-C., and Wang, C.-J. (2009). Extracorporeal Shock-Wave Therapy Enhanced Wound Healing via Increasing Topical Blood Perfusion and Tissue Regeneration in a Rat Model of STZ-Induced Diabetes. *Wound Repair Regen.* 17, 522–530. doi:10.1111/j.1524-475x.2009.00504.x

Lau, T. T., Wang, C., and Wang, D.-A. (2010). Cell Delivery with Genipin Crosslinked Gelatin Microspheres in Hydrogel/microcarrier Composite. *Composites Sci. Techn.* 70, 1909–1914. doi:10.1016/j.compscitech.2010.05.015

Li, Y., Rodrigues, J., and Tomás, H. (2012). Injectable and Biodegradable Hydrogels: Gelation, Biodegradation and Biomedical Applications. *Chem. Soc. Rev.* 41, 2193–2221. doi:10.1039/c1cs15203c

Li, Z., Guo, S., Yao, F., Zhang, Y., and Li, T. (2013). Increased Ratio of Serum Matrix Metalloproteinase-9 against TIMP-1 Predicts Poor Wound Healing in Diabetic Foot Ulcers. *J. Diabetes Its Complications* 27, 380–382. doi:10.1016/j.jdiacomp.2012.12.007

Liang, H.-C., Chang, W.-H., Liang, H.-F., Lee, M.-H., and Sung, H.-W. (2004). Crosslinking Structures of Gelatin Hydrogels Crosslinked with Genipin or a Water-Soluble Carbodiimide. *J. Appl. Polym. Sci.* 91, 4017–4026. doi:10.1002/app.13563

Liang, H.-C., Chang, W.-H., Lin, K.-J., and Sung, H.-W. (2003). Genipin-crosslinked Gelatin Microspheres as a Drug Carrier for Intramuscular Administration:*In Vitro* Andin Vivo Studies. *J. Biomed. Mater. Res.* 65A, 271–282. doi:10.1002/jbm.a.10476

Matoori, S., Veves, A., and Mooney, D. J. (2021). Advanced Bandages for Diabetic Wound Healing. *Sci. Transl Med.* 13, eabe4839. doi:10.1126/scitranslmed.abe4839

Nakazaki, M., Morita, T., Lankford, K. L., Askenase, P. W., and Kocsis, J. D. (2021). Small Extracellular Vesicles Released by Infused Mesenchymal Stromal Cells Target M2 Macrophages and Promote TGF-β Upregulation, Microvascular Stabilization and Functional Recovery in a Rodent Model of Severe Spinal Cord Injury. *J. Extracellular Vesicles* 10. doi:10.1002/jev2.12137

Newsom, J. P., Payne, K. A., and Krebs, M. D. (2019). Microgels: Modular, Tunable Constructs for Tissue Regeneration. *Acta Biomater.* 88, 32–41. doi:10.1016/j.actbio.2019.02.011

Nguyen, T. T., Ding, D., Wolter, W. R., Pérez, R. L., Champion, M. M., Mahasenan, K. V., et al. (2018). Validation of Matrix Metalloproteinase-9 (MMP-9) as a Novel Target for Treatment of Diabetic Foot Ulcers in Humans and Discovery of a Potent and Selective Small-Molecule MMP-9 Inhibitor that Accelerates Healing. *J. Med. Chem.* 61, 8825–8837. doi:10.1021/acs.jmedchem.8b01005

Nourian Dehkordi, A., Mirahmadi Babaheydari, F., Chehelgerdi, M., and Raeisi Dehkordi, S. (2019). Skin Tissue Engineering: Wound Healing Based on Stem-Cell-Based Therapeutic Strategies. *Stem Cel Res Ther* 10, 111. doi:10.1186/s13287-019-1212-2

Nyame, T. T., Chiang, H. A., Leavitt, T., Ozambela, M., and Orgill, D. P. (2015). Tissue-Engineered Skin Substitutes. *Plast. Reconstr. Surg.* 136, 1379–1388. doi:10.1097/prs.0000000000001748

Patel, S., Srivastava, S., Singh, M. R., and Singh, D. (2019). Mechanistic Insight into Diabetic Wounds: Pathogenesis, Molecular Targets and Treatment Strategies to Pace Wound Healing. *Biomed. Pharmacother.* 112, 108615. doi:10.1016/j.biopha.2019.108615

Piard, C., Jeyaram, A., Liu, Y., Caccamese, J., Jay, S. M., Chen, Y., et al. (2019). 3D Printed HUVECs/MSCs Cocultures Impact Cellular Interactions and Angiogenesis Depending on Cell-Cell Distance. *Biomaterials* 222, 119423. doi:10.1016/j.biomaterials.2019.119423

Plikus, M. V., Guerrero-Juarez, C. F., Ito, M., Li, Y. R., Dedhia, P. H., Zheng, Y., et al. (2017). Regeneration of Fat Cells from Myofibroblasts during Wound Healing. *Science* 355, 748–752. doi:10.1126/science.aai8792

Qian, X., Guo, L., Sigen, A., Gao, Y., and Wang, W. (2018). Injectable Hyperbranched Poly(β-Amino Ester) Hydrogels with On-Demand Degradation Profile to Match Wound Healing Process. *Chem. Sci.* 9, 2179–2187.

Rustad, K. C., Wong, V. W., Sorkin, M., Glotzbach, J. P., Major, M. R., Rajadas, J., et al. (2012). Enhancement of Mesenchymal Stem Cell Angiogenic Capacity and Stemness by a Biomimetic Hydrogel Scaffold. *Biomaterials* 33, 80–90. doi:10.1016/j.biomaterials.2011.09.041

Santoro, M., Tatara, A. M., and Mikos, A. G. (2014). Gelatin Carriers for Drug and Cell Delivery in Tissue Engineering. *J. Controlled Release* 190, 210–218. doi:10.1016/j.jconrel.2014.04.014

Shabbir, A., Cox, A., Rodriguez-Menocal, L., Salgado, M., and Badiavas, E. V. (2015). Mesenchymal Stem Cell Exosomes Induce Proliferation and Migration of Normal and Chronic Wound Fibroblasts, and Enhance Angiogenesis *In Vitro*. *Stem Cell Dev.* 24, 1635–1647. doi:10.1089/scd.2014.0316

Shi, M., Xuan, L., Zhang, Y., Wang, D., Ye, F., Shi, X., et al. (2019b). Synergistic Effects of thermal Treatment and Encapsulation of Calcium Phosphate Nanoparticles on Enhancing Dimensional Stability and Osteogenic Induction Potential of Free-Standing PLGA Electrospun Membranes. *Colloids Surf. B: Biointerfaces* 183, 110437. doi:10.1016/j.colsurfb.2019.110437

Shi, M., Zhang, H., Song, T., Liu, X., Gao, Y., Zhou, J., et al. (2019a). Sustainable Dual Release of Antibiotic and Growth Factor from pH-Responsive Uniform Alginate Composite Microparticles to Enhance Wound Healing. *ACS Appl. Mater. Inter.* 11, 22730–22744. doi:10.1021/acsami.9b04750

Sivadas, N., O'Rourke, D., Tobin, A., Buckley, V., Ramtoola, Z., Kelly, J. G., et al. (2008). A Comparative Study of a Range of Polymeric Microspheres as Potential Carriers for the Inhalation of Proteins. *Int. J. Pharmaceutics* 358, 159–167. doi:10.1016/j.ijpharm.2008.03.024

Solorio, L., Zwolinski, C., Lund, A. W., Farrell, M. J., and Stegemann, J. P. (2010). Gelatin Microspheres Crosslinked with Genipin for Local Delivery of Growth Factors. *J. Tissue Eng. Regen. Med.* 4, 514–523. doi:10.1002/term.267

Sung, B., Krieger, J., Yu, B., and Kim, M. H. (2018). Colloidal Gelatin Microgels with Tunable Elasticity Support the Viability and Differentiation of Mesenchymal Stem Cells under Pro-inflammatory Conditions. *J. Biomed. Mater. Res.* 106, 2753–2761. doi:10.1002/jbm.a.36505

Tabata, Y. (1998). Protein Release from Gelatin Matrices. *Adv. Drug Deliv. Rev.* 31, 287–301. doi:10.1016/s0169-409x(97)00125-7

Takemitsu, H., Zhao, D., Yamamoto, I., Harada, Y., Michishita, M., and Arai, T. (2012). Comparison of Bone Marrow and Adipose Tissue-Derived Canine Mesenchymal Stem Cells. *BMC Vet. Res.* 8, 150. doi:10.1186/1746-6148-8-150

Tao, S.-C., Guo, S.-C., Li, M., Ke, Q.-F., Guo, Y.-P., and Zhang, C.-Q. (2017). Chitosan Wound Dressings Incorporating Exosomes Derived from MicroRNA-126-Overexpressing Synovium Mesenchymal Stem Cells Provide Sustained Release of Exosomes and Heal Full-Thickness Skin Defects in a Diabetic Rat Model. *Stem Cell Translational Med.* 6, 736–747. doi:10.5966/sctm.2016-0275

Tomaszewski, C. E., Constance, E., Lemke, M. M., Zhou, H., Padmanabhan, V., Arnold, K. B., et al. (2019). Adipose-derived Stem Cell-Secreted Factors Promote Early Stage Follicle Development in a Biomimetic Matrix. *Biomater. Sci.* 7, 571–580. doi:10.1039/c8bm01253a

Turner, P. A., Thiele, J. S., and Stegemann, J. P. (2017). Growth Factor Sequestration and Enzyme-Mediated Release from Genipin-Crosslinked Gelatin Microspheres. *J. Biomater. Sci. Polym. Edition* 28, 1826–1846. doi:10.1080/09205063.2017.1354672

Wimmer, R. A., Leopoldi, A., Aichinger, M., Wick, N., Hantusch, B., Novatchkova, M., et al. (2019). Human Blood Vessel Organoids as a Model of Diabetic Vasculopathy. *Nature* 565, 505–510. doi:10.1038/s41586-018-0858-8

Wu, Y., Chen, L., Scott, P. G., and Tredget, E. E. (2010). Mesenchymal Stem Cells Enhance Wound Healing through Differentiation and Angiogenesis. *Stem Cells* 25, 2648–2659. doi:10.1634/stemcells.2007-0226

Wynn, T. A., Chawla, A., and Pollard, J. W. (2013). Macrophage Biology in Development, Homeostasis and Disease. *Nature* 496, 445–455. doi:10.1038/nature12034

Yang, Z., Huang, R., Zheng, B., Guo, W., Li, C., He, W., et al. (2021). Highly Stretchable, Adhesive, Biocompatible, and Antibacterial Hydrogel Dressings for Wound Healing. *Adv. Sci.* 8, 2003627. doi:10.1002/advs.202003627

Zhao, X., Liu, S., Yildirimer, L., Zhao, H., Ding, R., Wang, H., et al. (2016). Injectable Stem Cell-Laden Photocrosslinkable Microspheres Fabricated Using Microfluidics for Rapid Generation of Osteogenic Tissue Constructs. *Adv. Funct. Mater.* 26, 2809–2819. doi:10.1002/adfm.201504943

Conflict of Interest: The authors declare that the research was conducted in the absence of any commercial or financial relationships that could be construed as a potential conflict of interest.

Publisher's Note: All claims expressed in this article are solely those of the authors and do not necessarily represent those of their affiliated organizations or those of the publisher, the editors, and the reviewers. Any product that may be evaluated in this article, or claim that may be made by its manufacturer, is not guaranteed or endorsed by the publisher.

Copyright © 2022 Shi, Gao, Lee, Song, Zhou, Yan and Li. This is an open-access article distributed under the terms of the Creative Commons Attribution License (CC BY). The use, distribution or reproduction in other forums is permitted, provided the original author(s) and the copyright owner(s) are credited and that the original publication in this journal is cited, in accordance with accepted academic practice. No use, distribution or reproduction is permitted which does not comply with these terms.

frontiers | Frontiers in Bioengineering and Biotechnology

ORIGINAL RESEARCH
published: 11 April 2022
doi: 10.3389/fbioe.2022.844177

β-Cyclodextrin and Oligoarginine Peptide-Based Dendrimer-Entrapped Gold Nanoparticles for Improving Drug Delivery to the Inner Ear

Jia Luo[1], *XueXin Lin*[1], *LiLing Li*[1], *JingQian Tan*[2] *and Peng Li*[1]*

[1]Department of Otolaryngology Head and Neck Surgery, The Third Affiliated Hospital of Sun Yat-Sen University, Guangzhou, China, [2]Department of Otolaryngology Head and Neck Surgery, The Eighth Affiliated Hospital of Sun Yat-Sen University, Shenzhen, China

Here, we developed a safe and highly effective nanocarrier using β-cyclodextrin (β-CD) and oligoarginine peptide (Arg8)-modified dendrimer-entrapped gold nanoparticles (Au@CD-PAMAM-Arg8), with a diameter of 5 nm, for improved delivery of dexamethasone (Dex) to the inner ear. The properties and *in vivo* distribution of the Au@CD-PAMAM-Arg8 were assessed *in vitro*, and a streptomycin (SM) ototoxicity model was used *in vivo*. Flow cytometry analysis of HEIOC1 cells treated with Au@CD-PAMAM-Arg8 and Au @CD-PAMAM at different time intervals indicated that cell uptake efficiency of the drug delivery carrier Au@CD-PAMAM-Arg8 was higher than that of Au @CD-PAMAM. Au@CD-PAMAM-Arg8 carrying Dex (Au@CD-PAMAM-Arg8/Dex) were mainly distributed in hair cells, the spiral ganglion, lateral wall, and nerve fibers and had stronger protective effects on the inner ear than Dex administration alone. *In vivo* tracer tests revealed that tympanic injection was significantly more effective than posterior ear injection, muscle injection, and tail vein injection, whereas clinical retro-auricular injection could not increase the efficiency of drug delivery into the ear. Electrocochleography results showed that Au@CD-PAMAM-Arg8/Dex significantly improved hearing in C57/BL6 mice after SM exposure. These findings indicate that Au@CD-PAMAM-Arg8 may be the useful drug carriers for the treatment of inner ear diseases.

Keywords: drug delivery, dexamethasone, inner ear, spiral ganglion, outer hair cells, nerve fibers

OPEN ACCESS

Edited by:
Kaili Lin,
Shanghai Jiao Tong University, China

Reviewed by:
Di Huang,
Massachusetts Eye and Ear Infirmary and Harvard Medical School, United States
Lesan Yan,
Wuhan University of Technology, China

***Correspondence:**
Peng Li
lp76@163.net

Specialty section:
This article was submitted to Biomaterials, a section of the journal Frontiers in Bioengineering and Biotechnology

Received: *27 December 2021*
Accepted: *24 February 2022*
Published: *11 April 2022*

Citation:
Luo J, Lin X, Li L, Tan J and Li P (2022) β-Cyclodextrin and Oligoarginine Peptide-Based Dendrimer-Entrapped Gold Nanoparticles for Improving Drug Delivery to the Inner Ear. Front. Bioeng. Biotechnol. 10:844177. doi: 10.3389/fbioe.2022.844177

1 INTRODUCTION

Approximately 250 million people worldwide suffer from disabling hearing loss and do not receive effective treatment (Holley, 2005). The main reason for treatment failure is the inability to deliver drugs effectively to the inner ear. Systemic intravenous administration, local tympanic injection, and surgery are the three most common modalities for treating ear diseases. The blood labyrinth barrier (BLB) filling with efflux pump proteins is an obstacle for reaching the hair cells or the spiral ganglion cells after systemic administration (Saito et al., 2001). It is difficult to deliver drugs through the round window membrane (RWM) to the inner ear via tympanic administration mainly because of the low expression of receptors on the RWM and the lipophilic nature of the cell membranes that prevents polar bioactive molecules such as proteins, peptides, and oligonucleotides from efficiently entering the inner ear (Kim, 2017; Zhang L. et al., 2018).

Nanoparticles can overcome anatomical barriers and efficiently deliver encapsulated drugs to the target cells and organelles, and their usefulness in treating inner ear diseases remains to be fully exploited (Daraee et al., 2016; Lee et al., 2018).

By engineering nanoparticles with strong transmembrane penetration ability, biocompatibility, and sufficient cavity structure for drug loading, better drug delivery efficiency and specific cell targeting can be achieved (**Scheme 1A**). Poly amidoamine (PAMAM) dendrimers are widely used synthetic hyperbranched polymers with a high degree of monodispersity, polyvalency, and controlled molecular architecture. After modification, such as glycosylation and acylation, they have good biocompatibility and low toxicity (Markowicz et al., 2021). Compared to other common nanocarriers for drug-targeted delivery, such as solid lipid nanoparticles, micelles, and polymeric nanoparticles, PAMAM dendrimers are nonimmunogenic and have controlled molecular architecture and uniform particle size (Eichman et al., 2000). In addition, their internal cavity structure can improve the dispersibility of loaded drugs, and a large number of external end groups (-NH2, -COOH, and -OH surface groups) can be used to realize different targeting molecular ligands and fluorescent probe modifications (Parimi et al., 2010; Malinga-Drozd et al., 2021). Poly amidoamine (PAMAM) dendrimers can be modified with various groups with different functions (Tomalia et al., 1985; Tomalia et al., 1986), such as fluorophores, targeting ligands, and drugs, thereby expanding their applications to a variety of biological diagnostics and therapeutics (Shakhbazau et al., 2010; Labieniec-Watala and Watala, 2015). Third-generation poly amidoamine (PAMAM) dendrimers delivery systems have been developed for effective drug delivery to the inner ear. β-cyclodextrin (β-CD), considered safe by the US Federal Drug Administration (Crumling et al., 2012), is used to increase the biocompatibility of the PAMAM nano-system. The Au @CD-PAMAM system was developed by reducing $HAuCl_4$ with PAMAM-β-CD. GNPs, surfaces of which are easily modified to deliver drugs, nucleic acids, and target tumors, have CT imaging capability and can reduce the cytotoxicity of vectors by peripheral modification of polyethylene glycol chains dendrimers (Nam et al., 2009; Hou et al., 2016) or by embedding into the internal cavity of dendrimers (Shan et al., 2012; Xiong et al., 2019) with remarkably strengthened cellular uptake and intracellular release efficiency (Hou et al., 2015). For better cellular internalization, Au @CD-PAMAM-Arg8 (Au-DENPs) have been synthesized by linking an oligoarginine peptide (Arg8) through the amide reaction (Maitani and Hattori, 2009). Peptides with low arginine levels can easily penetrate cell membranes as efficiently as other cell penetrating peptides (CPPs) and can enter the nucleus (Roy et al., 2010). Biofilms, such as RWM, have negatively charged surfaces; therefore, the uptake of drug delivery vectors into cells requires positively charged surfaces to bind to them. Cellular internalization achieved by macropinocytosis of oligoarginine peptide (Arg8) nanoparticles can improve drug penetration through the circular window membrane (Carlisle et al., 2001). The mechanism may be that binding to the cell surface through ion interactions between positively charged Arg8 and negatively charged surface proteoglycan induces megalocytosis (Nakase et al., 2004; Kitagishi et al., 2013).

Dexamethasone (Dex) can bind to glucocorticoid and mineralocorticoid receptors, which are widely expressed in the cochlea, thus preventing inflammation and maintaining lymphatic balance (Dinh et al., 2008; Meltser and Canlon, 2011). Several animal studies have shown that the intratympanic injection of free Dex can effectively alleviate SM ototoxicity (Kinis et al., 2013; Gül et al., 2017). Dex is also used to treat sudden sensorineural hearing loss, Meniere's disease, and noise-induced hearing loss (Haynes et al., 2007; Stachler et al., 2012).

Therefore, in this study, we developed Dex-loaded nanoparticles for the effective delivery of Dex to the inner ear. A series of *in vitro* and *ex vivo* experiments were conducted (**Scheme 1B–D**). We also evaluated the biodistribution, cytotoxicity, and drug delivery efficiency of these nanoparticles (**Scheme 1D**) in an animal model (**Scheme 1B, C**).

2 EXPERIMENTAL SECTION

2.1 Materials

β-CD, Tween 80, 1-(3-dimethylaminopropyl)-3-ethylcarbondiimide hydrochloric acid (EDC) 98.5%, sodium borohydride 98%, N-hydroxy succinimide (NHS) 98%, and chloroauric acid 97% were purchased from Shanghai Macklin Biochemical Technology Co., Ltd. (Shanghai City, China). Dexamethasone was purchased from Sigma-Aldrich, Co. (Saint Louis, MO, United States). Arg8 peptides 98% were obtained from Hangzhou Dan gang Biotechnology Co., Ltd. (Hangzhou City, China). Dexamethasone fluorescein (Dex-FITC) was obtained from Invitrogen (Carlsbad, CA). Triton X-100 and dimethyl sulfoxide 99.0% (DMSO) were acquired from Wuhan Google Biotechnology Co., Ltd. (Wuhan City, China). Phosphate-buffered saline (PBS, pH 7.4) was purchased from Gibco (Grand Island, NY). The dialysis membrane (mol. wt. cut-off (MWCO): 1 kDa, 2 kDa) was purchased from Spectrum Laboratories (Rancho Dominguez, CA). Two-month-old C57/BL6 mice (30–40 g) were purchased from the Guangdong Experimental Animal Center. (Guangdong, China). All the animal experiments were conducted using protocols approved by the Experimental Animal Ethics Committee of the Rui ye Model Animal Center (Ethics Number: 20210111008).

2.2 Materials

2.2.1 Description of PAMAM-β-CD

β-CD was used as a precursor for the nanoparticles. PAMAM-β-CD synthesis: β-CD (63.2 mg) and CDI (90.28 mg) were dissolved in DMSO (10 ml) with continuous stirring for 6 h, and the third-generation polyamide amine dendritic macromolecule (G3 PAMAM) (57.93 mg, 2.227 mol) dissolved in dimethyl sulfoxide (DMSO) was added dropwise to the solution with constant mechanical stirring (650 rpm) at room temperature for 3 days. The suspension was dialyzed against 0.01 M phosphate-buffered saline (PBS) using a 2-kDa dialysis bag for 24 h and purified using ultrapure water for 2 days to eliminate free chemical residues. The

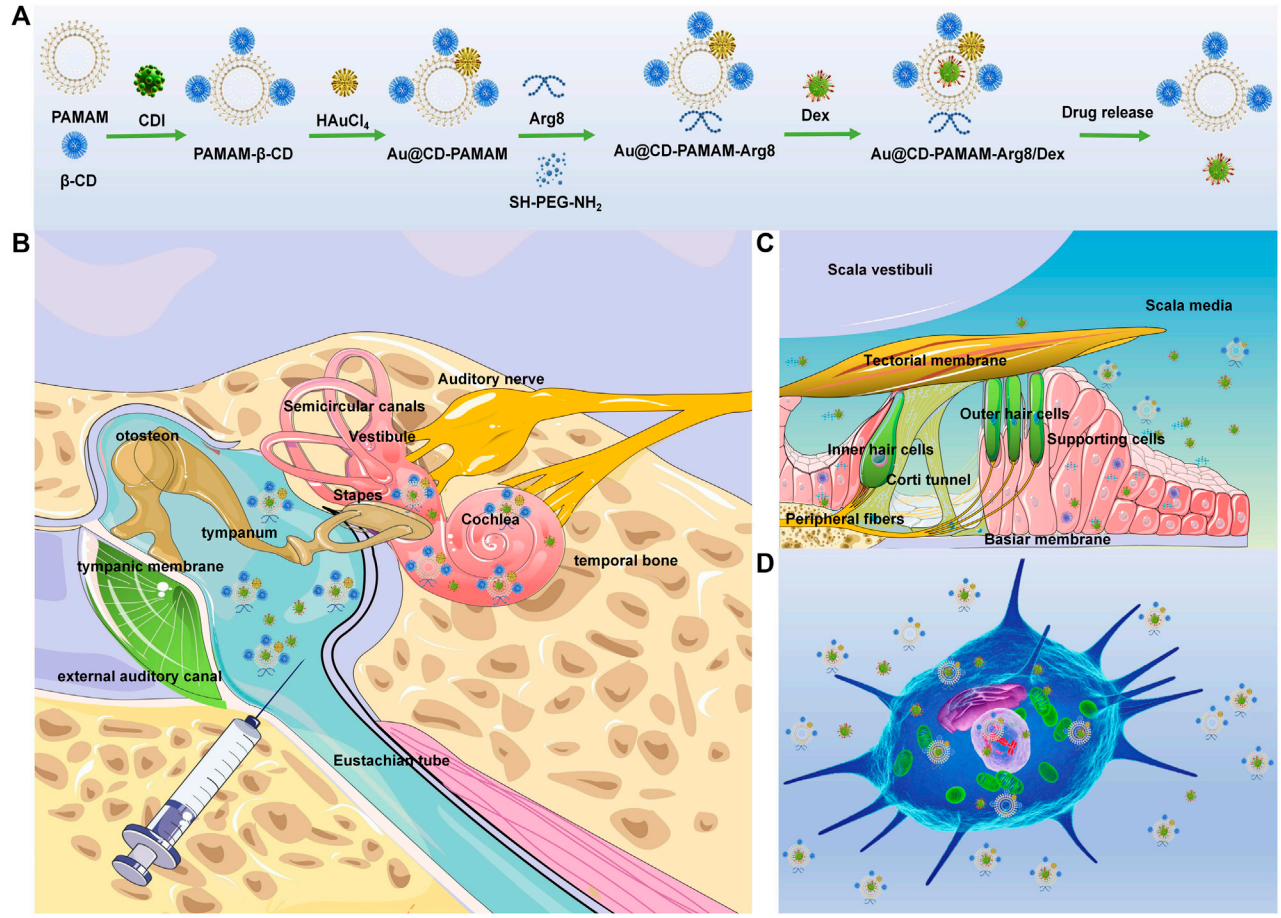

SCHEME 1 | (A) Chemical synthesis of Au @PAMAM-β-CD-Arg8/Dex. **(B)** Retro-auricular RWM approach: the location of target cells (spiral ganglion, organ of Corti, and spiral ligament) and delivery route of Au @PAMAM-β-CD-Arg8/Dex nanoparticles in the inner ear through tympanic cavity injection. **(C)** OHCs are located on the basement membrane in scala media, with the scala vestibuli on top and the scala tympani below. Au @PAMAM-β-CD-Arg8/Dex targeted to hair cells, supporting cells, and other structures. **(D)** Schematic diagram of nanometers entering HEIOC1 cells.

product was then freeze-dried, and the final white powder product (G3. NH_2-β-CD) was stored at −20°C.

2.2.2 Synthesis of Au @CD-PAMAM

Au @CD-PAMAM was produced by adding the G3. NH_2-β-CD solution into an aqueous solution of chloroauric acid ($HAuCl_4$) under continuous intense agitation for 30 min. Then, the aqueous solution of sodium borohydride ($NaBH_4$) was quickly added five times to continue the reaction for 4 h. Subsequently, the copolymers were purified in distilled water using a 2-kDa dialysis bag for 72 h and then isolated by freeze-drying.

2.2.3 Preparation of Nanocomposites With Drugs

Arg8 polypeptides (lipid concentration: 1.5 mg/ml), EDC (lipid concentration: 0.2 mg/ml), and NHS (lipid concentration: 0.4 mg/ml) were added into PBS (pH = 7.4) and stirred at room temperature for 4 h. The drug-loaded nanomaterial powder (Au@CD-PAMAM)was dissolved in PBS, and then the commixture of the two solutions was obtained and allowed to react overnight at roomtemperature. The mixture was freeze-dried to obtain the drug-loaded nanocompositematerial with targeted properties of Au @CD-PAMAM-Arg8(Au-DENPs). The free chemical residues were removed by dialysis using a 1-kDa MWCO membrane. Dexamethasone (Dex) dissolved in DMSO (concentration: 2 mg/ml) was added to the Au-DENPs. The mixed solution was stirred overnight at room temperature, filtrated with a 2-kDa MWCO membrane and freeze-dried to get Au @CD-PAMAM-Arg8/Dex (Au DENPs-Dex).

2.3 Material Characterization

2.3.1 Characterization of Nanoparticle Carriers

The ^{1}H NMR hydrogen spectrum of G3 NH_2-β-CD was recorded using a Bruker AV III 500 MHz NMR spectrometer (Wang et al., 2021). The FT-IR spectra of the G3. NH_2-β-CD and Au @CD-PAMAM nanoparticles in the range of 4,000–500 cm^{-1} were examined by the potassium bromide tablet method. The morphology of Au @PAMAM-β-CD-Arg8 was determined by cold-emission, high-resolution transmission electron microscopy (TEM, JEM-2010F, JEOL., Ltd.). The size distribution and zeta potentials of the targeted drug-loaded nanocomposite suspensions

were measured by the dynamic light scattering (DLS) technique using a Nano-ZS 90 Zetasizer (Malvern, America) at 25°C. The zeta potential (ζ) was determined by using laser Doppler electrophoresis (LDE) (Qiu et al., 2018; Wang et al., 2021). *In vitro* CT images of each concentration of the NPs (0.005, 0.01, 0.02, 0.04, 0.08, and 0.16 M) were captured using a single-source CT imaging system (Aquilion ONE 320 CT, Canon Medical Systems). All CT scans were performed at 100 kV voltage, 80 mA current, and a slice thickness of 0.625 nm. CT images were recorded, and the HU values of each sample were obtained by using built-in software.

2.3.2 Drug-Loading Capacity and Drug Release *In Vitro*

The loading content (%) and loading efficiency (%) of Au-DENPs-Dex were measured by high-performance liquid chromatography [HPLC (Thermo Fisher U3000)] at following time points: 0.5, 1, 3, 5, 8, 24, 48, and 72 h (Yoon et al., 2015). The test conditions were as follows: a series of Dex solutions with different concentrations (1,000, 500, 250, 125, 62.5, 31.25, 15.6, 7.8, and 3.9 μg/m L), a mobile phase of water and acetonitrile (60: 40 v/v), sample injection volume of 20 μL, flow rate of 1.0 ml/min, column temperature of 30°C, and detection wavelength of 240 nm (Zhao et al., 2021).

2.4 Cell Experiments

2.4.1 Cell Culture

Although HEIOC1 cells were undifferentiated, both hair cell and support cell markers were expressed on them (Tan et al., 2020). The HEIOC1 cells were cultured in the high-glucose Dulbecco's modified Eagle's medium (high-glucose DMEM; Sigma-Aldrich, Saint Louis, United States) mixed with 10% fetal bovine serum (FBS; Gibco, BRL) and 1% penicillin-SM (Sigma, Saint Louis, United States). The cells were cultured in a humidified 10% CO_2 environment at 37°C. The mouse fibroblasts L929 cells were maintained in the DMEM complete medium supplemented with 10% FBS and 1% penicillin-SM at 33°C in a humidified incubator with 10% CO_2.

2.4.2 Cytotoxicity

The cytotoxicity of Au @CD-PAMAM against HEIOC1 cells and L929 cells was quantitatively detected by the CCK-8 method. L929 cells and HEIOC1 cells at a density of 5,000 cells/well were inoculated into a 96-well plate and placed in a CO_2 incubator for overnight culture and wall sticking. A medium with different concentrations of Au @CD-PAMAM (concentrations of Au @CD-PAMAM in HEIOC1 cells: 1, 5, 10, 50, 100, 200, 400, 600, and 800 ug/mL and concentrations of Au @CD-PAMAM in L929 cells: 50,100,200,400,600, and 800 ug/mL) and 0.01 M PBS was used as the control. Cells were detected by the CCK-8 method after culture for 24 h (Su et al., 2019). The microplate reader (Bio-Rad Laboratories, Hercules, CA) was used to determine the optical densities of the samples at 450 nm.

2.4.3 Cellular Uptake

Cell uptake and intracellular localization of FITC-labeled Au-DENPs-Dex (0.6 mg/ml) in HEIOC1 cell were investigated after 0.5, 2, and 6 h of treatment using confocal microscopy (LSM880 Live Configuration Variotwo VRGB; Zeiss, Jena, Germany). The HEIOC1 cells were treated with FITC-labeled Au-DENPs-Dex at the maximum safe dose, determined by the cytotoxicity test. The cells were fixed with 4% paraformaldehyde (PA) solution after incubation and stained with DAPI (Sigma, Saint Louis, United States). A confocal microscope was used to observe the treated cells (Zambito et al., 2021).

2.4.4 The Targeting of Nanoparticle Carriers

Cell uptake of the Au-DENPs complex with and without Arg8 functionalization was analyzed to confirm Arg8's targeting ability. HEIOC1 cells were cultured overnight in a 96-well plate, and then FITC-labeled Au@PAMAM-β-CD-Arg8, FITC-labeled Au@PAMAM-β-CD (0.2 mg/ml), and 0.01 M PBS (pH = 7.4) were added and incubated for 0.5, 2, and 6 h. Cellular uptake efficiency in each group was quantified by flow cytometry. The untreated cells were used as negative controls. The corresponding fluorescence intensity (three parallel for each well) was quantified using Flow Jo 7.6.1 software.

2.5 Animal Experiments

2.5.1 Nanoparticle Distribution in the Cochlea

Surgery: male C57/BL6 mice aged 2 months were anesthetized with intraperitoneal (I. p.) injection pentobarbitone (with 0.5% pentobarbital sodium at the dosage of 0.02 ml/g body weight) and placed on a temperature-controlled heating mat to hold body temperature at 37°C in the supine position. An incision along the posterior auricular sulcus was made, and the left-side of the otic vesicle was exposed, in which a small hole was made with an insulin syringe. Next, the maximum safe dose of Au-DENPs-Dex (0.4 mg/ml), FITC-labeled Au-DENPs (80 ug/mL), or free Dex (5 mg/ml) was injected into the tympanum until the cavity was filled. Bone wax was used to plug the hole after injection (JOHON, Shen Zheng City, China), and the wound was sutured. After surgery, baytril (1 mg/kg; Sigma-Aldrich, Saint Louis, MO, United States) was used to treat middle ear infection by intraperitoneal injection once daily (Yang et al., 2018).

After 0.5, 2, 3, 24, and 72 h of injection of Au-DENPs-Dex (0.4 mg/ml, 100 μL) and free Dex (5 mg/ml, 100 μL) into the middle ear cavity (n = 5/group, control group: n = 5), immunohistochemical staining with an antibody-targeting Dex was conducted. The ABC HRP Kit and a peroxidase substrate (Vector, Burlingame, CA) were used to detect nanoparticle distribution in the inner ear at different time points (Riquelme et al., 2010).

After 3 and 24 h of intratympanic injection and 3 h of tail intravenous injection of FITC-labeled Au-DENPs (0.01 M PBS was used as control), the cochlear basilar membranes of the group subjected to intratympanic injection for 3 h (n = 2/group) were incubated with Alexa Fluor 660-conjugated phalloidin to label actin, which is heavily expressed in the stereocilia and the cuticular plate of outer hair cells (OHCs), inner hair cells (IHCs), and pillar cells (PCs) and DAPI (Sigma-Aldrich, Saint Louis, United States). The other membranes were incubated with anti-β-tubulin III antibody (Abcam, United Kingdom) to label never fibers (NFs) and spiral ganglion neurons (SGNs) and then immersed in a solution consisting of secondary antibody conjugated with Alexa Fluor 555 (1:200, Solarbio, Beijing City,

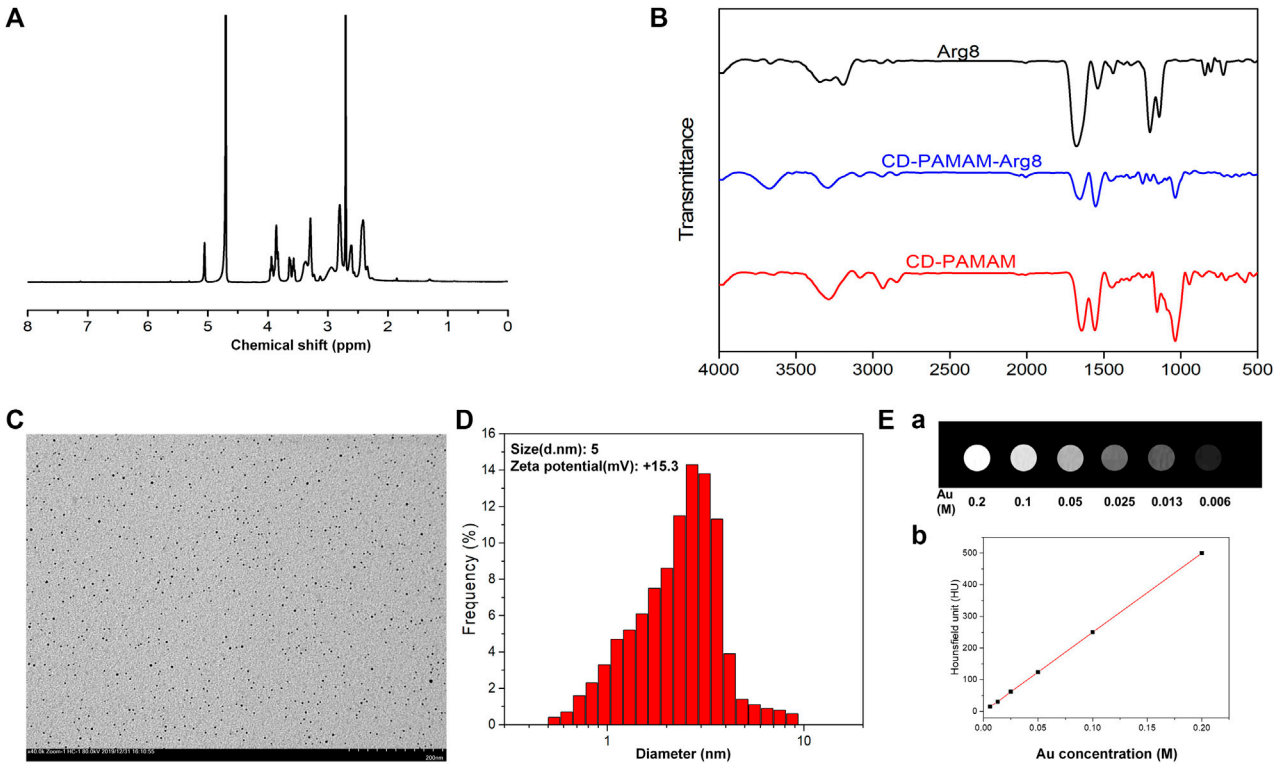

FIGURE 1 | (A) ^{1}H NMR spectrum of G_3-β-CD (β-CD). **(B)** FT-IR spectra of Arg8, Au@CD-PAMAM-Arg8, and Au @CD-PAMAM. **(C)** TEM image and **(D)** particle size distribution of Au@CD-PAMAM-Arg8. **(E)** Au @CD-PAMAM CT images of different concentrations.

China) normal goat serum, Triton X-100, and 0.01 M PBS as well as with DAPI. Then, the membranes were studied under a confocal microscope (Zeiss LSM-880) (Ding et al., 2011; Ding et al., 2012; Wang et al., 2017; Zhang J. et al., 2018) to determine the distribution of FITC-loaded nanoparticles in the inner ear after the two different injection methods.

2.5.2 Nanoparticle Distribution *In Vivo*

A total of sixteen mice, aged 2 months, were injected with 100 μL of FITC-labeled Au-DENPs (2 mg/kg) into the tympanum, posterior ear, muscle, and tail vein. After 0.5, 1, 3, 5, and 7 h, fluorescent optical imaging was performed by using a small animal imaging system (FX Pro Bruker) to evaluate the enrichment of FITC-labeled Au-DENPs *in vivo* following the different injection methods. The mice were anesthetized and placed on the imaging stage. The excitation wavelength is 495 nm, and the emission wavelength was 519 nm. Acquisition and image analysis were performed using Living 302 Image 4.4.1 software.

The mice were injected with 100 μL of Au-DENPs (2 mg/kg) via the left tympanum and tail vein. The animals were euthanized after 5 h and the main organs (heart, liver, spleen, lung, kidney, and bilateral cochlear) were excised and subjected to induced coupled plasma atomic emission spectroscopy (ICP-AES) to explore the distribution of the nanoparticles *in vivo*.

2.5.3 Toxicity Evaluation *In Vivo*

A total of twelve male C57/BL6 mice, aged 2 months, were divided into four groups (n = 3/group). The control group mice did not undergo surgery or treatment, and the other three groups received Au-DENPs-Dex, Au-DENPs, or Au @CD-PAMAM treatment via caudal vein injection (0.6 mg/ml; 100 uL). The mice were euthanized 2 weeks later, and H&E staining was conducted to observe the cytotoxicity of the nanoparticles in the main organs (heart, liver, spleen, lung, and kidney).

2.6 Drug Delivery Efficiency of the Nanoparticles in the SM Ototoxicity Animal Model

2.6.1 Cytotoxicity and Therapeutic Effects in Cells

The HEIOC1 cells were treated with the fresh complete medium with various concentrations of SM (0, 1, 2, 5, 10, 15, 20, 30, and 40 mg/ml) to determine the optimal dosing concentration of SM. In another 96-well plate, the HEIOC1 cells were dealt with the best dosing concentration of SM after pretreatment with six different concentrations (1, 5, 10, 15, 20, and 30 μg/ml) of Au-DENPs-Dex and Dex alone; 0.01 M PBS was used as the control group (Zhao et al., 2021). Then, the cytotoxicity of SM to HEIOC1 and the efficacy of free Dex and Au-DENPs-Dex in treating SM ototoxicity were quantitatively detected by the CCK-8 method to verify drug delivery efficiency of nanoparticles.

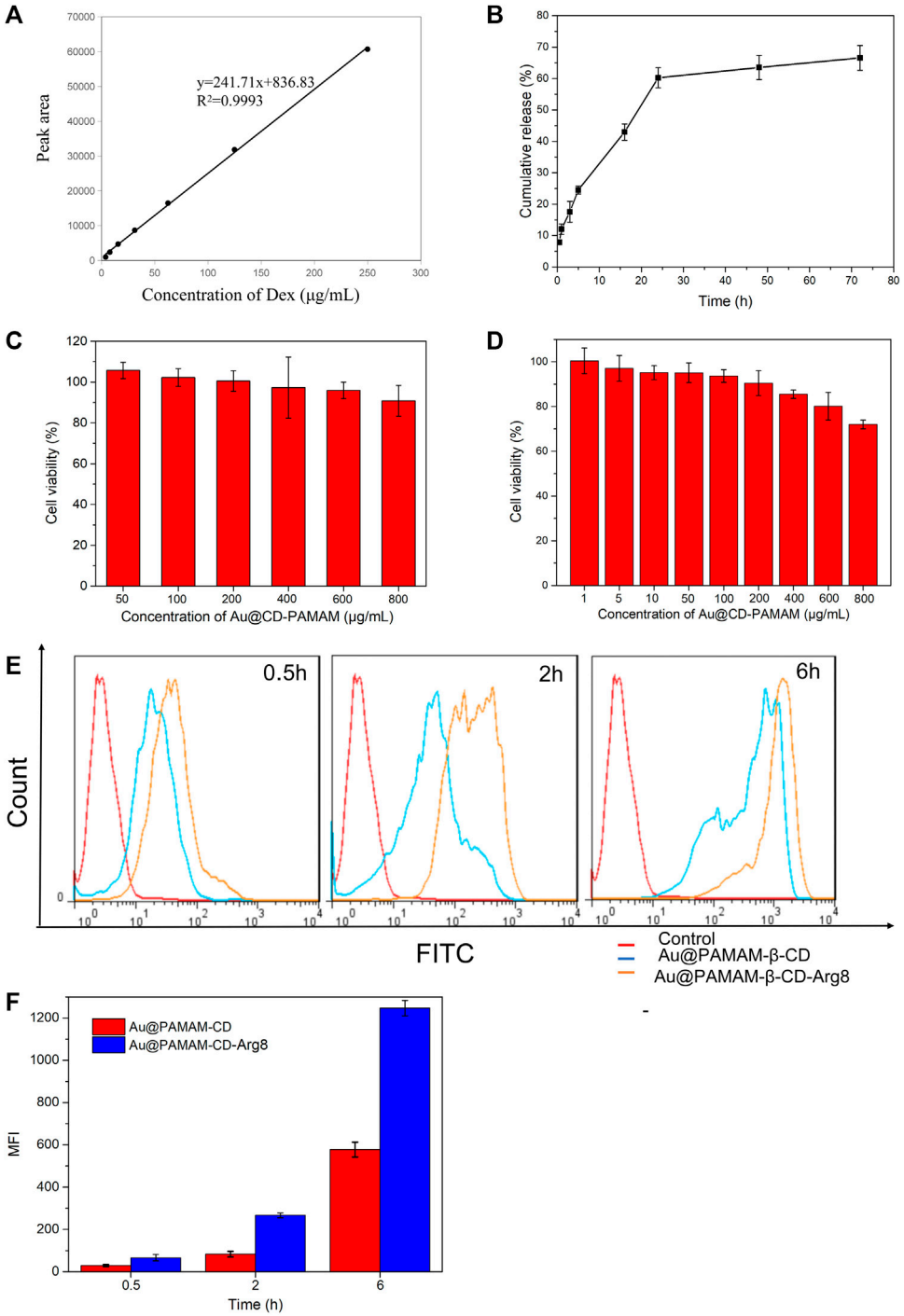

FIGURE 2 | (A) Standard curve of Dex. **(B)** Release curve of Dex. **(C)** L929 cell cytotoxicity. **(D)** HEIOC1 cell cytotoxicity. **(E)** Targeting of nanoparticle carriers. **(F)** Quantitative analysis of gold nanoparticles expression in HEIOC1 cells at different time intervals.

2.6.2 Cytotoxicity and Therapeutic Effects in Animals

Compared with auditory brainstem response (ABR) *in vivo*, compound action potential (CAP) in electrocochleography (ECochG) was good in reflecting the functional status of the peripheral auditory neurons and cochlear sensory epithelium following SM damage. The mice were anesthetized 3 days after tympanic cavity injection of Au-DENPs-Dex mixed with SM, mixture of SM and Dex, SM (concentration of Au-DENPs-Dex or Dex: 30 μg/ml; SM: 37.5 mg/ml, 100 μL), or 0.01 M PBS. After exposing the left facial nerve to set a silver wire into the facial

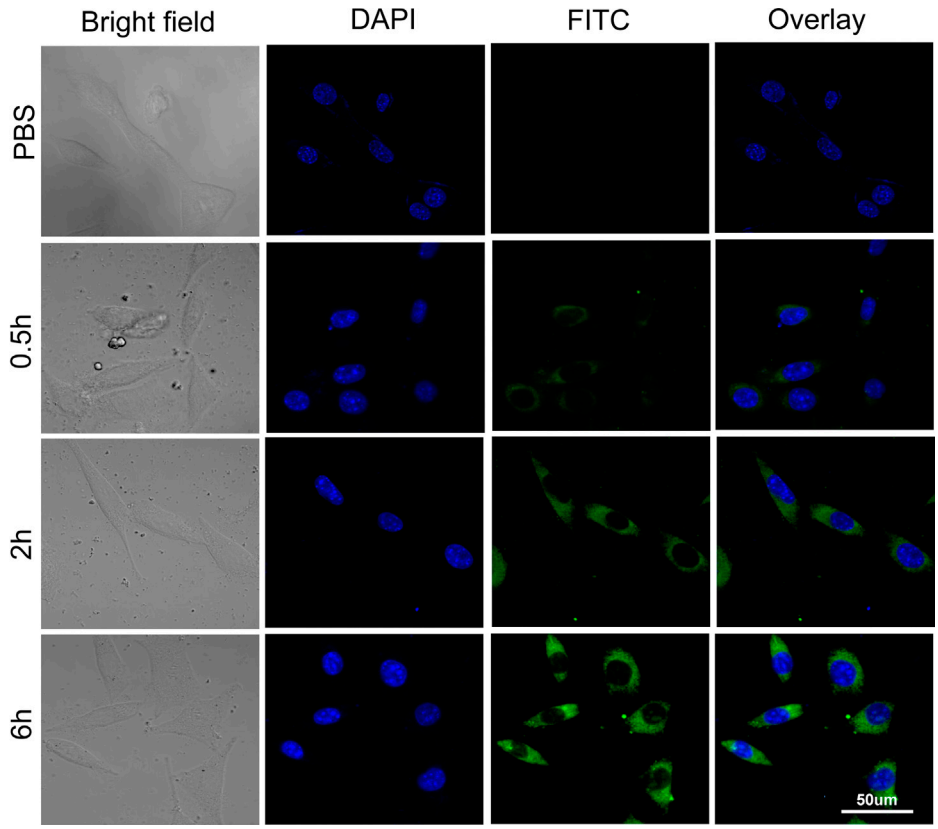

FIGURE 3 | Cell uptake of FITC-labeled Au-DENPs in HEIOC1 cells at 0.5, 2, and 6 h.

nerve canal for CAP recording, the reference electrode and ground electrode were inserted subcutaneously at the earlobe of the test ear and the opposite earlobe, respectively (Li et al., 2021). The data were collected by using an analyzer (Neurosoft LLC, Russia). ECochG click was generated in response to tones (1, 2, 3, 4, 6, 8, 16, and 32 kHz) between 100 and 20 dB in 5 dB increments.

After CAP recording, the mice were euthanized, and the basement membranes were stained with anti-β-tubulin III antibody, secondary antibody conjugated with Alexa Fluor 488, Alexa Fluor 660-conjugated phalloidin, and DAPI to evaluate the damage caused to hair cells, spiral ganglion cells, nerve fibers behind the inner hair cells, and ganglion cells following treatment of SM, Au-DENPs-Dex, and Dex alone (Ding et al., 2011; Zhang J. et al., 2018).

3 RESULTS AND DISCUSSION

3.1 Properties of Nanoparticle Carriers

The characteristic ^{1}H NMR peaks of the G3 PAMAM dendrimer and β-CD in the presence of G3-β-CD are shown in **Figure 1A**. The chemical shift between 2.25 and 2.34 ppm is due to the methylene skeleton of the G3 PAMAM dendrimer, whereas the proton peaks around 3.5–4 and 5 ppm are due to the β-CD group. The FT-IR spectra of the prepared samples, Arg8, Au-DENPs, and Au @CD-PAMAM are shown in **Figure 1B**. The IR-Vis spectrum of Arg8 showed a single deep Soret band ranging from 1,750 to 1,650 nm, indicating intermolecular self-aggregation. With a concomitant increase in the new signals upon the addition of Au @CD-PAMAM, the single deep Soret band reduced. The λ max of the Soret band (1,320–1,250 nm) and a broad and deep band (800–630 nm) in the final spectra was in good agreement with that of the inclusion complex of Au @CD-PAMAM. Upon the addition of Au-DENPs to the solution, the double Soret band ranging from 1,750 to 1,650 nm gradually declined (Kermanian et al., 2021).

The transmission electron microscopy (TEM) image of G3-β-CD is shown in **Figure 1C**. The prepared Au @CD-PAMAM was small with an average size of about 2.9 nm and was spherical shaped. It showed good dispersion in aqueous solutions, with uniform particle size distribution. Some research studies considered that the shape and size of the drug-carrier particle greatly influence the ability to pass into the organ of Corti and uptake into cells. Nanoparticles less than 200 nm can effectively penetrate through the RWM (Kim et al., 2015). The size of our nanoparticles, characterized by dynamic light scattering, was uniform and small, averaging about 5 nm (**Figure 1D**),

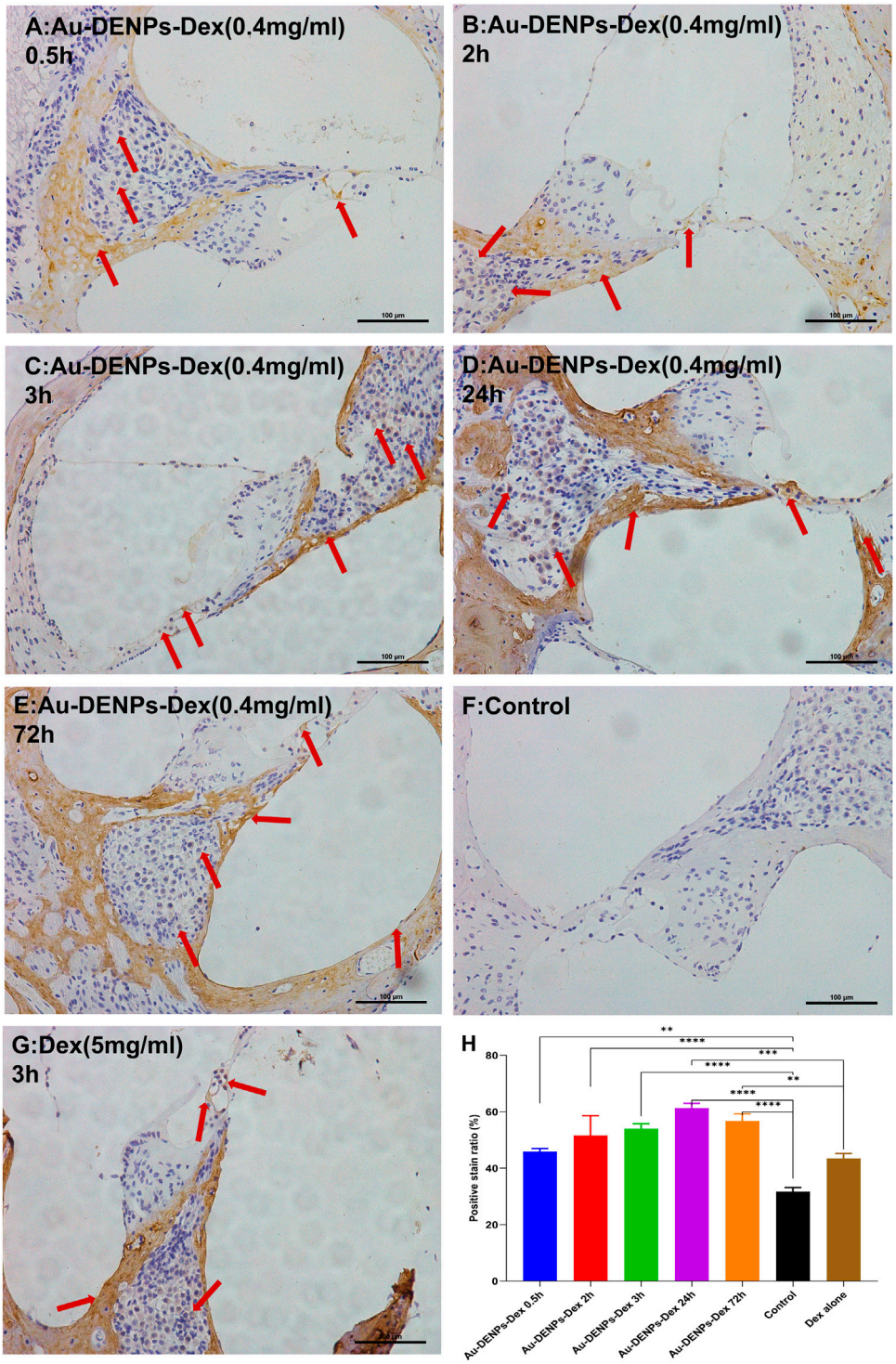

FIGURE 4 | Immunostaining for dexamethasone (Dex) after injection of Au-DENPs-Dex, free Dex, and PBS. **(A–E)** Tympanum injection of Au-DENPs-Dex (400 ug/ml) for 0.5, 2, 3, 24, and 72 h, respectively. **(F)** Tympanum injection of 0.01 M PBS for the control group. **(G)** Tympanum injection of free Dex (5 mg/ml) for 3 h as a positive group. **(H)** positive staining rate of each group. *$p < 0.05$, **$p < 0.01$, ***$p < 0.001$, and ****$p < 0.0001$.

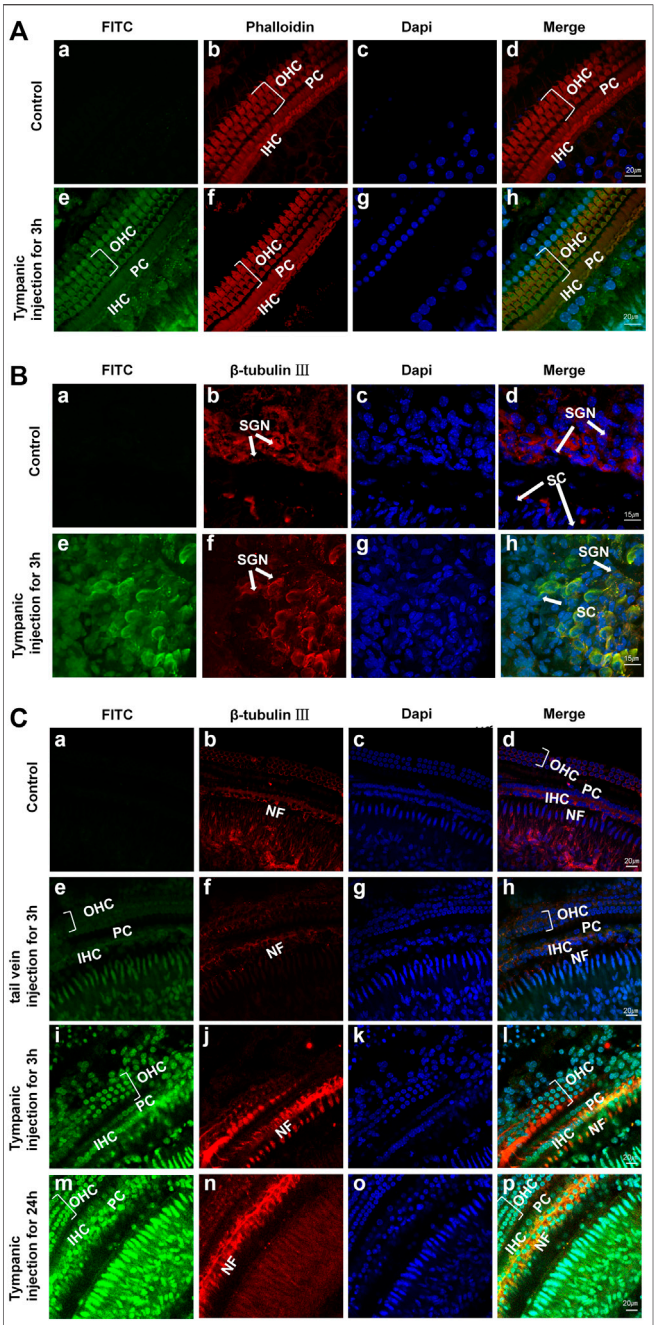

FIGURE 5 | (A,B) Confocal microscopy images of OHCs, IHCs, and SGNs in adult mice after 3 h of PBS (a–d: control group) and FITC-labeled Au-DENPs treatment (e–h) by tympanum injection (n = 2 per group). **(C)** Confocal microscopy images of the organ of Corti in adult mice after nanoparticles delivery by tail vein injection for 3 h and tympanum injection for 3 and 24 h and control group (n = 2 per group). Green represents FITC-labeled Au-DENPs nanoparticles **(A,C),** and red represents OHCs and IHCs stained with phalloidin in (A) or SGN and NF stained with β-tubulin **III** in **(B,C)**. DAPI was used to label nuclei **(A–C)**.

consistent with the TEM results. Biofilms, such as RWM, have negatively charged surfaces, which can bind with a positively charged Arg8 to increase the uptake into hair cells (Zhang L. et al., 2018). Zeta potential measurements revealed that our samples of Au-DENPs nanoparticles were positively charged (+15.3 mV).

As shown in **Figure 1E**, the CT image gradually brightened with the increase in Au concentration. When Au concentration was 0.1 m, the luminance of the CT image was obviously enhanced. Compared with the clinical use of Omnipaque, Au @CD-PAMAM had a high HU value at the same concentration, suggesting that Au @CD-PAMAM has a potential clinical value as a CT imaging contrast agent.

3.2 Drug Loading and Release

The relationship between different concentrations of Au-DENPs-Dex solution and peak area was measured by HPLC. The standard curve equation Y = 241.71× +836.83, R2 = 0.9993 was obtained, and the drug loading was 1.3% (**Figure 2A**). Dex was loaded onto Au-DENPs. The particle diameter was about 5 nm, which was similar to that before drug loading. The loading efficacy was 93.1 ± 7.6% (1.3%). According to recent studies, Dex remains in the outer lymphatic fluid of the cochlea for not more than 12 h after a single tympanum administration (Sun et al., 2015). However, our nanoparticles remained in the dendritic structure for a longer period owing to hydrophobic interactions. Burst release was observed at 24 h, after which the release rate decreased. After 70 h, the release rate of Dex was 70%, indicating that our nanoparticles have long-lasting effects (**Figure 2B**).

3.3 Cytotoxicity and Absorption Rates of Nanoparticle Carriers

Au @CD-PAMAM showed mild toxicity at 0.8 mg/ml in L929 cells (**Figure 2C**) and at 0.4 mg/ml in HEIOC1 cells (**Figure 2D**). Cellular internalization achieved by oligoarginine peptide (Arg8) nanoparticles can improve drug penetration through the circular window membrane into the cells of the inner ear and even into their nuclei, thus delivering the drugs to the specific target. The results of our flow cytometry analysis confirm this. The relative fluorescence intensity of Au-DENPs (Au@CD-PAMAM-Arg8) was enhanced to a great extent compared to that of the Au @CD-PAMAM nanoparticles, and the uptake increased exponentially from 0.5 to 6 h (**Figures 2E,F**). These findings indicate that Arg8 can increase the transmembrane ability of nanoparticles.

3.4 Cellular Uptake

The results of the confocal microscopy studies were in line with those of flow cytology analysis. After 0.5 h of treatment with FITC-labeled Au-DENPs (0.4 mg/ml) nanocarriers, green FITC fluorescence was detected at the periphery of the cell nuclei stained with DAPI. The staining intensity gradually increased with time, and the fluorescence could be clearly observed in the cells and the nuclei after 6 h. These findings confirm that Arg8-conjugated nanoparticles can penetrate the cell membrane and reach the nuclei (**Figure 3**).

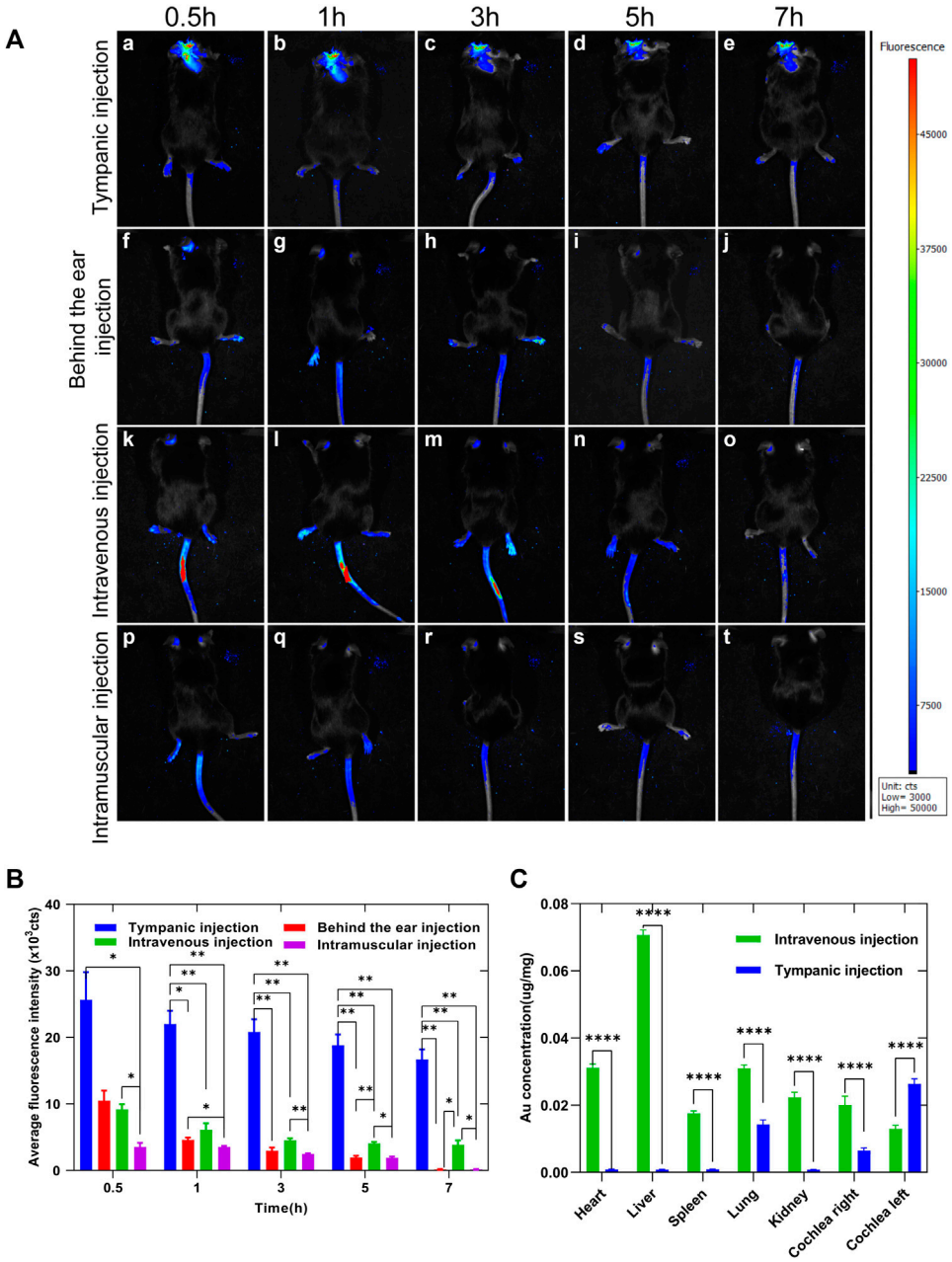

FIGURE 6 | (A) Enrichment of Au-DENPs in the cochlea by different injection methods after 0.5, 1, 3, 5, and 7 h using a small animal imaging system. **(B)** Quantitative fluorescence of temporal bone after injection in tympanum, posterior auricular sulcus, vein, and muscle. **(C)** Gold content in the main organs after 5 h of tympanum and intravenous injection of Au-DENPs (2 mg/kg) with ICP-AES.*$p < 0.05$, **$p < 0.01$, ***$p < 0.001$, and ****$p < 0.0001$.

3.5 Nanoparticle Distribution in the Cochlea

Most drugs, such as steroids, used in inner-ear disease are hydrophobic and not conducive to cellular internalization. However, Au-DENPs-Dex showed uptake of Dex on the spiral ganglion cells, the modiolus, the medial side, hair cells, and the lateral wall after 0.5 h of treatment; this increased markedly after 24 and 72 h (**Figures 4A,D,E**). Moreover, in our study, the positive staining rate of the group treated for 3 h with Au-DENPs-Dex (400 ug/mL) was significantly higher than that of the group treated with Dex alone (5 mg/ml) (**Figures 4C,F**). This confirmed that Arg8 and β-CD-conjugated nanoparticles are likely to improve absorption of hydrophobic drugs by cells and facilitate rapid action of these drugs. As Dex is encapsulated in nanoparticles, the distribution of Dex indirectly reflects the distribution of the nanoparticles. Nanoparticles began to appear around the spiral ganglion cells,

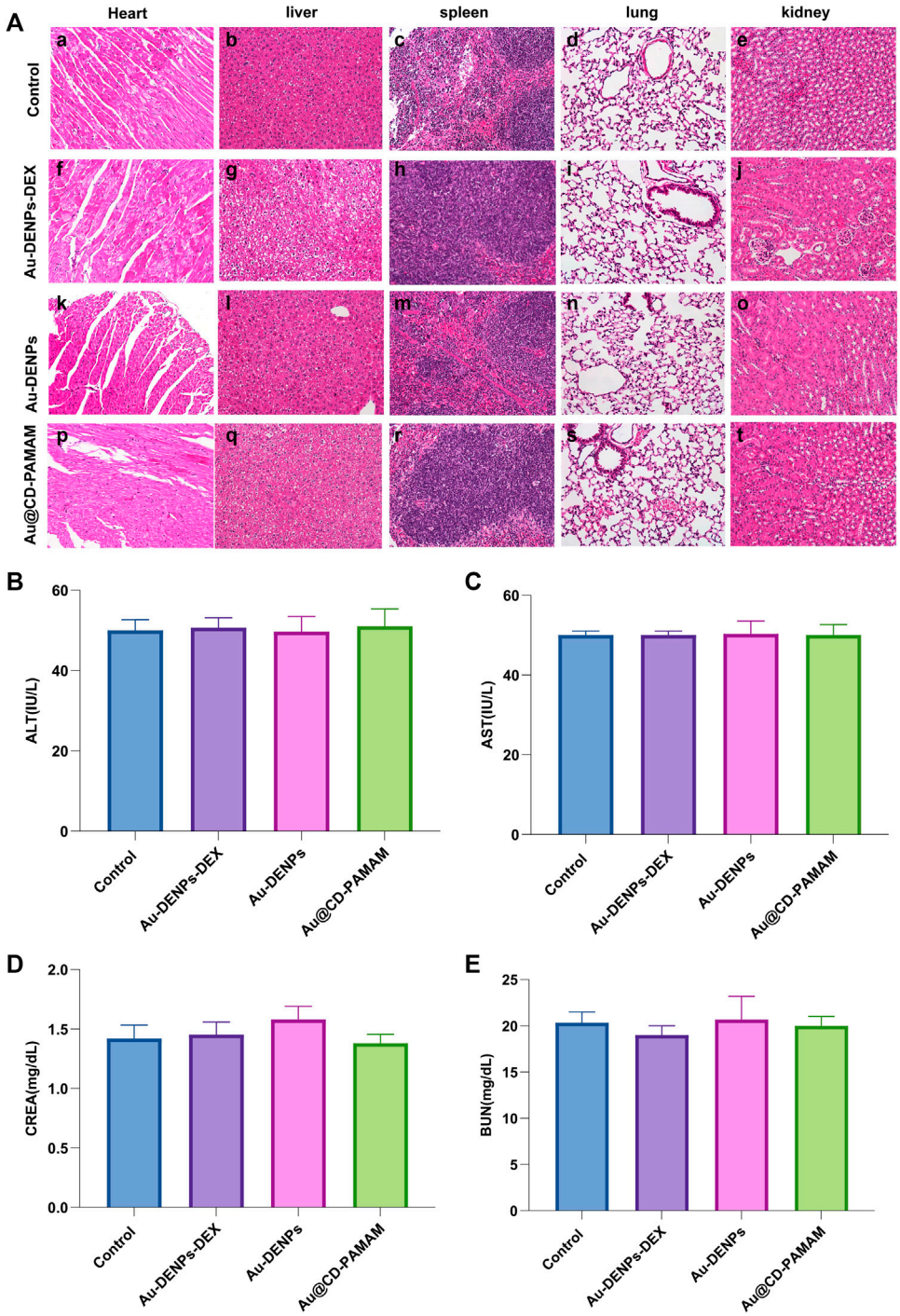

FIGURE 7 | (A) Systemic biosafety assessment. H&E staining of the heart, liver, spleen, lung, and kidney of mice from each group 2 weeks after treatment. Scale bar = 100 μm. Assessment of acute toxicity effects of **(B)** ALT, **(C)** AST, **(D)** CREA, and **(E)** BUN of each group (*n* = 3 per group).

modiolus, and medial side 0.5 h after administration and were present in the vicinity of OHCs and IHCs after 2 h, as shown in **Figure 4B**. However, according to recent research, in parts of the inner ear, such as Reissner's membrane, the organ of Corti, and the stria vascularis, tight junctions (TJs) directly exerted profound effects on intercellular sealing for complete perilymph and endolymph compartmentalization and prevented leakage of solutes through a paracellular pathway (Kitajiri et al., 2004). Therefore, we conjectured that absorption through the modiolus or limbus and diffusion to the hair cells were the main routes through which nanoparticles in the

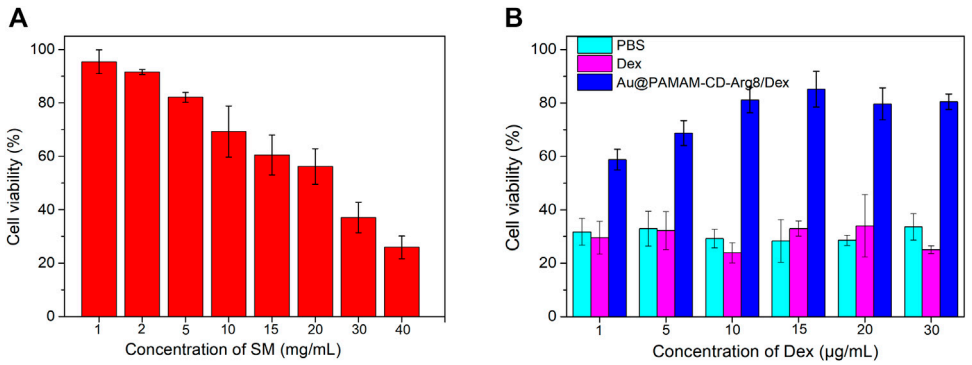

FIGURE 8 | (A) Ototoxicity induced by SM at different concentrations. **(B)** Therapeutic effects of Dex alone and Au@CD-PAMAM-Arg8/Dex on streptomycin ototoxicity.

perilymph approached the hair cells, instead of through the tight junctions in the superior margin of the intercellular space of the organ of Corti, which is linked with the endolymph.

Studies have shown that SM ototoxicity is mainly manifested in the nerve endings associated with the auditory receptors, OHCs, IHCs, and SGN (Wang et al., 2017; Ding et al., 1993; Cui et al., 2015). Hence, it is greatly important to administer a large drug dose in OHCs, IHCs, nerve fibers, and SGN; however, drugs or genes in the perilymph have more difficulty reaching the organ of Corti than reaching the spiral ligament or the spiral ganglion (Ding et al., 2014). Our confocal microscopy images of the cochlea delivery of FITC-labeled Au-DENPs (80 ug/mL, 100 uL) showed that FITC uptake mainly appeared in OHCs and IHCs especially in NF and SGN in adult mice after tympanum injection (**Figures 5A–C**) and tail intravenous injection (**Figure 5C, e**). The fluorescence was the strongest for tympanic injection in the 24-h group (**Figure 5C m**) and the weakest for tail vein injection in the 3-h group. Furthermore, the fluorescence of the spiral ganglion was significantly stronger than that of the hair cells 3 h after intratympanic injection (**Figures 5A,B**). Both the hair cells and SGN were not damaged after exposure. Moreover, a recent anatomical study of the human cochlea revealed that perforated structures at the modiolar surface of the scala tympani (ST) and the scala vestibuli (SV) allowed fluid exchanges between the modiolar space/vascular tree, the perilymph, and the spiral ligament (Rask-Andersen et al., 2006). Our nanoparticles, with a diameter of 5 nm, are much smaller than those used in other experiments (diameter >200 nm) (Zhao et al., 2021). These results suggest that the size of nanoparticles affects absorption, and drugs with a small size in the perilymph reach the modiolus or limbus more easily. This further demonstrates the potential of our nanoparticles in the management of inner-ear disease.

3.6 Nanoparticle Distribution *In Vivo* With Different Injection Methods

Fluorescent optical imaging was performed on mice to evaluate the enrichment and metabolism of Au-DENPs in the cochlea by different injection methods at different time periods. Accumulation of the fluorescent tracer reflected the number of nanoparticles entering the inner ear when various injection methods were used. The nanoparticles entering the inner ear reached maximal levels at 0.5 h (**Figure 6**) and gradually declined after 7 h (**Figure 6A** e, j, o, t and **Figure 6B**). The intratympanic injection route afforded the most intense fluorescent signals of FITC, followed by the intravenous, intramuscular, and retro-auricular sulcus injection routes (in that order). The results were analyzed by quantitative analysis of cochlea imaging data, and the results of quantitative analysis were significantly consistent with those obtained from *in vivo* imaging (**Figure 6B**). Many doctors choose posterior ear injection in clinics to increase the efficiency of drugs in the inner ear; however, we found that the amount of Au-DENPs entering the vessels of the inner ear by retro-auricular injection was similar to that by intramuscular injection (**Figure 6A, f, p**), and this basically confirmed that the effects of intramuscular injection were similar to those of retro-auricular sulcus injection in clinics. Fluorescent optical imaging only showed nanocarriers in the capillaries of the inner ear. While this did not mean that the nanocarriers crossed the blood–labyrinth barrier (BLB) and entered the epithelial cells of the inner ear labyrinth and the inner ear, **Figure 5 C (a-d and e-h)** shows that FITC fluorescence could be observed in the spiral ganglion cells and hair cells of the intravenous injection group, indicating that our nanoparticles could enter the inner ear through the BLB, and they had the potential to target focus of diseases in the inner ear.

3.7 Nanoparticle Distribution in Visceral Organs With the ICP-AES Test

ICP-AES was used to measure the distribution of gold elements in important organs. As shown in **Figure 6C**, the absolute gold content decreased in all organs. However, after left tympanum injection, Au-DENPs were relatively enriched in the left cochlea and lung and relatively low in other organs. In contrast, after intravenous injection, Au-DENPs were mainly enriched in the liver, heart, and lung, and low in the cochlea, with no observable difference between the left and right cochlea. This can be seen from ICP-AES results shown in **Figure 6C**. Therefore, tympanic injection of nanomedicine is an appropriate way to treat diseases of the inner ear (**Figure 6C**).

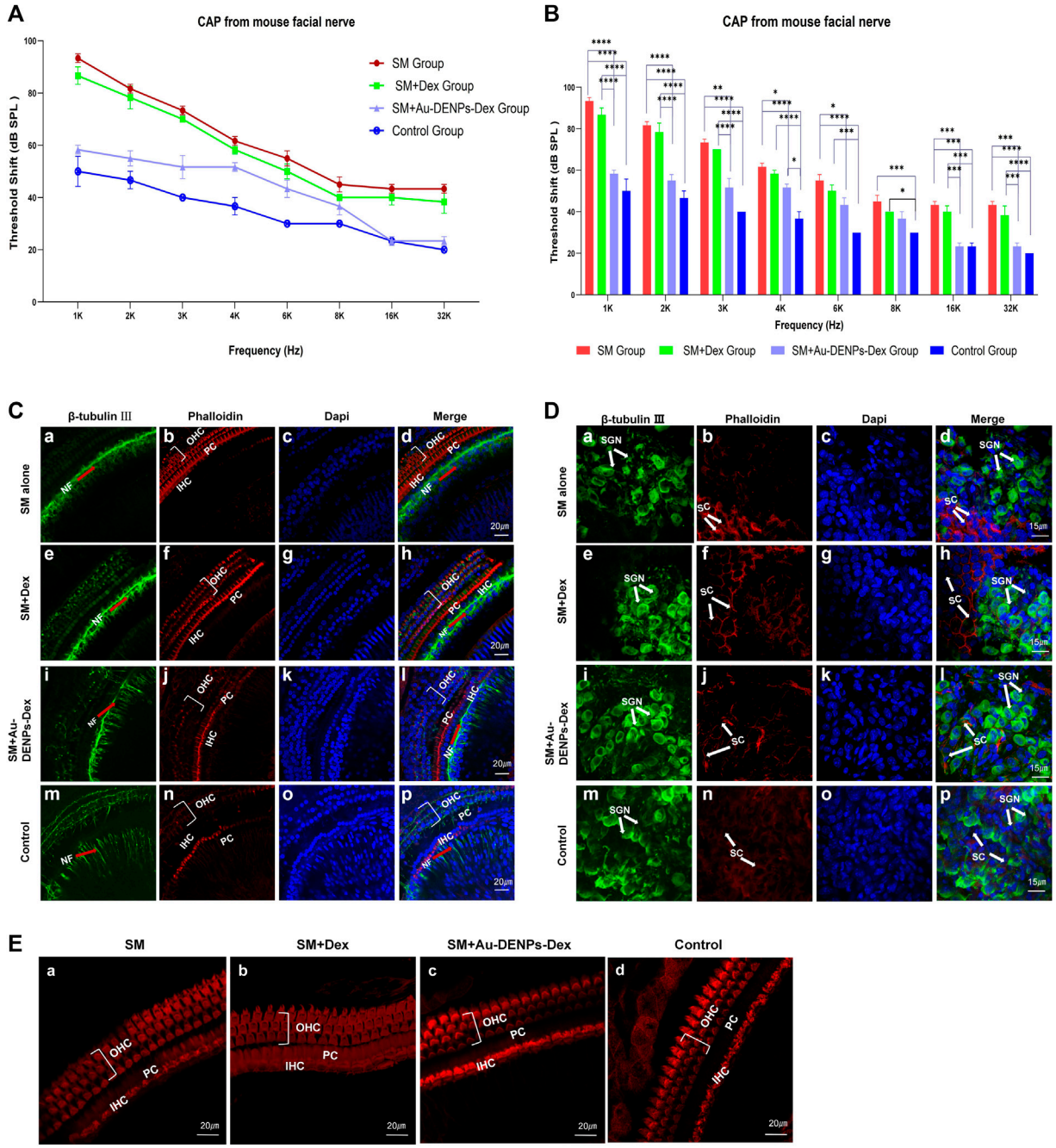

FIGURE 9 | (A) Rapid changes in the CAP threshold of mice recorded from the facial nerve after treatment with streptomycin alone, streptomycin mixed with Dex, and streptomycin mixed with Au-DENPs-Dex (Au@CD-PAMAM-Arg8/Dex). **(B)** Comparison of hearing improvement among each group in response to 1,2,3,4, 6, 8, 16, and 32 kHz; *$p < 0.05$, **$p < 0.01$, ***$p < 0.001$, and ****$p < 0.0001$. The damage of nerve endings below the inner hair cells **(C)**, spiral ganglion cells **(D)**, and OHCs and IHCs **(E)** with different treatment methods under confocal microscopy.

3.8 Toxicity Evaluation of Nanoparticles

H&E staining was used to evaluate the systemic biosafety of Au-DENPs-Dex *in vivo* 2 weeks after treatment. Compared to the control group, all treatment groups (Au-DENPs-Dex group, Au-DENPs group, Au @CD-PAMAM group, or control group) had no obvious morphological changes or tissue damage (**Figure 7A**). The liver functionality (AST/ALT) (**Figures 7B**,C) and renal functionality (CREA/BUN) (**Figures 7D**,E) in each group was within the normal range, indicating that the nanoparticles exerted no obvious biological toxicity.

3.9 Drug Delivery Efficiency of Nanoparticles by the SM Ototoxicity Model

3.9.1 Assessment of Therapeutic Effect

As shown in **Figure 8A**, an increase in SM concentration led to a gradual decrease in cell activity. An SM concentration of 30 mg/ml was used as an ototoxicity model to explore the therapeutic effects of treatments using Au-DENPs-Dex and dexamethasone only. As the concentration of Au-DENPs-Dex nanoparticles accumulated, the cell viability gradually increased. The cell viability of the Au-DENPs-Dex nanoparticles group, at the same concentration, was higher than that of both Dex only and 0.01 M PBS groups (**Figure 8B**). It indicated that the therapeutic effect of our nanoparticles is superior to that of direct drug administration at the cellular level.

3.9.2 Auditory Function Evaluation *In Vivo*

After SM treatment, overproduction of ROS contributed to the production of pro-inflammatory cytokines, which severely exacerbated inflammation in the cochlea (Ding et al., 1993; Wrzesniok et al., 2013; Cui et al., 2015). The administration of Dex can reduce pro-inflammatory cytokines (Shan et al., 2012; Xiong et al., 2019). To further explore the drug delivery efficiency of nanoparticles, CAP thresholds recorded from the facial nerve for 1, 2, 3, 4, 6, 8, 16, and 32 kHz were performed 3 days after surgery, to investigate hearing function *in vivo*. There was a significant effect from SM alone, SM mixed with Dex, SM mixed with Au-DENPs-Dex treatment, and control groups on CAP thresholds [$F(3, 64) = 188.7$, $p < 0.0001$]. Hearing losses in the SM and SM mixed with Dex groups were significant compared to the control and SM mixed with Au-DENPs-Dex groups. (**Figures 9A,B**). Almost no hearing loss was reported in the SM mixed with Au-DENPs-Dex group. CAP thresholds in the SM group (ranging from 93.3 dB SPL at 1 kHz to 43.3 dB at 32 kHz) increased more than those in the SM mixed with Au-DENPs-Dex group (ranging 58.3 dB SPL at 1 kHz to 23.3 dB SPL at 32 kHz). This shows that Au-DENPs-Dex is effective for reducing SM-induced injury. The therapeutic effect of nanoparticles is greater than that of direct administration.

3.9.3 Assessment of Therapeutic Effects *In Vivo*

Confocal microscopy images of nerve endings below the inner hair cells (**Figure 9C**), spiral ganglion cells (**Figure 9D**), and hair cells (**Figure 9E**) were used to explore the therapeutic effect of Au-DENPs-Dex and Dex on SM ototoxicity. In the SM mixed with Au-DENPs-Dex and control groups, a thick bundle of NF can be seen running medial and parallel to the row of IHC (**Figures 9C l,p**), and thin fascicles of NF project out radially from the thick fiber bundle in the direction of the OHC. Many blue-labeled nuclei were observed in the outer sulcus cell (OSC) area radial to the OHC (**Figures 9C l,p**), while the longitudinal NF bundle was medial to the row of IHC in the SM group.

The longitudinally oriented fascicle of NF medial to the IHC in the SM (**Figure 9C, a**) and SM mixed with Dex groups (**Figure 9C, e**) was severely damaged and the thickness was less than that in the control (**Figure 9C, m**) and SM mixed with Au-DENPs-Dex groups (**Figure 9C i**). SGNs were described as large, round, blue-labeled nuclei surrounded with the green cytoplasm marked with β-tubulin III; numerous diminutive blue-labeled nuclei appeared in the circumambient support cells labeled with phalloidin (**Figures 9D a,e,i,m**). However, mostly β-tubulin-labeled SGNs were eliminated (**Figures 9D d,h**), and the soma and nuclei were shrunken in the SM or SM mixed with Dex groups (**Figures 9D d,h**) compared to the control and SM mixed with Au-DENPs-Dex groups (**Figures 9D p,l**). In addition, there was no significant difference in hair cells of each group; stereocilia and hair cells in all frequency regions of the organ of Corti in each group exhibited almost no damage and appeared similar to those of the control (**Figure 9E**).

We observed an apparent recovery in the morphology of nerve fibers, nerve endings below the inner hair cell, and SGN in the SM mixed with Au-DENPs-Dex group compared to the SM and SM mixed with free Dex groups (**Figure 9**), supporting the concept that acute cochlear damage caused by low concentrations of streptomycin mainly occurred in the nerve fibers, nerve endings below the inner hair cell, and SGN. Destruction of the efferent endings by SM leads to an increase in the auditory threshold. It is evident that Au-DENPs-Dex is significant for SM ototoxicity. These results indicate that the systemic toxicity of nanomaterials is negligible and has a potential clinical value in SM-induced ototoxic injury or other inner ear disease.

4 CONCLUSION

In summary, we successfully developed a safe and highly effective nano-drug carrier based on β-CD and Arg8-modified gold nanoparticles, Au-DENPs, targeted to inner ear diseases, which can be loaded with Dex and has promising treatment effects over Dex alone. We also verified that Au-DENPs-Dex is mainly distributed in SGN, hair cells, and supporting cells in the cochlea, which are major damage sites in cases of tinnitus and deafness. *In vivo* tracer tests showed that the effect of tympanic injection was significantly better than that of posterior ear injection, muscle injection, and tail vein injection, and clinical retro-auricular injection cannot increase the efficiency of administering drugs into the ear. The SM ototoxicity model verified the efficiency and potential of drug carriers for loading drugs *in vivo*. This research suggests that Au-DENPs are a potential new drug carrier, and the clinical application of Au-DENPs-Dex in acute inner ear injury is promising.

DATA AVAILABILITY STATEMENT

The original contributions presented in the study are included in the article/Supplementary Material; further inquiries can be directed to the corresponding author.

ETHICS STATEMENT

All animal experiments were conducted under protocols approved by the Experimental Animal Ethics Committee of the Rui ye Model Animal Center (Ethics Number: 20210111008).

AUTHOR CONTRIBUTIONS

The manuscript was written through contributions of JL and PL. All authors have given approval to the final version of the manuscript. Conception and design: PL and JL; Collection and assembly of data: JL; Provision of study materials and experimenter: JL; Data analysis and interpretation: JL, XL, LL, and JT; Final approval of manuscript: all authors.

FUNDING

This research was supported by the National Natural Science Foundation of China (NSFC) (No. 82071050), National Natural Science Foundation of China (NSFC) (No. 2020G2RPYMS12), and Science and Technology Planning Project of Guangzhou, China (No. 201803010093).

REFERENCES

Carlisle, R. C., Bettinger, T., Ogris, M., Hale, S., Mautner, V., and Seymour, L. W. (2001). Adenovirus Hexon Protein Enhances Nuclear Delivery and Increases Transgene Expression of Polyethyleneimine/plasmid DNA Vectors. *Mol. Ther.* 4, 473–483. doi:10.1006/mthe.2001.0472

Crumling, M. A., Liu, L., Thomas, P. V., Benson, J., Kanicki, A., Kabara, L., et al. (2012). Hearing Loss and Hair Cell Death in Mice Given the Cholesterol-Chelating Agent Hydroxypropyl-β-Cyclodextrin. *PLoS One* 7 (12), e53280. doi:10.1371/journal.pone.0053280

Cui, C., Liu, D., and Qin, X. (2015). Attenuation of SM Ototoxicity by Tetramethylpyrazine in guinea Pig Cochlea. *Otolaryngol. Head Neck Surg.* 152 (5), 904–911. doi:10.1177/0194599814565594

Daraee, H., Eatemadi, A., Abbasi, E., Fekri Aval, S., Kouhi, M., and Akbarzadeh, A. (2016). Application of Gold Nanoparticles in Biomedical and Drug Delivery. *Artif. Cell Nanomedicine, Biotechnol.* 44 (1), 410–422. doi:10.3109/21691401.2014.955107

Ding, D., Allman, B. L., and Salvi, R. (2012). Review: Ototoxic Characteristics of Platinum Antitumor Drugs. *Anat. Rec. (Hoboken)* 295 (11), 1851–1867. doi:10.1002/ar.22577

Ding, D., Salvi, R., and Roth, J. A. (2014). Cellular Localization and Developmental Changes of Zip8, Zip14 and Transferrin Receptor 1 in the Inner Ear of Rats. *Biometals* 27 (4), 731–744. doi:10.1007/s10534-014-9765-0

Ding, D., Jin, X., and Huangfu, M. (1993). Blocking Effect of SM Sulfate on Auditory Conduction. *J. Audiol. Speech Dis.* 1, 29–31.

Ding, D., Roth, J., and Salvi, R. (2011). Manganese Is Toxic to Spiral Ganglion Neurons and Hair Cells *In Vitro*. *Neurotoxicology* 32, 233–241. doi:10.1016/j.neuro.2010.12.003

Dinh, C. T., Haake, S., Chen, S., Hoang, K., Nong, E., Eshraghi, A. A., et al. (2008). Dexamethasone Protects Organ of Cortiexplants against Tumor Necrosis Factor-Alpha-Induced Loss of Auditory Hair Cellsand Alters the Expression Levels of Apoptosis-Related Genes. *Neuroscience* 157 (2), 405–413. doi:10.1016/j.neuroscience.2008.09.012

Eichman, J. D., Bielinska, A. U., Kukowska-Latallo, J. F., and Baker, J. R., Jr (2000). The Use of PAMAM Dendrimers in the Efficient Transfer of Genetic Material into Cells. *Pharm. Sci. Techn. Today* 3 (7), 232–245. doi:10.1016/s1461-5347(00)00273-x

Gül, A., Şengül, E., Yılmaz, B., Özkurt, F. E., Akdağ, M., Keleş, A., et al. (2017). The Protective Effect of Intratympanic Dexamethasone on SM Ototoxicity in Rats. *Ear Nose Throat J.* 96 (6), 12–17.

Haynes, D. S., O'Malley, M., Cohen, S., Watford, K., and Labadie, R. F. (2007). Intratympanic Dexamethasone for Sudden Sensorineural Hearing Loss after Failure of Systemic Therapy. *Laryngoscope* 117, 3–15. doi:10.1097/01.mlg.0000245058.11866.15

Holley, M. C. (2005). Keynote Review: The Auditory System, Hearing Loss and Potential Targets for Drug Development. *Drug Discov. Today* 10 (19), 1269–1282. doi:10.1016/s1359-6446(05)03595-6

Hou, W., Wei, P., Kong, L., Guo, R., Wang, S., and Shi, X. (2016). Partially PEGylated Dendrimer-Entrapped Gold Nanoparticles: A Promising Nanoplatform for Highly Efficient DNA and siRNA Delivery. *J. Mater. Chem. B* 4, 2933–2943. doi:10.1039/c6tb00710d

Hou, W., Wen, S., Guo, R., Wang, S., and Shi, X. (2015). Partially Acetylated Dendrimer-Entrapped Gold Nanoparticles with Reduced Cytotoxicity for Gene Delivery Applications. *J. Nanosci. Nanotechnol.* 15, 4094–4105. doi:10.1166/jnn.2015.9618

Kermanian, M., Sadighian, S., Ramazani, A., Naghibi, M., Khoshkam, M., and Ghezelbash, P. (2021). Inulin-Coated Iron Oxide Nanoparticles: A Theranostic Platform for Contrast-Enhanced MR Imaging of Acute Hepatic Failure. *ACS Biomater. Sci. Eng.* 7 (6), 2701–2715. doi:10.1021/acsbiomaterials.0c01792

Kim, D. K. (2017). Nanomedicine for Inner Ear Diseases: A Review of Recent *In Vivo* Studies. *Biomed. Res. Int.* 2017, 3098230. doi:10.1155/2017/3098230

Kim, D. K., Park, S. N., Park, K. H., Park, C. W., Yang, K. J., Kim, J. D., et al. (2015). Development of a Drug Delivery System for the Inner Ear Using Poly (Amino Acid)-Based Nanoparticles. *Drug Deliv.* 22 (3), 367–374. doi:10.3109/10717544.2013.879354

Kinis, V., Ozbay, M., Bakir, S., Sengul, E., Yorgancilar, E., Keles, A., et al. (2013). The Effect of Corticosteroid against SM Ototoxicity. *J. Craniofac. Surg.* 24 (5), 1726–1730. doi:10.1097/scs.0b013e3182a232a5

Kitagishi, H., Hatada, S., Itakura, T., Maki, Y., Maeda, Y., and Kano, K. (2013). Cellular Uptake of Octaarginine-Conjugated Tetraarylporphyrin Included by Per-O-Methylated β-cyclodextrin. *Org. Biomol. Chem.* 11 (19), 3203–3211. doi:10.1039/c3ob27248f

Kitajiri, S. I., Furuse, M., Morita, K., Saishin-Kiuchi, Y., Kido, H., Ito, J., et al. (2004). Expression Patterns of Claudins, Tight junction Adhesion Molecules, in the Inner Ear. *Hear. Res.* 187 (1-2), 25–34. doi:10.1016/s0378-5955(03)00338-1

Labieniec-Watala, M., and Watala, C. (2015). PAMAM Dendrimers: Destined for success or Doomed to Fail? Plain and Modified PAMAM Dendrimers in the Context of Biomedical Applications. *J. Pharm. Sci.* 104 (1), 2–14. doi:10.1002/jps.24222

Lee, J. H., Lee, M. Y., Lim, Y., Knowles, J., and Kim, H. W. (2018). Auditory Disorders and Future Therapies with Delivery Systems. *J. Tissue Eng.* 9, 2041731418808455. doi:10.1177/2041731418808455

Li, W., Li, D., Chen, N., Liu, P., Han, S., Wang, L., et al. (2021). Recording of Electrocochleography from the Facial Nerve Canal in Mice. *J. Neurosci. Methods* 360, 109256. doi:10.1016/j.jneumeth.2021.109256

Maitani, Y., and Hattori, Y. (2009). Oligoarginine-PEG-lipid Particles for Gene Delivery. *Expert Opin. Drug Deliv.* 6 (10), 1065–1077. doi:10.1517/17425240903156366

Malinga-Drozd, M., Uram, Ł., Wróbel, K., and Wołowiec, S. (2021). Chiral Recognition of Homochiral Poly (Amidoamine) Dendrimers Substituted with R- and S-Glycidol by Keratinocyte (HaCaT) and Squamous Carcinoma (SCC-15) Cells *In Vitro*. *Polymers* 13 (7), 1049. doi:10.3390/polym13071049

Markowicz, J., Uram, Ł., Wołowiec, S., and Rode, W. (2021). Biotin Transport-Targeting Polysaccharide-Modified PAMAM G3 Dendrimer as System Delivering α-Mangostin into Cancer Cells and C. elegans Worms. *Int. J. Mol. Sci.* 22 (23), 12925. doi:10.3390/ijms222312925

Meltser, I., and Canlon, B. (2011). Protecting the Auditory System with Glucocorticoids. *HearRes* 281 (1-2), 47–55. doi:10.1016/j.heares.2011.06.003

Nakase, I., Niwa, M., Takeuchi, T., Sonomura, K., Kawabata, N., Koike, Y., et al. (2004). Cellular Uptake of Arginine-Rich Peptides: Roles for Macropinocytosis and Actin Rearrangement. *Mol. Ther.* 10 (6), 1011–1022. doi:10.1016/j.ymthe.2004.08.010

Nam, H. Y., Nam, K., Hahn, H. J., Kim, B. H., Lim, H. J., Kim, H. J., et al. (2009). Biodegradable PAMAM Ester for Enhanced Transfection Efficiency with Low Cytotoxicity. *Biomaterials* 30, 665–673. doi:10.1016/j.biomaterials.2008.10.013

Parimi, S., Barnes, T. J., Callen, D. F., and Prestidge, C. A. (2010). Mechanistic Insight into Cell Growth, Internalization, and Cytotoxicity of PAMAM Dendrimers. *Biomacromolecules* 11 (2), 382–389. doi:10.1021/bm9010134

Qiu, J., Kong, L., Cao, X., Li, A., Wei, P., Wang, L., et al. (2018). Enhanced Delivery of Therapeutic siRNA into Glioblastoma Cells Using Dendrimer-Entrapped Gold Nanoparticles Conjugated with β-Cyclodextrin. *Nanomaterials (Basel)* 8 (3), 131. doi:10.3390/nano8030131

Rask-Andersen, H., Schrott-Fischer, A., Pfaller, K., and Glueckert, R. (2006). Perilymph/modiolar Communication Routes in the Human Cochlea. *Ear Hear* 27 (5), 457–465. doi:10.1097/01.aud.0000233864.32183.81

Riquelme, R., Cediel, R., Contreras, J., la Rosa Lourdes, R. D., Murillo-Cuesta, S., Hernandez-Sanchez, C., et al. (2010). A Comparative Study of Age-Related Hearing Loss in Wild Type and Insulin-like Growth Factor I Deficient Mice. *Front. Neuroanat.* 4, 27. doi:10.3389/fnana.2010.00027

Roy, S., Johnston, A. H., Newman, T. A., Glueckert, R., Dudas, J., Bitsche, M., et al. (2010). Cell-specific Targeting in the Mouse Inner Ear Using Nanoparticles Conjugated with a Neurotrophin-Derived Peptide Ligand: Potential Tool for Drug Delivery. *Int. J. Pharm.* 390, 214–224. doi:10.1016/j.ijpharm.2010.02.003

Saito, T., Zhang, Z. J., Tokuriki, M., Ohtsubo, T., Noda, I., Shibamori, Y., et al. (2001). Expression of P-Glycoprotein Is Associated with that of Multidrug Resistance Protein 1 (MRP1) in the Vestibular Labyrinth and Endolymphatic Sac of the guinea Pig. *Neurosci. Lett.* 303 (3), 189–192. doi:10.1016/s0304-3940(01)01738-4

Shakhbazau, A., Isayenka, I., Kartel, N., Goncharova, N., Seviaryn, I., Kosmacheva, S., et al. (2010). Transfection Efficiencies of PAMAM Dendrimers Correlate Inversely with Their Hydrophobicity. *Int. J. Pharm.* 383 (1-2), 228–235. doi:10.1016/j.ijpharm.2009.09.020

Shan, Y., Luo, T., Peng, C., Sheng, R., Cao, A., Cao, X., et al. (2012). Gene Delivery Using Dendrimer-Entrapped Gold Nanoparticles as Nonviral Vectors. *Biomaterials* 33, 3025–3035. doi:10.1016/j.biomaterials.2011.12.045

Stachler, R. J., Chandrasekhar, S. S., Archer, S. M., Rosenfeld, R. M., and Schwartz, S. R. (2012). American Academy of Otolaryngology-Head and Neck Surgery. Clinical Practice Guideline: Sudden Hearing Loss. *Otolaryngol. Head Neck Surg.* 146 (3 Suppl. l), S1–S35. doi:10.1177/0194599812436449

Su, Z., Xiong, H., Pang, J., Lin, H., Lai, L., Zhang, H., et al. (2019). LncRNA AW112010 Promotes Mitochondrial Biogenesis and Hair Cell Survival: Implications for Age-Related Hearing Loss. *Oxid Med. Cel Longev* 2019, 6150148. doi:10.1155/2019/6150148

Sun, C., Wang, X., Zheng, Z., Chen, D., Wang, X., Shi, F., et al. (2015). A Single Dose of Dexamethasone Encapsulated in Polyethylene Glycol-Coated Polylactic Acid Nanoparticles Attenuate Cisplatin-Induced Hearing Loss Following Round Window Membrane Administration. *Int. J. Nanomedicine* 10, 3567–3579. doi:10.2147/IJN.S77912

Tan, X., Zhou, Y., Agarwal, A., Lim, M., Xu, Y., Zhu, Y., et al. (2020). Systemic Application of Honokiol Prevents Cisplatin Ototoxicity without Compromising its Antitumor Effect. *Am. J. Cancer Res.* 10 (12), 4416–4434.

Tomalia, D. A., Baker, H., Dewald, J., Hall, M., Kallos, G., Martin, S., et al. (1985). A New Class of Polymers: Starburst-Dendritic Macromolecules. *Polym. J.* 17, 117–132. doi:10.1295/polymj.17.117

Tomalia, D. A., Baker, H., Dewald, J., Hall, M., Kallos, G., Martin, S., et al. (1986). Dendritic Macromolecules: Synthesis of Starburst Dendrimers. *Macromolecules* 19, 2466–2468. doi:10.1021/ma00163a029

Wang, N., Liu, C., Yao, W., Zhou, H., Yu, S., Chen, H., et al. (2021). A Traceable, GSH/pH Dual-Responsive Nanoparticles with Spatiotemporally Controlled Multiple Drugs Release Ability to Enhance Antitumor Efficacy. *Colloids Surf. B Biointerfaces* 205, 111866. doi:10.1016/j.colsurfb.2021.111866

Wang, P., Li, H., Yu, S., Jin, P., Hassan, A., and Du, B. (2017). Minocycline Attenuates Streptomycin-Induced Cochlear Hair Cell Death by Inhibiting Protein Nitration and Poly (ADP-Ribose) Polymerase Activation. *Neurosci. Lett.* 656, 83–88. doi:10.1016/j.neulet.2017.07.028

Wrzesniok, D., Beberok, A., Otreba, M., and Buszman, E. (2013). Effect of SM on Melanogenesis and Antioxidant Status in Melanocytes. *Mol. Cel Biochem* 383, 77–84. doi:10.1007/s11010-013-1756-x

Xiong, Z., Alves, C. S., Wang, J., Li, A., Liu, J., Shen, M., et al. (2019). Zwitterion-functionalized Dendrimer-Entrapped Gold Nanoparticles for Serum-Enhanced Gene Delivery to Inhibit Cancer Cell Metastasis. *Acta Biomater.* 99, 320–329. doi:10.1016/j.actbio.2019.09.005

Yang, K. J., Son, J., Jung, S. Y., Yi, G., Yoo, J., Kim, D. K., et al. (2018). Optimized Phospholipid-Based Nanoparticles for Inner Ear Drug Delivery and Therapy. *Biomaterials* 171, 133–143. doi:10.1016/j.biomaterials.2018.04.038

Yoon, J. Y., Yang, K. J., Kim, D. E., Lee, K. Y., Park, S. N., Kim, D. K., et al. (2015). Intratympanic Delivery of Oligoarginine-Conjugated Nanoparticles as a Gene (Or Drug) Carrier to the Inner Ear. *Biomaterials* 73, 243–253. doi:10.1016/j.biomaterials.2015.09.025

Zambito, G., Deng, S., Haeck, J., Gaspar, N., Himmelreich, U., Censi, R., et al. (2021). Fluorinated PLGA-PEG-Mannose Nanoparticles for Tumor-Associated Macrophage Detection by Optical Imaging and MRI. *Front. Med. (Lausanne)* 8, 712367. doi:10.3389/fmed.2021.712367

Zhang, J., Sun, H., Salvi, R., and Ding, D. (2018). Paraquat Initially Damages Cochlear Support Cells Leading to Anoikis-like Hair Cell Death. *Hear. Res.* 364, 129–141. doi:10.1016/j.heares.2018.03.014

Zhang, L., Xu, Y., Cao, W., Xie, S., Wen, L., and Chen, G. (2018). Understanding the Translocation Mechanism of PLGA Nanoparticles across Round Window Membrane into the Inner Ear: a Guideline for Inner Ear Drug Delivery Based on Nanomedicine. *Int. J. Nanomedicine* 13, 479–492. doi:10.2147/ijn.s154968

Zhao, Z., Han, Z., Naveena, K., Lei, G., Qiu, S., Li, X., et al. (2021). ROS-responsive Nanoparticle as a Berberine Carrier for OHC-Targeted Therapy of Noise-Induced Hearing Loss. *ACS Appl. Mater. Inter.* 13 (6), 7102–7114. doi:10.1021/acsami.0c21151

Conflict of Interest: The authors declare that the research was conducted in the absence of any commercial or financial relationships that could be construed as a potential conflict of interest.

Publisher's Note: All claims expressed in this article are solely those of the authors and do not necessarily represent those of their affiliated organizations, or those of the publisher, the editors, and the reviewers. Any product that may be evaluated in this article, or claim that may be made by its manufacturer, is not guaranteed or endorsed by the publisher.

Copyright © 2022 Luo, Lin, Li, Tan and Li. This is an open-access article distributed under the terms of the Creative Commons Attribution License (CC BY). The use, distribution or reproduction in other forums is permitted, provided the original author(s) and the copyright owner(s) are credited and that the original publication in this journal is cited, in accordance with accepted academic practice. No use, distribution or reproduction is permitted which does not comply with these terms.

frontiers | Frontiers in Bioengineering and Biotechnology

REVIEW
published: 13 May 2022
doi: 10.3389/fbioe.2022.908751

Advances in Regenerative Sports Medicine Research

Liren Wang[1,2†], Jia Jiang[1,2,3†], Hai Lin[4], Tonghe Zhu[5], Jiangyu Cai[1,4], Wei Su[1], Jiebo Chen[1], Junjie Xu[1], Yamin Li[1], Jing Wang[1], Kai Zhang[4] and Jinzhong Zhao[1,2,3]**

[1]Department of Sports Medicine, Shanghai Jiao Tong University Affiliated Sixth People's Hospital, Shanghai, China, [2]Regenerative Sports Medicine and Translational Youth Science and Technology Innovation Workroom, Shanghai Jiao Tong University School of Medicine, Shanghai, China, [3]Regenerative Sports Medicine Lab of the Institute of Microsurgery on Extremities, Shanghai Jiao Tong University Affiliated Sixth People' Hospital, Shanghai, China, [4]National Engineering Research Center for Biomaterials, Sichuan University, Chengdu, China, [5]School of Chemistry and Chemical Engineering, Shanghai Engineering Research Center of Pharmaceutical Intelligent Equipment, Shanghai Frontiers Science Research Center for Druggability of Cardiovascular Non-Coding RNA, Institute for Frontier Medical Technology, Shanghai University of Engineering Science, Shanghai, China

OPEN ACCESS

Edited by:
Kaili Lin,
Shanghai Jiao Tong University, China

Reviewed by:
Dejian Li,
Fudan University Pudong Medical Center, China
Xingge Yu,
Shanghai Ninth People's Hospital, China

***Correspondence:**
Kai Zhang
kaizhang@scu.edu.cn
Jinzhong Zhao
jzzhao@sjtu.edu.cn

†These authors contributed equally to this work

Specialty section:
This article was submitted to Biomaterials, a section of the journal Frontiers in Bioengineering and Biotechnology

Received: 31 March 2022
Accepted: 21 April 2022
Published: 13 May 2022

Citation:
Wang L, Jiang J, Lin H, Zhu T, Cai J, Su W, Chen J, Xu J, Li Y, Wang J, Zhang K and Zhao J (2022) Advances in Regenerative Sports Medicine Research. Front. Bioeng. Biotechnol. 10:908751. doi: 10.3389/fbioe.2022.908751

Regenerative sports medicine aims to address sports and aging-related conditions in the locomotor system using techniques that induce tissue regeneration. It also involves the treatment of meniscus and ligament injuries in the knee, Achilles' tendon ruptures, rotator cuff tears, and cartilage and bone defects in various joints, as well as the regeneration of tendon–bone and cartilage–bone interfaces. There has been considerable progress in this field in recent years, resulting in promising steps toward the development of improved treatments as well as the identification of conundrums that require further targeted research. In this review the regeneration techniques currently considered optimal for each area of regenerative sports medicine have been reviewed and the time required for feasible clinical translation has been assessed. This review also provides insights into the direction of future efforts to minimize the gap between basic research and clinical applications.

Keywords: regenerative medicine, sports medicine, meniscus, rotator cuff, cartilage, tendon-to-bone, bone

INTRODUCTION

Regenerative medicine utilizes innovative approaches to explore and develop materials that can be used to replace, repair, improve, or reproduce tissues and organs in the human body (Brody, 2016). Sports medicine focuses on aspects of physical health, including the treatment and prevention of exercise-related injuries and aging-related problems that hinder the function of the locomotor system (**Figure 1**) (Baby, 2000; Foster, 2015; Kweon, et al., 2019). In the clinical practice of sports medicine, the prevention and treatment of conditions consequently depend on the structural and functional restoration of various related tissues and structures in the locomotor system. When structural integrity cannot be restored through repair, approaches that induce tissue regeneration become necessary, to prevent or delay the use of non-organic structures such as artificial joints. Thus, we explore the field of regenerative sports medicine, which is defined as a science that focuses on the restoration of the structural and functional integrity of the locomotor system, using techniques that induce the regeneration of tissue structures or organs. The approaches currently used in regenerative sports medicine include the utilization of organic and non-organic materials at various structural levels. From a clinical perspective, regenerative sports medicine deals with sports and aging-related conditions in different parts of the locomotor system, such as the menisci, ligaments, tendons, cartilages, and bones.

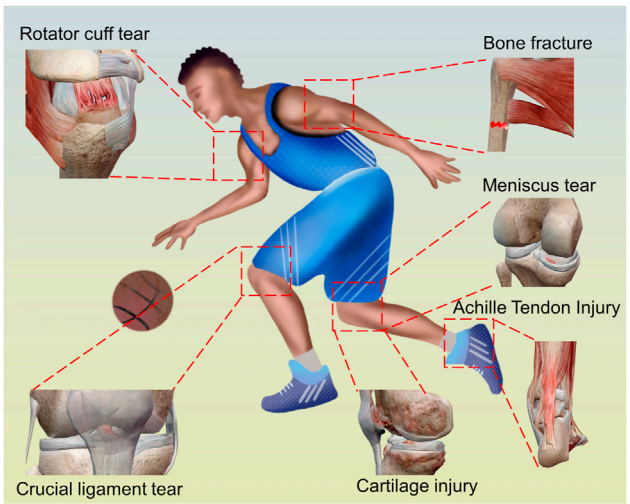

FIGURE 1 | Sports medicine related injuries.

A meniscus tear is a common knee disorder (Abrams, et al., 2013) that is irreparable in many cases, and consequently, must be addressed *via* structural restoration with a partial or total meniscectomy to restore its function. Previously, allograft and synthetic menisci have been used with unfavorable or inconsistent clinical results, and thus meniscus regeneration strategies are desirable; however, they require further investigation and development (Southworth, et al., 2020; Li, et al., 2021; Veronesi, et al., 2021). Knee ligament injuries often result in ligament deficiency and joint instability and necessitate ligament reconstruction (Pike, et al., 2019). To prevent the donor site morbidity that can occur with autografts, the high failure rate with allografts, and the non-graft-bone healing associated with non-receiver transformable synthetic ligaments, receiver transformable regenerative ligaments are considered an alternative choice (Wang C. et al., 2021). Chronic Achilles' tendon rupture often results in tendon defects that make the direct opposition of the separated tendon ends impossible and graft bridging a necessary choice; consequently, there is demand for regenerative or receiver transformable artificial Achilles' tendons (Arshad, et al., 2021). Rotator cuff tears are mainly an aging-related condition and quite often irreparable; thus, rotator cuff grafts are required to repair defects and restore the native force chain (Novi, et al., 2018). Though various graft choices are available (Sunwoo and Murrell, 2020), receiver transformable artificial rotator cuff patches are currently considered the ideal option. Sports-related cartilage injuries and osteoarthritis are the main conditions addressed in clinical sports medicine. Clinical approaches such as micro-fractures and autogenous osteochondral graft transplantations are the main strategies used to treat small cartilage defects (Beck, et al., 2016; Guo, et al., 2018), while for large cartilage defects, cartilage regeneration is required. Bone defects, fractures, or osteotomies, osteoporosis, and osteonecrosis in the locomotor system, such as glenoid and humeral head bone defects with shoulder dislocations, glenoid bone absorption with severe shoulder osteoarthritis (OA), bone defects with high tibial osteotomy, and tibial plateau depression fractures with knee dislocations, may require bone structure regeneration (Xie C. et al., 2021). In tendon or ligament-to-bone repair, the most important goal is to restore a normal tendon–bone connection with an important fibrocartilage layer (Tits and Ruffoni, 2021). However, after soft tissue-to-bone repair the cartilage layer has been found to reappear inconsistently, which makes tendon–bone interface regeneration a critical issue (Patel, et al., 2018).

In general, regenerative sports medicine has high clinical requirements. In recent years, there has been a large amount of research in this field leading to promising outcomes. In this review, we have assessed the recent progress and assessed the time required for feasible clinical translation of the new techniques and products.

RESEARCH PROGRESS IN SPECIFIC FIELDS OF REGENERATIVE SPORTS MEDICINE

Meniscus Regeneration

Meniscus Physiology and the Hurdles in Regeneration

The menisci are the semilunar and wedge-shaped fibrocartilaginous tissues between the articular cartilage of the femur and tibia plateau. They have complex 3D structures to absorb shock and distribute its load through collagen fibers which are specifically aligned in a circumferential pattern. The unique zonal phenotypes in the meniscus are histologically and physiologically characterized by two distinct regions: the avascular inner zone (white–white zone), which mainly consists of glycosaminoglycan and type-II collagen with a rounded chondrocyte-like cellular phenotype, and the vascular outer zone (red–red zone), which predominantly contains higher type-I collagen with an elongated ligament-like cellular phenotype. Moreover, these two regions are separated by a middle region (red–white zone), which is a mixture of the inner and outer zones. The limited vascularity of the meniscus indicates a poor healing ability, especially in the avascular white–white zone. Thus, the major hurdles in meniscus regeneration include the inability to replicate its native anisotropic zonal structure and hence, its specialized mechanical function. Moreover, avascularity due to its unique structural properties, and the tibiofemoral articular environment that hinders the healing potency both mechanically and biochemically, have made it challenging for biomedical scientists to create matched engineering constructs for meniscus regeneration.

Surgical Techniques for Meniscus Regeneration

Partial lesions or defects in the meniscus reduce its propensity to heal spontaneously because of mechanical stimuli from the tibiofemoral motions and the avascularity in the white–white zone, leading to degeneration over time. Advances in techniques and tissue engineering strategies have enabled researchers to attempt to repair or regenerate these meniscal defects. Some biological promotion techniques are recommended in clinical

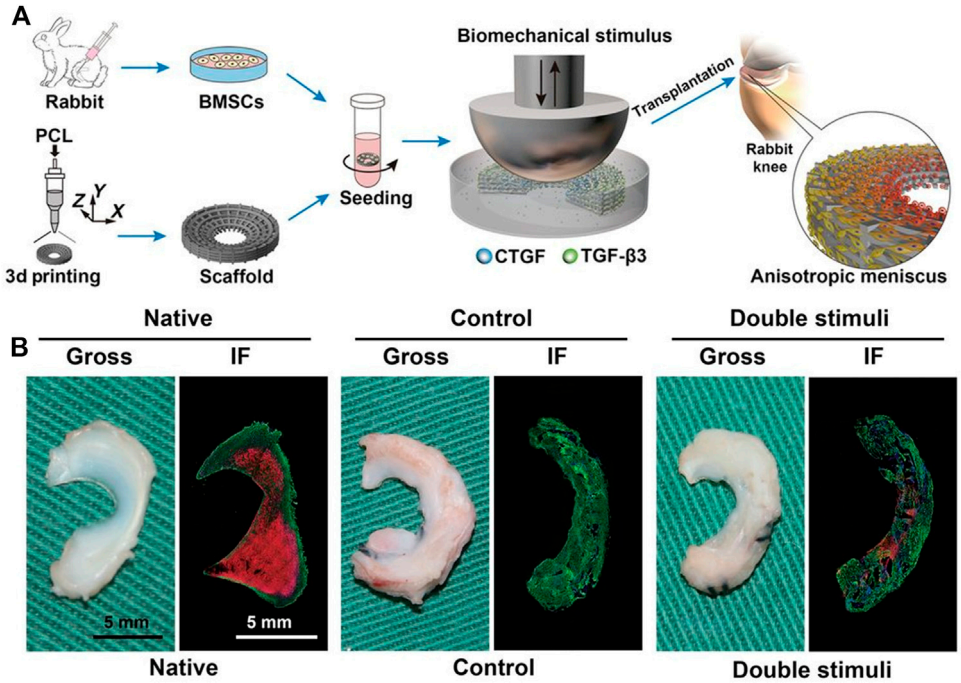

FIGURE 2 | Orchestrated biomechanical, structural, and biochemical stimuli for engineering anisotropic meniscus. **(A)** Schematic diagrams for reconstruction of functional anisotropic meniscus; **(B)** Gross view and low-magnification immunofluorescence (IF) images of native or regenerated menisci at 24 weeks after *in vivo* implantation in rabbit knees. Green, COL-1; red, COL-2. Copyright 2019 American Association for the Advancement of Science.

scenarios to augment meniscus repair, such as the introduction of bone marrow stem cells using marrow venting techniques, the exogenous addition of fibrin clot, and the stimulation of adjacent healthy meniscus and synovium (Taylor and Rodeo, 2013; Dean, et al., 2017; Kwon, et al., 2019). Notably, concurrent anterior cruciate ligament (ACL) reconstruction that used bone tunnel to release the cells and growth factors from the bone marrow, has been proven to enhance meniscal repair (Chahla, et al., 2017; Dean, et al., 2017; Westermann, et al., 2017; Tagliero, et al., 2018; DePhillipo, et al., 2019). Moreover, partial meniscus replacements offer promising approaches to treat patients with segmental meniscus defects. Both collagen meniscus implants (CMI) from the USA and polyurethane polymeric implants (Actifit) from Europe have been shown to improve clinical outcomes and substantially relieve pain in patients with meniscus defects in both medium- and long-term follow-ups (van Tienen, et al., 2009; Bulgheroni, et al., 2015).

Tissue Engineering Strategies for Meniscus Regeneration

Current surgical techniques have failed to promote meniscus regeneration, while many natural or synthetic materials, such as decellularized extracellular matrices, alginate, hyaluronan, polylactides, polyglycolides, and silk have been successfully utilized as scaffolds for meniscus engineering (Makris, et al., 2011). Among these scaffolds, decellularized extracellular matrices derived from the white–white and red–red regions of the meniscus have been shown to promote the differentiation of MSCs toward fibroblastic and fibrochondrocyte phenotypes (Shimomura, et al., 2017). Other types include injectable hydrogels that can be used to address structural defects due to their ability to form structural adaptations (Athanasiou, et al., 2013; Liu, et al., 2017). While scaffolds are beneficial due to their ability to incorporate growth factors and their initial mechanical stability, they also indicate recapitulation of the mechanical and biochemical architecture of the native meniscus, with matched stiffness and ingredient gradients (Higashioka, et al., 2014; Steele, et al., 2014; Zhu, et al., 2018; Zitnay, et al., 2018). Notably, when engineering menisci for regeneration, although an obvious choice for cell source might be fibrochondrocytes, regeneration effects are best when fibrochondrocytes are cocultured with other cell subsets (Hadidi, et al., 2016; Koh, et al., 2017; Son and Levenston, 2017; Sasaki, et al., 2018; Xie, et al., 2018). Zhang C. H. et al. (2018) used a pre-mechanically stimulated poly (ε-caprolactone) (PCL) scaffold, cocultured with rabbit bone marrow stem cells, for meniscus replacement and found that the pretreated scaffold was a better choice for inducing tissue regeneration (**Figure 2**).

Current Clinical Studies and the Challenges in Clinically Translating Meniscus Regeneration

Currently, a few scaffolds for meniscus engineering are undergoing clinical trials with a focus on cell-based therapies. Cell Bandage, a collagen sponge embedded with autologous bone marrow-derived MSCs, was applied in clinical practice to close the torn edges and defects of the meniscus, and is assumed to potentially promote healing. In another clinical trial in humans, a

chondrogenic composed of allogeneic bone marrow-derived MSCs was administered to the knee, and reported to effectively decrease visual analog scale pain scores. While meniscus repair products for clinical applications are currently lacking, preliminary outcomes suggest that cell-based therapies are a positive and promising road ahead; however, they have also identified challenges that must be overcome. In the clinical translation of engineered meniscus products, an insufficient source of autologous cells is the primary issue. The use of non-articular cells, however, seems to be a potential strategy to alleviate the scarcity of cells for autologous meniscus therapies (Makris, et al., 2011; Utomo, et al., 2016). Additionally, the high-quality autologous neo-tissues required to consistently regenerate the meniscus are difficult to obtain, as demonstrated by the large biological variability observed between donors (Martin, et al., 2017; Vapniarsky, et al., 2018; Kwon, et al., 2019). Therefore, well-characterized allogeneic tissues and cell banks should be established to enable suitable neo-tissues to be provided stably and avoid disease transmission, and this is likely to solve the intractable problem of biological variability. Furthermore, mechanical biomimicry when engineering the meniscus should be achieved, as the native meniscus allows for frictionless tibiofemoral joint movement and load distribution, which may be related to positive long-term healing outcomes (Elder and Athanasiou, 2009; MacBarb, et al., 2013; Huwe, et al., 2018). If the meniscus can be successfully generated after overcoming the aforementioned challenges, then the avascular white–white zone of the meniscus leads to difficulties in both implant protection and its integration into existing native tissues (Arvayo, et al., 2018; Vapniarsky, et al., 2018). For surgeons and biomechanical researchers, developing appropriate techniques and protocols to enhance the vascular supply to implants should be a priority (Vapniarsky, et al., 2018; Kwon, et al., 2019). In addition to vascularity, the engineering meniscus must also adjust to the inflammatory microenvironment, especially in an injured or diseased joint with its complex biochemical conditions. Therefore, modifications by decellularization and antigen removal when engineering the meniscus are required to minimize the immunoreaction of xenogeneic or allogeneic menisci to ensure implant survival and integration. Li et al. (2021) fabricated silk/graphene oxide-based meniscus scaffolds, which consisted of tannic acid and Sr^{2+}. The scaffold exerts anti-inflammatory and reactive oxygen species elimination effects, which protect against cartilage degeneration and delay OA development after meniscus injury.

The promising progression which will ultimately lead to the application of tissue-engineered therapies for meniscus regeneration in clinical practice, is evident in current clinical trials. In the near future, tissue engineering strategies may rapidly emerge for the development of meniscus regeneration products, which could potentially provide long-term solutions for patients.

Cruciate Ligament Regeneration

Common Strategies for Cruciate Ligament Regeneration

Knee crucial ligament injuries are common in sports medicine, and often occur during adolescence and young adulthood (Petersonand Krabak, 2014). Ligament reconstruction is the main solution to prevent subsequent cartilage and meniscus damage, thus improving quality of life (Mastrokalos, et al., 2005; Petersonand Krabak, 2014). Clinically, autografts and allografts are the two most common graft types used for surgical ligament reconstruction (Cai J. Y. et al., 2021). However, donor site morbidity remains an inevitable problem associated with their use (Yilgor, et al., 2012), and allografts carry additional risks of disease transmission, infection, rejection, low availability and quality, and high failure rates (Jackson, et al., 1993). Xenografts [porcine bone-patellar tendon–bone (BTB)] were harvested by Galili et al. and treated with recombinant alpha-galactosidase and glutaraldehyde for ACL reconstruction (Galili and Stone, 2021). The authors have completed preclinical trials with monkeys and progressed to clinical trials, and they have reported no significant differences in the functional performances of the porcine BTB group and cadaveric allograft group at the 24 months follow up, if the missing/contaminated cases were excluded (Stone, et al., 2007; Van Der Merwe, et al., 2020). The potential advantages of the xenografts are that they could help address the quality concerns and availability problems that occur with allografts. However, like allografts, xenografts also have the disadvantages including the possibility for disease transmission, infection, and rejection. Moreover, the process of utilizing an animal originated graft with human tissue, namely graft "humanization," is difficult and will require further investigation (Van Der Merwe, et al., 2020). To address this, artificial ligaments have been developed in recent years. To date, those ligaments that are clinically available, have been made of non-degradable materials or non-receiver transformable materials, such as polyethylene terephthalate (PET) and polyethylene, which are characterized by their hydrophobic properties and inferior biocompatibility and lead to poor graft-host bone healing after implantation (**Figure 3**) (Ai, et al., 2017; Cai J. et al., 2021). The development of receiver transformable artificial ligaments is another scope and direction for future ligament research.

Artificial Materials for Cruciate Ligament Regeneration

Teuschl *et al.* (Teuschl, et al., 2016) fabricated novel degradable silk fiber-based artificial ligaments and used biological materials, biodegradable polymers, and composite materials in ligament fabrication for ACL reconstruction in a sheep model. The silk ligaments could induce new tissue ingrowth and stimulate ACL regeneration *in vivo*. However, the balance between the degradation rate of the materials and the regeneration and remodeling rate of the tissues was not controllable. Furthermore, it is unknown whether the regenerated tissues could maintain the function of the knee at a level similar to that of the native ACL, as functional recovery and a return to sports cannot be fully evaluated in quadruped animal models.

The combined use of receiver transformable and non-transformable materials is an additional option. Mengsteab *et al.* (Mengsteab, et al., 2020) incorporated PET fibers into the poly (L-lactic) acid (PLLA) bioengineered ACL matrix to fabricate a PET/PLLA hybrid ligament. The hybrid ligament

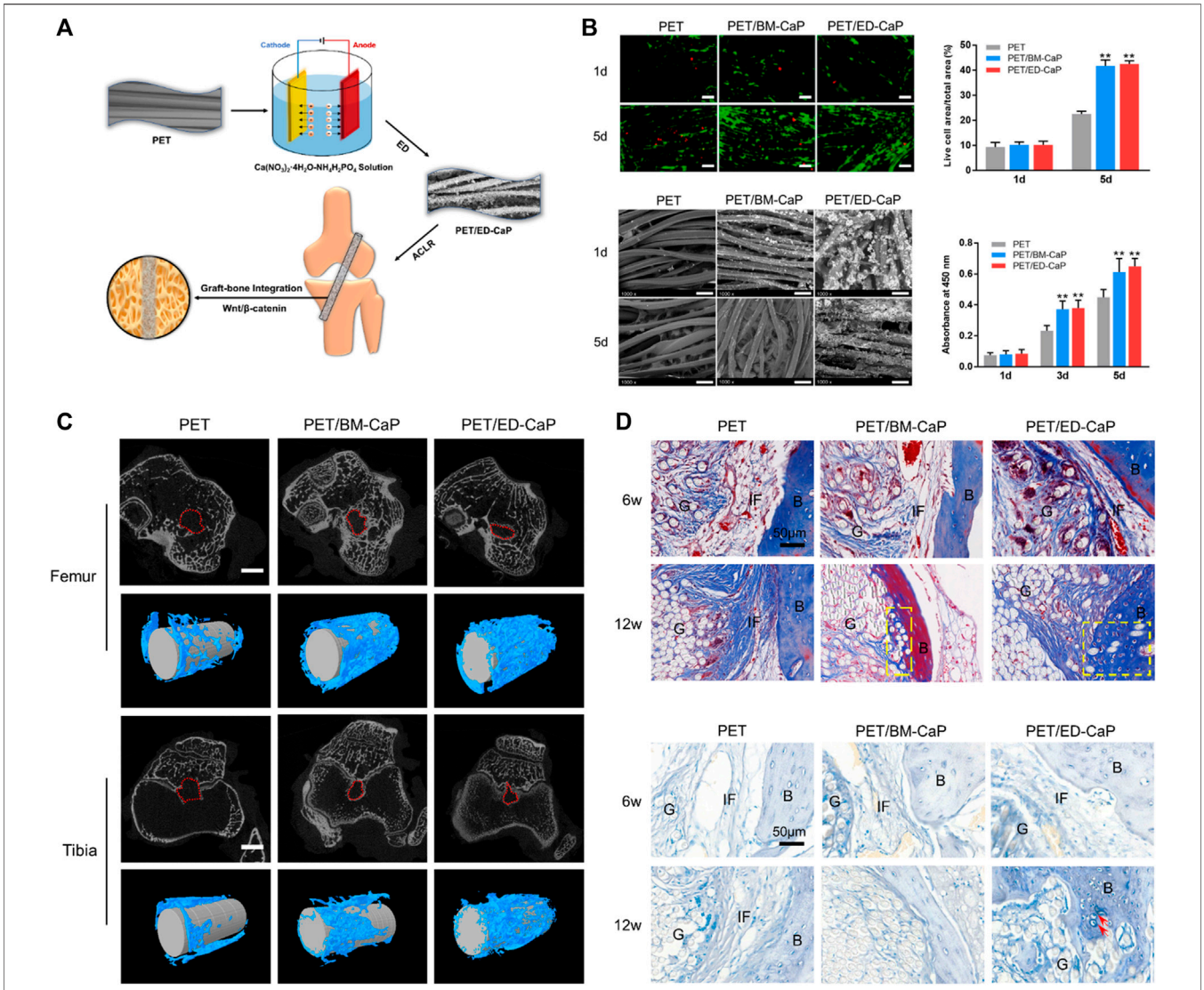

FIGURE 3 | Electrodeposition of calcium phosphate onto polyethylene terephthalate artificial ligament enhances graft-bone integration after anterior cruciate ligament reconstruction. **(A)** Electrodeposition of calcium phosphate onto polyethylene terephthalate artificial ligament; **(B)** The viability and SEM morphology of MC3T3-E1 in the PET, PET/BM-CaP and PET/ED-CaP groups; **(C)** Micro-CT analysis of the PET, PET/BM-CaP and PET/ED-CaP groups at 12 weeks after surgery; **(D)** Masson and toluidine blue staining results of pathological sections in the PET, PET/BM-CaP and PET/ED-CaP groups at 6 and 12 weeks after surgery. Copyright 2021 Elsevier.

demonstrated great peak loads and promoted the regeneration of ACL in a rabbit model.

Future Perspectives

Despite these encouraging results, further work is required to optimize the properties of newly developed grafts for crucial ligament reconstruction of the knee. We believe that decellularized scaffolds with ready-made collagen and degradable artificial ligaments are the two most promising graft types for ligament reconstruction in future clinical practice. However, prior to application, issues regarding ligament development must be addressed, as it is vital that the host-graph response be regulated and controlled. Moreover, there is a need to explore the regenerative competent microenvironment, which is the articular cavity that can induce tissue ingrowth into the graft. For clinical use, the functional assessment of the knee is more important than the regeneration and healing assessment, as the regenerated or remodeled ligament should be able to mimic the function of the native ligament.

Achilles Tendon Regeneration

Surgical Techniques for Achilles Tendon Repair

End-to-end repair of the chronic Achilles tendon is appropriate when the gap is 2 cm or less, while the V-Y technique, turndown flaps, autograft tendon transfer, and reconstructions using

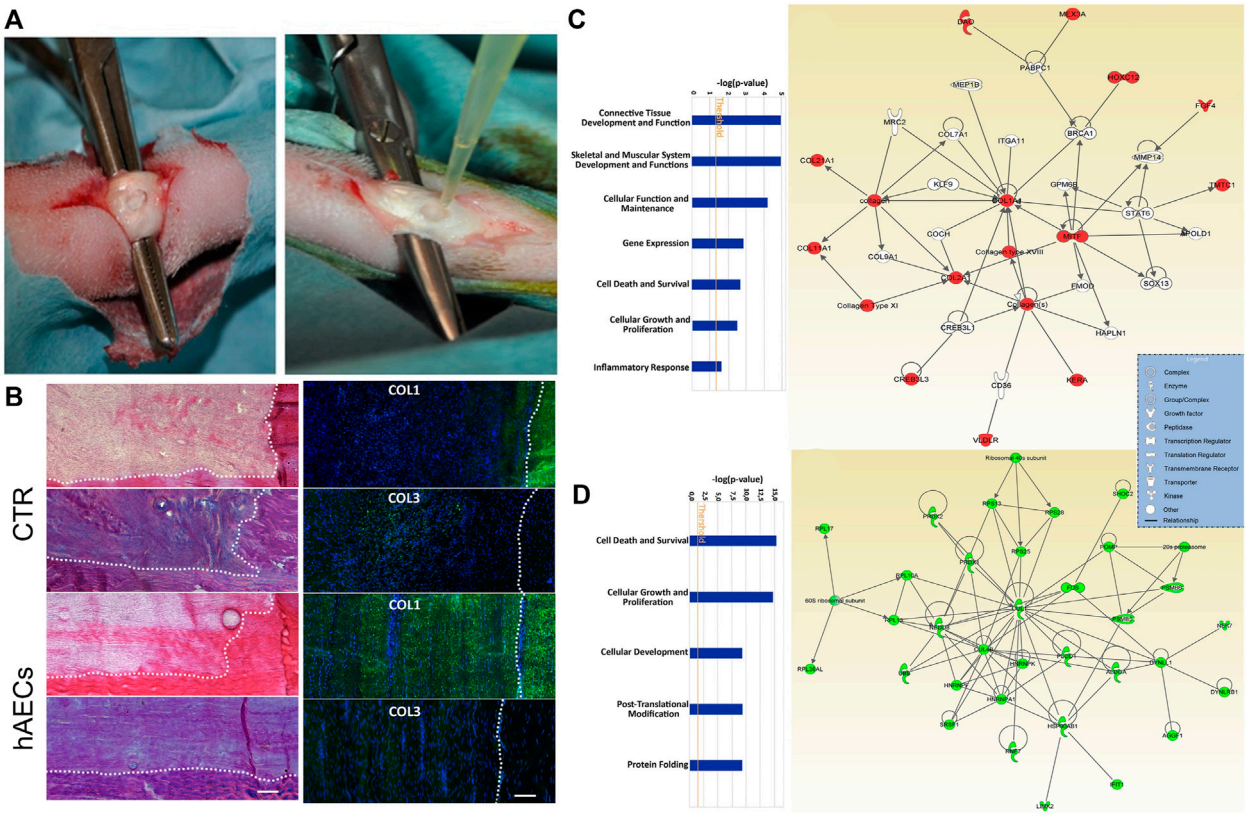

FIGURE 4 | Therapeutic potential of hAECs for early Achilles tendon defect repair through regeneration. **(A)** Circular defects of 5 mm created in the Achilles tendons. One defect was filled with fibrin glue, whereas the contralateral with 10 × 106 PKH26-stained cells suspended in fibrin glue (bottom); **(B)** Representative haematoxylin–eosin-, Herovici and immunofluorescent staining of CTR (control) and human amniotic epithelial cell (hAEC)-treated tendons. **(C)** Key functions associated with genes found to be up-regulated in hAECs and the top-scored network; **(D)** Key functions associated with genes found to be down-regulated in hAECs and the top-scored network. Copyright 2017 Wiley.

allograft, xenogeneic, or synthetic biomaterials are required for larger defects with or without the preservation of the paratenon (Kraeutler, et al., 2017; Maffulli, et al., 2018; Muller, et al., 2018; Chen and Hunt, 2019). Regardless of the multiple surgical management strategies, the ideal treatment for tendon injury is to promote Achilles tendon regeneration after gap formation (Sun, et al., 2018).

Strategies for Achilles Tendon Repair

The literature on Achilles tendon regeneration is limited mostly to laboratory studies using porcine small intestinal submucosa (Badylak, et al., 1995), acellular tendon matrix (Gungormus, et al., 2015; Zhang C. H. et al., 2018), and collagen (Sun, et al., 2018) or collagen gel (Shen, et al., 2010) as scaffolds. Moreover, exogenous cell transplantations such as for tenocytes (Gungormus, et al., 2015) and human amniotic epithelial cells (Barboni, et al., 2018) have been applied but restricted by the cell source, immune rejection, ethics, and injured microenvironment (**Figure 4**) (Harris, et al., 2004; Sun, et al., 2018). Chemokines like SDF-1α and recombinant SDF-1α containing a collagen-binding domain (CBD) have also been reported to promote endogenous tendon regeneration by inducing extracellular matrix production and avoiding the above drawbacks of exogenous cell transplantation in clinical applications (Shen, et al., 2010; Sun, et al., 2018). The local application of combined ascorbic acid and T_3 also showed the potential benefits for accelerated tendon healing (Oliva, et al., 2019). Platelet-rich fibrin (PRF), with the delivery of cytokine and growth factor, induced more organized collagen fibers *in vivo* and promoted tenocyte viability and tenogenic phenotypic differentiation *in vitro* (Wong, et al., 2020). Similarly, platelet-rich plasma (PRP) is widely used and has been proven to be effective for tendon healing *in vivo* (Chiou, et al., 2015). However, Zhang et al. (Zhang C. H. et al., 2018) found that the combined PRP was no better at repair-augmenting effects than the scaffolds alone for Achilles tendon regeneration.

Future Perspectives

Promising laboratory findings reported in the literature suggest that there will be important implications for the practical application and clinical translation of tendon regeneration (Cai C. et al., 2021; Cai et al., 2022; Wang et al., 2022). However, few clinical studies have been reported to date, and most are case reports and small case series (Chen and Hunt, 2019) with a few

translational animal models (dog, horse, *etc.*) (Sun, et al., 2018; Badylak, et al., 1995; Gungormus, et al., 2015; Zhang C. H. et al., 2018; Shen, et al., 2010). Additionally, therapeutic perspectives are not achievable until the critical challenges relating to the scaffold, cell, or chemokine use (source, induction condition, genomic compatibility, dose, *etc.*) are solved. The combination of scaffold implanted with cell or chemokines, however, is encouraging for future studies and promising for human clinics.

Rotator Cuff Regeneration

Treatment of Rotator Cuff Repairs Is an Ongoing Challenge

Rotator cuff defects are the main issues that occur in shoulder repair, and the rate of surgical failure is reportedly up to 94%, especially for large and massive tears after simple repairs (McElvany, et al., 2015; Lewington, et al., 2017; Saveh-Shemshaki, et al., 2019). Various scaffolds have been used to replace the native tissue structures in rotator cuff repairs. Most scaffolds consist chiefly of extracellular matrix and chemical polymer, which provides a bridge for connecting tendon and bone tissues, and adsorbs the fibroblast secreted collagen matrix (Guevara, et al., 2020). These scaffolds have been utilized in rotator cuff tendon tissue engineering for several decades (Steinhaus, et al., 2016; Zhao, et al., 2017). They usually combine bioactive substances to promote rotator cuff regeneration, such as stem cells and growth factors. There are currently three types of rotator cuff tendon scaffold used: xeno-patches, allo-matrices, and synthetic films (Steinhaus, et al., 2016; Coons and Alan, 2006; Wang D. et al., 2021). However, imperfect tissue regeneration is an ongoing problem.

Xeno-Patches for Rotator Cuff Repair

Xeno-patches extracted from extracellular matrices are effective bioactive scaffolds for tendon engineering and can be applied in surgical implantations to rotator cuff defects (McGovern, et al., 2018). The acellular xenografts derived from the porcine dermis and small intestine were used in a large animal model for infraspinatus repair to evaluate the effects of tendon regeneration. Nicholson et al. (Nicholson, et al., 2007) found that intestinal and porcine dermis patches were almost replaced by tendon-like tissues at 24-week, but a foreign body reaction was observed in the conjunction site of the tendon and xenograft. Ultimately, the cause of failure was the same for the dermal and intestinal groups. The potential immune reaction and associated chronic foreign body responses were the main concerns. This reaction may result from the residual DNA in the Xeno-tissue, even if processed by decellularization. Another problem is the hyper acute rejection caused by α-Gal. The α-Gal epitope exists in non-primate mammals (Naso, et al., 2011; Platts-Mills, et al., 2021), and therefore, the epitope antibody is produced in humans, which specifically binds to xeno-tissue.

Allo-Matrices for Rotator Cuff Repair

Allo-matrices originated from decellularized cadaveric human tissues and were found to have the capability to bridge tendon tissue defects, with a low risk of tissue-scaffold rejection (Fini, et al., 2012). A study by Adams et al. (Adams, et al., 2006) explored the histological and biomechanical processes of allo-matrices, by utilizing allo-dermal matrices to bridge tendon and bone in an animal model for infraspinatus repair. The fibroblast infiltration and new collagen deposition were surrounded by dermal matrices 6 weeks after implantation, and at 24 weeks, a more mature tendon-like tissue was formed in the allo-dermal group. The biomechanical properties of the regenerated tissues were promising. However, there were only small-scale clinical trials conducted to evaluate their performance (Zhao, et al., 2017). Even though no serious allo-matrix related complications were observed, and clinical outcomes appeared to be good, some potential problems still existed. Similar to the xeno-patches, there were concerns about the residual DNA. The residual DNA may cause immune inflammatory reactions and increase the proliferation of the scaring tissue (Lewington, et al., 2017). There is also evidence that the mechanical properties of the allogenic matrices are decreased when compared with that of the auto-tendons. To better induce tendon–bone interface regeneration, Chen et al. (2019) added recombinant SDF-1α to the decellularized bone–fibrocartilage–tendon composite and injected synovium-derived mesenchymal stem cells (SMSCs) into the repair site. They found that the fabricated scaffold was better at recruiting the SMSCs and resulted in well regeneration of the tendon–bone interface 8 weeks after surgery. However, the option proposed in this study is too complicated for clinical application. Neither the addition of recombinant SDF-1α nor the injection of stem cells has been approved by the administration (**Figure 5**).

Synthetic Polymers for Rotator Cuff Repair

Owing to the ongoing focus on immune reactions for both the xeno-patches and allo-matrices, synthetic polymers that are of great interest for tendon regeneration engineering have been identified (Qiu, et al., 2021; Zhao, et al., 2021). Degradable polymers, including PLLA, poly-dioxanone (PDO), and poly (lactic-co-glycolic) acid (PLGA) have been used as supports to create multifunctional scaffolds. These synthetic films consisting of regularly arranged fibers exhibit stronger mechanical characteristics than the scaffolds derived from bio-tissues (Gachon and Mesquida, 2021). The controllable arrangement plays a role in cell migration, with fibroblasts well aligned with the axis of the polymer fibers when compared to the un-aligned films in a random orientation. The polymer film had fewer immune responses when compared with that of the xeno-and allo-patches, indicating that it could be a potential scaffold to bridge the tendon gap. Yokoya et al. (Yokoya, et al., 2012) used the PLGA sheet to repair the full-thickness defect of the rotator cuff in a rabbit model and observed that a greater proportion of type-I collagen was generated in the PLGA sheet with mesenchymal stem cells. The repaired site also had a better ultimate strength when compared with that of the controls without mesenchymal stem cells. Studies that have explored synthetic films have achieved encouraging results, but the products of the polymer film degradation were identified as a concern (Silva, et al., 2020). High levels of chemical composite have a toxic effect on fibroblast proliferation and inhibit collagen deposition. These toxic effects vary with different polymers, and therefore,

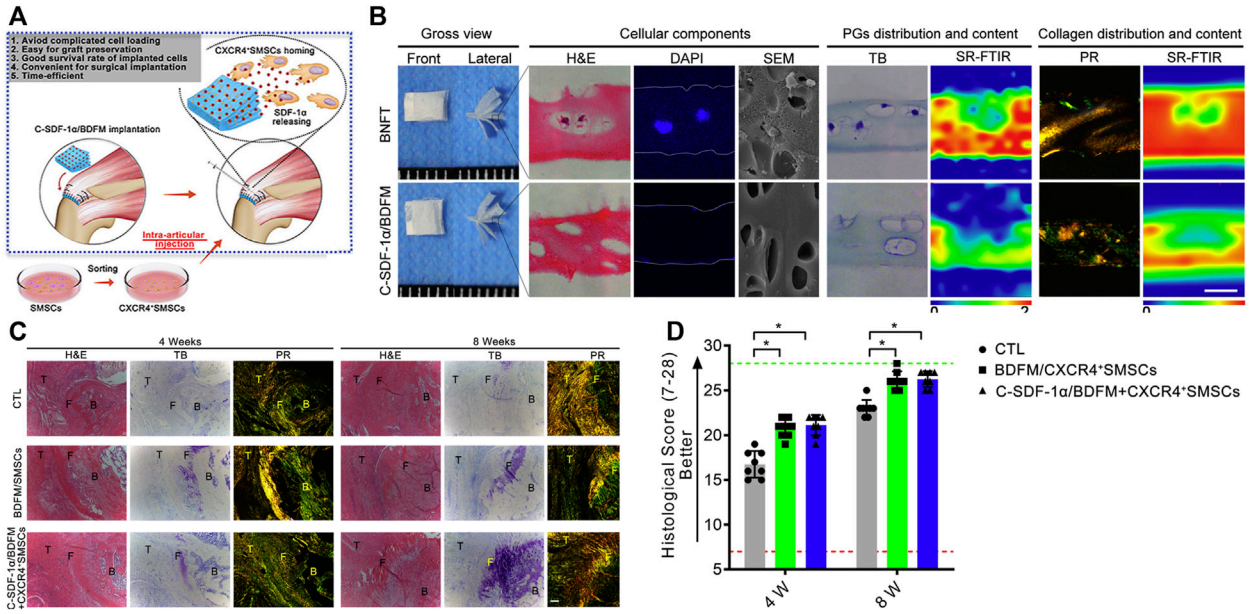

FIGURE 5 | Functional decellularized fibrocartilaginous matrix graft for rotator cuff enthesis regeneration: A novel technique to avoid *in-vitro* loading of cells. **(A)** Developing a cell-free graft with chemotaxis to recruit postoperative injected cells; **(B)** Macroscopic observation, histological analysis, and synchrotron radiation-Fourier transform infrared spectroscopy analysis of the book-type nature fibrocartilage tissues and C-SDF-1α/BDFM, sections stained with hematoxylin and eosin (H&E), DAPI, toluidine blue (TB), and picrosirius red (PR); **(C,D)** Histological analyses of regenerated fibrocartilage during RC healing. Copyright 2020 Elsevier.

more research is required to ensure that the degradation product levels are safe.

Future Perspectives

These bio-scaffolds are assumed to offer ideal structural binding sites for tissue integration. Synthetic films have the advantage of mechanical properties and low rates of immune reaction. Several scaffolds have emerged in recent years; however, they have not yet been used in routine clinical surgery (Zurina, et al., 2020). The ideal scaffold should be able to meet the mechanical strength of the cuff tendon and provide bioactive binding sites that promote fibroblast-mediated healing and tendon regeneration.

Cartilage and Osteochondral Regeneration

Simple Cartilage Regeneration

The common types of joint bone defects include partial cartilage injury, full-thickness cartilage injury, and osteochondral defect (Chow, et al., 2004; Shkhyan, et al., 2018; Kato, et al., 2019). The repair and regeneration of damaged cartilage tissue is one of the most challenging problems in the field of tissue engineering and regenerative medicine.

Until now, promoting cartilage regeneration has been one of the greatest difficulties in the field of regenerative medicine, due to the limited self-healing ability of cartilage tissues (Wang, et al., 2020; Zhang, et al., 2020). Natural and synthetic substances are the two main biomaterials used to restore cartilage (Chae, et al., 2021; Qiao, et al., 2021; Schuurmans, et al., 2021). The aim is mainly to improve cell adhesion and promote the growth and dynamic migration of regenerative tissues. Scaffolds are not only regarded as physical substrates, but in the biological environment, scaffolds are related to each other through clear chemical exchanges and physical stimulation through cells and adjacent tissues. Therefore, scaffolds are mainly used to support cell culture, infiltration, proliferation, and differentiation caused by signal factors and mechanical stimulation (Gardner, et al., 2016; Lynch, et al., 2016). Scaffolds are dissimilated into categories such as nanomaterials, biomimetic materials, biological enhancers, and hydrogels, and they can be used to bind chondrocytes or can be placed at cartilage defect sites. Hua et al. (2021) fabricated multifunctional hybrid optical crosslinking (HPC) hydrogels by photopolymerization and photopolymerization of imine crosslinking. Loaded with chondrocytes, the scaffold was used for cartilage defect repairing through arthroscopy in a pig model. Six months after implantation, an ideal layer of cartilage was regenerated. However, the development of an optimal scaffold that can induce cartilage regeneration is ongoing. The other critical issue in isolated cartilage regeneration is how to increase the adherence of the regenerated cartilage to the bone underneath.

Scaffolds for Osteochondral Regeneration

A method to repair osteochondral defects, the terminal stage of a cartilage defects, is urgently required (Eldridge, et al., 2020; Hall, et al., 2021; Kim, et al., 2021). At present, serious defects can only be treated by arthroplasty (Pirosa, et al., 2021; Xie J. et al., 2021). However, the commonly used artificial joints based on non-degradable materials, such as metals and ceramics have some disadvantages, including their high cost, limited biocompatibility, foreign body rejection, and long-term loosening (Labek, et al., 2011; Valdes, et al., 2012; Sakellariou, et al., 2016). Achieve

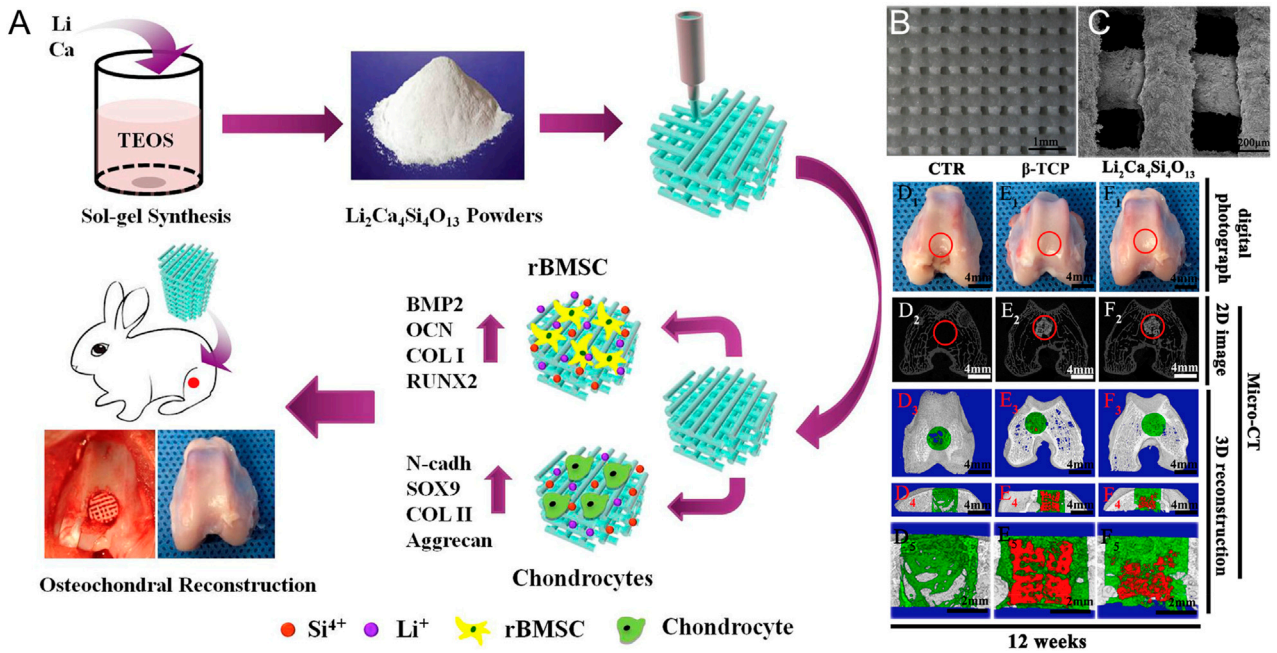

FIGURE 6 | 3D printing of a lithium-calcium-silicate crystal bioscaffold with dual bioactivities for osteochondral interface reconstruction. **(A)** Schematic illustration of application of Li2Ca4Si4O13 scaffolds for osteochondral reconstruction; **(B)** SEM images of 3D-printed $Li_2Ca_4Si_4O_{13}$ scaffolds after fabrication and **(C)** after soaking in the simulated body fluids for 14 days; Macro-photographs showed the defects in the control group and the other two experimental groups (**D_1**: blank control without scaffolds, **E_1**: pure β-TCP scaffolds, **F_1**: $Li_2Ca_4Si_4O_{13}$ scaffolds) at 12 weeks of post-surgery; (D_2 – F_2) showed 2D projection images of the three experimental groups at week 12; (D_3 – F_3) showed the transverse view of 3D reconstruction images of the three experimental groups at week 12; (D_4 – F_4) showed the sagittal view of 3D reconstruction images of the three experimental groups at week 12. Copyright 2019 Elsevier.

bone–cartilage composite tissue regeneration and permanent joint physiological function reconstruction remains a challenging problem. Using biomimetic scaffolds to induce *in situ* osteochondral regeneration is expected to be an important option for future joint function reconstruction (**Figure 6**) (Radhakrishnan, et al., 2018; Chen et al., 2019; Xu, et al., 2019; Zhu, et al., 2019). The tissue engineering of osteochondral integrated scaffolds imitates a normal osteochondral structure, as well as the natural osteochondral components in composition, to achieve a double bionics structure and components, which will eventually enable the effective repair and regeneration of osteochondral defects. However, due to the complex anatomical structure and component content of normal bone and cartilage, as well as the dynamic changes in time and space that occur in the regeneration area, the repair and regeneration of the osteochondral defect area is not just a simple "filling" of new tissue. It requires subchondral bone regeneration to support hyaline cartilage, and hyaline cartilage is closely combined with bone to generate cartilage–bone interface integration and thus the concurrent regeneration of both cartilage and bone.

To achieve a breakthrough in osteochondral regeneration, we must focus on preparing integrated bionic scaffolds that accurately simulate the microenvironment of osteochondral regeneration, and solve the following key scientific problems: *1*) accurate simulation of 3D shapes, multi gradient structures, regional specific matrix components, and the microenvironment factors of joints to prepare a bionic osteochondral scaffold (Choe, et al., 2021; Lee, et al., 2021; Liu, et al., 2021); *2*) achievement of osteochondral tissue regeneration and biological joint construction *in vitro*; and *3*) realization of the industrialization of integrated bionic stents and clinical transformations of the biological joints. The accumulation of separate tissue regeneration research for the cartilage and bone and the application of emerging cutting-edge technologies in recent years has facilitated breakthroughs regarding these technical problems.

At present, osteochondral scaffolds are commonly used in experimental research and clinical applications including natural biomaterial scaffolds, synthetic scaffolds, bioceramic scaffolds, bioactive glass, extracellular matrix scaffolds, and composite scaffolds.

The biological and mechanical properties of various tissue-engineered osteochondral scaffolds are different due to their different components and structures. For example, although natural biological scaffolds have the advantage of good biocompatibility, high cell affinity and degradability, which are conducive to adhesion and proliferation following the infiltration and recruitment of cells, they also have disadvantages, such as poor mechanical properties, rapid degradation rates, and limited sources. Synthetic scaffolds and bioceramics have good mechanical properties, strong plasticity, controllable degradation, and unrestricted wide sources. Their corresponding disadvantages are poor biocompatibility, low

cell affinity, lack of hydrophilicity of some scaffolds, and their degradation products may have certain toxicities. With the development of tissue engineering, to overcome the shortcomings of single materials, two or more materials have been combined according to the principles of complementary characteristics and advantages, to design an ideal scaffold that can meet the needs of osteochondral tissue engineering.

Composite scaffolds combine the advantages of individual scaffolds, such as a controllable degradation rate, good cell compatibility, good hydrophilicity, and appropriate biomechanical strength. Su et al. (2021) prepared cartilage layers *via* collagen II and chitosan with a pore diameter of approximately 100 μm and a bone layer *via* the PLGA with a pore diameter of 500 μm. The chondrocytes labeled by nano magnetic particles were planted on this biphasic scaffold to observe their growth, proliferation, and distribution on the scaffold, to further investigate the effects of this method on the repair and regeneration of bone and cartilage. The experimental results showed that the combination of a scaffold structure and cells labeled by novel technology has good application prospects for repairing regenerated osteochondral defects.

Biomedical Material Fabrication in Osteochondral Regeneration

Rapid progress in biomedical material fabrication has been made in the field of osteochondral regeneration, including 3D bioprinting, electrospinning, aerogels, hydrogels, and drug loaded microspheres (Deng, et al., 2021; Gao, et al., 2021; Jiang, et al., 2021). However, there are still some challenges, such as the accuracy and stability of 3D biological printing technologies and the flexibility and function of the products. A potential clinical application of bioprinting is to develop "*in vivo* bioprinting" technology, which can accurately "print" cell materials on the damaged parts with the help of handheld print heads, to directly repair cartilage defects of different shapes and thicknesses. This technique has great potential for the development of individualized treatment plans and will help to eliminate the need for a secondary surgery.

In addition to 3D printing technologies, tissue-engineered hydrogel scaffolds have also been utilized in cartilage repair. However, it is difficult for hydrogels to meet the advantages of high porosity, good mechanical properties, toxicity, biocompatibility, and a controllable degradation cycle. Most of the hydrogels can only satisfy one or two advantages. A composite hydrogel that can synchronize the degradation rate with the regeneration rate of cartilage tissue could be promising as a repairing material for the treatment of cartilage defects.

The applicational prospects for tissue engineering electrospinning scaffolds is optimistic, with high porosity and bionic extracellular matrix structures, but there are still many problems that must be addressed, such as: *1*) electrospinning scaffolds seriously affecting the adhesion, proliferation, and differentiation of seed cells on materials; *2*) solving the contradictions between the mechanical strength and degradation rates of materials; and *3*) unclear the teratogenicity and tumorigenicity of materials in the human body.

While the tissue engineering of osteochondral integrated scaffolds can solve some of the existing problems in traditional treatments, there are also shortcomings. If there is no in-depth study on the mechanisms for the repair and regeneration of osteochondral integrated scaffolds, it is impossible to clarify the repair and regeneration mechanisms for the defect area from a microscopic cellular and molecular level. Moreover, the osteochondral integrated scaffold has double bionics for its structure and composition, which cannot be compared with the normal osteochondral structure at both biological and mechanical levels; further, special materials similar to the natural osteochondral structure-cannot be found. In addition, the calcified layer and tidal line play important roles in the structure of bone and cartilage, but the integrated bionic scaffold is still difficult to completely biomimic these unique structures. Therefore, at present, the problem of the calcification of the cartilage layer and easy separation between the two layers of biphasic and multiphasic scaffolds has not yet been solved. Nevertheless, use of new preparation technologies and methods, such as 3D printing and electrospinning technologies, discovery or synthesis of new scaffold materials, and cooperation between medicine, industry, materials, biological structures, biomechanics, and integrated bionic scaffolds can finally solve the clinical scientific problem of osteochondral defects.

Bone Regeneration

Bone defects, fractures or osteotomies, osteoporosis, and osteonecrosis in the locomotor system may require bone-structure restoration to achieve regeneration (McFarland, et al., 2016; Khira and Salama, 2017; Choi and Rhee, 2017; Zhang Y. et al., 2018). Some examples of such cases are glenoid and humeral head bone defects occurring in shoulder dislocations, glenoid bone absorption in cases of severe shoulder osteoarthritis (OA), bone defects occurring in high tibial osteotomy, and tibial plateau depression fractures in cases of knee dislocation. Bone regeneration is defined as the process wherein bone-grafting materials are replaced by newly formed bone (Wei et al., 2022). Till now, autologous grafts have been suggested as the gold standard for bone regeneration. However, the accompanying donor-site complications and the limited availability of autografts hamper their extensive use in clinical applications. Meanwhile, allogeneic bone grafts are challenged by vascularization issues and disease transmission risks (Giannoudis, et al., 2005; Laurencin, et al., 2006). Thus, there is an urgent need for the development of biomaterials in sports medicine. There are different strategies used to treat bone defects, such as *1*) simple artificial bone material, *2*) artificial bone material with bioactive factors, and *3*) artificial bone material with stem cells.

The ideal scaffold would have an appropriate hierarchical architecture that would permit normal metabolic activity as well as the migration, proliferation, and differentiation of cells together with angiogenesis and bone ingrowth. As an example, a highly porous scaffold would have a greater surface area that

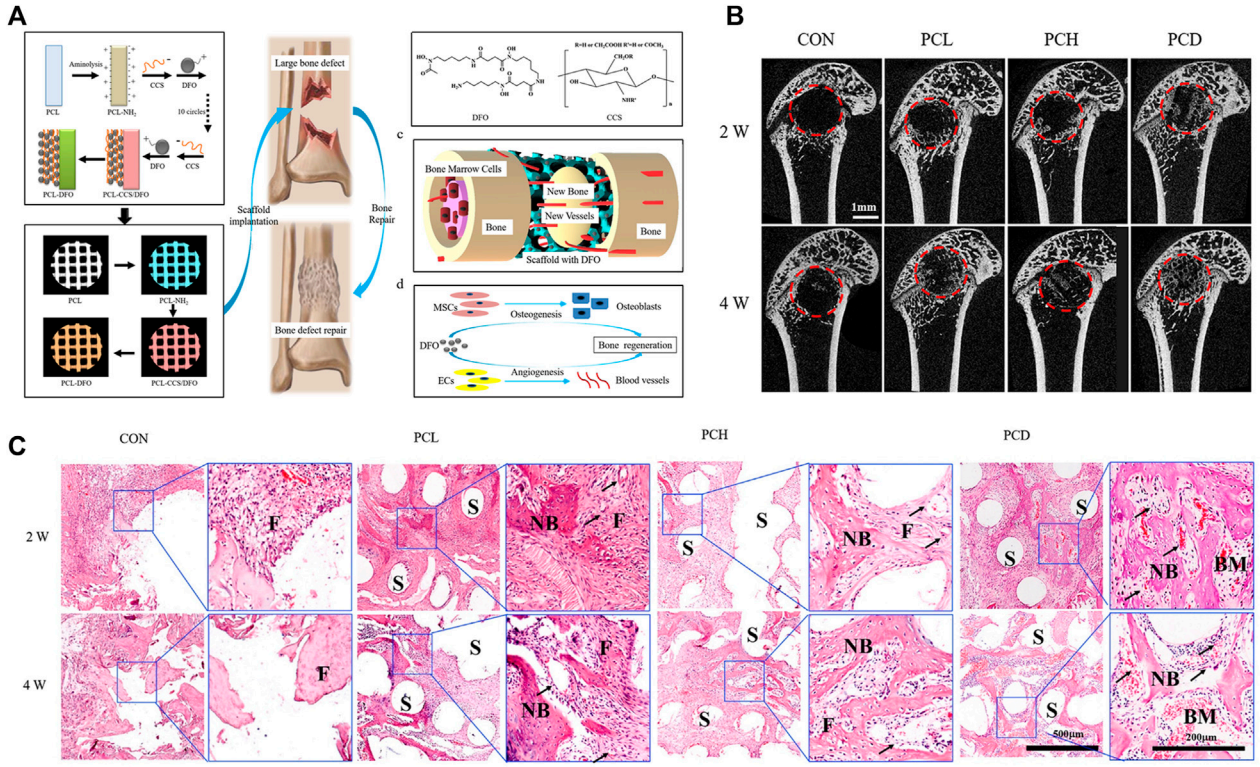

FIGURE 7 | Vascularized 3D printed scaffolds for promoting bone regeneration. **(A)** Schematic diagram of bridging deferoxamine (DFO) on the surface of 3D printed polycaprolactone (PCL) scaffold and its biological function for bone regeneration in bone defect model; **(B)** Micro-CT analysis of the effect of scaffolds on bone repair *in vivo*; **(C)** Representative images of hematoxylin-eosin (HE) staining of the decalcificated bones slice, showing the new formed tissue including the fibrous tissue (F), newly mineralized bone tissue (NB) and the structure of scaffolds (S). Copyright 2019 Elsevier.

would promote improved osteogenic effects by allowing greater mass exchange and adsorption of growth factors (Wu, et al., 2014; Tang, et al., 2016). The pore size of the scaffold is also critical for good bone regeneration, as the presence of smaller pores leads to hypoxic conditions that promote pre-osteogenic osteochondral formation while larger interconnected pores promote directional osteogenesis (Karageorgiou and kaplan, 2005; Zhang, et al., 2013). Porous surfaces also stimulate interactions and linkages between the implant and the bone, and the pore size is critical for bone integration. For example, it was found that while 300-μm pores produced the most lamellar bone, the process of osseointegration was longer than with 200-μm pores (Xu, et al., 2011).

In this review, we have focused on research over the past 5 years into the optimization of the architectural, chemical, and surface features of bone graft substitutes (BGS) for the promotion of bone regeneration and osteointegration. Three-dimensional printing permits the creation of BGS tailored for the individual patient by optimization of both mechanical and structural characteristics. The optimizing structure permits specific correspondence between the BGS and the patient's body, leading to more rapid postoperative recovery (Tan, et al., 2017). Although titanium is most commonly used for 3D printing, materials such as bioceramics and polymers such as polyetheretherketon (PEEK), which allow custom design, are only being investigated at the pre-clinical stage at the moment (Mustafa, et al., 2011; Li, et al., 2017a; Yang, et al., 2017). The issues that are being addressed in the use of these novel ceramic materials include optimal mechanical characteristics, architectural design, and chemical properties to enhance both porosity and degradability. Optimal surface characteristics are vital for osteogenic cell adhesion to the BGS, leading to the promotion of new bone growth (Colquhoun and Tanner, 2015; Fernandez-Yague, et al., 2015; Babaie and Bhaduri, 2018). These properties can be manipulated by coatings that promote bone regeneration.

As bone repair is a complex process that is dependent on various growth factors, we discuss the application of active biomolecules for promoting bone repair (Krishnan, et al., 2006; Carragee, et al., 2011; Polak, et al., 2011; Kim, et al., 2012; Santo, et al., 2013; Mumith, et al., 2017). These applications can be divided into three approaches are three approaches: *1*) the application of recombinant growth factors, individually or as mixtures, together with a natural or calcium phosphate matrix, such as BMP-2 (Infuse bone graft), BMP-7 (OP-1 putty), and rhPGDF-BB (Augment bone graft®); *2*) the use of ECM-derived peptides targeting cellular receptors, such as B2A (B2A2-K-NS) and P-15; *3*) the use of small molecules targeting pathways that influence none mass, including parathyroid hormone (PTH), Nel-like molecule-1 (NELL-1), and LIM mineralization protein-1 (LMP-1). These molecules may affect bone mass directly or indirectly by inhibiting negative modulators of bone mass and thus promoting increased bone mass.

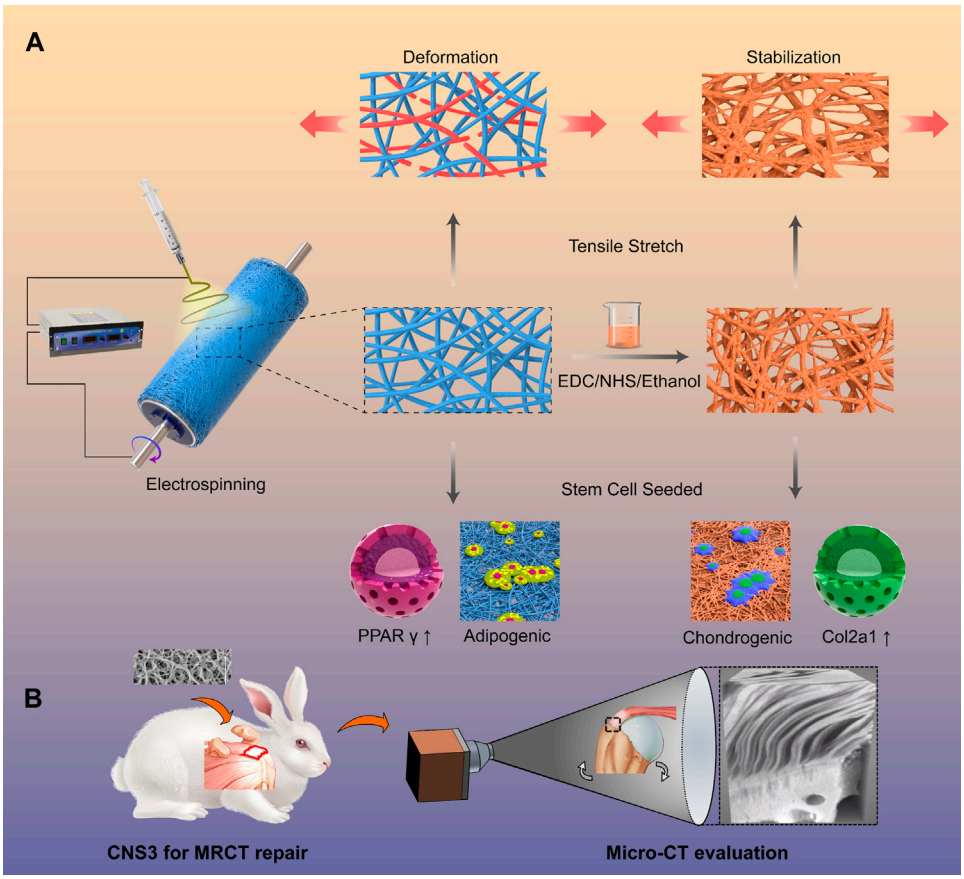

FIGURE 8 | Crimped nanofiber scaffold mimicking tendon-to-bone interface for fatty-infiltrated massive rotator cuff repair. **(A)** Schemata of fabrication of the crimped nanofibrous scaffold for massive rotator cuff tear repairing; **(B)** Representative micro-computed tomography (micro-CT) images of the proximal humerus and quantitative analysis. Copyright 2022 Elsevier.

The third approach used stem cells as part of a cell-based construct. This requires the presence of progenitor cells allowing the formation of new tissue through interaction with host cells, stimulatory factors, and support providing cells with 3D cues for new tissue formation. The progenitor cells used include bone marrow stromal cells (BMSCs), adipose-derived mesenchymal cells (ASCs) and periosteum-derived stem cells (PDSCs) (Ingber, et al., 2006; Bolander, et al., 2016; Bolander, et al., 2017). However, the necessity of pre-incubating the biomaterial with the cells complicates the engineering process considerably and also reduces the viability of the cells, leading to high production costs. In addition, the scaffolds may not have sufficient ability to promote vascularization *in vivo* and may thus be unable to maintain cell and tissue viability (Lenas, et al., 2009). Because of these issues, this approach has not proved popular in clinical practice.

Bone tissue engineering approaches were devised to address the shortcomings of bone grafts and alloplasts and to promote the repair of bone defects and fractures. Both biological derivatives and synthetic materials have been used for scaffold fabrication, singly or in combination. The developments in the field include the use of scaffolds together with gene therapy and stimulatory factors (Farberg, et al., 2012; Pountos, et al., 2016; El Bialy, et al., 2017; Yan, et al., 2019), while recent advances in the 3D printing of scaffolds open new directions for effective bone regeneration (Ding, et al., 2013; Gong, et al., 2015; Lee, et al., 2017; Li, et al., 2018) (**Figure 7**). Nevertheless, many challenges remain. Recent reports have emphasized the importance of local microenvironments for the success of these scaffolds. In addition, more understanding of the precise functions of the active biomolecular constituents, such as their influence on inflammation or bone precursor cells, is required. The precise control and delivery of these molecules in the correct doses are necessary to prevent undesirable side effects. There is intensive research in the form of pre-clinical studies to understand the underlying mechanisms of these therapies and their effective applications. Translation to clinical practice also requires many regulatory steps and costs.

Tendon–Bone Interface Regeneration

Poor Tendon–Bone Interface Healing After Tendon/Ligament Reconstruction

One of the main problems in the functional reconstruction of tendons and ligaments is the poor healing of the tendon–bone

TABLE 1 | Common sports medicine injuries and their promising treatment methods.

Common sports medicine injury	Clinical gold standard treatment	Shortage
Meniscus tear	Meniscectomy or meniscal repair	Progression of osteoarthritis and decreased sports function
Cruciate ligament tear	Autograft reconstruction	Decreased mechanical property of ligament
Achilles tendon tear	Surgical repair	Decreased sports function
Rotator cuff tear	Partial repair or rotator cuff reconstruction	The recurrence rate is 40–94%
Cartilage tear	Conservative treatment	Progression of osteoarthritis
Bone defect	Autograft	Limited source
Tendon-to-bone injury	None	—

TABLE 2 | Promising treatments' advantage and disadvantage.

Potential regeneration methods	Advantage	Disadvantage
Allograft	Ideal biocompatibility and bioactivity	Limited source and donor site injury
Xeno-patches	Wide range of sources	Risk of infection and immunological rejection
Natural materials	Biocompatibility	Limited bioactivity and mechanical property
Non-biodegradable artificial synthetic material	Mechanical property and ideal structural machinability	Structural failure in the long-term
Biodegradable artificial synthetic material	Relatively good mechanical property and Structural machinability	The balanced control of degenerative and regenerative rate; Toxicity of some degeneration product

interface (Yang, et al., 2017; Xing, et al., 2020, Zhu, C., et al., 2021). Natural tendon–bone interfaces can be categorized into four portions: tendon, uncalcified fibrocartilage, calcified fibrocartilage, and bone (Weimin, et al., 2013; Liu, et al., 2019). The transition of the structures effectively prevents the structural damage caused by a sudden tension, by gradually distributing tension across the interface (Lu and Thomopoulos, 2013). From a mechanical perspective, this structure perfectly connects ligament and bone tissue with an elasticity modulus of 200 MPa and 20 GPa, respectively, which also increases the strength of the insertion to avoid the avulsion of the tendon. However, after injury, even with proper surgical treatments, scar tissue takes the place of the transitional structure in the tendon–bone interface, which greatly decreases its mechanical properties (Zhu, J., et al., 2021). Hence, inducing the regeneration of natural tendon–bone interfaces is a major issue when treating tendon–bone interface injuries.

Scaffolds Fabricated for Tendon–Bone Interface Regeneration

A decellularized extracellular matrix is a common option for tendon–bone interface regeneration, as it possesses ideal biocompatibility and a natural microstructure. Through a combination of physical, chemical, and enzymatic treatments, Su et al. (2019) successfully fabricated decellularized triphasic hierarchical bone–fibrocartilage–tendon composites, with the preservation of natural microstructures and mineralization. After 8 weeks implantation occurred into the tibia bone tunnel, and the fabricated decellularized bone–fibrocartilage–tendon composite induced a notably larger amount of bone regeneration in the bone tunnel when compared with that of simple decellularized tendon tissue. However, it is still unclear whether the decellularized bone–fibrocartilage–tendon composite can induce cartilage regeneration between the tendon–bone interface, which is the main issue in tendon–bone interface regeneration. Additionally, the fabrication procedure of decellularized bone–fibrocartilage–tendon composite is relatively complicated. It is quite difficult to achieve a balance between the preservation of the natural microstructure and the elimination of remnant cell debris and consequently, there is no current gold standard method for the field.

Decellularized small intestinal submucosa (SIS) has been generated for use as a commercial medical implant as numerous studies have indicated that many bioactive factors can be preserved, even after the decellularization procedure (Meng, et al., 2021; Singh, et al., 2021). However, unlike the decellularized bone–fibrocartilage–tendon composite, decellularized SIS scaffolds lack the required microstructures between the tendon–bone interface. Even though decellularized SIS has been successfully used in many other tissue repair processes, recent clinical studies jointly suggested that the use of decellularized SIS did not (Su, et al., 2021)result in better clinical results when used for rotator cuff repair surgery (Iannotti, et al., 2006; Bryant, et al., 2016). The retear rate and American Shoulder and Elbow Surgeons shoulder score were not improved, which indicated that the tendon–bone interface regeneration was not properly induced by a decellularized SIS scaffold (Sclamberg, et al., 2004).

When compared with a natural extracellular matrix, artificial polymer scaffolds have advantages, including good quality control reliability and microstructure adjustability. Nevertheless, unlike a natural extracellular matrix, the artificial polymer scaffold lacks biocompatibility, biodegradability, and

inducibility; highlighting the need to select appropriate materials. PLGA and PCL are common material options that have been deemed safe by the Food and Drug Administration (Li, et al., 2015). By electrospinning, the fabricated scaffold is equipped with the similar microstructure when compared with that of a natural extracellular matrix (Hua, et al., 2021). However, the microstructures of the tendon–bone interfaces are very different from the extracellular matrices of other tissues (Rossetti, et al., 2017). The orientation of fiber in the extracellular matrix of the tendon–bone interface changes from aligned-to-random, suggesting that the fabricated scaffold should also mimic the transitional microstructure differences (Deymier-Black, et al., 2015). Xie C. et al. (2021) fabricated electrospun scaffolds with aligned-to-random microstructures and morphologies of the tendon fibroblasts were cultured on the scaffold, and were organized and haphazardly oriented, respectively. In addition to the differences in the microstructures, there is also a gradient density for calcium in the tendon–bone interface. As PLGA and PCL are bioinert materials, which cannot induce bone regeneration, bioactive factors were commonly added to the scaffolds. In a previous study, we produced a PCL scaffold combined with gradient calcium phosphate silicate (CPS) content and found that the multilayer gradient composite effectively increased tendon–bone healing at the tear site, where better tissue cellularity and gradient mineralized cartilage formation were observed (Su, et al., 2021). Wang D. et al. (2021) crosslinked nanofibrous scaffolds to fabricate a scaffold, which simulates the microstructure of the natural tendon-to-bone interface, and 3 months after implantation in rabbit, it fully regenerated the unique 3D structure of the tendon-to-bone interface (**Figure 8**). However, the aforementioned studies were also too complicated for application in industrial production. Controlling the fiber orientation transition and gradient density of calcium is difficult using the current industry techniques.

Expectations in Tendon–Bone Interface Regeneration

To date, no medical implant for tendon–bone healing has been developed. Considering the difficulties in balancing the biocompatibility, biodegradability, inducibility, microstructure, and gradient density of the calcium, the time frame for a relevant implant is not short; however, it will be improved with time. Previous studies have either presented procedures that are too sophisticated or added bioactive materials not approved by the Food and Drug Administration. Scaffolds that can effectively induce tendon–bone interface healing, are easy to manufacture, and are highly reliable, are urgently required.

MATERIALS FOR SPORTS MEDICINE INJURY

Autografts are recommended as the "gold standard" for most common sports medicine injuries, including ACL tears and bone defects (Cho, 1975; Clancy, et al., 1982; Howe, et al., 1991). Although autografts contribute to an increased healing rate, both structurally and functionally, donor site injury and limited tissue sources restrict their applications (Piva, et al., 2009). Allografts can not only reduce surgery time but also reduce damage and complication at the donor site. However, a long-term follow-up study indicated that, when compared with autografts, allografts could prolong the post-surgery recovery time, increase the incidence of infection, and the risk of spreading infectious diseases (Dahlstedt, et al., 1989; Good, et al., 1989; Greenberg, et al., 2010).

Natural biological materials are one of the major material sources of tissue engineering. SIS is a natural, acellular, degenerable, extracellular collagen matrix material which is mainly composed of helically interweaving type-I and -III collagen (Badylak, et al., 1989; Badylak, et al., 1995). Studies confirmed that using SI as an ACL supplementary repair could contribute to neuro-vascularization and cell growth (Nguyen, et al., 2015). However, Badylak et al. (1989) found that there was a reduced tensile resistance in the mucous membrane of the small intestine after 3 months in the experiment for goat ACL reconstruction, which could not meet the prerequisite in clinical biomechanics. Silk is a natural material and highly recommended for its desirable biocompatibility and mechanical strength (Li, et al., 2014; Teuschl, et al., 2016). However, the uncontrollable speed of silk degeneration, limited cellular affinity, and unstable mechanical strength immediately after surgery all imposed restrictions on its application (Soong and Kenyon, 1984).

Non-degradable polyester materials, such as PET, are another option as they are equipped with high mechanical strength. Ligament advanced reinforcement system (LARS) is a representative product of non-degradable artificial ligaments and it was advantageous to the patients who needed to be back to the field with a high-level performance. Considering its disadvantages, such as poor hydrophilicity, inertness, and no osteogenic active ingredient, the LARS ligament would lead to the formation of a scar at the ligament-bone interface and loss of long-term effectiveness (Li, et al., 2012; Tiefenboeck, et al., 2015). Some studies have focused on surface coatings to improve bioinert material defects. Studies have shown that coating the surface of LARS ligaments with fibroin or hydroxyapatite can effectively promote the degradation of LARS ligaments and the tendon–bone healing of inert material in the bone tunnel (Ai, et al., 2017; Cai, et al., 2018; Wang, et al., 2018). However, there are still problems with the current technique, such as nonuniform surface coating on the ligament and binding force, which greatly limits the clinical applications of the products.

Single polymer/macromolecular based scaffolds (such as polylactic acid and poly (caprolactone)) have been recently developed and are being explored for potential clinical use (Correia Pinto, et al., 2017; Erisken, et al., 2008; Zhang, et al., 2005). Such scaffolds can be equipped with relatively good mechanical properties and structural machinability which can be adjusted for different requirements. Research has indicated that they can gradually degrade in 600 days and maintain a certain degree of strength, which provides stable conditions for tissue regeneration (Blaker, et al., 2011). Most of the absorbable polymer materials have a low hydrophilicity and cellular affinity. Furthermore, polylactic acid can produce acid metabolites during the degeneration process and thus cannot form real tissue inductivity (Lu, et al., 2005; Cardwell, et al., 2014). For

successful tissue engineering, the single polymer/macromolecular based scaffolds should meet several criteria (Zhao, et al., 2014a; Zhao, et al., 2014b; Zhao, et al., 2015; Li, et al., 2017b). First, good biocompatibility and mechanical properties should be confirmed *in vitro* to lay the foundation for further *in vivo* implantation. During degeneration, the initial, middle-stage, and final grafts should cooperate with induced regenerative tissues to support sufficient strength. Finally, the toxicity of the degeneration product should be strictly limited.

SUMMARY

There is a high demand for tissue regeneration techniques in the field of sports medicine, which make regenerative sports medicine crucial for the treatment of injuries and diseases in the locomotor system. There are several conundrums, however, that are limiting the application of these techniques (**Tables 1**, **2**). The first issue is how to restore like for like, i.e., how to recreate tissues that mimic the native tissues in both structure and function. The second issue is how to fabricate a structure that can overcome the defects of the native structure to ensure that its function is improved and the potential for reinjury is reduced.

For meniscus regeneration, tissue engineering strategies could potentially generate a meniscus like cellular or acellular structure with or without growth factors. Progress has already been made in restoring its native anisotropy and zonal organization. Further research should be conducted to understand how to restore its hooping effect from the collagen structure and the connection between the anterior and posterior horns and the tibia, as well as how to ensure its healing to the peripheral capsule ligament and how to obtain sustained vitalization of the neonatal structure to reduce the risk of reinjury.

For cruciate ligament, rotator cuff, and Achilles' tendon regeneration, the goal is to obtain a viable type-I collagen dominated fibrous structure that can heal to the bone and soft tissue it connects. For the collagen regeneration-inducing technique that utilizes degradable synthetic material as the main construct, there is still a long way to go before it will be able to induce the regeneration of sufficient volumes of collagen. The collagen transformation-inducing technique is more practical with readily available collagen. However, vitalizing the structure in the intraarticular environment, obtaining a mature ligament or tendon structure with sufficient final strength, and achieving satisfactory ligament or tendon–bone healing requires further investigation.

Osteochondral regeneration induced with a biomimetic scaffold is a promising strategy to solve the problem of cartilage regeneration and cartilage–bone adhesion. Progress has been achieved in the development of a scaffold simulate native osteochondral construct with regard to its microstructure, components, and bioactive stimulator. Breakthroughs are still required, however, to obtain a scaffold that can induce bone, cartilage, and the bone–cartilage interface with desired biological and mechanical features throughout the regeneration induction process, and to obtain semi-finished or finished osteochondral products that can be directly used for implantation.

In bone regeneration, obtaining an appropriate scaffold and bioactive molecules does not seem to be a problem. However, precisely controlling the release of the bioactive molecules to avoid undesirable side effects requires further investigation.

For tendon–bone interface regeneration, the goal is to obtain a layer of fibrocartilage between the tendon and the bone. However, neither simple structure materials nor complicated scaffolds can be used clinically to achieve this goal.

The increasing incidence of sports medicine injury is posing clinical challenges to surgeons worldwide. Approaches in the field of regenerative sports medicine will present promising options for the structural and functional restoration of the locomotor system. Unlike tissue regeneration in other systems of the body, the to-be-regenerated structure in the locomotor system should be capable of bearing various types of forces during regeneration without exhibiting obvious deformation and should restore the native connection of the regenerated structure to the different surrounding tissues. The future of sports medicine injury repairing scaffolds relies on using optimal components for the structural materials, bionic 3D structures, which simulate natural structures, and long-lasting viability of the regenerated structure with bioactivity.

AUTHOR CONTRIBUTIONS

LW: Reviewing articles, Writing and original draft, Format conducting.JJ: Reviewing articles, Writing and original draft. HL: Reviewing articles, Writing and original draft. TZ: Reviewing articles, Writing and original draft. JCa: Reviewing articles, Writing and original draft. WS: Reviewing articles, Writing and original draft. JCh: Reviewing articles, Writing and original draft. JX: Reviewing articles, Writing and original draft. YL: Reviewing articles, Writing and original draft. JW: Reviewing articles, Writing and original draft. KZ: Conceptualization, Supervision, Writing - review and editing, Project administration. JZ: Funding acquisition, Conceptualization, Supervision, Writing - review and editing, Project administration.

FUNDING

This work was supported by National Natural Science Foundation of China (Grant No. 81902186, 81671920, 31972923, 81871753, 81772341), National Key Research and Development Program of China (Grant No. 2018YFC1106200, 2018YFC1106201, 2018YFC1106202), and Technology Support Project of Science and Technology Commission of Shanghai Municipality of China (Grant No. 19441901700, 19441901701, 19441902800).

REFERENCES

Abrams, G. D., Frank, R. M., Gupta, A. K., Harris, J. D., McCormick, F. M., and Cole, B. J. (2013). Trends in Meniscus Repair and Meniscectomy in the United States, 2005-2011. *Am. J. Sports Med.* 41 (10), 2333–2339. doi:10.1177/0363546513495641

Adams, J. E., Zobitz, M. E., Reach, J. S., An, K. N., and Steinmann, S. P. (2006). Rotator Cuff Repair Using an Acellular Dermal Matrix Graft: an In Vivo Study in a Canine Model. *Arthroscopy* 22 (7). doi:10.1016/j.arthro.2006.03.016

Ai, C., Sheng, D., Chen, J., Cai, J., Wang, S., Jiang, J., et al. (2017). Surface Modification of Vascular Endothelial Growth Factor-Loaded Silk Fibroin to Improve Biological Performance of Ultra-high-molecular-weight Polyethylene via Promoting Angiogenesis. *Int. J. Nanomedicine* 12. doi:10.2147/IJN.S148845

Arshad, Z., Lau, E. J. S., Leow, S. H., and Bhatia, M. (2021). Management of Chronic Achilles Ruptures: a Scoping Review. *Int. Orthop*. doi:10.1007/s00264-021-05102-5

Arvayo, A. L., Wong, I. J., Dragoo, J. L., and Levenston, M. E. (2018). Enhancing Integration of Articular Cartilage Grafts via Photochemical Bonding. *J. Orthop. Res.* 36 (9). doi:10.1002/jor.23898

Athanasiou, K. A., Eswaramoorthy, R., Hadidi, P., and Hu, J. C. (2013). Self-organization and the Self-Assembling Process in Tissue Engineering. *Annu. Rev. Biomed. Eng.* 15. doi:10.1146/annurev-bioeng-071812-152423

Babaie, E., and Bhaduri, S. B. (2018). Fabrication Aspects of Porous Biomaterials in Orthopedic Applications: A Review. *ACS Biomater. Sci. Eng.* 4 (1). doi:10.1021/acsbiomaterials.7b00615

Baby, B. (2000). What Is Sports Medicine? Medical Students Don't Know. *Br. J. Sports Med.* 34 (1), 73. doi:10.1136/bjsm.34.1.73-a

Badylak, S. F., Lantz, G. C., Coffey, A., and Geddes, L. A. (1989). Small Intestinal Submucosa as a Large Diameter Vascular Graft in the Dog. *J. Surg. Res.* 47 (1). doi:10.1016/0022-4804(89)90050-4

Badylak, S. F., Tullius, R., Kokini, K., Shelbourne, K. D., Klootwyk, T., Voytik, S. L., et al. (1995). The Use of Xenogeneic Small Intestinal Submucosa as a Biomaterial for Achilles Tendon Repair in a Dog Model. *J. Biomed. Mater Res.* 29 (8). doi:10.1002/jbm.820290809

Barboni, B., Russo, V., Gatta, V., Bernabò, N., Berardinelli, P., Mauro, A., et al. (2018). Therapeutic Potential of hAECs for Early Achilles Tendon Defect Repair through Regeneration. *J. Tissue Eng. Regen. Med.* 12 (3). doi:10.1002/term.2584

Beck, A., Murphy, D. J., Carey-Smith, R., Wood, D. J., and Zheng, M. H. (2016). Treatment of Articular Cartilage Defects with Microfracture and Autologous Matrix-Induced Chondrogenesis Leads to Extensive Subchondral Bone Cyst Formation in a Sheep Model. *Am. J. Sports Med.* 44 (10), 2629–2643. doi:10.1177/0363546516652619

Blaker, J. J., Nazhat, S. N., Maquet, V., and Boccaccini, A. R. (2011). Long-term In Vitro Degradation of PDLLA/bioglass Bone Scaffolds in Acellular Simulated Body Fluid. *Acta Biomater.* 7 (2). doi:10.1016/j.actbio.2010.09.013

Bolander, J., Ji, W., Geris, L., Bloemen, V., Chai, Y. C., Schrooten, J., et al. (2016). The Combined Mechanism of Bone Morphogenetic Protein- and Calcium Phosphate-Induced Skeletal Tissue Formation by Human Periosteum Derived Cells. *Eur. Cell Mater* 31. doi:10.22203/ecm.v031a02

Bolander, J., Ji, W., Leijten, J., Teixeira, L. M., Bloemen, V., Lambrechts, D., et al. (2017). Healing of a Large Long-Bone Defect through Serum-free In Vitro Priming of Human Periosteum-Derived Cells. *Stem Cell Rep.* 8 (3). doi:10.1016/j.stemcr.2017.01.005

Brody, H. (2016). Regenerative Medicine. *Nature* 540 (7632). doi:10.1038/540s49a

Bryant, D., Holtby, R., Willits, K., Litchfield, R., Drosdowech, D., Spouge, A., et al. (2016). A Randomized Clinical Trial to Compare the Effectiveness of Rotator Cuff Repair with or without Augmentation Using Porcine Small Intestine Submucosa for Patients with Moderate to Large Rotator Cuff Tears: a Pilot Study. *J. Shoulder Elb. Surg.* 25 (10). doi:10.1016/j.jse.2016.06.006

Bulgheroni, E., Grassi, A., Bulgheroni, P., Marcheggiani Muccioli, G. M., Zaffagnini, S., and Marcacci, M. (2015). Long-term Outcomes of Medial CMI Implant versus Partial Medial Meniscectomy in Patients with Concomitant ACL Reconstruction. *Knee Surg. Sports Traumatol. Arthrosc.* 23 (11). doi:10.1007/s00167-014-3136-9

Cai, C., Wang, W., Liang, J., Li, Y., Lu, M., Cui, W., et al. (2021). MMP-2 Responsive Unidirectional Hydrogel-Electrospun Patch Loading TGF-β1 siRNA Polyplexes for Peritendinous Anti-Adhesion. *Adv. Funct. Mater.* 31 (6). doi:10.1002/adfm.202008364

Cai, C., Zhang, X., Li, Y., Liu, X., Wang, S., Lu, M., et al. (2022). Self-Healing Hydrogel Embodied with Macrophage-Regulation and Responsive-Gene-Silencing Properties for Synergistic Prevention of Peritendinous Adhesion. *Adv. Mater.* 34 (5). doi:10.1002/adma.202106564

Cai, J., Wang, J., Ye, K., Li, D., Ai, C., Sheng, D., et al. (2018). Dual-layer Aligned-Random Nanofibrous Scaffolds for Improving Gradient Microstructure of Tendon-To-Bone Healing in a Rabbit Extra-articular Model. *Int. J. Nanomedicine* 13. doi:10.2147/IJN.S165633

Cai, J. Y., Xu, J. J., Kang, Y. H., Li, Y. F., Wang, L. R., Yan, X. Y., et al. (2021). Acceleration of Ligamentization and Osseointegration Processes after Anterior Cruciate Ligament Reconstruction with Autologous Tissue-Engineered Polyethylene Terephthalate Graft. *Ann. Transl. Med.* 9 (9). doi:10.21037/atm-20-8048

Cai, J., Zhang, Q., Chen, J., Jiang, J., Mo, X., He, C., et al. (2021). Electrodeposition of Calcium Phosphate onto Polyethylene Terephthalate Artificial Ligament Enhances Graft-Bone Integration after Anterior Cruciate Ligament Reconstruction. *Bioact. Mater* 6 (3). doi:10.1016/j.bioactmat.2020.08.037

Cardwell, R. D., Dahlgren, L. A., and Goldstein, A. S. (2014). Electrospun Fibre Diameter, Not Alignment, Affects Mesenchymal Stem Cell Differentiation into the Tendon/ligament Lineage. *J. Tissue Eng. Regen. Med.* 8 (12). doi:10.1002/term.1589

Carragee, E. J., Hurwitz, E. L., and Weiner, B. K. (2011). A Critical Review of Recombinant Human Bone Morphogenetic Protein-2 Trials in Spinal Surgery: Emerging Safety Concerns and Lessons Learned. *Spine J.* 11 (6). doi:10.1016/j.spinee.2011.04.023

Chae, S., Lee, S. S., Choi, Y. J., Hong, D. H., Gao, G., Wang, J. H., et al. (2021). *3D Cell-Printing of Biocompatible and Functional Meniscus Constructs Using Meniscus-Derived Bioink*. Amsterdam: Biomaterials, 267.

Chahla, J., Dean, C. S., Matheny, L. M., Mitchell, J. J., Cinque, M. E., and LaPrade, R. F. (2017). Outcomes of Inside-Out Meniscal Repair in the Setting of Multiligament Reconstruction in the Knee. *Am. J. Sports Med.* 45 (9). doi:10.1177/0363546517698944

Chen, C., and Hunt, K. J. (2019). Open Reconstructive Strategies for Chronic Achilles Tendon Ruptures. *Foot Ankle Clin.* 24 (3). doi:10.1016/j.fcl.2019.04.002

Chen, L., Deng, C., Li, J., Yao, Q., Chang, J., Wang, L., et al. (2019). *3D Printing of a Lithium-Calcium-Silicate Crystal Bioscaffold with Dual Bioactivities for Osteochondral Interface Reconstruction*. Amsterdam: Biomaterials.

Chiou, G. J., Crowe, C., McGoldrick, R., Hui, K., Pham, H., and Chang, J. (2015). Optimization of an Injectable Tendon Hydrogel: the Effects of Platelet-Rich Plasma and Adipose-Derived Stem Cells on Tendon Healing In Vivo. *Tissue Eng. Part A* 21 (9-10). doi:10.1089/ten.TEA.2014.0490

Cho, K. O. (1975). Reconstruction of the Anterior Cruciate Ligament by Semitendinosus Tenodesis. *J. Bone & Jt. Surg. Am. Volume)* 57 (5). doi:10.2106/00004623-197557050-00003

Choe, R., Devoy, E., Jabari, E., Packer, J. D., and Fisher, J. P. (2021). *Biomechanical Aspects of Osteochondral Regeneration: Implications and Strategies for 3D Bioprinting*. New York: Tissue Eng Part B Rev.

Choi, Y. Y., and Rhee, S. J. (2017). Medial Opening Wedge High Tibial Osteotomy in Patients with Posttraumatic Medial Tibial Plateau Bone Defect: A Case Report. *Int. J. Surg. Case Rep.* 41. doi:10.1016/j.ijscr.2017.10.020

Chow, J. C., Hantes, M. E., Houle, J. B., and Zalavras, C. G. (2004). Arthroscopic Autogenous Osteochondral Transplantation for Treating Knee Cartilage Defects: a 2- to 5-year Follow-Up Study. *Arthroscopy* 20 (7). doi:10.1016/j.arthro.2004.06.005

Clancy, W. G., Jr., Nelson, D. A., Reider, B., and Narechania, R. G. (1982). Anterior Cruciate Ligament Reconstruction Using One-Third of the Patellar Ligament, Augmented by Extra-articular Tendon Transfers. *J. Bone & Jt. Surg. Am. Volume)* 64 (3). doi:10.2106/00004623-198264030-00004

Colquhoun, R., and Tanner, K. E. (2015). Mechanical Behaviour of Degradable Phosphate Glass Fibres and Composites-A Review. *Biomed. Mater* 11 (1). doi:10.1088/1748-6041/11/1/014105

Coons, D. A., and Alan Barber, F. (2006). Tendon Graft Substitutes-Rotator Cuff Patches. *Sports Med. Arthrosc. Rev.* 14 (3). doi:10.1097/00132585-200609000-00011

Correia Pinto, V., Costa-Almeida, R., Rodrigues, I., Guardao, L., Soares, R., and Miranda Guedes, R. (2017). Exploring the In Vitro and In Vivo Compatibility of PLA, PLA/GNP and PLA/CNT-COOH Biodegradable Nanocomposites: Prospects for Tendon and Ligament Applications. *J. Biomed. Mater Res. A* 105 (8). doi:10.1002/jbm.a.36075

Dahlstedt, L. J., Netz, P., and Dalen, N. (1989). Poor Results of Bovine Xenograft for Knee Cruciate Ligament Repair. *Acta Orthop. Scand.* 60 (1). doi:10.3109/17453678909150079

Dean, C. S., Chahla, J., Matheny, L. M., Mitchell, J. J., and LaPrade, R. F. (2017). Outcomes after Biologically Augmented Isolated Meniscal Repair with Marrow Venting Are Comparable with Those after Meniscal Repair with Concomitant Anterior Cruciate Ligament Reconstruction. *Am. J. Sports Med.* 45 (6). doi:10.1177/0363546516686968

Deng, C., Yang, J., He, H., Ma, Z., Wang, W., Zhang, Y., et al. (2021). 3D Bio-Printed Biphasic Scaffolds with Dual Modification of Silk Fibroin for the Integrated Repair of Osteochondral Defects. *Biomater. Sci.* 9 (14). doi:10.1039/d1bm00535a

DePhillipo, N. N., Dekker, T. J., Aman, Z. S., Bernholt, D., Grantham, W. J., and LaPrade, R. F. (2019). Incidence and Healing Rates of Meniscal Tears in Patients Undergoing Repair during the First Stage of 2-Stage Revision Anterior Cruciate Ligament Reconstruction. *Am. J. Sports Med.* 47 (14). doi:10.1177/0363546519878421

Deymier-Black, A. C., Pasteris, J. D., Genin, G. M., and Thomopoulos, S. (2015). Allometry of the Tendon Enthesis: Mechanisms of Load Transfer between Tendon and Bone. *J. Biomech. Eng.* 137 (11). doi:10.1115/1.4031571

Ding, C., Qiao, Z., Jiang, W., Li, H., Wei, J., Zhou, G., et al. (2013). Regeneration of a Goat Femoral Head Using a Tissue-specific, Biphasic Scaffold Fabricated with CAD/CAM Technology. *Biomaterials* 34 (28). doi:10.1016/j.biomaterials.2013.05.038

El Bialy, I., Jiskoot, W., and Reza Nejadnik, M. (2017). Formulation, Delivery and Stability of Bone Morphogenetic Proteins for Effective Bone Regeneration. *Pharm. Res.* 34 (6). doi:10.1007/s11095-017-2147-x

Elder, B. D., and Athanasiou, K. A. (2009). Systematic Assessment of Growth Factor Treatment on Biochemical and Biomechanical Properties of Engineered Articular Cartilage Constructs. *Osteoarthr. Cartil.* 17 (1). doi:10.1016/j.joca.2008.05.006

Eldridge, S. E., Barawi, A., Wang, H., Roelofs, A. J., Kaneva, M., Guan, Z., et al. (2020). Agrin Induces Long-Term Osteochondral Regeneration by Supporting Repair Morphogenesis. *Sci. Transl. Med.* 12 (559). doi:10.1126/scitranslmed.aax9086

Erisken, C., Kalyon, D. M., and Wang, H. (2008). Functionally Graded Electrospun Polycaprolactone and Beta-Tricalcium Phosphate Nanocomposites for Tissue Engineering Applications. *Biomaterials* 29 (30). doi:10.1016/j.biomaterials.2008.06.022

Farberg, A. S., Jing, X. L., Monson, L. A., Donneys, A., Tchanque-Fossuo, C. N., Deshpande, S. S., et al. (2012). Deferoxamine Reverses Radiation Induced Hypovascularity during Bone Regeneration and Repair in the Murine Mandible. *Bone* 50 (5). doi:10.1016/j.bone.2012.01.019

Fernandez-Yague, M. A., Abbah, S. A., McNamara, L., Zeugolis, D. I., Pandit, A., and Biggs, M. J. (2015). Biomimetic Approaches in Bone Tissue Engineering: Integrating Biological and Physicomechanical Strategies. *Adv. Drug Deliv. Rev.* 84. doi:10.1016/j.addr.2014.09.005

Fini, M., Bondioli, E., Castagna, A., Torricelli, P., Giavaresi, G., Rotini, R., et al. (2012). Decellularized Human Dermis to Treat Massive Rotator Cuff Tears: In Vitro Evaluations. *Connect. Tissue Res.* 53 (4). doi:10.3109/03008207.2011.649929

Foster, T. E. (2015). Redefining the Value of Sports Medicine. *Am. J. Sports Med.* 43 (7), 1573–1574. doi:10.1177/0363546515590803

Gachon, E., and Mesquida, P. (2021). Mechanical Strain Alters the Surface Charge of Collagen Fibrils. *ACS Nano*. doi:10.1021/acsnano.1c00682

Galili, U., and Stone, K. R. (2021). *In Situ* "Humanization" of Porcine Bioprostheses: Demonstration of Tendon Bioprostheses Conversion into Human ACL and Possible Implications for Heart Valve Bioprostheses. *Bioeng. (Basel)* 8 (1). doi:10.3390/bioengineering8010010

Gao, J., Ding, X., Yu, X., Chen, X., Zhang, X., Cui, S., et al. (2021). Cell-Free Bilayered Porous Scaffolds for Osteochondral Regeneration Fabricated by Continuous 3D-Printing Using Nascent Physical Hydrogel as Ink. *Adv. Healthc. Mater* 10 (3). doi:10.1002/adhm.202001404

Gardner, O. F., Fahy, N., Alini, M., and Stoddart, M. J. (2016). Differences in Human Mesenchymal Stem Cell Secretomes during Chondrogenic Induction. *Eur. Cell Mater* 31. doi:10.22203/ecm.v031a15

Giannoudis, P. V., Dinopoulos, H., and Tsiridis, E. (2005). Bone Substitutes: an Update. *Injury* 36 (Suppl. 3). doi:10.1016/j.injury.2005.07.029

Gong, T., Xie, J., Liao, J., Zhang, T., Lin, S., and Lin, Y. (2015). Nanomaterials and Bone Regeneration. *Bone Res.* 3. doi:10.1038/boneres.2015.29

Good, L., Odensten, M., Pettersson, L., and Gillquist, J. (1989). Failure of a Bovine Xenograft for Reconstruction of the Anterior Cruciate Ligament. *Acta Orthop. Scand.* 60 (1). doi:10.3109/17453678909150080

Greenberg, D. D., Robertson, M., Vallurupalli, S., White, R. A., and Allen, W. C. (2010). Allograft Compared with Autograft Infection Rates in Primary Anterior Cruciate Ligament Reconstruction. *J. Bone & Jt. Surg. Am. Volume)* 92 (14). doi:10.2106/JBJS.I.00456

Guevara, J. A., Entezari, V., Ho, J. C., Derwin, K. A., Iannotti, J. P., and Ricchetti, E. T. (2020). An Update on Surgical Management of the Repairable Large-To-Massive Rotator Cuff Tear. *J. Bone Jt. Surg. Am.* 102 (19). doi:10.2106/JBJS.20.00177

Gungormus, C., Kolankaya, D., and Aydin, E. (2015). *Histopathological and Biomechanical Evaluation of Tenocyte Seeded Allografts on Rat Achilles Tendon Regeneration*. Amsterdam: Biomaterials, 51.

Guo, T., Noshin, M., Baker, H. B., Taskoy, E., Meredith, S. J., Tang, Q., et al. (2018). *3D Printed Biofunctionalized Scaffolds for Microfracture Repair of Cartilage Defects*. Amsterdam: Biomaterials, 185.

Hadidi, P., Paschos, N. K., Huang, B. J., Aryaei, A., Hu, J. C., and Athanasiou, K. A. (2016). Tendon and Ligament as Novel Cell Sources for Engineering the Knee Meniscus. *Osteoarthr. Cartil.* 24 (12). doi:10.1016/j.joca.2016.07.006

Hall, G. N., Tam, W. L., Andrikopoulos, K. S., Casas-Fraile, L., Voyiatzis, G. A., Geris, L., et al. (2021). *Patterned, Organoid-Based Cartilaginous Implants Exhibit Zone Specific Functionality Forming Osteochondral-like Tissues in Vivo*. Amsterdam: Biomaterials, 273.

Harris, M. T., Butler, D. L., Boivin, G. P., Florer, J. B., Schantz, E. J., and Wenstrup, R. J. (2004). Mesenchymal Stem Cells Used for Rabbit Tendon Repair Can Form Ectopic Bone and Express Alkaline Phosphatase Activity in Constructs. *J. Orthop. Res.* 22 (5). doi:10.1016/j.orthres.2004.02.012

Higashioka, M. M., Chen, J. A., Hu, J. C., and Athanasiou, K. A. (2014). Building an Anisotropic Meniscus with Zonal Variations. *Tissue Eng. Part A* 20 (1-2). doi:10.1089/ten.TEA.2013.0098

Howe, J. G., Johnson, R. J., Kaplan, M. J., Fleming, B., and Jarvinen, M. (1991). Anterior Cruciate Ligament Reconstruction Using Quadriceps Patellar Tendon Graft. Part I. Long-Term Followup. *Am. J. Sports Med.* 19 (5). doi:10.1177/036354659101900505

Hua, Y., Xia, H., Jia, L., Zhao, J., Zhao, D., Yan, X., et al. (2021). Ultrafast, Tough, and Adhesive Hydrogel Based on Hybrid Photocrosslinking for Articular Cartilage Repair in Water-Filled Arthroscopy. *Sci. Adv.* 7 (35). doi:10.1126/sciadv.abg0628

Huwe, L. W., Brown, W. E., Hu, J. C., and Athanasiou, K. A. (2018). Characterization of Costal Cartilage and its Suitability as a Cell Source for Articular Cartilage Tissue Engineering. *J. Tissue Eng. Regen. Med.* 12 (5). doi:10.1002/term.2630

Iannotti, J. P., Codsi, M. J., Kwon, Y. W., Derwin, K., Ciccone, J., and Brems, J. J. (2006). Porcine Small Intestine Submucosa Augmentation of Surgical Repair of Chronic Two-Tendon Rotator Cuff Tears. A Randomized, Controlled Trial. *J. Bone Jt. Surg. Am.* 88 (6). doi:10.2106/JBJS.E.00524

Ingber, D. E., Mow, V. C., Butler, D., Niklason, L., Huard, J., Mao, J., et al. (2006). Tissue Engineering and Developmental Biology: Going Biomimetic. *Tissue Eng.* 12 (12). doi:10.1089/ten.2006.12.3265

Jackson, D. W., Grood, E. S., Goldstein, J. D., Rosen, M. A., Kurzweil, P. R., Cummings, J. F., et al. (1993). A Comparison of Patellar Tendon Autograft and Allograft Used for Anterior Cruciate Ligament Reconstruction in the Goat Model. *Am. J. Sports Med.* 21 (2). doi:10.1177/036354659302100203

Jiang, G., Li, S., Yu, K., He, B., Hong, J., Xu, T., et al. (2021). A 3D-Printed PRP-GelMA Hydrogel Promotes Osteochondral Regeneration through M2 Macrophage Polarization in a Rabbit Model. *Acta Biomater.* 128. doi:10.1016/j.actbio.2021.04.010

Karageorgiou, V., and Kaplan, D. (2005). Porosity of 3D Biomaterial Scaffolds and Osteogenesis. *Biomaterials* 26 (27). doi:10.1016/j.biomaterials.2005.02.002

Kato, Y., Chavez, J., Yamada, S., Hattori, S., Takazawa, S., and Ohuchi, H. (2019). A Large Knee Osteochondral Lesion Treated Using a Combination of Osteochondral Autograft Transfer and Second-Generation Autologous Chondrocyte Implantation: A Case Report. *Regen. Ther.* 10. doi:10.1016/j.reth.2018.10.002

Khira, Y. M., and Salama, A. M. (2017). Treatment of Locked Posterior Shoulder Dislocation with Bone Defect. *Orthopedics* 40 (3). doi:10.3928/01477447-20170308-07

Kim, H. S., Mandakhbayar, N., Kim, H. W., Leong, K. W., and Yoo, H. S. (2021). *Protein-reactive Nanofibrils Decorated with Cartilage-Derived Decellularized Extracellular Matrix for Osteochondral Defects*. Amsterdam: Biomaterials, 269.

Kim, J. W., Jung, I. H., Lee, K. I., Jung, U. W., Kim, C. S., Choi, S. H., et al. (2012). Volumetric Bone Regenerative Efficacy of Biphasic Calcium Phosphate-Collagen Composite Block Loaded with rhBMP-2 in Vertical Bone Augmentation Model of a Rabbit Calvarium. *J. Biomed. Mater Res. A* 100 (12). doi:10.1002/jbm.a.34278

Koh, R. H., Jin, Y., Kang, B. J., and Hwang, N. S. (2017). Chondrogenically Primed Tonsil-Derived Mesenchymal Stem Cells Encapsulated in Riboflavin-Induced Photocrosslinking Collagen-Hyaluronic Acid Hydrogel for Meniscus Tissue Repairs. *Acta Biomater.* 53. doi:10.1016/j.actbio.2017.01.081

Kraeutler, M. J., Purcell, J. M., and Hunt, K. J. (2017). Chronic Achilles Tendon Ruptures. *Foot Ankle Int.* 38 (8). doi:10.1177/1071100717709570

Krishnan, V., Bryant, H. U., and Macdougald, O. A. (2006). Regulation of Bone Mass by Wnt Signaling. *J. Clin. Investig.* 116 (5). doi:10.1172/JCI28551

Kweon, C. Y., Hagen, M. S., and Gee, A. O. (2019). What's New in Sports Medicine. *J. Bone Jt. Surg. Am.* 101 (8), 669–674. doi:10.2106/JBJS.19.00007

Kwon, H., Brown, W. E., Lee, C. A., Wang, D., Paschos, N., Hu, J. C., et al. (2019). Surgical and Tissue Engineering Strategies for Articular Cartilage and Meniscus Repair. *Nat. Rev. Rheumatol.* 15 (9). doi:10.1038/s41584-019-0255-1

Labek, G., Thaler, M., Janda, W., Agreiter, M., and Stockl, B. (2011). Revision Rates after Total Joint Replacement: Cumulative Results from Worldwide Joint Register Datasets. *J. Bone Jt. Surg. Br.* 93 (3). doi:10.1302/0301-620X.93B3.25467

Laurencin, C., Khan, Y., and El-Amin, S. F. (2006). Bone Graft Substitutes. *Expert Rev. Med. Devices* 3 (1). doi:10.1586/17434440.3.1.49

Lee, S. H., Moon, J. H., Jeong, C. M., Bae, E. B., Park, C. E., Jeon, G. R., et al. (20172017). The Mechanical Properties and Biometrical Effect of 3D Preformed Titanium Membrane for Guided Bone Regeneration on Alveolar Bone Defect. *Biomed. Res. Int.*doi:10.1155/2017/7102123

Lee, S. J., Nam, Y., Rim, Y. A., Lee, K., Ju, J. H., and Kim, D. S. (2021). Perichondrium-inspired Permeable Nanofibrous Tube Well Promoting Differentiation of hiPSC-Derived Pellet toward Hyaline-like Cartilage Pellet. *Biofabrication*. doi:10.1088/1758-5090/ac1e76

Lenas, P., Moos, M., and Luyten, F. P. (2009). Developmental Engineering: a New Paradigm for the Design and Manufacturing of Cell-Based Products. Part I: from Three-Dimensional Cell Growth to Biomimetics of In Vivo Development. *Tissue Eng. Part B Rev.* 15 (4). doi:10.1089/ten.TEB.2008.0575

Lewington, M. R., Ferguson, D. P., Smith, T. D., Burks, R., Coady, C., and Wong, I. H. (2017). Graft Utilization in the Bridging Reconstruction of Irreparable Rotator Cuff Tears: A Systematic Review. *Am. J. Sports Med.* 45 (13). doi:10.1177/0363546517694355

Li, H., Li, P., Yang, Z., Gao, C., Fu, L., Liao, Z., et al. (2021). Meniscal Regenerative Scaffolds Based on Biopolymers and Polymers: Recent Status and Applications. *Front. Cell Dev. Biol.* 9. doi:10.3389/fcell.2021.661802

Li, H., Yao, Z., Jiang, J., Hua, Y., Chen, J., Li, Y., et al. (2012). Biologic Failure of a Ligament Advanced Reinforcement System Artificial Ligament in Anterior Cruciate Ligament Reconstruction: a Report of Serious Knee Synovitis. *Arthroscopy* 28 (4). doi:10.1016/j.arthro.2011.12.008

Li, T., Peng, M., Yang, Z., Zhou, X., Deng, Y., Jiang, C., et al. (2018). 3D-printed IFN-Gamma-Loading Calcium Silicate-Beta-Tricalcium Phosphate Scaffold Sequentially Activates M1 and M2 Polarization of Macrophages to Promote Vascularization of Tissue Engineering Bone. *Acta Biomater.* 71. doi:10.1016/j.actbio.2018.03.012

Li, X., Cheng, R., Sun, Z., Su, W., Pan, G., Zhao, S., et al. (2017b). Flexible Bipolar Nanofibrous Membranes for Improving Gradient Microstructure in Tendon-To-Bone Healing. *Acta Biomater.* 61. doi:10.1016/j.actbio.2017.07.044

Li, X., He, J., Bian, W., Li, Z., Zhang, W., Li, D., et al. (2014). A Novel Silk-Based Artificial Ligament and Tricalcium Phosphate/polyether Ether Ketone Anchor for Anterior Cruciate Ligament Reconstruction - Safety and Efficacy in a Porcine Model. *Acta Biomater.* 10 (8). doi:10.1016/j.actbio.2014.05.015

Li, X., Wang, Y., Zhao, Y., Liu, J., Xiao, S., and Mao, K. (2017a). Multilevel 3D Printing Implant for Reconstructing Cervical Spine with Metastatic Papillary Thyroid Carcinoma. *Spine (Phila Pa 1976)* (22), 42. doi:10.1097/BRS.0000000000002229

Li, Y. H., Wang, Z. D., Wang, W., Ding, C. W., Zhang, H. X., and Li, J. M. (2015). The Biocompatibility of Calcium Phosphate Cements Containing Alendronate-Loaded PLGA Microparticles In Vitro. *Exp. Biol. Med. (Maywood)* 240 (11). doi:10.1177/1535370215579142

Liu, M., Zeng, X., Ma, C., Yi, H., Ali, Z., Mou, X., et al. (2017). Injectable Hydrogels for Cartilage and Bone Tissue Engineering. *Bone Res.* 5. doi:10.1038/boneres.2017.14

Liu, Q., Yu, Y., Reisdorf, R. L., Qi, J., Lu, C. K., Berglund, L. J., et al. (2019). *Engineered Tendon-Fibrocartilage-Bone Composite and Bone Marrow-Derived Mesenchymal Stem Cell Sheet Augmentation Promotes Rotator Cuff Healing in a Non-weight-bearing Canine Model*. Amsterdam: Biomaterials.

Liu, S., Li, P., Liu, X., Wang, P., Xue, W., Ren, Y., et al. (2021). Bioinspired Mineral-Polymeric Hybrid Hyaluronic Acid/poly (Gamma-glutamic Acid) Hydrogels as Tunable Scaffolds for Stem Cells Differentiation. *Carbohydr. Polym.* 264. doi:10.1016/j.carbpol.2021.118048

Lu, H. H., Cooper, J. A., Jr., Manuel, S., Freeman, J. W., Attawia, M. A., Ko, F. K., et al. (2005). Anterior Cruciate Ligament Regeneration Using Braided Biodegradable Scaffolds: In Vitro Optimization Studies. *Biomaterials* 26 (23). doi:10.1016/j.biomaterials.2004.11.050

Lu, H. H., and Thomopoulos, S. (2013). Functional Attachment of Soft Tissues to Bone: Development, Healing, and Tissue Engineering. *Annu. Rev. Biomed. Eng.* 15. doi:10.1146/annurev-bioeng-071910-124656

Lynch, M. E., Chiou, A. E., Lee, M. J., Marcott, S. C., Polamraju, P. V., Lee, Y., et al. (2016). Three-Dimensional Mechanical Loading Modulates the Osteogenic Response of Mesenchymal Stem Cells to Tumor-Derived Soluble Signals. *Tissue Eng. Part A* 22 (15-16). doi:10.1089/ten.TEA.2016.0153

MacBarb, R. F., Chen, A. L., Hu, J. C., and Athanasiou, K. A. (2013). Engineering Functional Anisotropy in Fibrocartilage Neotissues. *Biomaterials* 34 (38). doi:10.1016/j.biomaterials.2013.09.026

Maffulli, N., Oliva, F., Maffulli, G. D., Buono, A. D., and Gougoulias, N. (2018). Surgical Management of Chronic Achilles Tendon Ruptures Using Less Invasive Techniques. *Foot Ankle Surg.* 24 (2). doi:10.1016/j.fas.2017.02.002

Makris, E. A., Hadidi, P., and Athanasiou, K. A. (2011). The Knee Meniscus: Structure-Function, Pathophysiology, Current Repair Techniques, and Prospects for Regeneration. *Biomaterials* 32 (30). doi:10.1016/j.biomaterials.2011.06.037

Martin, F., Lehmann, M., Sack, U., and Anderer, U. (2017). Featured Article: In Vitro Development of Personalized Cartilage Microtissues Uncovers an Individualized Differentiation Capacity of Human Chondrocytes. *Exp. Biol. Med. (Maywood)* 242 (18). doi:10.1177/1535370217728498

Mastrokalos, D. S., Springer, J., Siebold, R., and Paessler, H. H. (2005). Donor Site Morbidity and Return to the Preinjury Activity Level after Anterior Cruciate Ligament Reconstruction Using Ipsilateral and Contralateral Patellar Tendon Autograft: a Retrospective, Nonrandomized Study. *Am. J. Sports Med.* 33 (1). doi:10.1177/0363546504265926

McElvany, M. D., McGoldrick, E., Gee, A. O., Neradilek, M. B., and Matsen, F. A. (2015). Rotator Cuff Repair: Published Evidence on Factors Associated with Repair Integrity and Clinical Outcome. *Am. J. Sports Med.* 43 (2). doi:10.1177/0363546514529644

McFarland, E. G., Huri, G., Hyun, Y. S., Petersen, S. A., and Srikumaran, U. (2016). Reverse Total Shoulder Arthroplasty without Bone-Grafting for Severe Glenoid Bone Loss in Patients with Osteoarthritis and Intact Rotator Cuff. *J. Bone Jt. Surg. Am.* 98 (21). doi:10.2106/JBJS.15.01181

McGovern, J. A., Griffin, M., and Hutmacher, D. W. (2018). Animal Models for Bone Tissue Engineering and Modelling Disease. *Dis. Model. Mech.* 11 (4). doi:10.1242/dmm.033084

Meng, C., Su, W., Liu, M., Yao, S., Ding, Q., Yu, K., et al. (2021). Controlled Delivery of Bone Morphogenic Protein-2-Related Peptide from Mineralised

Extracellular Matrix-Based Scaffold Induces Bone Regeneration. *Mater Sci. Eng. C Mater Biol. Appl.* 126. doi:10.1016/j.msec.2021.112182

Mengsteab, P. Y., Otsuka, T., McClinton, A., Shemshaki, N. S., Shah, S., Kan, H. M., et al. (2020). Mechanically Superior Matrices Promote Osteointegration and Regeneration of Anterior Cruciate Ligament Tissue in Rabbits. *Proc. Natl. Acad. Sci. U. S. A.* 117 (46). doi:10.1073/pnas.2012347117

Muller, S. A., Evans, C. H., Heisterbach, P. E., and Majewski, M. (2018). The Role of the Paratenon in Achilles Tendon Healing: A Study in Rats. *Am. J. Sports Med.* 46 (5). doi:10.1177/0363546518756093

Mumith, A., Coathup, M., Chimutengwende-Gordon, M., Aston, W., Briggs, T., and Blunn, G. (2017). Augmenting the Osseointegration of Endoprostheses Using Laser-Sintered Porous Collars: an In Vivo Study. *Bone Jt. J.* 99-B (2). doi:10.1302/0301-620X.99B2.BJJ-2016-0584.R1

Mustafa, S. F., Evans, P. L., Bocca, A., Patton, D. W., Sugar, A. W., and Baxter, P. W. (2011). Customized Titanium Reconstruction of Post-traumatic Orbital Wall Defects: a Review of 22 Cases. *Int. J. Oral Maxillofac. Surg.* 40 (12). doi:10.1016/j.ijom.2011.04.020

Naso, F., Gandaglia, A., Iop, L., Spina, M., and Gerosa, G. (2011). First Quantitative Assay of Alpha-Gal in Soft Tissues: Presence and Distribution of the Epitope before and after Cell Removal from Xenogeneic Heart Valves. *Acta Biomater.* 7 (4). doi:10.1016/j.actbio.2010.11.030

Nguyen, D. T., Dellbrugge, S., Tak, P. P., Woo, S. L., Blankevoort, L., and van Dijk, N. C. (2015). Histological Characteristics of Ligament Healing after Bio-Enhanced Repair of the Transected Goat ACL. *J. Exp. Orthop.* 2 (1). doi:10.1186/s40634-015-0021-5

Nicholson, G. P., Breur, G. J., Van Sickle, D., Yao, J. Q., Kim, J., and Blanchard, C. R. (2007). Evaluation of a Cross-Linked Acellular Porcine Dermal Patch for Rotator Cuff Repair Augmentation in an Ovine Model. *J. Shoulder Elb. Surg.* 16 (5 Suppl. l). doi:10.1016/j.jse.2007.03.010

Novi, M., Kumar, A., Paladini, P., Porcellini, G., and Merolla, G. (2018). Irreparable Rotator Cuff Tears: Challenges and Solutions. *Orthop. Res. Rev.* 10, 93–103. doi:10.2147/ORR.S151259

Oliva, F., Maffulli, N., Gissi, C., Veronesi, F., Calciano, L., Fini, M., et al. (2019). Combined Ascorbic Acid and T3 Produce Better Healing Compared to Bone Marrow Mesenchymal Stem Cells in an Achilles Tendon Injury Rat Model: a Proof of Concept Study. *J. Orthop. Surg. Res.* 14 (1). doi:10.1186/s13018-019-1098-9

Patel, S., Caldwell, J. M., Doty, S. B., Levine, W. N., Rodeo, S., and Soslowsky, L. J. (2018) Integrating Soft and Hard Tissues via Interface Tissue Engineering. *J. Orthop. Res.*, 36(4).doi:10.1002/jor.23810

Peterson, J. R., and Krabak, B. J. (2014). Anterior Cruciate Ligament Injury: Mechanisms of Injury and Strategies for Injury Prevention. *Phys. Med. Rehabil. Clin. N. Am.* 25 (4). doi:10.1016/j.pmr.2014.06.010

Pike, A. N., Patzkowski, J. C., and Bottoni, C. R. (2019). Meniscal and Chondral Pathology Associated with Anterior Cruciate Ligament Injuries. *J. Am. Acad. Orthop. Surg.* 27 (3), 75–84. doi:10.5435/JAAOS-D-17-00670

Pirosa, A., Gottardi, R., Alexander, P. G., Puppi, D., Chiellini, F., and Tuan, R. S. (2021). *An in Vitro Chondro-Osteo-Vascular Triphasic Model of the Osteochondral Complex*. Amsterdam: Biomaterials, 272.

Piva, S. R., Childs, J. D., Klucinec, B. M., Irrgang, J. J., Almeida, G. J., and Fitzgerald, G. K. (2009). Patella Fracture during Rehabilitation after Bone-Patellar Tendon-Bone Anterior Cruciate Ligament Reconstruction: 2 Case Reports. *J. Orthop. Sports Phys. Ther.* 39 (4). doi:10.2519/jospt.2009.2864

Platts-Mills, T. A., Hilger, C., Jappe, U., Hage, M., Gadermaier, G., Spillner, E., et al. (2021). *Carbohydrate Epitopes Currently Recognized as Targets for IgE Antibodies*. Allergy.

Polak, S. J., Levengood, S. K., Wheeler, M. B., Maki, A. J., Clark, S. G., and Johnson, A. J. (2011). Analysis of the Roles of Microporosity and BMP-2 on Multiple Measures of Bone Regeneration and Healing in Calcium Phosphate Scaffolds. *Acta Biomater.* 7 (4). doi:10.1016/j.actbio.2010.12.030

Pountos, I., Panteli, M., Lampropoulos, A., Jones, E., Calori, G. M., and Giannoudis, P. V. (2016). The Role of Peptides in Bone Healing and Regeneration: a Systematic Review. *BMC Med.* 14. doi:10.1186/s12916-016-0646-y

Qiao, Z., Lian, M., Han, Y., Sun, B., Zhang, X., Jiang, W., et al. (2021). *Bioinspired Stratified Electrowritten Fiber-Reinforced Hydrogel Constructs with Layer-specific Induction Capacity for Functional Osteochondral Regeneration*. Amsterdam: Biomaterials, 266.

Qiu, J., Ahn, J., Qin, D., Thomopoulos, S., and Xia, Y. (2021). Biomimetic Scaffolds with a Mineral Gradient and Funnel-Shaped Channels for Spatially Controllable Osteogenesis. *Adv. Healthc. Mater*.

Radhakrishnan, J., Manigandan, A., Chinnaswamy, P., Subramanian, A., and Sethuraman, S. (2018). *Gradient Nano-Engineered* in Situ *Forming Composite Hydrogel for Osteochondral Regeneration*. Amsterdam: Biomaterials, 162.

Rossetti, L., Kuntz, L. A., Kunold, E., Schock, J., Muller, K. W., Grabmayr, H., et al. (2017). The Microstructure and Micromechanics of the Tendon-Bone Insertion. *Nat. Mater* 16 (6). doi:10.1038/nmat4863

Sakellariou, V. I., Poultsides, L. A., Ma, Y., Bae, J., Liu, S., and Sculco, T. P. (2016). Risk Assessment for Chronic Pain and Patient Satisfaction after Total Knee Arthroplasty. *Orthopedics* 39 (1). doi:10.3928/01477447-20151228-06

Santo, V. E., Gomes, M. E., Mano, J. F., and Reis, R. L. (2013). Controlled Release Strategies for Bone, Cartilage, and Osteochondral Engineering--Part I: Recapitulation of Native Tissue Healing and Variables for the Design of Delivery Systems. *Tissue Eng. Part B Rev.* 19 (4). doi:10.1089/ten.TEB.2012.0138

Sasaki, H., Rothrauff, B. B., Alexander, P. G., Lin, H., Gottardi, R., Fu, F. H., et al. (2018). In Vitro Repair of Meniscal Radial Tear with Hydrogels Seeded with Adipose Stem Cells and TGF-Beta3. *Am. J. Sports Med.* 46 (10). doi:10.1177/0363546518782973

Saveh-Shemshaki, N., Laurencin, S. N. L., and Laurencin, C. T. (2019). Nanofiber-based Matrices for Rotator Cuff Regenerative Engineering. *Acta Biomater.* 94. doi:10.1016/j.actbio.2019.05.041

Schuurmans, C. C. L., Mihajlovic, M., Hiemstra, C., Ito, K., Hennink, W. E., and Vermonden, T. (2021). *Hyaluronic Acid and Chondroitin Sulfate (Meth) acrylate-based Hydrogels for Tissue Engineering: Synthesis, Characteristics and Pre-clinical Evaluation*. Amsterdam: Biomaterials, 268.

Sclamberg, S. G., Tibone, J. E., Itamura, J. M., and Kasraeian, S. (2004). Six-month Magnetic Resonance Imaging Follow-Up of Large and Massive Rotator Cuff Repairs Reinforced with Porcine Small Intestinal Submucosa. *J. Shoulder Elb. Surg.* 13 (5). doi:10.1016/j.jse.2004.03.005

Shen, W., Chen, X., Chen, J., Yin, Z., Heng, B. C., Chen, W., et al. (2010). The Effect of Incorporation of Exogenous Stromal Cell-Derived Factor-1 Alpha within a Knitted Silk-Collagen Sponge Scaffold on Tendon Regeneration. *Biomaterials* 31 (28). doi:10.1016/j.biomaterials.2010.05.040

Shimomura, K., Rothrauff, B. B., and Tuan, R. S. (2017). Region-Specific Effect of the Decellularized Meniscus Extracellular Matrix on Mesenchymal Stem Cell-Based Meniscus Tissue Engineering. *Am. J. Sports Med.* 45 (3). doi:10.1177/0363546516674184

Shkhyan, R., Van Handel, B., Bogdanov, J., Lee, S., Yu, Y., Scheinberg, M., et al. (2018). Drug-induced Modulation of Gp130 Signalling Prevents Articular Cartilage Degeneration and Promotes Repair. *Ann. Rheum. Dis.* 77 (5). doi:10.1136/annrheumdis-2017-212037

Silva, M., Ferreira, F. N., Alves, N. M., and Paiva, M. C. (2020). Biodegradable Polymer Nanocomposites for Ligament/tendon Tissue Engineering. *J. Nanobiotechnology* 18 (1). doi:10.1186/s12951-019-0556-1

Singh, H., Purohit, S. D., Bhaskar, R., Yadav, I., Bhushan, S., Gupta, M. K., et al. (2021). Biomatrix from Goat-Waste in Sponge/gel/powder Form for Tissue Engineering and Synergistic Effect of Nanoceria. *Biomed. Mater* 16 (2). doi:10.1088/1748-605x/abdb74

Son, M. S., and Levenston, M. E. (2017). Quantitative Tracking of Passage and 3D Culture Effects on Chondrocyte and Fibrochondrocyte Gene Expression. *J. Tissue Eng. Regen. Med.* 11 (4). doi:10.1002/term.2022

Soong, H. K., and Kenyon, K. R. (1984). Adverse Reactions to Virgin Silk Sutures in Cataract Surgery. *Ophthalmology* 91 (5). doi:10.1016/s0161-6420(84)34273-7

Southworth, T. M., Naveen, N. B., Tauro, T. M., Chahla, J., and Cole, B. J. (2020). Meniscal Allograft Transplants. *Clin. Sports Med.* 39 (1), 93–123. doi:10.1016/j.csm.2019.08.013

Steele, J. A., McCullen, S. D., Callanan, A., Autefage, H., Accardi, M. A., Dini, D., et al. (2014). Combinatorial Scaffold Morphologies for Zonal Articular Cartilage Engineering. *Acta Biomater.* 10 (5). doi:10.1016/j.actbio.2013.12.030

Steinhaus, M. E., Makhni, E. C., Cole, B. J., Romeo, A. A., and Verma, N. N. (2016). Outcomes after Patch Use in Rotator Cuff Repair. *Arthroscopy* 32 (8). doi:10.1016/j.arthro.2016.02.009

Stone, K. R., Walgenbach, A. W., Turek, T. J., Somers, D. L., Wicomb, W., and Galili, U. (2007). Anterior Cruciate Ligament Reconstruction with a Porcine

Xenograft: a Serologic, Histologic, and Biomechanical Study in Primates. *Arthroscopy* 23 (4). doi:10.1016/j.arthro.2006.12.024

Su, W., Guo, J., Xu, J., Huang, K., Chen, J., Jiang, J., et al. (2021). Gradient Composite Film with Calcium Phosphate Silicate for Improved Tendon-To-Bone Intergration. *Chem. Eng. J.* 404. doi:10.1016/j.cej.2020.126473

Sun, J., Mou, C., Shi, Q., Chen, B., Hou, X., Zhang, W., et al. (2018). *Controlled Release of Collagen-Binding SDF-1alpha from the Collagen Scaffold Promoted Tendon Regeneration in a Rat Achilles Tendon Defect Model*. Amsterdam: Biomaterials, 162.

Sunwoo, J. Y., and Murrell, G. A. C. (2020). Interposition Graft Repair of Irreparable Rotator Cuff Tears: A Review of Biomechanics and Clinical Outcomes. *J. Am. Acad. Orthop. Surg.* 28 (19), e829. doi:10.5435/JAAOS-D-19-00500

Tagliero, A. J., Desai, V. S., Kennedy, N. I., Camp, C. L., Stuart, M. J., Levy, B. A., et al. (2018). Seventeen-Year Follow-Up after Meniscal Repair with Concomitant Anterior Cruciate Ligament Reconstruction in a Pediatric and Adolescent Population. *Am. J. Sports Med.* 46 (14). doi:10.1177/0363546518803934

Tan, X. P., Tan, Y. J., Chow, C. S. L., Tor, S. B., and Yeong, W. Y. (2017). Metallic Powder-Bed Based 3D Printing of Cellular Scaffolds for Orthopaedic Implants: A State-Of-The-Art Review on Manufacturing, Topological Design, Mechanical Properties and Biocompatibility. *Mater Sci. Eng. C Mater Biol. Appl.* 76. doi:10.1016/j.msec.2017.02.094

Tang, W., Lin, D., Yu, Y., Niu, H., Guo, H., Yuan, Y., et al. (2016). Bioinspired Trimodal Macro/micro/nano-Porous Scaffolds Loading rhBMP-2 for Complete Regeneration of Critical Size Bone Defect. *Acta Biomater.* 32. doi:10.1016/j.actbio.2015.12.006

Taylor, S. A., and Rodeo, S. A. (2013). Augmentation Techniques for Isolated Meniscal Tears. *Curr. Rev. Musculoskelet. Med.* 6 (2). doi:10.1007/s12178-013-9165-z

Teuschl, A., Heimel, P., Nurnberger, S., van Griensven, M., Redl, H., and Nau, T. (2016). A Novel Silk Fiber-Based Scaffold for Regeneration of the Anterior Cruciate Ligament: Histological Results from a Study in Sheep. *Am. J. Sports Med.* 44 (6). doi:10.1177/0363546516631954

Tiefenboeck, T. M., Thurmaier, E., Tiefenboeck, M. M., Ostermann, R. C., Joestl, J., Winnisch, M., et al. (2015). Clinical and Functional Outcome after Anterior Cruciate Ligament Reconstruction Using the LARS System at a Minimum Follow-Up of 10 Years. *Knee* 22 (6). doi:10.1016/j.knee.2015.06.003

Tits, A., and Ruffoni, D. (2021). Joining Soft Tissues to Bone: Insights from Modeling and Simulations. *Bone Rep.* 14, 100742. doi:10.1016/j.bonr.2020.100742

Utomo, L., van Osch, G. J., Bayon, Y., Verhaar, J. A., and Bastiaansen-Jenniskens, Y. M. (2016). Guiding Synovial Inflammation by Macrophage Phenotype Modulation: an In Vitro Study towards a Therapy for Osteoarthritis. *Osteoarthr. Cartil.* 24 (9). doi:10.1016/j.joca.2016.04.013

Valdes, A. M., Doherty, S. A., Zhang, W., Muir, K. R., Maciewicz, R. A., and Doherty, M. (2012). Inverse Relationship between Preoperative Radiographic Severity and Postoperative Pain in Patients with Osteoarthritis Who Have Undergone Total Joint Arthroplasty. *Semin. Arthritis Rheum.* 41 (4). doi:10.1016/j.semarthrit.2011.07.002

Van Der Merwe, W., Lind, M., Fauno, P., Van Egmond, K., Zaffagnini, S., Marcacci, M., et al. (2020). Xenograft for Anterior Cruciate Ligament Reconstruction Was Associated with High Graft Processing Infection. *J. Exp. Orthop.* 7 (1). doi:10.1186/s40634-020-00292-0

van Tienen, T. G., Hannink, G., and Buma, P. (2009). Meniscus Replacement Using Synthetic Materials. *Clin. Sports Med.* 28 (1). doi:10.1016/j.csm.2008.08.003

Vapniarsky, N., Huwe, L. W., Arzi, B., Houghton, M. K., Wong, M. E., Wilson, J. W., et al. (2018). Tissue Engineering toward Temporomandibular Joint Disc Regeneration. *Sci. Transl. Med.* 10 (446). doi:10.1126/scitranslmed.aaq1802

Veronesi, F., Di Matteo, B., Vitale, N. D., Filardo, G., Visani, A., Kon, E., et al. (2021). Biosynthetic Scaffolds for Partial Meniscal Loss: A Systematic Review from Animal Models to Clinical Practice. *Bioact. Mater* 6 (11). doi:10.1016/j.bioactmat.2021.03.033

Wang, C., Hu, Y., Zhang, S., Ruan, D., Huang, Z., He, P., et al. (2021). Application of Stem Cell Therapy for ACL Graft Regeneration. *Stem Cells Int.* doi:10.1155/2021/6641818

Wang, D., Zhang, X., Huang, S., Liu, Y., Fu, B. S., Mak, K. K., et al. (2021). *Engineering Multi-Tissue Units for Regenerative Medicine: Bone-Tendon-Muscle Units of the Rotator Cuff*. Amsterdam: Biomaterials, 272.

Wang, S., Ge, Y., Ai, C., Jiang, J., Cai, J., Sheng, D., et al. (2018). Enhance the Biocompatibility and Osseointegration of Polyethylene Terephthalate Ligament by Plasma Spraying with Hydroxyapatite In Vitro and In Vivo. *Int. J. Nanomedicine* 13. doi:10.2147/IJN.S162466

Wang, S., Lu, M., Wang, W., Yu, S., Yu, R., Cai, C., et al. (2022). Macrophage Polarization Modulated by NF-kappaB in Polylactide Membranes-Treated Peritendinous Adhesion. *Small* 18 (3). doi:10.1002/smll.202104112

Wang, Z., Han, L., Sun, T., Ma, J., Sun, S., Ma, L., et al. (2020). Extracellular Matrix Derived from Allogenic Decellularized Bone Marrow Mesenchymal Stem Cell Sheets for the Reconstruction of Osteochondral Defects in Rabbits. *Acta Biomater.* 118. doi:10.1016/j.actbio.2020.10.022

Wei, H., Cui, J., Lin, K., Xie, J., and Wang, X. (2022). Recent Advances in Smart Stimuli-Responsive Biomaterials for Bone Therapeutics and Regeneration. *Bone Res.* 10 (1). doi:10.1038/s41413-021-00180-y

Weimin, P., Dan, L., Yiyong, W., Yunyu, H., and Li, Z. (2013). Tendon-to-bone Healing Using an Injectable Calcium Phosphate Cement Combined with Bone Xenograft/BMP Composite. *Biomaterials* 34 (38). doi:10.1016/j.biomaterials.2013.09.018

Westermann, R. W., Duchman, K. R., Amendola, A., Glass, N., and Wolf, B. R. (2017). All-Inside versus Inside-Out Meniscal Repair with Concurrent Anterior Cruciate Ligament Reconstruction: A Meta-Regression Analysis. *Am. J. Sports Med.* 45 (3). doi:10.1177/0363546516642220

Wong, C. C., Huang, Y. M., Chen, C. H., Lin, F. H., Yeh, Y. Y., and Bai, M. Y. (2020). Cytokine and Growth Factor Delivery from Implanted Platelet-Rich Fibrin Enhances Rabbit Achilles Tendon Healing. *Int. J. Mol. Sci.* 21 (9). doi:10.3390/ijms21093221

Wu, Z., Tang, T., Guo, H., Tang, S., Niu, Y., Zhang, J., et al. (2014). In Vitro degradability, Bioactivity and Cell Responses to Mesoporous Magnesium Silicate for the Induction of Bone Regeneration. *Colloids Surf. B Biointerfaces* 120. doi:10.1016/j.colsurfb.2014.04.010

Xie, C., Ye, J., Liang, R., Yao, X., Wu, X., Koh, Y., et al. (2021). Advanced Strategies of Biomimetic Tissue-Engineered Grafts for Bone Regeneration. *Adv. Healthc. Mater* 10 (14). doi:10.1002/adhm.202100408

Xie, J., Wang, Y., Lu, L., Liu, L., Yu, X., and Pei, F. (2021). Cellular Senescence in Knee Osteoarthritis: Molecular Mechanisms and Therapeutic Implications. *Ageing Res. Rev.* 70. doi:10.1016/j.arr.2021.101413

Xie, X., Zhu, J., Hu, X., Dai, L., Fu, X., Zhang, J., et al. (2018). A Co-culture System of Rat Synovial Stem Cells and Meniscus Cells Promotes Cell Proliferation and Differentiation as Compared to Mono-Culture. *Sci. Rep.* 8 (1). doi:10.1038/s41598-018-25709-w

Xing, S. G., Zhou, Y. L., Yang, Q. Q., Ju, F., Zhang, L., and Tang, J. B. (2020). Effects of Nanoparticle-Mediated Growth Factor Gene Transfer to the Injured Microenvironment on the Tendon-To-Bone Healing Strength. *Biomater. Sci.* 8 (23). doi:10.1039/d0bm01222j

Xu, C., Su, P., Chen, X., Meng, Y., Yu, W., Xiang, A. P., et al. (2011). Biocompatibility and Osteogenesis of Biomimetic Bioglass-Collagen-Phosphatidylserine Composite Scaffolds for Bone Tissue Engineering. *Biomaterials* 32 (4). doi:10.1016/j.biomaterials.2010.09.068

Xu, J., Feng, Q., Lin, S., Yuan, W., Li, R., Li, J., et al. (2019). *Injectable Stem Cell-Laden Supramolecular Hydrogels Enhance* in Situ *Osteochondral Regeneration via the Sustained Co-delivery of Hydrophilic and Hydrophobic Chondrogenic Molecules*. Amsterdam: Biomaterials, 210.

Yan, Y., Chen, H., Zhang, H., Guo, C., Yang, K., Chen, K., et al. (2019). *Vascularized 3D Printed Scaffolds for Promoting Bone Regeneration*. Amsterdam: Biomaterials, 190–191.

Yang, F., Chen, C., Zhou, Q., Gong, Y., Li, R., Li, C., et al. (2017). Laser Beam Melting 3D Printing of Ti6Al4V Based Porous Structured Dental Implants: Fabrication, Biocompatibility Analysis and Photoelastic Study. *Sci. Rep.* 7. doi:10.1038/srep45360

Yilgor, C., Yilgor Huri, P., and Huri, G. (20122012). Tissue Engineering Strategies in Ligament Regeneration. *Stem Cells Int.* doi:10.1155/2012/374676

Yokoya, S., Mochizuki, Y., Natsu, K., Omae, H., Nagata, Y., and Ochi, M. (2012). Rotator Cuff Regeneration Using a Bioabsorbable Material with Bone Marrow-Derived Mesenchymal Stem Cells in a Rabbit Model. *Am. J. Sports Med.* 40 (6). doi:10.1177/0363546512442343

Zhang, C. H., Jiang, Y. L., Ning, L. J., Li, Q., Fu, W. L., Zhang, Y. J., et al. (2018). Evaluation of Decellularized Bovine Tendon Sheets for Achilles Tendon Defect Reconstruction in a Rabbit Model. *Am. J. Sports Med.* 46 (11). doi:10.1177/0363546518787515

Zhang, J., Zhou, H., Yang, K., Yuan, Y., and Liu, C. (2013). RhBMP-2-loaded Calcium Silicate/calcium Phosphate Cement Scaffold with Hierarchically Porous Structure for Enhanced Bone Tissue Regeneration. *Biomaterials* 34 (37). doi:10.1016/j.biomaterials.2013.08.059

Zhang, M., Shi, J., Xie, M., Wen, J., Niibe, K., Zhang, X., et al. (2020). *Recapitulation of Cartilage/bone Formation Using iPSCs via Biomimetic 3D Rotary Culture Approach for Developmental Engineering*. Amsterdam: Biomaterials, 260.

Zhang, Y., Song, L., Li, X., and Fang, J. (2018). Flexion-valgus Unicondylar Tibial Plateau Depression Fracture Pattern: Classification and Treatment. *Injury* 49 (4). doi:10.1016/j.injury.2018.03.009

Zhang, Y. Z., Venugopal, J., Huang, Z. M., Lim, C. T., and Ramakrishna, S. (2005). Characterization of the Surface Biocompatibility of the Electrospun PCL-Collagen Nanofibers Using Fibroblasts. *Biomacromolecules* 6 (5). doi:10.1021/bm050314k

Zhao, S., Peng, L., Xie, G., Li, D., Zhao, J., and Ning, C. (2014a). Effect of the Interposition of Calcium Phosphate Materials on Tendon-Bone Healing during Repair of Chronic Rotator Cuff Tear. *Am. J. Sports Med.* 42 (8). doi:10.1177/0363546514532781

Zhao, S., Su, W., Shah, V., Hobson, D., Yildirimer, L., Yeung, K. W. K., et al. (2017). Biomaterials Based Strategies for Rotator Cuff Repair. *Colloids Surf. B Biointerfaces* 157. doi:10.1016/j.colsurfb.2017.06.004

Zhao, S., Xie, X., Pan, G., Shen, P., Zhao, J., and Cui, W. (2015). Healing Improvement after Rotator Cuff Repair Using Gelatin-Grafted poly(L-Lactide) Electrospun Fibrous Membranes. *J. Surg. Res.* 193 (1). doi:10.1016/j.jss.2014.08.019

Zhao, S., Zhao, J., Dong, S., Huangfu, X., Li, B., Yang, H., et al. (2014b). Biological Augmentation of Rotator Cuff Repair Using bFGF-Loaded Electrospun Poly(lactide-Co-Glycolide) Fibrous Membranes. *Int. J. Nanomedicine* 9. doi:10.2147/IJN.S59536

Zhao, X., Chen, X., Yuk, H., Lin, S., Liu, X., and Parada, G. (2021). Soft Materials by Design: Unconventional Polymer Networks Give Extreme Properties. *Chem. Rev.* 121 (8). doi:10.1021/acs.chemrev.0c01088

Zhu, C., Qiu, J., Thomopoulos, S., and Xia, Y. (2021). Augmenting Tendon-To-Bone Repair with Functionally Graded Scaffolds. *Adv. Healthc. Mater* 10 (9). doi:10.1002/adhm.202002269

Zhu, D., Tong, X., Trinh, P., and Yang, F. (2018). Mimicking Cartilage Tissue Zonal Organization by Engineering Tissue-Scale Gradient Hydrogels as 3D Cell Niche. *Tissue Eng. Part A* 24 (1-2). doi:10.1089/ten.TEA.2016.0453

Zhu, J., Shao, J., Chen, Y., Zhao, G., Li, L., Fu, Q., et al. (20212021). Fibrin Glue-Kartogenin Complex Promotes the Regeneration of the Tendon-Bone Interface in Rotator Cuff Injury. *Stem Cells Int*. doi:10.1155/2021/6640424

Zhu, Y., Kong, L., Farhadi, F., Xia, W., Chang, J., He, Y., et al. (2019). *An Injectable Continuous Stratified Structurally and Functionally Biomimetic Construct for Enhancing Osteochondral Regeneration*. Amsterdam: Biomaterials.

Zitnay, J. L., Reese, S. P., Tran, G., Farhang, N., Bowles, R. D., and Weiss, J. A. (2018). Fabrication of Dense Anisotropic Collagen Scaffolds Using Biaxial Compression. *Acta Biomater.* 65. doi:10.1016/j.actbio.2017.11.017

Zurina, I. M., Presniakova, V. S., Butnaru, D. V., Svistunov, A. A., Timashev, P. S., and Rochev, Y. A. (2020). Tissue Engineering Using a Combined Cell Sheet Technology and Scaffolding Approach. *Acta Biomater.* 113. doi:10.1016/j.actbio.2020.06.016

Conflict of Interest: The authors declare that the research was conducted in the absence of any commercial or financial relationships that could be construed as a potential conflict of interest.

The handling editor, KL, and Reviewer, XY, declared a shared parent affiliation with the authors LW, JJ, JC, WS, JCh, JX, YL, JW, JZ, at the time of review.

Publisher's Note: All claims expressed in this article are solely those of the authors and do not necessarily represent those of their affiliated organizations, or those of the publisher, the editors and the reviewers. Any product that may be evaluated in this article, or claim that may be made by its manufacturer, is not guaranteed or endorsed by the publisher.

Copyright © 2022 Wang, Jiang, Lin, Zhu, Cai, Su, Chen, Xu, Li, Wang, Zhang and Zhao. This is an open-access article distributed under the terms of the Creative Commons Attribution License (CC BY). The use, distribution or reproduction in other forums is permitted, provided the original author(s) and the copyright owner(s) are credited and that the original publication in this journal is cited, in accordance with accepted academic practice. No use, distribution or reproduction is permitted which does not comply with these terms.

frontiers | Frontiers in Bioengineering and Biotechnology

REVIEW
published: 13 May 2022
doi: 10.3389/fbioe.2022.895288

Approaches to Biofunctionalize Polyetheretherketone for Antibacterial: A Review

Yihan Wang[1,2], *Shutao Zhang*[1,2], *Bin'en Nie*[1,2], *Xinhua Qu*[1,2] *and Bing Yue*[1,2]*

[1]*Department of Bone and Joint Surgery, Renji Hospital, School of Medicine, Shanghai Jiaotong University, Shanghai, China,* [2]*Department of Orthopedics, Renji Hospital, School of Medicine, Shanghai Jiaotong University, Shanghai, China*

Due to excellent mechanical properties and similar elastic modulus compared with human cortical bone, polyetheretherketone (PEEK) has become one of the most promising orthopedic implant materials. However, implant-associated infections (IAIs) remain a challenging issue since PEEK is bio-inert. In order to fabricate an antibacterial bio-functional surface, modifications of PEEK had been widely investigated. This review summarizes the modification strategies to biofunctionalize PEEK for antibacterial. We will begin with reviewing different approaches, such as surface-coating modifications and controlled release of antimicrobials. Furthermore, blending modifications and 3D printing technology were discussed. Finally, we compare the effects among different approaches. We aimed to provide an in-depth understanding of the antibacterial modification and optimize the design of the PEEK orthopedic implant.

Keywords: PEEK, antibacterial properties, modification technology, polyetheretherketone, implant materials

OPEN ACCESS

Edited by:
Rui Guo,
Jinan University, China

Reviewed by:
Wei Luo,
Donghua University, China
Dejian Li,
Fudan University Pudong Medical Center, China

***Correspondence:**
Bing Yue
advbmp2@163.com

Specialty section:
This article was submitted to Biomaterials, a section of the journal Frontiers in Bioengineering and Biotechnology

Received: *13 March 2022*
Accepted: *31 March 2022*
Published: *13 May 2022*

Citation:
Wang Y, Zhang S, Nie B, Qu X and Yue B (2022) Approaches to Biofunctionalize Polyetheretherketone for Antibacterial: A Review. Front. Bioeng. Biotechnol. 10:895288. doi: 10.3389/fbioe.2022.895288

INTRODUCTION

The ideal orthopedic implant should possess good histocompatibility, good mechanical properties close to bone tissue, good bone–implant integration, and adequate antibacterial property (Liu et al., 2019). Currently, titanium is widely used in orthopedic clinical implants, followed by stainless steel, Mg, and other metals (Kim et al., 2020; Yang et al., 2020). However, the stress shielding effect of metal implants cannot be solved so far, which eventually leads to bone loss and loosening of implants (Heary et al., 2017; Mishchenko et al., 2020). Therefore, it is of great clinical and scientific significance to develop novel orthopedic implant materials. Among these, polyetheretherketone (PEEK) is a widely explored alternative orthopedic implant material. Since it was approved as a medical implant material by the FDA in the late 1990s, many researchers have paid attention to its application prospects in the field of orthopedic (Panayotov et al., 2016).

The average rate of orthopedic implant-associated infections (IAIs) is about 2–5%, even up to 30% of open fractures (Kuehl et al., 2019), which bring serious physical and psychological trauma to patients and generate a lot of medical expenses (Wang and Tang, 2019). Hip and knee arthroplasty has been a very mature technology in the treatment of terminal arthritis. Periprosthetic joint infections (PJIs) are the most serious complication, although the incidence is not high; it can be divided into acute and chronic infection based on the choice of clinical treatment (Otto-Lambertz et al., 2017). Whether the biofilm formatted on the surface of the prosthesis is one of the important factors determining acute or chronic infection needs further investigation. Compared with the treatment of acute infection by antibiotics, the treatment of chronic infection is more difficult. Two-stage revision is still the gold standard at present (Matar et al., 2021). PJI can lead to prosthesis loosening and dislocation, etc., and even if the infection is controlled by treatment, the long-term

Species	Prevalence in medical device infections (%)	Prevalence in knee arthroplasty infections (%)	Prevalence in hip arthroplasty infections (%)	Prevalence in infections involving external fixation (%)	Prevalence in infections involving internal fixation (%)
Staphylococcus aureus	31.7	21.1	22.2	54.5	47.8
	33.8	26.4	24.4	47.8	42.5
	13.0 (EU)[a]–31.0 (US)[a]	12.1 (EU)[a]–29.6 (US)[a]	13.6 (EU)[a]–32.6 (US)[a]	ND	ND
Coagulase-negative staphylococci	20.2 (US)[a]–39.3 (EU)[a]	21.7 (US)[a]–37.0 (EU)[a]	18.4 (US)[a]–40.7 (EU)[a]	ND	ND
Staphylococcus epidermidis	39.0	52.6	48.1	18.2	26.1
	31.5	41.8	43.6	15.2	21.9
Coagulase-negative staphylococci other than *Staphylococcus epidermidis*	11.6	ND	ND	ND	ND
	12.8	ND	ND	ND	ND
Streptococcus spp. and *Enterococcus* spp.	10.3 (US)[a]–14.5 (EU)[a]	10.3 (US)[a]–14.5 (EU)[a]	9.1 (US)[a]–12.1 (EU)[a]	ND	ND
Enterococcus faecalis	2.4	2.6	0.0	0.0	6.5
	4.4	0.5	3.5	8.7	5.3
Gram-negative bacteria	ND	4.5 (EU)[a]–6.4 (US)[a]	4.2 (EU)[a]–6.8 (US)[a]	ND	ND
Pseudomonas aeruginosa	6.1	10.5	3.7	18.2	4.3
	6.7	4.4	2.9	14.1	8.9
Escherichia coli	2.4	5.3	0.0	0.0	0.0
	1.6	ND	ND	ND	ND

EU, data from a European reference clinical setting; ND, not determined; US, data from a US reference clinical setting. [a]Infections after total arthroplasty.

FIGURE 1 | Major bacteria causing implant-associated infections. Reproduced from Arciola et al (2018). Copyright (2018), with permission from Springer Nature.

reoperation rate of joint revision is higher than that of uninfected patients (Clauss et al., 2020). In IAI, the most commonly cultured pathogens are Gram-positive; many other microorganisms can also be found (**Figure 1**). One of the reasons for the poor prognosis of IAI is failing to identify the pathogen species of infection at the first time. In addition, granulation tissue generated around the implant forms the immune depression area, which is prone to infection and colonization (Arciola et al., 2018). This is due to biofilm formation and then diffuses infection of surrounding tissues resulting in poor response to antibiotic therapy and may eventually lead to loosening or even shedding of the implants (Naik et al., 2015). Single-celled bacteria form biofilm through four stages: bacterial surface attachment, small colony formation, bacterial biofilm maturation, and dispersion separation (Bjarnsholt, 2013). The bacteria in the multilayer form of biofilm are in a static or dormant period, so they can resist clinical antibiotic treatment and phagocytes of the immune system (Zimmerli and Sendi, 2017; Masters et al., 2019). Therefore, the formation of bacterial biofilm will seriously affect the role of antibiotics and make treatment difficult. Until now, the incidence rate of IAI has not declined significantly even with strict aseptic techniques and application of broad-spectrum antibiotics (Wang and Tang, 2019). The modifications of implant materials to inhibit the initial bacterial adhesion and the formation of biofilms have great prospects in reducing the rate of IAI. Seeking new antibacterial implant materials is another way (Jiao et al., 2021), which requires abundant research resources. As new material needs to meet the requirements of biomechanics, histocompatibility, and osseointegration, meanwhile, it needs stable chemical properties, easy plasticity, low cost, and convenience for mass production. Consequently, surface biofunctionalization including chemical and physical modifications by antibacterial nanoparticles or compounds of existing approved materials to achieve antibacterial properties is a more efficient approach.

PEEK is an ideal bone substitute material due to its bio-inert property, safety, non-toxicity, wear-resistance, transmit radiation, strong plasticity, and mechanical properties close to the human cortical bone (Ya-Shum et al., 2018; Ma Z. et al., 2020; He et al., 2021). It had been successfully used as a biomaterial for arthroplasty construction and trauma and dental implant applications (**Table 1**). However, it also has drawbacks, for example, the unique structure leads to surface hydrophobicity that inhibits protein and cell adhesion (Ji et al., 2020), resulting in poor osseointegration and failure of the implant (Liao et al., 2020). In addition, it is easier to colonize bacteria and form biofilms due to its bio-inert property (Bock et al., 2017). Therefore, to make PEEK more suitable for orthopedic implant materials, it must be biofunctionalized to improve biocompatibility, osseointegration, and antibacterial properties. In recent years, the development of biomaterial modification has been greatly promoted relying on the

TABLE 1 | Clinical application of PEEK as implant.

Material	Model	Application	Patient	Observation	Outcome	Reference
Porous PEEK	3D-printed CAD models	Sub-periosteal implants in buccal cavity	5 patients	Follow-up for 12 months	All implants were not showing any signs of mobility, infection, or prosthetic fracture	Mounir et al. (2018)
PEEK-on-highly cross-linked polyethylene	Injection-molded	Joint prosthesis for TKA	10 patients (9 females and 1 male) with mean age 66.9 years	Imaging evaluations (10 cases at 1 and 3 months; 7 cases at 6 months)	The condition of periprosthetic bone volume and prosthesis position can be well assessed	Cai et al. (2022)
PEEK cage	—	Lumbar fusion with the interbody cage	1,094 patients (673 patients using a PEEK cage, while others using a Ti cage)	Meta-analysis from 11 studies	PEEK cage associated with lower odds of leg pain but lower fusion rate; no difference in subsidence rates and (VAS)-low back pain	Massaad et al. (2020)
Pure PEEK	3D-printed CAD model	Scapular prosthesis after tumor resection	A 16-year-old male	Follow-up at 1 month and 3 months	Constant shoulder score (CSS) was 68 points; the X-ray of the normal position of the shoulder joint; and no complications	Liu et al. (2018)
Pure PEEK	3D printed	Clavicle prosthesis after excision due to osteomyelitis	A 23-year-old female	Follow-up for 2 years	Pain VAS was 0/10 at 3 months; CSS was satisfactory with 88 points; no implant loosening or other complications during 2 years	Chang Chen et al. (2021)

progress of nanotechnology (Hochella et al., 2019). Modified biomaterials, such as nano-hydroxyapatite, have shown improved osseointegration over micro-hydroxyapatite (Panayotov et al., 2016; Lowe et al., 2020). PEEK also can get better modification effects and less inflammatory reaction due to nanotechnology (Gu et al., 2020). Nowadays, a large number of research studies have been carried out successfully *in vitro* and *in vivo* (Torstrick et al., 2018; Chepurnyi et al., 2020; Liu et al., 2020), but there is still a lack of in-depth understanding of the modification of antibacterial properties.

The clinical application of PEEK implants has continuously reported cases of infection (Roman et al., 2014; Chen et al., 2019; Tarallo et al., 2020; Hacherl et al., 2021). In this review, we focused on the antibacterial modification strategies of PEEK. Meanwhile, the biocompatibility and osseointegration are also taken into consideration on that the rapid integration of implant and surrounding tissue being crucial for preventing bacterial adhesion and colonization (Stones and Krachler, 2016). Because the implants cannot be absolutely sterile due to exposure to the air during the operation and there is no guarantee of any microbial colonization in the body for decades, only antibacterial modifications of the implant surface are futile. The formation of bacterial biofilm can be regarded as the competition of adhesion between bacteria and surrounding tissue cells (Subbiahdoss et al., 2009; Busscher et al., 2012), which was called "race for the surface," as first proposed by Gristina (1987). Ultimately, the objective of this article was to discuss the advantages and disadvantages of different modifications hoping to inspire and reference future research in this field.

Current Research on Biofunctionalized PEEK With Antibacterial

At present, there are many approaches to biofunctionalize PEEK for antibacterial, and fruitful results have been achieved (Poulsson et al., 2019). According to the biofunctionalization approaches as well as 3D printing technology, it can be divided into chemical modification and physical modification (**Figure 2**). Chemical modification is to functionalize the PEEK with antimicrobial particles or antimicrobial compounds. Physical modifications include changing the PEEK surface structure and particle blending and injection molding to form composites to meet application requirements. The authors screened the parts involving antibacterial properties in PEEK modification research in recent years, summarized, and discussed them hierarchically.

Chemical Modification

Nanoparticle Coating

The coating technique is the earliest and most widely used in PEEK surface modifications, such as magnetron sputtering (Liu et al., 2017), plasma treatment (Zhang Y. et al., 2021), and bioglass immobilization (Huo et al., 2021b). The advantage is that it can directly improve the biocompatibility, osseointegration, and antimicrobial properties of the PEEK, without destroying the mechanical properties of its matrix. However, there are drawbacks, such as the risk of coating peeling, which may lead to bone resorption and implant failure (Niu et al., 2020), and the cytotoxic risk of metal particles (AshaRani et al., 2009). To minimize the excessive absorption of metal particles, improvements can be made in terms of enhancing the firmness of the coating and the controlled release of the minimum effective concentration of metal ions. At present, there are two main ideas. One is to make nano-metal particle composites to enhance their adhesion. It is reported in the literature that silver nanocluster–silica composite was sprayed on the surface of PEEK composites by radio frequency sputtering. It was proved that it retained good antibacterial properties by bacterial experiments *in vitro*, while improving the stability of the coating, and silica regulating the release of silver ions, thereby

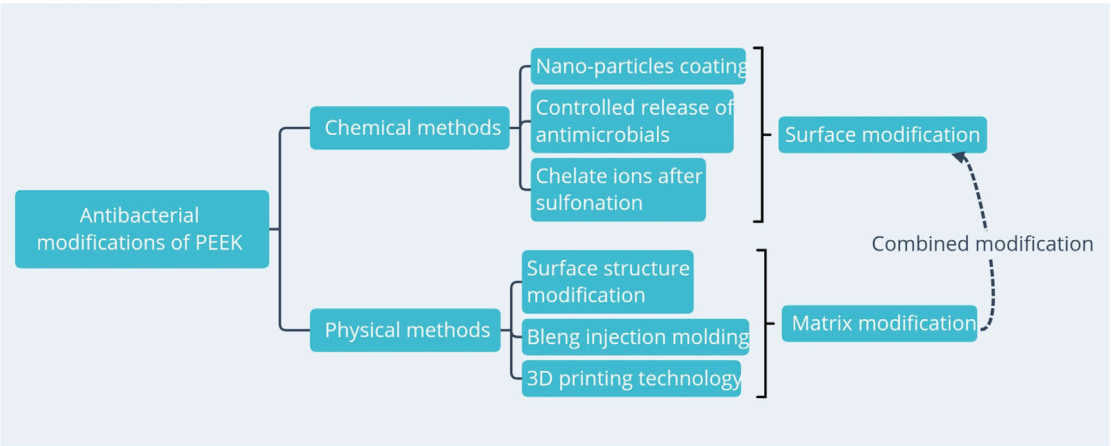

FIGURE 2 | Current research on biofunctionalized PEEK with antibacterial.

reducing cytotoxicity (Ur Rehman et al., 2017). Another approach is adding a controlled release coating on the particles to achieve the purpose of stabilizing the metal nanoparticles and controlling the release of metal ions. J. Kratochvíl and other scholars deposited copper nanoparticles on the surface of PEEK and further coated it with the fluorocarbon plasma polymer (C: F) film. The experimental results showed that when the thickness of the composite coating was 10 nm, it not only increased the coating stability and controlled release but also retained the antibacterial properties of copper ion and hindered the formation of biofilms (Kratochvíl et al., 2018). The same approach can be applied to silver nanoparticle coatings (Kylian et al., 2017). However, considering that orthopedic implants often exist in the human body for several years or even decades, no matter how low the cytotoxicity is in the short term, the risk of long-term excessive release and absorption of metals must be considered and verified. There is currently a lack of long-term *in vivo* trials of surface-modified PEEK coated with nano-metallic particles, thus lacking strong evidence for an in-depth discussion of its safety and antibacterial efficacy.

To avoid the cytotoxicity of metal particles, some researchers have explored non-metallic nanoparticles with antibacterial activity. Wang et al (2016) prepared red selenium and gray selenium nanocoatings on the surface of PEEK and found that short-term (<3 days) inhibited *Pseudomonas aeruginosa*, which could reduce infection and inhibit the formation of biofilms. Compared with nano-Ag particles, selenium nano-ions have been proven to be healthier, safer, and less cytotoxic (Perla and Webster, 2005). Buwalda et al (2020) immobilized ethylene glycol and dimethylamino ethyl acrylate on the surface of PEEK by UV radiation, and *in vitro* experiments demonstrated that it had a good inhibitory effect on *E. coli* and *S. aureus*. Non-metallic coatings also need to consider the antibacterial efficiency, such as the antimicrobial peptide of GL13K and 1-ethyl-3-(3-dimethyl aminopropyl) carbodiimide-mixed coating, of which 1-ethyl-3-(3-dimethyl aminopropyl) carbodiimide-mixed coating exhibited better antimicrobial performance than pure GL13K coating (Hu et al., 2021). Our group also carried out some work on biofunctionalized PEEK. We found that the PEEK surface modified with hydrofluoric acid and nitric acid (AFN) could promote M2 polarization of the macrophages and stimulate the differentiation of osteoblasts (Huo et al., 2021a).

In addition to that, PEEK was biofunctionalized with mesoporous bioactive glass (MBG) and loaded with A-485 for attenuating inappropriately activated immune responses and inhibiting osteoclastogenesis, thus promoting osteogenesis (**Figure 3**). Also, this MBG could also perform as long-lasting antibacterial agents for antibacterial. The advantage of PEEK surface coating modification is that the approach is simple and conducive to large-scale production, but the release of functional particles, the cytotoxicity of exfoliated particles, and the tissue inflammatory response still require in-depth research and long-term observation in the animal *in vivo* experiments.

Controlled Release of Antimicrobial Agents

The most common modification for antibacterial compounds or drugs is further polymerization on porous PEEK surfaces by polydopamine (PDA) coating. Polydopamine is inspired by mussels foot proteins and reported by Lee et al (2007) and has rapidly become a widely used method for surface decoration of materials, which can form functional nanocoatings on almost all material surfaces and can further polymerize other compounds (El Yakhlifi and Ball, 2020). Moreover, PDA coating exhibits synergistic antibacterial properties and can be used for photothermal therapy (Niyonshuti et al., 2020; Singh et al., 2020); thus, it has enormous potential in the biomedical field. The PEEK-PDA surface after antibacterial modification has also been proved with good biocompatibility and osseointegration (**Table 2**).

Silver nanoparticles (AgNPs) can destroy bacteria walls (Choi et al., 2008). AgNPs were reduced from $[Ag(NH3)2]^{+}$ utilizing the reducibility of the catechol in PDA, which exhibited superior and long-term antibacterial properties against *E. coli and S. aureus. However,* there were no notable differences in not only pro-

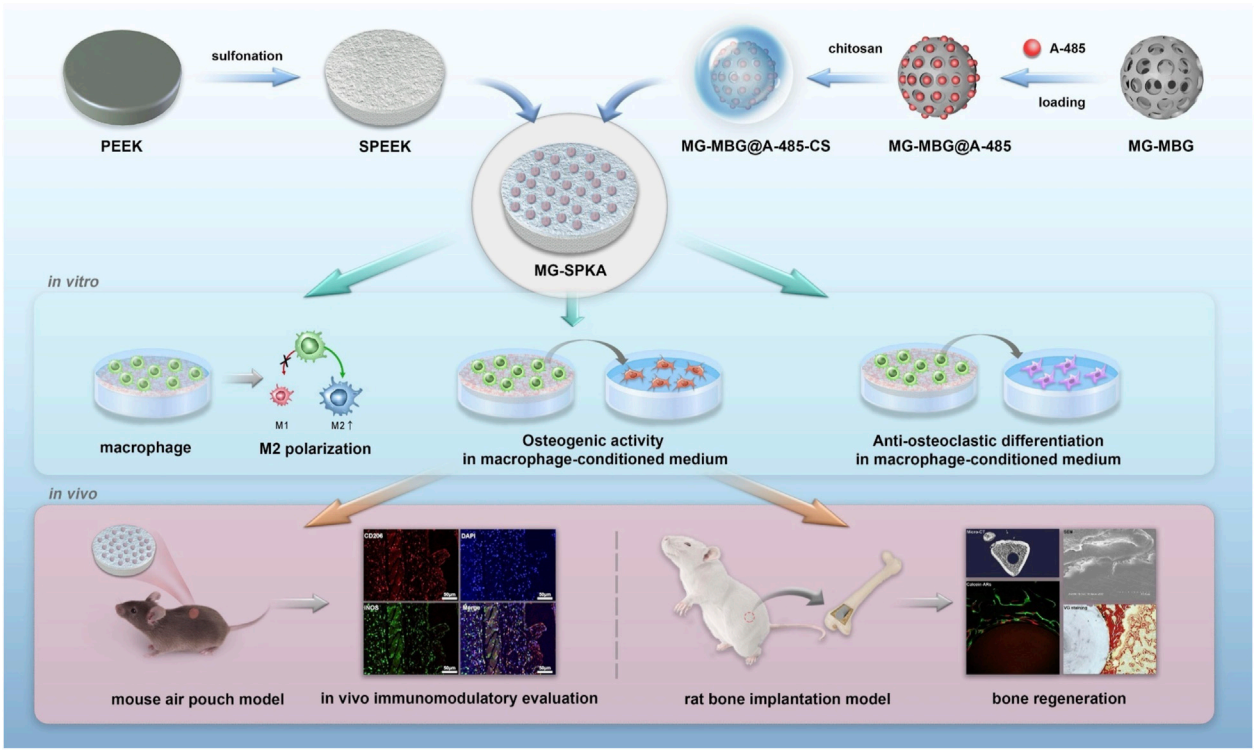

FIGURE 3 | Schematic diagram of the process used to prepare and evaluate the PEEK materials. Reproduced from Huo et al (2021c). Copyright (2021), with permission from Elsevier.

inflammatory but also anti-inflammatory gene expression between PEEK–PDA–Ag and blank groups which was significantly lower than that in the PEEK group due to the immunosuppressive effect of AgNPs (Gao et al.bgmj, 2017). In addition to antibacterial nanoparticles, integrating antibiotics are also one of the common modification approaches without worrying about the toxicity of metal ions. Sun et al (2021) prepared the SP-GS/PDA functional surface, which rapidly released gentamicin (GS) in the SBF solution. Its antibacterial activity sustained high during the initial 3 days but lost on day 4 due to the little residual content of GS. The long-term stable release of antibiotics with sub-lethal concentration is an urgent problem to be solved. However, Yan et al. (2018) explained different experimental results, and they believed that during the first day, neither AgNPs nor GS alone improved antibacterial activity significantly, yet the combination of them enhanced the antibacterial properties greatly. Thereafter, surface modification with AgNPs and copper oxide microspheres (μCuO) was explored. Yan et al (2020) proposed SP-CuO/Ag-enhanced osteogenesis while ensuring antibacterial properties. It can be seen that the effect of combined modification by multiple antibacterial particles is not a simple superposition, which needs further experimental exploration in the future. The biofunctionalized PEEK which is suitable for implant needs to not only enhance antibacterial properties but also improve histocompatibility and bone osteointegration. Some scholars have made attempts in this regard: Xu X. et al. (2019) considered that dexamethasone (DEX) was an osteoinducing and anti-inflammatory factor easing foreign body response to PEEK implants. They prepared PEEK-DEX/Mino liposome that was proved to be anti-inflammatory and osteogenic besides not reducing antibacterial properties. Modification of combined antibacterial metal nanoparticles was also explored. Compared with Zn−Mg-MOF74/PDA composite, DEX@Zn−Mg-MOF74/PDA composite coating on PEEK showed similar antibacterial properties but better osteogenic gene expressions (OPN and OCN) of rBMSCs observed by RT-PCR (Xiao et al., 2021). PDA coating has the advantage of simple operation and can integrate a variety of modification factors through interlayer. However, these experiments lack research on the wear resistance and stability of PDA coating. Chen et al. believed that the binding strength could be improved by argon plasma surface modification before PDA coating onto the PEEK (Chen et al., 2021). More similar attempts need to be verified in the future.

In addition, other coating modification techniques have also been applied: lawsone, an antibacterial compound that can be applied topically *in vivo* (Sultana et al., 2021), was made into a suspension with the bioactive glass powder and chitosan by Ur Rehman et al. (2018). It was found that lawsone maintained good antibacterial properties without affecting the biological activity of the material itself. Brushite (CaHPO4·2H2O) and gentamicin were coated on PEEK through a layer-by-layer (LBL) method with varied cycles. The antibacterial efficiency and osseointegration ability exhibited differences due to the

TABLE 2 | Controlled release of antimicrobial agents on the PEEK-PDA (2 mg/ml dopamine hydrochloride) surface.

Ion	Sample	Method	Bacterial strain	Antibacterial test	Antibacterial property	Mechanism	Biological effect	Reference
AgNPs	Tollens' reagent (0.02 mol/L) [ammonia into $AgNO_3$ solution (0.02 mol/L)]	PEEK-PDA immersed in the Tollens' reagent for 30 min	*E. coli* , S. *aureus*, and S. *aureus*	Plate counting and SEM IAI model in rat femur	97.9 ± 0.8% 99.8 ± 0.1% (antibacterial rate) *S. aureus* growth was significantly inhibited on the surface	Fast Ag+ release initially, then slow release for long-term	Showed low toxicity to MC3T3-E1 cell and possessed good biocompatibility and osseointegration	Gao et al. (2017)
AgNPs、SF/GS	$AgNO_3$–gentamicin (500 lg/mL in PBS) and silk fibroin	SP–PDA–Ag immersed into gentamicin followed by three silk layers	*E. coli* and S. *aureus*	Plate counting and SEM	Greatly enhanced the antibacterial effects and antiadhesion ability	The release rate of Ag+ and GS increased with decreasing pH	PDA and silk fibroin can balance cytocompatibility and antibacterial ability	Yan et al. (2018)
KR-12	KR-12 solution (1 mg/ml in 10 mM Tris–HCl buffer)	PEEK-PDA immersed in KR-12 solution under reverse nitrogen (N_2) flow overnight	S. *aureus* and S. *aureus*	Plate counting and SEM IAI model in rat femur	Effectively inhibited bacteria proliferation and biofilm formation *in vitro* and *in vivo*	Release of KR-12 which has a broad spectrum of antibacterial activity	rBMSCs: improved adhesion, proliferation, and osteogenic differentiation; in vivo: promoted osteointegration in rat femur	Meng et al. (2020)
GS	PDA and GS diluted in Tris–HCl solution (2 mg/ml and 3 mg/ml)	SPEEK was immersed in the left solution for 12 h	*E. coli* , S. *aureus*, and S. *aureus*	Plate counting IAI model in rat femur	Continuous antibacterial abilities. Imaging showed no evidence of osteomyelitis	GS release	Possessed good biocompatibility and the immunoregulatory ability	Sun et al. (2021)
Mino liposomes	Minocycline (Mino), liposome, and dexamethasone (DEX)	PEEK-PDA immersed in the Dex/Mino liposome solution obtained by the thin-film hydration method	S. mutans, P. gingivalis, and S. mutans	Plate counting and microbial viability assay kit-WST subcutaneous infection model of rats	Improved the antibacterial activity and inhibited the initial adhesion. The antibacterial efficiency was about 97.4%	Liposomal Mino releasing and benign cell adhesion on the functionalized PEEK surface	*In vitro*, improved osteogenic differentiation of human mesenchymal stem cells. *In vivo*, enhanced osteointegration	Xiao Xu et al. (2019)
Zn^{2+}–Mg^{2+}	$Mg(NO_3)_2{\cdot}6H_2O$、$Zn(NO_3)_2{\cdot}6H_2O$、2,5-dihydroxy-terephthalic acid (DHTA) dexamethasone (DEX)	PEEK-PDA was dipped in Zn–Mg-MOF74 composite obtained by hydrothermal synthesis and then coated by DEX	*E. coli*, S. *aureus*, and S. *aureus*	Plate counting and SEM fluorescence microscope subcutaneous infection model of rats	Significantly inhibited bacterial proliferation. Much smaller number of bacteria	Mg^{2+}, Zn^{2+}, and DHTA release. The alkaline microenvironment due to the coating degradation	Improved vascularization and osteogenic differentiation	Xiao et al. (2021)
Van-GNPs	vancomycin (Van)–Gelatin nanoparticles (GNPs)	Plasma modification (PDA/P-PEEK) combines two-step desolvation (Van-GNPs)	*S. aureus* and S. mutans	Plate counting and SEM	Inhibited bacteria adhesion and the cell membrane bursted on the Van-GNPs/ PEEK surface	Vancomycin release	Good osteogenesis without cytotoxicity	Tianjie Chen et al. (2021)

(Continued on following page)

TABLE 2 | (*Continued*) Controlled release of antimicrobial agents on the PEEK-PDA (2 mg/ml dopamine hydrochloride) surface.

Ion	Sample	Method	Bacterial strain	Antibacterial test	Antibacterial property	Mechanism	Biological effect	Reference
AgNPs–μCuO/SF	$Cu(NO_3)_2 \bullet 3H_2O$、AgNO3, Silk fibroin SPEEK	μCuO was prepared by hydrothermal solution followed by polymerization	*E. coli* and S. *aureus*	Plate counting and SEM	Effectively inhibited bacteria adhesion and biofilm formation	Cu^{2+} and Ag^{+} release	Showed better osteogenesis in the rabbit tibial defect model	Yan et al. (2020)

TABLE 3 | Sulfonated PEEK further chelates antibacterial ions.

Ion	Sample	Method	Bacterial strain	Antibacterial test	Antibacterial property	Antibacterial mechanism	Biological effect	Reference
GO	Graphene oxide powders	Dip-coating in GO–water suspension	*E. coli* and S. *aureus*	Plate counting and SEM	Effectively inhibited the proliferation of *E. coli* but failed S. *aureus*	Creates a neutralized surface state; induce oxidative stress and membrane stress	Higher ALP and osteogenic differentiation-related genes activity and more calcium nodule formation	Ouyang et al. (2018)
Ag^{+}/Zn^{2+}	Nacl, Alginate/Ag^{+}, and Chitosan/ZnO	Layer-by-layer on SPEEK (dip-coating)	*E. coli* and S. *aureus*	Plate counting and SEM	Greatly suppressed the growth of bacteria	The nano-Ag-containing interface and chitosan in conjunction	Enhanced expression of MG-63 ALP and osteogenesis-related genes	Deng et al. (2018)
SB	Sodium butyrate (SB)	Immersed into different concentrations of SB solution	S. *aureus* and S. *aureus*	Plate counting and SPM osteomyelitis model in rat femur	Significantly inhibited bacterial proliferation	The increased phagocytic activities of macrophages and ROS production	Enhanced osteogenic differentiation of rBMSCs and reduced bone destruction and osteolysis *in vivo*	Yang et al. (2019)
Ag^{+}/ZIF-8	$Zn(NO_3)_2$ $AgNO_3$ 2-methylimidazole (Hmim)	*In situ* growth (SPEEK@ZIF-8) and then self-assembled Ag^{+} layer by layer	*E. coli* and S. *aureus*	Plate counting and FESEM	Extraordinary antibacterial ability	Steady release behavior of Ag^{+} and Zn^{2+}	The cytotoxic effect of SPZA was slightly greater than that of SP due to the high concentration of bimetal ions	Yang et al. (2022)
MBD-14	MBD-14 lyophilized powder dissolved in phosphate-buffered solution	Dropped on hydrothermally treated SPEEK then lyophilized	S. *aureus*, *P. aeruginosa*, S. *aureus*, and *P. aeruginosa*	Plate counting and SEM osteomyelitis model in rat femur	Excellent antibacterial properties. Antibacterial effect increased with the concentration of MBD	MBD-14 long-term release	The expression of osteogenic differentiation-related genes and proteins was enhanced with increased MBD-14 concentration	Yuan et al. (2019)
Li^{+}/AMP	LiOH- $DOPA_4$-PEG_5-RWRWRW peptide solution	Layer-by-layer on SPEEK (dip-coating)	*E. coli,* S. *aureus*, and S. *aureus*	Plate counting, SEM, and TEM osteomyelitis model in rat femur	Inhibited the bacteria adhesion and survival antibacterial efficiency reached 95.03%	AMP sequence, RWRWRW, can kill bacteria	Li^{+} promoted the osseointegration and osteogenic differentiation activity	Ning Li et al. (2021)
SA (CGA)/BFP	SA and CGA solution (4 mg/ml) grafted with BFP	Dip-coating then activated by EDC and NHS in MES buffer	*E. coli* and S. *aureus*	Plate counting and SEM	Noticeable antibacterial effect and inhibited the bacteria adhesion	CGA release	SA enhanced biocompatibility and BFP stimulated the proliferation and differentiation of osteoblasts	He et al. (2019)

number of cycles (Xue et al., 2020). Different modification techniques will change the release concentration and time of antimicrobial compounds. Considering that too high concentration of a local drug may affect bone healing and produce cytotoxicity and very long release time may lead to local bacterial resistance. Ideal antimicrobial compound coating

modification should have broad-spectrum antibacterial, low toxicity, controlled release at minimum effective concentration, and ideal release time. In addition, some problems in this modification method to be verified are: whether the coating is stable; whether the antibacterial activity and release rate will be affected *in vivo*; as a bone implant, it will withstand different stress and friction; whether it can maintain the effective antimicrobial drug concentration per unit area. In a word, the surface coating approaches of PEEK antibacterial modification have been fruitful, but so far, most of the research is based on *in vitro* experiments, and the safety and effectiveness of *in vivo* experiments, especially under biomechanics conditions still lack long-term observation.

Chelated Antibacterial Ions After Sulfonation of PEEK

Sulfonated PEEK (SPEEK) fabricated by concentrated sulfuric acid makes the surface of PEEK form a negatively charged (-SO3H) interface, which repels the bacterial biofilm that is also negatively charged, thereby having antibacterial properties (Tomoglu et al., 2019). In addition, it can rely on ionic bonds to further chelate antibacterial ions to improve antibacterial performance (**Table 3**). Compared with the multi-coating adhesion methods, this approach retains the three-dimensional micro-nanostructure of the contact interface and may have stronger coating stability because of the chelation of positive and negative ion bonds. Silver is still one of the most widely used ions, and scholars have been exploring more synergies with other particles (Sikder et al., 2018; Yu et al., 2021). For example, compared with Ag-SPEEK, Ag/Zn-SPEEK (dual Ag^{+} and Zn^{2+}-decorated SPEEK) retained similar antibacterial properties but showed better cytocompatibility and osseointegration (Deng et al., 2018). In addition, the multiple assembly methods of modified ions produced different effects. Yang et al. (2022) fabricated zeolitic imidazolate framework-8 (ZIF-8) on SPEEK from 2-methylimidazole and Zn^{2+}, which possessed a high Ag^{+}-loading capacity. Experimental results demonstrated that SPZA had more effective antibacterial properties. The improvement of antibacterial activity was obtained not only by the synergy between different metal ions but also by the mixed modification of metal ions and antibacterial compounds. Li^{+} could enhance cell attachment, proliferation, differentiation, and implant–bone interface osseointegration of the antibacterial AMP coating on SPEEK (Li N. et al., 2021). Considering that antibiotics may lead to drug resistance and metal particles may lead to cytotoxicity, scholars pay attention to antimicrobial peptides (AMPs). However, AMPs are easily inactivated attributing to inducing autoimmune responses (Brandwein et al., 2017); consequently, an AMP from human elements is crucial to endophyte application. Recombinant mouse beta-defensin-14 (MBD-14) which has high homology as well as human beta-defensin-3 (HBD-3) was embellished on the SPEEK. The experimental result indicated that SP-MBD had good antibacterial activity, biocompatibility, and osteogenesis (Yuan et al., 2019). According to this idea, Yang et al. (2019) loaded sodium butyrate, a fermentation product of gut microbiota, onto the SPEEK surface and found that SB-SPEEK exhibited superior anti-infection capacity and induced new bone formation *in vitro and in vivo*. We can also combine AMPs and osteogenic promoters. Chlorogenic acid (CGA) has excellent antibacterial properties, and grafted peptide (BFP) is one of the most effective bone-inducing growth factors. He et al. (2019) fabricated a hydrogel of compound coating with sodium alginate (SA) on the SPEEK surface and revealed that SPEEK@SA (CGA)@BFP effectively inhibited bacterial proliferation and showed better bioaffinity. Any antibacterial modification method cannot sacrifice bone integrity and biocompatibility, and the detection of cytotoxicity is a crucial experiment before entering the clinical trial. Therefore, the research on antibacterial substances from biological sources has broad prospects.

However, sulfur may have negative effects on the human body, such as the synthesis of low-valent sulfurous compounds, to generate oxygen-free radicals, and damaged cells (Meng et al., 2005). Therefore, whether the corrosion and chemical composition changes of PEEK caused by concentrated sulfuric acid sulfonation can meet the safety requirements of long-term *in vivo* bone implants is worthy of further study. The balance of safety and antibacterial properties was explored by Ouyang et al. (2016). The research team washed SPEEK with water at different temperatures to obtain different residual sulfide concentrations on the surface. The higher the water temperature, the lower the residual sulfide concentration. *In vitro* experiments found that the antibacterial properties of SPEEK after treatment were not significantly reduced, especially the inhibitory effect on *Staphylococcus aureus*. The *in vivo* result was consistent with the *in vitro* experiments. In addition, the porous structure of SPEEK may have a profound impact on its biological properties. However, there is a lack of biomechanical research on bifunctional SPEEK in the aforementioned studies.

Physical Modification

Surface Structure Modification

As mentioned in the introduction, the surface structure of PEEK affects cell adhesion and is prone to bacterial film formation. When bacteria attach to nanopillars smaller than their volume, the bacterial wall will rupture (Wang et al., 2017), so the formation of a micro-nano three-dimensional structure can enhance its biological activity and antibacterial properties. At present, there are many approaches to modify the surface structure of PEEK, such as UV irradiation, plasma treatment (Liu et al., 2021), fluorination (Chen et al., 2017), and nitration (Li et al., 2019), while all reported excellent antibacterial properties. The most widely used approach is sulfonation. Different sulfonation times can form different nano-network structures on the surface of PEEK, which can improve biocompatibility. But too long sulfonation time will lead to a disordered porous structure (**Figure 4**). The literature proved that sulfonation for 5 min was the ideal time to modify the surface structure of PEEK (Ma R. et al., 2020). In addition, based on sulfonation, other structural modification methods such as plasma shock can be combined to form three-dimensional micro-nanostructures with specific functional groups, which can further improve cell adhesion and antibacterial activity (Wang et al., 2018).

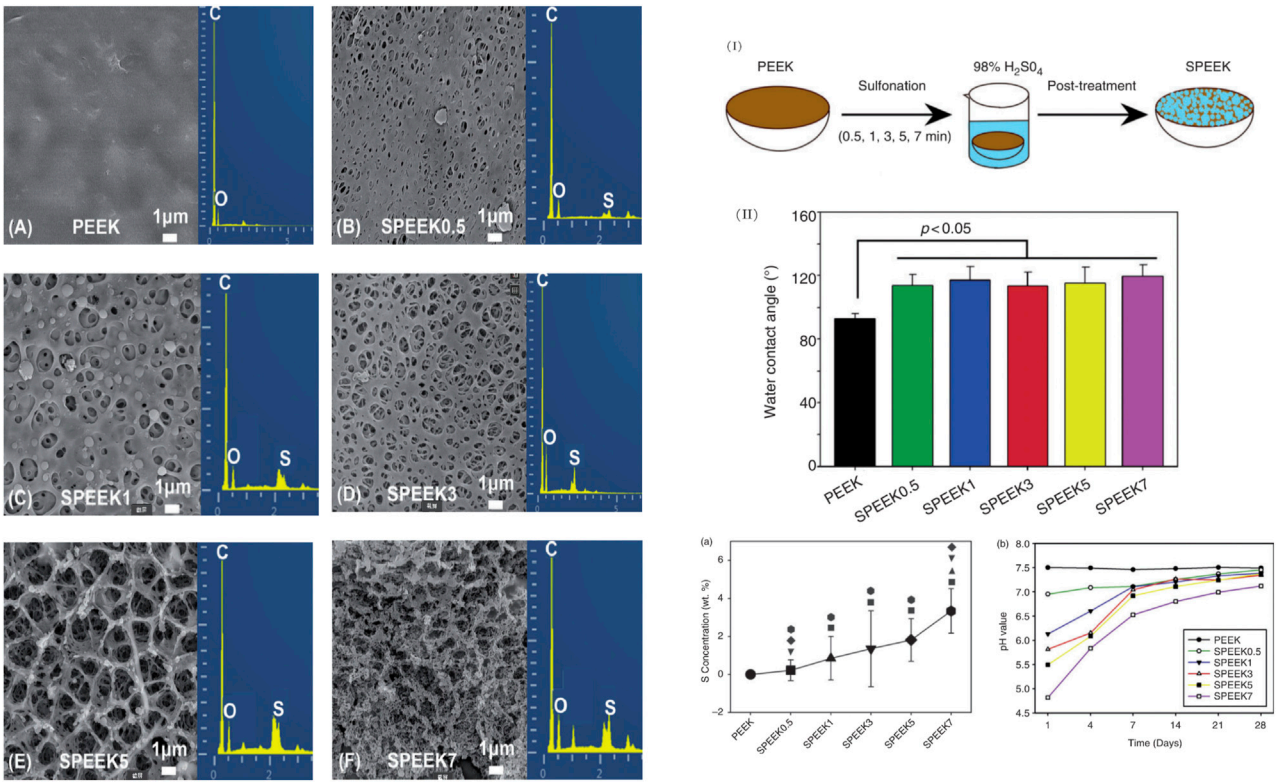

FIGURE 4 | Sulfonation of PEEK. **(I)** Sulfonation times: 0.5 min (SPEEK0.5), 1 min (SPEEK1), 3 min (SPEEK3), 5 min (SPEEK5), and 7 min (SPEEK7); untreated PEEK as the control. **(II)** Quantitative comparison of water contact angles. (a) S concentration of each group measured by EDS (the marks represent $p < 0.05$); (b) pH values at 1, 4, 7, 14, 21, and 28 days. **(A–F)** Morphology of the SPEEK surface characterized by SEM (left row) and chemical composition characterized by EDS (right row). Reproduced from Ma R. et al (2020). Copyright (2020), with permission from SAGE Publications.

Blend Injection Molding

Blending modification is to mix inorganic active substances into organisms to form biocomposites. This method has been proven by research studies to apply to the modification of bone endophytes and improve osteogenic activity and biocompatibility (Hajiali et al., 2017; Pang et al., 2019). Blend injection molding is characterized by improving the biomechanical properties of PEEK. As we know, the elastic modulus of pure PEEK (3.7–4.0 GPa) is lower than that of human cortical bone (7–30 GPa) (Ching et al., 2009). Tantalum is one of the metal materials that have been a hot topic studied in recent years. It has excellent histocompatibility and osseointegration, but the elastic modulus is too high. Scholars combined tantalum and PEEK into composite materials that proved to have good osseointegration and mechanical properties but with limited antibacterial property (Zhu et al., 2019; Hu et al., 2022). The antibacterial properties and osteogenic activity were further enhanced by further chelating the antibacterial compound genistein after sulfonation (Mei et al., 2021; Luo et al., 2022). Therefore, we believe that the relevant research on injection molding after particle blending should be tested to explore the changes in biomechanics.

At present, the antibacterial properties of blending modification have been extensively explored such as the common blending with antibacterial metal particles. PEEK and nano-zinc–magnesium silicate (nZMS) in different proportions have good antibacterial properties. When the nZMS content is 50%, the best antibacterial properties and mechanical properties are obtained (Tang et al., 2019). However, some scholars have found that metal particles affect histocompatibility or osseointegration performance after blending, so non-metallic particles are used. Silicon oxide and Si_3N_4 particles were incorporated into PEEK by melt blending, which had proved good antimicrobial properties with improved biocompatibility and osteogenic properties (Pezzotti et al., 2018; Hu et al., 2022). In addition to nanoparticles, antibacterial compounds can also be modified by blending: it was reported that chitosan, nanohydroxyapatite, and PEEK were made into mixed suspensions with different ratios, and all of them had good antibacterial effects on *S. aureus* and *E. coli*; moreover, chitosan could increase the stability of nanohydroxyapatite–PEEK binding (Abdulkareem et al., 2019). Blending modification still needs further research. In addition to the changes in biomechanical properties mentioned previously, most of the bioactive substances by blending modification are located in the matrix, which cannot be guaranteed with uniform and effective distribution, so the improvement of the surface properties is limited. For example, silver nanoparticles-coated

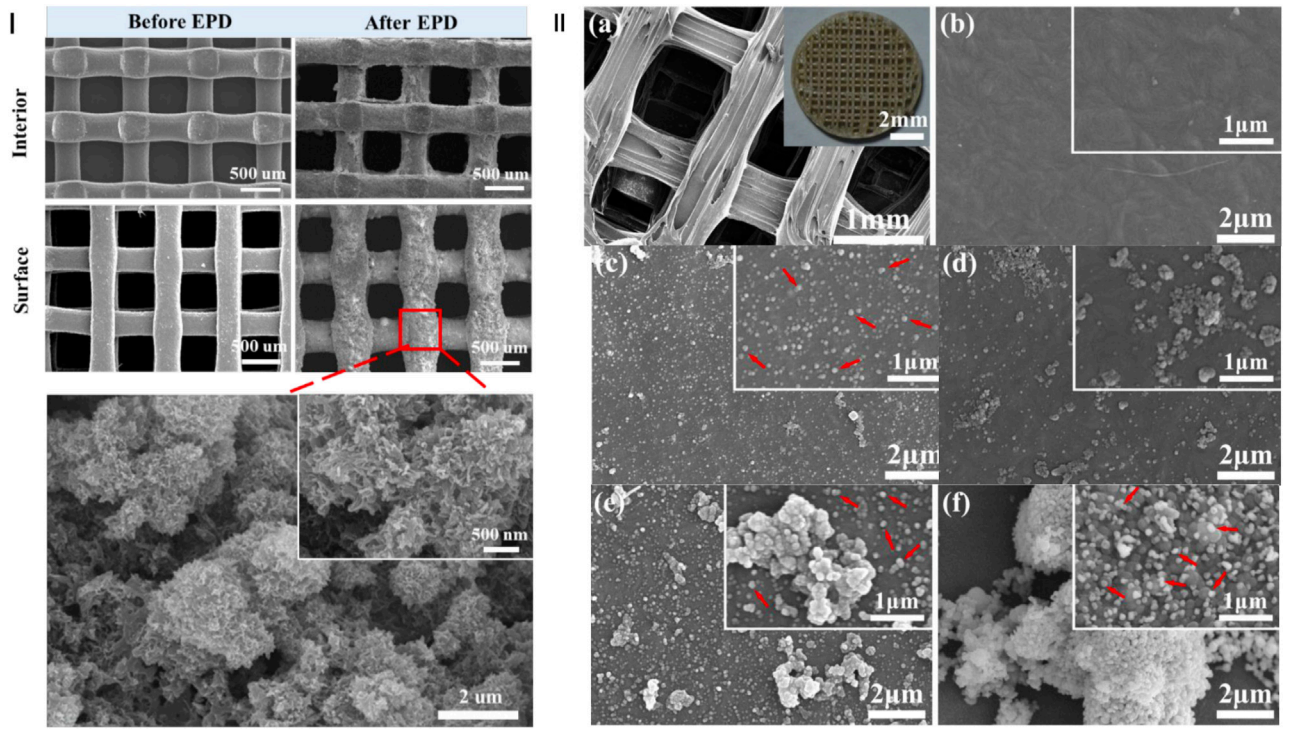

FIGURE 5 | Modification of 3D-printed PEEK. **(I)** SEM images of the 3D-printed PEEK/graphene composite scaffold before and after drug-laden hydroxyapatite-coating deposition. Adapted with permission from Zhu et al (2021). Copyright (2021) American Chemical Society. **(II)** SEM overview of the 3D-printed PEEK scaffolds. **(A)** SEM zoom images, **(B)** 3D-printed PEEK, **(C)** AgNP-decorated PEEK, **(D)** apatite-decorated PEEK, **(E)** "PDA–Ag–PDA–apatite" multilayers on PEEK, and **(F)** "PDA–apatite–PDA–Ag" multilayers on PEEK. Red arrows point to AgNPs. Adapted with permission from Deng et al (2020). Copyright (2020) American Chemical Society.

PEEK has been shown to have antibacterial activity. However, the composite-mixed silver nanoparticles or silver ions with the PEEK powder through injection molding exhibited uneven particle distribution and failed to inhibit the bacteria adhering to the surface of the PEEK composite (Jaekel, 2012). To solve this problem, we can make improvements in two aspects. One is through the modification of the surface structure; the PEEK composite will form a micro-nanostructure on the surface, which can make the co-polymer-mixed particles obtain greater surface exposure, resulting in improved bioactivity and antimicrobial properties (Niu et al., 2020). Another approach is injection molding by 3D printing technology with a reasonable distribution of particles. It can be concluded that the modification of PEEK does not need to be limited to a single approach, and the synergy of two or even more modification methods can be explored, which provides more and better possibilities for the development of PEEK implant.

Some nanomaterials can generate heat under the irradiation of near-infrared light to inhibit bacterial growth. The blending modification of PEEK and photothermal materials can be applied to photothermal therapy. Most bacteria die at 55°C due to protein denaturation (Pan et al., 2016). At the same time, near-infrared rays can penetrate tissue well with high safety. Taking advantage of these properties, the research on antibacterial properties of nanomaterials with photothermal effects has grown exponentially in recent years, such as graphene composite nanomaterials and noble metal particles or compounds (Xu J.-W. et al., 2019; Song et al., 2020). Among them, graphene and its derived materials also have a good drug-controlled release effect (Mousavi et al., 2020). Photothermal materials have broad prospects in the field of biomedicine.

3D Printing Technology

At present, 3D-printed PEEK implants have entered medical application (Basgul et al., 2018; Atef et al., 2021), which have also been extended to composites mixed with other bioactive particles (Oladapo et al., 2020; Manzoor et al., 2021; Rodzeń et al., 2021b), which can achieve mechanical properties close to human cortical bone and good contact interface biological activity (Li S. et al., 2021; Rodzeń et al., 2021a). Some 3D-printed composite antibacterial scaffolds reported in the literature also demonstrated their potential for antibacterial modification of materials (Yang et al., 2018; Allen et al., 2020; Wang et al., 2021). This research is of great significance to the development of PEEK in the medical field. Oladapo et al (2021) elaborates on the scientific mechanism and some solutions for modifying PEEK by 3D printing. 3D printing technology can better control the distribution of each nanoparticle, solve the problem of insufficient exposure of antibacterial particles at the contact interface in blend

injection molding to a certain extent, and also make the distribution of surface-modified particles more uniform and controllable, thereby improving biomechanics, surface properties, and antimicrobial activity of modified PEEK. Deng et al (2017) have produced 3D-printed PEEK decorated with nano-silver particles: *in vitro* experiments have shown that it has obvious inhibitory effects on Gram-positive bacteria (*S. aureus*) and Gram-negative bacteria (*E. coli*) and can destroy the biofilm formed After that, a "PDA–Ag–PDA" sandwich structure was further fabricated by 3D printing on a mesh-structured PEEK surface. *In vitro* experiments verified its intelligent-controlled release. When the pH decreased due to bacterial metabolism, Ag+ was released, and the experiments in mice also proved its good antibacterial properties and osseointegration (Deng et al., 2020). The 3D printing technique can also be used in photothermal therapy. It was reported in the literature that the antimicrobial drug-loaded hydroxyapatite (HA) coating was attached to the surface of a 3D-printed graphene/PEEK scaffold by electrophoretic deposition, and then the drug was released on-demand by near-infrared irradiation showing good bactericidal effect on *Escherichia coli* and MRSA (Zhu et al., 2021). At present, there are few reports on the antibacterial properties of 3D-printed PEEK. It may be because of the current shortcomings of 3D printing technology: first, its resolution is limited, the yield is low, and there are still difficulties and challenges in the manufacture of some sophisticated or complex structures (Tahayeri et al., 2018). Second, unlike sulfonation and other structural modifications to form a porous surface, 3D-printed PEEK forms a grid structure of both surface and matrix (**Figure 5**), so the mechanical property changes require further experimental research. However, it is believed that with the advancement of technology, especially the development of nanotechnology (Laird et al., 2021), 3D-printed PEEK must have broad prospects for the improvement of its osseointegration and antibacterial properties.

OUTLOOK

IAI is a *besorgniserregend* complication of orthopedic surgery with poor prognosis due to biofilm formation. The crucial factor is the initial bacteria adhesion onto implant interfaces. Therefore, it is very important to endow orthopedic implants with antibacterial properties. However, there are still a lot of experiments that need to be explored at present and in the future. First, the bacterial strains used in this literature are relatively single; *E. coli* and *S. aureus* are mostly used to represent Gram-negative and -positive bacteria. However, most implant infections in clinic are iatrogenic infections, the types of pathogens are diverse, and the incidence of drug-resistant bacteria is high. Therefore, the use of mixed pathogens in antibacterial experiments may better simulate implant infection than a single bacterial strain. Second, postoperative implant infections often occur within 4 weeks (Zhou et al., 2020) or even within 3 months (Borchardt and Tzizik, 2018). Considering the potential cytotoxicity and drug resistance risk of long-term antibacterial particles or compounds, the combination of chemical and physical modification should be explored more. The antibacterial particles or compounds on a physically modified PEEK provide a strong bactericidal effect in the early stage; then, the antibacterial structure alone can promote the attachment of surrounding tissues and the ability to resist the formation of biofilm achieving long-term antibacterial ability. Meanwhile, most of the surface chemical modifications of PEEK adopt conventional antibacterial metal particles or antibacterial drugs, while our group has reported the application potential of some non-antibacterial compounds in the treatment of IAI. Zhang et al (2020), Zhang S. et al (2021a), and Zhang S. et al (2021b) successively found and proved the antibacterial properties of flufenamic acid, diclofenac, and felodipine against implant biofilm and even drug-resistant bacteria such as MRSA infection. Finally, orthopedic implants not only need to resist long-term chemical erosion *in vivo* but also need to bear a variety of physical stress, such as friction, anti-fatigue, shear force, and violence due to different injury mechanisms. So, there is still a large amount of research work to be completed for the successful clinical transformation of antibacterial biofunctionalized PEEK: the stability of the coating under different stresses; whether the antibacterial substances could be released evenly and effectively; the granular reaction *in vivo*, and so on. The biomechanical examination also needs to be repeated after long-term implantation *in vivo*, and the detection of residual coating and the analysis of tissue around the implant are worthy of further exploration. In addition, with the improvement of 3D printing accuracy in the future, it will have a revolutionary impact on implant materials such as PEEK.

CONCLUSION

PEEK is the most exciting orthopedic implant material in the past 20 years. A large number of research studies have investigated the biofunctionalization of PEEK with antibacterial. Good antibacterial properties are not only one of the key elements for the success of implants but also can be used to treat difficult clinical diseases such as infection and osteomyelitis. This review summarized the research results of many scholars in recent years and analyzed the approaches to biofunctionalize PEEK for antibacterial and specific methods of modification and then looked forward to the future research direction and problems to be further solved, contributing to the development of the antibacterial scheme of polyetheretherketone.

AUTHOR CONTRIBUTIONS

YW was responsible for literature retrieval, analysis, and manuscript writing. SZ and B'eN were responsible for manuscript revision and opinion supplement. XQ was responsible for writing guidance and manuscript review. BY was responsible for guidance, hot spot analysis, cooperative division of labor, and final review before submission.

REFERENCES

Abdulkareem, M. H., Abdalsalam, A. H., and Bohan, A. J. (2019). Influence of Chitosan on the Antibacterial Activity of Composite Coating (PEEK/HAp) Fabricated by Electrophoretic Deposition. *Prog. Org. Coat.* 130, 251–259. doi:10.1016/j.porgcoat.2019.01.050

Allen, B., Moore, C., Seyler, T., and Gall, K. (2020). Modulating Antibiotic Release from Reservoirs in 3D-printed Orthopedic Devices to Treat Periprosthetic Joint Infection. *J. Orthop. Res.* 38 (10), 2239–2249. doi:10.1002/jor.24640

Arciola, C. R., Campoccia, D., and Montanaro, L. (2018). Implant Infections: Adhesion, Biofilm Formation and Immune Evasion. *Nat. Rev. Microbiol.* 16 (7), 397–409. doi:10.1038/s41579-018-0019-y

AshaRani, P. V., Low Kah Mun, G., Hande, M. P., and Valiyaveettil, S. (2009). Cytotoxicity and Genotoxicity of Silver Nanoparticles in Human Cells. *ACS Nano* 3 (2), 279–290. doi:10.1021/nn800596w

Atef, M., Mounir, M., Shawky, M., Mounir, S., and Gibaly, A. (2021). Polyetheretherketone Patient-Specific Implants (PPSI) for the Reconstruction of Two Different Mandibular Contour Deformities. *Oral Maxillofac. Surg.* 10, 1–11. doi:10.1007/s10006-021-00984-6

Basgul, C., Yu, T., MacDonald, D. W., Siskey, R., Marcolongo, M., and Kurtz, S. M. (2018). Structure-property Relationships for 3D-Printed PEEK Intervertebral Lumbar Cages Produced Using Fused Filament Fabrication. *J. Mater. Res.* 33 (14), 2040–2051. doi:10.1557/jmr.2018.178

Bjarnsholt, T. (2013). The Role of Bacterial Biofilms in Chronic Infections. *APMIS* 121 (136), 1–58. doi:10.1111/apm.12099

Bock, R. M., Jones, E. N., Ray, D. A., Sonny Bal, B., Pezzotti, G., and McEntire, B. J. (2017). Bacteriostatic Behavior of Surface Modulated Silicon Nitride in Comparison to Polyetheretherketone and Titanium. *J. Biomed. Mater. Res.* 105 (5), 1521–1534. doi:10.1002/jbm.a.35987

Borchardt, R. A., and Tzizik, D. (2018). Update on Surgical Site Infections. *Jaapa* 31 (4), 52–54. doi:10.1097/01.Jaa.0000531052.82007.42

Brandwein, M., Bentwich, Z., and Steinberg, D. (2017). Endogenous Antimicrobial Peptide Expression in Response to Bacterial Epidermal Colonization. *Front. Immunol.* 8, 1637. doi:10.3389/fimmu.2017.01637

Busscher, H. J., van der Mei, H. C., Subbiahdoss, G., Jutte, P. C., van den Dungen, J. J., Zaat, S. A., et al. (2012). Biomaterial-associated Infection: Locating the Finish Line in the Race for the Surface. *Sci. Transl Med.* 4 (153), 153rv10. doi:10.1126/scitranslmed.3004528

Buwalda, S., Rotman, S., Eglin, D., Moriarty, F., Bethry, A., Garric, X., et al. (2020). Synergistic Anti-fouling and Bactericidal Poly(ether Ether Ketone) Surfaces via a One-step Photomodification. *Mater. Sci. Eng. C* 111, 110811. doi:10.1016/j.msec.2020.110811

Cai, Z., Qu, X., Zhao, Y., Yuan, Z., Zheng, L., Long, T., et al. (2022). Preliminary Study on Immediate Postoperative CT Images and Values of the Modular Polyetheretherketone Based Total Knee Arthroplasty: An Observational First-In-Human Trial. *Front. Surg.* 9. doi:10.3389/fsurg.2022.809699

Chen, C., Yin, Y., Xu, H., Li, Z., Wang, F., and Chen, G. (2021). Personalized Three-Dimensional Printed Polyether-Ether-Ketone Prosthesis for Reconstruction after Subtotal Removal of Chronic Clavicle Osteomyelitis: a Case Report. *Medicine* 100 (17), e25703. doi:10.1097/md.0000000000025703

Chen, M., Ouyang, L., Lu, T., Wang, H., Meng, F., Yang, Y., et al. (2017). Enhanced Bioactivity and Bacteriostasis of Surface Fluorinated Polyetheretherketone. *ACS Appl. Mater. Inter.* 9 (20), 16824–16833. doi:10.1021/acsami.7b02521

Chen, T., Chen, Q., Fu, H., Wang, D., Gao, Y., Zhang, M., et al. (2021). Construction and Performance Evaluation of a Sustained Release Implant Material Polyetheretherketone With Antibacterial Properties. *Mater. Sci. Eng. C* 126, 112109. doi:10.1016/j.msec.2021.112109

Chen, Y., Zhang, L., Qin, T., Wang, Z., Li, Y., and Gu, B. (2019). Evaluation of Neurosurgical Implant Infection Rates and Associated Pathogens: Evidence from 1118 Postoperative Infections. *Neurosurg. Focus* 47 (2), E6. doi:10.3171/2019.5.Focus18582

Chepurnyi, Y., Chernogorskyi, D., Kopchak, A., and Petrenko, O. (2020). Clinical Efficacy of Peek Patient-specific Implants in Orbital Reconstruction. *J. Oral Biol. Craniofac. Res.* 10 (2), 49–53. doi:10.1016/j.jobcr.2020.01.006

Ching, W. Y., Rulis, P., and Misra, A. (2009). Ab Initio elastic Properties and Tensile Strength of Crystalline Hydroxyapatite. *Acta Biomater.* 5 (8), 3067–3075. doi:10.1016/j.actbio.2009.04.030

Choi, O., Deng, K. K., Kim, N.-J., Ross, L., Jr, Surampalli, R. Y., and Hu, Z. (2008). The Inhibitory Effects of Silver Nanoparticles, Silver Ions, and Silver Chloride Colloids on Microbial Growth. *Water Res.* 42 (12), 3066–3074. doi:10.1016/j.watres.2008.02.021

Clauss, M., Hunkeler, C., Manzoni, I., and Sendi, P. (2020). Debridement, Antibiotics and Implant Retention for Hip Periprosthetic Joint Infection: Analysis of Implant Survival after Cure of Infection. *J. Bone Jt. Infect.* 5 (1), 35–42. doi:10.7150/jbji.40924

Deng, L., Deng, Y., and Xie, K. (2017). AgNPs-decorated 3D Printed PEEK Implant for Infection Control and Bone Repair. *Colloids Surf. B: Biointerfaces* 160, 483–492. doi:10.1016/j.colsurfb.2017.09.061

Deng, Y., Shi, X., Chen, Y., Yang, W., and Chen, Z. G. (2020). A Bacteria-Triggered pH-Responsive Osteopotentiating Coating on 3D-Printed Polyetheretherketone Scaffolds for Infective Bone Defect Repair. *Ind. Eng. Chem. Res.* 59 (26), 12123–12135. doi:10.1021/acs.iecr.0c02107

Deng, Y., Yang, L., Huang, X., Chen, J., Shi, X., Yang, W., et al. (2018). Dual Ag/ZnO-Decorated Micro-/Nanoporous Sulfonated Polyetheretherketone with Superior Antibacterial Capability and Biocompatibility via Layer-by-Layer Self-Assembly Strategy. *Macromol. Biosci.* 18 (7), 1800028. doi:10.1002/mabi.201800028

El Yakhlifi, S., and Ball, V. (2020). Polydopamine as a Stable and Functional Nanomaterial. *Colloids Surf. B: Biointerfaces* 186, 110719. doi:10.1016/j.colsurfb.2019.110719

Gao, C., Wang, Y., Han, F., Yuan, Z., Li, Q., Shi, C., et al. (2017). Antibacterial Activity and Osseointegration of Silver-Coated Poly(ether Ether Ketone) Prepared Using the Polydopamine-Assisted Deposition Technique. *J. Mater. Chem. B* 5 (47), 9326–9336. doi:10.1039/c7tb02436c

Gristina, A. G. (1987). Biomaterial-centered Infection: Microbial Adhesion versus Tissue Integration. *Science* 237 (4822), 1588–1595. doi:10.1126/science.3629258

Gu, X., Sun, X., Sun, Y., Wang, J., Liu, Y., Yu, K., et al. (2020). Bioinspired Modifications of PEEK Implants for Bone Tissue Engineering. *Front. Bioeng. Biotechnol.* 8, 631616. doi:10.3389/fbioe.2020.631616

Hacherl, C.-C., Patel, N. A., Jones, K., Ruh, N. B., Gendreau, J. L., Abraham, M. E., et al. (2021). Characterizing Adverse Events of Cranioplasty Implants after Craniectomy: A Retrospective Review of the Federal Manufacturer and User Facility Device Experience Database. *Cureus* 13 (7), e16795. doi:10.7759/cureus.16795

Hajiali, F., Tajbakhsh, S., and Shojaei, A. (2017). Fabrication and Properties of Polycaprolactone Composites Containing Calcium Phosphate-Based Ceramics and Bioactive Glasses in Bone Tissue Engineering: A Review. *Polym. Rev.* 58 (1), 164–207. doi:10.1080/15583724.2017.1332640

He, M., Huang, Y., Xu, H., Feng, G., Liu, L., Li, Y., et al. (2021). Modification of Polyetheretherketone Implants: From Enhancing Bone Integration to Enabling Multi-Modal Therapeutics. *Acta Biomater.* 129, 18–32. doi:10.1016/j.actbio.2021.05.009

He, X., Deng, Y., Yu, Y., Lyu, H., and Liao, L. (2019). Drug-loaded/grafted Peptide-Modified Porous PEEK to Promote Bone Tissue Repair and Eliminate Bacteria. *Colloids Surf. B: Biointerfaces* 181, 767–777. doi:10.1016/j.colsurfb.2019.06.038

Heary, R. F., Parvathreddy, N., Sampath, S., and Agarwal, N. (2017). Elastic Modulus in the Selection of Interbody Implants. *J. Spine Surg.* 3 (2), 163–167. doi:10.21037/jss.2017.05.01

Hochella, M. F., Jr., Mogk, D. W., Ranville, J., Allen, I. C., Luther, G. W., Marr, L. C., et al. (2019). Natural, Incidental, and Engineered Nanomaterials and Their Impacts on the Earth System. *Science* 363 (6434), eaau8299. doi:10.1126/science.aau8299

Hu, C.-C., Kumar, S. R., Vi, T. T. T., Huang, Y.-T., Chen, D. W., and Lue, S. J. (2021). Facilitating GL13K Peptide Grafting on Polyetheretherketone via 1-Ethyl-3-(3-Dimethylaminopropyl)carbodiimide: Surface Properties and Antibacterial Activity. *Ijms* 23 (1), 359. doi:10.3390/ijms23010359

Hu, G., Zhu, Y., Xu, F., Ye, J., Guan, J., Jiang, Y., et al. (2022). Comparison of Surface Properties, Cell Behaviors, Bone Regeneration and Osseointegration between Nano Tantalum/PEEK Composite and Nano Silicon Nitride/PEEK Composite. *J. Biomater. Sci. Polym. Edition* 33 (1), 35–56. doi:10.1080/09205063.2021.1974812

Huo, S., Meng, X., Zhang, S., Yue, B., Zhao, Y., Long, T., et al. (2021a). Hydrofluoric Acid and Nitric Acid Cotreatment for Biofunctionalization of

Polyetheretherketone in M2 Macrophage Polarization and Osteogenesis. *J. Biomed. Mater. Res.* 109 (6), 879–892. doi:10.1002/jbm.a.37079

Huo, S., Wang, F., Lyu, Z., Hong, Q., Nie, B. e., Wei, J., et al. (2021b). Dual-functional Polyetheretherketone Surface Modification for Regulating Immunity and Bone Metabolism. *Chem. Eng. J.* 426, 130806. doi:10.1016/j.cej.2021.130806

Huo, S., Wang, F., Lyu, Z., Hong, Q., Nie, B. e., Wei, J., et al. (2021c). Dual-Functional Polyetheretherketone Surface Modification for Regulating Immunity and Bone Metabolism. *Chem. Eng. J.* 426 (32), 130806. doi:10.1016/j.cej.2021.130806

Jaekel, D. J. (2012). *Development and Fabrication of Silver Composite PEEK to Prevent Microbial Attachment and Periprosthetic Infection*. Philadelphia, PA: Drexel BIOMED 74, 1.

Ji, Y., Zhang, H., Ru, J., Wang, F., and Wei, J. (2020). Creating Micro-submicro Structure and Grafting Hydroxyl Group on PEEK by Femtosecond Laser and Hydroxylation to Synergistically Activate Cellular Response. *Mater. Des.* 199, 109413. doi:10.1016/j.matdes.2020.109413

Jiao, J., Zhang, S., Qu, X., and Yue, B. (2021). Recent Advances in Research on Antibacterial Metals and Alloys as Implant Materials. *Front. Cel. Infect. Microbiol.* 11, 693939. doi:10.3389/fcimb.2021.693939

Kim, T., See, C. W., Li, X., and Zhu, D. (2020). Orthopedic Implants and Devices for Bone Fractures and Defects: Past, Present and Perspective. *Engineered Regen.* 1, 6–18. doi:10.1016/j.engreg.2020.05.003

Kratochvíl, J., Štěrba, J., Lieskovská, J., Langhansová, H., Kuzminova, A., Khalakhan, I., et al. (2018). Antibacterial Effect of Cu/C:F Nanocomposites Deposited on PEEK Substrates. *Mater. Lett.* 230, 96–99. doi:10.1016/j.matlet.2018.07.082

Kuehl, R., Tschudin-Sutter, S., Morgenstern, M., Dangel, M., Egli, A., Nowakowski, A., et al. (2019). Time-dependent Differences in Management and Microbiology of Orthopaedic Internal Fixation-Associated Infections: an Observational Prospective Study with 229 Patients. *Clin. Microbiol. Infect.* 25 (1), 76–81. doi:10.1016/j.cmi.2018.03.040

Kylian, O., Kratochvil, J., Petr, M., Kuzminova, A., Slavinska, D., Biederman, H., et al. (2017). Ag/C:F Antibacterial and Hydrophobic Nanocomposite Coatings. *Funct. Mater. Lett.* 10 (3), 1750029–1750021. doi:10.1142/s1793604717500291

Laird, N. Z., Acri, T. M., Chakka, J. L., Quarterman, J. C., Malkawi, W. I., Elangovan, S., et al. (2021). Applications of Nanotechnology in 3D Printed Tissue Engineering Scaffolds. *Eur. J. Pharmaceutics Biopharmaceutics* 161, 15–28. doi:10.1016/j.ejpb.2021.01.018

Lee, H., Dellatore, S. M., Miller, W. M., and Messersmith, P. B. (2007). Mussel-inspired Surface Chemistry for Multifunctional Coatings. *Science* 318 (5849), 426–430. doi:10.1126/science.1147241

Li, N., Bai, J., Wang, W., Liang, X., Zhang, W., Li, W., et al. (2021). Facile and Versatile Surface Functional Polyetheretherketone with Enhanced Bacteriostasis and Osseointegrative Capability for Implant Application. *ACS Appl. Mater. Inter.* 13 (50), 59731–59746. doi:10.1021/acsami.1c19834

Li, S., Wang, T., Hu, J., Li, Z., Wang, B., Wang, L., et al. (2021b). Surface Porous Poly-Ether-Ether-Ketone Based on Three-Dimensional Printing for Load-Bearing Orthopedic Implant. *J. Mech. Behav. Biomed. Mater.* 120, 104561. doi:10.1016/j.jmbbm.2021.104561

Li, Y., Wang, J., He, D., GuoxiongZhuWu, G., Wu, G., and Chen, L. (2019). Surface Sulfonation and Nitrification Enhance the Biological Activity and Osteogenesis of Polyetheretherketone by Forming an Irregular Nano-Porous Monolayer. *J. Mater. Sci. Mater. Med.* 31 (1), 11. doi:10.1007/s10856-019-6349-0

Liao, C., Li, Y., and Tjong, S. C. (2020). Polyetheretherketone and its Composites for Bone Replacement and Regeneration. *Polymers* 12 (12), 2858. doi:10.3390/polym12122858

Liu, C., Bai, J., Wang, Y., Chen, L., Wang, D., Ni, S., et al. (2021). The Effects of Three Cold Plasma Treatments on the Osteogenic Activity and Antibacterial Property of PEEK. *Dental Mater.* 37 (1), 81–93. doi:10.1016/j.dental.2020.10.007

Liu, D., Fu, J., Fan, H., Li, D., Dong, E., Xiao, X., et al. (2018). Application of 3D-Printed PEEK Scapula Prosthesis in the Treatment of Scapular Benign Fibrous Histiocytoma: A Case Report. *J. Bone Oncol.* 12, 78–82. doi:10.1016/j.jbo.2018.07.012

Liu, X., Chen, C., Zhang, H., Tian, A., You, J., Wu, L., et al. (2019). Biocompatibility Evaluation of Antibacterial Ti–Ag Alloys with Nanotubular Coatings. *Ijn* Vol. 14, 457–468. doi:10.2147/ijn.S193569

Liu, X., Gan, K., Liu, H., Song, X., Chen, T., and Liu, C. (2017). Antibacterial Properties of Nano-Silver Coated PEEK Prepared through Magnetron Sputtering. *Dental Mater.* 33 (9), e348–e360. doi:10.1016/j.dental.2017.06.014

Liu, Y., Rath, B., Tingart, M., and Eschweiler, J. (2020). Role of Implants Surface Modification in Osseointegration: A Systematic Review. *J. Biomed. Mater. Res.* 108 (3), 470–484. doi:10.1002/jbm.a.36829

Lowe, B., Hardy, J. G., and Walsh, L. J. (2020). Optimizing Nanohydroxyapatite Nanocomposites for Bone Tissue Engineering. *ACS Omega* 5 (1), 1–9. doi:10.1021/acsomega.9b02917

Luo, S., Wang, P., Ma, M., Pan, Z., Lu, L., Yin, F., et al. (2022). Genistein Loaded into Microporous Surface of Nano Tantalum/PEEK Composite with Antibacterial Effect Regulating Cellular Response *In Vitro*, and Promoting Osseointegration *In Vivo*. *J. Mech. Behav. Biomed. Mater.* 125, 104972. doi:10.1016/j.jmbbm.2021.104972

Ma, R., Wang, J., Li, C., Ma, K., Wei, J., Yang, P., et al. (2020a). Effects of Different Sulfonation Times and post-treatment Methods on the Characterization and Cytocompatibility of Sulfonated PEEK. *J. Biomater. Appl.* 35 (3), 342–352. doi:10.1177/0885328220935008

Ma, Z., Zhao, X., Zhao, J., Zhao, Z., Wang, Q., and Zhang, C. (2020). Biologically Modified Polyether Ether Ketone as Dental Implant Material. *Front. Bioeng. Biotechnol.* 8. doi:10.3389/fbioe.2020.620537

Manzoor, F., Golbang, A., Jindal, S., Dixon, D., McIlhagger, A., Harkin-Jones, E., et al. (2021). 3D Printed PEEK/HA Composites for Bone Tissue Engineering Applications: Effect of Material Formulation on Mechanical Performance and Bioactive Potential. *J. Mech. Behav. Biomed. Mater.* 121, 104601. doi:10.1016/j.jmbbm.2021.104601

Massaad, E., Fatima, N., Kiapour, A., Hadzipasic, M., Shankar, G. M., and Shin, J. H. (2020). Polyetheretherketone versus Titanium Cages for Posterior Lumbar Interbody Fusion: Meta-Analysis and Review of the Literature. *Neurospine* 17 (1), 125–135. doi:10.14245/ns.2040058.029

Masters, E. A., Trombetta, R. P., de Mesy Bentley, K. L., Boyce, B. F., Gill, A. L., Gill, S. R., et al. (2019). Evolving Concepts in Bone Infection: Redefining "biofilm", "acute vs. Chronic Osteomyelitis", "the Immune Proteome" and "local Antibiotic Therapy". *Bone Res.* 7, 20. doi:10.1038/s41413-019-0061-z

Matar, H. E., Bloch, B. V., Snape, S. E., and James, P. J. (2021). Outcomes of Single- and Two-Stage Revision Total Knee Arthroplasty for Chronic Periprosthetic Joint Infection. *Bone Jt. J.* 103-B (8), 1373–1379. doi:10.1302/0301-620x.103b8.bjj-2021-0224.r1

Mei, S., Wang, F., Hu, X., Yang, K., Xie, D., Yang, L., et al. (2021). Construction of a Hierarchical Micro & Nanoporous Surface for Loading Genistein on the Composite of Polyetheretherketone/tantalum Pentoxide Possessing Antibacterial Activity and Accelerated Osteointegration. *Biomater. Sci.* 9 (1), 167–185. doi:10.1039/d0bm01306d

Meng, X., Zhang, J., Chen, J., Nie, B., Yue, B., Zhang, W., et al. (2020). KR-12 Coating of Polyetheretherketone (PEEK) Surface via Polydopamine Improves Osteointegration and Antibacterial Activity *In Vivo*. *J. Mater. Chem. B* 8 (44), 10190–10204. doi:10.1039/d0tb01899f

Meng, Z., Liu, Y., and Wu, D. (2005). Effect of Sulfur Dioxide Inhalation on Cytokine Levels in Lungs and Serum of Mice. *Inhalation Toxicol.* 17 (6), 303–307. doi:10.1080/08958370590922625

Mishchenko, O., Ovchynnykov, O., Kapustian, O., and Pogorielov, M. (2020). New Zr-Ti-Nb Alloy for Medical Application: Development, Chemical and Mechanical Properties, and Biocompatibility. *Materials* 13 (6), 1306. doi:10.3390/ma13061306

Mounir, M., Atef, M., Abou-Elfetouh, A., and Hakam, M. M. (2018). Titanium and Polyether Ether Ketone (PEEK) Patient-specific Sub-periosteal Implants: Two Novel Approaches for Rehabilitation of the Severely Atrophic Anterior Maxillary ridge. *Int. J. Oral Maxillofac. Surg.* 47 (5), 658–664. doi:10.1016/j.ijom.2017.11.008

Mousavi, S. M., Low, F. W., Hashemi, S. A., Lai, C. W., Ghasemi, Y., Soroshnia, S., et al. (2020). Development of Graphene Based Nanocomposites towards Medical and Biological Applications. *Artif. Cell Nanomedicine, Biotechnol.* 48 (1), 1189–1205. doi:10.1080/21691401.2020.1817052

Naik, K., Srivastava, P., Deshmukh, K., Monsoor S, M., and Kowshik, M. (2015). Nanomaterial-Based Approaches for Prevention of Biofilm-Associated Infections on Medical Devices and Implants. *J. Nanosci Nanotechnol* 15 (12), 10108–10119. doi:10.1166/jnn.2015.11688

Niu, Y., Guo, L., Hu, F., Ren, L., Zhou, Q., Ru, J., et al. (2020). Macro-Microporous Surface with Sulfonic Acid Groups and Micro-nano Structures of PEEK/Nano Magnesium Silicate Composite Exhibiting Antibacterial Activity and Inducing Cell Responses. *Ijn* Vol. 15, 2403–2417. doi:10.2147/ijn.S238287

NiyonshutiII, Krishnamurthi, V. R., Okyere, D., Song, L., Benamara, M., Tong, X., et al. (2020). Polydopamine Surface Coating Synergizes the Antimicrobial Activity of Silver Nanoparticles. *ACS Appl. Mater. Inter.* 12 (36), 40067–40077. doi:10.1021/acsami.0c10517

Oladapo, B. I., Ismail, S. O., Bowoto, O. K., Omigbodun, F. T., Olawumi, M. A., and Muhammad, M. A. (2020). Lattice Design and 3D-Printing of PEEK with Ca10(OH)(PO4)3 and *In-Vitro* Bio-Composite for Bone Implant. *Int. J. Biol. Macromolecules* 165 (Pt A), 50–62. doi:10.1016/j.ijbiomac.2020.09.175

Oladapo, B. I., Zahedi, S. A., Ismail, S. O., and Omigbodun, F. T. (2021). 3D Printing of PEEK and its Composite to Increase Biointerfaces as a Biomedical Material- A Review. *Colloids Surf. B: Biointerfaces* 203, 111726. doi:10.1016/j.colsurfb.2021.111726

Otto-Lambertz, C., Yagdiran, A., Wallscheid, F., Eysel, P., and Jung, N. (2017). Periprosthetic Infection in Joint Replacement. *Deutsches Ärzteblatt Int.* 114 (20), 347. doi:10.3238/arztebl.2017.0347

Ouyang, L., Deng, Y., Yang, L., Shi, X., Dong, T., Tai, Y., et al. (2018). Graphene-Oxide-Decorated Microporous Polyetheretherketone with Superior Antibacterial Capability and *In Vitro* Osteogenesis for Orthopedic Implant. *Macromol. Biosci.* 18 (6), 1800036. doi:10.1002/mabi.201800036

Ouyang, L., Zhao, Y., Jin, G., Lu, T., Li, J., Qiao, Y., et al. (2016). Influence of Sulfur Content on Bone Formation and Antibacterial Ability of Sulfonated PEEK. *Biomaterials* 83, 115–126. doi:10.1016/j.biomaterials.2016.01.017

Pan, W.-Y., Huang, C.-C., Lin, T.-T., Hu, H.-Y., Lin, W.-C., Li, M.-J., et al. (2016). Synergistic Antibacterial Effects of Localized Heat and Oxidative Stress Caused by Hydroxyl Radicals Mediated by Graphene/iron Oxide-Based Nanocomposites. *Nanomedicine: Nanotechnology, Biol. Med.* 12 (2), 431–438. doi:10.1016/j.nano.2015.11.014

Panayotov, I. V., Orti, V., Cuisinier, F., and Yachouh, J. (2016). Polyetheretherketone (PEEK) for Medical Applications. *J. Mater. Sci. Mater. Med.* 27 (7), 118. doi:10.1007/s10856-016-5731-4

Pang, H., Tian, H., Qiu, S., Wang, N., and Wang, Y.-Q. (2019). Progress of Titanium Strut for Cervical Reconstruction with Nano-Graphene Oxide Loaded Hydroxyapatite/polyamide Composite and Interbody Fusion after Corpectomy with Anterior Plate Fixation. *Artif. Cell Nanomedicine, Biotechnol.* 47 (1), 3094–3100. doi:10.1080/21691401.2019.1637883

Perla, V., and Webster, T. J. (2005). Better Osteoblast Adhesion on Nanoparticulate Selenium- A Promising Orthopedic Implant Material. *J. Biomed. Mater. Res.* 75A (2), 356–364. doi:10.1002/jbm.a.30423

Pezzotti, G., Marin, E., Adachi, T., Lerussi, F., Rondinella, A., Boschetto, F., et al. (2018). Incorporating Si3 N4 into PEEK to Produce Antibacterial, Osteocondutive, and Radiolucent Spinal Implants. *Macromol. Biosci.* 18 (6), 1800033. doi:10.1002/mabi.201800033

Poulsson, A. H. C., Eglin, D., and Geoff Richards, R. (2019). "Surface Modification Techniques of PEEK, Including Plasma Surface Treatment," in *PEEK Biomaterials Handbook*. 2nd Edn (ElsevierNetherlands), 179–201. doi:10.1016/b978-0-12-812524-3.00011-9

Rodzeń, K., McIvor, M. J., Sharma, P. K., Acheson, J. G., McIlhagger, A., Mokhtari, M., et al. (2021a). The Surface Characterisation of Fused Filament Fabricated (FFF) 3D Printed PEEK/Hydroxyapatite Composites. *Polymers* 13 (18), 3117. doi:10.3390/polym13183117

Rodzeń, K., Sharma, P. K., McIlhagger, A., Mokhtari, M., Dave, F., Tormey, D., et al. (2021b). The Direct 3D Printing of Functional PEEK/Hydroxyapatite Composites via a Fused Filament Fabrication Approach. *Polymers* 13 (4), 545. doi:10.3390/polym13040545

Roman, H. K., Berthier, P., Rouillon, T., Jean-Philippe, P., and Pierre, C. (2014). Severe Infectious Complications after PEEK-Derived Implant Placement: Report of Three Cases. *J. Oral Maxillofac. Surg. Med. Pathol.* 26 (4), 477–482. doi:10.1016/j.ajoms.2013.04.006

Sikder, P., Grice, C. R., Lin, B., Goel, V. K., and Bhaduri, S. B. (2018). Single-Phase, Antibacterial Trimagnesium Phosphate Hydrate Coatings on Polyetheretherketone (PEEK) Implants by Rapid Microwave Irradiation Technique. *ACS Biomater. Sci. Eng.* 4 (8), 2767–2783. doi:10.1021/acsbiomaterials.8b00594

Singh, I., Dhawan, G., Gupta, S., and Kumar, P. (2020). Recent Advances in a Polydopamine-Mediated Antimicrobial Adhesion System. *Front. Microbiol.* 11, 607099. doi:10.3389/fmicb.2020.607099

Song, J., Liu, H., Lei, M., Tan, H., Chen, Z., Antoshin, A., et al. (2020). Redox-Channeling Polydopamine-Ferrocene (PDA-Fc) Coating to Confer Context-dependent and Photothermal Antimicrobial Activities. *ACS Appl. Mater. Inter.* 12 (7), 8915–8928. doi:10.1021/acsami.9b22339

Stones, D. H., and Krachler, A. M. (2016). Against the Tide: the Role of Bacterial Adhesion in Host Colonization. *Biochem. Soc. Trans.* 44 (6), 1571–1580. doi:10.1042/bst20160186

Subbiahdoss, G., Kuijer, R., Grijpma, D. W., van der Mei, H. C., and Busscher, H. J. (2009). Microbial Biofilm Growth vs. Tissue Integration: "The Race for the Surface" Experimentally Studied. *Acta Biomater.* 5 (5), 1399–1404. doi:10.1016/j.actbio.2008.12.011

Sultana, T., Hossain, M., Rahaman, S., Kim, Y. S., Gwon, J.-G., and Lee, B.-T. (2021). Multi-functional Nanocellulose-Chitosan Dressing Loaded with Antibacterial Lawsone for Rapid Hemostasis and Cutaneous Wound Healing. *Carbohydr. Polym.* 272, 118482. doi:10.1016/j.carbpol.2021.118482

Sun, A. a., Lin, X., Xue, Z., Huang, J., Bai, X., Huang, L., et al. (2021). Facile Surface Functional Polyetheretherketone with Antibacterial and Immunoregulatory Activities for Enhanced Regeneration toward Bacterium-Infected Bone Destruction. *Drug Deliv.* 28 (1), 1649–1663. doi:10.1080/10717544.2021.1960924

Tahayeri, A., Morgan, M., Fugolin, A. P., Bompolaki, D., Athirasala, A., Pfeifer, C. S., et al. (2018). 3D Printed versus Conventionally Cured Provisional crown and Bridge Dental Materials. *Dental Mater.* 34 (2), 192–200. doi:10.1016/j.dental.2017.10.003

Tang, X., Dai, J., Sun, H., Nabanita, S., Petr, S., Wang, D., et al. (2019). Mechanical Strength, Surface Properties, Cytocompatibility and Antibacterial Activity of Nano Zinc-Magnesium Silicate/Polyetheretherketone Biocomposites. *J. Nanosci Nanotechnol* 19 (12), 7615–7623. doi:10.1166/jnn.2019.16727

Tarallo, L., Giorgini, A., Novi, M., Zambianchi, F., Porcellini, G., and Catani, F. (2020). Volar PEEK Plate for Distal Radius Fracture: Analysis of Adverse Events. *Eur. J. Orthop. Surg. Traumatol.* 30 (7), 1293–1298. doi:10.1007/s00590-020-02701-7

Tomoglu, S., Caner, G., Arabaci, A., and Mutlu, I. (2019). Production and Sulfonation of Bioactive Polyetheretherketone Foam for Bone Substitute Applications. *Int. J. Polymeric Mater.* 68 (18), 1167–1176. doi:10.1080/00914037.2018.1539985

Torstrick, F. B., Lin, A. S. P., Potter, D., Safranski, D. L., Sulchek, T. A., Gall, K., et al. (2018). Porous PEEK Improves the Bone-Implant Interface Compared to Plasma-Sprayed Titanium Coating on PEEK. *Biomaterials* 185, 106–116. doi:10.1016/j.biomaterials.2018.09.009

Ur Rehman, M. A., Bastan, F. E., Nawaz, Q., Goldmann, W. H., Maqbool, M., Virtanen, S., et al. (2018). Electrophoretic Deposition of Lawsone Loaded Bioactive Glass (BG)/chitosan Composite on Polyetheretherketone (PEEK)/BG Layers as Antibacterial and Bioactive Coating. *J. Biomed. Mater. Res.* 106 (12), 3111–3122. doi:10.1002/jbm.a.36506

Ur Rehman, M. A., Ferraris, S., Goldmann, W. H., Perero, S., Bastan, F. E., Nawaz, Q., et al. (2017). Antibacterial and Bioactive Coatings Based on Radio Frequency Co-sputtering of Silver Nanocluster-Silica Coatings on PEEK/Bioactive Glass Layers Obtained by Electrophoretic Deposition. *ACS Appl. Mater. Inter.* 9 (38), 32489–32497. doi:10.1021/acsami.7b08646

Wang, M., Bhardwaj, G., and Webster, T. (2017). Antibacterial Properties of PEKK for Orthopedic Applications. *Ijn* Vol. 12, 6471–6476. doi:10.2147/ijn.S134983

Wang, M., and Tang, T. (2019). Surface Treatment Strategies to Combat Implant-Related Infection from the Beginning. *J. Orthopaedic Translation* 17, 42–54. doi:10.1016/j.jot.2018.09.001

Wang, M., Yang, Y., Chi, G., Yuan, K., Zhou, F., Dong, L., et al. (2021). A 3D Printed Ga Containing Scaffold with Both Anti-infection and Bone Homeostasis-Regulating Properties for the Treatment of Infected Bone Defects. *J. Mater. Chem. B* 9 (23), 4735–4745. doi:10.1039/d1tb00387a

Wang, Q., Mejía Jaramillo, A., Pavon, J. J., and Webster, T. J. (2016). Red Selenium Nanoparticles and gray Selenium Nanorods as Antibacterial Coatings for PEEK Medical Devices. *J. Biomed. Mater. Res.* 104 (7), 1352–1358. doi:10.1002/jbm.b.33479

Wang, S., Deng, Y., Yang, L., Shi, X., Yang, W., and Chen, Z.-G. (2018). Enhanced Antibacterial Property and Osteo-Differentiation Activity on Plasma Treated

Porous Polyetheretherketone with Hierarchical Micro/nano-Topography. *J. Biomater. Sci. Polym. Edition* 29 (5), 520–542. doi:10.1080/09205063.2018.1425181

Xiao, T., Fan, L., Liu, R., Huang, X., Wang, S., Xiao, L., et al. (2021). Fabrication of Dexamethasone-Loaded Dual-Metal-Organic Frameworks on Polyetheretherketone Implants with Bacteriostasis and Angiogenesis Properties for Promoting Bone Regeneration. *ACS Appl. Mater. Inter.* 13 (43), 50836–50850. doi:10.1021/acsami.1c18088

Xu, J.-W., Yao, K., and Xu, Z.-K. (2019). Nanomaterials with a Photothermal Effect for Antibacterial Activities: an Overview. *Nanoscale* 11 (18), 8680–8691. doi:10.1039/c9nr01833f

Xu, X., Li, Y., Wang, L., Li, Y., Pan, J., Fu, X., et al. (2019b). Triple-functional Polyetheretherketone Surface with Enhanced Bacteriostasis and Anti-inflammatory and Osseointegrative Properties for Implant Application. *Biomaterials* 212, 98–114. doi:10.1016/j.biomaterials.2019.05.014

Xue, Z., Wang, Z., Sun, A. a., Huang, J., Wu, W., Chen, M., et al. (2020). Rapid Construction of Polyetheretherketone (PEEK) Biological Implants Incorporated with Brushite (CaHPO4·2H2O) and Antibiotics for Anti-infection and Enhanced Osseointegration. *Mater. Sci. Eng. C* 111, 110782. doi:10.1016/j.msec.2020.110782

Ya-Shum, C., Chen Lin, J.-H., Wu, Y.-R., Chang, C.-W., Chang, K.-C., Chen, C. C., et al. (2018). Characterizing the Differentiation of Osteoprogenitor Cells on Surface Modified Polyether-Ether-Ketone. *Surf. Coat. Techn.* 350, 904–912. doi:10.1016/j.surfcoat.2018.03.071

Yan, J., Xia, D., Zhou, W., Li, Y., Xiong, P., Li, Q., et al. (2020). pH-responsive Silk Fibroin-Based CuO/Ag Micro/nano Coating Endows Polyetheretherketone with Synergistic Antibacterial Ability, Osteogenesis, and Angiogenesis. *Acta Biomater.* 115, 220–234. doi:10.1016/j.actbio.2020.07.062

Yan, J., Zhou, W., Jia, Z., Xiong, P., Li, Y., Wang, P., et al. (2018). Endowing Polyetheretherketone with Synergistic Bactericidal Effects and Improved Osteogenic Ability. *Acta Biomater.* 79, 216–229. doi:10.1016/j.actbio.2018.08.037

Yang, C., Ouyang, L., Wang, W., Chen, B., Liu, W., Yuan, X., et al. (2019). Sodium Butyrate-Modified Sulfonated Polyetheretherketone Modulates Macrophage Behavior and Shows Enhanced Antibacterial and Osteogenic Functions during Implant-Associated Infections. *J. Mater. Chem. B* 7 (36), 5541–5553. doi:10.1039/c9tb01298b

Yang, X., Chai, H., Guo, L., Jiang, Y., Xu, L., Huang, W., et al. (2022). Corrigendum to '*In Situ* Preparation of Porous Metal-Organic Frameworks ZIF-8@Ag on Poly-Ether-Ether-Ketone with Synergistic Antibacterial Activity' [Colloids Surf. B: Biointerfaces 205 (2021) 111920]. *Colloids Surf. B: Biointerfaces* 209 (Pt 2), 112179. doi:10.1016/j.colsurfb.2021.112179

Yang, Y., Chu, L., Yang, S., Zhang, H., Qin, L., Guillaume, O., et al. (2018). Dual-functional 3D-Printed Composite Scaffold for Inhibiting Bacterial Infection and Promoting Bone Regeneration in Infected Bone Defect Models. *Acta Biomater.* 79, 265–275. doi:10.1016/j.actbio.2018.08.015

Yang, Y., He, C., Dianyu, E., Yang, W., Qi, F., Xie, D., et al. (2020). Mg Bone Implant: Features, Developments and Perspectives. *Mater. Des.* 185, 108259. doi:10.1016/j.matdes.2019.108259

Yu, Y., Sun, Y., Zhou, X., Mao, Y., Liu, Y., Ye, L., et al. (2021). Ag and Peptide Co-decorate Polyetheretherketone to Enhance Antibacterial Property and Osteogenic Differentiation. *Colloids Surf. B: Biointerfaces* 198, 111492. doi:10.1016/j.colsurfb.2020.111492

Yuan, X., Ouyang, L., Luo, Y., Sun, Z., Yang, C., Wang, J., et al. (2019). Multifunctional Sulfonated Polyetheretherketone Coating with Beta-Defensin-14 for Yielding Durable and Broad-Spectrum Antibacterial Activity and Osseointegration. *Acta Biomater.* 86, 323–337. doi:10.1016/j.actbio.2019.01.016

Zhang, S., Qu, X., Jiao, J., Tang, H., Wang, M., Wang, Y., et al. (2021a). Felodipine Enhances Aminoglycosides Efficacy against Implant Infections Caused by Methicillin-Resistant *Staphylococcus aureus*, Persisters and Biofilms. *Bioactive Mater.* 4, 272–289. doi:10.1016/j.bioactmat.2021.11.019

Zhang, S., Qu, X., Tang, H., Wang, Y., Yang, H., Yuan, W., et al. (2021b). Diclofenac Resensitizes Methicillin-Resistant *Staphylococcus aureus* to β -Lactams and Prevents Implant Infections. *Adv. Sci.* 8 (13), 2100681. doi:10.1002/advs.202100681

Zhang, S., Tang, H., Wang, Y., Nie, B. e., Yang, H., Yuan, W., et al. (2020). Antibacterial and Antibiofilm Effects of Flufenamic Acid against Methicillin-Resistant *Staphylococcus aureus*. *Pharmacol. Res.* 160, 105067. doi:10.1016/j.phrs.2020.105067

Zhang, Y., Wu, H., Yuan, B., Zhu, X., Zhang, K., and Zhang, X. (2021c). Enhanced Osteogenic Activity and Antibacterial Performance *In Vitro* of Polyetheretherketone by Plasma-Induced Graft Polymerization of Acrylic Acid and Incorporation of Zinc Ions. *J. Mater. Chem. B* 9 (36), 7506–7515. doi:10.1039/d1tb01349a

Zhou, W., Peng, X., Ma, Y., Hu, Y., Wu, Y., Lan, F., et al. (2020). Two-staged Time-dependent Materials for the Prevention of Implant-Related Infections. *Acta Biomater.* 101, 128–140. doi:10.1016/j.actbio.2019.10.023

Zhu, C., He, M., Sun, D., Huang, Y., Huang, L., Du, M., et al. (2021). 3D-Printed Multifunctional Polyetheretherketone Bone Scaffold for Multimodal Treatment of Osteosarcoma and Osteomyelitis. *ACS Appl. Mater. Inter.* 13 (40), 47327–47340. doi:10.1021/acsami.1c10898

Zhu, H., Ji, X., Guan, H., Zhao, L., Zhao, L., Liu, C., et al. (2019). Tantalum Nanoparticles Reinforced Polyetheretherketone Shows Enhanced Bone Formation. *Mater. Sci. Eng. C* 101, 232–242. doi:10.1016/j.msec.2019.03.091

Zimmerli, W., and Sendi, P. (2017). Orthopedic Biofilm Infections. *Apmis* 125 (4), 353–364. doi:10.1111/apm.12687

Conflict of Interest: The authors declare that the research was conducted in the absence of any commercial or financial relationships that could be construed as a potential conflict of interest.

Publisher's Note: All claims expressed in this article are solely those of the authors and do not necessarily represent those of their affiliated organizations or those of the publisher, the editors, and the reviewers. Any product that may be evaluated in this article, or claim that may be made by its manufacturer, is not guaranteed or endorsed by the publisher.

Copyright © 2022 Wang, Zhang, Nie, Qu and Yue. This is an open-access article distributed under the terms of the Creative Commons Attribution License (CC BY). The use, distribution or reproduction in other forums is permitted, provided the original author(s) and the copyright owner(s) are credited and that the original publication in this journal is cited, in accordance with accepted academic practice. No use, distribution or reproduction is permitted which does not comply with these terms.

frontiers | Frontiers in Bioengineering and Biotechnology

MINI REVIEW
published: 16 May 2022
doi: 10.3389/fbioe.2022.911180

The Osteoinductivity of Calcium Phosphate-Based Biomaterials: A Tight Interaction With Bone Healing

Yuchen Zhang[1†], Tianyu Shu[1†], Silin Wang[1], Zhongbo Liu[1], Yilong Cheng[2], Ang Li[1] and Dandan Pei[1]**

[1]Key Laboratory of Shaanxi Province for Craniofacial Precision Medicine Research, College of Stomatology, Xi'an Jiaotong University, Xi'an, China, [2]School of Chemistry, Xi'an Jiaotong University, Xi'an, China

Calcium phosphate (CaP)-based bioceramics are the most widely used synthetic biomaterials for reconstructing damaged bone. Accompanied by bone healing process, implanted materials are gradually degraded while bone ultimately returns to its original geometry and function. In this progress report, we reviewed the complex and tight relationship between the bone healing response and CaP-based biomaterials, with the emphasis on the *in vivo* degradation mechanisms of such material and their osteoinductive properties mediated by immune responses, osteoclastogenesis and osteoblasts. A deep understanding of the interaction between biological healing process and biomaterials will optimize the design of CaP-based biomaterials, and further translate into effective strategies for biomaterials customization.

Keywords: calcium phosphate, biomaterials, osteoinductivity, biodegradation, bone healing

OPEN ACCESS

Edited by:
Kaili Lin,
Shanghai Jiao Tong University, China

Reviewed by:
Fucong Tian,
Augusta University, United States
Xingge Yu,
Shanghai Ninth People's Hospital, China

****Correspondence:***
Ang Li
drliang@xjtu.edu.cn
Dandan Pei
peidandan@xjtu.edu.cn

[†]These authors have contributed equally to this work

Specialty section:
This article was submitted to Biomaterials, a section of the journal Frontiers in Bioengineering and Biotechnology

Received: *02 April 2022*
Accepted: *21 April 2022*
Published: *16 May 2022*

Citation:
Zhang Y, Shu T, Wang S, Liu Z, Cheng Y, Li A and Pei D (2022) The Osteoinductivity of Calcium Phosphate-Based Biomaterials: A Tight Interaction With Bone Healing. Front. Bioeng. Biotechnol. 10:911180. doi: 10.3389/fbioe.2022.911180

1 INTRODUCTION

The clinical intervention of bone healing is necessary for bone defects beyond the critical size, such as large segmental bone defects caused by severe trauma, tumor resection, cancer, congenital diseases, or small-scale alveolar bone defects (Davies et al., 2017; Majidinia et al., 2018). Given inevitable drawbacks of autografts (including donor site pain, increased operative time, risk of wound infection, and insufficient availability), many synthetic biomaterials have been specifically designed as an alternative for bone repair and regeneration (Pina et al., 2015; Xu et al., 2017; Stastny et al., 2019). Since the 1970s, calcium phosphate (CaP)-based bioceramics have received the most attention, and several of them [e.g., β-tricalcium phosphate (β-TCP) and hydroxyapatite (HA or HAP)] have already been clinically applied for orthopedic and maxillofacial surgery (Schaefer et al., 2011; Danoux et al., 2015).

For bone-filling purposes, CaPs have been utilized as bioactive components of solid ceramic, coatings, self-setting CaP cements (CPC), as well as advanced polymers, intending to function as a scaffold for bone formation (Parent et al., 2017). The family of CaP biomaterials comprises varying phase compositions, including HA [$Ca_{10}(PO_4)_6(OH)_2$], tricalcium phosphate [TCP, $Ca_3(PO_4)_2$], octacalcium phosphate [OCP, $Ca_8(HPO_4)_2(PO_4)_4{\cdot}5H_2O$], dicalcium phosphate dihydrate [DCPD, $CaHPO_4.2H_2O$], and amorphous calcium phosphate [ACP, $CaxHy(PO_4)z{\cdot}nH_2O$, n = 3–4.5; 15–20% H_2O], can be used in a variety of applications due to differences in solubility, stability, and mechanical strength (Jeong et al., 2019; Dorozhkin, 2021). CaP-based biomaterials provide a strong biomaterial/bone interface and demonstrate promising biological properties such as biodegradability, osteoconductivity, and in some cases even osteoinductivity (i.e., the ability of the material to induce *de novo* bone formation without the presence of osteogenic factors) (LeGeros,

2008; Chai et al., 2012; Stastny et al., 2019). In addition, CaPs can be manufactured in large quantities at relatively low cost, meeting the requirements of socially responsible tissue engineering and regenerative medicine (Habraken et al., 2016).

Much effort has been spent on optimizing biomechanical and physico-chemical properties to "engineer" materials for better "osteoinductivity" (Bigi and Boanini, 2017; Ruffini et al., 2021). In this context, the stiffness, porosity and pore size, surface microstructure, phase composition, and crystallinity have all been shown to affect the bone regeneration capacity of CaP-based materials. These bone-matching "static" physico-chemical parameters and the underlying osteogenesis mechanisms have been summarized in recent reviews for material design optimization (Habraken et al., 2016; Galvan-Chacon and Habibovic, 2017; Przekora, 2019; Dee et al., 2020). Nevertheless, the laboratory-prepared bone graft materials are often not successful in clinical application (Chen Z. et al., 2016). The regeneration capacity of biomaterials is usually evaluated by *in vitro* osteoblastic lineage (Diez-Escudero et al., 2017b), and *in vivo* bone histomorphology measurements (Yuan et al., 2000; Chiba et al., 2016). However, the biological process of bone healing to implanted materials has always been neglected. The mechanisms underlying bone healing are not simply led by osteoblasts, but a synergy of multiple systems involving a series of biological events including early inflammation response and long-term reconstruction process (Newman et al., 2021; Zhu et al., 2021). Therefore, the optimization and design of CaP-based biomaterials should keep pace with the rapid progress in bone healing biology, which eventually determines the *in vivo* fate of CaP-based biomaterials and bone healing effects.

In this review, we first summarized the biological process of bone healing and then focused on major developments in the bone healing response to CaP-based biomaterials. Understanding the interaction between biomaterials and host response during the bone healing process is important for improving the design of CaP-based biomaterials. Simultaneously, we also provide an outlook toward customizable CaP-polymer composite biomaterial strategies.

2 OVERVIEW OF BONE HEALING PROCESS

There are three overlapping stages of the bone healing process: inflammation, bone formation and bone remodeling (Maruyama et al., 2020; Newman et al., 2021; Zhu et al., 2021).

Inflammation begins immediately after the bone is broken and lasts for several days. Driven by cytokines, macrophages and other immune cells (granulocytes, lymphocytes, monocytes, etc.) infiltrate bone defects, which trigger inflammatory reactions, clean up bone-tissue debris, as well as form vascular tissue and granulation tissue (Maruyama et al., 2020). Macrophages demonstrate broad roles here in regulating bone tissue homeostasis. Under the stimulation of the locally ischemic and hypoxic environment, and cytokines [e.g., macrophage colony-stimulating factor (M-CSF) and receptor activator of NF-κB ligand (RANKL)], macrophages polarize towards "M1" type. They secrete a series of pro-inflammatory cytokines [e.g., tumor necrosis factor-α (TNF-α), interleukin-1 (IL-1), IL-6], which in turn recruit mesenchymal stem cells (MSCs), osteoprogenitor cells, and fibroblasts for tissue repair (Miron et al., 2016; Zhu et al., 2021). Macrophages transform towards M2 wound-healing type at the end of the inflammatory stage and secrete anti-inflammatory cytokines [e.g., IL-4, IL-10, and transforming growth factors beta (TGF-β)] in favor of establishing osteogenic environments (Oliveira et al., 2021).

During the bone formation process, there are two repair mechanisms depending on the location of the bone defect. The cancellous and inter-cortical bone regions are repaired by endochondral ossification, while the subperiosteal and adjacent soft tissue regions are repaired by intramembranous ossification (Zhu et al., 2021). In cancellous and inter-cortical bone regions, the recruited MSCs aggregate, proliferate and differentiate into chondrocytes. They secrete an avascular cartilage matrix, and the granulation tissue is gradually replaced by the fibrocartilage- and hyaline cartilage-rich soft callus (Nossin et al., 2021). Along with new blood vessel formation, endothelial cells, osteoblasts, and chondrocytes secrete matrix metalloproteinases to degrade the cartilage matrix. Mature hypertrophic chondrocytes undergo apoptosis or transition into osteoblast-like cells, which together with osteoblasts, contribute to the secretion of type I collagen and the extracellular matrix (ECM) mineralization. Finally, the soft callus is transformed into the disordered woven bone (Tsang et al., 2015; Fu et al., 2021). Once the periosteum and adjacent soft tissue regions are injured, the MSCs recruited from the periosteum, bone marrow, adjacent soft tissues, and peripheral circulation and osteoprogenitor cells within the periosteum initiate the intramembranous bone formation process. MSCs and osteoprogenitor cells differentiate into osteoblasts. These cells secrete and mineralize ECM, forming hard callus directly under the periosteum (Wang et al., 2020).

Bone remodeling is the final stage of bone healing and typically lasts for several months (ElHawary et al., 2021). As a dynamic process, the irregular woven bone is reconstructed by bone resorption and osteogenesis process under mechanical stimulation and further developed as mature lamellar bone (Frost, 2004; Loi et al., 2016; ElHawary et al., 2021). The crosstalk between osteoblasts and osteoclasts plays an important role in this phase. Bone ultimately returns to its original shape and restores the geometry and function of the damaged part (Zhu et al., 2021).

3 CALCIUM PHOSPHATE-BASED BIOMATERIALS PARTICIPATE IN BONE HEALING PROCESS

With similar composition to bone minerals, CaP-based biomaterials induce biological responses like those occur during bone healing (Diez-Escudero et al., 2017a). On the one hand, multiple cells involved in bone healing mediate the degradation and resorption of implanted materials. This is critical for CaP-based biomaterials to provide the space into which the bone and vascular tissues can grow (Rustom et al.,

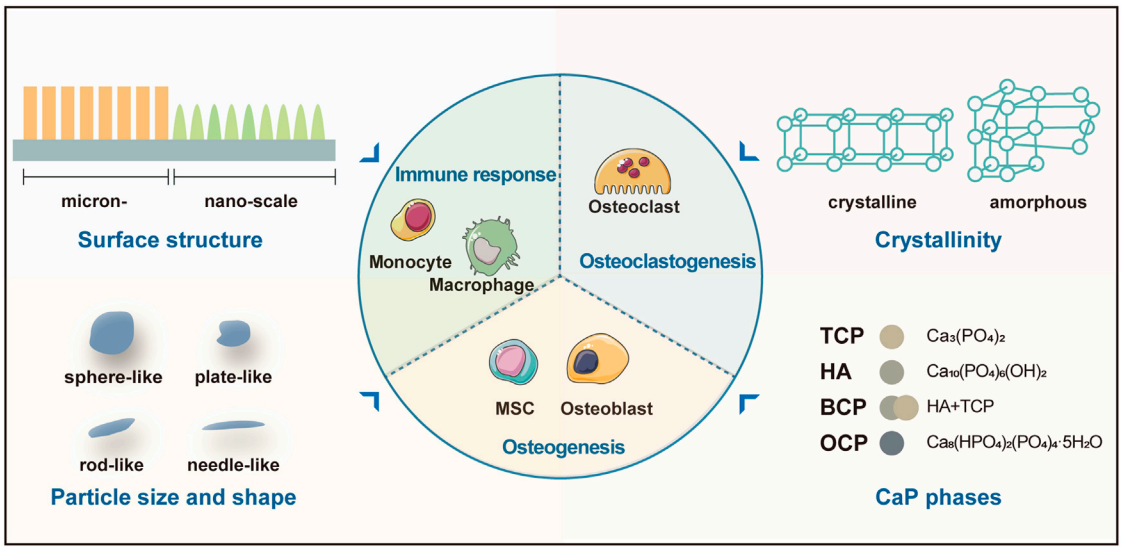

FIGURE 1 | The physico-chemical properties of CaP-based biomaterials affect the activity and function of immune cells, osteoclasts, and osteoblasts. Abbreviation: BCP, biphasic calcium phosphate; TCP, tricalcium phosphate; HA, hydroxyapatite; MSC, mesenchymal stem cell; OCP, octacalcium phosphate.

2019). The concomitant release of inorganic ions from the biodegradation of CaPs is also necessary for modifying the behavior of cells/tissues and enhances the osteoinductivity of the biomaterials (Tang et al., 2018). On the other hand, the osteoinductivity of CaP-based biomaterials is complicated *in vivo* as inflammation and osteoclastogenesis accompany the entire process of bone healing. Recent studies have pointed out that the physico-chemical properties of CaP-based biomaterials could affect the activity and function of immune cells and osteoclasts, and indirectly or directly affect osteogenesis, respectively (**Figure 1**). In this section, we will detail these tight and complex interactions between CaP-based biomaterials and bone healing responses.

3.1 Mechanisms of *in vivo* Biodegradation of Calcium Phosphate-Based Biomaterials

After implantation, the host body will first undergo a universal immune response to the materials. Proteins (e.g., fibrinogen, vitronectin, complement, and fibronectin) from blood and interstitial fluid will immediately adsorb on the material surface and then trigger an acute inflammation. Chemoattractants and cytokines such as platelet factor 4 (PF-4), platelet-derived growth factor (PDGF), and TGF-β lead to monocyte colonization and differentiate into macrophages and osteoclasts (Chen Z. et al., 2016; Galvan-Chacon and Habibovic, 2017). Meanwhile, CaP-based biomaterials will undergo degradation and resorption processes *in vivo* (Sheikh et al., 2015). Degradation is a physical process utilizing chemical dissolution or mechanical degradation. The disintegration and fragmentation of implants are often accompanied by the release of material particles (Sheikh et al., 2015; Galvan-Chacon and Habibovic, 2017). Biomaterial degradation paths the way for cell-mediated resorption processes that involve macrophages, osteoclasts, and multinucleated giant cells (Sheikh et al., 2015; Miron and Bosshardt, 2016; Xiao et al., 2016).

CaP particles can be directly engulfed *via* phagocytosis and intracellular digestion by macrophages and osteoclasts (size <10 μm), as well as giant cells (size between 10 and 100 μm) (Heymann et al., 2001; Wenisch et al., 2003; Nicolin et al., 2016). The particles, if larger than 100 μm, will undergo extracellular degradation within the acidic microenvironment created by osteoclasts (Galvan-Chacon and Habibovic, 2017). Solubility of the biomaterial (Yamada et al., 1997; Detsch et al., 2010; Wu and Uskokovic, 2016) and topographic characteristics such as specific surface area and the porosity content (Zimmer et al., 2013; Davison et al., 2014; Diez-Escudero et al., 2017b) are relevant physicochemical factors that influence the osteoclasts resorption activity.

In addition, cytokines released by monocytes/macrophages are responsible for the recruitment of osteoprogenitor cells and MSCs (Przekora, 2019). Cytokines such as M-CSF, RANKL and osteoprotegerin are responsible for stimulating osteoclastogenesis (Chen Z. et al., 2016). Contrary to previous beliefs that all inflammatory responses should be suppressed after biomaterial implantation, healing is promoted by suppression of extended chronic inflammatory responses (Miron and Bosshardt, 2016; Batool et al., 2021).

3.2 The Interaction Between Bone Healing Response and Calcium Phosphate-Based Biomaterials

3.2.1 Calcium Phosphate-Based Materials Regulate Osteoimmune

The concept of "osteoimmunomodulation" was proposed by Chen Z. et al. (2016) to emphasize the important roles of bone immune response in determining the *in vivo* fate of bone

substitute materials. Macrophages are major effector cells in determining the duration and intensity of material-induced immune responses and are indispensable for osteogenesis (Chen et al., 2014a; Xiao et al., 2021). Chen and his team (Chen et al., 2014b) demonstrated that macrophages switch to the M2 phenotype through the calcium-sensing receptor (CaSR) pathway in response to β-TCP powder extracts. At the same time, the secreted bone morphogenetic protein 2 (BMP-2), as well as anti-inflammatory genes (IL-10 and IL-1rα) were up-regulated, and inflammatory genes (IL-1β and IL-6) were significantly down-regulated in macrophages. When bone marrow mesenchymal stem cells (BMSCs) were cultured in macrophage/β-TCP extracts conditioned medium, the osteogenic differentiation of BMSCs was significantly enhanced. More recent studies also reported similar findings that under the stimulation of biphasic calcium phosphate (BCP) ceramics, the expression of anti-inflammatory cytokine (IL-10) and growth factors, including vascular endothelial growth factor (VEGF), PDGF, epidermal growth factor (EGF), BMP-2 and TGF-β1 was increased, which might synergistically create a pro-osteogenic micro-environment, resulting in MSCs recruitment and differentiation into osteoblasts (Chen X. et al., 2016; Wang et al., 2017). Compared with macrophage/BCP conditioned media, the degradation particles of BCP might play a more substantial role in this process (Wang et al., 2017). However, the increased expression of inflammatory factors [IL-6, monocyte chemoattractant protein-1 (MCP-1), and TNF-α] in macrophages was found by Wang et al. (2017), and the increment of these pro-inflammatory cytokines did not seem to inhibit the osteogenic differentiation of MSCs. The reason may be that the effects of inflammatory cytokines are dose-dependent, e.g., only IL-6 of high concentration (above 10 ng ml^{-1}) was proven to exhibit an inhibitory effect on BCP-induced osteogenesis (Chen X. et al., 2016). Further, more *in vivo* evaluations are needed for validating the immune-stimulated osteogenesis after CaP-based biomaterials implantation.

3.2.2 Calcium Phosphate-Based Materials Regulate Osteoclast-Mediated Osteogenesis

Bone resorption mediated by osteoclasts is tightly coupled with osteogenesis of osteoblasts (Chen et al., 2018; Kim et al., 2020). Substantial efforts have been made in modifying the properties of CaP-based materials to regulate the activities of osteoclasts. And the phases, surface structure, and crystallinity of CaP materials have been shown to control osteoclast activities (Takami et al., 2009; Davison et al., 2014; Uskokovic et al., 2019; Wang et al., 2021). Wang et al. (2021) prepared a series of CPC scaffolds with different calcium and phosphate ratios (Ca/P) and found that slight release of phosphate ions from CPC with higher Ca/P ratio (1.67) improved osteoclastogenesis. The released phosphate ions promoted osteoclast differentiation *via* increased affinity between RANKL and RANK, as well as robust NF-κB signaling transduction. Rat calvarial defect model further supported that CPC with high Ca/P ratio could ameliorate osteoclast-mediated bone healing. In addition to ions effects, the topographical structure and crystallinity of CaP materials could also be tuned to control osteoclast activities. For instance, Davison et al. (2014) indicated that β-TCP with submicron structure feature facilitated human peripheral blood monocytes differentiation into osteoclasts compared to microstructure. Similarly, another study pointed out that the surface structure of BCP affected osteoclastogenesis and bone ectopic formation after material implantation into the dorsal muscle of dogs (Davison et al., 2015). A recent study also showed that osteoclasts could sense the crystallinity of materials and higher crystallinity enhances metabolic and resorption activities of osteoclasts (Uskokovic et al., 2019).

In addition, the phases of CaPs in implanted materials could affect the osteoblasts-osteoclasts crosstalk *in vitro*. Shiwaku et al. (2015) found that osteoclasts cultured on BCPs with low HA content (5%) increased the expression of positive coupling factors, including sphingosine-kinase 1 (SPHK1) and collagen triple helix repeat containing 1 (Cthrc1). In a subsequent study, they cultured osteoclasts on HA/OCP or HA/TCP disks to investigate how the distinct chemical composition and crystal structure affect osteoclast formation and the osteoclasts-osteoblasts crosstalk. Both OCP and β-TCP had a similar ability to create multinucleated osteoclasts. OCP promoted the expression of complement component 3a (C3a) and β-TCP enhanced that of EphrinB2 (EfnB2) and Cthrc1 in osteoclasts, respectively. In turn, these secreted positive coupling factors promoted osteoblast differentiation and function (Shiwaku et al., 2019). Chemical properties, such as dissolution and precipitation around OCP and β-TCP crystals, may be factors that contribute to similar and different cellular responses in these CaP phases.

3.2.3 Biological Cell Responses to Internalized Calcium Phosphate Particles

Nanoscale CaP particles are produced from degradation or mechanical abrasion of macroscopic implants or direct implantation as nanoscale bone substitute materials (Epple, 2018). In all these cases, the surrounding tissue is subjected to calcium phosphate nanoparticles (CaP-NPs) at varying concentrations. Apart from small CaP-NPs (a few nm in diameter) that can directly penetrate the cell membrane on their own, almost all CaP nanoparticles are internalized by endocytosis and/or phagocytosis (Mahmoudi et al., 2011). Primary endosomes or phagosomes then fuse with cytoplasmic lysosomes to dissolve the CaP-NPs into calcium and phosphate. The cargo is eventually delivered into the cytoplasm (Epple, 2018). The CaP-NP-induced apoptotic pathway is mediated *via* a mitochondrial-dependent pathway (Xu et al., 2012; Xue et al., 2017). The sizes (Shi et al., 2009), surface topography and morphology (Zhao et al., 2007; Okada et al., 2010) and concentrations (Xu et al., 2012) of CaP-NPs have significant effects on the apoptotic level. The CaP-NPs are not cytotoxic *per se*, but the release of a large number of calcium ions after dissolution of the CaP-NPs is harmful. And apoptosis is induced by increased intracellular calcium ions concentration (Masouleh et al., 2017).

It is worthy that particles released from CaP materials degradation should not disturb the ability of bone-forming cells to form new bone. Therefore, in addition to studying the effect of materials' macroscopic properties on the osteogenic ability of MSCs/osteoblasts, more studies on the effects of

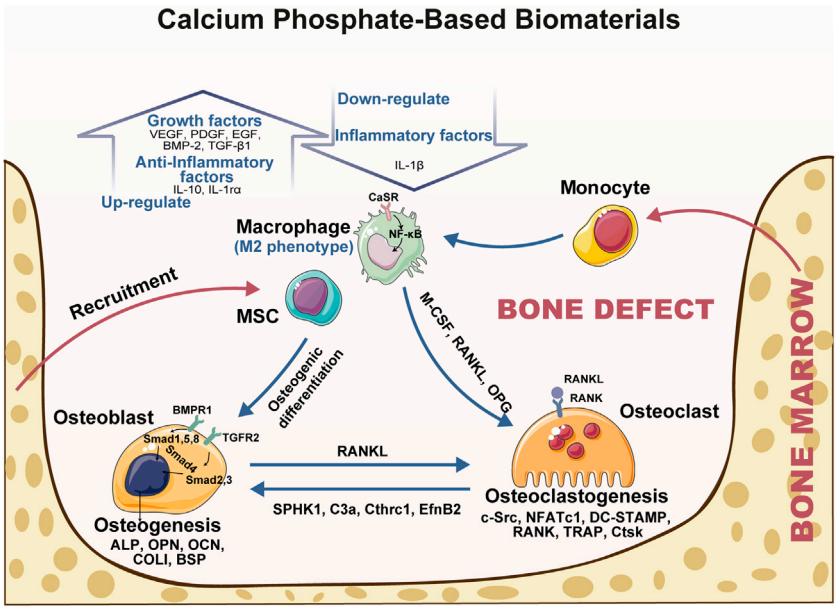

FIGURE 2 | The interactions between CaP-based biomaterials and bone healing response. The osteoinductivity of CaP-based biomaterials can be "programmed" by their physico-chemical properties and are necessary for modifying the behavior of immune cells, osteoclasts, and MSCs/osteoblasts. Under the simulation with CaP-based biomaterials, the expression of inflammatory factors (IL-1β) is decreased, and the production of anti-inflammatory cytokine (IL-10, IL-1rα), as well as growth factors (VEGF, PDGF, EGF, BMP-2, and TGF-β1) is increased in macrophages. The surface structure and crystallinity of CaP-based biomaterials can be sensed by osteoclasts and regulate their metabolically active and resorption capacity. All above synergistically create a pro-osteogenic micro-environment leading to effects on bone formation. Abbreviation: ALP, alkaline phosphatase; BMP-2, bone morphogenetic protein two; BSP, bone sialoprotein; CaSR, calcium-sensing receptor; C3a, complement component 3a; Cthrc1, collagen triple helix repeat containing one; COL-I, collagen I; Ctsk, cathepsin k. DC-STAMP, dendritic cell-specific transmembrane protein; EfnB2, EphrinB2; EGF, epidermal growth factor; IL, interleukin; SPHK1, sphingosine-kinase one; MCP-1, monocyte chemoattractant protein-1; M-CSF, macrophage colony-stimulating factor; NFATc1, nuclear factor of activated T cells one; OCN, osteocalcin; OPN, osteopontin; OPG, osteoprotegerin; PDGF, platelet derived growth factor; RANKL, receptor activator of NF-κB ligand; TGF-β, transforming growth factor beta; TNF-α, tumor necrosis factor-α; TRAP, tartrate-resistant acid phosphatase; VEGF, vascular endothelial growth factor.

CaP-NPs on these cells and the underlying mechanisms have been investigated (Albulescu et al., 2019; Khotib et al., 2021). Particle size, shape, and concentration will have different effects on the function, viability, proliferation, and extracellular matrix of osteoblasts (Sheikh et al., 2015; Li et al., 2022). CaP-NPs have dose-dependent effects on osteoblasts and the maximum number of nanoparticles a single osteoblast can tolerate is 50 (Pioletti et al., 2000). Small CaP particles (1–10 μm) are less biocompatible than large particles (>10 μm) on the viability, proliferation and gene expression of osteoblasts (Pioletti et al., 2000). The CaP-NPs with higher specific surface area could increase the adhesion of osteoblasts. However, Xu et al. (2012) found that larger specific surface areas of CaP-NPs might induce higher apoptosis rates in the concentration range of 20–100 μg/ml. Jin et al. (2017) have studied the effect of unfunctionalized calcium phosphate nanorods (HA; 20 nm in diameter and 80 nm in length) on MC3T3 cells. They observed an uptake by micropinocytosis and a significant cytotoxicity above 40 mg L^{-1}, which was caused by oxidative stress and lysosomal rupture. In a study using SAOS-2 osteoblasts, nano-HA were actively internalized and are retained within intracellular membrane-bound compartments. Dissolution of the nano-HA was observed within phagolysosomes. After 24 h of internalization, re-precipitation of needle-like minerals appears in the intracellular membrane-bound compartments (Rossi et al., 2018). These re-precipitated nanoparticles may provide a cellular protective mechanism against the cytotoxicity of rapidly elevated cytoplasmic calcium ions (Rossi et al., 2018).

In addition, particle size also significantly affects the activity of stimulating osteogenic differentiation. Yang et al. (2018) cultured MSCs with three different-sized nano-HA (~50, ~100, and ~150 nm, resp.) and found that smaller-sized nano-HA (~50 and ~100 nm) accelerated the expression of osteoblast-like cell osteogenic genes (Yang et al., 2018). This is in line with that smaller-sized nano-HA (40–1000 nm) appeared to be more effective in stimulating osteogenic differentiation of hMSCs (Weissenboeck et al., 2006). An *in vitro* enzymatic reaction route has been employed for generating biomimetic amorphous calcium phosphate (EACP) nanominerals (Jiang et al., 2018). The amorphous nanomineral is composed of organic-inorganic hybrid nanoparticles. Adenosine triphosphate (ATP) provides the pool of phosphate ions for EACP formation. After internalization of EACP into human bone marrow-derived mesenchymal stem cells (hBMSCs), the release of ADP/AMP biomolecules and calcium ions activate adenosine 5′-monophosphate (AMP)-activated protein kinase (AMPK) and induces autophagy and osteogenic differentiation of hBMSCs (Jiang et al., 2018).

4 CUSTOMIZABLE CALCIUM PHOSPHATE-POLYMER COMPOSITE BIOMATERIALS

Although humans share a set of bone healing mechanisms, the effects of bone healing vary in individuals, depending on the conditions of bone defects. Such diversities account for the different rates and effects of bone regeneration. Because these biomaterials are likely to be transplanted into an 'unfriendly' host, the disease state, and other specifics of the host, such as age, ongoing chronic inflammation and infection should be well understood and taken into consideration. Accordingly, the fabrication of a customizable bone graft to match the condition of the bone defect is important for efficient bone regeneration.

Customizable bone graft substitutes may be designed by following two principles: 1) Tailored external construction and internal structural mimicking of the microenvironment of the defect site. The specific technologies and methods relevant to the design and manufacture of such materials are summarized in another review (Forrestal et al., 2017). 2) Customized biodegradation rate that matches the new bone formation rate, which needs to be complemented by an appropriate *in vivo* bone healing response. In this context, introducing CaPs into smart hydrogel systems may be a promising solution.

Hydrogels possess good biocompatibility and tissue integration properties and serve as the carriers in drug systems and bone tissue engineering biomaterials (Forrestal et al., 2017; Mantha et al., 2019). In response to stimulus [including exogenous (thermoresponsively-, magnetically-, electroresponsively- or light-triggered) and internal physical/biochemical (pH-, redox- or enzyme-sensitive)], hydrogel systems can change their structures, compositions or conformations to support the release of encapsulated active species (Claassen et al., 2019; Wei et al., 2022). The specific microenvironment of bone healing process, such as specific immune environment or enzyme release, can be used to design corresponding intelligent stimulus-responsive biomaterials for rapid reactive bone therapy and bone regeneration. Enzyme-responsive systems provide enlightenments for the selection of biomolecules. The design of enzyme-responsive systems for drug delivery relies on esterase- or protease-mediated cleavage of esters or short peptide sequences, resulting in effective drug release (Ramasamy et al., 2017). By choosing an appropriate peptide sequence, enzyme-responsive materials may be designed to respond exclusively to a target enzyme (Ramasamy et al., 2017). To be specific, tissue-nonspecific alkaline phosphatase (TNAP) may be considered a candidate. The TNAP hydrolyzes inorganic pyrophosphate (PPi, a potent mineralization inhibitor) and ATP into monophosphate (Pi, inorganic phosphate) to control ECM mineralization (Bottini et al., 2018). Ideally, a matching peptide sequence can make polymers respond exclusively to TNAP. New bone formation that coordinates with the biodegradation of CaP-polymer composites may be achieved by harnessing the TNAP-response to achieve a customized biodegradation rate.

5 CONCLUSION

Synthetic biodegradable bone grafts are gradually being replaced by the patient's own bone. After implantation, tight and complex interactions occur between CaP-based biomaterials and the bone healing process. Multiple cells involved in bone healing mediate the materials' degradation and resorption, which is essential to provide the space into which the bone and vascular tissues can grow. The physico-chemical properties of materials are also necessary for modifying the behavior of cells/tissues and enhancing the osteoinductivity of the biomaterials. In light with previous studies, we summarized the osteoinductive mechanism of CaP-based biomaterials accompanying bone healing (**Figure 2**). Under the stimulation with CaP-based biomaterials, the expression of inflammatory factors (IL-1β) is decreased, and the production of anti-inflammatory cytokine (IL-10, IL-1rα), as well as growth factors (VEGF, PDGF, EGF, BMP-2 and TGF-β1) is increased in macrophages, which synergistically create a pro-osteogenic micro-environment. The surface topography and crystallinity of CaP-based biomaterials can be sensed by osteoclasts and regulate their metabolic activity and resorption capacity, then influencing bone formation. These material particles are eventually internalized into cells and are involved in the regulation of cell homeostasis and cell differentiation. Based on the in-depth understanding of the involvement of CaP-based biomaterials in the bone healing process, we propose the future design of these materials is to develop biomaterials with customizability, such as tailored geometry and biodegradation rate.

AUTHOR CONTRIBUTIONS

YZ and TS drafted the manuscript and contributed equally to this work. YZ, TS, SW, ZL, and YC investigated related publications. AL and DP reviewed and edited the work. All authors contributed to the article and approved the submitted version.

FUNDING

This work was financially supported by the National Natural Science Foundation of China (81870798, 82170927, and 82071078), the Natural Science Basic Research Program of Shaanxi Province (2022JC-57) and the Fundamental Research Funds for the Central Universities (xtr012019007 and sxtr042021004).

REFERENCES

Albulescu, R., Popa, A.-C., Enciu, A.-M., Albulescu, L., Dudau, M., Popescu, I. D., et al. (2019). Comprehensive *In Vitro* Testing of Calcium Phosphate-Based Bioceramics with Orthopedic and Dentistry Applications. *Materials* 12, 3704. doi:10.3390/ma12223704

Batool, F., Özçelik, H., Stutz, C., Gegout, P.-Y., Benkirane-Jessel, N., Petit, C., et al. (2021). Modulation of Immune-Inflammatory Responses through Surface Modifications of Biomaterials to Promote Bone Healing and Regeneration. *J. Tissue Eng.* 12, 204173142110414. doi:10.1177/20417314211041428

Bigi, A., and Boanini, E. (2017). Functionalized Biomimetic Calcium Phosphates for Bone Tissue Repair. *J. Appl. Biomaterials Funct. Mater.* 15, e313–e325. doi:10.5301/jabfm.5000367

Bottini, M., Mebarek, S., Anderson, K. L., Strzelecka-Kiliszek, A., Bozycki, L., Simão, A. M. S., et al. (2018). Matrix Vesicles from Chondrocytes and Osteoblasts: Their Biogenesis, Properties, Functions and Biomimetic Models. *Biochimica Biophysica Acta (BBA) - General Subj.* 1862, 532–546. doi:10.1016/j.bbagen.2017.11.005

Chai, Y. C., Carlier, A., Bolander, J., Roberts, S. J., Geris, L., Schrooten, J., et al. (2012). Current Views on Calcium Phosphate Osteogenicity and the Translation into Effective Bone Regeneration Strategies. *Acta Biomater.* 8, 3876–3887. doi:10.1016/j.actbio.2012.07.002

Chen, X., Wang, J., Wang, J., Zhu, X., Yang, X., Fan, Y., et al. (2016a). The Positive Role of Macrophage Secretion Stimulated by BCP Ceramic in the Ceramic-Induced Osteogenic Differentiation of Pre-osteoblasts via Smad-Related Signaling Pathways. *RSC Adv.* 6, 102134–102141. doi:10.1039/C6RA23362G

Chen, X., Wang, Z., Duan, N., Zhu, G., Schwarz, E. M., and Xie, C. (2018). Osteoblast-osteoclast Interactions. *Connect. Tissue Res.* 59, 99–107. doi:10.1080/03008207.2017.1290085

Chen, Z., Klein, T., Murray, R. Z., Crawford, R., Chang, J., Wu, C., et al. (2016b). Osteoimmunomodulation for the Development of Advanced Bone Biomaterials. *Mater. Today* 19, 304–321. doi:10.1016/j.mattod.2015.11.004

Chen, Z., Mao, X., Tan, L., Friis, T., Wu, C., Crawford, R., et al. (2014a). Osteoimmunomodulatory Properties of Magnesium Scaffolds Coated with β-tricalcium Phosphate. *Biomaterials* 35, 8553–8565. doi:10.1016/j.biomaterials.2014.06.038

Chen, Z., Wu, C., Gu, W., Klein, T., Crawford, R., and Xiao, Y. (2014b). Osteogenic Differentiation of Bone Marrow MSCs by β-tricalcium Phosphate Stimulating Macrophages via BMP2 Signalling Pathway. *Biomaterials* 35, 1507–1518. doi:10.1016/j.biomaterials.2013.11.014

Chiba, S., Anada, T., Suzuki, K., Saito, K., Shiwaku, Y., Miyatake, N., et al. (2016). Effect of Resorption Rate and Osteoconductivity of Biodegradable Calcium Phosphate Materials on the Acquisition of Natural Bone Strength in the Repaired Bone. *J. Biomed. Mat. Res.* 104, 2833–2842. doi:10.1002/jbm.a.35828

Claassen, C., Gerlach, T., and Rother, D. (2019). Stimulus-Responsive Regulation of Enzyme Activity for One-Step and Multi-Step Syntheses. *Adv. Synth. Catal.* 361, 2387–2401. doi:10.1002/adsc.201900169

Danoux, C. B. S. S., Bassett, D. C., Othman, Z., Rodrigues, A. I., Reis, R. L., Barralet, J. E., et al. (2015). Elucidating the Individual Effects of Calcium and Phosphate Ions on hMSCs by Using Composite Materials. *Acta Biomater.* 17, 1–15. doi:10.1016/j.actbio.2015.02.003

Davies, O. G., Cox, S. C., Williams, R. L., Tsaroucha, D., Dorrepaal, R. M., Lewis, M. P., et al. (2017). Annexin-enriched Osteoblast-Derived Vesicles Act as an Extracellular Site of Mineral Nucleation within Developing Stem Cell Cultures. *Sci. Rep.* 7, 12639. doi:10.1038/s41598-017-13027-6

Davison, N. L., ten Harkel, B., Schoenmaker, T., Luo, X., Yuan, H., Everts, V., et al. (2014). Osteoclast Resorption of Beta-Tricalcium Phosphate Controlled by Surface Architecture. *Biomaterials* 35, 7441–7451. doi:10.1016/j.biomaterials.2014.05.048

Davison, N., Su, J., Su, J., Yuan, H., van den Beucken, J., de Bruijn, J., et al. (2015). Influence of Surface Microstructure and Chemistry on Osteoinduction and Osteoclastogenesis by Biphasic Calcium Phosphate Discs. *eCM* 29, 314–329. doi:10.22203/ecm.v029a24

Dee, P., You, H. Y., Teoh, S.-H., and Le Ferrand, H. (2020). Bioinspired Approaches to Toughen Calcium Phosphate-Based Ceramics for Bone Repair. *J. Mech. Behav. Biomed. Mater.* 112, 104078. doi:10.1016/j.jmbbm.2020.104078

Detsch, R., Hagmeyer, D., Neumann, M., Schaefer, S., Vortkamp, A., Wuelling, M., et al. (2010). The Resorption of Nanocrystalline Calcium Phosphates by Osteoclast-like Cells. *Acta Biomater.* 6, 3223–3233. doi:10.1016/j.actbio.2010.03.003

Diez-Escudero, A., Espanol, M., Beats, S., and Ginebra, M.-P. (2017a). *In Vitro* degradation of Calcium Phosphates: Effect of Multiscale Porosity, Textural Properties and Composition. *Acta Biomater.* 60, 81–92. doi:10.1016/j.actbio.2017.07.033

Diez-Escudero, A., Espanol, M., Montufar, E. B., Di Pompo, G., Ciapetti, G., Baldini, N., et al. (2017b). Focus Ion Beam/Scanning Electron Microscopy Characterization of Osteoclastic Resorption of Calcium Phosphate Substrates. *Tissue Eng. Part C. Methods* 23 (2), 118–124. doi:10.1089/ten.TEC.2016.0361

Dorozhkin, S. V. (2021). Synthetic Amorphous Calcium Phosphates (ACPs): Preparation, Structure, Properties, and Biomedical Applications. *Biomater. Sci.* 9, 7748–7798. doi:10.1039/d1bm01239h

ElHawary, H., Baradaran, A., Abi-Rafeh, J., Vorstenbosch, J., Xu, L., and Efanov, J. I. (2021). Bone Healing and Inflammation: Principles of Fracture and Repair. *Semin. Plast. Surg.* 35, 198–203. doi:10.1055/s-0041-1732334

Epple, M. (2018). Review of Potential Health Risks Associated with Nanoscopic Calcium Phosphate. *Acta Biomater.* 77, 1–14. doi:10.1016/j.actbio.2018.07.036

Forrestal, D. P., Klein, T. J., and Woodruff, M. A. (2017). Challenges in Engineering Large Customized Bone Constructs. *Biotechnol. Bioeng.* 114, 1129–1139. doi:10.1002/bit.26222

Frost, H. M. (2004). A 2003 Update of Bone Physiology and Wolff's Law for Clinicians. *Angle Orthod.* 74, 3–15. doi:10.1043/0003-3219(2004)074<0003:AUOBPA>2.0.CO;2

Fu, R., Liu, C., Yan, Y., Li, Q., and Huang, R.-L. (2021). Bone Defect Reconstruction via Endochondral Ossification: A Developmental Engineering Strategy. *J. Tissue Eng.* 12, 204173142110042. doi:10.1177/20417314211004211

Galván-Chacón, V. P., and Habibovic, P. (2017). Deconvoluting the Bioactivity of Calcium Phosphate-Based Bone Graft Substitutes: Strategies to Understand the Role of Individual Material Properties. *Adv. Healthc. Mat.* 6, 1601478. doi:10.1002/adhm.201601478

Habraken, W., Habibovic, P., Epple, M., and Bohner, M. (2016). Calcium Phosphates in Biomedical Applications: Materials for the Future? *Mater. Today* 19, 69–87. doi:10.1016/j.mattod.2015.10.008

Heymann, D., Guicheux, J., and Rousselle, A. V. (2001). Ultrastructural Evidence *In Vitro* of Osteoclast-Induced Degradation of Calcium Phosphate Ceramic by Simultaneous Resorption and Phagocytosis Mechanisms. *Histol. Histopathol.* 16, 37–44. doi:10.14670/HH-16.37

Jeong, J., Kim, J. H., Shim, J. H., Hwang, N. S., and Heo, C. Y. (2019). Bioactive Calcium Phosphate Materials and Applications in Bone Regeneration. *Biomater. Res.* 23, 4. doi:10.1186/s40824-018-0149-3

Jiang, Y.-Y., Zhou, Z.-F., Zhu, Y.-J., Chen, F.-F., Lu, B.-Q., Cao, W.-T., et al. (2018). Enzymatic Reaction Generates Biomimic Nanominerals with Superior Bioactivity. *Small* 14, 1804321. doi:10.1002/smll.201804321

Jin, Y., Liu, X., Liu, H., Chen, S., Gao, C., Ge, K., et al. (2017). Oxidative Stress-Induced Apoptosis of Osteoblastic MC3T3-E1 Cells by Hydroxyapatite Nanoparticles through Lysosomal and Mitochondrial Pathways. *RSC Adv.* 7, 13010–13018. doi:10.1039/c7ra01008g

Khotib, J., Gani, M. A., Budiatin, A. S., Lestari, M. L. A. D., Rahadiansyah, E., and Ardianto, C. (2021). Signaling Pathway and Transcriptional Regulation in Osteoblasts during Bone Healing: Direct Involvement of Hydroxyapatite as a Biomaterial. *Pharmaceuticals* 14, 615. doi:10.3390/ph14070615

Kim, J.-M., Lin, C., Stavre, Z., Greenblatt, M. B., and Shim, J.-H. (2020). Osteoblast-osteoclast Communication and Bone Homeostasis. *Cells* 9, 2073. doi:10.3390/cells9092073

LeGeros, R. Z. (2008). Calcium Phosphate-Based Osteoinductive Materials. *Chem. Rev.* 108, 4742–4753. doi:10.1021/cr800427g

Li, X., Zhou, Q., Wu, Y., Feng, C., Yang, X., Wang, L., et al. (2022). Enhanced Bone Regenerative Properties of Calcium Phosphate Ceramic Granules in Rabbit Posterolateral Spinal Fusion through a Reduction of Grain Size. *Bioact. Mater.* 11, 90–106. doi:10.1016/j.bioactmat.2021.10.006

Loi, F., Córdova, L. A., Pajarinen, J., Lin, T.-h., Yao, Z., and Goodman, S. B. (2016). Inflammation, Fracture and Bone Repair. *Bone* 86, 119–130. doi:10.1016/j.bone.2016.02.020

Mahmoudi, M., Azadmanesh, K., Shokrgozar, M. A., Journeay, W. S., and Laurent, S. (2011). Effect of Nanoparticles on the Cell Life Cycle. *Chem. Rev.* 111, 3407–3432. doi:10.1021/cr1003166

Majidinia, M., Sadeghpour, A., and Yousefi, B. (2018). The Roles of Signaling Pathways in Bone Repair and Regeneration. *J. Cell Physiol.* 233, 2937–2948. doi:10.1002/jcp.26042

Mantha, S., Pillai, S., Khayambashi, P., Upadhyay, A., Zhang, Y., Tao, O., et al. (2019). Smart Hydrogels in Tissue Engineering and Regenerative Medicine. *Materials* 12, 3323. doi:10.3390/ma12203323

Maruyama, M., Rhee, C., Utsunomiya, T., Zhang, N., Ueno, M., Yao, Z., et al. (2020). Modulation of the Inflammatory Response and Bone Healing. *Front. Endocrinol.* 11, 386. doi:10.3389/fendo.2020.00386

Masouleh, M. P., Hosseini, V., Pourhaghgouy, M., and Bakht, M. K. (2017). Calcium Phosphate Nanoparticles Cytocompatibility versus Cytotoxicity: A Serendipitous Paradox. *Cpd* 23, 2930–2951. doi:10.2174/1570163814666170321115007

Miron, R. J., and Bosshardt, D. D. (2016). OsteoMacs: Key Players Around Bone Biomaterials. *Biomaterials* 82, 1–19. doi:10.1016/j.biomaterials.2015.12.017

Miron, R. J., Zohdi, H., Fujioka-Kobayashi, M., and Bosshardt, D. D. (2016). Giant Cells Around Bone Biomaterials: Osteoclasts or Multi-Nucleated Giant Cells? *Acta Biomater.* 46, 15–28. doi:10.1016/j.actbio.2016.09.029

Newman, H., Shih, Y. V., and Varghese, S. (2021). Resolution of Inflammation in Bone Regeneration: From Understandings to Therapeutic Applications. *Biomaterials* 277, 121114. doi:10.1016/j.biomaterials.2021.121114

Nicolin, V., Baldini, G., De Iaco, D., Bortul, R., Turco, G., and Nori, S. L. (2016). Looking for Calcium Phosphate Composite Suitable to Study Osteoclast Endocytosis: Preliminary Observations. *Transl. Med. UniSa* 14, 15–20.

Nossin, Y., Farrell, E., Koevoet, W. J. L. M., Datema, F., Somoza, R. A., Caplan, A. I., et al. (2021). The Releasate of Avascular Cartilage Demonstrates Inherent Pro-angiogenic Properties *In Vitro* and *In Vivo*. *Cartilage* 13 (2_Suppl. l), 559S–570S. doi:10.1177/19476035211047628

Okada, S., Ito, H., Nagai, A., Komotori, J., and Imai, H. (2010). Adhesion of Osteoblast-like Cells on Nanostructured Hydroxyapatite. *Acta Biomater.* 6, 591–597. doi:10.1016/j.actbio.2009.07.037

Oliveira, C. S., Leeuwenburgh, S., and Mano, J. F. (2021). New Insights into the Biomimetic Design and Biomedical Applications of Bioengineered Bone Microenvironments. *Apl. Bioeng.* 5, 041507. doi:10.1063/5.0065152

Parent, M., Baradari, H., Champion, E., Damia, C., and Viana-Trecant, M. (2017). Design of Calcium Phosphate Ceramics for Drug Delivery Applications in Bone Diseases: A Review of the Parameters Affecting the Loading and Release of the Therapeutic Substance. *J. Control. Release* 252, 1–17. doi:10.1016/j.jconrel.2017.02.012

Pina, S., Oliveira, J. M., and Reis, R. L. (2015). Natural-based Nanocomposites for Bone Tissue Engineering and Regenerative Medicine: A Review. *Adv. Mat.* 27, 1143–1169. doi:10.1002/adma.201403354

Pioletti, D. P., Takei, H., Lin, T., Van Landuyt, P., Jun Ma, Q., Yong Kwon, S., et al. (2000). The Effects of Calcium Phosphate Cement Particles on Osteoblast Functions. *Biomaterials* 21, 1103–1114. doi:10.1016/s0142-9612(99)00250-1

Przekora, A. (2019). The Summary of the Most Important Cell-Biomaterial Interactions that Need to Be Considered during *In Vitro* Biocompatibility Testing of Bone Scaffolds for Tissue Engineering Applications. *Mater. Sci. Eng. C* 97, 1036–1051. doi:10.1016/j.msec.2019.01.061

Ramasamy, T., Ruttala, H. B., Gupta, B., Poudel, B. K., Choi, H.-G., Yong, C. S., et al. (2017). Smart Chemistry-Based Nanosized Drug Delivery Systems for Systemic Applications: A Comprehensive Review. *J. Control. Release* 258, 226–253. doi:10.1016/j.jconrel.2017.04.043

Rossi, A. L., Longuinho, M. M., Tanaka, M. N., Farina, M., Borojevic, R., and Rossi, A. M. (2018). Intracellular Pathway and Subsequent Transformation of Hydroxyapatite Nanoparticles in the SAOS-2 Osteoblast Cell Line. *J. Biomed. Mat. Res.* 106, 428–439. doi:10.1002/jbm.a.36256

Ruffini, A., Sandri, M., Dapporto, M., Campodoni, E., Tampieri, A., and Sprio, S. (2021). Nature-inspired Unconventional Approaches to Develop 3D Bioceramic Scaffolds with Enhanced Regenerative Ability. *Biomedicines* 9, 916. doi:10.3390/biomedicines9080916

Rustom, L. E., Poellmann, M. J., and Wagoner Johnson, A. J. (2019). Mineralization in Micropores of Calcium Phosphate Scaffolds. *Acta Biomater.* 83, 435–455. doi:10.1016/j.actbio.2018.11.003

Schaefer, S., Detsch, R., Uhl, F., Deisinger, U., and Ziegler, G. (2011). How Degradation of Calcium Phosphate Bone Substitute Materials Is Influenced by Phase Composition and Porosity. *Adv. Eng. Mat.* 13, 342–350. doi:10.1002/adem.201000267

Sheikh, Z., Abdallah, M.-N., Hanafi, A., Misbahuddin, S., Rashid, H., and Glogauer, M. (2015). Mechanisms of *In Vivo* Degradation and Resorption of Calcium Phosphate Based Biomaterials. *Materials* 8 (11), 7913–7925. doi:10.3390/ma8115430

Shi, Z., Huang, X., Cai, Y., Tang, R., and Yang, D. (2009). Size Effect of Hydroxyapatite Nanoparticles on Proliferation and Apoptosis of Osteoblast-like Cells. *Acta Biomater.* 5, 338–345. doi:10.1016/j.actbio.2008.07.023

Shiwaku, Y., Neff, L., Nagano, K., Takeyama, K.-I., de Bruijn, J., Dard, M., et al. (2015). The Crosstalk between Osteoclasts and Osteoblasts Is Dependent upon the Composition and Structure of Biphasic Calcium Phosphates. *PLoS One* 10, e0132903. doi:10.1371/journal.pone.0132903

Shiwaku, Y., Tsuchiya, K., Xiao, L., and Suzuki, O. (2019). Effect of Calcium Phosphate Phases Affecting the Crosstalk between Osteoblasts and Osteoclasts *In Vitro*. *J. Biomed. Mat. Res.* 107, 1001–1013. doi:10.1002/jbm.a.36626

Stastny, P., Sedlacek, R., Suchy, T., Lukasova, V., Rampichova, M., and Trunec, M. (2019). Structure Degradation and Strength Changes of Sintered Calcium Phosphate Bone Scaffolds with Different Phase Structures during Simulated Biodegradation *In Vitro*. *Mater. Sci. Eng. C* 100, 544–553. doi:10.1016/j.msec.2019.03.027

Takami, M., Mochizuki, A., Yamada, A., Tachi, K., Zhao, B., Miyamoto, Y., et al. (2009). Osteoclast Differentiation Induced by Synthetic Octacalcium Phosphate through Receptor Activator of NF-Kb Ligand Expression in Osteoblasts. *Tissue Eng. Part A* 15 (12), 3991–4000. doi:10.1089/ten.TEA.2009.0065

Tang, Z., Li, X., Tan, Y., Fan, H., and Zhang, X. (2018). The Material and Biological Characteristics of Osteoinductive Calcium Phosphate Ceramics. *Regen. Biomater.* 5, 43–59. doi:10.1093/rb/rbx024

Tsang, K. Y., Chan, D., and Cheah, K. S. E. (2015). Fate of Growth Plate Hypertrophic Chondrocytes: Death or Lineage Extension? *Dev. Growth Differ.* 57, 179–192. doi:10.1111/dgd.12203

Uskoković, V., Janković-Častvan, I., and Wu, V. M. (2019). Bone Mineral Crystallinity Governs the Orchestration of Ossification and Resorption during Bone Remodeling. *ACS Biomater. Sci. Eng.* 5, 3483–3498. doi:10.1021/acsbiomaterials.9b00255

Wang, D., Gilbert, J. R., Zhang, X., Zhao, B., Ker, D. F. E., and Cooper, G. M. (2020). Calvarial versus Long Bone: Implications for Tailoring Skeletal Tissue Engineering. *Tissue Eng. Part B Rev.* 26, 46–63. doi:10.1089/ten.TEB.2018.0353

Wang, J., Liu, D., Guo, B., Yang, X., Chen, X., Zhu, X., et al. (2017). Role of Biphasic Calcium Phosphate Ceramic-Mediated Secretion of Signaling Molecules by Macrophages in Migration and Osteoblastic Differentiation of MSCs. *Acta Biomater.* 51, 447–460. doi:10.1016/j.actbio.2017.01.059

Wang, X., Yu, Y., Ji, L., Geng, Z., Wang, J., and Liu, C. (2021). Calcium Phosphate-Based Materials Regulate Osteoclast-Mediated Osseointegration. *Bioact. Mater.* 6, 4517–4530. doi:10.1016/j.bioactmat.2021.05.003

Wei, H., Cui, J., Lin, K., Xie, J., and Wang, X. (2022). Recent Advances in Smart Stimuli-Responsive Biomaterials for Bone Therapeutics and Regeneration. *Bone. Res.* 10, 17. doi:10.1038/s41413-021-00180-y

Weissenböck, M., Stein, E., Undt, G., Ewers, R., Lauer, G., and Turhani, D. (2006). Particle Size of Hydroxyapatite Granules Calcified from Red Algae Affects the Osteogenic Potential of Human Mesenchymal Stem Cells *In Vitro*. *Cells Tissues Organs* 182, 79–88. doi:10.1159/000093062

Wenisch, S., Stahl, J.-P., Horas, U., Heiss, C., Kilian, O., Trinkaus, K., et al. (2003). *In Vivo* mechanisms of Hydroxyapatite Ceramic Degradation by Osteoclasts: Fine Structural Microscopy. *J. Biomed. Mat. Res.* 67A, 713–718. doi:10.1002/jbm.a.10091

Wu, V. M., and Uskoković, V. (2016). Is There a Relationship between Solubility and Resorbability of Different Calcium Phosphate Phases *In Vitro* ? *Biochimica Biophysica Acta (BBA) - General Subj.* 1860, 2157–2168. doi:10.1016/j.bbagen.2016.05.022

Xiao, L., Shiwaku, Y., Hamai, R., Tsuchiya, K., Sasaki, K., and Suzuki, O. (2021). Macrophage Polarization Related to Crystal Phases of Calcium Phosphate Biomaterials. *Ijms* 22, 11252. doi:10.3390/ijms222011252

Xiao, W., Wang, Y., Pacios, S., Li, S., and Graves, D. T. (2016). Cellular and Molecular Aspects of Bone Remodeling. *Front. Oral Biol.* 18, 9–16. doi:10.1159/000351895

Xu, H. H., Wang, P., Wang, L., Bao, C., Chen, Q., Weir, M. D., et al. (2017). Calcium Phosphate Cements for Bone Engineering and Their Biological Properties. *Bone Res.* 5, 17056. doi:10.1038/boneres.2017.56

Xu, Z., Liu, C., Wei, J., and Sun, J. (2012). Effects of Four Types of Hydroxyapatite Nanoparticles with Different Nanocrystal Morphologies and Sizes on Apoptosis in Rat Osteoblasts. *J. Appl. Toxicol.* 32 (6), 429–435. doi:10.1002/jat.1745

Xue, Y., Chen, Q., and Sun, J. (2017). Hydroxyapatite Nanoparticle-Induced Mitochondrial Energy Metabolism Impairment in Liver Cells: *In Vitro* and *In Vivo* Studies. *J. Appl. Toxicol.* 37, 1004–1016. doi:10.1002/jat.3450

Yamada, S., Heymann, D., Bouler, J. M., and Daculsi, G. (1997). Osteoclastic Resorption of Calcium Phosphate Ceramics with Different Hydroxyapatite/β-Tricalcium Phosphate Ratios. *Biomaterials* 18, 1037–1041. doi:10.1016/s0142-9612(97)00036-7

Yang, X., Li, Y., Liu, X., Zhang, R., and Feng, Q. (2018). *In Vitro* Uptake of Hydroxyapatite Nanoparticles and Their Effect on Osteogenic Differentiation of Human Mesenchymal Stem Cells. *Stem Cells Int.* 2018, 1–10. doi:10.1155/2018/2036176

Yuan, H., Li, Y., de Bruijn, J., de Groot, K., and Zhang, X. (2000). Tissue Responses of Calcium Phosphate Cement: A Study in Dogs. *Biomaterials* 21, 1283–1290. doi:10.1016/S0142-9612(00)00016-8

Zhao, Y., Zhang, Y., Ning, F., Guo, D., and Xu, Z. (2007). Synthesis and Cellular Biocompatibility of Two Kinds of HAP with Different Nanocrystal Morphology. *J. Biomed. Mat. Res.* 83B, 121–126. doi:10.1002/jbm.b.30774

Zhu, G., Zhang, T., Chen, M., Yao, K., Huang, X., Zhang, B., et al. (2021). Bone Physiological Microenvironment and Healing Mechanism: Basis for Future Bone-Tissue Engineering Scaffolds. *Bioact. Mater.* 6, 4110–4140. doi:10.1016/j.bioactmat.2021.03.043

Zimmer, G., Rohrhofer, A., Lewis, K., Goessl, A., and Hoffmann, O. (2013). The Surface Microporosity of Ceramic Biomaterials Influences the Resorption Capacity of Osteoclasts. *J. Biomed. Mat. Res.* 101, 3365–3371. doi:10.1002/jbm.a.34639

Conflict of Interest: The authors declare that the research was conducted in the absence of any commercial or financial relationships that could be construed as a potential conflict of interest.

Publisher's Note: All claims expressed in this article are solely those of the authors and do not necessarily represent those of their affiliated organizations, or those of the publisher, the editors and the reviewers. Any product that may be evaluated in this article, or claim that may be made by its manufacturer, is not guaranteed or endorsed by the publisher.

Copyright © 2022 Zhang, Shu, Wang, Liu, Cheng, Li and Pei. This is an open-access article distributed under the terms of the Creative Commons Attribution License (CC BY). The use, distribution or reproduction in other forums is permitted, provided the original author(s) and the copyright owner(s) are credited and that the original publication in this journal is cited, in accordance with accepted academic practice. No use, distribution or reproduction is permitted which does not comply with these terms.

frontiers | Frontiers in Bioengineering and Biotechnology

ORIGINAL RESEARCH
published: 19 May 2022
doi: 10.3389/fbioe.2022.908585

Treatment of Acute Wounds With Recombinant Human-Like Collagen and Recombinant Human-Like Fibronectin in C57BL/6 Mice Individually or in Combination

Yunqing Dong[1,2†], Weidong Zhu[1,2†], Xiaoxuan Lei[2,3], Xin Luo[4], Qi Xiang[4], Xuanru Zhu[2], Qiao Pan[1,2], Panshi Jin[1,2] and Biao Cheng[1,2]*

[1]The First School of Clinical Medicine, Southern Medical University, Guangzhou, China, [2]Department of Burn and Plastic Surgery, General Hospital of Southern Theater Command of PLA, Guangzhou, China, [3]Department of Oral and Maxillofacial Surgery/Pathology, Amsterdam UMC and Academic Center for Dentistry Amsterdam (ACTA), Vrije Universiteit Amsterdam, Amsterdam Movement Science, Amsterdam, Netherlands, [4]Institute of Biomedicine and Guangdong Provincial Key Laboratory of Bioengineering Medicine, Jinan University, Guangzhou, China

OPEN ACCESS

Edited by:
Kaili Lin,
Shanghai Jiao Tong University, China

Reviewed by:
Jindan Wu,
Zhejiang Sci-Tech University, China
Chunmeng Shi,
Army Medical University, China

***Correspondence:**
Biao Cheng
chengbiaocheng@163.com

[†]These authors have contributed equally to this work and share first authorship

Specialty section:
This article was submitted to Biomaterials, a section of the journal Frontiers in Bioengineering and Biotechnology

Received: 30 March 2022
Accepted: 25 April 2022
Published: 19 May 2022

Citation:
Dong Y, Zhu W, Lei X, Luo X, Xiang Q, Zhu X, Pan Q, Jin P and Cheng B (2022) Treatment of Acute Wounds With Recombinant Human-Like Collagen and Recombinant Human-Like Fibronectin in C57BL/6 Mice Individually or in Combination. Front. Bioeng. Biotechnol. 10:908585. doi: 10.3389/fbioe.2022.908585

Wound repair is accomplished by the interaction between the cells involved in the repair and the extracellular matrix (ECM). Collagen is the main component of ECM, which is involved in transduction of signal, transportation of growth factors and cytokines. Fibronectin (FN) is also an important ECM, which participates in the initiation of fibroblast cell (FC) and promotes adhesion, migration, proliferation and differentiation of target cells. Compared with natural protein, the recombinant protein prepared by artificial method has the advantages of poor immunogenicity, wide range of sources, low cost and high activity. In this study, we used recombinant human-like collagen (RHC) and recombinant human-like fibronectin (rhFN) to treat acute wounds in C57BL/6 mice individually or in combination, and explored their effects on wound healing. Our study confirmed that these two recombinant proteins could effectively promote the proliferation, migration and adhesion of FCs. Meanwhile, it could positively regulate the healing speed and quality of acute wounds, re-epithelialization, collagen deposition, inflammation and angiogenesis. Moreover, we proved that the combination of the two was better than the treatment alone. Consequently, it has a good prospect as a new tissue material in the field of skin repair.

Keywords: recombinant human-like collagen (RHC), recombinant human-like fibronectin (rhFN), wound healing, fibroblast cell, re-epithelialization, collagen deposition, inflammation, angiogenesis

1 INTRODUCTION

Acute skin injury is very common, with high incidence rate and many complications. The prognosis is affected by many factors, such as the location, depth and area of the wound. If the acute skin injury can not be repaired in an orderly and timely manner, it may turn into a chronic refractory wound. Acute skin wound repair is a physiological process involving inflammatory cells, repair cells, ECM

Abbreviations: RHC, recombinant human-like collagen; rhFN, recombinant human-like fibronectin.

and a variety of growth factors, and ECM plays an important role in skin wound healing (Gurtner et al., 2008). Synthetic ECM and its key components are promising new materials for wound repair and tissue regeneration. ECM is the basis of extracellular microenvironment, which plays an important role in regulating biological behaviors such as proliferation, migration, adhesion, differentiation and apoptosis of cells, and can promote re-epithelialization, collagen deposition as well as regulate angiogenesis (Theocharis et al., 2016).

ECM is a complex three-dimensional network structure, which is composed of gel matrix and fibrous protein components. Fibrous proteins mainly contain collagen and elastin with structural support, as well as fibronectin (FN) and laminin (LN), which play a role in adhesion (Järveläinen et al., 2009). Collagen is not only the main component of ECM, but also the most abundant protein in human body. Most collagen can form structural scaffolds for wound healing and have good biocompatibility and degradability. It promotes tissue repair by promoting adhesion, chemotaxis and migration of cells (Colby and Prusiner, 2011). FN is also an important part of ECM. It can be used as a scaffold for cell migration, assist FCs to migrate to the wound, as well as promote collagen deposition and restore tissue structure (Patten and Wang, 2020). Previous studies have shown that collagen and FN are widely involved in all stages of wound repair (Mathew et al., 2021).

The wound healing process is complex regulated by many key factors, and collagen is widely involved in all stages of wound repair. In general, collagen transformation is slow, but it is accelerated during the remodeling and healing of skin injury (Jansen et al., 2018). In the early stage, collagen degradation fragments can recruit immune cells, such as monocytes-macrophages, to clear necrotic tissue and microorganisms (Yeung and Kelly, 2021). At the same time, in this primary stage, thrombin or collagen can release FN in platelets and help platelets bind firmly to fibrin and collagen in the form of covalent bonds to form thrombosis and cell matrix structures (Mosesson and Umfleet, 1970; Grinnell et al., 1981), which will contribute to the transition to the next phase. In the inflammatory stage, collagen will produce a strong and rapid inflammatory response, which is temporary and will subside soon, so as to promote wound healing. In the proliferative phase, on the one hand, collagen plays a chemotactic role, which significantly promotes the adhesion and effectively increases the proliferation of FN around the wound (Huang et al., 2012; Smithmyer et al., 2014; Lai et al., 2020). On the other hand, it can activate macrophages, induce the expression of various cytokines and growth factors, and promote angiogenesis (Lin et al., 2006; To and Midwood, 2011; Elbialy et al., 2020). Type I collagen can effectively stimulate angiogenesis *in vitro* and *in vivo* by recruiting endothelial cells to bind to specific integrin receptors. In addition, collagen can promote migration, re-epithelialization and collagen deposition of keratinocytes (Dang et al., 2015; Pal et al., 2016; Chen et al., 2019). At the same time, FN is mainly produced by FCs and macrophages in proliferative phase, which promotes the formation of granulation tissue, attracts endothelial cells and epithelial cells, promotes adhesion and migration of cells to matrix, and accelerates re-epithelialization (Cheng et al., 1988). Finally, in the process of wound remodeling, collagen, as a structural component of ECM, not only regulates the stable release of growth factors, intercellular adhesion and signal transduction, but also contributes to the elasticity of skin.

FN runs through all stages of wound repair. It can be used as a scaffold to recruit target cells to migrate to the wound and restore the tissue structure. Firstly, in the hemostatic period, platelets themselves do not participate in the agglutination of fibrinogen. FN derived plasma plays an important role in the accumulation and mutual adhesion of platelets, and firmly binds with fibrin and collagen in covalent form to form insoluble gel condensate (Eisinger et al., 2018). Next, in the middle stage of wound healing, FN gathers into a complex three-dimensional structure on the cell surface to regulate adhesion, migration, proliferation and apoptosis of cells in the process of skin wound healing. At the same time, collagen further forms the grid structure, which depends on the initial FN structure. In addition, as a non-specific opsonin, FN can mobilize and promote the phagocytic system to remove foreign bodies and purify the wound. Finally, in the stage of remodeling process, the temporary granulation tissue initially combined by FN and type III collagen is finally replaced by type I collagen (Lenselink, 2015). In addition, in the later stage of remodeling, FN plays a role by promoting the proliferation of α-smooth muscle actin (α-SMA) and assisting FCs to transform into myofibroblast cells (MFCs) with strong contractile effect (Sethi et al., 2002; Musiime et al., 2021; Spada et al., 2021).

However, the process of obtaining natural collagen is complex and costly. Similarly, the quantity of natural FN is limited and the price is expensive. In this study, specific functional fragments are selected by the institute of biomedicine and guangdong provincial key laboratory of bioengineering medicine of Jinan university in Guangzhou to obtain RHC and rhFN with high bioactivity and biocompatibility. RHC contains cell adhesion domains derived from natural type I collagen, which overcomes the limitations of natural animal-derived collagen. For example, the quality and purity of animal-derived collagen may affect performance, and non-human protein components may lead to an immune response in susceptible patients and a risk of contamination by pathogenic substances (Cheng et al., 2020; Deng et al., 2020). Similarly, in this study, rhFN selected fragments with fibronectin bioactivity, which overcomes the shortcomings of other methods. For instance, natural fibronectin extracted from human or animal blood and tissues is limited and expensive. At the same time, the molecular weight of wild-type fibronectin is too large to be recombined and expressed. In this experiment, we try to explore their effects on wound healing individually or in combination, and verify whether they have synergistic effect in human microenvironment.

2 MATERIALS AND METHODS

2.1 Construction of RHC and rhFN

The gene encoding RHC was cloned into the plasmids containing pET-3c (Invitrogen, United States) expression vector, and the

recombinant plasmid named pET3c-hlcollagen was constructed and transformed into *Escherichia coli* BL21 (DE3) (Invitrogen, United States). After that, the best expression conditions was selected by screening for ampicillin resistance and induction by isopropyl β-D-1-thiogalactopyranoside (Invitrogen, United States). A 50 L fermentor was used for generating large-scale production of RHC. In addition, RHC was purified by using affinity chromatography on a Ni Sepharose six Fast Flow (Sigma, Germany) column combined with gel filtration Sephadex G-25 (Sigma, Germany).

The gene encoding rhFN was cloned into the pPICZαA (Invitrogen, United States) expression vector to generate a recombinant plasmid named pPICZαA-rhFN. After linearizing the recombinant plasmid with sall enzyme (Takara, Japan), it was transferred into GS115 Pichia pastoris competent cells (Invitrogen, United States) and screened for positive transformants. Afterwords, recombinant human-like fibronectin was expressed by biological fermentation. Moreover, the nucleotide sequence was adapted by the host cell codon to optimize the expression of recombinant fibronectin.

2.2 Extraction and Identification of Dermal FCs

C57BL/6 mice were killed and their backs were depilated. Then they were washed with water and soaked in alcohol for 5 min. After that, the depilated skin on their backs was cut off and chopped with scissors as much as possible, which was then added wtih 0.2% collagenase (Sigma, Germany) and digested in the incubator for 1 h. Take out the digested skin, stop the digestion with DMEM medium, and then filter with a 70 μm cell filter, then centrifuge (1000 r, 5 min), remove the supernatant, and resuspend 10% FBS for inoculation. After the cells were stable, the primary cells were identified by immunofluorescence with 6-Diamidino-2-phenylindole dihydrochloride (DAPI) (Solarbio, China) and Fluoromount-G (SourthernBiotech, China).

2.3 Surface Characterization

The morphologies and structural properties of RHC and rhFN were characterized by scanning electron microscopy (Zeiss Sigma 300, Tescan, Germany). The excipients mannitol were added to RHC and rhFN, and they were frozen by gradient. The samples were placed on the table and coated with conductive carbon glue. After that, the lyophilized powder of RHC and rhFN were scanned and imaged by scanning electron microscope (SEM).

2.4 *In vitro* Studies

2.4.1 Biocompatibility Test

C57BL/6 mice dermal FCs were used to evaluate the biocompatibility of the materials. Different concentrations of RHC and rhFN (concentration to 0.01 μM/L, 0.1 μM/L, 1 μM/L, 10 μM/L, respectively) as well as equivalent phosphate buffer saline (PBS) (gibco, United States) were completely immersed in DMEM media (gibco, United States) supplemented and 1% (v/v) penicillin/streptomycin (gibco, United States). The dermal FCs were inoculated in 96-well plates (3×10^3 cells/well), and then added 100 μl of the above four media with 10% FBS (gibco, United States). Afterward, some cells in 96-well plates were culture at a specific point in time (24 h) at 37°C in a 5% CO_2 humidified incubator. First, these cells were detected by CCK-8, the above four culture medium of these cells in 96-well plates was changed every day. After being cultured for 1, 2 and 3 days, the cultured medium was changed to a 10% CCK-8 solution and incubated for another 2.5 h at 37°C, and the absorbance of cells was recorded by a microplate reader (Multiskan Go, Thermo, United States) at the wavelength of 450 nm. According to the results of the pre-experiment, the most suitable concentration was selected and the cells were laid again. Some cells were stained by using Live/Dead cell imaging kit (Dojindo, Japan) to determine whether they were live (green) or dead (red). For the Live/Dead staining, 100 μl of the Live/Dead stock solution was added to each well. After 15 min, the cells were washed twice and observed by an inverted fluorescence microscope (DMI3000B, Leica, Germany). Another part of the cells were used for CCK-8 assay. For the CCK-8 assay, The cell viability (%) was assessed using the following formula:

$$\text{Cell viability}\,(\%) = \left[(\text{ODDrug} - \text{ODBlank})/(\text{ODControl} - \text{ODBlank})\right] \times 100\%$$

2.4.2 Cell Migration Assay

The effects of RHC and rhFN on cell migration were measured by the scratch assay. The dermal FCs of C57BL/6 mice were inoculated in 24-well plates (1×10^5 cells/well) and grown to 80% to form a confluent monolayer. Cells were starved 6–8 h in FBS-free medium. Afterward, the cells were scratched with sterile pipet tips (200 μl) in the middle of the well and washed twice with PBS to mimic an incisional wound. Next, the artificial wound was covered by 1 ml FBS-free medium and was photographed by the microscope. As above, the pre-experiment of different concentrations of two recombinant proteins and equivalent PBS was carried out. The 24-well plates were replaced with the above media. Migration images were captured with a ×5 objective every 12 h for 36 h at 37°C and 5% CO_2. According to the results of the pre-experiment, the most suitable concentration was selected and the cells were laid again to conduct a formal scratch assay. The cell migration rate (%) was calculated using the following formula:

$$\text{Cell migration}\,(\%) = [(T0 - Tt)/T0] \times 100\%$$

where T0 is the scratch area at 0 h, and Tt is the scratch area without cell migration at different time points. Scratched wound area was quantified at each time-point using ImageJ 1.8.0 software (National Institutes of Health, United States).

2.4.3 Cell Adhesion Assay

The effects of RHC and rhFN on the adhesion were determined by the crystal violet (Beyotime, China) assay. The 48-well plates were coverd with the above three optimal concentrations of media and equivalent PBS, then dermal FCs were seeded in the same plates (2×10^4 cells/well). After 4 h, the cells were washed with PBS, fixed with 4% paraformaldehyde (PFA) (Sigma, Germany) solution for 20 min, and then washed with

PBS again. After that, the cells were stained with crystal violet for 10 min and washed with PBS for 3 times. The morphology of FCs was observed by the microscope. The adhesion area rate (%) was calculated using the following formula: Adhesion area (%) = Tt/T0×100% where T0 is the total area at 0 h, and Tt is the adhesion area after 4 hours. The images were analyzed with Image-Pro Plus 6. 0 (IPP 6.0) software (National Institutes of Health, United States) to calculate the proportion of cell adhesion area.

2.5 *In vivo* Studies

2.5.1 Establishment of Animal Model and Wound Healing Examination

Forty male C57BL/6 mice aged 6–8 weeks and weighed 25–30 g were provided from the Animal Research Centre of Guangdong (China). The animal study was reviewed and approved by the Institutional Animal Care and Use Committee (IACUC) of the General Hospital of the Southern Theatre Command (animal ethics approval number: scxk 2020–0054). Mice were anesthetized via intraperitoneal injection with 1% pentobarbital sodium solution (Sigma, Germany) (3 ml/kg), then their dorsal hairs were shaved and sterilized with iodophorthe. Each mouse was made into two pieces with the size of 1 × 1 cm round full-thickness skin defect. Three treatments were randomly applied to the wounds, while the control group was smeared with saline solution, and each wound was treated with a 0.5 ml dose of the respective treatment every day.

All wounds immediately after operation and five wounds randomly obtained from each group on days 3, 5, 7 and 10 post-surgery were harvested for wound closure analysis and morphological observation. The wounds were photographed with a Cannon digital camera (90 d, Cannon, Japan) and the wound area was measured using ImageJ software. Wound Healing Percentage (%) was determined by the following formula:

$$\text{Wound healing percentage}\,(\%) = [(W0 - Wt)/W0] \times 100\%$$

where W0 represents the immediate postoperative wound area, and Wt represents the wound area on days 3, 5, 7 and 10, respectively.

2.5.2 Histology Staining

The samples were collected and stained histologically on day 14. The excised patches, which contained the wound and normal tissue within 5 mm from the wound edge, were fixed in 4% PFA solution at 4°C over night, dehydrated with a gradient concentration of ethanol, embedded in paraffin (5 μm) and then sliced. The sections were collected and subsequently stained with haematoxylin and eosin (H&E) (Servicebio, China) and Masson (Servicebio, China) according to a manufacturer's instructions. The images of the stained samples were taken by the microtome (RM2016, Leica, China). The thickness of the neo-epidermis was measured by ImageJ software. The condition of collagen deposition was measured by IPP software. The thickness of neo-epidermis and the mean optical density of collagen fibers were calculated by the following formula:

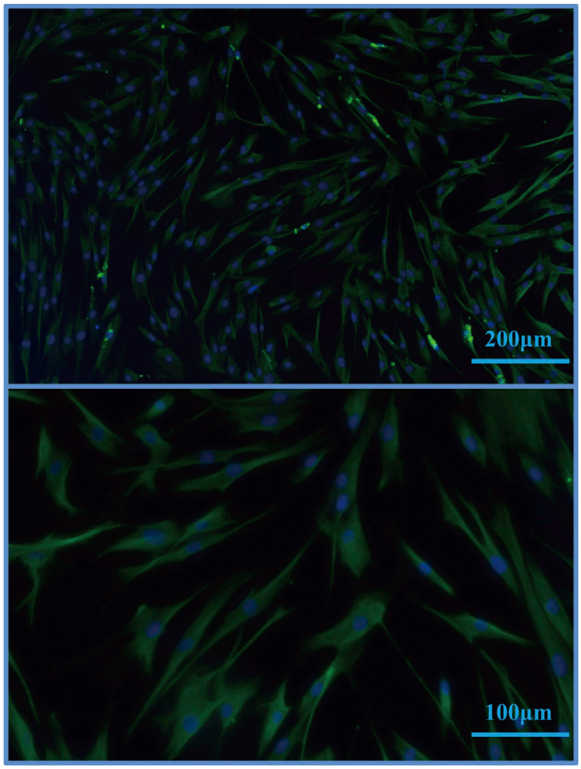

FIGURE 1 | Immunofluorescence identification images of FCs.

$$\text{Epithelial thickness} = \text{epithelial area}/\text{epithelial length}$$

$$\text{Mean optical density (MOD)} = \text{integrated option density (IOD)sum}/\text{area sum}$$

2.5.3 Immunohistochemistry Staining

The paraffin sections were dewaxed and rehydrated by xylene and gradient alcohol, and then were blocked in 3% hydrogen peroxide solution for 10 min at room temperature. Next, they were stained with primary antibodies to rabbit anti-TNF-α (1:100, abcam, United Kingdom), rabbit anti-IL-1β (1:100, abcam, United Kingdom), mouse anti-IL-6 (1:100, abcam, United Kingdom), mouse anti-TGF-β1 (1:100, abcam, United Kingdom), mouse-anti VEGF (1:100, abcam, United Kingdom) and mouse anti-α-SMA (1:100, abcam, United Kingdom) and incubated overnight at 4°C. Then, the sections were incubated with goat anti-mouse IgG (1:100, abcam, United Kingdom) and goat anti-rabbit IgG (1:100, abcam, United Kingdom) at 37°C for 50 min. After being washed in PBS thrice, they were detected with 3,3′-diaminobenzidine tetrahydrochloride solution (Agilent Dako, United States) for 10 min. Eventually, the nuclei were stained with hematoxylin., and the sections were also captured by microtome. Positive results of the average value of optical density were quantified by IPP software in a blinded fashion.

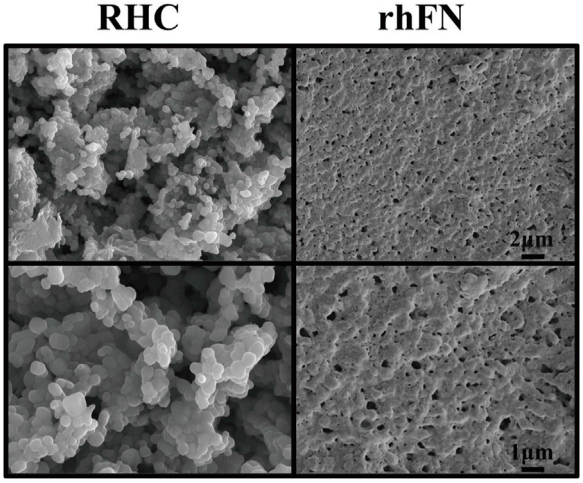

FIGURE 2 | SEM images of RHC and rhFN.

The expressions of various factors were calculated according to the following formula:

$$\text{MOD} = \text{IOD sum/area sum}$$

2.6 Statistical Analysis

SPSS 19.0 software was used to detect significant differences. All quantitative data were presented as mean ± standard deviation (SD). Statistical comparisons were analysed using one-way analysis of variance (ANOVA) and Bonferroni tests. In all figures, we used * to denote p-values, in which *($p < 0.05$), ** ($p < 0.01$), and *** ($p < 0.001$).

3 RESULTS

3.1 Immunofluorescence Identification of Dermal FCs

By immunofluorescence identification, the purity of the cell reached more than 90% (**Figure 1**).

3.2 Characterization Analysis

Recombinant human-like collagen and recombinant human-like fibronectin were self-assemble by lyophilization to form the noticeable but irregular reticular structure, which may be used as scaffolds to produce a marked effect of chemotaxis and adhesion by attracting various cells and growth factors (Meyer, 2019) (**Figure 2**).

3.3 Enhancement of Cell Biocompatibility

The biocompatibility test *in vitro* with C57BL/6 mice dermal FCs showed that RHC and rhFN had no cytotoxicity. The cells were stained with Live/Dead cell staining kit, which revealed that most of the cells were alive and almost no dead cells in all experimental groups (**Figure 3A**). Meanwhile, the CCK-8 assay was used to quantitatively measure the cell viability (According to the pre-experimental result, the optimal concentrations of these two recombinant proteins were both 1 μM/L). By detecting the OD value at 450 nm, all experimental groups had a higher cell viability (over 100%) compared with the control group on days 1, 2 and 3 (**Figure 3B**). On the third day, the cell viablity of RHC + rhFN group was significantly higher than that of the control group ($p < 0.05$), and there was no significant difference between the other groups. Both experiments revealed that RHC and rhFN were artificial biomaterials with good biocompatibility.

3.4 Promotion of Cell Migration

The scratch assay indicated that RHC and rhFN could promote cell migration (According to the pre-experimental result, which was proved again that the optimal concentrations were both 1 μM/L). The results showed that, in all experimental groups, wound closure by cell migration in FCs was significantly enhanced when compared with the control group, remarkably higher wound closure rates were observed in the rhFN and RHC + rhFN groups (**Figures 4A,B**). The faster migration in these groups was due to the fact that FN could stimulate the migration to the wound of FCs as a cell scaffold.

3.5 Promotion of Cell Adhesion

The crystal violet assay proved that RHC and rhFN could promote cell adhesion. Compared with the control group, the experimental groups significantly improved adhesion and showed a typical spindle shape of FC (**Figure 5A**). In addition, we also calculated the average area proportion of attached cells. Among all the groups, the RHC + rhFN group had the highest number of attached cells that were well-spread and exhibited a typical FC morphology (**Figure 5B**), which may due to the synergistic effect of these two proteins.

3.6 The Analysis of Wound Healing Rate

To probe into the effect of the above proteins on skin wound healing, a full-thickness skin defect model was established and the wound healing progress was analyzed at different time points after skin injury. The wound area of the model is basically same on day 0, about 1 cm^2. On post injury day (PID) 3 and 5, there was significant difference in wound healing rates between the experimental groups and the control group. On PID 3, wound healing rates in the RHC, rhFN and RHC + rhFN groups were (63.4 ± 5.2) % (66.2 ± 3.6) % and (73.3 ± 7.1) % respectively, which were significantly higher than (52.6 ± 3.1) % in the control group. On PID 5, wound healing rates in the RHC, rhFN and RHC + rhFN groups were (76.4 ± 5.0) %, (80.0 ± 2.0) % and (78.0 ± 7.0) % respectively, which were significantly higher than (63.7 ± 5.5) % in the control group. On PID 7 and 10, wound contractions in all experimental group were similar to that in the control group. On PID 10, the wounds in all groups basically healed (**Figures 6A,B**).

3.7 The Analysis of Histology

To further investigate the quality of the newly formed skin tissue of the wound site, the wound tissues were collected on PID 10 and the morphological changes of the skin layer were observed by H&E staining. It could be seen that all groups have entered the mature stage of wound repair at this time (**Figure 7A**). The wound contained a large number of mature capillaries. In addtion, the complete epidermal layer

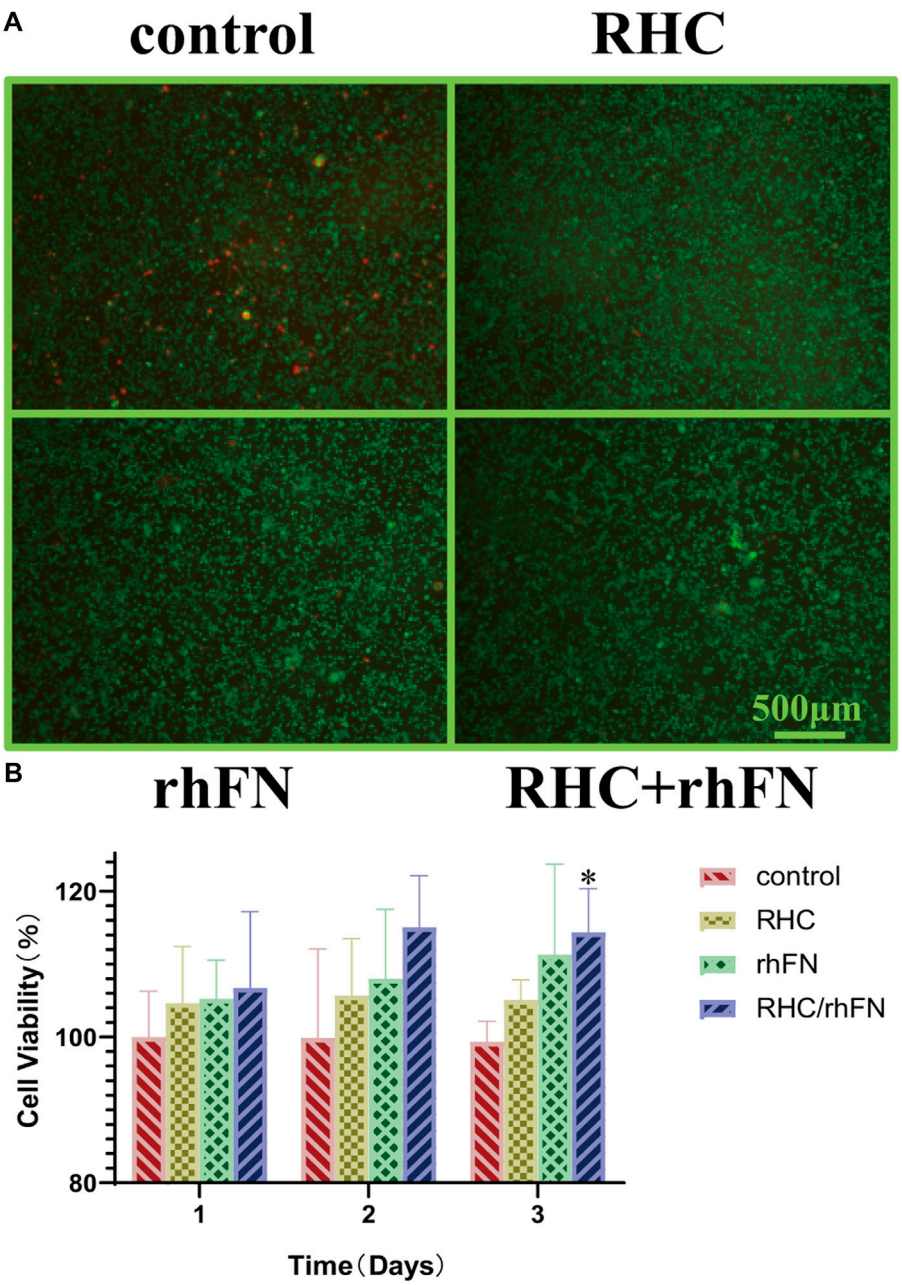

FIGURE 3 | The effect of RHC + rhFN on biocompatibility with FCs. **(A)** Live/Dead staining images of FCs at hour 24. Scale bar = 500 μm **(B)** Calculation and comparison of cell viability on days 1,2 and 3. Data are presented as the mean ± SD (n = 6). Statistical analysis: $*p < 0.05$.

was closely connected with the dermis to form the basal layer. At the same time, hair follicles, sebaceous glands and other skin accessory organs could be seen similarly (Zuijlen et al., 2003; Zheng et al., 2020). Compared with the control group, the thickness of the newly formed epidermal layers of all experimental groups were thicker, and the quantitative analysis showed that the average epithelial thickness in the RHC + rhFN group was significantly greater, while no difference was found between the other groups and the control group (**Figure 7B**).

Next, Masson staining was used to assess the collagen expression on PID 10 at wound site (**Figure 7A**). The results indicates that compared with the control group, the collagen deposition in the experimental groups had no significant difference, but arranged more regularly and orderly (**Figure 7C**).

3.8 The Analysis of Immunohistochemistry

Wound healing is an extremely complex inflammatory regulation process. Through immunohistochemical staining of pro-inflammatory factors (TNF-α, IL-1β and IL-6) and anti-inflammatory factor (TGF-

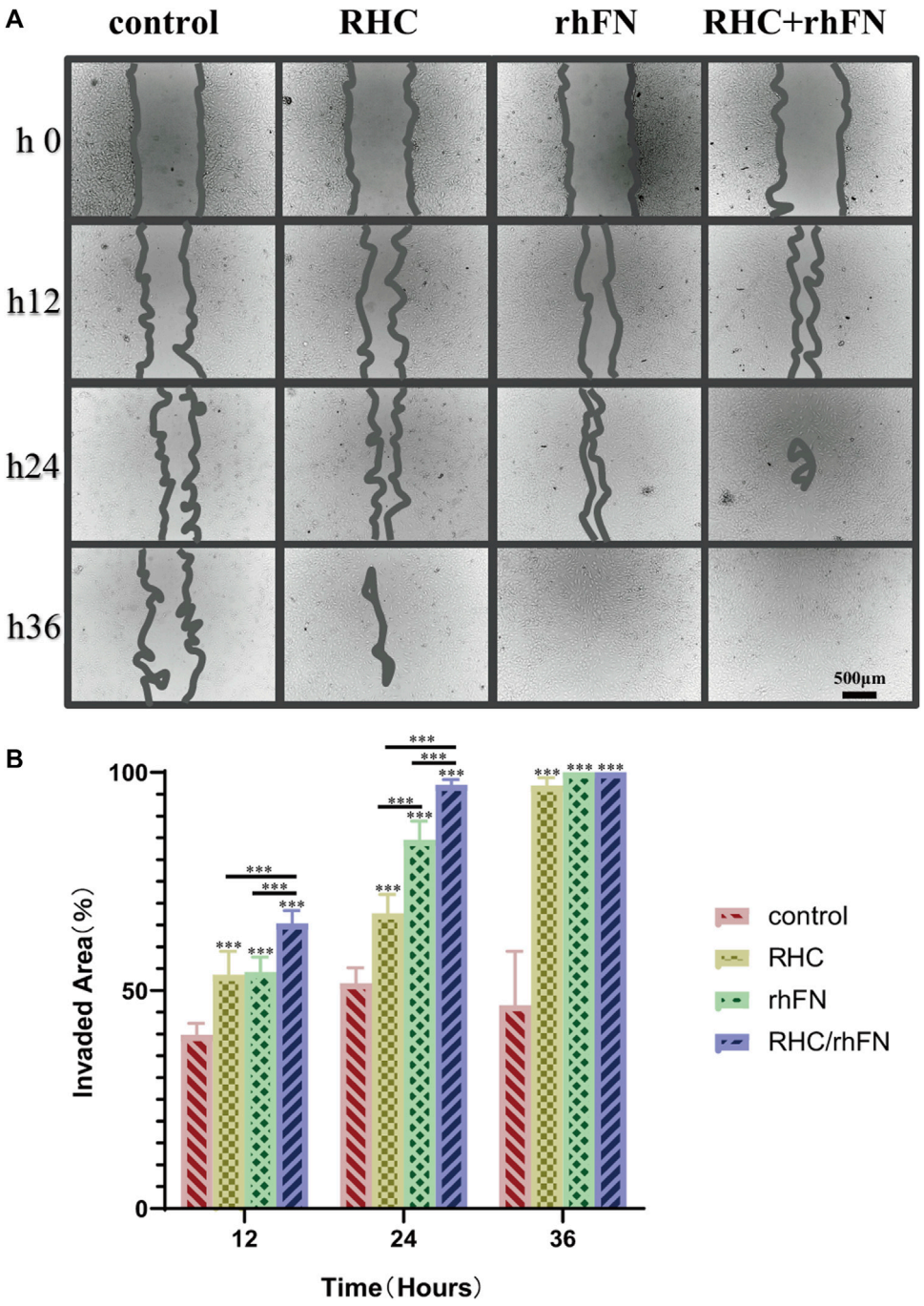

FIGURE 4 | The effect of RHC + rhFN on migration with FCs. **(A)** Scratch images of FCs at hours 12, 24 and 36. Scale bar = 500 μm. **(B)** Calculation and comparison of invaded area at hours 12, 24 and 36. Data are presented as the mean ± SD (n = 6). Statistical analysis: ***p < 0.001.

β1), to explore the mechanism of RHC and rhFN in promoting acute wound healing in C57BL/6 mice. By the results of immunohistochemistry evaluation, on PID 5 and 10, we observed that the RHC, rhFN and RHC + rhFN groups decreased the expression of pro-inflammatory cytokines (**Figures 8A–F**) and increase the expression of anti-inflammatory cytokine (**Figures 8G,H**).

To further confirm the positive impact of RHC and rhFN on angiogenesis, we detected the expression of Vascular endothelial growth factor (VEGF) as a vascular endothelial cell marker, and α-SMA as a parietal cell marker respectively. The results proved that, compared with the control group, on PID 5, the RHC and rhFN group enhanced VEGF production

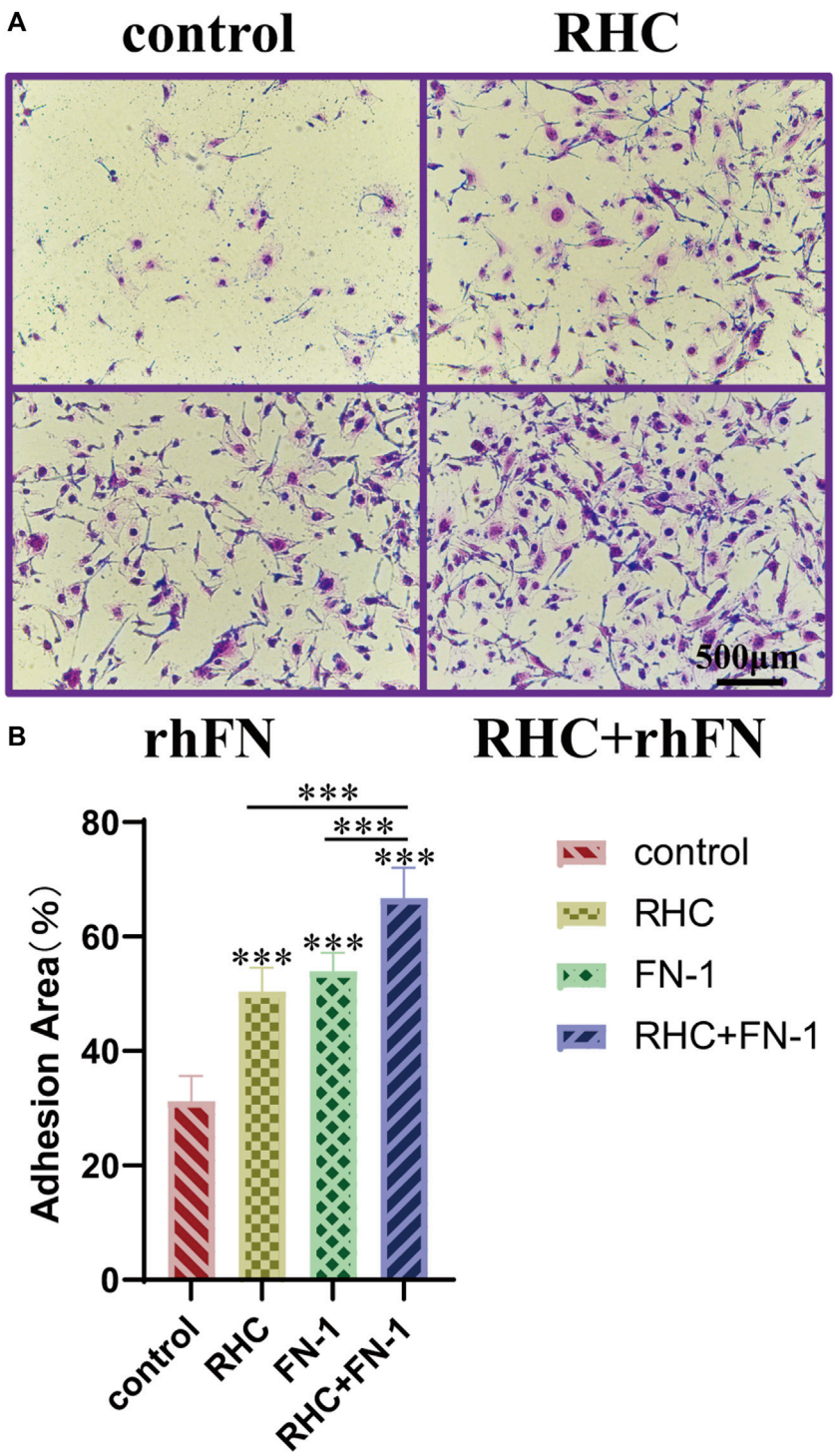

FIGURE 5 | The effect of RHC + rhFN on adhesion with FCs. **(A)** Crystal violet staining images of FCs at hour 4. Scale bar = 500 μm. **(B)** Calculation and comparison of adhesion area at hour 4. Data are presented as the mean ± SD (n = 6). Statistical analysis: ***p < 0.001.

(**Figures 8I,J**), and at the same time, α-SMA in the RHC and rhFN group was the most obvious, showing the higher vascular density on PID 5 and 10 (**Figures 8K,L**), both suggesting that combination therapy might have a positive impact on angiogenesis.

4 DISCUSSION

Acute skin injury refers to tissue damage and continuous destruction caused by external action in a short period of time. In the process of wound healing, if it stagnates or

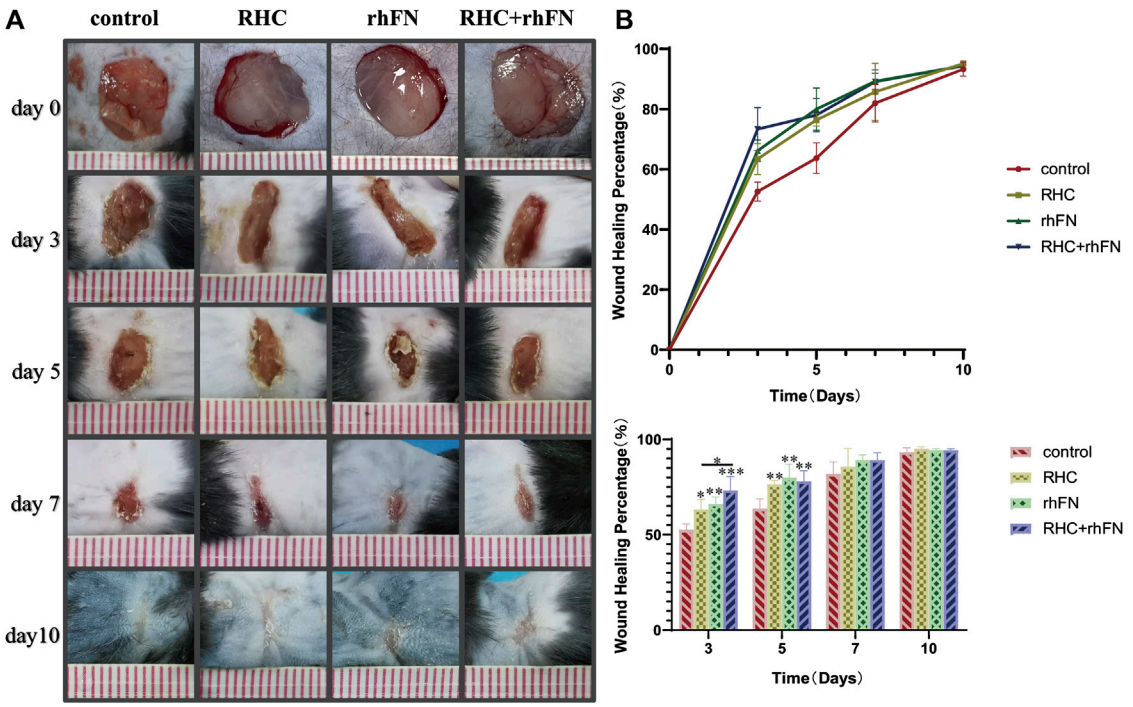

FIGURE 6 | The analysis of wound healing rate. **(A)** Representative photographs on PID 3, 5, 7 and 10. **(B)** Calculation and comparison of wound healing percentage on PID 3, 5, 7 and 10. Data are presented as the mean ± SD (n = 5). Statistical analysis: $*p < 0.05$, $**p < 0.01$, $***p < 0.001$.

worsens or even does not heal for a long time, it may develop into a chronic refractory wound (Ren et al., 2022). Therefore, the effective treatment of early wounds is very important to ensure the stable and orderly repair, and achieve early primary healing. At present, the clinical treatments of wound healing include a variety of interventions, such as topical dressing, biotherapy, physiotherapy and surgical treatment (Wei et al., 2021). In recent years, new bioactive materials for skin wound repair have attracted more and more attention (Hynes, 2009). In acute skin injury, collagen and FN stimulate FC formation, promote wound re-epithelialization and collagen deposition. In the meanwhile, they regulate the release of growth factors, histopathological changes, inflammatory response and angiogenesis, etc. (Manou et al., 2019). Due to poor solubility and immunogenicity, complex extraction methods and low efficiency, large molecular weight and multiple non functional domains, the application of nature protein in wound is limited. Therefore, the heterogeneity between species, the possibility of pathogen transfer and immunogenicity have prompted people to study alternative synthetic methods. Fortunately, with the progress of recombinant protein technology, the research on RHC and rhFN is increasing day by day, because of its good biocompatibility, safety, water solubility and easy production. Previous studies have successfully expressed RHC in *Escherichia coli* (Chi et al., 2011) and achieved mass production and ensured the homogeneity of different batches, as well as confirmed the effective application of recombinant collagen and derivatives combined with hydrogel in wound repair (Guo et al., 2019). Similarity, some scholars have successfully applied recombinant fibronectin and its derivatives to achieve bone repair (Xing et al., 2017; Liu et al., 2021). Consequently, these two recombinant proteins have a good prospect as a new tissue material in the field of skin repair.

According to the results of SEM, RHC and rhFN have a network structure similar to natural proteins and may act as scaffolds to attract various cells and growth factors. In previous studies, it has proved that collagen and FN can chemotactic FCs to migrate to the wound and stimulate the proliferation. Meanwhile, FCs begin to synthesize and secrete a large number of collagen fibers and matrix components to form granulation tissue to fill the wound, and converted into MFCs to promote wound contraction. In the later stage, FCs participate in tissue remodeling by secreting collagenase, and gradually apoptosis (Clark, 1993; Grinnell, 1994). We hypothesized that both recombinant proteins have binding sites of FCs and can chemotactic them, and they have synergistic effect in the process of wound repair. Combined with our experimental results *in vitro*, we have reason to believe that RHC and rhFN can promote the proliferation, migration and adhesion of FCs, and are largely interdependent and interactive, so as to jointly play the role of repair and reconstruction.

In order to further prove the effect of RHC and rhFN on wound healing *in vivo*, we used a full-thickness skin defect mouse model. In the early stage of wound repair, tissue defects are gradually filled with granulation tissue composed of new capillaries and proliferated FCs, accompanied by inflammatory cell infiltration, and its formation rate is closely related to the wound healing rate (Jiang and Scharffetter, 2020). The skin

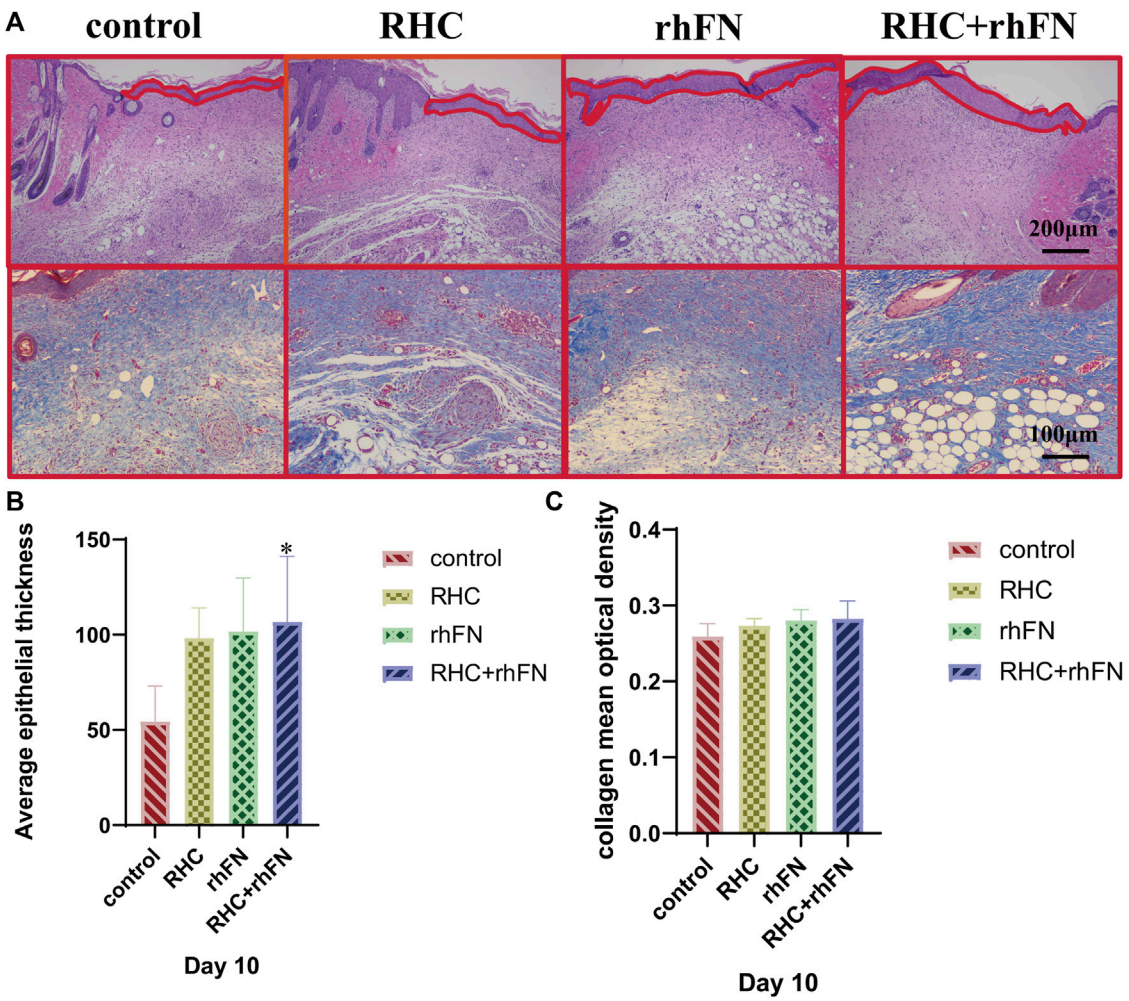

FIGURE 7 | The analysis of histology. **(A)** Representative H&E staining images on PID 10. Scale bar = 200 μm. Representative Masson staining images on PID 10. Scale bar = 100 μm. **(B)** Calculation and comparison of average epithelial thickness on PID 10. Data are presented as the mean ± SD (n = 5). Statistical analysis: $*p < 0.05$. **(C)**Calculation and comparison of collagen mean optical density on PID 10. Data are presented as the mean ± SD (n = 5). Statistical analysis: ns $p > 0.05$.

wound must undergo rapid re-epithelialization in order to achieve effective wound healing (Xu et al., 2020). The disorder of re-epithelialization is closely related to the delayed healing and the occurrence of chronic refractory wounds (Caedo-Dorantes and Caedo-Ayala, 2019). At the same time, a large amount of collagen will be generated during the remodeling period of wound healing with regularly and orderly arrangement, reducing the possibility of scar repair and improving the quality of tissue remodeling (Liu et al., 2010; Zhao et al., 2021). Our results showed that compared with the control group, RHC and rFN could significantly accelerate the speed of wound healing, especially in the combined treatment group. Besides, the combined application could increase the thickness of epithelium and improve the uniformity of collagen arrangement. Therefore, we are convinced of that RHC and rhFN play a role in the wound by promoting the early closure of the wound through a stronger degree of re-epithelialization and collagen deposition with orderly arrangement, which confirms the beneficial effect of recombinant protein on wound healing.

Inflammation is the basic response to tissue injury and invasion of pathogenic factors, as well as the inflammatory reaction initiates and regulates the process of wound repair (Li et al., 2022). Appropriate local inflammatory response can promote tissue repair, therefore, it is necessary to maintain the balance between pro-inflammatory and anti-inflammatory. According to previous studies, several pro-inflammatory cytokines play a defensive response in the early stage of wound repair by inducing inflammatory cells (Amaral et al., 2019; Huang et al., 2021). Known as is the key cytokine to initiate antibacterial inflammatory response, tumor necrosis factor-α (TNF-α) can induce activation and aggregation of inflammatory cells in the early stage. However, in the middle and late stages, too high concentration of TNF-α will cause excessive accumulation of inflammatory cells, which results in prolonged inflammatory period and poor wound healing (Ezoe

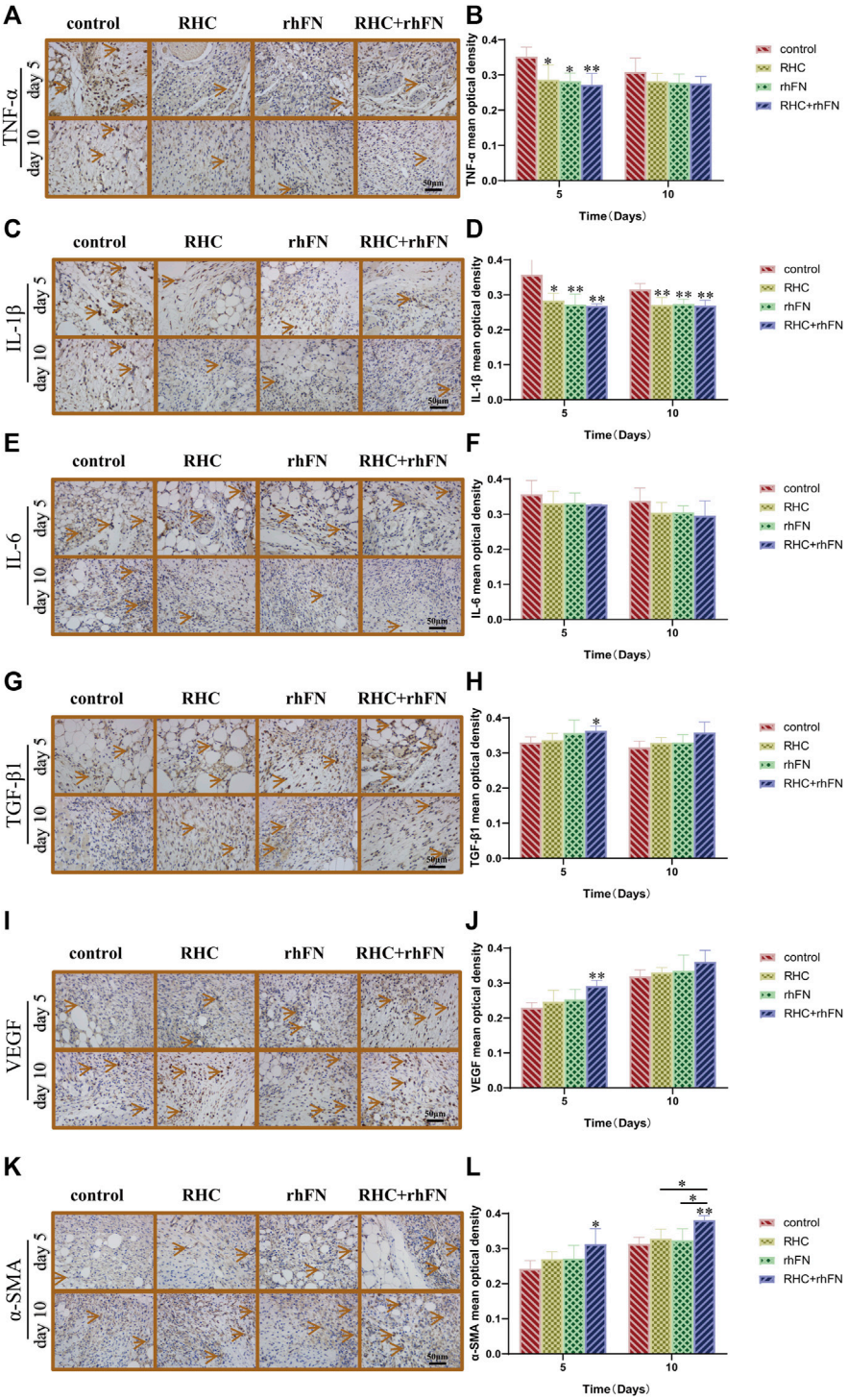

FIGURE 8 | The analysis of immunohistochemistry. **(A)** Representative images of TNF-α on PID 5 and 10. Scale bar = 50 μm. **(B)** Calculation and comparison of TNF-α on PID 5 and 10. Data are presented as the mean ± SD ($n = 5$). Statistical analysis: $*p < 0.05$, $**p < 0.01$. **(C)** Representative images of IL -1β on PID 5 and 10. Scale bar = 50 μm. **(D)** Calculation and comparison of IL -1β on PID 5 and 10. Data are presented as the mean ± SD ($n = 5$). Statistical analysis: $*p < 0.05$, $**p < 0.01$. **(E)** Representative images of IL -6 on PID 5 and 10. Scale bar = 50 μm. **(F)** Calculation and comparison of IL -6 on PID 5 and 10. Data are presented as the mean ± SD ($n = 5$). Statistical analysis: ns $p > 0.05$ **(G)** Representative images of TGF-β1 on PID 5 and 10. Scale bar = 50 μm **(H)** Calculation and comparison of TGF-β1 on PID 5 and 10. Data are presented as the mean ± SD ($n = 5$). Statistical analysis: $*p < 0.05$ **(I)** Representative images of VEGF on PID 5 and 10. Scale bar = 50 μm **(J)** Calculation and comparison of VEGF on PID 5 and 10. Data are presented as the mean ± SD ($n = 5$). Statistical analysis: $**p < 0.01$ **(K)** Representative images of α-SMA on PID 5 and 10. Scale bar = 50 μm **(L)** Calculation and comparison of α-SMA on PID 5 and 10. Data are presented as the mean ± SD ($n = 5$). Statistical analysis: $*p < 0.05$, $**p < 0.01$.

and Horikoshi, 1993; Jiang et al., 2017). High concentration of interleukin-1β (IL-1β) can induce the aggravation of inflammatory reaction by activating cell cascade reaction, while low concentration of IL-1β can be combined with TNF-α to stimulate inflammatory response and promote macrophages to produce growth factors to enhance wound healing indirectly (Fedyk et al., 2001; Broekman et al., 2016; Zhou et al., 2020). Similiar, as an immunomodulatory factor, interleukin-6 (IL-6) can activate lymphocytes and promote the synthesis of reactive protein and immunoglobulin in the acute phase of repair, but down-regulate in the late stage so as to inhibit inflammation (Edara et al., 2020). Besides, transforming growth factor-β1 (TGF-β1) is a kind of multifunctional growth factor that plays an important role in wound repair (Song et al., 2002; Peters et al., 2005), which can make FCs and inflammatory cells gather to the wound site and induce granulation tissue growth, re-epithelization and collagen deposition, as well as promote the deposition of new ECM and angiogenesis (that is, granulation tissue formation) (Kishi et al., 1999). Our experiments further proved that RHC and rFN could effectively maintain tissue dynamic balance by down-regulating pro-inflammatory cytokines (TNF- α, IL-1β and IL-6) and up-regulating anti-inflammatory cytokines (TGF- β1), thus promoting skin wound repair, especially in the combined treatment group. Hence, we have a firm believe that the recombinant proteins with functional domains can produce the effect similar to natural protein. At the beginning, it produces a strong and rapid inflammatory reaction, but this reaction is temporary and subside soon, so as to promote the progress of wound healing smoothly in the next stage, and the two have synergistic effect.

Wound healing requires the participation of a variety of cells, cytokines and nutrients, and adequate oxygen supply (Eelen et al., 2020; Wei et al., 2020). As the medium of biological material transportation, blood vessel is an indispensable part in the process of wound repair. Therefore, it is necessary to restore the blood supply of damaged tissues as soon as possible and promote angiogenesis (Demidova-Rice et al., 2012; Dulmovits and Herman, 2012). By binding to the corresponding receptors on vascular endothelial cells, VEGF can strongly promote the proliferation of vascular endothelial cells and FCs in vascular adventitia, increase the permeability of neovascularization, and become the main growth factor that initiates the process of angiogenesis in granulation tissue (Werner and Grose, 2003; White et al., 2021). Vascular adventitia cells are mainly FCs after injury, FCs can be transformed into MFCs. MFCs can proliferate and migrate to neointima through the injured media, which plays an important role in the occurrence and development of vascular remodeling, and its characteristic structure is the expression of α-SMA in the cytoplasm (Sartore et al., 2001; Gingras et al., 2009; Hussain et al., 2019). In our study, the combination of RHC and rFN produced the highest expression of VEGF and α-SMA, which increased the number of neovascularization around the wound. This would determine the quality of wound healing, thus further formalizing the positive role of the combination of the two.

Based on the full-thickness skin defect mouse model, we speculate that RHC and rhFN can be widely used in wound treatment and regenerative medicine, especially in combination. Compared with the traditional extracted proteins, the new synthesized recombinant proteins have the advantages of good water solubility, easy processing, high safety, low immunogenicity, high biological activity, low cost, high preparation purity and high expression. However, due to the defects of the current technology, there are still some deficiencies. For example, most of the prepared recombinant proteins are short peptides with functional domain and lack of three-dimensional spatial structure, which makes it impossible to carve all the functions of the original protein. Moreover, they are not stable and easy to decompose and fail, so they need the specific preservation and have a short-term application. At the same time, our research also has some limitations. Firstly, the healing period of acute wound in mice is too short to observe the slight difference among RHC, rhFN and RHC + rhFN, and chronic wound and pig model may be closer to the process of human wound healing comparatively. Secondly, the prepared RHC and rhFN are in a liquid state, and they may be lost after smearing the wound, suggesting that it can be combined with hydrogel and other means to ensure the stable existence in the wound in order to perform a more effective therapeutic role. Only by solving the above problems will RHC and rhFN be of great help to our medical treatment in the future.

5 CONCLUSION

In this study, RHC and rhFN were used individually or in combination to explore the treatment of synthetic recombinant human-like collagen and recombinant human-like fibronectin on acute wounds. In this basic experiment, we verified that RHC and rhFN could improve proliferation, migration and adhesion of FCs effectively *in vitro*. In addtion, RHC and rhFN could accelerate wound healing in C57BL/6 mice and showed better re-epithelialisation and orderly structrue of collagen deposition. Moreover, RHC and rhFN could significantly maintain inflammatory balance by down-regulating pro-inflammatory factor (TNF-α,IL-1β and IL-6) and up-regulating anti-inflammatory factor (TGF-β1) as well as enhance vascularization by increasing the expression of VEGF and α-SMA. Besides, RHC and rhFN are easy to be produced on a large scale and have the clear basic mechanism of action. In conclusion, although there are still some molecular mechanisms that need to be further studied, we firmly believe that both recombinant human-like collagen and recombinant human fibronectin play a great role in wound healing and regenerative medicine.

DATA AVAILABILITY STATEMENT

The original contributions presented in the study are included in the article/Supplementary Material, further inquiries can be directed to the corresponding author.

ETHICS STATEMENT

The animal study was reviewed and approved by the Institutional Animal Care and Use Committee (IACUC) of the General Hospital of the Southern Theatre Command.

AUTHOR CONTRIBUTIONS

BC and YD contributed to the conception and design of the study. YD, WZ, XL, QP, PJ, and XZ performed the study. YD and WZ organized the database. YD, WZ, XL, XL, and QX carried out data analysis. YD wrote the manuscript and BC Modified the manuscript. All authors read and approved the submitted version.

FUNDING

This study was supported by National Key Research and Development Plan of China (2017YFC1103301), Military Medical Innovation Special Projects (18CXZ029), National Natural Science Foundation of China (82172223) and The Key Areas Research and Development Program of Guangzhou (202103030003).

ACKNOWLEDGMENTS

The authors would like to thank Yadong Hang and Qi Xiang (Institute of Biomedicine and Guangdong Provincial Key Laboratory of Bioengineering Medicine, Jinan University, Guangzhou, China) for providing RHC and rhFN.

REFERENCES

Amaral, R. J. F. C., Zayed, N. M. A., Pascu, E. I., Cavanagh, B., Hobbs, C., Santarella, F., et al. (2019). Functionalising Collagen-Based Scaffolds with Platelet-Rich Plasma for Enhanced Skin Wound Healing Potential. *Front. Bioeng. Biotechnol.* 7, 371. doi:10.3389/fbioe.2019.00371

Broekman, W., Amatngalim, G. D., de Mooij-Eijk, Y., Oostendorp, J., Roelofs, H., Taube, C., et al. (2016). TNF-α and IL-1β-activated Human Mesenchymal Stromal Cells Increase Airway Epithelial Wound Healing *In Vitro* via Activation of the Epidermal Growth Factor Receptor. *Respir. Res.* 17, 3. doi:10.1186/s12931-015-0316-1

Caedo-Dorantes, L., and Caedo-Ayala, M. (2019). Skin Acute Wound Healing: A Comprehensive Review. *Int. J. Inflamm.*, 2019, 1–15. doi:10.1155/2019/3706315

Chen, J., Gao, K., Liu, S., Wang, S., Elango, J., Bao, B., et al. (2019). Fish Collagen Surgical Compress Repairing Characteristics on Wound Healing Process *In Vivo*. *Mar. Drugs* 17 (1). doi:10.3390/md17010033

Cheng, C. Y., Martin, D. E., Leggett, C. G., Reece, M. C., and Reese, A. C. (1988). Fibronectin Enhances Healing of Excised Wounds in Rats. *Archives Dermatology* 124 (2), 221–225. doi:10.1001/archderm.124.2.221

Cheng, Y., Li, Y., Huang, S., Yu, F., Bei, Y., Zhang, Y., et al. (2020). Hybrid Freeze-Dried Dressings Composed of Epidermal Growth Factor and Recombinant Human-like Collagen Enhance Cutaneous Wound Healing in Rats. *Front. Bioeng. Biotechnol.* 8, 742. doi:10.3389/fbioe.2020.00742

Chi, L., Fan, D.-D., Ma, X.-X., Mi, Y., Luo, Y.-E., Zhu, C.-H., et al. (2011). A Genetic Algorithm for the Optimization of the Thermoinduction Protocol for High-Level Production of Recombinant Human-like Collagen from *Escherichia coli*. *Biotechnol. Appl. Biochem.* 58, 175–184. doi:10.1002/bab.25

Clark, R. A. F. (1993). Regulation of Fibroplasia in Cutaneous Wound Repair. *Am. J. Med. Sci.* 306 (1), 42–48. doi:10.1097/00000441-199307000-00011

Colby, D. W., and Prusiner, S. B. (2011). Cold Spring Harbor Perspectives in Biology. *Cold Spring Harb. Perspect. Biol.* 3 (1), 13363–13383. doi:10.1101/cshperspect.a006833

Dang, Q. F., Liu, H., Yan, J. Q., Liu, C. S., Liu, Y., Li, J., et al. (2015). Characterization of Collagen from Haddock Skin and Wound Healing Properties of its Hydrolysates. *Biomed. Mat.* 10 (1), 015022. doi:10.1088/1748-6041/10/1/015022

Demidova-Rice, T. N., Durham, J. T., and Herman, I. M. (2012). Wound Healing Angiogenesis: Innovations and Challenges in Acute and Chronic Wound Healing. *Adv. Wound Care* 1 (1), 17–22. doi:10.1089/wound.2011.0308

Deng, A., Yang, Y., Du, S., Yang, X., Pang, S., Wang, X., et al. (2020). Preparation of a Recombinant Collagen-Peptide (RHC)-conjugated Chitosan Thermosensitive Hydrogel for Wound Healing. *Mater. Sci. Eng. C* 119, 111555. doi:10.1039/c3bm60319a

Dulmovits, B. M., and Herman, I. M. (2012). Microvascular Remodeling and Wound Healing: A Role for Pericytes. *Int. J. Biochem. Cell. Biol.* 44 (11), 1800–1812. doi:10.1016/j.biocel.2012.06.031

Edara, V. V., Nooka, S., Proulx, J., Stacy, S., Ghorpade, A., and Borgmann, K. (2020). β-Catenin Regulates Wound Healing and IL-6 Expression in Activated Human Astrocytes. *Biomedicines* 8 (11), 479. doi:10.3390/biomedicines8110479

Eelen, G., Treps, L., Li, X., and Carmeliet, P. (2020). Basic and Therapeutic Aspects of Angiogenesis Updated. *Circ. Res.* 127 (2), 310–329. doi:10.1161/circresaha.120.316851

Eisinger, F., Patzelt, J., and Langer, H. F. (2018). The Platelet Response to Tissue Injury. *Front. Med.* 5, 317. doi:10.3389/fmed.2018.00317

Elbialy, Z. I., Atiba, A., Abdelnaby, A., Al-Hawary, I. I., Elsheshtawy, A., El-Serehy, H. A., et al. (2020). Collagen Extract Obtained from Nile tilapia (*Oreochromis niloticus* L.) Skin Accelerates Wound Healing in Rat Model via up Regulating VEGF, bFGF, and α-SMA Genes Expression. *BMC Vet. Res.* 16 (1), 352. doi:10.1186/s12917-020-02566-2

Ezoe, K., and Horikoshi, T. (1993). Tumor Necrosis Factor-α Increased the Integrin α2β1 Expression and Cell Attachment to Type I Collagen in Human Dermal Fibroblasts. *Biochem. Biophysical Res. Commun.* 192 (1), 281–287. doi:10.1006/bbrc.1993.1411

Fedyk, E. R., Jones, D., Critchley, H. O. D., Phipps, R. P., Blieden, T. M., and Springer, T. A. (2001). Expression of Stromal-Derived Factor-1 Is Decreased by IL-1 and TNF and in Dermal Wound Healing. *J. Immunol.* 166 (9), 5749–5754. doi:10.4049/jimmunol.166.9.5749

Gingras, M., Farand, P., Safar, M. E., and Plante, G. E. (2009). Adventitia: the Vital Wall of Conduit Arteries. *J. Am. Soc. Hypertens.* 3 (3), 166–183. doi:10.1016/j.jash.2009.03.002

Grinnell, F., Billingham, R. E., and Burgess, L. (1981). Distribution of Fibronectin during Wound Healing *In Vivo*. *J. Investigative Dermatology* 76 (3), 181–189. doi:10.1111/1523-1747.ep12525694

Grinnell, F. (1994). Fibroblasts, Myofibroblasts, and Wound Contraction. *J. Cell. Biol.* 124 (4), 401–404. doi:10.1083/jcb.124.4.401

Guo, Y., Xu, B., Wang, Y., Li, Y., Si, H., Zheng, X., et al. (2019). Dramatic Promotion of Wound Healing Using a Recombinant Human-like Collagen and bFGF Cross-Linked Hydrogel by Transglutaminase. *J. Biomaterials Sci. Polym. Ed.* 30, 1591–1603. doi:10.1080/09205063.2019.1652416

Gurtner, G. C., Werner, S., Barrandon, Y., and Longaker, M. T. (2008). Wound Repair and Regeneration. *Nature* 453 (7193), 314–321. doi:10.1038/nature07039

Huang, R., Hu, J., Qian, W., Chen, L., and Zhang, D. (2021). Recent Advances in Nanotherapeutics for the Treatment of Burn Wounds. *Burns Trauma* 9, tkab026. doi:10.1093/burnst/tkab026

Huang, X., Yang, N., Fiore, V. F., Barker, T. H., Sun, Y., Morris, S. W., et al. (2012). Matrix Stiffness-Induced Myofibroblast Differentiation Is Mediated by Intrinsic Mechanotransduction. *Am. J. Respir. Cell. Mol. Biol.* 47 (3), 340–348. doi:10.1165/rcmb.2012-0050oc

Hussain, M., Wei, L. N., Dan, L., Naing, M. W., and Ng, K. W. (2019). Healing of Chronic Wounds -An Update of Recent Developments and Future Possibilities. *Tissue Eng. Part B Rev.* 25 (5), 429–444. doi:10.1039/D0BM00391C

Hynes, R. O. (2009). The Extracellular Matrix: Not Just Pretty Fibrils. *Science* 326 (5957), 1216–1219. doi:10.1126/science.1176009

Jansen, K. A., Licup, A. J., Sharma, A., Rens, R., Mackintosh, F. C., and Koenderink, G. H. (2018). The Role of Network Architecture in Collagen Mechanics. *Biophysical J.* 114 (11), 2665–2678. doi:10.1016/j.bpj.2018.04.043

Järveläinen, H., Sainio, A., Koulu, M., and Wight, T. N. (2009). Extracellular Matrix Molecules: Potential Targets in Pharmacotherapy. *Pharmacol. Rev.* 61 (2), 198–223. doi:10.1124/pr.109.001289

Jiang, D., and Scharffetter, K. (2020). Mesenchymal Stem Cells Adaptively Respond to Environmental Cues Thereby Improving Granulation Tissue

Formation and Wound Healing. *Front. Cell. Dev. Biol.* 8, 697. doi:10.3389/fcell.2020.00697

Jiang, Y., Wang, X., Cheng, Y., Peng, J., Xiao, J., Tang, D., et al. (2017). Associations between Inflammatory Gene Polymorphisms (TNF-α 308G/A, TNF-α 238G/A, TNF-β 252A/G, TGF-B1 29T/C, IL-6 174G/C and IL-10 1082A/G) and Susceptibility to Osteosarcoma: a Meta-Analysis and Literature Review. *Oncotarget* 8 (57), 97571–97583. doi:10.18632/oncotarget.18813

Kishi, K., Nakajima, H., and Tajima, S. (1999). Differential Responses of Collagen and Glycosaminoglycan Syntheses and Cell Proliferation to Exogenous Transforming Growth Factor β 1 in the Developing Mouse Skin Fibroblasts in Culture. *Br. J. Plastic Surg.* 52 (7), 579–582. doi:10.1054/bjps.1999.3163

Lai, C.-S., Tu, C.-W., Kuo, H.-C., Sun, P.-P., and Tsai, M.-L. (2020). Type II Collagen from Cartilage of *Acipenser baerii* Promotes Wound Healing in Human Dermal Fibroblasts and in Mouse Skin. *Mar. Drugs* 18 (10), 511. doi:10.3390/md18100511

Lenselink, E. A. (2015). Role of Fibronectin in Normal Wound Healing. *Int. Wound J.* 12 (3), 313–316. doi:10.1111/iwj.12109

Li, A., Li, L., Zhao, B., Li, X., Liang, W., Lang, M., et al. (2022). Antibacterial, Antioxidant and Anti-inflammatory PLCL/gelatin Nanofiber Membranes to Promote Wound Healing. *Int. J. Biol. Macromol.* 194, 914–923. doi:10.1016/j.ijbiomac.2021.11.146

Lin, H., Chen, B., Sun, W., Zhao, W., Zhao, Y., and Dai, J. (2006). The Effect of Collagen-Targeting Platelet-Derived Growth Factor on Cellularization and Vascularization of Collagen Scaffolds. *Biomaterials* 27 (33), 5708–5714. doi:10.1016/j.biomaterials.2006.07.023

Liu, X., Li, P., Chen, X.-Y., and Zhou, Y.-G. (2010). c-Ski Promotes Skin Fibroblast Proliferation but Decreases Type I Collagen: Implications for Wound Healing and Scar Formation. *Clin. Exp. Dermatology* 35 (4), 417–424. doi:10.1111/j.1365-2230.2009.03606.x

Liu, Z., Wu, Y., Dai, H., Li, S., Zhu, Y., Chen, Y., et al. (2021). A New Recombinant Fibronectin/Cadherin Protein-Hydrophobically Modified Glycol Chitosan/Paclitaxel Layer-By-Layer Self-Assembly Strategy for the Postoperative Therapy of Osteosarcoma and Correlated Bone Injury. *J. Biomed. Nanotechnol.* 17, 1765–1777. doi:10.1166/jbn.2021.3159

Manou, D., Caon, I., Bouris, P., Triantaphyllidou, I. E., Giaroni, C., Passi, A., et al. (2019). The Complex Interplay between Extracellular Matrix and Cells in Tissues. *Methods Mol. Biol.* 1952, 1–20. doi:10.1007/978-1-4939-9133-4_1

Mathew, S. S., Roy, S., and Sen, C. K. (2021). Collagen in Wound Healing. *Bioengineering* 8 (5), 63. doi:10.3390/bioengineering8050063

Meyer, M. (2019). Processing of Collagen Based Biomaterials and the Resulting Materials Properties. *Biomed. Eng. online* 18, 24. doi:10.1186/s12938-019-0647-0

Mosesson, M. W., and Umfleet, R. A. (1970). The Cold-Insoluble Globulin of Human Plasma. *J. Biol. Chem.* 245 (21), 5728–5736. doi:10.1016/s0021-9258(18)62713-9

Musiime, M., Chang, J., Hansen, U., Kadler, K. E., Zeltz, C., and Gullberg, D. (2021). Collagen Assembly at the Cell Surface: Dogmas Revisited. *Cells* 10 (3), 662. doi:10.3390/cells10030662

Pal, P., Srivas, P. K., Dadhich, P., Das, B., Maity, P. P., Moulik, D., et al. (2016). Accelerating Full Thickness Wound Healing Using Collagen Sponge of Mrigal Fish (Cirrhinus Cirrhosus) Scale Origin. *Int. J. Biol. Macromol.* 93, 1507–1518. doi:10.1016/j.ijbiomac.2016.04.032

Patten, J., and Wang, K. (2020). Fibronectin in Development and Wound Healing. *Adv. Drug Deliv. Rev.* 170, 353–368. doi:10.1016/j.addr.2020.09.005

Peters, T., Sindrilaru, A., Hinz, B., Hinrichs, R., Menke, A., Al-Azzeh, E. A. D., et al. (2005). Wound-healing Defect of CD18−/− Mice Due to a Decrease in TGF-B1 and Myofibroblast Differentiation. *Embo J.* 24 (19), 3400–3410. doi:10.1038/sj.emboj.7600809

Ren, H., Zhao, F., Zhang, Q., Huang, X., and Wang, Z. (2022). Autophagy and Skin Wound Healing. *Burns Trauma* 10 (3), 1–11. doi:10.1093/burnst/tkac003

Sartore, S., Chiavegato, A., Faggin, E., Franch, R., Puato, M., Ausoni, S., et al. (2001). Contribution of Adventitial Fibroblasts to Neointima Formation and Vascular Remodeling. *Circulation Res.* 89 (12), 1111–1121. doi:10.1161/hh2401.100844

Sethi, K. K., Yannas, I. V., Mudera, V., Eastwood, M., McFarland, C., and Brown, R. A. (2002). Evidence for Sequential Utilization of Fibronectin, Vitronectin, and Collagen during Fibroblast-Mediated Collagen Contraction. *Wound Repair Regen.* 10 (6), 397–408. doi:10.1046/j.1524-475X.2002.10609.x

Smithmyer, M. E., Sawicki, L. A., and Kloxin, A. M. (2014). Hydrogel Scaffolds as *In Vitro* Models to Study Fibroblast Activation in Wound Healing and Disease. *Biomater. Sci.* 2, 634–650. doi:10.1039/C3BM60319A

Song, Q. H., Klepeis, V. E., Nugent, M. A., and Trinkaus-Randall, V. (2002). TGF-beta1 Regulates TGF-Beta1 and FGF-2 mRNA Expression during Fibroblast Wound Healing. *Mol. Pathol. MP* 55 (3), 164–176. doi:10.4049/jimmunol.090192910.1136/mp.55.3.164

Spada, S., Tocci, A., Di Modugno, F., and Nisticò, P. (2021). Fibronectin as a Multiregulatory Molecule Crucial in Tumor Matrisome: from Structural and Functional Features to Clinical Practice in Oncology. *J. Exp. Clin. Cancer Res.* 40 (1), 102. doi:10.1186/s13046-021-01908-8

Theocharis, A. D., Skandalis, S. S., Gialeli, C., and Karamanos, N. K. (2016). Extracellular Matrix Structure. *Adv. Drug Deliv. Rev.* 97, 4–27. doi:10.1016/j.addr.2015.11.001

To, W. S., and Midwood, K. S. (2011). Plasma and Cellular Fibronectin: Distinct and Independent Functions during Tissue Repair. *Fibrogenes. Tissue Repair* 4 (1), 21. doi:10.1186/1755-1536-4-21

Wei, P., Zhong, C., Yang, X., Shu, F., Xiao, S., Gong, T., et al. (2020). Exosomes Derived from Human Amniotic Epithelial Cells Accelerate Diabetic Wound Healing via PI3K-AKT-mTOR-Mediated Promotion in Angiogenesis and Fibroblast Function. *Burns Trauma* 8 (20), 1–17. doi:10.1093/burnst/tkaa020

Wei, S., Xu, P., Yao, Z., Cui, X., and Cheng, B. (2021). A Composite Hydrogel with Co-delivery of Antimicrobial Peptides and Platelet-Rich Plasma to Enhance Healing of Infected Wounds in Diabetes. *Acta Biomater.* 124 (2), 205–218. doi:10.1016/j.actbio.2021.01.046

Werner, S., and Grose, R. (2003). Regulation of Wound Healing by Growth Factors and Cytokines. *Physiol. Rev.* 83 (3), 835–870. doi:10.1152/physrev.2003.83.3.835

White, M., Briquez, P. S., White, D., and Hubbell, J. A. (2021). VEGF-A, PDGF-BB and HB-EGF Engineered for Promiscuous Super Affinity to the Extracellular Matrix Improve Wound Healing in a Model of Type 1 Diabetes. *npj Regen. Med.* 6 (76), 1–12. doi:10.1038/s41536-021-00189-1

Xing, J., Mei, T., Luo, K., Li, Z., Yang, A., Li, Z., et al. (2017). A Nano-Scaled and Multi-Layered Recombinant Fibronectin/cadherin Chimera Composite Selectively Concentrates Osteogenesis-Related Cells and Factors to Aid Bone Repair. *Acta Biomater.* 53, 470–482. doi:10.1016/j.actbio.2017.02.016

Xu, P., Wu, Y., Zhou, L., Yang, Z., and Cheng, B. (2020). Platelet-rich Plasma Accelerates Skin Wound Healing by Promoting Re-epithelialization. *Burns Trauma* 8 (28), 1–14. doi:10.1093/burnst/tkaa028

Yeung, D. A., and Kelly, N. H. (2021). The Role of Collagen-Based Biomaterials in Chronic Wound Healing and Sports Medicine Applications. *Bioengineering* 8 (1), 8. doi:10.3390/bioengineering8010008

Zhao, B., Zhang, X., Zhang, Y. L., Lu, Y., and Zhang, J. (2021). Human Exosomes Accelerate Cutaneous Wound Healing by Promoting Collagen Synthesis in A Diabetic Mice Model. *Stem Cells Dev.* 30, 922–933. doi:10.1089/scd.2021.0100

Zheng, Y., Yuan, W., Liu, H., Huang, S., Bian, L., and Guo, R. (2020). Injectable Supramolecular Gelatin Hydrogel Loading of Resveratrol and Histatin-1 for Burn Wound Therapy. *Biomater. Sci.* 8, 4810–4820. doi:10.1039/d0bm00391c

Zhou, D., Liu, T., Wang, S., He, W., Qian, W., and Luo, G. (2020). Effects of IL-1β and TNF-α on the Expression of P311 in Vascular Endothelial Cells and Wound Healing in Mice. *Front. Physiol.* 11, 545008. doi:10.3389/fphys.2020.545008

Zuijlen, P. P. M., Ruurda, J. J. B., van Veen, H. A., van Marle, J., van Trier, A. J. M., Groenevelt, F., et al. (2003). Collagen Morphology in Human Skin and Scar Tissue: No Adaptations in Response to Mechanical Loading at Joints. *Burns* 29 (5), 423–431. doi:10.1016/s0305-4179(03)00052-4

Conflict of Interest: The authors declare that the research was conducted in the absence of any commercial or financial relationships that could be construed as a potential conflict of interest.

Publisher's Note: All claims expressed in this article are solely those of the authors and do not necessarily represent those of their affiliated organizations, or those of the publisher, the editors and the reviewers. Any product that may be evaluated in this article, or claim that may be made by its manufacturer, is not guaranteed or endorsed by the publisher.

Copyright © 2022 Dong, Zhu, Lei, Luo, Xiang, Zhu, Pan, Jin and Cheng. This is an open-access article distributed under the terms of the Creative Commons Attribution License (CC BY). The use, distribution or reproduction in other forums is permitted, provided the original author(s) and the copyright owner(s) are credited and that the original publication in this journal is cited, in accordance with accepted academic practice. No use, distribution or reproduction is permitted which does not comply with these terms.

frontiers | Frontiers in Bioengineering and Biotechnology

ORIGINAL RESEARCH
published: 19 May 2022
doi: 10.3389/fbioe.2022.899293

Biomimetic Design and Fabrication of Sericin-Hydroxyapatite Based Membranes With Osteogenic Activity for Periodontal Tissue Regeneration

Piaoye Ming[1,2], *Pengcheng Rao*[1,3], *Tianli Wu*[1,2], *Jianghua Yang*[1], *Shi Lu*[1,2], *Binbin Yang*[1], *Jingang Xiao*[1,2,3]* *and Gang Tao*[1]*

[1]Luzhou Key Laboratory of Oral and Maxillofacial Reconstruction and Regeneration, The Affiliated Stomatological Hospital of Southwest Medical University, Luzhou, China, [2]Department of Oral Implantology, The Affiliated Stomatological Hospital of Southwest Medical University, Luzhou, China, [3]Department of Oral and Maxillofacial Surgery, The Affiliated Hospital of Southwest Medical University, Luzhou, China

The guided tissue regeneration (GTR) technique is a promising treatment for periodontal tissue defects. GTR membranes build a mechanical barrier to control the ingrowth of the gingival epithelium and provide appropriate space for the regeneration of periodontal tissues, particularly alveolar bone. However, the existing GTR membranes only serve as barriers and lack the biological activity to induce alveolar bone regeneration. In this study, sericin-hydroxyapatite (Ser-HAP) composite nanomaterials were fabricated using a biomimetic mineralization method with sericin as an organic template. The mineralized Ser-HAP showed excellent biocompatibility and promoted the osteogenic differentiation of human periodontal membrane stem cells (hPDLSCs). Ser-HAP was combined with PVA using the freeze/thaw method to form PVA/Ser-HAP membranes. Further studies confirmed that PVA/Ser-HAP membranes do not affect the viability of hPDLSCs. Moreover, alkaline phosphatase (ALP) staining, alizarin red staining (ARS), and RT-qPCR detection revealed that PVA/Ser-HAP membranes induce the osteogenic differentiation of hPDLSCs by activating the expression of osteoblast-related genes, including ALP, Runx2, OCN, and OPN. The unique GTR membrane based on Ser-HAP induces the differentiation of hPDLSCs into osteoblasts without additional inducers, demonstrating the excellent potential for periodontal regeneration therapy.

Keywords: sericin, nano-hydroxyapatite, biomimetic membranes, human periodontal membrane stem cells, osteogenic differentiation

OPEN ACCESS

Edited by:
Kaili Lin,
Shanghai Jiao Tong University, China

Reviewed by:
Dejian Li,
Fudan University Pudong Medical Center, China
Yajun Shuai,
Zhejiang University, China

***Correspondence:**
Jingang Xiao
xiaojingang@swmu.edu.cn
Gang Tao
taogang@swmu.edu.cn

Specialty section:
This article was submitted to Biomaterials, a section of the journal Frontiers in Bioengineering and Biotechnology

Received: *18 March 2022*
Accepted: *18 April 2022*
Published: *19 May 2022*

Citation:
Ming P, Rao P, Wu T, Yang J, Lu S, Yang B, Xiao J and Tao G (2022) Biomimetic Design and Fabrication of Sericin-Hydroxyapatite Based Membranes With Osteogenic Activity for Periodontal Tissue Regeneration. Front. Bioeng. Biotechnol. 10:899293. doi: 10.3389/fbioe.2022.899293

INTRODUCTION

The repair of periodontal bone defects caused by periodontitis, infection, and trauma remains a challenge in clinical treatment (Orlandi et al., 2021). The guided tissue regeneration (GTR) technique is the mainstay therapy for periodontal bone defects. This generally combines bone meal with a GTR membrane to promote alveolar bone reconstruction. GTR membranes are most frequently used to restrain the ingrowth of fibrous tissue and create a suitable space for alveolar bone regeneration (Aral et al., 2020; Zhang et al., 2021; Zheng et al., 2021). Ideal GTR membranes should have an appropriate mechanical strength and be able to induce the osteogenic differentiation of autologous stem cells at the site of the alveolar bone defect (Liao et al., 2021; Woo et al., 2021). Currently, GTR membranes

are prepared by combining the advantages of different biomaterials into composites. Inorganic materials (HAP, Zinc, tricalcium phosphate, etc.) and polymers (chitosan, gelatin, PCL, PLGA, etc.) were used for periodontal tissue regeneration. Wu et al. successfully fabricated biocompatible chitin hydrogel films incorporated with ZnO and found that composite GTR membrane has excellent antibacterial abilities and can effectively promote periodontal repair (Wu et al., 2021). However, the most frequently used GTR membranes still have limitations, such as high cost, poor mechanical properties, and a lack of osteogenic activity. Therefore, the development of low-cost GTR membranes with good biocompatibility and excellent osteogenic function has attracted increasing attention (Nguyen et al., 2021; Tedeschi et al., 2021).

Sericin, a soluble protein extracted from domestic silkworm cocoons, contains 17–18 amino acids, including glycine, serine, alanine, and tyrosine. Due to its high carboxyl, amino, and hydroxyl group content, sericin has exhibited diverse biological activities, including anti-apoptosis and anti-oxidation properties (Zhao et al., 2014; Lamboni et al., 2015; Li et al., 2021). In addition, the biological activity of sericin in promoting cell migration and differentiation has been demonstrated (Martínez-Mora et al., 2012; Nayak et al., 2013). Sericin has excellent biocompatibility and biodegradability, making it attractive for the development of tissue engineering materials. The application of sericin has been studied for a range of tissue repairs, including sericin catheters for peripheral nerve regeneration, sericin scaffolds for cartilage repair, and sericin hydrogels for wound repair. Qi et al. (2020) prepared a photo-crosslinked sericin/graphene oxide hydrogel and found that the sericin composite scaffold exhibited good biocompatibility, cell adhesion, proliferation, and osteogenic induction property. However, the use of sericin as a GTR membrane for periodontal bone repair has not yet been explored. Therefore, we aimed to use sericin to prepare a GTR membrane with osteogenic properties, with the objective of effectively promoting the osteogenic differentiation of endogenous stem cells and the repair of periodontal bone defects.

Hydroxyapatite (HAP) is the most commonly used osteogenic material in bone tissue engineering owing to its similar biodegradability, crystal structure, and chemical properties to those of biological apatite (Fihri et al., 2017). HAP simultaneously releases Ca and P during its degradation process, giving it the potential to promote bone regeneration in bone tissue engineering (D'Elia et al., 2020). The formation of bone involves a series of complex events, with the critical step being the mineralization of calcium phosphate on the extracellular matrix (ECM) to form HAP crystals. Numerous natural and synthetic polymers have been used as templates for growing HAP and creating scaffold materials with osteogenic activity. Recently, hydroxyapatite fabricated using proteins has attracted widespread attention as an organic template (Raina et al., 2020; Bal et al., 2021; Zhu et al., 2021). Cai et al. (2010) showed that the crystallization of HAP could be affected by introducing proteins into the system. Tao reported a simple, one-step, "green" synthetic strategy using sericin as a biomineralized template for AgNPs synthesis to prepare sericin-AgNPS sponge dressings. The dressing has excellent biocompatibility and antimicrobial activity properties making it a competitive candidate for an effective wound dressing (Tao et al., 2019). Proteins contain a variety of active groups that can be used as templates for HAP deposition in the formation of protein/HAP nanocomposites. Similarly, sericin protein can be used as a biomineralization template for the deposition of HAP.

In this study, the effect of sericin on the mineralization of HAP was investigated, and it was found that increasing the sericin concentration led to a gradual decrease in HAP particle size. Polyvinyl alcohol (PVA), a biocompatible, biodegradable, non-toxic, and hydrophilic synthetic polymer, was widely used to prepare biomedical materials. It is a semi-crystalline polymer with excellent strength and flexibility that are crucial for biomaterials applications (Pan et al., 2021; Zhou et al., 2021). Polyvinyl alcohol (PVA) was combined with Ser-HAP and subjected to three freeze/thaw cycles to prepare PVA/Ser-HAP membranes (**Scheme 1A,B**). FESEM was used to characterize the morphological features of the PVA/Ser-HAP membranes. ARS and ALP staining were used to investigate the effect of the PVA/Ser-HAP membranes on the osteogenic differentiation of hPDLSCs. In addition, the expression of osteogenic-related genes, including ALP, runt-related transcription factor (Runx2), osteopontin (OPN), and osteocalcin (OCN) were assayed. The feasibility of using the PVA/Ser-HAP membrane as a new GTR membrane was verified (**Scheme 1C**). This study provides substantial support for the biomimetic design and preparation of sericin-based GTR membranes.

MATERIALS AND METHODS

Materials

Silkworm cocoons were obtained from the Seri Cultural Research Institute, China Academy of Agriculture Science (Jiangsu, China). Calcium chloride ($CaCl_2$), polyvinyl alcohol (PVA), and monosodium phosphate (NaH_2PO_4) were purchased from Macklin Biochemical Technology Co., Ltd. (Shanghai, China). Sodium carbonate anhydrous (Na_2CO_3) was purchased from Solarbio Technology Co., Ltd. (Beijing, China). And sodium hydroxide (NaOH) was obtained from Kelong Chemicals Co., Ltd. (Chengdu, China). All other reagents, including α-modified eagle's medium (α-MEM; Gibco, CA, United States), fetal bovine serum (FBS; Gibco, United States), 1% penicillin-streptomycin (Beyotime, United States), 0.25% trypsin-EDTA (Gibco, CA, United States), 4% paraformaldehyde (Sigma-Aldrich), Live/Dead® Viability Kit (Thermo Fisher Scientific, United States), Cell Counting Kit-8 (CCK-8, APE-BIO, United States), BCIP/NBT alkaline phosphatase color development kit (Beyotime, China), alizarin red staining solution (ARS, Cyagen, China), Total RNA extraction kit (TianGen, China), and RevertAid First Strand cDNA Synthesis Kit (Thermo Fisher Scientific, Waltham, United States), were used directly without further purification.

Isolation of Sericin

Sericin was extracted from silkworm cocoons using a previously described high temperature and alkaline degumming method

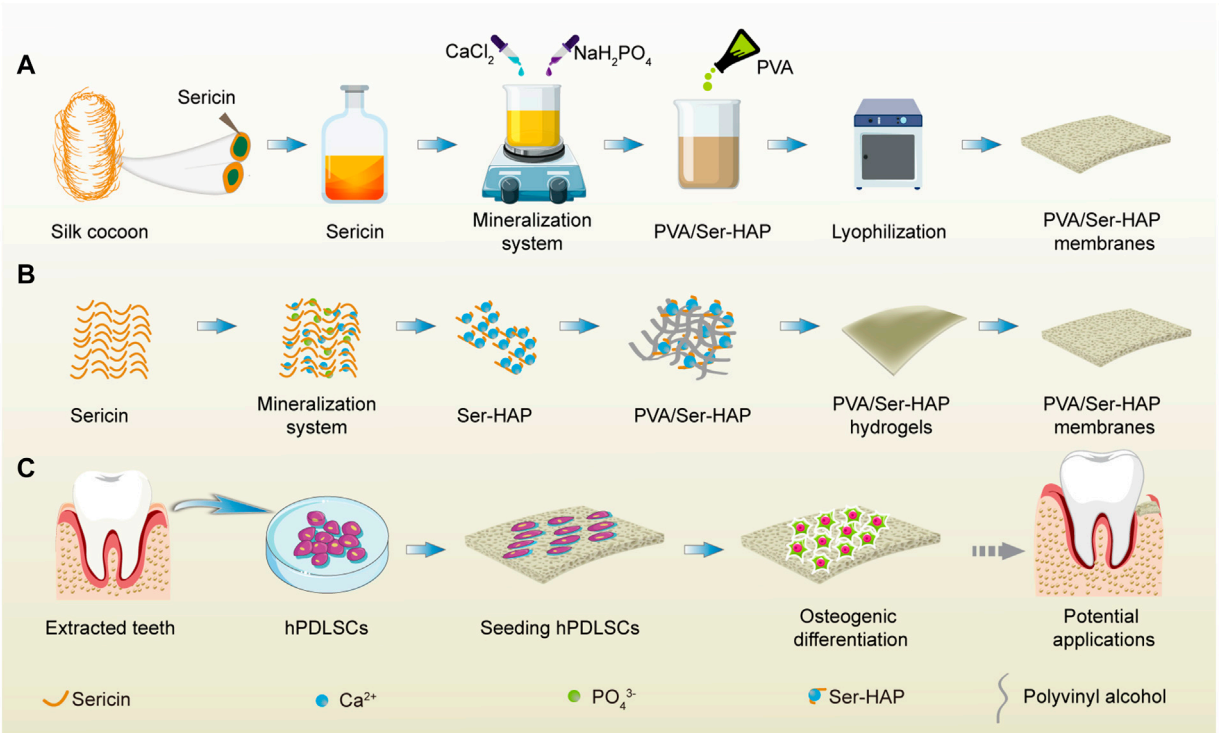

SCHEME 1 | A schematic illustration of the fabrication and application of PVA/Ser-HAP membrane. **(A)** The preparation process of PVA/Ser-HAP membrane; **(B)** Proposed schematic diagram depicting sericin-mediated nucleation of HAPs and preparation of PVA/Ser-HAP membrane; **(C)** The osteogenic differentiation of hPDLSCs on mineralized PVA/Ser-HAP membrane and potential periodontal tissue regeneration application for PVA/Ser-HAP membrane.

(Tao et al., 2021). Briefly, 10 g of silkworm cocoon was weighed and washed three times with deionized water. The pre-prepared cocoons were then placed in 250 ml of ultrapure water containing 2% (w/v) sodium carbonate. The mixture was allowed to boil at 120°C for 30 min to remove silk fibroin. The solution was then filtered and centrifuged at 3000 rpm for 5 min to remove insoluble residues and then dialyzed (MWCO: 3500 Da) for 48 h to remove hetero-ions. Finally, the sericin powder was obtained by freeze-drying and stored at 4°C before use.

Synthesis and Characterization of Sericin-HAP Particles

Sericin protein-mediated HAP mineralization was carried out using the co-precipitation method. Sericin concentrations of 0, 10, 50, and 100 μg/ml were used to investigate the effect of sericin concentration on the mineralization of HAP. Briefly, 2.22 g of $CaCl_2$ was dissolved in 50 ml of deionized water with various amounts of sericin to give solution A, and 1.44 g of NaH_2PO_4 was dissolved in an equal volume of deionized water (50 ml) to give solution B. The two solutions were then combined, heated to 52°C, and stirred for 2 h. Throughout the process, the pH of the mixed solution was measured using a pH Tester 10 (Eutech Instruments, United States) and adjusted with 0.1 M NaOH to maintain a pH of 11 ± 0.1. The final solution was aged at 4°C for 24 h, and then dried at 60°C for 24 h. The four resulting composites were denoted Ser0-HAP, Ser10-HAP, Ser50-HAP, and Ser100-HAP according to the concentration of sericin used: 0, 10, 50, and 100 μg/ml, respectively. For the Ser100-HAP group, the settling time was extended from 2 to 8 h to explore the effect of mineralization time on HAP nucleation.

The morphology and elemental composition of the Ser-HAP particles were determined using a transmission electron microscope (TEM, JEM-2100, Japan) equipped with energy dispersive spectroscopy (EDS). X-ray photoelectron spectroscopy (XPS, Shimadzu Kratos AXIS Ultra DLD, Nagoya, Japan) was used to assess the surface elemental composition. Fourier transform infrared (FTIR, Thermo Fisher Scientific, MA, United States) spectra in the range 4000–500 cm^{-1} with a resolution of 2 cm^{-1} were used to verify the surface functional groups. X-ray diffraction (XRD, PANalytical X'Pert powder, Almelo, Netherland) in the 2θ range 10°–70° was used to verify the formation of HAP particles.

Fabrication and Characterization of the PVA/Ser-HAP Membranes

PVA (4%, w/v) solution was prepared by dissolving 4 g of PVA in 100 ml of deionized water and stirring at 100°C for 1 h to allow complete dissolution. The 1% (w/v) sericin solution was mixed with (4%, w/v) PVA solution at a 1:1 ratio at 80°C with continuous stirring for 30 min Ser100-HAP particles were then added to the

TABLE 1 | Primer sequences.

Primer name	Forward (5–3′)	Reverse (5–3′)
Runx2	CACTGGCGCTGCAACAAGA	CATTCCGGAGCTCAGCAGAATAA
ALP	GGACCATTCCCACGTCTTCAC	CCTTGTAGCCAGGCCCATTG
OCN	CTAAGAAGTTTCGCAGAC	TGTCCCAATCAGAAGG
OPN	GATGAATCTGATGAACTGGTCACTG	GGTGATGTCCTCGTCTGTAGCA
β-actin	GATGAGATTGGCATGGCTTT	CACCTTCACCGTTCCAGTTT

mixture and stirred for 30 min. The concentration of Ser100-HAP particles was 0, 10, 50, or 100 μg/ml, and the corresponding membranes were denoted PVA/Ser-HAP0, PVA/Ser-HAP1, PVA/Ser-HAP2, PVA/Ser-HAP3, respectively. The mixtures were then poured into a 24-well plate to form PVA/Ser-HAP membranes. The membranes were frozen (−20°C) and thawed 3 times to improve their mechanical properties. Finally, the composite membranes were obtained by freeze-drying for 24 h using a SCIENTZ-12N Freezer Dryer (Ningbo, China). The PVA/Ser-HAP membranes were coated with platinum, and then the surface topography was analyzed by FESEM. The trace elements in the membrane were analyzed using energy dispersive spectroscopy (EDS).

Hydrophilicity and Degradation of PVA/Ser-HAP Membranes *In Vitro*

Composite membranes with the same dimensions were immersed in deionized water at 37°C. The initial dried weight was denoted W0. The swollen weight was determined when the swelling became stable and designated W1. The swelling ratio (SR) was calculated using **Eq. 1**.

$$SR(\%) = (W1 - W0)/W0 \times 100\% \quad (1)$$

On days 0, 7, 14, 21, 28, 35, and 63, the samples were dried. The weight was determined and designated W2. The degradation ratio (DR) was then calculated using **Eq. 2** (Thangprasert et al., 2019; Prakash et al., 2020).

$$DR(\%) = (W0 - W2)/W0 \times 100\% \quad (2)$$

Culture and Identification of hPDLSCs

This study was approved by the ethics committee of Southwest Medical University. Informed consent was obtained from all of the human participants. Healthy teeth were collected from five people receiving orthodontic treatment in the Department of Oral and Maxillofacial Surgery, The Affiliated Stomatological Hospital of Southwest Medical University. The tissue blocks were isolated from the root surface but not the apex, washed and cultured in α-modified eagle's medium, and incubated in a humidified atmosphere with 5% CO_2 at 37°C. The medium was changed every 3 days until the cells reached 80% confluency. The hPDLSCs were then purified by monoclonal culture as previously described (Zhu and Liang, 2015; Li et al., 2017; Li et al., 2021). In short, P0 cells were inoculated in 96-well plates at a concentration of 500 cells/mL for single cell-derived colony selection. The cells were then sub-cultured with 0.25% trypsin-EDTA and P3 cells were used in the subsequent experiments.

When the third-generation cells reached 70%–80% confluency, they were treated with 0.25% trypsin-EDTA and washed three times with phosphate buffered saline (PBS). hPDLSCs (5×10^5/ml) were then incubated with human antibodies for CD31 (FITC), CD34 (APC), CD45 (FITC), CD73 (PE), CD90 (FITC), and CD105 (FITC) (Bio-legend, CA, United States) at 4°C. Flow cytometry (FACSCalibur, CA, United States) was then used to detect stem cell surface markers of the samples. The data were analyzed using Win MDI 2.8 software (The Scripps Institute, West Lafayette, IN, United States).

Cytocompatibility of Sericin and Ser-HAP Particles

In this study, Live/Dead staining and CCK-8 assay were used to investigate the proliferation of cells treated with sericin and Ser-HAP particles. Briefly, hPDLSCs were inoculated in 24-well plates (5×10^3 cells/well) and cultured in α-modified eagle's medium supplemented with 10% FBS and 1% penicillin-streptomycin. The medium was replaced with a serum-free medium containing different concentrations of sericin, while for the Ser-HAP particles, the culture medium was replaced with a complete medium. After co-culturing for 48 h, hPDLSCs were incubated in Live/Dead staining solution for 30 min at room temperature and observed using a fluorescence microscope. A CCK-8 assay was then carried out according to a previously described method (Wang et al., 2015). Briefly, 90 μL of α-modified eagle's medium was mixed with 10 μL of CCK-8 and incubated for 1.5 h at 37°C. The solutions were then analyzed at 450 nm using a microplate reader (TECAN Infinite M200PRO, China).

Biocompatibility of the PVA/Ser-HAP Membranes

The PVA/Ser-HAP membranes were sterilized under ultraviolet light for 2 h and placed in 24-well plates. A hPDLSC suspension (0.5 ml, 1×10^5 cells/mL) was seeded on the membranes. After co-culture for 48 h, the Live/Dead staining of hPDLSCs was performed according to the manufacturer's instructions. For the CCK-8 assay, the culture fluid was discarded, and α-modified eagle's medium containing 10% CCK-8 solution was added. After incubation at 37°C for 1.5 h, the solution was added to 96-well plates and measured at 450 nm using a microplate reader (TECAN Infinite M200PRO, China).

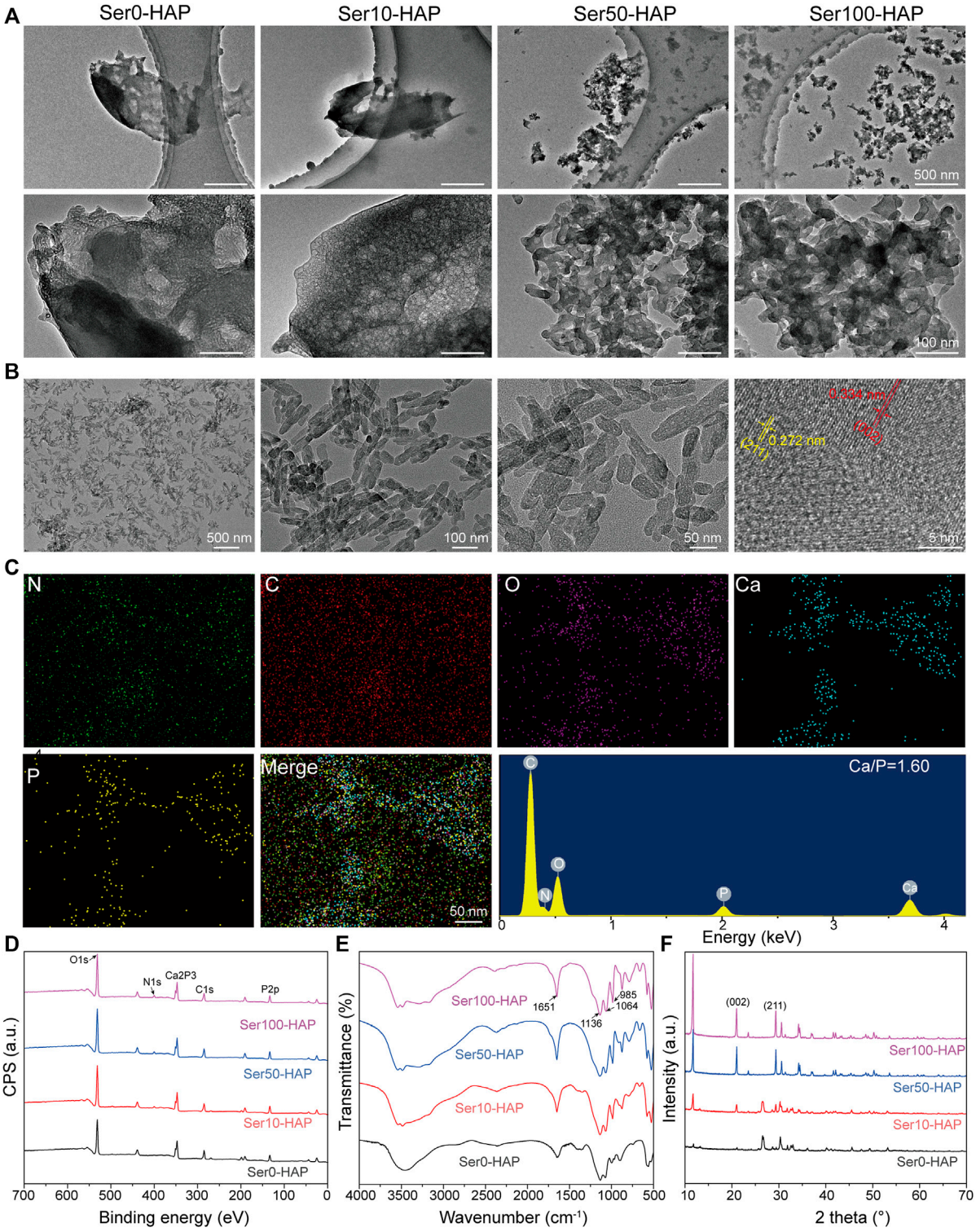

FIGURE 1 | Surface morphology and characterization of Ser-HAP. **(A)** TEM micrographs of Ser-HAP particles; **(B)** TEM and HRTEM images of Ser100-HAP particles; **(C)** EDS analysis of Ser100-HAP particles; **(D)** XPS spectra; **(E)** FTIR spectra; and **(F)** XRD patterns of Ser-HAP particles.

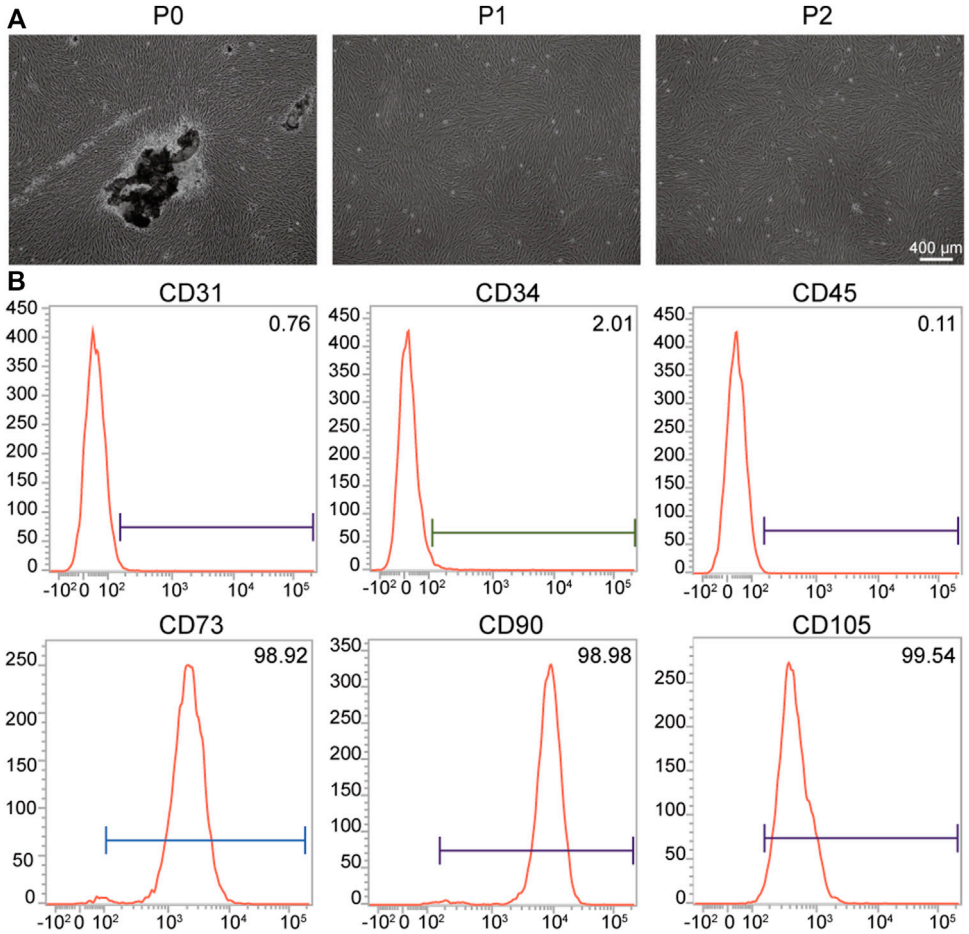

FIGURE 2 | Culture and identification of hPDLSCs. **(A)** Morphology of hPDLSCs; **(B)** Flow cytometry analysis of the indicated cell surface marker expression in hPDLSCs.

Cell Morphology on PVA/Ser-HAP Membranes

The morphology of hPDLSCs grown on the PVA/Ser-HAP membranes was analyzed using filamentous actin (F-actin) staining. hPDLSCs (2×10^4 cells/well) were seeded on the PVA/Ser-HAP membranes. After culturing for 3 or 5 days, the membranes were washed three times with PBS and fixed with 4% paraformaldehyde at 4°C for 30 min. The F-actin and cell nuclei of the hPDLSCs were stained with rhodamine phalloidin and 4-6-diamidino-2-phenylindole (DAPI), respectively, for 15 min. The samples were then sealed with 10% glycerin containing fluorescent anti-crack agent. Finally, the morphology of the hPDLSCs was observed using confocal laser microscopy (Nikon, Tokyo, Japan). All the operations were performed in the dark.

Alkaline Phosphatase Staining

hPDLSCs (2×10^4 cells/well) were seeded in a 24-well plate and cultured in a non-osteogenic induction medium containing different kinds of Ser-HAP particles. All of the Ser-HAP particles were at a concentration of 50 μg/ml. After co-culture for 3 or 5 days, 4% cold paraformaldehyde was used to fix the hPDLSCs for 15 min. The hPDLSCs were then stained with BCIP/NBT alkaline phosphatase color development kit for 1 h at 37°C.

To evaluate the osteogenic performance of the PVA/Ser-HAP membrane, the non-osteogenic induction medium was first prepared with the extract of the PVA/Ser-HAP membrane. The extract of materials was centrifuged at 3000 r/min for 10 min and filtered by sterilizing filter (Millipore, Canada). Subsequently, hPDLSCs (2×10^4 cells/well) were seeded in a 24-well plate with normal media and allowed to reach 80% fusion. The normal media were then replaced with the leaching liquors as described above. After co-culture for 3 or 5 days, alkaline phosphatase staining was performed in the same way as described above. For quantification, the data was processed by utilizing ImageJ.

Alizarin Red Staining

hPDLSCs (2×10^4 cells/well) were seeded in a 24-well plate and co-cultured with the leaching liquors of the PVA/Ser-HAP membranes as described above. After culturing for 21 days, the hPDLSCs were fixed with 4% cold paraformaldehyde for 30 min

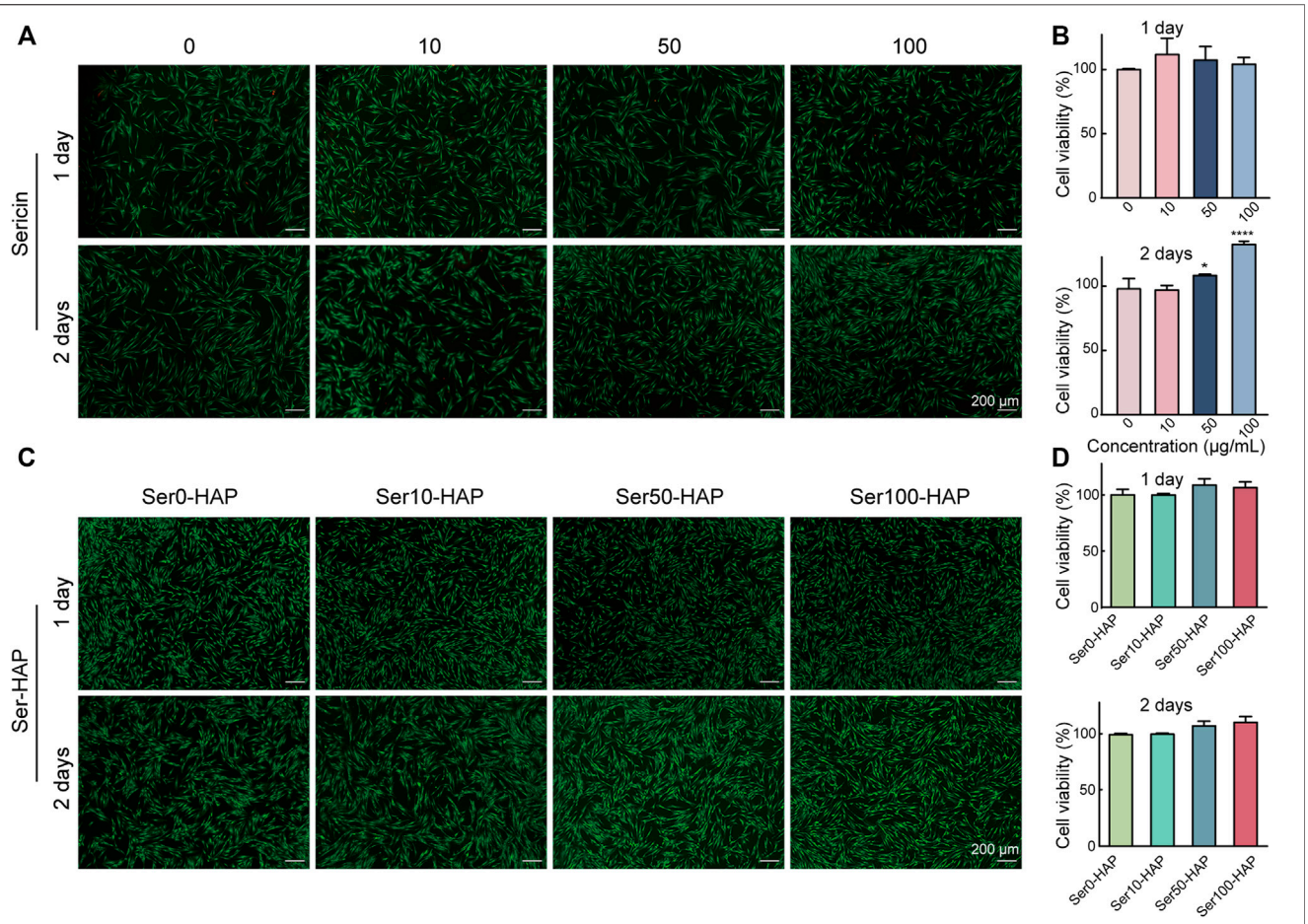

FIGURE 3 | Cytocompatibility of sericin solution and the Ser-HAP particles. **(A)** Live/Dead staining and **(B)** CCK-8 assay of sericin at 1 and 2 days; **(C)** Live/Dead staining and **(D)** CCK-8 assay of Ser-HAP particles at 1 and 2 days.

at 4°C and then incubated with alizarin red stain at 37°C for 1 h. Subsequently, the calcium deposition was imaged using fluorescence microscopy. For quantification, the data was processed by utilizing ImageJ.

Osteogenic Gene Expression

Real-time fluorescence quantitative PCR (RT-qPCR) was used to evaluate the expression of the osteogenic genes of hPDLSCs, including ALP, Runx 2, OPN, and OCN. β-Actin was used as a reference gene. Following co-culture for 3 or 5 days, hPDLSCs were lysed with a Total RNA extraction kit and RNA was collected according to the manufacturer's instructions. The cDNA was then obtained using a Revert Aid First Strand cDNA Synthesis Kit according to the manufacturer's instructions. All primers were compounded by Shenggong Bioengineering Co., Ltd. (Shanghai, China). The primer sequences for RT-qPCR are shown in **Table 1**. All experiments were performed in triplicate and analyzed using the $2^{-\Delta\Delta CT}$ method (Xing et al., 2021).

Statistical Analysis

All experiments were repeated in triplicate independently. The representative data were manifested by mean ± standard deviation (SD). One-way analysis of variance (ANOVA) was used to analyze the differences between groups. A p-value of <0.05 was accepted as statistical significance. ($^{*}p < 0.05$, $^{**}p < 0.01$, $^{***}p < 0.001$, $^{****}p < 0.001$).

RESULTS AND DISCUSSION

Characterization of Ser-HAP Particles

The morphology of the Ser-HAP particles was determined using TEM. As shown in **Figure 1A**, the Ser-HAP particles gradually decreased in size with increasing sericin concentration from 0 to 100 μg/ml. The 0 and 10 μg/ml sericin groups contained aggregated particles, while the 50 and 100 μg/ml sericin groups produced dispersed particles with more uniform particle size. This result indicates that the concentration of sericin affected the HAP mineralization process. According to previous reports, the nucleation of HAP is triggered by the anionic side chains in the protein combining with calcium ions (Kundu et al., 2008; Wang et al., 2010; Chen et al., 2016). Therefore, as the sericin content increased 10–100 μg/ml, the amount of acidic amino acids also increased, promoting the nucleation of HAP.

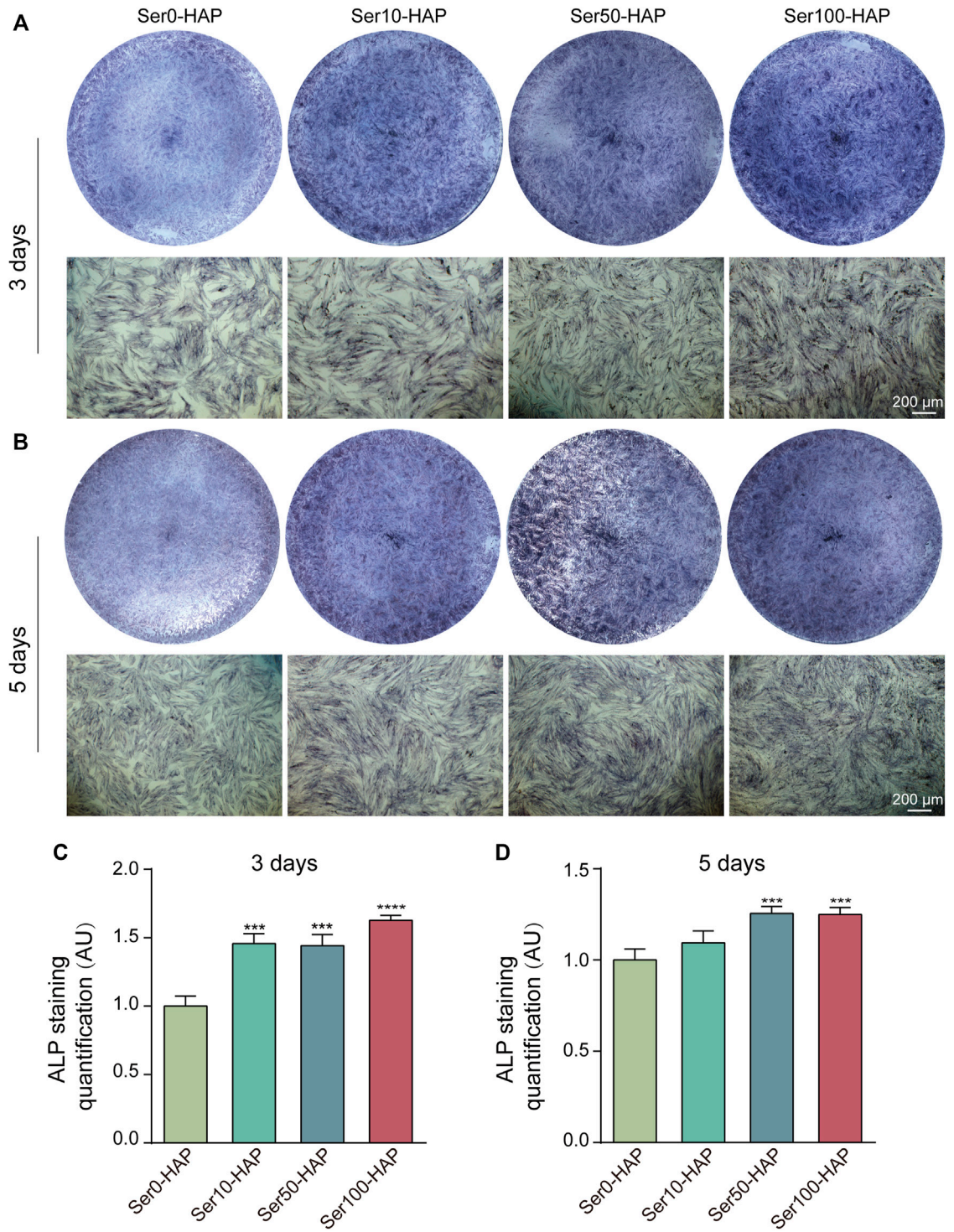

FIGURE 4 | ALP staining of hPDLSCs after culture with Ser-HAP for 3 days **(A)** and 5 days **(B)**; Quantitative analysis of ALP staining at 3 **(C)** and 5 days **(D)**.

The effect of mineralization time on HAP nucleation was explored (**Figure 1B**). When the mineralization time was increased to 8 h, the mineralized HAP crystals in the 100 μg/ml sericin group showed a nanoplate-like structure. The nanoplate crystals were approximately 50–70 nm in length and 15–20 nm in width, which is close to the morphology of natural HAP (Gao et al., 2016). The high-resolution image revealed d-spacings of 0.334 and 0.272 nm, corresponding to the distance of the (002) plane and (211) plane of HAP, respectively (Zheng et al., 2019). EDS analysis showed that C,

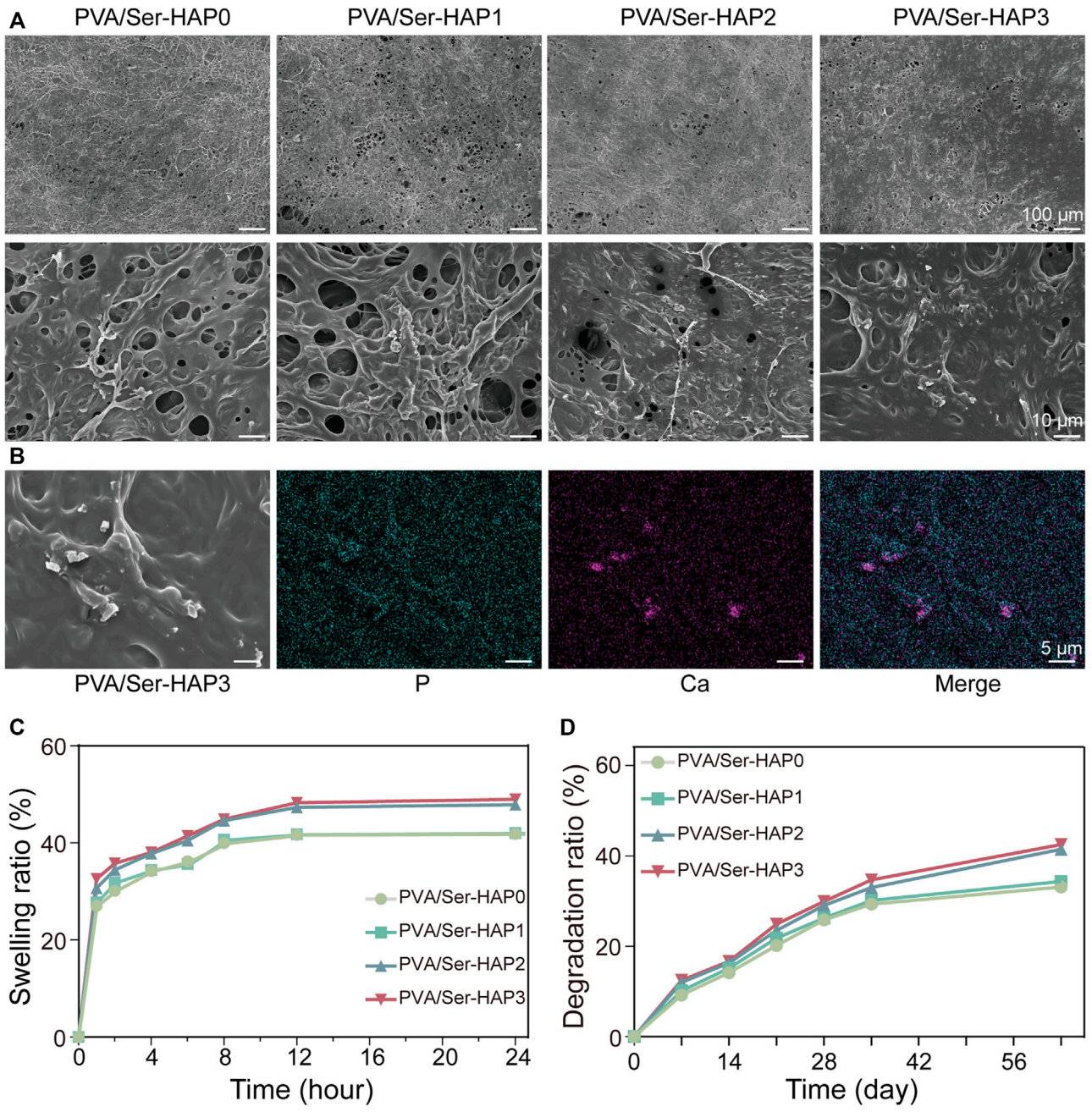

FIGURE 5 | Surface morphology and characterization of PVA/Ser-HAP membranes. **(A)** SEM micrographs of PVA/Ser-HAP membranes; **(B)** Elemental mapping of P and Ca in the PVA/Ser-HAP3 membrane; **(C)** Swelling and **(D)** degradation of the PVA/Ser-HAP membranes.

N, O, Ca, and P were evenly distributed on Ser100-HAP (**Figure 1C**). The molar ratio of Ca to P was 1.60, which is close to the 1.67 value of natural HAP (Xia et al., 2021).

XPS analysis was carried out to detect the surface atomic composition and chemical characteristics of the Ser-HAP samples. The XPS spectrum of Ser-HAP shows three strong peaks at 290, 400, and 530 eV, which are attributed to C 1s, N 1s, and O 1s, respectively (**Figure 1D**). In addition, the Ser-HAP sample exhibited photoelectron peaks at 134 eV (P 2p), 190 eV (P 2s), and 347 eV (Ca 2p), which correspond to the characteristic peaks of crystalline HAP. The carbon peaks of the C-C bond (C 1s, 284.8 eV) and the nitrogen peak of C–NH_2 (N 1s, 400 eV) were also observed for the Ser10-HAP, Ser50-HAP, and Ser100-HAP groups, indicating that sericin was integrated into HAP (Teotia et al., 2017).

The chemical structure of the Ser-HAP samples was characterized by FTIR spectroscopy (**Figure 1E**). The absorption peaks located at 1136, 1064, and 985 cm^{-1} are

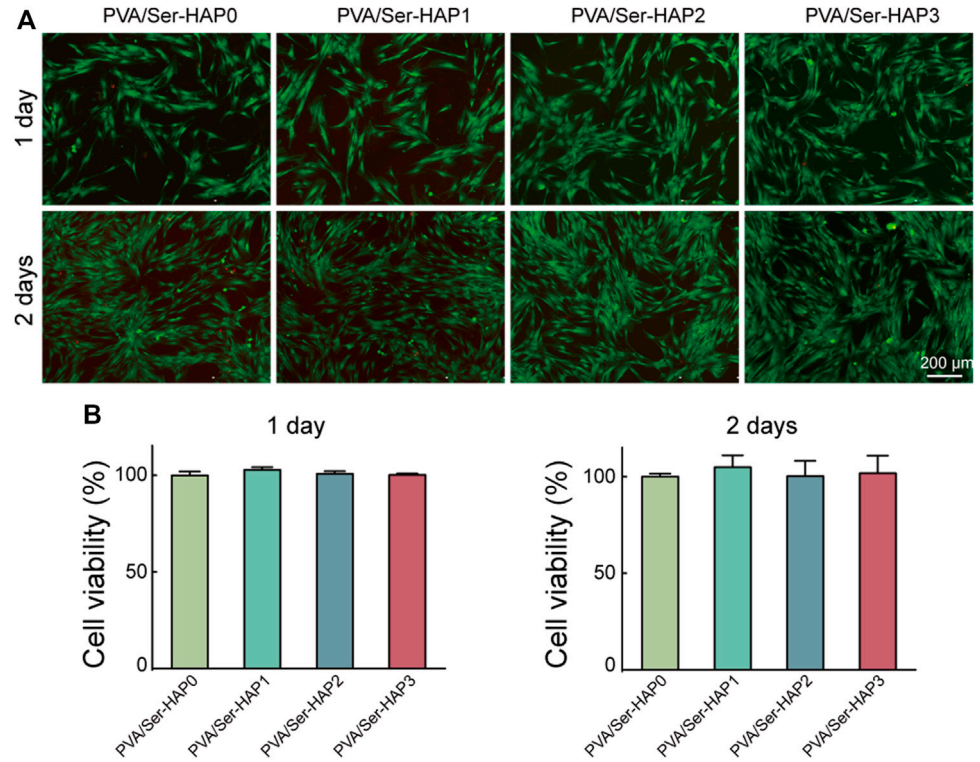

FIGURE 6 | Biological compatibility of PVA/Ser-HAP membranes. Live/Dead staining **(A)** and CCK-8 assay **(B)** of hPDLSCs on the PVA/Ser-HAP membranes.

attributed to the P-O stretching vibration mode and are the characteristic absorption peaks of HAP (Cai et al., 2010). Moreover, as the sericin content increased from 10 μg/ml (**Figure 1E**, Ser0-HAP) to 100 μg/ml (**Figure 1E**, Ser100-HAP), the amide I peak shifted from 1640–1651 cm^{-1}, indicating that more sericin was integrated into the HAP particles (Radha et al., 2018; Veiga et al., 2020; Yu et al., 2021).

XRD analysis was used to determine the phase composition of the Ser-HAP sample. A small peak around 11.66° was observed, which may be due to the HAP lattice as previously reported (Radha et al., 2018). The sharp peaks at 21.2° and 32.1° are assigned to the (002) and (211) planes of HAP (**Figure 1F**). The intensity of these two peaks increased with the sericin concentration, indicating that sericin affected the nucleation of HAP. All the results showed that the sericin content plays an essential role in the nucleation of HAP particles, and sericin was successfully introduced into HAP (Takeuchi et al., 2005; Cai et al., 2010; Liu et al., 2013; Yang et al., 2014; Zhang et al., 2019; Veiga et al., 2020).

Culture and Phenotypic Characterization of hPDLSCs

hPDLSCs, a type of mesenchymal stem cells (MSCs) derived from the periodontal tissue, exhibit strong differentiation into osteoblasts and have therefore attracted increasing attention in the field of periodontal bone tissue regeneration (Zhao et al., 2019). As shown in **Figure 2A**, the black part was human periodontal ligament tissue, and the cells that emerge from the human periodontal tissue present a spindle shape. The results of flow cytometry show that the MSC surface markers CD73 (98.92%), CD90 (98.98%), and CD105 (99.54%) were positive. However, low expressions of the hematopoietic stem cell surface markers CD31 (0.76%), CD34 (2.01%), and CD45 (0.11%) were observed (**Figure 2B**). All of the results suggest that the isolated hPDLSCs had the potential for osteogenic differentiation and were not mixed with hematopoietic stem cells or endothelial cells (Liu et al., 2020; Peng et al., 2021; Rao et al., 2021).

Cytocompatibility of Sericin and Ser-HAP Particles

To evaluate the cell biocompatibility of sericin and Ser-HAP particles in-depth, Live/Dead staining and a CCK-8 assay were used to examine the effects of sericin and Ser-HAP particles on the viability of hPDLSCs. Following incubation for 24 h, there was no significant difference in the viability of hPDLSCs treated with different concentrations of sericin (10, 50, and 100 μg/ml) compared with the control group. After incubation for 48 h, the cell viability of the 50 μg/ml group was slightly higher ($*p < 0.05$) than those of the 0 and 10 μg/ml groups, and the cell viability of the 100 μg/ml group was the highest ($**p < 0.01$) (**Figures 3A,B**). We speculate that in a serum-free environment, the amino acids in sericin serve as an energy source for cell metabolism and promote the growth of hPDLSCs (Lamboni et al., 2015; Wu et al., 2021). As shown in **Figures 3C,D**, Live/Dead staining and

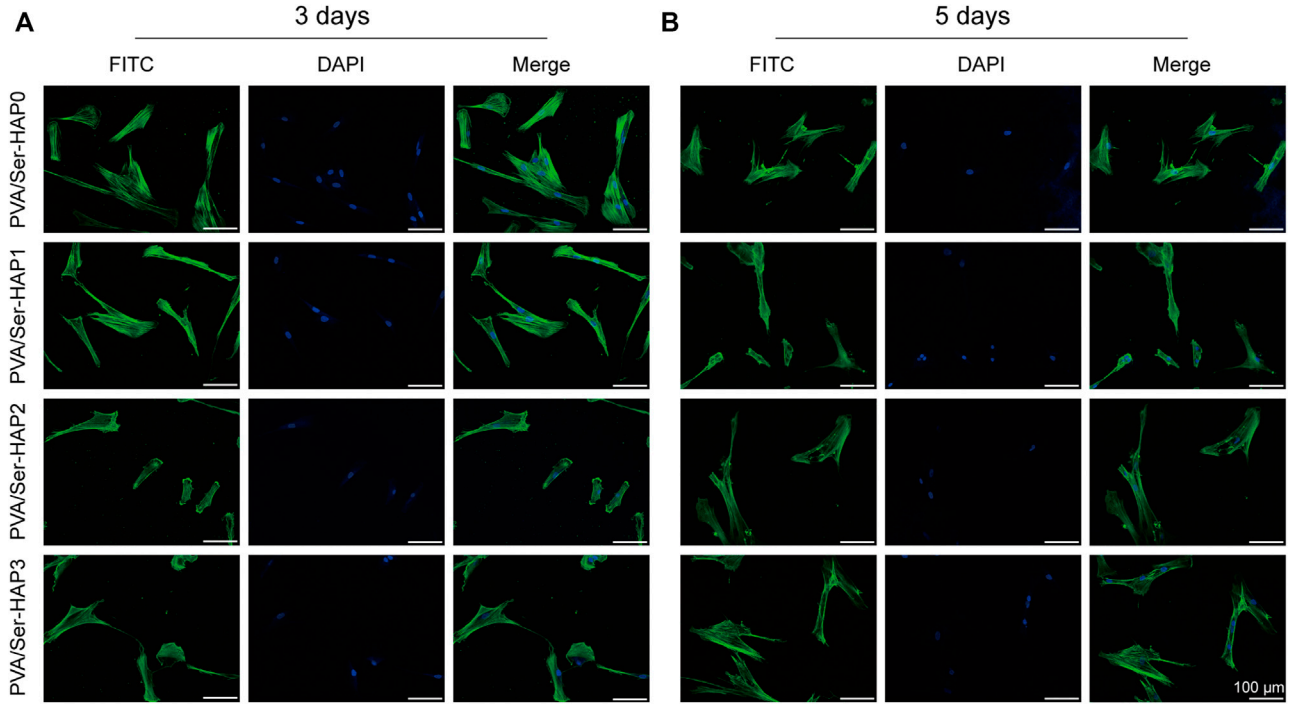

FIGURE 7 | Morphology of hPDLSCs after seeding on PVA/Ser-HAP membranes for 3 days **(A)** and 5 days **(B)**. Green, cytoskeleton stained with phalloidin; Blue, nuclei stained with DAPI.

the CCK-8 assay indicated that Ser-HAP particles did not significantly affect the cell viability of hPDLSCs. Sericin and Ser-HAP were found to have excellent cytocompatibility, which lays the foundations for the application of sericin-based scaffolds in periodontal tissue engineering (He et al., 2017).

Effects of Ser-HAP Particles on the Osteogenic Differentiation of hPDLSCs

HAP, the main artificial substitute for alveolar bone, has the ability to promote the differentiation of stem cells into osteoblasts (Pan et al., 2020). ALP staining was used to detect the osteoinductive effect of different Ser-HAP samples on hPDLSCs. As shown in **Figures 4A,B**, the ALP secreted by hPDLSCs was stained blue. The results show that the expression of ALP in the Ser0-HAP, Ser10-HAP, Ser50-HAP, and Ser100-HAP groups gradually increased on days 3 and 5 (**Figures 4A–D**). All the results indicate that the osteogenic properties of Ser-HAP were improved in comparison to pure HAP (Ser0-HAP group). This observation is attributed to sericin protein promoting the formation of nanoscale HAP particles, which significantly increased the surface area to volume ratio of HAP and thus accelerated the release rates of calcium and phosphorus.

Surface Topography of PVA/Ser-HAP Membranes

Based on the available data, Ser100-HAP particles were selected for preparing PVA/Ser-HAP membranes by mixing with 4% (w/v) polyvinyl alcohol and 1% (w/v) sericin. FESEM images were acquired to reveal the morphology of the PVA/Ser-HAP membranes. **Figure 5A** shows that both the pure PVA/Ser membrane and the PVA/Ser-HAP membrane had rough surfaces, indicating that the introduction of Ser-HAP did not significantly affect the surface morphology of the membrane. Previous studies have shown that rough surfaces are conducive to improving the adhesion and migration of hPDLSCs on composite membranes during periodontal bone repair (Deligianni et al., 2001). In addition, EDS mapping showed that Ca and P were homogenously distributed in the PVA/Ser-HAP3 membrane (**Figure 5B**). And it has been reported that calcium-enriched areas may be the active site of mineralization during bone formation (Huang et al., 2020).

In Vitro Hydrophilicity and Degradation of PVA/Ser-HAP Membranes

The ideal GTR membrane should retain an appropriate amount of water, which allows it to mimic the physiological functions of the original tissue and promote the proliferation and adhesion of cells (Prakash et al., 2019). The swelling kinetics of the PVA/Ser-HAP membranes were therefore explored (**Figure 5C**). All of the membranes swelled rapidly in the few minutes before reaching equilibrium. There was no significant difference in the swelling kinetics of the PVA/Ser-HAP0 and PVA/Ser-HAP1 membranes. During the soaking process of PVA/Ser-HAP membranes, with the release of Ser100-HAP NPs, the pores of the polymer PVA/Ser-HAP membranes were unblocked. Therefore, the swelling performance of PVA/Ser-HAP2 and PVA/Ser-HAP3 changed

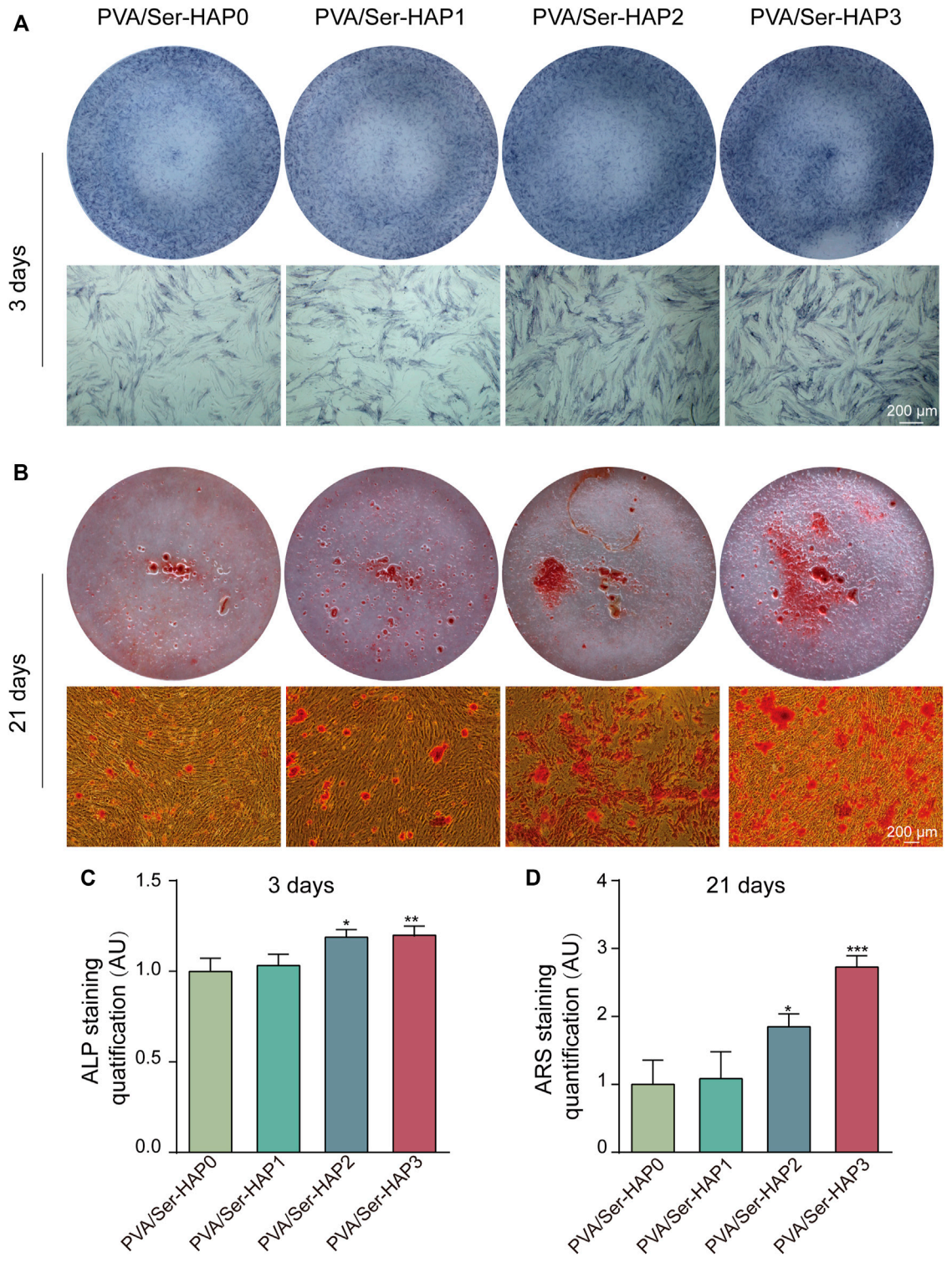

FIGURE 8 | (A) ALP staining of the hPDLSCs following cultured by extracts of PVA/Ser-HAP membranes for 3 days; **(B)** Alizarin red staining of the hPDLSCs after cultured by extracts of the membranes for 21 days; **(C)** Quantitative analysis of ALP staining at 3 days; **(D)** Quantitative analysis of Alizarin red staining at 21 days.

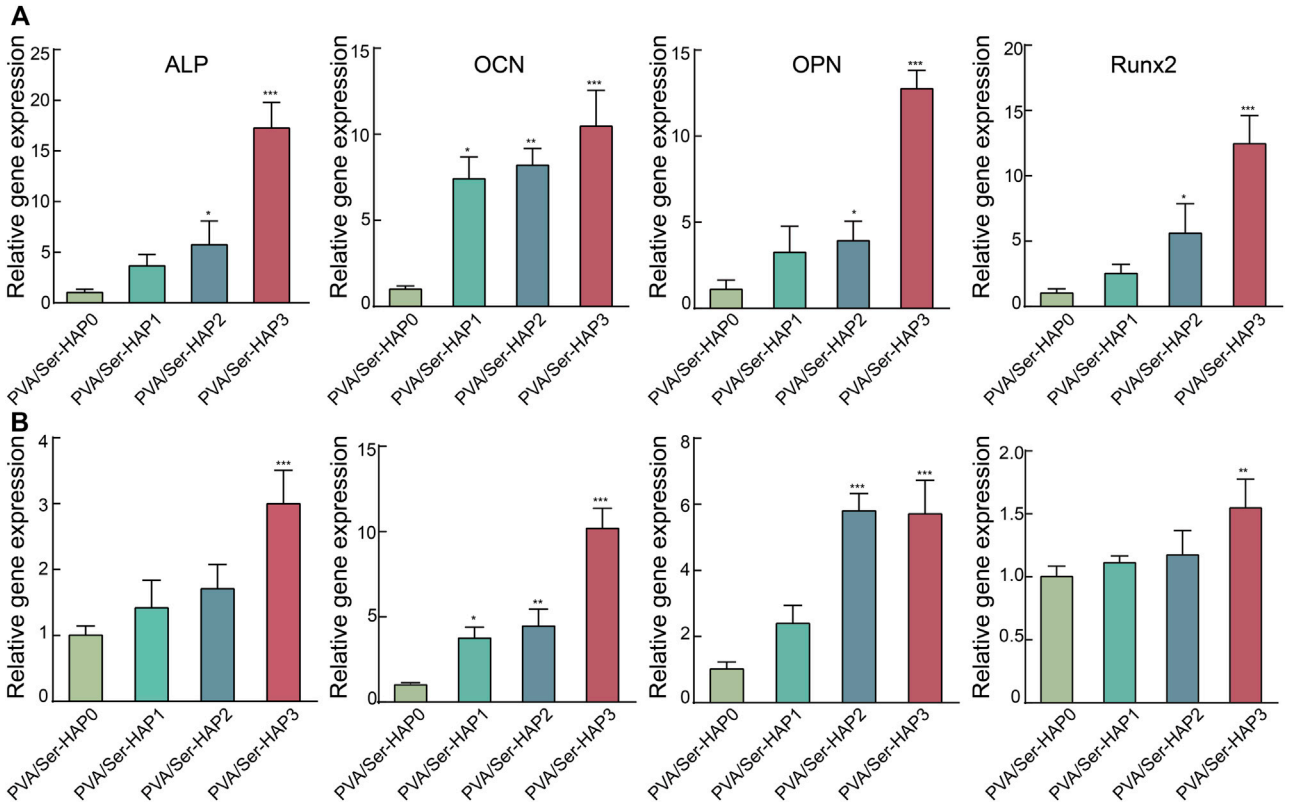

FIGURE 9 | RT-qPCR analysis of the ALP, OCN, OPN, and Runx2 expression of hPDLSCs following cultured by extracts of the PVA/Ser-HAP membranes for 3 days **(A)** and 5 days **(B)**.

slightly with increasing HAP content (Prakash et al., 2019). The complete degradability of the membrane is very important for clinical applications (Liu et al., 2020). The degradation behavior of the PVA/Ser-HAP membranes was measured by weight loss (**Figure 5D**). All membranes showed similar degradation rates during the first 3 weeks, then the weight losses of the membranes reached 33%–42% at 9 weeks. The PVA/Ser-HAP3 membrane shows slightly higher degradation due to the release of more HAP. These results indicate that the PVA/Ser-HAP membranes were appropriately hygroscopic and degradable, which are important properties for their application in periodontal tissue engineering (Catori et al., 2021).

Cytocompatibility of PVA/Ser-HAP Membranes

Biological compatibility is crucial for the application of GTR membranes in periodontal tissue regeneration engineering. The viability of hPDLSCs seeded on PVA/Ser-HAP membranes for 1 or 2 days was investigated using Live/Dead staining. **Figure 6A** shows the morphology of hPDLSCs adhered to various membranes, and indicates good cell vitality. Following the culture of hPDLSCs on the four PVA/Ser-HAP membranes for 2 days, the number of cells increased significantly, indicating that they have excellent biocompatibility (Nitti et al., 2021). In addition, CCK-8 analysis showed no significant difference in the cell viability after culture on the four PVA/Ser-HAP membranes for 1 or 2 days (**Figure 6B**).

Cell Morphology of hPDLSCs on PVA/Ser-HAP Membranes

After 3 or 5 days of culture, the cells were stained for F-actin and nuclei, and then the morphology of the hPDLSCs on the PVA/Ser-HAP membranes was characterized by confocal microscopy (Wu et al., 2021). **Figure 7** shows that the hPDLSCs on the membranes were spindle-shaped, and there was no significant difference in cell morphology between the different groups. Generally, spindle-shaped hPDLSCs with extended pseudopods indicate strong membrane attachment, while round hPDLSCs without pseudopods indicate almost no affinity for the membrane (Huang et al., 2020). These results indicate that the PVA/Ser-HAP membrane has good biocompatibility, and the cells adhered to the membrane surfaces well. These characteristics demonstrate the potential for application of the membranes in periodontal regeneration.

Osteogenic Differentiation of hPDLSCs Cultured With PVA/Ser-HAP Membranes

ALP staining, ARS, and RT-qPCR were used to analyze the osteogenic differentiation of hPDLSCs seeded on the four

membranes. Following 3 days of treatment, the expression of ALP in the PVA/Ser-HAP2 and PVA/Ser-HAP3 groups was significantly up-regulate compared with that of the PVA/Ser-HAP0 group (**Figures 8A,C**). These findings indicate that the PVA/Ser-HAP membranes markedly promoted the early osteogenic differentiation of hPDLSCs. As a late marker of the mineralization stage, ARS staining is used to study the production of calcium nodules (Zhu et al., 2020). As shown in **Figures 8B,D**, after co-cultured with hPDLSCs for 21 days, the PVA/Ser-HAP3 group showed the most apparent calcium mineral nodules, while the PVA/Ser-HAP0 group showed fewer calcium mineral nodules. These findings indicate that PVA/Ser-HAP membranes effectively promote the late osteogenic differentiation of hPDLSCs.

HAP has outstanding osteoconductive properties (Deligianni et al., 2001; Maleki-Ghaleh et al., 2021). A previous study reported that HAP promoted osteogenic differentiation of BMSCs through upregulation of ALP, OPN, and OCN (Yang et al., 2014). In addition, Runx2, a vital transcription factor for osteogenic differentiation, is closely related to the p38 MAPK pathway and can be triggered by HAP during osteoblast differentiation (Hiragami et al., 2005). To further verify the osteoinductivity of the PVA/Ser-HAP membranes, the expression of osteogenic genes by hPDLSCs cultured on the membranes was determined. **Figure 9** shows that the expression of osteogenic genes, including Runx2, ALP, OPN, and OCN, were significantly upregulated on the PVA/Ser-HAP3 membrane at 3 and 5 days, compared with on the PVA/Ser-HAP0 membrane ($p < 0.01$). The results indicate that the PVA/Ser-HAP membrane induces the expression of osteogenic proteins and genes and has the potential to induce the repair of alveolar bone defects.

CONCLUSION

We successfully synthesized Ser-HAP nanoparticles using sericin as an organic template. The sericin concentration and mineralization time were found to affect the nucleation of HAP. Ser-HAP nanoparticles exhibited excellent biocompatibility and promoted osteogenic differentiation of hPDLSCs. The Ser100-HAP nanoparticles were subsequently combined with PVA, and biomimetic PVA/Ser-HAP membranes were prepared by repeated freezing and thawing. Further studies showed that PVA/Ser-HAP membranes did not affect the viability of hPDLSCs. Most importantly, ALP staining, ARS, and RT-qPCR detection showed that PVA/Ser-HAP membranes promoted osteogenic differentiation of hPDLSCs. These findings suggest that PVA/Ser-HAP membranes have excellent potential for application in periodontal regeneration and repair therapy.

DATA AVAILABILITY STATEMENT

The original contributions presented in the study are included in the article/Supplementary Material, further inquiries can be directed to the corresponding authors.

ETHICS STATEMENT

The studies involving human participants were reviewed and approved by the Ethics committee of Southwest Medical University. The patients/participants provided their written informed consent to participate in this study.

AUTHOR CONTRIBUTIONS

PM: conceptualization, formal analysis, methodology, and writing-original draft. PR: methodology and investigation resources. TW, JY, SL, and BY: methodology and investigation. JX: formal analysis, writing-review and editing, funding acquisition. GT: conceptualization, formal analysis, writing-original draft, writing-review and editing and funding acquisition.

FUNDING

This work was funded by the National Natural Science Foundation of China (81870746), Open Project of the State Key Laboratory of Oral Disease Research (SKLOD2021OF08), Luzhou Science and Technology Program (2020-JYJ-39, 2021-RCM-114), Scientific Research Foundation of Southwest Medical University (2020ZRZD011), Key Program of Southwest Medical University (2021ZKZD009), Project of Stomatological Institute of Southwest Medical University (2021XJYJS01), and Joint project of Luzhou Municipal People's Government and Southwest Medical University (2020LZXNYDZ09). Scientific Research Foundation of the Affiliated Stomatological Hospital of Southwest Medical University (2020QY02, 202007).

REFERENCES

Aral, K., Milward, M. R., Kapila, Y., Berdeli, A., and Cooper, P. R. (2020). Inflammasomes and Their Regulation in Periodontal Disease: A Review. *J. Periodont Res.* 55 (4), 473–487. doi:10.1111/jre.12733

Bal, Z., Korkusuz, F., Ishiguro, H., Okada, R., Kushioka, J., Chijimatsu, R., et al. (2021). A Novel Nano-Hydroxyapatite/synthetic Polymer/bone Morphogenetic Protein-2 Composite for Efficient Bone Regeneration. *Spine J.* 21 (5), 865–873. doi:10.1016/j.spinee.2021.01.019

Cai, Y., Mei, D., Jiang, T., and Yao, J. (2010). Synthesis of Oriented Hydroxyapatite Crystals: Effect of Reaction Conditions in the Presence or Absence of Silk Sericin. *Mater. Lett.* 64 (24), 2676–2678. doi:10.1016/j.matlet.2010.08.071

Catori, D. M., Fragal, E. H., Messias, I., Garcia, F. P., Nakamura, C. V., and Rubira, A. F. (2021). Development of Composite Hydrogel Based on Hydroxyapatite Mineralization over Pectin Reinforced with Cellulose Nanocrystal. *Int. J. Biol. Macromol.* 167, 726–735. doi:10.1016/j.ijbiomac.2020.12.012

Chen, X., Liu, Y., Yang, J., Wu, W., Miao, L., Yu, Y., et al. (2016). The Synthesis of Hydroxyapatite with Different Crystallinities by Controlling the Concentration of Recombinant CEMP1 for Biological Application. *Mater. Sci. Eng. C* 59, 384–389. doi:10.1016/j.msec.2015.10.029

D'Elía, N. L., Rial Silva, R., Sartuqui, J., Ercoli, D., Ruso, J., Messina, P., et al. (2020). Development and Characterisation of Bilayered Periosteum-Inspired Composite Membranes Based on Sodium Alginate-Hydroxyapatite Nanoparticles. *J. Colloid Interface Sci.* 572, 408–420. doi:10.1016/j.jcis.2020.03.086

Deligianni, D. D., Katsala, N. D., Koutsoukos, P. G., and Missirlis, Y. F. (2001). Effect of Surface Roughness of Hydroxyapatite on Human Bone Marrow Cell Adhesion, Proliferation, Differentiation and Detachment Strength. *Biomaterials* 22 (1), 87–96. doi:10.1016/s0142-9612(00)00174-5

Fihri, A., Len, C., Varma, R. S., and Solhy, A. (2017). Hydroxyapatite: A Review of Syntheses, Structure and Applications in Heterogeneous Catalysis. *Coord. Chem. Rev.* 347, 48–76. doi:10.1016/j.ccr.2017.06.009

Gao, X., Song, J., Ji, P., Zhang, X., Li, X., Xu, X., et al. (2016). Polydopamine-templated Hydroxyapatite Reinforced Polycaprolactone Composite Nanofibers with Enhanced Cytocompatibility and Osteogenesis for Bone Tissue Engineering. *ACS Appl. Mat. Interfaces* 8 (5), 3499–3515. doi:10.1021/acsami.5b12413

He, H., Tao, G., Wang, Y., Cai, R., Guo, P., Chen, L., et al. (2017). *In Situ* green Synthesis and Characterization of Sericin-Silver Nanoparticle Composite with Effective Antibacterial Activity and Good Biocompatibility. *Mater. Sci. Eng. C* 80, 509–516. doi:10.1016/j.msec.2017.06.015

Hiragami, F., Akiyama, J., Koike, Y., and Kano, Y. (2005). Enhancement of Hydroxyapatite-Mediated Three-dimensional-like Proliferation of Mouse Fibroblasts by Heat Treatment: Effects of Heat Shock-Induced P38 MAPK Pathway. *J. Biomed. Mat. Res.* 74A (4), 705–711. doi:10.1002/jbm.a.30362

Huang, Y.-z., Ji, Y.-r., Kang, Z.-w., Li, F., Ge, S.-f., Yang, D.-P., et al. (2020). Integrating Eggshell-Derived CaCO3/MgO Nanocomposites and Chitosan into a Biomimetic Scaffold for Bone Regeneration. *Chem. Eng. J.* 395, 125098. doi:10.1016/j.cej.2020.125098

Kundu, S. C., Dash, B. C., Dash, R., and Kaplan, D. L. (2008). Natural Protective Glue Protein, Sericin Bioengineered by Silkworms: Potential for Biomedical and Biotechnological Applications. *Prog. Polym. Sci.* 33 (10), 998–1012. doi:10.1016/j.progpolymsci.2008.08.002

Lamboni, L., Gauthier, M., Yang, G., and Wang, Q. (2015). Silk Sericin: A Versatile Material for Tissue Engineering and Drug Delivery. *Biotechnol. Adv.* 33 (8), 1855–1867. doi:10.1016/j.biotechadv.2015.10.014

Li, J., Wang, Z., Huang, X., Wang, Z., Chen, Z., Wang, R., et al. (2021). Dynamic Proteomic Profiling of Human Periodontal Ligament Stem Cells during Osteogenic Differentiation. *Stem Cell Res. Ther.* 12 (1), 98. doi:10.1186/s13287-020-02123-6

Li, M., Feng, C., Gu, X., He, Q., and Wei, F. (2017). Effect of Cryopreservation on Proliferation and Differentiation of Periodontal Ligament Stem Cell Sheets. *Stem Cell Res. Ther.* 8 (1), 77. doi:10.1186/s13287-017-0530-5

Li, Y., Gao, S., Shi, S., Xiao, D., Peng, S., Gao, Y., et al. (2021). Tetrahedral Framework Nucleic Acid-Based Delivery of Resveratrol Alleviates Insulin Resistance: from Innate to Adaptive Immunity. *Nano-Micro Lett.* 13 (1), 86. doi:10.1007/s40820-021-00614-6

Liao, J., Tian, T., Shi, S., Xie, X., Peng, S., Zhu, Y., et al. (2021). Broadening the Biocompatibility of Gold Nanorods from Rat to *Macaca fascicularis*: Advancing Clinical Potential. *J. Nanobiotechnol* 19 (1), 195. doi:10.1186/s12951-021-00941-1

Liu, J., Dai, Q., Weir, M. D., Schneider, A., Zhang, C., Hack, G. D., et al. (2020). Biocompatible Nanocomposite Enhanced Osteogenic and Cementogenic Differentiation of Periodontal Ligament Stem Cells *In Vitro* for Periodontal Regeneration. *Materials* 13 (21), 4951. doi:10.3390/ma13214951

Liu, J., Liu, Y., Kong, Y., Yao, J., and Cai, Y. (2013). Formation of Vaterite Regulated by Silk Sericin and its Transformation towards Hydroxyapatite Microsphere. *Mater. Lett.* 110, 221–224. doi:10.1016/j.matlet.2013.08.021

Liu, X., He, X., Jin, D., Wu, S., Wang, H., Yin, M., et al. (2020). A Biodegradable Multifunctional Nanofibrous Membrane for Periodontal Tissue Regeneration. *Acta Biomater.* 108, 207–222. doi:10.1016/j.actbio.2020.03.044

Maleki-Ghaleh, H., Hossein Siadati, M., Fallah, A., Zarrabi, A., Afghah, F., Koc, B., et al. (2021). Effect of Zinc-Doped Hydroxyapatite/graphene Nanocomposite on the Physicochemical Properties and Osteogenesis Differentiation of 3D-Printed Polycaprolactone Scaffolds for Bone Tissue Engineering. *Chem. Eng. J.* 426, 131321. doi:10.1016/j.cej.2021.131321

Martínez-Mora, C., Mrowiec, A., García-Vizcaíno, E. M., Alcaraz, A., Cenis, J. L., and Nicolás, F. J. (2012). Fibroin and Sericin from *Bombyx mori* Silk Stimulate Cell Migration through Upregulation and Phosphorylation of C-Jun. *Plos One* 7 (7), e42271. doi:10.1371/journal.pone.0042271

Nayak, S., Dey, T., Naskar, D., and Kundu, S. C. (2013). The Promotion of Osseointegration of Titanium Surfaces by Coating with Silk Protein Sericin. *Biomaterials* 34 (12), 2855–2864. doi:10.1016/j.biomaterials.2013.01.019

Nguyen, H.-L., Tran, T. H., Hao, L. T., Jeon, H., Koo, J. M., Shin, G., et al. (2021). Biorenewable, Transparent, and Oxygen/moisture Barrier Nanocellulose/nanochitin-Based Coating on Polypropylene for Food Packaging Applications. *Carbohydr. Polym.* 271, 118421. doi:10.1016/j.carbpol.2021.118421

Nitti, P., Kunjalukkal Padmanabhan, S., Cortazzi, S., Stanca, E., Siculella, L., Licciulli, A., et al. (2021). Enhancing Bioactivity of Hydroxyapatite Scaffolds Using Fibrous Type I Collagen. *Front. Bioeng. Biotechnol.* 9, 631177. doi:10.3389/fbioe.2021.631177

Orlandi, M., Muñoz Aguilera, E., Marletta, D., Petrie, A., Suvan, J., and D'Aiuto, F. (2021). Impact of the Treatment of Periodontitis on Systemic Health and Quality of Life: A Systematic Review. *J. Clin. Periodontol.*, 585–596. doi:10.1111/jcpe.13554

Pan, Y., Li, P., Liang, F., Zhang, J., Yuan, J., and Yin, M. (2021). A Nano-Silver Loaded PVA/keratin Hydrogel with Strong Mechanical Properties Provides Excellent Antibacterial Effect for Delayed Sternal Closure. *Front. Bioeng. Biotechnol.* 9, 733980. doi:10.3389/fbioe.2021.733980

Pan, Y., Zhao, Y., Kuang, R., Liu, H., Sun, D., Mao, T., et al. (2020). Injectable Hydrogel-Loaded Nano-Hydroxyapatite that Improves Bone Regeneration and Alveolar Ridge Promotion. *Mater. Sci. Eng. CC* 116, 111158. doi:10.1016/j.msec.2020.111158

Peng, S., Shi, S., Tao, G., Li, Y., Xiao, D., Wang, L., et al. (2021). JKAMP Inhibits the Osteogenic Capacity of Adipose-Derived Stem Cells in Diabetic Osteoporosis by Modulating the Wnt Signaling Pathway through Intragenic DNA Methylation. *Stem Cell Res. Ther.* 121, 1–15. doi:10.1186/s13287-021-02163-6

Prakash, J., Kumar, T. S., Venkataprasanna, K. S., Niranjan, R., Kaushik, M., Samal, D. B., et al. (2019). PVA/alginate/hydroxyapatite Films for Controlled Release of Amoxicillin for the Treatment of Periodontal Defects. *Appl. Surf. Sci.* 495, 143543. doi:10.1016/j.apsusc.2019.143543

Prakash, J., Prema, D., Venkataprasanna, K. S., Balagangadharan, K., Selvamurugan, N., and Venkatasubbu, G. D. (2020). Nanocomposite Chitosan Film Containing Graphene Oxide/hydroxyapatite/gold for Bone Tissue Engineering. *Int. J. Biol. Macromol.* 154, 62–71. doi:10.1016/j.ijbiomac.2020.03.095

Qi, C., Deng, Y., Xu, L., Yang, C., Zhu, Y., Wang, G., et al. (2020). A Sericin/Graphene Oxide Composite Scaffold as a Biomimetic Extracellular Matrix for Structural and Functional Repair of Calvarial Bone. *Theranostics* 10 (2), 741–756. doi:10.7150/thno.39502

Radha, G., Venkatesan, B., Vellaichamy, E., and Balakumar, S. (2018). Structural, Mechanical and Biological Insights on Reduced Graphene Nanosheets Reinforced Sonochemically Processed Nano-Hydroxyapatite Ceramics. *Ceram. Int.* 44 (8), 8777–8787. doi:10.1016/j.ceramint.2018.02.021

Raina, D. B., Matuszewski, L.-M., Vater, C., Bolte, J., Isaksson, H., Lidgren, L., et al. (2020). A Facile One-Stage Treatment of Critical Bone Defects Using a Calcium Sulfate/hydroxyapatite Biomaterial Providing Spatiotemporal Delivery of Bone Morphogenic Protein-2 and Zoledronic Acid. *Sci. Adv.* 6 (48), eabc1779. doi:10.1126/sciadv.abc1779

Rao, P., Lou, F., Luo, D., Huang, C., Huang, K., Yao, Z., et al. (2021). Decreased Autophagy Impairs Osteogenic Differentiation of Adipose-Derived Stem Cells via Notch Signaling in Diabetic Osteoporosis Mice. *Cell. Signal.* 87, 110138. doi:10.1016/j.cellsig.2021.110138

Takeuchi, A., Ohtsuki, C., Miyazaki, T., Kamitakahara, M., Ogata, S.-i., Yamazaki, M., et al. (2005). Heterogeneous Nucleation of Hydroxyapatite on Protein: Structural Effect of Silk Sericin. *J. R. Soc. Interface.* 2 (4), 373–378. doi:10.1098/rsif.2005.0052

Tao, G., Cai, R., Wang, Y., Liu, L., Zuo, H., Zhao, P., et al. (2019). Bioinspired Design of AgNPs Embedded Silk Sericin-Based Sponges for Efficiently

Combating Bacteria and Promoting Wound Healing. *Mater. Des.* 180, 107940. doi:10.1016/j.matdes.2019.107940

Tao, G., Cai, R., Wang, Y., Zuo, H., and He, H. (2021). Fabrication of Antibacterial Sericin Based Hydrogel as an Injectable and Mouldable Wound Dressing. *Mater. Sci. Eng. C* 119, 111597. doi:10.1016/j.msec.2020.111597

Tedeschi, G., Guzman-Puyol, S., Ceseracciu, L., Benitez, J. J., Goldoni, L., Koschella, A., et al. (2021). Waterproof-breathable Films from Multi-Branched Fluorinated Cellulose Esters. *Carbohydr. Polym.* 271, 118031. doi:10.1016/j.carbpol.2021.118031

Teotia, A. K., Raina, D. B., Singh, C., Sinha, N., Isaksson, H., Tägil, M., et al. (2017). Nano-hydroxyapatite Bone Substitute Functionalized with Bone Active Molecules for Enhanced Cranial Bone Regeneration. *ACS Appl. Mat. Interfaces* 9 (8), 6816–6828. doi:10.1021/acsami.6b14782

Thangprasert, A., Tansakul, C., Thuaksubun, N., and Meesane, J. (2019). Mimicked Hybrid Hydrogel Based on Gelatin/PVA for Tissue Engineering in Subchondral Bone Interface for Osteoarthritis Surgery. *Mater. Des.* 183, 108113. doi:10.1016/j.matdes.2019.108113

Veiga, A., Castro, F., Reis, C. C., Sousa, A., Oliveira, A. L., and Rocha, F. (2020). Hydroxyapatite/sericin Composites: A Simple Synthesis Route under Near-Physiological Conditions of Temperature and pH and Preliminary Study of the Effect of Sericin on the Biomineralization Process. *Mater. Sci. Eng. C* 108, 110400. doi:10.1016/j.msec.2019.110400

Wang, F., Cao, B., and Mao, C. (2010). Bacteriophage Bundles with Prealigned Ca2+ Initiate the Oriented Nucleation and Growth of Hydroxylapatite. *Chem. Mat.* 22 (12), 3630–3636. doi:10.1021/cm902727s

Wang, Z., Wang, J., Jin, Y., Luo, Z., Yang, W., Xie, H., et al. (2015). A Neuroprotective Sericin Hydrogel as an Effective Neuronal Cell Carrier for the Repair of Ischemic Stroke. *ACS Appl. Mat. Interfaces* 7 (44), 24629–24640. doi:10.1021/acsami.5b06804

Woo, H. N., Cho, Y. J., Tarafder, S., and Lee, C. H. (2021). The Recent Advances in Scaffolds for Integrated Periodontal Regeneration. *Bioact. Mater.* 6 (10), 3328–3342. doi:10.1016/j.bioactmat.2021.03.012

Wu, C., Egawa, S., Kanno, T., Kurita, H., Wang, Z., Iida, E., et al. (2021). Nanocellulose Reinforced Silkworm Silk Fibers for Application to Biodegradable Polymers. *Mater. Des.* 202, 109537. doi:10.1016/j.matdes.2021.109537

Wu, T., Huang, L., Sun, J., Sun, J., Yan, Q., Duan, B., et al. (2021). Multifunctional Chitin-Based Barrier Membrane with Antibacterial and Osteogenic Activities for the Treatment of Periodontal Disease. *Carbohydr. Polym.* 269, 118276. doi:10.1016/j.carbpol.2021.118276

Wu, T., Yao, Z., Tao, G., Lou, F., Tang, H., Gao, Y., et al. (2021). Role of Fzd6 in Regulating the Osteogenic Differentiation of Adipose-Derived Stem Cells in Osteoporotic Mice. *Stem Cell Rev Rep* 17 (5), 1889–1904. doi:10.1007/s12015-021-10182-2

Xia, P., Zhang, K., Yan, S., Li, G., and Yin, J. (2021). Biomimetic, Biodegradable, and Osteoinductive Microgels with Open Porous Structure and Excellent Injectability for Construction of Microtissues for Bone Tissue Engineering. *Chem. Eng. J.* 414, 128714. doi:10.1016/j.cej.2021.128714

Xing, F., Chi, Z., Yang, R., Xu, D., Cui, J., Huang, Y., et al. (2021). Chitin-hydroxyapatite-collagen Composite Scaffolds for Bone Regeneration. *Int. J. Biol. Macromol.* 184, 170–180. doi:10.1016/j.ijbiomac.2021.05.019

Yang, M., Shuai, Y., Zhang, C., Chen, Y., Zhu, L., Mao, C., et al. (2014). Biomimetic Nucleation of Hydroxyapatite Crystals Mediated by *Antheraea pernyi* Silk Sericin Promotes Osteogenic Differentiation of Human Bone Marrow Derived Mesenchymal Stem Cells. *Biomacromolecules* 15 (4), 1185–1193. doi:10.1021/bm401740x

Yu, X., Shen, G., Shang, Q., Zhang, Z., Zhao, W., Zhang, P., et al. (2021). A Naringin-Loaded Gelatin-Microsphere/nano-Hydroxyapatite/silk Fibroin Composite Scaffold Promoted Healing of Critical-Size Vertebral Defects in Ovariectomised Rat. *Int. J. Biol. Macromol.* 193, 510–518. doi:10.1016/j.ijbiomac.2021.10.036

Zhang, Q., Ma, L., Zheng, S., Wang, Y., Feng, M., Shuai, Y., et al. (2019). Air-plasma Treatment Promotes Bone-like Nano-Hydroxylapatite Formation on Protein Films for Enhanced *In Vivo* Osteogenesis. *Biomater. Sci.* 7 (6), 2326–2334. doi:10.1039/c9bm00020h

Zhang, Y., Xie, X., Ma, W., Zhan, Y., Mao, C., Shao, X., et al. (2020). Multi-targeted Antisense Oligonucleotide Delivery by a Framework Nucleic Acid for Inhibiting Biofilm Formation and Virulence. *Nano-Micro Lett.* 121, 1–16. doi:10.1007/s40820-020-0409-3

Zhao, R., Li, X., Sun, B., Zhang, Y., Zhang, D., Tang, Z., et al. (2014). Electrospun Chitosan/sericin Composite Nanofibers with Antibacterial Property as Potential Wound Dressings. *Int. J. Biol. Macromol.* 68, 92–97. doi:10.1016/j.ijbiomac.2014.04.029

Zhao, Z., Liu, J., Schneider, A., Gao, X., Ren, K., Weir, M. D., et al. (2019). Human Periodontal Ligament Stem Cell Seeding on Calcium Phosphate Cement Scaffold Delivering Metformin for Bone Tissue Engineering. *J. Dent.* 91, 103220. doi:10.1016/j.jdent.2019.103220

Zheng, D. X., Kang, X. N., Wang, Y. X., Huang, Y. N., Pang, C. F., Chen, Y. X., et al. (2021). Periodontal Disease and Emotional Disorders: A Meta-analysis. *J. Clin. Periodontol.* 48 (2), 180–204. doi:10.1111/jcpe.13395

Zheng, J., Wu, F., Li, H., and Liu, M. (2019). Preparation of Bioactive Hydroxyapatite@halloysite and its Effect on MC3T3-E1 Osteogenic Differentiation of Chitosan Film. *Mater. Sci. Eng. CC* 105, 110072. doi:10.1016/j.msec.2019.110072

Zhou, T., Chen, S., Ding, X., Hu, Z., Cen, L., and Zhang, X. (2021). Fabrication and Characterization of Collagen/PVA Dual-Layer Membranes for Periodontal Bone Regeneration. *Front. Bioeng. Biotechnol.* 9, 630977. doi:10.3389/fbioe.2021.630977

Zhu, L., Chen, S., Liu, K., Wen, W., Lu, L., Ding, S., et al. (2020). 3D Poly (L-Lactide)/chitosan Micro/nano Fibrous Scaffolds Functionalized with Quercetin-Polydopamine for Enhanced Osteogenic and Anti-inflammatory Activities. *Chem. Eng. J.* 391, 123524. doi:10.1016/j.cej.2019.123524

Zhu, S., Zhang, X., Chen, X., Wang, Y., Li, S., Qiu, G., et al. (2021). Nano-hydroxyapatite Scaffold Based on Recombinant Human Bone Morphogenetic Protein 2 and its Application in Bone Defect Repair. *J. Biomed. Nanotechnol.* 17 (7), 1330–1338. doi:10.1166/jbn.2021.3110

Zhu, W., and Liang, M. (2015). Periodontal Ligament Stem Cells: Current Status, Concerns, and Future Prospects. *Stem Cells Int.* 2015, 1–11. doi:10.1155/2015/972313

Conflict of Interest: The authors declare that the research was conducted in the absence of any commercial or financial relationships that could be construed as a potential conflict of interest.

Publisher's Note: All claims expressed in this article are solely those of the authors and do not necessarily represent those of their affiliated organizations, or those of the publisher, the editors and the reviewers. Any product that may be evaluated in this article, or claim that may be made by its manufacturer, is not guaranteed or endorsed by the publisher.

Copyright © 2022 Ming, Rao, Wu, Yang, Lu, Yang, Xiao and Tao. This is an open-access article distributed under the terms of the Creative Commons Attribution License (CC BY). The use, distribution or reproduction in other forums is permitted, provided the original author(s) and the copyright owner(s) are credited and that the original publication in this journal is cited, in accordance with accepted academic practice. No use, distribution or reproduction is permitted which does not comply with these terms.

frontiers | Frontiers in Bioengineering and Biotechnology

ORIGINAL RESEARCH
published: 08 June 2022
doi: 10.3389/fbioe.2022.933135

Quercetin-Coating Promotes Osteogenic Differentiation, Osseointegration and Anti-Inflammatory Properties of Nano-Topographic Modificated 3D-Printed Ti6Al4V Implant

Nian Liu[1†], Hui Wang[1†], Zeyu Fu[2], Chuxi Zhang[1], Wenyu Hui[1], Jinyang Wu[1], Yong Zhang[1]* and Shilei Zhang[1]*

[1]Department of Oral and Cranio-Maxillofacial Surgery, Shanghai Ninth People's Hospital, College of Stomatology, Shanghai Jiao Tong University School of Medicine, National Clinical Research Center for Oral Diseases, Shanghai Key Laboratory of Stomatology and Shanghai Research Institute of Stomatology, Shanghai, China, [2]School of Materials and Chemistry, University of Shanghai for Science and Technology, Shanghai, China

The capabilities of osseointegration and anti-inflammatory properties are of equal significance to the bio-inert titanium implant surface. Quercetin has proved its capacities of activating anti-inflammation through macrophage modulation and promoting osteogenic differentiation. Herein, we fabricated quercetin-coating on nano-topographic modificated 3D-printed Ti6Al4V implant surface. Subsequently the biological cells responses *in vitro*, anti-inflammatory and osseointegration performance *in vivo* were evaluated. *In vitro* studies indicated that quercetin-coating can enhance the adhesion and osteogenic differentiation of rBMSCs, while modulating the polarization of macrophages from M1 to M2 phase and improving the anti-inflammatory and vascular gene expression. Moreover, quercetin-loaded implants reduced the level of peri-implant inflammation and ameliorated new bone formation and rapid osseoinegration *in vivo*. Quercetin-coating might provide a feasible and favorable scheme for endowing 3D-printed titanium alloy implant surface with enhanced the rapid osseointegration and anti-inflammatory properties.

Keywords: quercetin, three-dimensional printing, titanium alloy, micro-nano-topography, rapid osseointegration, macrophage polarization, anti-inflammation

OPEN ACCESS

Edited by:
Gang Wu,
VU Amsterdam, Netherlands

Reviewed by:
Zhihong Dong,
Chengdu University, China
Dejian Li,
Fudan University Pudong Medical Center, China

***Correspondence:**
Jinyang Wu
wujinyang7029@foxmail.com
Yong Zhang
zhangyong1362@163.com
Shilei Zhang
leinnymd@hotmail.com

[†]These authors have contributed equally to this work

Specialty section:
This article was submitted to Biomaterials, a section of the journal Frontiers in Bioengineering and Biotechnology

Received: *30 April 2022*
Accepted: *19 May 2022*
Published: *08 June 2022*

Citation:
Liu N, Wang H, Fu Z, Zhang C, Hui W, Wu J, Zhang Y and Zhang S (2022) Quercetin-Coating Promotes Osteogenic Differentiation, Osseointegration and Anti-Inflammatory Properties of Nano-Topographic Modificated 3D-Printed Ti6Al4V Implant. Front. Bioeng. Biotechnol. 10:933135. doi: 10.3389/fbioe.2022.933135

1 INTRODUCTION

Restoring large bone defects caused by tumor, trauma and osteoporosis is undoubtedly a great challenge, especially in load-bearing areas such as jaws and limbs (Hassan et al., 2019). The clinical use of autogenous bone grafts, as the current gold standard treatment, is limited due to the lack of donor site availability. Three-dimensional (3D) printed bone substitutes have been applied to produce almost all kinds of biomaterials in clinical practice (Bose et al., 2018), exhibiting multiple advantages like design flexibility and higher efficiency.

Titanium and its alloys are widely used in clinic because of their superior in mechanical properties and biocompatibility. Moreover, the extensibility of metal can realize the personalized and precise restoration through 3D printing. Yet the biological inertia of titanium alloys leads to unsatisfying

long-term implant survival, for the nonbiological Ti implants may induce a soft foreign body response that results in fibrous tissue formation (Goodman et al., 2013), infections and bone resorption in the implanted area (Civantos et al., 2017), thus hindering its potential clinical application.

The surface properties of implant materials, such as surface morphology and chemical composition, can directly impact the biological effects of cell adhesion, proliferation, differentiation, and ultimately affect the quality of osseointegration between implant and host bone (Chen et al., 2016). Current major strategies of titanium surface modification include physical modification, chemical modification and biochemical modification. With the advance of biochemical surface modification, bioactive agents such as protein, peptide, growth factor and drugs have been tentatively applied to implant surfaces, endowing the materials with multiple functions such as osteoinduction, osteoconduction and anti-inflammation.

Host's inflammatory response to the implantation is inevitable, which is an essential process of tissue regeneration. Implant osseointegration originates from the inflammatory driving process on and near the implant surface (Zhao et al., 2012). Before osteogenesis and angiogenesis, the initial inflammatory response of immune cells [macrophages (m Φ)/ monocytes] to the surface of the material determines the fate of the implant. Macrophages are plastic and dynamic that can polarize to classically activated inflammatory phenotype (M1) or alternatively activated inflammatory macrophages (M2) when stimulated by different signals (Kang et al., 2017). Characteristic M1 pro-inflammatory profile exerts a strong cytotoxic activity through production of nitric reactive species (inducible nitric oxide synthase, iNOS), apart from a Th1 pro-inflammatory response [interleukin-1β (IL-1β), IL-6] (Van den Bossche et al., 2017). Macrophages with this phenotype are beneficial for pathogens/tumour elimination but detrimental for the wound healing process (Zhang and Mosser, 2008). On the other hand, M2 anti-inflammatory profile, with mannose receptor (CD206) as typical surface markers, contributes to inflammation resolution and wound healing by producing anti-inflammatory cytokines such as IL-10 and angiogenesis mediators such as transforming growth factor-β (TGF-β) and vascular endothelial growth factor (VEGF) (Funes et al., 2018). M1 and M2 macrophages can transform into each other under external stimulation, and the transformation from M1 to M2 is the turning point from inflammation stage to repair stage (Landén et al., 2016). This functional plasticity of macrophages is the premise that the implant surface can play an immunomodulatory role. The physical and chemical properties of implant surface can affect the polarization of macrophages, and then affect the direction, degree and scope of the inflammatory process. Therefore, the design of implant materials should actively regulate the process of the inflammatory reaction rather than avoiding it, so as to make it turn to the direction conductive to tissue regeneration.

Recent reports threw light on the field that nano-structured surface can regulate the function of inflammatory response related cells, especially the function of macrophages by modulating the polarization between M1 and M2 phenotypes of macrophages and the secretion of cytokines (Vishwakarma et al., 2016). In addition to the change of implant surface structure, the introduction of various bioactive molecules (e.g., functional elements, growth/differentiation cytokines and small molecule drugs) loaded on the biomaterial surfaces can harness macrophage polarization to generate an osteogenic immune microenvironment, so as to regulate the direction, scope and degree of inflammation, which is ultimately beneficial to bone tissue regeneration (Chen et al., 2017; Dong et al., 2017). Surface modification with dual functions of enhancing osteogenesis and regulating macrophage polarization may be a promising solution to the bio-inertia of titanium alloy implants.

Quercetin is a flavonoid monomer compound of small polyphenolic molecules which widely exists in natural plants. It has many pharmacological effects such as anti-inflammation, anti-oxidation, anti-tumor, hypoglycemic and hypolipidemic (Russo et al., 2012). Recent reports illustrated that introducing quercetin onto nano-octahedral ceria could modulate the phenotypic switch of macrophages by not only inhibition of M1 polarization but also promotion of M2 polarization in periodontal disease (Wang Y et al., 2021). Meanwhile, numerous reports have confirmed its impacts on osteogenesis. Quercetin stimulated ALP activity of mesenchymal stem cells (MSCs) in a dose-dependent manner and up-regulated the expressions of ontogenetic marker proteins BGP and COL-1 besides the stimulation of MAPK/ERK signal pathway (Li et al., 2015). Quercetin could also promote OVX rBMSCs proliferation, osteogenic differentiation and angiogenic factor expression while rebuilding the balance of the RANKL/OPG system in a dose-dependent manner (Zhou et al., 2017). To sum up, quercetin might constitute an appropriate candidate as the loaded drug of titanium alloy implants to regulate macrophages polarization and enhance the osteogenesis at the same time.

However, in the deficiency of active functional groups on titanium surface, how to realize the effective loading of quercetin is an urgent problem to be resolved. Our previous research has successfully fabricated hierarchical micro/nano-topography on the Ti6Al4V implant surface through the combination of 3D-printing, alkali-heat treatment and subsequent hydrothermal treatment (Wang H et al., 2021). The graded micro/nano-topography, deposited with anatase phase of titanium dioxide (TiO_2) on the surface, possessed a high specific surface area to increase the adsorption of specific proteins that leading to better biocompatibility. Since quercetin has strong power to chelate metal cations (Sun et al., 2008), the drug was observed to be absorbed on TiO_2 in monomeric form by bidentate chelating the Ti atom in TiO_2 through two dissociated hydroxy functions at the catechol ring B (Zdyb and Krawczyk, 2016). 3D-printed Ti6Al4V implant with micro/nano-topography could also provide more binding sites for quercetin, so as to improve the drug-loading efficiency. Therefore, micro-nano hybrid 3D-printed titanium surface may be an ideal delivery carrier of quercetin.

In this study, we constructed the nano-topographic surface on micro-scaled 3D-printed Ti6Al4V implants on the basis of our prior research, then introduced quercetin-coating on the implant surface. The regulation on the biological behavior of macrophages and rBMSCs stimulated by quercetin-loading was evaluated,

TABLE 1 | Primer squences for real-time PCR.

Gene	Primers (F = forward; R = reverse)
VEGF-α	F: 5′-GTCCCATGAAGTGATCAAGTTC-3′
	R: 5′-TCTGCATGGTGATGTTGCTCTCTG-3′
TGF-β	F: 5′-CAGTACAGCAAGGTCCTTGC-3′
	R: 5′-ACGTAGTAGACGATGGGCAG-3′
IL-10	F: 5′-GCTCTTACTGACTGGCATGAG-3′
	R: 5′-CGCAGCTCTAGGAGCATGTG-3
CD206	F: 5′-AGACGAAATCCCTGCTACTG-3′
	R: 5′-CACCCATTCGAAGGCATTC-3′
INOS	F: 5′-GTTCTCAGCCCAACAATACAAGA-3′
	R: 5′-GTGGACGGGTCGATGTCAC-3
IL-1β	F: 5′-GCAACTGTTCCTGAACTCAACT-3′
	R: 5′-GCAACTGTTCCTGAACTCAACT-3′
GAPDH	F: 5′-AGGTCGGTGTGAACGGATTTG-3′
	R: 5′-TGTAGACCATGTAGTTGAGGTCA-3

TABLE 2 | Primer squences for real-time PCR.

Gene	Primers (F = forward; R = reverse)
OCN	F: 5′-GCCCTGACTGCATTCTGCCTCT-3′
	R: 5′-TCACCACCTTACTGCCCTCCTG-3
COL-I	F: 5′-GCCTCCCAGAACATCACCTA-3′
	R: 5′-GCAGGGACTTCTTGAGGTTG-3′
ALP	F: 5′-TATGTCTGGAACCGCACTGAAC-3′
	R: 5′-CACTAGCAAGAAGAAGCCTTTGG-3′
OPN	F: 5′-CCAAGCGTGGAAACACACAGCC-3′
	R: 5′-GGCTTTGGAACTCGCCTGACTG-3
β-actin	F: 5′-GTAAAGACCTCTATGCCAACA-3′
	R: 5′-GGACTCATCGTACTCCTGCT-3′

along with the observation of anti-inflammation and osseointegration performance in animal models.

2 MATERIALS AND METHODS

2.1 Materials Preparation

In this study, 3D-printed Ti6Al4V (Ti) samples were prepared as two shapes: square disks (10 mm in side length, 2 mm in thickness) and rod-like implants (2 mm in diameter, 3.5 mm in length), both were fabricated from 20 to 50 μm Ti6Al4V alloy powders as described in previous study (Zhang et al., 2019).

The samples were thoroughly ultrasonic cleaned in acetone, ethanol and distilled water to remove the adhered particles and then placed in polytetrafluoroethylene-lined metal reaction kettle with NaOH solution (5 mol/L) at 80°C for 6 h and next in deionized water at 200°C for 4 h to obtain the nanostructured topography, namely the nano-3D group (Wang et al., 2018).

Nano-3D samples were cleaned with deionized water, steam autoclaved and dried as described before *in vitro* or *in vivo* studies. Half of the nano-3D disks/implants were soaked into quercetin solution for drug-loading. Each piece of nano-3D samples was immersed in quercetin ethanol solution (0.05 mg/ml, 10 ml) in a 15 ml centrifuge tube. The samples were ultrasonic treated for 5 min and then placed at 4°C for 1 h. After gentle rinse with deionized water to remove the non-adsorbed quercetin, the nano-3D + quercetin samples were dried at room temperature and UV light sterilized for standby.

2.2 Surface Characterization of Materials

The surface topography of both groups was observed via scanning electron microscope (GeminiSEM 300, ZEISS, Germany). Raman spectroscope (RW 2000, Renishaw, England) was utilized to verify whether the quercetin was coated on the sample surface. The release of quercetin from the samples was determined by using a UV-vis spectrophotometer (IMPLEN, Germany). Quercetin-loaded nano-3D disks were soaked in phosphate buffer saline (PBS, Hyclone, United States) and shaken with 100 rpm at 37°C. The PBS was collected at 1, 4, 8, 12, 18, 24, 36 h and 2, 3, 4, 5, 6 days respectively, and the concentration of quercetin released was observed at 254 nm wavelength. The data were presented as the percentage of cumulative release in total: Cumulative amount of release (%) = 100 × M_t/M (M_t for the amount of quercetin released at time *t*; M for the total amount of quercetin). The surface wettability was observed by Optical Contact Angle and Interface Tension Meter SL200KS (SOLON TECK, China).

2.3 *In Vitro* Study

2.3.1 Cell Culturing

We employed macrophages (RAW 264.7 from Shanghai cell bank of Chinese Academy of Sciences) and rat BMSCs (rBMSCs) in the present study. The latter was isolated from two-week-old male Sprague Dawley rats (from Shanghai Bikai Animal Laboratory, China). Rats were sacrificed through cervical dislocation after general anesthesia, then peripheral soft tissue of dissected femora and tibiae was removed. The bone was resected at both sides of the metaphysis, then bone marrow contents were flushed into 10 cm cell culture dish containing alpha-modified Eagle's medium (α-MEM, Hyclone, United States) supplemented with 10% fetal bovine serum (FBS, Hyclone, United States) and 1% penicillin/streptomycin solution (Gibco, United States). The rBMSCs were incubated at 37°C in 5% CO_2 and the media was changed each 2 days, and third passages of rBMSCs were used in the following experiments.

2.3.2 Cell Adhesion and Proliferation

To assess the morphology of cells adhered on the samples, cells (RAW264.7: 1×10^5/ml, rBMSCs: 1×10^4/ml) were seeded onto each sample in a 24-well plate and cultured for 24 h respectively. Then samples were rinsed with PBS and fixed in 2.5% glutaraldehyde at 4°C overnight. After dehydration in graded ethanol series sequentially, samples were freezing dried and sputter coated with gold before SEM scanning (S-4800, Hitachi, Japan).

Cell proliferation was evaluated through Cell Counting Kit-8 (CCK-8, Beyotime, China) after culturing rBMSCs for 1, 4, 7 days and RAW 264.7 for 1, 3, 5 days respectively. Briefly, cells were seeded on samples (RAW264.7: 1×10^5/well, rBMSCs: 1×10^4/well) in 24-well plates and the media was changed every 2 days. At

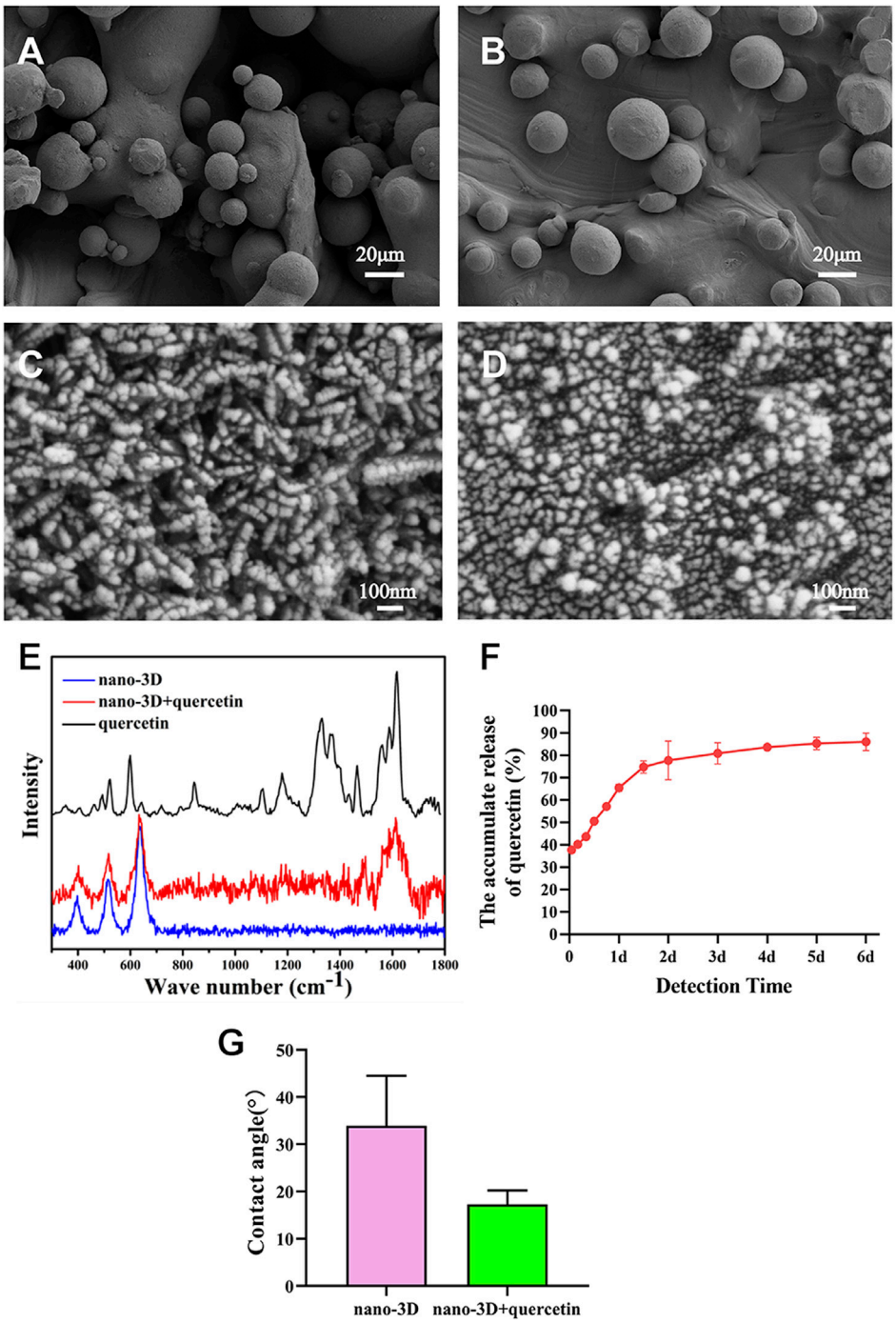

FIGURE 1 | SEM images of nano-3D **(A,C)** and nano-3D + quercetin **(B,D)** at low **(A,B)** and high magnifications **(C,D)**; Raman spectra analysis **(E)**, accumulative release percentage of quercetin loaded on the nano-3D samples at different times **(F)** and water contact angle **(G)** of nano-3D/nano-3D + quercetin sample surfaces (*$p < 0.05$).

each time point, every sample was transtrred into a new well and incubated in CCK-8 working solution for 2 h. The absorbance was measured at 450 nm wavelength using a microplate reader (Spectra Max M5, Molecular Devices, United States).

2.3.3 Quercetin-Coated Surface Modulating RAW 264.7 Polarization

After incubation on samples for 24 h, the culture medium of macrophages was collected and centrifuged. ELISA kits (Boster,

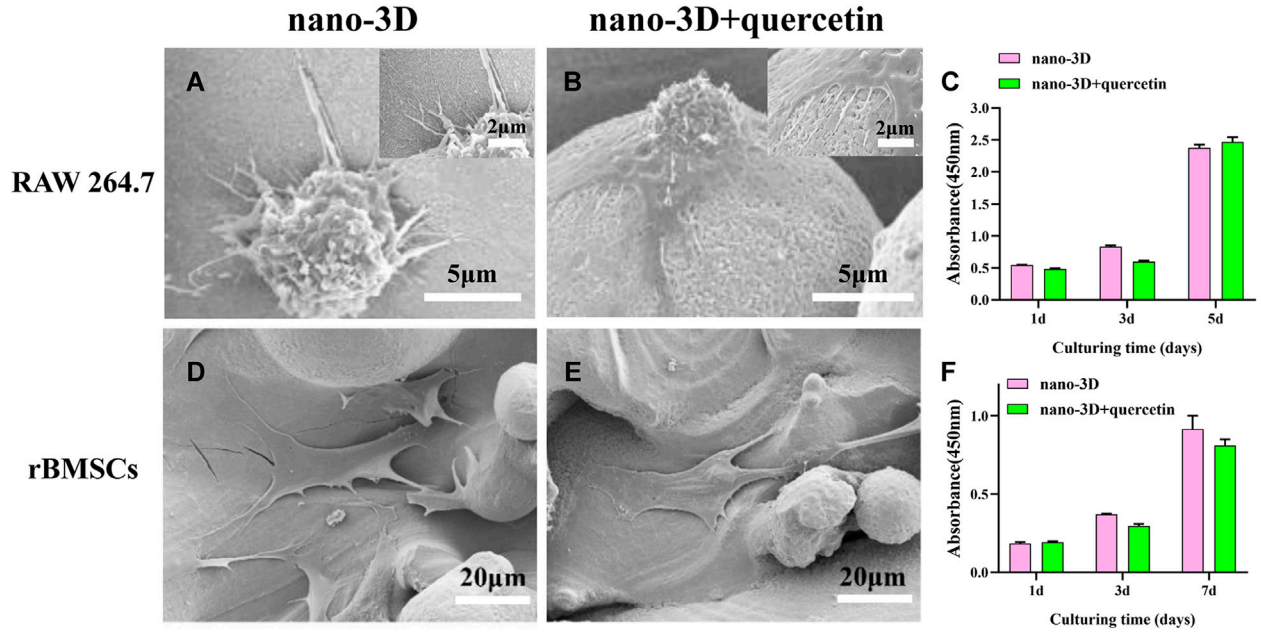

FIGURE 2 | SEM images of adherent RAW 264.7 **(A,B)** and rBMSCs **(D–E)** cultured on nano-3D **(A,D)** and nano-3D + quercetin **(B,E)**; CCK-8 analysis of RAW 264.7 **(C)** and rBMSCs **(F)** cultured on nano-3D and nano-3D + quercetin samples (*$p < 0.05$).

China) were used to examine the concentrations of IL-1β, VEGF-α and TGF-β in the supernatants according the manufacturer's instructions.

The gene expression level was determined by quantitative real-time polymerase chain reaction (qRT-PCR) assay so as to evaluate the related genes expression. The RAW 264.7 were seeded with a density of 4×10^6/well on the sample surfaces in 6-well plates. Total RNA was extracted and separated by RNAfast200 RNA Isolation Kits (Feijie, China) after 3 days, then reversely transcribed into cDNA through a Prime-Script RT reagent kit (Takara, Japan). The cDNA samples were 1:10 diluted in RNase-free water and stored at −20°C until the PCR reaction was performed. Primers used in the present study were synthesized commercially (Sangon, China), and are set out in **Table 1**. The real-time PCR procedure was performed with SYBR green PCR reaction mix (Takara, Japan) in Light Cycler® 96 Real-Time PCR System (Roche, Switzerland).

2.3.4 Quercetin-Coated Surface Promoting rBMSCs Osteogenic Differentiation

Alkaline phosphatase (ALP) activity and staining assay of rBMSCs cultured on the discs were measured at 4 and 7 days. Cells were seeded at a density of 4×10^4/well and at each time point, the samples were rinsed with PBS. For ALP staining, cells were fixed with 4% paraformaldehyde (PFA) and stained with ALP Color Development Staining Kit (Beyotime, China). After 12 h, stained materials were observed through optical microscope (Olympus, Japan). While for ALP activity assay, cells were lysed in 0.1% Triton ×100 buffer (Beyotime, China). After centrifugation, the supernatant was used to detect the ALP activity *via* ALP Assay Kit (Jiancheng, China), and the total protein concentration was determined with BCA Protein assay kit (Beyotime, China) according to the manufacturer's instruction. Finally, the ALP activity was calculated and normalized to the total protein level (U/g protein).

Besides, qRT-PCR assay was employed to investigate the related genes expression at 4 and 7 days so as to evaluate the effect of quercetin-coating on osteogenic differentiation, primers in this part are describedd in **Table 2**.

2.4 *In Vivo* Study

2.4.1 Surgical Procedures

SD rats weighted approximately 250 g were used in the present study. General anesthesia was conducted by intraperitoneal injection with pentobarbital sodium (30 mg/kg, Beyotime, China) and then the surgical area was shaved and washed with povidone iodine. A 1 cm-long incision was made through the skin, muscle and periosteum at the lateral side of femoral condyles to expose the implantation position. Subsequently, a hole of 2 mm in diameter and 3 mm in depth was prepared with a bur and the drilling procedure was accompanied with constant irrigation of sterile saline. Implants of nano-3D and nano-3D + quercetin were inserted into the left or right femoral condyle randomly and finally tissues were sutured in layers.

Animals were euthanized after 2 or 4 weeks of healing (n = 6 for each time point) and then the femoral condyles were resected and fixed in 4% PFA for further analysis.

2.4.2 Micro-Computed Tomography (Micro-CT Assay)

In order to evaluate the peri-implant new bone volumes *in vivo*, the harvested samples were scanned through micro-CT scanning system (Quantum GX, United States). The scanning parameters

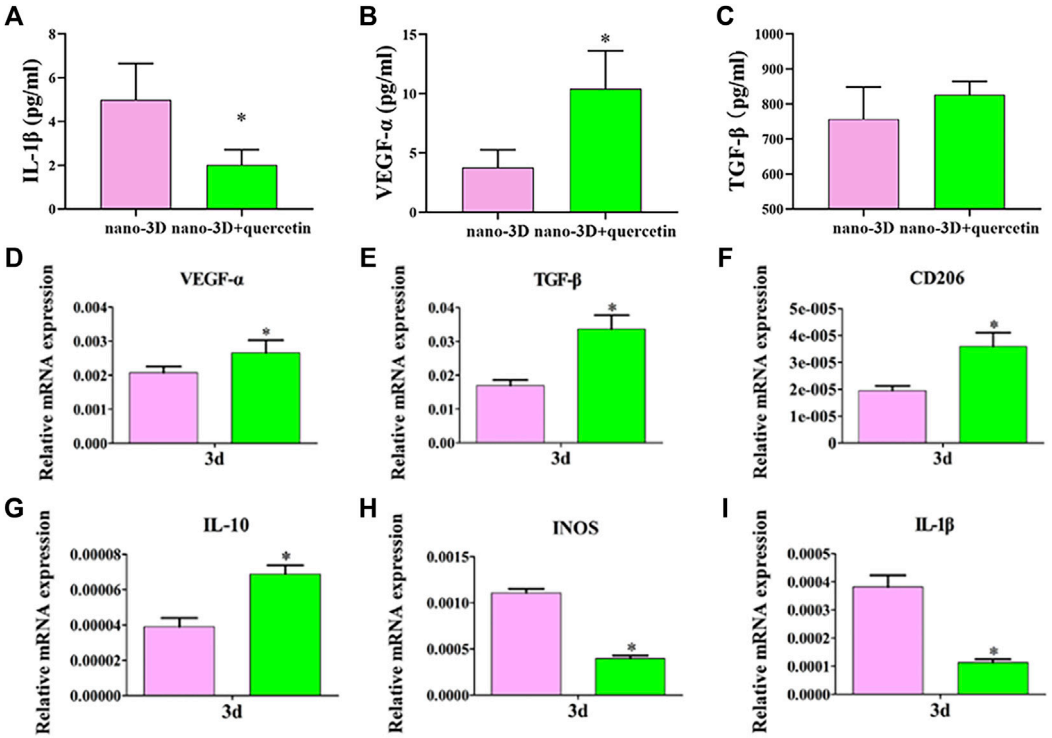

FIGURE 3 | Elisa results of IL-1β, VEGF-α and TGF-β at 24 h respectively **(A–C)** and relative genes expression of RAW 264.7 **(D–I)** on nano-3D and nano-3D + quercetin samples at 3 days (*$p < 0.05$).

were set at 90kV, 88 μA and 14 min, then the images were 3D-reconstructed in the voxel size of 25 μm, so as to calculate the ratio of bone volume to total volume (BV/TV) with the attached analysis software.

2.4.3 Histological and Histomorphometric Analysis

Hematoxylin and eosin (H&E) and immunofluorescence (IF) staining were performed on the peri-implant tissues harvested at 2 weeks. After decalcification for 1 month, the implants can be softly screwed out of the samples with tweezers, then the remaining tissues were embedded in paraffin and sectioned into 5 μm slices. The sections were stained with H&E to validate the inflammatory level, and the IF staining was employed to evaluate the macrophage phenotypes infiltrating the peri-implant tissues. The staining procedures were conducted according to the manufacturer's instruction with the antibodies (Affinity, United States).

The samples harvested at 4 weeks were dehydrated in graded ethanol series from 70% to 100% sequentially and embedded in methyl methacrylate (MMA) for undecalcified sectioning. The polymerized samples were longitudinally sectioned and polished with a Diamond Circular Saw Microtome and Micro Grinding System (Exakt 300, Germany). The sections were stained with Van Gieson's (VG) staining kit (Yuanye, China) and visualized under a light microscope (Olympus, Japan) for histological observation. For histomorphometric measurements, pictures captured by the digital camera attached to the microscope were analyzed, and the bone-to-implant contact (BIC) percentage was calculated *via* ImageJ.

2.5 Statistical Analysis

All quantitative data were performed as mean ± standard deviation (SD) and were statistically analyzed by *t*-test through GraphPad Prism 8.0 software. The difference was considered significant when p value was less than 0.05.

3 RESULTS AND DISCUSSION

3.1 Surface Characterization

As presented in **Figures 1A–D**, there was no significant difference in surface morphology between nano-3D and nano-3D + quercetin. This may be due to the fact that quercetin is a small molecular substance that cannot be observed on SEM. The Raman spectrum (**Figure 1E**) showed typical quercetin peak appeared on the surface of nano-3D + quercetin at about 1606 cm^{-1}, which indicated that quercetin had been successfully loaded on the surface of titanium scaffolds. The results of accumulative quercetin release (**Figure 1F**) showed significant quercetin release at 37.70 ± 0.39% in the first hour. Afterwards the quercetin release displayed a linear trend of steep increase to 74.75 ± 2.78% at 36 h, then gently increased until reaching 86.01 ± 3.91% at 6 days. These results implied that the nano-3D titanium alloy disks as a quercetin delivery carrier could provide effective

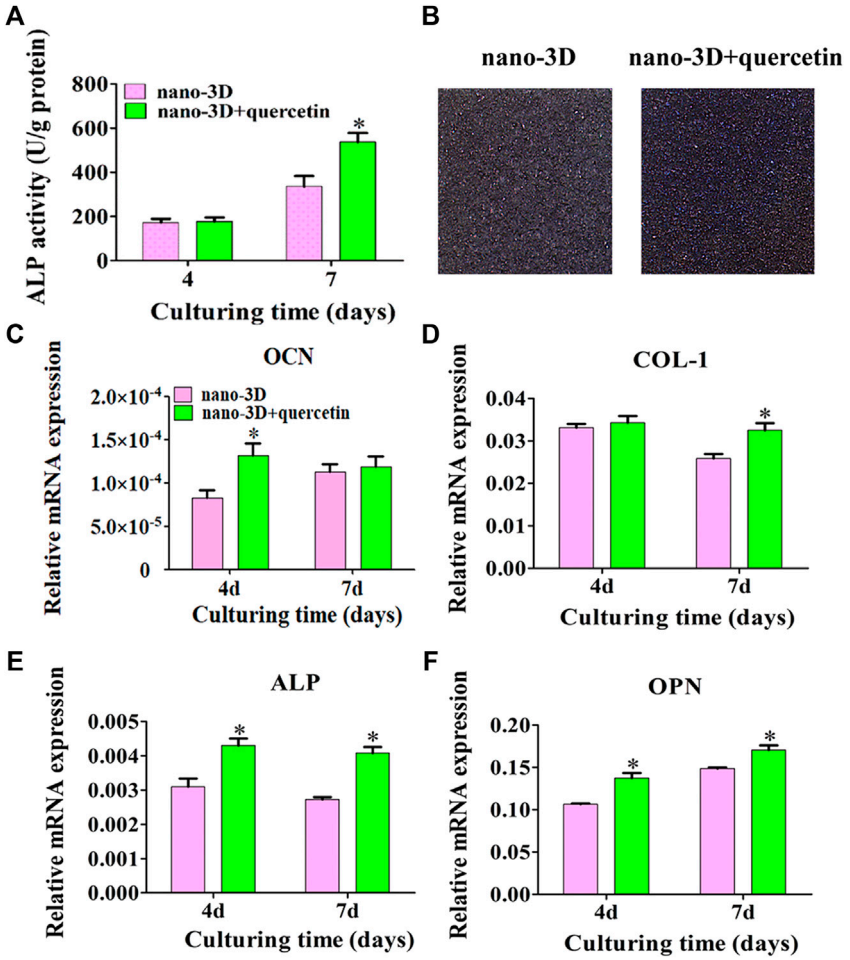

FIGURE 4 | ALP activity at 4/7 days **(A)** and staining at 7 days **(B)** of rBMSCs on nano-3D and nano-3D + quercetin sheets; Expression levels of OCN **(C)**, COL- I **(D)**, ALP **(E)** and OPN **(F)** in rBMSCs cultured on nano-3D and nano-3D + quercetin sheets at 4/7 days (*$p < 0.05$).

and stable drug release, and the release amount could quickly reach a high level at the first 2 days. Water contact angle analysis showed that the surface water contact angle of nano-3D + quercetin sample was lower than that of nano-3D group, but the difference was not statistically significant (**Figure 1G**). This may indicate that quercetin loading has little effect on the surface hydrophilicity of nano-modified 3D-printing implants.

3.2 Cell Adhesion and Proliferation

The SEM results of 24 h adhesion of RAW 264.7 (**Figures 2A,B**), the macrophages on both groups exhibited almost spherical shape, yet macrophages on the nano-3D + quercetin samples had more pseudopods, indicating more sufficient adhesion and spreading. As polarized M1 macrophages displayed round-like shape without any spreading in general, while M2 macrophages exhibiting spindle-shaped and better spreading morphology, the results might suggest that macrophages on the quercetin-loaded samples were more likely to polarize into M2 phenotype at the first day. Similar trends were also detected in the results of rBMSCs (**Figures 2D,E**), for that the cells on the surface of nano-3D + quercetin group were better adhered and spread with more plate-like and filiform pseudopods. Good adhesion plays an important role in cell proliferation and differentiation, however, CCK-8 analysis results (**Figures 2C,F**) showed no significant difference between the two groups, neither in rBMSCs nor in macrophages, indicating good cytocompatibilities of the quercetin-loading and quercetin at this concentration does not promote cell proliferation.

3.3 Quercetin-Coated Surface Modulating RAW 264.7 Polarization

To further verify the representative cytokines secreted by macrophages in M1/M2 phenotype, ELISA was implemented to determine the concentrations of IL-1β, VEGF-α and TGF-β. The results are shown in **Figures 3A–C**. The expression levels of IL-1β, the typical inflammatory cytokine mainly secreted by M1 macrophages, was significantly lower on quercetin-coated samples (**Figure 3A**). In contrast, macrophages on nano-3D + quercetin secreted the greater amounts of the anti-inflammatory

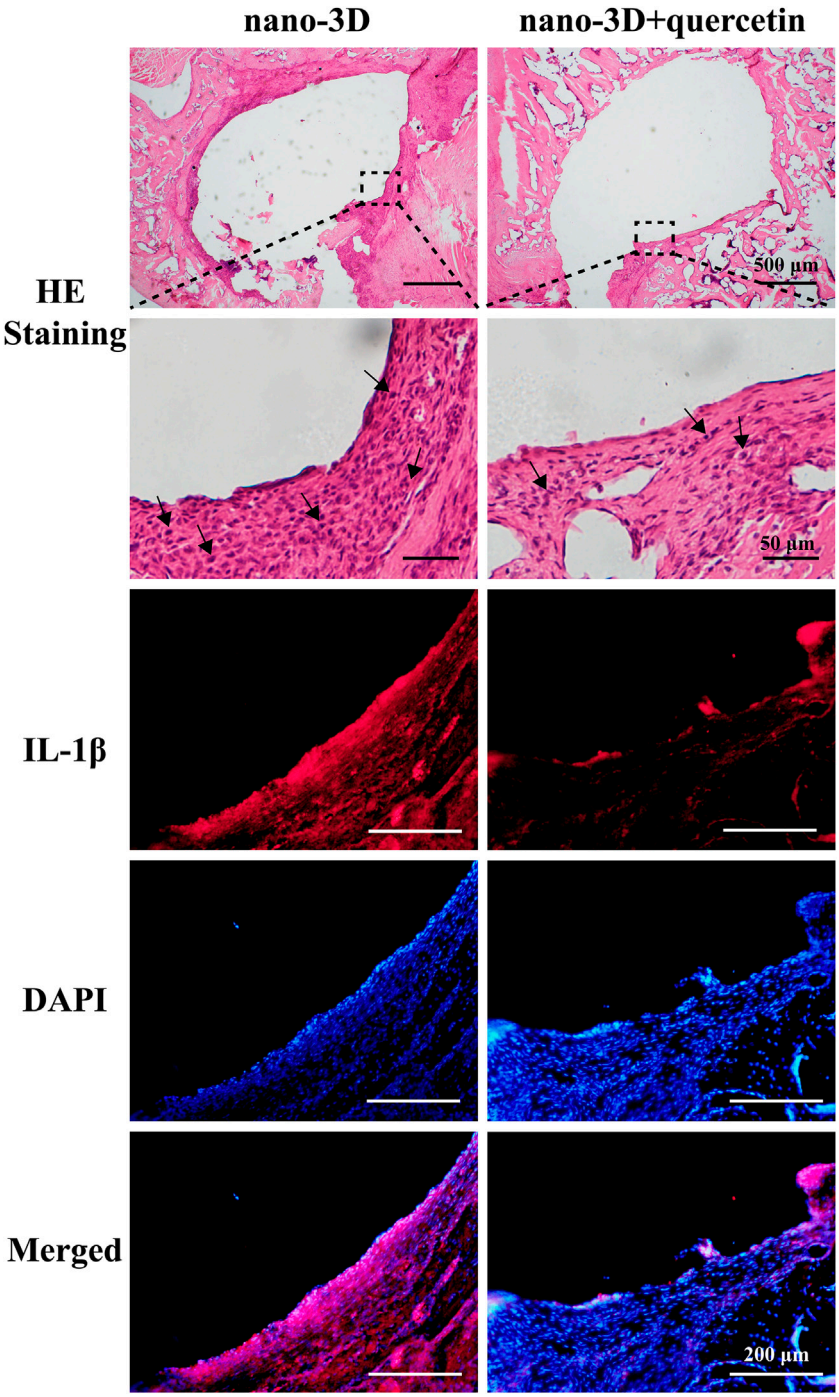

FIGURE 5 | H&E staining of the decalcified peri-implant tissues of nano-3D and nano-3D + quercetin at 2 weeks, black arrows indicate inflammatory cells such as macrophages, neutrophils, monocytes and lymphocytes; immunofluorescent staining results of the decalcified samples: red (IL-1β) and blue (DAPI).

cytokine VEGF-α largely produced by M2 macrophages (**Figure 3B**), yet no significant difference shown in TGF-β production between the two groups (**Figure 3C**).

Highly consistent with the ELISA results, as is presented in **Figures 3D–I**, the nano-3D + quercetin group was more conductive to the expression of anti-inflammatory phenotype (M2) related genes, such as VEGF-α, TGF-β, IL-10 and CD206, while reducing the expression of activated inflammatory macrophage (M1) related genes, such as iNOS and IL-1β, indicating that quercetin-coating could regulate the polarization of macrophages to M2 macrophages. M2 phenotype macrophages secrete a variety of immunoregulatory

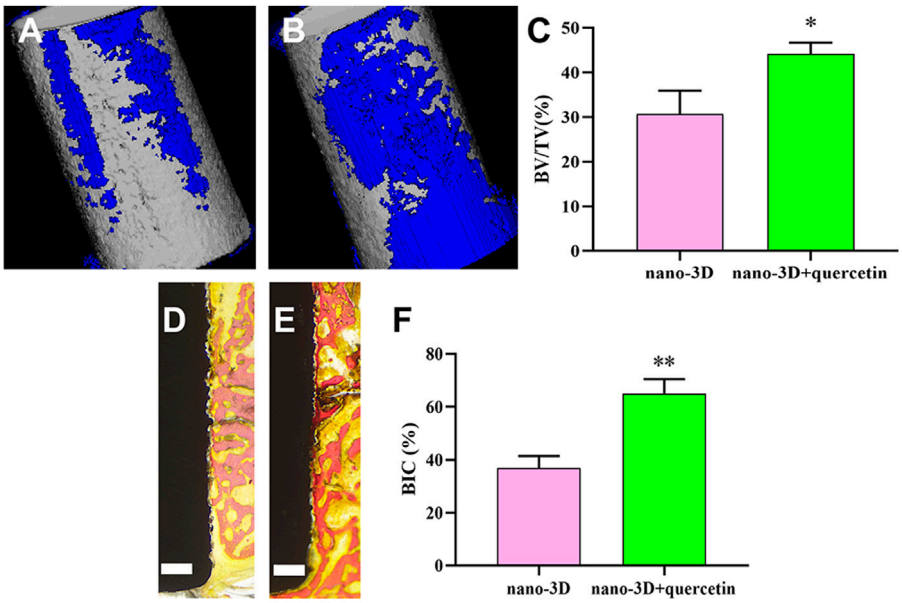

FIGURE 6 | 3D-reconstructed images of new bone formation (blue) around the implants (grey) of nano-3D **(A)** and nano-3D + quercetin **(B)** at 4 weeks, quantitative analysis of Micro-CT data: BV/TV ratio **(C)**. Van Gieson staining of undecalcified sections of nano-3D **(D)** and nano-3D + quercetin **(E)** at 4 weeks, scale bar = 300 μm, and the histomorphometric analysis of BIC percentage **(F)**, (*$p < 0.05$, **$p < 0.01$).

factors and chemokines to recruit and integrate fibroblasts, bone marrow mesenchymal cells, endothelial cells and other repair cells to the wound, thereby maintaining the tissue homeostasis and promoting the inflammatory response to enter the stage of tissue regeneration as soon as possible.

3.4 Quercetin-Coated Surface Promoting rBMSCs Osteogenic Differentiation

At 4 days, there was no significant difference in ALP activity between the two groups; at 7 days, the ALP expression on the surface of nano-3D + quercetin group increased significantly than that of nano-3D group (**Figure 4A**), and the ALP staining results (**Figure 4B**) confirmed the trend.

As demonstrated in **Figures 4C–F**, compared with the nano-3D group, the expression of osteogenesis related genes such as OCN, ALP and OPN on the surface of nano-3D + quercetin group increased significantly at 4 days, except that no significant difference shown in the expression of COL- I between the two groups. While at 7 days, the expression of COL-I, ALP and OPN on the surface of nano-3D + quercetin increased significantly, and the difference was statistically significant compared to the other group, besides no significant difference shown in the gene expression of OCN between the two groups at the time.

The results of quantitative detection of ALP expression and qRT-PCR exhibited similar trends that ALP and osteogenic related gene expression were higher in nano-3D + quercetin group, which implied that quercetin-coating was more favorable for osteogenic differentiation of rBMSCs.

3.5 Capability of Anti-Inflammation of Quercetin-Coated Nano-3D Implants

The images of H&E staining in **Figure 5** demonstrated the pathological changes in the peri-implant tissues. Compared to the quercetin-loaded group, the nano-3D sections showed more severe inflammatory state with abundant inflammatory cells infiltration, such as monocytes, neutrophils and macrophages. To further investigate the therapeutic effects of quercetin against inflammation, the level of inflammation-associated cytokine in the peri-implant tissues were observed by IF. The representative pro-inflammatory M1 biomarker IL-1β positive cells were notably detected in nano-3D group and significantly decreased in the quercetin-loaded samples, showing the anti-inflammatory effects of quercetin at the inflammatory site.

3.6 Capability of Osteogenesis and Osseointegration of Quercetin-Coated Nano-3D Implants

After implantation for 4 weeks, 3D-reconstructed images of nano-3D (**Figure 6A**) and nano-3D + quercetin (**Figure 6B**) showed that the volume of new bone formation in the quercetin-coated group was obviously larger than that in the non-coating group. The quantitative results of BV/TV (**Figure 6C**) also illustrated the difference, which the new bone formation ration of nano-3D + quercetin implants was significantly higher than the other group.

Moreover, the VG staining results of hard tissue slices showed a trend in consistence with the CT analysis, that there was more new bone formed around the surface of quercetin-coated implants (**Figure 6E**) compared to the nano-3D samples (**Figure 6D**). The

quantitative analysis of new bone area percentages demonstrated that BIC percentage of nano-3D + quercetin group is markedly higher than that of the non-coating group (**Figure 6F**).

To sum up, histological and histomorphometric results implied that the nano-structural modified 3D-printed Ti6Al4V with quercetin coating could enhance the capacities of osteogenesis and osseointegration around the implants *in vivo*.

Taking the *in vitro* and *in vivo* observations into account, the quercetin-coated nano-topographic modificated 3D-printed Ti6Al4V manifested superiority compared to the control group, which may owe to the capabilities of stimulating osteogenic differentiation and anti-inflammation of quercetin(Angellotti et al., 2020).

4 CONCLUSION

In the present study, we successfully loaded quercetin onto the surface of nano-structural modified 3D-printed Ti6Al4V implants, and then confirmed that quercetin-coating can promote the adhesion of macrophages and modulate the polarization from M1 to M2 phase, thus to improve the anti-inflammatory and vascular gene expression gene expression of the macrophages. Meanwhile, the nano-structural modified 3D-printed Ti6Al4V loaded with quercetin can promote the adhesion and osteogenic differentiation of rBMSCs. Quercetin-loading provided a feasible and favorable scheme for endowing 3D-printed titanium alloy implant surface with enhanced rapid osseointegration and anti-inflammatory properties, and the specific mechanisms of quercetin promoting osteogenesis and anti-inflammation through modulating polarization are worthy of further study.

DATA AVAILABILITY STATEMENT

The raw data supporting the conclusion of this article will be made available by the authors, without undue reservation.

ETHICS STATEMENT

The animal study was reviewed and approved by Institutional Animal Care and Use Committee of Shanghai Jiaotong University (Shanghai, China).

AUTHOR CONTRIBUTIONS

NL and HW performed the experiments and wrote the original draft. ZF and WH helped to perform the surgical procedures. CZ helped to prepare the manuscript. JW, YZ and SL led the conceptualization and project administration, and supervised the writing and editing of the manuscript. All authors contributed to the article and approved the submitted version.

ACKNOWLEDGMENTS

The authors acknowledge the support provided by the Shanghai Science and Technology Committee (20S31902200 and 20XD1433400), and Shanghai Ninth People's Hospital, Shanghai Jiao Tong University School of Medicine (JYLJ201918076, JYJC201802 and MDT project 201906).

REFERENCES

Angellotti, G., Murgia, D., Campisi, G., and De Caro, V. (2020). Quercetin-Based Nanocomposites as a Tool to Improve Dental Disease Management. *Biomedicines* 8, 504. doi:10.3390/biomedicines8110504

Bose, S., Robertson, S. F., and Bandyopadhyay, A. (2018). Surface Modification of Biomaterials and Biomedical Devices Using Additive Manufacturing. *Acta Biomater.* 66, 6–22. S1742706117306797. doi:10.1016/j.actbio.2017.11.003

Chen, X., Zhi, X., Pan, P., Cui, J., Cao, L., Weng, W., et al. (2017). Matrine Prevents Bone Loss in Ovariectomized Mice by Inhibiting RANKL-induced Osteoclastogenesis. *FASEB J.* 31, 4855–4865. doi:10.1096/fj.201700316r

Chen, Z., Klein, T., Murray, R. Z., Crawford, R., Chang, J., Wu, C., et al. (2016). Osteoimmunomodulation for the Development of Advanced Bone Biomaterials. *Mater. Today* 19 (6), 304–321. S1369702115003788. doi:10.1016/j.mattod.2015.11.004

Civantos, A., Martínez-Campo, E., Ramos, V., Elvira, C., Gallardo, A., and Abarrategi, A. (2017). Titanium Coatings and Surface Modifications: Toward Clinically Useful Bioactive Implants. *ACS Biomaterials Sci. Eng.* 3 (7), 1245–1261. doi:10.1021/acsbiomaterials.6b00604

Dong, X., Chang, J., and Li, H. (2017). Bioglass Promotes Wound Healing through Modulating the Paracrine Effects between Macrophages and Repairing Cells. *J. Mat. Chem. B* 5, 5240–5250. doi:10.1039/c7tb01211j

Funes, S. C., Rios, M., Escobar-Vera, J., and Kalergis, A. M. (2018). Implications of Macrophage Polarization in Autoimmunity. *Immunology* 154, 186–195. doi:10.1111/imm.12910

Goodman, S. B., Yao, Z., Keeney, M., and Fan, Y. J. B. (2013). The Future of Biologic Coatings for Orthopaedic Implants. *Biomaterials* 34 (13), 3174–3183. doi:10.1016/j.biomaterials.2013.01.074

Hassan, M. N., Yassin, M. A., Suliman, S., Lie, S. A., Gjengedal, H., and Mustafa, K. (2019). The Bone Regeneration Capacity of 3D-Printed Templates in Calvarial Defect Models: A Systematic Review and Meta-Analysis. *Acta Biomater.* 91, 1–23. doi:10.1016/j.actbio.2019.04.017

Kang, H., Kim, S., Wong, D. S. H., Jung, H. J., Lin, S., Zou, K., et al. (2017). Remote Manipulation of Ligand Nano-Oscillations Regulates Adhesion and Polarization of Macrophages *In Vivo*. *Nano Lett.* 17, 6415–6427. doi:10.1021/acs.nanolett.7b03405

Landén, N. X., Li, D., and Ståhle, M. (2016). Transition from Inflammation to Proliferation: a Critical Step during Wound Healing. *Cell. Mol. Life Sci.* 73, 3861–3885. doi:10.1007/s00018-016-2268-0

Li, Y., Wang, J., Chen, G., Feng, S., Wang, P., Zhu, X., et al. (2015). Quercetin Promotes the Osteogenic Differentiation of Rat Mesenchymal Stem Cells via Mitogen-Activated Protein Kinase Signaling. *Exp. Ther. Med.* 9 (6), 2072–2080. doi:10.3892/etm.2015.2388

Russo, M., Spagnuolo, C., Tedesco, I., Bilotto, S., and Russo, G. L. (2012). The Flavonoid Quercetin in Disease Prevention and Therapy: Facts and Fancies. *Biochem. Pharmacol.* 83, 6–15. doi:10.1016/j.bcp.2011.08.010

Sun, S., Chen, W., Cao, W., Zhang, F., Song, J., and Chengrui, T. (2008). Research on the Chelation between Quercetin and Cr(III) Ion by Density Functional Theory (DFT) Method. *J. Mol. Struct. THEOCHEM* 860 (1-3), 40–44. doi:10.1016/j.theochem.2008.03.020

Van den Bossche, J., O'Neill, L. A., and Menon, D. (2017). Macrophage Immunometabolism: Where Are We (Going)? *Trends Immunol.* 38 (6), 395–406. doi:10.1016/j.it.2017.03.001

Vishwakarma, A., Bhise, N. S., Evangelista, M. B., Rouwkema, J., Dokmeci, M. R., Ghaemmaghami, A. M., et al. (2016). Engineering Immunomodulatory Biomaterials to Tune the Inflammatory Response. *Trends Biotechnol.* 34, 470–482. doi:10.1016/j.tibtech.2016.03.009

Wang, H., Liu, J., Wang, C., Shen, S. G., Wang, X., and Lin, K. (2021). The Synergistic Effect of 3D-Printed Microscale Roughness Surface and Nanoscale

Feature on Enhancing Osteogenic Differentiation and Rapid Osseointegration. *J. Mater. Sci. Technol.* 63, 18–26. doi:10.1016/j.jmst.2019.12.030

Wang, H., Zhang, X., Wang, H., Zhang, J., Li, J., Ruan, C., et al. (2018). Enhancing the Osteogenic Differentiation and Rapid Osseointegration of 3D Printed Ti6Al4V Implants via Nano-Topographic Modification. *J. Biomed. Nanotechnol.* 14, 707–715. doi:10.1166/jbn.2018.2551

Wang, Y., Li, C., Wan, Y., Qi, M., and Wang, L. J. S. (2021). Quercetin-Loaded Ceria Nanocomposite Potentiate Dual-Directional Immunoregulation via Macrophage Polarization against Periodontal Inflammation. *Small* 17 (41), 2101505. doi:10.1002/smll.202101505

Zdyb, A., and Krawczyk, S. (2016). Characterization of Adsorption and Electronic Excited States of Quercetin on Titanium Dioxide Nanoparticles. *Spectrochimica Acta Part A Mol. Biomol. Spectrosc.* 157, 197–203. doi:10.1016/j.saa.2016.01.006

Zhang, J., Zhou, W., Wang, H., Lin, K., and Chen, F. (2019). 3D-printed Surface Promoting Osteogenic Differentiation and Angiogenetic Factor Expression of BMSCs on Ti6Al4V Implants and Early Osseointegration *In Vivo*. *J. Mater. Sci. Technol.* 35, 336–343. doi:10.1016/j.jmst.2018.09.063

Zhang, X., and Mosser, D. (2008). Macrophage Activation by Endogenous Danger Signals. *J. Pathol.* 214, 161–178. doi:10.1002/path.2284

Zhao, L., Liu, L., Wu, Z., Zhang, Y., and Chu, P. K. (2012). Effects of Micropitted/nanotubular Titania Topographies on Bone Mesenchymal Stem Cell Osteogenic Differentiation. *Biomaterials* 33, 2629–2641. doi:10.1016/j.biomaterials.2011.12.024

Zhou, Y., Wu, Y., Ma, W., Jiang, X., Takemra, A., Uemura, M., et al. (2017). The Effect of Quercetin Delivery System on Osteogenesis and Angiogenesis under Osteoporotic Conditions. *J. Mater. Chem. B* 5 (3), 612–625. doi:10.1039/c6tb02312f

Conflict of Interest: The authors declare that the research was conducted in the absence of any commercial or financial relationships that could be construed as a potential conflict of interest.

Publisher's Note: All claims expressed in this article are solely those of the authors and do not necessarily represent those of their affiliated organizations, or those of the publisher, the editors and the reviewers. Any product that may be evaluated in this article, or claim that may be made by its manufacturer, is not guaranteed or endorsed by the publisher.

Copyright © 2022 Liu, Wang, Fu, Zhang, Hui, Wu, Zhang and Zhang. This is an open-access article distributed under the terms of the Creative Commons Attribution License (CC BY). The use, distribution or reproduction in other forums is permitted, provided the original author(s) and the copyright owner(s) are credited and that the original publication in this journal is cited, in accordance with accepted academic practice. No use, distribution or reproduction is permitted which does not comply with these terms.

frontiers | Frontiers in Bioengineering and Biotechnology

ORIGINAL RESEARCH
published: 14 June 2022
doi: 10.3389/fbioe.2022.939199

Stem Cells-Loaded 3D-Printed Scaffolds for the Reconstruction of Alveolar Cleft

Dongyuan Luo[†], *Boying Chen*[†] *and Yu Chen*[*]

Guangzhou Women and Children's Medical Center, Guangzhou, China

The advances in the field of tissue engineering and regenerative medicine have opened new vistas for the repair of alveolar clefts. However, the currently available biomaterials used for the repair of alveolar clefts have poor mechanical properties and biocompatibility, which hinders the treatment outcomes. Here, we aimed to develop 3D printed biomimetic scaffolds that fuses β-tricalcium phosphate (β-TCP) and bone marrow mesenchymal stem cells (BMSCs) for improving the repair of alveolar clefts. The methacrylate gelatin (GelMA) was mixed with β-TCP for the preparation of GelMA/β-TCP hybrid scaffolds via 3D printing platform and chemically cross-linking with UV light. The physicochemical properties of the hydrogel scaffolds were characterized. Moreover, the survival state, proliferation ability, morphological characteristics, and osteogenic induction of BMSCs were examined. The prepared hybrid scaffolds showed good biocompatibility and mechanical properties. BMSCs attached well to the scaffolds and proliferated, survived, differentiated, and stimulated osteogenesis for the reconstruction of alveolar clefts. We expect that use of the prepared hybrid hydrogel scaffold can improve the outcomes of alveolar cleft repair in clinic and expand the application of hybrid hydrogel in tissue engineering repair.

Keywords: alveolar cleft, β-tricalcium phosphate, methacrylated gelatin, 3D printing, bone marrow mesenchymal stem cells

OPEN ACCESS

Edited by:
Rui Guo,
Jinan University, China

Reviewed by:
Yabin Zhu,
Ningbo University, China
Jiali Tan,
Sun Yat-sen University, China

***Correspondence:**
Yu Chen
2768201492@qq.com

[†]*These authors have contributed equally to this work*

Specialty section:
This article was submitted to Biomaterials, a section of the journal Frontiers in Bioengineering and Biotechnology

Received: *08 May 2022*
Accepted: *26 May 2022*
Published: *14 June 2022*

Citation:
Luo D, Chen B and Chen Y (2022) Stem Cells-Loaded 3D-Printed Scaffolds for the Reconstruction of Alveolar Cleft. Front. Bioeng. Biotechnol. 10:939199. doi: 10.3389/fbioe.2022.939199

1 INTRODUCTION

Alveolar cleft, which results from a fusion disorder between the embryonic globular process and the maxillary process, is the most difficult challenge in the sequence therapy of cleft lip and palate. Approximately 75% of all patients with cleft lip and palate have concomitant alveolar cleft (Cho-Lee et al., 2013). Effective repair of alveolar cleft can improve the treatment outcomes in patients with cleft lip and palate. The alveolar cleft can be reconstructed either with autologous cancellous tissue or with tissue-engineered scaffolds. The latter approach is associated with relatively higher safety and comfort, by precluding the need for secondary injury to the body. Tissue engineering scaffolds can provide space for cell growth, differentiation, adhesion, and migration in the fissure area. In addition, the ideal scaffolds should exhibit good biocompatibility and degradability, which are beneficial for the growth of osteoblasts and blood vessels. For the reconstruction of alveolar cleft, the scaffold should be good at bone conduction and conducive to certain bone induction. Currently, several materials are used for bone repair, such as metal, hydroxyapatite, and carbon nanotubes. Among these, the hydroxyapatite and other synthetic bio-ceramic tissue-engineered bone scaffolds have been widely used for repair of bone defects (LeGeros, 2002; Klijn et al., 2012). Application of these

materials effectively shortens the operation time and precludes the need for cutting the autologous bone, thus reducing the pain and complications. However, the non-deformability and non-biodegradability of these synthetic tissue-engineered bone scaffolds hinder the tooth eruption and orthodontic treatment (Feinberg et al., 1989; Chin et al., 2005). Especially during the bone healing period, the scaffolds tend to shift when exposed to stress (Letic-Gavrilovic et al., 2003). Therefore, they are not a suitable base for the movement of teeth and reconstruction of dental arch. Further research is required to develop biological absorbable scaffolds for bone reconstruction of alveolar cleft.

Biological 3D printing technology has been widely used in tissue repair engineering due to its high controllable accuracy and simple operation. In the field of tissue engineering, biological 3D printing technology can accurately control the morphology of scaffold material and the distribution of cells inside scaffolds. Moreover, the technology can enable construction of artificial tissues, which are highly similar to the human tissue structure. These structures show distinct advantage over previous scaffolds. 3D printing technology ensures that the printed scaffolds have the optimal anatomical configuration for *in-situ* implantation. Therefore, biological 3D printing technology has been applied in personalized medical models, permanent human implants, bionic scaffolds, drug testing models, controllable and sustained-release drugs, and other aspects, promoting the continuous development of biomedicine. Besides the bioactive tissue scaffolds, functional cells are required for alveolar cleft repair, so as to accelerate the reconstruction. Stem cells have been used in the treatment of a variety of diseases. Several reports have described the application of stem cells in alveolar cleft. Therefore, combining three-dimensional scaffolds with suitable stem cells is expected to have a good repair effect (Bajestan et al., 2017). Stem cells derived from a wide range of sources, such as bone marrow-derived stem cells (BMSCs) (Sousa et al., 2014), adipose tissue-derived stem cells (Benazzo et al., 2014), embryo-derived stem cells (Liu et al., 2014), and dental tissue-derived stem cells (Hilkens et al., 2014) have been used in the repair of alveolar cleft. Currently, BMSCs are being widely used in bone tissue engineering and bone defect repair due to the ability of proliferation and multidirectional differentiation potential. Thus, they can induce stable bone tissue formation *in vivo*, with no obvious bone absorption phenomenon. Moreover, these can help achieve sustained treatment effect for a long time (Middleton and Tipton, 2000; Ramakrishna et al., 2004; Hibi et al., 2006; Gimbel et al., 2007).

In this study, we developed 3D hydrogel scaffolds composed of GelMA and β-TCP. We determined the mechanical properties of GelMA/β-TCP scaffolds through electronic universal materials testing machine and then observed the microstructure of freeze-dried hydrogel scaffolds by scanning electron microscopy (SEM). The results showed good biocompatibility and biomechanical properties of hydrogel, which can contribute to the adhesion, proliferation, and differentiation of cells *in vivo*. The interaction between BMSCs and GelMA/β-TCP scaffolds was investigated. We found that the BMSCs adhered well to the hydrogel scaffold, and showed normal cell morphology, proliferation, and differentiation. With the rapid advances in 3D printing technology and tissue engineering, development of 3D printing materials loaded with stem cells for alveolar cleft bone grafting is of great clinical significance. Leveraging the two technologies can help address problems such as insufficient control of accuracy of scaffold structure, randomness of stem cell distribution, and weak mechanical strength. Our results have important implications for the application of 3D GelMA/β-TCP hybrid scaffolds in alveolar cleft bone grafting.

2 MATERIALS AND METHODS

2.1 Preparation of 3D GelMA/β-TCP Scaffolds

2.1.1 Printing of GelMA Scaffolds

Briefly, 5 g of GelMA was dissolved into 100 ml ultrapure water in a 37°C water bath. The GelMA solution was placed into the 20 ml steel syringe and then transferred to 4 °C for 30 min. The steel nozzle was maintained at 26°C and placed into the syringe for another 30 min. The temperature of printer platform was maintained at 3°C. Hydrogel microfilaments were dispensed to the base plate through the nozzle by applying pneumatic pressure of 360 kPa. The mechanical parameters were set at the crosshead velocity of 360 mm/min using 25 G nozzle. The distance between nozzle and surface of base plate was maintained around 0.2 mm. Subsequently, the scaffolds were solidified by illumination with the light source of 3W at 405 nm for 50 s. The GelMA scaffolds with dimensions of $10 \times 10 \times 2\ mm^3$ were fabricated.

2.1.2 Printing of GelMA/β-TCP Scaffolds

β-TCP was mixed into the 5% GelMA (w/v) solution to achieve final concentration of 1% β-TCP (w/v) at 37 °C. The mixture of GelMA/β-TCP solution was placed into a 20 ml steel syringe and then transferred to 4°C for 30 min. The steel nozzle was maintained at 25°C and placed into the syringe for another 30 min. Meanwhile, the temperature of printer platform was adjusted to 3°C. Hydrogel microfilaments were dispensed to the base plate through the nozzle by applying pneumatic pressure of 360 kPa. The mechanical parameters were set at the crosshead velocity of 360 mm/min using 25 G nozzle. The distance between nozzle and surface of base plate was maintained around 0.2 mm. Subsequently, the scaffolds were solidified by illumination with the light source of 3W at 405 nm for 50 s. The GelMA/β-TCP scaffolds with dimensions of $10 \times 10 \times 2\ mm^3$ were fabricated.

2.2 Characterization of GelMA/β-TCP Scaffold

Cylindrical hydrogel of 8.8 mm diameter and 5.5 mm height were placed between the parallel plates in the electronic universal materials testing machine for the detection of Young's modulus. The strain rate was controlled for 15% per minute, while the cylindrical hydrogel deformation varied from 0% to

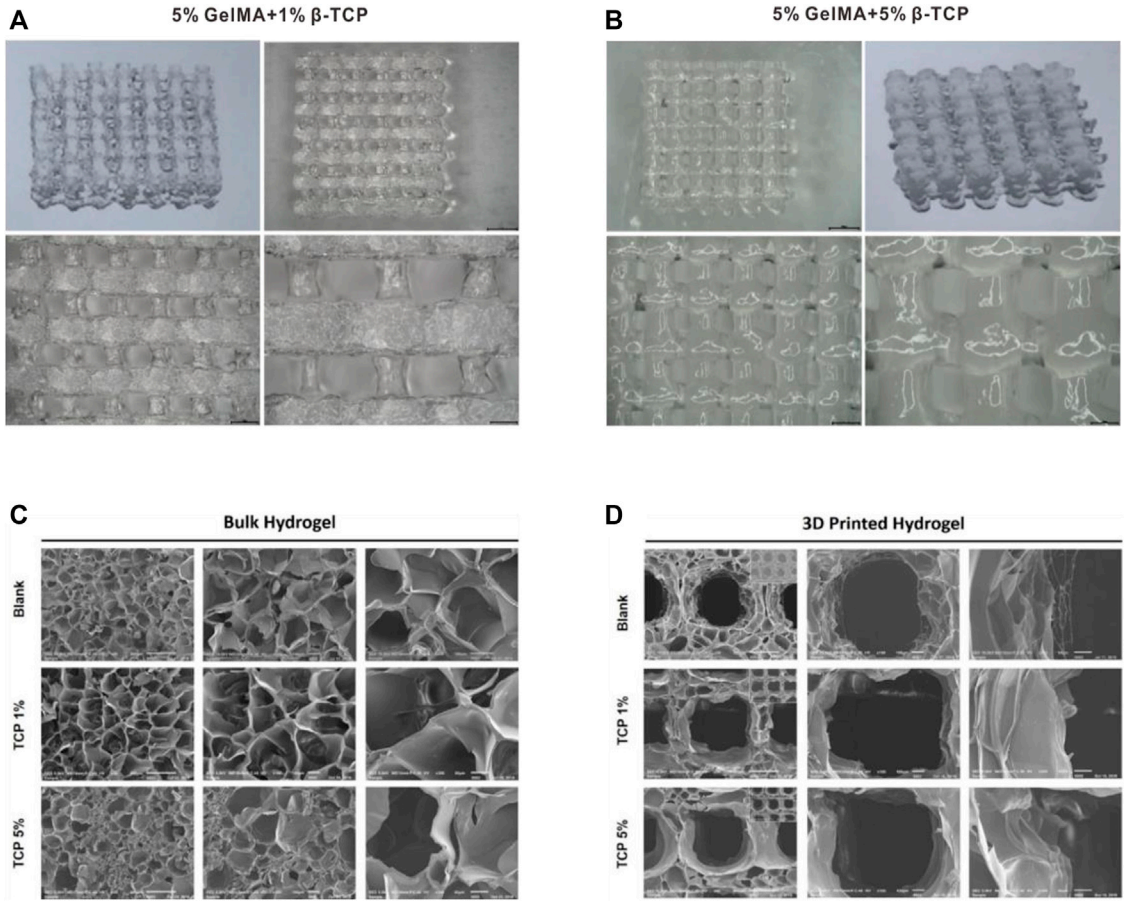

FIGURE 1 | Morphological characteristics of gel scaffolds. Morphology of hydrogels composed of 5% GelMA (w/v) with 1% β-TCP (w/v) **(A)** and 5% GelMA (w/v) with 5% β-TCP (w/v) **(B)**. Lyophilized hydrogels observed by scanning electron microscopy **(C)**. 3D printed hydrogel scaffolds observed by scanning electron microscopy **(D)**.

75%. The changes in the stress and strain monitored by the machine were recorded. The slope of the strain segment in the first 10% of the stress-strain curve was the hydrogel compression modulus.

2.3 Morphological Analysis of GelMA/β-TCP Scaffold

The morphology of the fabricated GelMA/β-TCP scaffolds was examined by SEM. Before the detection, the hydrogels were flash-frozen in the refrigerator at -80°C. Then, the samples were cut into 2 × 2 mm^2 with the scalpel. Subsequently, the small samples were transferred to be lyophilized. Finally, the treated hydrogels were fixed on the special stubs for examination by SEM.

2.4 Effect of GelMA/β-TCP on Proliferation of BMSCs

For evaluation of BMSCs proliferation, 0.5 ml of 5% GelMA, 5% GelMA +1%β-TCP, and 5% GelMA +5% β-TCP were added to the 12-well plate and solidified by illumination with the light source of 3W at 405 nm for 50 s as described above. The *in-situ* hydrogels were soaked in 75% alcohol for 2 h and then supplemented with DMEM/F12 complete medium overnight. BMSCs were inoculated in each well at the density of 1×10^5 cells/mL. There were four parallel groups in the experiment. The cell proliferation was assessed with the addition of 50 μL CCK8 reagent at days 1, 4, 7, and 10 for 3 h. Subsequently, the cells were detected by microplate reader (absorbance: 450 nm). The proliferation of BMSCs was assessed by the OD450 values.

2.5 Effect of GelMA/β-TCP on the Viability of BMSCs

For evaluation of the viability of BMSCs in the GelMA/β-TCP scaffold, the scaffolds were treated with alcohol and DMEM/F12 medium according to the procedure described above. Subsequently, the scaffolds were placed in 12-well plates, and each well was inoculated with 1×10^4 BMSCs for continuous culture of 10 days. The GelMA/β-TCP scaffolds

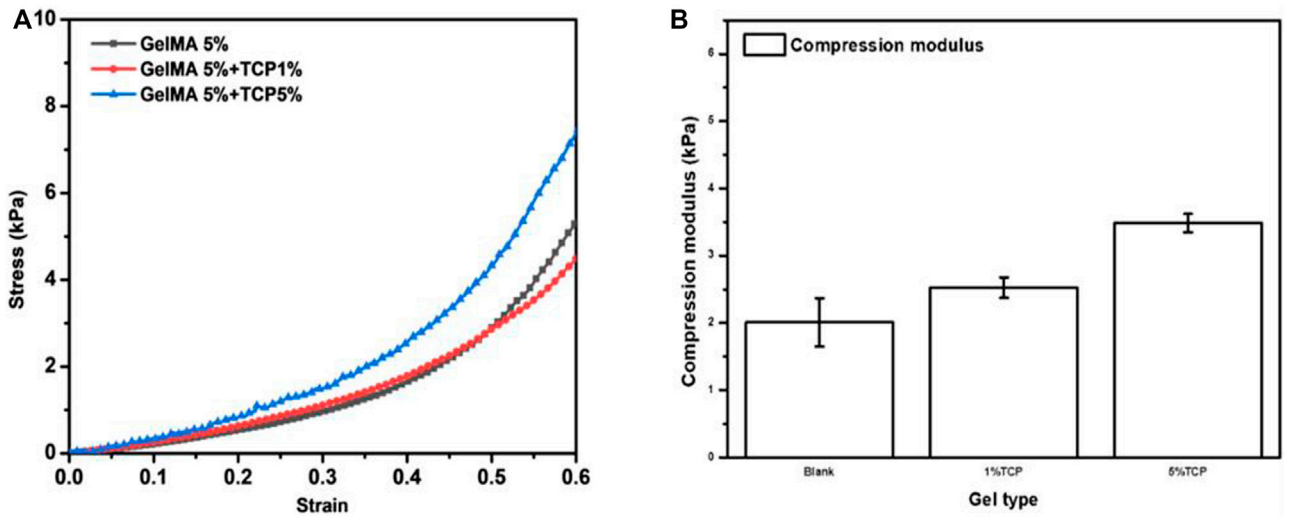

FIGURE 2 | Mechanical properties of GelMA/β-TCP hydrogels **(A)** The stress-strain curves of different hydrogels. **(B)** Anti-stress modulus of different hydrogel calculated by the changes in stress to strain (n = 4).

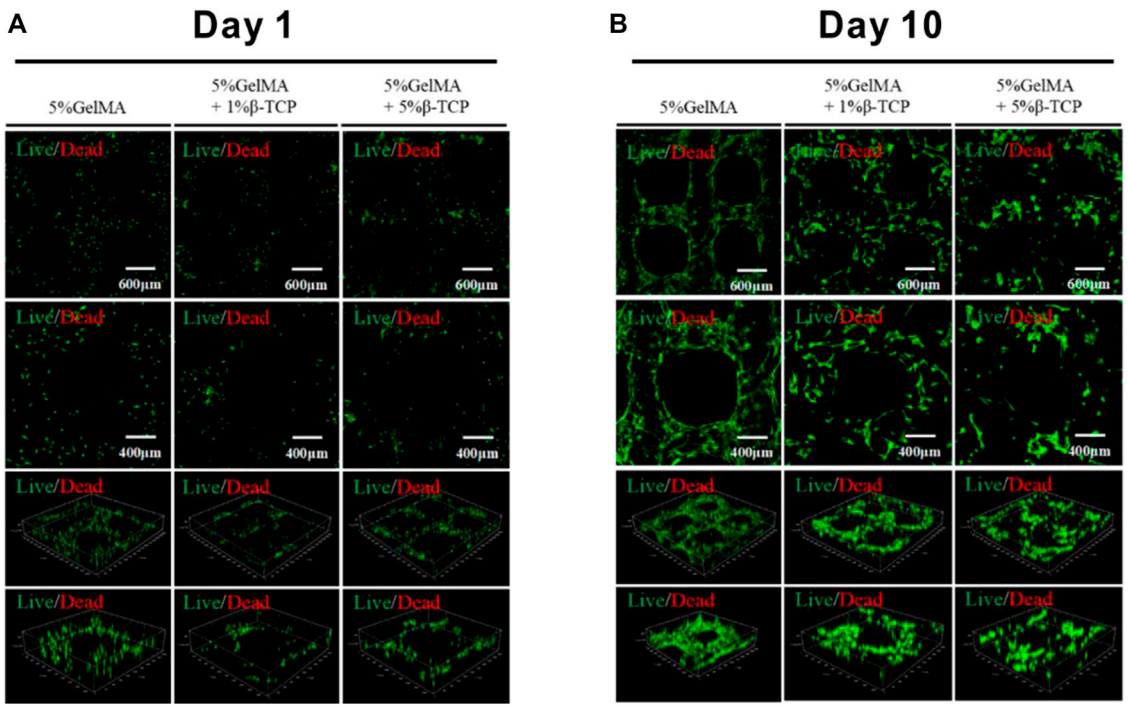

FIGURE 3 | Viability of BMSCs attached to the surface of hydrogel scaffolds. The surviving BMSCs attached to the different scaffolds were identified through immunofluorescence staining after incubation for 1 day **(A)** or 10 days **(B)**.

were removed after inoculation of 1 and 10 days for dead/alive staining analysis. 2 μM of calcein AM and 8 μM of propidium iodide (PI) were mixed for preparation of the working solution. The scaffold was washed thrice with 1×PBS. Then the prepared working solution was added and incubated with the cells for 45 min at room temperature. After incubation, the scaffolds were washed again with 1×PBS. Anti-fluorescence quenching agent was added into the samples and the samples were imaged by Olympus FV3000 scanning laser confocal microscope. Green fluorescence indicated the alive cells marked by the calcitanin AM, while red fluorescence indicated the dead cells marked with PI.

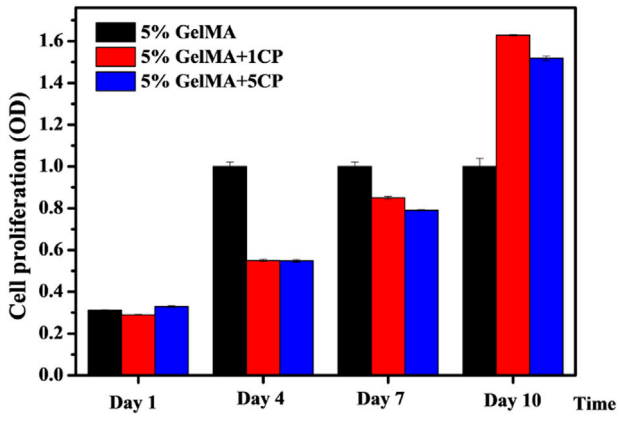

FIGURE 4 | Proliferation of rat BMSCs attached to the surface of GelMA/β-TCP hydrogel scaffolds. BMSCs were incubated into hydrogel scaffolds for culture. Cell proliferation was assessed from day 1 to day 10 using CCK8 assay (n = 4).

2.6 Effect of GelMA/β-TCP on the Morphology of BMSCs

For assessing the morphology of BMSCs in the GelMA/β-TCP scaffold, the scaffolds were treated with alcohol and DMEM/F12 medium as described above. Subsequently, the scaffolds were placed in 12-well plates, and each well was inoculated with 1×10^4 BMSCs for continuous culture of 10 days. The GelMA/β-TCP scaffolds were removed after inoculation for 10 days for cytoskeleton staining analysis. The scaffold was washed thrice with 1×PBS and immersed in 4% paraformaldehyde for 0.5 h and then washed 3 times. Then, 0.5% TritonX-100 was added into the scaffolds for 10 min. The washing operations were repeated as above. Subsequently, the cells loaded hydrogels were immersed into the 1 mg/ml phalloidine for 0.5 h and then transferred to the 1 μg/ml DAPI for 10 min. After staining of antibody, anti-fluorescence quenching agent was added to the scaffolds and stored at 4°C. For analysis of immunofluorescence staining results, images were collected by Olympus FV3000 scanning laser confocal microscope and analyzed for growth of BMSCs.

2.7 Effect of GelMA/β-TCP on Osteogenic Differentiation of BMSCs

For evaluation of osteogenic differentiation, the BMSCs loaded scaffolds were fixed with 4% paraformaldehyde for 15 min at room temperature. Subsequently, the scaffolds were washed thrice with 1×PBS. Subsequently, the scaffolds were stained with ALP dyes. BCIP/NBT is the common substrate for alkaline phosphatase. BCIP can be hydrolyzed to a highly reactive product that reacts with NBT to form an insoluble NBT-Formazan of dark blue or blue-purple color. The scaffolds were incubated with the dye at room temperature for 2 h. Then, the dyeing solution was removed and washed twice with distilled water to stop the color reaction. The cells were imaged by light microscopy.

3 RESULTS

3.1 Characterization of Hydrogel Scaffolds

We successfully prepared GelMA scaffolds via the 3D printing platform according to the methods described above. For improving the bio-absorbability and biomechanical properties, β-TCP was added into the reaction system to fabricate the hybrid GelMA/β-TCP hydrogel scaffolds. The microstructure of 5% GelMA (w/v) with 1% β-TCP (w/v) and 5% GelMA (w/v with 5% β-TCP (w/v) scaffolds was examined and the difference of stiffness and mesh pore size was investigated. The microstructure of 5% GelMA (w/v) with 1% β-TCP (w/v) scaffolds exhibited clear meshes, uniform pores, and uniform wire diameters (**Figure 1A**). The width of mesh pore ranged from 474 to 929 μm. The microstructure of 5% GelMA (w/v) with 5% β-TCP (w/v) scaffolds was similar with mesh pore widths ranging from 437 to 673 μm (**Figure 1B**). To further confirm the inner structure of hybrid scaffolds, we examined the microstructure of different hydrogels using SEM (**Figure 1C**). The pore wall of complete GelMA hydrogel was found to be smooth, and the pore wall roughness was increased with the addition of β-TCP from 1% to 5%. Some granular bulges on the smooth pore wall of the GelMA/β-TCP hydrogel were observable. The printed 3D hydrogel scaffolds freeze-dried were observed by scanning electron microscopy (**Figure 1D**). As shown in the results, the mesh aperture of Blank group was approximately 500–600 μm. By contrast, the mesh aperture of hybrid GelMA/β-TCP was approximately 600–800 μm. These results suggested that 3D hydrogel scaffolds fused with β-TCP are more conducive to the attachment and growth of stem cells.

3.2 Mechanical Properties of GelMA/β-TCP Hydrogels

The above results showed that we were able to print a relatively ideal structural morphology; however, this was far from enough for the use of biological scaffolds *in vivo*. Biological scaffolds must also have excellent biomechanical properties. Therefore, the mechanical properties of GelMA/β-TCP hydrogel were investigated. The anti-stress properties of GelMA, 5% GelMA (w/v) with incorporation of 1% β-TCP (w/v) and 5% GelMA (w/v) with incorporation of 5% β-TCP (w/v) hydrogels were tested. As shown in **Figure 2A**, the anti-stress ability of 5% GelMA (w/v) with the addition of 5% β-TCP (w/v) hybrid hydrogels was significantly greater than that of GelMA and 5% GelMA (w/v) with the addition of 1% β-TCP (w/v) hydrogel. When the tension was less than 0.5, there was no difference in the anti-stress strength of GelMA and 5% GelMA (w/v) with the addition of 1% β-TCP (w/v) hybrid hydrogels; however, when the tension exceeded 0.5, the anti-stress strength of GelMA was stronger than that of 5% GelMA (w/v) with the addition of 1% β-TCP (w/v). Moreover, we assessed the mechanical properties of the three different hydrogels. As shown in **Figure 2B**, the addition of β-TCP increased the anti-stress properties of hybrid hydrogels. These results suggested that the addition of β-TCP can improve the biomechanical properties of hydrogel scaffolds and contribute to its application for *in vivo* tissue repair.

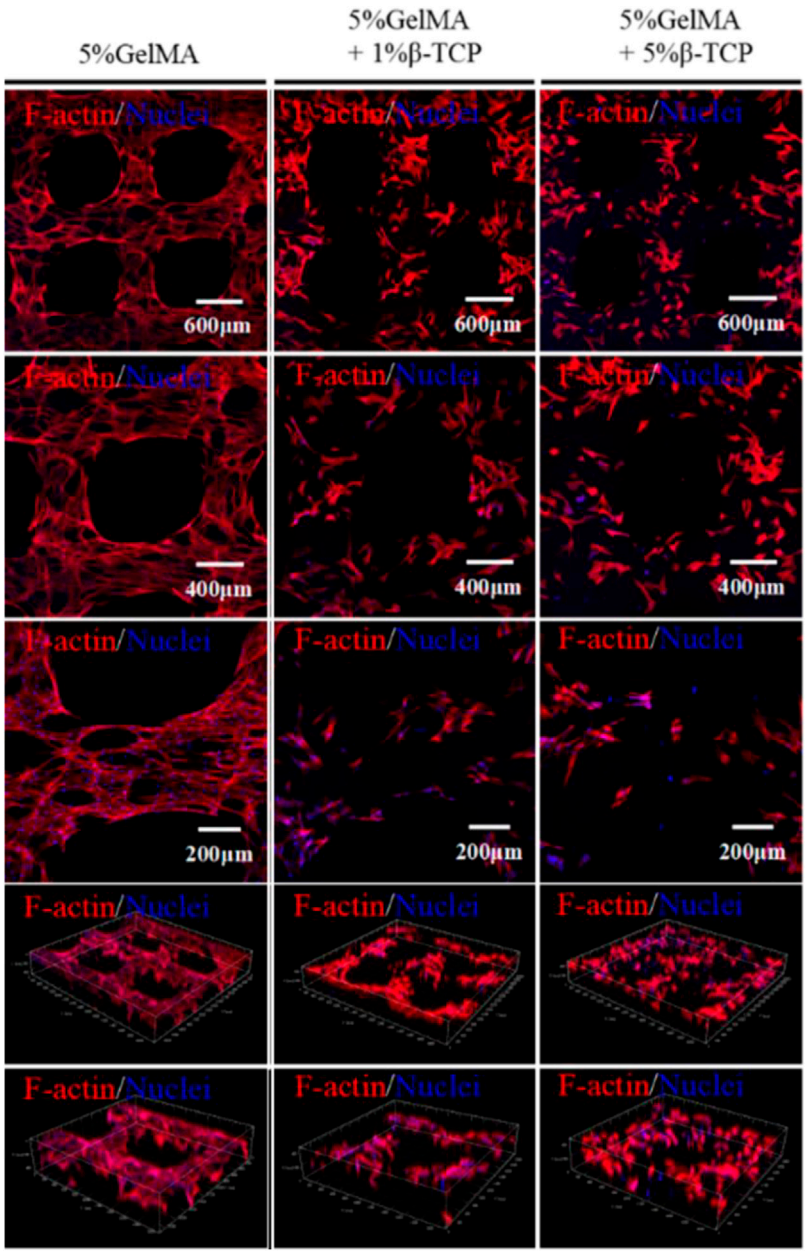

FIGURE 5 | Cytoskeleton structure of rat BMSCs attached to the surface of the GelMA/β-TCP hydrogel scaffolds. After continuous culture of 10 days, the GelMA/β-TCP hydrogel scaffold loaded with BMSCs was taken out for cytoskeleton staining with Rhodamine labeled Phalloidin, and nuclear staining with DAPI. Images were captured by scanning laser confocal microscope.

3.3 Survival of BMSCs on the Surface of GelMA/β-TCP Hydrogels

After successful preparation of the hybrid hydrogel scaffolds with uniform morphology and excellent bio-mechanical performance, we assessed whether BMSCs can survive on the surface of the scaffolds. BMSCs sourced from mice were incubated with the scaffolds. The survival of BMSCs was determined 1 day and 10 days after the inoculation, respectively. The survival rate of BMSCs was close to 100% after 1-day inoculation (**Figure 3A**). Further, the cells were evenly distributed on the surface of the scaffolds. After 10 days, the scaffolds attached with BMSCs were taken out for immunofluorescence staining with the AM/PI kit. As shown in **Figure 3B** the cell survival rate was >95%. Compared to the GelMA group, the BMSCs in the 5% GelMA with 1% β-TCP group and the 5% GelMA with 5% β-TCP group were more densely distributed. These results confirmed that the prepared scaffolds did not influence the activity of the attached cells.

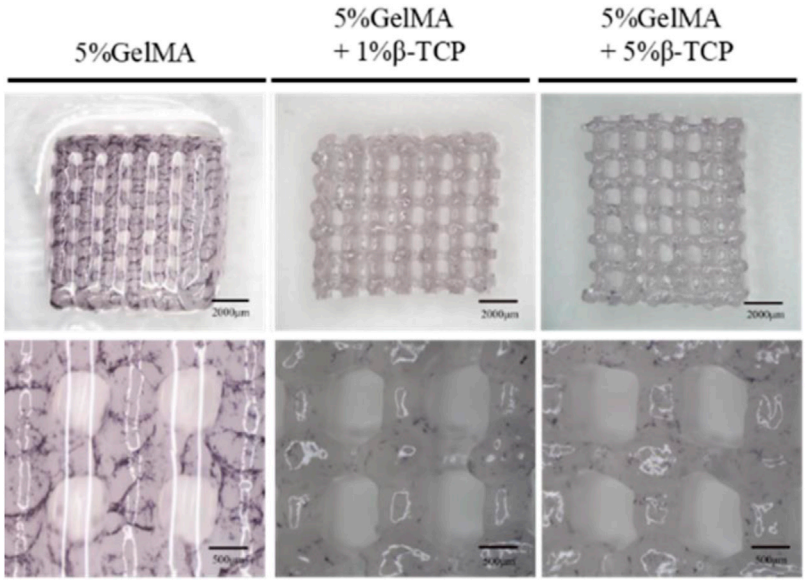

FIGURE 6 | Osteogenic ability of rat BMSCs attached to the surface of the GelMA/β-TCP hydrogel material. The hybrid hydrogel scaffolds loaded with BMSCs were cultured continuously for 21 days. ALP reaction was performed in the scaffolds, and then images were captured by optical microscope.

3.4 Proliferation of BMSCs on the Surface of GelMA/β-TCP Hydrogels

In order to reconstruct alveolar cleft, bionic scaffolds need to be able to induce bone, guide bone, and induce osteogenic differentiation of stem cells. Therefore, we explored the proliferation of rat BMSCs induced by the prepared hybrid scaffold. As shown in **Figure 4**, there was no significant difference in the proliferation of BMSCs on the surface of GelMA scaffolds and GelMA/β-TCP hybrid hydrogel scaffolds after 1 day. We also assessed the proliferation of BMSCs on day 4 and day 7. It was found that the proliferation of rat BMSCs attached on the surface of GelMA scaffolds was better than that of the other GelMA/β-TCP hybrid hydrogel scaffolds. However, after 10 days, the proliferation of rat BMSCs attached on the surface of GelMA/β-TCP hybrid hydrogel scaffolds was much better than that of GelMA scaffolds. These results suggested that with the extension of culture time, the GelMA/β-TCP hybrid hydrogel scaffolds were more conducive to the adhesion and proliferation of rat BMSCs. These findings indicate the suitability of hybrid hydrogel scaffolds fabricated by the GelMA/β-TCP for *in vivo* application for alveolar cleft reconstruction.

3.5 Morphology of Rat BMSCs Attached to the Surface of GelMA/β-TCP Hydrogel Scaffolds

The above experiments demonstrated that BMSCs could adhere to the hybrid hydrogel scaffolds and proliferate. To further verify that BMSCs were not abnormal proliferators, the morphology of rat BMSCs attached to the surface of GelMA/β-TCP hydrogel scaffolds was observed by fluorescence microscopy. When the GelMA/β-TCP hydrogel scaffolds loaded with BMSCs were cultured continuously for 10 days, the scaffold was removed for immunofluorescence staining of the skeleton. The coverage rate of BMSCs in the 5% GelMA with 1% β-TCP and 5% GelMA with 5% β-TCP groups was found to be lower than that in the 5% GelMA group (**Figure 5**). In addition, the morphology of the skeletons showed differences between them. We hypothesized that such differences were due to some biological behaviors such as cell differentiation.

3.6 Osteogenic Induction of Rat BMSCs on the Surface of GelMA/β-TCP Hydrogel Scaffolds

To further illustrate the influence of hydrogel scaffolds on the osteogenic ability of BMSCs in each group, the fabricated hydrogel scaffolds loaded with BMSCs were continuously induced and cultured for 21 days. Subsequently, the scaffolds were removed and subjected to alkaline phosphatase staining. Alkaline phosphatase expression was obvious in 5% GelMA group after 21 days (**Figure 6**). Lesser expression was found in 5% GelMA with 1% β-TCP and 5% GelMA with 5% β-TCP groups. These results indicated that the hydrogels composed of GelMA and β-TCP were inferior to GelMA hydrogel in terms of osteogenic induction ability, but the hydrogels fabricated with GelMA and β-TCP still exhibited partial osteogenic induction ability. These results showed that although the prepared GelMA/β-TCP hybrid hydrogel scaffolds showed limited osteogenic induction, it was sufficient for the reconstruction of alveolar cleft.

4 DISCUSSION

Reconstruction of alveolar cleft is an important step in the sequential treatment of cleft lip and palate. However, there are

still many controversies about the treatment of alveolar cleft. In the 1970s, Boyne and Sands (Boyne and Sands, 1972; Boyne and Sands, 1976) proposed the use of autologous cancellous bone for reconstruction and repair of alveolar cleft. In addition, they also suggested that bone grafting must be performed with autologous iliac cancellous bone before the emergence of cusp teeth in order to achieve good clinical results. Therefore, grafting of iliac cancellous bone mixed with dentition stage to repair alveolar cleft is widely used (Murthy and Lehman, 2005). Tissue regeneration engineering has developed rapidly in recent years. Tissue engineering scaffolds have been widely used as candidate graft materials for alveolar fissure reconstruction. This help reduce the occurrence of pain and complications by precluding the need for cutting the body bone. However, most tissue-engineered scaffolds have exhibited non-absorbability and non-deformability, which hinder tooth eruption and bone movement required for orthodontic treatment (Feinberg et al., 1989; Chin et al., 2005). Moreover, they are prone to shift when stressed during healing (Letic-Gavrilovic et al., 2003), failing to provide appropriate matrix for tooth movement and reconstruction of the dental arch. Therefore, development of bio-absorbable scaffold material with bone inducible activity is a key imperative for repair of alveolar cleft.

Based on the disadvantages of the bio-materials mentioned above, we sought to identify new materials that can be induced for bone induction. The GelMA hydrogel was first reported by Van den Bulcke in 2000 (Van Den Bulcke et al., 2000). GelMA hydrogel is mainly made up of methylacrylamide with Irgacure 2959 as light initiator, and the GelMA hydrogel is prepared by the illumination of UV light. The GelMA hydrogel has been successfully applied for the development of 3D vascular network. For example, Chen (Chen et al., 2012) and Lin (Lin et al., 2013) showed that endothelial cluster cells (ECFC) and mesenchymal stem cells (MSCs) loaded GelMA hydrogel can be used as attached stent for the study of vascular formation *in vivo* and *in vitro*. Moreover, the application of 3D printing technology allows fabrication of GelMA hydrogel with unique morphology, patterns, and 3D structure, which facilitates the provision of nutrients and oxygen to support the surrounding tissue cells and the removal of metabolic products. However, the mechanical performance of GelMA hydrogel is very poor, which is another key point in the design of scaffolds materials. The β-calcium phosphate (β-TCP) is a bio-ceramic that has the potential to improve biomechanical properties and can be used for the preparation of engineered bones via 3D printing techniques (Ma et al., 2019; Beheshtizadeh et al., 2021; Kaimonov et al., 2021). Here, we sought to combine the best of GelMA hydrogel and β-TCP and adjust the ratio of the two to achieve optimal performance of osteogenic scaffolds. We identified and prepared three different scaffolds of 5% GelMA without β-TCP, 5% GelMA with 1% β-TCP, and 5% GelMA with 5% β-TCP. Their microstructures were examined by SEM. We found that the printed structure of different scaffolds was clear with uniform pore size. Further the width of the grids was moderate, which is beneficial for the attachment of stem cells. In addition, we also explored the mechanical load performance of different hydrogels, and found that the anti-pressure performance of hydrogels improved with increase in the β-TCP ratio.

The affinity of BMSCs and hybrid hydrogels determines the biological activity of scaffolds for the reconstruction of alveolar cleft. We inoculated BMSCs into the hydrogel scaffolds for culture. After 10 days, the BMSCs were found to have attached on the hydrogel scaffolds. The cell survival rate was approximately 95%. Moreover, with the extension of incubation time, the hybrid gels were more conducive to the adhesion and proliferation of BMSCs. In addition, osteogenic ability is an important functional indicator of gel scaffolds. After 21 days of culture, the cells were analyzed by alkaline phosphatase staining. The results demonstrated the osteogenic ability of GelMA/β-TCP hybrid gels, which is important for the reconstruction of alveolar cleft.

In conclusion, we successfully developed novel graft materials of GelMA/β-TCP for alveolar cleft reconstruction. In our preliminary experiment, the 3D hybrid hydrogel materials of GelMA/β-TCP exhibited the basic properties required for the reconstruction of alveolar cleft. It was found to induce osteogenic differentiation of BMSCs. We believe that the technique can help improve the outcomes of clinical alveolar cleft reconstruction and expand the application of hydrogel scaffolds in the field of tissue engineering repair.

DATA AVAILABILITY STATEMENT

The raw data supporting the conclusion of this article will be made available by the authors, without undue reservation.

AUTHOR CONTRIBUTIONS

DL developed the concept, carried out the experiments, and performed statistical analyses. DL and BY collected information and wrote the manuscript. YC supervised the experiments and wrote the manuscript.

FUNDING

This research was funded by the internal fund from the Youth Pilot Project of the Guangzhou Women and Children's Medical Center (YIP-2018-038).

REFERENCES

Bajestan, M. N., Rajan, A., Edwards, S. P., Aronovich, S., Cevidanes, L. H. S., Polymeri, A., et al. (2017). Stem Cell Therapy for Reconstruction of Alveolar Cleft and Trauma Defects in Adults: A Randomized Controlled, Clinical Trial. *Clin. Implant Dent. Relat. Res.* 19 (5), 793–801. doi:10.1111/cid.12506

Beheshtizadeh, N., Azami, M., Abbasi, H., and Farzin, A. (2021). Applying Extrusion-Based 3D Printing Technique Accelerates Fabricating Complex

Biphasic Calcium Phosphate-Based Scaffolds for Bone Tissue Regeneration. *J. Adv. Res.* doi:10.1016/j.jare.2021.12.012

Benazzo, F., Botta, L., Scaffino, M. F., Caliogna, L., Marullo, M., Fusi, S., et al. (2014). Trabecular Titanium Can Induce *In Vitro* Osteogenic Differentiation of Human Adipose Derived Stem Cells without Osteogenic Factors. *J. Biomed. Mater. Res. Part A* 102, 2061–2071. doi:10.1002/jbm.a.34875

Boyne, P. J., and Sands, N. R. (1976). Combined Orthodontic-Surgical Management of Residual Palato-Alveolar Cleft Defects [J]. *Am. J. Orthod.* 70 (1), 20–37. doi:10.1016/0002-9416(76)90258-x

Boyne, P. J., and Sands, N. R. (1972). Secondary Bone Grafting of Residual Alveolar and Palatal Clefts. *J. Oral Surg.* 30 (2), 87–92.

Chen, Y. C., Lin, R. Z., Qi, H., Yang, Y., Bae, H., and Melero-Martin, J. M. (2012). Functional Human Vascular Network Generated in Photocrosslinkable Gelatin Methacrylate Hydrogels. *Adv. Funct. Mat.* 22, 2027–2039. doi:10.1002/adfm.201101662

Chin, M., Ng, T., Tom, W. K., and Carstens, M. (2005). Repair of Alveolar Clefts with Recombinant Human Bone Morphogenetic protein(rhBMP-2) in Patients with Clefts. *J. Craniofac Surg.* 16 (5), 778–789. doi:10.1097/01.scs.0000166802.49021.01

Cho-Lee, G. Y., García-Díez, E. M., Nunes, R. A., Martí-Pagès, C., Sieira-Gil, R., Rivera-Baró, A., et al. (2013). Review of Secondary Alveolar Cleft Repair. *Ann. Maxillofac. Surg.* 3 (1), 46–50. doi:10.4103/2231-0746.110083

Feinberg, S. E., Weisbrode, S. E., and Heintschel, G. (1989). Radiographic and Histological Analysis of Tooth Eruption through Calcium Phosphate Ceramics in the Cat. *Arch. Oral Biol.* 34 (12), 975–984. doi:10.1016/0003-9969(89)90055-1

Gimbel, M., Ashley, R. K., Sisodia, M., Gabbay, J. S., Wasson, K. L., Heller, J., et al. (2007). Repair of Alveolar Cleft Defects: Reduced Morbidity with Bonne Marrow Stem Cells in a Resorbable Matrix. *J. Craniofac Surg.* 18 (4), 895–901. doi:10.1097/scs.0b013e3180a771af

Hibi, H., Yamada, Y., Ueda, M., and Endo, Y. (2006). Alveolar Cleft Osteoplasty Using Tissue-Engineered Osteogenic Material[J]. *Int. J. Oral Maxillofac. Surg.* 35 (6), 551–555. doi:10.1016/j.ijom.2005.12.007

Hilkens, P., Fanton, Y., Martens, W., Gervois, P., Struys, T., Politis, C., et al. (2014). Pro-angiogenic Impact of Dental Stem Cells *In Vitro* and *In Vivo*. *Stem Cell Res.* 12, 778–790. doi:10.1016/j.scr.2014.03.008

Kaimonov, M. R., Safronova, T. V., Filippov, Y., Shatalova, T. B., and Preobrazhenskii, I. I. (2021). Calcium Phosphate Powder for Obtaining of Composite Bioceramics. *Inorg. Mater. Appl. Res.* 12 (1), 34–39. doi:10.1134/s2075113321010135

Klijn, R. J., van den Beucken, J. J., Félix Lanao, R. P., Veldhuis, G., Leeuwenburgh, S. C., Wolke, J. G., et al. (2012). There Different Strategies to Obtain Porous Calcium Phosphate Cements: Com Parison of Perform an Ceinaratskull Bone Augmentation Model. *Tissue Eng. Part A* 18 (11-12), 1171–1182. doi:10.1089/ten.TEA.2011.0444

LeGeros, R. Z. (2002). Properties of Osteoconductive Biomaterials: Calcium Phosphates. *Clin. Orthop. Relat. Res.* (395), 81–98. doi:10.1097/00003086-200202000-00009

Letic-Gavrilovic, A., Piattelli, A., and Abe, K. (2003). Nerve Growth Factor Beta (NGF Beta) Delivery via a collagen/hydroxyapatite(Col/HAp) Composite and its Effects on New Bone Ingrowth. *J. Mater Sci. Mater Med.* 14 (2), 95–102. doi:10.1023/a:1022099208535

Lin, R.-Z., Chen, Y.-C., Moreno-Luna, R., Khademhosseini, A., and Melero-Martin, J. M. (2013). Transdermal Regulation of Vascular Network Bioengineering Using a Photopolymerizable Methacrylated Gelatin Hydrogel. *Biomaterials* 34 (28), 6785–6796. doi:10.1016/j.biomaterials.2013.05.060

Liu, X., Wang, P., Chen, W., Weir, M. D., Bao, C., and Xu, H. H. (2014). Human Embryonic Stem Cells and Macroporous Calcium Phosphate Construct for Bone Regeneration in Cranial Defects in Rats. *Acta Biomater.* 10, 4484–4493. doi:10.1016/j.actbio.2014.06.027

Ma, C., Ma, Z., Yang, F., Wang, J., and Liu, C. (2019). Poly (Propylene Fumarate)/β-Calcium Phosphate Composites for Enhanced Bone Repair[J]. *Biomed. Mater.* 14 (4), 045002. doi:10.1088/1748-605x/ab12ae

Middleton, J. C., and Tipton, A. J. (2000). Synthetic Biodegradable Polymers as or Thopaedic Devices. *Biomaterials* 21 (23), 2335–2346. doi:10.1016/s0142-9612(00)00101-0

Murthy, A. S., and Lehman, J. A. (2005). Evaluation of Alveolar Bone Grafting: a Survey of ACPA Teams. *Cleft Palate Craniofac J.* 42 (1), 99–101. doi:10.1597/03-045.1

Ramakrishna, S., Huang, Z. M., Kmar, G. V., Batchelor, A. W., Mayer, J., et al. (2004). *An Introduction to Biocomposites*. 5 Toh Tuck Link Singapore: London: Imperial College Press, 36. doi:10.1142/9781860945205_0001

Sousa, B. R., Parreira, R. C., Fonseca, E. A., Amaya, M. J., Tonelli, F. M., Lacerda, S. M., et al. (2014). Human Adult Stem Cells from Diverse Origins: an Overview from Multiparametric Immunophenotyping to Clinical Applications. *Cytom. A* 85, 43–77. doi:10.1002/cyto.a.22402

Van Den Bulcke, A. I., Bogdanov, B., De Rooze, N., Schacht, E. H., Cornelissen, M., and Berghmans, H. (2000). Structural and Rheological Properties of Methacrylamide Modified Gelatin Hydrogels. *Biomacromolecules* 1, 31–38. doi:10.1021/bm990017d

Conflict of Interest: The authors declare that the research was conducted in the absence of any commercial or financial relationships that could be construed as a potential conflict of interest.

Publisher's Note: All claims expressed in this article are solely those of the authors and do not necessarily represent those of their affiliated organizations, or those of the publisher, the editors and the reviewers. Any product that may be evaluated in this article, or claim that may be made by its manufacturer, is not guaranteed or endorsed by the publisher.

Copyright © 2022 Luo, Chen and Chen. This is an open-access article distributed under the terms of the Creative Commons Attribution License (CC BY). The use, distribution or reproduction in other forums is permitted, provided the original author(s) and the copyright owner(s) are credited and that the original publication in this journal is cited, in accordance with accepted academic practice. No use, distribution or reproduction is permitted which does not comply with these terms.

frontiers | Frontiers in Bioengineering and Biotechnology

ORIGINAL RESEARCH
published: 17 June 2022
doi: 10.3389/fbioe.2022.900274

A Modified Hyaluronic Acid–Based Dissolving Microneedle Loaded With Daphnetin Improved the Treatment of Psoriasis

Shiya Peng[1†], Liuhanghang Cheng[2,3,4†], Qian Wu[1], Yuanchao Li[1], Lei Ran[1], Wei Wang[1], Ke Huang[1], Rong Zhu[1], Sihong Xue[1], Chunli Zhou[1], Weidong Zhu[5,6], Biao Cheng[6], Xiaobing Fu[2,3,4] and Rupeng Wang[1]**

[1]Department of Dermatology and Rheumatology Immunology, Xinqiao Hospital, Third Military Medical University (Army Medical University), Chongqing, China, [2]Research Center for Tissue Repair and Regeneration Affiliated to the Medical Innovation Research Department and Fourth Medical Center, PLA General Hospital and PLA Medical College, Beijing, China, [3]PLA Key Laboratory of Tissue Repair and Regenerative Medicine and Beijing Key Research Laboratory of Skin Injury, Repair and Regeneration, Beijing, China, [4]Research Unit of Trauma Care, Tissue Repair and Regeneration, Chinese Academy of Medical Sciences, Beijing, China, [5]The First School of Clinical Medicine, Southern Medical University, Guangzhou, China, [6]Department of Burn and Plastic Surgery, General Hospital of Southern Theater Command, Guangzhou, China

Psoriasis is a common chronic immune-inflammatory disease. Challenges exist in the present treatment of psoriasis, such as difficulties in transdermal drug administration and severe side effects. We hope to achieve a better therapeutic outcome for psoriasis treatment. By using modified soluble microneedles (MNs) loaded with daphnetin, the psoriasis symptoms of mice, the abnormal proliferation of keratinocytes, and the secretion of inflammatory factors were significantly reduced. *In vitro*, daphnetin is proven to inhibit the NF-κB signaling pathway and to inhibit the proliferation of HaCaT cells and the release of inflammatory factors, especially CCL20. This research showed that the modified microneedle loaded with daphnetin optimized transdermal drug delivery and relieved the symptoms of psoriasis more effectively. The novel route of Daph administration provides a future research direction for the treatment of psoriasis.

Keywords: psoriasis, daphnetin, hyaluronic acid microneedles, inflammatory factor, CCL20

OPEN ACCESS

Edited by:
Rui Guo,
Jinan University, China

Reviewed by:
Bing Tang,
First Affiliated Hospital of Sun Yat-sen University, China
Wei Wang,
Tianjin University, China

****Correspondence:***
Xiaobing Fu
fuxiaobing@vip.sina.com
Rupeng Wang
wrp71@163.com

[†]These authors have contributed equally to this work

Specialty section:
This article was submitted to Biomaterials, a section of the journal Frontiers in Bioengineering and Biotechnology

Received: *20 March 2022*
Accepted: *04 April 2022*
Published: *17 June 2022*

Citation:
Peng S, Cheng L, Wu Q, Li Y, Ran L, Wang W, Huang K, Zhu R, Xue S, Zhou C, Zhu W, Cheng B, Fu X and Wang R (2022) A Modified Hyaluronic Acid–Based Dissolving Microneedle Loaded With Daphnetin Improved the Treatment of Psoriasis. Front. Bioeng. Biotechnol. 10:900274. doi: 10.3389/fbioe.2022.900274

1 INTRODUCTION

Characterized by its skin erythema and scales symptomatically and hyperkeratosis with dyskeratosis and massive lymphocyte infiltration pathologically, psoriasis, as a common chronic immune disease, has affected over 125 million people worldwide (Nestle et al., 2009; Lowes et al., 2014; Armstrong and Read, 2020; Vicic et al., 2021). Skin damage is triggered and aggravated by the Koebner phenomenon (Weiss et al., 2002). The progression of psoriasis is associated with a variety of cells types, including dendritic cells, neutrophils, endothelial cells, fibroblasts, keratinocytes, and lymphocytes, among which, keratinocytes and T cells play an important role in the inflammatory response of psoriasis (Georgescu et al., 2019; Shin et al., 2020). Keratinocytes proliferate abnormally under the stimulation of many factors and secrete a series of chemokines such as CXCL1, CXCL2, CXCL8, and CCL20 (8). These chemokines recruit a variety of inflammatory cells to infiltrate locally and produce IL-1β, IL-23, TNF-α, and other inflammatory factors with keratinocytes to amplify the inflammatory response of psoriasis (Albanesi et al., 2018). T cells, especially Vγ4+ T cells, play a key role among the recruited inflammatory cells (Zhu et al., 2017). CCR6-

expressing Vγ4+ T cells can be recruited by CCL20 and secrete IL-17A, IL-22, and IFN-γ in response to IL-1β, IL-23, and TNF-α (Homey et al., 2000). IL-17A, IL-22, and IFN-γ can promote the abnormal proliferation of keratinocytes to form a positive feedback loop (Furue et al., 2020a) and continuously aggravate the inflammatory response of psoriasis. The clearance of CCL20 has been proven to significantly decrease the infiltration of γδ T cells in mice and relieve the symptoms of psoriasis (Mabuchi et al., 2013). Therefore, reducing the release of inflammatory factors associated with epidermal cells and inflammatory cells is one of the important therapeutic concepts (Kim et al., 2021).

Daphnetin (7,8-dihydroxycoumarin) is isolated from Daphne Korean Nakai and used for cancer and inflammatory disease treatment because of its antiproliferation and anti-inflammation effects (Pei et al., 2021). Previous research has shown the therapeutic effectiveness of Daph (in a cream form) in a psoriasis mouse model (Gao et al., 2020). Daph was reported to inhibit the abnormal proliferation of keratinocytes by inhibiting the NF-κB signaling pathway, thus reducing the release of inflammatory factors and alleviating the symptoms of psoriasis. The effect of Daph on Vγ4+ T cells, however, has not been studied, and the expression of CCL-20, a key chemokine in the inflammatory ring between keratinocytes and Vγ4+ T cells, was not measured. In addition, in previous studies, Daph could only inhibit and improve psoriasis lesions and did not show a complete cure effect, so its therapeutic effect needs to be further improved.

Despite the acceptable therapeutic effectiveness of Daph cream in psoriasis, even and continuous intradermal drug distribution is expected. The thickened stratum corneum in psoriasis also affects the transdermal absorption of topical drugs. Therefore, instead of cream, we chose hyaluronic acid (HA) microneedles (MNs), which have been proven in many studies to be effective in intralesional drug delivery (Huang et al., 2020; Liu et al., 2020). In prior studies, hyaluronic acid–based soluble MN patches loaded with methotrexate for intralesional administration have also been shown to improve the therapeutic efficacy in psoriasis and reduce the side effects compared with oral administration (Du et al., 2019). However, there is no relevant study on the topic of soluble MNs loaded with Daph in psoriasis. In addition, we have improved the MNs by adding polyvinyl acetate (PVA) as a matrix and cellulose nanocrystals (CNCs) to enhance the strength of the needle tip.

In this study, we use the modified MN combined with Daph as described previously to improve the treatment of psoriasis at a lower drug dosage. The changes in keratinocytes and Vγ4+ T cells and the expression of key inflammatory factors released by them were detected *in vivo*. *In vitro*, we used mRNA sequencing and other techniques to comprehensively detect the effect of Daph on HaCaT cells and on the release of CCL-20 and the mechanism.

2 MATERIALS AND METHODS

2.1 Preparation of the HA/PVA/CNC Patches

First, 2 g CNC was dissolved in 18 ml 45% concentrated sulfuric acid and reacted in a water bath at 45°C for 6 h. The reaction was stopped with 200 ml of deionized water, and the suspension was centrifuged (3000 r/min). A dialysis bag was used for dialysis for 3 days until the pH of the suspension was close to neutral, and the suspension was stored at −20°C. The suspension was then lyophilized at -80°C to obtain CNC powder. Daph was dissolved in absolute ethanol (0.01%, w/v). For the preparation of the Daph-loaded MN patch, Daph solution was added to the dimethylsiloxane (PDMS) mold and bubbles were removed in a vacuum oven. CNC powder was dissolved in deionized water at room temperature (0.1%, w/v) and then placed in the PDMS mold and bubbles were removed in a vacuum oven. After the CNC was dried, HA solution was placed in the PDMS mold, and the bubbles were removed in a vacuum oven. The excess HA solution was removed, and PVA solution was added to the PDMS mold and the bubbles were removed in a vacuum oven. The PDMS mold was placed in the dark at room temperature for 4 days, and PVA solution was added four times during the process. Finally, the tips of the needle consisted of 30% HA and 0.1% CNC, and the substrate consisted of 30% PVA (**Supplementary Figure S1**).

2.2 Properties of the Microneedle Patches

2.2.1 Infrared Spectroscopy

Three–five mg CNC sample and potassium bromide powder are fully ground and mixed in a mortar. An appropriate amount of powder was pressed into tablets (20 mmHg, 5 min) and detected by using a Fourier infrared spectrometer (Bruker, Germany) at 4000–500 cm-1.

2.2.2 X-Ray Diffraction Pattern of Cellulose Nanocrystal

Rheological properties were detected by a 20-mm diameter stainless steel parallel plate swivel (Bruker, Germany). G′ represented the elastic modulus of the samples, and G″ represented the viscous modulus. At room temperature, the fixed strain was 1% and time scanning was performed and G′ and G″ were recorded. Dynamic strain scanning was then performed at room temperature from 0.1 to 1000 Hz to determine the linear viscoelastic range of hydrogels.

2.2.3 Cellulose Nanocrystal Particle Size Determination

The particle size of the CNC was determined by a Zeta Sizer Nano ZS (Malvern, England).

2.2.4 Transmission Electron Microscopy Characterization of Cellulose Nanocrystal

The microscopic characterization of the CNC was determined by transmission electron microscopy (Hitachi, Japan).

2.2.5 Appearance of the Microneedle Patches

The MN patch was put on an Mshot stereomicroscope (Mingmei, China), and the tip area of the patches was photographed. The freeze-dried patches were pasted on the copper table with carbon conductive adhesive and observed by using a scanning electron microscope (Philips, Netherlands).

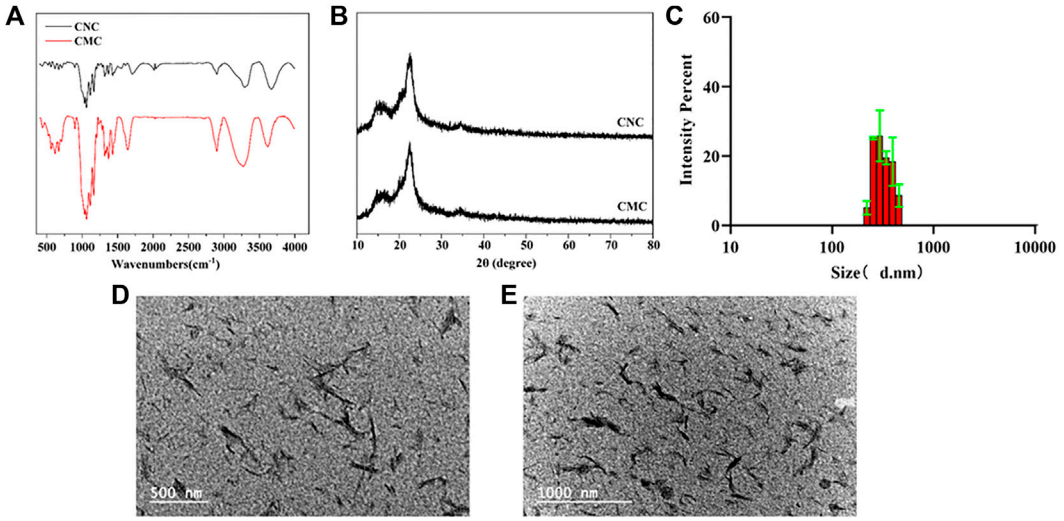

FIGURE 1 | Modification and characterization of the CNC: **(A)** Fourier transform infrared spectra of the CNC and CMC; **(B)** X-ray diffraction patterns of the CNC and CMC; **(C)** DLS image of the CNC; and **(D,E)** TEM images of the CNC at different magnifications. Data are shown as mean ± SE (*$p < 0.05$; **$p < 0.01$).

2.2.6 Tip Strength of the Microneedle Patches

The MN patch was put on the sample table of a universal material testing machine (BOSE, United States). The tip of the patch was up and compressed to 0.3 mm at a constant rate of 0.01 mm/s. The single-needle strength was calculated from the force recorded by the instrument, and the shape changes in the needle tip after compression were photographed by using a digital camera.

2.2.7 *In Vivo* Biocompatibility of the Microneedle Patches

The patches were pressed on the skin of nude mice for 5 min. The changes in the acupuncture area were observed at different time points and photos were taken.

2.3 *In Vivo* Puncture and Drug Release of the HA/PVA/CNC Patches

2.3.1 Penetration Test

The patch was pressed on isolated swine skin for 2 min, and then the tissue was fixed with 4% paraformaldehyde, embedded in paraffin, and sectioned. After hematoxylin and eosin (H&E) staining, the penetration was observed under a microscope.

2.3.2 Puncture Dissolution Test of the Tips

The patches were pressed on the back skin of nude mice and removed after 10 s, 30 s, 1, 2, and 5 min. The dissolution of the tips before and after puncture was observed and photographed under a light microscope.

2.3.3 Fluorescence Confocal Drug Permeation Test

Hydrophobic adriamycin was loaded onto the needle tip as a model fluorescent molecule since Daph was insoluble in water and its fluorescence was weak. After 0.5 h of swine skin puncture, the fluorescence penetration depth of needle tip drugs was scanned by using a laser confocal microscope (Zeiss, Germany).

2.4 Animals and Psoriasis-like Inflammation Model

The female C57/BL6 mice were obtained from the Experimental Animal Center of the Army Medical University and kept at 22–24°C and 50% humidity. All the mice had free access to food and water, and every mouse was kept in a cage.

All the mice were anesthetized with 1% pentobarbital solution (Sigma, United States), and a 2.5*3 cm area was selected on the back of the mouse and shaved carefully. Fifteen mice were randomized into five groups: control group (normal group), imiquimod (IMQ) group, Daph group, vehicle group, and vehicle + Daph group. Each mouse was applied with 62.5 mg IMQ ointment on the prepared back skin once daily, except for the control group. Gauze containing Daph (0.1 mg) was applied on the molding area of the Daph group and renewed every day. The vehicle group and vehicle + Daph group were treated once daily with Daph patches and Daph-free patches, respectively. Photos of the experimental skin area of all the mice were taken once a day, and all mice were killed on the seventh day for follow-up detection.

2.5 Psoriasis Area Severity Index (PASI) Score and Histological Analysis

The erythema and scales of mice in different groups were scored by the psoriasis area severity index (PASI) (41): 0, none; 1, slight; 2, moderate; 3, severe; and 4, very severe. The skin on the back modeling area was fixed with 4% paraformaldehyde dehydrated, paraffin-embedded, and made into 5-μm paraffin sections. Hematoxylin (Beyotime, China) and eosin (H&E) staining was performed for sections of each group. All sections were observed and counted under an optical

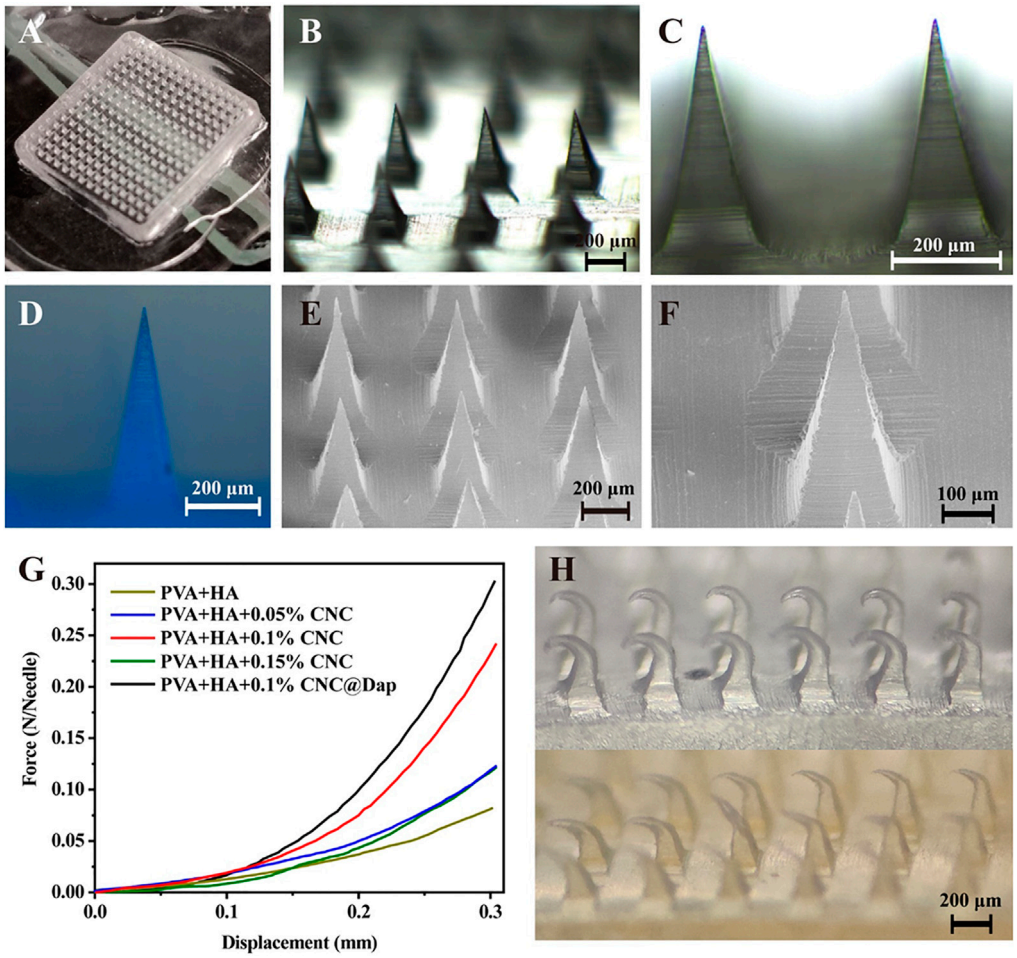

FIGURE 2 | Morphology and mechanical properties of the MN were determined. **(A–C)** Morphology of a blank MN under different magnification of an optical microscope. **(D)** Fluorescence image of a MN loaded with Daph at a scale of 200 μm. **(E, F)** Images of an MN under SEM at scales of 100 and 200 μm. **(G, H)** Test results of mechanical properties of the MN and optical microscope images of a blank MN (above) and drug-loaded MN (below) after compression, the microneedles in the blank and drug loading groups had corresponding morphological changes **(H)**.

microscope. Image-pro Plus 6.0 was used for the calculation of the epithelial thickness of the skin.

2.6 Immunohistochemistry and Immunofluorescence Staining

Gradient concentrations of xylene and alcohol were used for paraffin section dewaxing and hydration, and then the sections were heated for antigen retrieval. After cooling to room temperature, the sections were soaked in 3% H_2O_2 solution to inactivate the endogenous peroxidase (only for immunohistochemistry). All sections were treated with 10% goat serum for 30 min to block the antigen and then incubated with primary antibodies at 4°C overnight. The secondary antibody (Zhongshan Biology Co. Ltd, China) corresponding to the primary antibody was incubated at room temperature for 30 min. For immunohistochemistry staining, diaminobenzidine was used for antibody staining and hematoxylin (Beyotime, China) for nuclear staining. For immunofluorescence staining, DAPI was used for nuclear staining. The results were observed and photographed under a microscope (Olympus, Japan).

The primary antibodies used are described as follows: IL-1β (1: 200, Abcam, United Kingdom); IL-6 (1:200, Abcam, United Kingdom); IL-8 (1:200, Bioworld, United States); K1 (1:200, Abcam, United Kingdom); K6 (1:200, Thermo Fisher Scientific, United States); TNF-α (1:200, Abcam, United Kingdom); IL-23 (1:200, Abcam, United Kingdom);

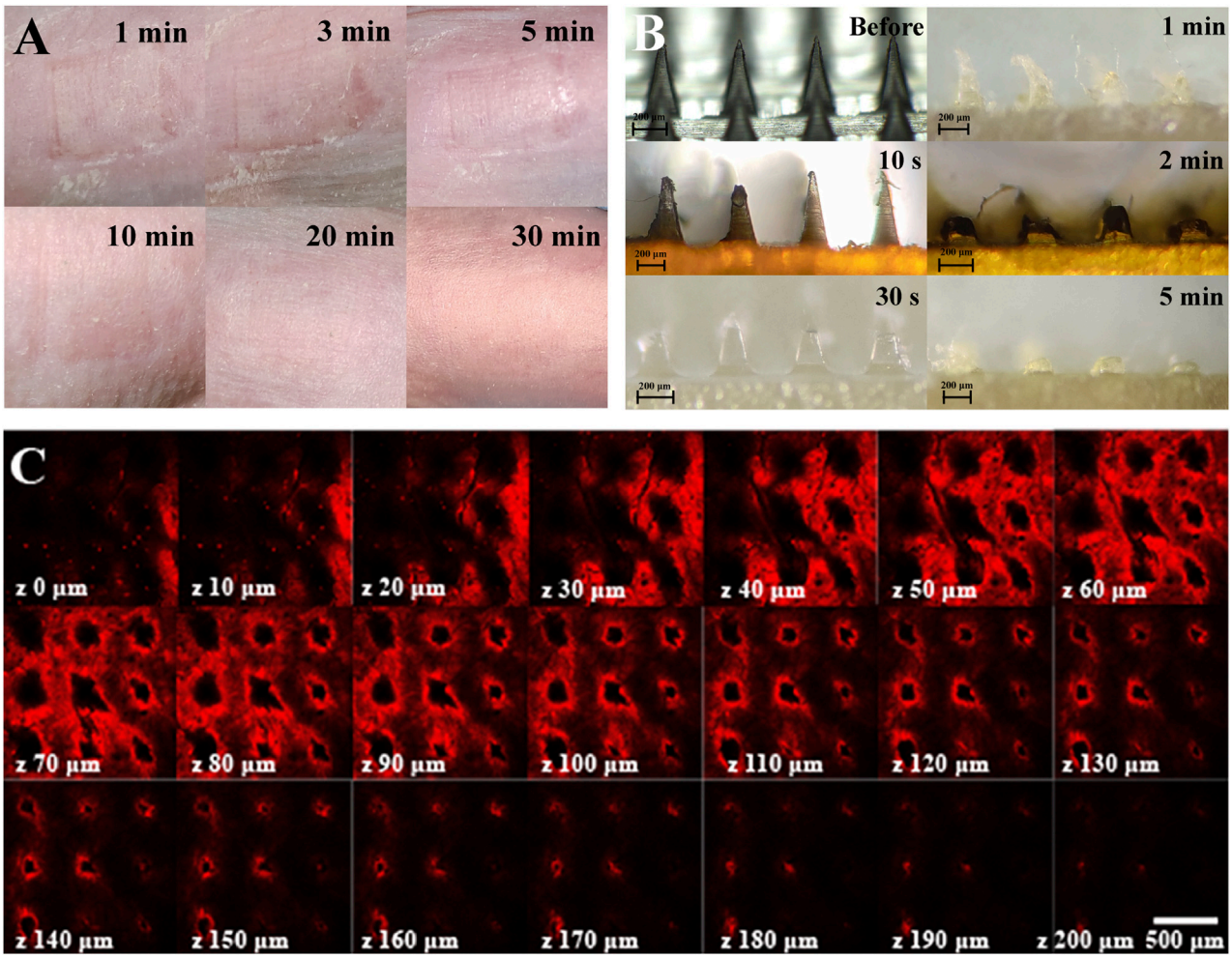

FIGURE 3 | Skin puncture test and drug release characterization of an MN. **(A)** Recovery of the skin puncture site *in vivo*. **(B)** Dissolved state of the MN in pig skin punctured by the MN at different time points. **(C)** Laser confocal image of drug penetration depth of fluorescein-loaded, MN-pierced pig skin, the scale is 500 μm.

CCL20 (1:100, Abcam, United Kingdom); IL-22; IL-17 (1:250, Abcam, United Kingdom); IFN-γ (1:200, Abcam, United Kingdom); and BrdU (Abcam, United Kingdom).

2.7 Isolation of Dermal Cells and Flow Cytometry

Skin samples were obtained from the back modeling area and the subcutaneous fascia was scraped off, then treated with 0.5% trypsin/GNK solution at 37°C for 2 h. After that, the dermis and epidermis were separated, The separated dermis and epidermis were cut into particles and then digested at 37°C for 1 h. Finally, the single-cell suspension was prepared by filtration with a 70-μm screen.

The single-cell suspensions were stained with monoclonal flow cytometry antibodies. For cell surface marker staining, anti CD16/32 was used for the nonspecific binding site and incubated with antibodies for 30 min at room temperature. For intracellular markers, the cells were incubated with a cocktail for 4 h and then stained for surface markers. After that, the cells were fixed with BD Cytofix Buffer and permeabilized with a Perm/Wash reagent. Finally, the cells were stained by intracellular antibodies and detected by using an Attune Acoustic Focusing Cytometer (Attune, Applied Biosystems AB, United States). The data were analyzed by Flowjo software.

The antibody used is described as follows: CD3 (BD Bioscience, United States); Vγ4 (BD Bioscience, United States); and IL-17 (BD Bioscience, United States).

2.8 Cell Culture and Biological Functions

Human HaCaT cells (Chinese Academy of Sciences, China) were cultured in a 5% CO_2 incubator at 37°C. The cells were passaged when they covered about 70% area of the culture bottle. The corresponding stimulation was performed as follows: the control group was cultured by a completed DMEM; the IMQ group was stimulated by 10 μg/ml IMQ; the Daph group was stimulated by 20 μM Daph; and the IMQ + Daph group was stimulated by both 10 μg/ml IMQ and 20 μM Daph.

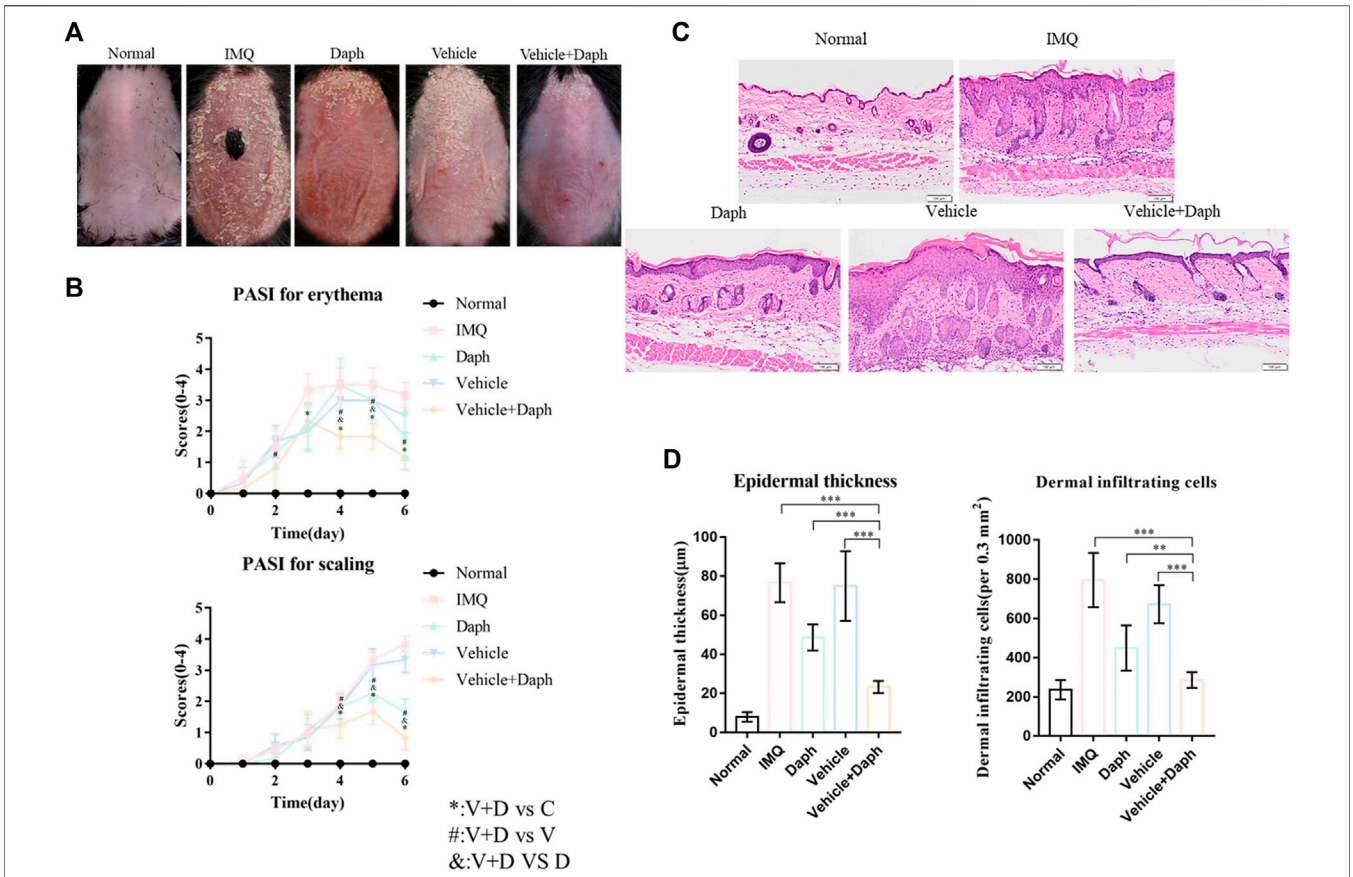

FIGURE 4 | Symptoms and histological results of psoriasis-like mice in different groups. **(A)** Photos of psoriasis modeling sites in different groups of mice. **(B)** H&E staining of psoriasis models in different groups of mice. **(C)** PASI scores of psoriatic mice in different groups. **(D)** Epidermal thickness and the number of inflammatory cells in each group. Data are shown as mean ± SE (*p < 0.05; **p <0.01).

2.8.1 Cytotoxicity

Cytotoxicity was detected by the CCK-8 method. The HaCaT cell suspension was cultured in a 96-well plate (2,000 cells/well). After cell adhesion, stimulating factors were added to the medium as mentioned previously. A total of 10 μL CCK-8 was added to the well after 0, 12, 24, 48, and 72 h and incubated at 37°C for 4 h. An OD value of 450 nm was detected by a microplate reader.

2.8.2 Cell Proliferation

An Edu test kit (Invitrogen, United States) was used for the detection of cell proliferation. According to the instruction, 5 μmol/L Edu was added into a well 3 h before the cells were stained. Finally, the result was detected by using a flow cytometer.

2.8.3 Apoptosis

HaCaT cells were collected after grouping stimulation was performed as described previously and washed in PBS. The cells were resuspended in 200 μL binding buffer (1×) and then treated according to the instruction of an Annexin V-FITC apoptosis kit (Thermo Fisher Scientific, United States). The result was detected by using a flow cytometer.

2.9 RNA Contraction, Quantitative Real-Time PCR (qPCR), and Western Blot

For the skin sample, the tissue was ground in liquid nitrogen, and then the RNA was isolated by TRIzol reagent (Ambion Life Technologies, United States). For the cells, RNA was extracted by using TRIzol directly. After the quantification of RNA concentration, cDNA was synthesized by using a reverse transcription kit (Takara, Japan). The cDNA was treated according to the instruction of the qPCR kit, and the result was detected by using an instrument (CFX Connect™, BIO-RAD, United States).

Primers:

Mouse:

β-actin:5′- AGAGGGAAATCGTGCGTGAC-3′(forward)
5′- CAATAGTGATGACCTGGCCGT-3′(reverse)
IL-6:5′- ACAGAAGGAGTGGCTAAGGA-3′(forward)
5′- AGGCATAACGCACTAGGTTT-3′(reverse)
IL-23:5′- ACCAAAGGAGGTGGATAGG-3′(forward)
5′- GGCAACAGCCATAGCATT-3′(reverse)
IL-1β:5′- AGTTGACGGACCCCAAA-3′(forward)
5′- TCTTGTTGATGTGCTGCTG-3′(reverse)
IL-22:5′- ATCTCTGATGGCTGTCCTG-3′(forward)

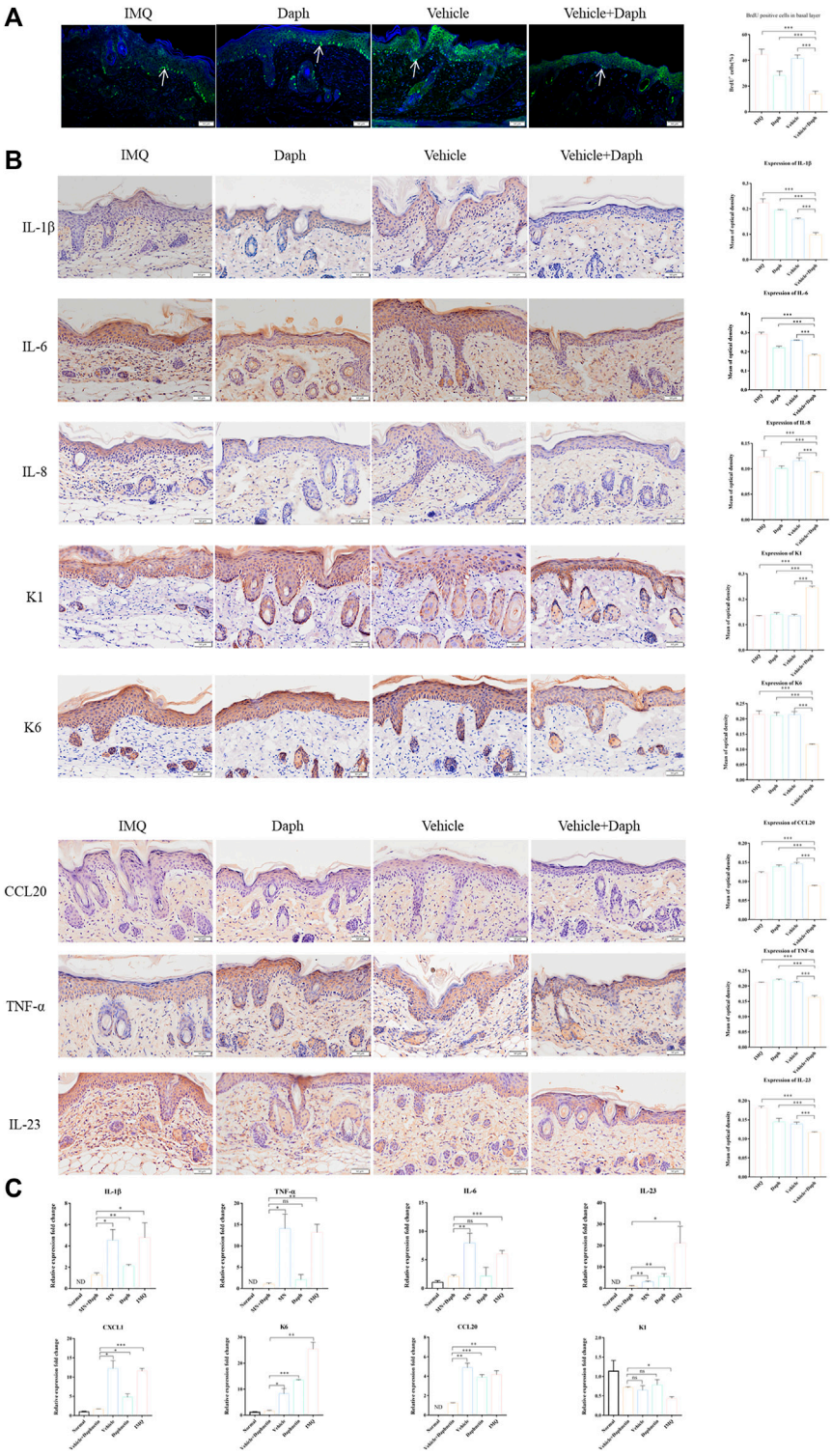

FIGURE 5 | Proliferation ratio of keratinocytes and the secretion of inflammatory factors in psoriatic mice were detected. **(A)** Proportion of keratinocytes in psoriasis modeling sites in each group; DAPI was labeled with blue fluorescence and BrdU was labeled with green fluorescence. **(B)** Immunohistochemical staining of major inflammatory factors (IL-1β, IL-23, TNF- α, IL-6, IL-8, and CCL20) secreted by keratinocytes and the expression of inflammatory factors were counted by the mean optical density. **(C)** qPCR detection results of skin-related inflammatory factors (IL-1β, IL-23, TNF- α, IL-6, CXCL1, and CCL20) at the mouse modeling site. Data are shown as mean ± SE (*$p < 0.05$; **$p < 0.01$).

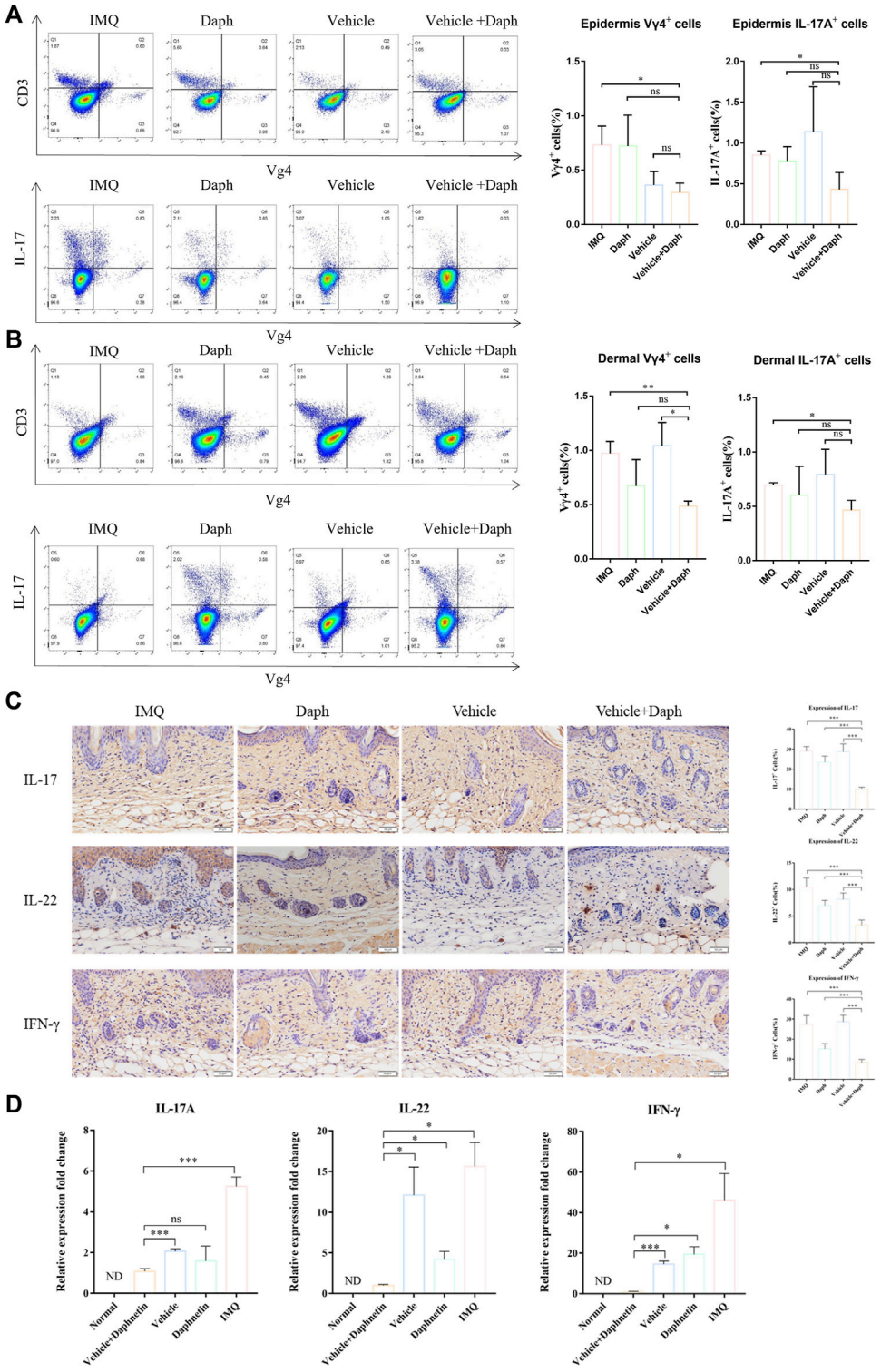

FIGURE 6 | Proportion of Vγ4+T cells and secretion of inflammatory factors in the skin at the modeling site were detected. **(A,B)** Proportion of Vγ4+T cells and the proportion of IL-17-secreting cells in the dermis and epidermis were detected by flow cytometry. **(C)** Immunohistochemical staining of major inflammatory factors (IL-17, IL-22, and IFN-γ) secreted by keratinocytes and the expression of inflammatory factors were counted by the proportion of positive cells. **(D)** PCR detection results of skin-related inflammatory factors (IL-17, IL-22, and IFN-γ) at the mouse modeling site. Data are shown as mean ± SE (*$p < 0.05$; **$p < 0.01$).

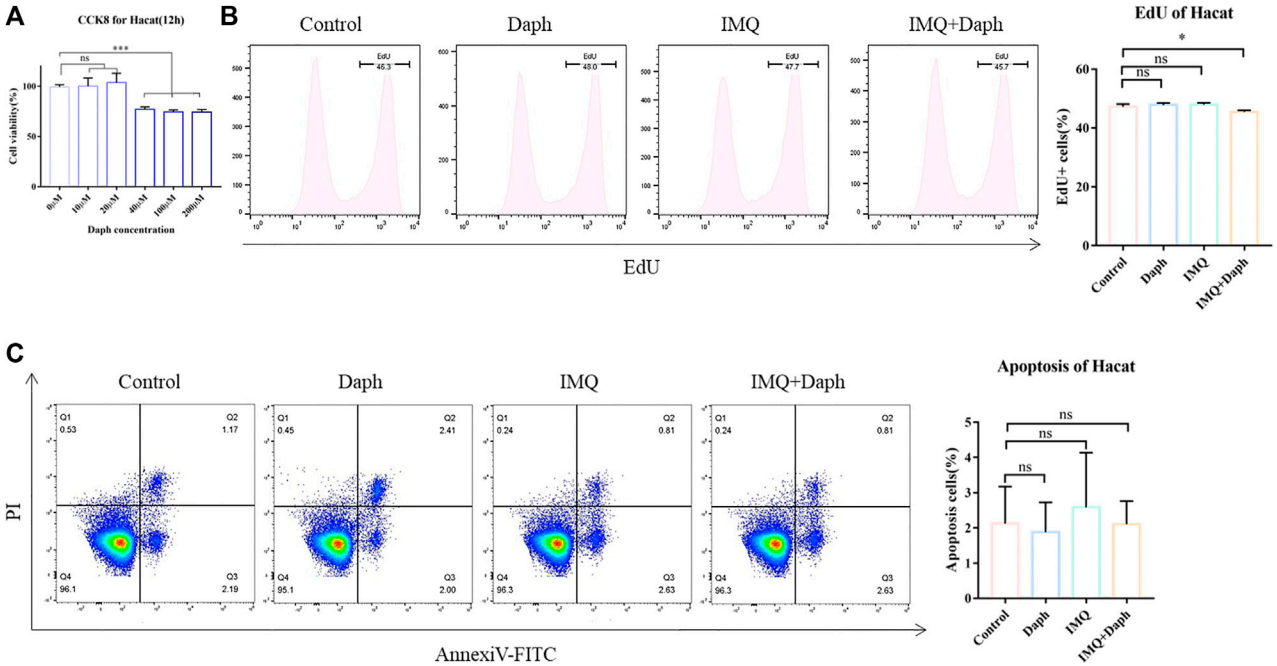

FIGURE 7 | HaCaT cell inflammation model was induced *in vitro* and the effect of Daph on its characteristics was detected. **(A)** CCK-8 was used to detect the effect of different concentrations of Daph on the activity of HaCaT cells. **(B)** Inflammatory state of HaCaT cells was induced by IMQ, and the effect of Daph on its proliferation was detected by an Edu test. **(C)** Effect of Daph on HaCaT cell apoptosis was detected. Data are shown as mean ± SE (*p < 0.05; **p < 0.01).

5′- GTATGGCTGCTGGAAGTTG-3′(reverse)
TNF-α:5′- CGCTGAGGTCAATCTGC-3′(forward)
5′- GGCTGGGTAGAGAATGGA-3′(reverse)
IL-17:5′- TCCAGGGAGAGCTTCATCTGTGTC-3′(forward)
5′- TTGGACACGCTGAGCTTTGAGG-3′(reverse)
KRT1:5′- GACTCGCTGAAGAGTGACCAGT-3′(forward)
5′- GGTCACGAACTCATTCTCTGCG-3′(reverse)
KRT6:5′- CTGTGAGTTTCTAATGGCCTGAGA-3′(forward)
5′- GAAACTTACATCACAGGACCAGTGA-3′(reverse)
IFN-γ:5′- CAGCAACAGCAAGGCGAAAAAGG-3′(forward)
5′- TTTCCGCTTCCTGAGGCTGGAT-3′(reverse)
CXCL1:5′- CTGGGATTCACCTCAAGAACATC-3′(forward)
5′- CAGGGTCAAGGCAAGCCTC-3′(reverse)
CXCL8:5′- CTTTGTCCATTCCCACTTCTGA-3′(forward)
5′- TCCCTAACGGTTGCCTTTGTAT-3′(reverse)
Human:
GAPDH:5′- TGTTGCCATCAATGACCCCTT-3′(forward)
5′- CTCCACGACGTACTCAGCG-3′(reverse)
CCL20:5′-TGCTGTACCAAGAGTTTGCTC-3′(forward)
5′- CGCACACAGACAACTTTTTCTTT-3′(reverse)
IL-6:5′- ACTCACCTCTTCAGAACGAATTG-3′(forward)
5′- CCATCTTTGGAAGGTTCAGGTTG-3′(reverse)
IL-8:5′- ACTGAGAGTGATTGAGAGTGGAC-3′(forward)
5′- AACCCTCTGCACCCAGTTTTC-3′(reverse)
TNF-α:5′- CCTCTCTCTAATCAGCCCTCTG-3′(forward)
5′- GAGGACCTGGGAGTAGATGAG -3′(reverse)
K6:5′- GGGTTTCAGTGCCAACTCAG-3′(forward)
5′- CCAGGCCATACAGACTGCGG -3′(reverse)

2.9.1 Western Blot

The protein of HaCaT cells was extracted by using RIPA lysis buffer (Beyotime, China) with protease and phosphatase inhibitors. A BCA protein assay kit (Thermo Fisher Scientific, United States) was used for the determination of protein concentration, and standard samples were prepared by boiling. The protein samples were passed through SDS-polyacrylamide gel electrophoresis and then transferred to the PVDF membrane. The membrane was blocked in 5% BSA and incubated with a primary antibody at 4°C overnight. After that, a secondary antibody was incubated at room temperature for 1 h. Finally, the membrane was incubated with a chemiluminescence substrate and visualized by the ChemiDoc™ XRS + system.

The antibody used is described as follows: CCL20 (1:1000, Abcam, United Kingdom); anti-p65 (1:1000, CST, United States); and -p-p65 (1:1000, CST, United States).

2.10 Ethics Approval

The animal study was reviewed and approved by the Medical and Ethics Committee of the Army Medical University, Chongqing, China.

2.11 Statistics Analysis

All data were analyzed by GraphPad Prism 5.0 and presented as the mean ± SD. p value <0.05 was considered statistically significant.

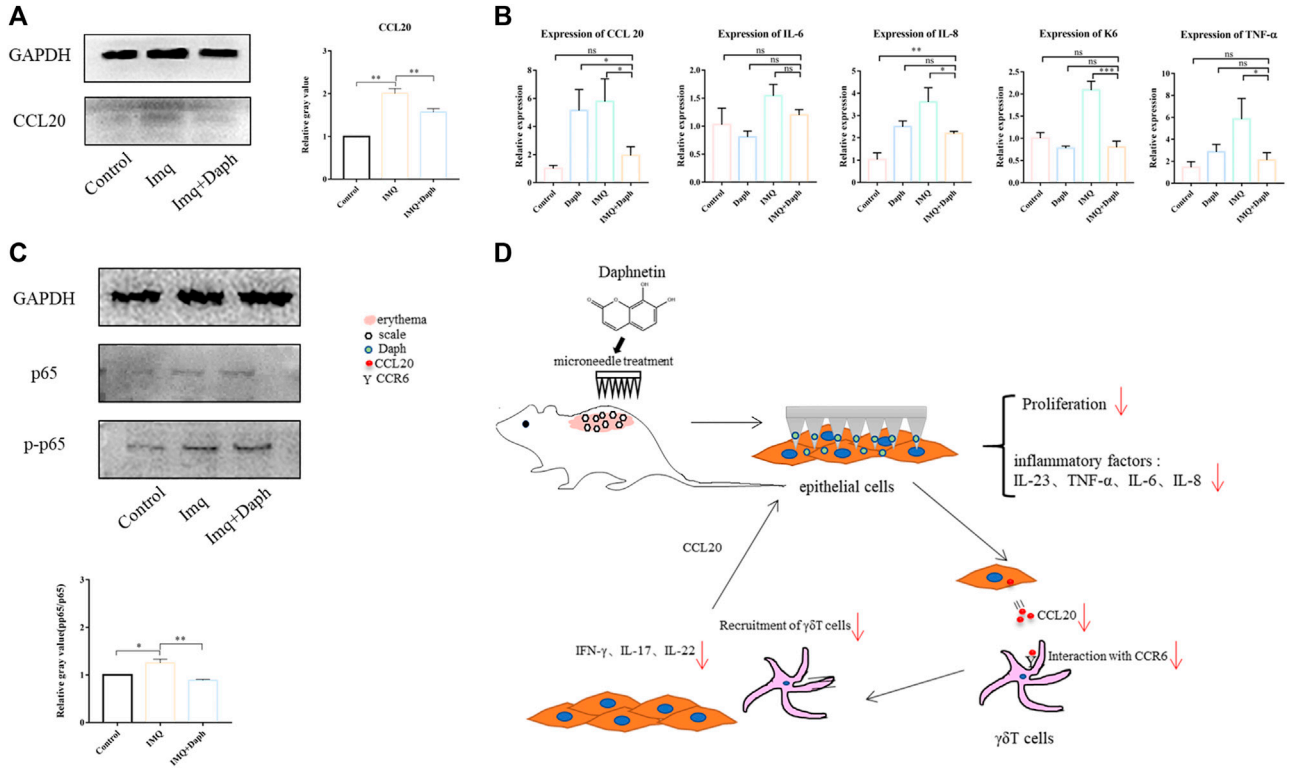

FIGURE 8 | Effects of Daph on the secretion of inflammatory factors and activation of the NF-κB signaling pathway in HaCaT cells were detected. **(A)** Effect of Daph on CCL20 secretion of HaCaT cells in the inflammatory state was detected by WB. **(B)** Effect of Daph on major inflammatory factors in HaCaT cells was detected by qPCR. **(C)** Effect of Daph on the activation of the NF-κB signaling pathway in HaCaT cells was detected by WB. **(D)** Schematic diagram of the mechanism of using MN-loaded Daph to treat psoriasis. Data are shown as mean ± SE (*$p < 0.05$; **$p < 0.01$).

3 RESULTS

3.1 Cellulose Nanocrystals Improved the Shape and Mechanical Properties of Microneedles

According to the results of the Fourier transform infrared spectrum of the CNC, the peaks at different positions represent the activities of different groups: the peaks at 3431 cm-1 and 1643 cm-1 represented stretching vibration and bending vibration, respectively, of the hydroxyl group (-OH) of cellulose; the peaks at 2901 cm-1 and 1371 cm-1 represented the stretching vibration and bending vibration, respectively, of CH; the peaks at 1016 cm-1 was attributed to the -CO- structure stretching vibration; the peaks at 1159-1 and 1111-1- were typical peaks of cellulose fingerprints; the peaks at 1277 cm-1 and 821 cm-1 were generated by sulfate groups of sulfuric acid (**Figure 1A**). XRD results showed that crystallization peaks appeared at 16.1°, 22.6°, and 34.6° of 2θ, which meant that the crystal structure of cellulose I can be maintained after acid hydrolysis. In particular, the XRD pattern of the CNC appeared at two new diffraction peaks, at 12.9° and 20.2° of 2θ, indicating the coexistence of cellulose I and cellulose II (**Figure 1B**). The average particle size of the prepared CNC is 220.2–458.7 nm (**Figure 1C**), and the CNC is evenly dispersed in a solution with homogeneous particle size (**Figure 1D,E**).

The prepared MN was observed by using a light microscope, fluorescence microscope, and scanning electron microscope. The blank MN without drug loading appeared with a 15 × 15 mm array (**Figure 2A**) and the single needle appeared as a transparent pyramid, of which the height was 600 μm and weight was 200 μm under a light microscope (**Figure 2B–F**). The surface of the MN was observed to be smooth and complete under the scanning electron microscope. According to the result, when 0.1% CNC is loaded, the force borne by a single MN was maximum, which could reach 0.23 N (**Figure 2G**). After compression, the microneedles in the blank and drug loading groups had corresponding morphological changes (**Figure 2H**).

3.2 Modified Microneedle Exhibited Good Drug Carriage and Subcutaneous Drug Delivery

The *in vitro* skin puncture experiment of nude mice showed that the skin could recover completely after 30 min of an MN patch puncture (**Figure 3A**). The MN was pressed on the back skin of nude mice and removed after 10 s, 30 s, 1, 2, and 5 min. The MN was observed to be dissolved completely after 5 min (**Figure 3B**), and the depth of delivery could be over 200 μm, that is, the subcutaneous layer (**Figure 3C**).

3.3 Daph-Loaded Microneedle Patch Could Alleviate the Symptoms of Psoriasis-Like Dermatitis Induced by IMQ in Mice

The model of psoriasis-like dermatitis was established in mice with IMQ, and the mice were observed daily and photographed. The modeling of psoriasis-like dermatitis was considered successful according to the photographs. Seven days after the modeling, the mice in the IMQ group showed apparent symptoms of erythema and scales compared with the mice in the control group. Compared with the Daph, vehicle, and IMQ groups, the vehicle + Daph group showed a significant reduction in erythema and the PASI score from day 4 post modeling (**Figure 4A,B**). The results of HE staining showed that after 7 days of modeling, the symptoms of abnormal epidermal thickening in the vehicle + Daph group were significantly reduced compared with those in other groups (**Figure 4C,D**).

3.4 Daph-Loaded Microneedle Patch Could Inhibit the Abnormal Proliferation of Vγ4+ T Cells and Reduce the Release of Inflammatory Factors of Keratinocytes in Psoriatic Dermatitis

In immunofluorescence staining, BrdU positive cells were in the proliferative stage. The results showed that the abnormal proliferation of keratinocytes in the vehicle + Daph group was significantly lower than that in the other groups (**Figure 5A**). Immunohistochemical results showed that keratinocyte inflammatory factors IL-8, IL-23, CCL20, and TNF-α decreased significantly in the vehicle + Daph group. The expression of keratinocyte-related marker K6 decreased in the vehicle + Daph group, while the expression of K1 increased (**Figure 5B**). According to the qPCR result of skin tissue, the expression of inflammatory molecules IL-1β, IL-23, TNF- α, IL-6, CXCL1, and CCL20 in the Daph group was lower than that in the IMQ and vehicle groups, while it was lowest in the vehicle + Daph group. The expression of keratinocyte-related markers K1 and K6 in the MN group was similar to that in the normal group (**Figure 5C**).

3.5 Daph-Loaded Microneedle Patch Inhibited Vγ4+T Cell Recruitment and Inflammatory Secretion

According to the results of flow cytometry, regardless of the dermis or epidermis, the proportion of Vγ4+T cells in the vehicle + Daph group was lower than that in other groups. In addition, the proportion of IL-17 Vγ4+T secreting cells in the vehicle + Daph group was also the lowest of all groups (**Figure 6A,B**). The results of immunohistochemical staining showed that the inflammatory factors IL-17, IL-22, and IFN-γ secreted by Vγ4+T cells in the vehicle + Daph group were significantly lower than those in other groups (**Figure 6C**). These factors were also detected by qPCR at the mRNA level, and the trends were the same as that of immunohistochemistry (**Figure 6D**).

3.6 Daph can Inhibit the Proliferation of HaCaT Cells *In Vitro* but Does Not Affect Apoptosis

Daph with a gradient concentration was added to the HaCaT cell culture medium. The CCK-8 assay showed that when the concentration of Daph was not more than 20 μM, it exhibited no cytotoxicity to normal HaCaT cells (**Figure 7A**). Therefore, 20 μM was selected as the Daph concentration *in vitro*. The inflammatory response of HaCaT cells was induced by IMQ *in vitro*. Edu results showed that Daph could inhibit the proliferation of HaCaT cells in an inflammatory environment (**Figure 7B**) but had no significant effect on apoptosis (**Figure 7C**).

3.7 Daph can Inhibit the Expression of Inflammatory Factors and the NF-κB Signaling Pathway in HaCaT Cells *in vitro*

The expression of CCL20 in HaCaT cells under an inflammatory environment was detected with Western blot. The results showed that after treating with Daph, the expression of CCL20 in HaCaT cells was downregulated (**Figure 8A**). IL-6, IL-8, CCL20, and TNF-α were detected at the mRNA level by qPCR. The results showed that the expression of inflammatory factors in HaCaT cells was inhibited after adding Daph (**Figure 8B**). One hour after adding Daph, the key signal molecule p65 of NF-κB was detected. The results showed that Daph could inhibit the phosphorylation of p65 and inhibit the NF-κB signaling pathway (**Figure 8C**).

4 DISCUSSION

The treatment of psoriasis is a challenge because of its pathogenic complexity (Greb et al., 2016; Dainichi et al., 2018). Some potential drugs and methods for the treatment of psoriasis were proposed in some studies recently (Hawkes et al., 2017), among which Daph showed a good symptom relief effect in the mouse psoriasis model (Gao et al., 2020). However, during the onset of psoriasis, Daph does not penetrate the thickened epidermis readily, making it difficult to reach the subcutaneous layer. As Daph is an unstable drug, it degrades rapidly, and thus does not maintain its therapeutic effect. Therefore, we chose the soluble MN to carry Daph and added the CNC to the MN for better mechanical properties. The MN can be used for transdermal administration as an effective alternative to traditional administration (Ahmed Saeed Al-Japairai et al., 2020). The inverted pyramid tip of modified MNs showed better mechanical properties and larger skin contact areas than the conical tip so that the MN could penetrate the skin better

and enhance the subcutaneous drug release. In addition, the modified MN is well-degradable *in vivo* and can deliver the drug to 200 μm in depth, which meets the demand for drug delivery *in vivo*.

The main symptoms of psoriasis are epidermal thickening, severe erythema, and scales (2). In the early stage of psoriasis, after being activated by various external factors, dendritic cells and keratinocytes start to show innate immune response through the secretion of innate immune molecules such as AMP (Mahil et al., 2016) and then induce the activation of T cells in the skin to secrete pro-inflammatory factors such as IL-17 and IL-22 (Cai et al., 2011). Recent studies have shown that the inhibition of the IL-23/IL-17 inflammatory axis plays an important role in the treatment and symptom relief of psoriasis (Ni and Lai, 2020). These pro-inflammatory factors stimulate the abnormal proliferation of keratinocytes and secrete a large number of chemokines and antimicrobial peptides, which could recruit more immune cells (Li et al., 2018). Inflammatory cells infiltrate the skin and form a positive inflammatory loop to mediate the occurrence and development of psoriasis, among which CCL20 plays a key role ((Homey et al., 2000), (Harper et al., 2009), (Furue et al., 2020b)). CCL20 secreted by keratinocytes induces CCR6-expressing T cells to infiltrate the skin and secrete a related inflammatory shadow, which promotes the further proliferation and differentiation of keratinocytes and amplifies this response (Shibata et al., 2015). Therefore, CCL20 has also been studied as a possible therapeutic target for psoriasis (Mabuchi et al., 2013; Getschman et al., 2017; Li et al., 2020). In this study, IMQ was used for the construction of a psoriasis-like dermatitis model in mice for its TLR7/8 activation effect (Gilliet et al., 2004). Using IMQ to construct the psoriasis model in mice is a mature disease model construction method (van der Fits et al., 2009; Swindell et al., 2017). After using an MN patch loading Daph, the symptoms of psoriasis-like dermatitis in mice were significantly relieved. In addition to the relieved symptoms, the production of various inflammatory factors, especially CCL20, was significantly reduced.

To identify the mechanism by which Daph reduces CCL20 secretion by keratinocytes, we used HaCaT cells for experimental verification *in vitro*. According to previous studies, Daph is an inhibitor of the NF-κB signaling pathway (Lv et al., 2018), and the NF-κB pathway is the key to regulating the production of CCL20 ((Shin et al., 2020), (Yu et al., 2021)). We used IMQ to construct the HaCaT cell inflammation model *in vitro*, added Daph as a stimulus, and then detected the associated biomarkers. As expected, after adding Daph, the NF-κB signaling pathway of HaCaT cells was inhibited and the expression of CCL20 decreased. In addition, the expression of other inflammatory factors also decreased, such as IL-8 and TNF-α. The *in vivo* results showed that the proportion of Vγ4+ T cells chemotaxed by CCL20 decreased significantly after treatment with MN patches loaded with Daph. IL-17, IL-22, and IFN-γ secreted by Vγ4+ T cells can again affect keratinocytes producing more inflammatory factors to form a positive inflammatory feedback loop (Bata-Csorgo et al., 1995). Therefore, we believe that the therapeutic effect of Daph in psoriasis relies on the inhibition of keratinocyte proliferation and the inhibition of CCL20, which disrupts the inflammatory loop of psoriasis. However, although the production of CCL20 is mainly regulated by the NF-κB pathway, it is also affected by P38/ERK/JNK and RIP4/STAT3 signaling pathways (Bae et al., 2018; Furue et al., 2019; Furue et al., 2020c). Whether Daph regulates these pathways remains to be further studied. However, Daph as a therapeutic drug for psoriasis is still in the experimental stage, and its therapeutic mechanism and safety need to be more perfect with clinical verification.

This study revealed that the modified hyaluronic acid MN, as a vehicle of drug administration, delivers the drug more effectively than having the drug applied alone topically in psoriasis. In addition, the mechanism of Daph in the treatment of psoriasis and inhibition of inflammatory response has been studied. Therefore, the MN patch used in this study can be ubiquitously applied in the research of psoriasis treatment. Daph and other drugs can be used in combination to obtain better therapeutic results.

5 CONCLUSION

In this research, we modified the hyaluronic acid MN for better morphology and mechanical properties. The modified MN was optimum for transdermal administration, and the symptoms of psoriatic mice were significantly alleviated by applying a Daph-loaded MN. *In vitro*, Daph can also inhibit the proliferation of HaCaT cells in the inflammatory state. Further studies showed that Daph could inhibit the NF-κB pathway, which was the key signaling pathway controlling the production of CCL20, an important inflammatory factor in terms of the pathogenesis of psoriasis. The use of modified MNs and the identification of a new mechanism of Daph in psoriasis treatment provide a new research direction for the psoriasis study (Onderdijk et al., 2017).

DATA AVAILABILITY STATEMENT

The raw data supporting the conclusions of this article will be made available by the authors, without undue reservation.

ETHICS STATEMENT

The animal study was reviewed and approved by the Laboratory Animal Welfare and Ethics Committee of the Third Military University.

AUTHOR CONTRIBUTIONS

The author contribution to the article is as follows: RW and XF designed the research; SP and QW finished the experiments of MN; SP, LC, and WW finished the experiments *in vivo*; KH, RZ, and SX finished the experiments *in vitro*; RW, XF, BC, CZ, and YL supervised the research; SP, LC, and YD collected and analyzed

the data; SP wrote the manuscript. All authors have read and approved the final version of the manuscript.

FUNDING

This study was funded by the National Nature Science Foundation of China (81271767) and Chongqing Nature Science Foundation (CSTC2018JCYJAX0222).

REFERENCES

Ahmed Saeed Al-Japairai, K., Mahmood, S., Hamed Almurisi, S., Reddy Venugopal, J., Rebhi Hilles, A., Azmana, M., et al. (2020). Current Trends in Polymer Microneedle for Transdermal Drug Delivery. *Int. J. Pharm.* 587, 119673. doi:10.1016/j.ijpharm.2020.119673

Albanesi, C., Madonna, S., Gisondi, P., and Girolomoni, G. (2018). The Interplay between Keratinocytes and Immune Cells in the Pathogenesis of Psoriasis. *Front. Immunol.* 9, 1549. doi:10.3389/fimmu.2018.01549

Armstrong, A. W., and Read, C. (2020). Pathophysiology, Clinical Presentation, and Treatment of Psoriasis. *JAMA* 323 (19), 1945–1960. doi:10.1001/jama.2020.4006

Bae, H. C., Jeong, S. H., Kim, J. H., Lee, H., Ryu, W.-I., Kim, M.-G., et al. (2018). RIP4 Upregulates CCL20 Expression through STAT3 Signalling in Cultured Keratinocytes. *Exp. Dermatol* 27 (10), 1126–1133. doi:10.1111/exd.13750

Bata-Csorgo, Z., Hammerberg, C., Voorhees, J. J., and Cooper, K. D. (1995). Intralesional T-Lymphocyte Activation as a Mediator of Psoriatic Epidermal Hyperplasia. *J. Invest. Dermatol* 105, 89S–94S. doi:10.1111/1523-1747.ep12316121

Cai, Y., Shen, X., Ding, C., Qi, C., Li, K., Li, X., et al. (2011). Pivotal Role of Dermal IL-17-Producing γδ T Cells in Skin Inflammation. *Immunity* 35 (4), 596–610. doi:10.1016/j.immuni.2011.08.001

Dainichi, T., Kitoh, A., Otsuka, A., Nakajima, S., Nomura, T., Kaplan, D. H., et al. (2018). The Epithelial Immune Microenvironment (EIME) in Atopic Dermatitis and Psoriasis. *Nat. Immunol.* 19 (12), 1286–1298. doi:10.1038/s41590-018-0256-2

Du, H., Liu, P., Zhu, J., Lan, J., Li, Y., Zhang, L., et al. (2019). Hyaluronic Acid-Based Dissolving Microneedle Patch Loaded with Methotrexate for Improved Treatment of Psoriasis. *ACS Appl. Mat. Interfaces* 11 (46), 43588–43598. doi:10.1021/acsami.9b15668

Furue, K., Ito, T., Tanaka, Y., Hashimoto-Hachiya, A., Takemura, M., Murata, M., et al. (2020). The EGFR-ERK/JNK-CCL20 Pathway in Scratched Keratinocytes May Underpin Koebnerization in Psoriasis Patients. *Int. J. Mol. Sci.* 21 (2), 434. doi:10.3390/ijms21020434

Furue, K., Ito, T., Tsuji, G., Nakahara, T., and Furue, M. (2020). The CCL20 and CCR6 axis in Psoriasis. *Scand. J. Immunol.* 91 (3), e12846. doi:10.1111/sji.12846

Furue, K., Ito, T., Tanaka, Y., Yumine, A., Hashimoto-Hachiya, A., Takemura, M., et al. (2019). Cyto/chemokine Profile of *In Vitro* Scratched Keratinocyte Model: Implications of Significant Upregulation of CCL20, CXCL8 and IL36G in Koebner Phenomenon. *J. Dermatological Sci.* 94 (1), 244–251. doi:10.1016/j.jdermsci.2019.04.002

Furue, M., Furue, K., Tsuji, G., and Nakahara, T. (2020). Interleukin-17A and Keratinocytes in Psoriasis. *Int. J. Mol. Sci.* 21 (4), 1275. doi:10.3390/ijms21041275

Gao, J., Chen, F., Fang, H., Mi, J., Qi, Q., and Yang, M. (2020). Daphnetin Inhibits Proliferation and Inflammatory Response in Human HaCaT Keratinocytes and Ameliorates Imiquimod-Induced Psoriasis-like Skin Lesion in Mice. *Biol. Res.* 53 (1), 48. doi:10.1186/s40659-020-00316-0

Georgescu, S. R., Tampa, M., Caruntu, C., Sarbu, M. I., Mitran, C. I., Mitran, M. I., et al. (2019). Advances in Understanding the Immunological Pathways in Psoriasis. *Int. J. Mol. Sci.* 20 (3), 739. doi:10.3390/ijms20030739

Getschman, A. E., Imai, Y., Larsen, O., Peterson, F. C., Wu, X., Rosenkilde, M. M., et al. (2017). Protein Engineering of the Chemokine CCL20 Prevents Psoriasiform Dermatitis in an IL-23-dependent Murine Model. *Proc. Natl. Acad. Sci. U.S.A.* 114 (47), 12460–12465. doi:10.1073/pnas.1704958114

Gilliet, M., Conrad, C., Geiges, M., Cozzio, A., Thürlimann, W., Burg, G., et al. (2004). Psoriasis Triggered by Toll-like Receptor 7 Agonist Imiquimod in the Presence of Dermal Plasmacytoid Dendritic Cell Precursors. *Arch. Dermatol* 140 (12), 1490–1495. doi:10.1001/archderm.140.12.1490

Greb, J. E., Goldminz, A. M., Elder, J. T., Lebwohl, M. G., Gladman, D. D., Wu, J. J., et al. (2016). Psoriasis. *Nat. Rev. Dis. Prim.* 2, 16082. doi:10.1038/nrdp.2016.82

Harper, E. G., Guo, C., Rizzo, H., Lillis, J. V., Kurtz, S. E., Skorcheva, I., et al. (2009). Th17 Cytokines Stimulate CCL20 Expression in Keratinocytes *In Vitro* and *In Vivo*: Implications for Psoriasis Pathogenesis. *J. Investigative Dermatology* 129 (9), 2175–2183. doi:10.1038/jid.2009.65

Hawkes, J. E., Chan, T. C., and Krueger, J. G. (2017). Psoriasis Pathogenesis and the Development of Novel Targeted Immune Therapies. *J. Allergy Clin. Immunol.* 140 (3), 645–653. doi:10.1016/j.jaci.2017.07.004

Homey, B., Dieu-Nosjean, M.-C., Wiesenborn, A., Massacrier, C., Pin, J.-J., Oldham, E., et al. (2000). Up-Regulation of Macrophage Inflammatory Protein-3α/CCL20 and CC Chemokine Receptor 6 in Psoriasis. *J. Immunol.* 164 (12), 6621–6632. doi:10.4049/jimmunol.164.12.6621

Huang, S., Liu, H., Huang, S., Fu, T., Xue, W., and Guo, R. (2020). Dextran Methacrylate Hydrogel Microneedles Loaded with Doxorubicin and Trametinib for Continuous Transdermal Administration of Melanoma. *Carbohydr. Polym.* 246, 116650. doi:10.1016/j.carbpol.2020.116650

Kim, N., Lee, S., Kang, J., Choi, Y. A., Jang, Y. H., Jeong, G. S., et al. (2021). Cudraxanthone D Ameliorates Psoriasis-like Skin Inflammation in an Imiquimod-Induced Mouse Model via Inhibiting the Inflammatory Signaling Pathways. *Molecules* 26 (19), 6086. doi:10.3390/molecules26196086

Li, H.-J., Wu, N.-L., Pu, C.-M., Hsiao, C.-Y., Chang, D.-C., and Hung, C.-F. (2020). Chrysin Alleviates Imiquimod-Induced Psoriasis-like Skin Inflammation and Reduces the Release of CCL20 and Antimicrobial Peptides. *Sci. Rep.* 10 (1), 2932. doi:10.1038/s41598-020-60050-1

Li, Y., Wu, J., Luo, G., and He, W. (2018). Functions of Vγ4 T Cells and Dendritic Epidermal T Cells on Skin Wound Healing. *Front. Immunol.* 9, 1099. doi:10.3389/fimmu.2018.01099

Liu, T., Luo, G., and Xing, M. (2020). Biomedical Applications of Polymeric Microneedles for Transdermal Therapeutic Delivery and Diagnosis: Current Status and Future Perspectives. *Adv. Ther.* 3 (9), 1900140. doi:10.1002/adtp.201900140

Lowes, M. A., Suárez-Fariñas, M., and Krueger, J. G. (2014). Immunology of Psoriasis. *Annu. Rev. Immunol.* 32, 227–255. doi:10.1146/annurev-immunol-032713-120225

Lv, H., Fan, X., Wang, L., Feng, H., and Ci, X. (2018). Daphnetin Alleviates Lipopolysaccharide/d-Galactosamine-Induced Acute Liver Failure via the Inhibition of NLRP3, MAPK and NF-Kb, and the Induction of Autophagy. *Int. J. Biol. Macromol.* 119, 240–248. doi:10.1016/j.ijbiomac.2018.07.101

Mabuchi, T., Singh, T. P., Takekoshi, T., Jia, G.-f., Wu, X., Kao, M. C., et al. (2013). CCR6 Is Required for Epidermal Trafficking of γδ-T Cells in an IL-23-Induced Model of Psoriasiform Dermatitis. *J. Investigative Dermatology* 133 (1), 164–171. doi:10.1038/jid.2012.260

Mahil, S. K., Capon, F., and Barker, J. N. (2016). Update on Psoriasis Immunopathogenesis and Targeted Immunotherapy. *Semin. Immunopathol.* 38 (1), 11–27. doi:10.1007/s00281-015-0539-8

Nestle, F. O., Kaplan, D. H., and Barker, J. (2009). Psoriasis. *N. Engl. J. Med.* 361 (5), 496–509. doi:10.1056/nejmra0804595

Ni, X., and Lai, Y. (2020). Keratinocyte: A Trigger or an Executor of Psoriasis? *J. Leukoc. Biol.* 108 (2), 485–491. doi:10.1002/jlb.5mr0120-439r

Onderdijk, A. J., Hekking-Weijma, I. M., Florencia, E. F., and Prens, E. P. (2017). Surgical Denervation in the Imiquimod-Induced Psoriasiform Mouse Model. *Methods Mol. Biol.* 1559, 75–81. doi:10.1007/978-1-4939-6786-5_6

Pei, Q., Hu, P., Zhang, H., Li, H., Yang, T., and Liu, R. (2021). Daphnetin Exerts an Anticancer Effect by Attenuating the Pro-inflammatory Cytokines. *J. Biochem. Mol. Toxicol.* 35 (6), 1–8. doi:10.1002/jbt.22759

SUPPLEMENTARY MATERIAL

The Supplementary Material for this article can be found online at: https://www.frontiersin.org/articles/10.3389/fbioe.2022.900274/full#supplementary-material

Supplementary Figure S1 | Schematic illustration showing the fabricating process of HA/PVA/CNC/Daph microneedle patches.

Shibata, S., Tada, Y., Hau, C. S., Mitsui, A., Kamata, M., Asano, Y., et al. (2015). Adiponectin Regulates Psoriasiform Skin Inflammation by Suppressing IL-17 Production from γδ-T Cells. *Nat. Commun.* 6, 7687. doi:10.1038/ncomms8687

Shin, J.-W., Kwon, M.-a., Hwang, J., Lee, S.-J., Lee, J.-H., Kim, H.-J., et al. (2020). Keratinocyte Transglutaminase 2 Promotes CCR6+ γδT-cell Recruitment by Upregulating CCL20 in Psoriatic Inflammation. *Cell Death Dis.* 11 (4), 301. doi:10.1038/s41419-020-2495-z

Swindell, W. R., Michaels, K. A., Sutter, A. J., Diaconu, D., Fritz, Y., Xing, X., et al. (2017). Imiquimod Has Strain-dependent Effects in Mice and Does Not Uniquely Model Human Psoriasis. *Genome Med.* 9 (1), 24. doi:10.1186/s13073-017-0415-3

van der Fits, L., Mourits, S., Voerman, J. S. A., Kant, M., Boon, L., Laman, J. D., et al. (2009). Imiquimod-induced Psoriasis-like Skin Inflammation in Mice Is Mediated via the IL-23/IL-17 axis. *J. Immunol.* 182 (9), 5836–5845. doi:10.4049/jimmunol.0802999

Vicic, M., Kastelan, M., Brajac, I., Sotosek, V., and Massari, L. P. (2021). Current Concepts of Psoriasis Immunopathogenesis. *Int. J. Mol. Sci.* 22 (21), 1154. doi:10.3390/ijms222111574

Weiss, G., Shemer, A., and Trau, H. (2002). The Koebner Phenomenon: Review of the Literature. *J. Eur. Acad. Dermatology Venereol. JEADV.* 16 (3), 241–248. doi:10.1046/j.1473-2165.2002.00406.x

Yu, Y., Xue, X., Tang, W., Su, L., Zhang, L., and Zhang, Y. (2021). Cytosolic-DNA-mediated STING-dependent Inflammation Contributes to the Progression of Psoriasis. *J. investigative dermatology*. 142. 898. doi:10.1016/j.jid.2021.08.430

Zhu, R., Cai, X., Zhou, C., Li, Y., Zhang, X., Li, Y., et al. (2017). Dermal Vγ4+T Cells Enhance the IMQ-Induced Psoriasis-like Skin Inflammatidon in Re-challenged Mice. *Am. J. Transl. Res.* 9 (12), 5347–5360.

Conflict of Interest: The authors declare that the research was conducted in the absence of any commercial or financial relationships that could be construed as a potential conflict of interest.

Publisher's Note: All claims expressed in this article are solely those of the authors and do not necessarily represent those of their affiliated organizations, or those of the publisher, the editors, and the reviewers. Any product that may be evaluated in this article, or claim that may be made by its manufacturer, is not guaranteed or endorsed by the publisher.

Copyright © 2022 Peng, Cheng, Wu, Li, Ran, Wang, Huang, Zhu, Xue, Zhou, Zhu, Cheng, Fu and Wang. This is an open-access article distributed under the terms of the Creative Commons Attribution License (CC BY). The use, distribution or reproduction in other forums is permitted, provided the original author(s) and the copyright owner(s) are credited and that the original publication in this journal is cited, in accordance with accepted academic practice. No use, distribution or reproduction is permitted which does not comply with these terms.

frontiers | Frontiers in Bioengineering and Biotechnology

REVIEW
published: 28 June 2022
doi: 10.3389/fbioe.2022.916967

Customized Barrier Membrane (Titanium Alloy, Poly Ether-Ether Ketone and Unsintered Hydroxyapatite/Poly-L-Lactide) for Guided Bone Regeneration

Yilin Shi[1,2,3], Jin Liu[1,2,3], Mi Du[1,2,3], Shengben Zhang[1,2,3], Yue Liu[1,2,3], Hu Yang[1,2,3], Ruiwen Shi[1,2,3], Yuanyuan Guo[1,2,3], Feng Song[1,2,3], Yajun Zhao[1,2,3] and Jing Lan[1,2,3]**

[1]Department of Implantology, School and Hospital of Stomatology, Cheeloo College of Medicine, Shandong University, Jinan, China, [2]Shandong Key Laboratory of Oral Tissue Regeneration, Jinan, China, [3]Shandong Engineering Laboratory for Dental Materials and Oral Tissue Regeneration, Jinan, China

OPEN ACCESS

Edited by:
Kaili Lin,
Shanghai Jiao Tong University, China

Reviewed by:
Xiangzhen Yan,
Tongji University, China
Antonio López-Valverde,
University of Salamanca, Spain

***Correspondence:**
Jing Lan
kqljf@sdu.edu.cn
Yajun Zhao
zhaoyajun_1@126.com

Specialty section:
This article was submitted to Biomaterials, a section of the journal Frontiers in Bioengineering and Biotechnology

Received: 10 April 2022
Accepted: 09 May 2022
Published: 28 June 2022

Citation:
Shi Y, Liu J, Du M, Zhang S, Liu Y, Yang H, Shi R, Guo Y, Song F, Zhao Y and Lan J (2022) Customized Barrier Membrane (Titanium Alloy, Poly Ether-Ether Ketone and Unsintered Hydroxyapatite/Poly-L-Lactide) for Guided Bone Regeneration. Front. Bioeng. Biotechnol. 10:916967. doi: 10.3389/fbioe.2022.916967

Sufficient bone volume is indispensable to achieve functional and aesthetic results in the fields of oral oncology, trauma, and implantology. Currently, guided bone regeneration (GBR) is widely used in reconstructing the alveolar ridge and repairing bone defects owing to its low technical sensitivity and considerable osteogenic effect. However, traditional barrier membranes such as collagen membranes or commercial titanium mesh cannot meet clinical requirements, such as lack of space-preserving ability, or may lead to more complications. With the development of digitalization and three-dimensional printing technology, the above problems can be addressed by employing customized barrier membranes to achieve space maintenance, precise predictability of bone graft, and optimization of patient-specific strategies. The article reviews the processes and advantages of three-dimensional computer-assisted surgery with GBR in maxillofacial reconstruction and alveolar bone augmentation; the properties of materials used in fabricating customized bone regeneration sheets; the promising bone regeneration potency of customized barrier membranes in clinical applications; and up-to-date achievements. This review aims to present a reference on the clinical aspects and future applications of customized barrier membranes.

Keywords: guided bone regeneration, customized, barrier membrane, titanium alloy, polyether ether ketone, unsintered hydroxyapatite/poly-L-lactide

1 INTRODUCTION

Sufficient bone volume is indispensable to achieve functional and aesthetic results in the fields of oral oncology, trauma, and implantology (Matsuo et al., 2010). The functional reconstruction of jawbone defects remains a major clinical challenge (Major et al., 2020; Kondo et al., 2022), and thus the effective repair and regeneration of maxillofacial and alveolar bone has great significance for maxillofacial reconstruction and oral function. Rapid developments in biomedical materials science and the continuous innovation and improvement of surgical procedures in clinical practice have increased the predictability of maxillofacial and alveolar bone reconstruction, and treatment options have increased. Currently, a variety of materials and surgical techniques have been

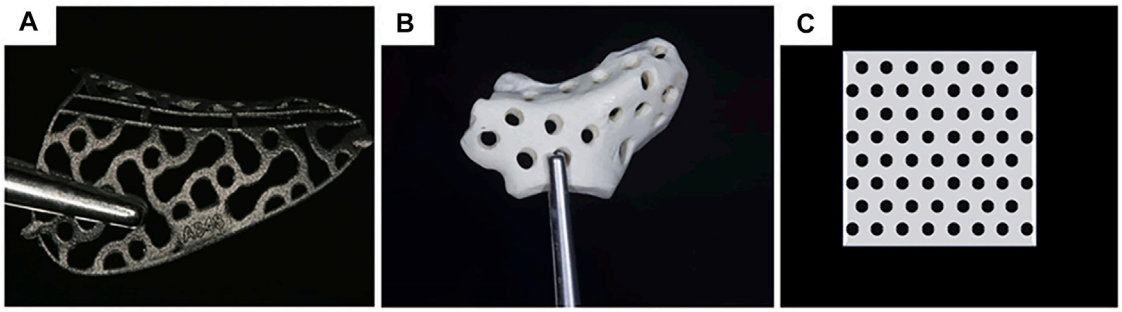

FIGURE 1 | Materials for customized mesh: **(A)** titanium alloy (Hartmann and Seiler, 2020); **(B)** PEEK (Mounir et al., 2019); **(C)** uHA/PLLA. Reproduced with permission from (Hartmann and Seiler, 2020) and (Mounir et al., 2019).

applied to vertical and horizontal bone augmentation, including bone-grafting techniques (Yamada and Egusa, 2018; Mangano et al., 2021), guided bone regeneration (Amaral Valladão et al., 2020) and distraction osteogenesis (Dimitriou et al., 2011). Each method varies and should be implemented according to clinicians' experiences and specific situations.

In guided bone regeneration (GBR), one of the most predictable methods for reconstructing maxillofacial and alveolar bones, a membrane is used to isolate soft tissues and thereby promote bone regeneration. The application of barrier membranes is a key factor in the success of GBR (Angelo et al., 2015). To date, a variety of barrier membranes have been developed to perform multiple functions in clinical applications and can be divided into resorbable or non-resorbable membranes (Rakhmatia et al., 2013). Resorbable barrier membranes, such as collagen membranes, are widely used clinically because they have high biocompatibility and no need for a second surgery to be removed (Lee et al., 2022). However, uncontrolled degradation, insufficient stiffness, and space maintenance often lead to inadequate bone regeneration (Zhou et al., 2021). Non-resorbable barrier membranes, such as titanium (Ti) mesh, have excellent mechanical properties, which can provide space for bone regeneration and reduce the volume of bone grafts. However, a traditional Ti mesh does not conform to the anatomical shape of a bone defect area, and the intraoperative cutting and bending of the Ti mesh may increase the risk of postoperative exposure and repeated mucosal irritation (Jung et al., 2014). Therefore, customized, three-dimensional (3D), and preformed barrier membranes with favorable mechanical properties are needed for ideal bone regeneration. Advances in modern 3D computer-aided planning and the application of computer-aided design or computer-aided manufacturing (Oberoi et al., 2018) have facilitated the fabrication of customized titanium (Ikawa et al., 2016), poly ether-ether ketone (PEEK) (El Morsy et al., 2020), and unsintered hydroxyapatite/poly-L-lactide (uHA/PLLA) (Matsuo et al., 2010) meshes to closely fit the anatomical shapes of bone defect areas for the accurate reconstruction of the 3D volume and position of the jaw (Vaquette et al., 2021).

This article outlines the basic workflow and advantages of modern 3D computer-aided surgery and critically analyzes materials (titanium alloy, PEEK, and uHA/PLLA; **Figure 1**) in the fabrication of customized barrier membranes, focusing on their uses in maxillofacial reconstruction and alveolar bone augmentation. Current developments in biomedical materials science and clinical aspects and future applications of patient-customized barrier membranes are discussed.

2 PROTOCOLS AND ADVANTAGES OF MODERN 3D COMPUTER-ASSISTED SURGERY

Modern 3D computer-assisted surgery (3D CAS), which combines 3D printing technology with 3D imaging techniques, has undergone remarkable developments in the past decades. As shown in **Figure 2**, several protocols are essential to 3D CAS: 1) information acquisition, 2) planning, 3) virtual operation, 4) 3D printing, and 5) surgery and postoperative analysis (Troulis et al., 2002; Prevost et al., 2019; Mian et al., 2022). Although potential errors occur in the fabrication of customized barrier membranes after tomography data acquisition, image processing, and 3D fabrication (Tian et al., 2021), technological developments in rapid prototyping systems have considerably contributed to the accurate and detailed replication of craniofacial devices (Sharma et al., 2021). A previous study scanned skulls using tomographic imaging and prototyped them through selective laser sintering and using a 3D printing technology. Comparison with the original skulls and analysis showed an error of only 2.10% for selective laser sintering and 2.67% for 3D printing. Stoop et al. obtained cone beam computerized tomography (CBCT) images of six patients with alveolar bone deficiencies. After prototyping their alveolar bone models and 3D printing customized resin grafts, they evaluated the fitness of the resin grafts to alveolar bone models and found that the mean marginal fit of the resin grafts was better in small defect zones (0.46 ± 0.20 mm) than in large defect zones (0.52 ± 0.18 mm) and all met clinical requirements (Silva et al., 2008, Stoop et al., 2019). The above results showed that data analysis and processing using CBCT allows the visualization of maxillofacial structures (Vannier et al., 1984) and facilitates analysis of bone abnormalities. 3D printing technology can constitute customized barrier membranes that

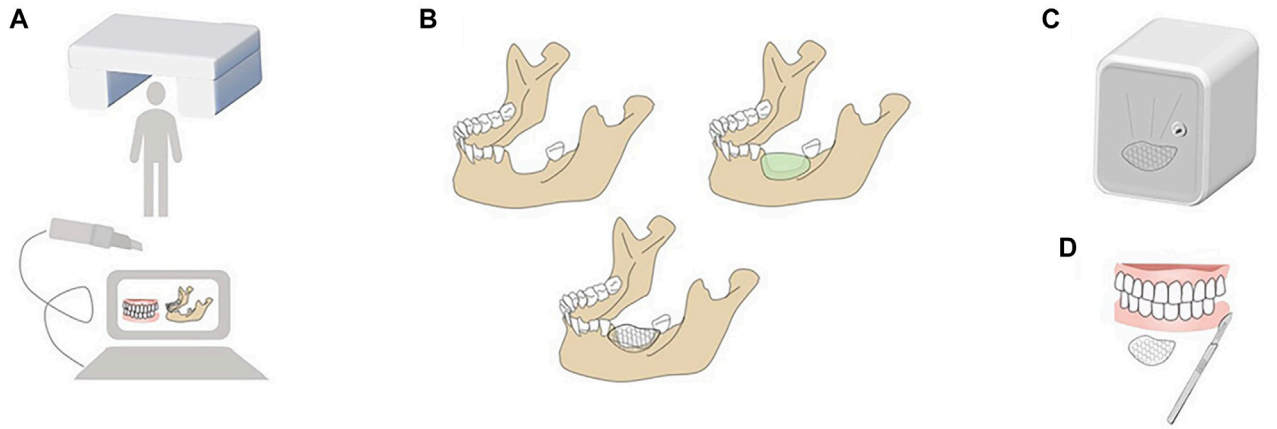

FIGURE 2 | Protocols of modern 3D CAS. **(A)** Information acquisition: Information is required by intraoral scanning and digital imaging and communications in medicine (DICOM) recording remaining alveolar bone, positioning of critical anatomic structure and soft tissue condition. **(B)** Planning and Virtual operation: Planning is to design the optimal scheme according to the size and range of defects virtually; Virtual operation is to define the best osteotomy boundary or bone grafting range according to the tumor boundary or defect condition in the software to realize virtual positioning design. **(C)** 3-D printing: 3D printing is an additional manufacturing technique that deposits materials layer by layer to construct predesigned models. **(D)** Surgery and Postoperative Analysis: Precise osteomy and accurate localization of the implant are prerequisites of successful operation. And postoperative CT scan is necessary to evaluate the designed and actual results and analyze why deviations occur and how to deal with them.

conform to complex tissue morphology (Kang et al., 2016). An efficient 3D CAS technology combining high-precision 3D printing and 3D imaging is a good option for alveolar bone augmentation and maxillofacial bone reconstruction.

According to the principle of "prosthetic guided regeneration," alveolar bone defects can be divided into four classes, as shown in **Figure 3** (Chiapasco and Casentini, 2018). For severe bone deficiency, Lizio et al. reconstructed 19 complex alveolar bone defects with a customized Ti mesh (Lizio et al., 2022). Morsy et al. rehabilitated 14 patients with severely atrophied alveolar ridges by using a customized PEEK mesh (El Morsy et al., 2020). Matsuo et al. applied customized uHA/PLLA meshes to patients with partial mandibular resection and achieved successful mandibular reconstruction (Matsuo et al., 2010). These successful cases indicate that customized barrier membranes in 3D CAS apply to a class 4 alveolar bone defect when a large horizontal or vertical bone defect or both occurs in an alveolar bone.

3 OPTIMIZATION OF BARRIER MEMBRANES

Barrier membranes in GBR act as protective films that maintain a stable bone regeneration environment, and an "ideal" barrier membrane is supposed to meet five basic principles (Scantlebury, 1993): biocompatibility (refers to the compatibility between hosts and biomaterials); space preservation (sufficient stiffness to support tissues above, maintain space, and withstand the pressure of mastication forces); selective permeability (prevention of soft tissue invasion while allowing osteogenic cells to proliferate); host tissue integration (for the embedding of surrounding host tissues); and clinical manipulation (ease of use and handling during clinical application). Through 3D printing and additional processes, the characteristics and biological performance of barrier membranes can be optimized by adjusting their microstructures given that their thickness, pore size, and roughness affect their mechanical performance and are directly related to bone formation ability.

3.1 Thickness

A customized membrane should have sufficient stiffness to create and maintain a suitable space for the intended bone regeneration, which is mainly related to the thickness of the membrane (Papia et al., 2022). A strong and thick membrane can withstand the pressures exerted by external forces, such as masticatory pressure. However, this also increases the risk of mucosal irritation and exposure (Levine et al., 2022). Therefore, determining the optimal thickness is crucial for customized membranes.

The thickness of Ti mesh commonly used ranges from 0.1 to 0.6 mm currently (Xie et al., 2020). For 3D printed Ti mesh, 0.4 mm-thick mesh is recommended, which can withstand sufficient strength and reduce irritation to mucosa, while 0.3 mm-thick mesh is suitable for the aesthetic zone with a missing tooth (Bai et al., 2019). PEEK, which has better tensile strength and elasticity, is closer to human bones than Ti and is widely used in cranioplasty (Panayotov et al., 2016). A previous study showed that a 0.6 mm-thick PEEK lattice with 2 mm pores could maintain space under masticatory pressure in the edentulous region (Li et al., 2022). For bioresorbable membranes, a certain thickness is essential for sufficient mechanical strength (Shikinami and Okuno, 1999). Studies have shown that a 0.8 mm-thick uHA-PLLA membrane could improve fine bone quality in mandibular reconstructions (Matsuo et al., 2010), and a single-folded 0.5 mm-thick uHA-PLLA membrane in orbital floor and medial wall reconstruction could facilitate the recovery of ophthalmologic function without

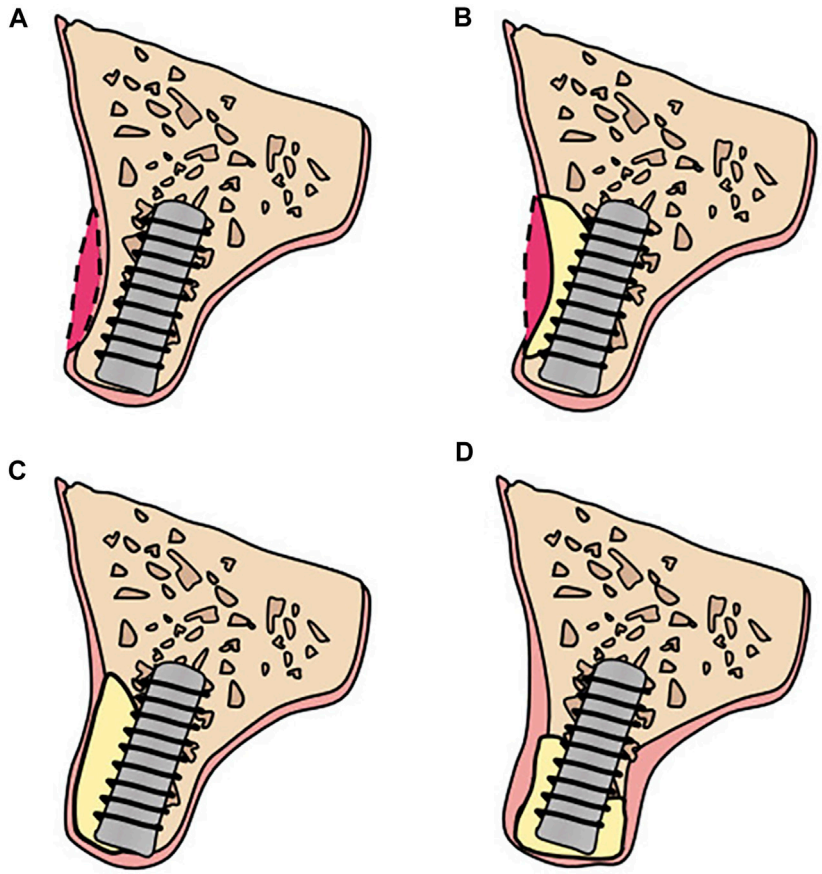

FIGURE 3 | Bone defects classification: **(A)** Class 1: ideal alveolar bone condition: implants can be placed in an ideal, restoration-driven location without augmenting the volume of alveolar ridge. Although soft tissue grafts are sometimes recommended; **(B)** Class 2: a moderate horizontal atrophy: a dehiscence or a fenestration of the buccal plate is present. Implants are placed combined with hard tissue augmentation procedures; **(C)** Class 3: large degree of horizontal defects: residual alveolar ridge allows for a two-stage implant placement. Sufficient bone graft volume and adequate healing time are indispensable; **(D)** Class 4: severe atrophy on height and width: the remaining alveolar bone is in poor condition and there are commonly two alternatives: (i) onlay bone grafting; (ii) GBR with autogenous particulate bone and/or xenogeneic bone using Ti mesh.

causing intraoperative or post-operative complications (Kanno et al., 2017). However, there is no consensus on the thickness of the uHA-PLLA membrane for GBR. These results showed that thickness affects the stiffness of a barrier membrane. Optimal thickness is crucial to meeting malleability requirements while maintaining strength. Studies on the exposure rates of the three customized barrier membranes with different thicknesses are still lacking, and further studies are needed to make a compromise between thickness and membrane exposure.

3.2 Pore Size

The pores of barrier membranes are channels for nutrient and oxygen exchanges and are closely related to the blocking ability of cells. Nonporous barrier membranes can prevent fibroblasts from growing into bone defects, but insufficient blood supply may delay bone regeneration (Celletti et al., 1994; Guo et al., 2020). A pore size of >100 μm is a prerequisite for the penetration of blood vessel-rich tissues and soft tissue healing (Chvapil et al., 1969). A previous report based on three-point bending tests and finite element analysis suggested that a customized Ti mesh with a large diameter (3–5 mm) possessed suitable mechanical properties, while animal and clinical evidence of its osteogenic effect was lacking (Bai et al., 2019). Similarly, Li et al. reported that a 0.6 mm-thick PEEK lattice with 2 mm pores could maintain space under masticatory pressure in the edentulous region, but they did not compare the biomechanical properties and osteogenic effect of PEEK mesh with different pore sizes (Li et al., 2022). The optimized pore size for uHA-PLLA barrier membranes is still unclear. A large pore size ensures efficient blood supply to a wound and is critical to integrating membranes into surrounding tissues and stabilization of bone grafts, but it may enable more connective tissues to grow in. Pseudo-periosteum, a layer of fibrous connective tissue with few blood vessels, is always observed between a Ti mesh and bone (Gutta et al., 2009). Whether large pore size contributes to bone formation remains controversial. A large aperture may accelerate early bone repair but has no effect on the final bone mass (Zellin and Linde, 1996; Zhang H. Y. et al., 2019). There are also studies proving that macroporous membranes are more effective in promoting bone regeneration than microporous

membranes (Gutta et al., 2009). The results indicate that the optimal pore size of membranes can be determined using advanced tools such as three-point bending tests and finite element analysis (Guo et al., 2021) to test the mechanical strength of different materials. Animal and clinical evidence are required to adjust the proper pore size to minimize soft tissue ingrowth without compromising nutrient exchange.

3.3 Roughness

Surface properties, especially roughness, can be easily manipulated using post-production surface treatments, such as acid etching, sandblasting, and electropolishing, and directly affect the interactions of implant–cell interfaces, which play an important role in cell responses, including adhesion, adsorption, and differentiation (Elias et al., 2008). Smooth surfaces can slow down biological processes at interfaces, and high roughness promotes bacterial adhesion and increases the possibility of implant failure. Optimal micro- and nano-roughness has been shown to promote osteoblast proliferation and differentiation (Rosales-Leal et al., 2009). For customized laser melting Ti mesh, an Ra value of 0.5 is recommended to promote osteoblast adhesion (Silva et al., 2009). Piotr Prochor et al. showed that an Ra value of 0.3 μm is the optimal roughness of a glass-reinforced PEEK and ensures high human osteoblast activity (Prochor and Mierzejewska, 2019). Meanwhile, the suitable roughness of uHA-PLLA for GBR is still unclear. To deliver the best possible clinical outcome, more studies are needed to define the optimal surface properties of 3D printed barrier membranes.

These studies suggest that a basic barrier membrane should possess abilities including biocompatibility, space preservation, selective permeability, host tissue integration, and clinical manipulation ability. The mechanical properties and biological performance of customized barrier membranes can be enhanced by optimizing their thickness, pore size, and roughness. Basic research is still needed as current research has not yet achieved a considerable balance between intrinsic properties and clinical needs.

4 ADVANCES IN 3D PRINTED BARRIER MEMBRANE FOR GUIDED BONE REGENERATION

4.1 Customized Ti Mesh

4.1.1 Properties of Customized Ti Mesh

The customized Ti mesh has good mechanical and biological properties. The physical traits of a selective laser melting (SLM) Ti mesh should be tested by tensile test, mean elongation strength, proof stress, or micro Vickers hardness to ensure impact and fracture stability (Sumida et al., 2015). Its high rigidity can maintain space and stabilize grafts, and its elasticity prevents the compression of the mucosa. Although a customized Ti mesh is thick and difficult to trim during operation (Silva et al., 2008), it conforms to alveolar bone morphology after selective laser sintering and 3D printing and prevents over-adjustment during surgery (Sumida et al., 2015). Moreover, corrosion resistance and biocompatibility ensure its stability (Her et al., 2012). Warnke et al. demonstrated the biocompatibility of patient-specific SLM Ti mesh at the cellular level through scanning electron microscopy, cell vitality staining, and biocompatibility testing (Warnke et al., 2009). Gyu-Un Jung et al. obtained fairly good bone regeneration results under a preformed Ti barrier membrane (Jung et al., 2014), and their histological results showed that newly regenerated bone was perfectly incorporated into the remaining allograft (Dellavia et al., 2021). These results indicate that a customized Ti mesh engineered with digital modeling technology and 3D printing technology is highly biocompatible, has the characteristics of high strength, good shape, high precision, simplicity, and convenience, can fit closely to the alveolar bone anatomy, and reconstruct the jaw precisely in terms of 3D volume and position.

4.1.2 Fabrication, Clinical Application, Complications of Customized Ti Mesh

Fabrication

Customized Ti devices are developed with two methods. One method is bending a commercial Ti mesh on a 3D printed augmented alveolar bone model (Li S. et al., 2021). EI Chaar et al. proposed a similar method (El Chaar et al., 2019). First, they prototyped a preoperative alveolar bone model and then used wax to raise the alveolar ridge contour before bending the Ti mesh. They achieved considerable results in clinical use in terms of bone gain (5.94–6.91 mm horizontally and 5.76–6.99 mm vertically). Another approach is to design a containment mesh directly on a virtually designed model and prototype it with SLM. Compared with a folded customized Ti mesh, a SLM Ti mesh is thicker and more difficult to trim during operation (Silva et al., 2008).

In the design process, the formation of a pseudo-periosteum and fixation scheme need to be considered. The pseudo-periosteum is a layer of connective tissue that can be observed above the newly formed bone (Dahlin et al., 1998), which may be relevant for bone graft protection, prevention of infection, and absorption. At present, we have not found reports on the formation of pseudo-periosteum beneath PEEK and uHA/PLLA-based customized barrier membranes. Formation of pseudo-periosteum has been reported beneath the Ti-reinforced polytetra-fluoroethylene membrane and Ti mesh membrane or Ti mesh plus resorbable membranes (Cucchi et al., 2019b; Giragosyan et al., 2022). The cause of pseudo-periosteum is not clear, but there may be multiple factors: 1) insufficient cell exclusion ability of the barrier membrane due to its pores (Xie et al., 2020; Choi et al., 2021), 2) the local biological immunological response (Giragosyan et al., 2022), 3) chronic bacterial infections (Croes et al., 2019), 4) the local hypoxic microenvironment (Zhuang et al., 2022), and 5) micromovement between the bone and the membrane (Wang and Boyapati, 2006). As formation of pseudo-periosteum is inevitable, a new augmentation section should be over-contoured to 1.5 mm to offset the volume of the pseudo-periosteum beneath a Ti mesh (Ciocca et al., 2013). Songhang Li et al. added an additional predetermined thickness of 0.5 mm

TABLE 1 | Summary of clinical studies with customized mesh for GBR.

Category	Reference	Method for making mesh	No. of patients	No.of graft sites	Thickness	Pore size	Roughness	Cover materials	Complication	Bone augmentationoutcome
Titanium mesh	Ciocca et al. (2011)	Type 2	1	1	0.6 mm	Square 1.0 mm holes	NA	None	NA	AHB: 3.41 ± 0.89 mm; AVB: 2.57 ± 0.86 mm
	Sumida et al. (2015)	Type 2	13	13	0.3 mm	Round 1.0 mm hole	Mirror polished	None	Mucosal rupture: 7.7%	NA
	Sagheb et al. (2017)	Type 2	17	21	NA	NA	NA	6 cases with a resorbable collagen membrane 13 cases with a double layer of collagen membrane and platelet-rich fibrin membranes	Mesh exposure: 33.3%	AHB: 5.50 ± 1.90 mm AVB: 6.50 ± 1.70 mm
	Ciocca et al. (2018)	Type 2	9	9	0.1 mm	Round 1.0-mm hole	NA	None	Mesh exposure: 66.7%	MAB: 1.72–4.10 mm (mean: 3.83 mm) MB: 2.14–6.88 mm (mean: 3.95 mm)
	Al-Ardah et al. (2018)	Type 1	1	1	NA	NA	NA	Platelet-rich fibrin membranes	NA	NA
	Cucchi et al. (2019a)	Type 2	1	1	NA	NA	NA	Plasma rich in growth factors membranes	NA	NA
	El Chaar et al. (2019)	Type 1*	17	17	NA	NA	NA	None	Mesh exposure: 35.3% Mesh failure: 11.8%	AHB: 5.94 mm AVB: 6.99 mm
	Ghanaati et al. (2019)	Type 2	7	NA	NA	NA	NA	Platelet-rich fibrin membranes	No signs of complications were observed in exposed open healing model	NA
	Takano et al. (2019)	Type 2	1	1	0.6 mm	NA	NA	None	NA	NA
	Hartmann et al. (2019)	Type 2	65	70	NA	NA	NA	Advanced- and injectable-platelet-rich fibrin and a collagen membrane	Mesh exposure: 37.1%	NA
	Hartmann and Seiler, (2020)	Type 2	55	68	NA	NA	NA	12 cases with advanced-platelet rich fibrin; 56 cases with a collagen membrane	Mesh exposure: 25.0%	Misch's classification:D1 (17.6%), D2 (52.9%), D3 (19.1%) and D4 (10.3%)

(Continued on following page)

TABLE 1 | (*Continued*) Summary of clinical studies with customized mesh for GBR.

Category	Reference	Method for making mesh	No. of patients	No.of graft sites	Thickness	Pore size	Roughness	Cover materials	Complication	Bone augmentationoutcome
	Cucchi et al. (2020)	Type 2	10	10	<0.5 mm	NA	NA	None	Mesh exposure: 10.0%	AVB: 4.5 ± 1.8 mm
	Tallarico et al. (2020)	Type 2	1	1	NA	NA	NA	None	NA	NA
	Hofferber et al. (2020)	Type 2	9	9	0.5 mm	NA	NA	Collagen membrane	Mesh exposure: 44.4%	AHB: 3.02 ± 0.84 mm AVB: 2.86 ± 1.09 mm
	Li et al. (2021b)	Type 1	21	22	NA	NA	NA	None	Mesh exposure: 9.1%	AHB: 4.11 mm (1.19–8.74) AVB: 2.48 mm (0.29–6.32)
	Li et al. (2021a)	Type 2	16	16	0.2 mm	Uniform apertures of 2.0 mm diameter	NA	Collagen membrane and concentrated growth factor matrix	Mesh exposure: 18.8% Wound dehiscence without mesh exposure: 6.3%	AHB:4.06 ± 2.37, 5.58 ± 2.65, and 5.26 ± 2.33 mm at levels of 0, 2, and 4 mm below the implant platform AVB: 3.55 ± 3.74 mm
	De Santis et al. (2021)	Type 2	5	12	NA	NA	NA	Collagen membrane	Mesh exposure: 8.3%	AHB: 3.60 ± 0.80 mm AVB: 5.20 ± 1.10 mm
	Chiapasco et al. (2021)	Type 2	41	53	NA	NA	NA	Collagen membrane	Mesh exposure: 20.8%	AHB: 6.35 ± 2.10 mm AVB: 4.78 ± 1.88 mm
	Nickenig et al. (2022)	Type 2	3	7	NA	NA	NA	Collagen membrane	No mesh exposure was observed	AHB: 3.70 mm (SD ± 0.59)
	Lizio et al. (2022)	Type 2	17	19	0.1–0.5 mm	NA	NA	None	Mesh exposure: 52.3% Mesh failure: 26.3%	Three-dimensional bone gain percentage: 88.2 ± 8.32% in 74% of the cases
PEEK mesh	Mounir et al. (2019)	Type 2	16	NA	2 mm	NA	NA	Collagen membrane	Mesh exposure: 1 case	Three-dimensional bone gain percentage: 31.8 ± 22.7%
	El Morsy et al. (2020)	Type 2	14	NA	NA	NA	NA	None	Mesh exposure: 1 case	AHB: 3.42 ± 1.10 mm AVB: 3.47 ± 1.46 mm
uHA/ PLLA mesh	Matsuo et al. (2010)	Type 1	2	2	0.8 mm	NA	NA	None	NA	Hounsfield unit value in new bone area was 790

Type 1, bend a commercial mesh on a 3D printed planned augmented alveolar bone model.
Type 1, use wax to raise a preoperative alveolar bone model before bending the mesh.*
Type 2, design the containment mesh directly on the virtually planned model and prototype it.
AVB, average vertical bone gain; AHB, average horizontal bone gain.
MAB, mandibular arch bone gain; MB, maxillary bone gain.
NA, not available.

buccally and 1.0 mm vertically in precision bone augmentation (Li S. et al., 2021). The fixation of a Ti mesh is supposed to stabilize blood clots and protect bone augmentation areas. However, Ciocca et al. used no screws to immobilize a customized Ti mesh and still achieved considerable bone augmentation following good fixation (Ciocca et al., 2011).

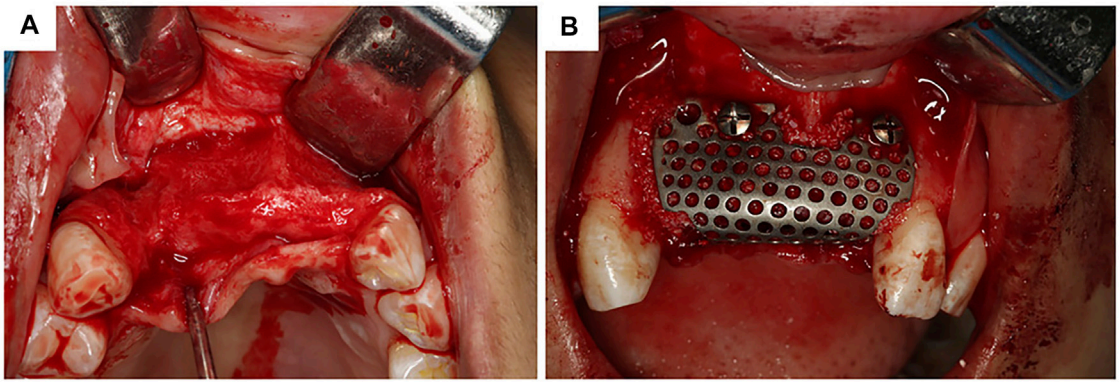

FIGURE 4 | Customized titanium mesh in clinical usage. **(A)** Exposure of alveolar bone ridge. **(B)**Fixation of customized titanium mesh.

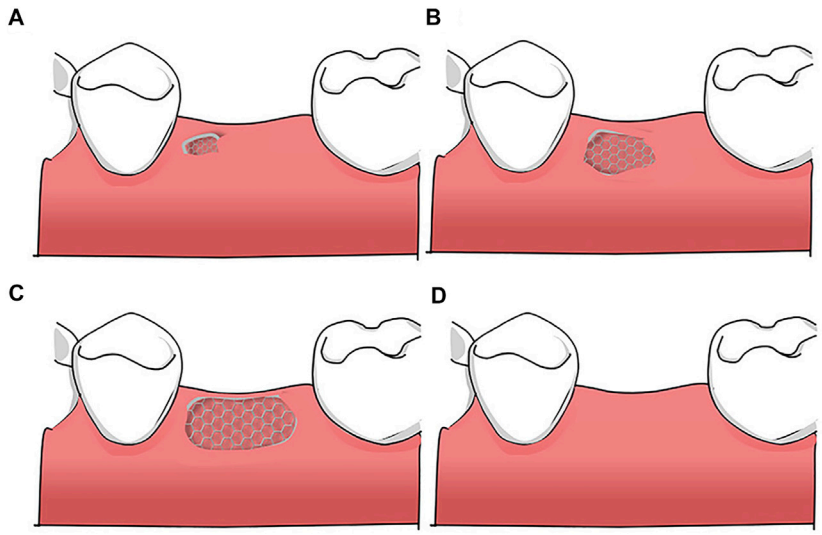

FIGURE 5 | Classification of mesh exposure: **(A)** minor exposure; **(B)** one tooth width exposure (premolar); **(C)** exposure of an entire mesh **(D)** no exposure.

These results show that pseudo-periosteum formation beneath a Ti mesh is inevitable. Besides, pseudo-periosteum can prevent infection and needs to be considered to design an over-contoured bone volume, and more research is needed in that area to truly understand its nature and importance to the guided bone regeneration process. A customized Ti mesh can be designed to precisely conform to the shape of an alveolar bone and fully engage existing undercuts, so few screws are required to ensure secure fixation.

Clinical Application

Ti and its alloys have been widely used in alveolar bone augmentation in atrophied posterior alveolar ridges and anterior aesthetic zones (**Table 1**; **Figure 4**). A study designed an L-shaped Ti mesh by preforming commercial Ti mesh on a model; a 2-year follow-up of 12 patients with a total of 16 implantation sites showed bone augmentation of 3.61 ± 1.50 mm vertically and 3.10 ± 2.06 mm horizontally (Zhang T. et al., 2019). Tallarico et al. have reported the successful application of customized Ti mesh in the anterior aesthetic area (Tallarico et al., 2020).

In maxillofacial reconstruction, a customized 3D printed Ti mesh has been applied to patients undergoing total maxillectomy for the reconstruction of maxillary contour and rehabilitation of orbital floor and orbital volume and has produced satisfactory results with few complications, such as exophthalmos and diplopia (Liu et al., 2019). On the basis of the "Dumbach Titam Mesh-System" (Stryken-Leibinger, Freiburg, Germany; (Cheung et al., 1994), which first applied a commercially available Ti mesh tray and particulate cancellous bone marrow in mandibular discontinuity reconstructions and achieved considerable results, Won-bum Lee et al. reported a case of successful secondary mandibular reconstruction in a large bone defect after using a Ti mesh and particulate cancellous

TABLE 2 | Comparison of three customized barrier membranes in GBR.

Category of customized membranes	Common advantages	Common disadvantages	Specific advantages	Disadvantages
Titanium mesh	1) Suitable for various bone defects, especially complex large bone defects 2) Easy to determine bone volume for bone reconstruction and facilitate bone-grafting design	Customized barrier membranes alone cannot prevent soft tissue ingrowth due to the pores, and the formation of pseudo-periosteum occupies osteogenic space and weakens osteogenic effect. (The formation of pseudo-periosteum beneath the PEEK and uHA/PLLA-based customized barrier has not been reported due to the lack of relevant literature.)	Thin and extensively applied in clinical usage	Radiopacity, high exposure rate and the need for secondary removal
PEEK mesh	3) More suitable for jaw anatomical morphology 4) Avoid manual shaping during the operation, which greatly shorten the during time		Radiolucent and has good tensile strength and elasticity similar to human bone with less mucous membrane irritation	Thick, costly, non-osteoconductive and needs a secondary removal. (Whether PEEK can reduce mesh exposure rate remains to be studied.)
uHA/PLLA mesh	5) The smooth external shape is conductive to fixation and secondary removal, which can reduce mucosal irritation and exposure time 6) Reduce the burden on surgeons and differences between different surgeons		Osteoconductive, radiolucent, bioresorbable and doesn't require a second surgical removal and has an elastic modulus similar to human bone	Thick and needs complicated production process. (Relevant literature is insufficient and further research is still needed.)

bone marrow after the failure of the fibula free flap technique; they obtained adequate bone augmentation for subsequent prothesis (Lee et al., 2018). The successful cases above demonstrate that a customized Ti mesh can reconstruct the jaw precisely in terms of 3D volume and position, offer a guarantee for the pre-operation plan, prevent manual shaping during operation, and greatly shorten operation time. It is suitable for various bone defects, especially complex large bone defects.

Complications

Ti mesh exposure is commonly associated with irritation to the mucosa because of its stiffness, sharp edges, and rough surfaces. Amely Hartmann et al. divided mesh and graft exposure into four classes (Hartmann et al., 2019): 1) minor exposure; 2) one tooth width exposure (premolar); 3) exposure of an entire mesh; and 4) no exposure (**Figure 5**). They found that age, periodontitis, diabetes, gender, tissue phenotype, and tobacco abuse are not associated with dehiscence probability, whereas tobacco abuse might accelerate graft loss when a mesh is exposed. These results are consistent with those of Lindfors et al., who showed that the success rate of bone augmentation was lower in smokers than in nonsmokers (Lindfors et al., 2010). A customized Ti mesh has a relatively low mesh exposure rate. In a clinical test, Sumida et al. equally divided 26 patients into two groups for alveolar bone augmentation surgery. One of the groups received customized Ti meshes, whereas the other received commercial Ti meshes. After post-operative follow-up, they observed that the exposure rates in the former (7.7%) were lower than those in the latter (23.1%). They attributed this result to the round and blunt shape of a customized Ti mesh (Sumida et al., 2015).

Dehiscence and mesh exposure can be prevented by properly managing soft tissues, and complete tension-free closure is indispensable during operation with single interrupted sutures and a deep mattress. Combination with collagen membranes does not reduce the exposure rate of a customized Ti mesh (Cucchi et al., 2021). Autologous bioactive materials, such as blood-based and platelet-rich plasma systems (Eppley et al., 2006; Torres et al., 2010), platelet-rich fibrin (Najeeb et al., 2017; Ghanaati et al., 2019), and concentrated growth factors (Wang et al., 2021b), have promising effects that improve soft-tissue healing. A previous clinical trial evaluated the effect of platelet-rich plasma on Ti mesh exposure. In the study, 15 patients were recruited and underwent alveolar bone augmentation with Ti mesh and platelet-rich plasma, and another 15 patients underwent alveolar bone augmentation only with Ti mesh. After a 6 month follow-up, the patients were recalled for evaluation and subsequent treatment. No exposure was observed in the platelet-rich plasma group compared with the group without platelet-rich plasma (Torres et al., 2010). This study showed that autologous bioactive materials contribute to soft-tissue healing. For wound dehiscence prevention, Masayuki Takano et al. reported a minimally invasive subperiosteal tunneling flap technique involving long labial incision, cervical palatal incision, and peritoneal-releasing incision (Takano et al., 2019). Although some studies showed that the premature (within 4–6 weeks) or delayed (after 6 weeks) exposure of Ti mesh has no effect on bone augmentation in the presence of a pseudo-periosteum (Ciocca et al., 2018), infection does compromise bone augmentation, and timely measures are still needed when exposure occurs, such as gentle cleaning and daily rinsing with 0.12% chlorhexidine or removing prematurely exposed meshes (Hartmann et al., 2019; Belleggia, 2021).

These results indicate that a customized mesh is round and blunt and more suitable for alveolar bone morphology, and they show low exposure rates. Selecting an appropriate surgical

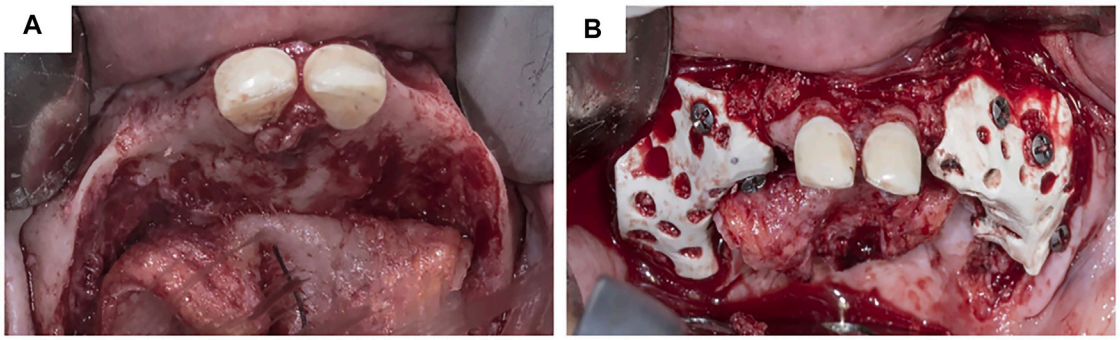

FIGURE 6 | Customized PEEK mesh in clinical usage. **(A)** Customized PEEK mesh. **(B)** Fixation of customized PEEK mesh. Reproduced with permission from El Morsy et al. (2020).

procedure and combining autologous bioactive materials can promote wound healing and reduce Ti mesh exposure. When a Ti mesh is exposed, timely measures are needed to control infection and prevent bone graft failure.

4.1.3 Advantages and Disadvantages of a Customized Ti Mesh

Apart from stabilizing graft material, creating enough space, and acting as a barrier membrane to guide bone regeneration in the same manner as a traditional Ti mesh does, patient-specific Ti, PEEK, and uHA/PLLA meshes have several benefits, as shown in **Table 2**. Besides, a customized Ti mesh is thinner and has more extensive clinical applications compared with PEEK and uHA/PLLA.

Customized Ti, PEEK, and uHA/PLLA barrier membranes are designed with pores to receive nutrients and blood from the periosteum to promote bone healing. However, soft tissue-derived cells can grow through the pores into the osteogenic region and weaken the osteogenic effect. Therefore, using a customized barrier membrane alone cannot prevent soft tissue ingrowth and pseudo-periosteum formation. More research is needed to address this limitation.

Customized Ti mesh also has its own disadvantages to address. Compared with traditional Ti mesh, customized Ti mesh can cause less membrane exposure because of its smooth round blunt shape. However, in some cases, the exposure rate of customized Ti mesh may reach an average of 20% or higher due to inherent stiffness (Sagheb et al., 2017). Besides, Ti mesh has no antibacterial ability and may need to be removed in the early stage of membrane exposure to avoid bone graft failure (Hartmann et al., 2019). A secondary surgery is still required to remove the Ti mesh (Zhou et al., 2021). In addition, the radiopacity of a Ti mesh may affect the imaging results of postoperative X-ray examinations.

To sum up, although customized Ti meshes are widely applied in GBR for alveolar bone augmentation and maxillofacial bone reconstruction, their inherent traits can lead to clinical complications and increase the complexity of treatment procedures. Relevant research should be directed towards increasing the antibacterial ability and osteogenic ability of Ti mesh to reduce membrane exposure and pseudo-periosteum formation.

4.2 PEEK-Based Customized Barrier Membrane

4.2.1 Mechanical and Biological Properties of PEEK

PEEK is a highly compatible polyaromatic semi-crystalline thermoplastic polymer (Gu et al., 2020; Ma et al., 2020) and has been approved by the US FDA Drug & Device Master File. *In vitro* experiments found no evidence of the mutagenic or cytotoxic effects of PEEK (Katzer et al., 2002). It has excellent mechanical properties, with an elastic modulus of 3.6 GPa, which can be increased to 18 GPa with the addition of carbon fiber, which is similar to the elastic modulus of cortical bone at 15 GPa. Furthermore, it has sufficient radiolucency and hardness, showing a flexural strength of 140–170 MPa to resist masticatory pressure (Schwitalla and Müller, 2013). These results reveal that PEEK has considerable biocompatibility and mechanical properties and can be used in repairing bone defects.

4.2.2 Fabrication, Clinical Application, and Limitations of PEEK

Patient-specific PEEK devices are virtually designed with specific software and fabricated from PEEK blocks with milling machines (El Morsy et al., 2020). Apart from cutting a scaffold, a fused deposition modeling 3D printer can also deposit customized PEEK scaffolds layer by layer with molten PEEK (Li et al., 2022).The devices are sterilized through immersion in 2.4% glutaraldehyde prior to surgery.

In the craniofacial field, PEEK has been widely used as a customized implant for repairing large skull defects (van de Vijfeijken et al., 2019; Yang et al., 2020) and mandibular reconstruction (Atef et al., 2021; Kang et al., 2021), and is often compared with Ti meshes in terms of price and operative time (Binhammer et al., 2020). Although customized PEEK implants can reduce operative duration to a certain extent compared with manually bent Ti meshes, they are more costly and are associated with an increased number of complications, such as infection (Rosinski et al., 2020).

As shown in **Table 1** and **Figure 6**, PEEK has been successfully used in augmenting atrophied alveolar ridges with vertical and horizontal bone gains of 3.47 mm (±1.46) and 3.42 (±1.1), respectively (El Morsy et al., 2020). In the formation of new bone mass, no statistical difference was found between prebent Ti mesh and patient-specific PEEK (Mounir et al., 2019). These results suggest that customized PEEK membranes can successfully augment severely atrophied alveolar bones. However, clinical samples are few, and given that PEEK does not possess any features of osteogenesis or osseointegration (Zhao et al., 2021), it cannot completely replace Ti meshes.

4.2.3 Advantages and Disadvantages of a Customized PEEK Mesh

Customized PEEK membranes have the same benefits as customized Ti meshes (**Table 2**). The above results indicate that PEEK has better tensile strength and elasticity than Ti, is more similar to human bone, and results in less mucous membrane irritation, which may reduce membrane exposure to some extent (Mounir et al., 2019). The radiographic property of a PEEK membrane has no effect on X-ray imaging. However, as PEEK is non-absorbable and non-osteoconductive and needs to be removed in a second operation (Zhao et al., 2021), it may not completely replace Ti mesh, and its high clinical cost may limit its potential use (Rosinski et al., 2020). Further studies should focus on enhancing its osteogenic and osseointegration ability as well as production efficiency problems.

4.3 uHA/PLLA-Based Customized Barrier Membrane

4.3.1 Properties and Advantages of uHA/PLLA

uHA/PLLA is a third-generation bio-resorbable material in oral and maxillo-facial medicine. It is processed with a specific forging protocol that combines uncalcined and u-HA particles (30 and 40% by weight) with PLLA (Shikinami and Okuno, 1999). PLLA belongs to the first generation of bioresorbable materials in osteosynthesis surgery. However, several disadvantages limit its potential use in maxillofacial medicine. First, insufficient strength and lack of osteoconduction properties make it unsuitable for stress-bearing zones. In addition, acidic degradation products can elicit an inflammatory reaction. Its crystallinity and hydrophobicity prevent its hydrolysis during the first 2 years, increasing resorption duration and delaying tissue degradation reactions (Kanno et al., 2018). Hydroxyapatite is radiopaque and osteoconductive and has been used as bone grafts in mandibular surgery. However, its high absorption rate, high infection rate, and inherent brittleness have limited its clinical application. uHA-PLLA combines the strengths of both materials through a unique forging process and offsets their respective weaknesses. uHA confers osteoconductivity on PLLA and enhances its strength (Shikinami and Okuno, 1999). uHA-PLLA has a mild hydrolysis reaction rate and can stably release PLLA fragments without causing tissue swelling, and thus it has been widely used in orthodontic treatment (Shikinami et al., 2005).

uHA-PLLA composites possess excellent biocompatibility and osteoconductivity and have been used in bone-fixation systems, such as plates and screws (Ueki et al., 2011). Yasuo Shikinami et al. compared F-PLLA-only rods with F-u-HA 30/40 rods implanted in a rabbit bone cavity and found that the F-PLLA-only group elicited an inflammatory response in the body because of the uneven release of PLLA particles. The F-u-HA 30/40 rods did not induce any adverse effects *in vivo*. These results showed that the uHA-PLLA composite is highly biocompatible (Shikinami et al., 2005). The uHA particles conferred osteoconductivity on PLLA, and newly formed bone was observed in uHA-PLLA sheets covering critical size defects compared with the PLLA in the rat model (Dong et al., 2019). A previous study confirmed that uHA-PLLA meshes are as effective as Ti meshes in bone augmentation (Moroi et al., 2013).

In addition, uHA-PLLA has excellent mechanical traits, with a modulus of 12 GPa, which is close to that of a cortical bone. The bending strength is 270 MPa, which is higher than that of PLLA and even higher than that of a human cortical bone. After 24 weeks, it can be maintained at 200 MPa, which is sufficient for normal bone regeneration (Shikinami and Okuno, 1999). Moreover, degradation *in vivo* takes 3–5 years, which is sufficient for bone healing, particularly the correction of large mandibular defects (Shikinami et al., 2005). These results show that uHA/PLLA combines the strengths of PLLA and hydroxyapatite, possessing excellent mechanical traits, biocompatibility, and osteoconductivity, and can be applied to bone tissue reconstruction.

4.3.2 Fabrication, Clinical Application and Prospect of uHA/PLLA Based Customized Barrier Membrane

Customized uHA/PLLA barrier membranes are usually prefabricated with the same fabrication method used for customized Ti meshes, that is, manipulating and bending commercial uHA/PLLA plates on stereolithographic models. A uHA/PLLA plate becomes soft after immersion in hot water at 60°C and is easily shaped with tweezers, but hardens when the temperature returns to 25°C (Moroi et al., 2013).

Akira Matsuo et al. fabricated a custom uHA-PLLA mesh tray for mandibular reconstruction by prototyping a mandibular stereolithography model and preforming HA-PLLA sheets based on that model to conform to a 3D contour (**Figure 7**) (Matsuo et al., 2010). One patient in their case report received dental implants 10 months after surgery and was followed up for 1 year. They obtained reliable and stable results. Although the duration from bone grafting to implant placement was insufficient to fully degrade uHA-PLLA, the alveolar part was easily removed, and the external part of the tray was preserved and suitable for implant placement. However, owing to the limited number of cases and short follow-up time, the result was not convincing (**Table 1**) (Matsuo et al., 2010). Akira Matsuo et al. assessed the fitness of a manually bent 0.8 mm-thick uHA-PLLA trays in dog models and revealed that the uHA-PLLA tray had a better fit to the lingual side of the alveolar bone than the manually bent Ti mesh, and no statistical difference was found on the buccal side. The CT value of the newly formed bone under the uHA-PLLA mesh was higher than that of the Ti mesh and was

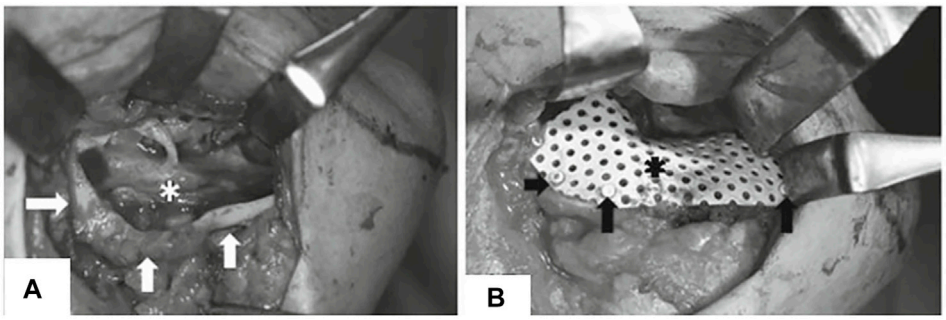

FIGURE 7 | Customized uHA-PLLA mesh in clinical usage. **(A)** Exposure of alveolar bone ridge. **(B)** Fixation of customized uHA-PLLA mesh. Reproduced with permission from Matsuo et al. (2010).

close to that of residual bone (Matsuo et al., 2012). These results show that a customized uHA-PLLA mesh can closely match an alveolar bone, maintain stable space, and achieve predictable bone regeneration. However, a few studies have reported the application of uHA-PLLA in GBR and 3D printing. More research is needed to explore its potential use in maxillofacial reconstruction and alveolar bone augmentation.

4.3.3 Advantages and Disadvantages of Customized uHA-PLLA Mesh

Bioresorbable materials with stiff strength and radiolucency, such as uHA-PLLA, may provide an alternative for predictable bone augmentation and the fabrication of customized barrier membranes (**Table 2**). A bioresorbable trait does not allow it to be removed in a second surgery. However, processes for manipulating and bending commercial uHA/PLLA plates on stereolithographic models (Moroi et al., 2013) are more complicated than processes for directly prototyping them, and relevant literature is insufficient. In summary, customized Ti devices are still the most mainstream protocol in GBR.

5. CURRENT PROGRESS AND FUTURE DIRECTIONS

5.1 Potential Solutions to Reduce Soft Tissue Ingrowth

Soft tissue ingrowth occupies osteogenic space and subsequently impairs the osteogenic effect. A non-porous barrier membrane can avoid fibrous tissue formation, but insufficient blood supply may delay bone regeneration (Guo et al., 2020). More research is needed on how to avoid soft tissue ingrowth for customized barrier membranes with pores. To date, numerous studies are trying to overcome this limitation. Collagen membranes have good soft tissue reactions and can reduce the migration of epithelial cells into the bone defects. Combined use of customized membranes and collagen membranes during GBR could ensure greater predictability with reduced soft tissue interposition (Borges et al., 2020). Surface modification could also help to reduce the growth of connective tissue. Nguyen et al. demonstrated that heat-treated Ti mesh subjected to anodization and cyclic precalcification could attach directly to the bone. However, connective tissues were found to grow between untreated Ti mesh and bone (Nguyen et al., 2016). Besides, cell occlusion effects are also affected by differences in superficial topography. It was found that the rough surface of an absorbable barrier membrane had more giant cells attached to it than the smooth surface contained more inflammatory cells, indicating that different surface topographies promote differential soft tissue responses (de Santana et al., 2010). Furthermore, Gutta and others demonstrated that macroporous Ti mesh (pore size 1.2 mm) significantly hindered soft tissue growth compared to microporous mesh (pore size 0.6 mm) (Gutta et al., 2009), suggesting that soft tissue ingrowth could be suppressed by changing the pore size. In addition, inspired by "Janus", a Janus membrane with the upper layer blocking the migration of fibroblasts and the bottom side promoting osteogenesis also provides researchers with a new direction (He et al., 2022).

Based on existing studies, several potential solutions can be suggested to reduce soft tissue ingrowth: 1) combined use of customized membrane with collagen membrane; 2) using screws to fix the customized membrane to prevent micromovement between the bone graft and the membrane; 3) pore size and surface topography optimization; 4) surface modification of membrane materials; 5) development and application of Janus membranes. Besides, in order to obtain sufficient bone mass, excessive bone augmentation can avoid insufficient bone volume caused by soft tissue ingrowth and pseudo-periosteum formation.

5.2 Enhancement of Bioactive Properties

Along with the progress of biomaterials, research for improving the bioactive properties of Ti alloys is advancing (Liu et al., 2020; Wang et al., 2021a; Wei et al., 2021). Xu et al. focused on the study of Cu ions with excellent antibacterial properties. By incorporating Cu ions into Ti alloys, they found that Ti6AL4V alloy meshes offer broad prospects for clinical application and exert considerable pro-angiogenic and anti-inflammatory effects (Xu et al., 2018). Thuy-Duong Thi Nguyen et al. coated Ti meshes with strontium-substituted calcium phosphate for surface modification and achieved better osseointegration compared with that in the untreated group in rat calvarial defect models

(Nguyen et al., 2019). Zhao et al. found that porous chitosan gelatin doxycycline coatings on the Ti mesh exhibited antibacterial effects (Zhao et al., 2022). The improvement of bioactive properties can enhance the bone-binding and antibacterial abilities of Ti mesh, which may help reduce the risk of exposure.

The absence of osteogenesis and osseointegration ability limits the clinical application of PEEK (Han et al., 2022), so numerous strategies have been proposed to strengthen its bioactivity. In recent years, PEEK implants have gone through three development phases: 1) mechanical property enhancement; 2) cytocompatibility and osteogenic ability enhancement; and 3) osseointegration and anti-inflammatory enhancement (Gu et al., 2020). Improvement in PEEK properties is usually achieved through surface modification (Frankenberger et al., 2021; Mehdizadeh Omrani et al., 2021; Jiang et al., 2022) and blending modification (Ma et al., 2020; Ren et al., 2020; Hu et al., 2022). Waser-Althaus et al. used oxygen and ammonia plasma to modify PEEK surfaces and enhance their hydrophilicity and protein adsorption capacity. *In vitro* tests showed that compared with pure PEEK, modified PEEK showed stronger osteogenic ability and could better promote the osteogenic differentiation of adipose-derived mesenchymal stem cells (Waser-Althaus et al., 2014). It was found that adding silicon nitride powder within a PEEK matrix can significantly enhance its osteoconductive and bacteriostatic properties (Pezzotti et al., 2018). Overall, endowing PEEK with antibacterial and bone-binding capabilities and applying it to GBR will certainly promote wound healing, reduce the barrier membrane exposure rate, and improve osteogenesis. In view of numerous articles about PEEK modification, a series of factors, such as complexity of processing, economic cost, and clinical practicability, must be considered in its future development.

5.3 Development of Biodegradable Materials

Biomaterials for tissue engineering are evolving from the first generation of metals and ceramics to the second generation of bioceramics (Brunello et al., 2020) and polymers (Babilotte et al., 2019) and to the third generation of absorbable metal materials (Rahman et al., 2020). In recent years, studies about biodegradable metal materials with excellent mechanical properties, such as magnesium-based alloys (Chen et al., 2018; Rahman et al., 2020; Yan et al., 2022) and zinc-based alloys (Jia et al., 2020), have grown dramatically. Magnesium-based alloys have good biocompatibility and mechanical properties and offset the rapid degradation of magnesium and hydrogen production. Asgari et al. prepared a magnesium oxide film coating on a Mg-based substrate and established a rat calvarial defect model. Their results revealed the improved osteo-compatibility and biodegradability of magnesium alloys (Asgari et al., 2019). Zinc-based alloys can improve the low strength and brittleness of pure zinc and provide a novel biodegradable material for orthopedic applications. For example, zinc-manganese biodegradable metals have been utilized in animal bone defect models and successfully promoted bone regeneration (Jia et al., 2020). These results suggest that the development of biodegradable materials can well solve the problem of secondary removal of non-absorbable membranes after GBR. Barrier membranes made of biodegradable materials should have good biocompatibility, good mechanical properties to maintain space, excellent properties to promote osteogenesis and reduce the risk of exposure. These properties will provide a promising prospect for GBR (Toledano-Osorio et al., 2021).

6 CONCLUSION

Developments in digital modeling and 3D printing technologies have produced materials, such as Ti alloy, PEEK, and uHA/PLLA, with excellent mechanical properties and good biocompatibility, which are used in fabricating customized bone regeneration sheets for GBR. These materials are predictable and stable solutions for maxillofacial reconstruction and alveolar bone augmentation. By comparison, little research has been performed on customized PEEK and uHA-PLLA meshes, and a customized Ti mesh is the most mainstream protocol in GBR, although it needs to be removed in a second operation. In addition, improvement of material properties endows Ti and PEEK with high antibacterial and osteogenic properties, and the emergence of novel biological materials is developing towards biological absorption, enhanced osteogenesis, and reduced membrane exposure, which will promote the application of customized absorbable barrier membranes in GBR.

AUTHOR CONTRIBUTIONS

YS, JL, MD, SZ, YL, HY, RS, YG and FS wrote and edited the article, YZ and JL provided supervision and feedback.

FUNDING

This work was supported by the National Natural Science Foundation of China (No. 82100977), the China Postdoctoral Science Foundation (2021M691930), and the Youth Scientific Research Funds of the School of Stomatology, Shandong University (2020QNJJ03).

REFERENCES

Al-Ardah, A. J., Alqahtani, N., AlHelal, A., Goodacre, B. J., Swamidass, R., Garbacea, A., et al. (2018). Using Virtual Ridge Augmentation and 3-Dimensional Printing to Fabricate a Titanium Mesh Positioning Device: A Novel Technique Letter. *J. Oral Implantol.* 44 (4), 293–299. doi:10.1563/aaid-joi-D-17-00160

Amaral Valladão, C. A., Jr., Freitas Monteiro, M., and Joly, J. C. (2020). Guided Bone Regeneration in Staged Vertical and Horizontal Bone Augmentation Using Platelet-Rich Fibrin Associated with Bone Grafts: A Retrospective Clinical Study. *Int. J. Implant. Dent.* 6 (1), 72. doi:10.1186/s40729-020-00266-y

Angelo, T., Marcel, W., Andreas, K., and Izabela, S. (2015). Biomechanical Stability of Dental Implants in Augmented Maxillary Sites: Results of a Randomized Clinical Study with Four Different Biomaterials and Prf and a Biological View on Guided Bone Regeneration. *BioMed Res. Int.* 2015, 1–17. doi:10.1155/2015/850340

Asgari, M., Yang, Y., Yang, S., Yu, Z., Yarlagadda, P. K. D. V., Xiao, Y., et al. (2019). Mg-Phenolic Network Strategy for Enhancing Corrosion Resistance and Osteocompatibility of Degradable Magnesium Alloys. *ACS Omega* 4 (26), 21931–21944. doi:10.1021/acsomega.9b02976

Atef, M., Mounir, M., Shawky, M., Mounir, S., and Gibaly, A. (2021). Polyetheretherketone Patient-specific Implants (Ppsi) for the Reconstruction of Two Different Mandibular Contour Deformities. *Oral Maxillofac. Surg* 26, 299–309. doi:10.1007/s10006-021-00984-6

Babilotte, J., Guduric, V., Le Nihouannen, D., Naveau, A., Fricain, J. C., and Catros, S. (2019). 3d Printed Polymer-Mineral Composite Biomaterials for Bone Tissue Engineering: Fabrication and Characterization. *J. Biomed. Mat. Res.* 107 (8), 2579–2595. doi:10.1002/jbm.b.34348

Bai, L., Ji, P., Li, X., Gao, H., Li, L., and Wang, C. (2019). Mechanical Characterization of 3d-Printed Individualized Ti-Mesh (Membrane) for Alveolar Bone Defects. *J. Healthc. Eng.* 2019, 1–13. doi:10.1155/2019/4231872

Belleggia, F. (2021). Exposure Management of a Titanium-Reinforced Dense Polytetrafluoroethylene Mesh Used in a Vertical Ridge Augmentation: A Case Report with 1-Year Follow-Up. *Clin. Adv. Periodontics*. Available at: https://pubmed.ncbi.nlm.nih.gov/34337897/ (Accessed August 2, 2021)

Binhammer, A., Jakubowski, J., Antonyshyn, O., and Binhammer, P. (2020). Comparative Cost-Effectiveness of Cranioplasty Implants. *Plast. Surg. (Oakv)* 28 (1), 29–39. doi:10.1177/2292550319880922

Borges, C. D. A., Faria, P. E. P., Pessôa de Oliveira, P. G. F., Sales de Melo Soares, M., Ricoldi, M. S. T., Costa, M. S., et al. (2020). Influence of Collagen Membrane on Bone Quality in Titanium Mesh Reconstructions-Study in Rats. *J. Periodontol.* 91 (12), 1673–1681. doi:10.1002/jper.19-0399

Brunello, G., Panda, S., Schiavon, L., Sivolella, S., Biasetto, L., and Del Fabbro, M. (2020). The Impact of Bioceramic Scaffolds on Bone Regeneration in Preclinical *In Vivo* Studies: A Systematic Review. *Materials* 13 (7), 1500. doi:10.3390/ma13071500

Celletti, R., Davarpanah, M., Etienne, D., Pecora, G., Tecucianu, J. F., Djukanovic, D., et al. (1994). Guided Tissue Regeneration Around Dental Implants in Immediate Extraction Sockets: Comparison of E-Ptfe and a New Titanium Membrane. *Int. J. Periodontics Restor. Dent.* 14 (3), 242

Chen, Y., Ye, S.-H., Sato, H., Zhu, Y., Shanov, V., Tiasha, T., et al. (2018). Hybrid Scaffolds of Mg Alloy Mesh Reinforced Polymer/Extracellular Matrix Composite for Critical-Sized Calvarial Defect Reconstruction. *J. Tissue Eng. Regen. Med.* 12 (6), 1374–1388. doi:10.1002/term.2668

Cheung, L. K., Samman, N., Tong, A. C. K., and Tideman, H. (1994). Mandibular Reconstruction with the Dacron Urethane Tray: A Radiologic Assessment of Bone Remodeling. *J. Oral Maxillofac. Surg.* 52 (4), 373–380. doi:10.1016/0278-2391(94)90440-5

Chiapasco, M., and Casentini, P. (2018). Horizontal Bone-Augmentation Procedures in Implant Dentistry: Prosthetically Guided Regeneration. *Periodontol. 2000* 77 (1), 213–240. doi:10.1111/prd.12219

Chiapasco, M., Casentini, P., Tommasato, G., Dellavia, C., and Del Fabbro, M. (2021). Customized Cad/Cam Titanium Meshes for the Guided Bone Regeneration of Severe Alveolar Ridge Defects: Preliminary Results of a Retrospective Clinical Study in Humans. *Clin. Oral Implants Res.* 32 (4), 498–510. doi:10.1111/clr.13720

Choi, I.-O., Oh, J.-S., Yu, S.-J., Kim, B.-O., and Lee, W.-P. (2021). Retrospective Analysis of the Effect of Three-Dimensional Preformed Titanium Mesh on Peri-Implant Non-contained Horizontal Defects in 100 Consecutive Cases. *Appl. Sci.* 11 (2), 872. doi:10.3390/app11020872

Ciocca, L., Fantini, M., De Crescenzio, F., Corinaldesi, G., and Scotti, R. (2013). Cad-Cam Prosthetically Guided Bone Regeneration Using Preformed Titanium Mesh for the Reconstruction of Atrophic Maxillary Arches. *Comput. Methods Biomechanics Biomed. Eng.* 16 (1), 26–32. doi:10.1080/10255842.2011.601279

Ciocca, L., Fantini, M., De Crescenzio, F., Corinaldesi, G., and Scotti, R. (2011). Direct Metal Laser Sintering (Dmls) of a Customized Titanium Mesh for Prosthetically Guided Bone Regeneration of Atrophic Maxillary Arches. *Med. Biol. Eng. Comput.* 49 (11), 1347–1352. doi:10.1007/s11517-011-0813-4

Ciocca, L., Lizio, G., Baldissara, P., Sambuco, A., Scotti, R., and Corinaldesi, G. (2018). Prosthetically Cad-Cam-Guided Bone Augmentation of Atrophic Jaws Using Customized Titanium Mesh: Preliminary Results of an Open Prospective Study. *J. Oral Implant* 44 (2), 131–137. doi:10.1563/aaid-joi-D-17-00125

Croes, M., Kruyt, M. C., Kruyt, M., Boot, W., Pouran, B., Braham, M., et al. (2019). The Role of Bacterial Stimuli in Inflammation-Driven Bone Formation. *eCM* 37, 402–419. doi:10.22203/eCM.v037a24

Cucchi, A., Bianchi, A., Calamai, P., Rinaldi, L., Mangano, F., Vignudelli, E., et al. (2020). Clinical and Volumetric Outcomes after Vertical Ridge Augmentation Using Computer-Aided-Design/Computer-Aided Manufacturing (Cad/Cam) Customized Titanium Meshes: A Pilot Study. *BMC Oral Health* 20 (1), 219. doi:10.1186/s12903-020-01205-4

Cucchi, A., Giavatto, M. A., Giannatiempo, J., Lizio, G., and Corinaldesi, G. (2019a). Custom-Made Titanium Mesh for Maxillary Bone Augmentation with Immediate Implants and Delayed Loading. *J. Oral Implant* 45 (1), 59–64. doi:10.1563/aaid-joi-D-18-00141

Cucchi, A., Sartori, M., Aldini, N., Vignudelli, E., and Corinaldesi, G. (2019b). A Proposal of Pseudo-periosteum Classification after Gbr by Means of Titanium-Reinforced D-Ptfe Membranes or Titanium Meshes Plus Cross-Linked Collagen Membranes. *Int. J. Periodontics Restor. Dent.* 39 (4), e157–e165. doi:10.11607/prd.e359810.11607/prd.3598

Cucchi, A., Vignudelli, E., Franceschi, D., Randellini, E., Lizio, G., Fiorino, A., et al. (2021). Vertical and Horizontal Ridge Augmentation Using Customized Cad/Cam Titanium Mesh with versus without Resorbable Membranes. A Randomized Clinical Trial. *Clin. Oral Implants Res.* 32 (12), 1411–1424. doi:10.1111/clr.13841

Dahlin, C., Simion, M., Nanmark, U., and Sennerby, L. (1998). Histological Morphology of the E-FTFE/tissue Interface in Humans Subjected to Guided Bone Regeneration in Conjunction with Oral Implant Treatment. *Clin. Oral Implant. Res.* 9 (2), 100–106. doi:10.1034/j.1600-0501.1998.090205.x

de Santana, R. B., de Mattos, C. M. L., Francischone, C. E., and Van Dyke, T. (2010). Superficial Topography and Porosity of an Absorbable Barrier Membrane Impacts Soft Tissue Response in Guided Bone Regeneration. *J. Periodontology* 81 (6), 926–933. doi:10.1902/jop.2010.090592

De Santis, D., Gelpi, F., Verlato, G., Luciano, U., Torroni, L., Antonucci, N., et al. (2021). Digital Customized Titanium Mesh for Bone Regeneration of Vertical, Horizontal and Combined Defects: A Case Series. *Medicina* 57 (1), 60. doi:10.3390/medicina57010060

Dellavia, C., Canciani, E., Pellegrini, G., Tommasato, G., Graziano, D., and Chiapasco, M. (2021). Histological Assessment of Mandibular Bone Tissue after Guided Bone Regeneration with Customized Computer-aided Design/computer-assisted Manufacture Titanium Mesh in Humans: A Cohort Study. *Clin. Implant Dent. Relat. Res.* 23 (4), 600–611. doi:10.1111/cid.13025

Dimitriou, R., Jones, E., McGonagle, D., and Giannoudis, P. V. (2011). Bone Regeneration: Current Concepts and Future Directions. *BMC Med.* 9, 66. doi:10.1186/1741-7015-9-66

Dong, Q. N., Kanno, T., Bai, Y., Sha, J., and Hideshima, K. (2019). Bone Regeneration Potential of Uncalcined and Unsintered Hydroxyapatite/Poly L-Lactide Bioactive/Osteoconductive Sheet Used for Maxillofacial Reconstructive Surgery: An *In Vivo* Study. *Materials* 12 (18), 2931. doi:10.3390/ma12182931

El Chaar, E., Urtula, A. B., Georgantza, A., Cruz, S., Fallah-Abed, P., Castaño, A., et al. (2019). Treatment of Atrophic Ridges with Titanium Mesh: A Retrospective Study Using 100% Mineralized Allograft and Comparing Dental Stone versus 3d-Printed Models. *Int. J. Periodontics Restor. Dent.* 39 (4), 491–500. doi:10.11607/prd.3733

El Morsy, O. A., Barakat, A., Mekhemer, S., and Mounir, M. (2020). Assessment of 3-dimensional Bone Augmentation of Severely Atrophied Maxillary Alveolar Ridges Using Patient-specific Poly Ether-ether Ketone (PEEK) Sheets. *Clin. Implant Dent. Relat. Res.* 22 (2), 148–155. doi:10.1111/cid.12890

Elias, C., Oshida, Y., Lima, J., and Muller, C. (2008). Relationship between Surface Properties (Roughness, Wettability and Morphology) of Titanium and Dental Implant Removal Torque. *J. Mech. Behav. Biomed. Mater.* 1 (3), 234–242. doi:10.1016/j.jmbbm.2007.12.002

Eppley, B. L., Pietrzak, W. S., and Blanton, M. (2006). Platelet-Rich Plasma: A Review of Biology and Applications in Plastic Surgery. *Plastic Reconstr. Surg.* 118 (6), 147e–159e. doi:10.1097/01.prs.0000239606.92676.cf

Frankenberger, T., Graw, C. L., Engel, N., Gerber, T., Frerich, B., and Dau, M. (2021). Sustainable Surface Modification of Polyetheretherketone (Peek) Implants by Hydroxyapatite/Silica Coating-An *In Vivo* Animal Study. *Materials* 14 (16), 4589. doi:10.3390/ma14164589

Ghanaati, S., Al-Maawi, S., Conrad, T., Lorenz, J., Rössler, R., and Sader, R. (2019). Biomaterial-Based Bone Regeneration and Soft Tissue Management of the Individualized 3d-Titanium Mesh: An Alternative Concept to Autologous Transplantation and Flap Mobilization. *J. Cranio-Maxillofacial Surg.* 47 (10), 1633–1644. doi:10.1016/j.jcms.2019.07.020

Giragosyan, K., Chenchev, I., Ivanova, V., and Zlatev, S. (2022). Immunological Response to Nonresorbable Barrier Membranes Used for Guided Bone Regeneration and Formation of Pseudo Periosteum: A Narrative Review. *Folia. Medica.* 64 (1), 13–20. doi:10.3897/folmed.64.e60553

Gu, X., Sun, X., Sun, Y., Wang, J., Liu, Y., Yu, K., et al. (2020). Bioinspired Modifications of Peek Implants for Bone Tissue Engineering. *Front. Bioeng. Biotechnol.* 8, 631616. doi:10.3389/fbioe.2020.631616

Guo, F., Huang, S., Hu, M., Yang, C., Li, D., and Liu, C. (2021). Biomechanical Evaluation of a Customized 3D-printed Polyetheretherketone Condylar Prosthesis. *Exp. Ther. Med.* 21 (4), 348. doi:10.3892/etm.2021.9779

Guo, H., Xia, D., Zheng, Y., Zhu, Y., Liu, Y., and Zhou, Y. (2020). A Pure Zinc Membrane with Degradability and Osteogenesis Promotion for Guided Bone Regeneration: *In Vitro* and *In Vivo* Studies. *Acta Biomater.* 106, 396–409. doi:10.1016/j.actbio.2020.02.024

Gutta, R., Baker, R. A., Bartolucci, A. A., and Louis, P. J. (2009). Barrier Membranes Used for Ridge Augmentation: Is There an Optimal Pore Size?. *J. Oral Maxillofac. Surg.* 67 (6), 1218–1225. doi:10.1016/j.joms.2008.11.022

Han, X., Gao, W., Zhou, Z., Yang, S., Wang, J., Shi, R., et al. (2022). Application of Biomolecules Modification Strategies on Peek and its Composites for Osteogenesis and Antibacterial Properties. *Colloids Surfaces B Biointerfaces* 215, 112492. doi:10.1016/j.colsurfb.2022.112492

Hartmann, A., Hildebrandt, H., Schmohl, J. U., and Kämmerer, P. W. (2019). Evaluation of Risk Parameters in Bone Regeneration Using a Customized Titanium Mesh: Results of a Clinical Study. *Implant Dent.* (6), 543–550. doi:10.1097/id.0000000000000933

Hartmann, A., and Seiler, M. (2020). Minimizing Risk of Customized Titanium Mesh Exposures - a Retrospective Analysis. *BMC Oral Health* 20 (1), 36. doi:10.1186/s12903-020-1023-y

He, Y., Wang, X., He, Y., Zhao, X., Lin, J., Feng, Y., et al. (2022). A Bioinspired Janus Polyurethane Membrane for Potential Periodontal Tissue Regeneration. *J. Mat. Chem. B* 10 (14), 2602–2616. doi:10.1039/d1tb02068d

Her, S., Kang, T., and Fien, M. J. (2012). Titanium Mesh as an Alternative to a Membrane for Ridge Augmentation. *J. Oral Maxillofac. Surg.* 70 (4), 803–810. doi:10.1016/j.joms.2011.11.017

Hofferber, C. E., Beck, J. C., Liacouras, P. C., Wessel, J. R., and Getka, T. P. (2020). Volumetric Changes in Edentulous Alveolar Ridge Sites Utilizing Guided Bone Regeneration and a Custom Titanium Ridge Augmentation Matrix (Ctram): A Case Series Study. *Int. J. Implant. Dent.* 6 (1), 83. doi:10.1186/s40729-020-00269-9

Hu, G., Zhu, Y., Xu, F., Ye, J., Guan, J., Jiang, Y., et al. (2022). Comparison of Surface Properties, Cell Behaviors, Bone Regeneration and Osseointegration between Nano Tantalum/Peek Composite and Nano Silicon Nitride/Peek Composite. *J. Biomaterials Sci. Polym. Ed.* 33 (1), 35–56. doi:10.1080/09205063.2021.1974812

Ikawa, T., Shigeta, Y., Hirabayashi, R., Hirai, S., Hirai, K., Harada, N., et al. (2016). Computer Assisted Mandibular Reconstruction Using a Custom-Made Titan Mesh Tray and Removable Denture Based on the Top-Down Treatment Technique. *J. Prosthodont. Res.* 60 (4), 321–331. doi:10.1016/j.jpor.2016.01.009

Jia, B., Yang, H., Han, Y., Zhang, Z., Qu, X., Zhuang, Y., et al. (2020). *In Vitro* and *In Vivo* Studies of Zn-Mn Biodegradable Metals Designed for Orthopedic Applications. *Acta Biomater.* 108, 358–372. doi:10.1016/j.actbio.2020.03.009

Jiang, J., You, D., Wang, Q., and Gao, G. (2022). Novel Fabrication and Biological Characterizations of Agnps-Decorated Peek with Gelatin Functional Nanocomposite to Improve Superior Biomedical Applications. *J. Biomaterials Sci. Polym. Ed.* 33 (5), 590–604. doi:10.1080/09205063.2021.2004632

Jung, G.-U., Jeon, J.-Y., Hwang, K.-G., and Park, C.-J. (2014). Preliminary Evaluation of a Three-Dimensional, Customized, and Preformed Titanium Mesh in Peri-Implant Alveolar Bone Regeneration. *J. Korean Assoc. Oral Maxillofac. Surg.* 40 (4), 181–187. doi:10.5125/jkaoms.2014.40.4.181

Kang, J., Zhang, J., Zheng, J., Wang, L., Li, D., and Liu, S. (2021). 3d-Printed Peek Implant for Mandibular Defects Repair - a New Method. *J. Mech. Behav. Biomed. Mater.* 116, 104335. doi:10.1016/j.jmbbm.2021.104335

Kanno, T., Sukegawa, S., Furuki, Y., Nariai, Y., Sekine, J., Tatsumi, H., et al. (20172018). Feasibility of Single Folded Unsintered Hydroxyapatite Particles/Poly-L-Lactide Composite Sheet in Combined Orbital Floor and Medial Wall Fracture ReconstructionOverview of Innovative Advances in Bioresorbable Plate Systems for Oral and Maxillofacial Surgery. *Jpn. Dent. Sci. Rev. Dent. Sci. Rev.* 2654 (23), 127–138. doi:10.1016/j.jdsr.2018.03.003

Katzer, A., Marquardt, H., Westendorf, J., Wening, J. V., and von Foerster, G. (2002). Polyetheretherketone-cytotoxicity and Mutagenicity *In Vitro*. *Biomaterials* 23 (8), 1749–1759. doi:10.1016/s0142-9612(01)00300-3

Kondo, T., Kanayama, K., Egusa, H., and Nishimura, I. (2022). Current Perspectives of Residual Ridge Resorption: Pathological Activation of Oral Barrier Osteoclasts. *J. Prosthodont. Res*. doi:10.2186/jpr.JPR_D_21_00333

Lee, J. S., Park, J. Y., Chung, H. M., Song, Y. W., and Strauss, F. J. (2022). Vertical Ridge Augmentation Feasibility Using Unfixed Collagen Membranes and Particulate Bone Substitutes: A 1- to 7-year Retrospective Single-cohort Observational Study. *Clin. Implant Dent. Rel Res.* doi:10.1111/cid.13084

Lee, W.-b., Choi, W.-h., Lee, H.-g., Choi, N.-r., Hwang, D.-s., and Kim, U.-k. (2018). Mandibular Reconstruction with a Ready-Made Type and a Custom-Made Type Titanium Mesh after Mandibular Resection in Patients with Oral Cancer. *Maxillofac. Plast. Reconstr. Surg.* 40 (1), 35. doi:10.1186/s40902-018-0175-z

Levine, R., Lai, P.-C., Manji, A., Bruce, J., Katwal, D., Chen, P.-H., et al. (2022). Implant Site Development Using Titanium Mesh in the Maxilla: A Retrospective Study of 58 Mesh Procedures in 48 Patients. *Int. J. Periodontics Restor. Dent.* 42 (1), 43–51. doi:10.11607/prd.5530

Li, L., Gao, H., Wang, C., Ji, P., Huang, Y., and Wang, C. (2022). Assessment of Customized Alveolar Bone Augmentation Using Titanium Scaffolds vs Polyetheretherketone (Peek) Scaffolds: A Comparative Study Based on 3d Printing Technology. *ACS Biomater. Sci. Eng.* 8, 2028–2039. doi:10.1021/acsbiomaterials.2c00060

Li, L., Wang, C., Li, X., Fu, G., Chen, D., and Huang, Y. (2021a). Research on the Dimensional Accuracy of Customized Bone Augmentation Combined with 3D -printing Individualized Titanium Mesh: A Retrospective Case Series Study. *Clin. Implant Dent. Relat. Res.* 23 (1), 5–18. doi:10.1111/cid.12966

Li, S., Zhang, T., Zhou, M., Zhang, X., Gao, Y., and Cai, X. (2021b). A Novel Digital and Visualized Guided Bone Regeneration Procedure and Digital Precise Bone Augmentation: A Case Series. *Clin. Implant Dent. Relat. Res.* 23 (1), 19–30. doi:10.1111/cid.12959

Lindfors, L. T., Tervonen, E. A. T., Sándor, G. K. B., and Ylikontiola, L. P. (2010). Guided Bone Regeneration Using a Titanium-Reinforced Eptfe Membrane and Particulate Autogenous Bone: The Effect of Smoking and Membrane Exposure. *Oral Surg. Oral Med. Oral Pathology, Oral Radiology, Endodontology* 109 (6), 825–830. doi:10.1016/j.tripleo.2009.12.035

Liu, B.-y., Cao, G., Dong, Z., Chen, W., Xu, J.-k., and Guo, T. (2019). The Application of 3d-Printed Titanium Mesh in Maxillary Tumor Patients Undergoing Total Maxillectomy. *J. Mater Sci. Mater Med.* 30 (11), 125. doi:10.1007/s10856-019-6326-7

Liu, J., Liu, J., Attarilar, S., Wang, C., Tamaddon, M., Yang, C., et al. (2020). Nano-Modified Titanium Implant Materials: A Way toward Improved Antibacterial Properties. *Front. Bioeng. Biotechnol.* 8, 576969. doi:10.3389/fbioe.2020.576969

Lizio, G., Pellegrino, G., Corinaldesi, G., Ferri, A., Marchetti, C., and Felice, P. (2022). Guided Bone Regeneration Using Titanium Mesh to Augment 3-

dimensional Alveolar Defects Prior to Implant Placement. A Pilot Study. *Clin. Oral Implants Res.* doi:10.1111/clr.13922

Ma, Z., Zhao, X., Zhao, J., Zhao, Z., Wang, Q., and Zhang, C. (2020). Biologically Modified Polyether Ether Ketone as Dental Implant Material. *Front. Bioeng. Biotechnol.* 8, 620537. doi:10.3389/fbioe.2020.620537

Major, R., Kowalczyk, P., Surmiak, M., Łojszczyk, I., Podgórski, R., Trzaskowska, P., et al. (2020). Patient Specific Implants for Jawbone Reconstruction after Tumor Resection. *Colloids Surfaces B Biointerfaces* 193, 111056. doi:10.1016/j.colsurfb.2020.111056

Mangano, C., Giuliani, A., De Tullio, I., Raspanti, M., Piattelli, A., and Iezzi, G. (2021). Case Report: Histological and Histomorphometrical Results of a 3-D Printed Biphasic Calcium Phosphate Ceramic 7 Years after Insertion in a Human Maxillary Alveolar Ridge. *Front. Bioeng. Biotechnol.* 9, 614325. doi:10.3389/fbioe.2021.614325

Matsuo, A., Chiba, H., Takahashi, H., Toyoda, J., and Abukawa, H. (2010). Clinical Application of a Custom-Made Bioresorbable Raw Particulate Hydroxyapatite/Poly-L-Lactide Mesh Tray for Mandibular Reconstruction. *Odontology* 98 (1), 85–88. doi:10.1007/s10266-009-0111-x

Matsuo, A., Takahashi, H., Abukawa, H., and Chikazu, D. (2012). Application of Custom-Made Bioresorbable Raw Particulate Hydroxyapatite/Poly-L-Lactide Mesh Tray with Particulate Cellular Bone and Marrow and Platelet-Rich Plasma for a Mandibular Defect: Evaluation of Tray Fit and Bone Quality in a Dog Model. *J. Cranio-Maxillofacial Surg.* 40 (8), e453–e460. doi:10.1016/j.jcms.2012.03.004

Mehdizadeh Omrani, M., Kumar, H., Mohamed, M. G. A., Golovin, K., S. Milani, A., and Kim, K. (2021). Polyether Ether Ketone Surface Modification with Plasma and Gelatin for Enhancing Cell Attachment. *J. Biomed. Mater Res.* 109 (5), 622–629. doi:10.1002/jbm.b.34726

Mian, S. H., Moiduddin, K., Elseufy, S. M., and Alkhalefah, H. (2022). Adaptive Mechanism for Designing a Personalized Cranial Implant and its 3d Printing Using Peek. *Polymers* 14 (6), 1266. doi:10.3390/polym14061266

Moroi, A., Ueki, K., Okabe, K., Marukawa, K., Sotobori, M., Mukozawa, A., et al. (2013). Comparison between Unsintered Hydroxyapatite/Poly-L-Lactic Acid Mesh and Titanium Mesh in Bone Regeneration of Rabbit Mandible. *Implant Dent.* 22 (3), 255–262. doi:10.1097/ID.0b013e31828336be

Mounir, M., Shalash, M., Mounir, S., Nassar, Y., and El Khatib, O. (2019). Assessment of Three Dimensional Bone Augmentation of Severely Atrophied Maxillary Alveolar Ridges Using Prebent Titanium Mesh vs Customized Poly-ether-ether-ketone (PEEK) Mesh: A Randomized Clinical Trial. *Clin. Implant Dent. Relat. Res.* 21 (5), 960–967. doi:10.1111/cid.12748

Najeeb, S., Khurshid, Z., Agwan, M. A. S., Ansari, S. A., Zafar, M. S., and Matinlinna, J. P. (2017). Regenerative Potential of Platelet Rich Fibrin (Prf) for Curing Intrabony Periodontal Defects: A Systematic Review of Clinical Studies. *Tissue Eng. Regen. Med.* 14 (6), 735–742. doi:10.1007/s13770-017-0079-5

Nguyen, T.-D., Moon, S.-H., Oh, T.-J., Seok, J.-J., Lee, M.-H., and Bae, T.-S. (2016). Comparison of Guided Bone Regeneration between Surface-Modified and Pristine Titanium Membranes in a Rat Calvarial Model. *Int. J. Oral Maxillofac. Implants.* 31 (3), 581–590. doi:10.11607/jomi.4317

Nguyen, T.-D. T., Jang, Y.-S., Kim, Y.-K., Kim, S.-Y., Lee, M.-H., and Bae, T.-S. (2019). Osteogenesis-Related Gene Expression and Guided Bone Regeneration of a Strontium-Doped Calcium-Phosphate-Coated Titanium Mesh. *ACS Biomater. Sci. Eng.* 5 (12), 6715–6724. doi:10.1021/acsbiomaterials.9b01042

Nickenig, H.-J., Riekert, M., Zirk, M., Lentzen, M.-P., Zöller, J. E., and Kreppel, M. (2022). 3d-Based Buccal Augmentation for Ideal Prosthetic Implant Alignment-An Optimized Method and Report on 7 Cases with Pronounced Buccal Concavities. *Clin. Oral Invest.* 26, 3999–4010. doi:10.1007/s00784-022-04369-1

Oberoi, G., Nitsch, S., Edelmayer, M., Janjić, K., Müller, A. S., and Agis, H. (2018). 3d Printing-Encompassing the Facets of Dentistry. *Front. Bioeng. Biotechnol.* 6, 172. doi:10.3389/fbioe.2018.00172

Panayotov, I. V., Orti, V., Cuisinier, F., and Yachouh, J. (2016). Polyetheretherketone (Peek) for Medical Applications. *J. Mater Sci. Mater Med.* 27 (7), 118. doi:10.1007/s10856-016-5731-4

Papia, E., Brodde, S. A. C., and Becktor, J. P. (2022). Deformation of Polyetheretherketone, Peek, with Different Thicknesses. *J. Mech. Behav. Biomed. Mater.* 125, 104928. doi:10.1016/j.jmbbm.2021.104928

Pezzotti, G., Marin, E., Adachi, T., Lerussi, F., Rondinella, A., Boschetto, F., et al. (2018). Incorporating Si_3N_4 into PEEK to Produce Antibacterial, Osteocondutive, and Radiolucent Spinal Implants. *Macromol. Biosci.* 18 (6), 1800033. doi:10.1002/mabi.201800033

Prevost, R., Kimakhe, J., Diep, D., Drouet, J., Benateau, H., and Veyssiere, A. (2019). The Significance of Computer-Assisted Surgery in Avoiding Double-Barrel Fibula Grafts in Reconstruction of the Horizontal Mandibular Ramus. *J. Stomatology, Oral Maxillofac. Surg.* 120 (2), 167–171. doi:10.1016/j.jormas.2018.09.004

Prochor, P., and Mierzejewska, Ż. A. (2019). Influence of the Surface Roughness of Peek Grf30 and Ti6al4v Slm on the Viability of Primary Human Osteoblasts Determined by the Mtt Test. *Materials* 12 (24), 4189. doi:10.3390/ma12244189

Rahman, M., Dutta, N. K., and Roy Choudhury, N. (2020). Magnesium Alloys with Tunable Interfaces as Bone Implant Materials. *Front. Bioeng. Biotechnol.* 8, 564. doi:10.3389/fbioe.2020.00564

Rakhmatia, Y. D., Ayukawa, Y., Furuhashi, A., and Koyano, K. (2013). Current Barrier Membranes: Titanium Mesh and Other Membranes for Guided Bone Regeneration in Dental Applications. *J. Prosthodont. Res.* 57 (1), 3–14. doi:10.1016/j.jpor.2012.12.001

Ren, L., Tang, S., Shen, X., Gao, C., Jung, Y. K., Wang, D., et al. (2020). Influences of Sodium Tantalite Submicro-Particles in Polyetheretherketone Based Composites on Behaviors of Rbmscs/Hge-1 Cells for Dental Application. *Colloids Surfaces B Biointerfaces* 188, 110723. doi:10.1016/j.colsurfb.2019.110723

Rosinski, C. L., Patel, S., Geever, B., Chiu, R. G., Chaker, A. N., Zakrzewski, J., et al. (2009). Effect of Roughness, Wettability and Morphology of Engineered Titanium Surfaces on Osteoblast-like Cell Adhesion. *Colloid Surf. A-Physicochem. Eng. Asp.* 365A Retrospective Comparative Analysis of Titanium Mesh and Custom Implants for Cranioplasty. *Neurosurg.* 86 (11), E15–e22. doi:10.1093/neuros/nyz358

Sagheb, K., Schiegnitz, E., Moergel, M., Walter, C., Al-Nawas, B., and Wagner, W. (2017). Clinical Outcome of Alveolar Ridge Augmentation with Individualized Cad-Cam-Produced Titanium Mesh. *Int. J. Implant. Dent.* 3 (1), 36. doi:10.1186/s40729-017-0097-z

Scantlebury, T. V. (1993). 1982-1992: A Decade of Technology Development for Guided Tissue Regeneration. *J. Periodontology* 64 (11 Suppl. l), 1129–1137. doi:10.1902/jop.1993.64.11s.1129

Schwitalla, A., and Müller, W.-D. (2013). Peek Dental Implants: A Review of the Literature. *J. Oral Implant.* 39 (6), 743–749. doi:10.1563/aaid-joi-d-11-00002

Sharma, N., Aghlmandi, S., Dalcanale, F., Seiler, D., Zeilhofer, H.-F., Honigmann, P., et al. (2021). Quantitative Assessment of Point-of-Care 3d-Printed Patient-specific Polyetheretherketone (Peek) Cranial Implants. *Ijms* 22 (16), 8521. doi:10.3390/ijms22168521

Shikinami, Y., Matsusue, Y., and Nakamura, T. (2005). The Complete Process of Bioresorption and Bone Replacement Using Devices Made of Forged Composites of Raw Hydroxyapatite Particles/poly -lactide (F-u-HA/PLLA). *Biomaterials* 26 (27), 5542–5551. doi:10.1016/j.biomaterials.2005.02.016

Shikinami, Y., and Okuno, M. (1999). Bioresorbable Devices Made of Forged Composites of Hydroxyapatite (HA) Particles and Poly-L-Lactide (Plla): Part I. Basic Characteristics. *Biomaterials* 20 (9), 859–877. doi:10.1016/s0142-9612(98)00241-5

Silva, D. N., Gerhardt de Oliveira, M., Meurer, E., Meurer, M. I., Lopes da Silva, J. V., and Santa-Bárbara, A. (2008). Dimensional Error in Selective Laser Sintering and 3d-Printing of Models for Craniomaxillary Anatomy Reconstruction. *J. Cranio-Maxillofacial Surg.* 36 (8), 443–449. doi:10.1016/j.jcms.2008.04.003

Silva, T. S. N., Machado, D. C., Viezzer, C., Silva Júnior, A. N., and Oliveira, M. G. d. (2009). Effect of Titanium Surface Roughness on Human Bone Marrow Cell Proliferation and Differentiation: An Experimental Study. *Acta Cir. Bras.* 24 (3), 200–205. doi:10.1590/s0102-86502009000300007

Sumida, T., Otawa, N., Kamata, Y., Kamakura, S., Mtsushita, T., Kitagaki, H., et al. (2015). Custom-Made Titanium Devices as Membranes for Bone Augmentation in Implant Treatment: Clinical Application and the Comparison with Conventional Titanium Mesh. *J. Cranio-Maxillofacial Surg.* 43 (10), 2183–2188. doi:10.1016/j.jcms.2015.10.020

Takano, M., Sugahara, K., Koyachi, M., Odaka, K., Matsunaga, S., Homma, S., et al. (2019). Maxillary Reconstruction Using Tunneling Flap Technique with 3d Custom-Made Titanium Mesh Plate and Particulate Cancellous Bone and

Marrow Graft: A Case Report. *Maxillofac. Plast. Reconstr. Surg.* 41 (1), 43. doi:10.1186/s40902-019-0228-y

Tallarico, M., Park, C.-J., Lumbau, A. I., Annucci, M., Baldoni, E., Koshovari, A., et al. (2020). Customized 3d-Printed Titanium Mesh Developed to Regenerate a Complex Bone Defect in the Aesthetic Zone: A Case Report Approached with a Fully Digital Workflow. *Materials* 13 (17), 3874. doi:10.3390/ma13173874

Tian, Y., Chen, C., Xu, X., Wang, J., Hou, X., Li, K., et al. (2021). A Review of 3d Printing in Dentistry: Technologies, Affecting Factors, and Applications. *Scanning* 2021, 1–19. doi:10.1155/2021/9950131

Toledano-Osorio, M., Manzano-Moreno, F. J., Ruiz, C., Toledano, M., and Osorio, R. (2021). Testing Active Membranes for Bone Regeneration: A Review. *J. Dent.* 105, 103580. doi:10.1016/j.jdent.2021.103580

Torres, J., Tamimi, F., Alkhraisat, M. H., Manchón, Á., Linares, R., Prados-Frutos, J. C., et al. (2010). Platelet-Rich Plasma May Prevent Titanium-Mesh Exposure in Alveolar Ridge Augmentation with Anorganic Bovine Bone. *J. Clin. Periodontol.* 37 (10), 943–951. doi:10.1111/j.1600-051X.2010.01615.x

Troulis, M. J., Everett, P., Seldin, E. B., Kikinis, R., and Kaban, L. B. (2002). Development of a Three-Dimensional Treatment Planning System Based on Computed Tomographic Data. *Int. J. Oral Maxillofac. Surg.* 31 (4), 349–357. doi:10.1054/ijom.2002.0278

Ueki, K., Okabe, K., Miyazaki, M., Mukozawa, A., Moroi, A., Marukawa, K., et al. (2011). Skeletal Stability after Mandibular Setback Surgery: Comparisons Among Unsintered Hydroxyapatite/Poly-L-Lactic Acid Plate, Poly-L-Lactic Acid Plate, and Titanium Plate. *J. Oral Maxillofac. Surg.* 69 (5), 1464–1468. doi:10.1016/j.joms.2010.06.187

van de Vijfeijken, S. E. C. M., Schreurs, R., Dubois, L., Becking, A. G., Becking, A. G., Dubois, L., et al. (2019). The Use of Cranial Resection Templates with 3d Virtual Planning and Peek Patient-specific Implants: A 3 Year Follow-Up. *J. Cranio-Maxillofacial Surg.* 47 (4), 542–547. doi:10.1016/j.jcms.2018.07.012

Vaquette, C., Mitchell, J., and Ivanovski, S. (2021). Recent Advances in Vertical Alveolar Bone Augmentation Using Additive Manufacturing Technologies. *Front. Bioeng. Biotechnol.* 9, 798393. doi:10.3389/fbioe.2021.798393

Wang, H.-L., and Boyapati, L. (2006). "PASS" Principles for Predictable Bone Regeneration. *Implant Dent.* 15 (1), 8–17. doi:10.1097/01.id.0000204762.39826.0f

Wang, X., Mei, L., Jiang, X., Jin, M., Xu, Y., Li, J., et al. (2021a). Hydroxyapatite-Coated Titanium by Micro-arc Oxidation and Steam-Hydrothermal Treatment Promotes Osseointegration. *Front. Bioeng. Biotechnol.* 9, 625877. doi:10.3389/fbioe.2021.625877

Wang, X., Wang, G., Zhao, X., Feng, Y., Liu, H., and Li, F. (2021b). Short-Term Evaluation of Guided Bone Reconstruction with Titanium Mesh Membranes and Cgf Membranes in Immediate Implantation of Anterior Maxillary Tooth. *BioMed Res. Int.* 2021, 1–9. doi:10.1155/2021/4754078

Warnke, P. H., Douglas, T., Wollny, P., Sherry, E., Steiner, M., Galonska, S., et al. (2009). Rapid Prototyping: Porous Titanium Alloy Scaffolds Produced by Selective Laser Melting for Bone Tissue Engineering. *Tissue Eng. Part C. Methods* 15 (2), 115–124. doi:10.1089/ten.tec.2008.0288

Waser-Althaus, J., Salamon, A., Waser, M., Padeste, C., Kreutzer, M., Pieles, U., et al. (2014). Differentiation of Human Mesenchymal Stem Cells on Plasma-Treated Polyetheretherketone. *J. Mater Sci. Mater Med.* 25 (2), 515–525. doi:10.1007/s10856-013-5072-5

Wei, J., Qiao, S., Zhang, X., Li, Y., Zhang, Y., Wei, S., et al. (2021). Graphene-Reinforced Titanium Enhances Soft Tissue Seal. *Front. Bioeng. Biotechnol.* 9, 665305. doi:10.3389/fbioe.2021.665305

Xie, Y., Li, S., Zhang, T., Wang, C., and Cai, X. (2020). Titanium Mesh for Bone Augmentation in Oral Implantology: Current Application and Progress. *Int. J. Oral Sci.* 12 (1), 37. doi:10.1038/s41368-020-00107-z

Xu, X., Lu, Y., Li, S., Guo, S., He, M., Luo, K., et al. (2018). Copper-Modified Ti6al4v Alloy Fabricated by Selective Laser Melting with Pro-angiogenic and Anti-inflammatory Properties for Potential Guided Bone Regeneration Applications. *Mater. Sci. Eng. C* 90, 198–210. doi:10.1016/j.msec.2018.04.046

Yamada, M., and Egusa, H. (2018). Current Bone Substitutes for Implant Dentistry. *J. Prosthodont. Res.* 62 (2), 152–161. doi:10.1016/j.jpor.2017.08.010

Yan, Z.-Y., Zhu, J.-H., Liu, G.-Q., Liu, Z.-C., Guo, C.-B., Cui, N.-H., et al. (2022). Feasibility and Efficacy of a Degradable Magnesium-Alloy Gbr Membrane for Bone Augmentation in a Distal Bone-Defect Model in Beagle Dogs. *Bioinorganic Chem. Appl.* 2022, 1–12. doi:10.1155/2022/4941635

Yang, J., Sun, T., Yuan, Y., Li, X., Yu, H., and Guan, J. (2020). Evaluation of Titanium Cranioplasty and Polyetheretherketone Cranioplasty after Decompressive Craniectomy for Traumatic Brain Injury: A Prospective, Multicenter, Non-Randomized Controlled Trial. *Med. (Baltim.).* 99 (30), e21251. doi:10.1097/md.0000000000021251

Zellin, G., and Linde, A. (1996). Effects of Different Osteopromotive Membrane Porosities on Experimental Bone Neogenesis in Rats. *Biomaterials* 17 (7), 695–702. doi:10.1016/0142-9612(96)86739-1

Zhang, H. Y., Jiang, H. B., Ryu, J.-H., Kang, H., Kim, K.-M., and Kwon, J.-S. (2019a). Comparing Properties of Variable Pore-Sized 3d-Printed Pla Membrane with Conventional Pla Membrane for Guided Bone/Tissue Regeneration. *Materials* 12 (10), 1718. doi:10.3390/ma12101718

Zhang, T., Zhang, T., and Cai, X. (2019b). The Application of a Newly Designed L-shaped Titanium Mesh for GBR with Simultaneous Implant Placement in the Esthetic Zone: A Retrospective Case Series Study. *Clin. Implant Dent. Relat. Res.* 21 (5), 862–872. doi:10.1111/cid.12726

Zhao, D., Dong, H., Niu, Y., Fan, W., Jiang, M., Li, K., et al. (2022). Electrophoretic Deposition of Novel Semi-permeable Coatings on 3d-Printed Ti-Nb Alloy Meshes for Guided Alveolar Bone Regeneration. *Dent. Mater.* 38 (2), 431–443. doi:10.1016/j.dental.2021.12.026

Zhao, H., Wang, X., Zhang, W., Wang, L., Zhu, C., Huang, Y., et al. (2021). Bioclickable Mussel-Derived Peptides with Immunoregulation for Osseointegration of Peek. *Front. Bioeng. Biotechnol.* 9, 780609. doi:10.3389/fbioe.2021.780609

Zhou, T., Chen, S., Ding, X., Hu, Z., Cen, L., and Zhang, X. (2021). Fabrication and Characterization of Collagen/Pva Dual-Layer Membranes for Periodontal Bone Regeneration. *Front. Bioeng. Biotechnol.* 9, 630977. doi:10.3389/fbioe.2021.630977

Zhuang, Y., Zhao, Z., Cheng, M., Li, M., Si, J., Lin, K., et al. (2022). HIF-1α Regulates Osteogenesis of Periosteum-Derived Stem Cells under Hypoxia Conditions via Modulating POSTN Expression. *Front. Cell Dev. Biol.* 10, 836285. doi:10.3389/fcell.2022.836285

Conflict of Interest: The authors declare that the research was conducted in the absence of any commercial or financial relationships that could be construed as a potential conflict of interest.

Publisher's Note: All claims expressed in this article are solely those of the authors and do not necessarily represent those of their affiliated organizations, or those of the publisher, the editors, and the reviewers. Any product that may be evaluated in this article, or claim that may be made by its manufacturer, is not guaranteed or endorsed by the publisher.

Copyright © 2022 Shi, Liu, Du, Zhang, Liu, Yang, Shi, Guo, Song, Zhao and Lan. This is an open-access article distributed under the terms of the Creative Commons Attribution License (CC BY). The use, distribution or reproduction in other forums is permitted, provided the original author(s) and the copyright owner(s) are credited and that the original publication in this journal is cited, in accordance with accepted academic practice. No use, distribution or reproduction is permitted which does not comply with these terms.

frontiers | Frontiers in Bioengineering and Biotechnology

ORIGINAL RESEARCH
published: 22 July 2022
doi: 10.3389/fbioe.2022.920766

Mesoporous Polydopamine Loaded Pirfenidone Target to Fibroblast Activation Protein for Pulmonary Fibrosis Therapy

Qi Fang[1], Shaoyu Liu[1], Jiangyu Cui[2], Ruiyue Zhao[1], Qian Han[2], Peng Hou[1], Youcai Li[1], Jie Lv[1], Xiaoyao Zhang[1], Qun Luo[2] and Xinlu Wang[1]**

[1]Department of Nuclear Medicine, The First Affiliated Hospital of Guangzhou Medical University, Guangzhou, China, [2]State Key Laboratory of Respiratory Diseases, Guangzhou Institute of Respiratory Diseases, The First Affiliated Hospital of Guangzhou Medical University, Guangzhou, China

Recently, fibroblast activation protein (FAP), an overexpressed transmembrane protein of activated fibroblast in pulmonary fibrosis, has been considered as the new target for diagnosing and treating pulmonary fibrosis. In this work, mesoporous polydopamine (MPDA), which is facile prepared and easily modified, is developed as a carrier to load antifibrosis drug pirfenidone (PFD) and linking FAP inhibitor (FAPI) to realize lesion-targeted drug delivery for pulmonary fibrosis therapy. We have found that PFD@MPDA-FAPI is well biocompatible and with good properties of antifibrosis, when ICG labels MPDA-FAPI, the accumulation of the nanodrug at the fibrosis lung *in vivo* can be observed by NIR imaging, and the antifibrosis properties of PFD@MPDA-FAPI *in vivo* were also better than those of pure PFD and PFD@MPDA; therefore, the easily produced and biocompatible nanodrug PFD@MPDA-FAPI developed in this study is promising for further clinical translations in pulmonary fibrosis antifibrosis therapy.

Keywords: mesoporous polydopamine, fibroblast activation protein, fibroblast activation protein inhibitor, pulmonary fibrosis, antifibrosis therapy

OPEN ACCESS

Edited by:
Gang Wu,
Academic Centre for Dentistry Amsterdam, Netherlands

Reviewed by:
Shuo Tang,
Sun Yat-sen University, China
Ekaterina Naumenko,
Kazan Federal University, Russia
Juan Chen,
Ningxia Medical University, China

****Correspondence:***
Qun Luo
luoqunx@163.com
Xinlu Wang
71Lu@163.com

Specialty section:
This article was submitted to Biomaterials, a section of the journal Frontiers in Bioengineering and Biotechnology

Received: *15 April 2022*
Accepted: *16 June 2022*
Published: *22 July 2022*

Citation:
Fang Q, Liu S, Cui J, Zhao R, Han Q, Hou P, Li Y, Lv J, Zhang X, Luo Q and Wang X (2022) Mesoporous Polydopamine Loaded Pirfenidone Target to Fibroblast Activation Protein for Pulmonary Fibrosis Therapy. Front. Bioeng. Biotechnol. 10:920766. doi: 10.3389/fbioe.2022.920766

1 INTRODUCTION

Pulmonary fibrosis is the terminal of many interstitial lung diseases (ILDs), it damages the normal lung structure, causes lung function decay, impairs the quality of life, and even leads to death by fibroblasts activated aberrantly and extracellular matrix (ECM) accumulated excessively (Rockey et al., 2015; Deng et al., 2020; Lai et al., 2021). Idiopathic pulmonary fibrosis (IPF) is a very common ILD, manifesting progressive pulmonary fibrosis with unclear etiology, the middle survival time of IPF is 2–5 years (Fernández Pérez et al., 2010; Ley et al., 2011; Nathan et al., 2011; Raghu et al., 2011). Nowadays, the critical treatment for IPF is antifibrosis therapy, for example, pirfenidone (PFD). PFD had finished the phase three trial, represented a good effect on patients with IPF, but often comes along with gastrointestinal (GI) adverse events (AE), which may be brought by the oral administration (King et al., 2014; Lancaster et al., 2017).

Activated fibroblast is a key cell in pulmonary fibrosis pathogenesis, and fibroblast activation protein (FAP), a 97 kDa type II transmembrane protein, with dipeptidyl peptidase activity as one kind of serine protease, only overexpressed on the membrane of aberrantly activated fibroblast, had been proved that could be found at the remolding area of IPF and cancer (Garin-Chesa et al., 1990; Acharya et al., 2006; Keane et al., 2013). So FAP has become the target of pulmonary fibrosis diagnosis and therapy, which

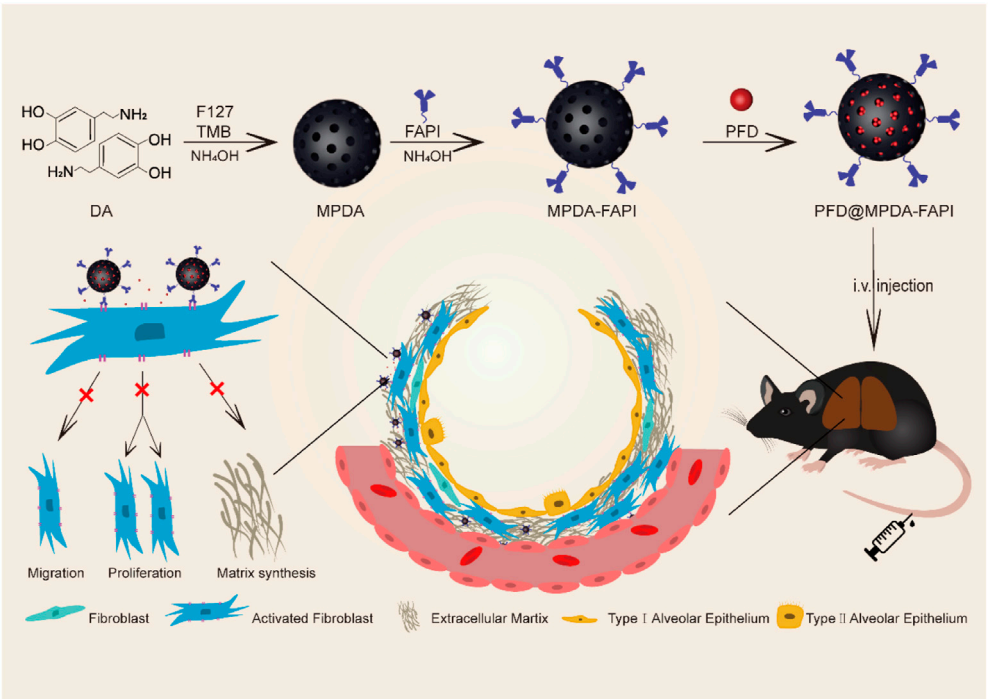

SCHEME 1 | Schematic illustration of the synthetic procedures and therapy mechanisms of PFD@MPDA-FAPI.

interests many researchers (Wenlong et al., 2015; Lin et al., 2019; Wu et al., 2020; Bergmann et al., 2021; Rohrich et al., 2022). It had been reported that FAP inhibitor (FAPI) labeled by radionuclide could reveal the FAP expression in patients with ILD, (Bergmann et al., 2021; Rohrich et al., 2022) positron emission tomography computed tomography (PET/CT) used FAPI as a tracer maybe is a promising imaging modality for ILDs to detect lesion earlier than CT, because CT only focuses on the change of structure, but FAPI PET/CT can observe the metabolism of the fibroblast before the change of anatomy. At the same time, Ma et al. have proved that bioluminescent probe target to FAP successfully indicated that the expression of FAP in the lung of the pulmonary fibrosis mice was increased (Lin et al., 2019). FAP is also has been proved that can play a role in antifibrosis therapy, Egger et al. (2017) reported that FAP inhibitor PT100 manifests antifibrosis properties in pulmonary fibrosis mice induced by bleomycin (BLM). Getting et al. found that FAP stimulates the activation of fibroblast (Wu et al., 2020). But in contrast, Kimura et al. found that the lack of FAP accelerates fibrosis. Meanwhile, Fan et al. (2016) found that FAP can accelerate the degradation and clearance of collagen. Therefore, the real role that FAP plays in fibrosis remains a mystery, but we may base the specific membrane protein to develop a class of target drug delivery nano.

There has been no nanodrug target to FAP for antifibrosis therapy before. Recently, nanodrugs that utilize nanoparticles as drug delivery carriers for targeting lesions, releasing drugs, improving pharmacokinetics, biocompatibility, and bioavailability interested people greatly (George et al., 2019; Altinoglu and Adali, 2020; Maghsoudi et al., 2020; Liu et al., 2021; Abd Al-Jabbar et al., 2022; Sultan et al., 2022). The mesoporous polydopamine (MPDA) is one of the most popular nanoparticles because of its intrinsic biocompatibility, facile preparation, and various easily modified surface groups (Seth et al., 2020; Lin et al., 2021; Zhu et al., 2021). Therefore, the nanodrug based on MPDA targets to FAP administrated by intravenous (IV) is one of the promising approaches for antifibrosis therapy without GI AE.

Here, we develop a nanodrug, PFD@MPDA-FAPI, based on MPDA, loading with PFD, and linking FAPI for antifibrosis therapy by FAP targeting drug delivery (**Scheme 1**), it is well biocompatibility and performs well at antifibrosis. MPDA was synthesized from dopamine hydrochloride with F127 and TMB as templates and then to remove template; NH_2-PEG_2-FAPI was conjugated to MPDA *via* condensation. PFD was loaded in the mesoporous on MPDA-FAPI. Compared to pure PFD and PFD@MPDA, PFD@MPDA-FAPI could target activated fibroblast *in vitro* and fibrosis lung *in vivo*, as well as improving the antifibrosis efficacy. This promising strategy demonstrates a new avenue for antifibrosis therapy.

2 EXPERIMENTAL SECTION

2.1 Materials

Dopamine hydrochloride (Aladdin, Shanghai, China) was used to synthesize MPDA; 1,3,5-trimethyl benzene (TMB) and F127 (Macklin, Shanghai, China) were used as the template. NH_2-PEG-FAPI (Tanzhenbio, Nanchang, China) was used for FAP targeting. Pirfenidone (Aladdin, Shanghai, China) is an antifibrosis drug. In immunohistochemical

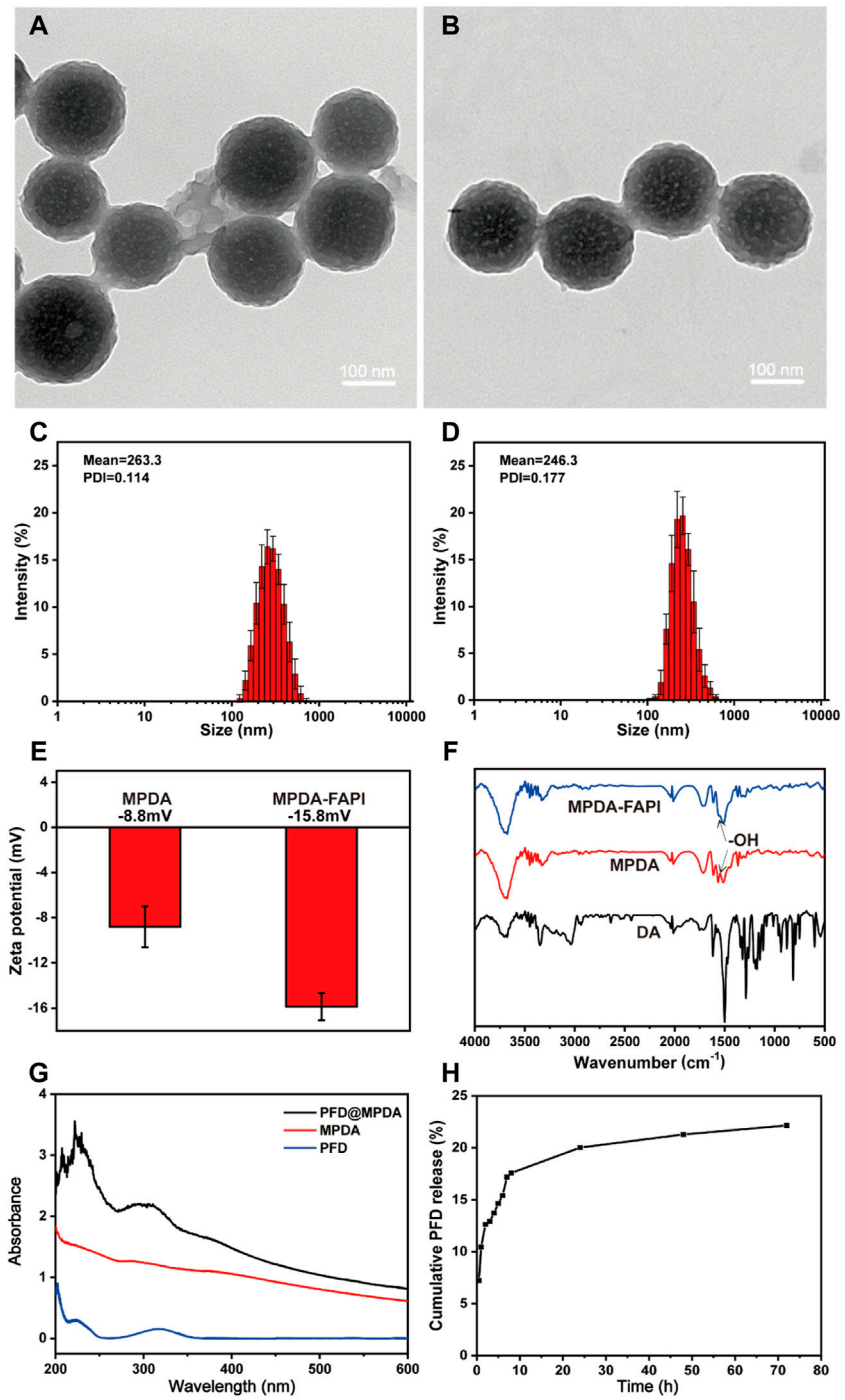

FIGURE 1 | TEM images of **(A)** MPDA and **(B)** MPDA-FAPI. Hydrodynamic diameters of **(C)** MPDA and **(D)** MPDA-FAPI. **(E)** Zeta potential of MPDA and MPDA-FAPI. **(F)** FTIR absorption spectrum of DA, MPDA, and MPDA-FAPI. **(G)** UV/Vis absorption spectrum of MPDA, PFD, and PFD@MPDA. **(H)** PFD released from PFD@MPDA at pH 7.4 for 72 h.

(IHC) staining, FN antibody (ab2413, Invitrogen) and FAP antibody (PA5-99458, Invitrogen) diluted 1:200, and α-SMA antibody (19245S, CST) diluted 1:800. For Western blot, FN antibody and FAP antibody diluted 1:1,000 was used. All other reagents were obtained from Aladdin.

2.2 Synthesis of MPDA and MPDA-FAPI

MPDA was synthesized by a facile approach. In short, 150 mg of dopamine hydrochloride was dissolved in 3 ml of deionized water, and 100 mg of F12 was dissolved in 3 ml of ethanol. The F127 solution was added to the dopamine solution, then

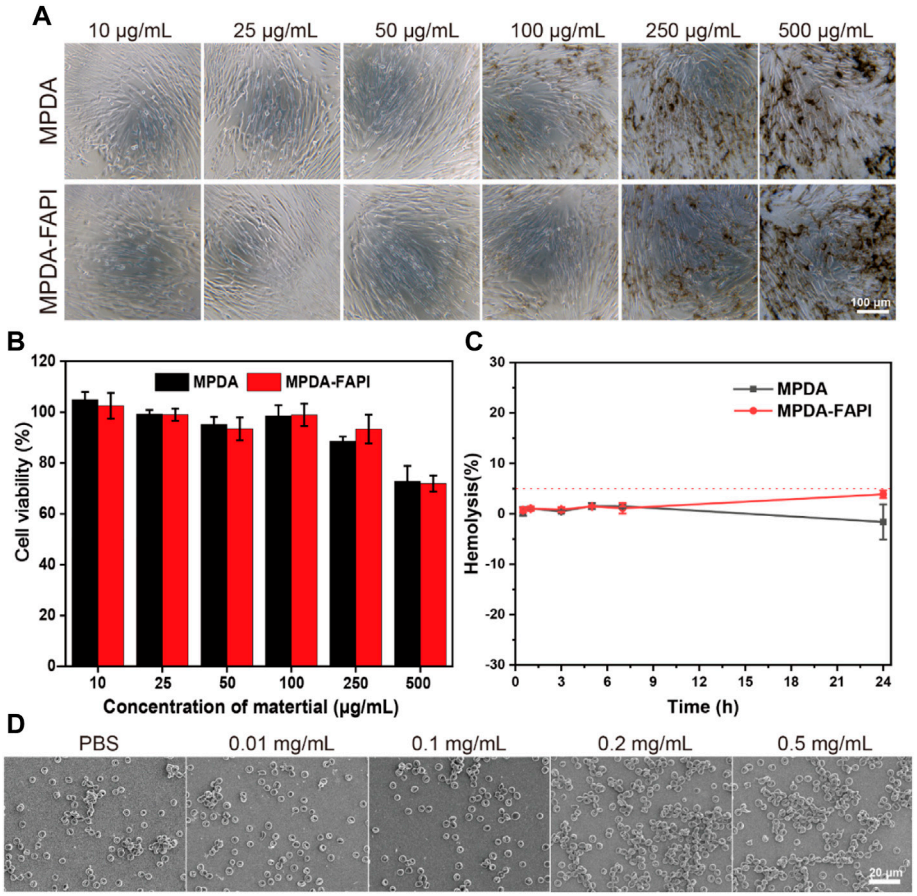

FIGURE 2 | (A,B) Cytotoxicity test of MPDA and MPDA-FAPI NPSs after incubation with HFL1 cells for 24 h. **(C)** Hemolysis percentage of red blood cells at 0.01 mg/ml of MPDA and MPDA-FAPI. **(D)** Morphology of red blood cell incubated with MPDA-FAPI.

added 160 μl of TMB, followed by 2 min of ultrasonic mixing, then 375 μl of 28% NH_4OH was added to the solution finally. After magnetic stirring for 2 h of the mixed solution, MPDA was obtained by centrifugal washing three times and resuspended in 1 ml deionized water. After drying, 1 ml MPDA solution weighs 1.5–2 mg. MPDA-FAPI was synthesized as follows. Then, 28% NH_4OH was used to adjust the pH of 3 ml MPDA solution to 9, then added 2 mg FAPI-NH_2-PEG, then the MPDA-FAPI was obtained by centrifugal washing after magnetic stirring at room temperature overnight.

2.3 Drug Loading and Release

First, 10 mg PFD was dissolved in 2 ml of methanol, then added PFD solution into 500 μl MPDA solution, magnetic stirring overnight and then centrifugally washing, finally resuspended the sediment in 1 ml deionized water to obtain MPDA@PFD. We tested the ultraviolet-visible (UV-Vis) absorbance of different concentrations of PFD to draw a standard curve of PFD, which is used for calculating the PFD concentration of nanodrug. The loading capacity is the weight ratio of PFD in MPDA@PFD. The 500 μl MPDA@PFD was sealed in a dialysis bag and put in a 15 ml tube with 2 ml PBS (pH 7.4) buffer solution, the mixture was shaken for 72 h a speed of 150 rpm. Periodically remove 0.5 ml of dialysate with a pipette gun and immediately add 0.5 ml of fresh PBS buffer to keep the constant total volume of the solution. After 72 h, the drug release was measured by the UV-Vis spectrophotometer.

2.4 Characterization

The morphology of MPDA and MPDA-FAPI were observed by using a transmission electron microscope (TEM). Firstly, prepared MPDA and MPDA-FAPI were dripped on the copper net, then dried and placed under the transmission electron microscope. The hydrodynamic diameter and the distribution of MPDA and MPDA-FAPI used dynamic light scattering (DLS) and zeta potential were measured by the laser nanometer particle size analyzer. The Fourier transform infrared (FTIR) spectrum and UV-vis spectrum of samples were obtained as follows. The proper amount of samples (DA, MPDA, and MPDA-FAPI) were grinded and pressed with KBr, respectively, then the prepared samples were detected by FTIR spectrometer, the scanning wavelength range was 500–4000 cm^{-1}. The appropriate number of samples (PFD, MPDA, and MPDA@PFD) were uniformly dispersed in the deionized water, using

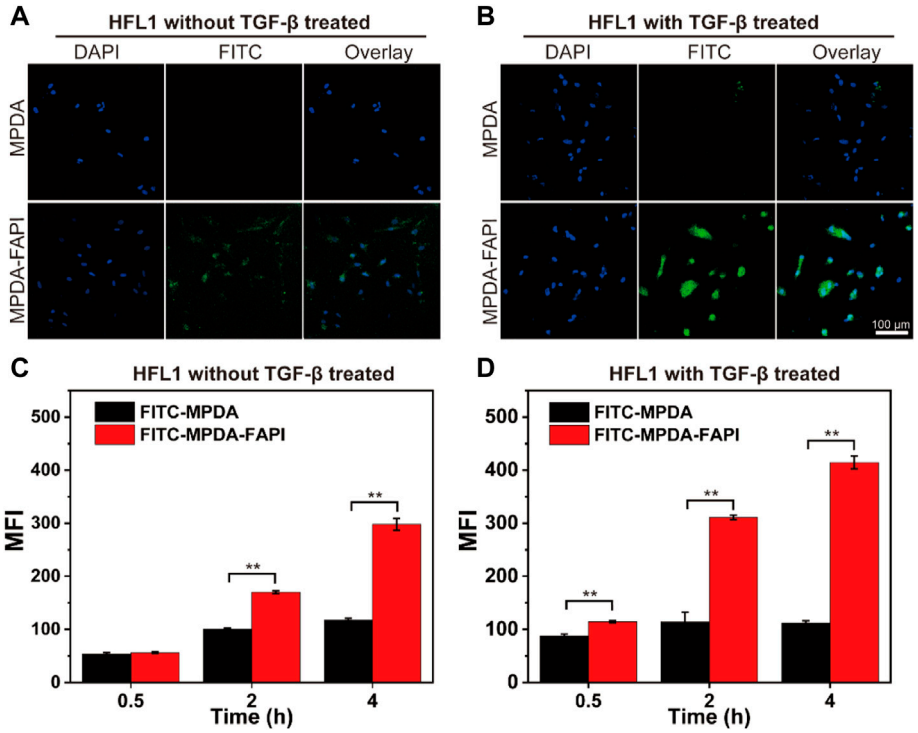

FIGURE 3 | (A,B) CLSM images of HFL1 cells (treated without/with TGF-β) uptake MPDA and MPDA-FAPI for 4 h. **(C,D)** Flow cytometer result of HFL1 cells (treated without/with TGF-β) uptake of MPDA and MPDA-FAPI (**$p < 0.01$).

the UV-Vis spectrophotometer to record the spectrum of samples within the range of 200–600 nm.

2.5 *In Vitro* Experience

2.5.1 Cell Culture

HFL1 (human fetal lung fibroblast, Procell CL-0106) was provided by Procell Life Science and Technology Co., cultured in Ham's F-12K with 10% fetal bovine serum (FBS) and 1% penicillin-streptomycin, cells were kept in a humidified atmosphere containing 5% CO_2 at 37°C.

2.5.2 Cytotoxicity and Blood Compatibility

For the cytotoxicity assay *in vitro*, HFL1 was first seeded into 96-well plates at a density of 5,000 cells per well overnight. Then, the original medium is then taken away and replaced with a fresh one containing various concentrations of nanoparticles and incubated for 24 h. The concentration of MPDA and MPDA-FAPI were 10–500 μg/ml. Finally, 100 μl, 0.1 μl/ml CCk8 solution was added to determine the relative cell viabilities among different concentration of nanoparticles treated groups as well as the untreated control.

Then, 200 μl 16% red blood cell suspension was incubated with MPDA and MPDA-FAPI (0.01 mg/ml), respectively, then centrifuged for 5 min, 1,000 × g at pre-set time points (1, 3, 6, 9, 18, and 24 h) to obtain supernatant. The Microplate Reader measured the absorbance of each supernatant at 540 nm to calculate the hemolysis rate. Whole blood was centrifuged with 1,000 × g for 5 min, then the lower red blood cells were collected, and incubated with MPDA-FAPI (0.01 mg/ml) for 15 min, then centrifuged to collect the red blood cell, then washed with PBS, and added 4% paraformaldehyde for 1 h. The fixed red blood cells were dehydrated with 70, 85, 95, and 100% ethanol, respectively, for 10 min. After the samples were dried, the samples were sprayed with gold, and the cell morphology was observed by scanning electron microscope (SEM).

2.5.3 Cellular Uptake Analyzed

FITC-MPDA and FITC MPDA-FAPI were prepared for cellular uptake experiment, obtained by stirring MPDA or MPDA-FAPI (1 ml) with FITC (300 μg) overnight, followed with centrifugally washed, and resuspended in 1 ml deionized water. Cellular uptake of FITC-MPDA and FITC-MPDA-FAPI were analyzed by endocytosis experiments. Specifically, HFL1 cells were seeded into a 24-well plate with a density of 5 × 10⁴ cells/holes, cultured overnight, and half of the holes were treated with 10 ng/ml TGF-β for 48 h. Then added to a complete medium containing 50 μg/ml FITC-MPDA or FITC-MPDA-FAPI. After incubating for 0.5, 2, and 4 h, the cells in each group were washed with PBS to remove the free material, digested with trypsin, and centrifuged to collect the cells. Finally, cells were resuspended by 200 μl PBS and detected by flow cytometry, the fluorescence intensity was measured by Flow JO 7.6.1 software.

The endocytosis of MPDA-FITC or MPDA-FAPI-FITC was also observed by confocal laser scanning. Specifically, HFL1 cells were first seeded in a cell culture dish with a density of 2 × 10⁵ cells per dish and then cultured overnight; then, two dishes of cells were treated with

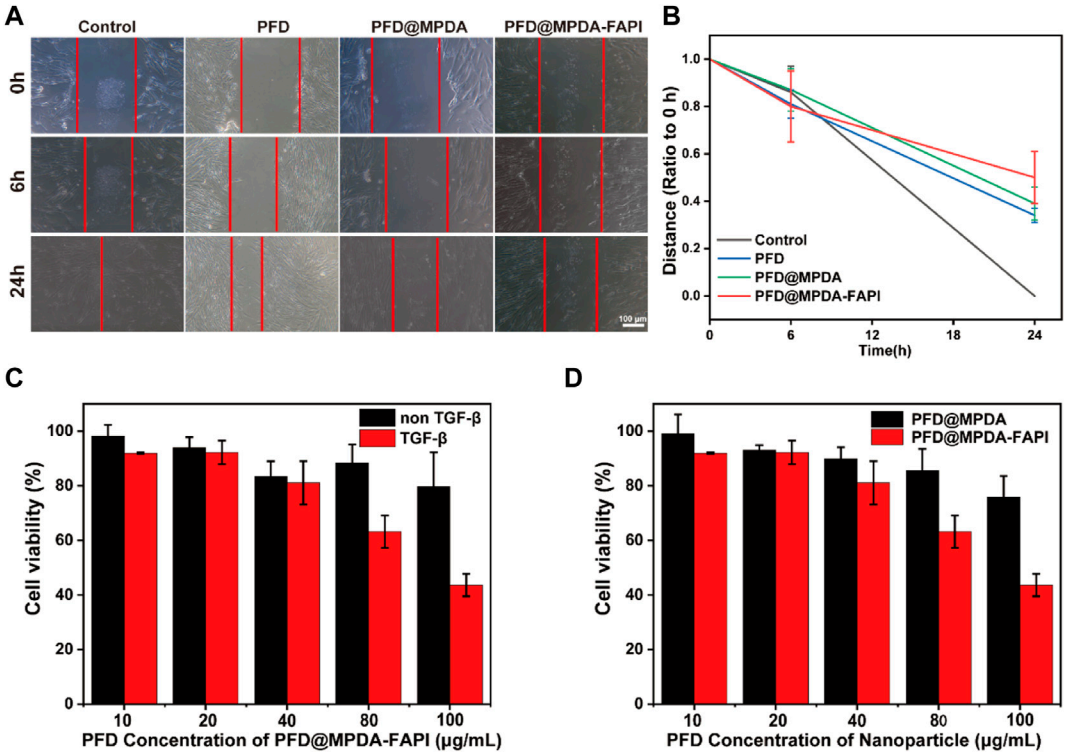

FIGURE 4 | (A,B) Scratch test results of HFL1-1 treated by TGF-β and incubated with PFD, PFD@MPDA, and PFD@MPDA-FAPI. **(C)** Proliferation test of PFD@MPDA-FAPI NPSs after incubation with HFL1 cells without/with TGF-β for 24 h. **(D)** Proliferation test of PFD@MPDA and PFD@MPDA-FAPI NPSs after incubation with HFL1-1 cells treated by TGF-β for 24 h (**$p < 0.01$).

TGF-β for 48 h and finally added to a complete medium containing 50 μg/ml FITC-MPDA or FITC-MPDA-FAPI. The cells were then washed with PBS after incubation for 4 h, then the cells were immobilized with 4% paraformaldehyde for 30 min and washed with PBS three times, the cell nucleus was stained with 1 ml DAPI in each dish for 15 min, and the cells were washed with PBS three times, and 2 ml PBS was added to each dish to keep the cell morphology, finally cells were observed and photographed with a laser confocal microscope.

2.5.5 Cell Proliferation Inhabitation

MTT assay was used to investigate the effects of MPDA@PFD and PFD@MPDA-FAPI on HFL1 with and without TGF-β treated. HFL1 cells were seeded into a 96-well plate at a density of 5,000 cells per hole and then cultured overnight. The original medium is then taken away and replaced with fresh complete media containing different concentrations of nanomaterials, the concentration of PFD in MPDA@PFD and MPDA-FAPII@PFD was in the range of 10–100 μg/ml, 50 μl, 1 mg/ml. MTT solution was then added to determine the relative cell viabilities among different concentration of nanoparticles treated groups as well as the untreated control.

2.5.6 Cell Scratches Experiment

HFL1 cells were seeded into a 24-well plate with a density of 5×10^4 cells per hole and cultured overnight, then treated with 10 ng/mg TGF-β for 48 h and scratched the bottom of the well to create artificial gaps in the cell. Then the cells were divided into three groups, incubated with 50 μg/ml MPDA@PFD, PFD@MPDA-FAPI, and PBS especially for 12 h, then washed with PBS, cultured in DMEM (serum-free), and photographed the gaps at the same position every different time (0, 6, and 24 h) by an inverted microscope, ImageJ software was used to measure and analyze the scratch area.

2.6 *In Vivo* Experience

2.6.1 Pulmonary Fibrosis Animal Model

C57BL/6 male mice (6–8 weeks, w ≈ 25 g) were used for the study. Animals were kept in a good environment. Drinking water and food were freely available. Mice were lightly anesthetized with 1.5% pentobarbital sodium, and BLM (2 mg/kg, YuanYe, Shanghai) was administered transtracheal *via* a laryngoscope (Yuyan, Shanghai). Micro CT (ALOKA LCT-200) was performed after 6 days to confirm the interstitial lung disease (**Supplementary Figure S5**).

2.6.2 *In Vivo* Imaging

MPDA and MPDA-FAPI are prepared for ICG/NIR imaging. The nanodrug labeled by ICG was obtained by stirring MPDA or MPDA-FAPI (1 ml) and 1 ml 1 mg/ml ICG overnight, followed by centrifugally washed and resuspended in 1 ml deionized water. ICG-MPDA and ICG-MPDA-FAPI were administrated *via* tail

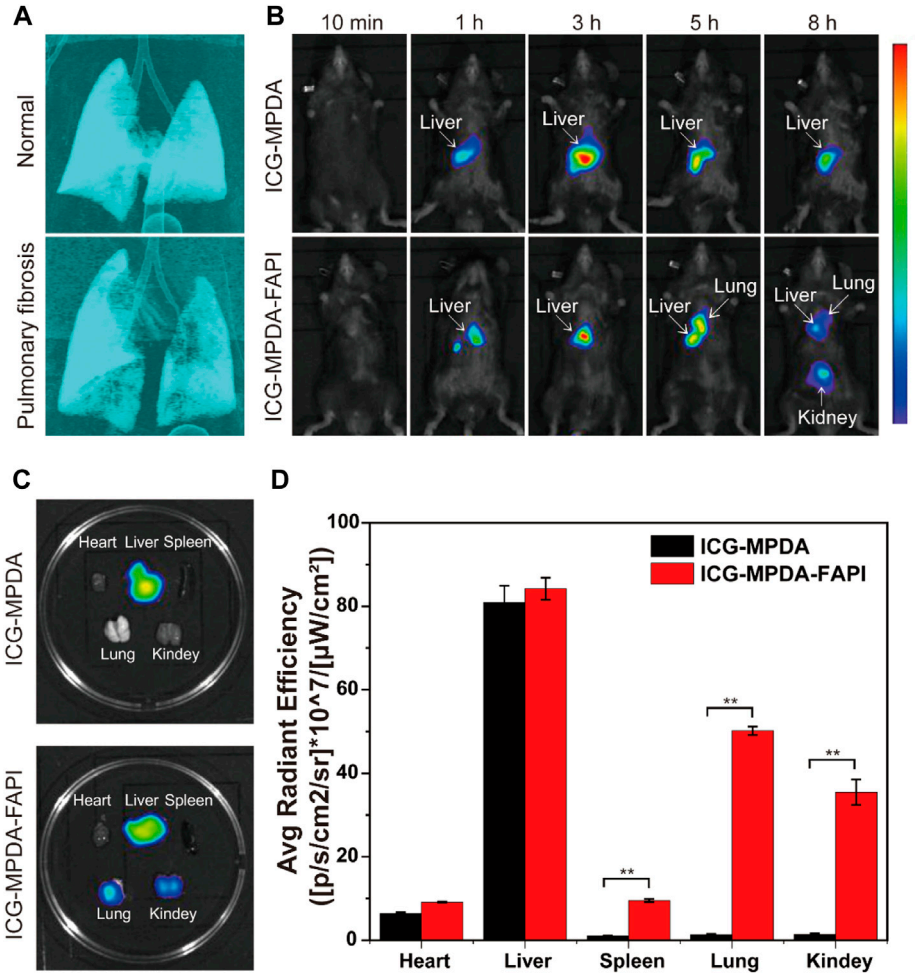

FIGURE 5 | (A) 3D CT of the normal lung and pulmonary fibrosis. **(B)** ICG-MPDA and ICG-MPDA-FAPI NIR fluorescence imaging *in vivo* of pulmonary fibrosis mice. **(C)** ICG-MPDA and ICG-MPDA-FAPI NIR fluorescence imaging of pulmonary fibrosis mice *in vitro*. **(D)** ICG-MPDA and ICG-MPDA-FAPI NIR fluorescence quantification of pulmonary fibrosis mice *in vitro*.

vein, and *in vivo* imaging was obtained after 10 min, 1, 3, 5, and 8 h administration of the pulmonary fibrosis mice. After 8 h imaging, the heart, liver, spleen, lungs, and kidneys were resected to quantify the radiant efficiency *in vitro*.

2.6.3 *In Vivo* Antifibrosis Therapy

Three healthy mice as the control group. Then, 15 pulmonary fibrosis mice were divided into five groups randomly, named NaCl, MPDA, PFD, PFD@MPDA, and PFD@MPDA-FAPI groups especially. Except for the control group, other groups of mice were pulmonary fibrosis, after 7 days induced by BLM, each group of mice was IV administrated with the corresponding drugs every 2 days regularly. In NaCl and MPDA groups, mice were IV injected with 120 μl NS and 120 μl MPDA solution, respectively. In the PFD, PFD@MPDA, and PFD@MPDA-FAPI groups, the dosage of PFD was 6 mg/kg. After three times of therapy, all the mice were sacrificed, right lungs were collected for WB analyses, and left lungs were collected for histological analyses.

2.6.4 Alveolitis and Fibrosis Grading

In histological analyses, HE staining and Masson staining were performed for grading alveolitis and fibrosis, the grading is according to the method of Szapiel et al. (1979). Alveolitis was evaluated with the HE stained sections and was graded using the criteria as follows: none (0), no alveolitis; mild (1+), thickening of the alveolar septum by a mononuclear cell infiltrate, with involvement limited to focal, pleural-based lesions occupying less than 20% of the lung and with good preservation of the alveolar architecture; moderate (2+), more widespread alveolitis involving 20–50% of the lung, although still predominantly pleural based; severe (3+), diffuse alveolitis involving more than 50% of the lung, with occasional consolidation of air spaces by the intra-alveolar mononuclear cells and some hemorrhagic areas within the interstitium and/or alveolus. The extent of fibrosis in these sections was graded using the following criteria: none (0), no evidence of fibrosis; mild (1+), focal regions of fibrosis involving less than 20% of the lung. Fibrosis involved

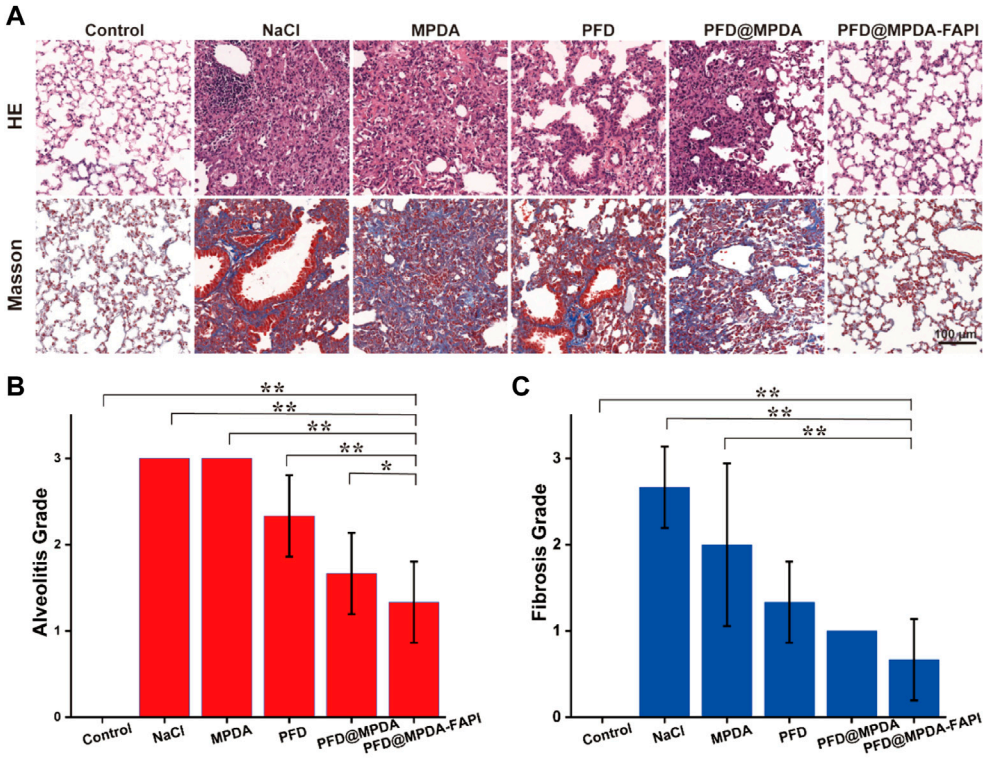

FIGURE 6 | (A) HE staining and Masson staining of lungs among different treatment groups. **(B,C)** Grade of alveolitis and fibrosis among different treatment groups.

the pleura and the interstitium of the subpleural parenchyma with some distortion of alveolar architecture; moderate (2+), more extensive fibrosis involving 20–50% of the lung and fibrotic regions mostly extending inward from the pleura and still focal; severe (3+), widespread fibrosis, involving more than 50% of the lung. Confluent lesions with extensive derangement of parenchymal architecture, including cystic air spaces lined by cuboidal epithelium.

2.6.5 IHC Staining

FN antibody and FAP antibody were diluted to 1:200, and α-SMA antibody was diluted to 1:800 for IHC staining. Image-Pro Plus was used to calculate the average optical density (AOD) of FN, FAP, and α-SMA among different groups.

2.6.6 Western Blot Analyses

The expression of FN and FAP in different groups was analyzed by WB. FN antibody and FAP antibody are diluted to 1: 1,000 for WB.

3 RESULT AND DISCUSSION

3.1 Synthesis and Characterization of MPDA, PFD@MPDA, and PFD@MPDA-FAPI

The synthetic procedures of MPDA, MPDA-FAPI, and PFD@MPDA-FAPI nanoparticles are depicted in **Scheme 1**. First, the soft templating method was used to synthesize MPDA. All these nanoparticles were obtained in the aqueous solution. As for the production of MPDA, F127, and TBM were chosen as templates, ethanol, and ammonia solution were used for cosolvent and the catalyst in the polymerization of DA, then *via* the π–π stacking interactions, PDA was self-assembled on the templates, MPDA NPs were finally obtained by removing of templates (Wu et al., 2019; Lin et al., 2021). Second, NH_2-PEG_2-FAPI was conjugated to MPDA *via* condensation of the amine groups on NH_2-PEG_2-FAPI and the dihydroxy indole groups on MPDA to form MPDA-FAPI. Finally, PFD was loaded onto MPDA and MPDA-FAPI by magnetic stirring to form PFD@MPDA and PFD@MPDA-FAPI.

TEM observations confirmed that MPDA and MPDA-FAPI NPs manifest the well-defined spherical morphology and mesoporous structure, as well as uniform size distribution (**Figures 1A,B**), and the huge surface area created by mesoporous structure, is suitable for drug loading. The average diameters of MPDA and MPDA-FAPI NPs are all about 200 nm. DLS measurement also demonstrates that no aggregation occurs of these nanoparticles, the average hydrodynamic diameters of MPDA and MPDA-FAPI nanoparticles are ≈263 and 246 nm, respectively (**Figures 1C,D**). Compared to the diameter of the dried sample used in TEM measurement, the hydrodynamic diameter is larger. The tiny variety of the nanoparticles' diameter between TEM and DLS results may occur by swelling effect, which is

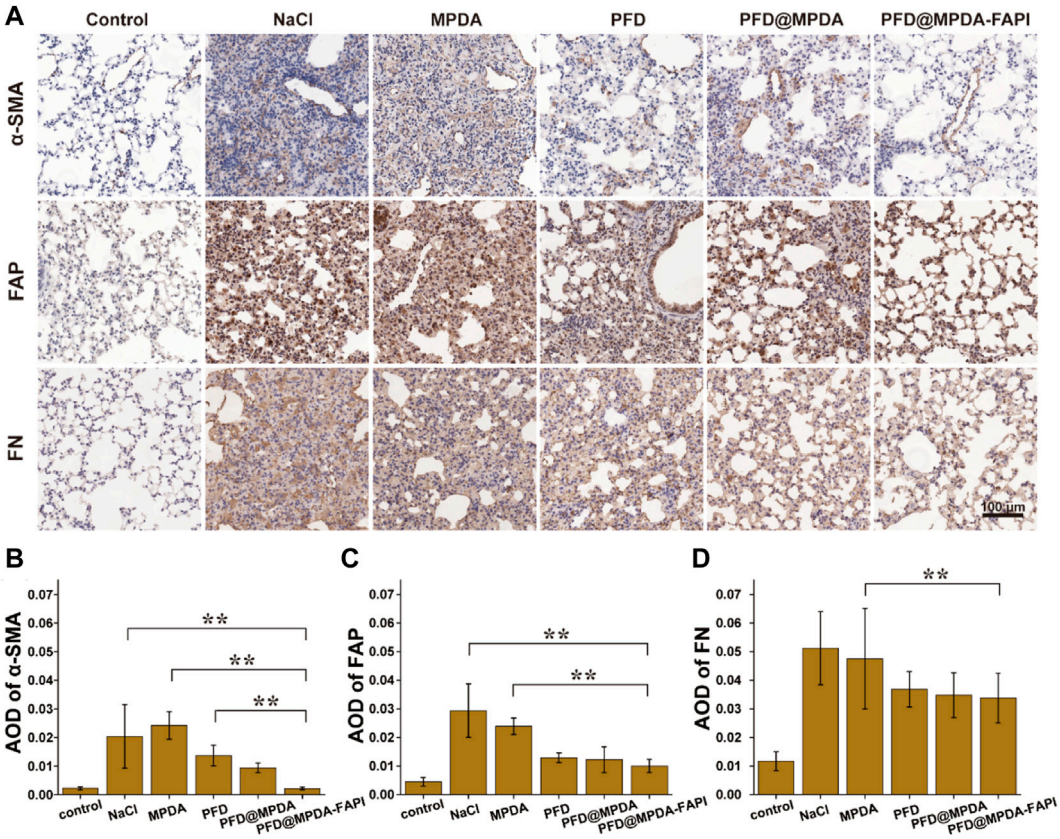

FIGURE 7 | (A) IHC staining for FN, FAP, and α-SMA among different treatment groups. **(B–D)** AOD of IHC staining for FN, FAP, and α-SMA among different treatment groups.

common in polymer material. The nanoscale diameter is safe for IV administration without pulmonary embolism risk. Meanwhile, the zeta potentials of MPDA and MPDA-FAPI nanoparticles are −8.8 and −15.8 mV, respectively (**Figure 1E**), the lower charge of MPDA-FAPI confirmed the conjugation of MPDA and the negatively charged NH_2-PEG_2-FAPI. FTNR spectrum can also prove the conjunction of MPDA and FAPI, the condensation of the amine groups on NH_2-PEG_2-FAPI with the hydroxy indole groups on MPDA, consuming the hydroxyl, because of hydroxyl on MPDA manifests a characteristic absorption band at 1,500 cm^{-1}, hence, the lower absorbance of MPDA-FAPI at 1,500 cm^{-1} proved the condensation of MPDA and NH_2-PEG_2-FAPI (**Figure 1F**).

3.2 Drug Loading and Release Properties

The UV-Vis absorption spectrum of PFD@MPDA clearly shows the characteristic absorption band of PFD at 319 nm (**Figure 1G**). Based on the standard curve of PFD (**Supplementary Figure S1**), the loading capacity (the weight ratio of PFD to MPDA) was calculated as 53% by measuring the PFD@MPDA absorbance at 319 nm. It is reported that the loading efficiency of MPDA is better than PDA without mesoporous (Chen et al., 2016; Peng et al., 2019), the satisfying loading efficiency of PFD@MPDA in our study may also be thanks to the large specific surface area brought by the mesoporous structure.

In vitro, the release of PFD from PFD@MPDA was investigated in PBS by a UV-Vis spectrophotometer. PFD released from PFD@MPDA was accumulated in a neutral solution (pH 7.4) mimicking *in vivo* environments. After 72 h, about 22% of PFD is released from PFD@MPDA at pH 7.4 (**Figure 1H**).

3.3 Cytotoxicity and Blood Compatibility

Biocompatibility is crucial for nanoparticles. Both MPDA and MPDA-FAPI nanoparticles of various concentrations (10–500 μg/ml) display negligible cytotoxicity after 24 h incubation with HFL1 cells. (**Figures 2A,B**), which proved that the nanoparticle does not harm normal HFL1 cells. After 72 h treated with MPDA and MPDA-FAPI (0.01 mg/ml), the hemolysis rate was less than 5% *in vitro* (**Figure 2C**). Also, the SEM result of RBC treated with MPDA-FAPI at various concentrations (10–500 μg/ml) shows normal morphology, consistent with the low hemolysis (**Figure 2D**). As expected, the biocompatibility of nanoparticle based on PDA is good because PDA is also the primary pigment of melanin, which naturally exist in the human body. Good biocompatibility allows nanoparticle utility in practice.

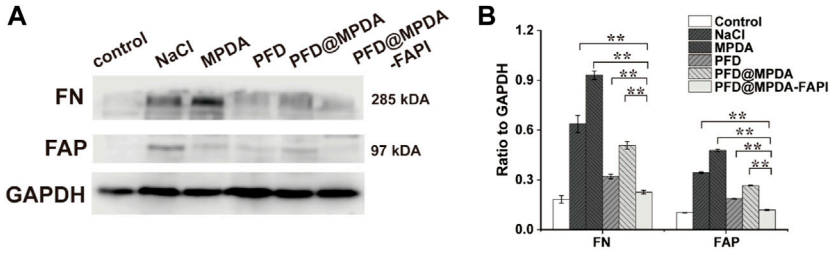

FIGURE 8 | (A,B) WB results of FN and FAP among different treatment groups (*$p < 0.05$).

3.4 Cellular Uptake and Localization of Nanoparticle

We observed the HFL1 treated without/with TGF-β uptake MPDA and MPDA-FAPI for 4 h by the confocal laser scanning microscope (CLSM), the highest cell uptake was observed for FITC-MPDA-FAPI in HFL1 with TGF-β treated (**Figures 3A,B**). The cellular uptake of MPDA and MPDA-FAPI for 0.5, 2, and 4 h were quantificationally investigated by a flow cytometer (**Figures 3C,D**). With the time changed, the uptake of nanodrug increased, and at each time point, the MFI of the FITC-MPDA-FAPI group is higher than FITC-MPDA no matter whether HFL1 was treated by TGF-β or not. We also found that the uptake of FITC-MPDA-FAPI is higher in HFL1 which is treated by TGF-β than the nontreated group, but the difference between FITC-MPDA uptake in HFL1 treated by TGF-β and nontreated groups was tiny (**Supplementary Figure S2**). As expected, the HFL1 treated with TGF-β and incubated with FITC-MPDA-FAPI for 4 h showed the highest MFI (414 ± 12), which is consistent with the CLSM result.

The higher uptake of MPDA-FAPI by HFL1 treated with TGF-β indicates that the MPDA-FAPI is successfully targeting the activated fibroblast and improving the uptake of nanodrug, which is beneficial for pulmonary fibrosis foci target drug delivery.

3.5 *In Vitro* Therapy of Nanoparticle

TGF-β is considered a key regulator in tissue fibrosis by promoting the overexpression of downstream fibrosis-related target genes. The HFL1 is activated *in vitro* and treated by TGF-β for 48 h, which can promote the proliferation and migration of HFL1, and also promote the expression of the biomarkers of fibrosis (such as FN and α-SMA). PFD can inhibit the activity of TGF-β and regulate the downstream signal of the TGF/Smad signal pathway, which has the properties of antifibrosis. Compared to pure PFD and PFD@MPDA, PFD@MPDA-FAPI can promote the drug uptake of HFL1, which manifest the best antifibrosis properties.

The effects of NPS-loaded PFD on the proliferation of HFL1 were analyzed by MTT assay. The results showed that PFD@MPDA-FAPI could inhibit the proliferation of HFL1 treated by TGF-β, while HFL1 without TGF-β treatment had not been significantly inhibited (**Figure 4C**). In addition, PFD@MPDA-FAPI performs better than PFD@MPDA in inhibiting the proliferation of HFL1 treated with TGF-β (**Figure 4D**). According to the results of the MTT assay, the 100 μg/ml PFD concentration of MPDA@PFD and MPDA@PFD-FAPI were chosen for the scratch test to measure HFL1 migration. The results showed that both PFD, PFD@MPDA, and PFD@MPDA-FAPI could inhibit the migration of HFL1 treated by TGF-β, and PFD@MPDA-FAPI performed best (**Figures 4A,B**).

The study suggested that PFD@MPDA-FAPI targeting FAP does better than PFD@MPDA on inhibitor the proliferation and migration of activated fibroblast, and had a tiny effect on the normal fibroblast, suggesting that nanoparticle target to FAP is useful in the therapy of pulmonary fibrosis.

3.6 *In Vivo* Biodistribution

Pulmonary fibrosis mice were induced by BLM (2 mg/kg) administered transtracheal *via* a laryngoscope, and after 6 days, micro-CT was performed to confirm the pulmonary fibrosis, then the next day *in vivo* NIR imaging was performed to explore the biodistribution of MPDA and MPDA-FAPI in pulmonary fibrosis mice. The 3D remolding of lungs based on micro-CT showed that, compared to healthy pulmonary, the normal airway structure in fibrosis lungs is reduced (**Figure 5A**). Only MPDA-FAPI has a significant accumulation in the lungs of pulmonary fibrosis mice (**Figure 5B**). After 8 h imaging, the major organs of mice were resected and quantified the radiant efficiency, the lung of the pulmonary fibrosis mouse injected with ICG-MPDA-FAPI also showed a high radiant efficiency, which was consistent with the *in vivo* ICG imaging (**Figures 5C,D**).

The ICG-MPDA and ICG-MPDA-FAPI were first observed in livers because the liver is a typical organ with the endothelial reticular system, in which Kupffer cells uptake nanoparticles. For ICG-MPDA, the accumulation only lasted in the liver; as for ICG-MPDA-FAPI, the nanoparticle gradually accumulates in fibrosis lung, in which FAP is overexpressed. At a later point, ICG-MPDA-FAPI accumulates in the kidneys because the hydrophilic PEG brought by the NH_2-PEG_2-FAPI may change the pharmacokinetic. The NIR imaging indicated the MPDA-FAPI is targeted to the overexpress FAP of fibrosis foci in *in vivo*, MPDA-FAPI is a successful FAP targeted nanodelivery carried out in *in vivo*.

3.7 *In Vivo* Antifibrosis Properties

After the nanodrug treatment, the weight of mice varies mild, which indicates the nanodrug is safe (**Supplementary Figure S6**).

The grades of alveolitis and fibrosis of the mice in the control group were both 0. Compared to the control group, NaCl, MPDA, and PFD@MPDA groups, the PFD@MPDA-FAPI shows the lowest grades of alveolitis and fibrosis (**Figures 6A–C**).

In IHC staining, the control group showed the lowest expression of α-SMA, FAP, and FN. Compared to the control group, the expression of α-SMA, FAP, and FN were increased in NaCl and MPDA groups. The expression of α-SMA, FAP, and FN in PFD, PFD@MPDA, and PFD@MPDA-FAPI groups decreased compared to NaCl and MPDA groups, and the PFD@MPDA-FAPI group manifested the lowest expression (**Figures 7A–D**).

The results of WB were generally consistent with the IHC staining. In WB analyses, the control group showed a low expression of FAP and FN. Compared to the control group, NaCl and MPDA groups show higher expression of FN and FAP. In the PFD@MPDA-FAPI group, the expression of FN and FAP were lower than in the PFD and PFD@MPDA groups, which indicated that the antifibrosis properties of PFD@MPDA-FAPI are the best (**Figures 8A,B**).

In the pathological produce of pulmonary fibrosis, alveolitis comes first, then the fibroblast is activated, expressed FAP, and then activated fibroblast differentiate to myofibroblast, which is a key cell-expressed α-SMA to produce excessive exocellular matrix (Yu and Tang, 2022). The excessive exocellular matrix is comprised of collagen fibers, which can be determined by Masson staining and FN IHC.

Therefore, the WB and IHC results of low FN, FAP, and α-SMA expression in the PFD@MPDA-FAPI group, indicate that PFD@MPDA-FAPI shows good antifibrosis properties *in vivo* and performed better than pure PFD and PFD@MPDA in generally.

We also analyzed the antifibrosis properties of nanodrug after six times treatments. The PFD@MPDA-FAPI also performed the best, which is similar to the result of three times of treatments (**Supplementary Figures S3, S4**). It is considered that the pulmonary fibrosis of mice induced by BLM may change with time, in general, the fibrosis lesion may subside and is close to normal at the end, (Degryse and Lawson, 2011) so it is hard to explain the difference between three times and six times treatment groups, but either three times or six times treatment, we can observe the pleasing antifibrosis properties of PFD@MPDA-FAPI.

4 CONCLUSION

PFD@MPDA-FAPI, a nanoparticle developed based on MPDA, loading PFD, and targeting FAP on activated fibroblast, performs better than pure PFD and MPDA@PFD in inhibiting the proliferation and migration of the activated fibroblast, which is crucial in antifibrosis therapy, and do no harm to normal fibroblast. The nanoparticle is safe for IV administration and can accumulate in the fibrosis lung *in vivo*, also manifesting a good antifibrosis property. PFD@MPDA-FAPI is a promising nanodrug for antifibrosis therapy without the side effects of the stomach caused by PFD orally administrated. In addition, given consideration that FAP is also overexpressed on cancer-associated fibroblast, the MPDA also manifests a photothermal property, so replacing the loading drug with an anticancer drug may also develop a new tumor target nanodrug, which may perform well in cancer therapy combined with chemotherapy and photothermal therapy.

DATA AVAILABILITY STATEMENT

The original contributions presented in the study are included in the article/**Supplementary Material**; further inquiries can be directed to the corresponding authors.

ETHICS STATEMENT

The animal study was reviewed and approved by the Animal Protection and Use Committee of Jinan University.

AUTHOR CONTRIBUTIONS

XW designed the study and gave instructions. QF performed the experiment, data analysis, and writing of the original draft. SL, JC, RZ, QH, PH, YL, JL, XZ, and QL helped perform the analysis with constructive discussions.

FUNDING

This research was supported in part by the Department of Science and Technology of Guangzhou and Guangzhou Medical University, the National Natural Science Foundation of China (No. 82001879), the Applied and Basic Research Foundation of Guangdong Province (No. 2020A1515110159), the Science and Technology Project of Guangzhou City (No. 202102010354), and the Zhongnanshan Medical Foundation of Guangdong Province (ZNSA-2020003).

SUPPLEMENTARY MATERIAL

The Supplementary Material for this article can be found online at: https://www.frontiersin.org/articles/10.3389/fbioe.2022.920766/full#supplementary-material

REFERENCES

Abd Al-Jabbar, S., Atiroğlu, V., Hameed, R. M., Guney Eskiler, G., Atiroğlu, A., Deveci Ozkan, A., et al. (2022). Fabrication of Dopamine Conjugated with Protein @metal Organic Framework for Targeted Drug Delivery: A Biocompatible pH-Responsive Nanocarrier for Gemcitabine Release on MCF-7 Human Breast Cancer Cells. *Bioorg. Chem.* 118, 105467. doi:10.1016/j.bioorg.2021.105467

Acharya, P. S., Zukas, A., Chandan, V., Katzenstein, A.-L. A., and Puré, E. (2006). Fibroblast Activation Protein: a Serine Protease Expressed at the Remodeling

Interface in Idiopathic Pulmonary Fibrosis. *Hum. Pathol.* 37 (3), 352–360. doi:10.1016/j.humpath.2005.11.020

Altinoglu, G., and Adali, T. (2020). Alzheimer's Disease Targeted Nano-Based Drug Delivery Systems. *Curr Drug Targets* 21 (7), 628–646. doi:10.2174/1389450120666191118123151

Bergmann, C., Distler, J. H. W., Treutlein, C., Tascilar, K., Müller, A.-T., Atzinger, A., et al. (2021). 68Ga-FAPI-04 PET-CT for Molecular Assessment of Fibroblast Activation and Risk Evaluation in Systemic Sclerosis-Associated Interstitial Lung Disease: a Single-Centre, Pilot Study. *Lancet Rheumatology* 3 (3), e185–e194. doi:10.1016/s2665-9913(20)30421-5

Chen, F., Xing, Y., Wang, Z., Zheng, X., Zhang, J., and Cai, K. (2016). Nanoscale Polydopamine (PDA) Meets π-π Interactions: An Interface-Directed Coassembly Approach for Mesoporous Nanoparticles. *Langmuir* 32 (46), 12119–12128. doi:10.1021/acs.langmuir.6b03294

Degryse, A. L., and Lawson, W. E. (2011). Progress toward Improving Animal Models for Idiopathic Pulmonary Fibrosis. *Am. J. Med. Sci.* 341 (6), 444–449. doi:10.1097/MAJ.0b013e31821aa000

Deng, Z., Fear, M. W., Suk Choi, Y., Wood, F. M., Allahham, A., Mutsaers, S. E., et al. (2020). The Extracellular Matrix and Mechanotransduction in Pulmonary Fibrosis. *Int. J. Biochem. Cell Biol.* 126, 105802. doi:10.1016/j.biocel.2020.105802

Egger, C., Cannet, C., Gérard, C., Suply, T., Ksiazek, I., Jarman, E., et al. (2017). Effects of the Fibroblast Activation Protein Inhibitor, PT100, in a Murine Model of Pulmonary Fibrosis. *Eur. J. Pharmacol.* 809, 64–72. doi:10.1016/j.ejphar.2017.05.022

Fan, M.-H., Zhu, Q., Li, H.-H., Ra, H.-J., Majumdar, S., Gulick, D. L., et al. (2016). Fibroblast Activation Protein (FAP) Accelerates Collagen Degradation and Clearance from Lungs in Mice. *J. Biol. Chem.* 291 (15), 8070–8089. doi:10.1074/jbc.M115.701433

Fernández Pérez, E. R., Daniels, C. E., St. Sauver, J., Hartman, T. E., Bartholmai, B. J., Yi, E. S., et al. (2010). Incidence, Prevalence, and Clinical Course of Idiopathic Pulmonary Fibrosis. *Chest* 137 (1), 129–137. doi:10.1378/chest.09-1002

Garin-Chesa, P., Old, L. J., and Rettig, W. J. (1990). Cell Surface Glycoprotein of Reactive Stromal Fibroblasts as a Potential Antibody Target in Human Epithelial Cancers. *Proc. Natl. Acad. Sci. U.S.A.* 87 (18), 7235–7239. doi:10.1073/pnas.87.18.7235

George, A., Shah, P. A., and Shrivastav, P. S. (2019). Natural Biodegradable Polymers Based Nano-Formulations for Drug Delivery: A Review. *Int. J. Pharm.* 561, 244–264. doi:10.1016/j.ijpharm.2019.03.011

Keane, F. M., Yao, T.-W., Seelk, S., Gall, M. G., Chowdhury, S., Poplawski, S. E., et al. (2013). Quantitation of Fibroblast Activation Protein (FAP)-specific Protease Activity in Mouse, Baboon and Human Fluids and Organs. *FEBS Open Bio* 4, 43–54. doi:10.1016/j.fob.2013.12.001

King, T. E., Jr., Bradford, W. Z., Castro-Bernardini, S., Fagan, E. A., Glaspole, I., Glassberg, M. K., et al. (2014). A Phase 3 Trial of Pirfenidone in Patients with Idiopathic Pulmonary Fibrosis. *N. Engl. J. Med.* 370 (22), 2083–2092. doi:10.1056/NEJMoa1402582

Lai, Y., Wei, X., Ye, T., Hang, L., Mou, L., and Su, J. (2021). Interrelation between Fibroblasts and T Cells in Fibrosing Interstitial Lung Diseases. *Front. Immunol.* 12, 747335. doi:10.3389/fimmu.2021.747335

Lancaster, L. H., de Andrade, J. A., Zibrak, J. D., Padilla, M. L., Albera, C., Nathan, S. D., et al. (2017). Pirfenidone Safety and Adverse Event Management in Idiopathic Pulmonary Fibrosis. *Eur. Respir. Rev.* 26 (146), 170057. doi:10.1183/16000617.0057-2017

Ley, B., Collard, H. R., and King, T. E., Jr. (2011). Clinical Course and Prediction of Survival in Idiopathic Pulmonary Fibrosis. *Am. J. Respir. Crit. Care Med.* 183 (4), 431–440. doi:10.1164/rccm.201006-0894CI

Lin, K., Gan, Y., Zhu, P., Li, S., Lin, C., Yu, S., et al. (2021). Hollow Mesoporous Polydopamine Nanospheres: Synthesis, Biocompatibility and Drug Delivery. *Nanotechnology* 32 (28), 285602. doi:10.1088/1361-6528/abf4a9

Lin, Y., Ma, Z., Li, Z., Gao, Y., Qin, X., Zhang, Z., et al. (2019). Bioluminescent Probe for Monitoring Endogenous Fibroblast Activation Protein-Alpha. *Anal. Chem.* 91 (23), 14873–14878. doi:10.1021/acs.analchem.9b02117

Liu, B., Yang, W., Che, C., Liu, J., Si, M., Gong, Z., et al. (2021). A Targeted Nano Drug Delivery System of AS1411 Functionalized Graphene Oxide Based Composites. *ChemistryOpen* 10 (4), 408–413. doi:10.1002/open.202000226

Maghsoudi, S., Taghavi Shahraki, B., Rabiee, N., Fatahi, Y., Dinarvand, R., Tavakolizadeh, M., et al. (2020). Burgeoning Polymer Nano Blends for Improved Controlled Drug Release: A Review. *Int. J. Nanomedicine* 15, 4363–4392. doi:10.2147/ijn.S252237

Nathan, S. D., Shlobin, O. A., Weir, N., Ahmad, S., Kaldjob, J. M., Battle, E., et al. (2011). Long-term Course and Prognosis of Idiopathic Pulmonary Fibrosis in the New Millennium. *Chest* 140 (1), 221–229. doi:10.1378/chest.10-2572

Peng, L., Hung, C.-T., Wang, S., Zhang, X., Zhu, X., Zhao, Z., et al. (2019). Versatile Nanoemulsion Assembly Approach to Synthesize Functional Mesoporous Carbon Nanospheres with Tunable Pore Sizes and Architectures. *J. Am. Chem. Soc.* 141 (17), 7073–7080. doi:10.1021/jacs.9b02091

Raghu, G., Collard, H. R., Egan, J. J., Martinez, F. J., Behr, J., Brown, K. K., et al. (2011). An Official ATS/ERS/JRS/ALAT Statement: Idiopathic Pulmonary Fibrosis: Evidence-Based Guidelines for Diagnosis and Management. *Am. J. Respir. Crit. Care Med.* 183 (6), 788–824. doi:10.1164/rccm.2009-040GL

Rockey, D. C., Bell, P. D., and Hill, J. A. (2015). Fibrosis - A Common Pathway to Organ Injury and Failure. *N. Engl. J. Med.* 372 (12), 1138–1149. doi:10.1056/NEJMra1300575

Röhrich, M., Leitz, D., Glatting, F. M., Wefers, A. K., Weinheimer, O., Flechsig, P., et al. (2022). Fibroblast Activation Protein-specific PET/CT Imaging in Fibrotic Interstitial Lung Diseases and Lung Cancer: A Translational Exploratory Study. *J. Nucl. Med.* 63 (1), 127–133. doi:10.2967/jnumed.121.261925

Seth, A., Gholami Derami, H., Gupta, P., Wang, Z., Rathi, P., Gupta, R., et al. (2020). Polydopamine-Mesoporous Silica Core-Shell Nanoparticles for Combined Photothermal Immunotherapy. *ACS Appl. Mat. Interfaces* 12 (38), 42499–42510. doi:10.1021/acsami.0c10781

Sultan, M. H., Moni, S. S., Madkhali, O. A., Bakkari, M. A., Alshahrani, S., Alqahtani, S. S., et al. (2022). Characterization of Cisplatin-Loaded Chitosan Nanoparticles and Rituximab-Linked Surfaces as Target-specific Injectable Nano-Formulations for Combating Cancer. *Sci. Rep.* 12 (1), 468. doi:10.1038/s41598-021-04427-w

Szapiel, S. V., Elson, N. A., Fulmer, J. D., Hunninghake, G. W., and Crystal, R. G. (1979). Bleomycin-induced Interstitial Pulmonary Disease in the Nude, Athymic Mouse. *Am. Rev. Respir. Dis.* 120 (4), 893–899. doi:10.1164/arrd.1979.120.4.893

Wenlong, L., Leilei, Y., Wei, F., Yi, C., Jing, T., Lanzhi, M., et al. (2015). Luciferase Expression Is Driven by the Promoter of Fibroblast Activation Protein-α in Murine Pulmonary Fibrosis. *Biotechnol. Lett.* 37 (9), 1757–1763. doi:10.1007/s10529-015-1855-8

Wu, D., Duan, X., Guan, Q., Liu, J., Yang, X., Zhang, F., et al. (2019). Mesoporous Polydopamine Carrying Manganese Carbonyl Responds to Tumor Microenvironment for Multimodal Imaging-Guided Cancer Therapy. *Adv. Funct. Mat.* 29 (16), 1900095. doi:10.1002/adfm.201900095

Wu, G., Xie, B., Lu, C., Chen, C., Zhou, J., and Deng, Z. (2020). microRNA-30a Attenuates TGF-β1-Induced Activation of Pulmonary Fibroblast Cell by Targeting FAP-α. *J. Cell Mol. Med.* 24 (6), 3745–3750. doi:10.1111/jcmm.15020

Yu, Q. Y., and Tang, X. X. (2022). Irreversibility of Pulmonary Fibrosis. *Aging Dis.* 13 (1), 73–86. doi:10.14336/ad.2021.0730

Zhu, M., Shi, Y., Shan, Y., Guo, J., Song, X., Wu, Y., et al. (2021). Recent Developments in Mesoporous Polydopamine-Derived Nanoplatforms for Cancer Theranostics. *J. Nanobiotechnol* 19 (1), 387. doi:10.1186/s12951-021-01131-9

Conflict of Interest: The authors declare that the research was conducted in the absence of any commercial or financial relationships that could be construed as a potential conflict of interest.

Publisher's Note: All claims expressed in this article are solely those of the authors and do not necessarily represent those of their affiliated organizations, or those of the publisher, the editors, and the reviewers. Any product that may be evaluated in this article, or claim that may be made by its manufacturer, is not guaranteed or endorsed by the publisher.

Copyright © 2022 Fang, Liu, Cui, Zhao, Han, Hou, Li, Lv, Zhang, Luo and Wang. This is an open-access article distributed under the terms of the Creative Commons Attribution License (CC BY). The use, distribution or reproduction in other forums is permitted, provided the original author(s) and the copyright owner(s) are credited and that the original publication in this journal is cited, in accordance with accepted

frontiers | Frontiers in Bioengineering and Biotechnology

ORIGINAL RESEARCH
published: 22 July 2022
doi: 10.3389/fbioe.2022.940735

Real-Time MRI Monitoring of GelMA-Based Hydrogel-Loaded Kartogenin for *In Situ* Cartilage Regeneration

Hanyuan Zhang[1,2,3], *Weijun Fang*[4], *Tingting Zhao*[4], *Huabing Zhang*[4], *Liang Gao*[5,6], *Jingya Li*[1,2], *Rujing Wang*[1] *and Weiping Xu*[1,2,7]*

[1]Institute of Intelligent Machines, Chinese Academy of Sciences, Hefei, China, [2]Department of Biological Physics, University of Science and Technology of China, Hefei, China, [3]Department of Orthopedics, The First Affiliated Hospital of Anhui Medical University, Hefei, China, [4]School of Basic Medical Sciences, Anhui Medical University, Hefei, China, [5]Hua Tuo Institute of Medical Innovation (HTIMI), Wuhan, China, [6]Sino Euro Orthopaedics Network, Berlin, Germany, [7]The First Affiliated Hospital of USTC, Division of Life Sciences and Medicine, University of Science and Technology of China, Hefei, China

The cartilage has poor ability to mount a sufficient healing response. Herein, kartogenin (KGN), an emerging stable non-protein compound with the ability to recruit bone marrow mesenchyme stem cells (BMSCs) to promote chondrogenic differentiation, was grafted onto dopamine-Fe(III) chelating nanoparticles, followed by involving a gelatin- and dextran-based injectable hydrogel to mimic the extracellular matrix to promote cartilage repair. The *in vitro* results demonstrated that KGN underwent long-term sustained release behavior and availably promoted the deep migration of BMSC cells in yielding hydrogels. Furthermore, *in vivo* New Zealand white rabbits' cartilage defect model repairing results showed that cartilage defect obtained significant regeneration post operation in the 12th week, and the defect edge almost disappeared compared to adjacent normal cartilage tissue. Meanwhile, the T_2-weighted magnetic resonance imaging (MRI) property resulting from dissociative Fe (III) can significantly monitor the degradation degree of the implanted hydrogels in the defect site. This integrated diagnosis and treatment system gives insight into cartilage regeneration.

Keywords: kartogenin, cartilage regeneration, dopamine, magnetic resonance imaging (MRI), hydrogels

OPEN ACCESS

Edited by:
Rui Guo,
Jinan University, China

Reviewed by:
Chenggong Yan,
Southern Medical University, China
Zuyong Wang,
Hunan University, China

***Correspondence:**
Weiping Xu
weipingx@ustc.edu.cn

Specialty section:
This article was submitted to Biomaterials, a section of the journal Frontiers in Bioengineering and Biotechnology

Received: *10 May 2022*
Accepted: *06 June 2022*
Published: *22 July 2022*

Citation:
Zhang H, Fang W, Zhao T, Zhang H, Gao L, Li J, Wang R and Xu W (2022) Real-Time MRI Monitoring of GelMA-Based Hydrogel-Loaded Kartogenin for In Situ Cartilage Regeneration. Front. Bioeng. Biotechnol. 10:940735. doi: 10.3389/fbioe.2022.940735

INTRODUCTION

Cartilage has a rather limited ability for self-repair and regeneration due to its unique avascular microstructure and low cell density (Zhang et al., 2020a; Zhang et al., 2020b). Although the common treatment methods for cartilage injury in clinical, including marrow stimulation, autografts and matrix-induced autologous chondrocyte implant, can alleviate the pain, they also have limited problems such as ectopic cartilage damage, insufficient donors and immune rejection (Yan et al., 2020a; Satapathy et al., 2020; Wang et al., 2020; Yin et al., 2020; Naghizadeh et al., 2021). Hence, it is still a challenge to obtain natural hyaline cartilage and restore its function. Current studies utilized three-dimensional scaffolds to fill defects to suppress cartilage deterioration development caused by the peak force values on the uneven surface (Zhou et al., 2017; Liu et al., 2020a; Rogan et al., 2020; Yao et al., 2020). In addition, the scaffolds provide a mimetic extracellular matrix (ECM) for chondrocytes (Huang et al., 2015; Yang et al., 2019a). However, due to the inherent low density

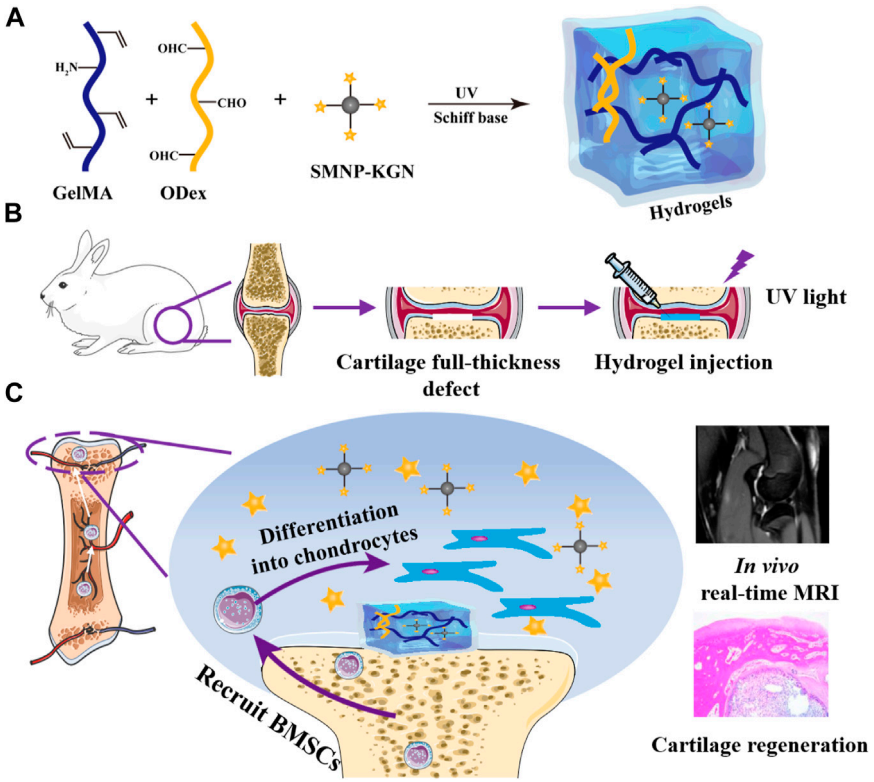

SCHEME 1 | Schematic diagram of the research. **(A)** Hydrogel; **(B)** full-thickness defect surgical procedure; **(C)** GelMA/ODex/SMNP-KGN hydrogel recruits BMSC and promotes its differentiation into chondrocytes.

of chondrocytes, it is difficult to achieve effective cartilage regeneration only by providing chondrocytes with a mimicking ECM (Zhang et al., 2019; Benmassaoud et al., 2020; Dai et al., 2020). Although some researchers make attempts to promote repair by cell injection or the integrated cell-scaffold resulting from 3D printing, these approaches also encounter limitations, including the appropriate number of cells, immune rejection, and the risk of infection caused by bacteria and viruses (van Buul et al., 2011; Abdollahiyan et al., 2020). Therefore, it is particularly important to choose an effective signal stimulation to evoke the self-repair of cartilage.

In recent years, the emerging small molecule kartogenin (KGN) has high stability *in vitro*. It can recruit BMSCs to home to cartilage sites and further induce BMSCs to differentiate into chondrocytes, which has inspired researchers' interest to use it in cartilage diseases (Zhang et al., 2017; Yang et al., 2019b; Yan et al., 2020b). However, the related study demonstrated that single KGN injections in the joint hardly promoted cartilage regeneration owing to the loss of KGN due to the effect of blood circulation (Xu et al., 2015). Although coating KGN on the surface of nanomaterials can achieve an improved sustainable release effect, the simple physical interactions can still easily cause obvious burst release, which can barely accomplish the long-term repair process (Yin et al., 2017; Sun et al., 2018).

Another important problem is that owing to the long-term repair process, it is necessary to observe the degree of repair intermittently in clinic and adopt some external intervention for the regulation of a treatment scheme to obtain the desired effect. Therefore, it is a key and urgent challenge to integrate the function of monitoring materials in a real-time and non-invasive manner. Magnetic resonance imaging (MRI), which has deep penetration capabilities, has served as a safe imaging tool for monitoring molecular changes with high resolution, the absorption states of implanted materials, and the remodeling of regenerated tissue (Kotecha et al., 2013; Ukai et al., 2015). It is also widely and effectively applied in clinical investigations (Chen et al., 2013). In the past, MRI has been utilized to visualize and assess tissue-engineered constructs due to its superior distinguishing capabilities for soft tissue (van Buul et al., 2011).

Hydrogels based on natural biomaterials have been widely used in the study of hard tissue repair, such as bone and cartilage (Zhou et al., 2018). They can mimic the ECM and serve as a carrier for *in situ* drug release. Gelatin and dextran are two of the most used biomaterials for constructing the hydrogel for biomedical use. They both have excellent biocompatibility, abundant chemical groups for modification, and biodegradability. Researchers used the two chemical-modified biomaterials to construct double crosslinked hydrogel and realized the *in situ* application (Zhou et al., 2018; Zhao et al.,

2022; Zhou et al., 2022). Moreover, hydrogels can stabilize and uniformly disperse nanoparticles, which can be chosen as an ideal carrier for drugs (Liu et al., 2020b).

Based on the above background, KGN is a stable chemical component compared to protein, cells or growth factors, which allows KGN to work long term *in vivo*. One issue that needs be addressed is the development of suitable carriers to achieve sustained release of KGN. Fe (III) has long been used in MRI monitoring, and nanoparticles combined with dopamine can enhance its biocompatibility. In this research, the dopamine-Fe (III) chelating nanoparticles covalently bound to KGN and dropped into hydrogel was designed to realize the *in situ* long-term release. The prepared hydrogels can effectively fill the irregular cartilage defects, the mechanical strength of which can be adjusted by changing the construction ratio. Released KGN can effectively recruit BMSCs to the internal hydrogel and induce them to differentiate into chondrocytes. Fe (III) can effectively provide significant T_2-weighted imaging, which can monitor the hydrogel state and regenerated cartilage in a real-time and non-invasive manner (**Scheme 1**).

MATERIALS AND METHODS

Materials

Gelatin (Gel) from porcine skin was purchased from Sigma-Aldrich (Shanghai, China). Dextran (Dex, Mw = 70 KDa) was purchased from J&K (Beijing, China). Methacrylic anhydride, sodium periodate, ethylene glycol, dopamine hydrochloride, ferric chloride hexahydrate ($FeCl_3$ $6H_2O$), kartogenin (KGN) and photo-initiator 2-hydroxy-4'-(2-hydroxyethoxy)-2-methylpropiophenone (Irgacure 2959) were purchased from Aladdin Industrial Corporation (Shanghai, China). BMSCs were purchased from Guangzhou Chuangseed Biomedical Materials Co., Ltd. All other chemical reagents were purchased from Sigma-Aldrich and used without further purification.

Synthesis and Characterization of GelMA and ODex

GelMA was synthesized according to the previously described procedure (Camci-Unal et al., 2013). Briefly, 10 g of gelatin was dissolved in 100 ml of PBS at 50°C with continuous stirring. Then, 8 ml of methacrylic anhydride was added to the gelatin solution and stirred for 3 h at 50°C. The reaction solution was diluted with 300 ml of PBS and then dialyzed against distilled water (molecule weight cut-off = 12–14 kDa) for 1 week at 40°C to remove unreacted reagents. The final product was obtained by lyophilizing at −80°C.

Oxidized dextran (ODex) was synthesized as follows: 1 g of dextran was dissolved in 10 ml of purified water to obtain 10% (w/v) solution, and then oxidized with 2 ml of sodium periodate with a concentration of 100 mg/ml. The reaction was carried out in the dark for 20 h at room temperature and the theoretical oxidation was about 20% (Zhu et al., 2018). Ethylene glycol was added to the reaction solution to stop the oxidation process. The resulting solution was then dialyzed exhaustively against deionized water (molecule weight cut-off = 7–12 kDa) and lyophilized at −80°C to obtain the final product.

The successful synthesis of final product GelMA and ODex was characterized by Fourier Transform Infrared Spectrometer (FT-IR, Bruker, VERTEX 70, Germany) with a resolution of 4 cm^{-1}. The potassium bromide (KBr) tablet method was used for preparing test samples and a blank KBr tablet was used as background.

Synthesis and Characterization of MRI Contrast Agent SMNP and Therapeutic Agent SMNP-KGN Nanoparticles

As for the synthesis of contrast agent synthetic melanin nanoparticles (SMNP) (Li et al., 2016), 45 mg of dopamine hydrochloride and different amounts of ferric chloride hexahydrate was fully dissolved in 130 ml of deionized water, stirring at room temperature for 1 h. Subsequently, 20 ml of tris buffer was quickly injected into the above solution. It was observed that the color of solution immediately turned red and gradually turned black after 0.5 h. After stirring for another 1.5 h, the targeted SMNP nanoparticles were separated by centrifugation and washed three times with deionized water.

The SMNP-KGN nanoparticles were prepared by amidation: 20 mg of hydrophobic KGN powder was dissolved in 20 ml of dimethyl sulfoxide (DMSO) solution, and then 200 mg of SMNP nanoparticles were added to the KGN solution and sonicated for 20 min to obtain a homogeneous mixture. Next, the mixture was shaken (120 r/min) at 37°C in the shaker for 24 h. The precipitated SMNP-KGN nanoparticles were collected by centrifuging (8000 r/min) and lyophilized at −80°C. The successful synthesis of SMNP-KGN was characterized by (FT-IR, Bruker, VERTEX 70, Germany). The morphology and diameter of the resulting SMNP-KGN were characterized by TEM (H-800; Hitachi, Japan) and DLS (Zetasizer Nano ZS, Malvern, the United Kingdom).

The Preparation and Characterization of Gel-Dex/SMNP-KGN Hydrogels

The hydrogel pre-solution was obtained by dissolving GelMA and ODex in PBS buffer at different compositions with 0.1% (w/v) photo-initiator I2959 and placed at 37°C. The GelMA solution was fixed at a final concentration of 5% (w/v) and the concentration of ODex was varied. The mass ratio of GelMA and ODex ranged from 1/9 to 9/1. Next the prepared SMNP-KGN nanoparticles were added and sonicated to obtain homogeneous mixing. Hydrogel was finally obtained by UV (365 nm) crosslinking.

The rheological experiments of the prepared hydrogels were carried out in strain-controlled mode on a rotary rheometer (Kinexus Pro$^+$, Malvern, United Kingdom) with a parallel plate (20 mm) at room temperature. The strain and frequency were selected from the linear viscoelastic region, which were 1% and 1 Hz separately. The dynamic frequency sweep experiments were carried out in the range of 0.1–10 Hz at 1% strain to identify the linear viscoelastic range of the hydrogel. The GelMA/ODex

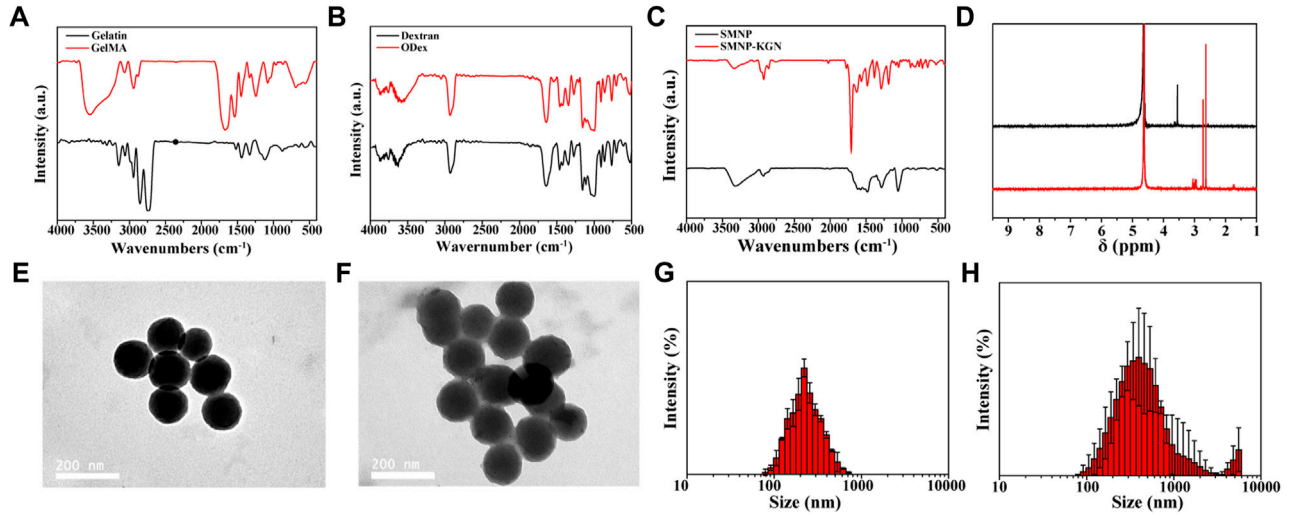

FIGURE 1 | Chemical construction of synthesized materials and characterization of nanoparticles. **(A)** FT-IR spectrum of gelatin and GelMA; **(B)** FT-IR spectrum of dextran and ODex; **(C)** FT-IR spectrum of SMNP and SMNP-KGN; **(D)** ^{1}H NMR spectrum of SMNP and SMNP-KGN; TEM image of **(E)** SMNP and **(F)** SMNP-KGN nanoparticles; hydration diameter statistics of **(G)** SMNP and **(H)** SMNP-KGN obtained by dynamic light scattering.

hydrogels' morphology were observed using a scanning electron microscope (SEM, LEO1530 VP, 5 kV electron beam; Philips, Netherlands) after sputter coating with gold.

In Vitro Release Behavior of KGN

In vitro release behavior of KGN was evaluated as follows: the hydrogel containing SMNP-KGN was immersed in 3 ml of PBS buffer (pH = 7.4) at 37°C. At specified time intervals, 1 ml of incubation solution was taken, and residual solution was supplemented with 1 ml of PBS. The amount of KGN released was determined by UV spectrophotometry and the absorption peak of KGN was 278.4 nm.

In Vitro MR Imaging Stability

The MR images were acquired on a Bruker 7.0 T magnet with Avance II hardware equipped with a 72 mm quadrature transmit/receive coil. T_1 contrast was determined by selecting regions of interest using the software ParaVision version 5.1. The parameters for 7.0 T MRI are TR = 750.0 ms, TE = 12.6 ms, echo = 1/1, FOV = 6.91/3.12 cm, slice thickness = 2 mm, nex = 2 mm, matrix = 256 × 116.

In Vitro Proliferation and Migration Performance of BMSCs

BMSCs proliferation was examined with Cell Counting Kit-8 (CCK-8) at 450 nm on days 1, 3, and 5 after seeding. The hydrogel samples (1.0 g) with different compositions of Fe (III) were incubated in 10 ml of DMEM at 37°C with shaken (100 rpm) for 24 h, the hydrogels were taken out and the DMEM culture medium was obtained as hydrogel extracts. BMSCs were seeded on 48-well plates with 5,000 cells per well. After BMSCs adhered to the wall of 48-well plate, 200 μL of different hydrogel extracts were added to each well, and then the 48-well plate was cultured at 37°C in an incubator containing 5% CO_2 atmosphere. At the selected time point, the culture medium was replaced by CCK-8 working solution and cultured at 37 °C for another 1h, the OD value at 450 nm was read by microplate reader (SpectraMax® M5, Molecular Devices, United States) following the instructions in the manual. To evaluate the cell migration performance of composite hydrogels, BMSCs were seeded on the surface of the hydrogel samples in a 6 well plate at the concentration of 2.5×10^5 per well for 3 days, and then washed by PBS to remove unadhered cells. The different top surface was observed and taken by microscope after cutting. Migrated cell dots were quantitatively evaluated using Image-Pro Plus (v.6.0) software.

In Vitro Characterization of the Ability of BMSC Differentiate Into Chondrocytes

The expression of glycosaminoglycan (GAG), type I collagen and type II collagen in BMSCs co-cultured with the hydrogel extracts were measured to characterize the potential of BMSCs to differentiate into chondrocytes.

A 1,9-dimethylmethylene blue (DMMB) dye binding assay was utilized to detect the GAG content. The samples were collected at days 7, 14, and 28 and digested with papain solution (1 mg ml^{-1} papain in 0.1 M phosphate buffer with 5 mM L-cysteine hydrochloride and 5 mM EDTA) for 18 h at 60°C. After centrifugation at 1000 *g* for 15 min, 20 μL of supernatant from each specimen was mixed with 200 μL of DMMB dye (16 mg of DMMB in 1 L of water containing 3.04 g of glycine, 2.37 g of NaCl, and 95 ml of 0.1 M hydrochloric acid) for 30 min at 37°C. The GAG content was standardized using shark chondroitin 6-sulfates.

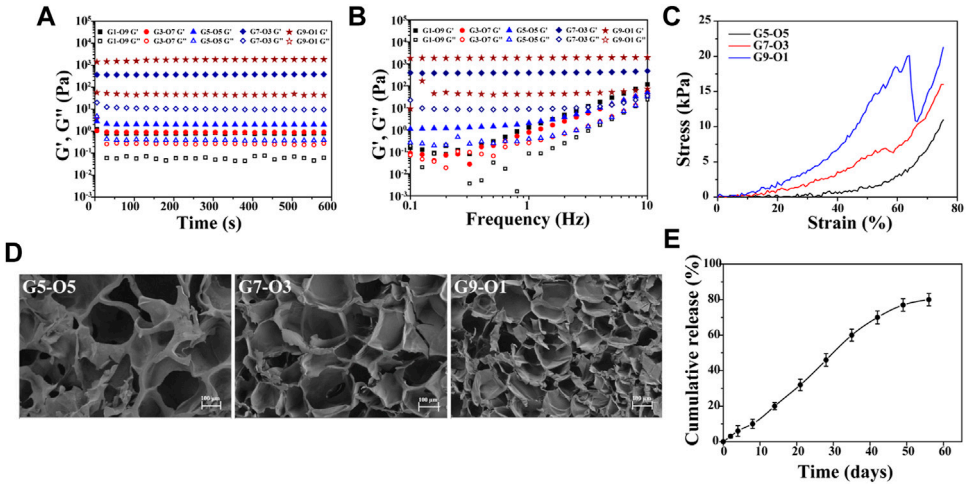

FIGURE 2 | (A) Time-sweep sequence and **(B)** frequency sweep of hydrogel with different mass ratio; **(C)** strain-stress curve of G5-O5, G7-O3, and G9-O1 hydrogel; **(D)** SEM images of cross-sections of three hydrogels. **(E)** Release curve of KGN obtained from GelMA/ODex/SMNP-KGN hydrogel.

The DNA content was measured with Hoechst 33258 diluent and normalized to a certified calf thymus DNA standard. Absorbance and fluorescence values were immediately determined after the incubation time using a SpectraMax® M5 multimode microplate reader (Molecular Devices). The cartilage-specific gene (collagen I and collagen II) expression level of the GelMA/ODex, GelMA/ODex/SMNP and GelMA/ODex/SMNP-KGN hydrogel co-cultured with BMSCs for 14 days were evaluated by real-time PCR.

Rabbit Cartilage Defect Model Construction

All animal procedures were approved by the Laboratory Animal Center of Anhui Medical University. Twenty-seven adult male New Zealand white rabbits (2.5–3 kg, 5–6 months old) were fed for 1 week to adapt to the environment before surgery. The rabbit was anesthetized by injecting 3% (w/v) pentobarbital (1 ml/kg) through the ear vein and put in the supine position. The hair on the joint was removed and the surgical site then disinfected with iodophor. The skin and surface tissue along the lateral side of the patella was cut to expose the knee joint. A drill with a core diameter of 4 mm was used to create a full-thickness cartilage defect with a diameter of 4 mm and a depth of 4 mm in the center of the joint. Subsequently, the hydrogel pre-solution was added on the defect and crosslinked using UV light. After the hydrogel formed, the skin was sutured layer by layer and disinfected. Penicillin was injected in the first 3 days after the surgery to prevent infection. After 6 and 12 weeks of treatment, the articular cartilage was collected and fixed with 4% paraformaldehyde.

For histological staining, the fixed articular cartilage was decalcified with 10% ethylenediaminetetraacetic acid EDTA for 3 months until softened, then dehydrated and embedded in paraffin. The samples were cut into 5 μm sections for further staining. H&E, Masson, toluidine blue, and PAS staining were carried out to assess the regeneration of cartilage.

In Vivo MRI Evaluation

All animals were anesthetized for MRI observation after surgery at 0, 6 and 12 weeks. The parameters for 7.0 T MRI are TR = 750.0 ms, TE = 12.6 ms, echo = 1/1, FOV = 6.91/3.12 cm, slice thickness = 2 mm, nex = 2 mm, matrix = 256 × 116.

Statistical Analysis

The data are expressed as the mean standard deviation of at least 3 parallel samples. All statistical analysis were performed using SPSS software (ver. 16.0; SPSS Inc., United States). Significance analysis is obtained through one-way ANOVA, and at $p < 0.05$ were considered statistically significant: (*) for $p < 0.05$, (**) for $p < 0.01$, (***) for $p < 0.001$.

RESULTS AND DISCUSSION

The Synthesis of Hydrogel Precursor GelMA and ODex and MRI Imaging-Therapeutic Agents SMNP-KGN Nanoparticles

The matrix occupies 95% of the total volume of cartilage, and the organic components in a cartilage matrix are mainly proteins, such as collagen. As one of the collagen derivatives, gelatin exhibits unique properties such as similar biological properties to collagen, lower antigenicity and desired biocompatibility. However, due to the excessively fast degradation rate and insufficient mechanical strength, its application in hard tissue repair is limited (Levett et al., 2014).

In this study, gelatin was modified by methacryloyl and served as a candidate of functioned hydrogels. The successful synthesis of GelMA was demonstrated by the FT-IR absorption peaks at 1634 cm^{-1} (amide I band), 1530 cm^{-1} (amide II band) and 1446 cm^{-1} (amide III band), corresponding to the stretching vibration of C=O bond, bending vibration of -NH bond and plane vibration of -CN and -NH bonds, respectively (**Figure 1A**).

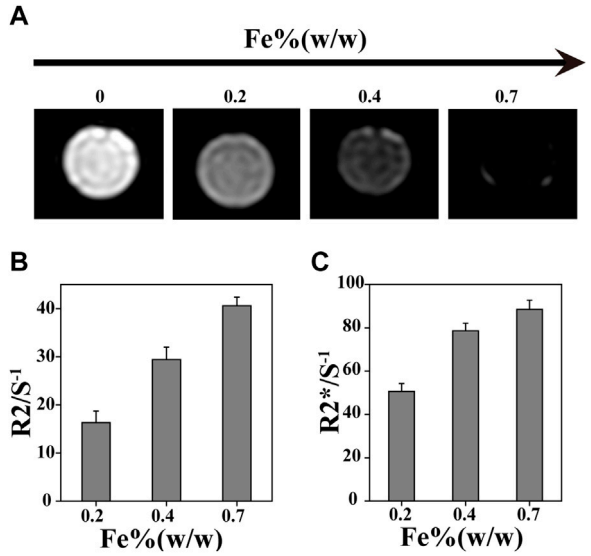

FIGURE 3 | *In vitro* MR imaging ability. **(A)** MRI with different Fe concentration. **(B)** R2/S^{-1} and **(C)** R2*/S^{-1} value obtained from MR images.

Although GelMA alone can form hydrogel, this hydrogel is completely formed by a chemical cross-linked network and generally has poor fatigue resistance. Articular cartilage, as a connection between bones, needs to withstand cyclic pressure, so only using GelMA as hydrogel cannot meet actual needs. Double cross-linked network hydrogels can effectively solve the problem of poor mechanical properties of single network hydrogels.

Dextran has the similar structure to natural chondroitin and has recently been applied in cartilage repair (Jin et al., 2010; Wang et al., 2017). It can be modified by a variety of chemical methods, among which the most common modification method is sodium periodate oxidation to obtain aldehyde groups. Aldehydated dextran can easily form hydrogels with amino-rich organics through a Schiff base. This dynamically reversible Schiff base crosslinked hydrogel also plays an important role in the field of biomedicine.

Previous research indicates that oxidized dextran (ODex) can form Schiff bases with unreacted amino groups in GelMA, and the GelMA/ODex hydrogel has better fatigue resistance than GelMA after crosslinked by UV light (Liu et al., 2020b). This kind of interpenetrating polymer network (IPN) can dissipate external energy well, so that the hydrogel still maintains good mechanical properties after being subjected to multiple compression cycles. Therefore, ODex is introduced into the interaction with GelMA to produce a hydrogel with double crosslinks, thereby improving the mechanical properties of hydrogel that matches natural cartilage. The successful synthesis of ODex was proved according to the FT-IR spectrum and the characteristic adsorption peak of ODex at 1722 cm^{-1} was attributed to the vibration of the aldehyde group (**Figure 1B**).

SMNP, a new type of nanoparticle based on dopamine, maintains the good biocompatibility of dopamine and at the same time has a high Fe (III) ion content, which has great potential as an MRI contrast agent. Through the amino groups on the surface of SMNP, KGN can be easily grafted to the surface of SMNP by amide reaction, thereby prolonging the retention time and exerting a long-term effect in the body. **Figure 1C** showed the successful synthesis of SMNP-KGN. The emerging peak at 1710 cm^{-1} and weakened peak at 1535 cm^{-1} was ascribed to the vibrations of carboxyl groups of KGN and amino groups of SMNP, respectively. The ^{1}H NMR spectrum also shows the successful synthesis of SMNP-KGN (**Figure 1D**). The morphology and diameter of SMNP and SMNP-KGN was

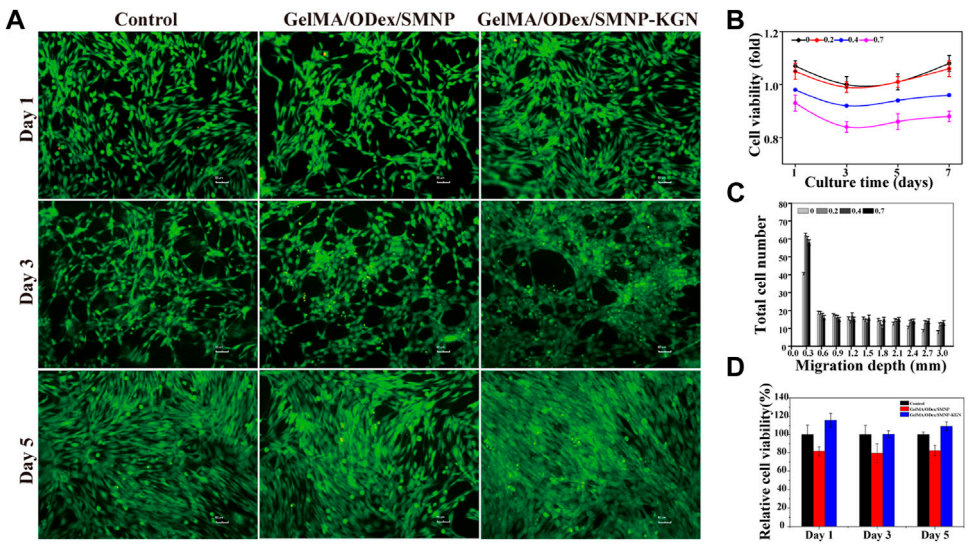

FIGURE 4 | Cytocompatibility of hydrogels. **(A)** Live/dead staining of BMSCs cultured with hydrogel extracts; **(B)** cell viability of BMSCs cultured with SMNP with different Fe content; **(C)** migration depth of SMNP-KGN with different Fe (III) content; **(D)** cell viability of GelMA/ODex/SMNP and GelMA/ODex/SMNP-KGN hydrogel.

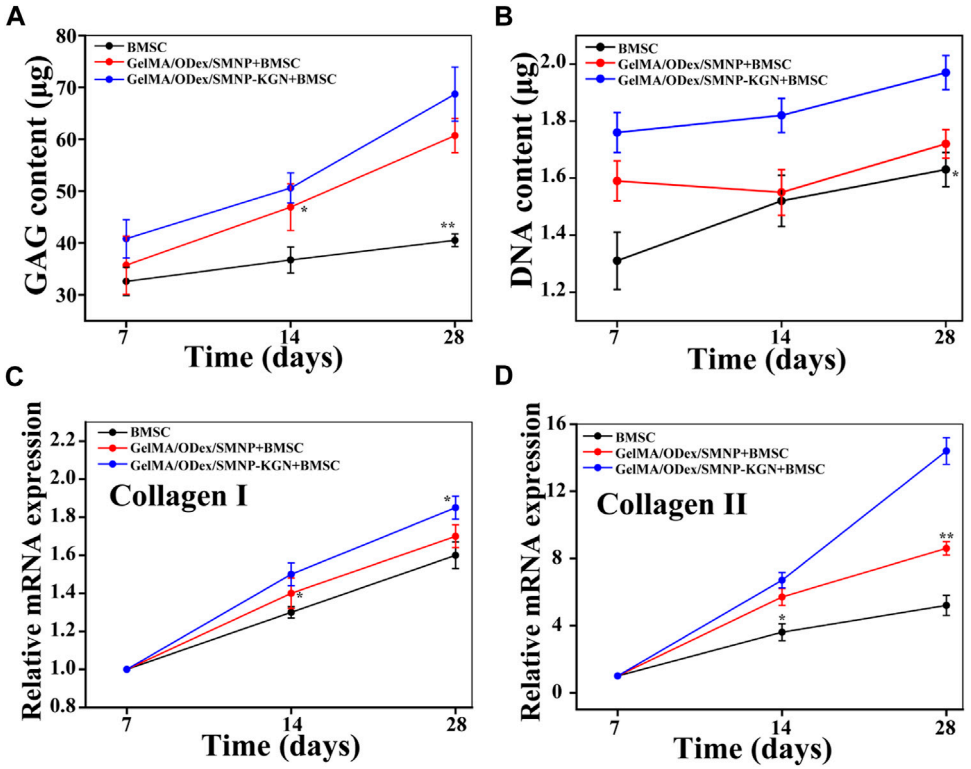

FIGURE 5 | (A) GAG and **(B)** DNA content of cartilage matrix deposition after BMSCs co-cultured with hydrogel. Relative mRNA expression of **(C)** collagen II and **(D)** collagen I.

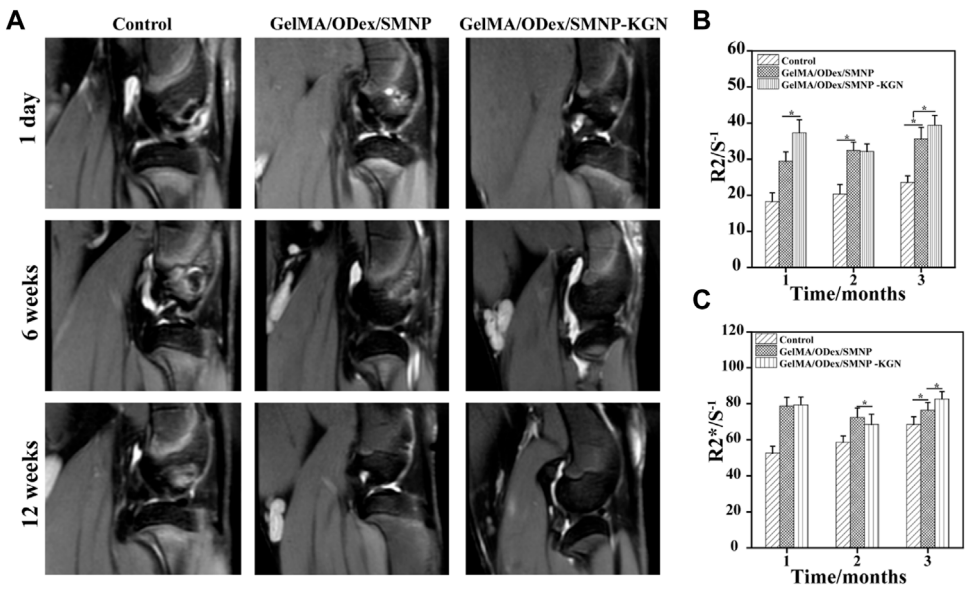

FIGURE 6 | (A) *In vivo* T2-weight MR image of articular cartilage. **(B)** R2/S-1 and **(C)** R2*/S-1 value obtained from MR images.

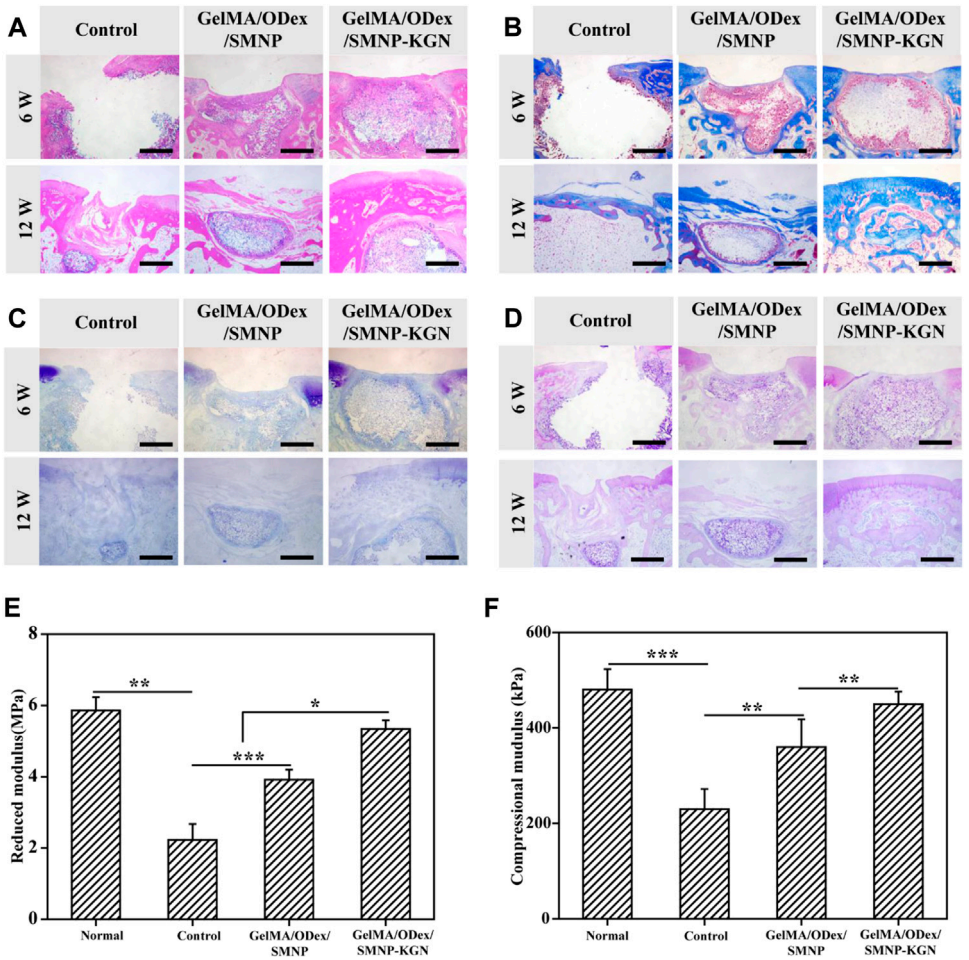

FIGURE 7 | Evaluation of the effect of cartilage regeneration *in vivo*. **(A)** H&E, **(B)** Masson, **(C)** toluidine, and **(D)** PAS staining of defect cartilage at 6 and 12 weeks. Scale bar = 200 μm. **(E)** Reduced modulus and **(F)** compressional modulus of regenerated cartilage in 12 weeks.

characterized through TEM and DLS. SMNP appeared as a sphere with an average diameter of 130 mm (**Figures 1E,G**). It was found the shape of SMNP-KGN was not significantly changed but the diameter of the complex increased slightly compared to SMNP (**Figures 1F,H**).

Rheological Properties and Morphology of GelMA/ODex Hydrogel

Hydrogel was regarded as the solid material with apparent viscoelasticity reflecting viscosity and elasticity by compressional deformation that frequently occurs in the cartilage repair. Rheological behavior of various components of hydrogels was conducted (**Figures 2A,B**). The results showed that the storage modulus (G') and the viscous modulus (G") of all hydrogels remained stable, indicating the hydrogel was fully formed. But the storage modulus increased over the proportion of GelMA increasing. For instance, the storage modulus at the maximal value was 1401 Pa for G9-O1, 366.8 Pa for G7-O3, 2.7 Pa for G5-O5, 1.035 Pa for G3-O7, and 1.218 Pa for G1-O9, indicating that the addition of GelMA was pivotal to improve the storage modulus (**Figure 2A**). It is worth noting that G3-O7 and G1-O9 did not form hydrogel, because the higher concentration of ODex affected the photo-crosslinking of GelMA, so these two groups were not used in the following tests. In addition, there was no significant change in storage modulus after applying a shearing force ranging from 1 to 10 Hz, but the viscosity modulus showed the changing trend over the various content of GelMA and ODex, especially the G5-O5, G3-O7 and G1-O9 group (**Figure 2B**). Previous literature has reported that hydrogels with storage modulus about 1,000 Pa are more conducive to protecting and maintaining the chondrocyte phenotype (Liu et al., 2018), thus the hydrogel that was prepared was suitable for cartilage regeneration.

A static compression test was conducted to further analyze the mechanical properties of three different hydrogels. As shown in **Figure 2C**, the stress was increased as GelMA concentration increasing. However, the G9-O1 hydrogel with the highest content of GelMA failed to dissipate the huge external pressure in time due to the higher cross-linking

density of C=C double bonds and the low content of Schiff base bonds and ruptured under 60% strain. This phenomenon was also observed in the study of Liu et al. Pure GelMA hydrogel has higher compression stress due to the tighter covalently cross-linking between C=C double bonds (Liu et al., 2020b).

The morphology of hydrogels with various ratios of GelMA was observed by SEM (**Figure 2D**). The results showed all hydrogels exhibited similar interconnected pore morphology. The interconnectivity of the macro-pores of the hydrogels for cartilage regeneration is essential to assure cell seeding or cell invasion from subchondral bone (Mok et al., 2018). Subsequently, the pore size and quantity decreased, and the smooth pore wall became thick over the GelMA increasing. The average pore size of the G7-O3 hydrogel was about 100 μm, which could support chondrocyte growth. In addition, it can be inferred that pore size was significantly correlated with the degree of crosslinking between molecular chains. The crosslinking density became higher with the increase of G7 content. Therefore G7-O3 was applied in pivotal proportion for further research according to the above results.

The Potential of Hydrogels as MRI Contrast and Cartilage Therapeutics Agent

Further, the *in vitro* release behavior of KGN loaded in 0.4% Fe (III) labeled hydrogels was investigated (**Figure 2E**). It was observed that the release was slow in the first 10 days, and then accelerated in the medium term, and the release trend flattened out eventually. The release behavior can be inferred that the crosslinking point between the macromolecular chain in the hydrogels was gradually hydrolyzed and broken, and then the macromolecules were decomposed into small molecules. The deconstruction of hydrogel accelerated the release of SMNP-KGN nanoparticles; thus, a higher release speed could be seen from day 10 to day 40. The cumulative release of KGN reached 80% on the 56th day, which was close to the release rate obtained by directly coating the KGN in PLGA microspheres according to previous literature that reported an effective cartilage repair effect (Shi et al., 2016).

In vivo real-time non-destructive monitoring of tissue repair is very important for guiding clinical medication. MRI can effectively observe cartilage structure, and the SMNP that was prepared is a new type of contrast agent with great potential for MRI. Hydrogels were labeled by SMNP-KGN with various content of Fe (III), and then conducted for T_2-weighted MR images. It was found that $1/T_2$ value showed an obvious increase with the increase of Fe (III) content resulting in hyperintense image in the labeled group, and in reverse hypointense in the blank group, indicating that Fe (III)-chelated nanoparticles can enhance T_2-weighted MR images (**Figures 3A–C**).

In Vitro Proliferation and Migration of BMSCs Cultured With Hydrogel

To verify the biocompatibility of hydrogel, CCK-8 was used to detect the cell viability of BMSCs co-cultured with the hydrogel extract, and the cells were stained with a live-dead staining kit. **Figure 4Bfig4** shows that the higher content of Fe (III) increased the cytotoxicity of SNMP nanoparticles, but 0.2% Fe contained in SMNP did not show obvious cytotoxicity. KGN has an important effect to recruit BMSCs to differentiation into chondrocyte. Cell starch assay was conducted to assess the promoting migration ability of SMNP-KGN. A significant migration depth of 0.3 mm of BMSCs appeared in the presence of SMNP-KGN with different Fe content; low migration appeared in the control group in return (**Figure 4C**). But when the migration depth exceeded 0.3 mm, there was no significant difference in the migration rate of BMSCs. The phenomenon could be ascribed to the effect of KGN that had the ability of protecting chondrocyte and promoting the migration of BMSCs as previously reported. Meanwhile, it is proved that the Fe content used in this study does not inhibit cell proliferation and migration. SMNP containing 0.2% Fe also behavior the MRI contrast ability and it was therefore chosen for the following study. Previous studies demonstrated that Fe concentrations higher than 25 μg Fe/mL showed an inhibiting effect on chondrogenesis of hBMSCs (Chen et al., 2018); the concentration of Fe (III) in SMNP-KGN labeled hydrogel was lower than the reported value, thus the hydrogel that was prepared would not affect the chondrogenesis of hBMSCs.

The cytotoxicity of GelMA/ODex hydrogels containing SMNP and SNMP-KGN was further studied. In the live/dead staining image (**Figure 4A**), BMSCs showed a good spread morphology, and no obvious dead cells (red) were seen, and the living cells (green) were in good condition. The CCK-8 assay results demonstrated though GelMA/ODex/SMNP hydrogel had a certain inhibitory effect on cell proliferation, but the addition of KGN can significantly protect cells and accelerate cell proliferation (**Figure 4D**).

In Vitro Ability of Hydrogel to Induce BMSC to Differentiate Into Chondrocytes

Next,:BMSCs were co-cultured with hydrogels to analyze the ability of hydrogel that induce BMSCs to differentiate into chondrocytes. The deposited cartilage matrix and the relative expression of cartilage matrix coding genes was investigated. Compared with the GelMA/Odex hydrogel, the GAG secretion content in the SMNP containing the hydrogel cultured group was up regulated and the expression level in KGN-SMNP containing the hydrogel cultured group was the highest. The secretion rate in the latter 14 days in the SMNP containing hydrogel was higher than that in the first 14 days, while the control group (GelMA/Odex hydrogel) only showed a slightly increasing trend (**Figure 5A**). The total glycosaminoglycan (GAG) contents were normalized to the DNA content and showed a robust and sustained increase (**Figure 5B**).

Collagen is one of the main components of cartilage, among which hyaline cartilage mainly contains collagen II (fibrocartilage mainly contains collagen I). It was determined the content of collagen I and collagen II expressed by BMSCs after co-cultured with hydrogel. As shown in **Figures 5C**,D, compared with the control group, the expression of collagen II in the GelMA-Odex/

SMNP-KGN was significantly upregulated over time. The expression of collagen I in each group remained basically unchanged and was significantly lower than that of collagen II, indicating that the hydrogel has the potential to promote the differentiation of BMSCs to form hyaline cartilage *in vitro*, rather than forming fibrocartilage.

In Vivo Full-Thickness Defect Cartilage Regeneration Assessment of Hydrogel

To evaluate the effect of hydrogel in promoting cartilage regeneration, we caused full-thickness damage to the articular cartilage of rabbits and injected the hydrogel *in situ* to completely fill the damaged area to evaluate the promotion effect of cartilage regeneration.

SMNP labeled hydrogels were implanted in cartilage defect and monitored by MRI (**Figure 6A**). As shown, hyperintense image appeared in all the groups incipiently and SMNP labeled hydrogels showed more remarkable light signal compared to the control group, which was mainly ascribed to water and Fe (III) enhancing the T_2-weighted MR images. At the 6th week, the control group kept the hyperintense, whereas the experiment groups showed weak hyperintense and strong hypointense. Combining the results of gross observation, it can be inferred that severe inflammation has not relieved over time in the control group, however the other groups treated with hydrogels emerged a repaired effect, along with hydrogels degradation that caused the loss of contrast agent, thus decreasing $1/T_2$ value. In addition, it can be found that more obvious hypointense and higher R2 and R2* value was detected in the hydrogels group with KGN, indicating that the accelerated deposition of calcium ions happened at the defect site enhancing the T_2-weight imaging (Yang et al., 2019b). At 12 weeks, GelMA-ODex/SMNP-KGN group showed a strong shadow similar to the surrounding normal cartilage tissues, which demonstrated that KGN speeded up the process of cartilage regeneration, and that the complex hydrogels mostly degraded after the *in vivo* implantation for 12 weeks (**Figures 6B,C**).

The therapeutic effect of the GelMA-ODex/SMNP-KGN hydrogel was further evaluated through histological staining. At the 6th week, an obvious fracture surface was observed in the blank control group by H&E staining (**Figure 7A**). Despite the occurrence of improvement in the production of cartilage matrix in the GelMA/ODex/SMNP group, the discontinue feature existed all the time. The GelMA-ODex/SMNP-KGN group was mostly filled with cartilage matrix without observed inflammation. At the 12th week, the control group still retained the defect state, verifying the truth that cartilage lacked the innate ability to mount enough healing response. Nevertheless, it was interesting to find that the GelMA-ODex/SMNP group seemed to contain remarkable matrix filling compared to the control group. But the regenerated tissue appeared different and displayed distinct boundaries from the surrounding normal hyaline cartilage. As for the GelMA-ODex/SMNP-KGN group, the regenerated cartilage matrix coincided with normal cartilage matrix and remarkably recovered the cartilage defect flushing with the native tissue.

In 12 weeks of Masson staining, the GelMA/ODex/SMNP-KGN hydrogel treated group showed less collagen deposition than the other two groups (**Figure 7B**). But PAS and toluidine blue (TB) staining images showed that the experimental group had obvious glycosaminoglycan deposition (**Figures 7C,D**). At the 12th week, discontinuous sections were hardly observed in the GelMA/ODex/SMNP-KGN hydrogel treated group, which showed abundant new collagen consistent with that of the surrounding normal cartilage. Although the GelMA/ODex/SMNP hydrogel treated group was filled with partial matrix, it seems to be different with normal tissue, which can be ascribed to an inflammation response. The blank group still showed incomplete cross-sections.

To verify the functional recovery of regeneration cartilage, the mechanical properties were evaluated (**Figures 7E,F**). It was found that the reduced modulus and compressional modulus of the experimental group were higher than those of the other groups and were close to the strength of normal cartilage tissue, which was consistent with the histological results. Meanwhile, it is found that the blank group cannot support the role of force in the empty state, while the GelMA/ODex/SMNP hydrogel treated group will form fibrotic cartilage.

The reason for the better repair effect of the GelMA/ODex/SMNP hydrogel treated group may be the SMNP-KGN nanoparticles carried in the hydrogel. SMNP-KGN nanoparticles was gradually released from hydrogel during its degradation process as shown in MRI results, and KGN was released to the defect tissue under the action of weaker amide bonds. The released KGN could recruit BMSC cells to the defect site, further inducing differentiation into chondrocytes, and making up for the defect of hyaline cartilage, and accelerating cartilage matrix deposition and remodeling.

CONCLUSION

In summary, an injectable GelMA/ODex/SMNP-KGN hydrogel was successfully prepared. This kind of hydrogel can be injected to fill damaged cartilage *in situ*, which solves the problem that the scaffold cannot adapt to the shape of the defect. In addition, SMNP-KGN nanoparticles, which have both MRI contrast and cartilage treatment functions, were loaded in hydrogel to realize non-destructive monitoring of the injured site, and recruit surrounding BMSCs to differentiate into chondrocytes to form hyaline cartilage. The histological results further showed that cartilage defect was regenerated significantly at the 12th week after GelMA/ODex/SMNP-KGN hydrogel injection, and the defect edge almost disappeared compared to adjacent normal cartilage tissue. In addition, the mechanical property of regenerated hyaline cartilage was similar to that of normal cartilage. This hydrogel with integrated diagnosis and treatment function will provide a new method for clinical treatment of articular cartilage injury diseases.

DATA AVAILABILITY STATEMENT

The raw data supporting the conclusions of this article will be made available by the authors, without undue reservation.

ETHICS STATEMENT

The animal study was reviewed and approved by the Laboratory Animal Center of Anhui Medical University.

AUTHOR CONTRIBUTIONS

HaZ: investigation, methodology, data curation, formal analysis, writing original draft. WF: investigation, methodology, data curation, formal analysis, writing—original draft. TZ: investigation, discussion, writing—review and editing. HaZ: investigation, methodology. JL: investigation. LG: supervision, conceptualization, methodology, writing—review and editing. RW: writing—review and editing. WX: conceptualization, methodology, formal analysis, data curation, writing—review and editing, supervision, funding acquisition.

FUNDING

This work was supported by the National Natural Science Foundation of China (No. 52072360, 51672004), the Key Research and Development Program of Anhui Province (China, No. 1804h08020252), and the Natural Science Foundation of Anhui Province (China, No. 1608085MH176, 1908085QB65).

REFERENCES

Abdollahiyan, P., Oroojalian, F., Mokhtarzadeh, A., and Guardia, M. (2020). Hydrogel-Based 3D Bioprinting for Bone and Cartilage Tissue Engineering. *Biotechnol. J.* 15 (12), 2000095. doi:10.1002/biot.202000095

Benmassaoud, M. M., Gultian, K. A., DiCerbo, M., and Vega, S. L. (2020). Hydrogel Screening Approaches for Bone and Cartilage Tissue Regeneration. *Ann. N.Y. Acad. Sci.* 1460 (1), 25–42. doi:10.1111/nyas.14247

Camci-Unal, G., Cuttica, D., Annabi, N., Demarchi, D., and Khademhosseini, A. (2013). Synthesis and Characterization of Hybrid Hyaluronic Acid-Gelatin Hydrogels. *Biomacromolecules* 14 (4), 1085–1092. doi:10.1021/bm3019856

Chen, J., Wang, F., Zhang, Y., Jin, X., Zhang, L., Feng, Y., et al. (2013). *In Vivo* MRI Tracking of Polyethylenimine-Wrapped Superparamagnetic Iron Oxide Nanoparticle-Labeled BMSCs for Cartilage Repair. *Cartilage* 4 (1), 75–82. doi:10.1177/1947603512455194

Chen, Z., Yan, C., Yan, S., Liu, Q., Hou, M., Xu, Y., et al. (2018). Non-invasive Monitoring of *In Vivo* Hydrogel Degradation and Cartilage Regeneration by Multiparametric MR Imaging. *Theranostics* 8 (4), 1146–1158. doi:10.7150/thno.22514

Dai, M., Sui, B., Hua, Y., Zhang, Y., Bao, B., Lin, Q., et al. (2020). A Well Defect-Suitable and High-Strength Biomimetic Squid Type II Gelatin Hydrogel Promoted *In Situ* Costal Cartilage Regeneration via Dynamic Immunomodulation and Direct Induction Manners. *Biomaterials* 240, 119841. doi:10.1016/j.biomaterials.2020.119841

Huang, G. X., Arany, P. R., and Mooney, D. J. (2015). Modeling and Validation of Multilayer Poly(Lactide-Co-Glycolide) Scaffolds for *In Vitro* Directed Differentiation of Juxtaposed Cartilage and Bone. *Tissue Eng. Part A* 21 (15-16), 2228–2240. doi:10.1089/ten.TEA.2015.0089

Jin, R., Moreira Teixeira, L. S., Dijkstra, P. J., van Blitterswijk, C. A., Karperien, M., and Feijen, J. (2010). Enzymatically-crosslinked Injectable Hydrogels Based on Biomimetic Dextran-Hyaluronic Acid Conjugates for Cartilage Tissue Engineering. *Biomaterials* 31 (11), 3103–3113. doi:10.1016/j.biomaterials.2010.01.013

Kotecha, M., Klatt, D., and Magin, R. L. (2013). Monitoring Cartilage Tissue Engineering Using Magnetic Resonance Spectroscopy, Imaging, and Elastography. *Tissue Eng. Part B Rev.* 19 (6), 470–484. doi:10.1089/ten.teb.2012.0755

Levett, P. A., Melchels, F. P. W., Schrobback, K., Hutmacher, D. W., Malda, J., and Klein, T. J. (2014). A Biomimetic Extracellular Matrix for Cartilage Tissue Engineering Centered on Photocurable Gelatin, Hyaluronic Acid and Chondroitin Sulfate. *Acta biomater.* 10 (1), 214–223. doi:10.1016/j.actbio.2013.10.005

Li, Y., Xie, Y., Wang, Z., Zang, N., Carniato, F., Huang, Y., et al. (2016). Structure and Function of Iron-Loaded Synthetic Melanin. *ACS Nano* 10 (11), 10186–10194. doi:10.1021/acsnano.6b05502

Liu, H., Cheng, Y., Chen, J., Chang, F., Wang, J., Ding, J., et al. (2018). Component Effect of Stem Cell-Loaded Thermosensitive Polypeptide Hydrogels on Cartilage Repair. *Acta biomater.* 73, 103–111. doi:10.1016/j.actbio.2018.04.035

Liu, H., Zhu, X., Guo, H., Huang, H., Huang, S., Huang, S., et al. (2020). Nitric Oxide Released Injectable Hydrogel Combined with Synergistic Photothermal Therapy for Antibacterial and Accelerated Wound Healing. *Appl. Mater. Today* 20, 100781. doi:10.1016/j.apmt.2020.100781

Liu, X., Song, S., Huang, J., Fu, H., Ning, X., He, Y., et al. (2020). HBC-nanofiber Hydrogel Scaffolds with 3D Printed Internal Microchannels for Enhanced Cartilage Differentiation. *J. Mat. Chem. B* 8 (28), 6115–6127. doi:10.1039/d0tb00616e

Mok, S.-W., Fu, S.-C., Cheuk, Y.-C., Chu, I.-M., Chan, K.-M., Qin, L., et al. (2018). Intra-Articular Delivery of Quercetin Using Thermosensitive Hydrogel Attenuate Cartilage Degradation in an Osteoarthritis Rat Model. *CARTILAGE* 11 (4), 490–499. doi:10.1177/1947603518796550

Naghizadeh, Z., Karkhaneh, A., Nokhbatolfoghahaei, H., Farzad-Mohajeri, S., Rezai-Rad, M., Dehghan, M. M., et al. (2021). Cartilage Regeneration with Dual-drug-releasing Injectable Hydrogel/microparticle System: *In Vitro* and *In Vivo* Study. *J. Cell Physiol.* 236 (3), 2194–2204. doi:10.1002/jcp.30006

Rogan, H., Ilagan, F., Tong, X., Chu, C. R., and Yang, F. (2020). Microribbon-hydrogel Composite Scaffold Accelerates Cartilage Regeneration *In Vivo* with Enhanced Mechanical Properties Using Mixed Stem Cells and Chondrocytes. *Biomaterials* 228, 119579. doi:10.1016/j.biomaterials.2019.119579

Satapathy, M. K., Manga, Y. B., Ostrikov, K. K., Chiang, W.-H., Pandey, A., Lekha, R., et al. (2020). Microplasma Cross-Linked Graphene Oxide-Gelatin Hydrogel for Cartilage Reconstructive Surgery. *ACS Appl. Mat. Interfaces* 12 (1), 86–95. doi:10.1021/acsami.9b14073

Shi, D., Xu, X., Ye, Y., Song, K., Cheng, Y., Di, J., et al. (2016). Photo-Cross-Linked Scaffold with Kartogenin-Encapsulated Nanoparticles for Cartilage Regeneration. *Acs Nano* 10 (1), 1292–1299. doi:10.1021/acsnano.5b06663

Sun, X., Wang, J., Wang, Y., and Zhang, Q. (2018). Collagen-based Porous Scaffolds Containing PLGA Microspheres for Controlled Kartogenin Release in Cartilage Tissue Engineering. *Artif. Cells Nanomed Biotechnol.* 46 (8), 1957–1966. doi:10.1080/21691401.2017.1397000

Ukai, T., Sato, M., Ishihara, M., Yokoyama, M., Takagaki, T., Mitani, G., et al. (2015). Usefulness of Using Laser-Induced Photoacoustic Measurement and 3.0 Tesla MRI to Assess Knee Cartilage Damage: a Comparison Study. *Arthritis Res. Ther.* 17, 383. doi:10.1186/s13075-015-0899-4

van Buul, G. M., Kotek, G., Wielopolski, P. A., Farrell, E., Bos, P. K., Weinans, H., et al. (2011). Clinically Translatable Cell Tracking and Quantification by MRI in

Cartilage Repair Using Superparamagnetic Iron Oxides. *PloS one* 6 (2), e17001. doi:10.1371/journal.pone.0017001

Wang, Q., Li, X., Wang, P., Yao, Y., Xu, Y., Chen, Y., et al. (2020). Bionic Composite Hydrogel with a Hybrid Covalent/noncovalent Network Promoting Phenotypic Maintenance of Hyaline Cartilage. *J. Mat. Chem. B* 8 (20), 4402–4411. doi:10.1039/d0tb00253d

Wang, X., Li, Z., Shi, T., Zhao, P., An, K., Lin, C., et al. (2017). Injectable Dextran Hydrogels Fabricated by Metal-free Click Chemistry for Cartilage Tissue Engineering. *Mater. Sci. Eng. C* 73, 21–30. doi:10.1016/j.msec.2016.12.053

Xu, X., Shi, D., Shen, Y., Xu, Z., Dai, J., Chen, D., et al. (2015). Full-thickness Cartilage Defects Are Repaired via a Microfracture Technique and Intraarticular Injection of the Small-Molecule Compound Kartogenin. *Arthritis Res. Ther.* 17 (1), 20. doi:10.1186/s13075-015-0537-1

Yan, W., Xu, X., Xu, Q., Sun, Z., Jiang, Q., and Shi, D. (2020). Platelet-rich Plasma Combined with Injectable Hyaluronic Acid Hydrogel for Porcine Cartilage Regeneration: a 6-month Follow-Up. *Regen. Biomater.* 7 (1), 77–90. doi:10.1093/rb/rbz039

Yan, W., Xu, X., Xu, Q., Sun, Z., Lv, Z., Wu, R., et al. (2020). An Injectable Hydrogel Scaffold with Kartogenin-Encapsulated Nanoparticles for Porcine Cartilage Regeneration: A 12-Month Follow-Up Study. *Am. J. Sports Med.* 48 (13), 3233–3244. doi:10.1177/0363546520957346

Yang, W., Zheng, Y., Chen, J., Zhu, Q., Feng, L., Lan, Y., et al. (2019). Preparation and Characterization of the Collagen/cellulose Nanocrystals/USPIO Scaffolds Loaded Kartogenin for Cartilage Regeneration. *Mater. Sci. Eng. C* 99, 1362–1373. doi:10.1016/j.msec.2019.02.071

Yang, W., Zhu, P., Huang, H., Zheng, Y., Liu, J., Feng, L., et al. (2019). Functionalization of Novel Theranostic Hydrogels with Kartogenin-Grafted USPIO Nanoparticles to Enhance Cartilage Regeneration. *ACS Appl. Mat. Interfaces* 11 (38), 34744–34754. doi:10.1021/acsami.9b12288

Yao, Y., Wang, P., Li, X., Xu, Y., Lu, G., Jiang, Q., et al. (2020). A Di-self-crosslinking Hyaluronan-Based Hydrogel Combined with Type I Collagen to Construct a Biomimetic Injectable Cartilage-Filling Scaffold. *Acta biomater.* 111, 197–207. doi:10.1016/j.actbio.2020.05.007

Yin, H., Wang, J., Gu, Z., Feng, W., Gao, M., Wu, Y., et al. (2017). Evaluation of the Potential of Kartogenin Encapsulated poly(L-Lactic Acid-Co-Caprolactone)/collagen Nanofibers for Tracheal Cartilage Regeneration. *J. Biomater. Appl.* 32 (3), 331–341. doi:10.1177/0885328217717077

Yin, N., Tan, X., Liu, H., He, F., Ding, N., Gou, J., et al. (2020). A Novel indomethacin/methotrexate/MMP-9 siRNA *In Situ* Hydrogel with Dual Effects of Anti-inflammatory Activity and Reversal of Cartilage Disruption for the Synergistic Treatment of Rheumatoid Arthritis. *Nanoscale* 12 (15), 8546–8562. doi:10.1039/d0nr00454e

Zhang, J., Yun, S., Du, Y., Zannettino, A. C. W., and Zhang, H. (2020). Fabrication of a Cartilage Patch by Fusing Hydrogel-Derived Cell Aggregates onto Electrospun Film. *Tissue Eng. Part A* 26 (15-16), 863–871. doi:10.1089/ten.TEA.2019.0318

Zhang, J., Yuan, T., Zheng, N., Zhou, Y., Hogan, M. V., and Wang, J. H.-C. (2017). The Combined Use of Kartogenin and Platelet-Rich Plasma Promotes Fibrocartilage Formation in the Wounded Rat Achilles Tendon Entheses. *Bone & Jt. Res.* 6 (4), 231–244. doi:10.1302/2046-3758.64.bjr-2017-0268.r1

Zhang, Y., Cao, Y., Zhao, H., Zhang, L., Ni, T., Liu, Y., et al. (2020). An Injectable BMSC-Laden Enzyme-Catalyzed Crosslinking Collagen-Hyaluronic Acid Hydrogel for Cartilage Repair and Regeneration. *J. Mat. Chem. B* 8 (19), 4237–4244. doi:10.1039/d0tb00291g

Zhang, Y., Zhu, D., Wei, Y., Wu, Y., Cui, W., Liuqin, L., et al. (2019). A Collagen Hydrogel Loaded with HDAC7-Derived Peptide Promotes the Regeneration of Infarcted Myocardium with Functional Improvement in a Rodent Model. *Acta biomater.* 86, 223–234. doi:10.1016/j.actbio.2019.01.022

Zhao, X., Li, S., Du, X., Li, W., Wang, Q., He, D., et al. (2022). Natural Polymer-Derived Photocurable Bioadhesive Hydrogels for Sutureless Keratoplasty. *Bioact. Mater.* 8, 196–209. doi:10.1016/j.bioactmat.2021.07.001

Zhou, F., Hong, Y., Zhang, X., Yang, L., Li, J., Jiang, D., et al. (2018). Tough Hydrogel with Enhanced Tissue Integration and *In Situ* Forming Capability for Osteochondral Defect Repair. *Appl. Mater. Today* 13, 32–44. doi:10.1016/j.apmt.2018.08.005

Zhou, F., Zhang, X., Cai, D., Li, J., Mu, Q., Zhang, W., et al. (2017). Silk Fibroin-Chondroitin Sulfate Scaffold with Immuno-Inhibition Property for Articular Cartilage Repair. *Acta biomater.* 63, 64–75. doi:10.1016/j.actbio.2017.09.005

Zhou, L., Zhou, L., Wei, C., and Guo, R. (2022). A Bioactive Dextran-Based Hydrogel Promote the Healing of Infected Wounds via Antibacterial and Immunomodulatory. *Carbohydr. Polym.* 291, 119558. doi:10.1016/j.carbpol.2022.119558

Zhu, Q., Jiang, M., Liu, Q., Yan, S., Feng, L., Lan, Y., et al. (2018). Enhanced Healing Activity of Burn Wound Infection by a Dextran-HA Hydrogel Enriched with Sanguinarine. *Biomater. Sci.* 6 (9), 2472–2486. doi:10.1039/c8bm00478a

Conflict of Interest: The authors declare that the research was conducted in the absence of any commercial or financial relationships that could be construed as a potential conflict of interest.

Publisher's Note: All claims expressed in this article are solely those of the authors and do not necessarily represent those of their affiliated organizations, or those of the publisher, the editors and the reviewers. Any product that may be evaluated in this article, or claim that may be made by its manufacturer, is not guaranteed or endorsed by the publisher.

Copyright © 2022 Zhang, Fang, Zhao, Zhang, Gao, Li, Wang and Xu. This is an open-access article distributed under the terms of the Creative Commons Attribution License (CC BY). The use, distribution or reproduction in other forums is permitted, provided the original author(s) and the copyright owner(s) are credited and that the original publication in this journal is cited, in accordance with accepted academic practice. No use, distribution or reproduction is permitted which does not comply with these terms.

frontiers | Frontiers in Bioengineering and Biotechnology

TYPE Review
PUBLISHED 25 July 2022
DOI 10.3389/fbioe.2022.921284

Check for updates

OPEN ACCESS

EDITED BY
Gang Wu,
VU Amsterdam, Netherlands

REVIEWED BY
Jinshan Guo,
Southern Medical University, China
Wei Xia,
Uppsala University, Sweden

*CORRESPONDENCE
Weijiang Dong,
dongwj@xjtu.edu.cn
Rui Zou,
rainy@xjtu.edu.cn
Lin Niu,
niulin@xjtu.edu.cn

†These authors have contributed equally to this work

SPECIALTY SECTION
This article was submitted to Biomaterials, a section of the journal Frontiers in Bioengineering and Biotechnology

RECEIVED 15 April 2022
ACCEPTED 04 July 2022
PUBLISHED 25 July 2022

CITATION
Dong S, Zhang Y, Mei Y, Zhang Y, Hao Y, Liang B, Dong W, Zou R and Niu L (2022), Researching progress on bio-reactive electrogenic materials with electrophysiological activity for enhanced bone regeneration. *Front. Bioeng. Biotechnol.* 10:921284. doi: 10.3389/fbioe.2022.921284

COPYRIGHT
© 2022 Dong, Zhang, Mei, Zhang, Hao, Liang, Dong, Zou and Niu. This is an open-access article distributed under the terms of the Creative Commons Attribution License (CC BY). The use, distribution or reproduction in other forums is permitted, provided the original author(s) and the copyright owner(s) are credited and that the original publication in this journal is cited, in accordance with accepted academic practice. No use, distribution or reproduction is permitted which does not comply with these terms.

Researching progress on bio-reactive electrogenic materials with electrophysiological activity for enhanced bone regeneration

Shaojie Dong[1,2,3†], Yuwei Zhang[1,2†], Yukun Mei[1,2†], Yifei Zhang[1,2], Yaqi Hao[1,2,3], Beilei Liang[1,2,3], Weijiang Dong[4*], Rui Zou[1,2*] and Lin Niu[1,2,3*]

[1]Key Laboratory of Shaanxi Province for Craniofacial Precision Medicine Research, College of Stomatology, Xi'an Jiaotong University, Xi'an, China, [2]Clinical Research Center of Shaanxi Province for Dental and Maxillofacial Diseases, Xi'an, China, [3]Department of Prosthodontics, College of Stomatology, Xi'an Jiaotong University, Xi'an, China, [4]School of Basic Sciences of Xi'an Jiaotong University Health Science Center, Xi'an, China

Bone tissues are dynamically reconstructed during the entire life cycle phase, which is an exquisitely regulated process controlled by intracellular and intercellular signals transmitted through physicochemical and biochemical stimulation. Recently, the role of electrical activity in promoting bone regeneration has attracted great attention, making the design, fabrication, and selection of bioelectric bio-reactive materials a focus. Under specific conditions, piezoelectric, photoelectric, magnetoelectric, acoustoelectric, and thermoelectric materials can generate bioelectric signals similar to those of natural tissues and stimulate osteogenesis-related signaling pathways to enhance the regeneration of bone defects, which can be used for designing novel smart biological materials for engineering tissue regeneration. However, literature summarizing studies relevant to bioelectric materials for bone regeneration is rare to our knowledge. Consequently, this review is mainly focused on the biological mechanism of electrical stimulation in the regeneration of bone defects, the current state and future prospects of piezoelectric materials, and other bioelectric active materials suitable for bone tissue engineering in recent studies, aiming to provide a theoretical basis for novel clinical treatment strategies for bone defects.

KEYWORDS

electrogenesis, bone regeneration, electrical stimulation, bio-reactive material, electrophysiological activity

1 Introduction

Critical-sized bone defects caused by cleft palate, trauma, infection, tumors, and other genetic or environmental factors exhibit a non-negligible incidence rate and remain difficult to regenerate (Geng et al., 2021; Westhauser et al., 2021; Li et al., 2022). Traction osteogenesis, autologous bone transplantation, and allogeneic bone transplantation are commonly used for bone restoration in the clinic, whereas the effect of these methods is restricted by insufficient sources, bone lesions, secondary injury, potential antigenicity, infection, and other undefined concerns of donors (Terpos et al., 2021).

With the prosperous development of biomaterials, new possibilities for the restoration of massive bone defects have been provided. Among them, bone-implanted biomaterials can be roughly sorted into three generations, referred to as bioinert materials, bioactive materials, and bio-reactive materials. As the first generation of biomaterials, bioinert materials were initially developed during the 1960s–1980s, which included artificial joints, bone nails, and bone plates for internal fixation. These inert biomaterials, which are most widely used in humans, exhibit attractive biocompatibility in the long term during the post-implanted stage (Senra and Marques, 2020). Since traditional inanimate medical metals, polymers, ceramics, and other conventional materials make no adaptive response to changes in bone defects, they can hardly meet the actual needs in the clinic or fulfill the requirements of developing modern biomaterials. Thus, researchers in the field of biomedical materials had started to shift their attention from biocompatibility to bioactivity in the 1980s. Therefore, the second generation of biomedical materials was proposed, which were characterized by controllable degradation, ion exchange capability, polycondensation, and even stimulation of osteoblasts under physiological conditions, ultimately contributing to the formation of new bone (Im, 2020). However, the aforementioned biomaterials have no bidirectional interaction with bone tissues under physiological load or biochemical stimulation, which is a common disadvantage. In recent years, the requirement for new strategies for treating bone defects has increased, leaving new opportunities and challenges for the development of next-generation biomedical materials. Significantly, to keep with the progress of biology and biomaterial science, researchers are forging ahead to incorporate this new opportunity into specific groundbreaking biomaterials. Discoveries in molecular biology are now opening new frontiers for the design of biomaterials and brand paths to biomaterials that will work with normal physiology and integrate into the human body seamlessly (Gocha and Mcdonald, 2020; Kim et al., 2021). In addition to the innate functions of supporting, replacing, and restoring, new properties, such as biologically inducing activity, would be incorporated. In this context, third-generation bio-reactive materials that can transfer environmental factors to specific signals to induce cell responses at the molecular level have been proposed. These bio-reactive materials can trigger reactions with osteogenesis-related cell integrin proteins and induce proliferation, differentiation, and secretion of extracellular matrix (ECM) to promote tissue regeneration. Therefore, simulating body tissue composition and structure to realize functional simulation has become the mainstream direction of third-generation biomaterials (Gaharwar et al., 2020).

Nevertheless, third-generation materials still have the potential for further improvement. With the gradual clarification of the physiological mechanism of bone restoration and electrical response, bioelectric active materials have been increasingly studied and have shown fascinating effects and potential. Relevant studies have revealed the existence of both piezoelectricity and inverse piezoelectricity in the bone, which may be key factors in the bone healing process enhanced by low-intensity biophysical–electric stimulation. Meanwhile, with the recognition of wound electrical activity as a long-lasting and regulated response, it was demonstrated that natural, endogenous electric fields and electric current could arise spontaneously after the wound of tissues, which might be necessary for the healing of defects (Cheah et al., 2021; Wang et al., 2022). Regretfully, it is rarely found that the design, classification, and application of existing or potential bioelectric materials that can be utilized for the restoration of bone defects are systemically researched. Therefore, the functional mechanisms, synthetic pathways, and application of electrogenic materials in the field of bone regeneration are reviewed herein, aiming to provide a comprehensive perspective for the design, fabrication, and utilization of novel bioelectric active materials.

2 Electrical stimulation enhanced bone regeneration

The electroactivity of biological tissue is the basic attribute of life phenomena and plays an irreplaceable role in the process of metabolism (Chiranjeevi and Patil, 2020). There is also much evidence of endogenous electrical signals that play key roles in regulating the development and regeneration of many tissues (So et al., 2020; Casella et al., 2021). With the further clarification of bone tissue composition, it has been found that natural bone tissue is closely related to bioelectricity, that is, the bone has the same electroactivity as other living tissues. Half a century ago, the piezoelectric property of the bone was first reported (Fukada and Yasuda, 1964). Since the application of electrical stimulation in the treatment of tibial anterior foot ptosis in the 1960s (Liberson et al., 1961), after years of technical innovation, electrical stimulation technology has become a reliable method to treat patients with paralysis.

Electrical stimulation, such as pulsed electromagnetic field, pulsed alternating current, direct current, and electrostatic field, has been proven to be beneficial to the growth and repair of new bone in many animal experiments and clinical practices (Khatua et al., 2020; Sahm et al., 2020; Devet et al., 2021). Clinically, electrical stimulation osteogenesis can be roughly divided into implantation and non-implantation methods. In the first method, all or a part of the electrical stimulation device is implanted into a wound through surgery, which belongs to invasive electrical stimulation. After treatment, the electrode often needs to be removed, which usually leads to infection and secondary injury; in the second method, it is generally the external electrical stimulation of the fracture part and belongs to noninvasive electrical stimulation. It can neither stimulate the fracture site accurately nor guaranty the effectiveness of stimulation.

Subsequently, it has been proven that bioelectrical signals, endogenous electric field, and external electrical stimulation play an important role in regulating cell behavior in the field of bone repair, such as osteoblasts, chondrocytes, fibroblasts, and smooth muscle cells (Yu et al., 2021; Wei et al., 2022). Therefore, researchers are looking for electroactive materials that can simulate the microenvironment and transmit signals that stimulate osteoblast-related cell responses.

In recent years, numerous innovative biomaterials that can accelerate regenerating effects by transmitting physiological electrical cues and enhancing the electrical environment without external stimulation devices have been found. Thus, an opportunity for the local cure of diseases is provided by accurately regulating cell behavior. Optical, electrical, ultrasonic, and magnetic external energy have great potential to trigger electronic stimulations due to their noninvasive and accurate characteristics (Kang et al., 2018; Zhang et al., 2019; Trinh et al., 2020).

3 Current and potential electrogenic materials for enhanced bone regeneration

3.1 Piezoelectric materials

The phenomenon of "piezoelectricity," which means pressure—originating from the Greek word "piezein," was first discovered in 1880 (Mould, 2007). With the proposal of "Wolf's law," people began to realize that complexes composed of collagen fibrils with a dense arrangement of hydroxyapatite particles in bone tissue would reshape their structure in response to external stress. Moreover, the latest studies suggest that various biological tissues, such as keratin, tendons, cartilage, dentin, and cementum, possess remarkable piezoelectric properties, which may be attributed mainly to the components of collagen (Kim et al., 2020). Due to the piezoelectric property, collagen can generate electrical signals in response to loaded forces. For instance, dense bone contains a large amount of type I collagen, and its piezoelectric constant is approximately 0.7 pC/N (Puppi et al., 2010).

Piezoelectric materials, as their name implies, are characterized by the piezoelectric effect, which can convert mechanical pressure into an electrical signal (Zaszczynska et al., 2020). As a sensitive mechanical–electrical transduction platform, piezoelectric materials can utilize physiological deformation of bone tissue with movement to generate instant bioelectric stimulation and transfer it into biomimetic electrophysiological signals to obtain appropriate physiological functions (Kapat et al., 2020).

The *in vivo* working mechanism of piezoelectric materials determines their clinical value to a large degree. Electroactive piezoelectric scaffolds simulating the piezoelectric coefficient of natural tissue can generate electrical signals along with the loaded stress, and the generated charge and electric dipole stimulates bone remodeling and growth by opening the voltage-gated calcium channel (Figure 1). The calcium/calmodulin pathway of osteocytes thus activated to produce transforming growth factor β and act on osteoblasts, osteoclasts, and other cells promotes osteogenic differentiation, proliferation, and tissue restoration (Jacob et al., 2018).

Since piezoelectric type II collagen is abundant in cartilage, it affects cell membrane receptors with changes in electric charge and finally acts on the nucleus to promote cartilage regeneration (Figure 2) (Reddi and, 2000; Jacob et al., 2019; Zhang et al., 2020).

Piezoelectric materials are most concerned about the polarization ability of piezoelectric bodies under pressure. Therefore, it is necessary to introduce the most commonly used piezoelectric constant ("d_{ij}" constant) which reflects the linear response relationship between the piezoelectric physical quantity and electrical quantity. The first subscript "i" represents the direction of polarization (or applied electric field) and the second subscript "j" represents the direction of applied stress (or induced strain). It is the expression of the amount of charge generated by the material on the applied stress and the strain experienced by the material applying the unit electric field. Piezoelectric materials are a family of both organic (mostly polymers) and inorganic materials that can convert mechanical force into electricity and *vice versa* (Figure 3). Piezoelectric materials can be roughly divided into piezoelectric polymers and piezoelectric ceramics, as mentioned above, which can be used alone or together in tissue engineering. Concretely, it is also classified into four different categories: 1) naturally occurring piezocrystals, 2) piezoceramics (titanates, lead-based, and lead-free ceramics), 3) piezopolymers, and 4) piezocomposites (Kapat et al., 2020). Next, we will take piezoelectric polymer and piezoelectric ceramics as the main representatives to introduce piezoelectric biomaterials.

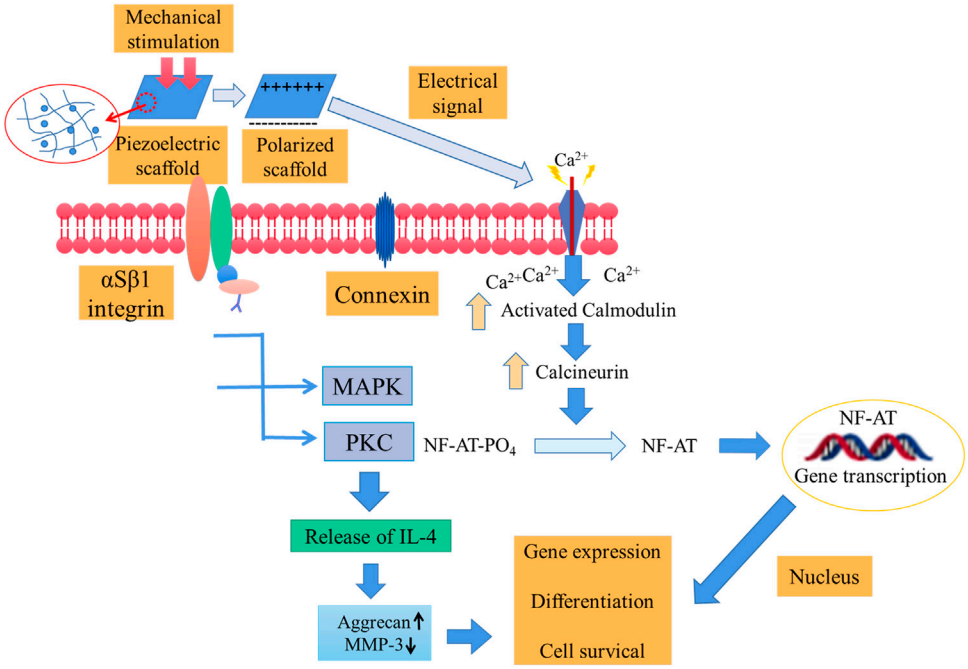

FIGURE 1
Schematic diagram of the activation of signal transduction pathways in response to electrical and mechanical stimulation. Mechanical stimulation is transformed into electrical signals to activate voltage-gated Ca^{2+} channels. The further increase in the intracellular Ca^{2+} concentration activates the calcium-modulated protein which then further activates calcineurin (calcium and calmodulin-dependent serine/threonine protein phosphatase). The activated calcineurin can dephosphorylate NF-AT and transfer it to the nucleus, where it acts as a transcription factor together with other related proteins. Additionally, mechanical stimulation can activate mechanical receptors in the membrane, thereby activating PKC and MAPK signaling cascades. These cascades lead to the synthesis of proteoglycans, and the inhibition of IL-1 and proteoglycans can be broken down (Jacob et al., 2018).

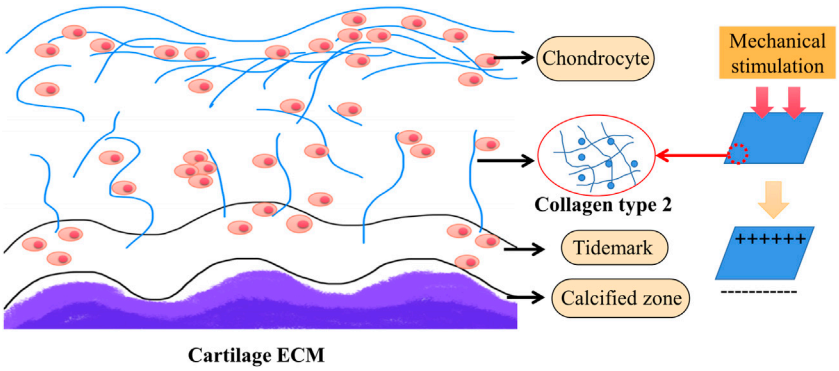

FIGURE 2
The mechanism of cartilage regeneration. Cartilage is rich in type II collagen. Piezoelectric collagen affects cell membrane receptors with changes in charge and ultimately acts on the nucleus to promote cartilage regeneration (Jacob et al., 2018; Jacob et al., 2019).

3.1.1 Piezoelectric polymer

Piezoelectric polymers include PVDF (polyvinylidene fluoride), PHBV (poly-3-hydroxybutyrate-3-hydroxyvalerate), polyamides, poly-l-lactic acid (PLLA), and biopolymers such as cellulose, collagen, chitin, and others. Piezoelectric polymers have the advantage of processing flexibility, which represents higher strength and impact resistance than inorganic materials (Jacob et al., 2018). To obtain the

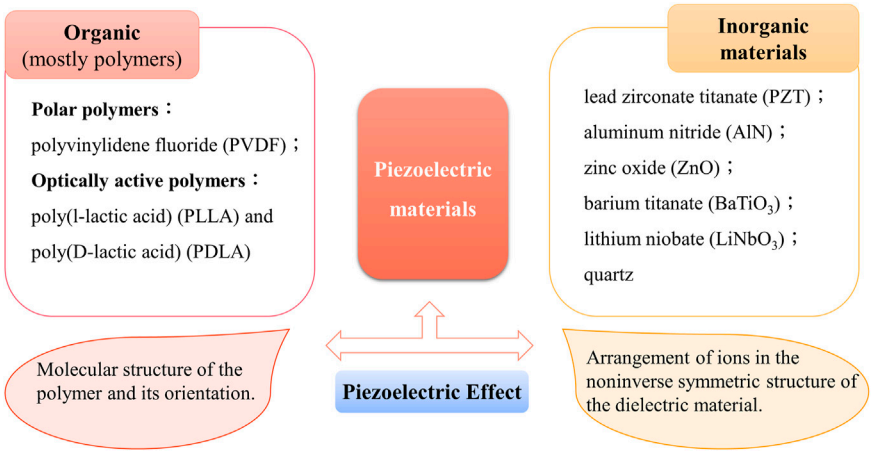

FIGURE 3
Representative materials of the piezoelectric material family and their causes of the piezoelectric effect. Piezoelectric materials are a family of organic and inorganic materials (Chorsi et al., 2019).

characteristics of piezoelectricity, piezoelectric polymers often require elaborately designed permanent molecular dipoles, the ability to align or orient molecular dipoles, maintain alignment once achieved, and experience large strains under mechanical stress (Fousek et al., 1999; Xu et al., 2018).

PVDF is one of the most famous piezoelectric copolymers with a piezoelectric coefficient of 20 pC/N and five crystal polymorphisms, namely, the nonpolar α- (most common), β-, γ-, δ-, and ε-phases (Li et al., 2019a). The β-PVDF phase shows excellent piezoelectric and ferroelectric properties. Because of its high flexibility and nontoxicity, PVDF has been used in various ways, from tissue engineering scaffolds to implantable automatic force devices and other biomedical applications (Hamzah et al., 2021). After corona polarization of PVDF scaffolds, the negatively charged surface that is formed promotes better adhesion and proliferation of myoblasts (Martins et al., 2013). When mechanically stimulated, the surface of piezoelectric PVDF generates an electric current, which enhances the proliferation and osteogenic differentiation of osteoblasts and adipose stem cells (Zhang et al., 2018). The *in vivo* evaluation results of the piezoelectric PVDF film confirmed its applicability as a candidate for bone-repairing substitutes (Wang et al., 2018).

Problems of improving hydrophilicity are an obstacle for PVDF in serving as a biological piezoelectric coating in bone defect repair. Thus, a polarized HA/PVDF coating is prepared to reduce the contact angle of the material by 66.9%. When the piezoelectric coefficient of the 20-pC/N HA/PVDF biological piezoelectric coating reaches 1.52 pC/N, the contact angle of the coating becomes 31.7° in the process of contact with the body fluid or tissue fluid, which is lower than the surface of the previous hydrophobic material and would greatly reduce the adsorption of cells and proteins on the surface that is conducive to tissue restoration at the later stage (Wu et al., 2020). In addition, when the charge is not high enough to cause a beneficial cellular response, it is necessary to improve the piezoelectric properties of the scaffold. Researchers manufactured core-shell composite submicron fibers of PVDF with the addition of graphene oxide and reported that the piezoelectric constant increased by 426% when compared with neat PVDF fibers (Diabor et al., 2019). It was found that when the content of graphene oxide was higher than 0.1 wt.%, the composition of PVDF in the (GO)/PVDF nanocomposite films would have a phase transition from the mixed state of the α- and β- to the high purity state of the β-phase. When the content of graphene oxide was higher than 2 wt.%, the Young's modulus and tensile strength of PVDF increased by 192 and 92%, respectively (El Achaby et al., 2012).

P(VDF-TrFE) are copolymers of vinylidene fluoride (VDF) and trifluoroethylene (TrFE), possessing ideal cell compatibility and conduciveness to trigger the integrin-mediated FAK signaling pathway, finally upregulating the osteogenic differentiation of MSCs (Shen et al., 2021; Zhu et al., 2022). The piezoelectric coefficient of the copolymers reached the highest value of 30 pC/N (Fukada, 1998). PVDF and PVDF TrFE have been mixed with starch or cellulose, similar to natural polymers, to produce porous structures conducive to tissue growth to develop scaffold structures suitable for tissue restoration and regeneration, especially for bone tissue engineering (Pereira et al., 2014). Polyamides have limited application in tissue engineering due to difficult degradation, which needs to be further modified. Modified polyamide–hydroxyapatite composite can promote osteogenesis after 12 weeks of implantation (Wang et al., 2007).

Natural biopolymer polymers are becoming increasingly important in tissue engineering because of their degradability and low toxicity, which are conducive to biological signal

transduction, cell adhesion, and cell response. However, their physical properties are not sufficient, and their biological properties may be lost in the process of mixing with other materials. In addition, appropriate screening and treatment are needed to avoid disease transmission and immune rejection. Appropriate chemical or physical treatment helps overcome the above problems. Cellulose is the most abundant natural polymer on Earth, with excellent biocompatibility, high tensile strength, and shear properties (Diabor et al., 2019; Dou et al., 2021). The shear piezoelectric coefficient (d_{14}), which is a representative indicator of high tensile strength, is 0.2 pC/N (Kim et al., 2006). Although small pore size or dense reticular fibers limit cell infiltration, it can be improved by adding an appropriate pore-forming agent. In addition, studies have shown that cellulose has the ability to promote cell adhesion, especially chondrocytes, osteocytes, endothelial cells, and smooth muscle cells (Zaborowska Bodin et al., 2010). Therefore, it is a piezoelectric material suitable for bone and cartilage tissue engineering. Collagen is a biological protein and an important part of the bone, cartilage, tendons, teeth, and blood vessels. It has the desired biocompatibility, cell binding performance, hydrophilicity, low antigenicity, and *in vivo* absorption capability and has been used in the field of bone and cartilage regeneration. However, the limitations of collagen, such as low mechanical stiffness, rapid degradation, and toxicity of adding a crosslinking agent, should be overcome before it can be widely applied in the clinic (Jacob et al., 2018).

3.1.2 Piezoelectric ceramics

Piezoelectric ceramics are polycrystalline (Narayan et al., 2018) and have a high piezoelectric coefficient, for example, barium titanate, zinc oxide, potassium sodium niobate (KNN), lithium sodium potassium niobate (LKNN), and boron nitride. Generally, inorganic piezoelectric materials are biocompatible or can be biocompatible after being encapsulated, while lead-based ceramics have limited applications in tissue engineering due to their cytotoxicity. Lead-free piezoelectric ceramics may be another option. Other ceramics also have dose-dependent toxicity, which are suitable for tissue engineering to a certain extent. Lead-free piezoelectric ceramics can be divided into five systems, such as the barium titanate, niobate base, bismuth layer, sodium bismuth titanate, and tungsten bronze systems. Among them, the barium titanate system and the niobate system are the most widely studied. The former is well known in relevant theories and applications, and the latter niobate ceramics have been developed since 2004, when the modification of lithium, tantalum, and antimony in the KNN ceramic texture structure experienced breakthroughs and attracted much attention (Saito et al., 2004). Barium titanate (BTO) is a piezoelectric ceramic with high biocompatibility that was independently discovered by American scientists and former Soviet scientists in 1946, the d_{33} coefficient of which reached 191 pC/N (Mindlin, 1972). The piezoelectric property of BTO was first discovered as a sort of strong dielectric compound material with a high dielectric constant and low dielectric loss. Due to its early discovery, stable chemical properties and good piezoelectric properties, BTO occupied the leading position in early piezoelectric materials and became a research hotspot. Yamashita et al. (1996) soaked polarized barium titanate and HA composite (HABT) ceramics in simulated body fluid (SBF) for different times. The results show that a large number of bone-like apatite crystals were formed on the negatively charged surface, while only NaCl was deposited on the surface of the opposite electrode. Hwang et al. (2002) further studied the osteoapatite-inducing ability of barium titanate ceramics with different polarization degrees. Similar results were obtained when polarized barium titanate was placed in simulated body fluid (SBF). It was found that the higher the degree of polarization was, the greater the calcium phosphorus ratio would be, which could be attributed to the electrostatic adsorption effect (Masataka et al., 2001).

As an electroactive biomaterial, barium titanate ceramics have poor temperature stability and are liable to deteriorate, preventing the cytotoxicity of titanium and barium ions from being ignored under long-term physiological conditions. These shortcomings limit its further application in the biological field.

Lead-free niobate piezoelectric materials, as previous studies have indicated, enhance the proliferation and osteogenic activity of osteoblasts for rapid bone regeneration. To ensure adequate mechanical strength and piezoelectric properties of the piezoelectric ceramics, Li is added. The relatively considerable biocompatibility of ferroelectric lithium niobate (LN) has been demonstrated by culturing and fluorescence imaging MC3T3 osteoblast cells for up to 11 days. While rapid bone regeneration was discovered, mineralization was observed for all LN surfaces at 20 days, whereas no mineral was observed on electrostatically neutral control glass surfaces until day 30. Qualitatively, for 30 and 40 days, there appears to be more mineralization on charged than on uncharged surfaces (Carville et al., 2015). KNN and LKNN are also lead-free Li-doped piezoelectric ceramics with piezoelectric coefficients of 63 pC/N and 98 pC/N, respectively. When exposed to the bioenvironment, the cytotoxicity of Li would slightly increase during the release process when compared with that of KNN (Yu et al., 2012). After all, the addition of Li could be a mixed blessing, under the condition of slight loss of biocompatibility, Li improves the strength and piezoelectric properties of the material, which is worthy of medical implantation and long-term electrophysiological osteogenesis.

3.2 Optoelectronic materials

As a highly orthogonal external stimulus, light has the unique ability to accurately manipulate the cellular signal system, which has been widely used in materials science, chemistry, biology, and drug delivery systems. In particular, light can be used as a

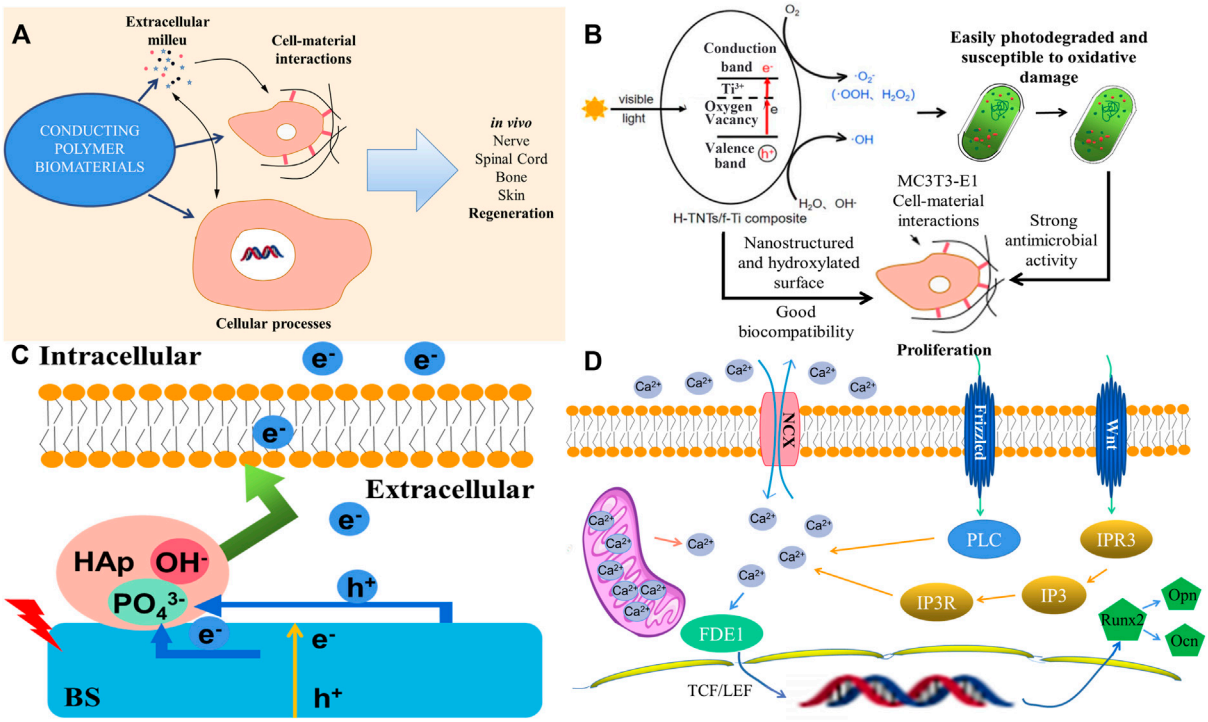

FIGURE 4
The mechanism and effect of photoelectric-responsive materials. **(A)** Conducting polymers and their effects on the tissue environment, cell outcomes, and *in vivo* regeneration. **(B)** Diagram of the interaction between photoelectrons and cells. **(C)** Diagram of the Ti-BS/HAp osteogenic differentiation mechanism under 808 nm irradiation. **(D)** Schematic representations of antibacterial activity for the H-TNTs/f-Ti composite under visible light irradiation (Fu et al., 2019; Petty et al., 2020; Zhao et al., 2021).

noninvasive external energy source to monitor and trigger the spatiotemporal dynamics of cell signals. To regulate the cell signal transduction process, attempts have been made to covalently connect photostability chemical groups to signal molecules necessary for cell function (Zhu et al., 2018; Tang and Wang, 2021; Wakiyama et al., 2021). In search of suitable and stable donors, optoelectronic materials have come into sight during this exploring process.

Nevertheless, not all light can penetrate through deep tissue or be harmless to healthy histocytes. Only a few types of electromagnetic waves with specific wavelengths have harmless tissue penetration properties; among them, near infrared (NIR, wavelength from 780 to 2,526 nm) light irradiation has been demonstrated to cause negligible damage to cells when compared to other short wavelength lasers that can produce phototoxic side effects. Moreover, NIR light is absorbed mainly by nanoparticles that react to NIR light and barely by water or surrounding tissues. In addition, this whole process is difficult to interfere with by solvents or the surrounding environment (Zhang et al., 2016; Li et al., 2019b).

Optoelectronic materials are highly sensitive to NIR light, which can widely absorb and convert laser energy into electrical stimulation to activate the downstream signaling pathway. Photosensitive optoelectronic materials with good biocompatibility, such as polymers, bismuth sulfide (BS), manganese dioxide nanoparticles, and other materials with photothermal conversion efficiency, could achieve remote, precise, and noninvasive NIR irradiation and control cell differentiation behavior *in vitro* as well as tune the photoelectric microenvironment *in vivo* (Fu et al., 2019; Wang et al., 2020). Conducting polymers (CPs) have unique electroactive and photoelectric properties, such as bulk mixed electronic/ionic conduction, making it possible to manufacture multifunctional biomaterials those passively affect cell response, regulate the electric field, charge injection or drug delivery, and actively affect the process of tissue regeneration (Figure 4A) (Petty et al., 2020). A photoelectric-responsive material–hydrogenated TiO_2 nanotube/Ti foil (H-TNT/f-Ti) composite with a higher visible photoelectric response and more hydroxyl functional groups has also been fabricated, which inhibits proliferation of *Streptococcus mutans* and *Porphyromonas gingivalis* which are the main cause of implant failures. Moreover, the proliferation of MC3T3-E1 cells on the hydroxylated surface was promoted, and improved biocompatibility with osteogenic cells was observed. As shown in Figure 4B, the photocurrent produced by the photoelectric

response guarantees antibacterial activity and better biocompatibility with MC3T3-E1 cells for proliferation, thus providing a simple and effective method to significantly improve dental implant efficacy (Zhao et al., 2021).

A study used bismuth sulfide/hydroxyapatite (BS/HAP) film to create a rapid and repeatable photoelectric response microenvironment around the implant. Under NIR light irradiation, the corresponding increase in photocurrent on BS/HAP films was mainly attributed to the depletion of holes through PO_4^{3-} from HAp and interfacial charge transfer by HAp compared with BS. Electrons activated the Na^+ channels of mesenchymal stem cells (MSCs) and changed cell adhesion in the intermediate environment. RNA sequencing showed that when photoelectrons were transferred to the cell membrane, sodium flux and membrane potential depolarized and changed the cell shape. At the same time, calcium flux and FDE1 expression were upregulated. Moreover, TCF/LEF in the nucleus began to be transcribed and regulated the downstream genes involved in osteogenic differentiation through the Wnt/Ca^{2+} signaling pathway. In this study, NIR light–activated photoelectrons with BS/HAP film were transferred to the intracellular space controlled cell fate, directed osteogenic differentiation *in vitro*, and promoted bone regeneration *in vivo* (Figure 4C). The specific reaction mechanism is shown in Figure 4D. The Wnt/Ca^{2+} signaling pathway, a known membrane sensor and osteogenic marker, was upregulated in Ti-BS/HAp after light irradiation. Calcium then entered the cell nucleus to influence TCF/LEF through FDE1. Downstream genes related to osteogenic differentiation were activated. The Wnt/Ca^{2+} signaling pathway affects the intracellular Ca^{2+} concentration to modify osteogenic differentiation (Fu et al., 2019). However, although light is a relatively harmless energy source, it is mostly used for the regeneration and reconstruction of superficial tissues. Considering the limitation of penetration, frequent *in vitro* irradiation, and the complexity of biological tissue defects, the development of optoelectronic materials in the field of bone regeneration is limited to a certain extent.

3.3 Magnetoelectric materials

To overcome the penetrating limitation of optoelectronic materials, researchers switched their attention to magnetic fields, which have been put into clinical application and exhibit ideal penetration ability as well as minimal cytotoxicity on living tissues (Roessler et al., 2005).

The relationship between magnetism and polarization is the classical research content of physics. It is well known that the key physical property of magnetoelectric materials, or multiferroic materials, is the coupling between magnetism and polarization, that is, magnetoelectricity (Dong et al., 2019a). In solids, magnetism and electricity are derived from spin and charge degrees of freedom, respectively. In recent years, the intersection between these two fascinating topics has developed and become a new branch of condensed matter physics called magnetoelectricity (Fiebig et al., 2016; Dong et al., 2019b). The first phenomenon of the magnetoelectric effect was observed in the dielectric material, which was magnetized when passing through an electric field. Chun et al. (2010) reported that there was a large magnetoelectric (ME) effect in aluminum-substituted y-hexagonal $Ba_{0.5}Sr_{1.5}Zn_2(Fe_{1-x}Al_x)_{12}O_{22}$. The amazing enhancement of ME effect by Al substitution could be preliminarily attributed to the reduction of magnetocrystalline anisotropy, which magnetizes along the plane perpendicular to the hexagonal axis. For the unique magnetoelectric effect, magnetoelectric materials can realize mutual transformation of the magnetic field and electric field and control electric polarization through a magnetic field or magnetic polarization through an electric field, which is widely used in magnetoelectric sensors, microwave devices, and magnetic recording.

Recently, an MNC-(AuNP RGD) heterodimer nanoswitch was developed, which was composed of AuNPs flexibly coupled to an RGD coating by a magnetic nanocage (Kang et al., 2018). This study provides initial evidence of physical and reversible ligand thawing for controlling stem cell adhesion through magnetic nanoswitches. Magnetic nanoswitches can also help regulate various cell functions *in vivo*. Moreover, such a physical, noninvasive, noncontact, and reversible nanoswitch can potentially improve the performance of material implants and promote the regenerative treatment of stem cells, such as osteogenic differentiation.

Magnetic nanoparticle techniques offer a number of important advantages over conventional, mechanically preconditioned, induced tissue engineering scaffolds, such as compression or fluid flow–based perfusion, by the precise control and duration of the levels of forces that can be applied to cells within a three-dimensional construct (Holtorf et al., 2005; Jafari et al., 2019). A new magnetic particle technology that allows highly local mechanical forces to be directly applied to a specific region of the ion channel structure was also reported. The results showed that manipulating the particles in the extracellular ring region extended for TREK-1 lead to a change in the whole cell current, which is consistent with the change in TREK-1 activity. follow-upKnowing the potential role of magnetic particle, follow-up studies should be carried out focusing on the usage as a tool to treat ion channel dysfunction caused by human diseases (Hughes et al., 2008). Furthermore, a study investigated remote magnetic field activation of magnetic nanoparticle–tagged mechanosensitive TREK-1 receptors on the cell membrane of human bone marrow stromal cells for use in osteoprogenitor cell delivery systems and the activation of *in vitro* and *in vivo* differentiation toward an osteochondral lineage, from which these cell manipulation strategies offer

tremendous therapeutic opportunities in soft and hard tissue regeneration (Kanczler et al., 2010).

The aforementioned studies and reports do not clearly answer how the new generation of biomagnetoelectric materials control polarization through the magnetic field, from which the direct evidence of this association needs further exploration. However, the magnetic field, as a kind of mechanical stimulation, leads to the potential regulation of cells and triggers subsequent changes in whole-cell currents to promote osteogenic differentiation. In the future, the use of a magnetic field as the direct source of bioelectric stimulation acting on osteoblast-related cells is the direction we strive to explore.

3.4 Acoustoelectric materials

After considering physical, noninvasive, and noncontact external energy that can be converted into electrical energy, such as light energy and magnetic fields, researchers turn their attention to the strategy of sound-generated electricity. Compared with the external energy sources mentioned before, the tissue penetration ability and stability of ultrasonic waves are more desirable. Furthermore, as a kind of green energy, ultrasonic waves have less possible tissue toxicity and more availability because of economic effects.

Two-dimensional materials, such as graphene and molybdenum disulfide, are suitable for surface acoustic wave (SAW) device integration (Mas-Ballesté et al., 2011). The electric field associated with the propagation of the back wave on the piezoelectric substrate can be used to transmit carriers over a macro distance at the speed of sound in these materials, which results in an acoustoelectric (AE) current, a phenomenon in which electromotive force is produced by the action of sound waves propagating in semiconductors. This effect has been studied in other nanostructures which are applied to metrology and quantum information (Morocha and Rozhkov, 2018; Poole and Nash, 2018).

To our knowledge, there is no specific literature to support that acoustoelectric materials have entered the field of tissue engineering at present. However, a few studies have proven the relationship between acoustoelectric and piezoelectric mechanisms. Herein, these basic theories and concepts of piezoelectric materials need to be further reviewed to understand the relationships between them. Under the applied mechanical pressure, the electrical characteristics of piezoelectric materials change with the deformation of crystal structure and shape. This phenomenon is called the positive piezoelectric effect. By contrast, when a voltage is applied to the crystal, its structure and shape will also change with it. This phenomenon is called the reverse piezoelectric effect. A number of acoustic and electroacoustic devices, such as crystal pickups, crystal oscillators, and loudspeakers, can be fabricated by utilizing the piezoelectric effect. Previous studies have indicated that when the longitudinal wave propagates in the semiconductor, additional periodic potential field waves are generated, and the period of the wave is the same as that of the sound wave. In atomic semiconductors, sound waves will produce a distorted periodic potential field, and the amplitude is small at this time. In a piezoelectric semiconductor, a sound wave will produce a piezoelectric periodic potential field, while the wave amplitude is very large. If an electron passes through at this moment, when the mean free path of the electron is smaller than the wavelength of the sound wave, the electron will continue to suffer from the scattering of phonons and lose energy such that the electron is captured by the trough of the periodic potential field generated by the sound wave. Meanwhile, when the sound wave propagates, the electron is pulled forward by the sound wave potential field and results in an electromotive force, which is the effect of "sound waves producing electrical effect" or acoustoelectric effect. This is the basic principle of applying the sound electricity effect to sound power generation (Morocha and Rozhkov, 2018; Ghosh, 2019; Mansoorzare and Abdolvand, 2019). Researchers use boron nitride (BNNT) as a nanocarrier to carry charged/mechanical stimulation on demand in the cell system. After the internalization of BNNTs, electrical stimulation is transmitted to tissues or cells through a wireless mechanical source (i.e., ultrasound). That is, the electric stimulation of cells is generated by internalized BNNT nanoparticles after external ultrasonic irradiation, which utilizes ultrasound as the mechanical stress on piezoelectric BNNTs to produce electrical stimulation to enhance cell differentiation (Figure 5) (Ciofani et al., 2008).

Because of the maturity of the theory of piezoelectric effect osteogenesis, the application of the acoustoelectric effect can creatively apply sound waves to generate bioelectricity to promote osteogenesis, in which the piezoelectric effect plays a bridge and intermediary role from "acoustic wave generates electricity" to "bone regeneration." In brief, it is believed that acoustoelectric materials can be expected in the future.

3.5 Thermoelectric materials

Since the discovery of the Seebeck effect and Peltier effect in the early 19th century, the theoretical basis for the application of thermoelectric energy converters and thermoelectric refrigeration has been gradually enriched (Yamamoto et al., 2021). In the past few decades, thermoelectric materials (TEs) have attracted considerable attention in the consumer market due to their outstanding reliable, lightweight, and noiseless features (Lei et al., 2021; Zhou et al., 2021).

As the name suggests, TE can realize the mutual transformation between heat and electric energy. It is reasonable to consider whether heat energy could be converted, especially biological body temperature and external room temperature difference, into electric energy and further use

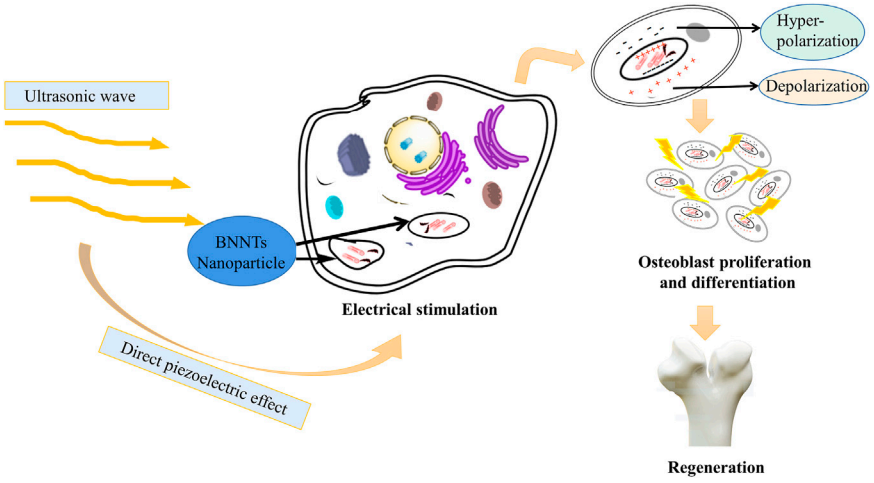

FIGURE 5
BNNT nanoparticles can internalize external ultrasonic irradiation into electrical stimulation. Under the direct piezoelectric effect, ultrasound, as a mechanical stress, is transformed into electrical stimulation and then promotes proliferation and differentiation of osteoblasts (Jacob et al., 2018).

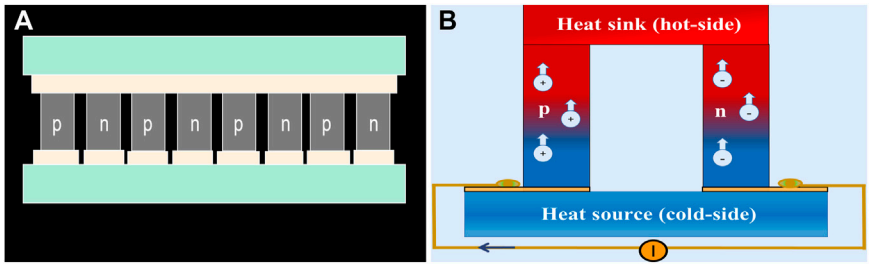

FIGURE 6
The construction and schematic diagram of TE materials. **(A)** TE materials consist of several thermocouples composed of p-type and n-type thermoelectric legs, which are electrically in series and thermally in parallel. **(B)** Once electric current is applied, charge carriers, electrons in n-type, and holes in p-type would transfer heat in the module from one side to the other (Kishore et al., 2019).

energy that has been ignored in the field of tissue engineering. In terms of the implementation path, there is an obvious temperature gradient from the body nucleus to the body surface, which is the basis for the conversion of heat energy into electrical energy, and the generated microcurrent, which is a continuous and stable output under physiological adaptation, which further activates the proliferation and differentiation of osteoblasts through the above electroresponsive stimulation osteogenesis mechanism due to external stimuli-responsive bone therapy. It is an established fact that the classical theory of electrical stimulation osteogenesis has been demonstrated to accelerate bone regeneration and maintain BMSC stemness both in animal experiments and clinical practice by upregulating bone morphogenetic proteins under electrical stimulation, thus ultimately stimulating the calcium–calmodulin pathway, transforming growth factor-β (TGF-β), and other cytokines (Wei et al., 2022). In terms of the implementation scheme, the appropriate TE carrier should be the medium to accelerate osteogenesis. This requires the material itself to make full use of the temperature gradient of the human body or the temperature difference between the human body and its environment, to have a reasonable conversion efficiency that reaches the current threshold required for osteogenesis, to form a good closed circuit and overcome the extremely high thermal resistance of the environment between the human body and ambient air. To realize these requirements, researchers need to further understand and explore appropriate thermoelectric carriers (Kishore et al., 2019). Hence, the evaluation criteria and classification of thermoelectric materials will be briefly introduced in this review.

The thermoelectric performance of a material can be defined as the thermoelectric figure of merit ZT ($ZT = S^2\sigma T/\kappa$) to

evaluate, where "S" is the thermoelectric power or Seebeck coefficient, "T" is the absolute temperature, "σ" is conductivity, and "κ" is the thermal conductivity. To have a high thermoelectric merit ZT, the material must have a high Seebeck coefficient (S), electron conductivity, and low thermal conductivity (Xiao et al., 2014).

Electrothermal materials can be divided into three categories according to their operating temperature. First, bismuth telluride and its alloy are widely used in thermoelectric coolers with optimal operating temperatures less than 450°C. The second is lead telluride and its alloy, which are widely used in thermoelectric generators with an optimal operating temperature of approximately 1,000°C. The third is silicon germanium alloy, which is also widely used in thermoelectric generators with an optimal operating temperature of approximately 1,300°C (Chen et al., 2018; Feng et al., 2018).

Due to the biocompatibility issue of lead-containing materials, restriction of the optimal operating temperature, cost performance of mass production, toxic organic solvents in the production process, and the absence of obvious temperature differences in the human body under constant temperature conditions, the clinical application of thermoelectric materials is limited to effectively converting heat energy into electric energy. However, some thermoelectric materials can generate microcurrents in a temperature environment. For example, highly robust and flexible thermoelectric (TE) films based on n-type Ag_2Te nanoshuttle/polyvinylidene fluoride by solution treatment without surfactant are prepared, which achieves a favorable power performance of more than 30 μW $(mK^2)^{-1}$ at room temperature. In addition, the synthetic fabric also shows application potential in flexible electronic devices, as the performance change after 1,000 bending cycles can be ignored (Zhou et al., 2018). Unfortunately, TE is still infrequent in the field of bone defect regeneration, partly because the requirements for materials and conditions are rigorous, and both p- and n-type TE materials with equivalent performance are required to construct high-performance TE devices to form a closed loop, indicating that a p-type flexible TE counterpart is highly desirable (Figure 6A) (Snyder and Toberer, 2012).

At present, thermoelectric materials have already entered the field of medicine and health care. Embedding a thermoelectric generator (TEG) in a biological body is a promising way to supply electronic power in the long term for an implantable medical device (IMD). Through theoretical analysis, it has been found that the highest temperature gradient occurs near the skin surface of the human body, which suggests a candidate site for implanting and positioning the TEG. As the calculation shows, cooling the skin surface to 277 K can make the highest temperature difference reach up to 1.4 K. While heating the skin surface to 313 K, the maximum temperature difference is no more than 0.119 K (Yang et al., 2007).

In addition, using the temperature difference between the natural environment and the body surface is also a reasonable way to increase the temperature difference. The basic strategy of wearable TEGs is that after the current is applied, the carriers move while the charge carriers, holes in p-type, and electrons in n-type legs transfer heat from one side of the module to the other (Figure 6B). However, the skin temperature of the human body is different in different parts of the body and increases with increasing ambient temperature. During generations of natural evolution, human skin becomes a poor conductor of heat, as does ambient air, making TEGs operate in an extremely high thermally resistive environment; moreover, the shallow location may limit their scope of application (Kishore et al., 2019).

The future tendency is to synergistically optimize and integrate all the effective factors to further improve the TE performance such that highly efficient TE materials and devices can be more beneficial to daily lives (Yang et al., 2018).

4 Future prospective of electrogenesis bio-reactive materials

Piezoelectric and optoelectronic materials are the two earliest researched kinds of materials used in tissue engineering. Piezoelectric materials are widely used in the repair of load-bearing tissues. Although photoelectric materials are limited by phototoxicity, weak penetration ability, frequent irradiation by operators, and inappropriateness for deep wound repair, optoelectronic materials are more likely to be used for accurate stimulation of superficial tissues that are easily penetrated by near-infrared light. At present, except for piezoelectric and optoelectronic materials, a large number of experiments *in vivo* and *in vitro* have not proven to effectively promote bone tissue regeneration, which only stays in the theoretical stage, leaving a gap that we need to make an effort to fill in the future.

Piezoelectric materials are more mature in the field of electromechanical sensors than in tissue engineering. Nevertheless, it can be deduced that electroactive scaffolds can generate an electric field according to small mechanical vibrations and regulate the effective electric field characteristics of natural ECM observed during tissue development, regeneration, or repair. Photoelectric materials are only partially used for superficial tissue repair at present. Acoustoelectric and magnetoelectric materials, two materials with better penetration ability than photoelectric materials, also lack much clinical scientific research support. The thermoelectric material itself does not need an external invasive power supply and does not need frequent operation (such as irradiation) by the operator. Its mechanism is to use the temperature difference between the inherent body temperature and the external environment to further stimulate bone tissue repair. However, considering that the organism is a constant temperature condition, it is only suitable for the repair of defects under the condition of a possible temperature difference between the superficial and the body.

TABLE 1 Representative bio-reactive electrogenic materials and their electric constants.

Type	Representative material	Electric constant	Reference
Piezoelectric materials	PVDF	d_{ij} constant, 20 pC/N	Li et al. (2019a)
	HA/PVDF	d_{ij} constant, 1.5 pC/N	Wu et al. (2020)
	P(VDF-TrFE)	d_{ij} constant, 30 pC/N	Fukada (1998)
	Barium titanate	d_{ij} constant, 191 pC/N	Mindlin (1972)
	Potassium sodium niobate or lithium-doped potassium sodium niobate	d_{ij} constant 63 pC/N or 98 pC/N	Yu et al. (2012)
Optoelectronic materials	Bismuth sulfide/hydroxyapatite film	Photocurrent density, 25 μA cm^{-2} (under NIR light, 0.29 W cm^{-2})	Fu et al. (2019)
	Hydrogenated TiO_2 nanotube/Ti foil	Photocurrent density, 4 μA cm^{-2} (under visible light, 100 mW cm^{-2})	Zhao et al. (2021)
Magnetoelectric materials	MNC–(AuNP RGD) heterodimer nanoswitch	Unstated	Kang et al. (2018)
Acoustoelectric materials	Graphene nanoribbons	Exhibiting linear dependence on surface acoustic wave intensity and frequency	Poole and Nash (2018)
Thermoelectric materials	Ag_2Te nanoshuttle/polyvinylidene fluoride	Thermoelectric efficiency, 30 μW $(mK^2)^{-1}$	Zhou et al. (2018)

Indisputably, in addition to the necessary biocompatibility, the application of a new material should also consider biodegradability, physical and chemical stability, and properties that can simulate the microenvironment *in vivo* and be used as a platform for carrying "seed" cells and growth factors.

The osteogenesis potential of bio-reactive electrogenic materials encouraged the personalized and comprehensive synergetic application to make the utmost of their advantages and avoid their disadvantages. For instance, the combination of acoustoelectric and piezoelectric materials can comprehensively improve the bone repair efficiency than using one of them alone. Meanwhile, developing the process of preparing nanosized materials according to their characteristics and nanobioelectric active materials themselves will be more conducive to simulating the physiological microenvironment and promoting repair. Apart from the treatment of bone defects, electrostimulation can further modulate a myriad of biological processes, from cell cycle, migration, proliferation, and differentiation to neural conduction, muscle contraction, embryogenesis, and tissue regeneration. Recent advances in electroactive biomaterials are systematically overviewed for modulation of stem cell fate and tissue regeneration, which mainly include nerve regeneration, bone tissue engineering, and cardiac tissue engineering (Snyder and Toberer, 2012). When confronting the problems of premature degradation and insufficient performance of drugs and biomaterials, it is essential to build a suitable material carrier system for packaging and modification. Commercial products, such as alginates, gelatin, and chitosan, are widely used in biomedical applications such as drug delivery, cell encapsulation, anti-adhesion materials, and tissue engineering scaffolds because of their biocompatibility, providing a novel strategy to develop a suitable carrier to promote bone restoration.

As a representative of new advanced bone repair materials, bio-reactive electrogenic materials have the properties of being noninvasive, independent of external power supply, ergonomic, and as the product of the progress of materials science and physiology, showing favorable effects and bright prospects in tissue reparation and reconstitution (Table 1).

However, limited by the degradation rate, Young's modulus, stiffness, efficiency, cytotoxicity to the body, the lack of appropriate carrier, the lack of economic effect, and the aftereffect observation of the materials, there are still inherent defects in the program of material processing and the materials themselves. Energy conversion materials such as thermoelectric and optoelectric materials are important to green energy systems, but at present, their energy conversion efficiency is relatively low. Ground-breaking design and fabrication technology for novel bioelectric active osteogenic materials will play an important role in the diagnosis and treatment of bone tissue defects.

5 Summary

In terms of interaction activity, the above bio-reactive electrogenic materials are utilized as carriers to convert physical stimuli such as mechanical pressure, sound waves, light waves, magnetic fields, and temperature differences into microcurrents and act on osteoblast-related cells through the established classical theory of electrical stimulation osteogenesis by upregulating bone morphogenetic proteins under electrical stimulation, thus ultimately stimulating the calcium–calmodulin pathway, TGF-β, and other cytokines. Although the corresponding biological evidence needs to be accumulated over time, the valuable role of bio-reactive electrogenic materials would be self-evident. Overall, an appropriate

material carrier is vital for the output current for osteogenesis under physiological conditions, which requires a large number of experimental explorations and subsequent staged clinical trials in the future.

Author contributions

SD, YZ, and YM wrote the original draft; YZ, YH, and BL reviewed and edited the manuscript; SD, WD, RZ, and LN supervised the study and acquired funding for the same. All the authors listed have made a direct, substantial, and intellectual contribution to the work and approved it for publication.

Funding

This work is supported by the National Natural Science Foundation of China (81970981, 82102221), Project to Enhance the Base of Innovation Ability of Xi'an City—Medical Research (21YXYJ0123), and Fundamental Research Funds of Xi'an Jiaotong University for Free Exploration and Innovation—Project for Teacher (XZY012021069).

Conflict of interest

The authors declare that the research was conducted in the absence of any commercial or financial relationships that could be construed as a potential conflict of interest.

Publisher's note

All claims expressed in this article are solely those of the authors and do not necessarily represent those of their affiliated organizations, or those of the publisher, the editors, and the reviewers. Any product that may be evaluated in this article, or claim that may be made by its manufacturer, is not guaranteed or endorsed by the publisher.

References

Carville, N. C., Collins, L., Manzo, M., Gallo, K., Lukasz, B. I., Mckayed, K. K., et al. (2015). Biocompatibility of ferroelectric lithium niobate and the influence of polarization charge on osteoblast proliferation and function. *J. Biomed. Mat. Res. A* 103 (8), 2540–2548. doi:10.1002/jbm.a.35390

Casella, A., Panitch, A., and Leach, J. K. (2021). Endogenous electric signaling as a blueprint for conductive materials in tissue engineering. *Bioelectricity* 3 (1), 27–41. doi:10.1089/bioe.2020.0027

Cheah, Y. J., Buyong, M. R., and Yunus, M. H. M. (2021). Wound healing with electrical stimulation technologies: A review. *Polymers* 13 (21), 3790. doi:10.3390/polym13213790

Chen, X. Q., Dai, W., Wu, T., Luo, W., Yang, J. P., Jiang, W., et al. (2018). Thin film thermoelectric materials: Classification, characterization, and potential for wearable applications. *Coatings* 8 (7), 244. doi:10.3390/coatings8070244

Chiranjeevi, P., and Patil, S. A. (2020). Strategies for improving the electroactivity and specific metabolic functionality of microorganisms for various microbial electrochemical technologies. *Biotechnol. Adv.* 39, 107468. doi:10.1016/j.biotechadv.2019.107468

Chorsi, M. T., Curry, E. J., Chorsi, H. T., Das, R., Baroody, J., Purohit, P. K., et al. (2019). Piezoelectric biomaterials for sensors and actuators. *Adv. Mat.* 31 (1), 1802084. doi:10.1002/adma.201802084

Chun, S. H., Yi, S. C., Oh, Y. S., Jaiswal-Nagar, D., Haam, S. Y., Kim, I., et al. (2010). Realization of giant magnetoelectricity in helimagnets. *Phys. Rev. Lett.* 104 (3), 037204. doi:10.1103/physrevlett.104.037204

Ciofani, G., Raffa, V., Menciassi, A., and Dario, P. (2008). Preparation of boron nitride nanotubes aqueous dispersions for biological applications. *J. nanosci. nanotechnol.* 8 (12), 6223–6231. doi:10.1166/jnn.2008.18375

Devet, T., Jhirad, A., Pravato, L., and Wohl, G. R. (2021). Bone bioelectricity and bone-cell response to electrical stimulation: A review. *Crit. Rev. Biomed. Eng.* 49 (1), 1–19. doi:10.1615/critrevbiomedeng.2021035327

Diabor, E., Funkenbusch, P., and Kaufmann, E. E. (2019). Characterization of cassava fiber of different genotypes as a potential reinforcement biomaterial for possible tissue engineering composite scaffold application. *Fibers Polym.* 20 (2), 217–228. doi:10.1007/s12221-019-8702-9

Dong, S., Xiang, H., and Dagotto, E. (2019). Magnetoelectricity in multiferroics: a theoretical perspective. *Natl. Sci. Rev.* 6 (4), 629–641. doi:10.1093/nsr/nwz023

Dong, S., Xiang, H., and Elbio, D. (2019). Magnetoelectricity in multiferroics: a theoretical perspective. *Natl. Sci. Rev.* 6 (4), 629–641. doi:10.1093/nsr/nwz023

Dou, C. Y., Li, Z., Gong, J. X., Li, Q. J., Qiao, C. S., Zhang, J. F., et al. (2021). Bio-based poly (gamma-glutamic acid) hydrogels reinforced with bacterial cellulose nanofibers exhibiting superior mechanical properties and cytocompatibility. *Int. J. Biol. Macromol.* 170, 354–365. doi:10.1016/j.ijbiomac.2020.12.148

El Achaby, M., Arrakhiz, F. Z., Vaudreuil, S., Essassi, E. M., and Qaiss, A. (2012). Piezoelectric β-polymorph formation and properties enhancement in graphene oxide – PVDF nanocomposite films. *Appl. Surf. Sci.* 258 (19), 7668–7677. doi:10.1016/j.apsusc.2012.04.118

Feng, J. J., Zhu, W., and Deng, Y. (2018). An overview of thermoelectric films: Fabrication techniques, classification, and regulation methods. *Chin. Phys. B* 27 (4), 047210. doi:10.1088/1674-1056/27/4/047210

Fiebig, M., Lottermoser, T., Meier, D., and Trassin, M. (2016). The evolution of multiferroics. *Nat. Rev. Mat.* 1 (8), 16046. doi:10.1038/natrevmats.2016.46

Fousek, J., Cross, L. E., and Litvin, D. B. (1999). Possible piezoelectric composites based on the flexoelectric effect. *Mater. Lett.* 39 (5), 287–291. doi:10.1016/s0167-577x(99)00020-8

Fu, J., Liu, X., Tan, L., Cui, Z., Wu, S., Liang, Y., et al. (2019). Photoelectric responsive extracellular matrix for bone engineering. *ACS Nano* 13 (11), 13581–13594. doi:10.1021/acsnano.9b08115

Fukada, E. (1998). New piezoelectric polymers. *Jpn. J. Appl. Phys.* 37 (5B), 2775–2780. doi:10.1143/jjap.37.2775

Fukada, E., and Yasuda, I. (1964). Piezoelectric effects in collagen. *Jpn. J. Appl. Phys.* 3 (8), 502B. doi:10.1143/jjap.3.502b

Gaharwar, A. K., Singh, I., and Khademhosseini, A. (2020). Engineered biomaterials for *in situ* tissue regeneration. *Nat. Rev. Mat.* 5 (9), 686–705. doi:10.1038/s41578-020-0209-x

Geng, B. J., Li, P., Fang, F. L., Shi, W. Y., Glowacki, J., Pan, D. Y., et al. (2021). Antibacterial and osteogenic carbon quantum dots for regeneration of bone defects infected with multidrug-resistant bacteria. *Carbon* 184, 375–385. doi:10.1016/j.carbon.2021.08.040

Ghosh, S. (2019). "Fdsoi on lithium niobate Al_2O_3 wafer-bonding for acoustoelectric rf microdevices," in 20th International Conference on Solid-State Sensors, Actuators and Microsystems and Eurosensors XXXIII (TRANSDUCERS and EUROSENSORS), Berlin, Germany, 22 August 2019, 535–538.

Gocha, A., and Mcdonald, L. (2020). Better bodies with biomaterials: How ceramic and glass contribute to the $110B global market for implantable biomaterials. *Am. Ceram. Soc. Bull.* 99 (9), 17–31.

Hamzah, M. S. A., Ab Razak, N. A., Ng, C., Azize, A. H. A., Sukor, J. A., Fhong, S. C., et al. (2021). Preparation of the electrospun polyvinylidene fluoride /polyvinyl alcohol scaffold as a potential tissue replacement. *Ium Eng. J.* 22 (1), 245–258. doi:10.31436/iiumej.v22i1.1548

Holtorf, H. L., Jansen, J. A., and Mikos, A. G. (2005). Flow perfusion culture induces the osteoblastic differentiation of marrow stromal cell-scaffold constructs in the absence of dexamethasone. *J. Biomed. Mat. Res. A* 72A (3), 326–334. doi:10.1002/jbm.a.30251

Hughes, S., Mcbain, S., Dobson, J., and El Haj, A. J. (2008). Selective activation of mechanosensitive ion channels using magnetic particles. *J. R. Soc. Interface* 5 (25), 855–863. doi:10.1098/rsif.2007.1274

Hwang, K. S., Song, J. E., Jo, J. W., Yang, H. S., Park, Y. J., Rawls, H. R., et al. (2002). Effect of poling conditions on growth of calcium phosphate crystal in ferroelectric BaTiO3 ceramics. *J. Mat. Sci. Mat. Med.* 13 (1), 133–138. doi:10.1023/a:1013671526975

Im, G. I. (2020). Biomaterials in orthopaedics: the past and future with immune modulation. *Biomater. Res.* 24 (1), 7. doi:10.1186/s40824-020-0185-7

Jacob, J., More, N., Kalia, K., and Kapusetti, G. (2018). Piezoelectric smart biomaterials for bone and cartilage tissue engineering. *Inflamm. Regen.* 38 (1), 2. doi:10.1186/s41232-018-0059-8

Jacob, J., More, N., Mounika, C., Gondaliya, P., Kalia, K., Kapusetti, G., et al. (2019). Smart piezoelectric nanohybrid of poly(3-hydroxybutyrate-co-3-hydroxyvalerate) and barium titanate for stimulated cartilage regeneration. *ACS Appl. Bio Mat.* 2 (11), 4922–4931. doi:10.1021/acsabm.9b00667

Jafari, J., Han, X. L., Palmer, J., Tran, P. A., and O'connor, A. J. (2019). Remote control in formation of 3D multicellular assemblies using magnetic forces. *ACS Biomater. Sci. Eng.* 5 (5), 2532–2542. doi:10.1021/acsbiomaterials.9b00297

Kanczler, J. M., Sura, H. S., Magnay, J., Green, D., Oreffo, R. O. C., Dobson, J. P., et al. (2010). Controlled differentiation of human bone marrow stromal cells using magnetic nanoparticle technology. *Tissue Eng. Part A* 16 (10), 3241–3250. doi:10.1089/ten.tea.2009.0638

Kang, H., Jung, H. J., Wong, D., Kim, S. K., Lin, S., Kai, F. C., et al. (2018). Remote control of heterodimeric magnetic nanoswitch regulates the adhesion and differentiation of stem cells. *J. Am. Chem. Soc.* 140 (18), 5909–5913. doi:10.1021/jacs.8b03001

Kapat, K., Shubhra, Q. T. H., Zhou, M., and Leeuwenburgh, S. (2020). Piezoelectric nano-biomaterials for biomedicine and tissue regeneration. *Adv. Funct. Mat.* 30 (44), 1909045. doi:10.1002/adfm.201909045

Khatua, C., Bhattacharya, D., and Balla, V. K. (2020). *In situ* electrical stimulation for enhanced bone growth: A mini-review. *Med. Devices Sens.* 3 (4), e10090. doi:10.1002/mds3.10090

Kim, D., Han, S. A., Kim, J. H., Lee, J. H., Kim, S. W., Lee, S. W., et al. (2020). Biomolecular piezoelectric materials: From amino acids to living tissues. *Adv. Mat.* 32 (14), 1906989. doi:10.1002/adma.201906989

Kim, J., Yun, S., and Ounaies, Z. (2006). *Macromolecules* 39 (12), 4202–4206. doi:10.1021/ma060261e

Kim, S. K., Kim, Y. H., Park, S., and Cho, S. W. (2021). Organoid engineering with microfluidics and biomaterials for liver, lung disease, and cancer modeling. *Acta Biomater.* 132, 37–51. doi:10.1016/j.actbio.2021.03.002

Kishore, R. A., Nozariasbmarz, A., Poudel, B., Sanghadasa, M., and Priya, S. (2019). Ultra-high performance wearable thermoelectric coolers with less materials. *Nat. Commun.* 10 (1), 1765. doi:10.1038/s41467-019-09707-8

Lei, B. W., Bai, S. X., Ju, S., Yin, C. P., Chen, C., Zhang, J. W., et al. (2021). Review on advances in thermoelectric conversion using ion-conducting polymers. *Mat. Res. Express* 8 (6), 062001. doi:10.1088/2053-1591/ac0364

Li, Y., Du, Z., Liu, X. P., Ma, M. M., Yu, D. Q., Lu, Y., et al. (2019). Near-infrared activated black phosphorus as a nontoxic photo-oxidant for alzheimer's amyloid-beta peptide. *Small* 15 (24), 1901116. doi:10.1002/smll.201901116

Li, Y., Liao, C., and Tjong, S. C. (2019). Electrospun polyvinylidene fluoride-based fibrous scaffolds with piezoelectric characteristics for bone and neural tissue engineering. *Nanomater. (Basel)* 9 (7), 952. doi:10.3390/nano9070952

Li, Y. N., Ge, J., Luo, M., Niu, W., Ling, X. W., Xu, K., et al. (2022). Elastomeric self-healing antibacterial bioactive nanocomposites scaffolds f or treating skull defect. *Appl. Mater. Today* 26, 101254. doi:10.1016/j.apmt.2021.101254

Liberson, W., Holmquest, H., and Scott, M. (1961). Functional electrotherapy: Stimulation of the common peroneal nerve synchronised with the swing phase of gait of hemiplegic subjects. *Archives Phys. Med. Rehabilitation* 42, 202–205.

Mansoorzare, H., and Abdolvand, R. (2019). "Acoustoelectric amplification in lateral-extensional composite piezo-silicon resonant cavities," in Joint Conference of the IEEE International Frequency Control Symposium and European Frequency and Time Forum, Orlando, FL, USA, 14-18 April 2019, 3. EFTF/IFC).2019

Martins, P. M., Ribeiro, S., Ribeiro, C., Sencadas, V., Lan Ce Ros-Men De, Z. S., Gama, F. M., et al. (2013). Effect of poling state and morphology of piezoelectric poly (vinylidene fluoride) membranes for skeletal muscle tissue engineering. *RSC Adv.* 3 (39), 17938. doi:10.1039/c3ra43499k

Mas-Ballesté, R., Gómez-Navarro, C., Gómez-Herrero, J., and Zamora, F. (2011). 2D materials: to graphene and beyond. *Nanoscale* 3 (1), 20–30. doi:10.1039/c0nr00323a

Masataka, Ohgaki, Takashi, Kizuki, Mihoko, Katsura, and Yamashita, K. (2001). Manipulation of selective cell adhesion and growth by surface charges of electrically polarized hydroxyapatite. *J. Biomed. Mat. Res.* 57 (3), 366–373. doi:10.1002/1097-4636(20011205)57:3<366:aid-jbm1179>3.0.co;2-x

Mindlin, R. D. (1972). Elasticity, piezoelectricity and crystal lattice dynamics. *J. Elast.* 2 (4), 217–282. doi:10.1007/bf00045712

Morocha, A. K., and Rozhkov, A. S. (2018). Electron transport by a transverse acoustoelectric stoneley wave. *Semiconductors* 52 (15), 1915–1918. doi:10.1134/s1063782618150083

Mould, R. F. (2007). Pierre curie, 1859–1906. *Curr. Oncol.* 14 (2), 74–82. doi:10.3747/co.2007.110

Narayan, B., Malhotra, J. S., Pandey, R., Yaddanapudi, K., Nukala, P., Dkhil, B., et al. (2018). Electrostrain in excess of 1% in polycrystalline piezoelectrics. *Nat. Mat.* 17 (5), 427–431. doi:10.1038/s41563-018-0060-2

Pereira, J. D. a. S., Camargo, R., Filho, J., Alves, N., and Constantino, C. (2014). Biomaterials from blends of fluoropolymers and corn starch - implant and structural aspects. *Mater. Sci. Eng. C* 36, 226–236. doi:10.1016/j.msec.2013.12.008

Petty, A. J., Keate, R. L., Jiang, B., Ameer, G. A., and Rivnay, J. (2020). Conducting polymers for tissue regeneration *in vivo*. *Chem. Mat.* 32 (10), 4095–4115. doi:10.1021/acs.chemmater.0c00767

Poole, T., and Nash, G. R. (2018). Acoustoelectric photoresponse of graphene nanoribbons. *J. Phys. D. Appl. Phys.* 51 (15), 154001. doi:10.1088/1361-6463/aab3ec

Puppi, D., Chiellini, F., Piras, A. M., and Chiellini, E. (2010). Polymeric materials for bone and cartilage repair. *Prog. Polym. Sci.* 35 (4), 403–440. doi:10.1016/j.progpolymsci.2010.01.006

Reddi and, A. H. (2000). Morphogenesis and tissue engineering of bone and cartilage: Inductive signals, stem cells, and biomimetic biomaterials. *Tissue Eng.* 6 (4), 351–359. doi:10.1089/107632700418074

Roessler, K., Donat, M., Lanzenberger, R., Novak, K., and Beisteiner, R. (2005). Evaluation of preoperative high magnetic field motor functional MRI (3 Tesla) in glioma patients by navigated electrocortical stimulation and postoperative outcome. *J. Neurology Neurosurg. Psychiatry* 76 (8), 1152–1157. doi:10.1136/jnnp.2004.050286

Sahm, F., Ziebart, J., Jonitz-Heincke, A., Hansmann, D., Dauben, T., Bader, R., et al. (2020). Alternating electric fields modify the function of human osteoblasts growing on and in the surroundings of titanium electrodes. *Int. J. Mol. Sci.* 21 (18), 6944. doi:10.3390/ijms21186944

Saito, Y., Takao, H., Tani, T., Nonoyama, T., Takatori, K., Homma, T., et al. (2004). Lead-free piezoceramics. *Nature* 432 (7013), 84–87. doi:10.1038/nature03028

Senra, M. N. R., and Marques, M. D. V. (2020). Synthetic polymeric materials for bone replacement. *J. Compos. Sci.* 4 (4), 191. doi:10.3390/jcs4040191

Shen, S. X., He, X. Z., Chen, X. Y., Dong, L. Q., Cheng, K., Weng, W. J., et al. (2021). Enhanced osteogenic differentiation of mesenchymal stem cells on P(VDF-TrFE) layer coated microelectrodes. *J. Biomed. Mat. Res.* 109 (12), 2227–2236. doi:10.1002/jbm.b.34884

Snyder, G. J., and Toberer, E. S. (2012). Complex thermoelectric materials. *Nat. Mat.* 7 (2), 105–114. doi:10.1038/nmat2090

So, J. Y., Lee, J., Ahn, Y., Kang, D., Jung, W., Bae, W. G., et al. (2020). The synergistic effect of biomimetic electrical stimulation and extracellular-matrix-mimetic nanopattern for upregulating cell activities. *Biosens. Bioelectron. X.* 167, 112470. doi:10.1016/j.bios.2020.112470

Tang, Y. Y., and Wang, G. J. (2021). NIR light-responsive nanocarriers for controlled release. *J. Photochem. Photobiol. C Photochem. Rev.* 47, 100420. doi:10.1016/j.jphotochemrev.2021.100420

Terpos, E., Zamagni, E., Lentzsch, S., Drake, M. T., Garcia-Sanz, R., Abildgaard, N., et al. (2021). Treatment of multiple myeloma-related bone disease: recommendations from the bone working group of the international myeloma working group. *Lancet Oncol.* 22 (3), E119–E130. doi:10.1016/s1470-2045(20)30559-3

Trinh, M. T., Smail, G., Makhal, K., Yang, D. S., Kim, J., Rand, S. C., et al. (2020). Observation of magneto-electric rectification at non-relativistic intensities. *Nat. Commun.* 11 (1), 5296. doi:10.1038/s41467-020-19125-w

Wakiyama, H., Kato, T., Furusawa, A., Choyke, P. L., and Kobayashi, H. (2021). Near infrared photoimmunotherapy of cancer; possible clinical applications. *Nanophotonics* 10 (12), 3135–3151. doi:10.1515/nanoph-2021-0119

Wang, A., Liu, Z., Ming, H., Wang, C., Zhang, X., Shi, B., et al. (2018). Piezoelectric nanofibrous scaffolds as *in vivo* energy harvesters for modifying

fibroblast alignment and proliferation in wound healing. *Nano Energy* 43, 63–71. doi:10.1016/j.nanoen.2017.11.023

Wang, H., Li, Y., Zuo, Y., Li, J., Ma, S., Cheng, L., et al. (2007). Biocompatibility and osteogenesis of biomimetic nano-hydroxyapatite/polyamide composite scaffolds for bone tissue engineering. *Biomaterials* 28 (22), 3338–3348. doi:10.1016/j.biomaterials.2007.04.014

Wang, J., Lin, J. W., Chen, L., Deng, L. F., and Cui, W. G. (2022). Endogenous electric-field-coupled electrospun short fiber via collecting wound exudation. *Adv. Mater.* 34 (9), 2108325. doi:10.1002/adma.202108325

Wang, S., Zheng, H., Zhou, L., Cheng, F., Zhang, Q., Zhang, H., et al. (2020). Injectable redox and light responsive MnO2 hybrid hydrogel for simultaneous melanoma therapy and multidrug-resistant bacteria-infected wound healing. *Biomaterials* 260, 120314. doi:10.1016/j.biomaterials.2020.120314

Wei, H. P., Cui, J. J., Lin, K. L., Xie, J., and Wang, X. D. (2022). Recent advances in smart stimuli-responsive biomaterials for bone therapeutics and regeneration. *Bone Res.* 10 (1), 17. doi:10.1038/s41413-021-00180-y

Westhauser, F., Arango-Ospina, M., Losch, S., Wilkesmann, S., Lehner, B., Ali, M. S., et al. (2021). Selective and caspase-independent cytotoxicity of bioactive glasses towards giant cell tumor of bone derived neoplastic stromal cells but not to bone marrow derived stromal cells. *Biomaterials* 275, 120977. doi:10.1016/j.biomaterials.2021.120977

Wu, C., Tang, Y., Mao, B., Zhao, K., and Wu, Z. (2020). Rapid apatite induction of polarized hydrophilic HA/PVDF bio-piezoelectric coating on titanium surface. *Surf. Coatings Technol.* 405 (28), 126510. doi:10.1016/j.surfcoat.2020.126510

Xiao, C., Li, Z., Li, K., Huang, P., and Xie, Y. (2014). Decoupling interrelated parameters for designing high performance thermoelectric materials. *Acc. Chem. Res.* 47 (4), 1287–1295. doi:10.1021/ar400290f

Xu, C. W., Jin, L., Zhang, L., Wang, C. F., Huang, X., He, X. B., et al. (2018). Pressure-crystallized piezopolymer/ionomer/graphene quantum dot composites: A novel poling-free dynamic hybrid electret with enhanced energy harvesting properties. *Compos. Sci. Technol.* 164, 282–289. doi:10.1016/j.compscitech.2018.06.010

Yamamoto, K., Iguchi, R., Miura, A., Zhou, W. N., Sakuraba, Y., Miura, Y., et al. (2021). Phenomenological analysis of transverse thermoelectric generation and cooling performance in magnetic/thermoelectric hybrid systems. *J. Appl. Phys.* 129 (22), 223908. doi:10.1063/5.0055475

Yamashita, K., Oikawa, N., and Umegaki, T. (1996). Acceleration and deceleration of bone-like crystal growth on ceramic hydroxyapatite by electric poling. *Chem. Mat.* 8 (12), 2697–2700. doi:10.1021/cm9602858

Yang, L., Chen, Z. G., Dargusch, M. S., and Zou, J. (2018). High performance thermoelectric materials: Progress and their applications. *Adv. Energy Mat.* 8 (6), 1701797. doi:10.1002/aenm.201701797

Yang, Y., Wei, X.-J., and Liu, J. (2007). Suitability of a thermoelectric power generator for implantable medical electronic devices. *J. Phys. D. Appl. Phys.* 40 (18), 5790–5800. doi:10.1088/0022-3727/40/18/042

Yu, B., Qiao, Z. G., Cui, J. J., Lian, M. F., Han, Y., Zhang, X., et al. (2021). A host-coupling bio-nanogenerator for electrically stimulated osteogenesis. *Biomaterials* 276, 120997. doi:10.1016/j.biomaterials.2021.120997

Yu, S. W., Kuo, S. T., Tuan, W. H., Tsai, Y. Y., and Wang, S. F. (2012). Cytotoxicity and degradation behavior of potassium sodium niobate piezoelectric ceramics. *Ceram. Int.* 38 (4), 2845–2850. doi:10.1016/j.ceramint.2011.11.056

Zaborowska, M., Bodin, A., Backdahl, H., Popp, J., Goldstein, A., and Gatenholm, P. (2010). Microporous bacterial cellulose as a potential scaffold for bone regeneration. *Acta Biomater.* 6 (7), 2540–2547. doi:10.1016/j.actbio.2010.01.004

Zaszczynska, A., Gradys, A., and Sajkiewicz, P. (2020). Progress in the applications of smart piezoelectric materials for medical devices. *Polymers* 12 (11), 2754. doi:10.3390/polym12112754

Zhang, C., Liu, W., Cao, C., Zhang, F., Tang, Q., Ma, S., et al. (2018). Modulating surface potential by controlling the β phase content in poly(vinylidene fluoridetrifluoroethylene) membranes enhances bone regeneration. *Adv. Healthc. Mat.* 7 (11), 1701466. doi:10.1002/adhm.201701466

Zhang, W., Ling, C., Li, X. L., Sheng, R. W., Liu, H. Y., Zhang, A. N., et al. (2020). Cell-free biomimetic scaffold with cartilage extracellular matrix-like architectures for *in situ* inductive regeneration of osteochondral defects. *ACS Biomater. Sci. Eng.* 6 (12), 6917–6925. doi:10.1021/acsbiomaterials.0c01276

Zhang, X. S., Huan, Y., Li, K., Tian, H., Shen, H. T., Li, M., et al. (2019). Enhanced photocatalytic activity and cycle stability driven by ultrasonic vibration for ferroelectric photocatalysts. *Iet Nanodielectrics* 2 (1), 48–53. doi:10.1049/iet-nde.2018.0039

Zhang, Y., Huang, L., Li, Z., Ma, G., Zhou, Y., Han, G., et al. (2016). Illuminating cell signaling with near-infrared light-responsive nanomaterials. *ACS Nano* 10 (4), 3881–3885. doi:10.1021/acsnano.6b02284

Zhao, Y., Lu, R., Wang, X., Huai, X. C., Wang, C. Y., Wang, Y. J., et al. (2021). Visible light-induced antibacterial and osteogenic cell proliferation properties of hydrogenated TiO2 nanotubes/Ti foil composite. *Nanotechnology* 32 (19), 195101. doi:10.1088/1361-6528/abe156

Zhou, C., Dun, C., Ge, B., Ke, W., Shi, Z., Liu, G., et al. (2018). Highly robust and flexible n-type thermoelectric film based on Ag2Te nanoshuttle/polyvinylidene fluoride hybrids. *Nanoscale* 10, 14830–14834. doi:10.1039/c8nr04883e

Zhou, W. N., Yamamoto, K., Miura, A., Iguchi, R., Miura, Y., Uchida, K., et al. (2021). Seebeck-driven transverse thermoelectric generation. *Nat. Mat.* 20 (4), 463–467. doi:10.1038/s41563-020-00884-2

Zhu, P. J., Lai, C. H., Cheng, M. W., He, Y. H., Xu, Y., Chen, J. H., et al. (2022). Differently charged P (VDF-TrFE) membranes influence osteogenesis through differential immunomodulatory function of macrophages. *Front. Mat.* 8, 790753. doi:10.3389/fmats.2021.790753

Zhu, X. Y., Yuan, L., Hu, X. X., Zhang, L. L., Liang, Y. X., He, S. Y., et al. (2018). Construction of a fluorine substituted chromenylium-cyanine near-infrared fluorophore for ratiometric sensing. *Sensors Actuators B Chem.* 259, 219–225. doi:10.1016/j.snb.2017.12.008

frontiers | Frontiers in Bioengineering and Biotechnology

TYPE Original Research
PUBLISHED 23 September 2022
DOI 10.3389/fbioe.2022.957263

Check for updates

OPEN ACCESS

EDITED BY
Muhammad Wajid Ullah,
Jiangsu University, China

REVIEWED BY
Ahmed El-Fiqi,
Dankook University, South Korea
Ranjith Kumar Kankala,
Huaqiao University, China
Kaushik Chatterjee,
Indian Institute of Science (IISc), India

*CORRESPONDENCE
Jenneke Klein-Nulend,
j.kleinnulend@acta.nl

†These authors have contributed equally to this work and share first authorship

SPECIALTY SECTION
This article was submitted to Biomaterials, a section of the journal Frontiers in Bioengineering and Biotechnology

RECEIVED 30 May 2022
ACCEPTED 22 August 2022
PUBLISHED 23 September 2022

CITATION
Abbasi-Ravasjani S, Seddiqi H, Moghaddaszadeh A, Ghiasvand M-E, Jin J, Oliaei E, Bacabac RG and Klein-Nulend J (2022), Sulfated carboxymethyl cellulose and carboxymethyl κ-carrageenan immobilization on 3D-printed poly-ε-caprolactone scaffolds differentially promote pre-osteoblast proliferation and osteogenic activity.
Front. Bioeng. Biotechnol. 10:957263.
doi: 10.3389/fbioe.2022.957263

COPYRIGHT
© 2022 Abbasi-Ravasjani, Seddiqi, Moghaddaszadeh, Ghiasvand, Jin, Oliaei, Bacabac and Klein-Nulend. This is an open-access article distributed under the terms of the Creative Commons Attribution License (CC BY). The use, distribution or reproduction in other forums is permitted, provided the original author(s) and the copyright owner(s) are credited and that the original publication in this journal is cited, in accordance with accepted academic practice. No use, distribution or reproduction is permitted which does not comply with these terms.

Sulfated carboxymethyl cellulose and carboxymethyl κ-carrageenan immobilization on 3D-printed poly-ε-caprolactone scaffolds differentially promote pre-osteoblast proliferation and osteogenic activity

Sonia Abbasi-Ravasjani[1†], Hadi Seddiqi[1†], Ali Moghaddaszadeh[2], Mohammad-Ehsan Ghiasvand[3], Jianfeng Jin[1], Erfan Oliaei[4], Rommel Gaud Bacabac[5] and Jenneke Klein-Nulend[1*]

[1]Department of Oral Cell Biology, Academic Centre for Dentistry Amsterdam (ACTA), Amsterdam Movement Sciences, University of Amsterdam and Vrije Universiteit Amsterdam, Amsterdam, Netherlands, [2]Department of Biomedical Engineering, Science and Research Branch, Islamic Azad University, Tehran, Iran, [3]Department of Mechanical Engineering, Amir Kabir University of Technology, Tehran, Iran, [4]Fiber and Polymer Technology, KTH Royal Institute of Technology, Stockholm, Sweden, [5]Medical Biophysics Group, Department of Physics, University of San Carlos, Cebu City, Philippines

The lack of bioactivity in three-dimensional (3D)-printing of poly-ϵ-caprolactone (PCL) scaffolds limits cell-material interactions in bone tissue engineering. This constraint can be overcome by surface-functionalization using glycosaminoglycan-like anionic polysaccharides, e.g., carboxymethyl cellulose (CMC), a plant-based carboxymethylated, unsulfated polysaccharide, and κ-carrageenan, a seaweed-derived sulfated, non-carboxymethylated polysaccharide. The sulfation of CMC and carboxymethylation of κ-carrageenan critically improve their bioactivity. However, whether sulfated carboxymethyl cellulose (SCMC) and carboxymethyl κ-carrageenan (CM-κ-Car) affect the osteogenic differentiation potential of pre-osteoblasts on 3D-scaffolds is still unknown. Here, we aimed to assess the effects of surface-functionalization by SCMC or CM-κ-Car on the physicochemical and mechanical properties of 3D-printed PCL scaffolds, as well as the osteogenic response of pre-osteoblasts. MC3T3-E1 pre-osteoblasts were seeded on 3D-printed PCL scaffolds that were functionalized by CM-κ-Car (PCL/CM-κ-Car) or SCMC (PCL/SCMC), cultured up to 28 days. The scaffolds' physicochemical and mechanical properties and pre-osteoblast function were assessed experimentally and by finite element (FE) modeling. We found that the surface-functionalization by SCMC and CM-κ-Car did not change the scaffold geometry and structure but decreased the elastic modulus. Furthermore, the scaffold surface roughness and hardness increased and the scaffold became more hydrophilic. The FE modeling results implied resilience up to 2% compression strain, which was below the yield stress for all scaffolds. Surface-functionalization by SCMC decreased *Runx2* and *Dmp1* expression, while surface-functionalization by CM-κ-Car increased *Cox2* expression at day 1.

Surface-functionalization by SCMC most strongly enhanced pre-osteoblast proliferation and collagen production, while CM-κ-Car most significantly increased alkaline phosphatase activity and mineralization after 28 days. In conclusion, surface-functionalization by SCMC or CM-κ-Car of 3D-printed PCL-scaffolds enhanced pre-osteoblast proliferation and osteogenic activity, likely due to increased surface roughness and hydrophilicity. Surface-functionalization by SCMC most strongly enhanced cell proliferation, while CM-κ-Car most significantly promoted osteogenic activity, suggesting that surface-functionalization by CM-κ-Car may be more promising, especially in the short-term, for *in vivo* bone formation.

KEYWORDS

bio-functionalization, bone tissue engineering, carboxymethylated κ-carrageenan, finite element modeling, PCL (poly-ε-caprolactone), pre-osteoblast, 3D-printed scaffold, sulfated carboxymethyl cellulose

1 Introduction

Bone tissue engineering requires three-dimensional (3D)-bioactive scaffolds mimicking bone in their structural, chemical, and mechanical properties in order to support cell adhesion, proliferation, and differentiation (Moghaddaszadeh et al., 2021). 3D printing is a favorable technology for producing bone scaffolds with controlled physical and mechanical properties, as well as a hierarchical structure analogous to the bone matrix (Entezari et al., 2019). Poly-ε-caprolactone (PCL) is a commonly used 3D-printable biomaterial (Joseph et al., 2020). It is approved by the United States Food and Drug Administration (FDA) for internal use in the human body, since it is biocompatible and biodegradable, and has a slow degradation rate and favorable mechanical properties (Joseph et al., 2020). Unfortunately, the absence of essential surface features in 3D-printed PCL scaffolds, lacks the inherent mechanical cues for cell attachment, which consequently impairs osteogenesis and *in vivo* integration (Dong et al., 2017). Therefore, it is hypothesized that the bioactivity of these scaffolds can be improved by strategic surface-functionalization.

Numerous surface functionalization techniques including physical (e.g., plasma treatment), chemical (e.g., hydrolysis), or biological (e.g., coating and immobilization of biologically active molecules on the surface) approaches have been implemented to improve the bioactivity of PCL scaffolds (Dwivedi et al., 2020). Glycosaminoglycan (GAG)-like anionic polysaccharides are also widely used for biomaterial functionalization, because of their ability to facilitate cell adhesion, proliferation, and differentiation (Malliappan et al., 2022). Among several kinds of anionic polysaccharides, carboxymethyl cellulose (CMC; a plant-based carboxymethylated polysaccharide) (Seddiqi et al., 2021), and κ-carrageenan (a seaweed-derived sulfated polysaccharide) (Cao et al., 2021) have attracted attention for tissue engineering applications. The ease of chemical functionalization, hydrophilicity, favorable mechanical properties, and biocompatibility make CMC and κ-carrageenan interesting for tissue engineering applications (Cao et al., 2021; Zennifer et al., 2021). The chemical modification of anionic polysaccharides by sulfate and carboxymethyl groups is an important route to enhance their bioactivity (Palhares et al., 2021). The chemical structure of sulfated CMC (SCMC) is similar to heparan sulfate, which facilitates cell adhesion, proliferation, and differentiation (Bhutada et al., 2021). Moreover, it has been shown that carboxymethylated κ-carrageenan (CM-κ-Car) promotes biodegradability, cytocompatibility, stem cell adhesion, cell growth, and osteogenic differentiation (Madruga et al., 2021). However, the effect of SCMC and CM-κ-Car on osteoblast precursor cell adhesion, proliferation, and osteogenic differentiation still needs to be assessed.

In this study, CMC was first sulfated and κ-carrageenan carboxymethylated before their use for surface functionalization of PCL. Then PCL scaffolds were 3D-printed with a regular structure by depositing the strands layer-by-layer with an alternating 0/90° lay-down pattern, since this pattern provides optimal mechanobiological behavior (Saatchi et al., 2020). Afterwards, the effect of surface-functionalization of 3D-printed PCL scaffolds by SCMC or CM-κ-Car was tested experimentally based on the scaffold's physicochemical and mechanical properties, as well as on the osteogenic response of embedded pre-osteoblasts. Moreover, finite element (FE) modeling was used to quantify the von Mises stress distribution and magnitude under uniform 2% compression strain deformation.

2 Materials and methods

2.1 Sulfation of carboxymethyl cellulose

CMC was allowed to react with the SO_3/pyridine complex at room temperature to prepare SCMC as described previously (Hoseinpour et al., 2018). CMC was activated in dimethylacetamide (Merck, Darmstadt, Germany) for 1 h at 80°C while stirring. SO_3/pyridine complex was prepared through the reaction of pyridine (Merck) and chlorosulfonic acid (Merck).

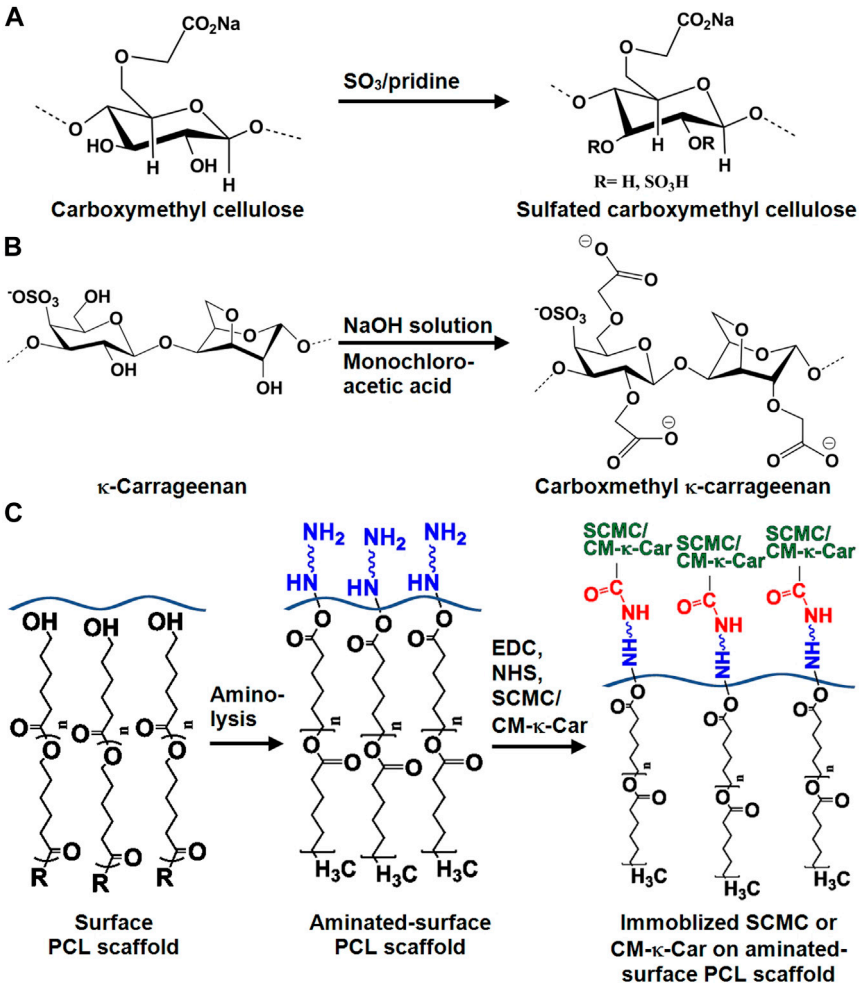

FIGURE 1
Chemical structure of SCMC and CM-κ-Car surface-functionalized 3D-printed PCL scaffolds. **(A)** Chemical conversion of carboxymethyl cellulose to SCMC. **(B)** Chemical conversion of κ-carrageenan to CM-κ-Car. **(C)** Schematic illustration of surface-functionalization by SCMC or CM-κ-Car of 3D-printed PCL scaffolds. PCL, poly-ε-caprolactone; SCMC, sulfated carboxymethyl cellulose; CM-κ-Car, carboxymethyl κ-carrageenan.

SO_3/pyridine complex was added to activated CMC, and the reaction was allowed to stir at ambient temperature for 1 h (Figure 1A). The SCMC obtained was dissolved in 0.5 M sodium hydroxide (NaOH; Merck), precipitated in 100% ethanol, and washed in a graded ethanol series [ethanol/water (v/v): 20/80, 40/60, 60/40, 80/20, and 100% ethanol, respectively] to remove remaining salts. Finally, SCMC was dried under vacuum at 50°C.

2.2 Carboxymethylation of κ-carrageenan

CM-κ-Car was synthesized in two steps as described previously (Ilanlou et al., 2019). Briefly, alkalization of κ-carrageenan was achieved using NaOH to form alkoxy-κ-carrageenan at 35°C for 1 h under stirring, followed by etherification of alkoxy-κ-carrageenan with monochloroacetic acid (Merck, Darmstadt, Germany) for 12 h under stirring to prepare CM-κ-Car (Figure 1B). The CM-κ-Car (sediment) was frozen at −80°C for 24h, and freeze-dried.

2.3 Characterization of sulfated carboxymethyl cellulose and carboxymethyl κ-carrageenan

2.3.1 Fourier transform infrared spectroscopy of sulfated carboxymethyl cellulose and carboxymethyl κ-carrageenan

Fourier transform infrared spectroscopy (FTIR; Thermo Nicolet Avatar 370, San Diego, CA, United States) was used

to study the chemical structures of CMC, SCMC, κ-carrageenan, and CM-κ-Car.

2.3.2 ^{1}H and ^{13}C nuclear magnetic resonance spectroscopy of sulfated carboxymethyl cellulose and carboxymethyl κ-carrageenan

The ^{1}H and ^{13}C nuclear magnetic resonance (NMR) spectra of the CMC, SCMC, κ-carrageenan, and CM-κ-Car samples were recorded on a Bruker AMX-500 NMR spectrometer at ambient temperature. The samples were dissolved in D_2O (35 mg/ml). Chemical shifts (in ppm) were expressed relative to the resonance. MestreNova software (Version 9.0, Mestrelab Research S.L., Santiago de Compostela, Spain) was used to process the data, which included a 90° shifted square sine-bell apodization window. Baseline and phase correction were conducted in both directions.

2.3.3 Degree of substitution of carboxymethyl κ-carrageenan

The degree of substitution (DS) value of CM-κ-Car was estimated from potentiometric titration. CM-κ-Car (4 g/L) was dissolved in 0.1 M hydrochloric acid (Merck), and titrated with 0.1 M NaOH. The pH values were measured with a pH meter (Mettler Toledo, Columbus, OH, United States) as incremental volumes of NaOH solution were added (Muzzarelli et al., 1984). The DS value was calculated by the following equation:

$$DS = (385\times A)/(1000 - 80 \times A), A = (V2 - V1)_{NaOH} \times C_{NaOH}/m_{CM-K-Car} \quad (1)$$

where A is the amount of–CH_2COOH and–CH_2COONa per gram CM-κ-Car. Samples were analyzed in triplicate.

2.4 Three-dimensional-printing of poly-ε-caprolactone scaffolds

PCL scaffolds (l × w × h:10 mm × 10 mm × 10 mm; volume: 1,000 mm^3) were printed using a 3DPLN2 bioprinter (3DPL, Tehran, Iran) with a Thermo polymer extruder equipped with a needle (inner diameter: 700 μm). PCL (Mw 80 kDa; Sigma-Aldrich®, St. Louis, MO, United States) was heated to 100°C before being extruded at 2 bar through a pre-heated needle. PCL strands were plotted layer-by-layer with an alternating 0°/90° lay-down pattern. In total, 30 scaffolds were printed for this study.

2.5 Surface-functionalization of three-dimensional-printed poly-ε-caprolactone scaffolds by sulfated carboxymethyl cellulose or carboxymethyl κ-carrageenan

3D-printed PCL scaffolds were aminolysed with 10% (w/v) 1,6-hexandiamine (Merck, Darmstadt, Germany) in isopropanol (Merck) at 37°C for 1 h, followed by rinsing with deionized water (Figure 1C). For SCMC immobilization, the aminolysed scaffolds were immersed in 1.5% (w/v) SCMC in 0.05 M 2-(N-morpholino) ethanesulfonic acid (pH 6.0; MES; Sigma-Aldrich, St. Louis, MO, United States) buffer solution containing 1.5 mg/ml 1-ethyl-3-(3-dimethylaminopropyl)-carbodiimide (EDC; Sigma-Aldrich) and 1.5 mg/ml N-hydroxysulfosuccinimide (NHS; Thermo Fisher Scientific, Rockville, IL, United States) at ambient temperature for 8 h, followed by rinsing with PBS (Figure 1C). For CM-κ-Car immobilization, 2 mg/ml CM-κ-Car in 0.5 M MES buffer solution containing 1.6 mg/ml EDS and 3.2 mg/ml NHS was prepared under stirring for 1 h at 37°C. Then aminolysed scaffolds were immersed in CM-κ-Car for 4 h at 37°C, rinsed with sodium dihydrogen phosphate (Merck) for 2 h, and rinsed with PBS for 12 h (Figure 1C).

2.6 Scaffold characterization

2.6.1 Elemental composition

The elemental composition of the 3D-printed PCL, PCL/SCMC, and PCL/CM-κ-Car scaffolds was evaluated with energy dispersive spectroscopy (EDS; Zeiss, Oberkochen, Germany) analysis. Scaffolds were assayed in triplicate.

2.6.2 Hydrophilicity

To determine a possible effect of surface functionalization by SCMC or CM-κ-Car on the hydrophilicity of a flat PCL surface prepared by solvent casting, the surface was functionalized by SCMC or CM-κ-Car, thereby avoiding possible effects from the curvature and roughness in the scaffolds. The static water contact angle of PCL, PCL/SCMC, and PCL/CM-κ-Car sheets was measured according to ASTM D7334 standard (ASTM, 2013). A video contact angle system (Sony color video camera, Tokyo, Japan) was used to capture water contact angle images. The water contact angle was determined using ImageJ. Sheets were analyzed in triplicate.

2.6.3 Surface topography and morphology

The surface topography and morphology of 3D-printed PCL, PCL/SCMC, and PCL/CM-κ-Car scaffolds were observed by scanning electron microscopy (SEM). Scaffolds were coated with a layer of gold using an Edwards Sputter Coater S150B (Edwards, Burgess Hill, United Kingdom), and imaged using a Zeiss EVO LS-15 scanning electron microscope (Zeiss, Oberkochen, Germany) with an accelerating voltage of 20 kV.

2.6.4 Void size and strand diameter

Ten voids and strands per scaffold were measured using ImageJ (https://imagej.net/downloads). Scaffolds were assayed in triplicate.

2.6.5 Surface roughness

The surface roughness of 3D-printed PCL, PCL/SCM, and PCL/CM-κ-Car scaffolds was determined using a non-contact optical profilometer (Fanavari Kahroba Co., Tehran, Iran). The scaffolds were scanned at 0.5 μm resolution. Data from profilometer were analyzed using Gwyddion (an open-source software package; see gwyddion.net) to determine 3D-scaffold surface topography and average surface roughness. Measurements were performed in triplicate. Scaffolds were analyzed in triplicate.

2.6.6 Surface charge

The zeta potential of the surface of 3D-printed PCL, PCL/SCMC, and PCL/CM-κ-Car scaffolds was assessed in 1 mmol/L KCl solution, pH 5.7, at room temperature, using a clamping cell (60 mm × 60 mm) mounted in a SurPASS™3 Electrokinetic Analyzer (Anton Paar GmbH, Graz, Austria), with polymethyl methacrylate film as reference. Scaffolds were analyzed in triplicate.

2.6.7 Surface chemical composition

Attenuated total reflection-Fourier transform infrared spectroscopy (ATR-FTIR; Thermo Nicolet Avatar 370, San Diego, CA, United States) was used to identify functional groups, chemical interactions, and possible alteration of 3D-printed PCL, PCL/SCMC, and PCL/CM-κ-Car scaffolds. Scaffolds were analyzed in triplicate.

2.6.8 Total protein adsorption

To determine total protein adsorption on 3D-printed PCL, PCL/SCMC, and PCL/CM-κ-Car scaffolds, the scaffolds were incubated in α-MEM supplemented with 10% FBS at 37°C for 24 h. The scaffolds were then washed with PBS to remove weakly adsorbed proteins and incubated in 2% sodium dodecyl sulfate (Sigma-Aldrich) for 20 h. The total amount of protein was determined by using a BCA Protein Assay reagent Kit (PierceTM, Rockford, lll, United States), and the absorbance was read at 540 nm with a Synergy HT® spectrophotometer (BioTek Instruments, Winooski, VT, United States). Scaffolds were tested in triplicate.

2.6.9 Mechanical properties

3D-printed PCL, PCL/SCMC, and PCL/CM-κ-Car scaffolds were tested for their compressive strength using an STM 20 universal testing machine (Santam, Tehran, Iran) with a 200 N load cell at a rate of 1 mm/min at ambient temperature (25°C). Scaffolds were compressed up to 80% of their original length. Stress values were determined by dividing the load by the cross-sectional area of each scaffold (21 mm^2). Stress-strain curves were plotted, and compressive ultimate strength was assessed. Surface hardness was measured using a Shore durometer (Shore D; Santam; Tehran, Iran). Scaffolds were tested in triplicate.

2.7 Finite element modeling

2.7.1 Geometry of the model

A 3D-scaffold (l × w × h: 5 mm × 5 mm × 5 mm) with a strand diameter of 0.5 mm, and a void size of 0.7 mm was designed using commercial software (COMSOL Multiphysics 5.4, Stockholm, Sweden), and used for FE modeling.

2.7.2 Mechanical behavior of the scaffolds

FE modeling was used to measure von Mises stress magnitude and distribution on the 3D-printed PCL scaffolds without or with surface-functionalization, under uniform 2% compression strain. This analysis confirmed no plastic deformation of the scaffolds under the conditions mentioned. The 3D structure of the scaffolds was modeled by considering the scaffold as a homogenous and isotropic linear elastic material. The bottom surface of the scaffolds was fixed, and a displacement-controlled boundary condition was applied to the top surface of the scaffolds. The final displacement was set as an equivalent vertical strain of 2%, which was within the range of elastic deformation for this composite material (Baptista and Guedes, 2020). The models were meshed using 208,779 tetrahedra, 116,514 triangles, 29,652 edges, and 5220 vertex elements. Table 1 provides detailed information on the model parameters used for modeling.

The computed reaction force (F_R) defines the scaffold's effective elastic modulus (E) according to Eq. 2:

$$E = F_R/(A \times \varepsilon) \quad (2)$$

where the average strain $\varepsilon = 0.02$, and the cross-sectional area of the compression A = 21 mm^2.

2.8 Cell culture and pre-osteoblast bioactivity

2.8.1 Cell culture, and seeding onto the scaffolds

MC3T3-E1 pre-osteoblasts (American Type Culture Collection, Manassas, VA, United States) were grown and maintained in α-Minimum Essential Medium (α-MEM; Gibco, Life Technologies, Walthan, MA, United States), supplemented with 10% fetal bovine serum (FBS; Gibco, Life Technologies, Waltham, MA, United States), and 1% PSF (antibiotic antimycotic solution, Sigma-Aldrich®, St. Louis, MO, United States), in a humidified incubator with 5% CO_2 in air at 37°C. After reaching 75% confluency, cells were detached using 0.25% trypsin (Gibco, Invitrogen, Waltham, MA, United States) and 0.1% ethylenediaminetetraacetic acid (Merck, Darmstadt, Germany) in PBS at 37°C. Cells were then resuspended at 5×10^6 cells/ml in osteogenic medium consisting of α-MEM supplemented with 10% FBS, 1% PSF, 50 μg/ml ascorbic acid (Sigma-Aldrich®, St. Louis, MO, United States), and 10 mM β-

TABLE 1 Parameters and default values used in the FE modeling.

Type of scaffold	Parameter	Expression	Value	References
PCL	E (MPa)	Elastic modulus	162.2	
	ϑ	Poisson's ratio	0.3	(Liu et al., 2020)
PCL/SCMC	E (MPa)	Elastic modulus	147.5	
	ϑ	Poisson's ratio	0.3	
PCL/CM-κ-Car	E (MPa)	Elastic modulus	119.5	
	ϑ	Poisson's ratio	0.3	

PCL, poly-ε-caprolactone; SCMC, sulfated carboxymethyl cellulose; CM-κ-Car, carboxymethyl κ-carrageenan.

glycerophosphate (Sigma-Aldrich®, St. Louis, MO, United States).

Cell seeding was performed by spreading ten 10 µl drops of a 5×10^5 cells/cm^3 cell suspension onto the scaffold surface in 24-well culture plates. Cell-seeded scaffolds were incubated for 3 h at 5% CO_2 in the air at 37°C to allow cell attachment. To prevent evaporation, 100 µl osteogenic medium was added every 30 min during this period. Then osteogenic medium (1,500 µl/well) was added, and cell-seeded scaffolds were cultured for up to 28 days. The culture medium was changed every 2 days. Cell seeding efficiency, morphology, spreading, gene expression, and proliferation were assessed as described below. At days 7, 14, 21, and 28, scaffolds were collected and cut into 8 equal parts (l × w × h: 5 mm × 5 mm × 5 mm; volume: 125 mm^3), since cell distribution from the scaffold's top to bottom was relatively homogeneous. Each part of all types of scaffold was compared with respect to collagen production, ALP activity, and matrix mineralization (see below). For comparison between groups, parts from the same location in the scaffolds were used (Zamani et al., 2018).

2.8.2 Cell morphology and spreading

Cell morphology and spreading on 3D-printed PCL, PCL/SCMC, and PCL/CM-κ-Car scaffolds were observed an imaged by SEM after 4 h, 12 h, and 3 days of culture. Cell-seeded scaffolds were fixed using 4% glutaraldehyde, followed by dehydration in a graded ethanol series (50, 70, 80, 90, and 100%). Cell-seeded scaffolds were coated with a layer of gold using an Edwards Sputter Coater S150B, and imaged using a Zeiss EVO LS-15 scanning electron microscope with an accelerating voltage of 20 kV.

2.8.3 Cell seeding efficiency

To determine seeding efficiency, cell-seeded scaffolds were kept under static conditions for 8 h following cell seeding to guarantee sufficient time for cell attachment and adaptation to a specific scaffold architecture. The cell-seeded scaffolds, in a 24-well culture plate ("old plate"), were washed twice with PBS, and transferred to a new 24-well culture plate. Seeding efficiency was assessed by determining the number of cells attached to the wells of the "old plate" as well as the number of cells attached to the scaffolds, using AlamarBlue® fluorescent assay (Invitrogen, Frederick, MD, United States), according to the manufacturer's instructions. We determined a linear relationship between AlamarBlue® fluorescence and cell number (data not shown). Fresh osteogenic medium with 10% AlamarBlue® was added to the wells of the "old plate" and each scaffold until the solution completely covered the top of the scaffolds. Both scaffolds and "old plate" were incubated in AlamarBlue® solution for 4 h in a humidified incubator with 5% CO_2 at 37°C. The solution was harvested from the scaffolds and the "old plate", and the fluorescence was measured at 530 nm with a Synergy HT® spectrophotometer. Scaffolds were washed twice with PBS to remove AlamarBlue®, and incubated in a humidified incubator with 5% CO_2 in air at 37°C. Seeding efficiency was calculated according to the following equation:

$$\text{Seeding efficiency } (\%) = \frac{number\ of\ cells\ attached\ to\ scaffold}{number\ of\ cells\ attached\ to\ scaffold\ +\ number\ of\ cells\ attached\ to\ plate} \times 100 \quad (3)$$

Three independent experiments with 3 constructs per group were assayed in triplicate.

2.8.4 Analysis of gene expression

After 1 or 7 days of culture, total RNA was extracted using TRIzol® reagent (Life Technologies, Waltham, MA, United States), and stored at -80°C prior to analysis. Complementary DNA (cDNA) was synthesized using the First Strand cDNA Synthesis kit (Thermo Fisher Scientific, Vilnius, Lithuania). cDNA was stored at −20°C prior to real-time-polymerase chain reaction (RT-PCR) analysis, and diluted 5× for gene expression analysis. RT-PCR reactions were performed using 1 µl cDNA per reaction and LightCycler® 480 SYBR® Green I Mastermix (Roche Diagnostics, Mannheim, Germany) in a LightCycler® 480 (Roche Diagnostics). RT-PCR conditions for all genes were as follows: 10 min pre-incubation at 95°C, followed by 45 cycles of amplification at 95°C for 10 s, 56°C for 5 s, 72°C for 10 s, and 78°C for 5 s, after which melting curve analysis was performed. With LightCycler® software (version 1.2), crossing points were assessed and plotted versus the serial dilution of known concentrations of the internal standard (Jin et al., 2021).

TABLE 2 Primers used in real time PCR.

Gene	Forward primer sequence (5′-3′)	Reverse primer sequence (5′-3′)
Runx2	ATGCTTCATTCGCCTCAC	ACTGCTTGCAGCCTTAAAT
Ocn	CAGACACCATGAGGACCATCTT	GGTCTGATAGCTCGTCACAA
Ki67	CCCTCAGCAAGCCTGAGAA	AGAGGCGTATTAGGAGGCAAG
Fgf2	GGCTTCTTCCTGCGCATCCA	TCCGTGACCGGTAAGTATTG
Cox2	TTGCTGTTCCAATCCATGTCA	GGTGGGCTTCAGCAGTAATTTG
Dmp1	CGGCTGGTGGACTCTCTAAG	CGGGGTCGTCGCTCTGCATC
Pbgd	AGTGATGAAAGATGGGCAACT	TCTGGACCATCTTCTTGCTGA

Runx2, runt-related transcription factor 2; *Ocn,* osteocalcin; *Ki67,* antigen KI-67; *Fgf2,* fibroblast growth factor-2; *Cox2,* cyclooxygenase-2; *Dmp1,* dentin matrix acidic phosphoprotein 1; *Pbgd,* porphobilinogen deaminase.

Target proliferation marker gene *Ki67* and osteogenic marker genes *Runx2*, *Cox2, Ocn, Fgf2,* and *Dmp1* were analyzed. Gene expression levels were calculated relative to the housekeeping gene *Pbgd*. Primer sequences are listed in Table 2. Three independent experiments with five scaffolds were performed.

2.8.5 Cell proliferation

MC3T3-E1 pre-osteoblast proliferation was assessed by determining the cell number in the scaffolds at days 3, 7, 14, 21, and 28, and by dividing these numbers by the cell number in the scaffolds at day 1, using AlamarBlue® fluorescent assay, as described above, using Eq. 1. At each time point, scaffolds were transferred to a new plate, AlamarBlue® was added, and the fluorescence was measured. After performing the AlamarBlue® assay on each day, scaffolds were washed twice with PBS, and incubated in osteogenic medium in a humidified incubator with 5% CO_2 at 37°C. Data was obtained from three scaffolds from three independent experiments (n = 3).

2.8.6 Alkaline phosphatase activity and protein assay

Alkaline phosphatase (ALP) activity was measured to determine the osteoblastic phenotype of MC3T3-E1 pre-osteoblasts on 3D-printed PCL, PCL/SCMC, and PCL/CM-κ-Car scaffolds. On days 7, 14, 21, and 28 of cell culture on the scaffolds, one part (1/8th) of the cell/scaffold construct was subjected to cell lysis. Cells were lysed with milli-Q water, and freeze-thawed 3 times to determine ALP activity and protein content. P-nitrophenyl-phosphate (Merck, Darmstadt, Germany) at pH 10.3 was used as the substrate for ALP as described earlier (Kroeze et al., 2011). The absorbance was read at 410 nm. ALP activity was expressed as μmol/μg total cellular protein. The amount of protein was determined by using a BCA Protein Assay reagent Kit (Pierce™, Rockford, lll, United States), and the absorbance was read at 540 nm with a Synergy HT® spectrophotometer (BioTek Instruments, Winooski, VT, United States). Constructs were assayed in triplicate.

ALP protein was stained after 7, 14, 21, and 28 days of culture. One part (1/8th) of the cell/scaffold construct was washed 3 times with PBS, and fixed with 4% formaldehyde in PBS for 15 min at 37°C. The BCIP/NBT (5-bromo-4-chloro-3-indolyl phosphate (BCIP)/nitro blue tetrazolium (NBT) phosphatase color development kit (Roche Diagnostics, Mannheim, Germany) was used for the colorimetric detection of ALP intensity by incubation for 30 min at 37°C. Optical images were taken using a stereomicroscope.

2.8.7 Collagen production

Total collagen production by MC3T3-E1 pre-osteoblasts on 3D-printed scaffolds was visualized and quantified using a picrosirius red stain kit (Chondrex, Inc., Redmond, WA, United States). After 7, 14, 21, and 28 days of culture, one part (1/8th) of the cell/scaffold construct was washed with PBS thrice and fixed in 4% formaldehyde. Fixed constructs were stained for 2 h with picrosirius red at room temperature. Then, constructs were washed twice with acidified water (5 ml acetic acid/L distilled water) to remove the unbound stain, and collagen production was visualized using a Nikon SMZ-10 stereomicroscope (Nikon, Tokyo, Japan) and a Leica inverted microscope (Leica Microsystems, Wetzlar, Germany). For semiquantitative collagen analysis, picrosirius red stain was eluted from the constructs using 0.2 M NaOH/methanol (1:1, v/v) for 30 min under shaking. A 100 μl of this solution per well of a 96-well plate (Greiner, Bio-One, Alphen aan den Rijn, Netherlands) was used to determine the absorbance at 490 nm, with a microplate reader (BioRad Laboratories Inc., Veenendaal, Netherlands). Constructs were weighed after 24 h of air drying at room temperature. Data were normalized to the weight of the dried construct and expressed as absorbance/g. Constructs were assayed in triplicate.

2.8.8 Matrix mineralization

ECM mineralization by MC3T3-E1 pre-osteoblasts attached to the scaffolds was analyzed after 7, 14, 21, and 28 days of culture. To determine mineralization, one part (1/8th) of the cell/scaffold construct was washed with PBS, and fixed in 4%

glutaraldehyde for 15 min at 37°C. Fixed constructs were incubated in 40 mM Alizarin Red staining solution (Merck, Darmstadt, Germany), pH 4.3, at room temperature for 30 min, and washed extensively with deionized water to remove the unreacted dye. Optical images were taken using a stereomicroscope. For quantitative mineralization analysis, the red-stained mineralized nodules were dissolved with 5% sodium dodecyl sulfate (Merck) in 0.5 N HCL at room temperature under shaking. Then, 100 µl of the solution was added per well of a 96-well plate (Techno Plastic Products, Trasadingen, Switzerland) to measure the absorbance at 405 nm with a microplate reader (BioRad Laboratories Inc., Veenendaal, Netherlands). Scaffolds were air-dried at room temperature for 24 h and weighed. The absorbance values were normalized to the weight of the scaffolds and expressed as absorbance/g. Constructs were assayed in triplicate.

2.9 Statistical analysis

All data are expressed as mean ± standard deviation (SD) from at least three independent, separate experiments. Data were analyzed using one-way ANOVA, and the significance of differences among means of contact angle, elastic modulus, comprehensive strength, surface roughness, strand diameter, void size, zeta potential, surface hardness, and protein adsorption were determined by post-hoc comparisons, using Bonferroni's method. Two-way analysis of variance with pairwise comparison was used to assess differences among means of marker gene expression, pre-osteoblast proliferation, ALP activity, collagen production, and matrix mineralization between groups and over time. Differences were considered significant if $p < 0.05$. Statistical analysis was performed using GraphPad Prism® 8.0 (GraphPad Software Inc.).

3 Results

3.1 Chemical structure and composition of sulfated carboxymethyl cellulose and carboxymethyl κ-carrageenan

The chemical structure and composition of CMC, SCMC, κ-Car, and CM-κ-Car were determined by FTIR spectroscopy, and ^{1}H NMR and ^{13}C NMR spectroscopy (Figure 2).

3.1.1 Fourier transform infrared spectroscopy spectra of sulfated carboxymethyl cellulose and carboxymethyl κ-carrageenan

CMC characteristic peaks were detected at 3,570 (OH stretching), 2,920 (asymmetric CH stretching), 1,620 (COOH stretching), 1,430 (CH_2 stretching), 1,330 (CH stretching), and 1,056 (CH–O–CH_2 stretching) (Bhutada et al., 2021). After sulfation of CMC, two new bonds appeared at 1,270 and 727 cm^{-1} in the SCMC spectra, corresponding to the stretching vibration bands of S=O and S–O–C (Figure 2A) (Bhutada et al., 2021). In the spectra of κ-Car, characteristic peaks were detected at 3,350 (OH stretching), 2,940 (asymmetric CH stretching), 1,260 (S=O stretching), and 845 cm^{-1} (S–O–C stretching) (Mobarak et al., 2012). After carboxymethylation of κ-Car, new characteristic peaks appeared at 1,604 and 1760 cm^{-1} in CM-κ-Car spectra corresponding to the stretching vibration band of –COO^{-}, indicating carboxymethylation of κ-Car (Figure 2B) (Mobarak et al., 2012; Ilanlou et al., 2019). In addition, the increase in the intensity of the absorption peak at 1,417 cm^{-1} (symmetric –C–O stretching) confirmed carboxymethylation of κ-Car (Mobarak et al., 2012).

3.1.2 ^{1}H nuclear magnetic resonance and ^{13}C nuclear magnetic resonance spectra of sulfated carboxymethyl cellulose and carboxymethyl κ-carrageenan

The chemical structures of CMC, SCMC, κ-Car, and CM-κ-Car were studied by ^{1}H NMR and ^{13}C NMR spectra (Figure 2). The ^{1}H NMR spectrum of CMC revealed the expected signals of 7 protons (H1-H7) (Figure 2C). The signals of H2–H7 were shown as a group of overlapping peaks between 3.17 and 4.23 ppm (Figure 2C) (Bhutada et al., 2021). The ^{1}H NMR spectrum of SCMC revealed downfield displacement of CMC proton signals due to the addition of electron-withdrawing sulfate (SO_4^{-}) groups (Figure 2C) (Bhutada et al., 2021). The signal of H1 (anomeric proton) of CMC (4.76 ppm) shifted downfield (5.36 ppm), which could be ascribed to de-shielding of the C2 sulfate group (Figure 2C). The chemical shifts of C2–C5 in CMC were between 71.26 and 75.01 ppm (Figure 2D) (Fan et al., 2014). After sulfation, the C2 and C3 shifted to lower field positions, since they were directly attached to electronegative sulfate ester groups. The C4 and C5 shifted to higher field positions, since they were indirectly attached to sulfate ester groups (Figure 2D) (Fan et al., 2014).

The ^{1}H NMR spectrum of κ-carrageenan and CM-κ-Car revealed peaks ranging between 3 and 5 ppm (Figure 2E) (Mobarak et al., 2012). The existence of new peaks around 3.17–3.35 confirmed the substitution of a carboxymethyl group to a hydroxyl group in κ-carrageenan (Figure 2E) (Mobarak et al., 2012). The presence of a new peak at 178 ppm was attributed to a carboxylated carbon in CM-κ-Car, which confirmed the carboxylation of κ-carrageenan (Figure 2F) (Mobarak et al., 2012). The DS value of CM-κ-Car was 0.92 ± 0.004 [Values are mean ± SD (n = 3)].

3.2 Surface chemistry, hydrophilicity, and topography

The elemental composition of 3D-printed PCL scaffolds with or without surface functionalization was analyzed by EDX

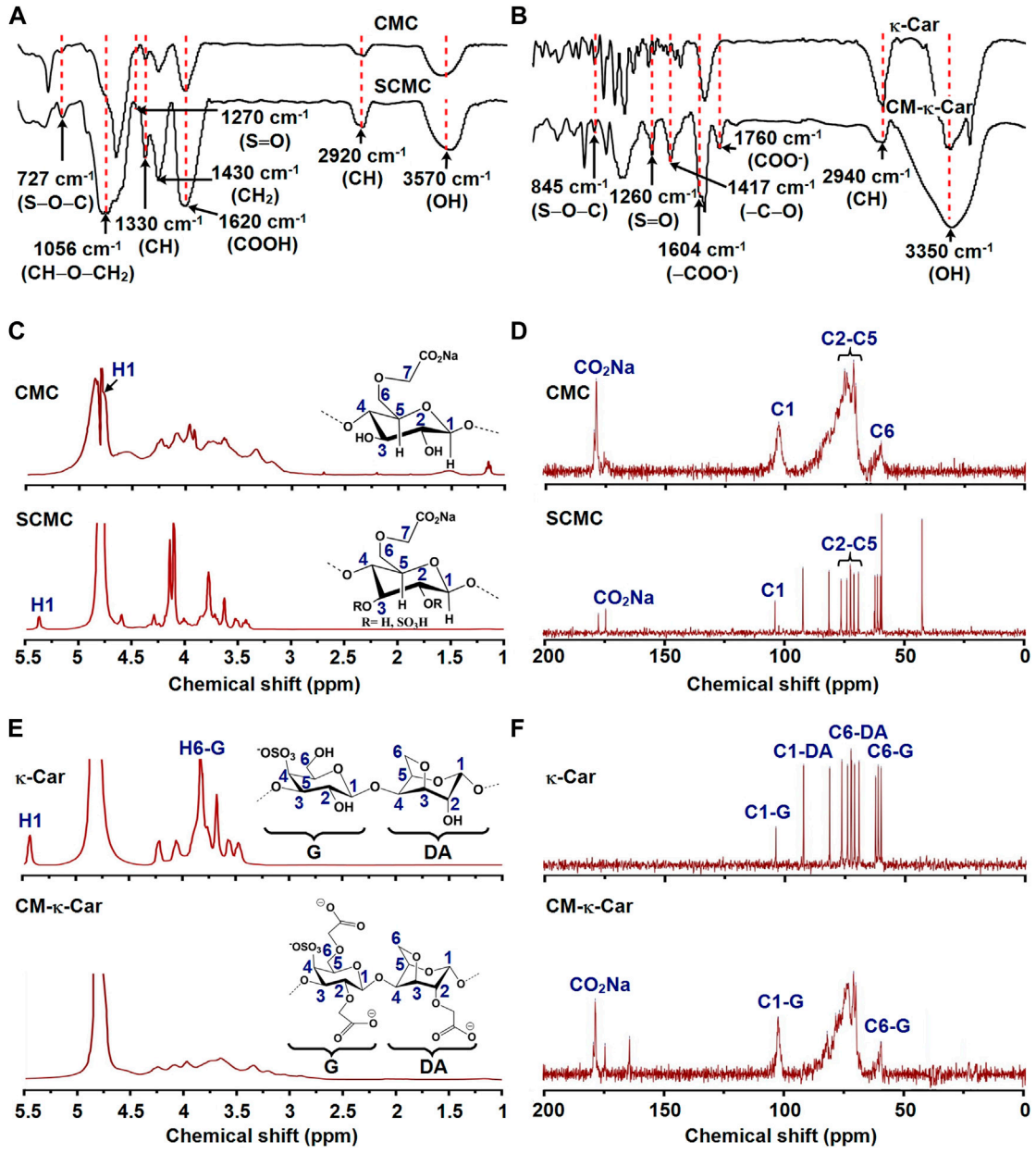

FIGURE 2
Effect of functionalization of CMC by sulfate groups and κ-Car by carboxymethyl groups on chemical composition and structure. **(A)** FTIR spectra of CMC and SCMC. **(B)** FTIR spectra of κ-Car and CM-κ-Car. FTIR, Fourier-transform infrared spectroscopy; CMC, carboxymethyl cellulose; SCMC, sulfated carboxymethyl cellulose; κ-Car, κ-carrageenan; CM-κ-Car, carboxymethyl κ-carrageenan. **(C)** ^{1}H NMR spectra of CMC and SCMC. **(D)** ^{13}C NMR spectra of CMC and SCMC. **(E)** ^{1}H NMR spectra of κ-Car and CM-κ-Car. **(F)** ^{13}C NMR spectra of κ-Car and CM-κ-Car. NMR, Nuclear magnetic resonance; CMC, carboxymethyl cellulose; SCMC, sulfated carboxymethyl cellulose; κ-Car, κ-carrageenan; CM-κ-Car, carboxymethyl κ-carrageenan.

spectral analysis (Figures 3A,B). EDX spectra of 3D-printed PCL scaffolds indicated the presence of carbon [C; 55.95 ± 1.95 wt% (mean ± SD)], and oxygen (O; 41.05 ± 1.49 wt%) (Figure 3B). EDX spectra of 3D-printed PCL/SCMC scaffolds indicated the presence of carbon (C; 34.20 ± 1.80 wt%), oxygen (O; 24.35 ± 0.35 wt%), and sulfur (S; 15.50 ± 1.98 wt%) (Figure 3B). EDX spectra of 3D-printed PCL/CM-κ-Car scaffolds indicated the presence of carbon (C; 33.35 ± 0.65 wt%), oxygen (O; 20.45 ± 1.63 wt%), and sulfur (S; 19.75 ± 0.21 wt%) (Figure 3B). Surface-functionalization by SCMC or CM-κ-Car was validated by the

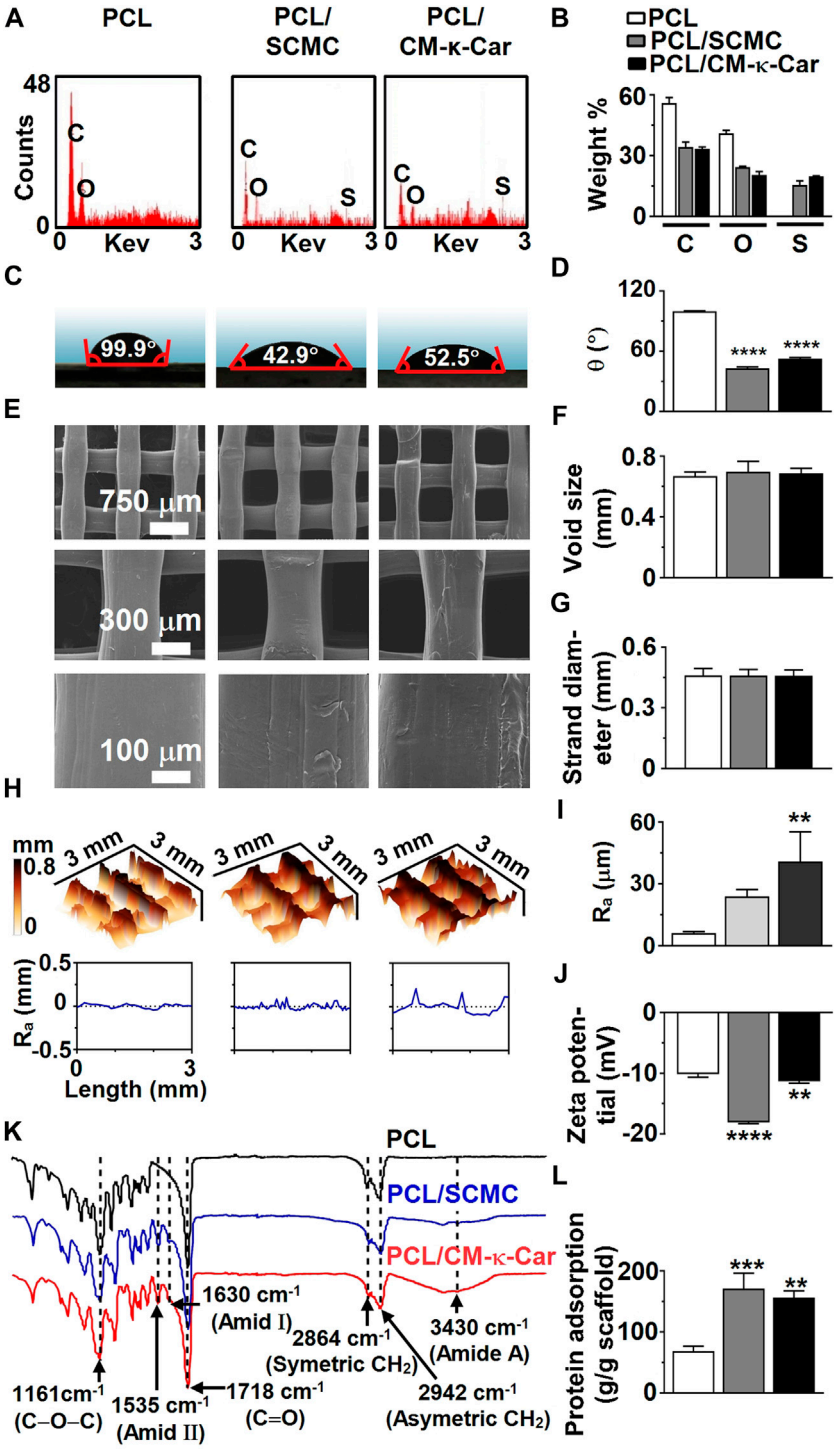

FIGURE 3
Effect of surface-functionalization of 3D-printed PCL scaffolds by SCMC or CM-κ-Car on surface chemistry, hydrophilicity, and topography. **(A)** EDX spectra indicating chemical elements. **(B)** Weight percent of carbon, oxygen, nitrogen, and sulfate. **(C)** Water contact angle on surface of scaffolds. **(D)** Average water contact angle. **(E)** SEM images showing the structure, morphology, and surface topography of the strands inside the scaffolds. **(F)** Void size. **(G)** Strand diameter. **(H)** 3D-view of scaffold surface topography showing surface-functionalization-dependent variation in surface roughness distribution and magnitude. R_a, average surface roughness. **(I)** Average surface roughness. **(J)** Zeta potential. **(K)** FTIR spectra indicating functional groups. **(L)** Protein adsorption on surface of scaffolds. Values are mean ± SD (n = 3). ***Significantly different from unfunctionalized 3D-printed PCL scaffold, $p < 0.0005$; ****$p < 0.0001$. PCL, poly-ε-caprolactone; SCMC, sulfated carboxymethyl cellulose; CM-κ-Car, carboxymethyl κ-carrageenan; EDX, energy dispersive X-ray spectroscopy; FTIR, Fourier-transform infrared spectroscopy, C, carbon; O, oxygen; N, nitrogen; S, sulfate. *Significantly different from unfunctionalized 3D-printed PCL scaffold, $p < 0.05$, ****$p < 0.0001$. PCL, poly-ε-caprolactone; SCMC, sulfated carboxymethyl cellulose; CM-κ-Car, carboxymethyl κ-carrageenan; SEM, scanning electron microscopy.

increment in the percentage of sulfur on PCL/SCMC and PCL/CM-κ-Car scaffolds (Figure 3B). Surface-functionalization by CM-κ-Car created higher sulfate groups (1.27-fold) on the surface of 3D-printed PCL scaffolds compared to SCMC (Figure 3B).

The hydrophilicity of the 3D-printed PCL scaffolds was analyzed by water contact angle measurement (Figures 3C,D). Surface-functionalization by SCMC and CM-κ-Car did affect the hydrophilicity of scaffolds (Figure 3C). The water contact angle was lower on PCL/SCMC (0.43-fold, $p < 0.0001$) and PCL/CM-κ-Car (0.53-fold, $p < 0.0001$) scaffolds than on unfunctionalized PCL scaffolds (Figure 3D). In addition, the water contact angle was lower on PCL/SCMC scaffolds (0.82-fold) than on PCL/CM-κ-Car scaffolds (Figure 3D).

Unfunctionalized 3D-printed PCL scaffolds had a regular structure with a smooth surface (Figure 3E). Surface-functionalization of PCL scaffolds by SCMC or CM-κ-Car resulted in surface irregularity with a surface topology exhibiting small peaks and troughs (Figure 3E). Surface-functionalization by SCMC or CM-κ-Car did not change the void size and strand diameter of PCL scaffolds (Figures 3F,G). Surface-functionalization by SCMC and CM-κ-Car had an effect on the PCL scaffolds' surface roughness distribution and magnitude (Figure 3H). The average surface roughness was higher on PCL/CM-κ-Car (6.62-fold, $p < 0.005$), but not PCL/SCMC, than on unfunctionalized PCL scaffolds (Figure 3I). The zeta potential was measured to determine the (negative) surface charge of the PCL (−10.14 ± 0.50 mV), PCL/SCMC (−18.09 ± 0.22 mV), and PCL/CM-κ-Car (−11.34 ± 0.30 mV) scaffolds (Figure 3J). The surface charge was negatively higher on PCL/SCMC scaffolds (1.78-fold, $p < 0.0001$) and PCL/CM-κ-Car scaffolds (1.12-fold, $p < 0.005$) than on unfunctionalized PCL scaffolds (Figure 3J).

The FTIR spectra of unfunctionalized 3D-printed PCL scaffolds showed PCL characteristic peaks at 2,942 cm^{-1} [asymmetric (CH_2) stretching], 2,864 cm^{-1} [symmetric (CH_2) stretching], 1718 cm^{-1} [carbonyl (C=O) group stretching], and 1,161 cm^{-1} [ester bond (C–O–C) stretching] (Figure 3K) (Zamani et al., 2018). The FTIR spectra of surface-functionalized scaffolds by SCMC and CM-κ-Car showed characteristic peaks at wavelengths 3,430 (amid A), 1,630 (amid I), and 1,535 cm^{-1} (amid II; Figure 3K) (Ilanlou et al., 2019; Alamry and Khan, 2021).

Surface-functionalization by SCMC and CM-κ-Car did affect protein adsorption on 3D-printed PCL scaffolds (Figure 3L). Protein adsorption was higher on PCL/SCMC (2.49-fold, $p < 0.0005$) and PCL/CM-κ-Car (2.28-fold, $p < 0.005$) scaffolds than on unfunctionalized PCL scaffolds (Figure 3L).

3.3 Mechanical properties

The von Mises stress distribution was less homogeneous on unfunctionalized PCL scaffolds than on PCL/SCMC and PCL/CM-κ-Car scaffolds (Figure 4A). The maximum von Mises stress for 2% compression strain ranged between 10.1 and 13.4 MPa for all types of scaffolds (Figure 4B). In all types of scaffolds, the maximal von Mises stress did not exceed the yield stress of bulk materials (Figure 4B). The surface-functionalization by SCMC and CM-κ-Car on PCL scaffolds did not significantly change the compressive strength (Figure 4C). The surface hardness was higher on PCL/SCMC (1.64-fold, $p < 0.0005$) and PCL/CM-κ-Car scaffolds (PCL/CM-κ-Car: 1.61-fold, $p < 0.0005$) compared to unfunctionalized PCL scaffolds (Figure 4D). The elastic modulus was lower on PCL/CM-κ-Car scaffolds (0.74-fold, $p < 0.05$), but not PCL/SCMC scaffolds, compared to unfunctionalized PCL scaffolds (Figure 4E). The variation in mean values of FE modeling and experimental results was only 8%–14%, which is generally accepted in validating FE modeling results by experimental data (Figure 4E) (Gupta et al., 2004). The surface-functionalization by SCMC and CM-κ-Car did not change the stress-strain relationship (Figure 4F).

3.4 Pre-osteoblast spreading, attachment, and gene expression

Surface-functionalization by SCMC and CM-κ-Car had an effect on pre-osteoblast morphology and spreading, as visualized by SEM imaging, on 3D-printed PCL scaffolds after 4 h of culture (Figure 5A). Pre-osteoblasts did not spread well on the surface of unfunctionalized PCL scaffolds and exhibited a slightly spherical morphology (Figure 5A). Surface-functionalization by SCMC and CM-κ-Car improved cell spreading on 3D-printed PCL scaffolds (Figure 5A). Well-spread cells with a natural spindle-shaped morphology were observed on the surface of PCL/SCMC and PCL/CM-κ-Car scaffolds (Figure 5A). Surface-functionalization by SCMC and CM-κ-Car did not change the pre-osteoblast seeding efficiency on 3D-printed PCL scaffolds after 8 h (Figure 5B). Seeding efficiency ranged between 75% (on PCL scaffolds) and 82% (on PCL/CM-κ-Car scaffolds) (Figure 5B).

Surface-functionalization by SCMC and CM-κ-Car did affect the expression of a proliferation marker gene and osteogenesis-related genes in pre-osteoblasts cultured on 3D-printed PCL scaffolds after 1 and 7 days (Figure 5C). *Ki67* gene expression was higher on 3D-printed PCL scaffolds compared to SCMC (0.30-fold, $p < 0.005$) and CM-κ-Car (0.42-fold, $p < 0.005$) surface-functionalized scaffolds after 1 day, but after 7 days, only PCL/SCMC (0.09-fold, $p < 0.05$) exhibited lower *Ki67* gene expression compared to PCL scaffolds. *Cox2* mRNA levels were higher on PCL/CM-κ-Car scaffolds (3.00-fold, $p < 0.005$), but not on PCL/SCMC scaffolds, compared to unfunctionalized PCL scaffolds after 1 day (Figure 5C). *Cox2* mRNA levels were not significantly different on all 3D-printed PCL scaffolds, with or without surface-functionalization at day 7 (Figure 5C). *Runx2* mRNA levels were higher on PCL/SCMC scaffolds, but not on PCL/CM-κ-Car scaffolds, after 1 day (0.26-fold, $p < 0.005$) or after 7 days (0.20-fold, $p < 0.0005$) compared with unfunctionalized PCL

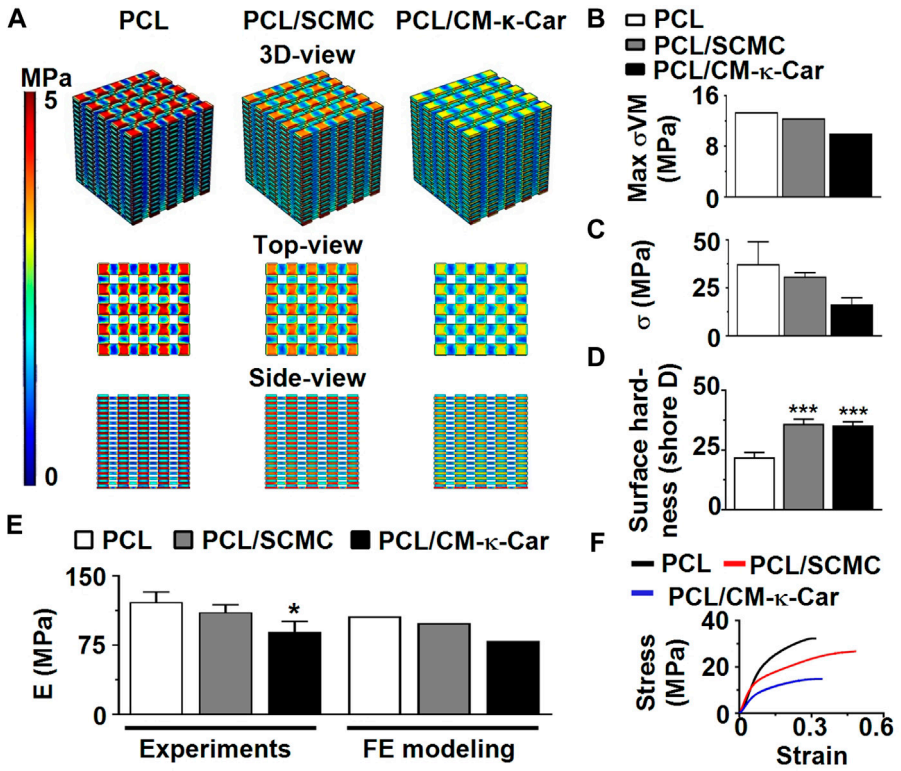

FIGURE 4
Effect of 3D-printed PCL scaffold surface-functionalization by SCMC or CM-κ-Car on mechanical properties. **(A)** 3D-view, top-view, and side-view of von Mises stress distribution on the scaffolds as a result of uniform 2% compression strain deformation determined by FE modeling. **(B)** Maximum von Mises stress. **(C)** Compressive strength. **(D)** Surface hardness. **(E)** Elastic modulus determined experimentally and by FE modeling. **(F)** Stress-strain curve. Values are mean ± SD (n = 3). *Significantly different from unfunctionalized 3D-printed PCL scaffold, $p < 0.05$, ****$p < 0.0001$. PCL, poly-ε-caprolactone; SCMC, sulfated carboxymethyl cellulose; CM-κ-Car, carboxymethyl κ-carrageenan; FE, finite element modeling.

scaffolds (Figure 5C). There were no significant differences in *Ocn* and *Fgf2* gene expression between 3D-printed PCL scaffolds with or without surface-functionalization after 1 or 7 days (Figure 5C). *Dmp1* mRNA levels were lower on PCL/SCMC scaffolds (0.51-fold, $p < 0.05$), but not on PCL/CM-κ-Car scaffolds, compared to unfunctionalized PCL scaffolds after 1 day (Figure 5C). However, *Dmp1* mRNA levels did not change on 3D-printed PCL scaffolds with or without surface-functionalization after 7 days (Figure 5C).

3.6 Pre-osteoblast proliferation

Surface-functionalization by SCMC and CM-κ-Car affected pre-osteoblast spreading and proliferation as visualized by SEM imaging, on 3D-printed PCL scaffolds after 4 h, 12 h, 3 days, and 28 days of culture (Figure 6A). Well-spread and proliferating cells were observed on the surface of PCL/SCMC and PCL/CM-κ-Car scaffolds (Figure 6A). Surface-functionalization by SCMC or CM-κ-Car did change pre-osteoblast proliferation on 3D-printed PCL scaffolds after 7, 14, 21, and 28 days in relation to day 1 (Figure 6B). At day 3, pre-osteoblast proliferation was similar on all types of scaffolds, while at day 7, pre-osteoblast proliferation was significantly higher on PCL/CM-κ-Car scaffolds (2.50-fold, $p < 0.0001$), but not on the PCL/SCMC scaffolds, than on unfunctionalized PCL scaffolds (Figure 6B). At day 14, pre-osteoblast proliferation was significantly higher on PCL/SCMC scaffolds (1.67-fold, $p < 0.05$) and on PCL/CM-κ-Car scaffolds (2.66-fold, $p < 0.0001$) than on unfunctionalized PCL scaffolds (Figure 6B). After 21 days, cell proliferation was higher on PCL/SCMC (1.73-fold, $p < 0.0001$) and PCL/CM-κ-Car (1.66-fold, $p < 0.0005$) scaffolds, and after 28 days, when cell proliferation was also higher on PCL/SCMC (1.89-fold, $p < 0.0005$) and on PCL/CM-κ-Car (1.30-fold, $p < 0.05$) scaffolds than on unfunctionalized scaffolds (Figure 6B).

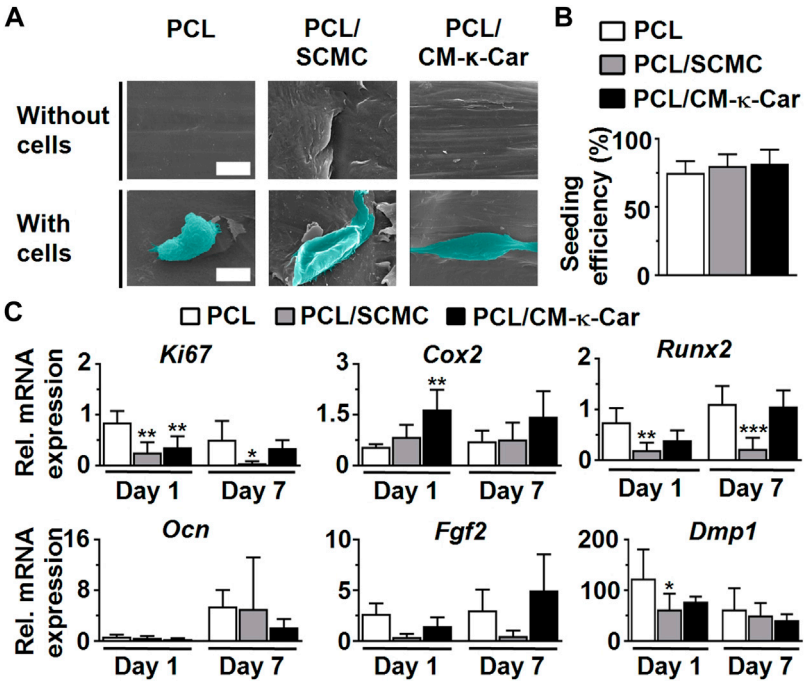

FIGURE 5
Effect of 3D-printed PCL scaffold surface-functionalization by SCMC or CM-κ-Car on MC3T3-E1 pre-osteoblast spreading, attachment, and gene expression. **(A)** SEM images showing pre-osteoblast morphology and spreading after 4 h. Scale bar: 10 μm. **(B)** Pre-osteoblast seeding efficiency. **(C)** Expression of osteogenic (*Runx2*, *Ocn*, *Dmp1*), proliferation (*Ki67*), and angiogenic-related (*Fgf2*) genes by MC3T3-E1 pre-osteoblasts after 1 and 7 days. Values are normalized to *Pbgd* expression. Values are mean ± SD ($n = 3$). *Significantly different from unfunctionalized 3D-printed PCL scaffolds, $p < 0.05$, ***$p < 0.0005$, ****$p < 0.0001$. PCL, poly-ε-caprolactone; SCMC, sulfated carboxymethyl cellulose; CM-κ-Car, carboxymethyl κ-carrageenan; SEM, scanning electron microscopy.

3.7 Alkaline phosphatase activity and protein

The osteoinductive ability of the scaffolds was evaluated by measuring ALP activity. ALP activity (blue) was increased, i.e., more intense blue staining, on PCL/CM-κ-Car scaffolds after 14, 21, and 28 days of culture compared to all other scaffolds (Figure 7A). At day 7, ALP activity was similar on all types of scaffolds (Figure 7B). At day 14, ALP activity was higher in PCL/SCMC (6.05-fold, $p < 0.005$) and on PCL/CM-κ-Car (6.02-fold, $p < 0.005$) scaffolds than on unfunctionalized scaffolds. Also, at day 21, ALP activity was higher on PCL/SCMC (2.90-fold, $p < 0.0001$) and on PCL/CM-κ-Car (3.14-fold, $p < 0.0001$) scaffolds than on unfunctionalized scaffolds (Figure 7B). Finally, at day 28, ALP activity was higher on PCL/SCMC (1.97-fold, $p < 0.0001$) and on PCL/CM-κ-Car (2.94-fold, $p < 0.0001$) scaffolds than on unfunctionalized PCL scaffolds (Figure 7B).

3.8 Collagenous matrix production

Collagen production (red) was enhanced, i.e., more intense red staining, on PCL/SCMC scaffolds after 7, 14, 21, and 28 days of culture compared to all other scaffolds (Figure 8A). At day 7, collagen production was higher on PCL/SCMC (1.73-fold, $p < 0.05$) scaffolds, but not on PCL/CM-κ-Car scaffolds, than on unfunctionalized PCL scaffolds (Figure 8B). At day 14, collagen production was similar on all types of scaffolds (Figure 8B). At day 21, collagen production was higher on PCL/SCMC (3.62-fold, $p < 0.0001$) scaffolds, but not on PCL/CM-κ-Car scaffolds, than on unfunctionalized PCL scaffolds (Figure 8B). At day 28, collagen production was higher on PCL/SCMC (3.95-fold, $p < 0.0001$) and on PCL/CM-κ-Car (2.35-fold, $p < 0.0001$) scaffolds than on unfunctionalized PCL scaffolds (Figure 8B).

3.9 Matrix mineralization

Surface-functionalization by SCMC and CM-κ-Car did affect matrix mineralization on 3D-printed PCL scaffolds after 7, 14, 21, and 28 days (Figure 9A). Matrix mineralization (red) was increased, i.e., more intense red staining, on PCL/CM-κ-Car scaffolds after 28 days of culture compared to all other scaffolds (Figure 9A). At days 7 and 14, matrix mineralization was similar on all types of scaffolds (Figure 9B). At day 21, matrix mineralization was

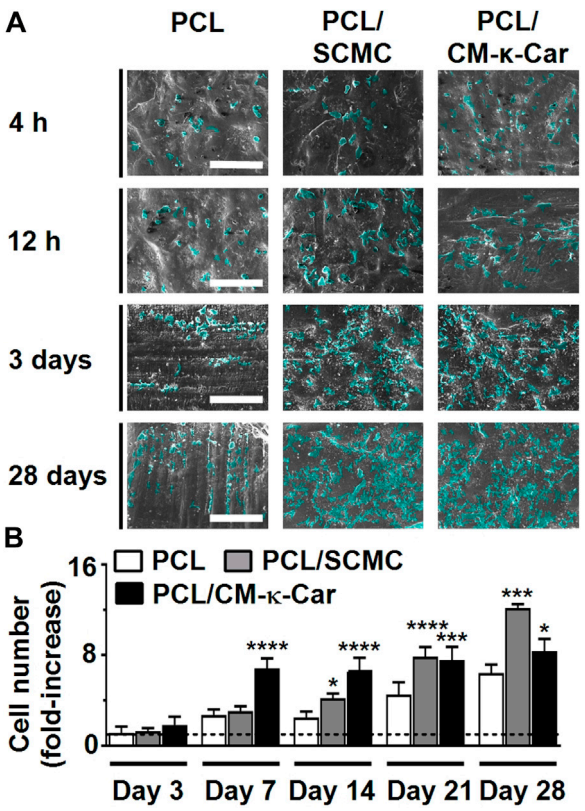

FIGURE 6
Effect of 3D-printed PCL scaffold surface-functionalization by SCMC or CM-κ-Car on MC3T3-E1 pre-osteoblast proliferation. **(A)** SEM images showing pre-osteoblasts after 4 h, 12 h, 3 days, and 28 days of culture. Scale bar: 200 μm. **(B)** Quantification of pre-osteoblast proliferation after 3, 7, 14, 21, and 28 days relative to day 1. Values are mean ± SD ($n = 3$). *Significantly different from unfunctionalized 3D-printed PCL scaffolds, $p < 0.05$, **$p < 0.005$, ****$p < 0.0001$. PCL, poly-ε-caprolactone; SCMC, sulfated carboxymethyl cellulose; CM-κ-Car, carboxymethyl κ-carrageenan; SEM, scanning electron microscopy.

higher on PCL/CM-κ-Car (2.11-fold, $p < 0.005$) scaffolds, but not on PCL/SCMC scaffolds, than on unfunctionalized PCL scaffolds (Figure 9B). At day 28, mineralization was higher on PCL/SCMC (2.12-fold, $p < 0.05$) and PCL/CM-κ-Car (4.23-fold, $p < 0.0001$) scaffolds than on unfunctionalized PCL scaffolds (Figure 9B).

4 Discussion

PCL is widely used to fabricate 3D-printed scaffolds. However, cell attachment and/or proliferation are not supported by PCL, resulting from a lack of bioactivity (Park et al., 2021). Surface-functionalization by bioactive agents can significantly improve the biological properties of 3D-printed PCL scaffolds (Park et al., 2021). Anionic polysaccharides, like CMC and κ-carrageenan, are used as naturally-derived bioactive agents for bone tissue engineering, based on their bone-like biological properties to facilitate cell adhesion, proliferation, and differentiation (Singh et al., 2016; Goonoo et al., 2017). The bioactivity of CMC and κ-carrageenan can be effectively increased by chemical modification, e.g., by sulfation and/or carboxymethylation (Madruga et al., 2020; Bhutada et al., 2021). The current study aimed to investigate the effects of surface-functionalization by SCMC or CM-κ-Car on the physicochemical and mechanical properties of 3D-printed PCL scaffolds, as well as the osteogenic response of pre-osteoblasts. We hypothesized that surface-functionalization by SCMC or CM-κ-Car on a 3D-printed PCL scaffold significantly affects the scaffold's physicochemical and mechanical properties, as well as the osteogenic response of pre-osteoblasts. We found that 1) Surface-functionalization by SCMC or CM-κ-Car did not change the scaffold geometry and structure; 2) Surface-functionalization by SCMC or CM-κ-Car similarly increased surface charge, hydrophilicity, surface roughness, and hardness; 3) Using FE-modeling, on all types of scaffolds the maximal von Mises stress for 2% compression strain did not exceed the yield stress for the bulk-material, showing that the scaffold will not show irreversible deformation when in use; 4) Surface-functionalization by SCMC, but not CM-κ-Car, decreased *Runx2* and *Dmp1* expression, while surface-functionalization by CM-κ-Car, but not by SCMC, increased *Cox2* expression; and 5) Surface-functionalization by SCMC most strongly enhanced proliferation and collagen production, while CM-κ-Car most significantly increased ALP activity and mineralization. Thus, our results revealed increased osteogenic differentiation potential in PCL/CM-κ-Car scaffolds compared to PCL/SCMC scaffolds *in vitro*, suggesting that surface-functionalization by CM-κ-Car may be more promising, especially in the short-term, for *in vivo* bone formation.

Our data confirmed that sulfation of CMC and carboxymethylation of k-carrageenan successfully occurred, suggesting improved CMC and k-carrageenan bioactivity (Hoseinpour et al., 2018; Madruga et al., 2020). Sulfation of carboxymethyl cellulose increases ALP activity and expression of osteogenic genes, e.g., osterix and noggin (Peschel et al., 2012). Carboxymethylation of k-carrageenan increases cytocompatibility, biodegradability, cell adhesion and growth, and osteogenic differentiation of stem cells (Madruga et al., 2021).

The surface chemical composition of scaffolds regulates osteoblast function and differentiation (Zreiqat et al., 2005). We found that the oxygen concentration on the surface of the strands in the PCL/SCMC scaffolds was higher compared to PCL/CM-κ-Car scaffolds, indicating the presence of more carboxymethyl groups in the PCL/SCMC scaffolds compared to PCL/CM-κ-Car scaffolds. Since carboxymethylation of poly (2-hydroxyethyl methacrylate) pellets has been shown to

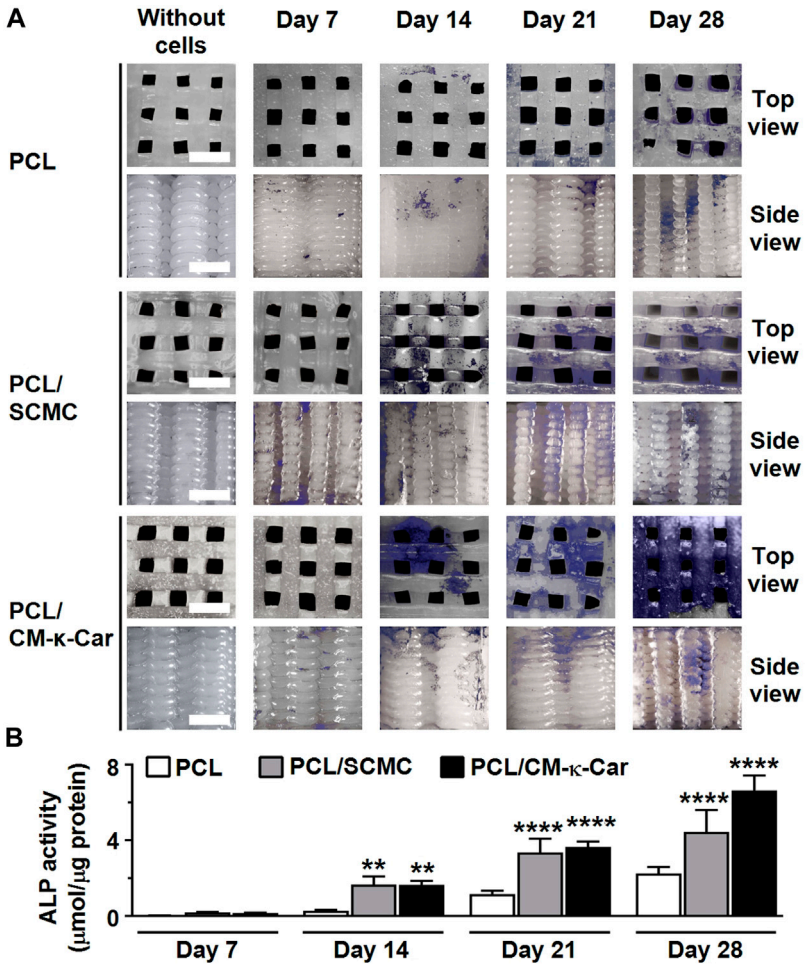

FIGURE 7
Effect of 3D-printed PCL scaffold surface-functionalization by SCMC or CM-κ-Car on ALP activity of MC3T3-E1 pre-osteoblasts after 7, 14, 21, and 28 days. **(A)** ALP staining (purple). Scale bar: 1.5 mm. **(B)** Quantification of ALP activity. Values are mean ± SD (n = 3). **Significantly different from control 3D-printed PCL scaffolds, $p < 0.005$, ****$p < 0.0001$. PCL, poly-ε-caprolactone; SCMC, sulfated carboxymethyl cellulose; CM-κ-Car, carboxymethyl κ-carrageenan.

enhance osteoblast adherence and proliferation (Filmon et al., 2002), our results suggest that PCL/SCMC scaffolds are more favorable than PCL/CM-κ-Car scaffolds for pre-osteoblast attachment and proliferation. We also found that the sulfur concentration on the surface of the strands in the PCL/CM-κ-Car scaffolds was higher compared to PCL/SCMC scaffolds, illustrating more sulfate groups in the PCL/CM-κ-Car scaffolds compared to PCL/SCMC scaffolds. Since sulfate groups promote osteogenic differentiation (Ruiz Velasco et al., 2011), our findings suggest that PCL/CM-κ-Car scaffolds stimulate osteogenic differentiation more strongly than PCL/SCMC scaffolds.

Our data showed that surface functionalization of PCL scaffolds by SCMC or CM-κ-Car introduced polar molecules, *i.e.* oxygen and sulfur, at the surface, resulting in a more negatively charged scaffold surface. A negative surface charge improves osteogenic activity in Saos-2 and MC3T3-E1 cells (Radha et al., 2021). Therefore, a negative surface charge, as we found in our study, might suggest enhanced osteogenic activity as a result of SCMC or CM-κ-Car surface-functionalization.

Our data showed that 3D-printed PCL scaffolds had a regular structure and interconnected pores. Such a structure and porosity promote oxygen diffusion and cell proliferation (Seddiqi et al., 2020). As expected, surface-functionalization by SCMC and CM-κ-Car did not change the scaffolds' structure. Moreover, we found that the average void size of the surface-functionalized scaffolds ranged from 600 to 700 μm. Such a void size promotes cell growth and matrix mineralization *in vitro*, as well as bone formation *in vivo* (Ouyang et al., 2019). We also found that surface-functionalization by SCMC or CM-κ-Car resulted in surface irregularity with peaks and troughs, indicating that our surface functionalization affected protein adsorption and

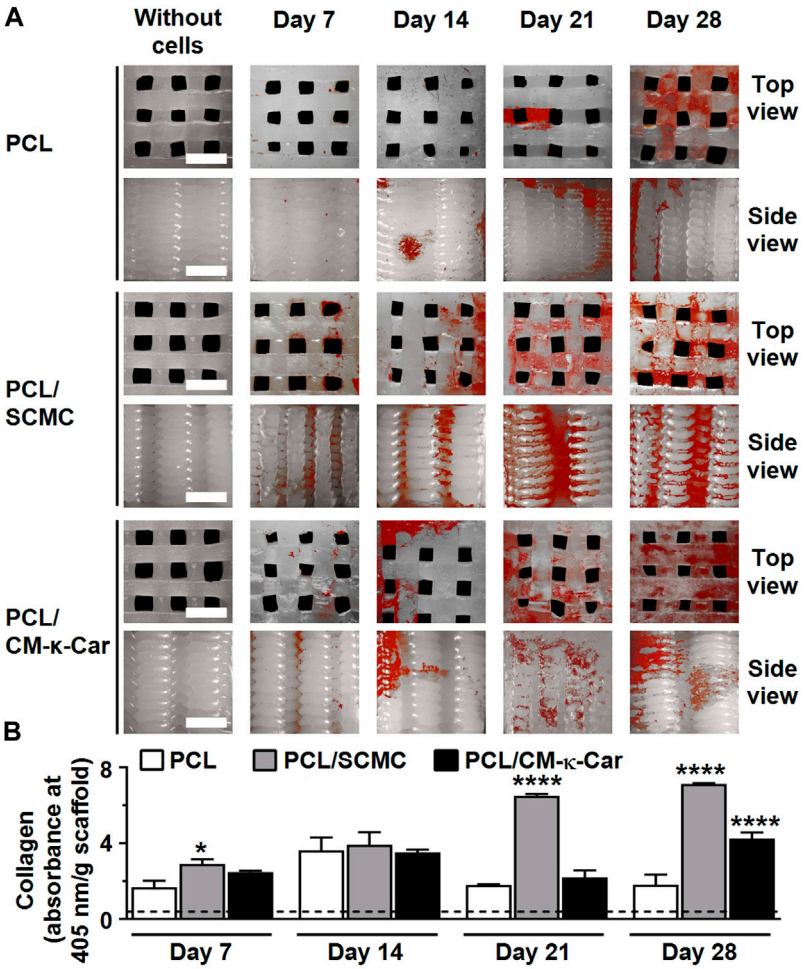

FIGURE 8
Effect of 3D-printed PCL scaffold surface-functionalization by SCMC or CM-κ-Car on collagen production by MC3T3-E1 pre-osteoblasts after 7, 14, 21, and 28 days. **(A)** Collagen staining (red). Collagenous matrix production, visualized by picrosirius red staining. Scale bar: 1.5 mm. **(B)** Quantification of collagen production. Values are mean ± SD (n = 3). *Significantly different from control 3D-printed PCL scaffolds, $p < 0.05$, ****$p < 0.0001$. PCL, poly-ε-caprolactone; SCMC, sulfated carboxymethyl cellulose; CM-κ-Car, carboxymethyl κ-carrageenan.

cell behavior, as has been shown for PCL films (Khampieng et al., 2018). Surface roughness, on a micron scale, improves cell attachment, viability, and osteogenic differentiation (Zhang et al., 2015; Lukaszewska-Kuska et al., 2018). We showed that surface-functionalization by SCMC or CM-κ-Car of PCL scaffolds changed surface roughness distribution, and slightly increased surface roughness. Surface-functionalization by CM-κ-Car most significantly increased surface roughness. Therefore, these surface-functionalized scaffolds might promote cell attachment, viability, and osteogenic differentiation *in vitro*, as has been observed for surface-modified titanium with increased surface roughness (Lukaszewska-Kuska et al., 2018).

Cells can only adhere to the surface of a biomaterial after protein from body fluid is adsorbed onto the biomaterial. Our data showed that surface functionalization of PCL scaffolds by SCMC or CM-κ-Car improves protein adsorption. This was expected since surface hydrophilicity and roughness enhance protein adsorption (Akkas et al., 2013). In addition, a negative surface charge aids protein adsorption through ionic and hydrogen bonding (Aramesh et al., 2015). The presence of sulfate groups on the scaffold surface also improves protein adsorption (Kim et al., 2010). Adsorbed proteins, such as fibronectin and vitronectin, activate the focal adhesion pathway, ECM-receptor interaction pathway, and regulate actin cytoskeleton formation (Yang et al., 2013). Enhanced fibronectin adsorption on a sulfated polymer-grafted surface stimulates the pre-osteoblast attachment (Felgueiras et al., 2015). Fibronectin also plays an important role in cell proliferation and differentiation (Linsley et al., 2013). Moreover, it has been shown that sulfated polymer grafting onto a scaffold surface increases the secretion of fibronectin and collagen by osteoblasts (Pavon-Djavid et al., 2007). The

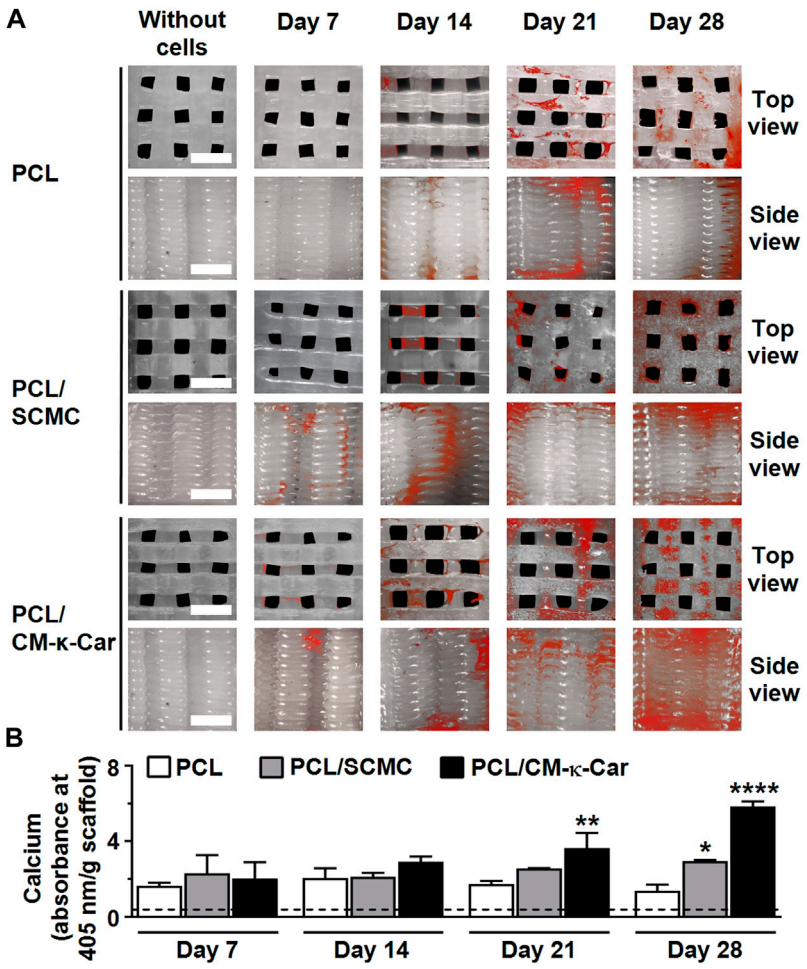

FIGURE 9
Effect of 3D-printed PCL scaffold surface-functionalization by SCMC or CM-κ-Car on matrix mineralization by MC3T3-E1 pre-osteoblasts after 7, 14, 21, and 28 days. **(A)** Mineral deposition staining (alizarin red). Scale bar: 1.5 mm. **(B)** Quantified mineral content. Values are mean ± SD (n = 3). *Significantly different from control 3D-printed PCL scaffolds, $p < 0.05$, **$p < 0.005$, ****$p < 0.0001$. PCL, polycaprolactone; SCMC, sulfated carboxymethyl cellulose; CM-κ-Car, carboxymethyl κ-carrageenan.

sulfated polysaccharide κ-Car promotes paxillin protein expression by pre-osteoblasts (Cao et al., 2021). Protein adsorption on a scaffold surface promotes cell adhesion, proliferation, and osteogenic differentiation (Gandavarapu et al., 2013). Therefore, our finding that cell attachment, proliferation and osteogenic activity were increased on surface-functionalized PCL scaffolds by SCMC or CM-κ-Car might be related to improved protein adsorption.

3D-printed scaffolds should have a favorable mechanical strength to meet the mechanical requirements for target bone tissue and should retain their structure to maintain their mechanical function after implantation (Zamani et al., 2020). Our data showed that surface functionalization of PCL scaffolds by SCMC or CM-κ-Car did not meaningfully change the elastic modulus and compressive strength. Note that the scaffolds were not meant to deform beyond the elastic, reversible region, and the ultimate compressive strength was controlled, as a safety feature. Therefore, the reduction in ultimate compressive strength had little importance to the functionality of the scaffolds. Furthermore, we showed that for all types of scaffolds the maximal von Mises stress for 2% compression strain was within the elastic region. We also showed that the surface hardness of the surface-functionalized scaffolds was remarkedly increased, which provided a more bone-like feature to promote osteogenic differentiation due to the stiffer surface, thus modulating mechano-transduction pathways (Shih et al., 2011).

Cell attachment and spreading are necessary steps toward the clinical translation of 3D scaffolds to be used for tissue engineering applications (Sobral et al., 2011). We found that the seeding efficiency of all surface-functionalized and

unfunctionalized 3D-printed PCL scaffolds was similar, likely because the same large 3D-scaffold structure enabled cell entrapment. Moreover, we found that pre-osteoblasts exhibited a slightly spherical morphology on unfunctionalized 3D-printed PCL scaffolds. This was expected since PCL is hydrophobic and lacks biological recognition sites (Park et al., 2021). In addition, we found that pre-osteoblasts exhibited a well-spread morphology on scaffolds that were surface-functionalized by SCMC or CM-κ-Car compared to PCL scaffolds. This can be explained by increased hydrophilicity, as well as by the presence of carboxyl and sulfate groups in the chemical structures of SCMC and CM-κ-Car.

Cell-material interaction is crucial for cell survival and cellular functions such as cell viability, proliferation, differentiation, and mineralization (Zamani et al., 2018). In our study, SCMC or CM-κ-Car surface-functionalized 3D-printed PCL scaffolds did not affect *Ki67* gene expression by pre-osteoblasts at day 1 and 7. Since proliferation was enhanced by SCMC or CM-κ-Car surface-functionalization, *Ki67* gene expression might be changed at a later time point. Surface-functionalization of all 3D-printed scaffolds did not affect *Ocn* and *Fgf2* gene expression at day 1 and 7, but did affect *Dmp1* expression at day 1. These three genes are known to be related to extracellular matrix (ECM) mineralization in the long term, and therefore their expression might not be affected significantly immediately upon exposure to a surface-functionalized PCL scaffold, but only at later time points. We found that 3D-printed PCL scaffold surface functionalization by SCMC or CM-κ-Car considerably affected the scaffold's physicochemical properties, which might have affected ECM mineralization *via* expression of other molecules, e.g., E11/gp38 glycoprotein or sclerostin (Prideaux et al., 2012). Future studies are needed to test this hypothesis. *Cox2* and *Runx2* gene expression were upregulated respectively downregulated by SCMC and CM-κ-Car surface functionalization. The downregulation of *Runx2* gene expression was unexpected and needs further experimentation for clarification. The SCMC or CM-κ-Car surface functionalization-stimulated osteogenic differentiation might mainly rely on *Cox2* activity in the short-term (before day 7). Based on the long-term data (ALP activity, collagen production, and matrix mineralization), other osteogenic genes were likely involved in osteogenic differentiation of pre-osteoblasts cultured on 3D-printed PCL scaffolds with or without surface functionalization.

3D scaffolds must promote cell proliferation inside their structures. Our data showed that cell proliferation was similar in all types of scaffolds after 3 days, but diverged after 7 days. SCMC or CM-κ-Car surface-functionalized 3D-printed PCL scaffolds did affect cell proliferation in a later stage of culture, i.e., after 14 days. Surface charge and wettability have been shown to affect early stage mineralization and bone cell–calcium phosphate interactions (Bodhak et al., 2009). Moreover, PCL scaffold roughness affects cell attachment and growth with minimal loss of mechanical strength (Gupta et al., 2019). Therefore, the increased proliferation as a result of SCMC or CM-κ-Car surface-functionalization as we found in the current study might be explained by enhanced surface hydrophilicity, roughness, and charge.

ALP activity and collagen production are important for bone formation (Jin et al., 2021). We found that ALP activity of pre-osteoblasts on 3D-printed PCL scaffolds without and with surface-functionalization by SCMC or CM-κ-Car was similar after 7 days. After 14, 21, and 28 days of culture, the pre-osteoblasts showed higher levels of ALP activity on surface-functionalized scaffolds, indicating enhanced osteogenic differentiation on surface-functionalized 3D-printed PCL scaffolds. This was expected since both sulfate and carboxymethyl groups enhance ALP activity of pre-osteoblasts (Nakaoka et al., 2010). We also found that PCL/CM-κ-Car scaffolds more strongly stimulate ALP activity compared to PCL/SCMC scaffolds after 28 days of culture. Moreover, our data showed that collagen production by pre-osteoblasts on SCMC or CM-κ-Car surface-functionalized 3D-printed PCL scaffolds was increased compared to unfunctionalized scaffolds after 21 and 28 days of culture. This was expected since sulfate groups enhance osteogenic differentiation of pre-osteoblasts (Miyazaki et al., 2008). We found that the oxygen concentration on the surface of the strand in the PCL/SCMC scaffolds was higher compared to PCL/CM-κ-Car scaffolds, resulting in enhanced hydrophilicity and cell proliferation. Since increased hydrophilicity enhances cell proliferation and collagen production (Ghilini et al., 2021), our results suggest that PCL/SCMC scaffolds more strongly stimulate cell proliferation and collagen production compared to PCL/CM-κ-Car scaffolds. However, since surface-functionalization by CM-κ-Car more strongly enhanced ALP activity, surface-functionalization by both SCMC and CM-κ-Car seems promising for stimulating bone formation.

An important factor for bone tissue engineering scaffolds is their ability to enhance matrix mineralization. We found that surface-functionalized 3D-printed PCL scaffolds by SCMC or CM-κ-Car facilitated matrix mineralization after 21 days. This increased matrix mineralization can be explained by the fact that surface-functionalization resulted in a more negative surface charge of the scaffolds due to the presence of carboxyl and sulfate groups, which enabled efficient interaction with calcium ions (Liu et al., 2014). We also found that surface-functionalization by CM-κ-Car resulted in more mineralization compared to SCMC, which might be due to the presence of more sulfate groups in the chemical structure of CM-κ-Car compared to SCMC, as well as to increased surface roughness of PCL/CM-κ-Car scaffolds compared to PCL/SCMC scaffolds. Therefore, our findings suggest that surface chemical composition, which determines surface ionic charge and zeta potential, as well as surface roughness, may be key factors in the regulation of pre-osteoblast proliferation and osteogenic activity, more than surface hardness and hydrophilicity.

5 Conclusion

In the present study, 3D-printed PCL scaffolds were successfully surface-functionalized by SCMC or CM-κ-Car. Surface-functionalized 3D-printed PCL scaffolds did possess higher surface hydrophilicity, negative charge, roughness, and hardness than unfunctionalized scaffolds, and improved MC3T3-E1 pre-osteoblast adhesion, proliferation, ALP activity, collagen production, and matrix mineralization. SCMC is superior to CM-κ-Car in promoting pre-osteoblast proliferation, but CM-κ-Car has an important advantage over SCMC in promoting osteogenic differentiation of pre-osteoblasts, suggesting surface-functionalization by CM-κ-Car may be more promising, especially in the short-term, for *in vivo* bone formation.

Our scaffolds have to be further studied regarding efficient vascularization for successful clinical implementation. Moreover, future research will have to elucidate whether these relatively small 3D-printed scaffolds can also be used in large critical sized bone defects without changing physicochemical characteristics and bioactivity. Finally, in view of clinical application of these surface-functionalized 3D-printed PCL scaffolds, their ability to promote cell behavior and bone formation should be investigated in bioreactors, *in-situ*, and *in vivo*.

Data availability statement

The data that support the findings of this study are openly available in the Figshare repository: https://figshare.com/s/acc742db2687855bed2d.

Author contributions

Conceptualization, SA-R, HS, and JK-N; Formal analysis, HS; Funding acquisition, RB; Investigation, SA-R, HS, AM, M-EG, and JJ; Methodology, SA-R, and HS; supervision, JK-N; Visualization, SA-R, and HS, writing—original draft preparation, SA-R, HA, and EO; writing—review and editing, SA-R, HS, AM, M-EG, JJ, EO, RB, and JK-N. All authors have read and agreed to the published version of the manuscript.

Funding

RG Bacabac was funded by DOST project No. 09438 (monitored by DOST-PCIEERD) and received logistic support from the USC-RDEPO and Department of Physics.

Conflict of interest

The authors declare that the research was conducted in the absence of any commercial or financial relationships that could be construed as a potential conflict of interest.

Publisher's note

All claims expressed in this article are solely those of the authors and do not necessarily represent those of their affiliated organizations, or those of the publisher, the editors and the reviewers. Any product that may be evaluated in this article, or claim that may be made by its manufacturer, is not guaranteed or endorsed by the publisher.

References

Akkas, T., Citak, C., Sirkecioglu, A., and Güner, F. S. (2013). Which is more effective for protein adsorption: Surface roughness, surface wettability or swelling? Case study of polyurethane films prepared from castor oil and poly (ethylene glycol). *Polym. Int.* 62, 1202–1209. doi:10.1002/pi.4408

Alamry, K. A., and Khan, A. (2021). Efficient and easily retrievable green modified carboxymethyl cellulose coated A. indica stem bark encapsulated metal nanoparticles towards the reduction of o-nitrophenol and azo dyes. *Appl. Nanosci.* 11, 1057–1074. doi:10.1007/s13204-021-01672-3

Aramesh, M., Shimoni, O., Ostrikov, K., Prawer, S., and Cervenka, J. (2015). Surface charge effects in protein adsorption on nanodiamonds. *Nanoscale* 7, 5726–5736. doi:10.1039/c5nr00250h

ASTM (2013). *D7490–13 Standard test method for measurement of the surface tension of solid coatings, substrates and pigments using contact angle measurements*. West Conshohocken, PA, United States: Astm.

Baptista, R., and Guedes, M. (2020). Morphological and mechanical characterization of 3D printed PLA scaffolds with controlled porosity for trabecular bone tissue replacement. *Mater. Sci. Eng. C* 118, 111528. doi:10.1016/j.msec.2020.111528

Bhutada, S. S., Sriram, M., and Katti, D. S. (2021). Sulfated carboxymethylcellulose conjugated electrospun fibers as a growth factor presenting system for tissue engineering. *Carbohydr. Polym.* 268, 118256. doi:10.1016/j.carbpol.2021.118256

Bodhak, S., Bose, S., and Bandyopadhyay, A. (2009). Role of surface charge and wettability on early stage mineralization and bone cell–materials interactions of polarized hydroxyapatite. *Acta Biomater.* 5, 2178–2188. doi:10.1016/j.actbio.2009.02.023

Cao, W., Jin, J., Wu, G., Bravenboer, N., Helder, M. N., Pathak, J. L., et al. (2021). K-Carrageenan stimulates pre-osteoblast proliferation and osteogenic differentiation: A potential factor for the promotion of bone regeneration? *Molecules* 26, 6131. doi:10.3390/molecules26206131

Dong, L., Wang, S.-J., Zhao, X.-R., Zhu, Y.-F., and Yu, J.-K. (2017). 3D-printed poly (ε-caprolactone) scaffold integrated with cell-laden chitosan hydrogels for bone tissue engineering. *Sci. Rep.* 7, 13412–13419. doi:10.1038/s41598-017-13838-7

Dwivedi, R., Kumar, S., Pandey, R., Mahajan, A., Nandana, D., Katti, D. S., et al. (2020). Polycaprolactone as biomaterial for bone scaffolds: Review of literature. *J. Oral Biol. Craniofac. Res.* 10, 381–388. doi:10.1016/j.jobcr.2019.10.003

Entezari, A., Roohani, I., Li, G., Dunstan, C. R., Rognon, P., Li, Q., et al. (2019). Architectural design of 3D printed scaffolds controls the volume and functionality of newly formed bone. *Adv. Healthc. Mat.* 8, 1801353. doi:10.1002/adhm.201801353

Fan, L., Zhou, X., Wu, P., Xie, W., Zheng, H., Tan, W., et al. (2014). Preparation of carboxymethyl cellulose sulfates and its application as anticoagulant and wound dressing. *Int. J. Biol. Macromol.* 66, 245–253. doi:10.1016/j.ijbiomac.2014.02.040

Felgueiras, H. P., Evans, M. D., and Migonney, V. (2015). Contribution of fibronectin and vitronectin to the adhesion and morphology of MC3T3-E1

osteoblastic cells to poly (NaSS) grafted Ti6Al4V. *Acta Biomater.* 28, 225–233. doi:10.1016/j.actbio.2015.09.030

Filmon, R., Grizon, F., Basle, M., and Chappard, D. (2002). Effects of negatively charged groups (carboxymethyl) on the calcification of poly (2-hydroxyethyl methacrylate). *Biomaterials* 23, 3053–3059. doi:10.1016/s0142-9612(02)00069-8

Gandavarapu, N. R., Mariner, P. D., Schwartz, M. P., and Anseth, K. S. (2013). Extracellular matrix protein adsorption to phosphate-functionalized gels from serum promotes osteogenic differentiation of human mesenchymal stem cells. *Acta Biomater.* 9, 4525–4534. doi:10.1016/j.actbio.2012.09.007

Ghilini, F., Fagali, N., Pissinis, D. E., Benítez, G., and Schilardi, P. L. (2021). Multifunctional titanium surfaces for orthopedic implants: Antimicrobial activity and enhanced osseointegration. *ACS Appl. Bio Mat.* 4, 6451–6461. doi:10.1021/acsabm.1c00613

Goonoo, N., Khanbabaee, B., Steuber, M., Bhaw-Luximon, A., Jonas, U., Pietsch, U., et al. (2017). κ-Carrageenan enhances the biomineralization and osteogenic differentiation of electrospun polyhydroxybutyrate and polyhydroxybutyrate valerate fibers. *Biomacromolecules* 18, 1563–1573. doi:10.1021/acs.biomac.7b00150

Gupta, D., Singh, A. K., Kar, N., Dravid, A., and Bellare, J. (2019). Modelling and optimization of NaOH-etched 3-D printed PCL for enhanced cellular attachment and growth with minimal loss of mechanical strength. *Mater. Sci. Eng. C* 98, 602–611. doi:10.1016/j.msec.2018.12.084

Gupta, S., Van Der Helm, F., Sterk, J., Van Keulen, F., and Kaptein, B. (2004). Development and experimental validation of a three-dimensional finite element model of the human scapula. *Proc. Inst. Mech. Eng. H.* 218, 127–142. doi:10.1243/095441104322984022

Hoseinpour, V., Ghaee, A., Vatanpour, V., and Ghaemi, N. (2018). Surface modification of PES membrane via aminolysis and immobilization of carboxymethylcellulose and sulphated carboxymethylcellulose for hemodialysis. *Carbohydr. Polym.* 188, 37–47. doi:10.1016/j.carbpol.2018.01.106

Ilanlou, S., Khakbiz, M., Amoabediny, G., Mohammadi, J., and Rabbani, H. (2019). Carboxymethyl kappa Carrageenan-modified decellularized small-diameter vascular grafts improving thromboresistance properties. *J. Biomed. Mat. Res. A* 107, 1690–1701. doi:10.1002/jbm.a.36684

Jin, J., Seddiqi, H., Bakker, A. D., Wu, G., Verstappen, J. F., Haroon, M., et al. (2021). Pulsating fluid flow affects pre-osteoblast behavior and osteogenic differentiation through production of soluble factors. *Physiol. Rep.* 9, e14917. doi:10.14814/phy2.14917

Joseph, B., James, J., Grohens, Y., Kalarikkal, N., and Thomas, S. (2020). Additive manufacturing of poly (ε-caprolactone) for tissue engineering. *JOM* 72, 4127–4138. doi:10.1007/s11837-020-04382-3

Khampieng, T., Yamassatien, V., Ekabutr, P., Pavasant, P., and Supaphol, P. (2018). Protein adsorption and cell behaviors on polycaprolactone film: The effect of surface topography. *Adv. Polym. Technol.* 37, 2030–2042. doi:10.1002/adv.21861

Kim, S., Pyo, H.-B., Ko, S. H., Ah, C. S., Kim, A., and Kim, W.-J. (2010). Fabrication of anionic sulfate-functionalized nanoparticles as an immunosensor by protein immobilization. *Langmuir* 26, 7355–7364. doi:10.1021/la9043717

Kroeze, R. J., Knippenberg, M., and Helder, M. N. (2011). Osteogenic differentiation strategies for adipose-derived mesenchymal stem cells. *Methods Mol. Biol.* 702, 233–248. doi:10.1007/978-1-61737-960-4_17

Linsley, C., Wu, B., and Tawil, B. (2013). The effect of fibrinogen, collagen type I, and fibronectin on mesenchymal stem cell growth and differentiation into osteoblasts. *Tissue Eng. Part A* 19, 1416–1423. doi:10.1089/ten.tea.2012.0523

Liu, H., Ahlinder, A., Yassin, M. A., Finne-Wistrand, A., and Gasser, T. C. (2020). Computational and experimental characterization of 3D-printed PCL structures toward the design of soft biological tissue scaffolds. *Mater. Design.* 188, 108488. doi:10.1016/j.matdes.2020.108488

Liu, H., Cheng, J., Chen, F., Hou, F., Bai, D., Xi, P., et al. (2014). Biomimetic and cell-mediated mineralization of hydroxyapatite by carrageenan functionalized graphene oxide. *ACS Appl. Mat. Interfaces* 6, 3132–3140. doi:10.1021/am4057826

Lukaszewska-Kuska, M., Wirstlein, P., Majchrowski, R., and Dorocka-Bobkowska, B. (2018). Osteoblastic cell behaviour on modified titanium surfaces. *Micron* 105, 55–63. doi:10.1016/j.micron.2017.11.010

Madruga, L. Y., Balaban, R. C., Popat, K. C., and Kipper, M. J. (2021). Biocompatible crosslinked nanofibers of Poly (Vinyl Alcohol)/carboxymethyl-kappa-carrageenan produced by a green process. *Macromol. Biosci.* 21, 2000292. doi:10.1002/mabi.202000292

Madruga, L. Y., Sabino, R. M., Santos, E. C., Popat, K. C., Balaban, R. d. C., and Kipper, M. J. (2020). Carboxymethyl-kappa-carrageenan: A study of biocompatibility, antioxidant and antibacterial activities. *Int. J. Biol. Macromol.* 152, 483–491. doi:10.1016/j.ijbiomac.2020.02.274

Malliappan, S. P., Yetisgin, A. A., Sahin, S. B., Demir, E., and Cetinel, S. (2022). Bone tissue engineering: Anionic polysaccharides as promising scaffolds. *Carbohydr. Polym.* 283, 119142. doi:10.1016/j.carbpol.2022.119142

Miyazaki, T., Miyauchi, S., Tawada, A., Anada, T., Matsuzaka, S., and Suzuki, O. (2008). Oversulfated chondroitin sulfate-E binds to BMP-4 and enhances osteoblast differentiation. *J. Cell. Physiol.* 217, 769–777. doi:10.1002/jcp.21557

Mobarak, N., Ramli, N., Ahmad, A., and Rahman, M. (2012). Chemical interaction and conductivity of carboxymethyl κ-carrageenan based green polymer electrolyte. *Solid State Ion.* 224, 51–57. doi:10.1016/j.ssi.2012.07.010

Moghaddaszadeh, A., Seddiqi, H., Najmoddin, N., Ravasjani, S. A., and Klein-Nulend, J. (2021). Biomimetic 3D-printed PCL scaffold containing a high concentration carbonated-nanohydroxyapatite with immobilized-collagen for bone tissue engineering: Enhanced bioactivity and physicomechanical characteristics. *Biomed. Mat.* 16, 065029. doi:10.1088/1748-605x/ac3147

Muzzarelli, R. A., Tanfani, F., Emanuelli, M., Pace, D. P., Chiurazzi, E., and Piani, M. (1984). Sulfated N-(carboxymethyl) chitosans: Novel blood anticoagulants. *Carbohydr. Res.* 126, 225–231. doi:10.1016/0008-6215(84)85380-x

Nakaoka, R., Yamakoshi, Y., Isama, K., and Tsuchiya, T. (2010). Effects of surface chemistry prepared by self-assembled monolayers on osteoblast behavior. *J. Biomed. Mat. Res. A* 94, 524–532. doi:10.1002/jbm.a.32714

Ouyang, P., Dong, H., He, X., Cai, X., Wang, Y., Li, J., et al. (2019). Hydromechanical mechanism behind the effect of pore size of porous titanium scaffolds on osteoblast response and bone ingrowth. *Mat. Des.* 183, 108151. doi:10.1016/j.matdes.2019.108151

Palhares, L. C., London, J. A., Kozlowski, A. M., Esposito, E., Chavante, S. F., Ni, M., et al. (2021). Chemical modification of glycosaminoglycan polysaccharides. *Molecules* 26, 5211. doi:10.3390/molecules26175211

Park, J., Lee, S. J., Jung, T. G., Lee, J. H., Kim, W. D., Lee, J. Y., et al. (2021). Surface modification of a three-dimensional polycaprolactone scaffold by polydopamine, biomineralization, and BMP-2 immobilization for potential bone tissue applications. *Colloids Surfaces B Biointerfaces* 199, 111528. doi:10.1016/j.colsurfb.2020.111528

Pavon-Djavid, G., Gamble, L., Ciobanu, M., Gueguen, V., Castner, D., and Migonney, V. (2007). Bioactive poly (ethylene terephthalate) fibers and fabrics: Grafting, chemical characterization, and biological assessment. *Biomacromolecules* 8, 3317–3325. doi:10.1021/bm070344i

Peschel, D., Zhang, K., Fischer, S., and Groth, T. (2012). Modulation of osteogenic activity of BMP-2 by cellulose and chitosan derivatives. *Acta Biomater.* 8, 183–193. doi:10.1016/j.actbio.2011.08.012

Prideaux, M., Loveridge, N., Pitsillides, A. A., and Farquharson, C. (2012). Extracellular matrix mineralization promotes E11/gp38 glycoprotein expression and drives osteocytic differentiation. *PloS one* 7, e36786. doi:10.1371/journal.pone.0036786

Radha, G., Venkatesan, B., Jaisankar, S. N., Rajashree, P., and Balakumar, S. (2021). Interplay between surface chemistry and osteogenic behaviour of sulphate substituted nano-hydroxyapatite. *Mat. Sci. Eng. C Mat. Biol. Appl.* 120, 111617. doi:10.1016/j.msec.2020.111617

Ruiz Velasco, C., Baud'Huin, M., Sinquin, C., Maillasson, M., Heymann, D., Colliec-Jouault, S., et al. (2011). Effects of a sulfated exopolysaccharide produced by Altermonas infernus on bone biology. *Glycobiology* 21, 781–795. doi:10.1093/glycob/cwr002

Saatchi, A. R., Seddiqi, H., Amoabediny, G., Helder, M. N., Zandieh-Doulabi, B., and Klein-Nulend, J. (2020). Computational fluid dynamics in 3D-printed scaffolds with different strand-orientation in perfusion bioreactors. *Iran. J. Chem. Chem. Eng.* 39, 307–320. doi:10.30492/IJCCE.2019.35867

Seddiqi, H., Oliaei, E., Honarkar, H., Jin, J., Geonzon, L. C., Bacabac, R. G., et al. (2021). Cellulose and its derivatives: Towards biomedical applications. *Cellulose* 28, 1893–1931. doi:10.1007/s10570-020-03674-w

Seddiqi, H., Saatchi, A., Amoabediny, G., Helder, M. N., Ravasjani, S. A., Aghaei, M. S. H., et al. (2020). Inlet flow rate of perfusion bioreactors affects fluid flow dynamics, but not oxygen concentration in 3D-printed scaffolds for bone tissue engineering: Computational analysis and experimental validation. *Comput. Biol. Med.* 124, 103826. doi:10.1016/j.compbiomed.2020.103826

Shih, Y. R. V., Tseng, K. F., Lai, H. Y., Lin, C. H., and Lee, O. K. (2011). Matrix stiffness regulation of integrin-mediated mechanotransduction during osteogenic differentiation of human mesenchymal stem cells. *J. Bone Min. Res.* 26, 730–738. doi:10.1002/jbmr.278

Singh, B., Panda, N., Mund, R., and Pramanik, K. (2016). Carboxymethyl cellulose enables silk fibroin nanofibrous scaffold with enhanced biomimetic potential for bone tissue engineering application. *Carbohydr. Polym.* 151, 335–347. doi:10.1016/j.carbpol.2016.05.088

Sobral, J. M., Caridade, S. G., Sousa, R. A., Mano, J. F., and Reis, R. L. (2011). Three-dimensional plotted scaffolds with controlled pore size gradients: Effect of

scaffold geometry on mechanical performance and cell seeding efficiency. *Acta Biomater.* 7, 1009–1018. doi:10.1016/j.actbio.2010.11.003

Yang, D., Lü, X., Hong, Y., Xi, T., and Zhang, D. (2013). The molecular mechanism of mediation of adsorbed serum proteins to endothelial cells adhesion and growth on biomaterials. *Biomaterials* 34, 5747–5758. doi:10.1016/j.biomaterials.2013.04.028

Zamani, Y., Amoabediny, G., Mohammadi, J., Seddiqi, H., Helder, M. N., Zandieh-Doulabi, B., et al. (2020). 3D-printed poly (Ɛ-caprolactone) scaffold with gradient mechanical properties according to force distribution in the mandible for mandibular bone tissue engineering. *J. Mech. Behav. Biomed. Mat.* 104, 103638. doi:10.1016/j.jmbbm.2020.103638

Zamani, Y., Mohammadi, J., Amoabediny, G., Visscher, D. O., Helder, M. N., Zandieh-Doulabi, B., et al. (2018). Enhanced osteogenic activity by MC3T3-E1 pre-osteoblasts on chemically surface-modified poly (ε-caprolactone) 3D-printed scaffolds compared to RGD immobilized scaffolds. *Biomed. Mat.* 14, 015008. doi:10.1088/1748-605x/aaeb82

Zennifer, A., Senthilvelan, P., Sethuraman, S., and Sundaramurthi, D. (2021). Key advances of carboxymethyl cellulose in tissue engineering & 3D bioprinting applications. *Carbohydr. Polym.* 256, 117561. doi:10.1016/j.carbpol.2020.117561

Zhang, H., Han, J., Sun, Y., Huang, Y., and Zhou, M. (2015). MC3T3-E1 cell response to stainless steel 316L with different surface treatments. *Mater. Sci. Eng. C* 56, 22–29. doi:10.1016/j.msec.2015.06.017

Zreiqat, H., Valenzuela, S. M., Nissan, B. B., Roest, R., Knabe, C., Radlanski, R. J., et al. (2005). The effect of surface chemistry modification of titanium alloy on signalling pathways in human osteoblasts. *Biomaterials* 26, 7579–7586. doi:10.1016/j.biomaterials.2005.05.024

frontiers | Frontiers in Bioengineering and Biotechnology

TYPE Original Research
PUBLISHED 20 October 2022
DOI 10.3389/fbioe.2022.1011853

Check for updates

OPEN ACCESS

EDITED BY
Roman Surmenev,
Tomsk Polytechnic University, Russia

REVIEWED BY
Xin Liu,
Shanghai Jiao Tong University School of Medicine, China
Visakh P. M,
Tomsk State University of Control Systems and Radio-Electronics, Russia

*CORRESPONDENCE
Janak L. Pathak,
j.pathak@gzhmu.edu.cn
Jenneke Klein-Nulend,
j.kleinnulend@acta.nl

SPECIALTY SECTION
This article was submitted to Biomaterials, a section of the journal Frontiers in Bioengineering and Biotechnology

RECEIVED 04 August 2022
ACCEPTED 11 October 2022
PUBLISHED 20 October 2022

CITATION
Cao W, Jin J, Wu G, Bravenboer N, Helder MN, Schulten EAJM, Bacabac RG, Pathak JL and Klein-Nulend J (2022), Kappa-carrageenan-Functionalization of octacalcium phosphate-coated titanium Discs enhances pre-osteoblast behavior and osteogenic differentiation. *Front. Bioeng. Biotechnol.* 10:1011853. doi: 10.3389/fbioe.2022.1011853

COPYRIGHT
© 2022 Cao, Jin, Wu, Bravenboer, Helder, Schulten, Bacabac, Pathak and Klein-Nulend. This is an open-access article distributed under the terms of the Creative Commons Attribution License (CC BY). The use, distribution or reproduction in other forums is permitted, provided the original author(s) and the copyright owner(s) are credited and that the original publication in this journal is cited, in accordance with accepted academic practice. No use, distribution or reproduction is permitted which does not comply with these terms.

Kappa-carrageenan-Functionalization of octacalcium phosphate-coated titanium Discs enhances pre-osteoblast behavior and osteogenic differentiation

Wei Cao[1,2], Jianfeng Jin[1], Gang Wu[1], Nathalie Bravenboer[3], Marco N. Helder[2], Engelbert A. J. M. Schulten[2], Rommel G. Bacabac[4], Janak L. Pathak[5]* and Jenneke Klein-Nulend[1]*

[1]Department of Oral Cell Biology, Academic Centre for Dentistry Amsterdam (ACTA), University of Amsterdam and Vrije Universiteit Amsterdam, Amsterdam Movement Sciences, Amsterdam, Netherlands, [2]Department of Oral and Maxillofacial Surgery/Oral Pathology, Amsterdam University Medical Centers and Academic Centre for Dentistry Amsterdam (ACTA), Vrije Universiteit Amsterdam, Amsterdam Movement Sciences, Amsterdam, Netherlands, [3]Department of Clinical Chemistry, Amsterdam University Medical Centers, Vrije Universiteit Amsterdam, Amsterdam Movement Sciences, Amsterdam, Netherlands, [4]Department of Physics, Medical Biophysics Group, University of San Carlos, Cebu City, Phlilippines, [5]Guangzhou Key Laboratory of Basic and Applied Research of Oral Regenerative Medicine, Affiliated Stomatology Hospital of Guangzhou Medical University, Guangdong Engineering Research Center of Oral Restoration and Reconstruction, Guangzhou, China

Bioactive coatings are promising for improving osseointegration and the long-term success of titanium dental or orthopaedic implants. Biomimetic octacalcium phosphate (OCP) coating can be used as a carrier for osteoinductive agents. κ-Carrageenan, a highly hydrophilic and biocompatible seaweed-derived sulfated-polysaccharide, promotes pre-osteoblast activity required for bone regeneration. Whether κ-carrageenan can functionalize OCP-coating to enhance osseointegration of titanium implants is unclear. This study aimed to analyze carrageenan-functionalized biomimetic OCP-coated titanium structure, and effects of carrageenan functionalization on pre-osteoblast behavior and osteogenic differentiation. Titanium discs were coated with OCP/κ-carrageenan at 0.125–2 mg/ml OCP solution, and physicochemical and biological properties were investigated. κ-Carrageenan (2 mg/ml) in the OCP coating of titanium discs decreased the pore size in the sheet-like OCP crystal by 41.32%. None of the κ-carrageenan concentrations tested in the OCP-coating did affect hydrophilicity. However, κ-carrageenan (2 mg/ml) increased (1.26-fold) MC3T3-E1 pre-osteoblast spreading at 1 h i.e., κ-Carrageenan in the OCP-coating increased pre-osteoblast proliferation (max. 1.92-fold at 2 mg/ml, day 1), metabolic activity (max. 1.50-fold at 2 mg/ml, day 3), and alkaline phosphatase protein (max. 4.21-fold at 2 mg/ml, day 3), as well as matrix mineralization (max. 5.45-fold at 2 mg/ml, day 21). κ-Carrageenan (2 mg/ml) in the OCP-coating increased gene expression of *Mepe* (4.93-fold) at day 14, and *Runx2* (2.94-fold), *Opn* (3.59-

fold), *Fgf2* (3.47-fold), *Ocn* (3.88-fold), and *Dmp1* (4.59-fold) at day 21 in pre-osteoblasts. In conclusion, κ-carrageenan modified the morphology and microstructure of OCP-coating on titanium discs, and enhanced pre-osteoblast metabolic activity, proliferation, and osteogenic differentiation. This suggests that κ-carrageenan-functionalized OCP coating may be promising for *in vivo* improvement of titanium implant osseointegration.

KEYWORDS

bone regeneration, κ-carrageenan, implant, OCP-coating, osteogenic differentiation, osteointegration, pre-osteoblast, titanium

1 Introduction

Titanium implants are widely used in dentistry, as well as for critical-sized bone defect reconstruction in orthopaedics (Haugen and Chen, 2022). Dental or orthopaedic implant osseointegration is crucial for prolonged implant success (Haugen and Chen, 2022). Osseointegration, the direct structural and functional connection between ordered living bone and the surface of a load-carrying implant, involves the incorporation of nonvital components of the living bone leading to an efficient, reliable, and predictable anchorage mechanism (Brånemark et al., 2001). However, titanium implants lack the biological properties needed for osseointegration, such as osteoconductivity and osteoinductivity (Das et al., 2019). Compromised osseointegration might lead to implant failure, which occurs more often in systemic and local diseases, such as diabetes, periodontitis, and osteoporosis, where the inflammatory environment alters osteoblast and osteoclast function thereby impairing the bone regeneration process (Chen et al., 2013; Haugen and Chen, 2022). Titanium implant surface modification approaches ensuring implant success in patients with inflammatory diseases are still in high demand (Das et al., 2019). Moreover, cost-effective approaches to improve titanium implant surface modifications, that can be easily translated to the clinic, need to be further explored. Various physicochemical and biological strategies are already available to improve the implant's biological properties, including calcium phosphate (CaP) coating (Liu et al., 2007; Kim et al., 2017), sandblast and acid etching (Wang et al., 2020), doping silicon and copper ions into high-energy shot peening-assisted micro-arc oxidation-treated coatings (Shen et al., 2020), and plasma spray (Wang et al., 2022). Among these methods, CaP coating is the most efficient and least expensive (Kim et al., 2017). CaP coatings are hydrophilic, which improves cell attachment, proliferation, and differentiation, leading to enhanced osseointegration and success rate of dental implants (Zheng et al., 2014; Kim et al., 2017). CaP-coated implants show good biological activity and osteoconductivity, but osteoinductivity is poor (Barrère et al., 1999). To tackle this issue, the incorporation of biologically active agents, e.g. bone morphogenetic protein-2 (BMP2), in a CaP-coating on an implant surface may be used to improve implant osseointegration.

Different strategies have been developed to lay down CaP-coatings on titanium implants, such as electrostatic or plasma spraying (Siebers et al., 2004), coating *via* sol gel phase shifting (Shen et al., 2015), high-temperature sintering (Kim et al., 2017), and magnetron sputtering (Wang et al., 2020). High-temperature sintering and electrostatic approaches destroy implant biological activity (Kim et al., 2017). A biomimetic CaP coating guarantees a slow, gradual, and local release of bioactive agents (e.g., BMP2) thereby mimicking the natural release of these factors from the bone matrix under physiological conditions (Liu et al., 2018). Also, biomimetic CaP coatings are promising as drug carrier. A CaP coating on scaffolds can be achieved by first precipitating amorphous CaP (ACP), followed by octacalcium phosphate (OCP) deposition including a drug or bioactive agent of interest (Wu et al., 2010).

OCP ($Ca_8(HPO_4)_2(PO_4)_4{\cdot}5H_2O$) is one of the precursors of hydroxyapatite during bone mineralization. OCP crystals are deposited on titanium through a two-step procedure (Barrère et al., 2001). A CaP coating on scaffolds is achieved by first precipitating amorphous CaP (ACP), followed by octa-CaP deposition, including a drug or bioactive agent of interest. A prominent advantage of using such an osteogenic agent/drug-containing CaP coating is that the biological activity of the agent/drug is preserved during coprecipitation with inorganic components at physiological temperature (37°C) and pH (7.4) (Lin et al., 2020). In addition, the crystal structure of CaP formed is more akin to that of the bone mineral than of tri-/tetracalcium phosphate and hydroxyapatite, which are produced at exceedingly high temperatures (>1,000°C) (Kokubo et al., 1990). Moreover, a minimum dose of drugs or biological agents can be incorporated in CaP coating to provide sustained drug or biological agent release for weeks in a cell-mediated manner (Wu et al., 2010). BMP2 and polymers have been incorporated in CaP coating to improve the biological activity and osteoinductivity of CaP-coated implants (Fini et al., 2002; Lin et al., 2020). CaP coating with BMP2 improves implant osteoinductivity (Vehof et al., 2001). Unfortunately, the clinical use of BMP2 is very expensive (Zheng et al., 2014). Therefore, the search for alternative cost-effective bioactive agents that can be incorporated in biomimetic CaP coating on an implant surface to improve implant osseointegration is still ongoing.

κ-Carrageenan is a natural polysaccharide extracted from diverse red seaweeds with abundant sulfate groups (Du et al., 2016). κ-Carrageenan has been used widely in the food industry to gel, thicken, and stabilize food products for decades, and its safety has been recognized based on a large database of animal studies (Geonzon et al., 2019). The structure of κ-carrageenan is similar to glycosaminoglycan (GAG), which is naturally found in human bone and cartilage. κ-Carrageenan has both chondrogenic and osteogenic potential based on its chondroitin-4-sulfate and dermatan sulfate (Mokhtari et al., 2019). Therefore, κ-carrageenan is considered to be a potent factor that can induce bone regeneration. Importantly, κ-carrageenan-functionalized graphene oxide (GO) has been shown to enhance the adhesion and proliferation of MC3T3-E1 pre-osteoblasts (Liu et al., 2014). Carrageenan nanocomposite hydrogel incorporated with dimethyloxallylglycine and whitlockite nanoparticles enhances osteogenic gene expression, e.g., RUNX2, COL1α-1, and OPN (Mokhtari et al., 2019). Collagen-hydroxyapatite/κ-carrageenan (COL-HAP/κ-Car) composite has been shown to have similar structural characteristics with natural bone (Feng et al., 2017). Moreover, κ-carrageenan/silk fibroin bioactive composite scaffolds are biocompatible, and can induce precursor cell proliferation and osteogenic differentiation (Nourmohammadi et al., 2017). An ideal therapeutic agent for bone substitute functionalization should have the potential to induce cellular activities required for bone regeneration including cell migration, adhesion, spreading, proliferation, and osteogenic differentiation (Zamani et al., 2018). Earlier we found that κ-carrageenan promotes migration, adhesion, spreading, and osteogenic differentiation of MC3T3-E1 pre-osteoblasts *in vitro* (Cao et al., 2021). Therefore, κ-carrageenan could be a potent factor to improve implant osteoinductivity and osseointegration when incorporated in a CaP coating of titanium implants.

In the present study, we aimed to functionalize titanium implants by incorporating κ-carrageenan at 0.125, 0.25, 0.5, 1, and 2 mg/ml in OCP coating by depositing κ-carrageenan and OCP simultaneously layer-by-layer on a titanium surface using a biomimetic co-precipitation technique. The physicochemical properties of the OCP coating without/with κ-carrageenan were characterized. MC3T3-E1 pre-osteoblast adhesion, metabolic activity, morphology, spreading, proliferation, alkaline phosphatase (ALP) activity, matrix mineralization, and osteogenic gene expression were assessed after seeding on OCP-coated titanium discs without/with κ-carrageenan.

2 Materials and methods

2.1 κ-Carrageenan

κ-Carrageenan was kindly supplied by Tokyo Chemical Industry Co., Ltd. (Tokyo, Japan), and was prepared as described earlier (Du et al., 2016). The freeze-dried pure κ-carrageenan (100%, wt/vol) was dissolved in deionized water at 28 mg/ml (stock solution) under stirring overnight at room temperature, sterilized by heating for 2 min to 90°C, and stored at 4°C.

2.2 Octacalcium phosphate coating without/with κ-carrageenan

Titanium discs (diameter: 10 mm; height: 1 mm; Baozhong, Shanxi, China) were immersed for 24 h at 37°C in 50 ml of a solution (adjusted to pH 6.5) containing 684 mM NaCl, 12.5 mM $CaCl_2{\cdot}2H_2O$, 5 mM $Na_2HPO_4{\cdot}2H_2O$, 21 mM $NaHCO_3$, and 7.5 mM $MgCl_2{\cdot}6H_2O$. An amorphous CaP layer was achieved in the presence of 7.5 mM $MgCl_2{\cdot}6H_2O$ to inhibit crystal growth. At the end of 24 h incubation, the pH of the solution had increased from 6.5 to 8.0. Coated discs were cleaned ultrasonically in deionized water for 10 min, and air-dried overnight at ambient temperature. The thin, dense layer of amorphous CaP formed served as a seeding substratum for the deposition of another more crystalline OCP layer. OCP-coated discs without/with κ-carrageenan were prepared by immersion of the amorphous CaP-coated discs for 48 h at 37°C in 50 ml of a super-saturated solution of OCP containing 40 mM HCl, 4 mM $CaCl_2{\cdot}2H_2O$, 136 mM NaCl, and 2 mM $Na_2HPO_4{\cdot}2H_2O$ (pH 7.4), as well as 0, 0.125, 0.25, 0.5, 1, or 2 mg κ-carrageenan/ml. The concentration of κ-carrageenan in food additives is 1–3 mg/ml (Du et al., 2016). Previously we showed that κ-carrageenan (0.125–2 mg/ml) dose-dependently increases pre-osteoblast proliferation and metabolic activity, with a maximum effect at 2 mg/ml (Cao et al., 2021). κ-Carrageenan (0.5 and 2 mg/ml) increases osteogenic differentiation by enhancing alkaline phosphatase activity, matrix mineralization, and expression of osteogenic markers *Opn*, *Dmp1*, and *Mepe* (Cao et al., 2021). All chemical components in the supersaturated OCP solution used for preparing the OCP-coated titanium discs should be completely dissolved to allow the development of the CaP coating. However, κ-carrageenan at >3 mg/ml resulted in OCP precipitation in the solution (Supplementary Figure S2). Therefore we used κ-carrageenan at 2 mg/ml OCP solution as the highest concentration (Supplementary Figure S2). Titanium discs with OCP coatings without/with κ-carrageenan were air-dried overnight at ambient temperature and used for experiments.

2.3 Characterization of octacalcium phosphate coating without/with κ-carrageenan

2.3.1 Surface morphology

The surface morphology of OCP-coated discs without/with κ-carrageenan was observed by scanning electron microscopy

(SEM; S-3400N II, Hitachi, Tokyo, Japan). Discs were coated with a layer of gold using magnetron sputter (Shinkku VD, MSP-1S, Mito, Japan), and imaged using an SEM with an accelerating voltage of 15 kV.

2.3.2 Elemental composition

The elemental composition of OCP coatings without/with κ-carrageenan was evaluated with energy dispersive X-ray spectroscopy (EDX; Model 55i, IXRF, Austin, Texas, United States) analysis. Discs were assayed in triplicate.

2.3.3 Surface chemical composition and crystalline phase

Raman spectroscopy (DXR3, Thermo Fisher Scientific, Waltham, MA, United States) was used to identify functional groups, chemical interactions, and possible alteration of OCP coatings with κ-carrageenan. To identify the crystalline phases of OCP coatings without/with κ-carrageenan, X-ray diffraction (XRD) analysis was performed using an X-ray diffractometer (Empyrean, Malvern, United Kingdom). Discs were assayed in triplicate.

2.3.4 Hydrophilicity

To determine the hydrophilicity of OCP coatings without/with κ-carrageenan, the static water contact angle was measured. A video contact angle system (Sony, Tokyo, Japan) was used to capture water contact angle images. The water contact angle was determined *via* ImageJ. Discs were analyzed in triplicate.

2.4 Protein release from octacalcium phosphate coating without/with κ-carrageenan

Protein release from OCP-coated discs without/with κ-carrageenan was determined using fluorescein isothiocyanate (FITC)-bovine serum albumin (BSA). Discs were incubated for 24 h in 1 ml PBS containing 10 mg FITC-BSA for up to 7 days at 37°C. Hundred μl samples of the solution were taken at 1, 2, 12, and 24 h, as well as after 7 days. Thousand μl PBS was replaced with fresh PBS after taking each sample. Fluorescent images of the discs were made using a fluorescent microscope (Leica, Wetzlar, Germany), and fluorescence intensity was quantified using ImageJ software (https://imagej.net/Fiji.Downloads) (Jin et al., 2019). Serial dilutions of FITC-BSA in PBS were used as a standard curve. The fluorescence intensity was monitored at 485 nm (excitation) and 528 nm (emission) in a microplate reader (Synergy, BioTek™, Winooski, VT, United States).

Protein adsorption onto titanium discs with or without κ-carrageenan was performed in α-MEM containing 10% fetal calf serum (FCS, Gibco, Paisly, United Kingdom). After incubation for 1, 12, or 24 h at 37°C, the discs were transferred into a new 48-well plate (one disc per well), and washed thoroughly with PBS. Five-hundred μl 1% sodium dodecyl sulfate (SDS; Sigma, St. Louis, MO, United States) was added per well for quantification of protein adsorption. The amount of protein was determined using a BCA Protein Assay Reagent kit (Thermo Fisher Scientific, Rockford, IL, United States), and the absorbance was read at 540 nm with a microplate reader (Synergy, BioTek™, Winooski, VT, United States). (Supplementary Figure S3)

2.5 MC3T3-E1 pre-osteoblast culture and bioactivity

2.5.1 Cell culture and seeding onto octacalcium phosphate-coated discs without/with κ-carrageenan

MC3T3-E1 pre-osteoblast (American Type Culture Collection, Manassas, VA, United States) were grown and maintained in α-Minimum Essential Medium (α-MEM; Gibco, Paisly, United Kingdom), supplemented with 10% fetal bovine serum (FBS; Gibco), and 1% PSF (antibiotic antimycotic solution, Sigma-Aldrich®, St. Louis, MO, United States), in a humidified incubator with 5% CO_2 in air at 37°C. After reaching 85% confluency, cells were detached using 0.25% trypsin (Gibco) and 0.1% ethylenediaminetetraacetic acid (EDTA, Merck, Darmstadt, Germany) in phosphate buffered saline (PBS; Gibco) at 37°C. Cells were then resuspended in α-MEM with 10% FBS and antibiotics, seeded in 96, 48, or 24-well culture plates (Greiner, Bio-one, Alphen a/d Rijn, Netherlands), and cultured for different periods, from 1 h up to 21 days, dependent on the outcome parameter measured (see below).

Cell seeding was done by seeding MC3T3-E1 pre-osteoblasts (5×10^3 cells/disc (cell proliferation), 1×10^4 cells/well (cell spreading, paxillin immunofluorescence staining), 1×10^5 cells/disc (cell metabolic activity, alkaline phosphatase (ALP) activity and protein assay, alizarin red staining, and osteogenic gene expression), onto OCP-coated titanium discs without/with κ-carrageenan, which were put in 48-well culture plates (Greiner). Cell-seeded discs were incubated for 8 h in 5% CO_2 in air at 37°C to allow cell attachment. Then osteogenic medium (250 μl/well) was added, and cell-seeded discs were cultured for up to 21 days. The culture medium was changed every 2 days. Cell adhesion, metabolic activity, morphology, spreading, proliferation, ALP activity, matrix mineralization, and osteogenic gene expression were assessed as described below. Ascorbic acid (Sigma; 0.1 mg/ml) and β-glycerophosphate (phosphate donor; Sigma; 10 mM) were added to the culture medium for determination of osteogenic gene expression, ALP activity, ALP protein, and matrix mineralization.

2.5.2 Cell adhesion and spreading

MC3T3-E1 pre-osteoblasts were seeded at 1×10^4 cells/well onto OCP-coated titanium discs without/with κ-carrageenan (2 mg/ml). Discs were put into 48-well plates (Greiner; 1 disc/

TABLE 1 Primer sequences used for real-time PCR.

Target gene	Primer sequence	
Runx2	Forward	ATGCTTCATTCGCCTCAC
	Reverse	ACTGCTTGCAGCCTTAAAT
Opn	Forward	AGTGATGAAAGATGGGCAACT
	Reverse	TCTGGACCATCTTCTTGCTGA
Fgf2	Forward	GGCTTCTTCCTGCGCATCCA
	Reverse	TCCGTGACCGGTAAGTATTG
Ocn	Forward	CAGACACCATGAGGACCATCTT
	Reverse	GGTCTGATAGCTCGTCACAA
Mepe	Forward	GGAGCACTCACTACCTGAC
	Reverse	TAGGCACTGCCACCATGT
Dmp1	Forward	CGGCTGGTGGACTCTCTAAG
	Reverse	CGGGGTCGTCGCTCTGCATC
PBGD	Forward	AGTGATGAAAGATGGGCAACT
	Reverse	TCTGGACCATCTTCTTGCTGA

Runx2, Runt-related transcription factor-2; Opn, osteopontin; Fgf2, fibroblast growth factor-2; Ocn, osteocalcin; Mepe, matrix extracellular phosphoprotein; Dmp1, dentin matrix protein-1; PBGD, porphobilinogen deaminase.

well) and incubated for 1 h. After incubation, the medium was removed, discs were washed twice with PBS, and fixed in 2.5% glutaraldehyde overnight at 4°C. After washing twice with deionized water, the discs were dehydrated using graded ethanol series (50, 70, 80, 90, 100%). Then, discs were air-dried overnight with hexamethyldisilane (HMDS; Sigma) in a chemical hood, followed by coating with a layer of gold using a magnetron sputter. Discs were imaged using an SEM with an accelerating voltage of 15 kV. For determination of cell surface area, cell length, and cell width, three regions of interest (ROI), measuring 250 × 175 μm, were defined on SEM images of OCP-coated titanium discs with/without κ-carrageenan. One ROI was positioned in the center of each disc, and two ROIs were evenly spaced (200 μm) from the center of each disc in opposite directions. The total number of cells in the three ROIs ranged from 20 to 25. Cell surface area, cell length, and cell width were calculated using an Analyze Particles cell plugin in ImageJ software.

2.5.3 Paxillin immunofluorescence staining

One hour after seeding MC3T3-E1 pre-osteoblasts onto OCP-coated titanium discs without/with κ-carrageenan (2 mg/ml), cells were fixed with 4% paraformaldehyde solution for 15 min at 37°C, treated with 0.2% Triton X-100 (Sigma) for 10 min, and non-essentially bound substances were blocked in 5% BSA for 30 min. Paxillin expression was analyzed by immunofluorescence staining using rhodamine-phalloidin cytoskeleton dye (Invitrogen, Fisher Scientific, Carlsbad, CA, United States) and p-paxillin pTy31 polyclonal rabbit IgG (ab32084, Abcam, Cambridgeshire, United Kingdom). The secondary antibody used was Alexa Fluor-488 goat anti-rat IgG (Abcam). Nuclei were stained blue with 1 μg/ml DAPI (Sigma). After glycerol mounting, cell imaging was performed by laser scanning confocal microscopy (LSCM; Nikon, A1R/A1, Tokyo, Japan). Fluorescence microscopy was also used to visualize paxillin at 488 nm wavelength, and ImageJ software was used for paxillin area quantification. For paxillin area quantification, three ROIs, measuring 50 × 50 μm, of each OCP-coated titanium disc with/without κ-carrageenan, were defined on fluorescent images. One ROI was positioned in the center of each disc, and two ROIs were evenly spaced (200 μm) from the center of each disc in opposite directions. Paxillin was visualized using fluorescence microscopy at 488 nm wavelength. ImageJ software was used for paxillin area quantification. The total cell number in the three ROIs ranged from 20 to 25.

2.5.4 Cell proliferation

MC3T3-E1 pre-osteoblast proliferation was assessed by DNA content quantification. Cells were cultured onto OCP-coated titanium discs without/with κ-carrageenan at 5×10^3 cells/disc in 48-well plates (Greiner) up to 3 days. Cell lysate was collected using lysis buffer, and DNA content per well was determined with the Cyquant Cell Proliferation Assay (Molecular Probes, Eugene, OR, United States) according to the manufacturer's protocol. Fluorescence intensity was read at 485 nm (excitation) and 528 nm (emission) in a microplate reader (Synergy).

2.5.5 Cell metabolic activity

To assess cell metabolic activity, MC3T3-E1 pre-osteoblasts were seeded on OCP-coated titanium discs without/with κ-carrageenan at $1{\times}10^5$ cells/disc in 48-well plates (Greiner), and cultured up to 7 days. The medium was removed, cells were washed with PBS, and α-MEM with 10% FBS and antibiotics was added. The PrestoBlue™ Assay (Invitrogen) was used to evaluate cell metabolic activity according to the manufacturer's instructions. In short, PrestoBlue™ reagent was added to the cells (10%, vol/vol), followed by 30 min incubation in a 5% CO_2 in air incubator with a humidified atmosphere at 37°C. The medium was harvested (100 μl/well) and transferred into a 96-wells black microplate (Greiner). Fluorescence intensity was determined at a wavelength of 560 nm (excitation) and 590 nm (emission), and quantified using a Multiskan™ FC Microplate Photometer (Thermo Fisher Scientific). Prestoblue™ fluorescence was linearly associated with DNA content (data not shown).

2.5.6 Alkaline phosphatase protein, alkaline phosphatase activity, and total protein assay

To assess the osteogenic phenotype of MC3T3-E1 pre-osteoblasts, cells were seeded at $1{\times}10^5$ cells/disc coated with OCP without or with κ-carrageenan and cultured for 3 or 7 days on OCP-coated titanium discs without/with κ-carrageenan, and ALP activity and protein content determined. ALP protein on OCP-coated

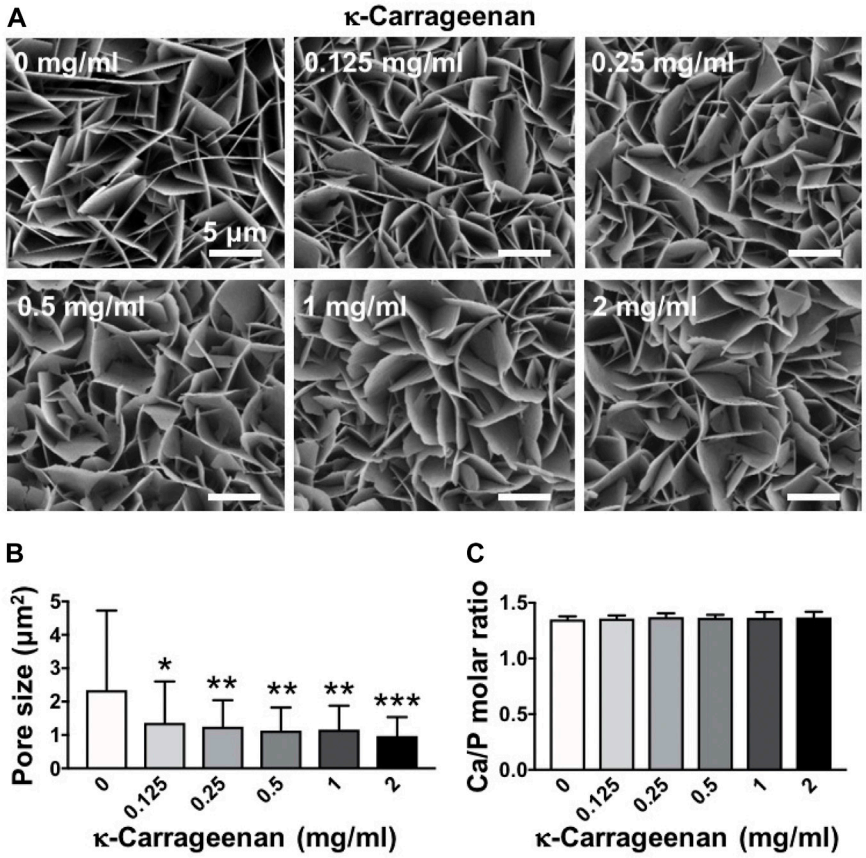

FIGURE 1
Dose-dependent effect of κ-carrageenan in octacalcium phosphate (OCP)-coating of titanium discs on surface morphology. **(A)** SEM micrographs. **(B)** Pore size. **(C)** Calcium/phosphate ratio. Values are mean ± SD. n = 9 from 3 independent experiments. Significant effect of κ-carrageenan, *$p < 0.05$, **$p < 0.01$, ***$p < 0.001$. Bar: 5 μm.

titanium discs without/with κ-carrageenan was stained at 3 and 7 days. The culture medium was removed and discs were washed 2 times with PBS, and fixed with 4% formaldehyde in PBS for 15 min at 37°C. ALP protein staining kit (Beyotime, Shanghai, China) was used for the colorimetric detection of ALP intensity, using 30 min incubation at 37°C. Optical images were taken using a stereomicroscope. Quantification of ALP protein was performed using ImageJ software. Note that the images were converted to gray scale 8. The stained ALP protein area was determined using the plugin of Analyze Particles. Three independent experiments providing 9 images of titanium discs (n = 3) were performed. To determine ALP activity, p-nitrophenyl phosphate (Merck) at pH 10.3 was used as a substrate. The absorbance was read at 405 nm in a microplate reader (Synergy). The amount of total protein was determined using a BCA Protein Assay Reagent kit (Thermo Fisher Scientific), and the absorbance was read at 540 nm with a microplate reader (Synergy). ALP activity was expressed as nmol/μg total protein.

2.5.7 Alizarin red staining and mineralized nodule quantification

Matrix mineralization was analyzed by alizarin red staining of MC3T3-E1 pre-osteoblasts seeded at 1×10^5 cells/disc coated with OCP without or with κ-carrageenan (0.5 or 2 mg/ml) and cultured for 21 days. Cells were fixed with 4% paraformaldehyde for 15 min, followed by rinsing with deionized water. Two hundred μl of 2% alizarin red solution in water, pH 4.3 (Alizarin Red S, Sigma-Aldrich, Los Angeles, CA, United States), was added per well for 30 min at room temperature. Then cells were washed with deionized water, and mineralization was quantified by dissolving the (red) mineralized matrix in 10% (vol/vol) cetylpyridinium chloride (Sigma) in 10 mM sodium phosphate solution (Sigma). Discs were de-stained for 1 h in 200 μl cetylpyridinium chloride solution on a rocking table, and the absorbance was read at 620 nm with a Multiskan FC (Thermo Fisher Scientific).

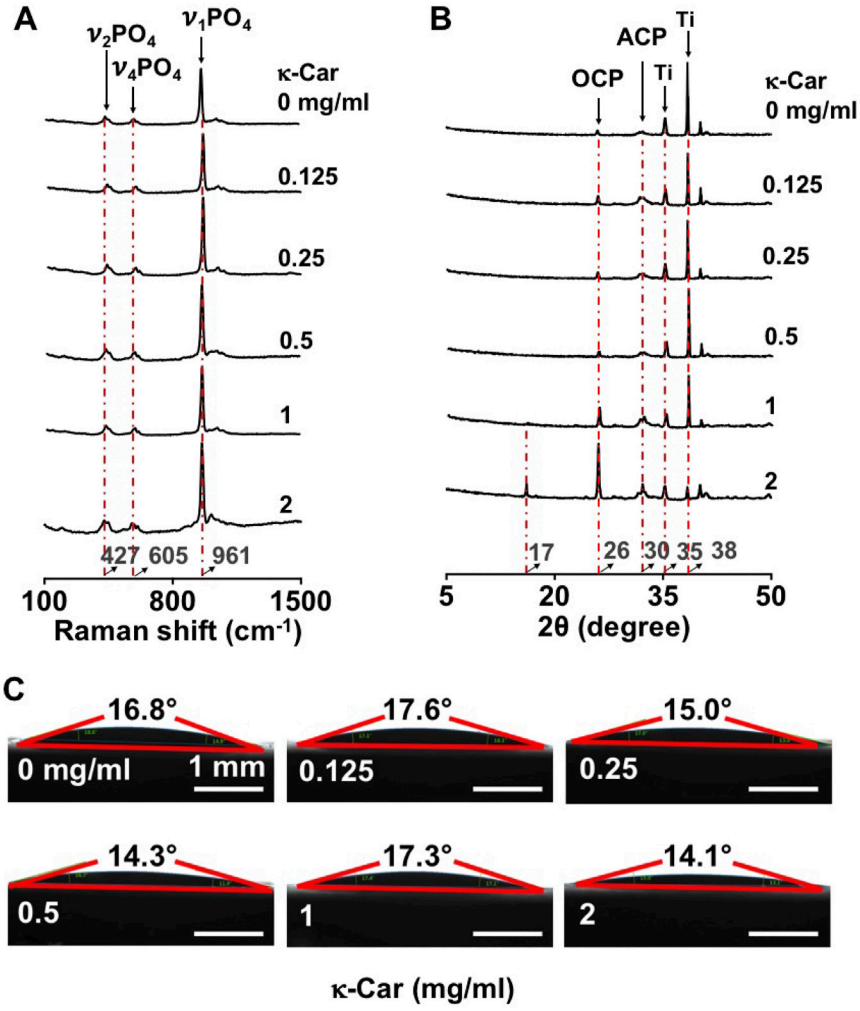

FIGURE 2
Effect of κ-carrageenan in OCP-coating of titanium discs on the crystalline phase and surface hydrophilicity of OCP-coating. **(A)** Raman spectra. **(B)** XRD spectra. **(C)** Surface hydrophilicity. κ-Car, κ-carrageenan. Bar: 1 mm.

2.5.8 Osteogenic gene expression

Total RNA was isolated from the MC3T3-E1 pre-osteoblasts seeded at 1×10^5 cells/disc coated with OCP without/with κ-carrageenan after 1, 14, and 21 days of culture using an Invitrogen RNA isolation kit (Invitrogen). cDNA synthesis was performed using 0.5–1 μg total RNA in 20 μl reaction mix consisting of 5 units Transcriptor Reverse Transcriptases (Roche Diagnostics, Basel, Switzerland), 1 mM of each dNTP (Invitrogen), 0.08 A_{260} units random primers (Roche Diagnostics), and 1x concentrated Transcriptor Reverse Transcriptase reaction buffer (Roche Diagnostics). Real-time PCR (RT-PCR) reactions were performed using the LightCycler® 480 SYBR green I Master reaction mix according to the manufacturer's instructions (Roche Diagnostics) in a Light Cycler 480 (Roche Diagnostics), and relative housekeeping gene expression (PBGD) and relative target gene expression, i.e. runt-related transcription factor 2 (*Runx2*), osteocalcin (*Ocn*), fibroblast growth factor 2 (*Fgf2*), dentin matrix protein 1 (*Dmp1*), and osteopontin (*Opn*) were determined. Primers (Invitrogen) used for RT-PCR are listed in Table 1. Values of target gene expression were normalized for *PBGD* gene expression.

2.6 Statistical analysis

Data are presented as mean ± standard deviation (SD). Data were analyzed using Graphpad Prism® 7.0 (GraphPad Software Inc., La Jolla, CA, United States). One-way analysis of variance (ANOVA) with Bonferroni's post hoc test was used to test differences between groups. A p-value <0.05 was considered statistically significant.

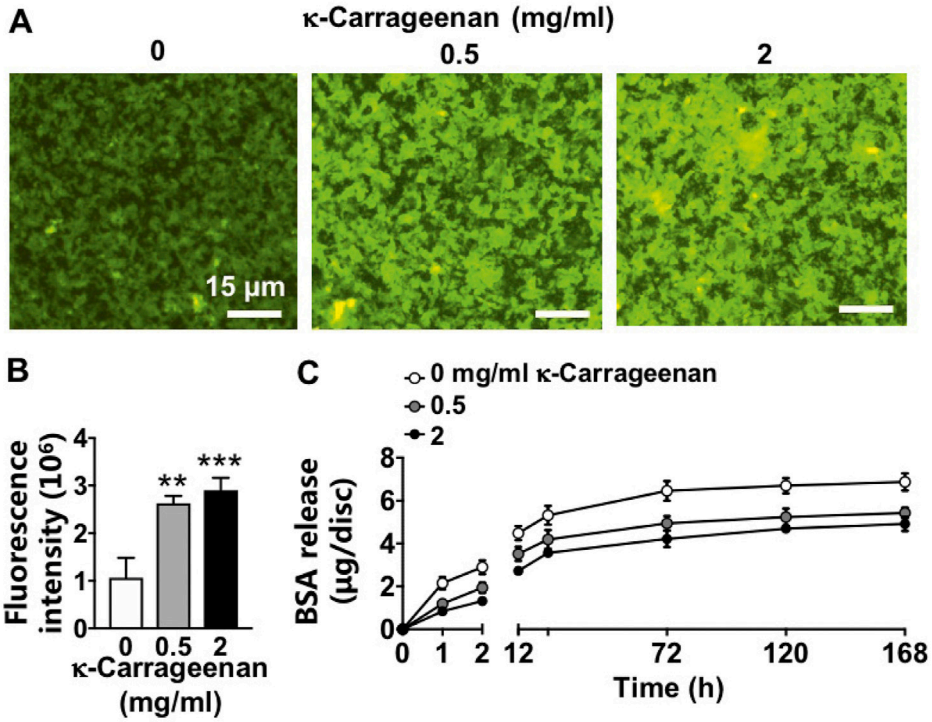

FIGURE 3
Effect of increasing κ-carrageenan concentration in OCP-coating of titanium discs on BSA release from OCP-coating up to day 7. Total amount of initial BSA incorporated per disc: 10 μg. **(A)** Fluorescent images of FITC-BSA on the surface of OCP-coating. **(B)** Quantification of fluorescence intensity on the surface of OCP-coating. **(C)** BSA release profile. Values are mean ± SD. n = 3 from 3 independent experiments. BSA, bovine serum albumin. Significant effect of κ-carrageenan, $^{**}p < 0.01$, $^{***}p < 0.001$. Bar: 15 μm.

3 Results

3.1 Surface morphology and elemental composition of octacalcium phosphate-coated titanium discs without/with κ-carrageenan

SEM images were taken to show the effect of increasing κ-carrageenan concentration (0–2 mg/ml) in OCP-coatings on surface morphology and microstructure. κ-carrageenan did affect the morphology, by changing the more straight sheet-like structure (0 mg/ml) into a more curved sheet-like structure at all concentrations tested (Figure 1A). κ-carrageenan significantly reduced the pore size in the sheet-like structure of OCP crystal by 41.32% (Figure 1B). The elemental composition of OCP-coated titanium discs without/with κ-carrageenan surface functionalization was analyzed by EDX spectroscopy. EDX spectra indicated the presence of calcium (Ca; 36.73 ± 1.44 wt%), and phosphate (P; 20.32 ± 1.08 wt%). To assess whether κ-carrageenan affects OCP crystallinity, the Ca/P ratio was calculated (Figure 1C). κ-carrageenan did not affect the Ca/P ratio of the OCP coating.

3.2 Chemical composition and hydrophilicity of octacalcium phosphate-coated titanium discs without/with κ-carrageenan

Raman spectroscopy of OCP-coated titanium discs without/with κ-carrageenan was performed to show the chemical composition of OCP, whereby the internal phosphate (PO_4^{3-}) modes were taken into consideration (Akiva et al., 2016). A strong band at 961 cm^{-1} was assigned to the totally symmetric stretching mode (ν1) of PO_4^{3-} group in OCP. Double (ν2) and triple (ν4) degenerate bending modes were observed at 427 cm^{-1} and 605 cm^{-1}. The XRD pattern of OCP-coated titanium discs without/with κ-carrageenan was also evaluated (Figure 2B). The titanium surface pattern showed a bump at 30° typical of a CaP amorphous state. The sharp peak at 26° was typical of triclinic OCP crystal. κ-Carrageenan (0.125–2 mg/ml) increased the intensity of crystallinity peaks corresponding to the crystal structure of OCP, with κ-carrageenan at 2 mg/ml showing the highest peak intensity. OCP containing κ-carrageenan at 2 mg/ml, but not at the other concentrations tested, resulted in a peak at 17° corresponding to diffraction in the OCP structure. The

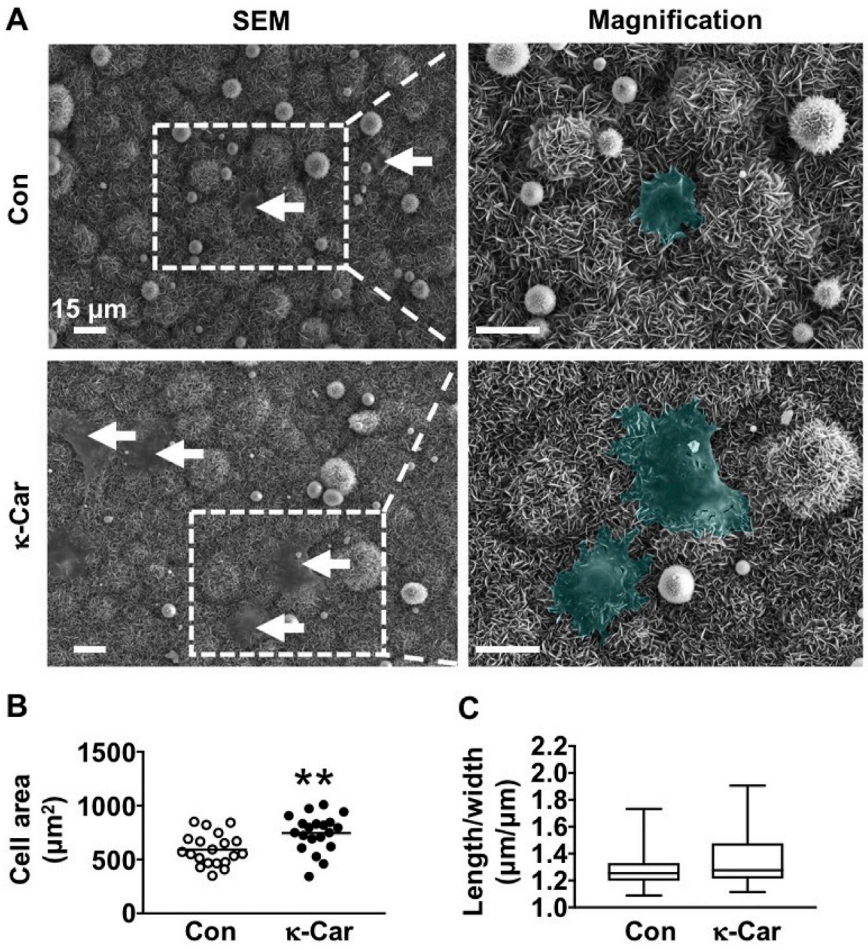

FIGURE 4
Effect of 2 mg/ml κ-carrageenan in OCP-coating of titanium discs on the spreading of MC3T3-E1 pre-osteoblasts at 1 h **(A)** SEM images of MC3T3-E1 pre-osteoblasts on OCP-coating. Arrows: cells (green). **(B)** Quantification of cell surface area. **(C)** Cell length/width ratio. Values are mean ± SD. n = 9 from 3 independent experiments. Significant effect of κ-carrageenan, $^{**}p < 0.01$. Con, control; κ-Car, κ-carrageenan; SEM, scanning electron microscopy. Bar: 15 μm. Magnification: 4×.

peaks at 35° and 38° were assigned to titanium. Water contact angle measurement revealed that the hydrophilicity of OCP-coated titanium discs without/with κ-carrageenan was similar (Figure 4C).

3.3 Protein release

FITC-BSA was incorporated in the OCP coating without/with κ-carrageenan, and BSA release kinetics were determined during 7 days (Figure 3). OCP coatings without κ-carrageenan showed less FITC-BSA (top view) compared to OCP coatings with κ-carrageenan at 0.5 mg/ml and 2 mg/ml (most FITC-BSA) after 7 days incubation (Figure 3A). Quantification of the fluorescence intensity at day 7 (Figure 3B) confirmed this observation indicating that BSA release decreased by adding κ-carrageenan to the OCP coating. The BSA release kinetics showed that the inhibition of BSA release by κ-carrageenan occurred especially during the first 2 h of incubation, with the strongest inhibition at 2 mg/ml (Figure 3C).

3.4 Pre-osteoblast spreading

SEM images revealed visual differences between MC3T3-E1 pre-osteoblasts spreading at OCP coating without and with κ-carrageenan (2 mg/ml) at 1 h after seeding (Figure 4A). κ-Carrageenan (2 mg/ml) significantly enhanced the cell surface area by 1.26-fold (Figure 4B). The cell length/width ratio remained unchanged by κ-carrageenan (Figure 4C).

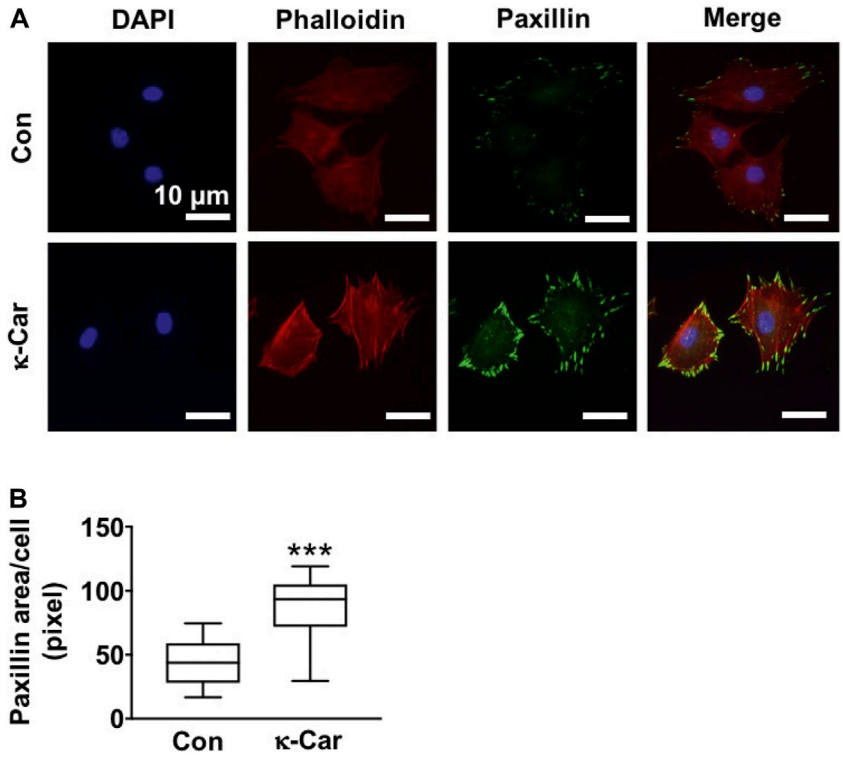

FIGURE 5
Effect of 2 mg/ml κ-carrageenan in OCP-coating of titanium discs on paxillin expression and distribution of MC3T3-E1 pre-osteoblasts at 1 h. **(A)** Cells stained for DAPI/phalloidin (blue/red) and paxillin (green). **(B)** Quantification of paxillin area in untreated control and κ-carrageenan-treated cells. Values are mean ± SD. n = 9 from 3 independent experiments. Significant effect of κ-carrageenan, ***$p < 0.001$. Con, control; κ-Car, κ-carrageenan. Bar: 10 μm.

3.5 Paxillin protein expression

Immunofluorescence staining of paxillin revealed clear clusters at the cell boundary of untreated control MC3T3-E1 pre-osteoblasts on OCP-coated titanium discs without/with κ-carrageenan (Figure 5). κ-Carrageenan (2 mg/ml) in the OCP coating resulted in more paxillin dots, resembling short rods (Figure 5A). Quantification of the area covered by paxillin dots indicated a significant (2.03-fold) increase in fluorescent paxillin area per cell after 1 h incubation (Figure 5B).

3.6 MC3T3-E1 pre-osteoblast proliferation and metabolic activity

The effect of increasing concentrations of κ-carrageenan in OCP coating on MC3T3-E1 pre-osteoblast proliferation and metabolic activity for 3 and 7 days, respectively, was determined (Figure 6). Cell proliferation as assessed by DNA content was most significantly enhanced by treatment with κ-carrageenan at 2 mg/ml from day 1–3 (maximum increase 1.92-fold, day 1) (Figure 6A). MC3T3-E1 pre-osteoblast metabolic activity was most significantly enhanced after treatment with 2 mg/ml κ-carrageenan from day 1–7 (maximum 1.50-fold increase, day 3) (Figure 6B).

3.7 Alkaline phosphatase activity and protein staining

ALP activity in MC3T3-E1 pre-osteoblasts was enhanced by κ-carrageenan at day 3 (0.5, 1, and 2 mg/ml) and day 7 (1 and 2 mg/ml), with 2 mg/ml showing the strongest effect (Figures 7A,B). At day 3, κ-carrageenan (0.5 and 2 mg/ml) also increased ALP protein by 2.85-fold (0.5 mg/ml) and 4.21-fold (2 mg/ml) (Figures 7C,D). At day 7, κ-carrageenan (2 mg/ml) increased ALP protein by 1.49-fold (Figures 7E,F).

3.8 Mineralized extracellular matrix production

OCP coating with κ-carrageenan (2 mg/ml) increased matrix mineralization in pre-osteoblasts after 21 days of culture

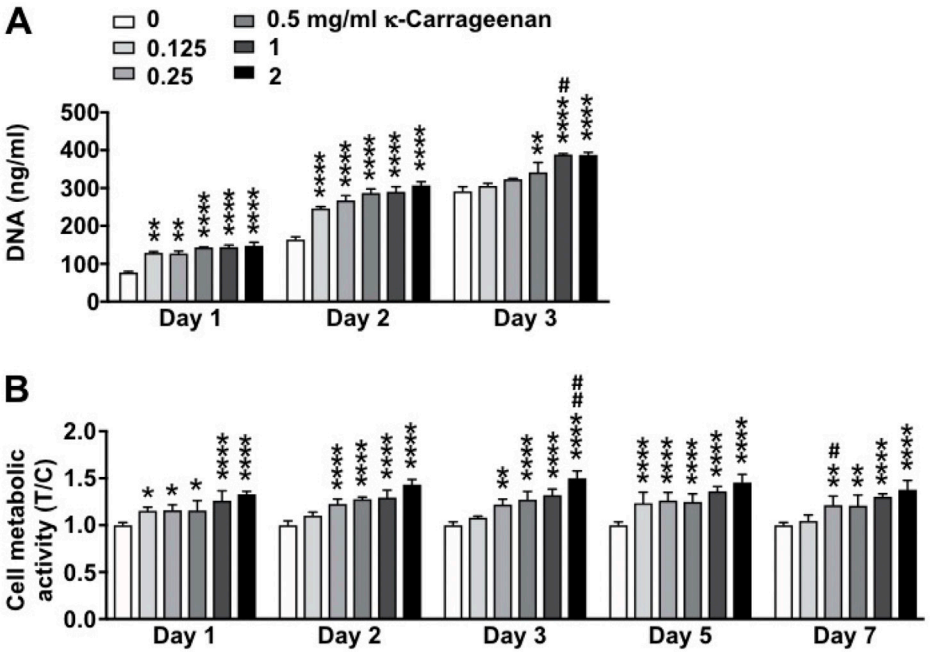

FIGURE 6
Dose-dependent effect of κ-carrageenan in OCP-coating of titanium discs on MC3T3-E1 pre-osteoblasts proliferation (day 1, 2, 3) and metabolic activity (day 1–7). **(A)** Total cellular DNA content. **(B)** Presto-blue cell metabolic activity. Data are expressed as κ-carrageenan-treated-over-control (T/C) ratio. Values are mean ± SD. $n = 3$ from 3 independent experiments. Significant effect of κ-carrageenan, $^{*}p < 0.05$, $^{**}p < 0.01$, $^{****}p < 0.0001$, $^{\#}p < 0.05$, $^{\#\#}p < 0.01$.

(Figure 8). Matrix mineralization (red) was increased by 5.45-fold, *i.e.* more intense red staining, on OCP-coated titanium discs with κ-carrageenan (Figures 8A,B).

3.9 Osteogenic gene expression

Gene expression of all osteogenic markers (*Runx2*, *Opn*, *Fgf2*, *Ocn*, *Mepe*, and *Dmp1*) was similar on OCP-coated titanium discs without/with κ-carrageenan at day 1. Gene expression of all markers was also similar at day 14, except for *Mepe* expression, which was increased (4.93-fold) in pre-osteoblasts on OCP coating with 2 mg/ml κ-carrageenan (Figure 9). OCP coating with κ-carrageenan (2 mg/ml) Increased mRNA levels of *Runx2* (2.94-fold), *Opn* (3.59-fold), *Fgf2* (3.47-fold), *OCn* (3.88-fold), and *Dmp1* (4.59-fold) compared to OCP-coated titanium discs without κ-carrageenan at day 21.

4 Discussion

This study aimed to explore whether κ-carrageenan can functionalize OCP coating on a titanium surface to enhance osseointegration of implants. We characterized κ-carrageenan-functionalized biomimetic OCP-coated titanium and tested the effect of carrageenan-functionalization on MC3T3-E1 pre-osteoblast behavior and osteogenic differentiation. We showed, for the first time, that κ-carrageenan can be co-precipitated with an OCP coating on the surface of titanium discs. κ-Carrageenan at all concentrations tested did affect the morphology of the OCP-coated titanium discs, i.e. it changed the more straight sheet-like structure of CaP into a more curved sheet-like structure. κ-Carrageenan significantly reduced the pore size in the sheet-like CaP structure. κ-Carrageenan in the OCP coating did not affect the coating's Ca/P ratio, chemical composition, or hydrophilicity. Moreover, we found that κ-carrageenan in the OCP coating increased pre-osteoblast spreading, proliferation, and metabolic activity, as well as ALP activity, matrix mineralization, and osteogenic gene expression. Thus, κ-carrageenan-functionalization of OCP-coated titanium discs enhanced pre-osteoblast behavior and osteogenic differentiation, suggesting that κ-carrageenan-functionalized OCP coating might improve osseointegration of titanium implants.

In the current study, we functionalized the OCP coating on the surface of titanium discs by coprecipitation with κ-carrageenan. CaP coatings on titanium implant surfaces have been widely investigated to integrate metallic implants with living bone (Das et al., 2019; Pazarceviren et al., 2021). OCP can be deposited onto a substratum using layer-by-layer deposition technology in a simulated *in vivo* microenvironment at 37°C

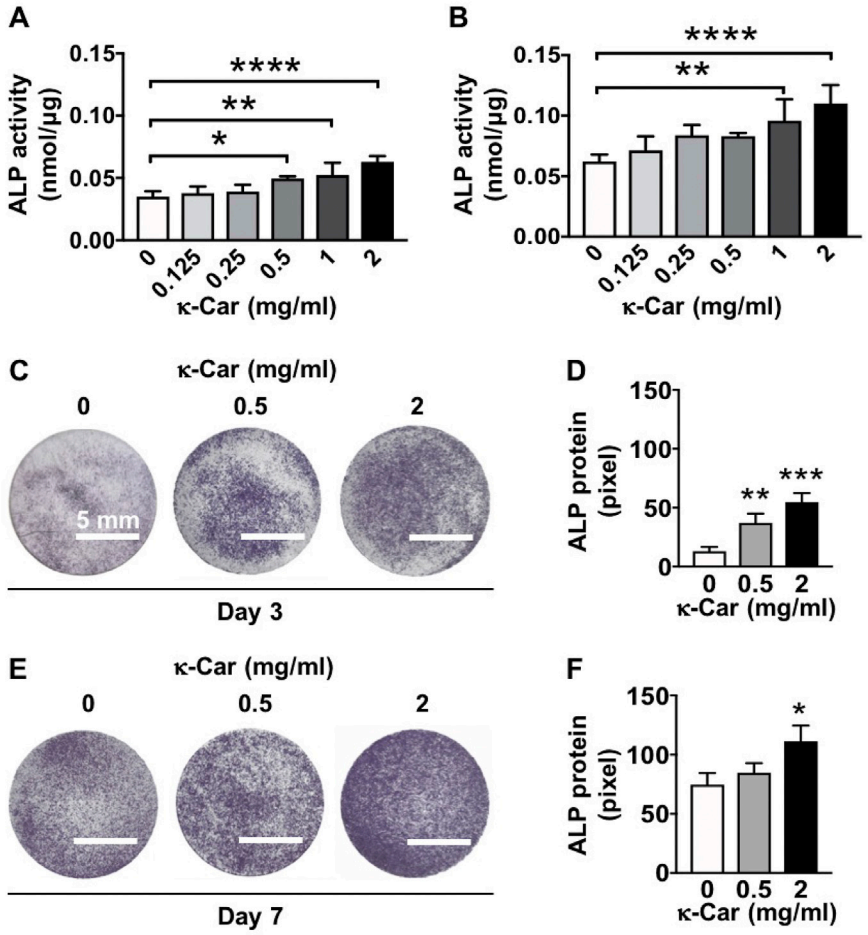

FIGURE 7
Dose-dependent effect of κ-carrageenan in OCP-coating of titanium discs on ALP activity of MC3T3-E1 pre-osteoblasts at day 3 and 7. **(A)** ALP activity at day 3. **(B)** ALP activity at day 7. **(C)** ALP protein staining at day 3. **(D)** Quantitive colorimetric results of ALP staining at day 3. **(E)** ALP protein staining at day 7. **(F)** Quantitive colorimetric results of ALP staining at day 7. Values are mean ± SD. $n = 3$ from 3 independent experiments. Significant effect of κ-carrageenan, $^{*}p < 0.05$, $^{**}p < 0.01$, $^{***}p < 0.001$, $^{****}p < 0.0001$. ALP, alkaline phosphatase; κ-Car, κ-carrageenan. Bar: 5 mm.

(Wu et al., 2010), rather than at a high temperature (>1,000°C) as needed for other types of CaP coating, e.g. hydroxyapatite or β-tricalcium phosphate (Takahashi et al., 2008). In our study, Raman spectroscopy showed three typical peaks at 427 (cm^{-}), 605 (cm^{-}), and 961 (cm^{-}) of phosphate (PO_4^{3-}) modes, the typical chemical composition of OCP. XRD showed a typical peak at 30° of amorphous CaP, as well as a typical peak at 26° of the crystal phase of OCP. These results indicate successful incorporation of κ-carrageenan in the OCP coating on a titanium surface using a biomimetic co-precipitation technique.

We found that κ-carrageenan at all concentrations tested did affect the morphology of OCP-coated titanium discs by changing the more straight sheet-like structure of CaP into a more curved sheet-like structure. Material surface morphology affects cell-material interaction (Zamani et al., 2018), as well as the response of bone tissue towards titanium implants *in vivo* (Levin et al., 2022). Moreover, κ-Carrageenan significantly reduced the pore size in the CaP sheet-like network structure, suggesting increased density of the OCP sheets, which might facilitate pre-osteoblast adhesion and spreading onto the OCP coating. Adhesion and spreading of osteoprogenitors are affected by integrin binding and focal adhesion formation (Kim et al., 2012). Paxillin, a fundamental focal adhesion-associated adapter that connects structural and signaling components, plays a major role in integrating multiple signals from the microenvironment. In the current study, the more curved OCP sheet-like structure was associated with the presence of κ-carrageenan in the coating, as well as with enhanced pre-osteoblast spreading and paxillin expression. This might indicate that κ-carrageenan in the OCP coating provides more sites for osteoblast recruitment, which might lead to enhanced bone formation, which would be beneficial for osseointegration.

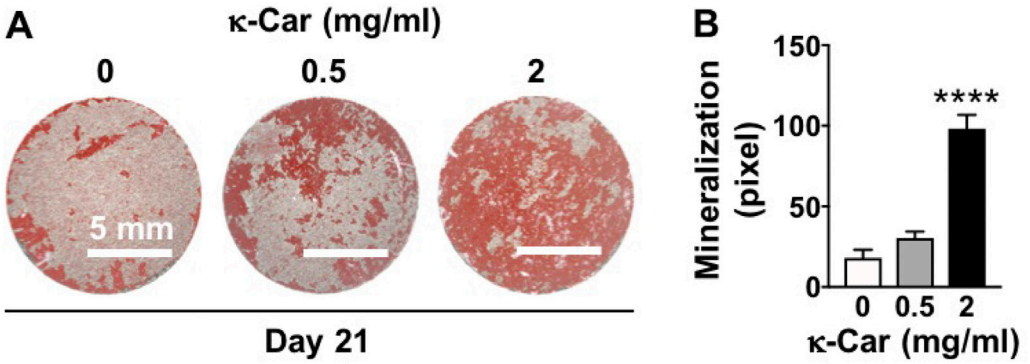

FIGURE 8
Dose-dependent effect of κ-carrageenan in OCP-coating of titanium discs on extracellular matrix mineralization in MC3T3-E1 pre-osteoblasts at day 21. **(A)** Alizarin red-stained mineralized matrix. **(B)** Quantitive colorimetric results of extracellular matrix mineralization. Values are mean ± SD. n = 3 from 3 independent experiments. Significant effect of κ-carrageenan, ****$p < 0.0001$. κ-Car, κ-carrageenan. Bar: 5 mm.

We found that κ-carrageenan did not affect the Ca/P ratio, chemical composition, or hydrophilicity of the OCP coating. The molar Ca/P ratio of CaP deposited onto titanium has been reported to vary between 1.31 and 2.05, being in the range of apatitic CaP (Nourmohammadi et al., 2017). We found an OCP Ca/P molar ratio of 1.40 ± 0.06 (mean ± SD, n = 3). This ratio resembles the reported OCP molar CaP ratio of 1.33 (Nourmohammadi et al., 2017), indicating that κ-carrageenan did not affect the chemical composition of the OCP coating, and thus can be successfully incorporated in the OCP coating. Hydrophilic surfaces tend to enhance cell adhesion, proliferation, differentiation, and bone mineralization in the early stage compared to hydrophobic surfaces (Arya & Kumar, 2020). We showed that κ-carrageenan did not affect the hydrophilicity of the coating, i.e. κ-carrageenan-functionalized OCP coating is attractive for osteoblast adhesion, and might be advantageous for osseointegration.

We found that the addition of κ-carrageenan to the OCP coating slowed down protein (BSA) release during the first 2 h of incubation, with the strongest inhibition at 2 mg/ml. This indicates that the protein release characteristics by addition of κ-carrageenan are beneficial for bone tissue engineering purposes. Biomimetic CaP-based coatings on implants can serve as a vehicle for the targeted delivery of osteogenic agents, e.g., BMP2, to the local implant environment (Liu et al., 2018). BMP2 stimulates both osteoprogenitor and osteoclast recruitment, proliferation, and differentiation. Thus, high concentrations of BMP2 released might promote the resorption of newly formed bone almost as soon as it has been laid down. Moreover, the high cost and local/systemic adverse effects of BMP2 limit its clinical application. Currently, natural polymers are widely used in the food industry, chemical engineering, and pharmaceutical applications (Caillol, 2020). These natural polymers are also used as bioactive interphases to enhance rapid, robust, and functional osseointegration between bone and implants (Caillol, 2020). One of these natural polymers is κ-carrageenan, which is naturally available in high amounts, and easy to extract (Du et al., 2016). Therefore, κ-carrageenan might be a promising factor for cost-effective clinical application. We found that κ-carrageenan slowed down the release of protein (BSA) during the early stage of release from the OCP coating. This indicates that our new OCP coating containing κ-carrageenan may be able to control the precise release rate of other osteogenic agents, e.g., BMP2, or drugs that are important for bone regeneration.

Cell adhesion, spreading, and metabolic activity are directly correlated with osseointegration and implant success (Zamani et al., 2018). Our data showed that κ-carrageenan-functionalized OCP coating on titanium discs robustly promoted pre-osteoblast spreading, as well as increased pre-osteoblast proliferation and metabolic activity, suggesting that κ-carrageenan-functionalized OCP coating is biocompatible and attractive to preosteoblasts and therefore likely to result in osseointegration and implant success. Moreover, biomimetic co-precipitation-based κ-carrageenan functionalization of OCP might also improve precursor cell spreading as well as metabolic activity, which would provide a basis for further research on the suitability of κ-carrageenan functionalization of OCP coating on dental titanium implants.

Osteogenic differentiation of attached and proliferated precursor cells into osteoblasts depositing new bone on the implant surface is another key biological process required for implant osseointegration (Zamani et al., 2018). We found that κ-carrageenan-functionalized OCP coating on titanium discs induced osteogenic differentiation of pre-osteoblasts, as indicated by the enhanced ALP activity, matrix mineralization, and osteogenic gene expression. κ-Carrageenan in the OCP coating enhanced osteogenic

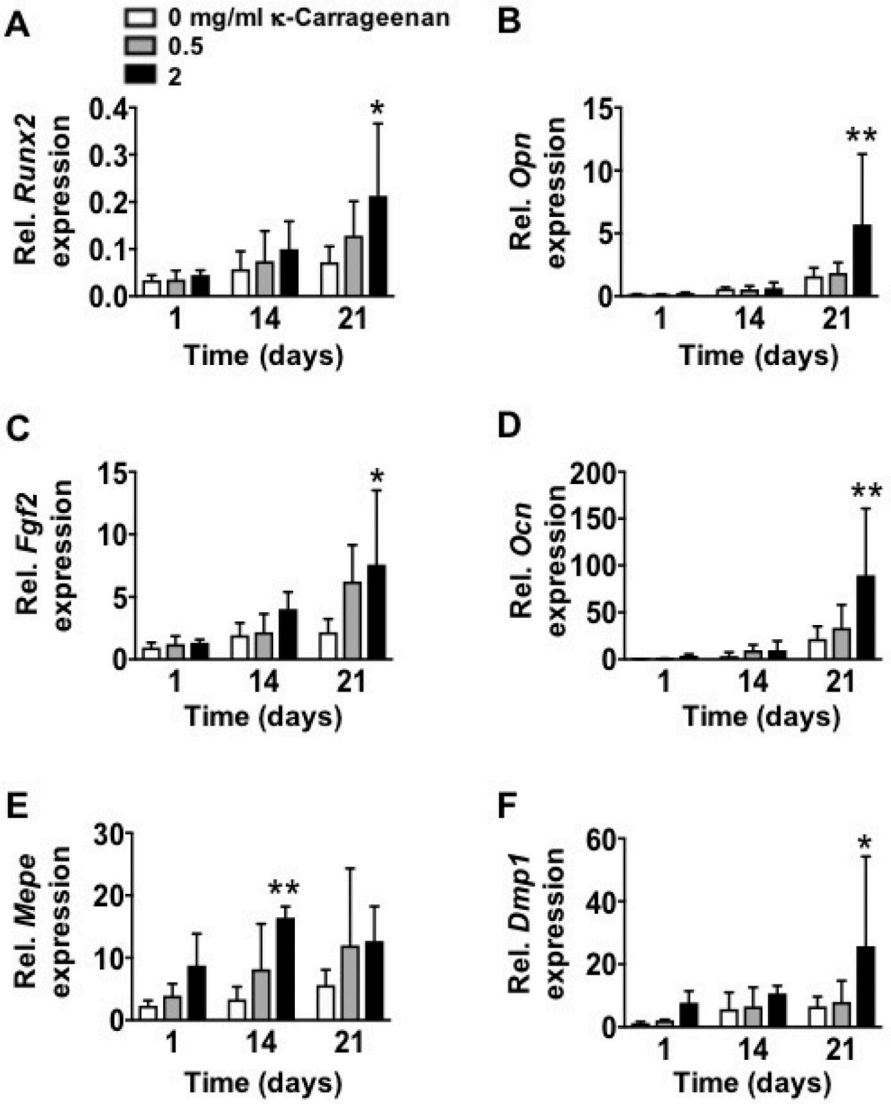

FIGURE 9
Effect of increasing κ-carrageenan concentration in OCP-coating of titanium discs on expression of osteogenic markers in MC3T3-E1 pre-osteoblasts at day 1, 14, and 21. Expression pattern of **(A)** *Runx2,* **(B)** *Opn,* **(C)** *Fgf2,* **(D)** *Ocn,* **(E)** *Mepe,* and **(F)** *Dmp1*. Values are mean ± SD. $n = 3$ from 3 independent experiments. Significant effect of κ-carrageenan, $^{*}p < 0.05$, $^{**}p < 0.01$. *Runx2*, Runt-related transcription factor-2; *Opn*, osteopontin; *Fgf2*, fibroblast growth factor-2; *Ocn*, osteocalcin; *Dmp1*, dentin matrix protein-1; *Mepe*, matrix extracellular phosphoprotein.

gene expression (*Mepe, Runx2*, *Opn*, *Fgf2*, *Ocn*, and *Dmp1)* in the long-term (14–21 days). *Runx2* is a key transcription factor associated with bone-related cell differentiation. In the cell cycle, *Runx2* plays a vital cell proliferation regulatory role in osteoblasts (Lucero et al., 2013). We found that κ-carrageenan in the OCP coating increased *Runx2* mRNA expression, which might be due to the effect of ascorbic acid and β-glycerophosphate in the osteogenic medium taken up by pre-osteoblasts after seeding on OCP coating containing κ-carrageenan at 21 days. *Opn* has an crucial role in endocrine-regulated and neuron-mediated bone mass, but is also involved in adhesion, proliferation, and migration of different bone cells (Vancea et al., 2021). *Ocn* has a significant role in the regulation of bone metabolism, and is secreted only by osteoblasts (Lee et al., 2007). *Fgf2* affects gene expression in osteoblasts in a biphasic fashion, depending on the osteoblast maturation stage (Pitaru et al., 1993). *Ocn* is involved in calcium ion homeostasis and bone mineralization, as is *Fgf2* (Globus et al., 1989). *Dmp1* is a non-collagenous extracellular matrix mineralization protein found in dentin and bone, similar as bone sialoprotein and *Opn*, which combines ligand N-linked glycoprotein family, and is part of the small integrin-binding ligand (Fisher et al., 2004). These osteogenic genes (*Opn, Ocn, Fgf2, and Dmp1*) are well related to extracellular

matrix mineralization in the long term. We found that κ-carrageenan enhanced expression of these osteogenic genes at 21 days. *Mepe* has a multifunctional role in the regulation of cell signaling, mineral homeostasis, and mineralization (Chrepa et al., 2017). In this study, κ-carrageenan did affect *Mepe* gene expression at 14 days, but not at 21 days, suggesting that κ-carrageenan affects *Mepe* expression only in the short term. *Mepe* belongs to the small integrin-binding ligands and influences the adhesion and differentiation of cells from the osteoblast cell lineage leading to increased bone formation (Sprowson et al., 2008). Therefore, the increased *Mepe* expression might be related to the improved cell spreading on the OCP coating containing κ-carrageenan. ALP activity and matrix mineralization are important for bone regeneration (Moghaddaszadeh et al., 2021). We found that κ-carrageenan in the OCP coating enhanced ALP activity and ALP protein in the short term (3, 7 days), as well as enhanced matrix mineralization in the long term (21 days) in pre-osteoblasts, suggesting stimulation of bone formation. κ-Carrageenan has already been shown to have chondrogenic, soft tissue, and osteogenic regenerative potential (Nourmohammadi et al., 2017; Gonzalez Ocampo et al., 2019; Mokhtari et al., 2019). κ-Carrageenan with gelatin, and sericin hydrogel composites improve cell viability of cryopreserved Saos-2 cells (Ashe et al., 2020). Moreover, we have shown earlier that exogenously added κ-carrageenan promotes migration, adhesion, spreading, and osteogenic differentiation of MC3T3-E1 preosteoblasts *in vitro* (Cao et al., 2021). These findings indicate that κ-carrageenan-functionalization of OCP-coated titanium surface results in implant osteoinductivity, thereby improving osseointegration.

In this study, we successfully incorporated κ-carrageenan in the OCP coating on a titanium surface using a biomimetic co-precipitation technique. We found that κ-carrageenan in the OCP coating increased pre-osteoblast spreading, proliferation, and metabolic activity, as well as ALP activity, matrix mineralization, and osteogenic gene expression suggesting that κ-carrageenan-functionalized OCP coating might improve osseointegration of titanium dental or orthopaedic implants. We found a positive effect of κ-carrageenan in OCP-coating on most pre-osteoblast activities. This is likely due to the fact that κ-carrageenan contains abundant sulfate groups, which mimic the charged proteins present in the extracellular matrix and ensures the practicality of κ-carrageenan for bone tissue engineering. This fits earlier literature findings that the structural similarity between κ-carrageenan and glycosaminoglycans improves osteoblast adhesion and proliferation (Gonzalez Ocampo et al., 2019). However, the exact molecular mechanisms for bone regeneration need further investigation. An ideal coating of a medical implant is biocompatible, osteoconductive, osteoinductive, and has optimal stiffness. During implantation, the surgical procedure may destroy the surface topography of the coating. Future studies will test the stiffness, thickness, and stability of the coating, and address the underlying mechanism of κ-carrageenan-increased MC3T3-E1 cell spreading, proliferation, and osteogenic differentiation. Recent advances in the field of cell-based therapeutics provide new perspectives for oral tissue regeneration. The development of large animal models, which overcome the limitations of rodent models and allow to emulate clinical situations, is crucial for the validation of regenerative strategies to move toward clinical application (Mangione et al., 2022). Canine models are successfully used in all oral tissue regeneration, notably implantology studies (Uijlenbroek et al., 2022). The findings of this study will be further verified using a canine mandibular peri-implant bone defect healing model.

5 Conclusion

In this study, we successfully incorporated κ-carrageenan in the OCP coating on a titanium surface using a biomimetic co-precipitation technique. κ-Carrageenan in OCP coating on titanium discs modified the morphology and microstructure of the OCP-coating, and enhanced pre-osteoblast metabolic activity, proliferation, and osteogenic differentiation. These findings suggest that κ-carrageenan-functionalized OCP coating may be promising, especially in the short term, for *in vivo* improvement of titanium dental and orthopaedic implant osseointegration.

Data availability statement

The original contributions presented in the study are included in the article/Supplementary Material, further inquiries can be directed to the corresponding authors.

Author contributions

Conceptualization, WC, GW, JK-N; Formal analysis, WC, JJ; Funding acquisition, WC, JP, JK-N; Investigation, WC, JJ; Supervision GW, NB, MH, ES, JP, JK-N; Writing-original draft preparation WC, JP, JK-N; Writing-review and editing, JJ, GW, NB, MH, ES, RB, JP, JK-N. All authors have read and agreed to the published version of the manuscript.

Funding

This work was granted by the China Scholarship Council (CSC, no. 201808440487). This work was also granted by Health-Holland (project no. LSHM19016, “BB”). Moreover, this work was granted by Guangzhou Municipal Science and Technology Project (no. 202201020236). RB was funded by DOST project no. 09438 (monitored by DOST-PCIEERD) and received logistic support from the USC-RDEPO and Department of Physics. JP was funded by the National Natural Science Foundation of China (no. 82150410451).

Conflict of interest

The authors declare that the research was conducted in the absence of any commercial or financial relationships that could be construed as a potential conflict of interest.

Publisher's note

All claims expressed in this article are solely those of the authors and do not necessarily represent those of their affiliated organizations, or those of the publisher, the editors and the reviewers. Any product that may be evaluated in this article, or claim that may be made by its manufacturer, is not guaranteed or endorsed by the publisher.

Supplementary material

The Supplementary Material for this article can be found online at: https://www.frontiersin.org/articles/10.3389/fbioe.2022.1011853/full#supplementary-material

References

Akiva, A., Kerschnitzki, M., Pinkas, I., Wagermaier, W., Yaniv, K., Fratzl, P., et al. (2016). Mineral formation in the larval zebrafish tail bone occurs via an acidic disordered calcium phosphate phase. *J. Am. Chem. Soc.* 138, 14481–14487. doi:10.1021/jacs.6b09442

Arya, G., and Kumar, V. (2020). Evaluation of osseintegration between traditional and modified hydrophilic titanium dental implants-Systematic analysis. *Natl. J. Maxillofac. Surg.* 11, 176–181. doi:10.4103/njms.njms_44_20

Ashe, S., Behera, S., Dash, P., Nayak, D., and Nayak, B. (2020). Gelatin carrageenan sericin hydrogel composites improves cell viability of cryopreserved SaOS-2 cells. *Int. J. Biol. Macromol.* 154, 606–620. doi:10.1016/j.ijbiomac.2020.03.039

Barrère, F., Layrolle, P., Van Blitterswijk, C. A., and De Groot, K. (2001). Biomimetic coatings on titanium: A crystal growth study of octacalcium phosphate. *J. Mat. Sci. Mat. Med.* 12, 529–534. doi:10.1023/a:1011271713758

Brånemark, R., Brånemark, P. I., Rydevik, B., and Myers, R. R. (2001). Osseointegration in skeletal reconstruction and rehabilitation: A review. *J. Rehabil. Res. Dev.* 38, 175–181.

Caillol, S. (2020). Special issue "natural polymers and biopolymers II. *Molecules* 26, 112. doi:10.3390/molecules26010112

Cao, W., Jin, J., Wu, G., Bravenboer, N., Helder, M. N., Pathak, J. L., et al. (2021). K-carrageenan stimulates pre-osteoblast proliferation and osteogenic differentiation: A potential factor for the promotion of bone regeneration? *Molecules* 26, 6131. doi:10.3390/molecules26206131

Chrepa, V., Austah, O., and Diogenes, A. (2017). Evaluation of a commercially available hyaluronic acid hydrogel (restylane) as injectable scaffold for dental pulp regeneration: An *in vitro* evaluation. *J. Endod.* 43, 257–262. doi:10.1016/j.joen.2016.10.026

Das, S., Dholam, K., Gurav, S., Bendale, K., Ingle, A., Mohanty, B., et al. (2019). Accentuated osseointegration in osteogenic nanofibrous coated titanium implants. *Sci. Rep.* 9, 17638. doi:10.1038/s41598-019-53884-x

Du, L., Brenner, T., Xie, J., and Matsukawa, S. (2016). A study on phase separation behavior in kappa/iota carrageenan mixtures by micro DSC, rheological measurements and simulating water and cations migration between phases. *Food Hydrocoll.* 55, 81–88. doi:10.1016/j.foodhyd.2015.11.004

Feng, W., Feng, S., Tang, K., He, X., Jing, A., and Liang, G. (2017). A novel composite of collagen-hydroxyapatite/kappa-carrageenan. *J. Alloys Compd.* 693, 482–489. doi:10.1016/j.jallcom.2016.09.234

Fini, M., Giavaresi, G., Aldini, N. N., Torricelli, P., Botter, R., Beruto, D., et al. (2002). A bone substitute composed of polymethylmethacrylate and α-tricalcium phosphate: Results in terms of osteoblast function and bone tissue formation. *Biomaterials* 23, 4523–4531. doi:10.1016/s0142-9612(02)00196-5

Fisher, L. W., Jain, A., Tayback, M., and Fedarko, N. S. (2004). Small integrin binding ligand **N** -linked glycoprotein gene family expression in different cancers. *Clin. Cancer Res.* 10, 8501–8511. doi:10.1158/1078-0432.ccr-04-1072

Geonzon, L. C., Bacabac, R. G., and Matsukawa, S. (2019). Network structure and gelation mechanism of kappa and iota carrageenan elucidated by multiple particle tracking. *Food Hydrocoll.* 92, 173–180. doi:10.1016/j.foodhyd.2019.01.062

Globus, R. K., Plouet, J., and Gospodarowicz, D. (1989). Cultured bovine bone cells synthesize basic fibroblast growth factor and store it in their extracellular matrix. *Endocrinology* 124, 1539–1547. doi:10.1210/endo-124-3-1539

Gonzalez Ocampo, J. I., Machado de Paula, M. M., Bassous, N. J., Lobo, A. O., Ossa Orozco, C. P., and Webster, T. J. (2019). Osteoblast responses to injectable bone substitutes of kappa-carrageenan and nano hydroxyapatite. *Acta Biomater.* 83, 425–434. doi:10.1016/j.actbio.2018.10.023

Haugen, H. J., and Chen, H. (2022). Is there a better biomaterial for dental implants than titanium?-a review and meta-study analysis. *J. Funct. Biomater.* 13, 46. doi:10.3390/jfb13020046

Jin, J., Fei, D., Zhang, Y., and Wang, Q. (2019). <p>Functionalized titanium implant in regulating bacteria and cell response</p>. *Int. J. Nanomedicine* 14, 1433–1450. doi:10.2147/ijn.s193176

Kim, H. D., Amirthalingam, S., Kim, S. L., Lee, S. S., Rangasamy, J., and Hwang, N. S. (2017). Bone tissue engineering: Biomimetic materials and fabrication approaches for bone tissue engineering (adv. Healthcare mater. 23/2017). *Adv. Healthc. Mat.* 6 (23), 1770120. doi:10.1002/adhm.201770120

Kim, M. C., Kim, C., Wood, L., Neal, D., Kamm, R. D., and Asada, H. H. (2012). Integrating focal adhesion dynamics, cytoskeleton remodeling, and actin motor activity for predicting cell migration on 3D curved surfaces of the extracellular matrix. *Integr. Biol. (Camb.)* 4, 1386–1397. doi:10.1039/c2ib20159c

Kokubo, T., Ito, S., Huang, Z. T., Hayashi, T., Sakka, S., Kitsugi, T., et al. (1990). Ca, P-rich layer formed on high-strength bioactive glass-ceramic A-W. *J. Biomed. Mat. Res.* 24, 331–343. doi:10.1002/jbm.820240306

Lee, N. K., Sowa, H., Hinoi, E., Ferron, M., Ahn, J. D., Confavreux, C., et al. (2007). Endocrine regulation of energy metabolism by the skeleton. *Cell* 130, 456–469. doi:10.1016/j.cell.2007.05.047

Levin, M., Spiro, R. C., Jain, H., and Falk, M. M. (2022). Effects of titanium implant surface topology on bone cell attachment and proliferation *in vitro*. *Med. Devices (Auckl.)* 15, 103–119. doi:10.2147/mder.s360297

Lin, X., Chen, J., Liao, Y., Pathak, J. L., Li, H., and Liu, Y. (2020). Biomimetic calcium phosphate coating as a drug delivery vehicle for bone tissue engineering: A mini-review. *Coatings* 10, 1118–1119. doi:10.3390/coatings10111118

Liu, H., Cheng, J., Chen, F., Hou, F., Bai, D., Xi, P., et al. (2014). Biomimetic and cell-mediated mineralization of hydroxyapatite by carrageenan functionalized graphene oxide. *ACS Appl. Mat. Interfaces* 6, 3132–3140. doi:10.1021/am4057826

Liu, Y., Enggist, L., Kuffer, A. F., Buser, D., and Hunziker, E. B. (2007). The influence of BMP-2 and its mode of delivery on the osteoconductivity of implant surfaces during the early phase of osseointegration. *Biomaterials* 28, 2677–2686. doi:10.1016/j.biomaterials.2007.02.003

Liu, Y., Schouten, C., Boerman, O., Wu, G., Jansen, J. A., and Hunziker, E. B. (2018). The kinetics and mechanism of bone morphogenetic protein 2 release from calcium phosphate-based implant-coatings. *J. Biomed. Mat. Res. A* 106, 2363–2371. doi:10.1002/jbm.a.36398

Lucero, C. M., Vega, O. A., Osorio, M. M., Tapia, J. C., Antonelli, M., Stein, G. S., et al. (2013). The cancer-related transcription factor Runx2 modulates cell proliferation in human osteosarcoma cell lines. *J. Cell. Physiol.* 228, 714–723. doi:10.1002/jcp.24218

Mangione, F., Salmon, B., EzEldeen, M., Jacobs, R., Chaussain, C., and Vital, S. (2022). Characteristics of large animal models for current cell-based oral tissue regeneration. *Tissue Eng. Part B Rev.* 28, 489–505. doi:10.1089/ten.teb.2020.0384

Moghaddaszadeh, A., Seddiqi, H., Najmoddin, N., Abbasi Ravasjani, S., and Klein-Nulend, J. (2021). Biomimetic 3D-printed PCL scaffold containing a high concentration carbonated-nanohydroxyapatite with immobilized-collagen for bone

tissue engineering: Enhanced bioactivity and physicomechanical characteristics. *Biomed. Mat.* 16 (6), 065029. doi:10.1088/1748-605x/ac3147

Mokhtari, H., Kharaziha, M., Karimzadeh, F., and Tavakoli, S. (2019). An injectable mechanically robust hydrogel of kappa-carrageenan-dopamine functionalized graphene oxide for promoting cell growth. *Carbohydr. Polym.* 214, 234–249. doi:10.1016/j.carbpol.2019.03.030

Nourmohammadi, J., Roshanfar, F., Farokhi, M., and Haghbin Nazarpak, M. (2017). Silk fibroin/kappa-carrageenan composite scaffolds with enhanced biomimetic mineralization for bone regeneration applications. *Mater. Sci. Eng. C* 76, 951–958. doi:10.1016/j.msec.2017.03.166

Pazarceviren, A. E., Tezcaner, A., and Evis, Z. (2021). Multifunctional natural polymer-based metallic implant surface modifications. *Biointerphases* 16, 020803. doi:10.1116/6.0000876

Pitaru, S., Kotev-Emeth, S., Noff, D., Kaffuler, S., and Savion, N. (1993). Effect of basic fibroblast growth factor on the growth and differentiation of adult stromal bone marrow cells: Enhanced development of mineralized bone-like tissue in culture. *J. Bone Min. Res.* 8, 919–929. doi:10.1002/jbmr.5650080804

Shen, S., Cai, S., Xu, G., Zhao, H., Niu, S., and Zhang, R. (2015). Influence of heat treatment on bond strength and corrosion resistance of sol-gel derived bioglass-ceramic coatings on magnesium alloy. *J. Mech. Behav. Biomed. Mat.* 45, 166–174. doi:10.1016/j.jmbbm.2015.02.005

Shen, X., Hu, W., Ping, L., Liu, C., Yao, L., Deng, Z., et al. (2020). Antibacterial and osteogenic functionalization of titanium with silicon/copper-doped high-energy shot peening-assisted micro-arc oxidation technique. *Front. Bioeng. Biotechnol.* 8, 573464. doi:10.3389/fbioe.2020.573464

Siebers, M. C., Walboomers, X. F., Leeuwenburgh, S. C., Wolke, J. G., and Jansen, J. A. (2004). Electrostatic spray deposition (ESD) of calcium phosphate coatings, an *in vitro* study with osteoblast-like cells. *Biomaterials* 25, 2019–2027. doi:10.1016/j.biomaterials.2003.08.050

Sprowson, A. P., McCaskie, A. W., and Birch, M. A. (2008). ASARM-truncated Mepe and AC-100 enhance osteogenesis by promoting osteoprogenitor adhesion. *J. Orthop. Res.* 26, 1256–1262. doi:10.1002/jor.20606

Takahashi, K., van den Beucken, J. J., Wolke, J. G., Hayakawa, T., Nishiyama, N., and Jansen, J. A. (2008). Characterization and *in vitro* evaluation of biphasic calcium pyrophosphate-tricalciumphosphate radio frequency magnetron sputter coatings. *J. Biomed. Mat. Res. A* 84, 682–690. doi:10.1002/jbm.a.31341

Uijlenbroek, H. J. J., Lin, X., Liu, T., Zheng, Y., Wismeijer, D., and Liu, Y. (2022). Bone morphogenetic protein-2 incorporated calcium phosphate graft promotes peri-implant bone defect healing in dogs: A pilot study. *Clin. Exp. Dent. Res.* doi:10.1002/cre2.613

Vancea, A., Serban, O., and Fodor, D. (2021). Relationship between osteopontin and bone mineral density. *Acta Endocrinol. (Copenh).* 17, 509–516. doi:10.4183/aeb.2021.509

Vehof, J. W., Mahmood, J., Takita, H., van't Hof, M. A., Kuboki, Y., Spauwen, P. H., et al. (2001). Ectopic bone formation in titanium mesh loaded with bone morphogenetic protein and coated with calcium phosphate. *Plastic Reconstr. Surg.* 108, 434–443. doi:10.1097/00006534-200108000-00024

Wang, L. N., Meng, Y. F., Feng, Y., Wang, H. C., Mao, L. B., Yu, S. H., et al. (2022). Amorphous precursor-mediated calcium phosphate coatings with tunable microstructures for customized bone implants. *Adv. Healthc. Mat.* 11, e2201248. doi:10.1002/adhm.202201248

Wang, L., Wang, W., Zhao, H., Liu, Y., Liu, J., and Bai, N. (2020). Bioactive effects of low-temperature argon-oxygen plasma on a titanium implant surface. *ACS Omega* 5, 3996–4003. doi:10.1021/acsomega.9b03504

Wu, G., Liu, Y., Iizuka, T., and Hunziker, E. B. (2010). Biomimetic coating of organic polymers with a protein-functionalized layer of calcium phosphate: The surface properties of the carrier influence neither the coating characteristics nor the incorporation mechanism or release kinetics of the protein. *Tissue Eng. Part C. Methods* 16, 1255–1265. doi:10.1089/ten.tec.2009.0588

Zamani, Y., Mohammadi, J., Amoabediny, G., Visscher, D. O., Helder, M. N., Zandieh-Doulabi, B., et al. (2018). Enhanced osteogenic activity by MC3T3-E1 pre-osteoblasts on chemically surface-modified poly(ε-caprolactone) 3D-printed scaffolds compared to RGD immobilized scaffolds. *Biomed. Mat.* 14, 015008. doi:10.1088/1748-605x/aaeb82

Zheng, Y., Wu, G., Liu, T., Liu, Y., Wismeijer, D., and Liu, Y. (2014). A novel BMP2-coprecipitated, layer-by-layer assembled biomimetic calcium phosphate particle: A biodegradable and highly efficient osteoinducer. *Clin. Implant Dent. Relat. Res.* 16, 643–654. doi:10.1111/cid.12050

Frontiers in
Bioengineering and Biotechnology

Accelerates the development of therapies, devices, and technologies to improve our lives

A multidisciplinary journal that accelerates the development of biological therapies, devices, processes and technologies to improve our lives by bridging the gap between discoveries and their application.

Discover the latest Research Topics

See more →

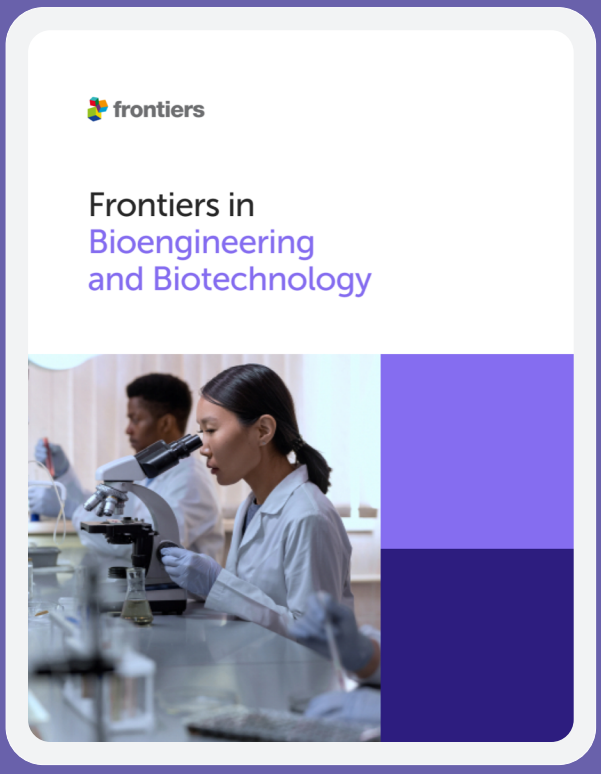

Frontiers

Avenue du Tribunal-Fédéral 34
1005 Lausanne, Switzerland
frontiersin.org

Contact us

+41 (0)21 510 17 00
frontiersin.org/about/contact